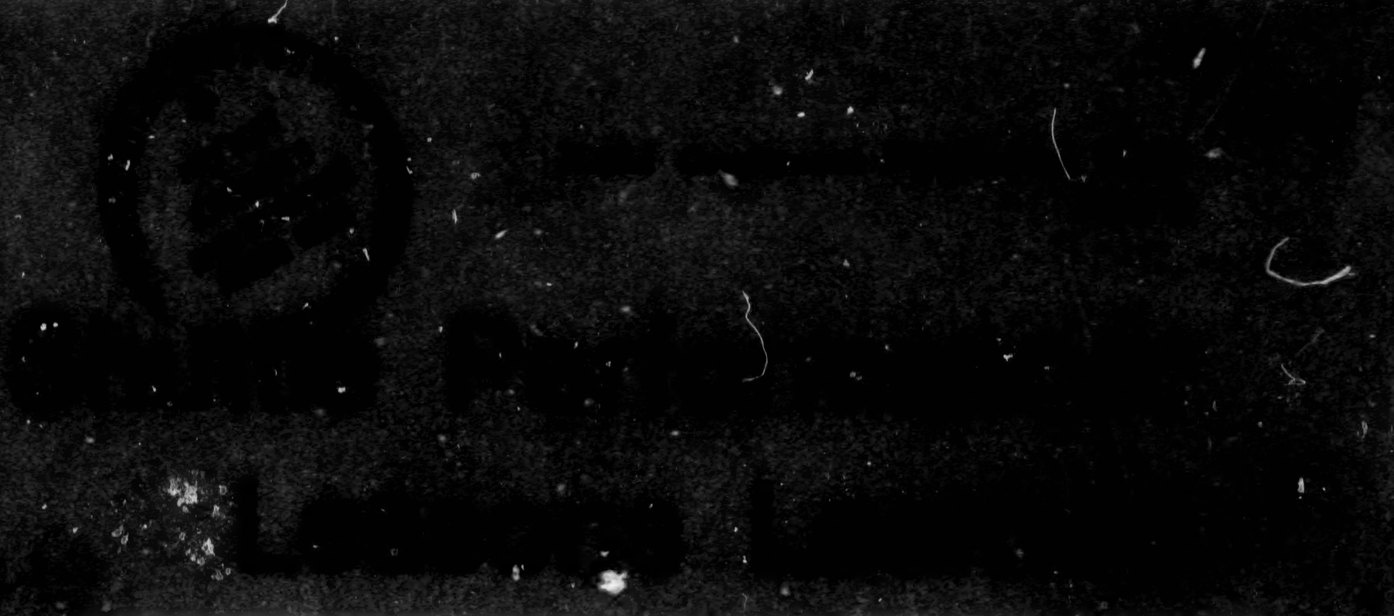

(NASA-CP-2283-Pt-2) SHUTTLE PERFORMANCE: N84-10144
LESSONS LEARNED, PART 2 (NASA) 746 p THRU
HC A99/MF A01 CSCL 22B N84-10170
Unclas
G3/16 44295

NASA Conference Publication 2283
Part 2

Shuttle Performance: Lessons Learned

Compiled by
James P. Arrington and Jim J. Jones
NASA Langley Research Center
Hampton, Virginia

Proceedings of a conference held at
NASA Langley Research Center
Hampton, Virginia
March 8-10, 1983

NASA
National Aeronautics
and Space Administration

Scientific and Technical
Information Branch

1983

PREFACE

Beginning with the first orbital flight of the Space Shuttle, a great wealth of flight data became available to the aerospace community. These data were immediately subjected to analyses by several different groups with different viewpoints and motivations.

The contractors, represented primarily by the prime contractor, Rockwell International, were concerned with verifying subsystems and correcting any deficiencies to make the vehicle operational. Having spent a decade or more in vehicle design and testing, the contractors were anxious to assess the quality of their product.

The contractors' counterparts within the NASA organization and its Project Office had a similar investment, and NASA immediately began to assess the measured performance of the vehicle against the wind tunnel data base and previous predictions. The primary motivation, in most cases, was the necessity to certify the vehicle for operational status.

Researchers at several NASA centers and elsewhere in the organization were anxious to reduce and analyze the data. They regarded the Shuttle as though it were a research vehicle, and the cornucopia of data from the Orbital Flight Test program was viewed as a magnificent opportunity to assess the state of the art in predicting the performance of a complex configuration throughout the speed range from entry to touchdown. Through the Orbiter Experiments Program, the researchers proposed and developed several instruments and experiments to supplement the basic developmental flight instrumentation. In some cases, the researchers were successful in having these instruments and experiments installed during the OFT flights.

The Air Force was also intensely interested in evaluating the flight data and independently assessed the Shuttle to ensure that it met their needs. Future launches from the Western Test Range will require greater crossrange than Kennedy-launched missions. Therefore, the Air Force was anxious to assess these first flights and their implications for higher crossrange on future entries.

Frequent telephone conferences were held during the Orbiter Flight Test program among representatives of each of the participating groups. Aerodynamics and the aerothermal performance were principal disciplines represented, and a general picture began to emerge in these areas. The vehicle's overall performance was well predicted in the design phase, but a number of discrepancies existed which warranted further investigation.

Although some of the results of these flight data analyses began to appear in AIAA conferences, papers in these conferences were usually intermixed with other papers and thus failed to give an overview of the vehicle's performance. Further, only a fraction of the interested parties described earlier were present to hear and discuss these papers.

We, at Langley, believed that it was an appropriate time to have a general convocation devoted to the interpretation of the Shuttle data and that this meeting would help provide a mechanism to collect and to distribute the results in a single publication. The conference was held at Langley on March 8-10, 1983, a little over 3 months after STS-5. Papers were solicited in the subject areas of ascent and entry

PRECEDING PAGE BLANK NOT FILMED

aerodynamics; guidance, navigation, and control; aerothermal environment prediction; thermal protection systems; and measurement techniques.

These volumes contain not only the contributed papers but also the invited papers by Mr. Robert Hoey of the Air Force Flight Test Center at Edwards Air Force Base, Major Steven Nagel of the Astronaut Office at Johnson Space Center, and Dr. Milton Silveira of NASA Headquarters. We have also included a few other papers that were not given orally but that contribute to the overall understanding of Shuttle performance.

The use of trade names or names of manufacturers in this report does not constitute an official endorsement of such products or manufacturers, either expressed or implied, by the National Aeronautics and Space Administration.

CONTENTS

PREFACE iii

Part 1*

ASCENT AERODYNAMICS I

Chairpersons: Tru E. Surber, Rockwell International
William I. Scallion, NASA Langley Research Center

PLUME BASE FLOW SIMULATION TECHNOLOGY 1
Barney B. Roberts, Rodney O. Wallace, and Joseph L. Sims

LAUNCH VEHICLE AERODYNAMIC DATA BASE DEVELOPMENT COMPARISON WITH FLIGHT DATA 19
J. T. Hamilton, R. O. Wallace, and C. C. Dill

SPACE SHUTTLE LAUNCH VEHICLE AERODYNAMIC UNCERTAINTIES: LESSONS LEARNED 37
J. T. Hamilton

LAUNCH VEHICLE AERODYNAMIC FLIGHT TEST RESULTS 41
L. M. Gaines, W. L. Osborn, and P. D. Wiltse

AERODYNAMIC ANALYSIS OF THE LOFT ANOMALY OBSERVED ON ORBITAL FLIGHT TESTS OF THE SPACE SHUTTLE 59
T. E. Surber and J. S. Stone

TECHNIQUES FOR ASSESSMENT OF ASCENT AERODYNAMIC CHARACTERISTICS OF THE SPACE SHUTTLE LAUNCH SYSTEM 79
Kenneth S. Leahy

ASCENT AERODYNAMICS II

Chairpersons: Barney B. Roberts, NASA Johnson Space Center
C. L. W. Edwards, NASA Langley Research Center

SUPERSONIC LOADS DUE TO SHUTTLE-ORBITER/EXTERNAL-TANK ATTACHMENT STRUCTURES 95
C. L. W. Edwards, P. J. Bobbitt, and W. J. Monta

SHUTTLE BOOSTER SEPARATION AERODYNAMICS 139
Mark K. Craig and Henry S. Dresser

SHUTTLE LAUNCH DEBRIS -- SOURCES, CONSEQUENCES, SOLUTIONS 159
Mark K. Craig

ASCENT AIR DATA SYSTEM RESULTS FROM THE SPACE SHUTTLE FLIGHT TEST PROGRAM 187
Ernest R. Hillje and Raymond L. Nelson

---

*Part 1 is presented under separate cover.

SPACE SHUTTLE ORBITER VENTING - LESSONS LEARNED.............................. 231
H. S. Lutfi and Raymond L. Nieder

DEVELOPMENT OF SPACE SHUTTLE IGNITION OVERPRESSURE ENVIRONMENT AND CORRELATION WITH FLIGHT DATA.. 259
S. Lai

ENTRY AERODYNAMICS I

Chairpersons: James C. Young, NASA Johnson Space Center
Bernard Spencer, Jr., NASA Langley Research Center

SPACE SHUTTLE ENTRY LONGITUDINAL AERODYNAMIC COMPARISONS OF FLIGHTS 1-4 WITH PREFLIGHT PREDICTIONS....................................... 283
Paul O. Romere and A. Miles Whitnah

A REVIEW OF PREFLIGHT ESTIMATES OF REAL-GAS EFFECTS ON SPACE SHUTTLE AERODYNAMIC CHARACTERISTICS.. 309
W. C. Woods, J. P. Arrington, and H. H. Hamilton II

EXPLANATION OF THE HYPERSONIC LONGITUDINAL STABILITY PROBLEM - LESSONS LEARNED.. 347
B. J. Griffith, J. R. Maus, and J. T. Best

SPACE SHUTTLE ORBITER REACTION CONTROL SUBSYSTEM FLIGHT DATA ANOMALIES.. 381
J. S. Stone, J. J. Baumbach, and B. B. Roberts

ANALYSIS OF SHUTTLE OSCILLATION IN THE MACH NUMBER = 1.7 TO MACH NUMBER = 1.0 RANGE.. 397
William T. Suit, Harold R. Compton, William I. Scallion,
James R. Schiess, and L. Sue Gahan

APPROACH TO ESTABLISHING THE EFFECT OF AEROELASTICITY ON AERODYNAMIC CHARACTERISTICS OF THE SPACE SHUTTLE ORBITER................................ 413
D. C. Schlosser and D. F. Dominik

ENTRY AERODYNAMICS II

Chairpersons: Donald C. Schlosser, Rockwell International
George M. Ware, NASA Langley Research Center

MINIMUM TESTING OF THE SPACE SHUTTLE ORBITER FOR STABILITY AND CONTROL DERIVATIVES... 447
Douglas R. Cooke

STABILITY AND CONTROL OVER THE SUPERSONIC AND HYPERSONIC SPEED RANGE.. 473
Harold R. Compton, James R. Schiess, William T. Suit,
William I. Scallion, and JoAnn W. Hudgins

PREDICTED AND FLIGHT TEST RESULTS OF THE PERFORMANCE, STABILITY AND CONTROL OF THE SPACE SHUTTLE FROM REENTRY TO LANDING....................... 509
Paul W. Kirsten, David F. Richardson, and Charles M. Wilson

LATERAL-DIRECTIONAL STABILITY INVESTIGATION OF THE SPACE SHUTTLE ORBITER AT MACH 6.. 525
Robert L. Calloway

AERODYNAMIC COEFFICIENT IDENTIFICATION PACKAGE DYNAMIC DATA ACCURACY DETERMINATIONS - LESSONS LEARNED.................................. 549
Michael L. Heck, John T. Findlay, and Harold R. Compton

REMOTELY DRIVEN MODEL CONTROL SURFACES FOR EFFICIENT WIND-TUNNEL OPERATIONS.. 573
George M. Ware, Bernard Spencer, Jr., and L. Raymond Gentry

GUIDANCE, NAVIGATION, AND CONTROL

Chairpersons: Kenneth J. Cox, NASA Johnson Space Center
Howard W. Stone, Jr., NASA Langley Research Center

SHUTTLE ASCENT GN&C POSTFLIGHT RESULTS... 581
Gene McSwain

THE APPLICATION OF AERODYNAMIC UNCERTAINTIES IN THE DESIGN OF THE ENTRY TRAJECTORY AND FLIGHT CONTROL SYSTEM OF THE SPACE SHUTTLE ORBITER.......... 595
Joe D. Gamble

SPACE SHUTTLE DESCENT FLIGHT CONTROL DESIGN REQUIREMENTS AND EXPERIMENTS... 617
G. Kafer and D. Wilson

USE OF NONLINEAR DAMPERS TO SUPPRESS SPACE SHUTTLE PAYLOAD MODES............. 629
Clint C. Browning and Gordon E. Hunter

APPROACH AND LANDING CHARACTERISTICS OF THE SPACE SHUTTLE ORBITER............ 637
Cynthia A. Bourne and Paul W. Kirsten

Part 2

AEROTHERMAL ENVIRONMENT I

Chairpersons: Dorothy B. Lee, NASA Johnson Space Center
David A. Throckmorton, NASA Langley Research Center

CALCULATION OF SHUTTLE BASE HEATING ENVIRONMENTS AND COMPARISON WITH FLIGHT DATA.. 653
Terry F. Greenwood, Young C. Lee, Robert L. Bender, and Robert E. Carter

TRENDS IN SHUTTLE ENTRY HEATING FROM THE CORRELATION OF FLIGHT TEST MANEUVERS.......... 687
James K. Hodge

FLIGHT TEST DERIVED HEATING MATH MODELS FOR CRITICAL LOCATIONS ON THE ORBITER DURING REENTRY.......... 703
Elam K. Hertzler and Paul W. Phillips

ORBITER ENTRY HEATING LESSONS LEARNED FROM DEVELOPMENT FLIGHT TEST PROGRAM.......... 719
J. W. Haney

SHUTTLE ORBITER BOUNDARY LAYER TRANSITION AT FLIGHT AND WIND TUNNEL CONDITIONS.......... 753
Winston D. Goodrich, Stephen M. Derry, and John J. Bertin

ORBITER WINDWARD SURFACE ENTRY HEATING: POST-ORBITAL FLIGHT TEST PROGRAM UPDATE.......... 781
M. H. Harthun, C. B. Blumer, and B. A. Miller

AEROTHERMAL ENVIRONMENT II

Chairpersons: John J. Bertin, University of Texas at Austin
E. Vincent Zoby, NASA Langley Research Center

VISCOUS SHOCK-LAYER PREDICTIONS OF THREE-DIMENSIONAL NONEQUILIBRIUM FLOWS PAST THE SPACE SHUTTLE AT HIGH ANGLE OF ATTACK.......... 805
M. D. Kim, S. Swaminathan, and Clark H. Lewis

CATALYTIC SURFACE EFFECTS ON SPACE SHUTTLE THERMAL PROTECTION SYSTEM DURING EARTH ENTRY OF FLIGHTS STS-2 THROUGH STS-5.......... 827
David A. Stewart, John V. Rakich, and Martin J. Lanfranco

ORBITER CATALYTIC/NONCATALYTIC HEAT TRANSFER AS EVIDENCED BY HEATING TO CONTAMINATED SURFACES ON STS-2 AND STS-3.......... 847
David A. Throckmorton, E. Vincent Zoby, and H. Harris Hamilton II

A REVIEW OF NONEQUILIBRIUM EFFECTS AND SURFACE CATALYSIS ON SHUTTLE HEATING.......... 865
Carl D. Scott

FILLER BAR HEATING DUE TO STEPPED TILES IN THE SHUTTLE ORBITER THERMAL PROTECTION SYSTEM.......... 891
D. H. Petley, D. M. Smith, C. L. W. Edwards, A. B. Patten, and H. H. Hamilton II

LEEWARD CENTERLINE AND SIDE FUSELAGE ENTRY HEATING PREDICTIONS FOR THE SPACE SHUTTLE ORBITER.......... 913
Vernon T. Helms III

THERMAL PROTECTION

Chairpersons: Howard E. Goldstein, NASA Ames Research Center
Richard E. Snyder, NASA Langley Research Center

SPACE SHUTTLE ORBITER REUSABLE SURFACE INSULATION FLIGHT RESULTS............. 949
Robert L. Dotts, James A. Smith, and Donald J. Tillian

LESSONS LEARNED FROM THE DEVELOPMENT AND MANUFACTURE OF CERAMIC REUSABLE SURFACE INSULATION MATERIALS FOR THE SPACE SHUTTLE ORBITERS................ 967
Ronald P. Banas, Donald R. Elgin, Edward R. Cordia, Kenneth N. Nickel, Edward R. Gzowski, and Lawrence Aguilar

LIFE CONSIDERATIONS OF THE SHUTTLE ORBITER DENSIFIED-TILE THERMAL PROTECTION SYSTEM.. 1009
Paul A. Cooper and James Wayne Sawyer

SHUTTLE TPS THERMAL PERFORMANCE AND ANALYSIS METHODOLOGY..................... 1025
W. E. Neuenschwander, D. U. McBride, and G. A. Armour

SPACE SHUTTLE ORBITER LEADING-EDGE FLIGHT PERFORMANCE COMPARED TO DESIGN GOALS.. 1065
Donald M. Curry, David W. Johnson, and Robert E. Kelly

SPACE SHUTTLE WING LEADING EDGE HEATING ENVIRONMENT PREDICTION DERIVED FROM DEVELOPMENT FLIGHT DATA.................................. 1083
John A. Cunningham and Joseph W. Haney, Jr.

MEASUREMENTS AND ANALYSIS

Chairpersons: Ernest R. Hillje, NASA Johnson Space Center
Harold R. Compton, NASA Langley Research Center

SUBSONIC LONGITUDINAL PERFORMANCE COEFFICIENT EXTRACTION FROM SHUTTLE FLIGHT DATA -- AN ACCURACY ASSESSMENT FOR DETERMINATION OF DATA BASE UPDATES...... 1111
John T. Findlay, G. Mel Kelly, Judy G. McConnell, Harold R. Compton

THE DEVELOPMENT OF AERODYNAMIC UNCERTAINTIES FOR THE SPACE SHUTTLE ORBITER.. 1169
James C. Young and Jimmy M. Underwood

THE CALIBRATION AND FLIGHT TEST PERFORMANCE OF THE SPACE SHUTTLE ORBITER AIR DATA SYSTEM... 1187
Alden S. Dean and Arthur L. Mena

COMPILING THE SPACE SHUTTLE WIND TUNNEL DATA BASE: AN EXERCISE IN TECHNICAL AND MANAGERIAL INNOVATIONS.................................. 1213
N. Dale Kemp

SHUTTLE FLIGHT PRESSURE INSTRUMENTATION: EXPERIENCE AND LESSONS FOR THE FUTURE.. 1255
P. M. Siemers III, P. F. Bradley, H. Wolf, P. F. Flanagan, K. J. Weilmuenster, and F. A. Kern

A COMPARISON OF MEASURED AND THEORETICAL PREDICTIONS FOR STS ASCENT AND ENTRY SONIC BOOMS.. 1277
Frank Garcia, Jr., Jess H. Jones, and Herbert R. Henderson

SUMMARY SESSION

Chairpersons: James P. Arrington, NASA Langley Research Center
Jim J. Jones, NASA Langley Research Center

SUMMARY SESSION: INTRODUCTION.. 1301

AFFTC OVERVIEW OF ORBITER-REENTRY FLIGHT-TEST RESULTS........................ 1303
Robert G. Hoey

FLYING THE ORBITER IN THE APPROACH/LANDING PHASE............................. 1317
Steven R. Nagel

THE BEGINNING OF A NEW AERODYNAMIC RESEARCH PROGRAM.......................... 1331
Milton A. Silveira

ASCENT AERODYNAMICS I & II... 1335
Tru E. Surber and Barney B. Roberts

ENTRY AERODYNAMICS I & II.. 1337
James C. Young and Donald C. Schlosser

GUIDANCE, NAVIGATION, AND CONTROL.. 1339
Kenneth J. Cox

AEROTHERMAL ENVIRONMENT I.. 1343
Dorothy B. Lee

AEROTHERMAL ENVIRONMENT II... 1345
E. Vincent Zoby

THERMAL PROTECTION... 1347
Howard E. Goldstein

MEASUREMENTS AND ANALYSIS.. 1349
Ernest R. Hillje

APPENDIX A: AEROELASTIC CHARACTERISTICS OF THE SPACE SHUTTLE EXTERNAL TANK CABLE TRAYS.. 1351
L. E. Ericsson and J. P. Reding

APPENDIX B: SHUTTLE CARRIER AERODYNAMICS.................................... 1371
Albert H. Eldridge

APPENDIX C: SPACE SHUTTLE THIRD FLIGHT (STS-3) ENTRY RCS ANALYSIS........... 1393
W. I. Scallion, H. R. Compton, W. T. Suit, R. W. Powell, T. A. Blackstock, and B. L. Bates

N84
10145

UNCLAS

N84 10145

CALCULATION OF SHUTTLE BASE HEATING ENVIRONMENTS AND COMPARISON WITH FLIGHT DATA

Terry F. Greenwood and Young C. Lee
NASA Marshall Space Flight Center
Marshall Space Flight Center, Alabama

Robert L. Bender
REMTECH, Incorporated
Huntsville, Alabama

Robert E. Carter
Lockheed Missiles and Space Company
Huntsville, Alabama

SUMMARY

The techniques, analytical tools, and experimental programs used initially to generate and later to improve and validate the Shuttle base heating design environments are discussed in this paper. In general, the measured base heating environments for STS-1 through STS-5 were in good agreement with the preflight predictions. However, some changes were made in the methodology after reviewing the flight data. This paper describes the flight data, compares preflight predictions with the flight data, and discusses improvements in the prediction methodology based on the data.

INTRODUCTION

The Space Shuttle base heating environment is a combination of SSME and SRM plume radiation, freestream air convective cooling, and reversed plume flow convective heating. Each base region component receives differing levels of radiation and convective heating depending upon its location relative to the plumes, base gas absorption, structural blockage, general base configuration, and local surface temperature. The radiation environment varies with the plume shape, and the incident radiation to any base location depends upon the emission/absorption and afterburning characteristics of each contribution plume and by the magnitude of attenuation of the base region gases. Convective cooling affects hot base surfaces during initial first-stage flight as cool freestream air is drawn through the base by the aspirating action of the plumes. At higher altitudes when the plumes become highly expanded and interact, hot gases from the SSME and SRM nozzle boundary layers are reversed into the base with resultant base convective heating to most base surfaces.

The Shuttle base configuration during 1st- and 2nd-stage ascent is shown in Figure 1. Those surfaces closest to the plumes - the SRB skirt trailing edge, the body flap trailing edge, and the SSME aft hat bands - receive the highest levels of radiation, approximately 16 Btu/ft^{2}sec at liftoff. Convective heating is most intense in the center heat shield region of the orbiter and in the upper center of the ET dome where levels of heating of 8 Btu/ft^{2}sec were measured at approximately 100,000 ft altitude. A spike in heating occurs during the last few seconds of SRM shutdown, producing an increase in radiation and convection well above nominal levels. Peak total heating during this period can exceed 25 Btu/ft^{2}sec at some locations.

A typical heating environment history at the center of the LH_2 tank aft dome is shown in Figure 2. Photographs of the plumes at several altitudes encompassing the full spectrum of base heating variations are presented in Figures 3 through 6. The thermal environment for the first 70 to 80 seconds of flight is dominated by SRM radiation. For the first 30 seconds, the plume radiation to the base surface is attenuated by base region outgassing. Beyond 30 seconds, radiation increases to near sea-level magnitudes followed by a gradual decrease until about 90 seconds (70,000 feet). Note also that convective cooling of the ET base occurs during the first 70 seconds of first-stage flight. Above 90 seconds, the plumes begin to strongly interact and recirculate hot gases with the peak convective effect occurring at about 75% SRM thrust and 100 seconds (100,000 feet). The SRM shutdown spike, noted at 128 seconds (166,000 feet), is visible in the plume photograph shown in Figure 6.

A more detailed look at the effect of the various flight events on the base heating environment can be seen in Figure 7. The environment shown in Figure 7 was measured in the center of the orbiter heat shield. This location was selected because it experiences heating throughout ascent and is sensitive to the various engine operational variations. As seen in this figure, the radiation environment early in flight is not significantly influenced by ignition, the roll maneuver, and throttling down to 65% thrust for max q. Radiation levels are reduced with altitude since plume gas temperatures decrease at a rate faster than the view factor of the expanding plume boundary increases. Freestream air convective cooling reduces total base heating until the plume boundaries intersect and recirculate rocket exhaust gasses toward the base at approximately 70 seconds. Convective heating, shown as the shaded areas in Figure 7, is dramatically affected by SRM thrust tailoff. If tailoff did not occur after 100 seconds, convective heating would continue to increase with increasing altitude during 1st-stage flight. Both radiation and convection increase during SRM shutdown, but the predominant effect at this base location is a dramatic increase in radiation. Both radiation and convection are constant during the high-altitude steady SSME performance period of 2nd-stage flight. Convection declines sharply when the SSMEs throttle down to 3g after 450 seconds. All base heating to the orbiter heat shield becomes negligible after main engine cut-off (MECO).

PREFLIGHT METHODOLOGY

Because of its extended reuse capability and flyback operational capability, the Shuttle thermal protection system (TPS) must be adequate but not grossly overdesigned. Any excess weight designed into the system because of an overdesigned TPS directly impacts payload capability and operating costs. Therefore, an extensive effort to accurately predict the ascent base heating environment was undertaken early in the Shuttle program. A paper[1] documenting the preflight Shuttle base heating methodology was presented at the JANNAF 10th Plume Technology Meeting. Important features of the preflight methodology are summarized in the following paragraphs. Radiation and convective heating components of the total environment prediction utilize different methods and are computed independently.

Radiation

SRM - The sea-level SRM plume radiation math model was originally based on experimental data taken on the Titan IIIC solid motors[2], geometrically scaled to the SRM size as shown in Figure 8(a). This sea-level model was subsequently updated based on ground tests of the SRM. In January 1977 (DM-1) and February 1978 (DM-2) the SRM was statically fired at the Thiokol Test Range in Utah (5000 ft elevation). Narrow-view-angle radiometer data were obtained along the plume centerline from the exit plane of the nozzle on DM-2. On both tests, wide-angle radiometer data were obtained at positions that simulated locations on the Shuttle vehicle. From these data, a new sea-level plume emissive power radiation model was developed.[3] This model consisted of a 12° cone-cylinder shape with the emissive power (E) changing along the centerline as shown in Figure 8(b).

Subsequent testing of the SRM at the Thiokol Utah Test Range (QM-2 and QM-3 in October 1979 and February 1980) provided narrow-view-angle radiometer measurements near the nozzle exit plane slightly higher than measurements taken on DM-1 and DM-2. Updating the emissive power of the first four plume segments of the SRM math model to values of $E = 70$, 59, 57, and 53 Btu/ft^{2}sec resulted in the plume model shown in Figure 8(c)[4] and a better correlation of the measured and predicted QM-2 and QM-3 heating rates. A comparison of the SRM plume radiation heating rates to the Shuttle vehicle made with this model (1980 updated model) compared to the older 1979 design model showed only slightly higher heating rates.

With the sea-level plume emissive power math model defined, radiation heating rates to various design points on the Shuttle were calculated using a radiation view factor computer program.[5] Initial predictions assumed no altitude variation. Later predictions (before flight data became available) considered altitude effects using a recently developed Monte Carlo radiation code[6] coupled with detailed, two-phase plume flow field calculations and the plume model shown in Figure 9.[7]

SSME - Radiation heating rates from the SSME plumes were calculated using a modified form of the basic NASA band model gaseous radiation program[8]. An extensive effort was made to correctly model the Mach disk region and the viscous shear layer of the plume (see Figure 10). At low to mid altitudes, the plumes do not interact, so detailed radiation calculations were made for each plume and the environment generated at a given design location by adding the contributions from each plume. The complex three-dimensional flow field occurring at high altitudes when the SSME plumes interact and reverse gases into the orbiter base region was approximated using two-dimensional techniques.[1]

Convection

Unlike radiation predictions, convective base heating predictions were based almost entirely on short duration, hot-firing model test data. Eight separate base heating tests were conducted to support the convective environment analysis as listed in Figure 11. The basic model used throughout these tests for first-stage condition was a 2.25% version of the fully integrated launch vehicle. These tests utilized short duration techniques that included hot-firing hydrogen-oxygen simulation of the SSME, hot-firing simulation of the booster SRM, and simulated external air flow over the model. The model used for second-stage test conditions was a 4% scale model of the orbiter base region, vertical fin, OMS pod, and body flap, which included hot-firing hydrogen-oxygen simulation of only the SSMEs. These tests were conducted in altitude chambers with no external flow, only a variable chamber back pressure.

During these tests, model heating rates and gas temperatures were measured over a range of simulated altitudes, and all factors affecting convective base heating were parametrically varied to provide a detailed base heating data base. When the flight conditions were established, this data base was used to extract the model heat transfer coefficient corresponding to the specific flight condition. The scaling techniques from model to full scale were based on the Colburn Turbulent Scaling Law. Details of these techniques are provided in Reference 1. Analytical predictions for the mass-averaged base gas recovery temperature were made by estimating the mass flow of exhaust products into the base region and then integrating the total energy flow in the nozzle boundary layer from the nozzle wall to this mass flow rate. Average temperature as a function of boundary layer mass flow is shown in Figure 12 for the exit plane of the SSME.

FLIGHT DATA

Base heating environment data have been measured on the four development flights as well as the first operational flight. A limited amount of data was obtained on STS-1 due to bad instrumentation initially installed on the orbiter and main engines and reduced instrumentation on the ET base. The bad instruments were replaced on STS-2, and a complete base heating data base was obtained on all subsequent flights with the single exception of the SRB data on STS-4, which was lost when the boosters sank following water impact. The flight instrumentation, operating conditions which affect base heating, and typical flight data are described in the following paragraphs.

Flight Parameters and Operating Characteristics

Shuttle flight parameters which influence base heating are: vehicle trajectory (Figure 13), vehicle angle of attack (Figure 14(a)), SRM chamber pressure history (Figure 14(b)), and SSME chamber pressure history (Figure 14(c)). Other flight and operating conditions affecting base heating, but not shown in this paper, include SSME and SRM gimbaling and vehicle side slip. Altitude and SRM thrust decay history have the most impact; other flight and operating conditions have a second-order effect. Model data indicate that SSME gimbaling can have significant effects on orbiter base heat shield 2nd-stage convective heating if the gimbal angles significantly deviate from current baseline nominal. However, on all Shuttle flights to date, the SSME gimbal angles flown on each flight have not varied from this nominal, and the measured flight data have been similar. The SRM and SSME chamber pressure histories shown in Figures 14(b) and 14(c) are typical for all engines for all flights.

The altitude histories during 1st-stage ascent have been remarkably similar on all five flights as have the engine operating conditions. Therefore, it was expected that the measured environments would be similar in magnitudes and trends. Flight-to-flight differences noted in the data are primarily a function of local flow field differences, gage contamination, TPS outgassing, flight-to-flight gage replacement and range changes, etc. The global base region flowfields, plume shapes, gas temperatures, and TPS and instrumentation temperature were generally the same on all flights.

Development Flight Instrumentation

Flight instrumentation to monitor ascent base heating consisted of total calorimeters, radiometers, and gas temperature probes. The number of instruments greatly increased from STS-1 to STS-2 and subsequent flights, and the quality of the measurements was also improved on STS-2 and subsequent flights at some base locations. A variety of different type gages and different mounting and data retrieval systems were used throughout the various base components. With the exception of the gas temperature measurements, the data were generally good, consistent from component to component, and were of significant value in understanding the base heating environments. Total calorimeter sensor temperatures were generally less than 200°F throughout ascent, so the measured total heating rates reflect an essentially cold wall convective component. Gas temperatures were measured for the ET and right SRB; no gas temperature measurements were taken on the orbiter and SSMEs.

Typical Flight Base Heating Data

Complete presentations of all base heating data for STS-1 through STS-5 are presented in References 9 through 13. As mentioned previously in the introductory discussion, the highest radiation heating occurs on aft-facing components at liftoff and during the SRB shutdown spike. Convective heating, which can be determined by subtracting radiation from the total heating at the same location, is often negative (convective cooling) during the early part of flight but generally peaks at the highest altitude where substantial booster thrust still occurs. This convective peak has occurred on all flights to date at approximately 100,000 feet altitude or 100 seconds into flight at a booster thrust level of 75%. Typical heating levels throughout the base region including outboard locations such as the vertical tail, body flap, and wing/elevon trailing edges are listed in Figure 15 at four times during a typical flight when the environments are distinctly different.

Typical heating rate histories for various base components are presented in Figures 16 through 23. The orbiter and main-engine data are characterized by significant heating through main engine cut-off. The SRB and ET aft dome environments terminate at SRB separation. It is apparent that all base components experienced a heating spike during the last seven seconds of SRM shutdown. The SRM plumes become brighter and have greater radiation potential during this time period as propellant residuals and liners are ejected through the nozzle and burn in the plume. All flights have shown significant amounts of luminous gases in the general base region surrounding the ET aft dome immediately following liftoff. These gases are hot SOFI ablation outgases released by the initial radiation heating load. They reduce the heat load by attenuating radiation to the base-region surfaces.

IMPROVED METHODOLOGY

Close examination of the flight data indicates that two changes were necessary in the basic SRM plume radiation prediction methodology. The sea-level radiation model was modified to account for the combustion zone between the SRMs resulting from the outgassing TPS material from the ET base combusting as it flows downstream between the SRM plumes. An altitude correction factor to modify sea-level SRM radiation rates to account for altitude changes was also developed from the flight experience. A discussion of these and other methodology changes is presented in Reference 14.

The Shuttle flight data generally validated the convective methodology. For most base surfaces, the agreement between prediction and flight data was good indicating that the scaling methods were correct. However, at three distinct base locations, the prediction methodology was obviously incorrect. These locations were the upper interior region of the orbiter base heat shield, the upper ET aft dome surface, and the outboard SRB skirt. At the upper heat shield location, the preflight methodology overpredicted convective heating during second stage. Conversely, the methodology underpredicted ET dome and outboard SRB skirt convective heating during the intense recirculation period at the end of first stage boost. Details of the improved methodology are described in the following paragraphs.

Radiation

SRM - Based on flight data from STS-1 and STS-2, the shape of the sea-level emissive power model was changed to a 15° cone with the same emissive powers for each segment as the 1980 design model, shown in Figure 24. The second change consists of the development of an altitude correction factor used to modify the sea-level SRM radiation rates to account for altitude variations (Figure 25). This procedure eliminates the launch stand correction factor that was present in the earlier methodology. The SRM altitude correction factor as depicted in Figure 25 is valid for any Shuttle trajectory (since it is a function of altitude only) except for the SRM shutdown spike, which occurs at the end of the SRM burn. Since this spike is a function of time (i. e., the last 7 seconds of SRM burnout, as shown in Figure 26), it is superimposed on the altitude plot at the appropriate altitude corresponding to 7 seconds before burnout and separation.

SSME - The general approach for calculating SSME plume radiation has not changed since Reference 1 was published. However, improvements in the SSME sea-level flowfield model have been made and incorporated in the model.[15] An improved emissive power SSME plume radiation model was developed from extensive gaseous radiation calculations made with the improved GASRAD computer code. The current SSME sea-level plume radiation model is shown in Figure 27.

Comparison of Preflight and Improved Radiation Methodology - STS-5 flight data are compared with the original design environment predictions (preflight methodology) and the operational flight predictions (improved methodology) in Figures 28 through 32. Each figure presents a comparison at a distinctly different base component location: center of the ET aft dome, the lower left corner of the orbiter heat shield, the SRB aft kick ring, the inboard aft hat band of the lower left SSME, and the sway strut of the ET/orbiter attach structure. For most locations, the improved methodology results in a radiation environment somewhat higher than the earlier design critical review (DCR) design environment and includes the SRM shutdown spike.

Convection

To update the convective heating methodology, flight data were substituted for the nominal model data base for the ET upper dome, SRB aft skirt, and the orbiter upper heat shield. Because the flight data were measured over a relatively narrow range of freestream and operating conditions, model data trends and distributions are retained in the up-dated methodology to encompass all possible flight conditions anticipated in future operational flights. The Shuttle flight data also showed less variation in convective heating over large surfaces, such as the orbiter heat shield, the OMS pod base, and the SSMEs, than had been indicated by the model data.

Original methods to predict base gas recovery temperature are unchanged in the up-dated methodology. No valid base gas temperature measurements were made anywhere in the Shuttle base region during the DFI flights. Gas probes, in general, have large uncertainties and potential errors and for these reasons the conservative gas temperatures derived from analytical methods will be retained.

Comparison of Pre-flight and Improved Convective Heating Methodology - Model data, design predictions (preflight methodology), flight data from STS-4, and the operational flight predictions (improved methodology) are compared for four different base locations in Figures 33 through 36. For some locations, e. g. - the ET dome, the operational flight environment encompasses the flight data and is approximately twice the magnitude of the DCR design environment. Conversely, operational predictions for the upper center region of the orbiter heat shield were substantially reduced from the original DCR environments.

REFERENCES

1. Greenwood, T. F., Seymour, D. C., and Bender, R. L.: "Base Heating Prediction Methodology Used for the Space Shuttle," Proceedings of the JANNAF 10th Plume Technology Meeting, Chemical Propulsion Information Agency, CPIA-29, Volume 2, San Diego, California, December 1977, pp. 253-312.

2. Kramer, O. G.: "Evaluation of Thermal Radiation From the Titan III Solid Rocket Motor Exhaust Plumes," Paper No. 70-842, AIAA 5th Thermophysics Conference, Los Angeles, July 1970.

3. Carter, R. E.: "Space Shuttle SRB Plumes-Thermal Radiation Model," LMSC-HREC TR D568530, Lockheed Missiles & Space Company, Huntsville, Alabama, December 1978.

4. Carter, R. E.: "Improved SRM Plume Radiation Design Heating," LMSC-HREC TN D698084, Lockheed Missiles & Space Company, Huntsville, Alabama, November 1980.

5. Lovin, J. K., and Lubkowitz, A. W.: "User's Manual (RADFAC) A Radiation View Factor Digital Computer Program," LMSC-HREC TN D148620, Lockheed Missiles & Space Company, Huntsville, Alabama, November 1969.

6. Watson, G. H., and Lee, A. L.: "Thermal Radiation Model for Solid Rocket Plumes," Journal of Spacecraft and Rockets, Volume 14, No. 11, November 1977, pp. 641-647.

7. Carter, R. E., and Lee, A. L.: "Space Shuttle SRB Plume Radiation Heating Rate Prediction With Altitude Corrections," LMSC-HREC TM D497262, Lockheed Missiles & Space Company, Huntsville, Alabama, September 1977.

8. Reardon, J. E.: "Prediction of Radiation From the Space Shuttle Main Engine to the Orbiter Base Region," RTR 011B-4, REMTECH, Inc., Huntsville, Alabama, May 1976.

9. NASA/Marshall Space Flight Center: "Space Shuttle STS-1 Final Flight Evaluation Report - Volume II - Base Heating Section VI," July 22, 1981.

10. Greenwood, T. F.: NASA/Marshall Space Flight Center Memo ED33-82-3, "STS-2 Flight Evaluation Report - Base Heating," January 15, 1982.

11. Greenwood, T. F.: NASA/Marshall Space Flight Center Memo ED33-82-25, "STS-3 Flight Evaluation Report - Base Heating," April 25, 1982.

12. Greenwood, T. F.: NASA/Marshall Space Flight Center Memo ED33-82-46, "STS-4 Flight Evaluation Report - Base Heating," August 10, 1982.

13. Greenwood, T. F.: NASA/Marshall Space Flight Center Memo ED33-82-65, "STS-5 Flight Evaluation Report - Base Heating," December 2, 1982.

14. Greenwood, T. F. et al.: "Development of Space Shuttle Base Heating Methodology and Comparison With Flight Data," Proceedings of the JANNAF 13th Plume Technology Meeting, Chemical Propulsion Information Agency, CPIA-357, vol. 1, Houston, Texas, April 1982, pp. 67-82.

15. Reardon, J. E., and Lee, Y.: "Space Shuttle Main Engine Plume Radiation Model," RTR 014-7, REMTECH, Inc., Huntsville, Alabama, December 1978.

1ST STAGE CONFIGURATION

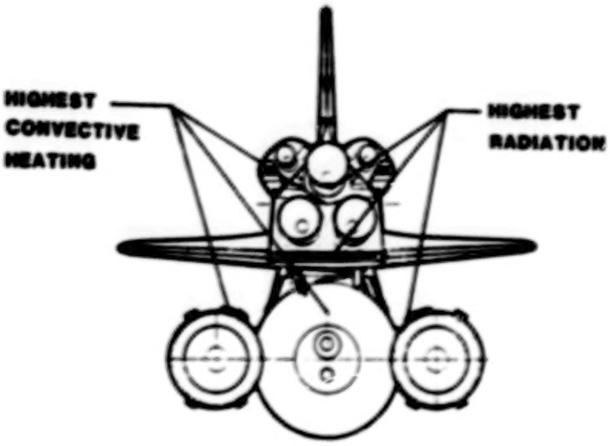
HIGHEST CONVECTIVE HEATING
HIGHEST RADIATION

2ND STAGE CONFIGURATION

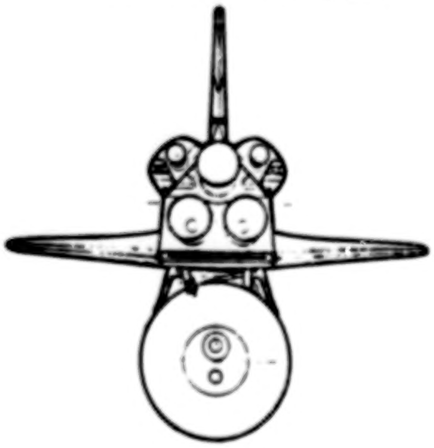

Figure 1.- Shuttle base configuration.

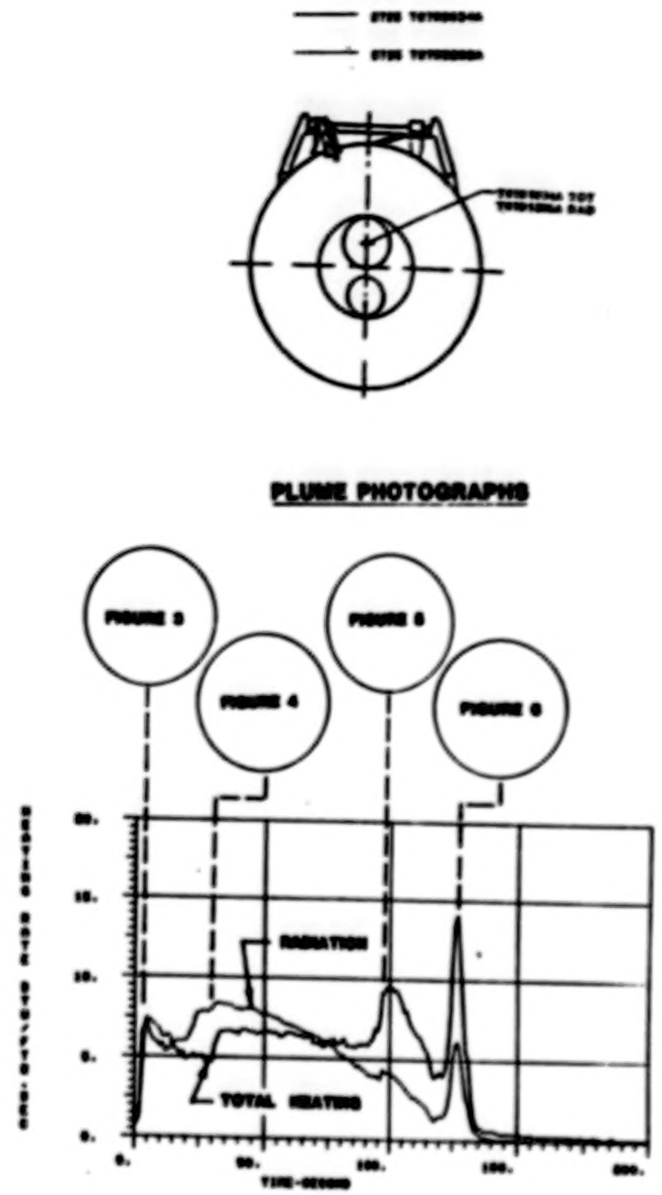

Figure 2.- Typical first-stage ascent base heating environment.

ORIGINAL PAGE IS
OF POOR QUALITY

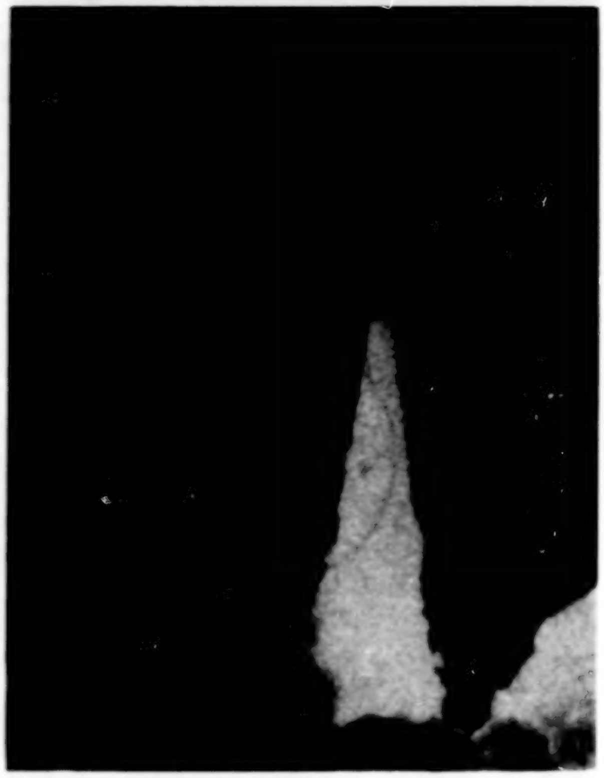

Figure 3.- Shuttle exhaust plumes at liftoff.

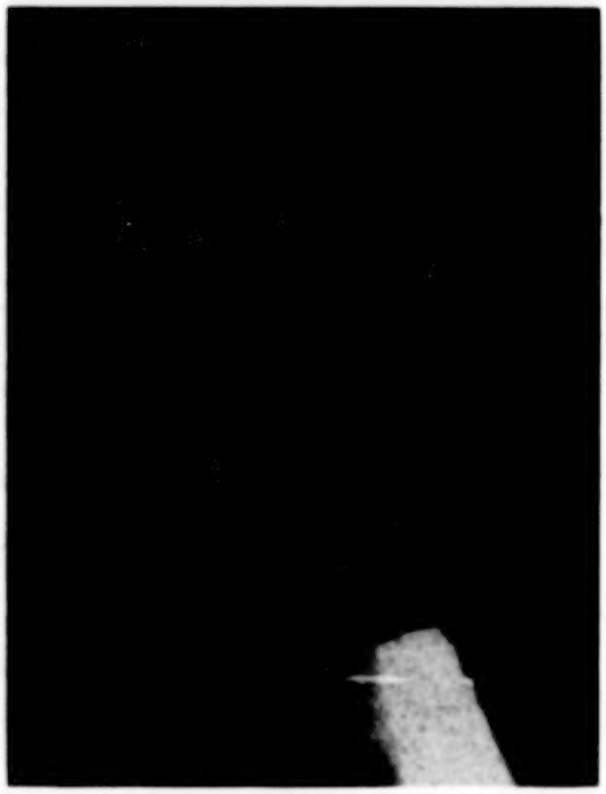

Figure 4.- Shuttle exhaust plumes at 7500 ft.

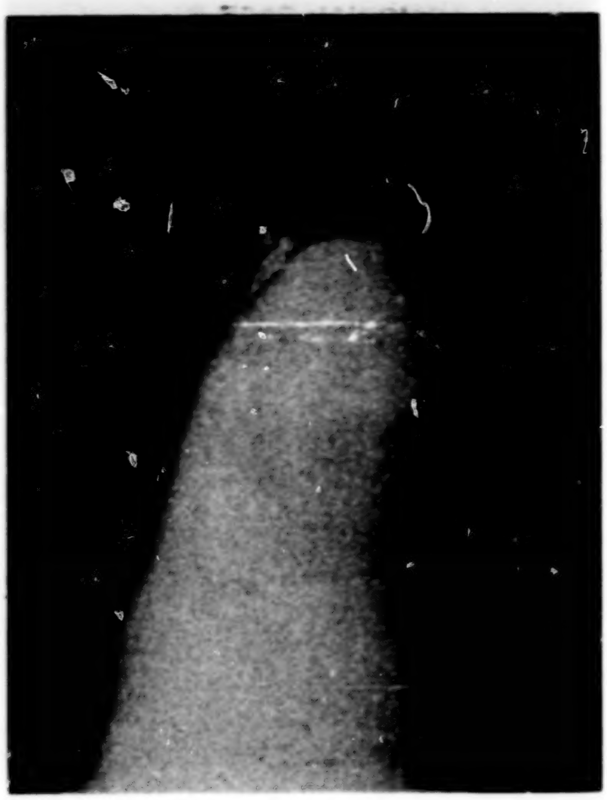

Figure 5.- Shuttle exhaust plumes at 90,000 ft.

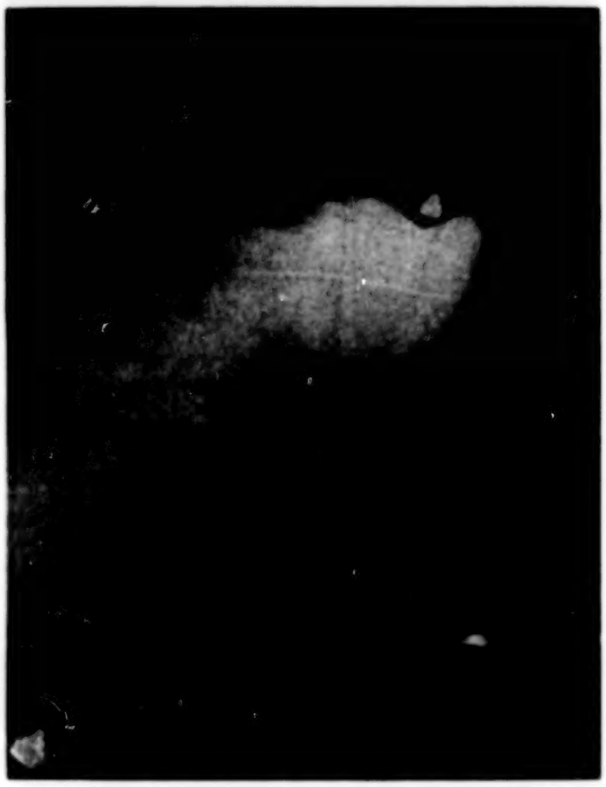

Figure 6.- Shuttle exhaust plumes at 166,000 ft.

ORIGINAL PAGE IS
OF POOR QUALITY

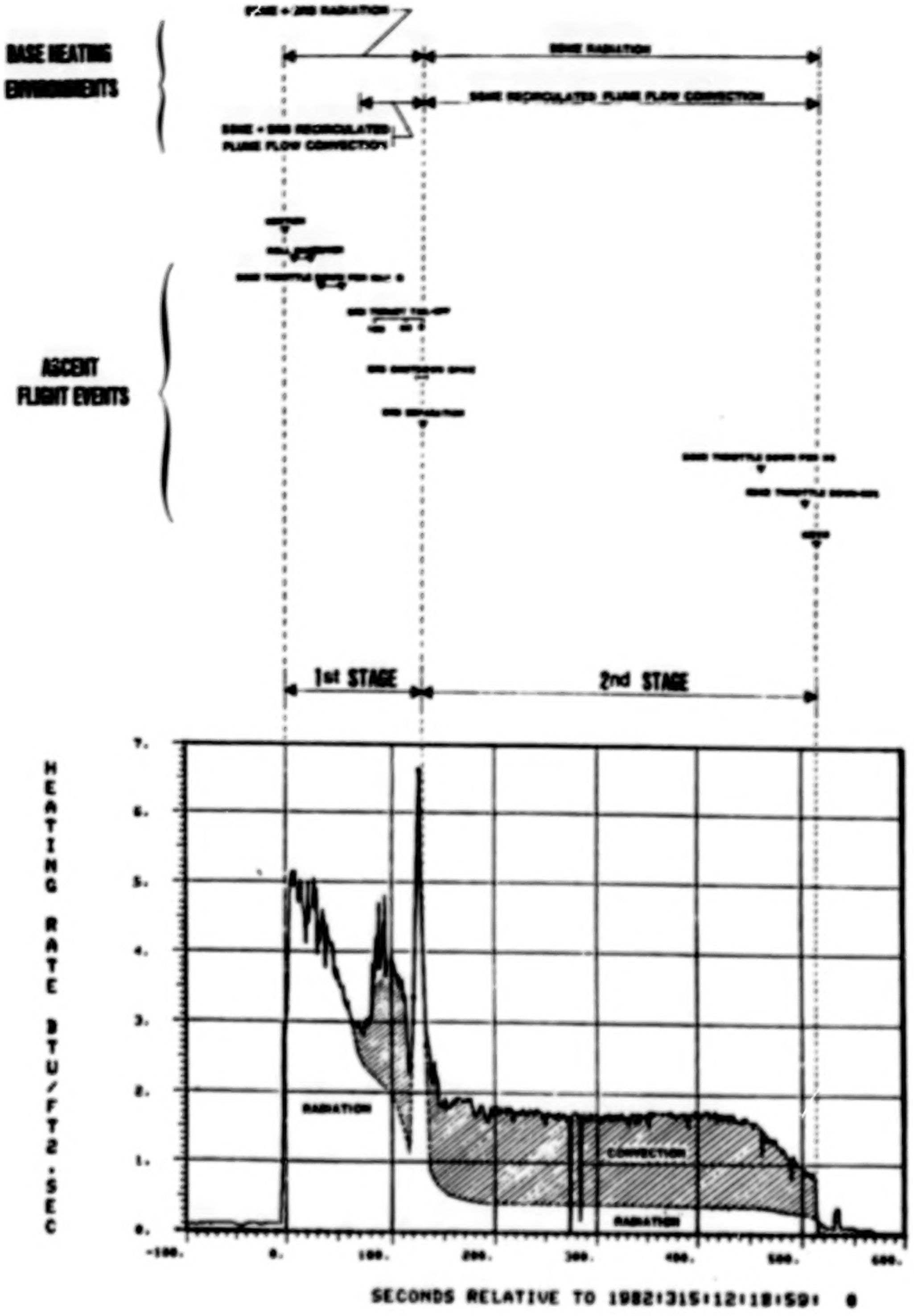

Figure 7.- Ascent flight events - typical orbiter heat shield environment.

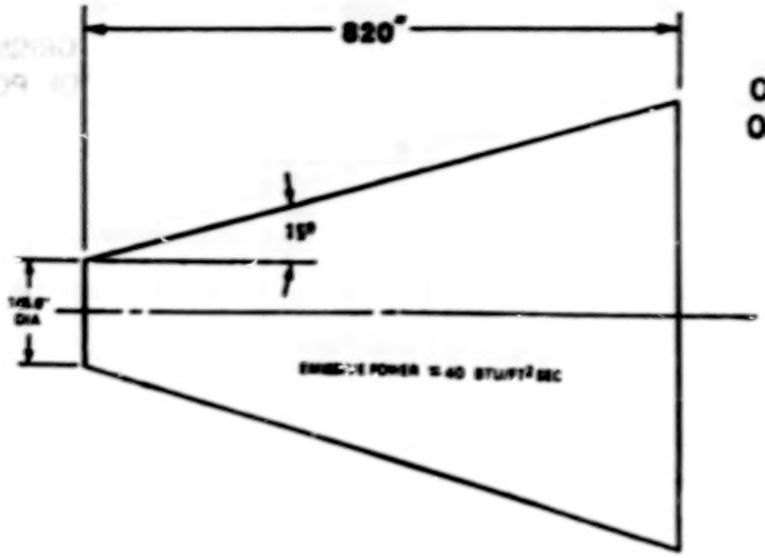
820"
15°
149.6" DIA
EMISSIVE POWER = 40 BTU/FT² SEC

(a) Original model (ref. 2).

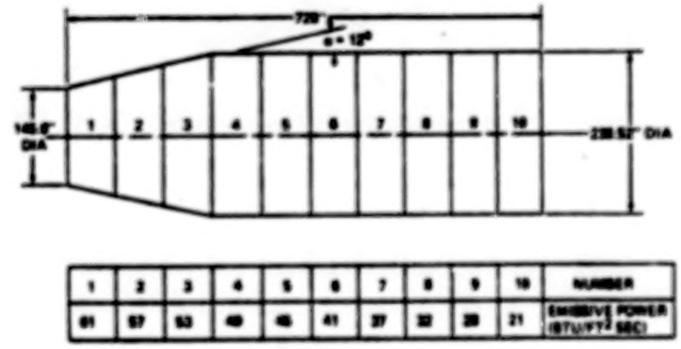
720"
α = 12°
149.6" DIA
1
2
3
4
5
6
7
8
9
10
238.52" DIA

1	2	3	4	5	6	7	8	9	10	NUMBER
61	57	53	49	45	41	37	32	28	21	EMISSIVE POWER (BTU/FT² SEC)

(b) 1979 design model (ref. 3).

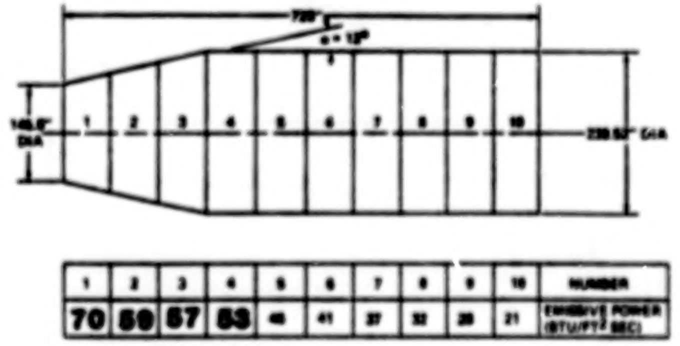
720"
α = 12°
149.6" DIA
1
2
3
4
5
6
7
8
9
10
238.52" DIA

1	2	3	4	5	6	7	8	9	10	NUMBER
70	59	57	53	45	41	37	32	28	21	EMISSIVE POWER (BTU/FT² SEC)

(c) 1980 up-dated design model (ref. 4).

Figure 8.- SRM sea-level plume radiation models.

SRB PLUME MODEL EMISSIVE POWERS VS ALTITUDE

No.	Altitude/Emissive Power (Btu/ft^2-sec)			
	42 Kft	82 Kft	102 Kft	136 Kft
1	36.990	32.731	29.586	25.763
2	32.850	24.506	17.963	14.696
3	26.880	16.394	11.183	7.947
4	22.472	12.390	7.695	5.093
5	17.566	9.236	5.869	3.534
6	13.654	6.500	4.011	2.212
7	11.507	5.040	3.065	1.449
8	8.397	3.621	1.945	1.023
9	5.625	2.256	1.403	0.725
10	3.163	1.628	0.000	0.496
∞	27.50	23.000	37.000	60.000

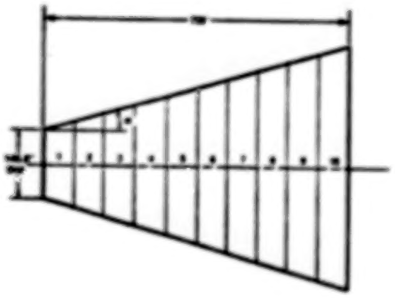
1
2
3
4
5
6
7
8
9
10

Figure 9.- SRM altitude plume model (ref. 7).

GEOMETRY AND EMISSIVE POWER OF THE SSME SEA LEVEL PLUME MODEL

SURFACE		Z-INCHES	R-INCHES	EMISSIVE POWER BTU/FT^2 · SEC
6° CONE		0 – 800	45-101	10-TRANSPARENT
CYLINDER		800-1000	100	10
DISK	1	60	30	70-OPAQUE
	2	100	30-40	60
	3	200	40-60	100
CYLINDER	1	60-100	30	40
	2	100-200	40	50
	3	200-800	50	50
	4	800-1000	50	30

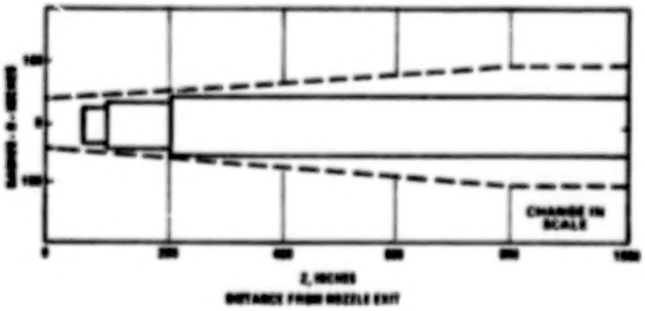
RADIUS - R - INCHES
100
0
100
CHANGE IN SCALE
0
200
400
600
800
1000
Z, INCHES
DISTANCE FROM NOZZLE EXIT

Figure 10.- SSME sea-level plume model (ref. 8).

ORIGINAL PAGE IS
OF POOR QUALITY

FIRST STAGE WIND TUNNEL TESTS

TEST	FACILITY	MACH NO.	NO. OF RUNS	MEASUREMENTS PER RUN	TIME PERIOD
IH-5	CALSPAN LUDWIEG TUBE	4.5	46	36	JAN-JULY 1974
IH-34	LEWIS 10X10	<3.5	36	98	JUNE - AUG 1975
IH-39	LEWIS 10X10	<3.5	163	136	OCT, 1976 APRIL, 1977
IH-75	CALSPAN LUDWEIG TUBE	3.5 AND 4.5	60	100	FALL, 1977

SECOND STAGE VACUUM TANK TESTS

TEST	FACILITY	NO. OF RUNS	MEASUREMENTS PER RUN	TIME PERIOD
OH-3	MSFC IBFF	38	24	MAY-AUG 1974
OH-64	LEWIS PLUM BROOK SPACE POWER	154	152	APRIL-JUNE 1975
OH-78	JSC CHAMBER A	266	179	JULY-NOV 1976
OH-79	JSC CHAMBER A	OPEN	OPEN	SPRING, 1978

Figure 11.- Shuttle base heating test program.

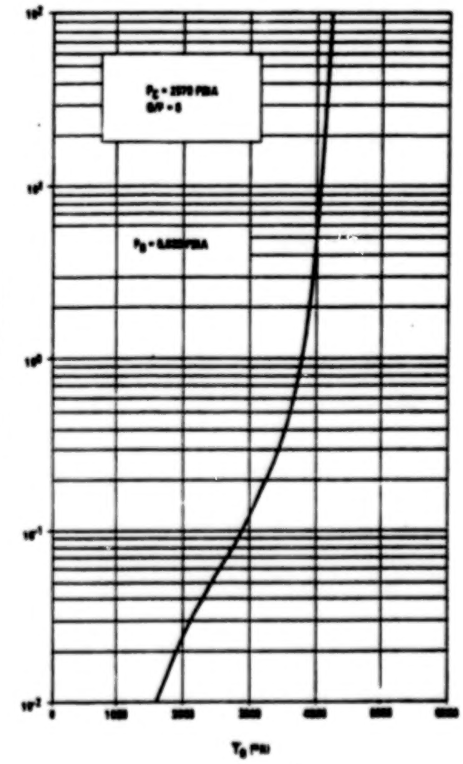

Figure 12.- Mass-averaged total temperature at the nozzle exit plane of the Space Shuttle orbiter main engine (ref. 1).

ORIGINAL PAGE IS
OF POOR QUALITY

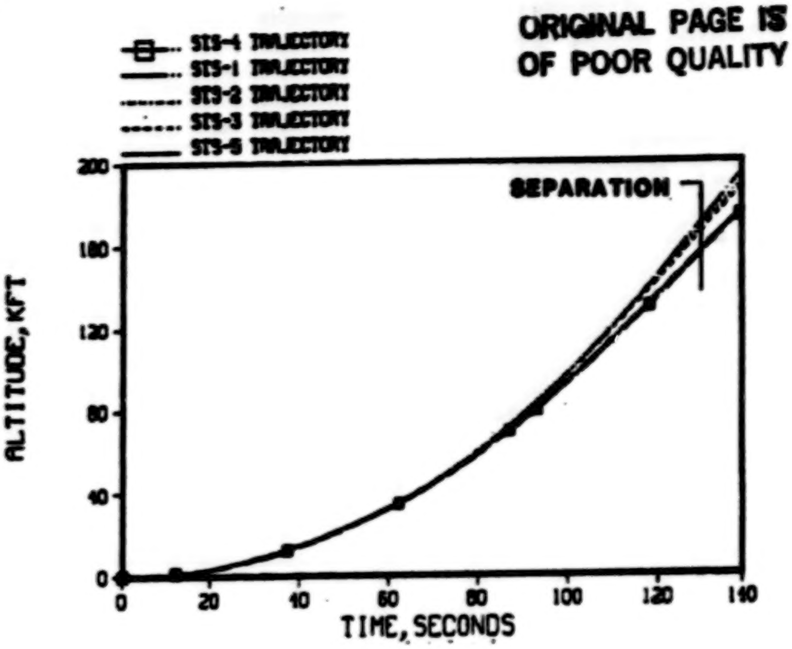

(a) First-stage flight.

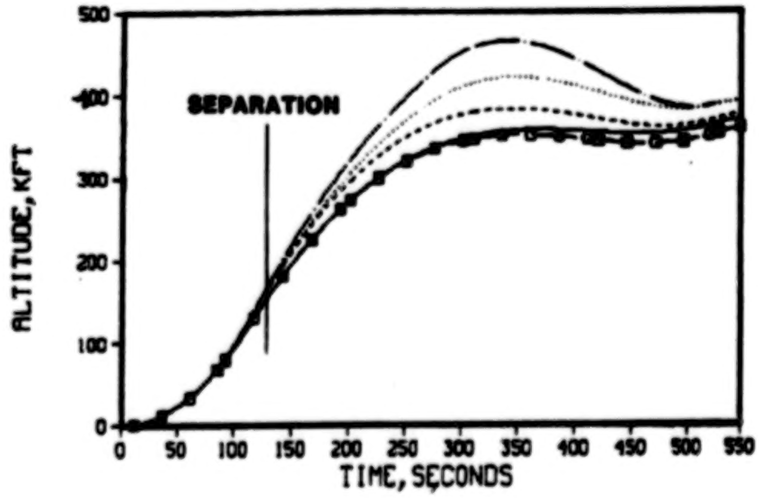

(b) First- and second-stage flight.

Figure 13.- Comparison of STS-1, STS-2, STS-3,
STS-4, and STS-5 trajectories.

ORIGINAL PAGE IS
OF POOR QUALITY

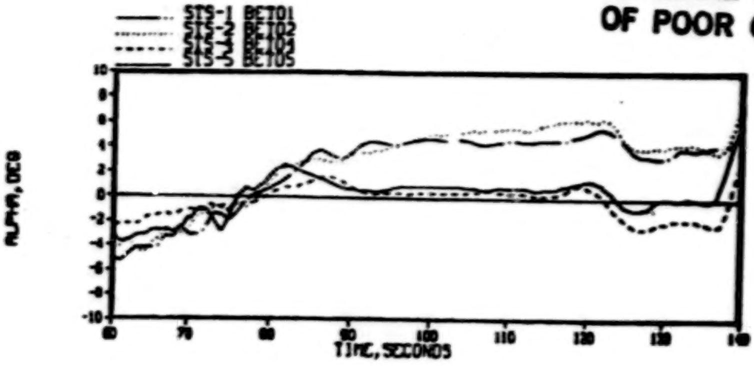

(a) Angle-of-attack histories for STS-1, STS-2, STS-4, and STS-5.

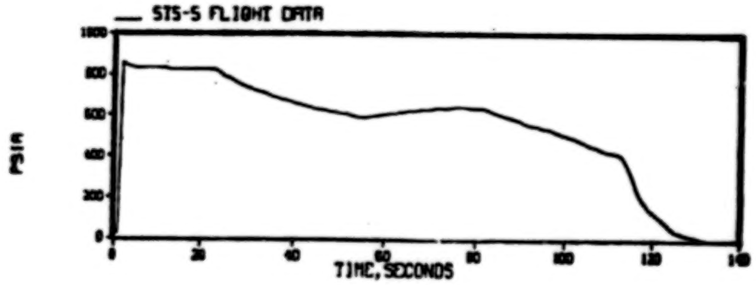

(b) R-SRB chamber pressure.

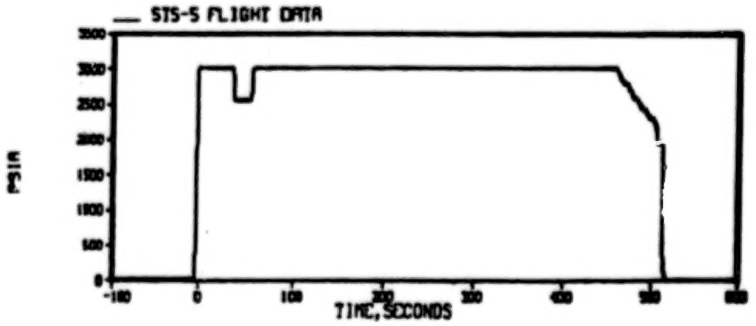

(c) SSME-3 chamber pressure.

Figure 14.- Flight parameters.

ORIGINAL PAGE IS
OF POOR QUALITY

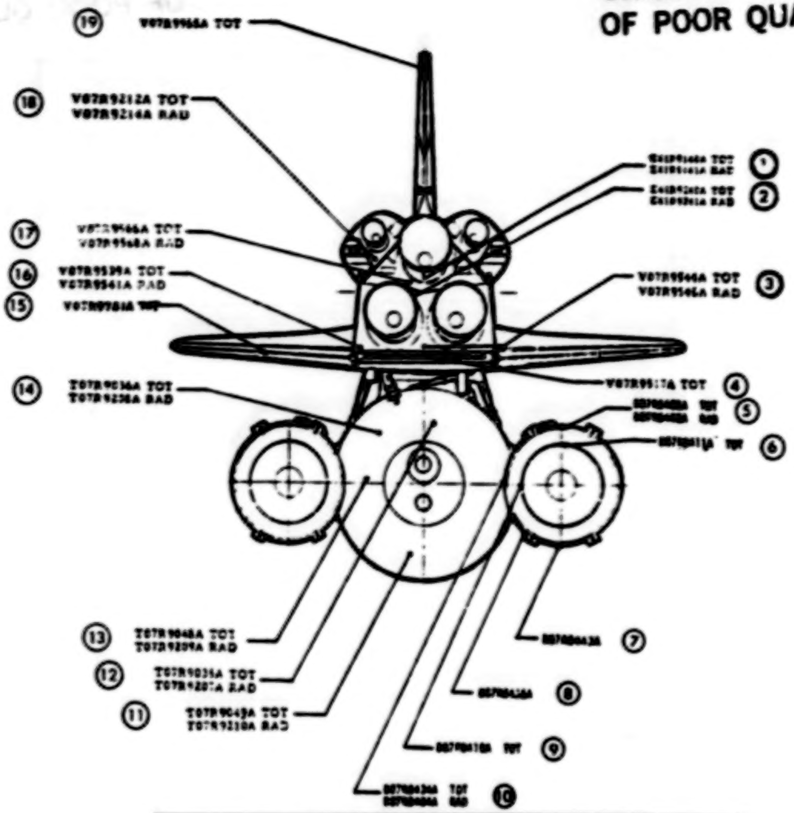
⑲ V07R9966A TOT
⑱ V07R9212A TOT
V07R9214A RAD
⑰ V07R9966A TOT
V07R9968A RAD
⑯ V07R9539A TOT
V07R9541A RAD
⑮ V07R9781A TOT
⑭ T07R9036A TOT
T07R9228A RAD
TOT
RAD ①
TOT
RAD ②
V07R9544A TOT
V07R9546A RAD ③
V07R9517A TOT ④
TOT
RAD ⑤
TOT ⑥
⑦
⑧
TOT ⑨
TOT
RAD ⑩
⑬ T07R9048A TOT
T07R9209A RAD
⑫ T07R9035A TOT
T07R9207A RAD
⑪ T07R9043A TOT
T07R9210A RAD

COMPONENT	LOC	HEATING RATE, BTU/FT.^{2} SEC								FLIGHT DATA
		10 SEC (780 FT)		100 SEC (98,000 FT)		126 SEC (158,500 FT)		300 SEC (409,000 FT)		
		RAD	TOT	RAD	TOT	RAD	TOT	RAD	TOT	
ORBITER										
HEAT SHIELD	③	5.10	3.70	2.70	4.75	4.85	6.10	0.30	1.00	
	⑯	4.65	2.85	2.40	3.95	5.10	5.12	0.10	0.30	
	⑰	4.00	2.70	1.70	4.15	2.91	4.38	0.30	1.55	
OMS POD	⑱	5.10	5.10	2.20	3.75	3.40	3.95	0.70	1.40	
VERTICAL TAIL	⑲	--	9.20	--	5.05	--	15.20	--	0.50	FIG. 20
ELEVON	⑮	--	5.20	--	4.00	--	8.25	--	0.10	FIG. 19
BODYFLAP	④	--	13.25	--	10.60	--	23.60	--	1.00	FIG. 18
SSME #1	①	9.00	13.25	3.20	9.05	11.23	26.80	0.80	2.50	FIG. 21
SSME #2	②	8.30	9.60	2.35	10.20	2.05	5.20	0.80	3.20	
RSRB										
NOZZLE	⑥	--	5.00	--	4.35	--	7.60			
	⑨	--	10.75	--	8.50	--	19.50*			
AFT SKIRT	⑤	8.50	11.40	1.85	5.20	7.00	15.40			FIG. 23
	⑦	--	0.10	--	1.35	--	2.60			
	⑧	--	0.70	--	2.65	--	6.30*			
	⑩	6.00	3.80	3.40	7.30	7.60	11.30*			
ET AFT DOME	⑪	3.55	3.00	1.85	3.95	2.75	8.30	0.00	0.00	
	⑫	3.50	3.80	2.10	5.30	6.35	11.70	0.00	0.00	FIG. 22
	⑬	3.00	4.60	1.75	6.50	3.55	12.10	0.00	0.00	
	⑭	2.55	5.00	1.25	6.35	3.60	14.05	0.00	0.00	

*OFFSCALE

Figure 15.- Base heating environment distribution.

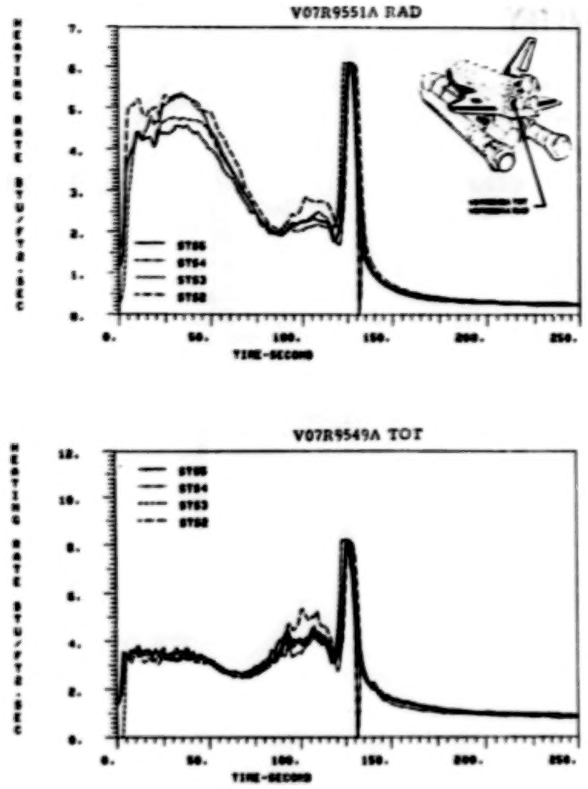

Figure 16.- Typical Shuttle flight data - orbiter heat shield.

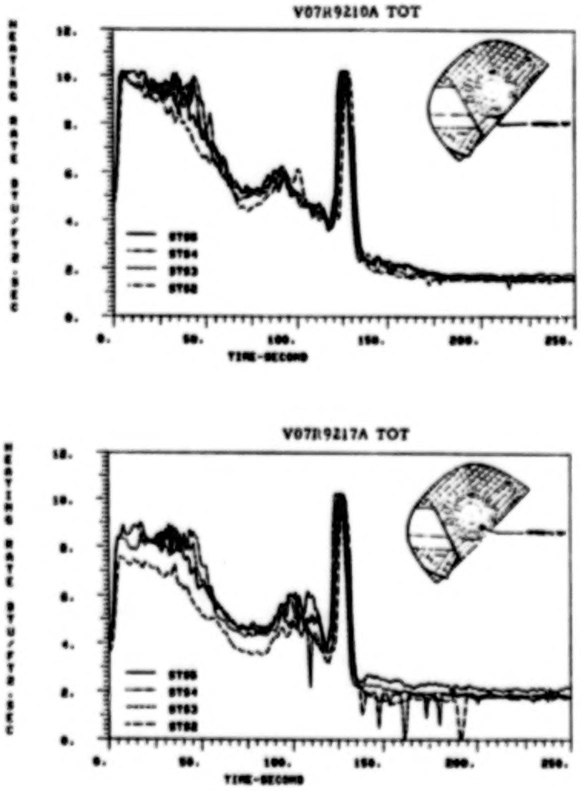

Figure 17.- Typical Shuttle flight data - OMS pod.

ORIGINAL PAGE IS
OF POOR QUALITY

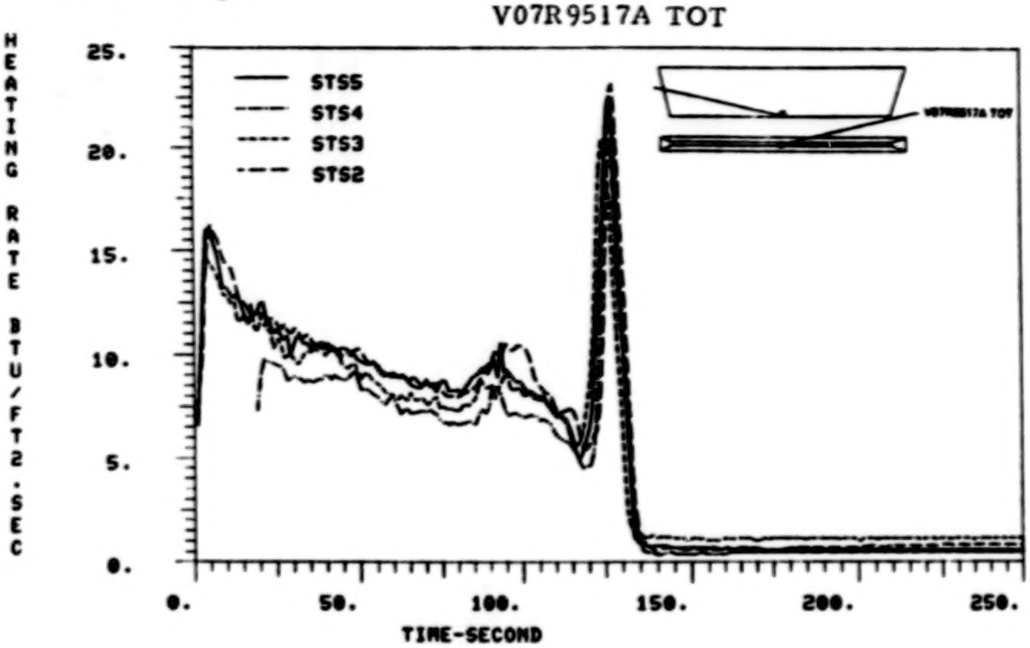

Figure 18.- Typical Shuttle flight data - body flap.

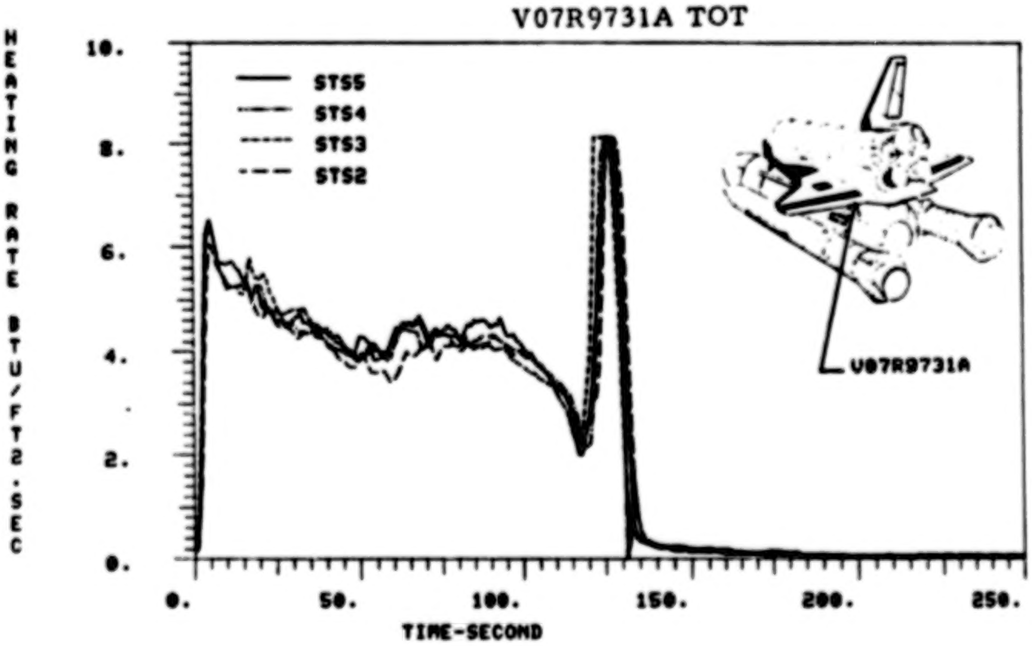

Figure 19.- Typical Shuttle flight data - elevon.

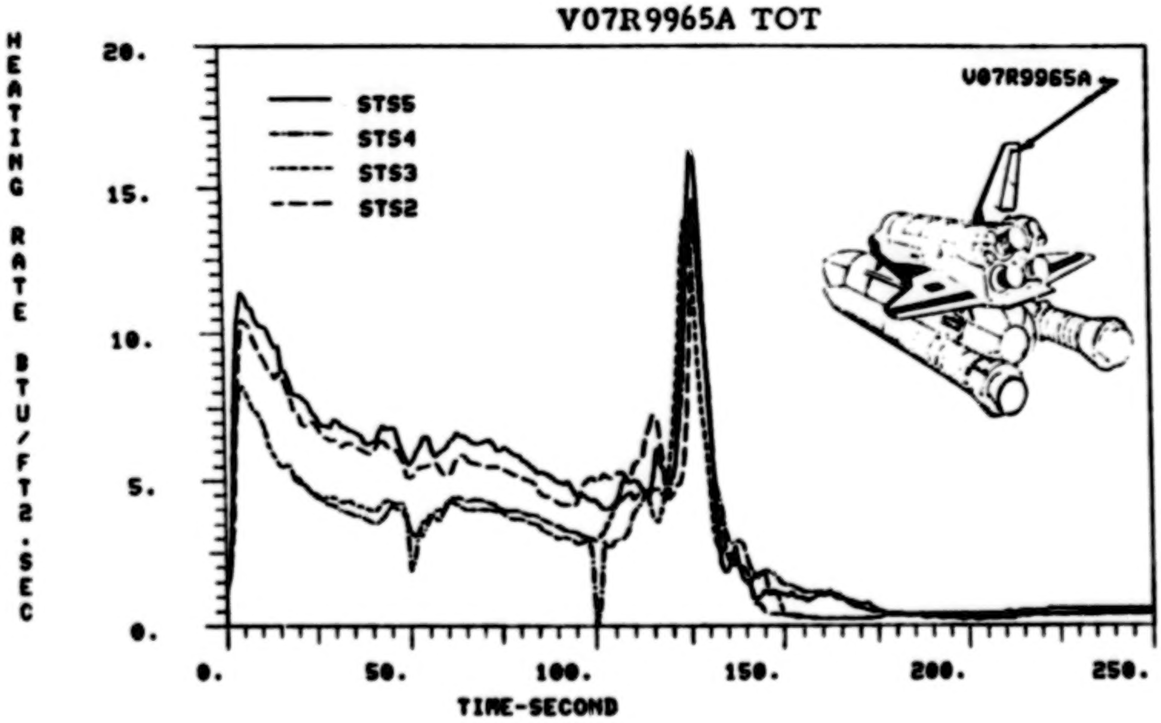

Figure 20.- Typical Shuttle flight data - vertical tail.

ORIGINAL PAGE IS
OF POOR QUALITY

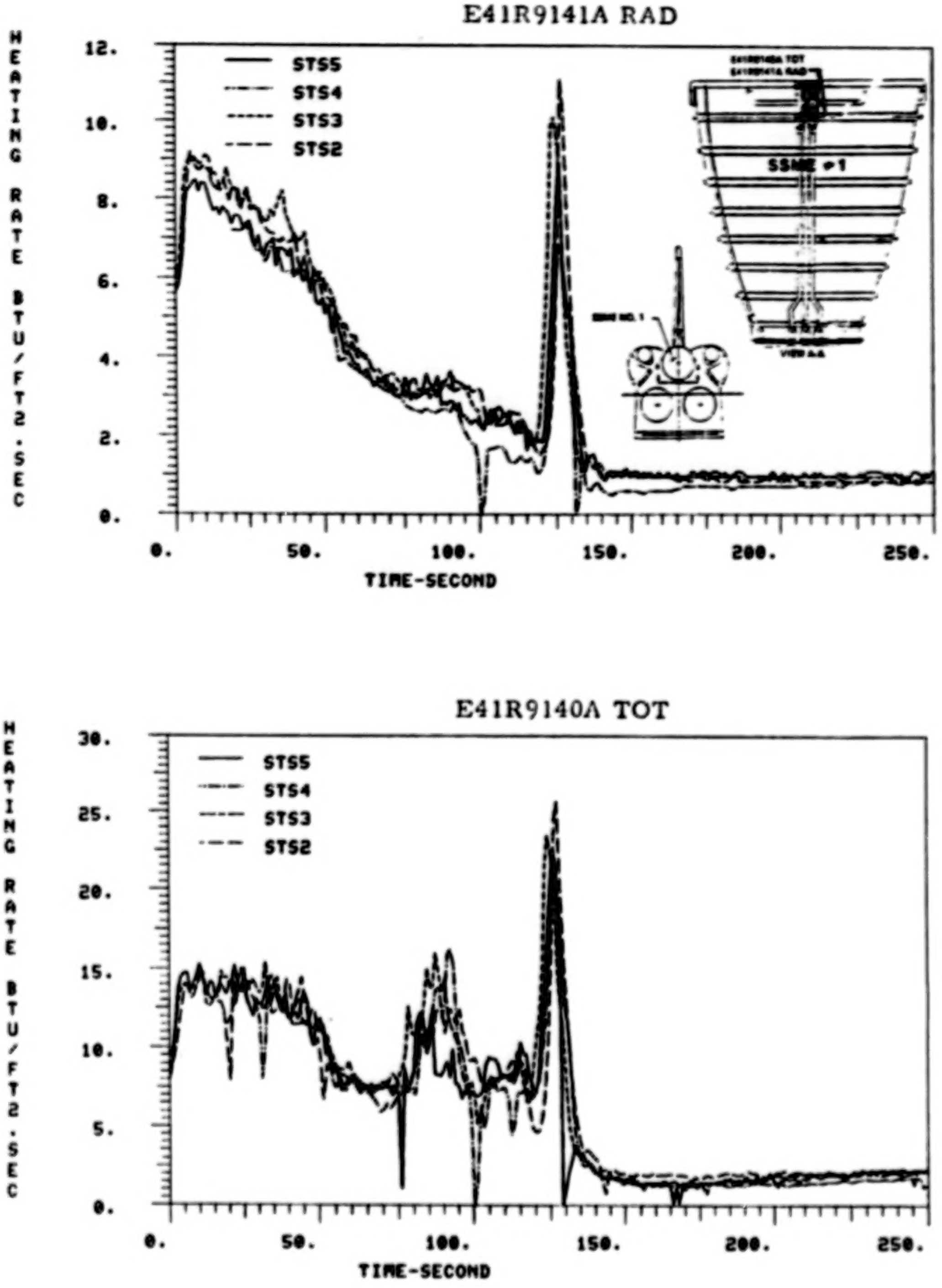

Figure 21.- Typical Shuttle flight data - SSME number 1.

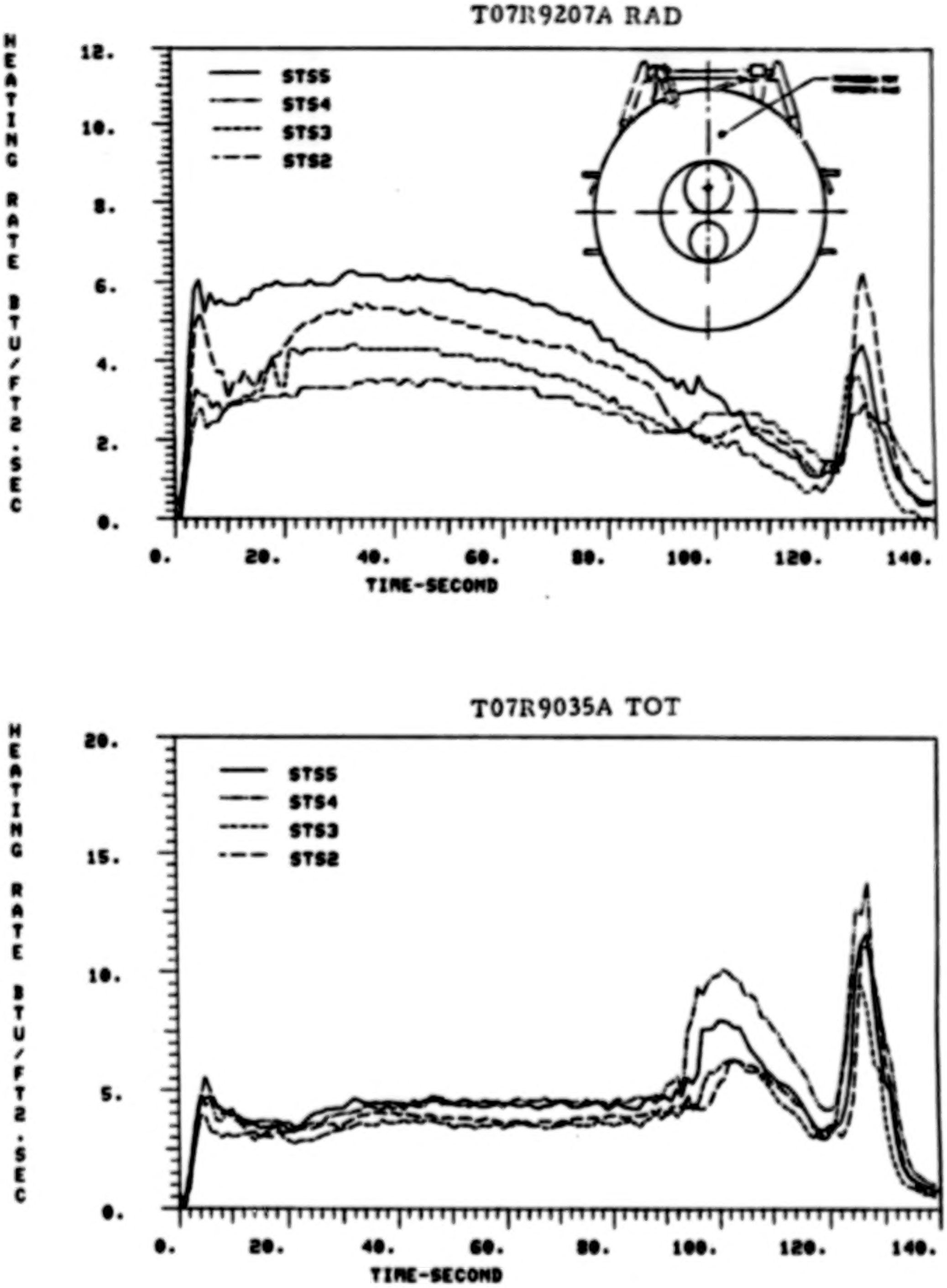

Figure 22.- Typical Shuttle flight data - external LH_2 tank aft dome.

B07R8402A RAD

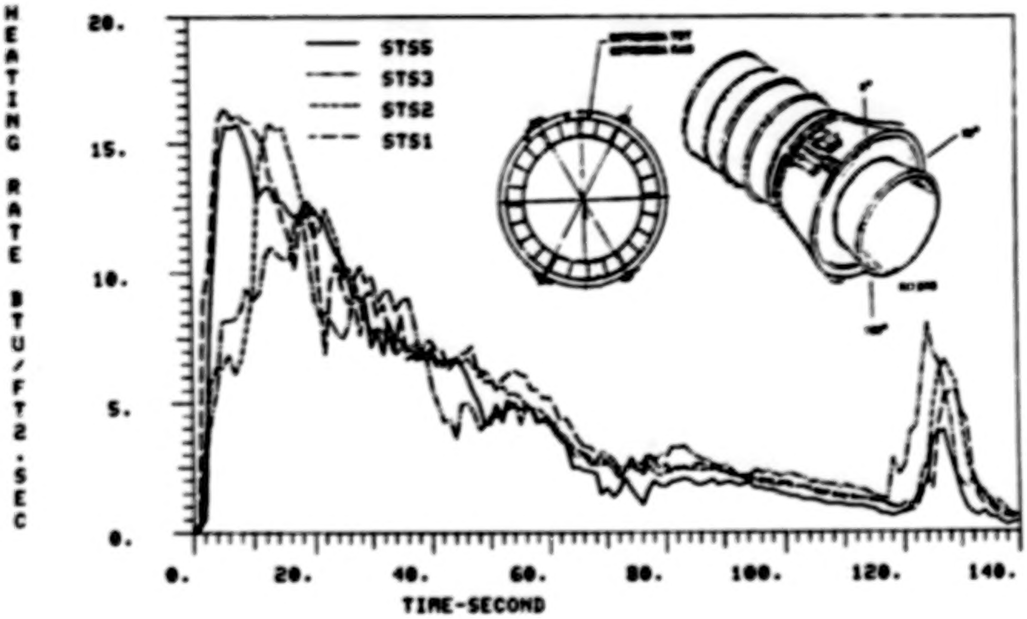

B07R8408A TOT

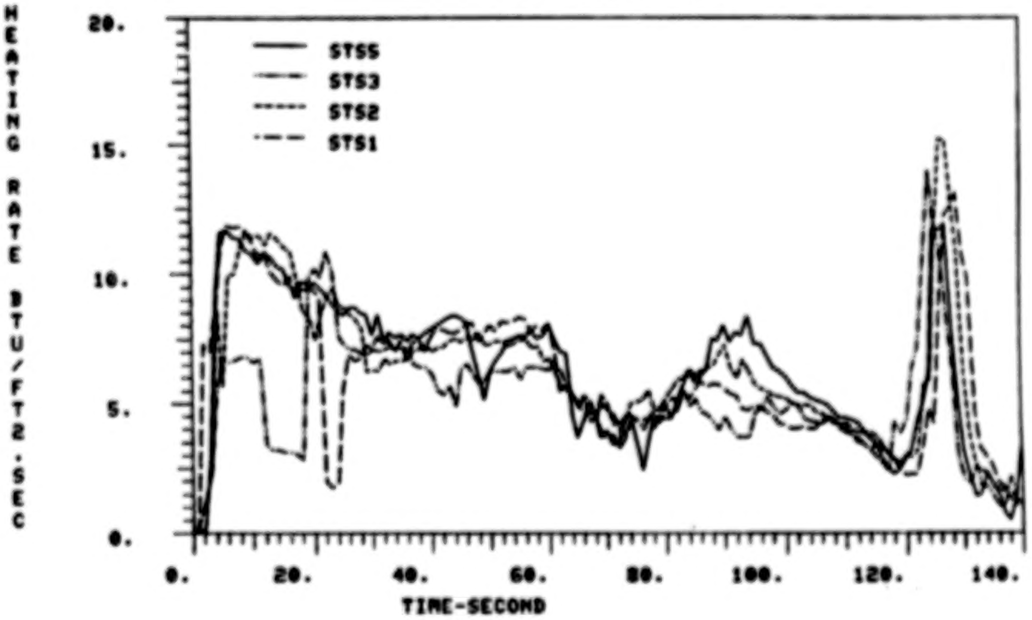

Figure 23.- Typical Shuttle flight data - right SRB aft skirt.

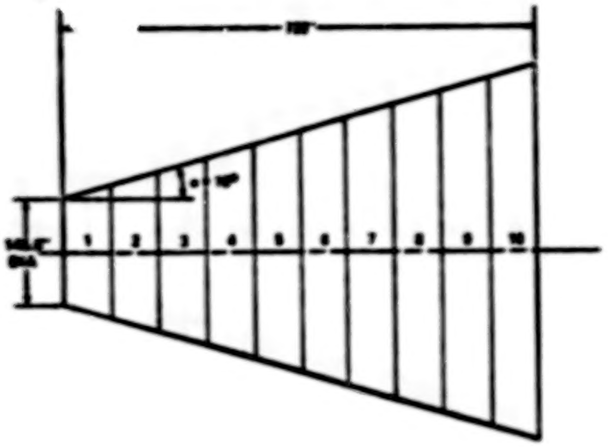

1	2	3	4	5	6	7	8	9	10	NUMBER
70	60	57	53	45	41	37	32	28	21	EMISSIVE POWER (BTU/FT² SEC)

Figure 24.- Current SRM sea-level plume radiation model (ref. 14).

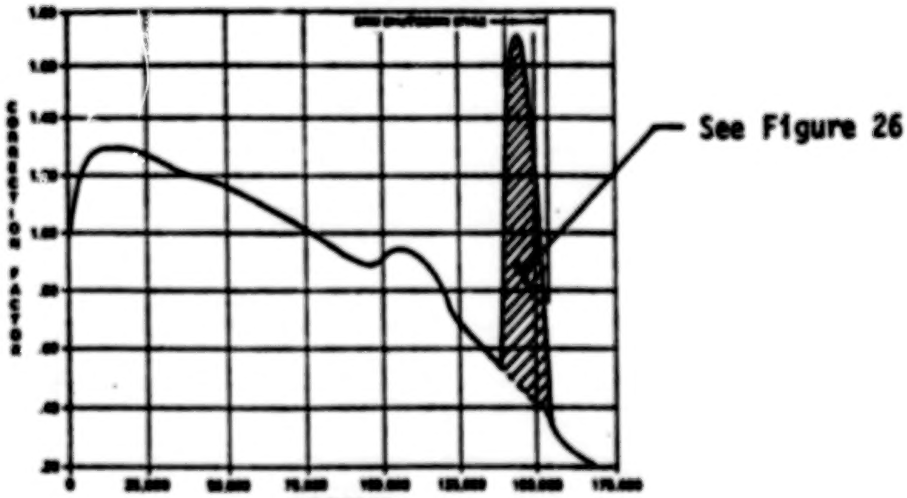

Figure 25.- SRM altitude correction factor (ref. 14).

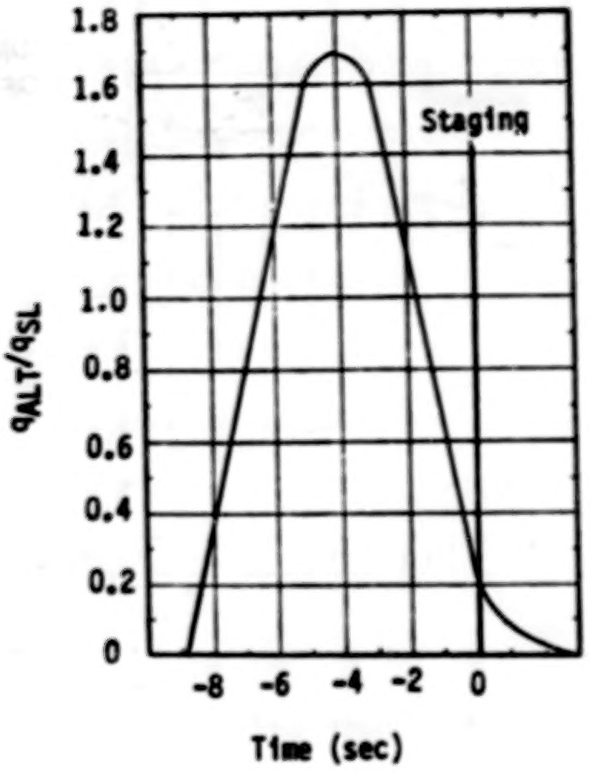

Figure 26.- SRM shutdown radiation spike (ref. 14).

SHAPE	EMISSIVE POWER BTU/FT^2–SEC	DISTANCE FROM EXIT INCHES	RADIUS INCHES
DISK 1 – TRANSPARENT	150	50	25
2 – TRANSPARENT	120	300	20–50
CYLINDER 1 – OPAQUE	60	50–300	20
2 – OPAQUE	60	300–600	50
3 – OPAQUE	40	600–1200	50
CONE – TRANSPARENT	12	100–1100	40–120

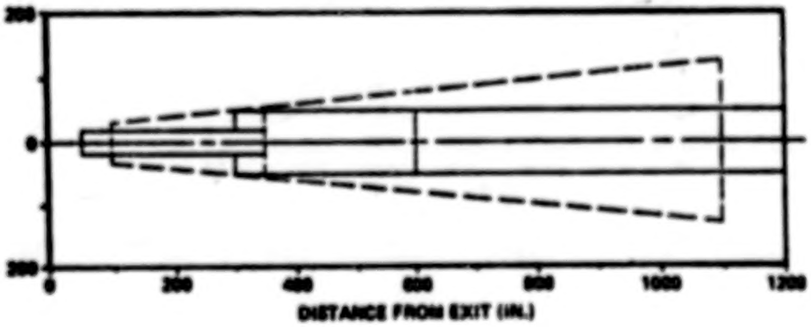
200
0
200
0
200
400
600
800
1000
1200
DISTANCE FROM EXIT (IN.)

Figure 27.- Current SSME sea-level plume radiation model (ref. 15).

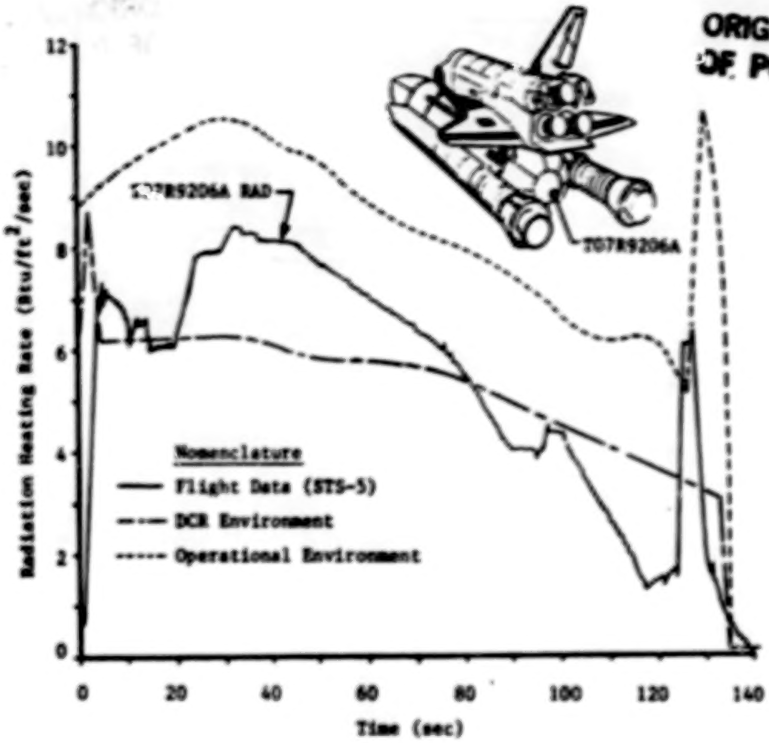

Figure 28.- External tank radiation base heating.

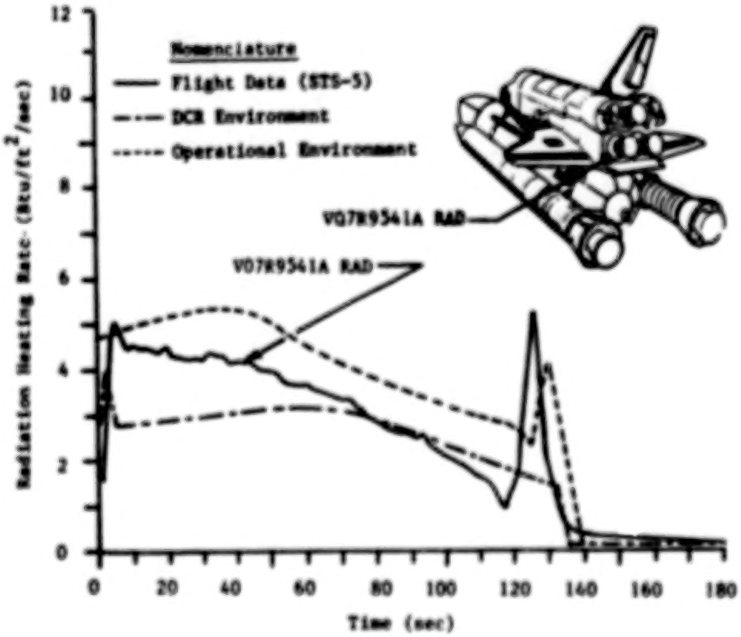

Figure 29.- Orbiter heat shield radiation base heating.

ORIGINAL PAGE IS
OF POOR QUALITY

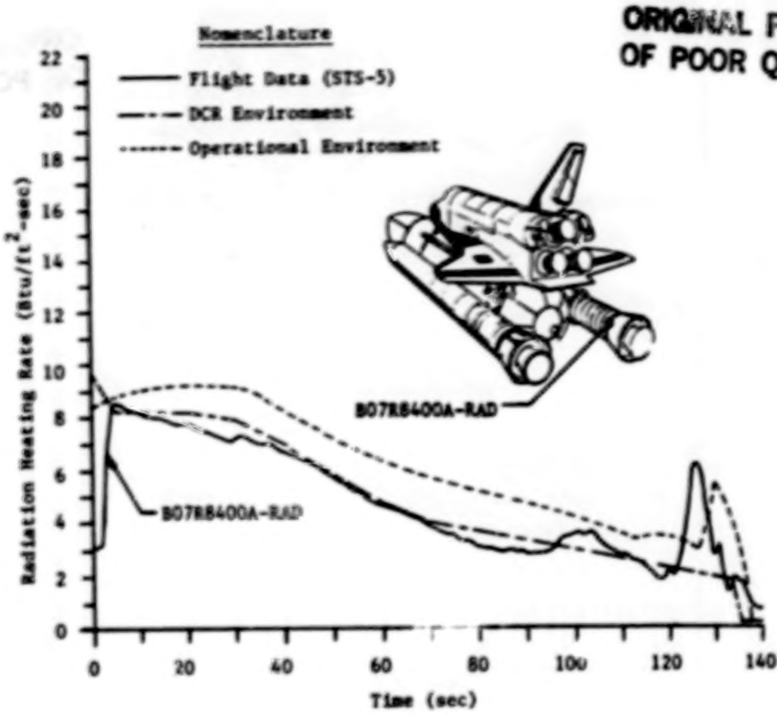

Figure 30.- SRB kick ring radiation base heating.

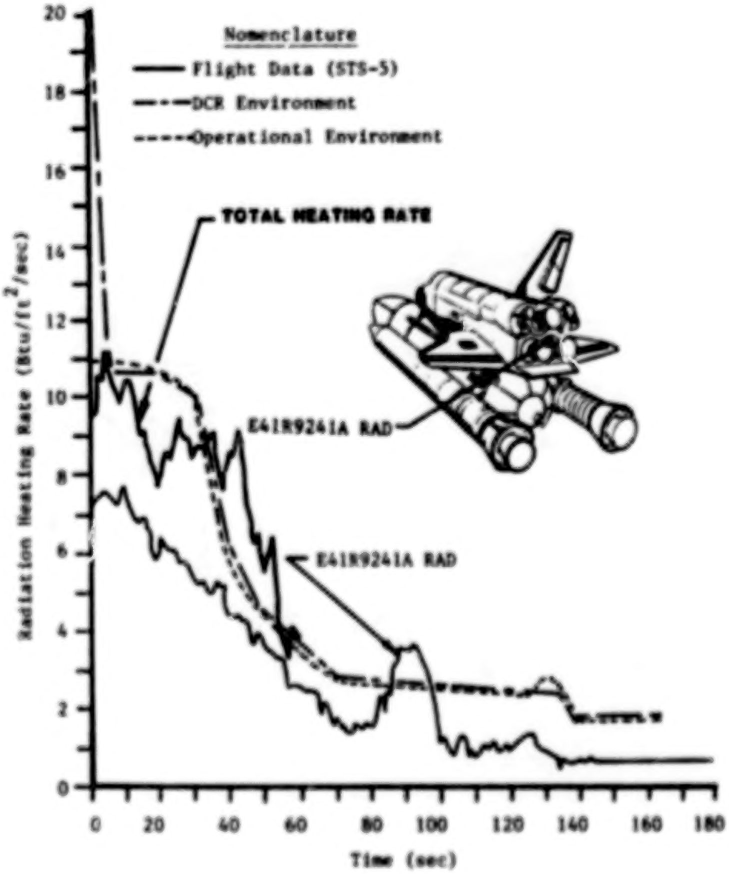

Figure 31.- SSME number 2 radiation base heating.

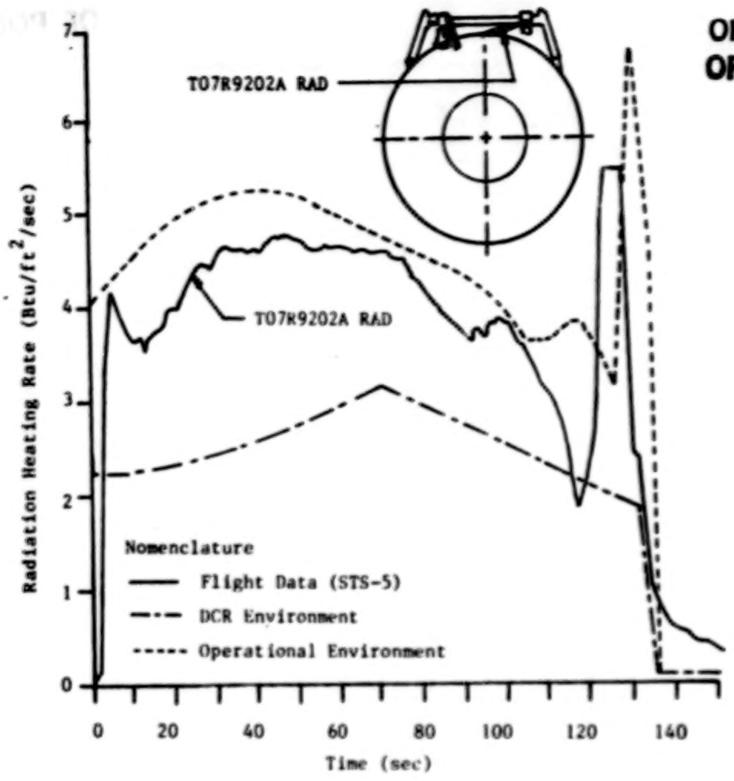

Figure 32.- ET/orbiter attach structure radiation base heating.

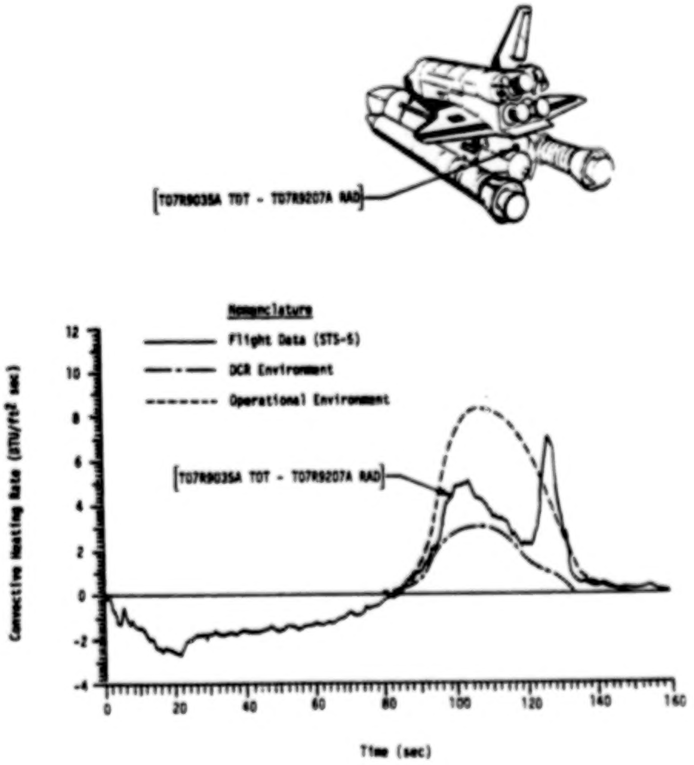

Figure 33.- External tank convective base heating.

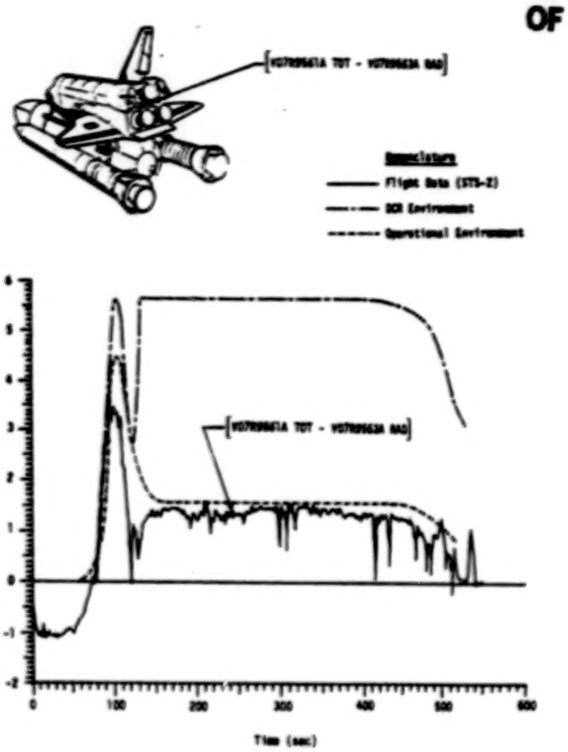

Figure 34.- Orbiter heat shield convective base heating.

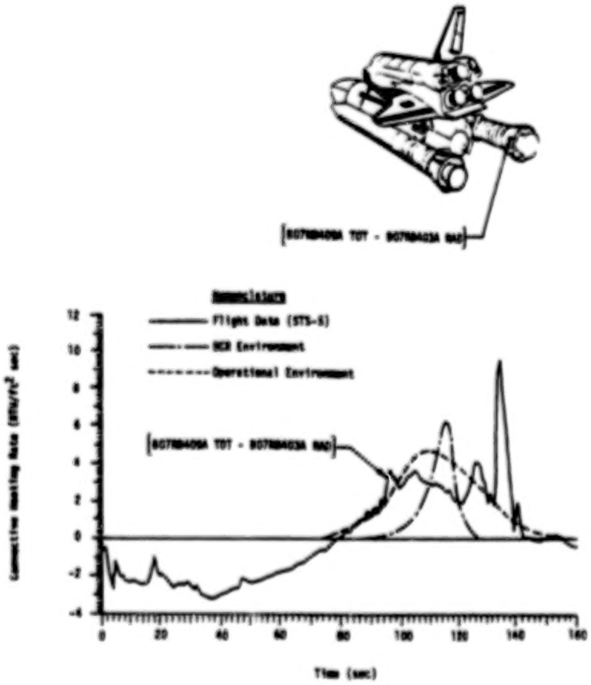

Figure 35.- SRB aft skirt convective base heating.

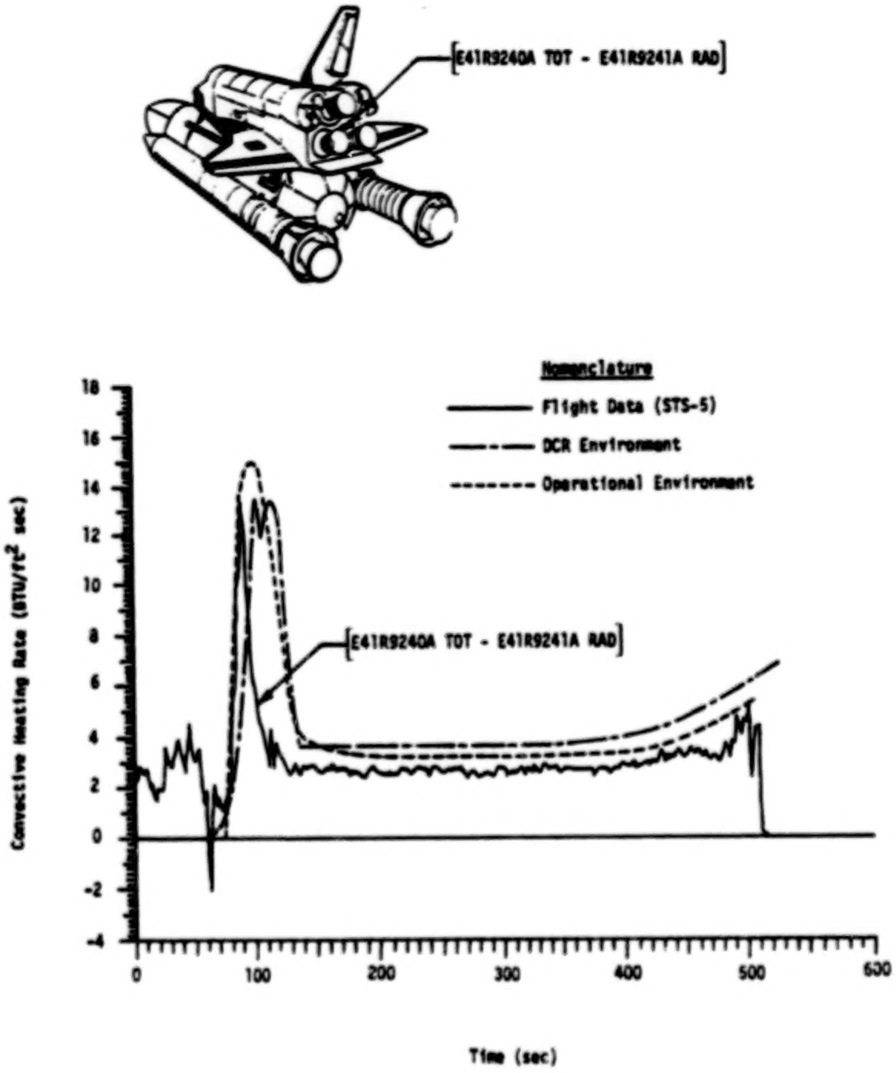

Figure 36.- SSME number 2 convective base heating.

N84
10146

UNCLAS

N84 10146 D2

TRENDS IN SHUTTLE ENTRY HEATING FROM THE CORRELATION OF FLIGHT TEST MANEUVERS

James K. Hodge
Air Force Institute of Technology
Wright-Patterson Air Force Base, Ohio

SUMMARY

A new technique was developed to systematically expand the aerothermodynamic envelope of the Space Shuttle Thermal Protection System (TPS). The technique required transient flight test maneuvers which were performed on the second, fourth, and fifth Shuttle reentries. Kalman filtering and parameter estimation were used for the reduction of embedded thermocouple data to obtain best estimates of aerothermal parameters. Difficulties in reducing the data were overcome or minimized. Thermal parameters were estimated to minimize uncertainties, and heating rate parameters were estimated to correlate with angle of attack, sideslip, deflection angle, and Reynolds number changes. Heating trends from the maneuvers allow for rapid and safe envelope expansion needed for future missions, except for some local areas.

INTRODUCTION

Because of the lifting capability of the Space Shuttle orbiter, its ranging capability and the aerodynamic heating to its TPS can vary significantly with attitude and in turn with the reentry trajectory. Flight simulators for most airplanes today have fairly standardized equations of motion in terms of linearized stability and control derivatives for example. No such capability existed for aerodynamic heating. Development of a standardized procedure on flight simulators was and is needed for manned reentry vehicles.

Most heat transfer data from wind tunnel tests for the orbiter were fairly standardized. The ratio of film transfer coefficient to a reference stagnation coefficient was tabulated as a function of angle of attack, sideslip, deflection angle, and Reynolds number. The wind tunnel data must be scaled to flight conditions, however, especially when the flow in the wind tunnel was transitional. Various theories to accomplish this were often buried in large programs which primarily output temperature time histories and were not appropriate for flight simulators or for mission planning. A simplified method (Ref. 1-2) was used for mission planning and was adapted and modified for flight simulators (Ref. 3-5). A one-dimensional thermal model was used to improve accuracy for bondline temperatures, and simplified heating ratios were modified to a tabulated form similar to the wind tunnel ratios, or scaled ratios could be used. An added advantage of this approach was flexibility for updating from flight test data.

A systems approach was used to develop the new technique for aerothermodynamic envelope expansion of the orbiter for operational missions at Vandenburg Air Force Base. A diagram of the approach is summarized by Figure 1. The systems approach essentially addresses operational needs for the life of the vehicle and not just

PRECEDING PAGE BLANK NOT FILMED

PAGE 686 INTENTIONALLY BLANK

needs for the next flight. Once the vehicle design was frozen, wind tunnel data and theory established a simulator data base for heating ratios. Tabulated heating ratios and a one-dimensional thermal model for several control points (Ref. 6) were programmed on the simulator at the Air Force Flight Test Center (AFFTC) to obtain both surface and bondline temperatures. Using the thermal model also allowed calculation of temperatures which would be measured by existing thermocouples in the TPS. Thus, not only were temperatures on future operational flights predicted, but thermocouple response during transient flight test maneuvers was also simulated. The data reduction technique for heating estimation, referred to as HEATEST, was developed to estimate heating parameters in a manner similar to estimation of stability and control derivatives during aerodynamic flight test maneuvers. Pushover-pullup (POPU) maneuvers and flap maneuvers caused sufficient thermocouple response to allow aerothermodynamic envelope expansion. The POPU allowed angle of attack envelope expansion (heating as a function of angle of attack) needed for more cross range. Flap maneuvers allowed axial center of gravity expansion (heating as a function of elevon and flap deflection.). Lateral center of gravity expansion (heating as a function of sideslip) could not be accomplished by maneuvers. By addressing the overall need for flexible and quick updating of the simulator data base, almost identical equations for the thermal model and heating rates were used in the data reduction program.

The data reduction program actually became a data correlation program when thermocouple data from flight test maneuvers were input. Maneuvers were designed to vary angle of attack, for example, while other variables were nearly constant. The heating rate at a given angle of attack was assumed to be the same, and thus to correlate. Otherwise, any hysteresis during a manuever would be due to error in the thermal model. Uncertainty was thus decreased by identifying this error by estimating thermal model parameters. Use of a Kalman filter further minimized other uncertainties due to modeling. Details of the technique are given in References 3,4,5, and 7.

Lessons have been learned by applying this new technique to thermocouple data from flight test maneuvers on the second and fourth Space Transportation Systems flights (STS-2 and STS-4). Another maneuver is also available from STS-5. Real-gas effects, internal radiative and convective cooling, and late transition are among heating trends which have been identified from thermocouple data, but only trends from transient flight test maneuvers will be emphasized in this paper.

THERMOCOUPLE INSTRUMENTATION

The excellent thermocouple instrumentation embedded in the orbiter TPS was designed for typical reentry profiles, and not for transient flight test maneuvers. For future vehicles, considerations for flight test maneuvers should be emphasized.

Surface thermocouples were installed in the TPS and covered with a thin coating of thickness ΔX_A. This coating was applied by hand and according to weight, not thickness. For a transient maneuver, error in the coating thickness can cause large uncertainty in the heating rate. Error in the specific heat and conductivity of the coating could also cause more uncertainty. Therefore, an effective coating thickness (equivalent to the surface thermocouple depth and including any significant wire heat capacity) was estimated during flight test maneuvers by the HEATEST program.

The coating thickness of High-temperature Reusable Surface Insulation (HRSI) was expected to be between 10 to 15 mils (0.025 to 0.04 cm). Estimates for coating thickness on HRSI have varied between a maximum of 21 mils (0.05 cm) at an outboard elevon location (V07T9730) to 15 mils at a lower surface location (V09T9527).

Nomex felt Flexible Resuable Surface Insulation (FRSI) coating was expected to be around 7 mils (0.02 cm). A location on the side of the Orbital Maneuvering System (OMS) pods were of primary concern because of discoloration of the FRSI during the first flight (STS-1). Because of the discoloration, the FRSI was apparently coated again, increasing the coating thickness. An estimate for the FRSI coating during the Mach 20 POPU on STS-2 was 20 mils (0.05 cm) at one location (V07T9976). However, a time skew of 3 seconds was also necessary for data correlation.

Time skews were identified as a serious problem based on estimates from simulated thermocouple data in Ref. 3. If thermocouple samples incorrectly led samples of the angle of attack by only one second, for example, estimates for the HRSI coating thickness became negative and physically unrealistic. If the thermocouple lagged by a second, then the estimates for coating thickness increased. Since the thermocouple and angle of attack were recorded on different recorders with no common clock, there was and is a concern over time skews. The actual sample time was also unknown within the sampling rate, which was once per second for thermocouples and angle of attack.

Thermocouples were not calibrated before the first flights. Most of the error associated with a calibration would probably only be in the form of a bias since calibration curves for thermocouples are well known. Most bias errors could be checked at ambient conditions inside the hangar within the data recorder resolution, which for the orbiter was an eight-bit word. This resolution was the primary noise source for the reduction of orbiter thermocouple data during transient maneuvers. Each thermocouple was scaled according to the anticipated maximum temperature at its location to minimize the resolution error. Calibration curves were then approximated by polynomials and an additional small error was introduced.

It is suggested that thermocouple installation on future vehicles with a low-conductivity thermal protection system be similar to the orbiter with the following improvements. A pressure transducer, surface thermocouple, and bondline thermocouple should be at the same location to enhance utilization of all measurements. A step input to the installed thermocouples with a known heat source should be used to verify the thermal model (at least at ambient conditions). The timing of the step input relative to the thermocouple samples is crucial to accurate estimation of the effective coating thickness. An accurate calibration curve could be practically used if all thermocouples of the same type are scaled identically and higher data resolution is used. Raw-data reduction would be simplified at the expense of more data storage capability. Real-time data links could possibly offset the additional data storage. In addition, fewer thermocouples may be necessary because of a better understanding of reentry heating gained from the thermocouple measurements on the orbiter. More flexibility in installing thermocouples at critical locations, which may not be identified until after a first flight, could also reduce the number of measurements. Although a higher sample rate is needed during flight test maneuvers, a lower sample rate may be sufficient for most of the reentry.

THERMOCOUPLE DATA REDUCTION

The reduction of thermocouple data using the HEATEST program was first successfully demonstrated by simulating thermocouple data on a typical lower surface location (Ref. 3). Thermocouple data on HRSI during a transient maneuver in a wind tunnel test was also reduced (Ref. 3, 4, and 5), but difficulty in estimating coating thickness was encountered. Thermocouple data from STS-1 were reduced in References 3 and 7, although data were lost above Mach 14 and there were no maneuvers. Thermocouple data from STS-2 and STS-4 have also been reduced (Ref. 4-6). The data reduction technique and the lessons learned concerning the technique are discussed.

The heating equations and one-dimensional model are referred to as the heating model and thermal model. These models were chosen to be nearly identical to the simulator equations. The ratio (denoted by a bar) of the heating rate (q) or film transfer coefficient (h) to an appropriate reference condition was assumed to be a linear function of the form

$$\begin{aligned}\bar{q} = \bar{q}_o &+ \bar{q}_\alpha (\alpha-\alpha_o) + \bar{q}_\beta (\beta-\beta_o) \\ &+ \bar{q}_{\log RE} (\log RE - \log RE_o) \\ &+ \bar{q}_{\delta e} (\delta e - \delta eo) + \bar{q}_{\delta bf} (\delta_{bf} - \delta_{bfo}) \qquad (1)\end{aligned}$$

where $\bar{q}_o$ is the magnitude or intercept at the reference conditions specified by the zero subscript on each variable. The subscripts on the heating ratio ($\bar{q}$) represent partial derivatives with respect to each variable. The variables are angle of attack (α), sideslip (β), logarithm of the freestream Reynolds number (log RE), elevon deflection angle (δe), and flap deflections (δ_{bf}). Second-order terms with second-derivative parameters were also added somtimes to account for nonlinearity. The heating model in the simulator was analogous to the linear equation when the heating parameters $\bar{q}_o$, $\bar{q}_\alpha$, $\bar{q}_\beta$, $\bar{q}_{\log RE}$, $\bar{q}_{\delta e}$, and $\bar{q}_{\delta bf}$ are functions of the appropriate variables. For data reduction during maneuvers, these parameters were assumed to be constant for short time durations, but to vary during the reentry. The heating rate was obtained by multiplying the ratio by the reference heating (q_r). The heating rate was input to the one-dimensional thermal model. A typical TPS cross section for Reusable Surface Insulation (RSI) is shown in Figure 2. The thermal-model equations were solved by the same finite-element (or finite-diffference) method as on the simulator and require initial conditions.

A simplified diagram of the HEATEST algorithm is shown in Figure 3. The MODEL block was identical to the simulator model except the sensitivity and covariance of the temperature at each node were also propagated in time. Initial conditions in the IC block were required for temperature (U), the sensitivity ($U_{\theta k}$) of the temperature to each parameter (θ_k), and the covariance (P) of the temperature. The parameters (θ_k) include both thermal and heating model parameters. The propagated or predicted temperature, sensitivity, and covariance are referred to as a priori values and are denoted by a minus superscript.

If a thermocouple measurement was available, then the a priori temperature was compared with the measured temperature in a Kalman filter algorithm (Ref. 3, 4, 5, and 7) which is referred to as a KALMAN UPDATE. Depending on the Kalman filter tuning (i.e., the uncertainty in the measurement and models), the a priori values were updated to a posteriori values which were donoted by a plus superscript. This process was repeated in a TIME LOOP until the end of a given time segment.

A Newton-Ralphson algorithm was then used to update heating and thermal parameters in the PARAMETER UPDATE block to satisfy a maximum likelihood function for each parameter (Ref. 3, 4, 5, and 7). With the updated parameter, the TIME LOOP was repeated. This process was repeated for a fixed number of iterations.

FLIGHT DATA REDUCTION

The HEATEST algorithm was applied to flight thermocouple data. Some difficulty was encountered due to data loss, initial condition generation, and excessive computer time.

Onboard thermocouple data were lost on STS-1 and STS-4, and only telemetry data were obtained. Therefore, the only flights with maneuvers and with thermocouple data are STS-2 and STS-5. Data from STS-5 were not available in time for this paper, but do not appear to change any results. Pressure measurements were lost on STS-2. Therefore, predicted pressures were used for determining RSI conductivity. Telemetry data from STS-4 partially covered both POPU maneuvers, but caused concern for initial conditions.

Errors in initial conditions were determined to be a source of error in heating parameter estimates based on studies with simulated thermocouple data (Ref. 3). For STS-2, initial conditions were generated by reducing all thermocouple data from entry interface to just prior to the maneuvers at approximately Mach 21. Initially, the on-board dynamic pressure and velocity were used to calculate density. When the pitch jets fired at low dynamic pressure, a large spike was caused in the dynamic pressure and thus in density. HEATEST estimated large angle of attack derivatives since no input variables except angle of attack were changing. If the pitch jets were input and the heating allowed to correlate with this variable, then the program should identify the error. Time segment size was increased instead. The initial conditions for STS-2 maneuvers should therefore be accurate, but excessive computer time was required.

Several methods to decrease the computer time were implemented. Most of the time was used to propagate the covariance. First an adiabatic wall type boundary condition was assumed only for the covariance at a few nodes from the surface. Another approximate initial condition generation procedure was based on a circuit analogy with an emperically determined time constant (Ref. 4-5). Finally, old inefficient library routines were replaced by new more efficient routines (Ref. 8). Analysis of the Mach-20 POPU at a lower surface location (V09T0527-V07T9531) with 14 nodes required 440 seconds on a Cyber 74. The new routines decreased the time to 44 seconds. Using the adiabatic wall assumption would decrease this further but would not allow the use of all in-depth thermocouples. Approximate initial conditions were generated 50 seconds prior to the maneuver and HEATEST was used for initial conditions for the POPU. The behavior of the Kalman filter at each measurement node was demonstrated as shown in Figure 4.

TRENDS FROM FLIGHT TEST MANEUVERS

Heating and thermal parameters were estimated during maneuvers. Estimates for effective coating thickness have already been discussed. Heating trends from these maneuvers were obtained at a few locations and are presented at a point representative of the lower surface, the elevon control surface and OMS pods on the upper surface.

Lower Surface

Because of the data loss on STS-4, a lower-surface location (V09T9527-V07T9531) with five embedded thermocouples was investigated. Time histories of the surface thermocouple and angle of attack of the Mach 20 POPU during STS-2 are shown in Figure 5. Time histories of the Mach 12 and 8 POPU during STS-4 are shown in Figures 6 and 7. Note that the pullup portion of the Mach 12 maneuver was unusually lon and that telemetry data started during the pushover. Note that the Mach 8 maneuver was short duration.

Results for the Mach 20 maneuver agreed well with wind tunnel data as shown in Figure 8. The trend in angle of attack agrees well and demonstrates that the linear assumption in angle of attack was valid.

The angle of attack heating derivative was lower at Mach 12. This could be a Mach effect or initial condition error caused by the data loss and transition to fully turbulent flow above 44 degrees angle of attack. As seen in Figure 6, the temperature was higher than the simulated temperature based on laminar heating rates In addition, as suggested by Hertzler (Ref. 6), the axial accelerometer measurement (axial drag) increased discretely for angles of attack above 44 degrees, typical of flow transition, and decreased back to laminar flow below 44 degrees. Thus, sensitivity of transition to angle of attack was demonstrated.

The flow was fully turbulent during the Mach 8 POPU. The higher heating magnitude and larger uncertainty bound are shown in Figure 7. The higher uncertainty was due to the short duration maneuver and perhaps to heating changes with Reynolds number. A Reynolds number derivative could not be estimated even when the angle of attack derivative was fixed. An alternate procedure used sequential five second time segments. The trend in Reynolds number, assuming the angle of attack trend was correct, is shown in figure 9.

Elevon Control Surface

Heating trends were sucessfully estimated at a location near the tip of the outboard elevon (V07T9730) for numerous maneuvers during STS-2. Time histories are shown for the Mach 21 flap maneuver and Mach 20 POPU in Figure 10. Because there was no thermocouple response, the flap maneuver at Mach 16 is not shown. The Mach 12 flap maneuver is shown in Figure 11.

Nonlinear heating trends in elevon deflection angle were evident as shown in Figure 12 for the Mach 21 maneuver. A second-order polynomial in elevon deflection was used. The cause of the increased heating above five degrees elevon deflection is unknown but could be due to a localized flow phenomenon or to transition to turbulent flow. There is a possibility that a local separation bubble would cause the hypersonic buffet reported on STS-4 when the elevon schedule was five degrees. Because there was no thermocouple response during the Mach 16 maneuver, the elevon heating derivative was zero. This result implies that the heating estimates at Mach 21 are more nonlinear.

Results from the Mach 12 flap maneuver for fully turbulent flow on the elevon are also shown in Figure 12. The data correlated poorly for negative deflection angles. A localized phenomenon or transitional flow at small deflections could cause this behavior. For envelope expansion, the trends at the larger deflection angles were of primary concern. The lower elevon heating allowed for a trade-off with the flap control surface.

Heating on the flap was lower than expected for a given deflection angle, but because of a shift in the basic pitching moment, larger flap or elevon deflections were required. The heating on the flap changed dramatically with flap deflection, angle of attack, and elevon deflection during STS-2 maneuvers. There was also a Reynolds number trend which made data correlation very difficult (Ref. 9).

Orbital Maneuvering System Pods

The primary concern for angle of attack envelope expansion was the upper surface, especially the OMS pods. Time histories for the Mach 20 POPU during STS-2 are shown in Figure 13. A large unexpected response occurred on the side of the OMS pod (V07T9976). Although a three-second time skew was necessary, the results from parameter estimates correlate well as shown in Figure 14. The flow impingement on the pod started at 37 degrees angle of attack instead of at 30 degrees as in the wind tunnel. In addition, estimates in Ref. 6 from STS-4 indicate less dependence on Reynolds number than in the wind tunnel. Visual inspection of FRSI discoloration as shown in Fig. 15 indicated a different pattern than expected based on predictions from wind tunnel data.

Investigation of transient maneuvers in the wind tunnel in Ref. 10 to estimate coating thickness demonstrated a similarity with the OMS pod heating. A three-second lag in the thermocouple response was found. A theoretical investigation in Ref. 11 of the lower heating magnitude reported in Ref. 3-5 confirmed the sensitivity of the heating to a discontinuity in wall temperature (or nonisothermal wall caused by an interface between different materials). The stainless-steel leading edge and HRSI test article on a flat plate in the wind tunnel had a step increase in wall temperature. On the OMS pod, there was a step decrease at the low-temperature RSI and FRSI interface as shown in Fig. 15. Therefore, the three-second time skew and some of the increased heating on the OMS pods may be attributed to the nonisothermal wall.

Numerous locations on the Orbiter have an interface between different materials and probably have the same nonisothermal-wall problem. One such local area would be the nose cap and HRSI interface where tiles have slumped due to increased heating as shown in Fig. 16. According to Ref. 11, such an interface near the leading edge would have a rapid recovery. The nose cap surface temperature peaks around Mach 18 corresponding to a POPU on STS-5. The nonisothermal wall effect would be largest at Mach 18. This effect should be considered when heating data is correlated and also for future designs.

REFERENCES

1. Evans, M.E.: Thermal Boundaries Analysis Program Document. NASA CR-151025, April 1975.

2. Space Shuttle Orbiter Entry Aerodynamic Heating Data Book. Rockwell Internationa Space Division Document Number SD73-SH-0814 C Revision, Books 1 and 2, Octobe 1978.

3. Hodge, J.K., Phillips, P.W., and Audley, D.R.: Flight Testing a Manned Lifting Reentry Vehicle (Space Shuttle) for Aerothermodynamic Performance. AIAA Paper 81-2421, November 1981.

4. Hodge, J.K., Audley, D.R., Phillips, P.W., and Hertzler, E.K.: Aerothermodynami Flight Envelope Expansion for a Manned Lifting Reentry Vehicle (Space Shuttle). Paper 3-A, AGARD CP-339, October 1982.

5. Hodge, J.K., and Audley D.R.: Aerothermodynamic Parameter Estimation from Space Shuttle Thermocouple Data During Transient Flight Test Maneuvers. AIAA Paper 83-0482, January 1983.

6. Hertzler, E.K. and Phillips, P.W.: Flight Test Derived Heating Math Models for Critical Locations on the Orbiter during Reentry. Shuttle Performance: Lessons Learned, NASA CP-2283, Part 2, 1983, pp. 703-718.

7. Audley, D.R., and Hodge, J.K.: Identifying the Aerothermodynamic Environment of the Space Shuttle Orbiter, Columbia. 6th IFAC Symposium on Identification and System Parameter Estimation, June 1982.

8. Sagstetter, P.W.: Numerical Computation of the Matrix Riccati Equation for Heat Propagation During Space Shuttle Reentry. Master's Thesis, AFIT/GCS/MA/82D-7, Air Force Institute of Technology, Wright-Patterson AFB, Ohio.

9. Wood, J.R.: Body Flap Heat Transfer Data from Space Shuttle Orbiter Entry Flight Test Maneuvers. Master's Thesis, AFIT/GA/AA/82D-12, Air Force Institut of Technology, Wright-Patterson AFB, Ohio.

10. Woo, Y.K.: Transient Heat-Transfer Measurement Technique in Wind Tunnel and Dat Analysis Technique Using System Identification Theory. Master's Thesis, AFIT/GAE/AA/82D-34, Air Force Institute of Technology, Wright-Patterson AFB, Ohio.

11. Cappelano, P.T.: Heat Transfer/Boundary Layer Investigation of Heating Discrepancies in Wind Tunnel Testing of Orbiter Insulating Articles. Master's Thesis AFIT/GA/AA/82D-3, Air Force Institute of Technology, Wright-Patterson AFB, Ohio.

ORIGINAL PAGE IS
OF POOR QUALITY

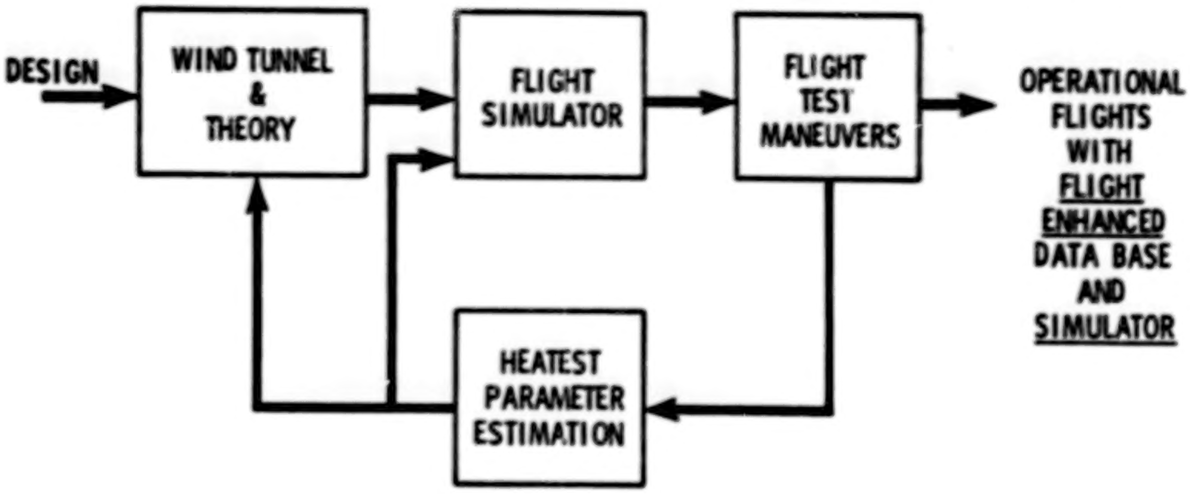
DESIGN
WIND TUNNEL & THEORY
FLIGHT SIMULATOR
FLIGHT TEST MANEUVERS
OPERATIONAL FLIGHTS WITH FLIGHT ENHANCED DATA BASE AND SIMULATOR
HEATEST PARAMETER ESTIMATION

Figure 1.- Systems approach to envelope expansion.

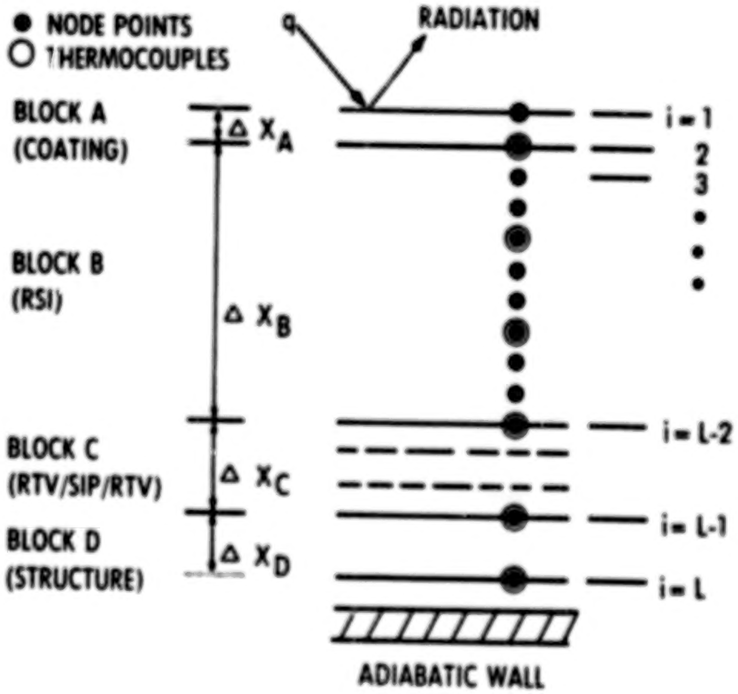
NODE POINTS
THERMOCOUPLES
q
RADIATION
BLOCK A (COATING)
Δ X_A
BLOCK B (RSI)
Δ X_B
BLOCK C (RTV/SIP/RTV)
Δ X_C
BLOCK D (STRUCTURE)
Δ X_D
i = 1
2
3
i = L-2
i = L-1
i = L
ADIABATIC WALL

Figure 2.- TPS model cross section.

ORIGINAL PAGE IS
OF POOR QUALITY

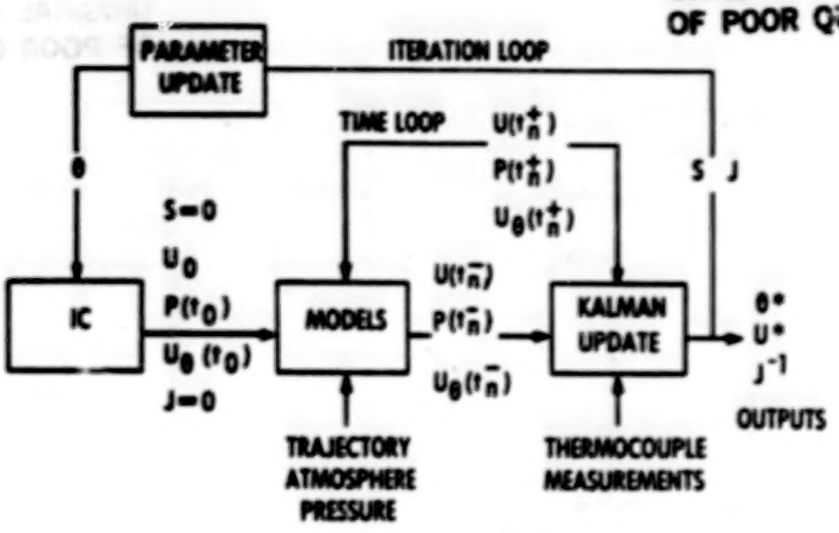
PARAMETER UPDATE
ITERATION LOOP
TIME LOOP
$U(t_n^+)$
$P(t_n^+)$
$U_\theta(t_n^+)$
S J
θ
S=0
U_0
$P(t_0)$
$U_\theta(t_0)$
J=0
IC
MODELS
$U(t_n^-)$
$P(t_n^-)$
$U_\theta(t_n^-)$
KALMAN UPDATE
θ*
U*
J^{-1}
OUTPUTS
TRAJECTORY
ATMOSPHERE
PRESSURE
THERMOCOUPLE
MEASUREMENTS

Figure 3.- Simplified HEATEST flow diagram.

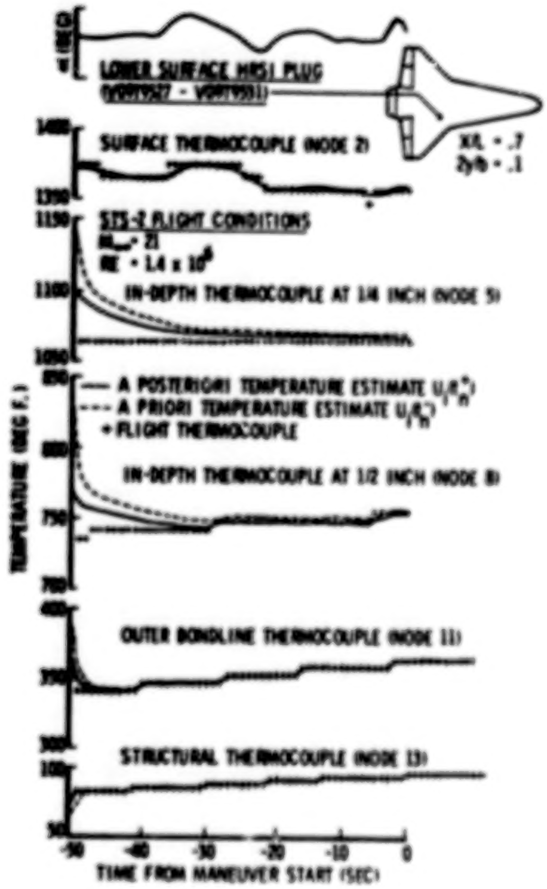

Figure 4.- Comparison of a priori and a posteriori temperature estimates of extended Kalman estimator starting from approximate initial conditions.

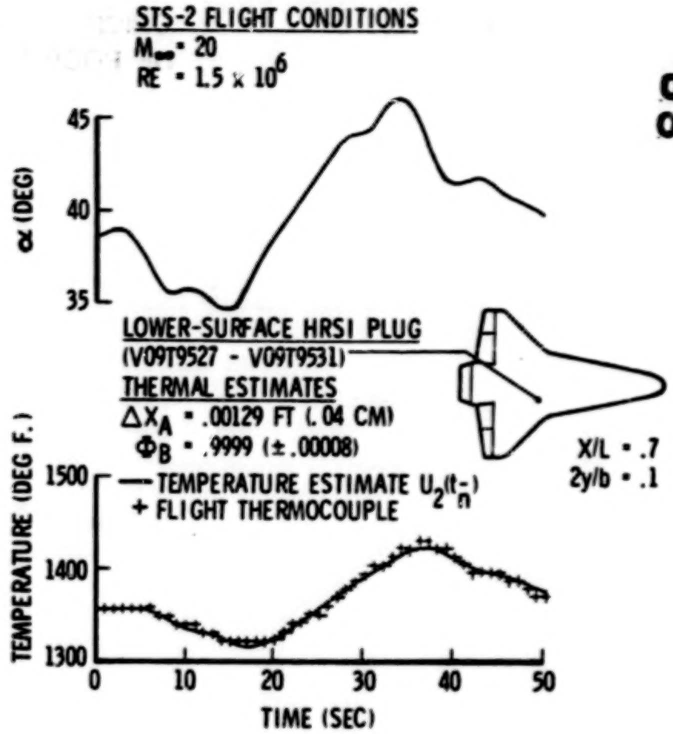

Figure 5.- Lower-surface-plug STS-2 flight thermocouple data (Mach 20 pushover-pullup maneuver).

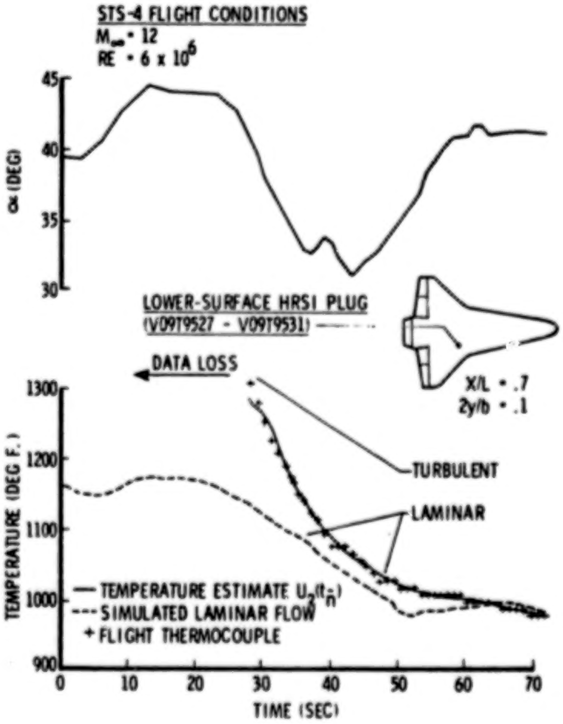

Figure 6.- Lower-surface-plug STS-4 flight thermocouple data with transition onset during Mach 12 pullup-pushover maneuver.

ORIGINAL PAGE IS
OF POOR QUALITY

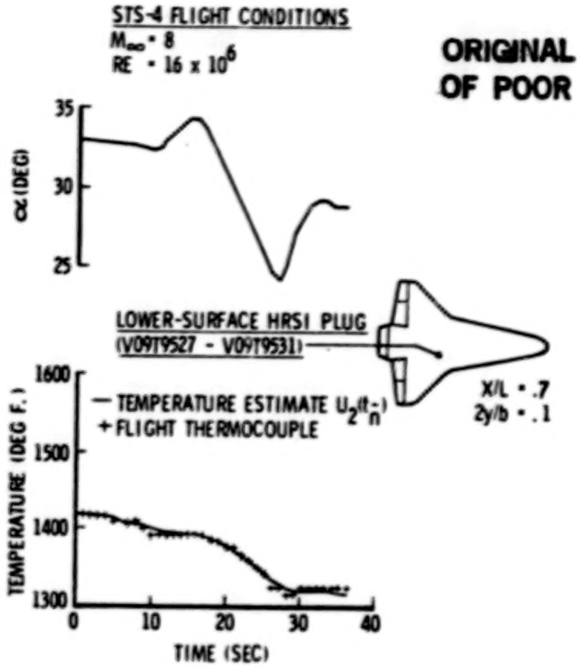

Figure 7.- Lower-surface-plug STS-4 flight thermocouple data for turbulent flow (Mach 8 pullup-pushover maneuver).

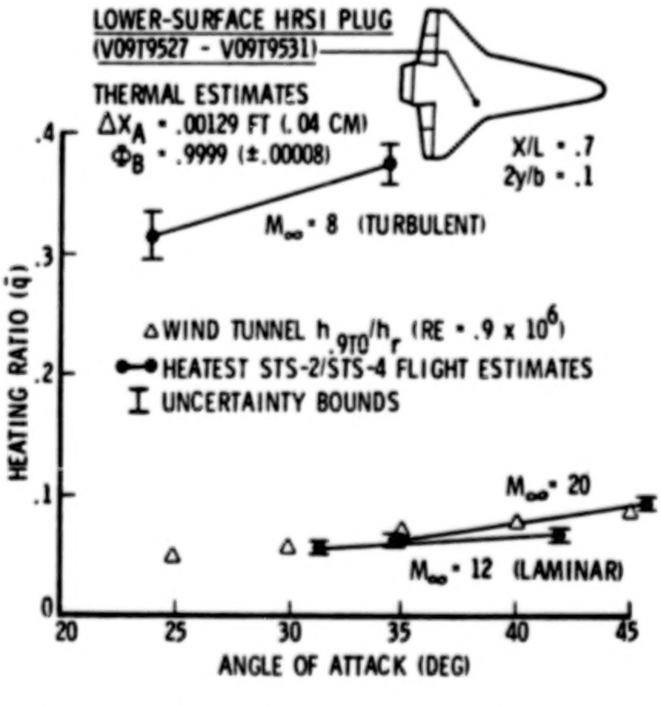

Figure 8.- Heating estimates for lower surface plug from STS-2/STS-4 flight thermocouple data.

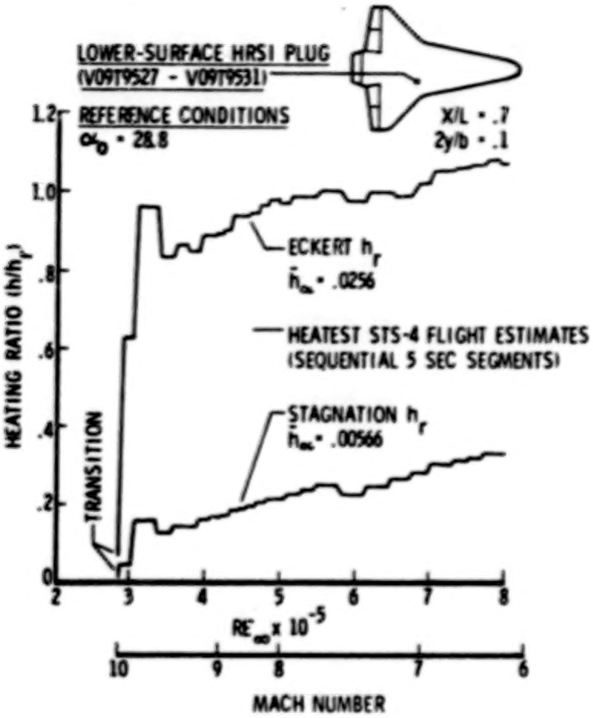

Figure 9.- Heating comparison for STS-4 thermocouple data using both stagnation and Eckert turbulent reference heating to show Reynolds number trends.

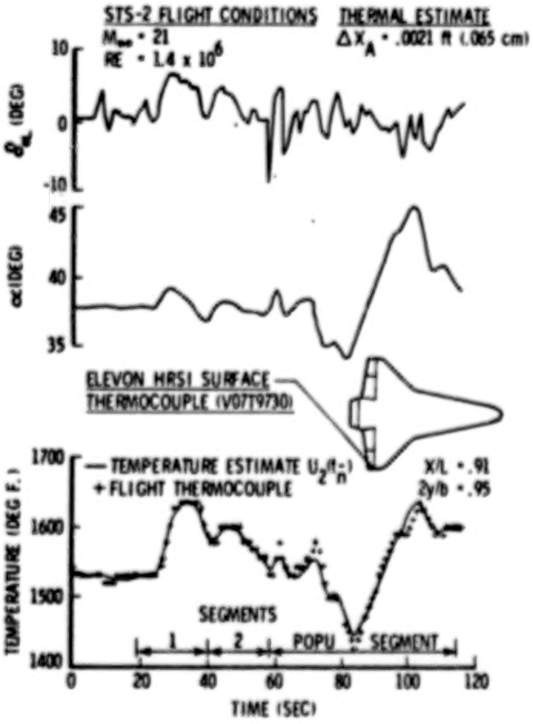

Figure 10.- Outboard elevon STS-2 flight thermocouple data (Mach 21 flap maneuver and Mach 20 pushover-pullup maneuver).

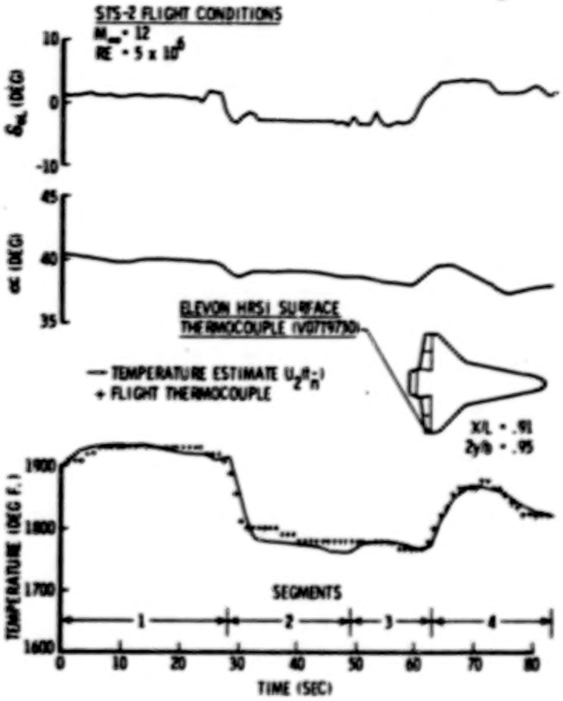

Figure 11.- Outboard elevon STS-2 flight thermocouple data (Mach 12 flap maneuver).

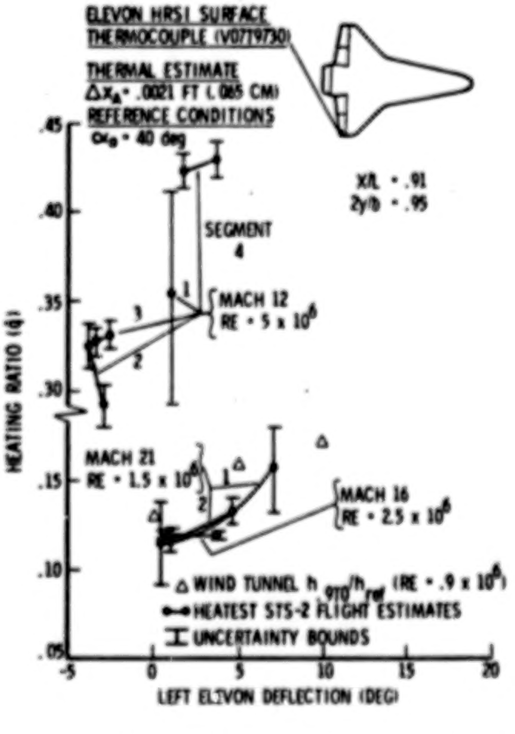

Figure 12.- Heating estimates for outboard elevon from STS-2 flight thermocouple data.

ORIGINAL PAGE IS
OF POOR QUALITY

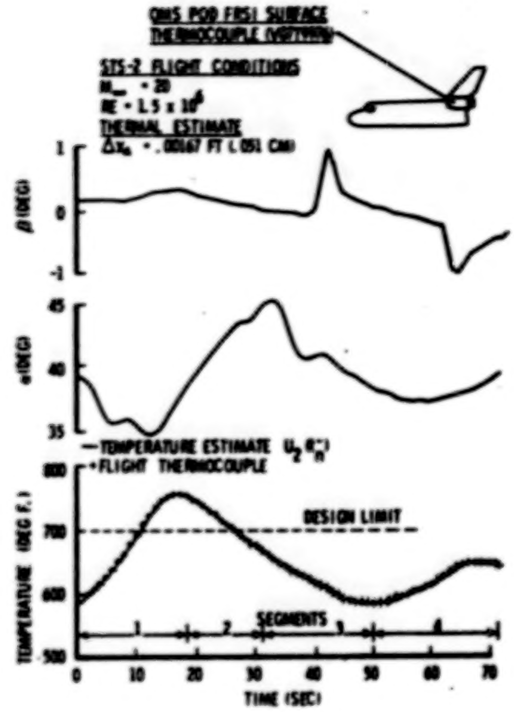

Figure 13.- OMS pod STS-2 flight thermocouple data (Mach 20 pushover-pullup maneuver).

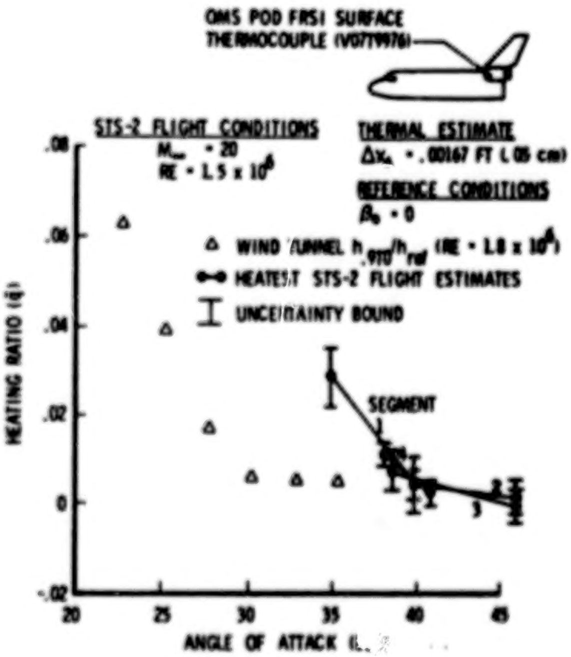

Figure 14.- Heating estimates for OMS pod from STS-2 flight thermocouple data (Mach 20 pushover-pullup maneuver).

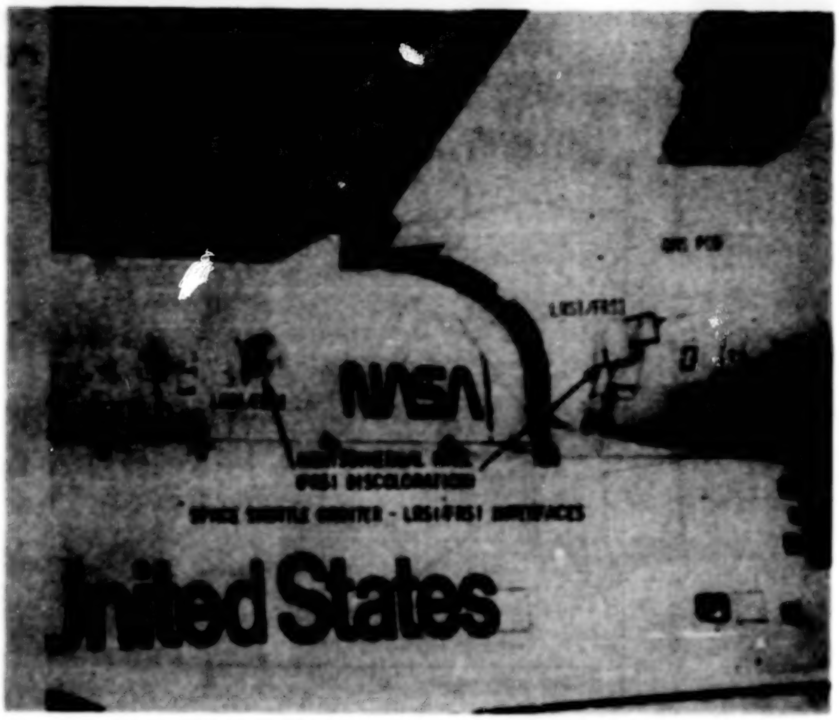
NASA
LRSI/FRSI
NONISOTHERMAL WALL
FRSI DISCOLORATION
SPACE SHUTTLE ORBITER - LRSI/FRSI INTERFACES
United States

Figure 15.- Space Shuttle orbiter LRSI/FRSI interfaces with a nonisothermal wall and FRSI discoloration.

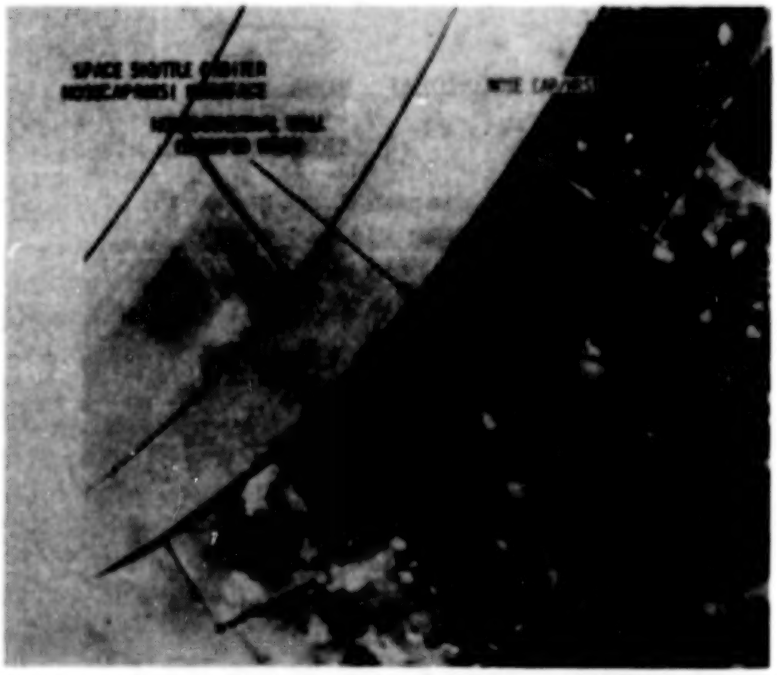
SPACE SHUTTLE ORBITER
NOSECAP/HRSI INTERFACE
NONISOTHERMAL WALL
SLUMPED HRSI
NOSE CAP/HRSI

Figure 16.- Space Shuttle orbiter nose CAP/HRSI interface with a nonisothermal wall and slumped HRSI.

N84
10147

UNCLAS

N84 10147 D3

FLIGHT TEST DERIVED HEATING MATH MODELS FOR CRITICAL LOCATIONS ON THE ORBITER DURING REENTRY

Elam K. Hertzler and Paul W. Phillips
Air Force Flight Test Center
Edwards Air Force Base, California

INTRODUCTION

An analysis technique was developed for expanding the aerothermodynamic envelope of the Space Shuttle orbiter without subjecting the vehicle to sustained flight at more stressing heating conditions. A transient analysis program was developed to take advantage of the transient maneuvers that were flown as part of this analysis technique. This program derived heat rates from flight test data for various locations on the orbiter. The flight-derived heat rates were used to update heating models based on predicted data. Future missions were then analyzed based on these flight-adjusted models.

This paper will present a technique for comparing flight and predicted heating-rate data and the extrapolation of the data to predict the aerothermodynamic environment of future missions.

ABBREVIATIONS AND SYMBOLS

AFFTC	Air Force Flight Test Center
deg F	degrees Fahrenheit
FRSI	Flexible Reusable Surface Insulation
HRSI	High Temperature Reusable Surface Insulation
KSC	Kennedy Space Center
LRSI	Low Temperature Reusable Surface Insulation
NASA	National Aeronautics and Space Administration
OMS	Orbital Maneuvering System
POPU	pushover-pullup
q	heating rate
q_{ref}	reference heating rate
Re_{∞}	free-stream Reynolds number
RTV	Room Temperature Vulcanized
STS-1,2,3,4,5	Space Transportation System flights 1, 2, 3, 4, and 5
TPS	Thermal Protection System

VAFB	Vandenberg AFB
X/L	longitudinal location nondimensionalized by the orbiter reference length
α	angle of attack, degrees
β	sideslip angle, degrees
δBF	bodyflap deflection, degrees
δe	elevator deflection, degrees

ANALYSIS TECHNIQUE

An analysis technique was developed (Figure 1) that allows accurate predictions of the aerothermodynamic environment of the Space Shuttle orbiter for future missions. Locations or control points were chosen based on the original NASA preflight selected control points (but at locations where temperature instrumentation was available) and the problem areas highlighted through analysis of wind tunnel data. A transient maneuver was designed where the Shuttle commander manually reduced the angle of attack of the orbiter to a predetermined point and then increased the angle of attack above the nominal (pushover-pullup (POPU)) so as to balance out the energy state of the orbiter. A transient analysis program was developed by the AFFTC that determined the change in the heating rate (nondimensionalized by a reference heating rate) with respect to angle of attack, sideslip, elevon deflection, or body flap deflection during the POPU maneuver. The transient analysis program utilized the actual flight trajectory, atmosphere, flight thermocouple data, one-dimensional thermal model, and material properties (Reference 1). An independent analysis program was also developed at the AFFTC that derived heat rates from the flight surface thermocouple data using an equilibrium temperature assumption and an empirically derived time constant in an algorithm which approximated the thermal properties of the coating. These two programs were applied to the flight data to update heating models for the AFFTC's control points which were originally based on both NASA contractor heating models and wind-tunnel-derived heating models. The final goal of this analysis was to use these flight-adjusted models to predict the surface and bondline temperatures for future missions. The predictions were calculated using a trajectory from a six-degree-of-freedom engineering simulator at the AFFTC and a one-dimensional thermal model.

This paper will not deal with the rigorous mathematical and statistical details of the computer programs utilized in this analysis. For details of this nature see References 2 and 3.

MATH MODELS

The AFFTC maintains nine thermodynamic math models, considered to be the most critical instrumented locations (control points), for the purpose of assessing the orbiter's ability to handle future missions. Figure 2 shows the locations of the various control points and their respective Thermal Protection System (TPS) materials along with the original NASA control points for comparison.

Lower Surface

The AFFTC heating math model on the centerline at X/L = 0.02 was originally comprised of the NASA contractor simplified heating model (Figure 3). The parameter estimation program was not utilized at this location due to the small response to angle of attack (as predicted) during the POPU maneuvers flown on STS-2, STS-4, and STS-5. The independent analysis program was used to obtain laminar heating levels for this location. The heating model was found to be conservative and was updated by reducing the heating levels by approximately 14 percent (Figure 4). Note that the flight-adjusted heating model matched the flight data quite well.

The AFFTC heating math model located on the centerline at X/L = 0.7 was originally the NASA contractor simplified heating model. The results from the transient analysis program for the STS-2 Mach 21 POPU dynamic test maneuver indicated that the laminar heating levels of the original heating model were conservative. The heating model was adjusted by reducing the laminar levels by approximately 14 percent. Additionally, the boundary layer transition in flight occurred at a higher Reynolds number (later in the entry) than predicted. Figure 5 shows a graphical representation of the original and flight-adjusted heating models. The independent analysis program was used to adjust the transitional and turbulent heating levels. The flight-adjusted heating model then provided a good comparison with flight data (Figure 6).

An off-centerline location at X/L = 0.7 was added which was more critical for missions with higher heat loads due to the thinness of the High Temperature Reusable Surface Insulation (HRSI) tiles in this region leading to increased bondline temperatures. (Bondline refers to the inner bondline which is representative of the structural skin temperature.) Similar methods of updating the heating model were applied to this location.

The AFFTC elevon control point was located at the left-hand outboard elevon tip and was originally based on a NASA contractor simplified heating model. Both the simplified and flight-adjusted heating models are graphically represented in Figure 7 (shown at zero deflection angle for simplicity). The model was updated with flight data results from both analysis programs. Figure 8 indicates how the original temperature predictions for STS-2 and those from the flight-adjusted model compare to the actual flight data. The actual transition occurred at a higher Reynolds number (i.e., later in the flight) than was the case for the original prediction.

The AFFTC body flap control point was located at the body flap edge and was based on the laminar portion of the NASA contractor simplified heating model for the centerline location. The simplified heating model contained information for body flap deflection angles of less than 15 degrees. Wind-tunnel-derived data was added to the flight-adjusted heating model in order to extend the model to body flap deflection angles of 22.5 degrees. The body flap edge location was chosen due to the consistently higher temperatures observed in the flight data when compared to the centerline thermocouple. Figure 9 indicates the adjustments made to the heating model utilizing results from the independent analysis program to extrapolate the laminar heating levels to the transitional and turbulent levels. The Mach 17 body flap sweep on STS-2 indicated an interaction between heating on the body flap and the elevon deflection angle. This phenomenon has not been incorporated into the model at present due to insufficient data. Figure 10 is the time history of the bodyflap edge thermocouple for STS-2 compared with predictions. The flight data indicated that the flow over the body flap may have been in a transitional/turbulent state for a large portion of the reentry before becoming fully turbulent. The original prediction of a rapid onset of boundary layer transition is obvious on this plot.

Results for the bondline temperatures at the X/L = 0.7 centerline location did not compare with flight test bondline measurements (Figure 11). One contributing factor was the late transition to turbulent flow, which led to a lower overall heat load. It was also determined that after the payload bay vent doors opened at Mach 2.5, the cool, atmospheric air allowed convective cooling to occur internally, which dissipated the heat soaking through to the backface of the structure, thereby reducing the bondline temperatures. (Backface refers to the back side of the substructure.) Additionally, the internal structure was cool enough to allow reradiation from the backface. Both the elevon tip and body flap edge were passively vented and were therefore subject to the free convective cooling effects. The lower backface of the control surfaces apparently radiated to the cooler backface of the upper surface. Terms to account for the free convective and radiative effects were applied to the one-dimensional thermal models for the fuselage and control surface control points. After the adjustments to the heating model were implemented, the bondline prediction for X/L = 0.02 was close to the actual flight data so the cooling effects were not applied.

Upper Surface

Two control points are located on the left Orbital Maneuvering System (OMS) pod (Figure 2). Postflight inspections have indicated that there are other problem areas on the upper surface (Reference 4) that will need to be modeled, but to date the OMS pod has received the most attention.

The aft OMS pod control point is located on the Flexible Reusable Surface Insulation (FRSI) at thermocouple V07T9976A. The wind-tunnel-derived and flight-adjusted heating models are shown on Figure 12. Figure 13 is a comparison of the thermocouple time history and predicted thermocouple response based on the heating models. A large discrepancy in the wind-tunnel-derived heating model and flight data was highlighted by the Mach 20 POPU maneuver indicated on Figure 13. The heating on the OMS pod is a function of angle of attack due to a vortex created at the wing glove area of the forward fuselage. (The heating is also dependent on Reynolds number and sideslip but to a lesser extent than angle of attack.) Specifically, as the angle of attack is reduced from the nominal 40 degree value, the vortex impinges on the OMS pod. Analysis of the wind tunnel data indicated that the impingement would occur abruptly at 30 degrees angle of attack, whereas the flight thermocouple data indicated that impingement began at about 37 degrees. Also, the effect of Reynolds number on the actual heating level due to the vortex impingement was underpredicted by the wind-tunnel-derived results. POPU maneuvers on flights two and four were analyzed with the parameter estimation program and the results were used to create the flight-adjusted model. Where flight data were not available, the flight-adjusted model was extrapolated based on trends.

Below 23 degrees angle of attack (Figure 12), the heating rate rapidly approaches the reference value (q/q_{ref} approaches 1) indicating attached flow conditions around the OMS pods. The yaw jet interaction effects were observed to disappear (Reference 5) at about the same flight condition, further supporting the likelihood of attached flow. The irregular shapes of the OMS pod heating models are probably related to sideslip effects rather than true irregularities with angle of attack as shown in the figure. There are insufficient data available at this time to separate and identify the angle of attack and sideslip effects.

The forward OMS pod control point was a recent development that was necessary in order to evaluate proposed changes to the OMS pod TPS. This location is on the Low Temperature Reusable Surface Insulation (LRSI) at thermocouple V07T9220A on OV-102. The heating model to date is adequate for a nominal 40-degree trajectory. However, for extrapolating to future missions more flight test information will be necessary to improve confidence.

The bondline temperatures for the OMS pod control points cannot be verified due to the absence of bondline instrumentation in these areas. The cooling effects applied to the lower surface were not felt to be appropriate for the OMS pod due to the existence of a thermal blanket behind the graphite epoxy structure.

Wing Leading Edge and Nose Cap

AFFTC wing leading edge and nose cap control points are located on the reinforced carbon-carbon wing leading edge (55 percent semispan) and the nose cap respectively. Both locations used the NASA contractor simplified heating models.

The wing leading edge control point simplified heating model is represented graphically in Figure 14. The models are considered to be of low confidence due to an inability to accurately model the three-dimensional aspects of the material and uncertainty in the interpretation of the flight test instrumentation. The close match between flight data and predictions shown in Figure 15 may, therefore, be fortuitous and no updating of the carbon/carbon heating models has been attempted.

The nose cap control point is not presented graphically since only one flight (STS-5) contained valid radiometer data from the nose cap. There is low confidence in the model due to the uncertainties discussed above (under the leading edge control point). In addition, the data from flight five indicated that the maximum heating was at the stagnation point on the nose cap instead of the sonic line where it was predicted to occur. Further attention is required in the future to produce high confidence math models of carbon/carbon material and to improve flight instrumentation so that valid comparisons can be made.

FUTURE MISSIONS

Flight test data to date have been used for the formation and/or updating of heating and thermal models for the orbiter TPS and aerothermal environment. However, the data have been limited due to the limited number of POPU maneuvers available and due to recorder malfunctions (STS-1, STS-4, and STS-5). In order for a high-confidence aerothermal model to be fully developed, additional reentry test maneuvers on an instrumented orbiter are needed. Design of future vehicles will benefit from a thorough understanding of angle of attack and Reynolds number effects on aerothermodynamic heating, especially for the upper surface. The maneuvers flown to date are indicated in Figure 16 along with the range of angle of attack capability required for operational flights. The lower angles of attack profile is associated with high crossrange entries like that required for an abort once around to Vandenberg AFB (VAFB). There is a lack of data below 30 degrees angle of attack and also between a Reynolds number of 5×10^6 and 15×10^6 which is extremely critical to the upper surface, specifically the OMS pods.

Figure 17 presents predicted surface and bondline temperatures for future reentries to both Kennedy Space Center (KSC), Florida, and VAFB, California. It is immediately obvious that the OV-102 OMS pod TPS is inadequate for any mission presented other than a 40-degree-angle-of-attack mission (nominal). Adequate margins exist at all other control points. AFFTC leading edge and nose cap points are of low confidence due to the uncertainties discussed earlier (nose cap prediction not presented).

There are other areas of concern that have not been dealt with by the AFFTC and are not subject matter of this report; for example, gap heating and tile slumping. Reference 4 presents more details.

LESSONS LEARNED

The reentry aerothermodynamic lessons learned are: windward-side heating predictions were conservative due to the combined effect of lower laminar heating levels, later-than-predicted transition to turbulent flow, and external atmospheric cooling. Structural peak temperatures were further reduced due to internal radiative and convective cooling. Leeside OMS pod heating, on the other hand, was underpredicted. Vortex impingement on the OMS pod occurred at a higher angle of attack than predicted (37 degrees rather than 30 degrees), and the unimpinged heating levels at 40 degrees angle of attack were higher than predicted.

CONCLUDING REMARKS

A flight test technique was developed and successfully used to verify predictive methods as well as select and update entry heating models. Discrepancies in heating predictions were identified. Basically, overprediction of windward-side heating and underprediction of leeside OMS pod heating were observed. The AFFTC flight test revised models have produced a good match of the respective test data for the first five orbital flights. High-confidence aerothermal models, particularly for the OMS pod, will require additional reentry heating flight test data. Design of future vehicles will benefit from continued orbiter testing through a thorough understanding of angle-of-attack and Reynolds number effects on aerothermodynamic heating, particularly on the upper surface.

REFERENCES

1. Space Shuttle Program Thermodynamic Design Data Book TPS Acreage Methods Validation, SD73-SH-0226, Volume 2, Book IIE, Rockwell International, Space Systems Group, Downey, CA, October 1981.

2. Hodge, J.K., Audley, D.R., Phillips, P.W., and Hertzler, E.K., Aerothermodynamic Flight Envelope Expansion for a Manned Lifting Reentry Vehicle (Space Shuttle), Flight Mechanics Symposium on Ground Flight Test Techniques and Correlation, Paper No. 3-A, AGARD CP-334, October 1982.

3. Hodge, J.K. and Audley, D.R., Aerothermodynamic Parameter Estimation from Space Shuttle Thermocouple Data During Transient Flight Test Maneuvers, 21st Aerospace Sciences Meeting, AIAA-83-0482, January 1983.

4. Hodge, J.K., Trends in Shuttle Entry Heating from the Correlation of Flight Test Maneuvers, Shuttle Performance: Lessons Learned, NASA CP-2238, Part 2, 1983, pp. 687-702.

5. Kirsten, P.W., Richardson, D.F., and Wilson, C.M., Predicted and Flight Test Results of the Performance, Stability, and Control of the Space Shuttle from Reentry to Landing, NASA CP-2283, Part 1, 1983, pp. 509-525.

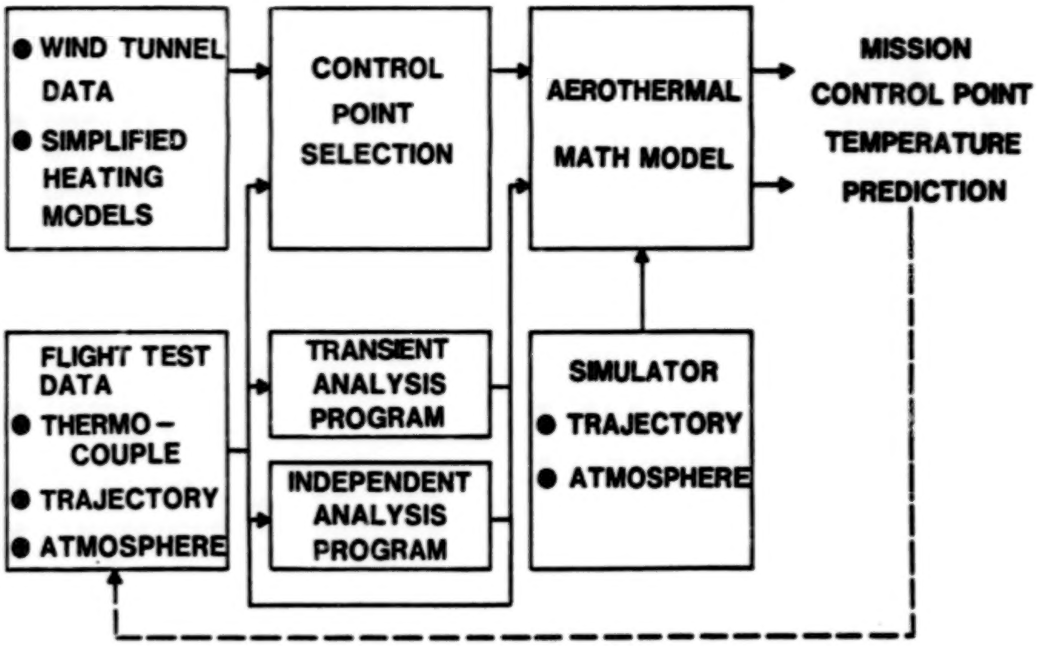
● WIND TUNNEL DATA
● SIMPLIFIED HEATING MODELS
CONTROL POINT SELECTION
AEROTHERMAL MATH MODEL
MISSION CONTROL POINT TEMPERATURE PREDICTION
FLIGHT TEST DATA
● THERMO-COUPLE
● TRAJECTORY
● ATMOSPHERE
TRANSIENT ANALYSIS PROGRAM
INDEPENDENT ANALYSIS PROGRAM
SIMULATOR
● TRAJECTORY
● ATMOSPHERE

Figure 1.- Analysis technique.

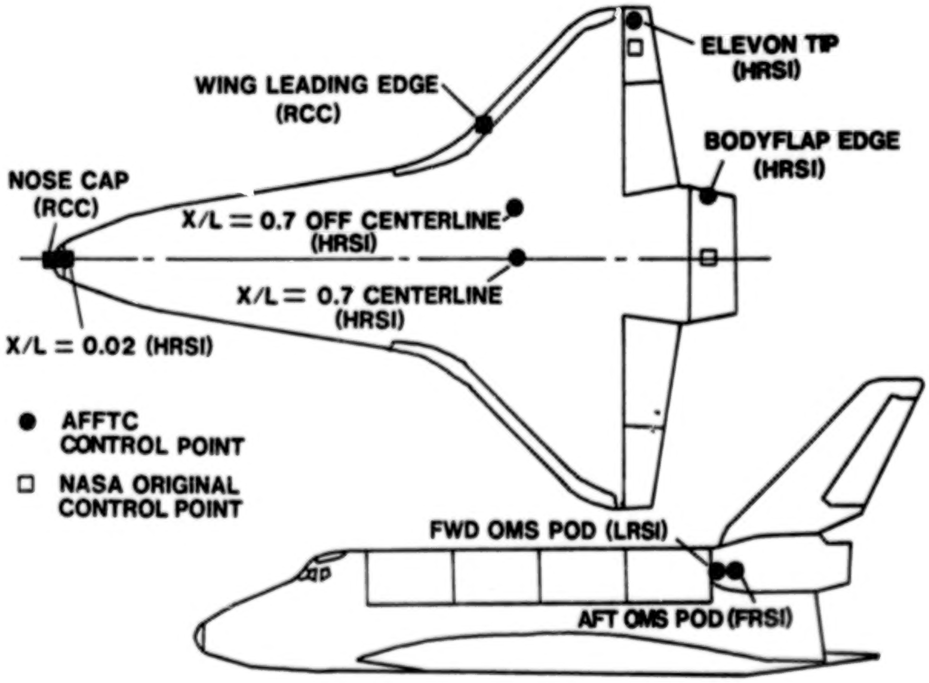
ELEVON TIP (HRSI)
WING LEADING EDGE (RCC)
BODYFLAP EDGE (HRSI)
NOSE CAP (RCC)
X/L = 0.7 OFF CENTERLINE (HRSI)
X/L = 0.7 CENTERLINE (HRSI)
X/L = 0.02 (HRSI)
● AFFTC CONTROL POINT
□ NASA ORIGINAL CONTROL POINT
FWD OMS POD (LRSI)
AFT OMS POD (FRSI)

Figure 2.- Temperature control points.

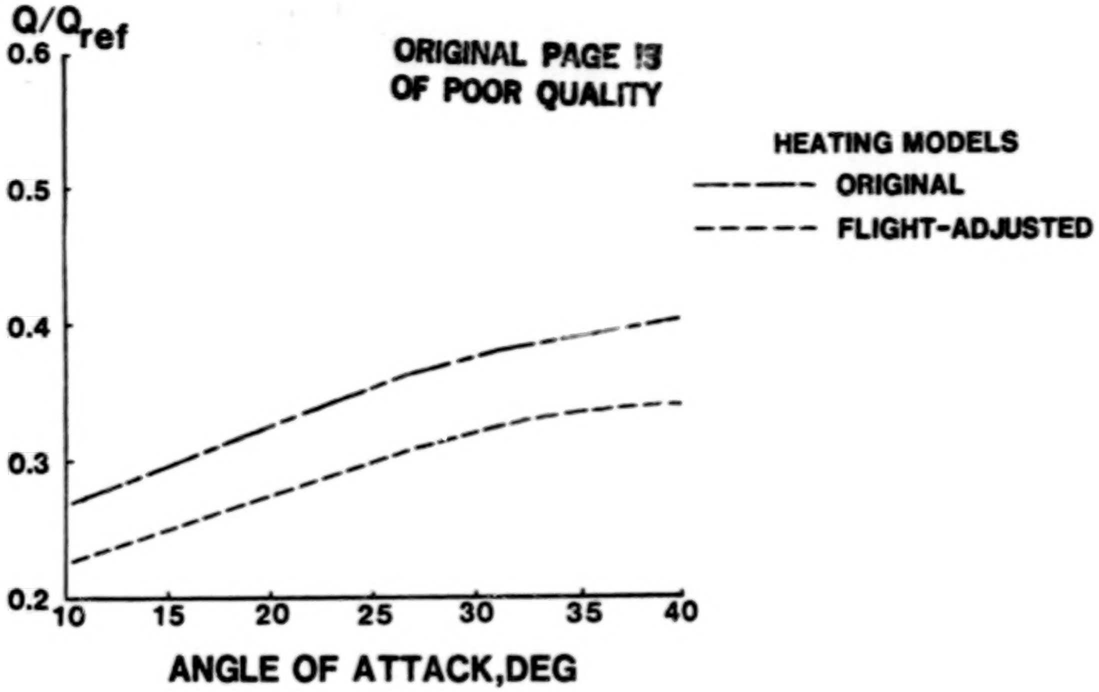

Figure 3.- Lower-surface heating model - forward location (X/L = 0.02).

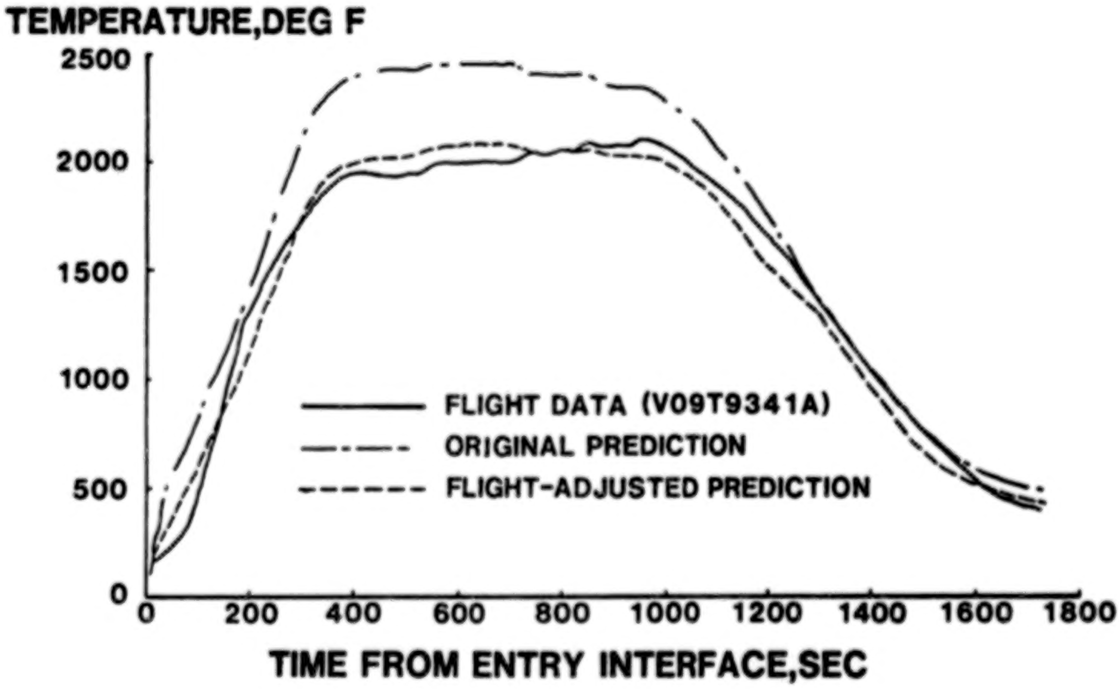

Figure 4.- Lower-surface temperature comparison - forward location (X/L = 0.02). STS-2.

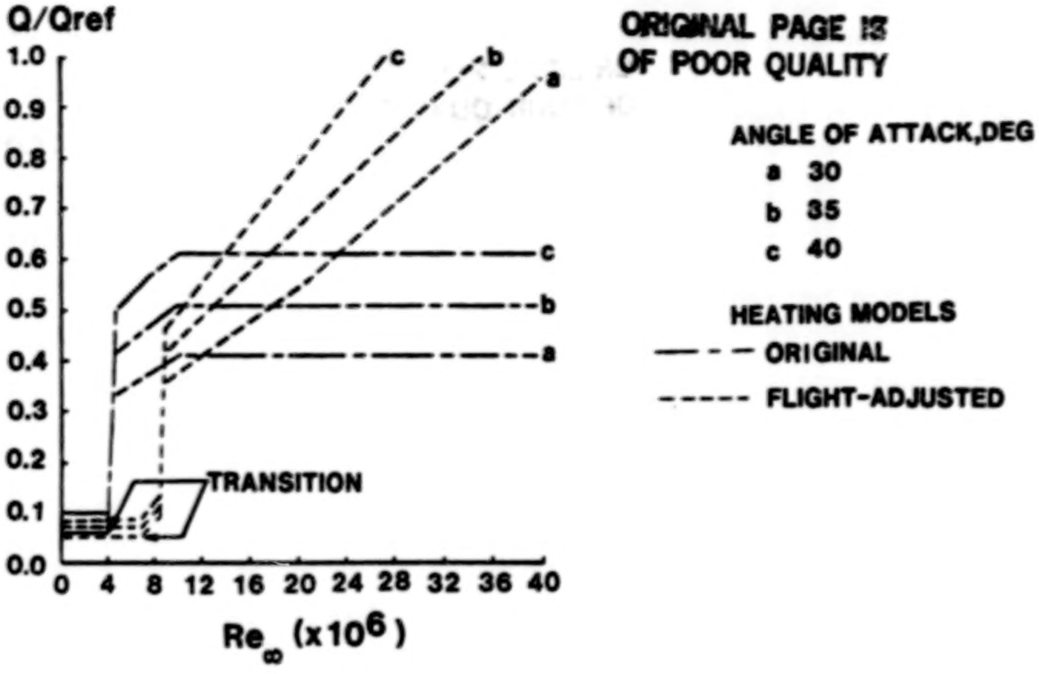

Figure 5.- Lower-surface heating model - aft location (X/L = 0.7 centerline).

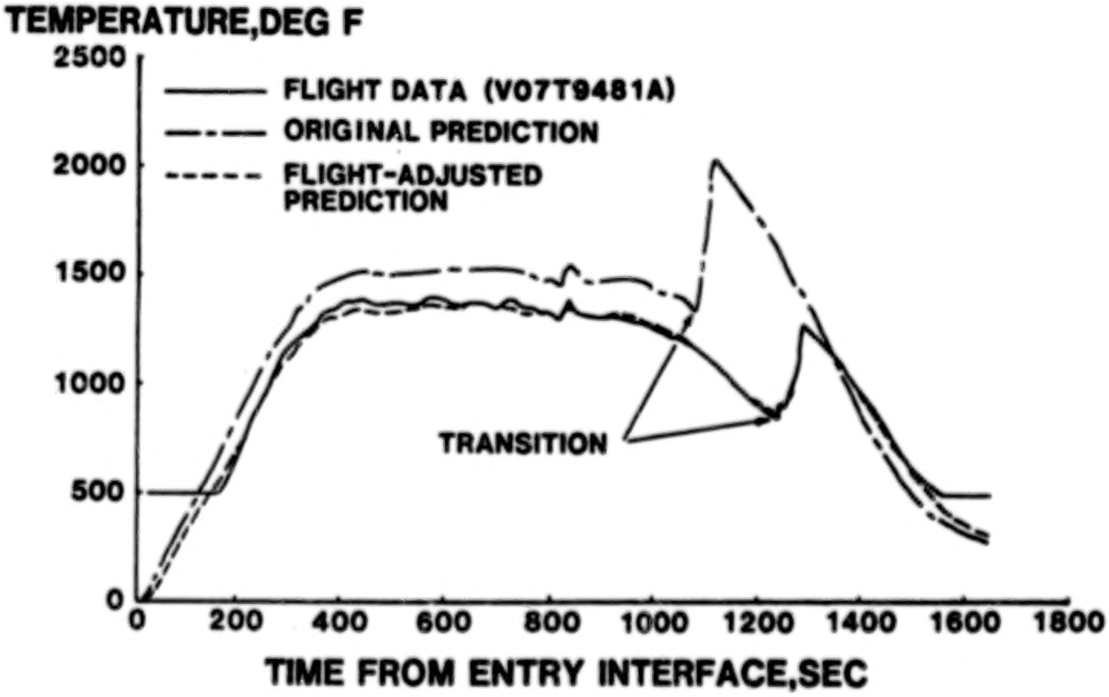

Figure 6.- Lower-surface temperature comparison - aft location (X/L = 0.7 centerline). STS-2.

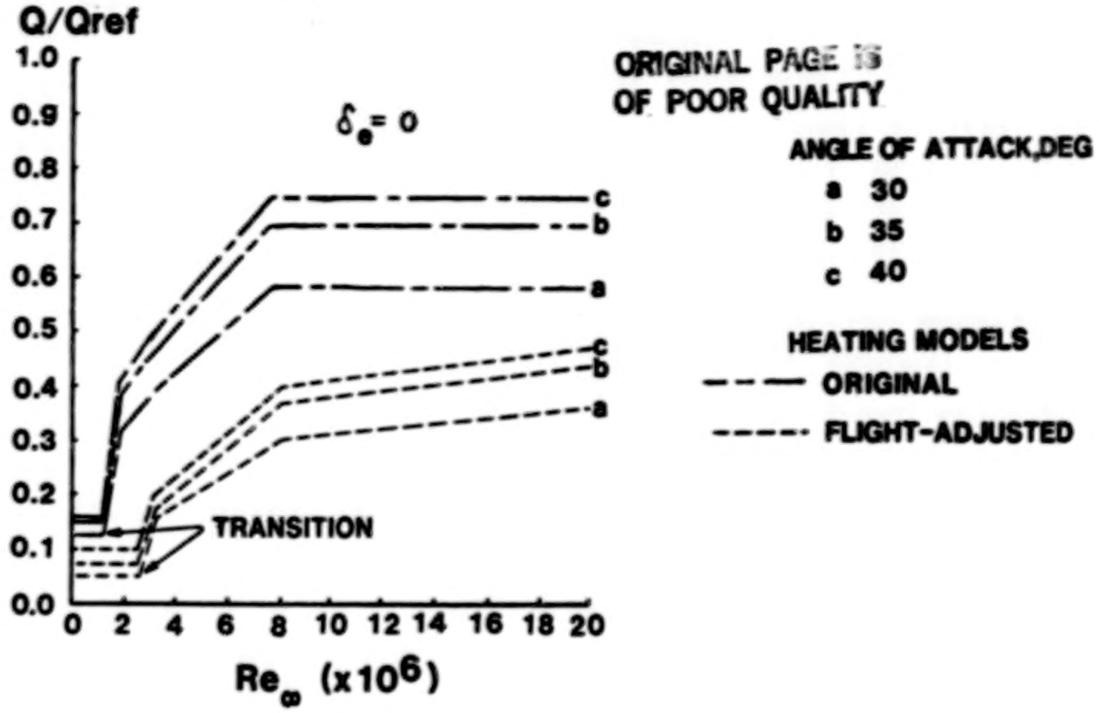

Figure 7.- Control surface heating model - elevon tip.

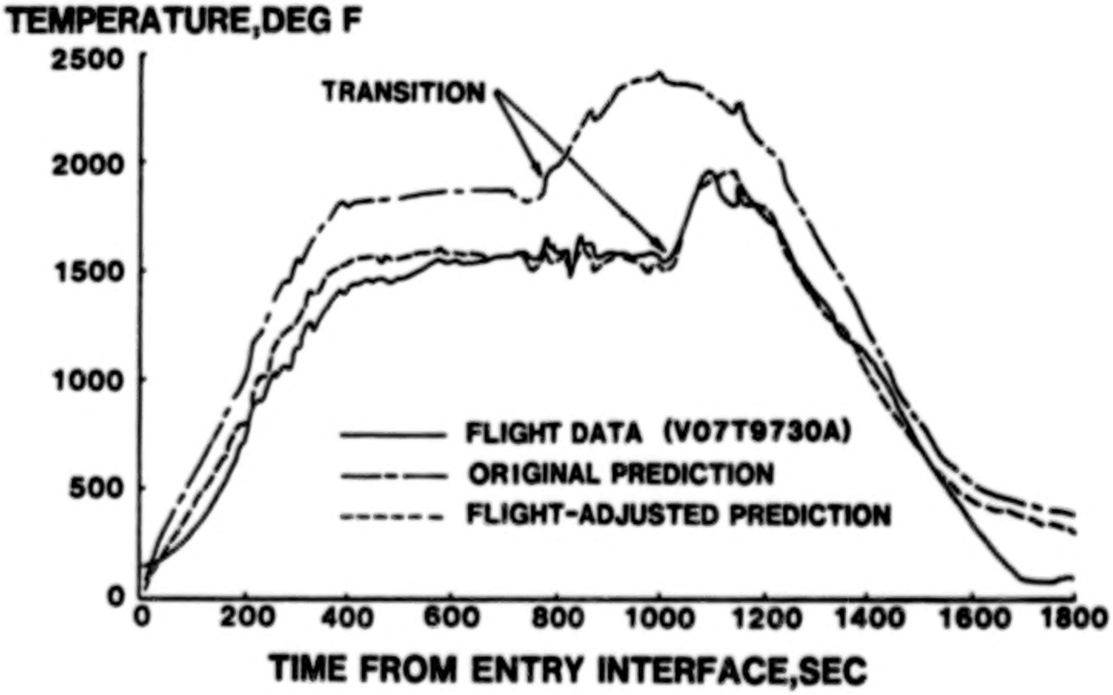

Figure 8.- Control surface temperature comparison - elevon tip. STS-2.

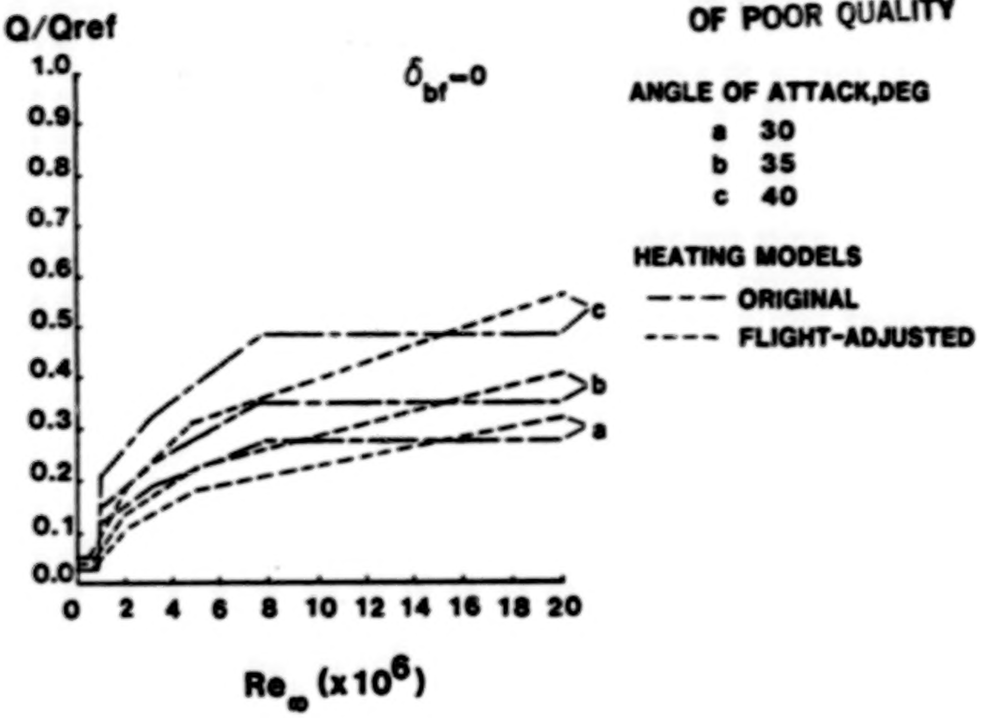

Figure 9.- Control surface heating model - bodyflap edge.

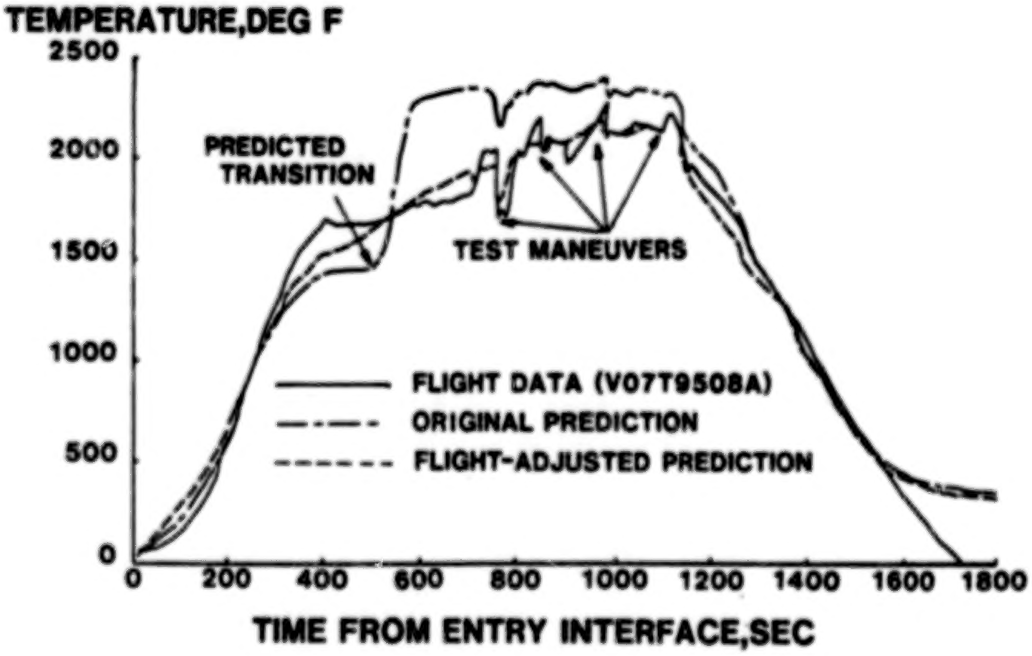

Figure 10.- Control surface temperature comparison - bodyflap edge. STS-2.

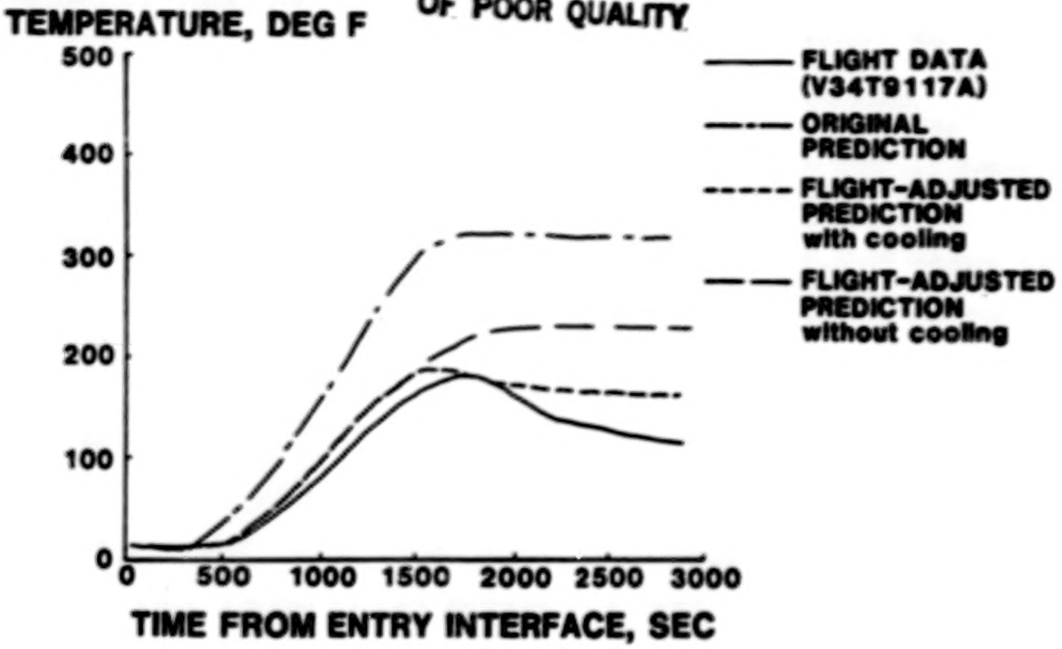

Figure 11.- Lower-surface bondline temperature comparison - aft location (X/L = 0.7 centerline). STS-2.

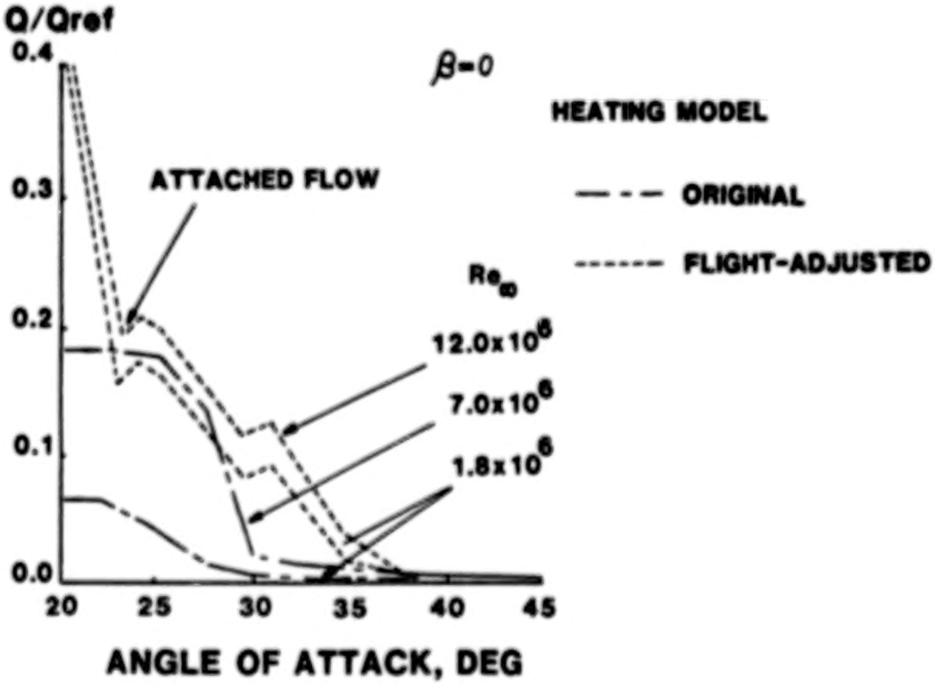

Figure 12.- OMS pod heating model - aft location.

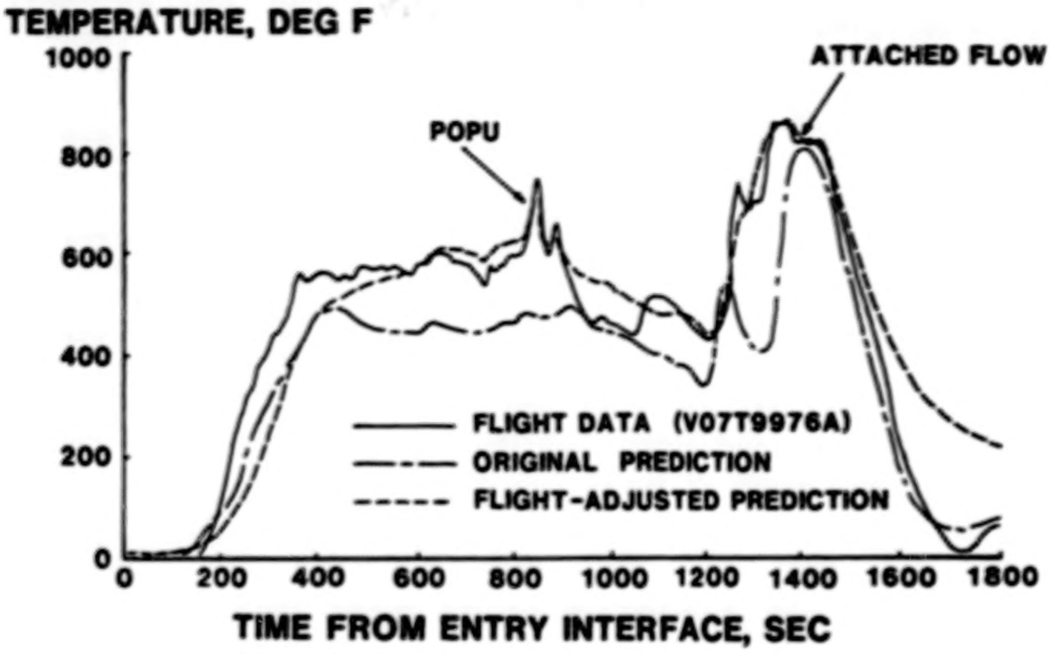

Figure 13.- OMS pod temperature comparison - aft location. STS-2.

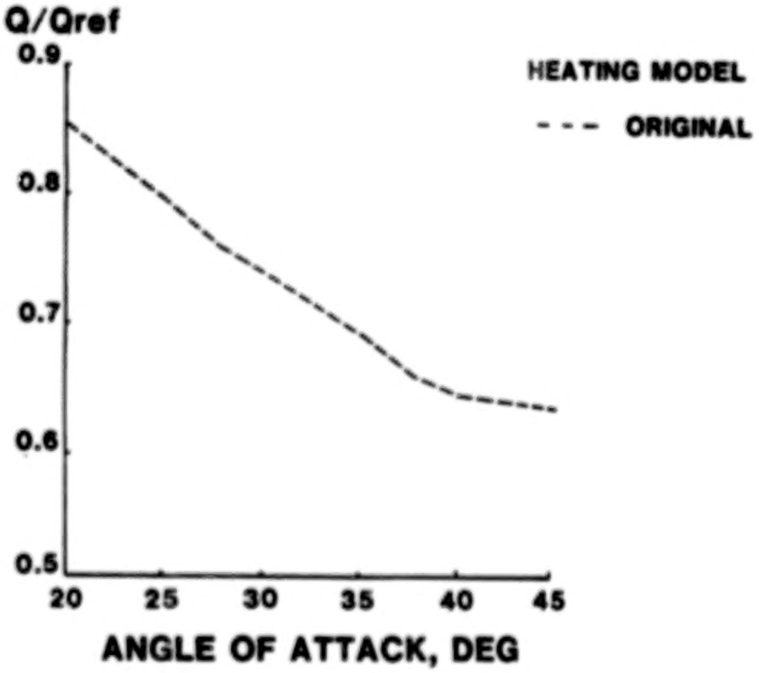

Figure 14.- Wing leading-edge heating model -
55-percent semispan location.

ORIGINAL PAGE IS OF POOR QUALITY

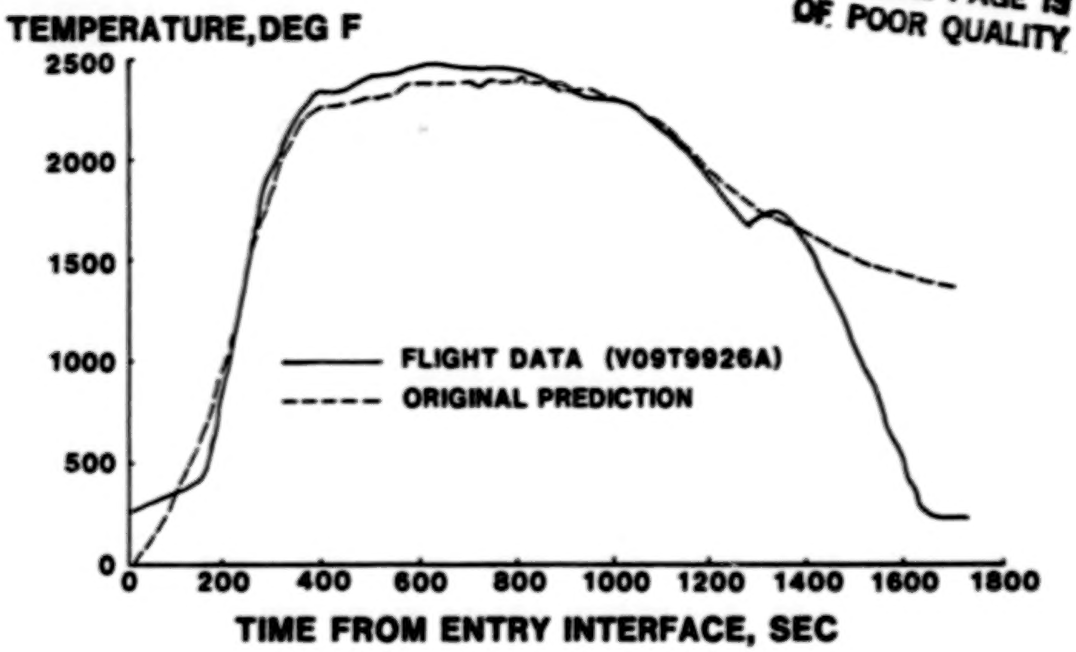

Figure 15.- Wing leading-edge temperature comparison - 55 percent semispan location. STS-2.

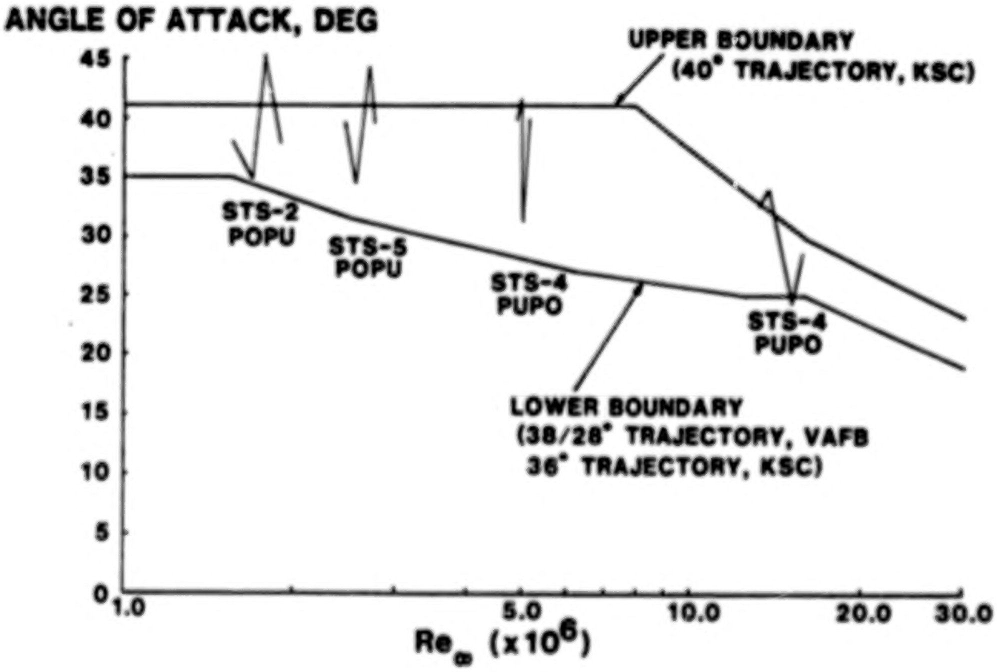

Figure 16.- Operational angle-of-attack envelope.

ORIGINAL PAGE IS
OF POOR QUALITY

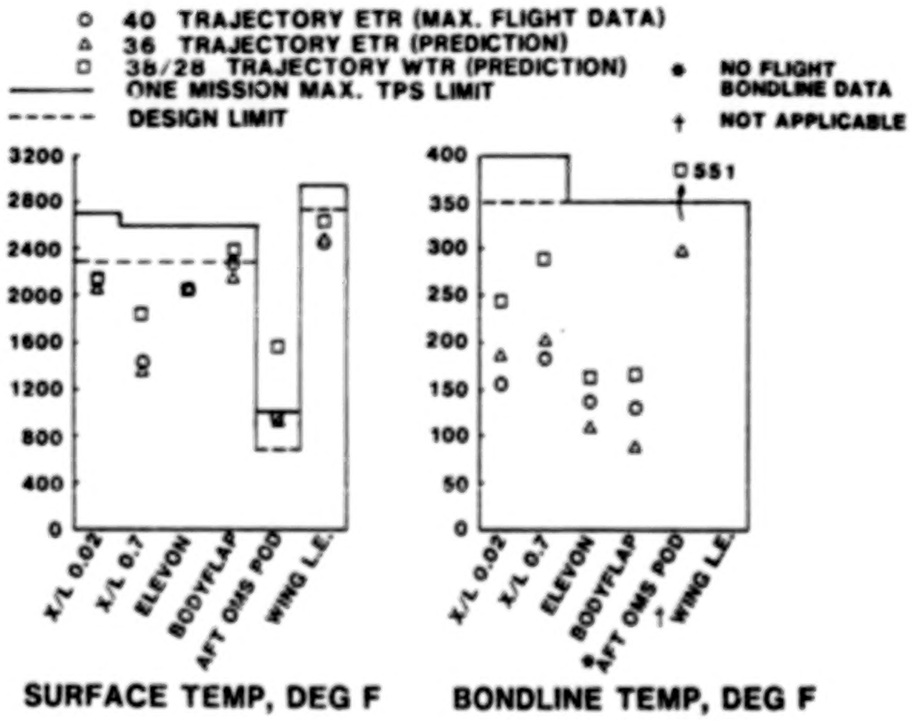

SURFACE TEMP, DEG F

BONDLINE TEMP, DEG F

Figure 17.- Maximum temperature comparison.

N84
10148

UNCLAS

N84 10148

ORBITER ENTRY HEATING LESSONS LEARNED FROM DEVELOPMENT FLIGHT TEST PROGRAM

J. W. Haney
Space Transportation and Systems Group
Rockwell International
Downey, California

SUMMARY

The Space Shuttle orbiter's thermal protection system (TPS), designed mainly on the basis of wind tunnel test data, has successfully completed its design, development, and flight test program. The flight test data provide an exceptional opportunity to evaluate the use of wind tunnel test data for the design of TPS for reentry vehicles. Comparisons of flight test data against wind tunnel data used to design the orbiter's TPS have been developed. These flight data, though still in the preliminary analysis phases, generally support the use of wind tunnel test data in the design of TPS for hypersonic reentry vehicles.

INTRODUCTION

At the onset of the design of the orbiter's TPS, wind tunnel data were relied upon heavily to develop aerothermodynamic prediction methods. These methods, either semiempirical correlations or validated analytical methods, were extrapolated to flight conditions in conjunction with an uncertainty analysis. Today, the process of methods verification based on flight test data has begun (figure 1).

This paper compares reentry flight test data from the first five flights of the Space Shuttle Columbia with the wind tunnel test data used to predict the environments on which the TPS design was based. In the process, basic design heating methods will be explained. The types of reentry missions on which data were obtained, instrumentation types and locations, and some current problems with available flight data are discussed. Differences between flight and wind tunnel test data are analyzed. Emphasis is placed on the orbiter leeside.

SYMBOLS

h	heat transfer coefficient
H	enthalpy
L	fuselage reference length (1,284.3 in.)
P	pressure

Pr	Prandtl number
R_e	Reynolds number
ST	Stanton number
T	temperature
V	velocity
X	axial length
α	angle of attack
β	angle of sideslip
δ	control surface deflection
θ^*	flow angle (body angle plus angle of attack)
μ	viscosity
ρ	density

Subscripts:

BF	body flap
E	elevon
e	boundary layer edge
FP	flat plate
o	stagnation
r	recovery
TR	transition
w	wall
θ	momentum thickness
∞	free stream

DESIGN HEATING APPROACH

Over a period of almost 12 years, from the start of the Phase A studies to the first orbital flight test (OFT) of Columbia, 50 wind tunnel tests (approximately 5,200 hours) were conducted for the purpose of developing aerothermodynamic math models to estimate entry heating environments. Through the course of this testing, configuration features were finalized, different facilities were investigated, and a large number of heating parameters were varied (figure 2). Even with all of this testing, the ability to directly simulate an entry trajectory was limited (figure 3). High Mach number with associated low Reynolds numbers were beyond the capability of wind tunnels. This inability to simulate was rationalized by the belief that correlations developed for lower Mach numbers (approximately 8) and higher Reynolds numbers could be accurately applied to other flight conditions.

Two different approaches were taken to utilize wind tunnel test data for environment definition. One approach, the simple geometric theory, was employed mainly on the orbiter lower surfaces. The other approach, wind tunnel data taken directly, was applied to the leeward surfaces.

The simple geometric theory approach subdivided the orbiter into simple shapes (spheres, cylinders, wedges, and cones) for which standard analytical solutions were in existence (figure 4). These simple geometric theories (mainly wedges and flatplates) were adjusted to match wind tunnel test data. The adjustments from the standard Eckert reference enthalpy flatplate solutions were to take into account such variations as streamline divergences and flow running lengths. These adjustment factors, developed for both laminar and turbulent boundary layers in the wind tunnel, were held constant when extrapolating to flight conditions.

The direct application of wind tunnel data for the upper surfaces was obtained by correlations of wind tunnel data (in terms of a nondimensional local film coefficient to that of a 1-ft-radius sphere) as a function of angle of attack, angle of sideslip (yaw), free-stream Reynolds number, and free-stream Mach number (figure 5). This essentially correlates the orbiter leeside into blunt body relationships. Regions of vortex scrubbing and flow impingement were allowed to vary somewhat beyond the wind tunnel values based on local pressure levels.

In addition to the basic use of wind tunnel test data, uncertainties were accounted for in order to have a conservative heating estimate for assessment of the first flight. Some conservatism was inherent in the analysis, such as assuming a fully catalytic surface. Other uncertainties were knowingly added (see figure 6). Uncertainties were determined individually by either analysis of wind tunnel data or by theoretical assumptions. These uncertainties were root sum squared together to obtain the final uncertainty values.

FLIGHT TEST DATA

The Space Shuttle orbiter development test program consisted of four test flights. However, problems in obtaining flight test data resulted in the addition of a fifth instrumented flight. The entry trajectories were shaped to be benign from an induced thermal point of view, with each flight having a vehicle angle of attack of 40 deg throughout most of the entry (figure 7). Emphasis was placed on maintaining adequate structural temperature margins. All five trajectories were similar, though STS-3 and STS-4 flights had slightly increased surface temperatures and reduced entry flight time.

Aerothermodynamic test data were obtained by three means: surface thermocouples, calorimeters, and surface pressure taps (figures 8a, 8b, and 8c).

Thermocouples were to be installed slightly below the outer mold line (OML) of the TPS. However, X-rays of tiles used in TPS certification testing indicated that the position of the thermocouple below the OML was not always constant. This was especially true of the felt reusable surface insulation (FRSI) located on the upper surfaces. Similarly, calibration of thermocouples on Columbia has indicated variations in response to a known induced environment. This condition becomes critical in assessing transient variations in environments and is currently being incorporated into the data analysis and verification process. This variation in response has been related to a variation in the effective depth of the thermocouples from the OML. All data presented in this paper considered the thermocouples to be reading surface temperature. These data will need to be adjusted once the effective depth or thermal math model of each thermocouple has been ascertained.

Calorimeters, used as a means of gathering data, were essentially available for only the first two development flights. The unanticipated responses of the calorimeters late in the STS-1 trajectory led to the removal of most and to their replacement with surface thermocouples. Unfortunately, after analyzing five flights of test data, the calorimeters appear to have been providing useful data during the first two test flights. The calorimeters, more sensitive than surface thermocouples, were quite responsive to vehicle attitude changes; however, the overall magnitude of the calorimeter readings remains in question.

Several unfortunate flight data problems reduced the total amount of available data so that only three entire flights of thermocouple, two entire flights of pressure, and one entire flight of calorimeter data were obtained during the OFT program. Partial data were obtained on both the first and fourth test flights.

FLIGHT TEST RESULTS

Lower Surface

In examining flight test data on the orbiter lower surfaces, three major statements can be made: (1) noncatalytic effects were present, (2) boundary layer transition occurred later than predicted, and (3) local pressures generally agreed with theory.

The noncatalytic effects not accounted for in the TPS design appear to be the most conservative element in that design. Figure 9 shows the differences between equilibrium (fully catalytic) and flight test data at two locations on the orbiter lower-surface centerline. Also evident is the agreement between the Spalding and Chi turbulent theory and flight data. Detailed discussions of noncatalytic effects are found in reference 1.

Roughness-induced boundary layer onset transition criterion was conservative for the first test flight; however, the TPS was actually designed based on a smooth-body criterion. Flight data indicate that transition occurs somewhat sooner than predicted by the smooth-body criterion developed from wind tunnel test data (figure 10). Detailed discussions of boundary layer transition and the orbiter may also be found in reference 1.

The local pressure levels (low-pressure gradient regions) on the orbiter lower surfaces were based on correlations of P_L/P as a function of free-stream Mach number, angle of attack, and local geometric angle. These correlations initially determined based on wedge and cone data were modified using orbiter wind tunnel test data, so that

$$P_L/P_\infty = 0.2397 + 1.161\ M_\infty \sin\theta^* + 1.060\ (M_\infty \sin\theta^*)^2 + 0.0487\ (M_\infty \sin\theta^*)^3$$

This approach provided excellent agreement with flight test data (figure 11).

Heating to the wing leading edge described in a separate paper (reference 2) can be summarized as follows. Outside of the shock impingement region, flight data agree well with the methods developed based on wind tunnel data; inside of the shock-influenced region, flight data were higher than wind-tunnel-based data.

Upper Surface

The main emphasis of this paper is the comparison of flight and wind tunnel data for the orbiter upper surfaces. Specifically, the fuselage side, payload bay door, wing upper surface, vertical tail, and orbital maneuvering system (OMS) pod will be discussed in this section. The wind tunnel test data used for comparisons with flight data are taken from references 3 through 10.

Fuselage Side

The flow on the orbiter fuselage side, as well as on many upper surface regions, is generally characterized by a separated flow region interrupted by vortex scrubbing (figure 12). The vortex is believed to develop from the junction of the wing glove and the fuselage side, and it traverses along the fuselage side at an angle similar to the vehicle angle of attack. This vortex scrubs the vertical surfaces of the fuselage and payload bay doors as indicated in figure 12. Once outside of the vortex zone, the heating drops rapidly to separation values. Derived from wind tunnel test data, the vortex location and strength were determined to be sensitive to angle of attack, yaw, and Reynolds number. The effects of varying these parameters in the wind tunnel were to shift the vortex forward or aft along the fuselage side.

In the regions of nonvortex attached flow (i.e., forebody side), flight data and wind tunnel data are in general agreement. In the wind tunnel, nondimensionalized heat transfer data in these same regions were insensitive to variations in Reynolds number and somewhat insensitive to angle of attack, which is indicative of laminar attached flow. There appears to be, however, some evidence of noncatalytic effects as seen on the lower surface in regions just aft of the nose cap (figure 13).

Moving aft along the side, at 30-percent body length, the agreement between flight and wind tunnel data is excellent in the range of Reynolds numbers tested in the wind tunnel (figure 14). For the case when Reynolds numbers are less than those tested in the wind tunnel, the heating is less than predicted. Above the Reynolds number limit of the wind tunnel, heating is generally equal to or greater than predictions. Wind tunnel data were not always correlated exactly when developing aeroheating math models. The correlation procedure (figure 5) sometimes did not lend itself to certain variations between parameters or physical locations. This is evident in figures 14b and 14c.

In regions strongly influenced by vortex scrubbing, the wind tunnel data underpredict flight test data (figure 15). The differences increase as the Reynolds numbers increase. The exact causes of this underprediction are not quite understood at present, but are believed to be related to the differences in specific heat ratios between wind tunnel and flight (1.4 versus 1.2). This difference should result in moving the vortex closer to the sidewall and increase the influence on heating. The other noticeable difference in flight data is the rapid rise in the temperature (heating rate) at a Reynolds number of approximately 2.0×10^6. This rise is quite evident with the $\alpha = 40$ deg data and can be implied with the limited $\alpha = 35$ deg and $\alpha = 30$ deg data. This rise in temperature reaches a level that is somewhat consistent with that of the lower angles of attack (an increase of 400 to 600 percent, figures 15b and 15c). The flow appears to be departing from a weak vortex and separated condition to that of a strong vortex and attached interaction.

Further aft on the orbiter's side (also strongly influenced by the vortex) is a region that, in the wind tunnel, did not experience any noticeable vortex scrubbing (figure 16). The flow in this region was separated at $\alpha = 40$ deg in the wind tunnel, but under flight conditions it experiences vortex scrubbing. Again note the rapid change in heating level at a Reynolds number of 2.0×10^6.

Payload Bay Door

In the wind tunnel, the flow on the payload bay doors was characterized by a pair of weak vortices traversing along the top of the doors; however, in flight these vortices do not appear to be attached at the high angle of attack, $\alpha = 40$ deg. During the TPS design phase of the Shuttle, much effort was made to correlate the wind tunnel test data on the payload bay doors. The correlating parameter used was Stanton number based on free-stream conditions. When this parameter is used for both flight and wind tunnel data, it can be seen that as the vehicle angle of attack is reduced, the differences between flight and wind tunnel are reduced (figures 17a, 17b, and 17c). Interestingly, Apollo and Shuttle leeside data are in general agreement for certain flight conditions (figure 18).

With the payload bay door wind tunnel data coming into better agreement for reduced angles of attack, this points to the need to maintain a view of the entire orbiter when extrapolating vehicle capability to more severe entries.

Wing Upper Surface

Of all the regions on the orbiter, the area most overpredicted by wind tunnel data was the wing upper surface. Wind tunnel data had indicated some vortex scrubbing on the outboard portion of the wing at a 40-deg angle of attack, with more severe scrubbing at the lower angles of attack. Analysis of oil flow data had indicated that this vortex was associated with the interaction of the bow and leading-edge shocks (figure 19).

The wing upper-surface wind tunnel data used the same correlation approach as the other upper-surface data; however, the vortex and its influence on heating were allowed to move in position from wind tunnel to flight as the shock interaction was predicted to move. (This amounted to about 10 percent of the wing span.)

The flight test data indicate that this vortex scrubbing is not present under flight conditions between a 30- and 40-deg angle of attack. In fact, the heating appears to be fairly constant outboard of 50-percent semispan, in direct contrast to the wind tunnel data (figure 20).

Inboard of the vortex-influenced region in the wind tunnel (i.e., $\leq$ 60-percent semispan), flight data indicate a similar chordwise trend in heating with that of the wind tunnel. The lowest heating on the wing upper surface consistently exists between 40- and 60-percent chord. This view of the wing upper-surface heating also illustrates the difference between wind tunnel and flight at 60- and 90-percent semispan (figures 21 and 22).

The cause of this greatly reduced heating, especially on the outboard wing upper surface, is not understood at the present time.

Vertical Tail

The vertical tail, as with other areas of the orbiter upper surface, can be divided into regions of nonvortex- and vortex-related flows. The vortex flow appears to be related to the fuselage side vortex based on oil flow data from the wind tunnel (figure 12). Generally, in those areas of nonvortex flow, the flight data and wind tunnel data are in agreement (figure 23). This applies mainly to the lower half of the vertical.

In those regions influenced by vortices, the flow has a pattern similar to the fuselage side. At the low Reynolds numbers, the flow appears to be separated and at a heating level below that of the wind tunnel. As with the fuselage side, flight data show a rapid rise in temperature (heating) at approximately a Reynolds number of 2.0×10^6. This results in an agreement between flight and wind tunnel data at the higher Reynolds numbers (figure 24).

OMS Pod

The OMS pod has been investigated in terms of flight test data probably more than any other upper surface region to date. This has been due to the critical factor the OMS pod plays in the ability of the orbiter to fly reduced angles of attack from the 40-deg angle of attack development flight test level.

The position of the OMS pod, extending from the orbiter side, makes it extremely susceptible to impingement of flow (vortices) as well as debris traversing along the fuselage side.

The OMS pod receives its peak heating twice during the orbiter's reentry. The upper surface of the pod peaks during the high-alpha portion of entry, while the side of the pod peaks at low angles of attack. Both instances appear to be vortex related. Heating on the side of the pod at a 40-deg angle of attack generally agreed with or was somewhat higher than wind tunnel data (figure 25). However, as the angle of attack decreased, the differences between flight and wind tunnel increased for the side of the pod.

The impinging vortex transforms the flow on the pod from separated to attached. First, the flow impinges at about 20 percent of the pod length. Then, as the angle of attack decreases or the Reynolds number increases, the attachment point moves forward. Once the flow becomes attached, changes in the major heating parameters have little influence on heating, based on wind tunnel data. However, in the transition phase between separation and attached flow, heating is extremely sensitive to small variations in angle of attack, yaw, and Reynolds number. Under flight conditions, it appears that the flow becomes attached at a higher angle of attack and at a lower Reynolds number than under wind tunnel conditions.

This sensitivity to angle of attack and flow attachment occurring earlier in flight was made evident based on data from several pitch maneuvers [push over/pull up (POPU)]. These maneuvers were planned to expose the orbiter to more severe angles of attack (lower) for short periods of time, thereby obtaining heat transfer data while not exposing the structure to any excessive heat loads. These transient maneuvers were performed at discrete velocities on STS-2 (21,000 ft/sec), STS-4 (12,000 ft/sec and 8,400 ft/sec), and STS-5 (18,000 ft/sec). The POPU maneuver was performed by varying the angle of attack by approximately 1 deg/sec from the nominal to the minimum, from the minimum to the maximum, and then back to the nominal angle of attack. Dwell time at the angle of attack extremes varies from 1 to 2 sec to almost 10 sec. This data, though only at the minimal angle of attack for less than 10 sec, indicated higher temperatures in flight than in the wind tunnel (figures 25b and 25c).

The element of uncertainty still in the POPU data is in determining the steady-state surface temperature (heating rate) from a thermocouple below the outer mold line (OML) experiencing only a few seconds of increased heating. The possible variation due to this uncertainty is shown in figures 26 and 27. This uncertainty relates not only to surface temperatures but to the total heat load influencing the structure temperature and thus to predictions of orbiter capability.

CONCLUDING REMARKS

The orbiter entry heating lessons learned from the development flight test program are significant, with many yet to be discovered. This development test program has provided quality entry aerothermodynamic data as a basis for these discoveries. These data, although still in the preliminary analysis phases, support the use of wind tunnel test data for the design of TPS's for hypersonic reentry vehicles and will allow more optimized TPS's for future vehicles. The design of these future vehicles will be further enhanced by both utilizing and developing analytical solutions derived from Navier-Stokes equations, thereby greatly reducing parametric design efforts and scaling-to-flight difficulties experienced with wind tunnel data.

REFERENCES

1. Harthun, M. H.; Blumer, C. B.; and Miller, B. A.: Orbiter Windward Surface Entry Heating—Post-Orbital Flight Test Program Update. Shuttle Performance: Lessons Learned, NASA CP-2283, Part 2, 1983, pp. 781-805.

2. Cunningham, J. A. and Haney, J. W.: Space Shuttle Wing Leading Edge Heating Environment Prediction Derived From Development Flight Data. Shuttle Performance: Lessons Learned, NASA CP-2283, Part 2, 1983,pp. 1083-1110.

3. An Investigation of Entry Heating on the 0.0175-Scale Space Shuttle Orbiter (Model 60-0) in the AEDC UKV Tunnel 'B'. NASA CR-160490, Vols 1-4, July 1980.

4. Results of Heat Transfer Tests on a 0.0175-Scale Space Shuttle Orbiter Model (56-0) in the AEDC VKF 'B' Hypersonic Wind Tunnel. NASA CR-144596, Mar. 1976.

5. Results of Heat Transfer Test in the Arnold Engineering Development Center - Von Karman Facility Tunnels A and B Utilizing Space Shuttle Orbiter Thin Skin Thermocouple Models 56-0, 60-0, and 83-0 Tests: OH 84B, OH 105, IH 102. NASA CR-160828, Vols 1-6, Aug. 1981.

6. Test Results From the NASA/Rockwell International Space Shuttle 0.0175-Scale Orbiter Models 56-0/60-0 and 0.04-Scale Orbiter Forebody Model 83-0 Conducted in the AEDC/VKF-B 50-Inch Hypersonic Wind Tunnel. NASA CR-167349, Vols 1-3, July 1982.

7. NASA/RI OH-111 Orbiter Abort Heating Test. NASA CR-167380, Vols 1-5, Sept. 1981.

8. Test Results From the NASA/Rockwell International Space Shuttle 0.0175-Scale Orbiter Models 56-0/60-0 and 0.04-Scale Orbiter Forebody Model 83-0 Conducted in the NASA/ARC 3.5-Foot Hypersonic Wind Tunnel. NASA CR-160844, Oct. 1981.

9. Results of Test on a 0.0175-Scale Model (60-0) of the Space Shuttle Orbiter to Determine Reentry Mode Convective Heat Transfer Rates on the Upper Wing Surface and SSME Nozzles in the AEDC VKF 'B' Hypersonic Wind Tunnel (OH98). NASA CR-160501, Vols 1 and 2, Sept. 1980.

10. Space Shuttle Orbital Maneuvering System Pod Heating Test at Mach Number 8. AEDC-TSR-80-V2, Jan. 1980.

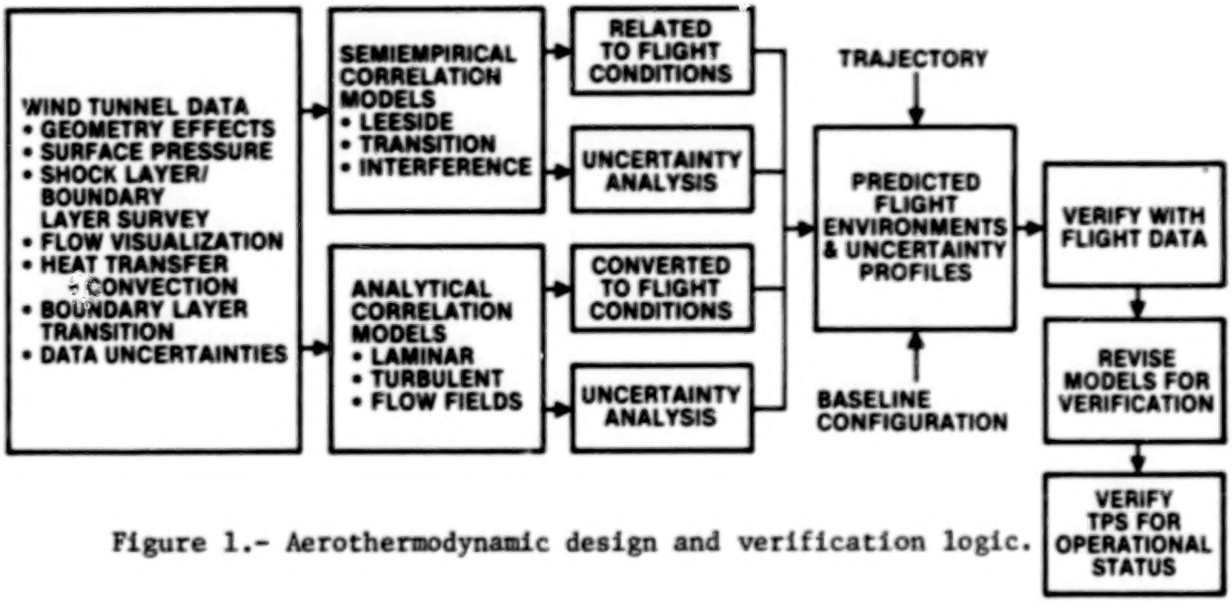
WIND TUNNEL DATA
• GEOMETRY EFFECTS
• SURFACE PRESSURE
• SHOCK LAYER/ BOUNDARY LAYER SURVEY
• FLOW VISUALIZATION
• HEAT TRANSFER
• CONVECTION
• BOUNDARY LAYER TRANSITION
• DATA UNCERTAINTIES
SEMIEMPIRICAL CORRELATION MODELS
• LEESIDE
• TRANSITION
• INTERFERENCE
ANALYTICAL CORRELATION MODELS
• LAMINAR
• TURBULENT
• FLOW FIELDS
RELATED TO FLIGHT CONDITIONS
UNCERTAINTY ANALYSIS
CONVERTED TO FLIGHT CONDITIONS
UNCERTAINTY ANALYSIS
TRAJECTORY
PREDICTED FLIGHT ENVIRONMENTS & UNCERTAINTY PROFILES
BASELINE CONFIGURATION
VERIFY WITH FLIGHT DATA
REVISE MODELS FOR VERIFICATION
VERIFY TPS FOR OPERATIONAL STATUS

Figure 1.- Aerothermodynamic design and verification logic.

- **50 WIND TUNNEL TEST**
- **5,250 HOURS**
- **~ 9 CONFIGURATIONS (07D-ATP, 089, 089B-MOD, 130 MOD, 139, 139 MOD, 140B, 147B, 140C-STS-1)**
- **7 FACILITIES: NASA LRC/VDT, NASA LRC/CF4, NASA LRC/CFHT, NASA AMES 3.5 FT, CALSPAN, AEDC-B, AEDC-F**
- **10 MODEL SCALES: 0.006, 0.01, 0.014, 0.0175, 0.025, 0.04, 0.08, 0.1, 0.111, FULL**
- **6 TYPES OF INSTRUMENTATION: THERMOCOUPLE, CALORIMETER, THIN FILM GAGE, PAINT, PRESSURE TAP, INFRARED**
- **4 TYPES OF DATA: TEMPERATURE, HEATING RATE, PRESSURE, BOUNDARY LAYER PROBES**
- **MACH NUMBERS:** **5.3 → 19**

R_E/FT	$0.5 \times 10^6 \rightarrow 9.0 \times 10^6$
α	$0^\circ \rightarrow 50^\circ$
β	$0^\circ \pm 0.5^\circ, \pm 1^\circ, \pm 2^\circ, + 5^\circ + 10^\circ$
δ_E	-30° TO $+ 10^\circ$
δ_{BF}	$0^\circ, 5^\circ, 10^\circ, 15^\circ, 22^\circ$

Figure 2.- Wind tunnel data base.

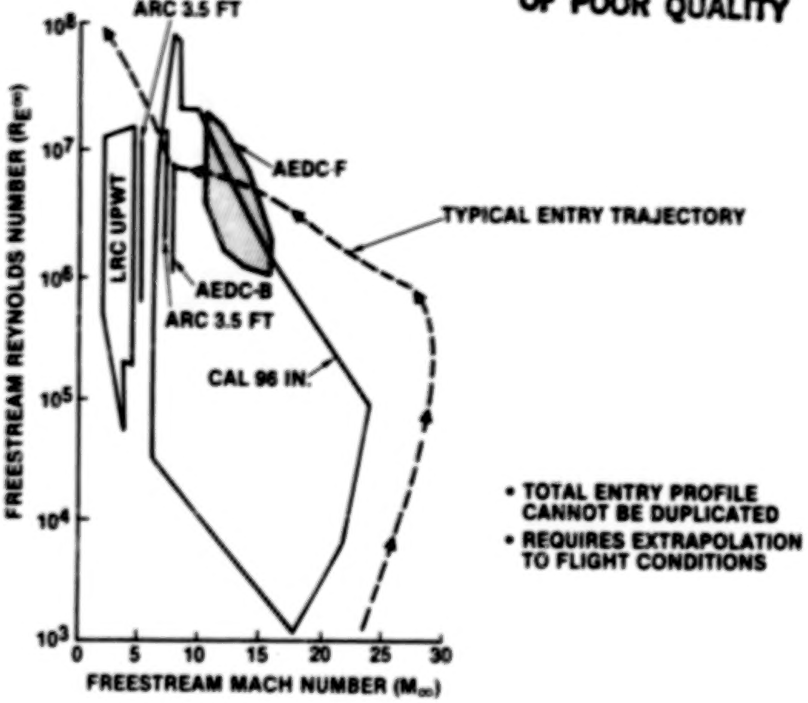

Figure 3.- Wind tunnel test simulation.

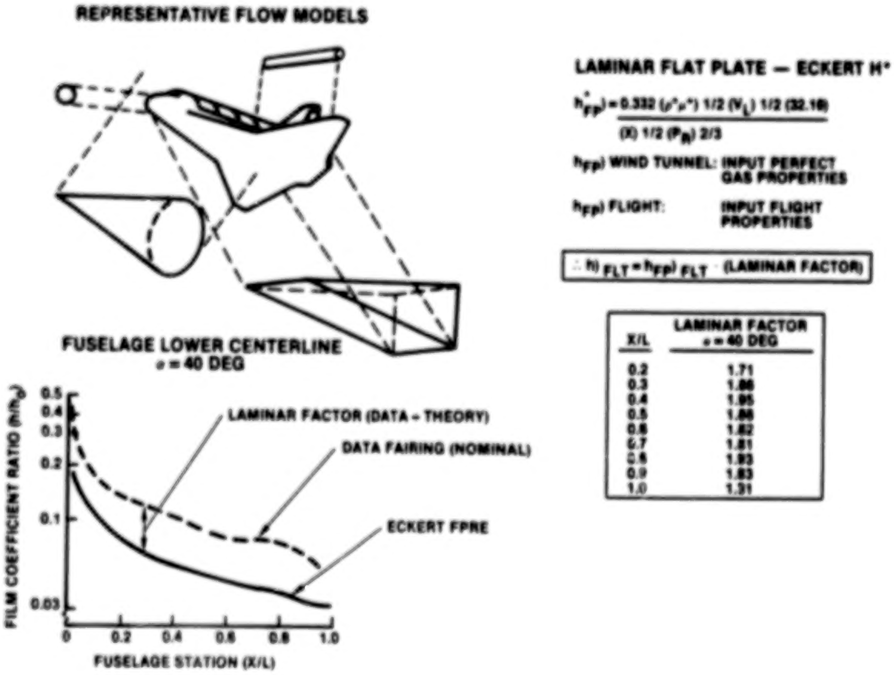
REPRESENTATIVE FLOW MODELS
FUSELAGE LOWER CENTERLINE
α = 40 DEG
LAMINAR FACTOR (DATA ÷ THEORY)
DATA FAIRING (NOMINAL)
ECKERT FPRE
FILM COEFFICIENT RATIO (h/h₀)
0.5
0.4
0.3
0.2
0.1
0.03
FUSELAGE STATION (X/L)
0
0.2
0.4
0.6
0.8
1.0
LAMINAR FLAT PLATE — ECKERT H*
h*_FP) = 0.332 (ρ*μ*) 1/2 (V_L) 1/2 (32.16) / (X) 1/2 (P_R) 2/3
h_FP) WIND TUNNEL: INPUT PERFECT GAS PROPERTIES
h_FP) FLIGHT: INPUT FLIGHT PROPERTIES
∴ h) FLT = h_FP) FLT · (LAMINAR FACTOR)

X/L	LAMINAR FACTOR α = 40 DEG
0.2	1.71
0.3	1.86
0.4	1.95
0.5	1.86
0.6	1.82
0.7	1.81
0.8	1.93
0.9	1.83
1.0	1.31

Figure 4.- Orbiter lower-surface methodology; slender body approach.

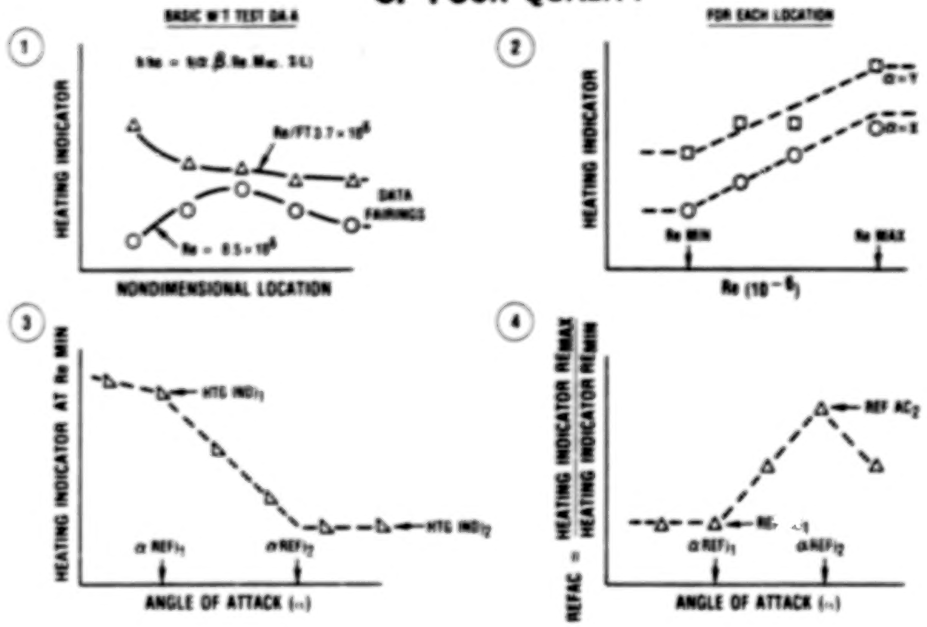

• SIMILAR PROCEDURE FOR β EFFECTS

Figure 5.- Orbiter upper-surface methodology.

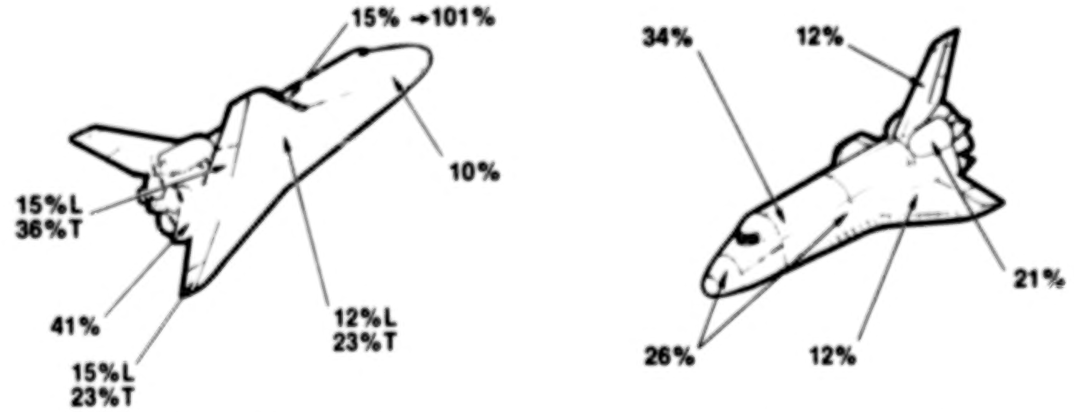
15% → 101%
10%
15%L
36%T
41%
15%L
23%T
12%L
23%T
34%
12%
21%
26%
12%

UNCERTAINTY CONSIDERATIONS

- WIND TUNNEL DATA SCATTER
- LOCAL PROPERTIES
- THEORY
- FLOW ORIGIN
- DEFLECTION EFFECTS
- SCALING TO FLIGHT
- DOUBLE SHOCK

UNCERTAINTY CONSIDERATIONS

- WIND TUNNEL DATA SCATTER
- SCALING TO FLIGHT

Figure 6.- Heating uncertainties for STS-1.

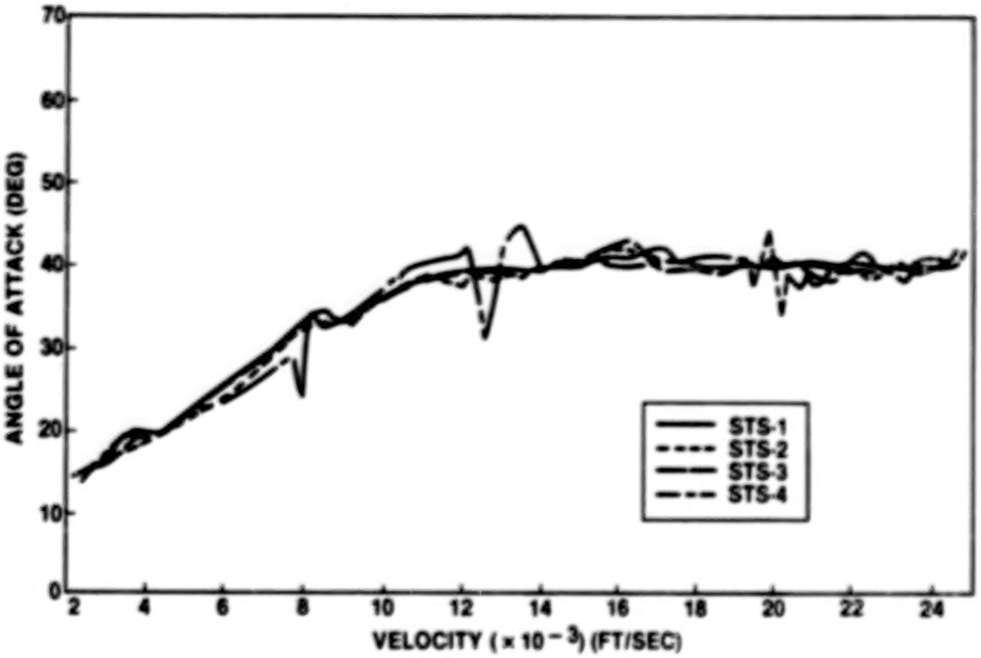

Figure 7.- Orbital flight test angle-of-attack experience.

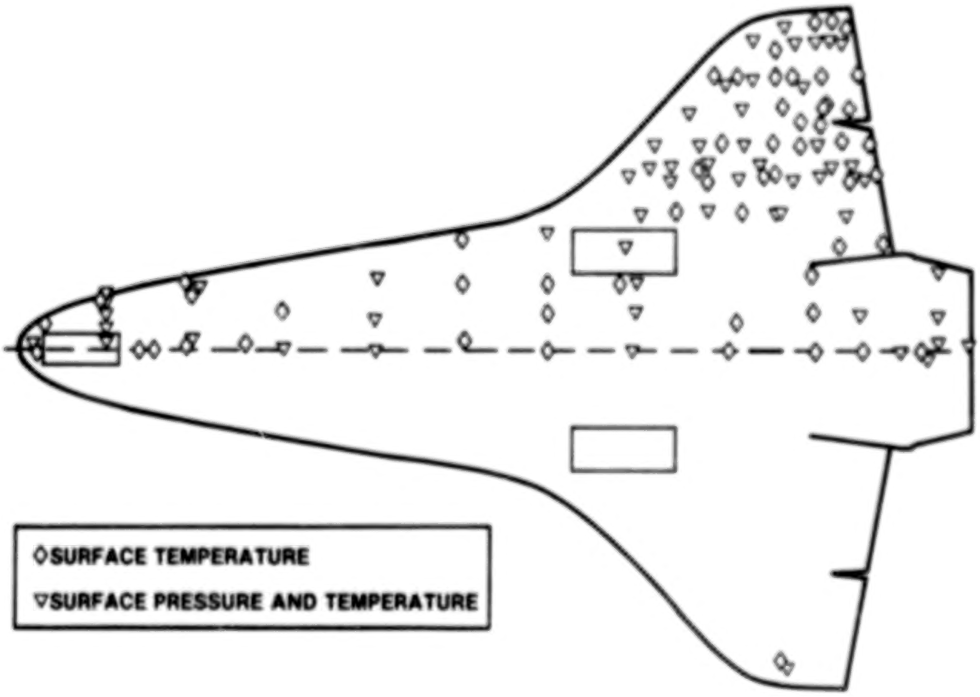
◇SURFACE TEMPERATURE
▽SURFACE PRESSURE AND TEMPERATURE

(a) Lower surface.

Figure 8.- Aerothermodynamic instrumentation locations.

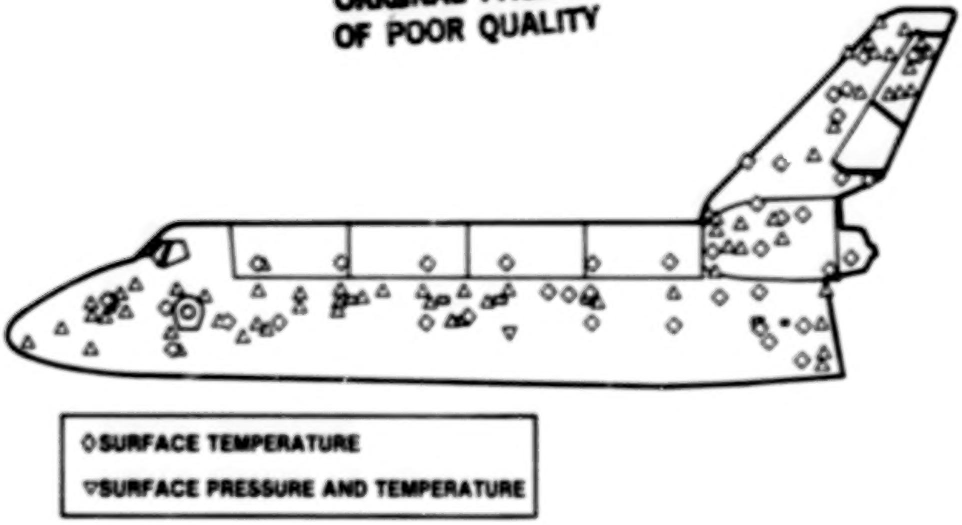
◇SURFACE TEMPERATURE
▽SURFACE PRESSURE AND TEMPERATURE

(b) Side surface.

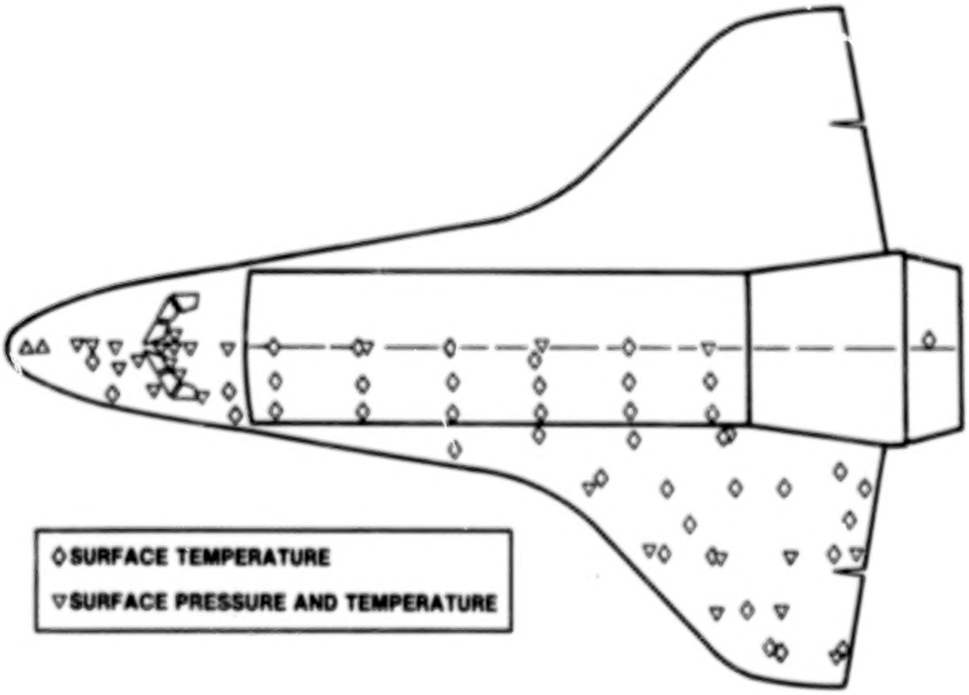
◇SURFACE TEMPERATURE
▽SURFACE PRESSURE AND TEMPERATURE

(c) Upper surface.

Figure 8.- Concluded.

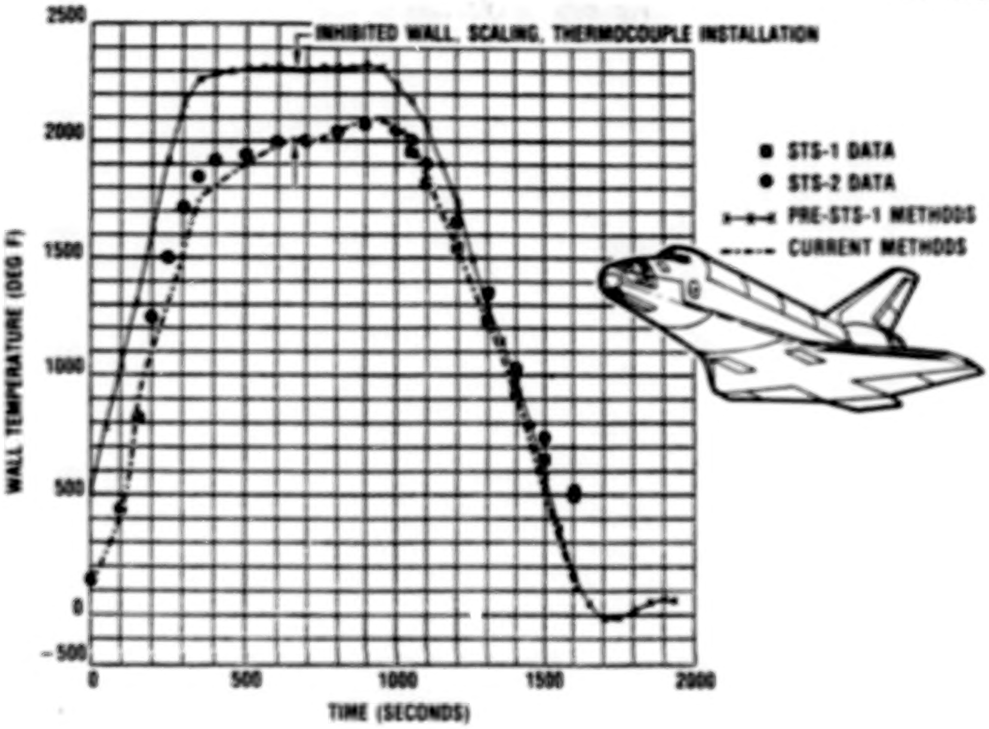

(a) Centerline - (X_o 268) (X/L = 0.025).

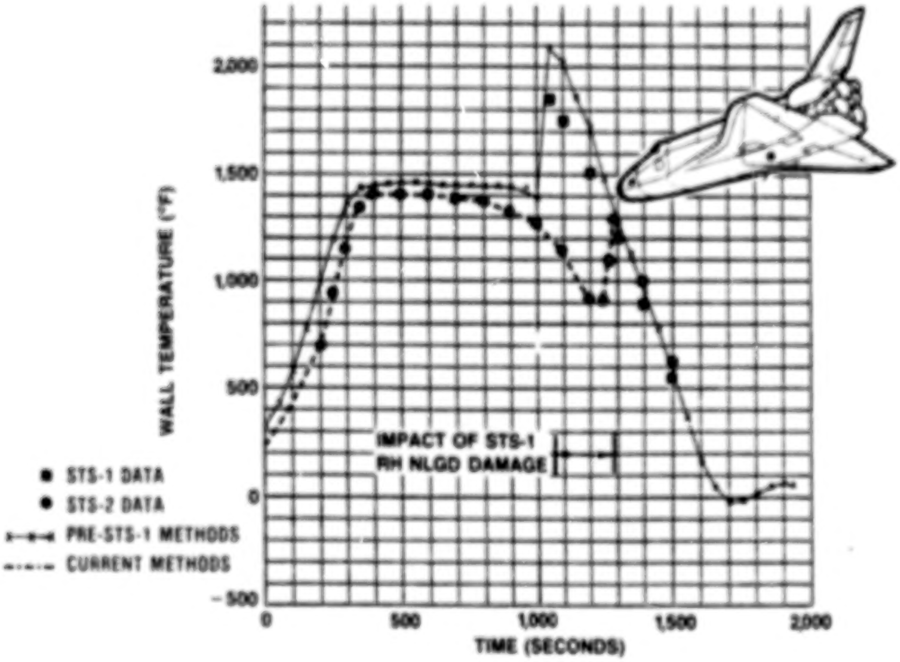

(b) Centerline - (X_o 1,128.0) (X/L = 0.70).

Figure 9.- Fuselage lower surface.

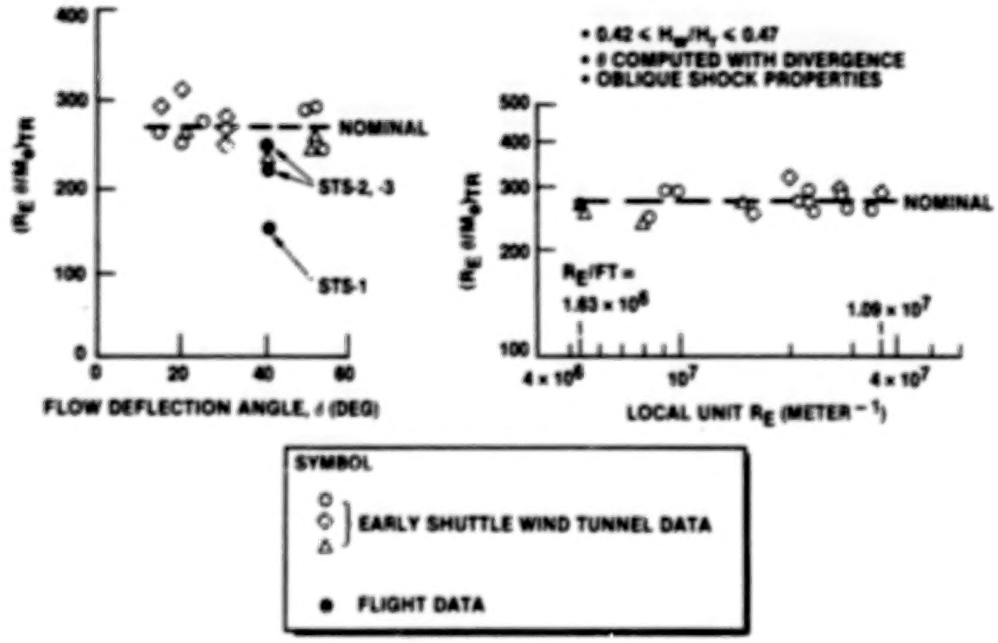

Figure 10.- Delta wing orbiter boundary layer transition correlation.

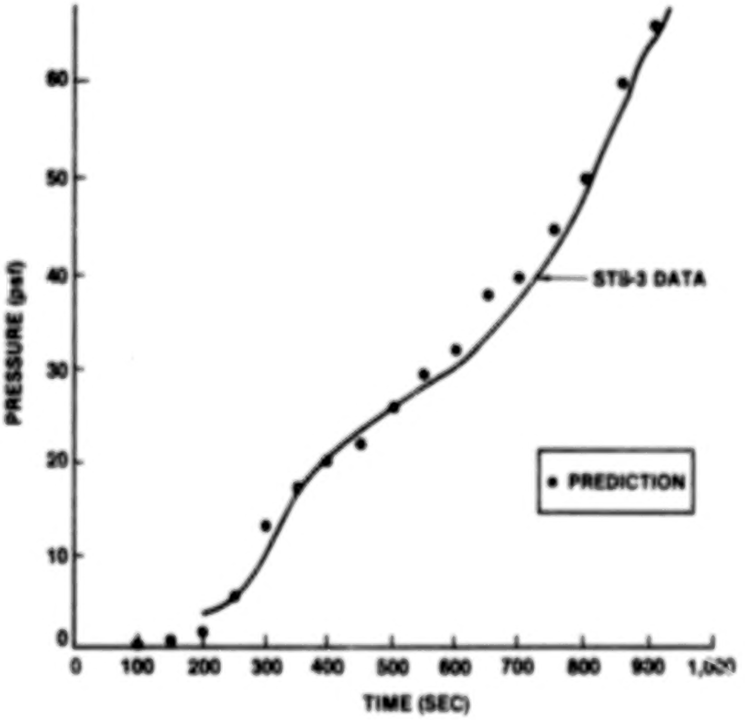

Figure 11.- STS-3 postflight lower centerline - X/L = 0.40 (V07P9472).

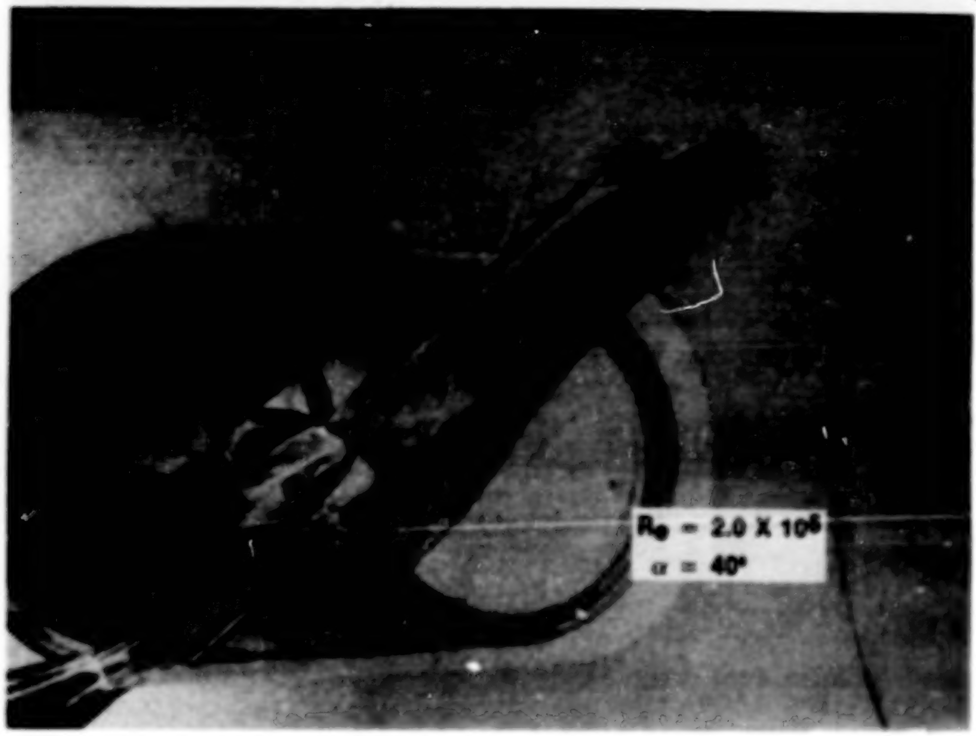
$R_e = 2.0 \times 10^6$
$\alpha = 40°$

(a) Oil flow patterns in wind tunnel. $\alpha = 40^{\circ}$.

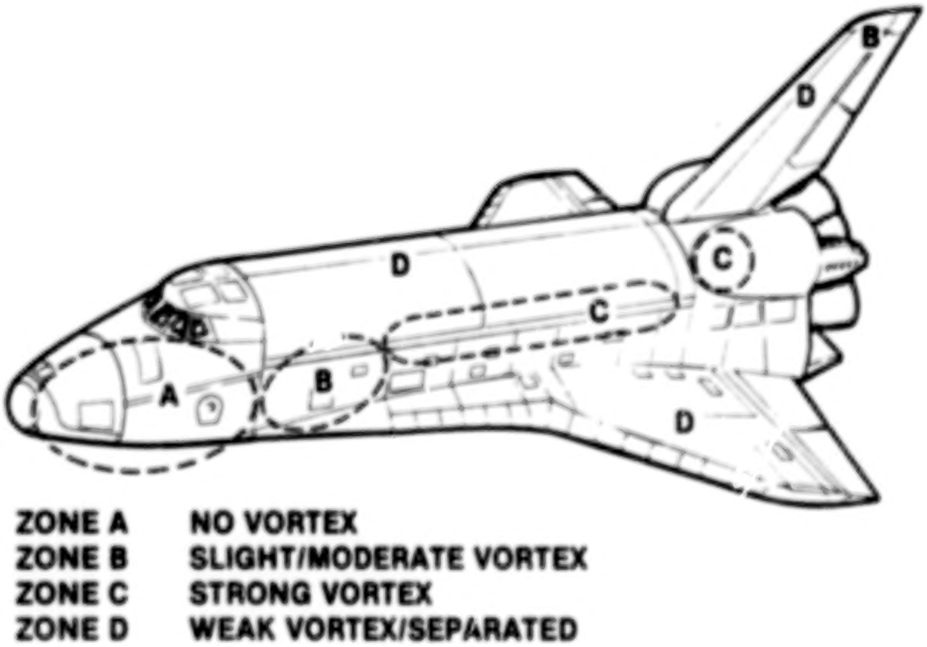
A
B
C
C
D
D
D
B
ZONE A NO VORTEX
ZONE B SLIGHT/MODERATE VORTEX
ZONE C STRONG VORTEX
ZONE D WEAK VORTEX/SEPARATED

(b) Leeside vortex flows.

Figure 12.- Fuselage side heating patterns.

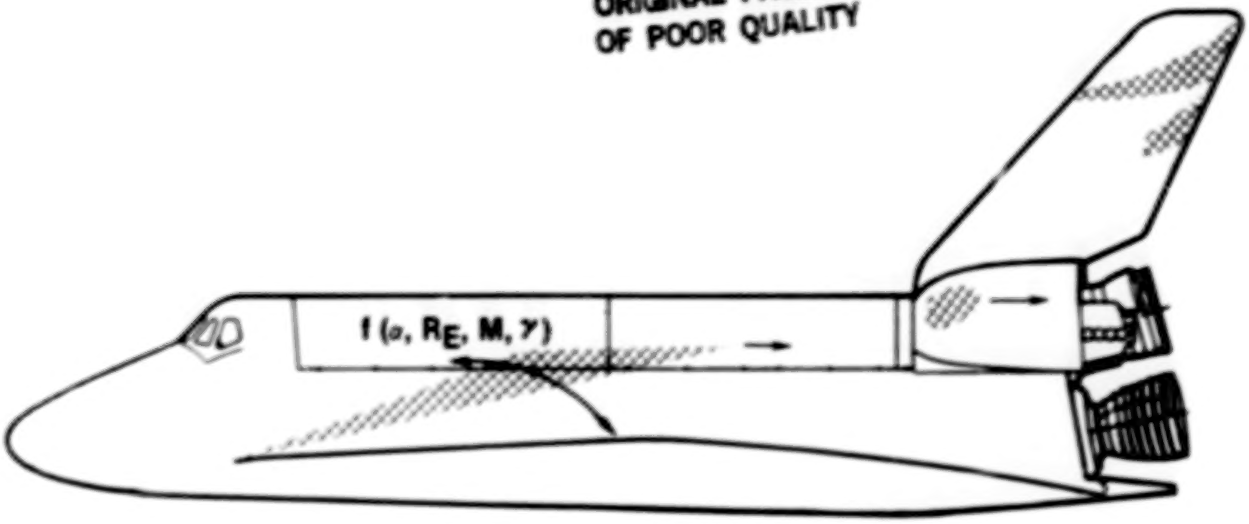

(c) Vortex scrubbing.

Figure 12.- Concluded.

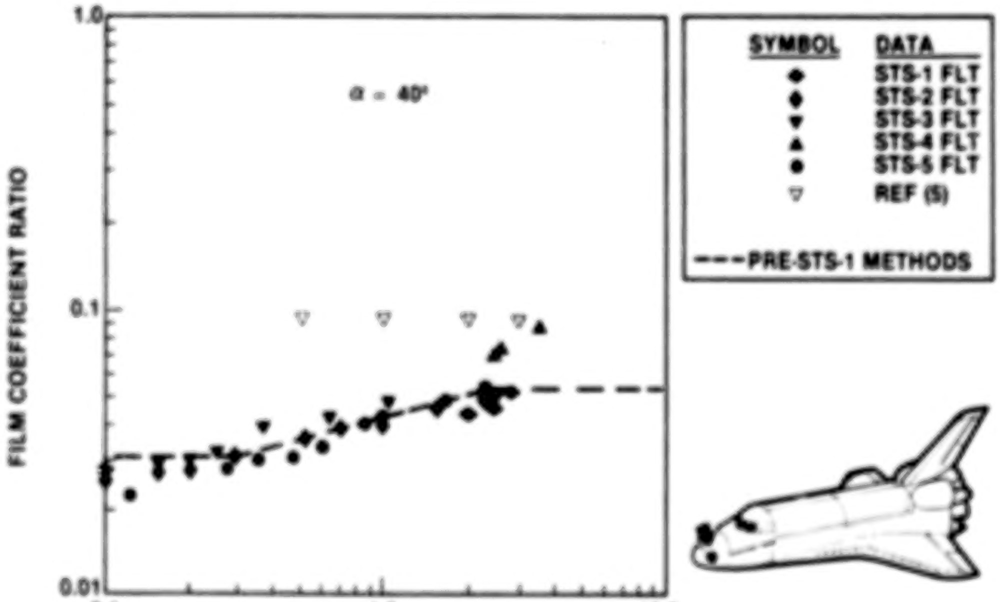

(a) α = 40°.

Figure 13.- Fuselage side heating correlation at location V07T9880.

ORIGINAL PAGE IS
OF POOR QUALITY

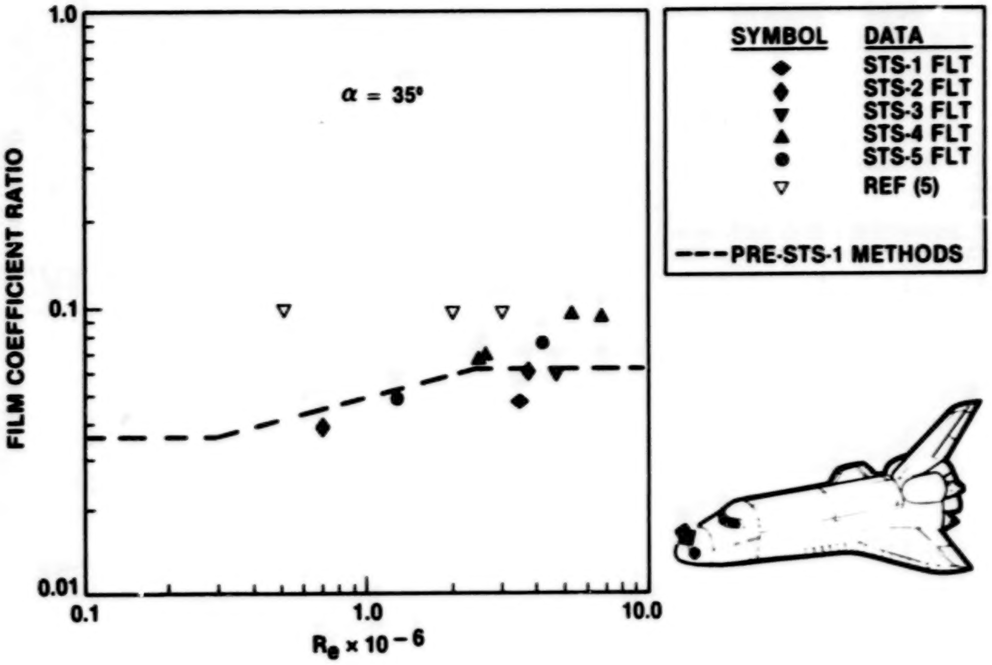

(b)α = 35°.

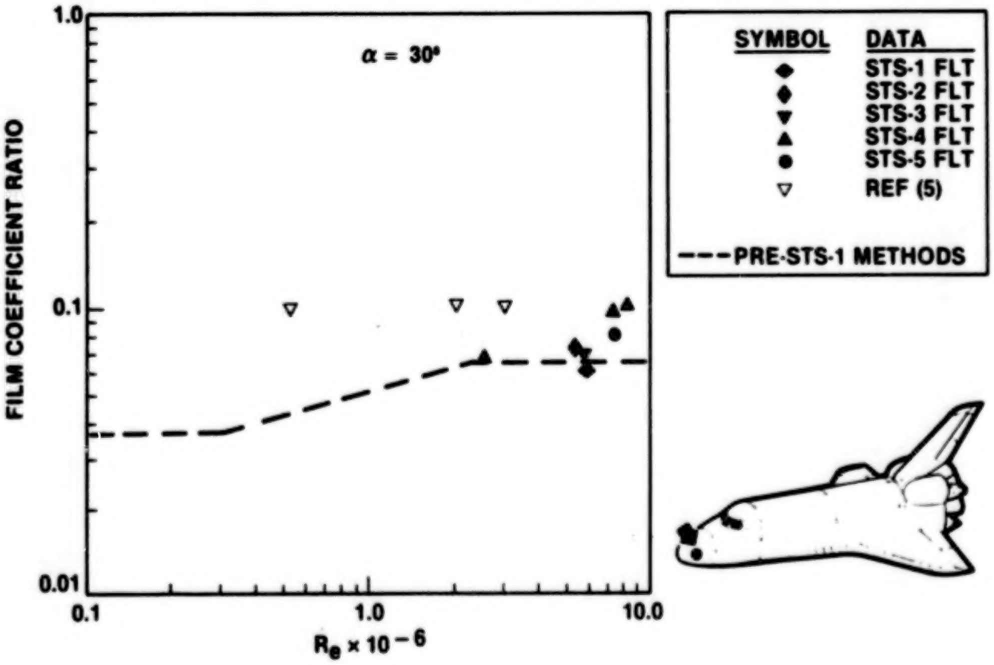

(c)α = 30°.

Figure 13.- Concluded.

C-2

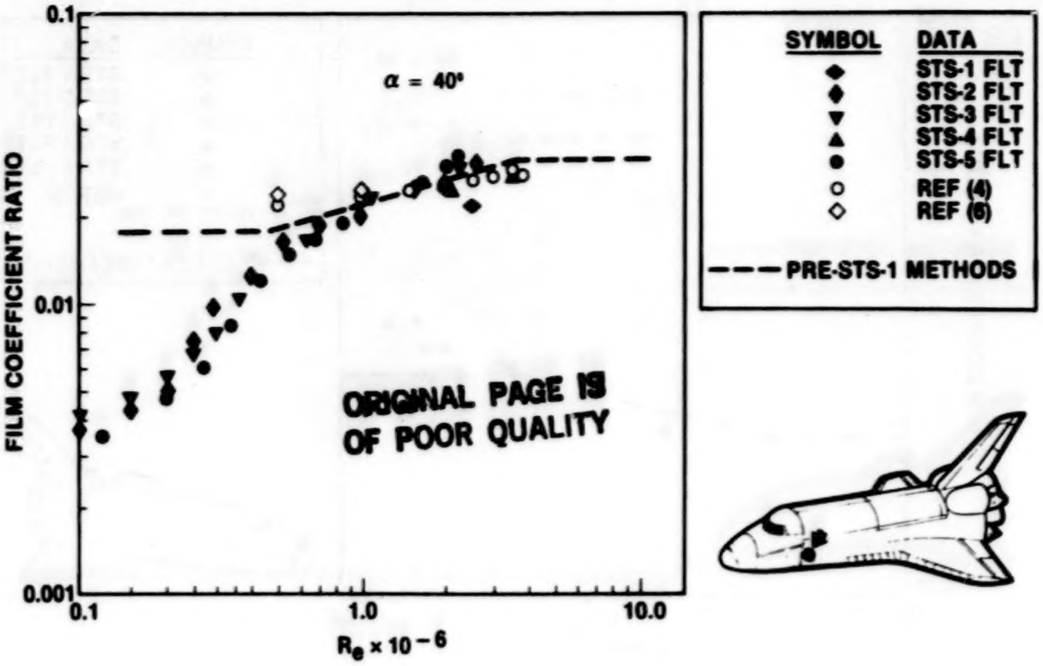

(a)$\alpha = 40^{\circ}$.

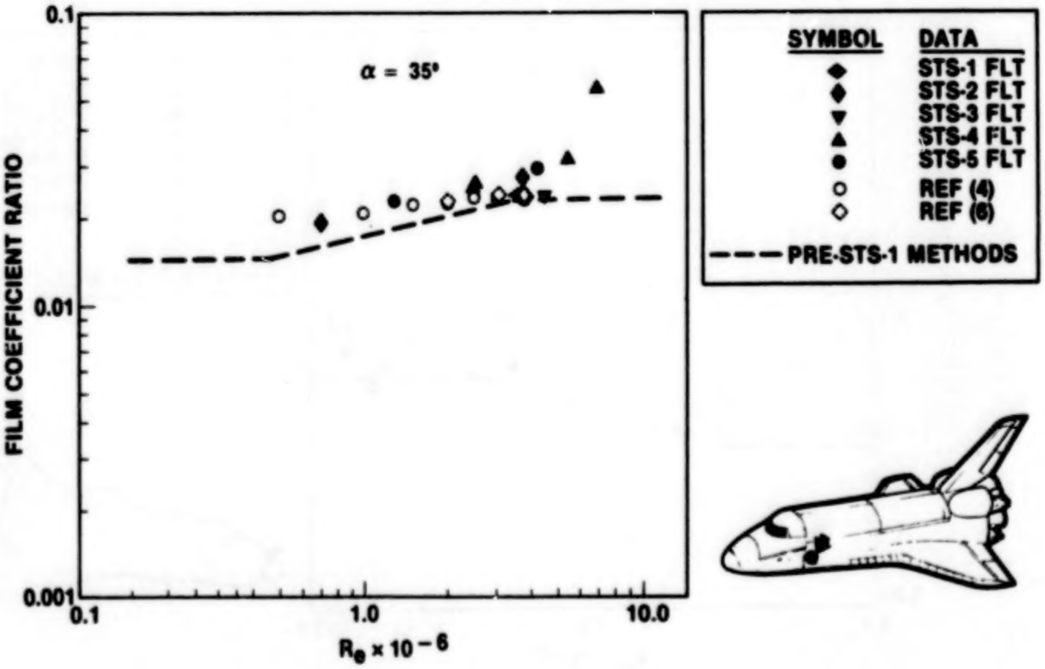

(b)$\alpha = 35^{\circ}$.

Figure 14.- Fuselage side heating correlation at location V07T9859.

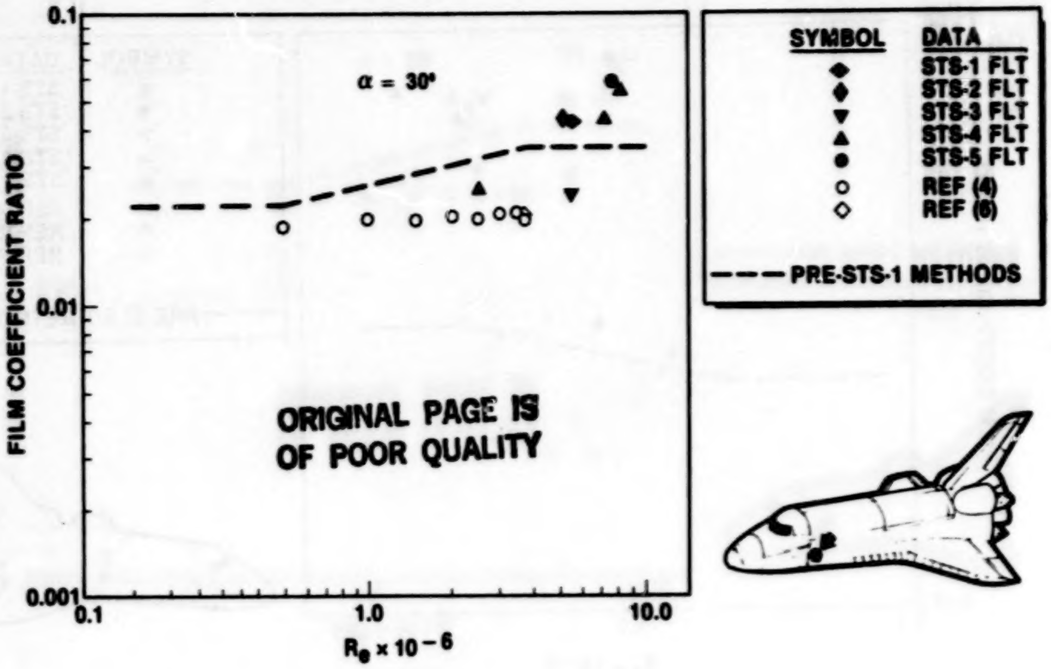

(c) α = 30°.

Figure 14.- Concluded.

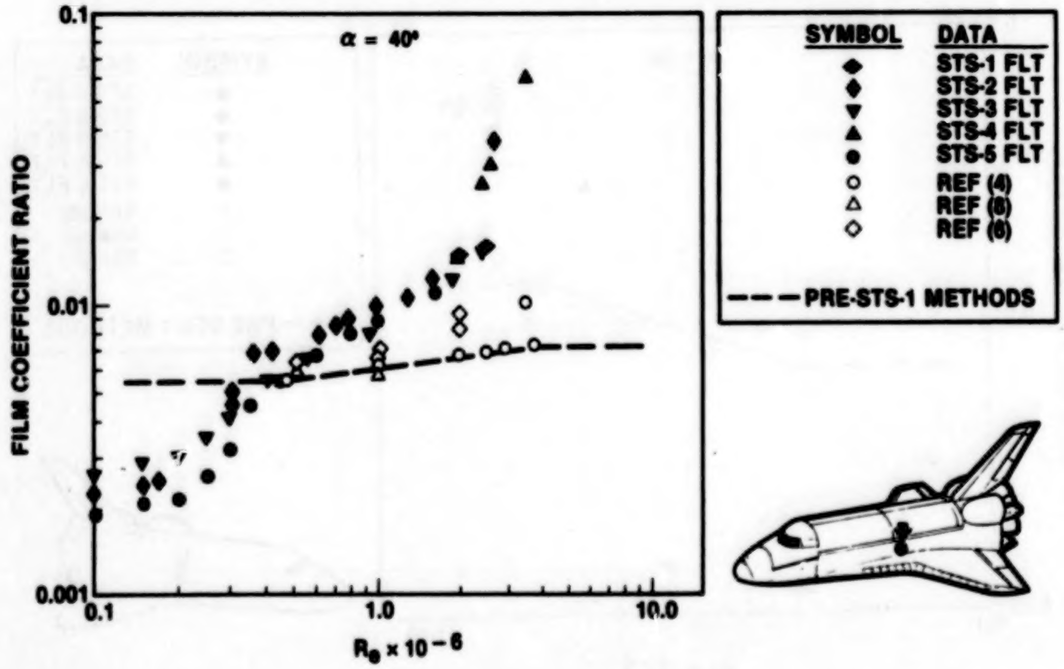

(a) α = 40°.

Figure 15.- Fuselage side heating correlation at location V07T9905.

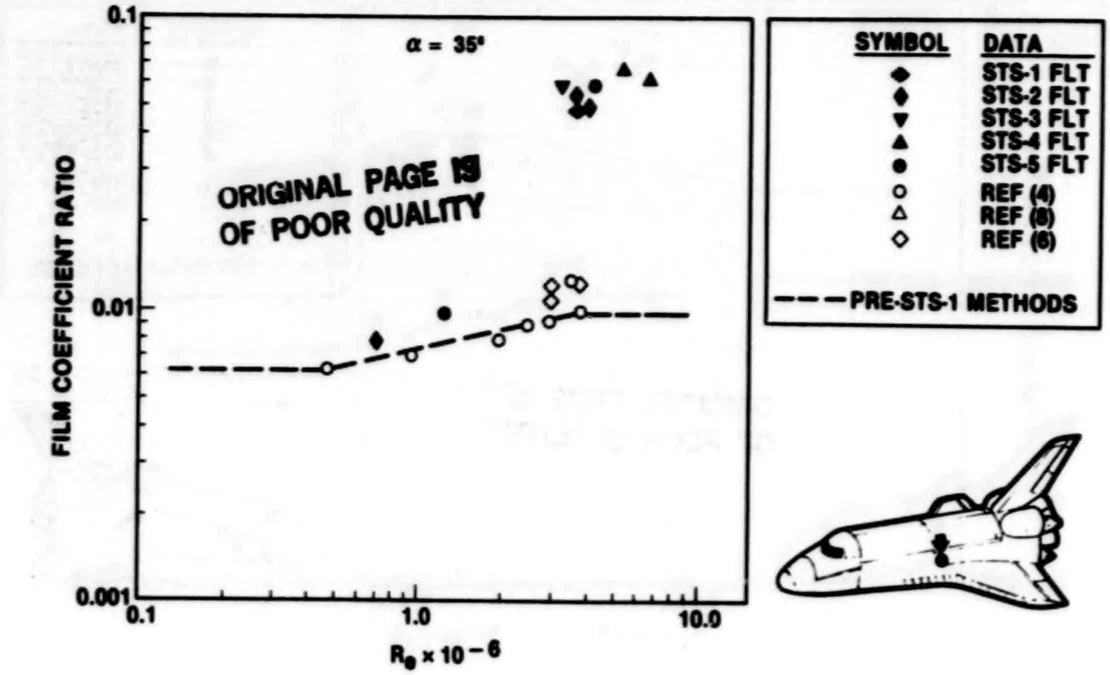

(b) α = 35°.

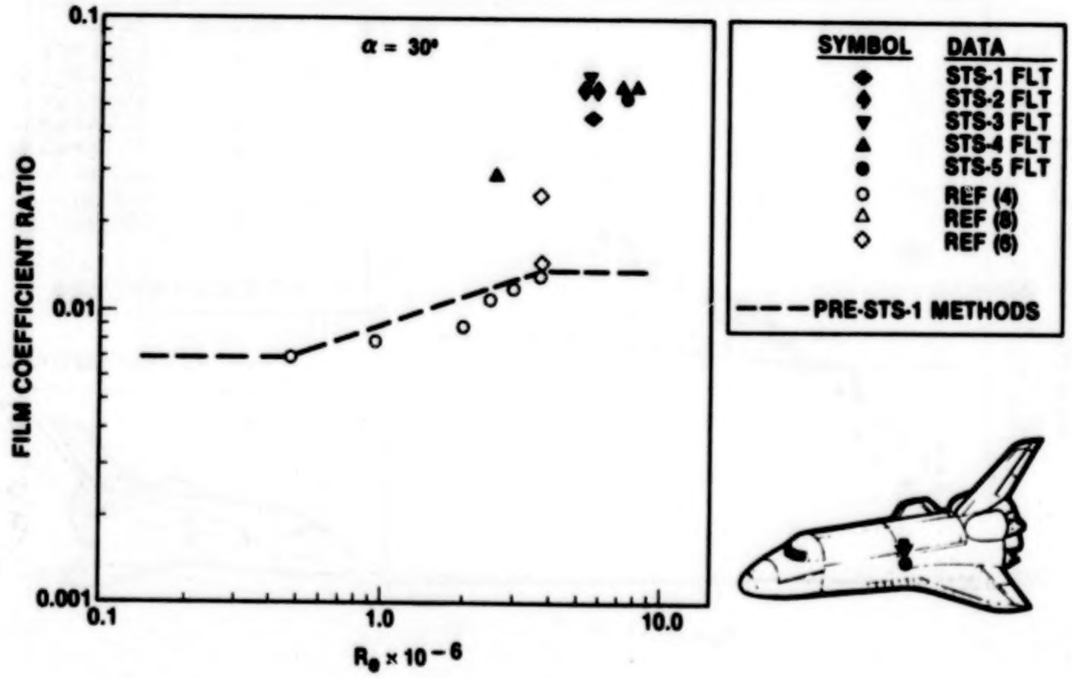

(c) α = 30°.

Figure 15.- Concluded.

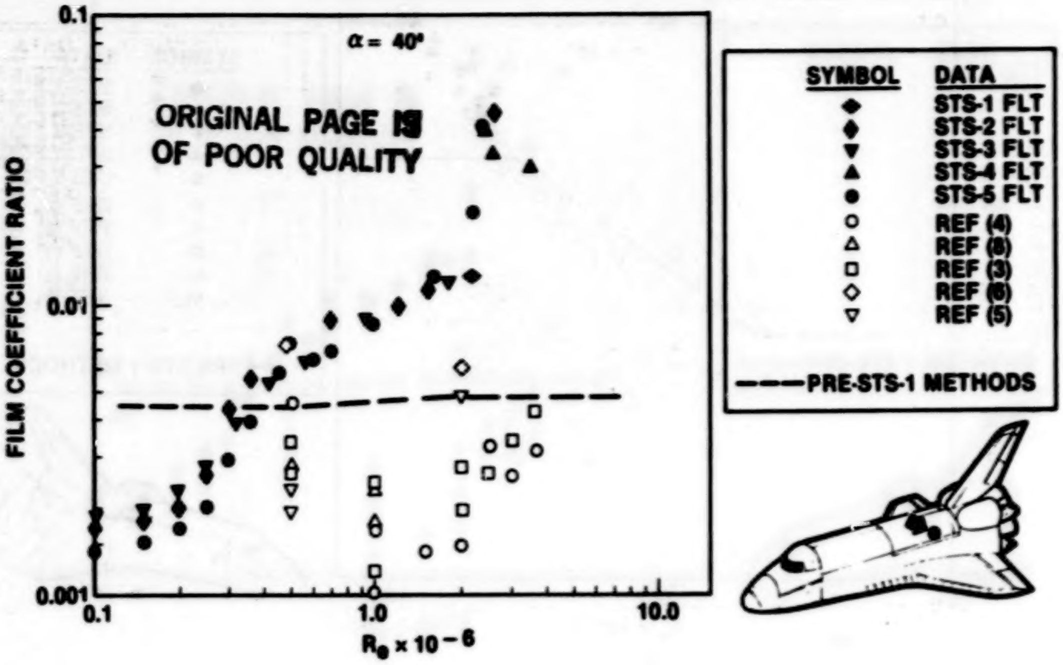

ORIGINAL PAGE IS OF POOR QUALITY

(a) α = 40

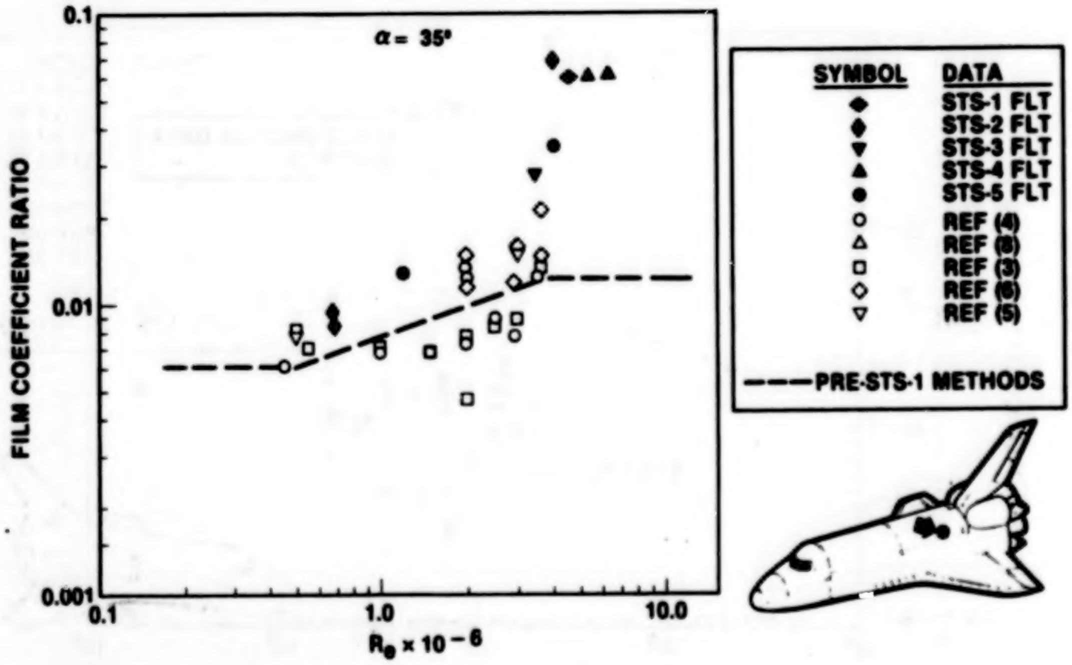

(b) α = 35°.

Figure 16.- Fuselage side heating correlation at location V07T9925.

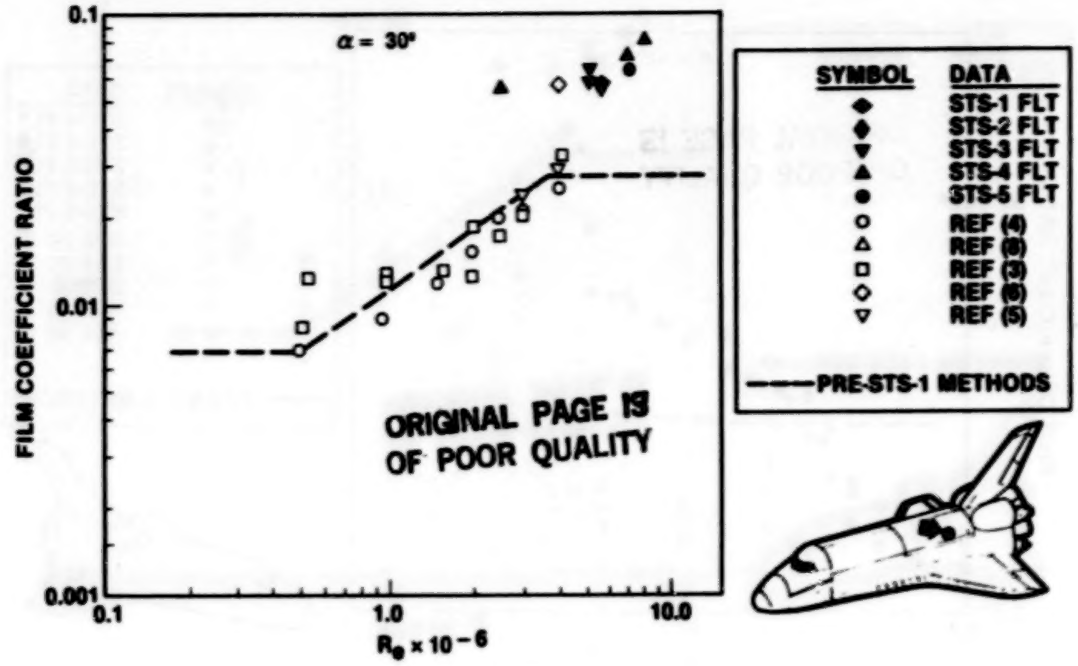

(c) α = 30°.

Figure 16.- Concluded.

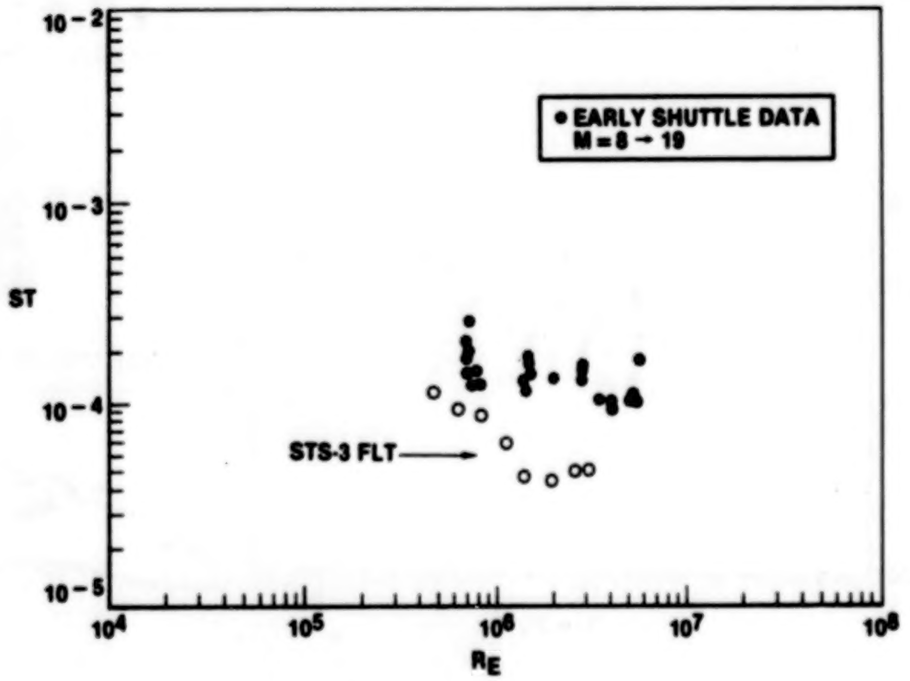

(a) ϕ = 180°, α = 40°, X/L = 0.7.

Figure 17.- Fuselage upper surface.

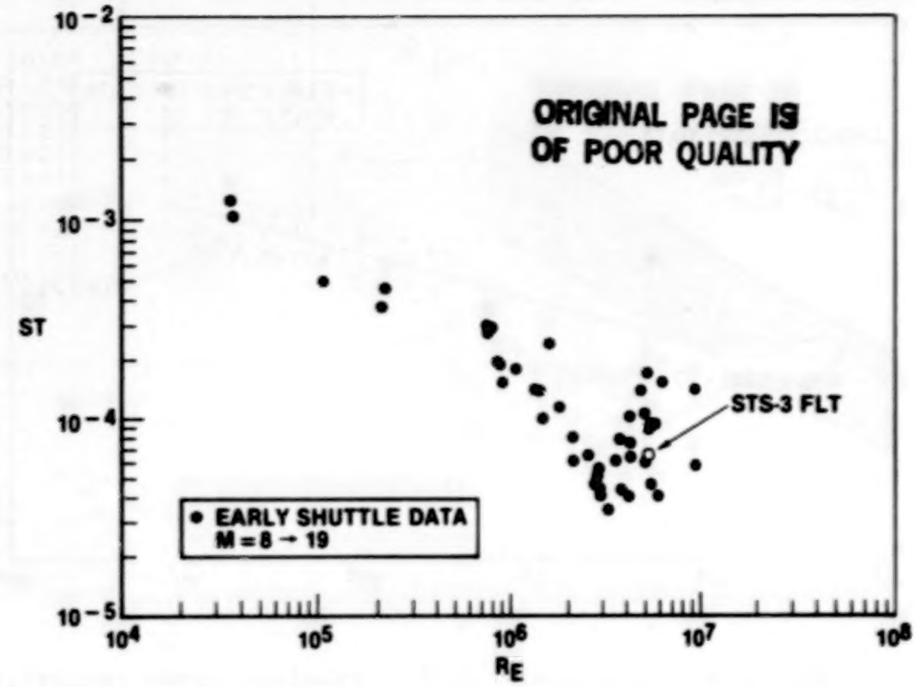

(b) ϕ = 180°, α = 35°, X/L = 0.7.

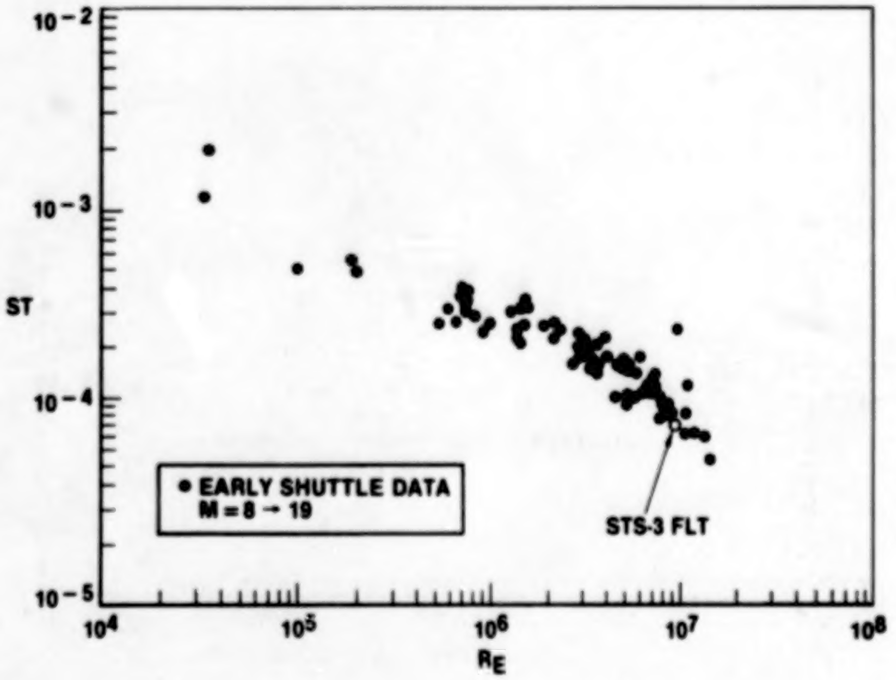

(c) ϕ = 180°, α = 30°, X/L = 0.7.

Figure 17.- Concluded.

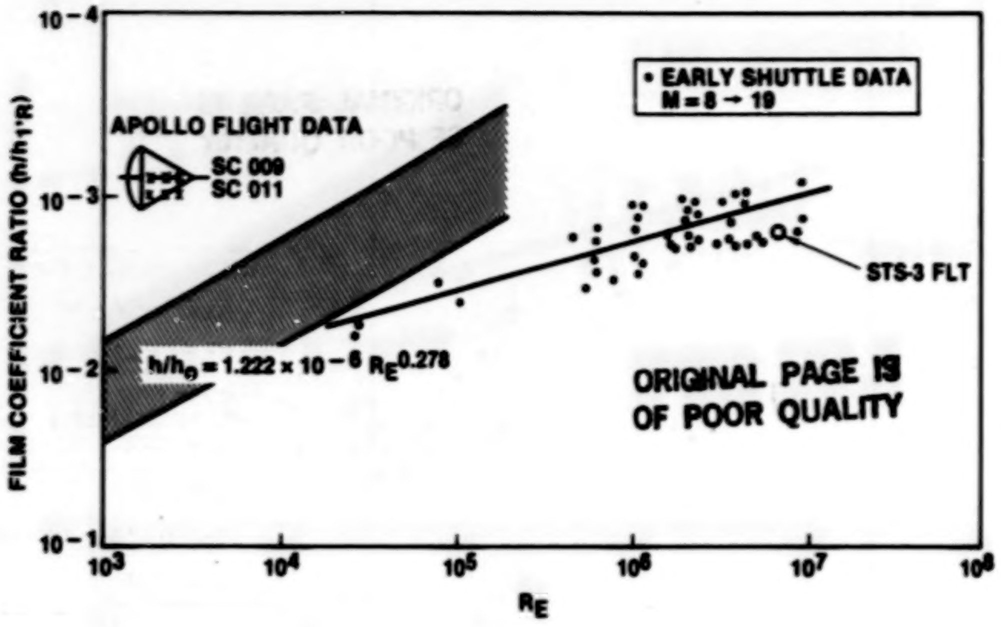

Figure 18.- Flight data versus wind tunnel. Fuselage upper centerline - $X/L = 0.5$, $\alpha = 30^{\circ}$.

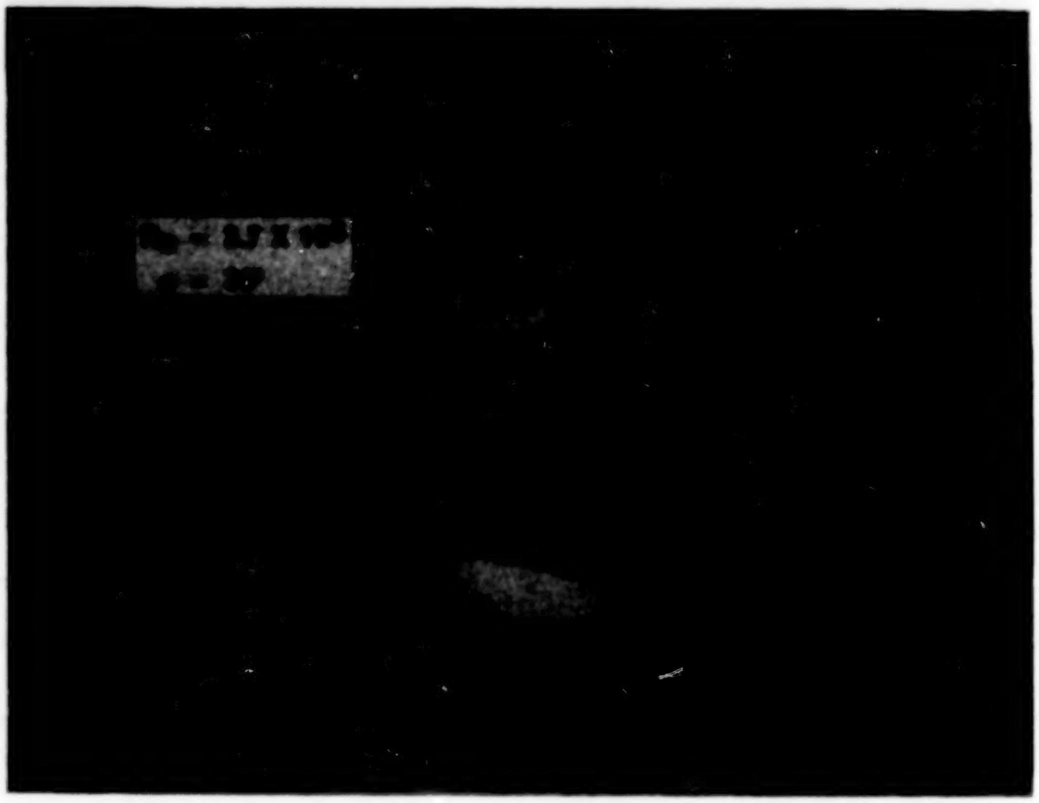

Figure 19.- Oil flow patterns in wind tunnel. $\alpha = 35^{\circ}$.

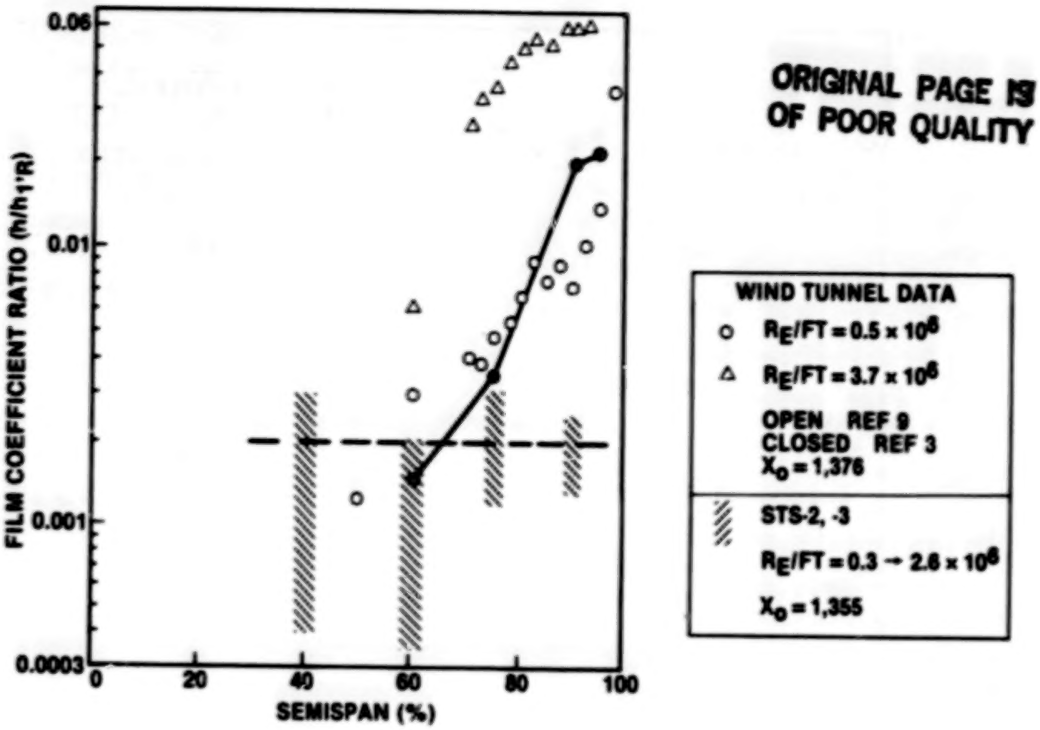

Figure 20.- Wing upper surface - spanwise variation.

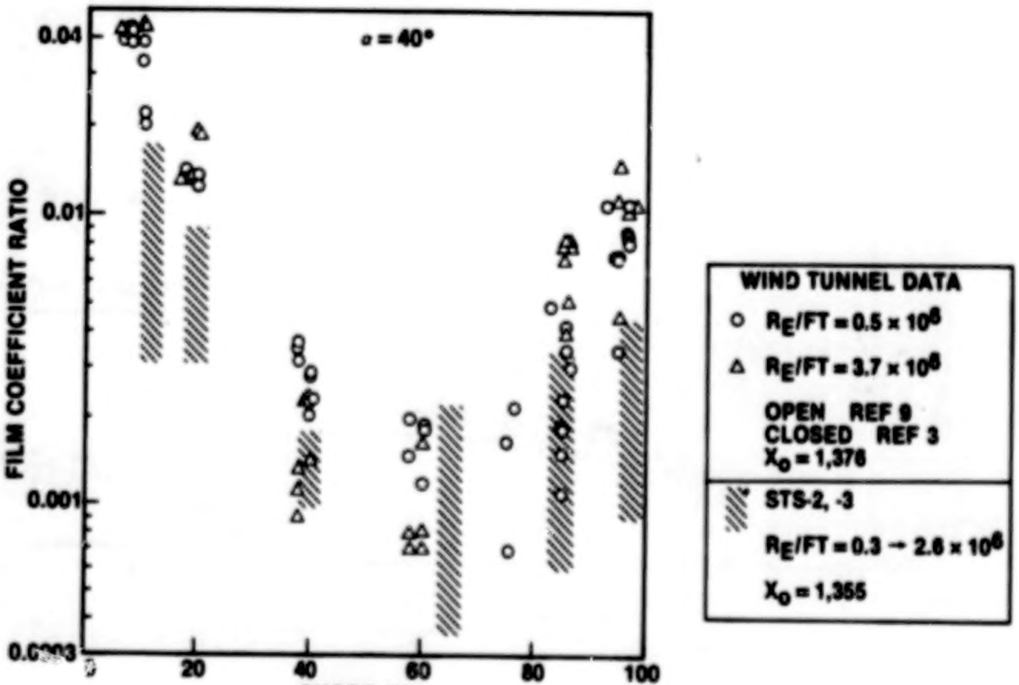

Figure 21.- Wing upper surface - 60-percent semispan.

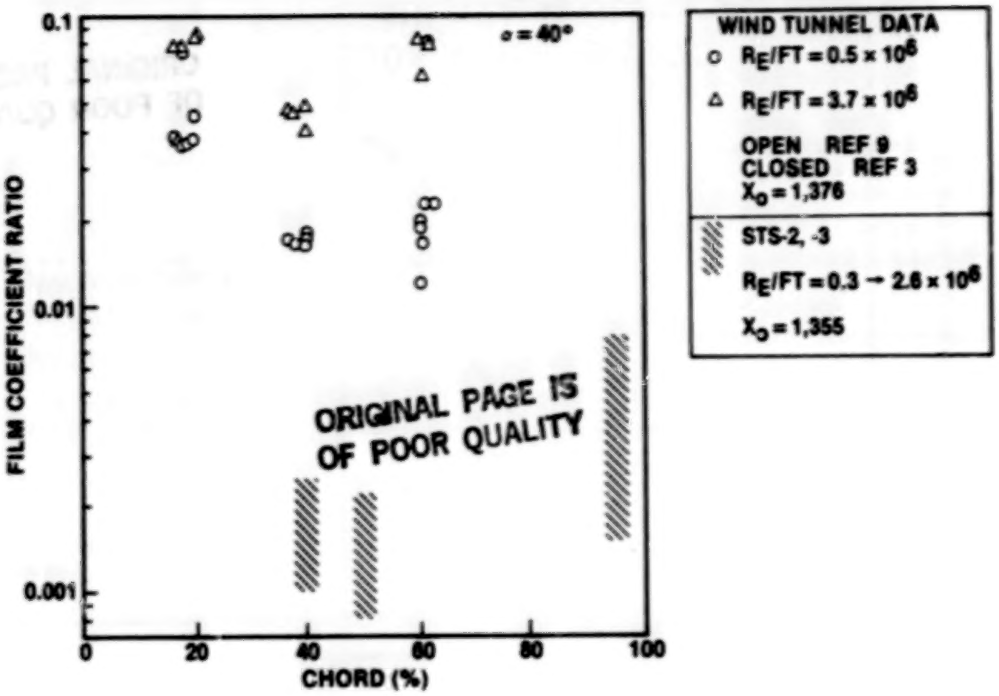

Figure 22.- Wing upper surface - 90-percent semispan.

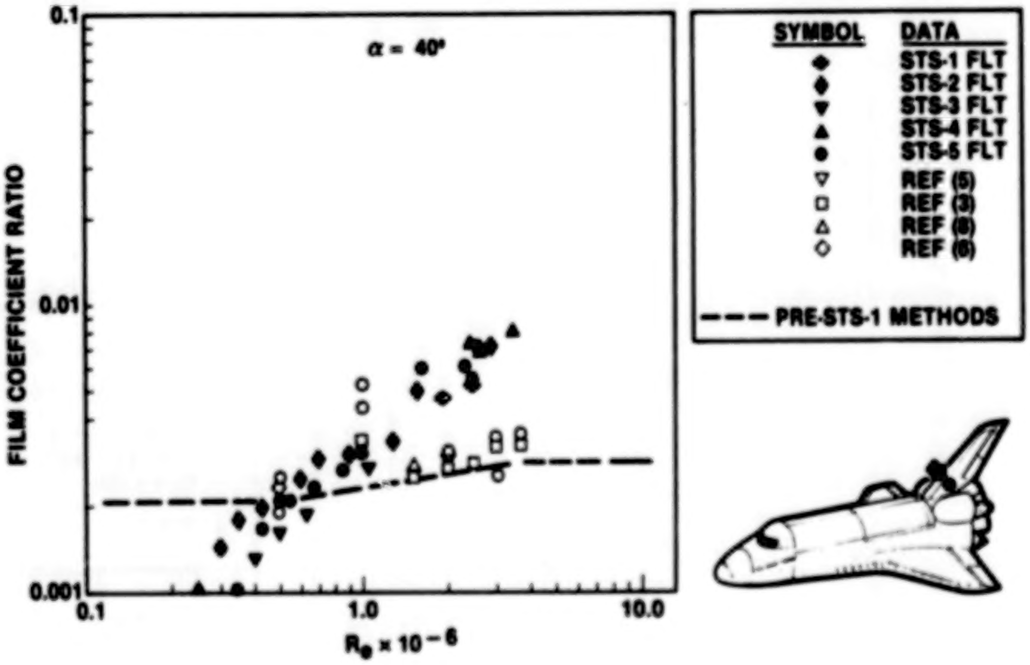

(a) α = 40°.

Figure 23.- Vertical tail heating correlation.

VERTICAL TAIL HEATING CORRELATION V07T9933

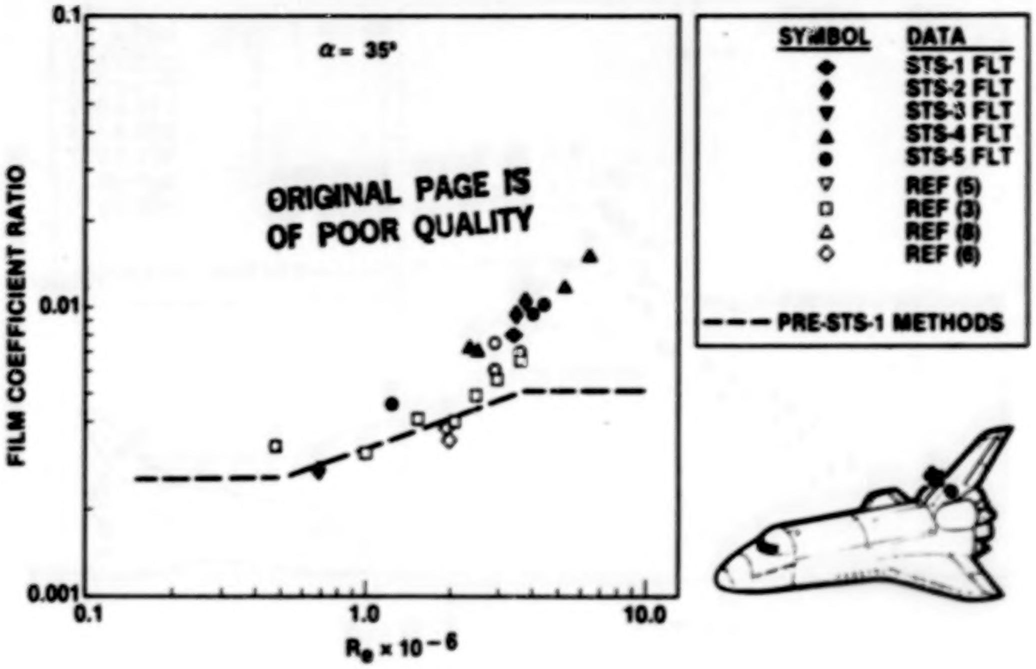

(b) $\alpha = 35^{\circ}$.

VERTICAL TAIL HEATING CORRELATION V07T9933

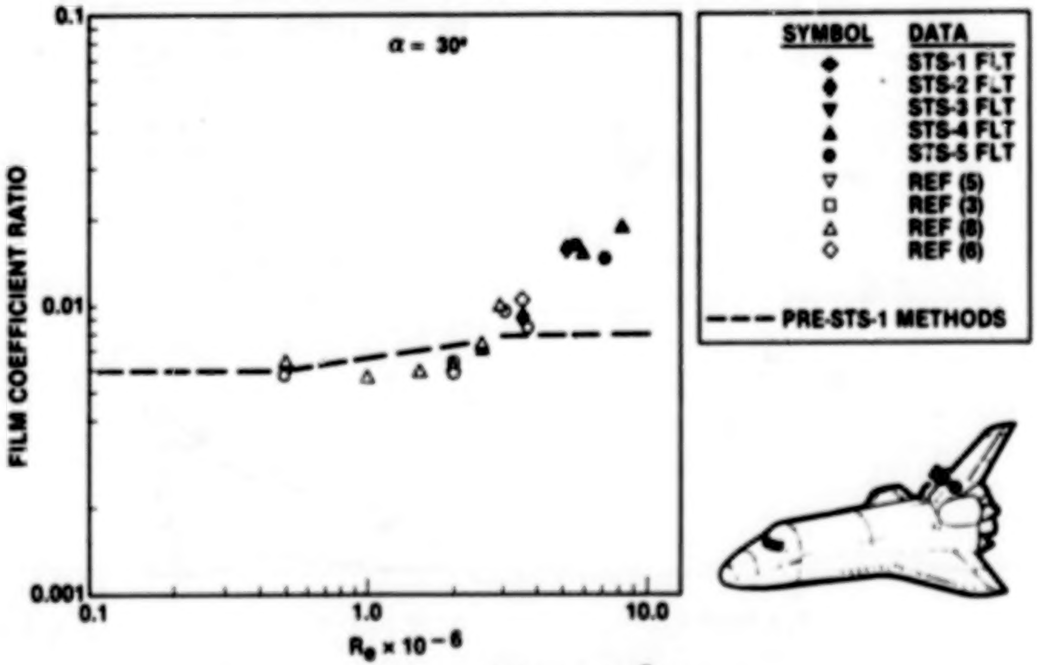

(c) $\alpha = 30^{\circ}$.

Figure 23.- Concluded.

VERTICAL TAIL CORRELATION V07T9941

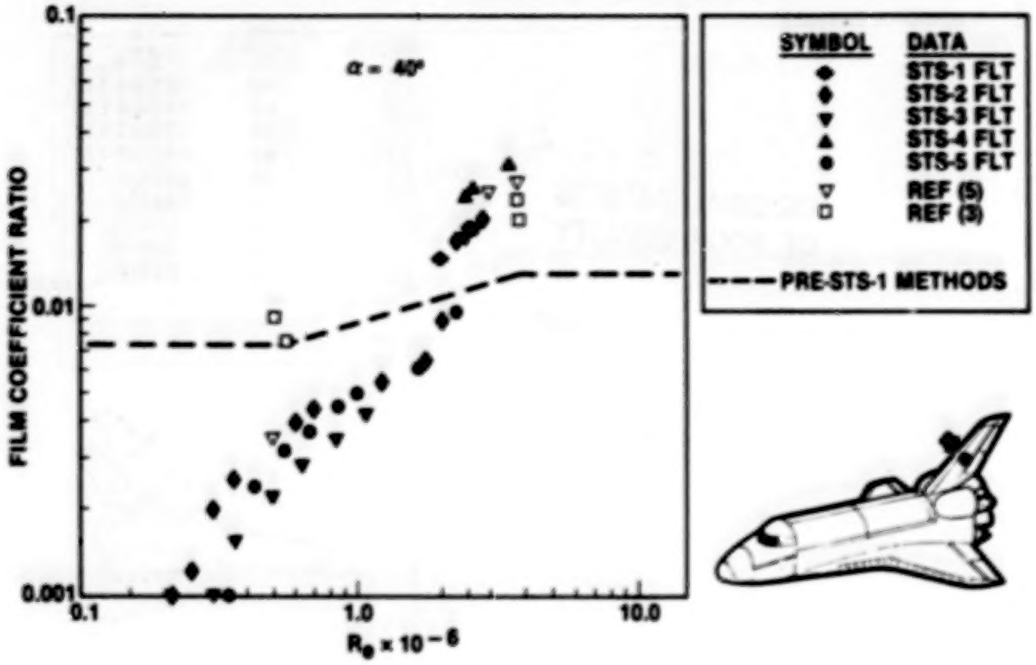

(a) α = 40°.

VERTICAL TAIL CORRELATION V07T9941

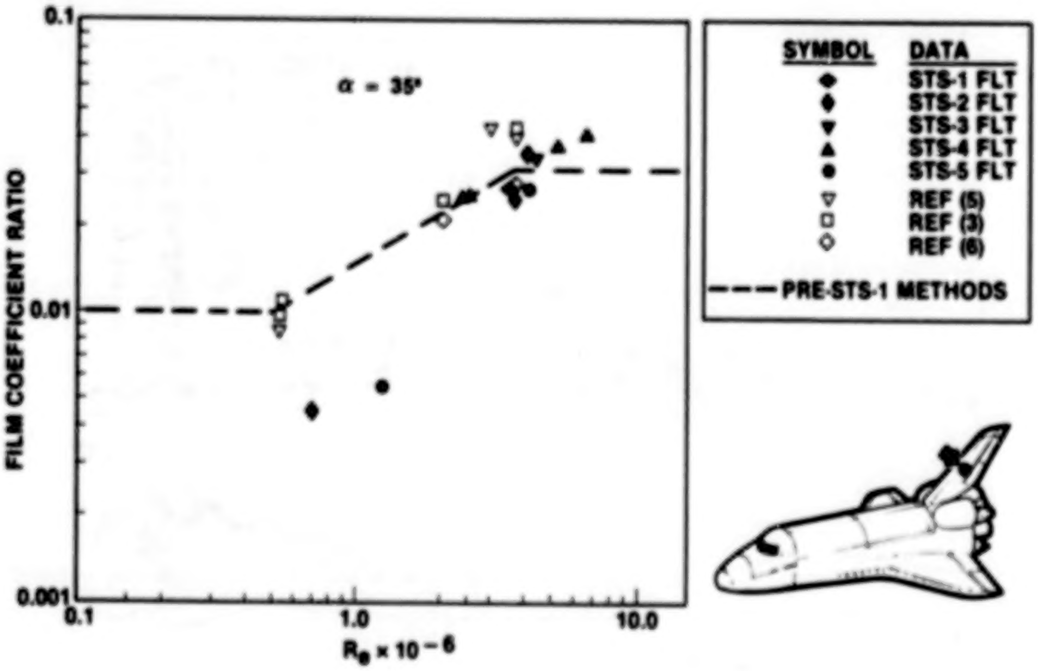

(b) α = 35°.

Figure 24.- Vertical tail correlation.

ORIGINAL PAGE IS
OF POOR QUALITY

VERTICAL TAIL CORRELATION V07T8941

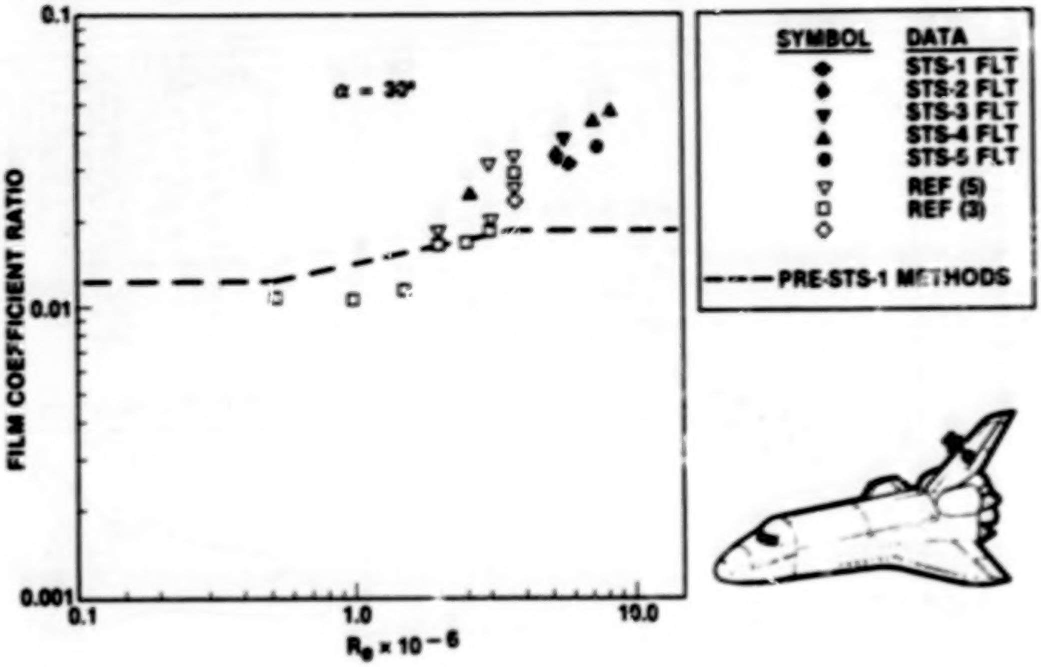

(c) α = 30°.

Figure 24.- Concluded.

OMS POD HEATING CORRELATION V07T9976

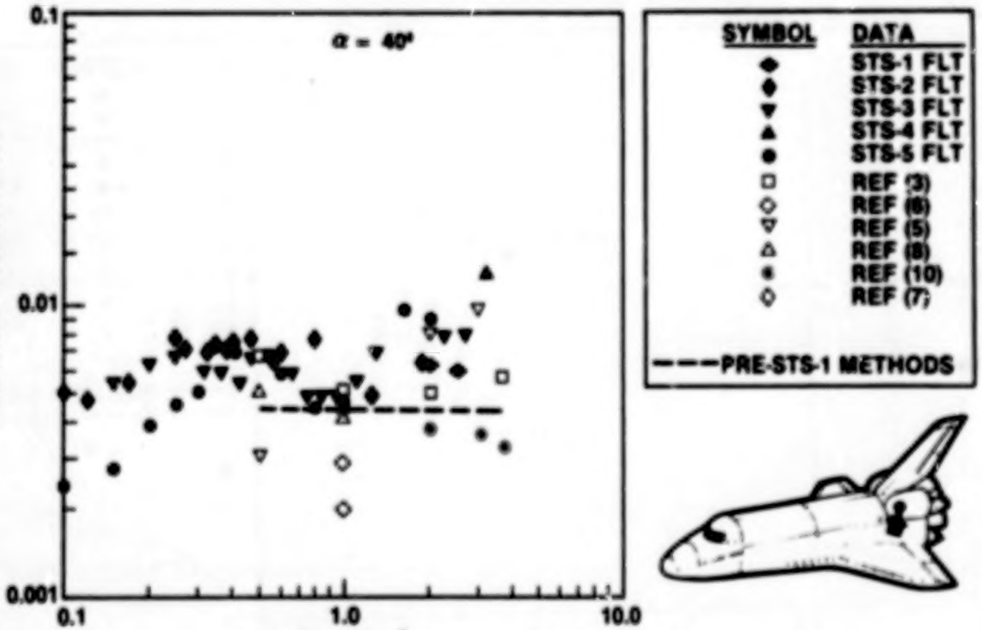

(a) α = 40°.

Figure 25.- Orbital Maneuvering System pod heating correlation.

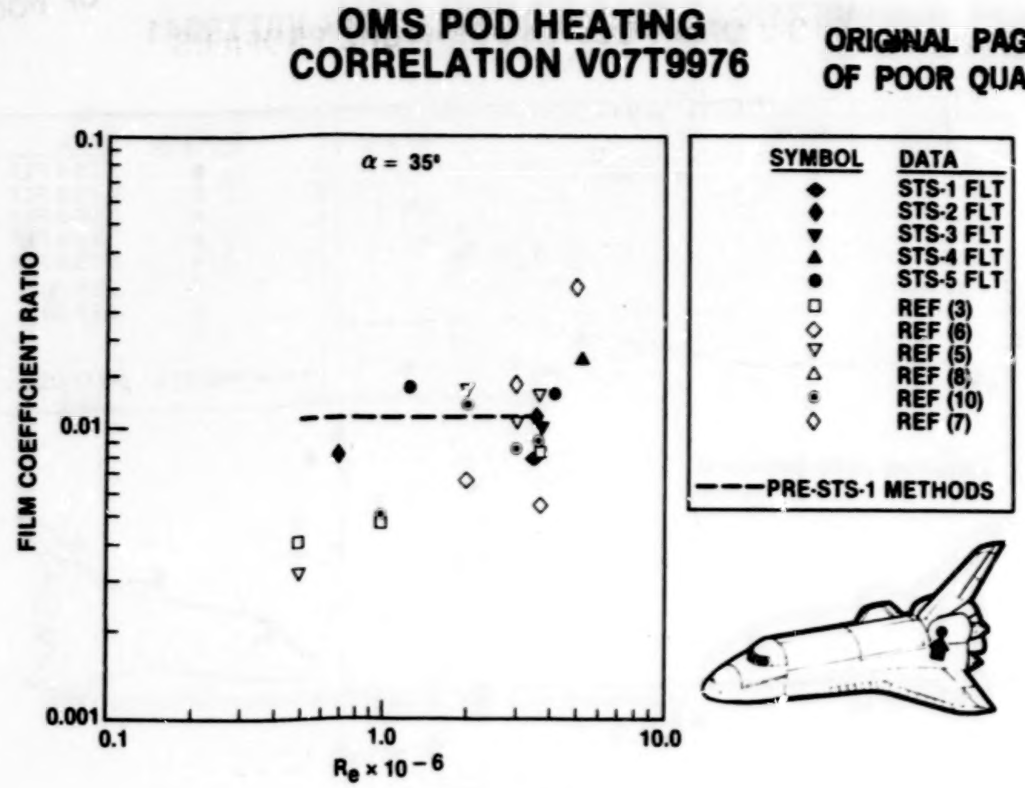

(b) α = 35°.

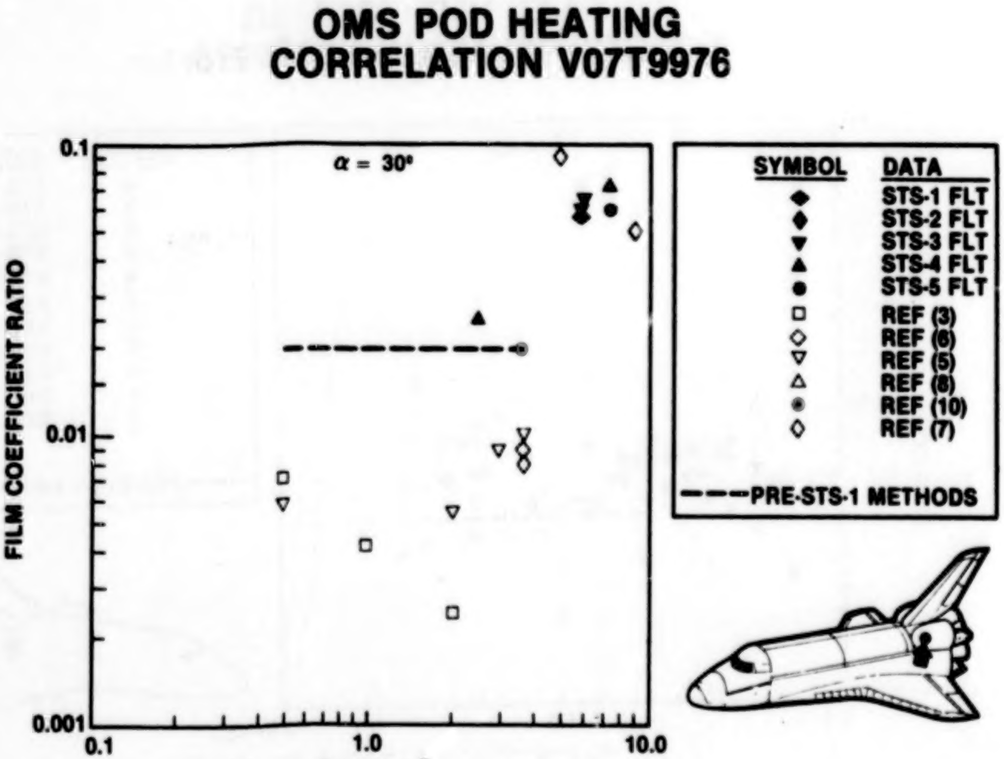

(c) α = 30°.

Figure 25.- Concluded.

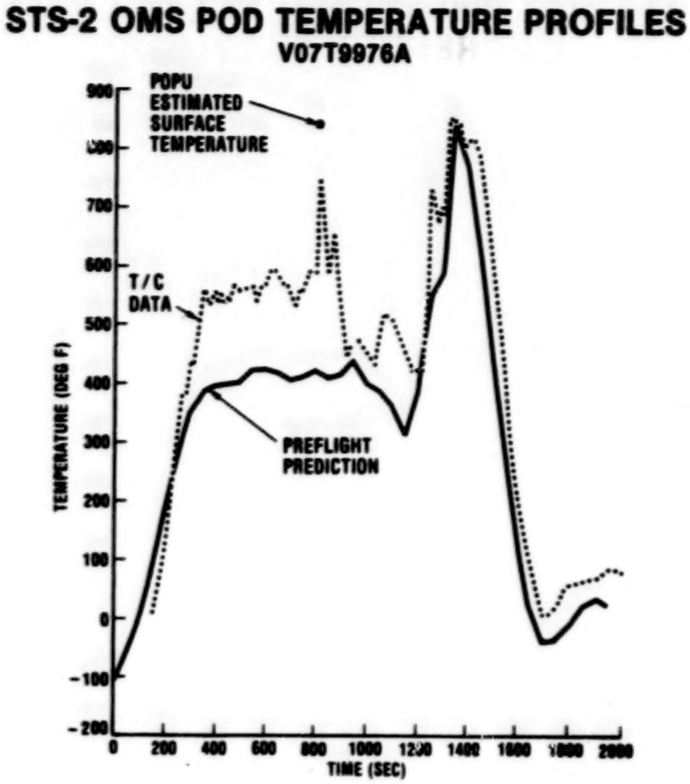

Figure 26.- STS-2 Orbital Maneuvering System pod temperature profiles (V07T9976A).

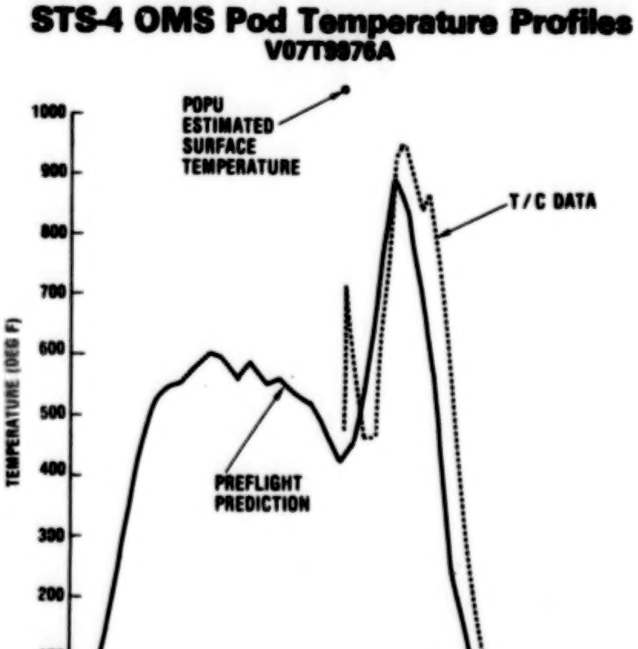

Figure 27.- STS-4 Orbital Maneuvering System pod temperature profiles (V07T9976A).

N84
10149

UNCLAS

N84 10149 D5

SHUTTLE ORBITER BOUNDARY LAYER TRANSITION AT FLIGHT AND WIND TUNNEL CONDITIONS

Winston D. Goodrich and Stephen M. Derry
NASA Johnson Space Center
Houston, Texas

John J. Bertin
The University of Texas at Austin
Austin, Texas

ABSTRACT

Hypersonic boundary layer transition data obtained on the windward centerline of the Shuttle orbiter during entry for the first five flights are presented and analyzed. Because the orbiter surface is composed of a large number of thermal protection tiles, the transition data include the effects of distributed roughness arising from tile misalignment and gaps. These data are used as a benchmark for assessing and improving the accuracy of boundary layer transition predictions based on correlations of wind tunnel data taken on both aerodynamically rough and smooth orbiter surfaces. By comparing these two data bases, the relative importance of tunnel free-stream noise and surface roughness on orbiter boundary layer transition correlation parameters can be assessed. This assessment indicates that accurate predications of transition times can be made for the orbiter at hypersonic flight conditions by using roughness-dominated wind tunnel data. Specifically, times of transition onset and completion can be accurately predicted using a correlation based on critical and effective values of a roughness Reynolds number previously derived from wind tunnel data.

INTRODUCTION

During the design, development, and construction of the Space Shuttle orbiter, concerns regarding the sensitivity of the thermal protection system (TPS) design to changes in heat transfer rates and loads caused by boundary layer transition were paramount. These concerns were fueled by very preliminary studies[1] which showed that the weight of the TPS changed by approximately 25%, depending on which of several "universal" transition prediction methodologies were used. Because at this time only a limited aerothermodynamic data base existed for vehicles as complex as the orbiter, the design, development, and construction processes for the TPS commenced before more specific correlations could be developed. In particular, the TPS was sized using smooth surface transition predictions derived from orbiter wind tunnel data and correlated with the popular transition parameter Re_θ/M. To prevent premature roughness-induced transition, smoothness constraints were placed on the TPS based on the "effective" roughness concept developed by van Driest and Blumer[2]. However, as the TPS was being fabricated, it became apparent that the initial smoothness requirements (k = 0.017" to 0.04") could not be achieved without expensive and lengthy manufacturing and installation efforts. This prompted the development of a more refined aerothermodynamic data base with complementary flow field analyses[3,4] resulting in more refined orbiter heating and boundary layer transition prediction methodologies.[5,6,7] Because the orbiter windward surface is composed of a large number of TPS tiles, the transition criterion had to

PAGE 752 INTENTIONALLY BLANK

PRECEDING PAGE BLANK NOT FILMED

include the effects of distributed roughness arising from tile misalignments and gaps. The individual tiles and gaps are visible in the photograph shown in Fig. 1.

Although the development of these methodologies could not always support the orbiter TPS design and construction schedule, the results were very useful in providing more quantitative estimates of aerothermodynamic uncertainties[8] necessary to support safety requirements for man-rated spacecraft operations. Furthermore, with regard to boundary layer transition, the analyses performed in Refs. 5, 6, and 7, which better defined the sensitivity of orbiter boundary layer transition to surface roughness caused by these TPS tile misalignments and gaps, allowed the stringent surface smoothness requirements initially imposed on the orbiter to be relaxed. In so doing, excessive concerns regarding TPS tile manufacturing and installation tolerances were also reduced, which contributed to an earlier rollout and flight schedule for the orbiter.

The transition methodology developed in Ref. 7, which was used extensively for making preflight assessments of the effects of surface roughness on orbiter boundary layer transition, is based on a relatively straightforward extrapolation of wind tunnel data correlations to flight conditions using local flow field parameters. This methodology requires precise geometric and dynamic flow simulation, which is a necessary condition for simulating both the magnitude and distribution of local flow field properties. Application to orbiter flight conditions was made on the premise that uncertainties in boundary layer transition data from hypersonic wind tunnels are always conservative; i.e., it is "well known" that boundary layer transition on a wind tunnel model occurs at lower Reynolds numbers than in flight because of disturbances or noise within the tunnel free stream. However, this premise is true only for aerodynamically smooth bodies, or bodies with roughness heights and/or other shock-layer-induced flow disturbances that do not dominate the transition process. Studies (Refs. 2, 9, and 10) aimed at defining the combined effects of roughness and free-stream disturbances for simple bodies with localized roughness elements have been conducted for the subsonic and supersonic flow regimes. Fewer studies have addressed the same issue for configurations as complicated as the orbiter while at hypersonic flow conditions and low values of T_w/T_o and with the additional complexity of having multiple sources of flow disturbances, such as distributed roughness elements, wind tunnel free-stream noise, and disturbances from the curved bow shock entropy gradient.

With the completion of the Space Transportation System (STS) test flights, a substantial aerothermodynamic data base has been compiled which provides the opportunity to evaluate the orbiter boundary layer transition prediction methodology. To this end, the primary purpose of this paper is to provide additional information and insight into the requirements for developing a reliable transition methodology based primarily on wind tunnel data because, in most cases, only wind tunnel data exist on a given configuration at the time that critical design decisions need to be made for the project. In addition, this paper will present transition data from the first five flights of the orbiter in a form usable to the technical community, make comparisons of these data with previously published wind tunnel data, show comparisons of predicted transition times with flight data, and use the results of these comparisons to assess and improve the accuracy of the current[7] orbiter boundary layer transition prediction methodology. Emphasis will be placed on reviewing the wind tunnel data in light of the STS flight data in order to establish a transition prediction methodology for the orbiter that will be less dependent on free-stream disturbances that exist in the wind tunnel. To accomplish this, the relative importance of tunnel free-stream noise and surface roughness on boundary layer transition distributions will be established from the data bases. In an effort to present the data as completely as possible, several common transition parameters were used in making the comparisons ($Re_{\infty,L}$, Re_x, Re_θ/M, and Re_k). Care was also taken to assure that comparable ranges of flow conditions and vehicle attitudes were used. Because most of the transition parameters are defined using local flow conditions, results will be limited to the orbiter windward centerline where flow conditions can be accurately predicted based on correlations of the 3-D flow field results of Ref. 3.

ORBITER FLIGHT TEST (OFT) PROGRAM

The OFT program, consisting of the first four STS flights, was designed to provide information to certify the hardware for the orbiter subsystems and the methodologies used to design these subsystems. This was safely accomplished by planning these flights to provide relatively benign conditions for the orbiter at first, with each successive flight progressively stressing the orbiter subsystems closer to design levels. The fifth flight, although officially an operational flight, also provided data of a redundant nature that can also be used for certification purposes. Transition data from all five flights were utilized to fulfill the purposes of this paper.

Flight Instrumentation

For these developmental flights, an onboard instrumentation system, referred to as the development flight instrumentation (DFI), provided the data necessary for certification studies. Although quite extensive, only the locations of the surface thermocouples (thermocouples located within selected TPS tiles which were in contact with the TPS coating) required for this study will be described. Additional information concerning the DFI instruments and locations can be found in Ref. 11. Instrumentation used to define transition along the orbiter windward centerline is depicted in Fig. 2. Detailed locations of these instruments, along with orbiter "body point" numbers and instrument identification numbers, are listed in Table 1.

Because of various malfunctions with the DFI data recorder, entry data for STS-1 and STS-4 were obtained by telemetry for the portion of entry occurring after blackout. Approximately the first 1050 seconds of data were lost for these flights. Despite these problems, the complete transition location history was obtained on STS-4 and roughly half of it was obtained in STS-1. Data were obtained through the complete entries of STS-2, STS-3, and STS-5.

Surface Roughness

To estimate the effects of surface roughness on transition, information defining the magnitude and distribution of roughness over the orbiter is necessary. Referring again to Fig. 1, the qualitative features of roughness resulting from the TPS tile misalignments and gaps are readily visible. The majority of these tiles are 6" square with gaps ranging from 0.045" to 0.06". However, quantitative features of these roughnesses are difficult to obtain and as yet have not been determined. Nevertheless, an estimate of the roughness was made for the purposes of this paper. This estimate was based on two sources of data. First, tile misalignment heights were measured on vibro-acousic test panels used to simulate the response of orbiter structural panels and TPS tiles to vibration and acoustic loads experienced during launch. Tile misalignment heights were measured before and after the tests. The measurements formed an approximate Gaussian distribution, with a mean value of approximately 0.03". Maximum values for these measurements were approximately 0.07".

Roughness estimates were also made using the distributions of allowable roughness used by the workers who installed the TPS tiles on the orbiter. As indicated in the Introduction, allowable roughness specifications were initially very stringent, but were eventually relaxed as more information was obtained on the effects of roughness on transition for the orbiter. Figure 3 illustrates the distribution of allowable roughness used to guide the initial installation of TPS tiles, in addition to the distribution used for the final phase of tile installation that was occurring at the time of orbiter rollout. The allowable roughness specifications used in the latter phase also included a specification on gap width ($k_a = (k^2 + (w - 0.045)^2)^{\frac{1}{2}}$). The effects of gaps were shown[12] to be somewhat less effective than misalignment height.

These are maximum allowable roughness distributions do not imply that all tiles were installed to these specifications. Because the tile installation procedures and materials used for the orbiter and the vibro-acoustic test models were nearly identical, similar Gaussian distributions of misalignment heights would be expected for each phase of the installation process. Therefore, the mean values can be estimated to be the average of the two ends of the distribution function for each installation phase (the average of zero and k_a, or $k_a/2$). Because the percentage of tiles installed during each phase was not readily available, and because of the nature of this estimate, the mean values of the final phase were used to provide an initial estimate of the surface roughness. This estimated roughness distribution is also shown in Fig. 3. This averaged roughness distribution and the vibro-acoustic model results were used as a guide in selecting roughness values to be used in calculating transition parameters that required roughness dimensions.

A significant, localized deviation to this roughness distribution occurred during the flight of STS-1. During this flight, ascent debris caused a large gouge (approximately 8" × 2" × 1" deep) in the TPS surface on the right forward landing gear door. This location is just off the centerline near $x = 0.05L$. The effect of this damage on the times of transition will be shown in a subsequent section.

Orbiter Test Conditions

The free-stream entry conditions for the OFT program are depicted in Fig. 4 by the dimensionless flow parameters $Re_{\infty,L}$ and M_∞. The range of these parameters used for the wind tunnel test program is also shown for reference. Identification of transition onset and completion is also indicated for each trajectory. Note that the onset value for STS-1 is not shown because of the DFI recorder malfunction. Also note that the location of transition onset is defined to be at the 99% length station (i.e., $x = 0.99L$). The location of transition completion was arbitrarily defined to be at $x = 0.1L$. This location was chosen because it essentially covered the complete orbiter centerline, and also because transition further forward occurred well past hypersonic flow conditions and was well outside the range of the wind tunnel data base. This occurred possibly because of the very favorable pressure gradient that is present along the forward 15% of the orbiter centerline. Predictions of the pressure distributions along the centerline are presented in Refs. 3 and 4. This result suggests that the orbiter roughness in this region is not as effective a boundary layer trip as the same roughness located further downstream.

This observation is basically consistent with the results presented by Morrisette[13], who showed that roughness in this region had to be two to seven times as large as roughness in low-pressure-gradient regions to be as effective at tripping the boundary layer.

The important point shown in Fig. 4 is that transition occurs over most of the centerline for a narrow range of relatively low free-stream Mach numbers. That is, transition starts near Mach 10, and is essentially complete near Mach 7. These conditions occur well past peak heating, and therefore contribute very little to the heat load experienced by the orbiter during entry. Also note that in terms of these parameters, the wind tunnel conditions provided a reasonable test environment.

To help relate these parameters to entry time, histories of free-stream Reynolds numbers are shown in Fig. 5 for all five flights. The times and values of $Re_{\infty,L}$ for transition onset and completion are also depicted, along with the range of $Re_{\infty,L}$ used in the wind tunnel test program. Because of planned trajectory differences, the times of transition onset and completion are observed to occur earlier with each successive OFT flight, except for STS-1, which has the earliest transition onset. This occurred because the TPS roughness on STS-1 was much greater than the other flights due to the previously discussed ascent debris damage. Note also that the values of $Re_{\infty,L}$ at transition onset and completion are approximately the same for each of the flights, with the exception of transition onset for STS-1. For operational purposes, this may be an adequate parameter for predicting transition, if the trajectories and roughness remain about the same.

Additional information regarding the entry trajectories is shown in Fig. 6, where histories of orbiter angle of attack are depicted along with the times of transition onset and completion. Note that, for all cases, the angles of attack for transition onset and completion are approximately 40° and 25°, respectively. For this angle-of-attack range, the wind tunnel data base indicated very little effect of angle of attack alone on transition.

The times used in the previous two figures were measured from entry interface, which is assumed to occur at approximately 4×10^5 feet altitude. For reference purposes, the Greenwich mean time (GMT) is listed in Table II along with the altitude, velocity, and angle of attack for each OFT mission. This will be useful when comparing these results to other interpretations of the flight data base.

DISCUSSION OF RESULTS

Temperature histories of the TPS surface, obtained from DFI surface thermocouples, were used to establish the times of boundary layer transition along the orbiter centerline. Locations of the instruments are shown in Fig. 2. Transition at a given instrument occurred when the temperature history deviated or jumped significantly from an otherwise smooth behavior. Figure 7 depicts typical surface temperature histories for instruments located along the centerline at $x = 0.1L$, $x = 0.5L$, and $x = 0.9L$ for STS-3. Transition times are indicated by the arrows. Examination of all the temperature histories in this manner was used to establish transition for all flights and instruments. Times of transition, along with all free-stream conditions necessary to calculate transition parameters, are listed in Table III for these flights and DFI instrument locations. Comparison of transition parameters obtained from these data will be made with wind tunnel test results in the next section.

Comparisons of Flight and Wind Tunnel Data

By comparing transition data from flight and hypersonic wind tunnels at comparable simulation conditions—and recognizing that the major difference in simulation parameters at these conditions was the level of free-stream noise—differences in transition results can be attributed to the presence of this free-stream noise. The objective of these comparisons will be to identify regions on the orbiter where these differences are at a minimum and use these results to improve the prediction methodology for the orbiter and to provide insight into the use of wind tunnel data for making similar predictions on other vehicles.

Free-Stream Conditions. The variations of the locations of transition with $Re_{\infty,L}$, calculated at the time of transition for these locations, are illustrated in Fig. 8. Also shown are the same parameters taken from the wind tunnel data base which used smooth and rough models. The first thing to note from this comparison is that the transition locations aft of $x = 0.15L$ appear to be much more sensitive to $Re_{\infty,L}$ for the flight data than the wind tunnel. In fact, at flight, transition moves forward to $x = 0.15L$ at approximately a constant Reynolds number. However, the Reynolds number at which this occurs varies somewhat from flight to flight. The behavior of the STS-1 data is an anomaly because of the additional surface roughness that occurred on this flight. However, these data do tend to follow the Reynolds number dependence of the wind tunnel data, possibly because of the overlapping effects of noise and roughness in the wind tunnel data. Also, because the very large localized roughness on STS-1 was off centerline, which may have caused early nonsymmetrical transition about the centerline, agreement with any correlation based on symmetrical data alone would be fortuitous. Insufficient data exist off centerline to verify this hypothesis. Another point concerning these data is that the wind tunnel and flight data are in relatively good agreement in the region between x/L of 0.1 to approximately 0.4. This suggests that the effects of free-stream noise may not be a significant factor in causing transition in this region because of other disturbances coming from surface roughness and the shock layer entropy gradient within the curved bow shock. Similar agreement will be shown for the transition parameters based on local flow conditions in the next section.

Local Flow Conditions. Predictions of local flow field and boundary layer properties have been made for most of the DFI locations along the orbiter centerline for the STS missions. These predictions were based on correlations of numerical flowfield solutions made for the orbiter windward surface for the design trajectory using the methods developed in Ref. 3. Parameters relevant to correlating transition data have been predicted for these instrument stations at times of transition for each trajectory. These predictions are listed in Table IV.

Selected flow parameters (M, Re_x, Re_θ/M, and Re_k) from Table IV are graphically illustrated in Fig. 9, along with these same parameters obtained from the wind tunnel test program. Figure 9(a) shows distributions of the local Mach number at the times of transition for each centerline station. With rare exception, transition values of local Mach number, M_{tr}, obtained at 30° and 40° angle of attack at wind tunnel conditions embrace the values of M_{tr} predicted at flight conditions. Basically, these results show that the wind tunnel conditions provided an excellent simulation of local Mach numbers for the flight conditions associated with transition. In addition, the values of M_{tr} at transition are relatively low (i.e., $M_{tr} \leq 2.5$).

In Fig. 9(b), distributions of local Reynolds numbers obtained from the flight and wind tunnel transition results are presented. As expected, transition values of the local Reynolds number, $Re_{x,tr}$, at flight conditions are almost always higher than values from the wind tunnel at comparable centerline locations. Actually, there is as much variation in the flight data as the wind tunnel data, which suggests that this parameter does not correlate the data very well. This is particularly true when both wind tunnel and flight data are considered. However, these distributions do reveal that some sources of flow disturbances may be present for the forward 40% of the orbiter, because both sets of data show a significant reduction in values of $Re_{x,tr}$ in this region. At flight conditions, these disturbances could come from a combination of shock layer gradients and surface roughness. In the wind tunnel, free-stream noise can be added to these disturbances. However, other factors may also be contributing this behavior and general lack of correlation using $Re_{x,tr}$. For example, $Re_{x,tr}$ alone does not correlate the effects of the boundary layer gradients or of surface roughness or temperature conditions, but only the effects of edge conditions.

In attempts to account for these differences and other flow parameters, investigators have developed a number of correlation parameters using various combinations of edge and boundary layer factors. Because it accounts for boundary layer properties as well as edge compressibility effects, Re_θ/M has evolved as one of the more popular forms of transition-correlating parameters and was selected here to represent this class of correlation parameter. Distributions of transition values of this parameter, $(Re_\theta/M)_{tr}$, for both wind tunnel and flight conditions are presented in Fig. 9(c). Again, possibly because of a combination of shock layer and surface roughness flow disturbances, significant reductions in the values of this parameter occur for the forward 40% of the orbiter at flight conditions. However, by using $(Re_\theta/M)_{tr}$ as a correlation parameter, the wind tunnel and flight data correlations are in better agreement in this region, but remain significantly different in the downstream region.

Thus far, the correlation parameters considered have not included the very important effects of surface roughness or of temperature. Braslow[14] and others have shown that the roughness Reynolds number, Re_k—a Reynolds number based on roughness height and boundary layer conditions at the top of the roughness—successfully correlates transition data over a range of local Mach numbers from approximately 0 to 4. In defining Re_k, values of surface roughness and temperature have to be known. For a given roughness, transition was shown[5,6,7] to be very sensitive to variations in surface temperature in the wind tunnel test program. This occurred because by cooling of the boundary layer, the density of the flow near the surface and at the top of the roughness would increase accordingly. Values of Re_k increased in proportion to the density. The effects of the changes in viscosity and velocity were less significant.

In the section covering surface roughness, the average roughness distribution was estimated to range from 0.03" to 0.1". To cover this range, transition values of the roughness Reynolds number, $Re_{k,tr}$, were calculated using three values of roughness: 0.03", 0.06", and 0.1". Values of $Re_{k,tr}$ for all three values of k, calculated using the surface temperature at flight, are listed in Table IV for all the flight transition times. Values of $Re_{k,tr}$ at wind tunnel conditions were calculated in Ref. 7 using the surface roughness and temperature conditions of the wind tunnel models. Figure 9(d) presents distributions of $Re_{k,tr}$ (using an average value of $k = 0.06"$) from the flight and wind tunnel data bases. As before, large differences in the flight and wind tunnel data bases exist downstream of the 40% station, probably because of wind tunnel noise. However, agreement between these two data bases has improved in the upstream region using the correlation parameter $Re_{k,tr}$, which accounts for not only edge and boundary layer conditions but also accounts for surface roughness and temperature conditions. This suggests that the effects of the surface conditions are dominant in the upstream region, while further downstream, the effects of tunnel noise dominate the transition process in wind tunnel tests. This further suggests that if transition distributions obtained from wind tunnel data were extrapolated to flight conditions, transition predictions would be conservative in the downstream region and reasonably reliable in the upstream region. This thought will be discussed in the next section, which compares predicted transition times with flight data for the orbiter centerline.

Transition Predictions

Using wind tunnel data alone, several transition prediction methodologies were developed in Refs. 5, 6, and 7. These methods all had one thing in common: the transition parameter (e.g., x_{tr}/L, $Re_{x,tr}$, $(Re_\theta/M)_{tr}$) used for making predictions of roughness-induced transition was correlated in terms of a departure from the same parameter correlated using smooth body data alone. This departure was functionally related to a roughness parameter (e.g., δ^*/k or Re_k) using the wind tunnel data. For more details on these parameters and correlations, see Ref. 7.

The correlation judged best suited for making preflight predictions was based on a departure of Re_θ/M from the smooth-body transition values as a function of $Re_{k,x=0.1L}$. This was selected because the smooth body prediction methodology was already based on Re_θ/M (see Fig. 9(c)). This correlation, reproduced from Ref. 7, is shown in Fig. 10. The normalized or relative transition parameter ξ is the ratio of Re_θ/M at roughness-induced transition conditions to Re_θ/M at smooth surface conditions (i.e., $\xi = (Re_\theta/M)_{tr,R}/(Re_\theta/M)_{tr,S}$). The reference roughness Reynolds number $Re_{k,x=0.1L}$ is calculated at the 10% centerline station for the conditions of transition. Several factors were involved in selecting $x = 0.1L$ as the reference location for calculating the transition parameter accounting for the effects of surface roughness and temperature. Initially, the orbiter was expected to have relatively uniform surface roughness, which suggested that any point might be adequate. Furthermore, at the time the correlation was developed, it was relatively difficult to calculate Re_k over the complete vehicle, but Re_k could be calculated relatively easily and accurately at $x = 0.1L$. However, the most important factor was the observation that when surface roughness and temperature effects did cause transition to move forward, transition would move to this general area. In addition, this location was at the end of the favorable pressure gradient region coming from the nose. Therefore, this location, which had the largest values of Re_k for low-pressure-gradient areas, would better reflect the effects of surface roughness on transition for the rest of the vehicle, which also had very low pressure gradients.

Also noted on Fig. 10 are the values of $Re_{k,x=0.1L}$ which cause transition to move forward at various rates on the orbiter. Surface roughness and cooling had no measurable effects on transition location for values of $Re_{k,x=0.1L}$ less than 30. This is defined as the incipient value of $Re_{k,x=0.1L}$ because it is the value that causes ξ to decrease just below unity. The effect of roughness and cooling on transition is minimal until $Re_{k,x=0.1L}$ reaches a value of 110, which is called the critical value. Above the critical value, the relative transition parameter decreases rapidly (transition moves rapidly upstream toward the nose) until $Re_{k,x=0.1L}$ reaches a value of 180. This is the minimum value of $Re_{k,x=0.1L}$ which will move transition the furthest forward for the test conditions. Therefore, 180 is defined as the effective value of $Re_{k,x=0.1L}$, because the roughness elements are now serving as effective tripping devices.

Preflight Predictions. The correlation shown in Fig. 10 served as the basic part of the preflight transition prediction methodology. The smooth surface transition correlation based on Re_θ/M, which is shown in Fig. 9(c), completes the methodology. To predict the locations of transition at flight, a history of the values of $Re_{k,x=0.1L}$ must be known for the trajectories. Such a history is shown in Fig. 11 for the STS trajectories. A nominal roughness value of 0.06" was used in calculating $Re_{k,x=0.1L}$. This value of k seemed to be a reasonable estimate based on all the considerations given in the roughness section. The effects of selecting different roughness sizes on the predictions of transition were investigated in Ref. 7 for the design trajectory.

To predict the location of transition for a given trajectory at a particular time, use Fig. 11 to determine the value of $Re_{k,x=0.1L}$ at this time. With this value, enter Fig. 10, and obtain a value of the relative transition parameter ξ. Knowing the smooth surface distribution of $(Re_\theta/M)_{tr,S}$ (as given by the correlation in Fig. 9(c)) and the value of ξ, the new value of $(Re_\theta/M)_{tr,R}$ that accounts for the effects of roughness on transition at this time can be calculated. With this value and a calculated distribution of Re_θ/M for this particular time, the roughness-induced transition location can be determined for this time. Histories of Re_θ/M have to be calculated for each trajectory. These calculations have been made for the five STS trajectories, and the resulting predictions of transition times are presented in Fig. 12 for the DFI locations given in Table IV. Predictions were not made for all the stations because local flow models were not available for the missing stations. The predicted times of transition follow the trends of the transition parameters shown in Figs. 8 and 9 in that the transition predictions based on wind tunnel data alone were very conservative downstream of the 30% to 40% stations. The exception observed for STS-1 in Fig. 12(a) occurs because of the previously mentioned TPS damage, resulting in a relatively large localized roughness just off centerline near the nose region. Predicted transition times forward of the 30% to 40% stations are in very good agreement with the data. These results are consistent with the previous discussion concerning roughness and the effects of free-stream disturbances on the tunnel data and resulting correlations. In addition, note that the predictions for x = 0.025L are very approximate because the prediction correlation did not include wind tunnel transition data from this very high pressure gradient region.

Postflight Comments. There are several ways that the prediction methodology can be improved. The first step would be to remove the smooth-surface data from the correlation parameter, because of its sensitivity to free-stream noise. However, as previously noted, even a large part of the rough-surface wind tunnel data in the downstream region seems to be sensitive to tunnel noise. To avoid this, one could simply correlate the flight data and possibly use the wind tunnel data to supplement the correlation. For example, for future operational flights, local values of Re_k that cause transition could be predicted by using the averages of the four previous flights. This methodology would be particularly useful if predictions of the effects of significant changes in roughness distributions are required. Also, by using this approach, the equivalent roughness size for STS-1 could be estimated by trial and error. This may be a good thing to do to support operational requirements. However, the primary objective of this paper is "to provide additional information and insight into the requirements for developing a reliable transition methodology based primarily on wind tunnel data . . .".

The very good agreement between the predicted and measured transition times in the 10% to 20% centerline region suggests that the wind tunnel simulations and correlation of transition in this region must have been very good. This must have occurred because surface roughness and shock layer disturbances dominated the transition process in this region at both wind tunnel and flight conditions. This was possible because of the relatively thin boundary layer and highly curved bow shock near the forward part of the orbiter. This is consistent with the discussion of Fig. 9(d). The fact that transition moves rapidly to the location of the effective roughness Reynolds number region, also in this region, is consistent with the findings of Ref. 7 shown in Fig. 10. One could conclude from this that transition times in this region could be predicted with the effective roughness Reynolds number obtained from the wind tunnel data.

This prediction of effective transition can be simply accomplished by entering Fig. 11 with the effective value of $Re_{k,x=0.1L}$ (i.e., 180) and extracting the times of effective transition in the 10% to 20% region for each trajectory. The results of this operation are shown in Fig. 12. The agreement with flight data is very good.

The fact that the flight transition moved forward so rapidly also suggests that the transition process occurs similarly to the process observed in the wind tunnel when the roughness Reynolds numbers were increasing from critical to effective values. The only difference between these tests was that for the wind tunnel tests the locations of transition were already on the orbiter when $Re_{k,x=0.1L}$ was critical, whereas for the flight tests transition was not yet on the orbiter. This occurred because tunnel noise and roughness both affect transition in the critical transition process, thus causing transition to be further forward at this time in the tunnel. Therefore, it could be possible to predict transition onset for the orbiter by using the critical value of $Re_{k,x=0.1L}$ (i.e., 110) just as was done using the effective value. These results are also indicated in Fig. 12. The agreement with transition onset is excellent for all flights except STS-1, which is as expected because of the differences in the surface roughness.

No attempt has been made to establish a prediction of the distribution of transition times between the critical and effective points. However, considering how quickly transition moves forward and the general uncertainties in the methodology, connecting the two points with a straight line should provide adequate predictions for design purposes.

CONCLUDING REMARKS

Surface temperature measurements from the windward centerline of the Shuttle orbiter have been used to define the locations of boundary layer transition during entry for the first five orbiter flights. Because the orbiter windward surface is composed of a large number of thermal protection tiles, the transition data include the effects of distributed roughness arising from tile misalignment and gaps. These data are used as a benchmark for assessing data from previous wind tunnel tests and for improving the accuracy of boundary layer transition predictions based on correlations of wind tunnel data taken on both aerodynamically rough and smooth orbiter models. Specifically, by comparing the data from these two environments, the relative importance of tunnel free-stream noise and of surface roughness on orbiter boundary layer transition predictions can be estimated. Based on these data, the following conclusions are made.

1) Free-stream disturbances dominate transition in the wind tunnel downstream of $x \cong 0.4L$. This conclusion is based on the observation that at early flight

times, transition locations based on wind tunnel data are significantly further upstream than those actually measured during flight. This occurs because the Reynolds number is relatively low, the boundary layer is relatively thick so that the tile-related roughness is submerged, and the wall temperature ratio, T_w/T_0, is low, which is usually considered as stabilizing. Because the wind tunnel simulation of local transition parameters was generally very good, "tunnel noise" is apparently a dominant factor in the transition process in the wind tunnel downstream of the 40% station. Since there are no corresponding background disturbances in the flight environment, transition occurs later in flight than one would predict using wind-tunnel-based correlations that use data from this noise-dominated region.

2) Surface roughness and, perhaps, shock layer disturbances dominate transition at both flight and wind tunnel conditions upstream of $x \cong 0.4L$. This is based on the fact that, at later flight times, the transition locations are in relatively good agreement with the predictions based on wind tunnel data. At these times, the Reynolds numbers are relatively high so that the boundary layer is relatively thin and, therefore, the tile-related roughness produces significant perturbations to the flow. Furthermore, the surface temperature has increased and T_0 has decreased, so that surface cooling is no longer as stabilizing as it was. Thus, the transition process is probably dominated by surface-roughness-induced perturbations and entropy gradient disturbances associated with the curved bow shock wave. Because the misaligned tiles are now serving as effective boundary layer trips, tunnel noise does not significantly influence the transition locations. Therefore, the measured locations of transition at flight are in relatively good agreement with wind-tunnel-based predictions.

3) Times of transition onset and completion at hypersonic flight conditions correspond to times when the reference roughness Reynolds number, $Re_{k,x=0.1L}$, reaches, respectively, its critical and effective values. These values, which are 110 and 180, respectively, were established from previous wind tunnel data analyses. This relationship can be used as a relatively simple improvement to the current transition prediction methodology. This is possible because these transition values are surface roughness dominated and, therefore, are relatively insensitive to the effects of wind tunnel noise.

SYMBOLS

k	height of the misaligned tiles
L	orbiter axial length, 107.75 ft
M	Mach number
Re_k	Reynolds number based on conditions at the top of the misaligned tile
Re_θ	Reynolds number based on local flow properties and the momentum thickness
$Re_{\infty,L}$	Reynolds number based on free-stream flow properties and the orbiter length
T	temperature

w	width of tile gaps
x	axial coordinate
α	angle of attack
δ^*	displacement thickness
θ	momentum thickness
ξ	relative transition location defined in Fig. 10

Subscripts:

o	evaluated at the stagnation conditions
tr	evaluated at the transition location
w	evaluated at the wall
∞	evaluated at the free-stream conditions

REFERENCES

1. Ried, R. C., Jr., Goodrich, W. D., Strouhal, G., and Curry, D. M., "The Importance of Boundary-Layer Transition to the Space Shuttle Design," Proceedings of the Boundary-Layer Transition Workshop held Nov. 3-5, 1971. Aerospace Report No. TOR-0172 (S2816-16) -5, Dec. 20, 1971.

2. van Driest, E. R., and Blumer, C. B., "Boundary-Layer Transition at Supersonic Speeds - Three-Dimensional Roughness Effects (Spheres)," Journal of the Aerospace Sciences, Aug. 1962, Vol. 29, No. 8, pp. 909-926.

3. Goodrich, W. D., Li, C. P., Houston, C. K., Chiu, P., and Olmedo, L., "Numerical Computations of Orbiter Flow Fields and Laminar Heating Rates", Journal of Spacecraft Rockets, May 1977, Vol. 14, No. 5, pp. 257-264.

4. Rakich, J. V. and Lanfranco, M. J., "Numerical Computation of Space Shuttle Laminar Heating and Surface Streamlines," Journal of Spacecraft and Rockets, May 1977, Vol. 14, No. 5, pp. 265-272.

5. Bertin, J. J., Idar, E. S., III, and Galanski, S. R., "Effect of Surface Cooling and Roughness on the Heating (Including Transition) to the Windward Plane-of-Symmetry of the Shuttle Orbiter", Aerospace Engineering Report 77002, Apr. 1977, The University of Texas at Austin.

6. Bertin, J. J., Idar, E. S., III, and Goodrich, W. D., "Effect of Surface Cooling and Roughness on Transition for the Shuttle Orbiter", Journal of Spacecraft and Rockets, March-April 1978, Vol. 15, No. 2., pp. 113-119.

7. Bertin, J. J., Hayden, T. E., and Goodrich, W. D., "Shuttle Boundary-Layer Transition Due to Distributed Roughness and Surface Cooling", Journal of Spacecraft and Rockets, Sept.-Oct. 1982, Vol. 19, No. 5, pp. 389-396.

8. Goodrich, W. D., Derry, S. M., and Maraia, R. J., "Effects of Aerodynamic Heating and TPS Thermal Performance Uncertainties on the Shuttle Orbiter," in Entry Heating and Thermal Protection, Vol. 69 of Progress in Astronautics and Aeronautics, Walter B. Olstad, ed. (1980) pp. 247-268.

9. Dryden, H. L., "Review of Published Data on the Effect of Roughness on Transition from Laminar to Turbulent Flow", Journal of the Aeronautical Sciences, July 1953, Vol. 20, No. 7, pp. 477-482.

10. Pate, S. R., "Induced Boundary-Layer Transition at Supersonic Speeds: Combined Effects of Roughness and Free-Stream Disturbances," May 1970, AIAA Paper 70-586.

11. Smith, J. A., "STS-3 Structural and Aerodynamic Pressure and Aerothermodynamic and Thermal Protection System Measurement Locations," Thermal Technology Branch ES3-82-1, NASA Johnson Space Center JSC 17889, Houston, TX, January 15, 1982.

12. Bertin, J. J. and Keisner, A., "Effects of Step and/or Gap Tile Misalignment on Shuttle Transition," Aerospace Engineering Report 78003, The University of Texas at Austin, June 1978.

13. Morrisette, E. L., "Roughness Induced Transition Criteria for Space Shuttle-Type Vehicles," Journal of Spacecraft and Rockets, February 1976, Vol. 13, No. 2, pp. 118-120.

14. Braslow, A. L., "A Review of Factors Affecting Boundary-Layer Transition", NASA TND-3384, Apr. 1966.

TABLE I.- IDENTIFICATION AND LOCATION OF FLIGHT THERMOCOUPLES USED FOR SPECIFYING THE TIMES OF BOUNDARY LAYER TRANSITION

Instrument identification number	Body point number	$\frac{x}{L}$	X,[a] in.	Y, in.
V09T9341	1020	0.0257	268.0	+1.2
V07T9452	1100	0.099	361.7	-4.9
V07T9462	1140	0.141	416.5	0.0
V07T9463	1160	0.164	446.2	-3.9
V07T9464	1200	0.196	486.5	-6.6
V09T9381	1250	0.257	565.0	-4.2
V09T9421	1300	0.288	604.7	-8.4
V07T9468	1300	0.299	618.9	0.0
V07T9471	1400	0.404	754.7	0.0
V09T9521	1500	0.501	878.9	-12.8
V07T9478	1600	0.598	1003.8	0.0
V07T9481	1700	0.695	1128.0	0.0
V07T9487	1800	0.801	1265.0	0.0
V07T9489	1900	0.900	1391.5	0.0
V09T9751	1950	0.952	1458.2	0.0
V07T9492	1990	0.993	1511.1	+1.3

[a] $X = x + 235$.

TABLE II.- MISSION TIMES USED TO DEFINE ENTRY INTERFACE FOR EACH FLIGHT, ALONG WITH SELECTED TRAJECTORY PARAMETERS

Mission number	Alt, ft	V_∞, ft/sec	α, deg	Mission time (GMT), sec
STS-1	399840	24555.8	41.22	9049750
STS-2	400141	24516.9	41.09	27550239
STS-3	400102	24451.5	40.97	7745683
STS-4	400049	24439.6	40.97	16040426.6
STS-5	400200	24398.0	40.83	27698594.9

TABLE III.- FREE-STREAM CONDITIONS AT TIMES OF BOUNDARY LAYER TRANSITION ALONG THE ORBITER WINDWARD PITCH PLANE

$\frac{x_{tr}}{L}$[a]	Time, sec	Alt, k-ft	V_∞, ft/sec	α, deg	T_∞, °R	P_∞, $\frac{\text{lb}_f}{\text{ft}^2}$	$\rho_\infty \times 10^5$, $\frac{\text{slugs}}{\text{ft}^3}$	M_∞	$Re_{\infty,L}$ $\times 10^{-6}$
					STS-1				
0.025	1716	33.8	722	7.8	394	548.5	81.16	0.74	211.
0.1	1357	121.1	5402	23.6	440	9.646	1.279	5.26	22.72
0.14	1320	131.3	6239	26.4	447	6.242	0.81	6.02	19.
0.16	1272	144.3	7377	30.5	463	3.683	0.4634	6.99	10.78
0.20	1272	144.3	7377	30.5	463	3.683	0.4634	6.99	10.78
0.26	1231	154.9	8469	34.5	480	2.448	0.2974	7.89	7.72
0.3	1220	156.4	8783	33.7	480	2.306	0.2800	8.17	7.53
0.4	1139	171.5	11279	38.6	464	1.278	0.1605	10.68	5.69
0.5	1136	172.2	11374	38.7	464	1.249	0.1568	10.77	5.61
0.6	<1052	184.7	14179	39.5	455	0.7535	0.0964	13.56	4.37
0.7									
0.8	No data prior to 1052 sec.								
0.9									
0.99									
					STS-2				
0.025	1710	41.	837	5.3	380	392.2	60.11	0.88	186.5
0.1	1340	129.9	6479	25.6	439	5.912	0.7853	6.31	16.8
0.14	1319	135.0	6962	27.8	449	4.790	0.62	6.7	13.95
0.16	1279	145.9	7952	31.9	466	3.093	0.39	7.51	9.63
0.2	1289	143.4	7704	30.8	459	3.414	0.4341	7.34	10.63
0.26	1268	148.3	8235	33.	474	2.809	0.3454	7.72	8.81
0.3	1262	149.3	8396	33.4	474	2.702	0.3319	7.86	8.62
0.4	1261	149.5	8424	33.5	474	2.687	0.3305	7.9	8.59
0.5	1249	150.5	8758	33.2	474	2.585	0.3179	8.21	8.62
0.6	1240	151.5	9014	33.1	475	2.488	0.3055	8.44	8.51
0.7	1233	152.8	9214	33.2	476	2.363	0.2893	8.62	8.22
0.8	1232	153.	9242	33.2	476	2.345	0.2869	8.64	8.17
0.9	1232	153.	9242	33.3	476	2.345	0.2869	8.64	8.17
0.99	1200	160.	10212	36.6	472	1.795	0.2215	9.59	7.02
					STS-3				
0.025	1630	39.1	772	5.1	384	423.2	64.33	0.8	182.7
0.1	1252	131.4	6386	26.6	447	6.032	0.7873	6.17	16.32
0.14	1183	149.2	8100	32.7	480	2.959	0.3591	7.54	8.91
0.16	1183	149.2	8100	32.7	480	2.959	0.3591	7.54	8.91
0.2	1183	149.2	8100	32.7	480	2.959	0.3591	7.54	8.91
0.26	1183	149.2	8100	32.7	480	2.959	0.3591	7.54	8.91
0.3	1183	149.2	8100	32.7	480	2.959	0.3591	7.54	8.91
0.4	1183	149.2	8100	32.7	480	2.959	0.3591	7.54	8.91
0.5	1183	149.2	8100	32.7	480	2.959	0.3591	7.54	8.91
0.6	1148	153.9	9084	33.5	482	2.473	0.2990	8.44	8.29
0.7	1120	159.4	9911	36.0	482	2.006	0.2424	9.21	7.34
0.8	1107	162.6	10329	37.5	480	1.772	0.2152	9.62	6.81
0.9	1106	162.9	10362	37.5	480	1.755	0.2132	9.65	6.77
0.99	1182	168.7	11134	38.7	474	1.402	0.1723	10.43	5.94
					STS-4				
0.025	1524	43.8	880	5.6	382	345.2	52.7	0.92	171.2
0.1	1178	129.	6510	24.9	454	7.309	0.9381	6.23	19.56
0.14	1152	135.8	7201	27.1	461	5.538	0.6994	6.84	15.93
0.16	1131	142.7	7805	29.2	472	4.221	0.5207	7.33	12.61
0.2	1028	174.7	11028	40.4	478	1.218	0.1486	10.3	5.04
0.26	1028	174.7	11028	40.4	478	1.218	0.1486	10.3	5.04
0.3	1028	174.7	11028	40.4	478	1.218	0.1486	10.3	5.04
0.4	1028	174.7	11028	40.4	478	1.218	0.1486	10.3	5.04
0.5	1028	174.7	11028	40.4	478	1.218	0.1486	10.3	5.04
0.6	1028	174.7	11078	40.4	478	1.218	0.1486	10.3	5.04
0.7	1027	175.2	11058	40.4	477	1.194	0.1459	10.33	4.97
0.8	1029	174.1	10998	40.3	479	1.242	0.1514	10.26	5.11
0.9	1028	174.7	11028	40.4	478	1.218	0.1486	10.3	5.04
0.99	1029	174.1	10998	40.3	479	1.242	0.1514	10.26	5.11
					STS-5				
0.025	1607	41.3	839	6.9	391	373.9	55.82	0.87	169.7
0.1	1215	135.8	6893	27.9	442	5.224	0.6895	6.69	15.57
0.14	1140	154.5	8881	35.1	457	2.418	0.3085	8.48	8.73
0.16	1140	154.5	8881	35.1	457	2.418	0.3085	8.48	8.73
0.2	1140	154.5	8881	35.1	457	2.418	0.3085	8.48	8.73
0.26	1125	157.9	9328	36.7	458	2.108	0.2684	8.90	7.97
0.3	1125	157.9	9328	36.7	458	2.108	0.2684	8.90	7.97
0.4	1125	157.9	9328	36.7	458	2.108	0.2684	8.90	7.97
0.5	1125	157.9	9328	36.7	458	2.108	0.2684	8.90	7.97
0.6	1122	158.5	9406	37.0	457	2.057	0.2625	8.98	7.87
0.7	1122	158.5	9406	37.0	457	2.057	0.2625	8.98	7.87
0.8	1122	158.5	9406	37.0	457	2.057	0.2625	8.98	7.87
0.9	1118	159.8	9563	37.5	455	1.955	0.2506	9.15	7.67
0.99	1120	159.1	9484	37.3	456	2.006	0.2565	9.06	7.77

[a] Instruments at x = 0.29L and 0.95L have been omitted because of redundancy and data quality.

ORIGINAL PAGE IS
OF POOR QUALITY

TABLE IV.- LOCAL FLOW CONDITIONS AT TIMES OF BOUNDARY LAYER TRANSITION ALONG THE ORBITER WINDWARD PITCH PLANE

x_{tr}/L [a]	Time, sec	M	Re_x $\times 10^{-6}$	Re_θ/M	T_w, °R	T_w/T_o	Re_k, k (in.) = 0.03	Re_k, k (in.) = 0.06	Re_k, k (in.) = 0.1
				STS-1					
0.025	1716	0.67	4.93	991	849	1.94	4145	9019	15100
0.1	1357	2.13	1.96	247	1264	0.478	155	494	1129
0.2	1272	2.03	1.56	218	1869	0.447	63	189	404
0.26	1231	1.84	1.37	208	1403	0.287	49	142	292
0.4	1139	2.01	1.73	217	1615	0.263	39	108	214
0.5	1136	2.01	2.14	240	1597	0.258	37	104	206
0.6	<1052	2.20	2.27	239	1517	0.183	31	82	163
0.7									
0.8	No data prior to 1052 sec.								
0.9									
0.99									
				STS-2					
0.025	1710	0.8	4.45	819	630	1.44	3572	8112	13650
0.1	1340	2.06	1.26	205	1540	0.443	111	336	734
0.2	1289	2.05	1.48	211	1421	0.322	62	182	387
0.26	1268	1.94	1.63	217	1410	0.296	59	163	339
0.4	1261	2.05	2.69	274	1414	0.289	53	158	331
0.5	1249	2.11	3.37	300	1421	0.28	52	153	321
0.6	1240	2.15	3.91	321	1346	0.257	49	147	307
0.7	1233	2.15	4.44	338	1321	0.248	46	138	289
0.8	1232	2.15	5.04	362	1346	0.252	45	134	282
0.9	1232	2.31	4.95	342	1309	0.245	34	104	222
0.99	1200	2.29	3.7	293	1086	0.189	24	73	154
				STS-3					
0.025	1630	0.74	4.35	881	850	1.96	3468	7909	13320
0.1	1252	2.0	1.24	208	1400	0.411	117	337	733
0.2	1183	1.89	1.19	199	1460	0.313	55	159	331
0.26	1183	1.92	1.6	221	1390	0.298	57	167	348
0.4	1183	2.04	2.84	269	1434	0.306	56	167	353
0.5	1183	2.04	3.55	316	1379	0.294	53	159	337
0.6	1148	2.10	3.84	319	1355	0.257	50	147	307
0.7	1120	2.02	3.81	321	1472	0.262	45	131	268
0.8	1107	1.99	4.04	334	1414	0.245	42	121	247
0.9	1106	2.13	3.81	310	1397	0.241	31	93	192
0.99	1082	2.24	3.26	278	1036	0.170	23	67	138
				STS-4					
0.025	1524	0.83	4.1	748	866	1.94	3222	7445	12560
0.1	1178	2.10	1.52	221	1501	0.427	137	413	902
0.2	1028	1.57	0.6	155	1826	0.311	32	86	168
0.26	1028	1.62	0.81	169	1635	0.277	35	92	179
0.4	1028	1.82	1.49	213	1746	0.293	36	98	193
0.5	1028	1.82	1.86	237	1578	0.265	35	99	188
0.6	1028	1.82	2.29	259	1511	0.253	34	94	186
0.7	1027	1.82	2.56	277	1472	0.246	32	91	181
0.8	1029	1.82	3.01	303	1470	0.247	32	92	185
0.9	1028	1.97	2.9	282	1460	0.245	25	73	149
0.99	1029	2.08	2.85	271	1406	0.236	21	61	126
				STS-5					
0.025	1607	0.78	3.74	776	822	1.96	3216	7319	12320
0.1	1215	1.94	1.13	201	1471	0.387	108	317	674
0.2	1140	1.81	1.02	194	1578	0.311	53	151	304
0.26	1125	1.76	1.22	203	1530	0.290	52	144	287
0.4	1125	1.92	2.23	256	1482	0.278	52	148	302
0.5	1125	1.92	2.76	285	1481	0.278	50	144	295
0.6	1122	1.90	3.24	311	1395	0.260	47	138	284
0.7	1122	1.90	3.77	335	1321	0.247	46	135	279
0.8	1122	1.90	4.34	360	1395	0.260	45	133	275
0.9	1118	2.02	4.04	334	1347	0.249	34	102	213
0.99	1120	2.15	4.07	322	1134	0.211	27	83	177

[a] Locations limited to DFI stations where local flow correlations were developed.

Figure 1.- Photograph of Columbia (OV-102) windward surface showing the TPS tiles and resulting distributed roughness caused by tile gaps and misalignments.

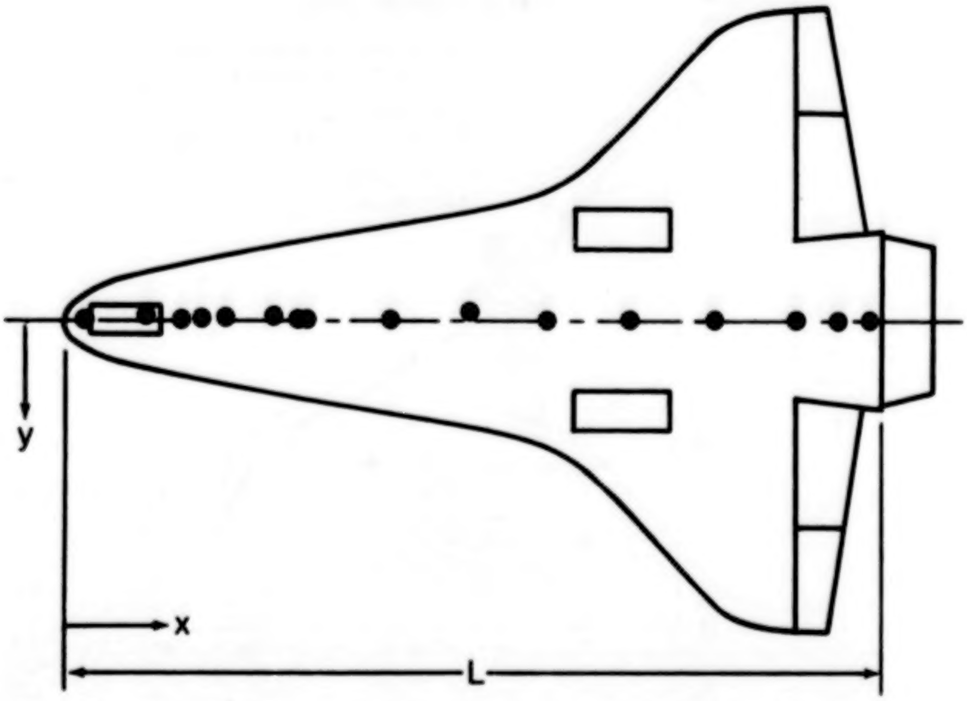

Figure 2.- Locations of surface temperature measurements along orbiter windward centerline. See Table I for detailed locations and instrument numbers.

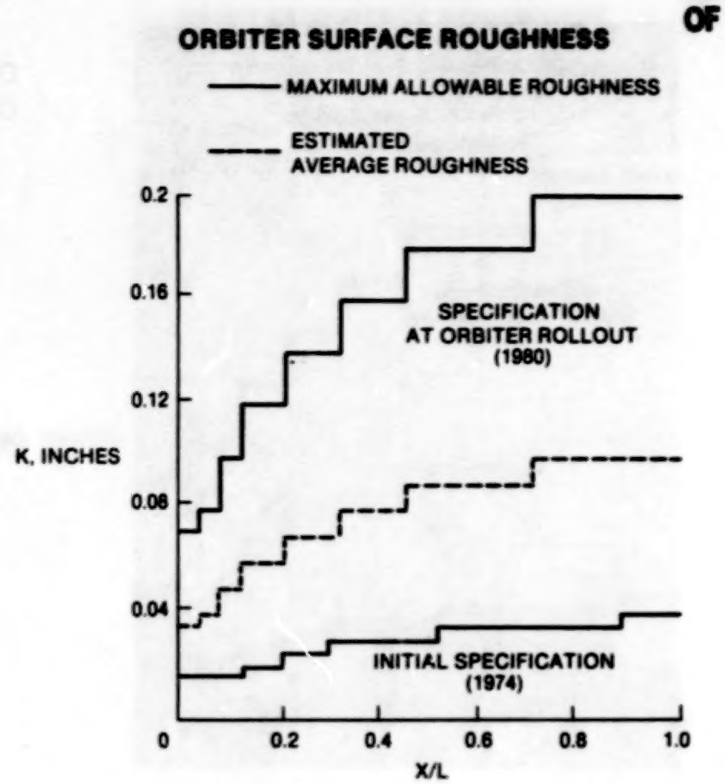

Figure 3.- Distribution of maximum allowable and estimated average surface roughness for the orbiter centerline.

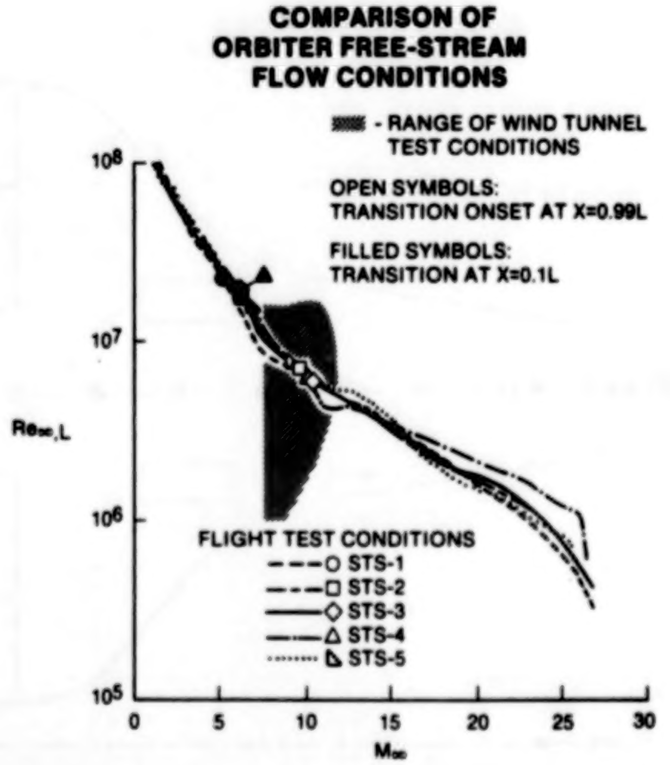

Figure 4.- Comparison of free-stream flow parameters for flight and wind tunnel test conditions.

ORIGINAL PAGE IS
OF POOR QUALITY

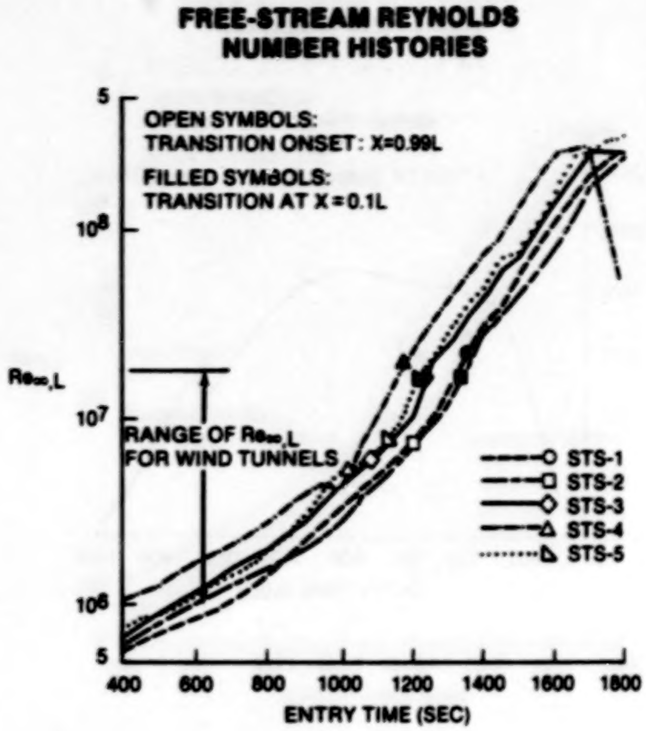

Figure 5.- Histories of free-stream Reynolds numbers for the STS trajectories.

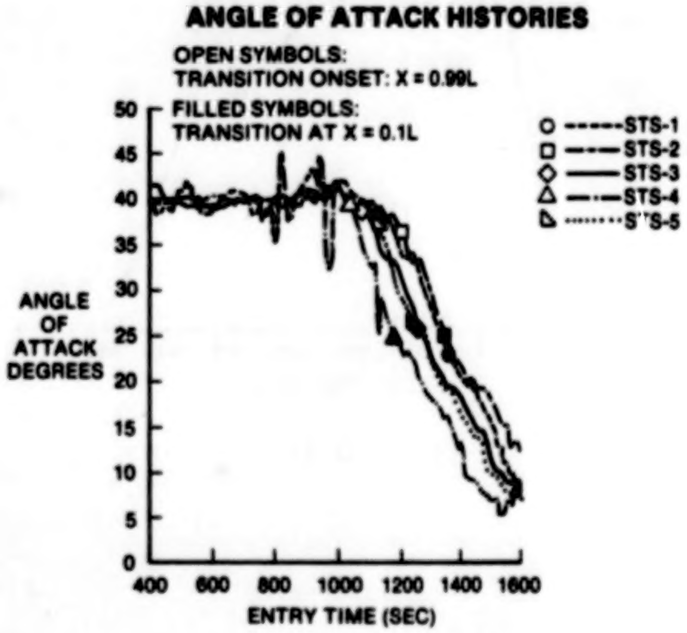

Figure 6.- Angle of attack histories for the STS trajectories.

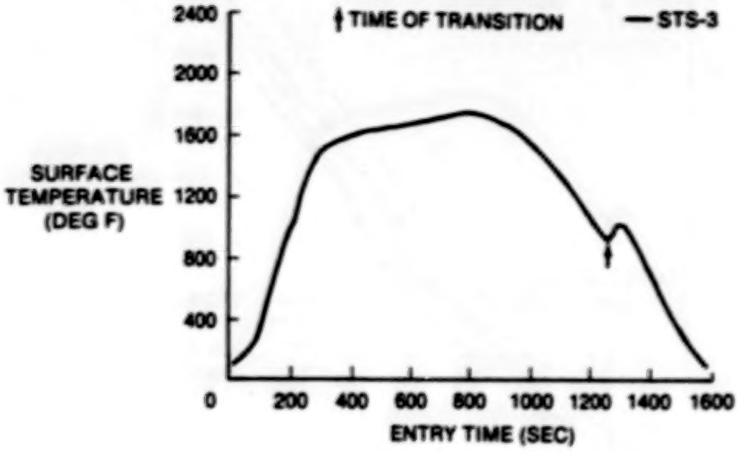

(a) x = 0.1L.

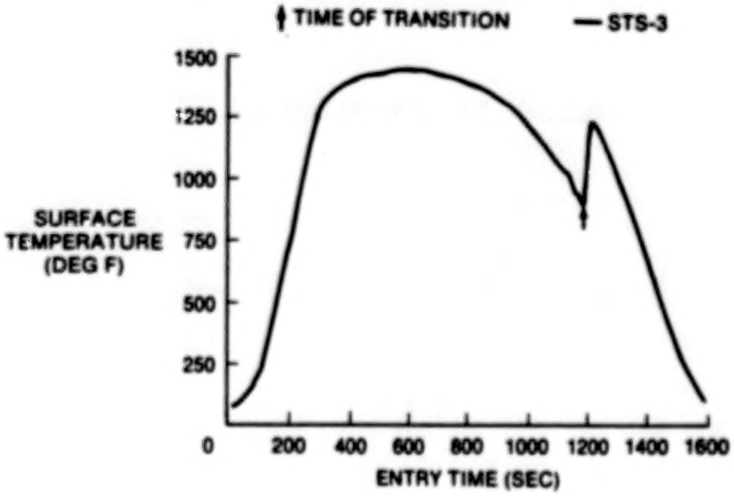

(b) x = 0.5L.

Figure 7.- Typical surface temperature histories used to locate times of transition.

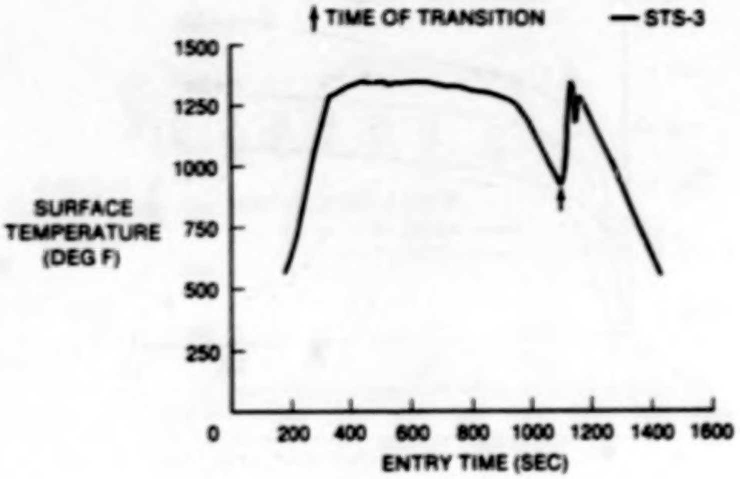

(c) x = 0.9L.

Figure 7.- Concluded.

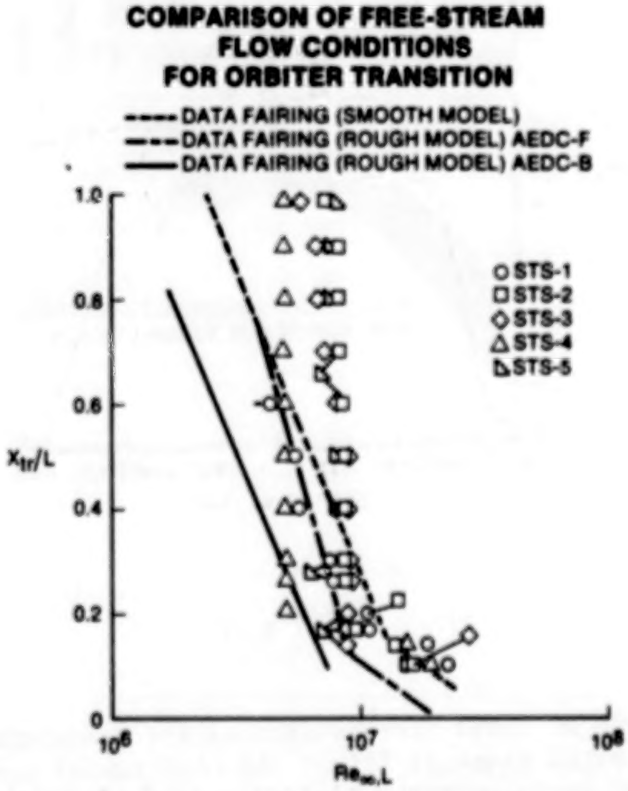

Figure 8.- Comparisons of $Re_{\infty,L}$ for transition along the orbiter windward pitch plane at flight and wind tunnel conditions.

ORIGINAL PAGE IS
OF POOR QUALITY

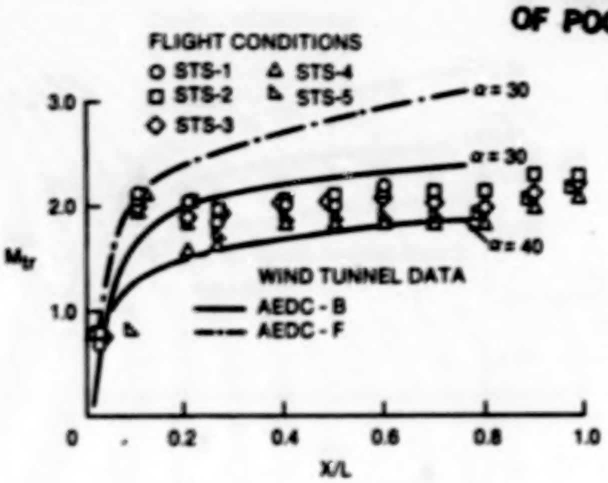

(a) Mach number.

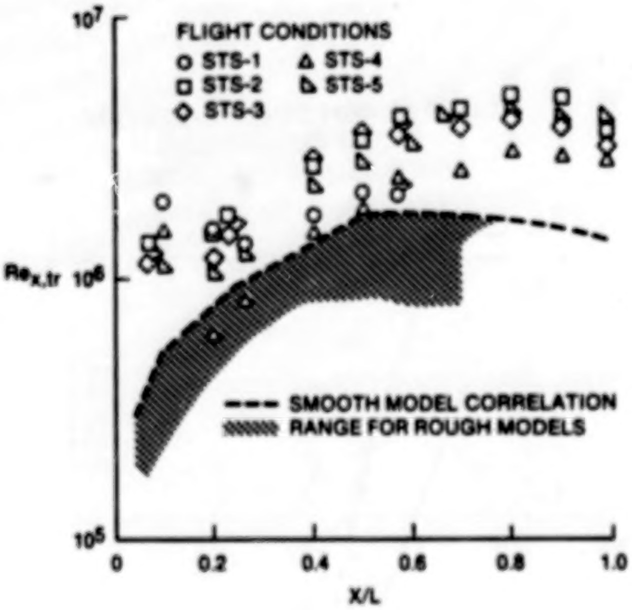

(b) $Re_{x,tr}$.

Figure 9.- Comparisons of local flow conditions for transition along the orbiter windward pitch plane at flight and wind tunnel conditions.

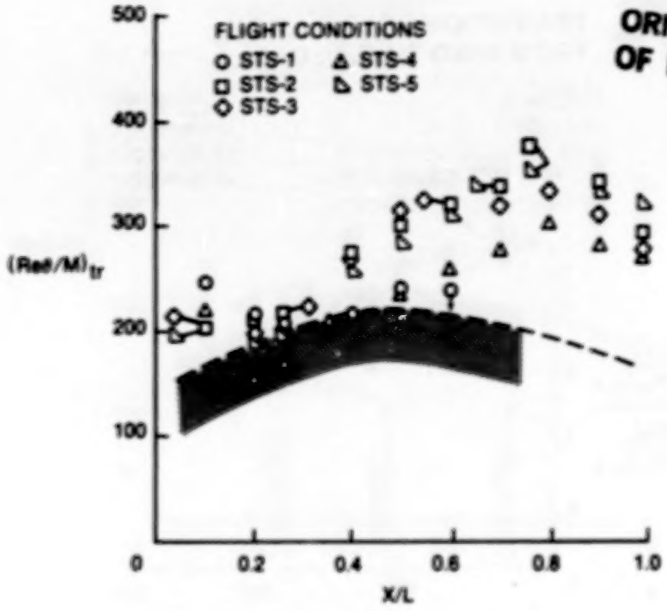

(c) $(Re_\theta/M)_{tr}$.

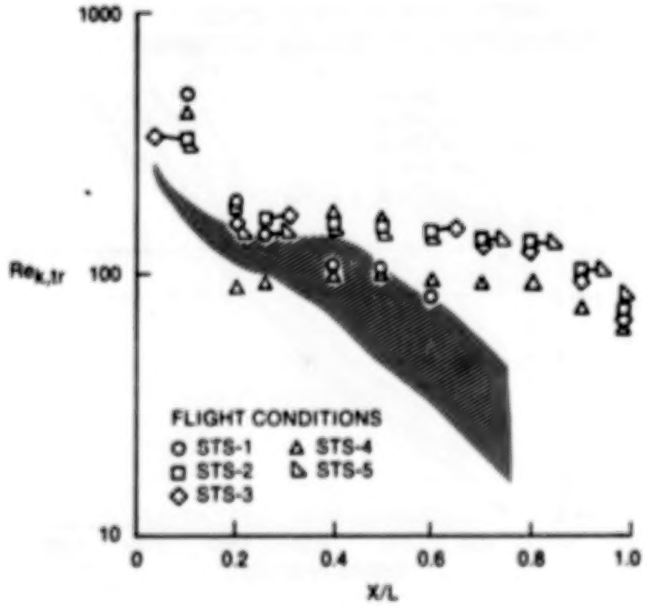

(d) $Re_{k,tr}$.

Figure 9.- Concluded.

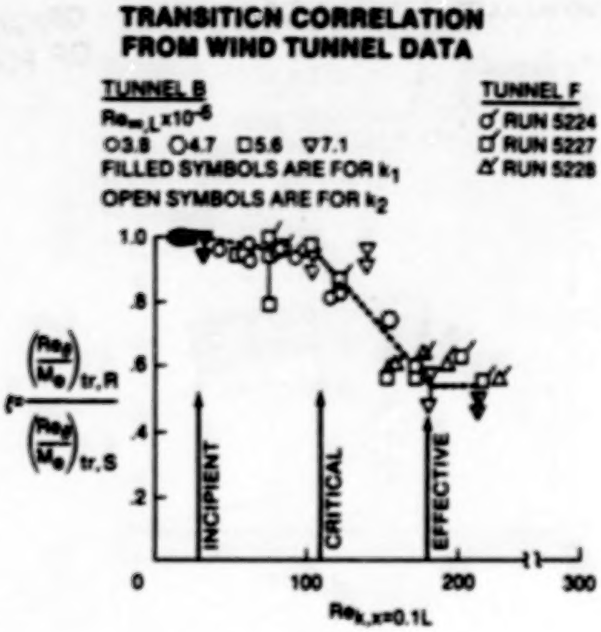

Figure 10.- Correlation of the relative transition parameter as a function of $Re_{k,x=0.1L}$ (Ref. 7).

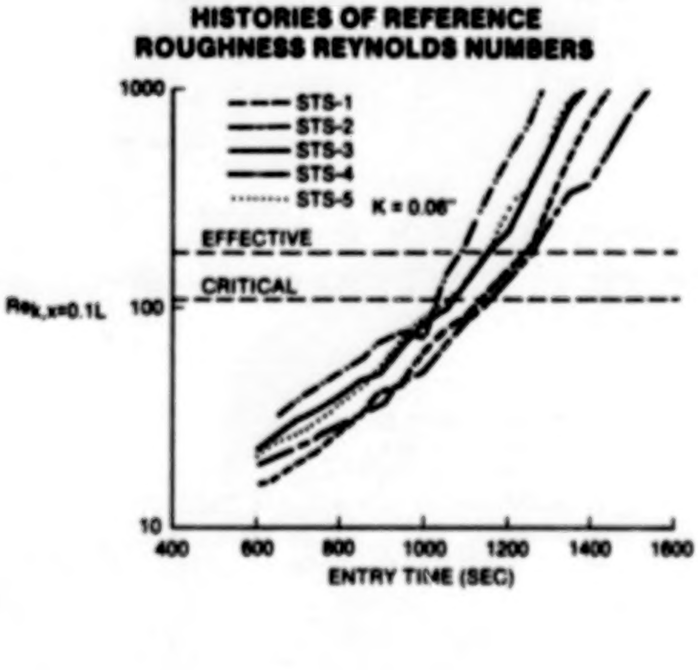

Figure 11.- Histories of $Re_{k,x=0.1L}$ for k = 0.06" for the STS trajectories.

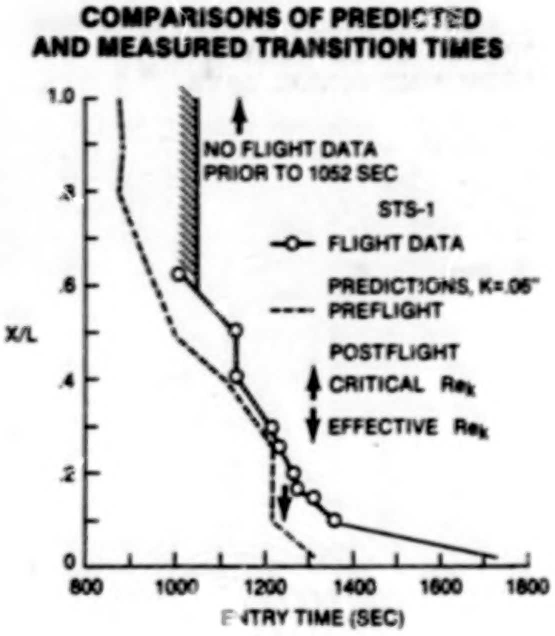

(a) STS-1.

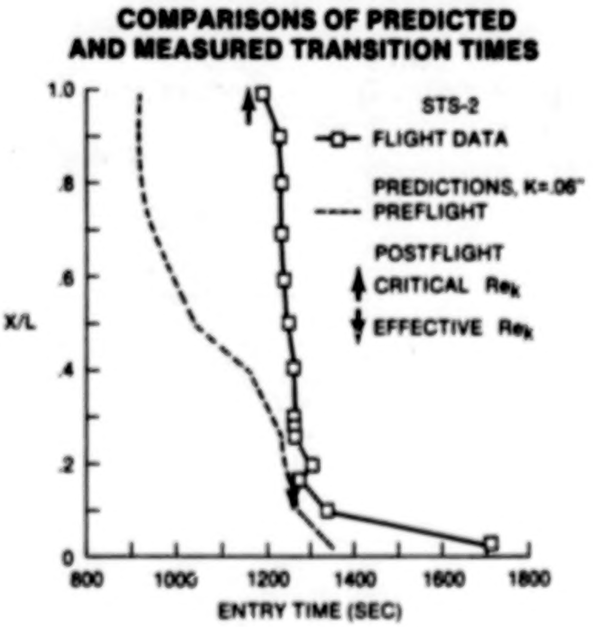

(b) STS-2.

Figure 12.- Comparisons of predicted and measured transition times for the first five STS trajectories.

ORIGINAL PAGE IS
OF POOR QUALITY

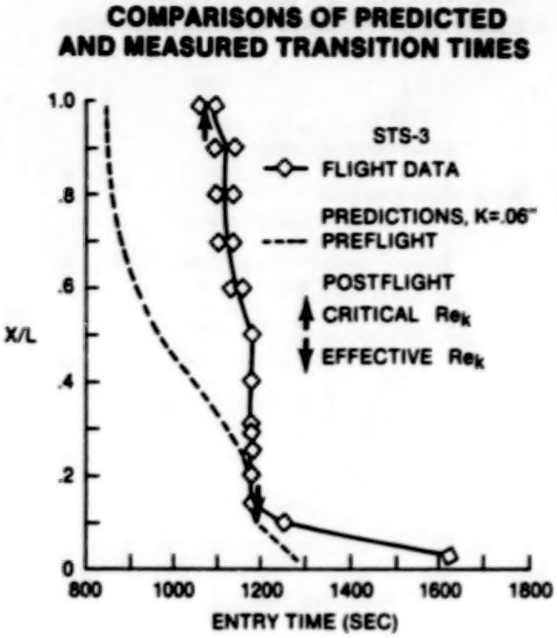

(c) STS-3.

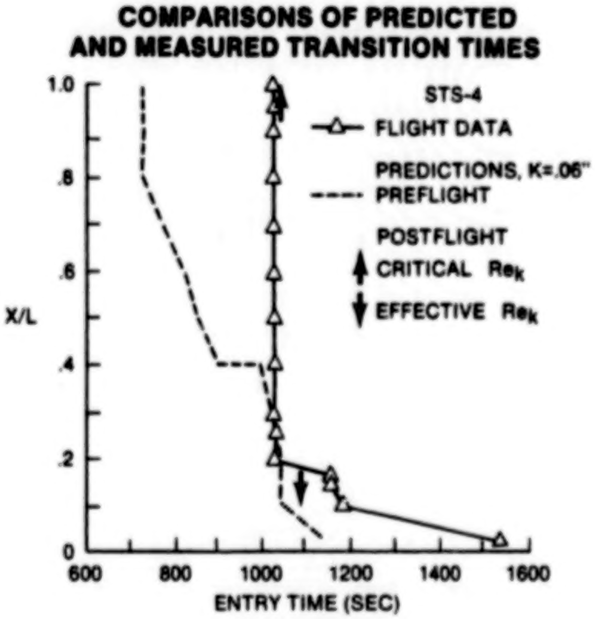

(d) STS-4.

Figure 12.- Continued.

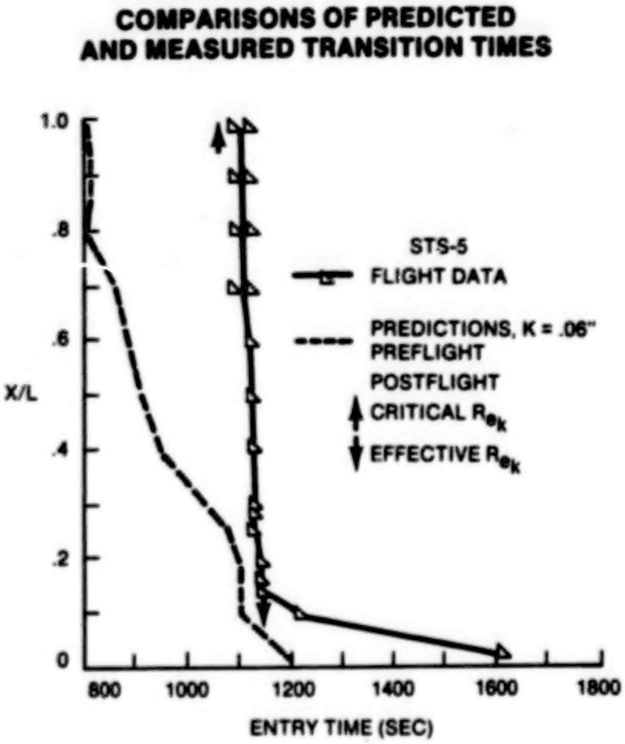

(e) STS-5.

Figure 12.- Concluded.

N84
10150

UNCLAS

N84 10150 D6

ORBITER WINDWARD SURFACE ENTRY HEATING: POST-ORBITAL FLIGHT TEST PROGRAM UPDATE

M. H. Harthun, C. B. Blumer, and B. A. Miller
Space Transportation and Systems Group
Rockwell International
Downey, California

SUMMARY

Correlations of orbiter windward surface entry heating data from the first five flights are presented with emphasis on boundary layer transition and the effects of catalytic recombination. Results show that a single-roughness boundary layer transition correlation developed for spherical-element trips works well for the orbiter tile system. Also, an engineering approach for predicting heating in nonequilibrium flow conditions shows good agreement with the flight test data in the time period of significant heating. The results of these correlations, when used to predict orbiter heating for a high-cross-range mission, indicate that the thermal protection system on the windward surface will perform successfully in such a mission.

INTRODUCTION

The design of the orbiter thermal protection system (TPS) was based on the following logic: the most severe operational mission was selected to define the design heating environments, but nominal trajectory parameters, nominal heating methods, nominal material properties, and an aerodynamically smooth surface were assumed in order to save weight. Safety margins for the flight test program were created by the lower orbit inclinations and reduced cross range requirements during these flights, which reduced the severity of the thermal environments. The aerothermodynamic objective of the flight test program was to obtain data to update the heating methodology, which then could be used to support verification of the TPS for operational use. To this end, development flight instrumentation (DFI) was installed on the vehicle to obtain data in critical locations. Data from the flight test program were expected to demonstrate that margins would also exist for the operational missions, even though a nominal design approach had been taken.

This paper presents the projected operational capability of the TPS (specifically the windward surfaces) in light of the lessons learned from the flight test program regarding entry aerodynamic heating.

PRECEDING PAGE BLANK NOT FILMED

PAGE 780 INTENTIONALLY BLANK

SYMBOLS

C	constant in equation 7
C_{P_f}	frozen specific heat
g	gravitational constant
h	local heat transfer coefficient
H	enthalpy
k	roughness element height
L	orbiter reference length
M	Mach number
N	constant in equation 7
P	local pressure
q	heat flux
Re_k	trip Reynolds number, $\rho_\delta u_\delta k/\mu_\delta$
Re_{x_k}	trip position Reynolds number, $\rho_\delta u_\delta x_k/\mu_\delta$
$Re_{\delta*}$	displacement thickness Reynolds number at the trip position for effective tripping, $\rho_\delta u_\delta \delta^*/\mu_\delta$
Re_θ	momentum thickness Reynolds number, $\rho_\delta u_\delta \theta/\mu_\delta$
R_o	universal gas constant
T	temperature
u	velocity
x	axial coordinate
x_k	trip position measured from stagnation point
x_t	transition position measured from stagnation point
y	spanwise coordinate
Z	compressibility
α	angle of attack
δ^*	displacement thickness of boundary layer
θ	momentum thickness of boundary layer

ρ	density
μ	viscosity
η	defined in equation 6
γ_R	defined in equation 7

Subscripts

av	adiabatic wall
D	dissociation
eff	effective
eq	equilibrium
f	frozen
ne	nonequilibrium
w	wall conditions
δ	boundary layer edge conditions

FLIGHT TEST PROGRAM

Flight Conditions

The Orbital Flight Test (OFT) program consisted of four flights, STS-1 through -4. Aerodynamic heating data were acquired by a DFI system with an on-board recorder. The fifth flight, STS-5, although an operational flight, also provided aeroheating data since the DFI system was utilized. In all five flights, the orbiter entered the atmosphere from low Earth orbits at inclinations ranging from 28.5 deg to 40 deg. Peak heating generally occurred when the vehicle angle of attack was 40 deg, and the thermal equivalent cross range flown was approximately 720 nmi.

Instrumentation

The entry aerodynamic heating data on the lower surface of the orbiter were obtained primarily from thermocouples installed in the outer surface of the high-temperature reusable surface insulation (HRSI) and in contact with the reaction cured glass (RCG) tile coating. These instruments, fabricated from a 10-mil platinum-platinum 13-percent rhodium wire, were located as shown in figure 1. In addition to the thermocouples, the lower fuselage surface was instrumented with pressure taps and calorimeters. A more detailed description of the DFI system can be found in reference 1.

RESULTS AND DISCUSSION

Data from the flight test program show that heating on the upper surfaces was generally less than predictions based on wind tunnel test data. The exception is the area influenced by the vortex emanating from the wing-glove/body junction. This area includes the fuselage side, payload bay door, and orbital maneuvering subsystem (OMS) pod. Possible reasons for the higher heating in flight are presented in reference 2.

The lower surfaces experienced less heating than expected during flight due to two phenomena: delayed boundary layer transition and reduced catalytic recombination. Therefore, this paper focuses on the knowledge gained from the flight test program with regard to these two topics.

Boundary Layer Transition

One of the major considerations in defining the entry heating environment was the time at which boundary layer transition occurs. The design philosophy was to specify the heating environment with a "smooth surface" transition. Smooth surface transition was defined as the transition conditions measured on a smooth wind tunnel model and correlated and extrapolated to flight by using $Re_\theta/M_\delta = f$ (angle of attack, body location). It was anticipated that the wind tunnel would provide a conservative transition value due to free-stream turbulence and that transition during flight would be induced by surface roughness.

Orbiter Surface Description. The TPS on the lower surface of the orbiter is composed primarily of insulating tiles with nominal surface dimensions of 6 in. by 6 in. The tiles are spaced by nominal gaps of 0.045 in. during installation to provide clearance for differential thermal expansion (contraction) between the tile and the orbiter's aluminum structure during flight. The tile edges are rounded to avoid stress concentrations in the glassy coating. Some tile surface irregularities exist due to manufacturing techniques or to surface slumping when the tile coating is fired; in addition, installation tolerances result in steps between tiles. The foregoing is not the description of an aerodynamically smooth surface; in fact, the many combinations of steps, gaps, and tile irregularities produce an incredibly complex surface in terms of roughness definition.

Several types of measurements were used to inspect the orbiter surface. Steps and gaps between adjacent tiles were measured after installation. Subsequent visual inspections indicated that in a significant number of cases, the step measurements did not identify the worst steps. As a result, a "profilometer" was built to measure the tile surface. The profilometer follows the principle of microsurface analyzers but on a much larger scale. It traces a path 50 in. long on the orbiter surface with three transducers spaced 0.25 in. laterally. An electronic plotter simultaneously plots the results, expanding the vertical scale 25 times so that a 0.001-in. surface displacement may be resolved.

A typical trace is shown in figure 2. Profile locations were selected on the basis of a visual inspection of the surface, always looking for the worst TPS installations. A set of 16 of these locations was also measured after each of the first four flights. No significant changes occurred from flight to flight at these locations. Measurement variations within 0.015 in. were observed, which is almost within the variation of repeated setups at the same location.

During the evolution of the thermal protection system, exploratory wind tunnel tests were performed on smooth orbiter models that were grooved to simulate tile gaps. It was discovered that grooves parallel to the surface streamlines produced strong boundary layer tripping disturbances whereas grooves perpendicular to streamlines produced much weaker disturbances. Subsequent experiments indicated that a 15-deg angle between gap and flow direction was sufficient to avoid the parallel-gap tripping effect. These observations resulted in the tile orientation pattern shown in figure 1.

Analysis. To develop analytical tools to define allowable TPS installation tolerances and further relate the completed orbiter surface configuration to the observed transition during flight, existing wind-tunnel-based boundary layer transition research was used. As previously stated, it was presumed that transition would be caused by single or isolated roughness elements that are three dimensional in character. The reasoning that leads to this assumption is as follows.

First, it has been demonstrated (ref. 3) that in supersonic flow three-dimensional roughnesses (spheres) are more effective trips than two-dimensional roughnesses (wires perpendicular to flow). By analogy, tile edges where the step and gap are uniform may be thought of as two-dimensional roughnesses and tile corners or intersections as three-dimensional roughnesses. If the tile edge and corner steps are the same, then the corner should produce the dominant disturbance. Also, wind tunnel tests (ref. 4) showed that spacing three-dimensional roughnesses laterally at a distance of four roughness heights (4k) was sufficient to prevent interaction between roughnesses; that is, it allows each element to act as if it were the only roughness element present. The maximum anticipated roughness is on the order of $k = 0.1$ in.; therefore, disturbance spacing greater than 0.4 in. should not cause interaction.

Finally, figure 3 shows schematically how three-dimensional roughness size variation affects transition location. In section A of figure 3, between ① and ② the roughness has very little effect on the natural or smooth wall transition, indicating that the roughness disturbances do not dominate the boundary layer before they decay. The region between ② and ③ is characterized by a small change in roughness size, causing a large change in transition position. The curve to the right of ③ again shows only a small change in transition position with roughness size when transition is close to the trip. Point ③ is defined as the "effective trip" size, i.e., the smallest trip that will cause transition near the trip. In this discussion, only the left side of figure 3, section A, up to point ③ is of concern. Section B of figure 3 shows the effect of increasing trip size. The boundary layer is very discriminating as to the roughness sizes that affect transition. Since the roughness distribution was not expected to be uniform, a relatively small number of discrete roughnesses were expected to cause transition, and there was a low probability that these disturbances would interact with one another. The conclusion was that single-roughness-element transition research would be an appropriate basis for the analytical tools. (It will be shown later that the observed transition patterns on the orbiter are consistent with the above assumptions.)

Equation 6 of reference 5 is

$$Re_k = 33.4 \left[1 + 0.90\left(\frac{T_w}{T_\delta} - 1\right) + 0.28\left(\frac{T_{aw}}{T_\delta} - 1\right)\right] Re_{x_k}^{1/4} \qquad (1)$$

which represents the conditions for an effective spherical element trip. This equation is for flow on a cone and includes variations in Mach number and heat transfer. Reference 5 also notes that the bracketed term in equation 1 is nearly equal to $(\delta^*/x_k)\sqrt{Re_{x_k}}$. Empirically, equation 2 represents a slight improvement:

$$\frac{\delta^*}{x}\sqrt{Re_{x_k}} = 1.09 \left[1 + 0.90\left(\frac{T_w}{T_\delta} - 1\right) + 0.28\left(\frac{T_{aw}}{T_\delta} - 1\right)\right] \qquad (2)$$

Substituting equation (2) into equation (1) yields

$$k/\delta^* = 30.7 \, Re_{x_k}^{-1/4} \qquad (3)$$

which also includes heat transfer and compressibility effects for flow over a cone. Equation 3, which matches the data of references 4 and 5 about as well as the previous equations, will be used to extrapolate to orbiter flight conditions because of its simplicity. Fortunately, the assumption of conical flow also is a good approximation for the orbiter lower surface for $x/L \leq 0.5$.

Figure 4 is a typical curve of effective roughness size versus streamwise location along the orbiter centerline at a specific flight condition as predicted from equation 3. The displacement thickness (δ^*) was calculated by using a finite-difference boundary layer computer code called GLTS (ref. 6). Obviously, the nose and wing leading edge are the most critical regions for surface roughness.

Wind Tunnel Tests. Wind tunnel tests were performed at Arnold Engineering Development Center Tunnel B at $M_\infty = 8$ to verify the applicability of equations 1 or 3 for the orbiter configuration. These tests used a 0.04-scale model of the orbiter forebody ($x/L \leq 0.5$). For the first series of tests, spherical roughnesses were mounted on the model at $x/L = 0.05$, 0.11, or 0.17. The models were solid copper forward of the trip to provide an isothermal boundary layer from the stagnation point to the roughness. Aft of the trip, the models were made of an alumina-filled epoxy, and the phase-change paint technique was used to obtain transition data. The roughness elements were spheres with diameters of 0.015, 0.020, 0.025, and 0.031 in. These data are compared with the cone data of reference 5 in figure 5. The second series of tests replaced the spherical roughness elements with a simulated tile array, including gaps between the tiles, as shown in figure 6. One tile in the array was displaced by shimming to create a step. Steps varied from 0 to 0.025 in. at 0.005-in. increments in the previously mentioned x/L stations. Gaps surrounding the stepped tile were 0, 0.010, or 0.020 in.

The results of this series of tests were less definitive than the results for the spherical roughness tests; however, several conclusions were made: (1) increasing the gap surrounding the stepped tile increased the tripping effect of the step; (2) with a 0.010-in. gap around the stepped tile, a step equal to approximately one half of the spherical roughness diameter (height) produced an equivalent transition pattern; and (3) the effect of the gap was most pronounced at the forward test station (i.e., $x/L = 0.05$). One variable that was not included was the tile edge radius. The model tile edges are essentially sharp (as machined), whereas the orbiter tile edge radius varies from about 0.050 to 0.100 in., or about the same as the observed steps. The edge radius may also be a significant variable when the step, edge radius, and the adjacent gap are all roughly the same dimension. Reference 7 suggests that increasing the solid volume at the top of the trip (i.e., reducing the edge radius) increases the effectiveness of the trip; however, the observed factor of two in trip size is much larger than trip-shape-factor effects previously observed.

Flight Test Results. The orbiter flight test program provided a boundary layer transition experiment of unprecedented proportion. Five flights were made with the DFI system operating. Transition-sensing instrumentation on the lower surface consisted of 94 platinum-platinum, 13-percent rhodium thermocouples installed in the tile outer surface coating and distributed over the left side of the orbiter with one thermocouple on the right wing tip as shown in figure 1. Data were recorded for each instrument at one-second intervals throughout the entry. A typical surface-temperature-versus-time record is shown in figure 7. The surface temperature is practically equal to radiation equilibrium temperature. The DFI data were recorded on board and telemetered in real time. Telemetered data were restricted to the latter part of entry because the orbiter was out of range of the receiving antennas early in the entry. On flights STS-1 and -4, failure of the on-board recorder limited the data.

In figure 7, the beginning of transition is the departure from the laminar temperature at 1,263 sec; the end of transition is the attainment of the turbulent temperature at 1,280 sec. The beginning of transition is used hereafter to correlate transition events. The transition interval is the difference between the beginning and end of transition and is characteristically less than 30 sec for flight test data, which represents a change in the Reynolds number of less than 20 percent. This abrupt transition zone is one indication of roughness-induced transition. Another indication of roughness-caused transition is the sudden forward movement illustrated in section A of figure 3. For the flight test data, roughness-caused transition is manifested as the simultaneous transition over some region of the surface observed in the data. Section B of figure 3 shows that transition caused by an effective roughness originates from a point somewhat downstream of the roughness and then spreads as a wedge of turbulence. This wedge crosses streamlines at a constant angle between 5 deg and 7 deg for supersonic boundary layer edge Mach numbers from 2 to 4, respectively (ref. 3). For a conical flow, the turbulent spreading still crosses streamlines at the above angle, but the turbulent front takes on a curved shape due to the streamline spreading. To map the transition regions on the orbiter, regions of constant transition time were associated with one tripping event. Again, the results were consistent with the assumption that single roughness elements cause transition.

Figures 8 through 12 show patterns developed from the flight test data. A spreading angle of 7 deg (assuming a conical flow field) appears to best fit the data although some variations might be expected due to surface Mach number and surface flow field variations with orbiter angle of attack at the transition time. The spacing of instruments also causes some uncertainty in the position of the transition fronts. Thermocouple locations are indicated on the maps. Surface streamline patterns were developed from contamination streaks on the TPS surface after STS-1. These patterns agreed with wind tunnel oil flow patterns used for the conical flow field assumption for $x/L \leq 0.5$. Streak patterns were used for $x/L > 0.5$.

For the first flight, STS-1, surface temperature data were only available after 1,050 sec entry time (entry time = 0 sec at altitude = 400,000 ft) due to a failure of the on-board recorder. At the time of data acquisition, the flow on the aft fuselage and right wing tip instruments was turbulent. Postflight inspection revealed a gouge in a tile on the right nose landing gear door (NLGD) that was approximately 8 in. long x 1 in. wide x 1 in. deep. Plotting the turbulent spreading from this anomaly gives the pattern shown in figure 8. Transition time for this roughness was set at about 1,000 sec based on an increase in the axial force coefficient along with an elevon asymmetry indicating higher drag on the right side. The asymmetry disappeared at 1,252 sec when the left-hand nose tripped. The tripping event at 1,252 sec is significant because it was repeated for flights STS-1, -2, -3, and -5, and because it was the event that affected the largest surface area on subsequent flights. It is observed that transition is propagated along the wing stagnation streamline (i.e., transition along the wing leading edge occurs at the same time as transition on the forward fuselage). After the flight, the left NLGD surface was inspected visually for large tile steps. The largest apparent step, measured at 0.085 in., was at a lateral tile corner at $x/L = 0.056$ and $y = 10$ in. This is the projection shown in the profilometer trace in figure 2. Surprisingly good agreement exists between this roughness location and the forward extrapolation of the turbulence spreading zone. Equation 3 gives an effective roughness height of 0.080 in. for this location at 1,252 sec. It appears that equation 3 works quite well without an adjustment for roughness shape factor. Two other forward fuselage tripping events occurred at 1,140 sec and 1,230 sec (fig. 8).

Figure 8 also shows that transition occurs on the wing at times ranging from 1,150 sec to 1,235 sec. The number and location of thermocouples in each turbulent wedge do not define the apex of the wedges accurately enough to identify a specific roughness for each tripping event; however, the tripping appears to be related to the wing leading edge or the tile interface region immediately behind the leading edge. The boundary layer on the swept-wing leading edge is already unstable, indicating that the allowable roughness on the leading edge must be less than in the nose region to produce the same transition time, assuming similar roughnesses exist on the wing and on the fuselage. The inboard turbulent wedge is caused by the main landing gear door outboard edge. Note the two transition times (i.e., 1,193/1,226 sec). This notation designates a significant transition event followed by a return to or movement toward a laminar surface temperature, followed by a second transition. The last time is the beginning of the transition that stays turbulent. In this instance, a dip in the angle of attack causes the roughness not to be an effective trip from 1,200 sec to 1,226 sec. Transition on the elevons occurs from before data acquisition at 1,050 sec to 1,155 sec and can be associated with the wing/elevon gap and elevon deflection angle.

The STS-2 and STS-1 trajectories were similar, and as figure 9 shows, the transition patterns and times were also similar. The primary difference was the absence of the gouge on the right hand nose during flight two. Significantly early transition occurs only downstream of the external tank attachment door and on the body flap of the aft fuselage for STS-2. The left NLGD tripping event occurs at 1,263 sec in STS-2 and appears to extrapolate forward to the same roughness location as in STS-1. An aft fuselage transition at 1,250 sec is extrapolated forward to the right NLGD; however, uncertainty in this location is noted. The wing pattern is substantially the same as in STS-1. The early transition on the body flap (i.e., between 500 sec and 700 sec) can be attributed to boundary layer separation caused by the flap's 15 deg down deflection.

STS-3 results (fig. 10) are similar to STS-1 and STS-2 with earlier transition times due to trajectory differences. Also, the transition pattern is somewhat more complicated. A substantial portion of the fuselage and wing transition occurred at 1,180 sec but appeared tentative and finally occurred 13 sec later. The origin of this event is assigned to the NLGD centerline thermal barrier. The left NLGD tripping occurred cleanly at 1,293 sec and overran the tentative 1,180 sec event. Right side events occurred at 1,112/1,145 sec and at 1,162 sec with the double time explainable as an α transient. The wing pattern closely resembles flights one and two. Right-hand-side transition events must be inferred from downstream patterns that cross the centerline or affect the right-hand wing tip.

Results from STS-4 (fig. 11) are notably different from the previous flights in that transition occurred over almost the entire lower surface due to a single tripping event at 1,030 sec. The apex of the transition appears to be in line with the microphone on the left NLGD. One significant difference was that transition occurred when the angle of attack was 40 deg rather than 32 to 34 deg for STS-1 through -3.

The STS-5 transition map is shown in figure 12. A right-side event is noted at 1,093/1,121 sec on the aft fuselage whereas the right wing tip tripped only at 1,121 sec, indicating that the 1,093 sec event is not far enough forward to spread onto the wing. The 1,125-sec event is consistent in location with the left-hand NLGD tripping on flights 1 through 3. Tripping occurred near the front of the left-hand NLGD at 1,145 sec. Less wing tripping was evident during STS-5 than on the first three flights.

To compare data from each instrumented flight, equation 3 was used to calculate the size of a fictitious roughness at $X/L = 0.1$ at the time of tripping in the left NLGD region. Results are presented in table I. The calculations indicate a nearly constant effective roughness size ($k_{av} = 0.113$ in.) for flights -1 through -3 and -5, even though the trajectory parameters changed substantially. The larger roughness ($k_{eff} = 0.133$ in.) calculated for STS-4 has not been explained, but this roughness size is large enough to cause transition before the observed wing tripping times on the other flights. This could explain the single-event tripping in STS-4.

It is concluded that: (1) a single roughness site on the left NLGD tripped the boundary layer on four of the five flights; (2) this roughness (k_{eff}) remained essentially unchanged through the flight test program; (3) transition from this roughness was obscured by earlier transition from a larger roughness in STS-4; and (4) an analytical method that predicts the effective roughness size has been extended from wind tunnel conditions to entry flight conditions.

Catalytic Recombination

The design of the orbiter TPS was accomplished by predicting heating based on the assumption of equilibrium flow. The methods used are described in reference 8. The approach to predict heating on the lower surface of the orbiter consisted of breaking the vehicle down into simple geometric shapes, predicting the heating for the assumed shape and modifying the prediction to match wind tunnel data. The resulting correlation was extrapolated to flight conditions using real-gas properties. The methods are incorporated in the Rockwell International Aeroheating Computer Program (ref. 9) which was formulated as a design instrument to estimate ascent or entry heating for simple geometric shapes. An inability to predict nonequilibrium boundary layer heating and a lack of knowledge about the catalytic behavior of the TPS tile coating precluded a design approach based on these phenomena. However, results from plasma arc heater tests during the TPS development test program indicated the inhibiting characteristics of the tile baseline coating may reduce aerodynamic heating. During the test program, the heating to the TPS coating in a plasma environment could be approximated by using

$$\dot{q}_{TEST} = \dot{q}_{eq} \left[\frac{H_{aw} - H_w - \eta H_D}{H_{aw} - H_w} \right] \tag{4}$$

where η was found to be 0.7 ± 0.1 (ref. 10). However, characterization of the dissociated nonequilibrium gases produced by the arc heaters was difficult and the tile coating was often contaminated. These phenomena precluded a confident update of the aeroheating prediction methods prior to the OFT program.

__Analysis__. Flight test data from STS-1 were acquired only during the last part of the entry trajectory. As a result, little was learned relative to the catalytic recombination characteristics of the orbiter TPS. During the second flight, data were acquired throughout the entry profile. The results showed that during the laminar flow regime, the heating over the fuselage lower surface was significantly less than predicted by the equilibrium heating methods (fig. 13). This data presented good insight into the potential reduction of aeroheating due to the inhibiting characteristics of the TPS coating. In addition, in STS-2, the orbiter experiments (OEX) catalytic surface effects (CSE) experiment sponsored by the NASA Ames Research Center was initiated. The results from this experiment dramatically illustrated the significance of catalytic recombination on the orbiter entry heating. These experiments were continued in subsequent flights and the results reported in other sources such as references 11 and 12.

To estimate the effects of a partially catalytic wall on aeroheating, equation 4 was applied to orbiter entry with consideration for frozen boundary layer properties:

$$\dot{q}_{ne} = \dot{q}_{eq} \left[\frac{H_{aw_f} - C_{p_f} T_w - \eta H_D}{(H_{aw} - H_w)_{eq}} \right] \tag{5}$$

By reviewing and interpreting the results of research in the field of nonequilibrium aeroheating, a relationship was obtained for η in terms of flight variables and the thermochemical properties of the TPS tile surface:

$$\eta = 1 - \frac{P_g \gamma_R}{h_{eq} \sqrt{2\pi R_o Z_f T_w}} \qquad (6)$$

The variable, γ_R, represents the number of recombined atoms of oxygen and nitrogen normalized by the total number of uncombined atoms at the edge of the boundary layer. An Arrhenius relation was assumed for γ_R:

$$\gamma_R = N \text{ EXP } (^{-C}/T_w) \qquad (7)$$

The DFI data from STS-2 was used to determine the values for N and C. The resulting correlation is

$$\gamma_R = 0.05787 \text{ EXP } (-6876/T_w) \qquad (8)$$

The nonequilibrium aeroheating was estimated by using equations 5, 6, and 8.

Flight Test Results. When this semi-empirical technique is applied to the STS-2, trajectory results are as shown in figures 13, 14, and 15, where surface temperature data and predictions are compared as a function of time at three stations along the fuselage lower centerline. Figure 13 also includes a prediction for equilibrium flow using the methodology referred to earlier. Figure 16 shows a crossplot of figures 13, 14, and 15 at two times during the trajectory. The second time cut selected was 1,200 sec since this is just prior to the time of boundary layer transition and the prediction technique for nonequilibrium heating has been assumed to be valid only during the laminar flow regime. The maximum deviation between the prediction model and data for these two time cuts is approximately 7 percent.

The results for STS-3 are shown in figures 17, 18, 19, and 20, and in general are similar to the results shown for STS-2.

Both figures 16 and 20 show excellent agreement between estimated surface temperature and measured flight temperature distributions for the later flight times. These times correspond to the onset of flow transition and the approach of the free stream to equilibrium chemistry conditions. This would enhance the validity of the equilibrium heating technique. The results of analyses of STS-5 data are still preliminary; however, a comparison of the overall results with those from previous flights is included in table III.

Table II presents average temperature deviations between estimated and measured values in the time period between 400 and 1,100 sec for three orbiter flights, STS-2, -3, and -5. These data are remarkably consistent and demonstrate the accuracy of the correlation (equation (5)) based on STS-2 flight data.

At the beginning of entry, 0 to 300 sec, the results from this engineering technique displayed larger differences compared to flight data than in the time period from 400 to 1,100 sec. This may be for two reasons: the application of a continuum flow model partially modified to account for low density flow, and the application of a radiation equilibrium assumption during the time of significant conduction into the TPS as compared to the incoming convective heating. However, during this time period, the impact of aeroheating on heat load (structure temperature) or peak surface temperature is not of major significance.

TPS Capability Projection

A preliminary analysis has been conducted to project the capability of the orbiter TPS for flying high-cross-range missions using the results from the OFT program as discussed in this paper and applying them to the computed trajectory for such a mission. The mission selected was entry from an orbital inclination of 104 deg with a cross-range requirement of 940 n.mi. achieved by flying a 38 to 28 deg angle of attack profile. Using the heat load of a one-foot-radius sphere as an indicator, this mission is approximately 50 percent more severe than the worst of the OFT flights and approximately 30 percent more severe than the TPS design trajectory (fig. 21). Nevertheless, based on the favorable results of the OFT program, it is projected that the windward surface TPS has the capability to accomplish this mission. This conclusion is drawn by comparing the predicted maximum surface temperatures and heat loads for this mission with TPS design values. As illustrated in table III, the maximum surface temperatures do not exceed the design values. At most locations, the heat loads (driver for structure bondline temperature) are less than the design values. Although there are locations where the design values are exceeded, the vehicle can accommodate these environments satisfactorily. Additional flight data and analyses are required to verify the TPS capability.

CONCLUDING REMARKS

Consistent and reliable correlations of the orbiter flight test heating data were obtained relative to boundary layer transition and catalytic recombination. The application of these correlations in predicting the heating of the orbiter for a high-cross-range mission indicates that the TPS on the windward surfaces has the capability for successfully performing this mission. This result tends to validate the unique design approach used for the orbiter TPS.

An understanding of boundary layer transition and catalytic recombination is not only significant for verifying the orbiter TPS, but is also helpful in the design of effective thermal protection systems for future entry vehicles. Therefore, it is recommended that high priority be given to the continued analysis and understanding of these phenomena.

REFERENCES

1. Smith, J. A., "STS-3 Structural and Aerodynamic Pressure, Aerothermodynamic and Thermal Protection System Measurement Locations," SMD/NASA/JSC, No. 17889, Jan. 15, 1982.

2. Haney, J. W., "Orbiter Entry Heating Lessons Learned From Development Flight Test Program," Shuttle Performance: Lessons Learned, NASA CP-2283, Part 2, 1983, pp. 719-951.

3. Van Driest, E. R. and W. D. McCauley, "The Effect of Controlled Three-Dimensional Roughness on Boundary Layer Transition at Supersonic Speeds," Journal of the Aerospace Sciences, Vol. 27, No. 4, pp. 261-272, Apr. 1980.

4. Van Driest, E. R. and C. B. Blumer, "Boundary-Layer Transition at Supersonic Speeds - Three-Dimensional Roughness Effects (Spheres)," Journal of the Aerospace Sciences, Vol. 29, No. 8, pp. 909-916, Aug. 1962.

5. Van Driest, E. R. and C. B. Blumer, "Boundary-Layer Transition at Supersonic Speeds: Roughness Effects with Heat Transfer," American Institute of Aeronautics and Astronautics Journal, Vol. 6, No. 4, pp. 603-607, Apr. 1968.

6. Waiter, S. A. and L. P. LeBlanc, "Solution of the Equations of the Compressible Boundary Layer (Laminar, Transition, Turbulent) by an Implicit Finite Difference Technique," Astronautica Acta, Vol. 16, pp. 265-275, 1971.

7. Morrisetti, E. L., D. R. Stone, and A. H. Whitehead, "Boundary Layer Tripping with Emphasis on Hypersonic Flows," Viscous Drag Reduction, Plenum Press, N.Y., pp. 33-51, 1969.

8. Lee, D. B. and M. H. Harthun, "Aerothermodynamic Entry Environment of the Space Shuttle Orbiter," AIAA Paper 82-0821, presented at the AIAA/ASME 3rd Joint Thermophysics Fluids, Plasma and Heat Transfer Conference, St. Louis, MO, June 7-11, 1982.

9. Miller, B. A., "XF0002 Aeroheating Computer Program Engineering Description and User's Guide," SOD 80-0150, Aug. 1982 Rev.

10. Miller, B. A., "Coldarc-Dissociated Air Flow Effects During Plasma Arc Testing," Cosmic Program Abstract, Computer Software Management and Information Center, University of Georgia, Nov. 1982.

11. Stewart, D. A., J. V. Rakich, and M. J. Lanfranco, "Catalytic Surface Effects Experiment on the Space Shuttle," AIAA Paper 81-1143, June 1981.

12. Rakich, J. V., D. A. Stewart, and M. J. Lanfranco, "Results of a Flight Experiment on the Catalytic Efficiency of the Space Shuttle Heat Shield," AIAA Paper 81-0944, June 1982.

ORIGINAL PAGE IS
OF POOR QUALITY

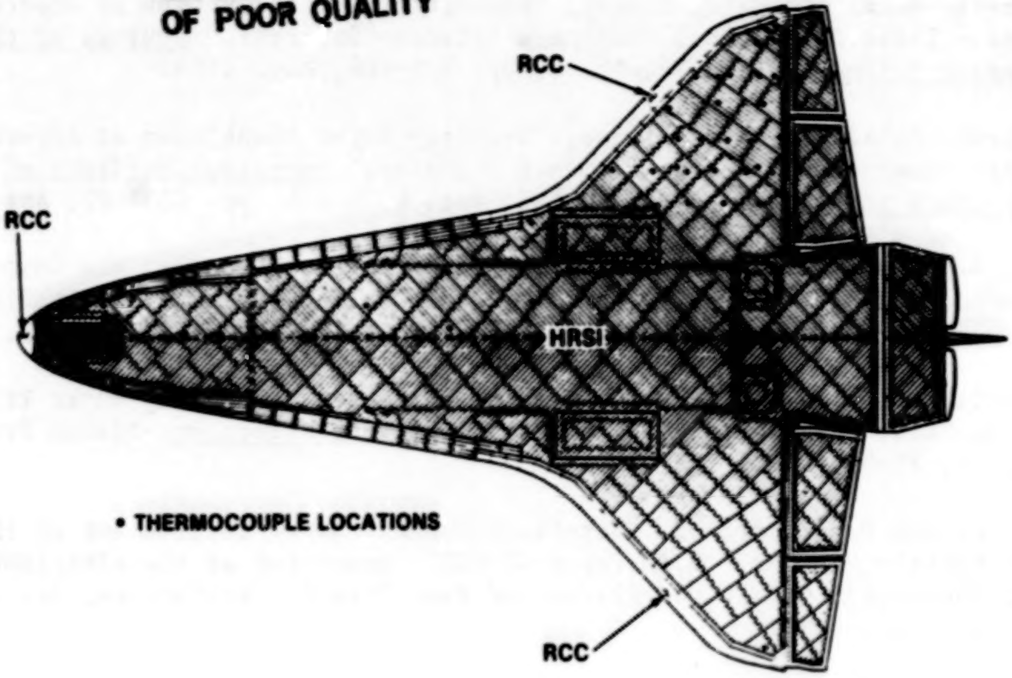
RCC
RCC
HRSI
• THERMOCOUPLE LOCATIONS
RCC

Figure 1.- Orbiter lower surface tile pattern and surface thermocouple layout.

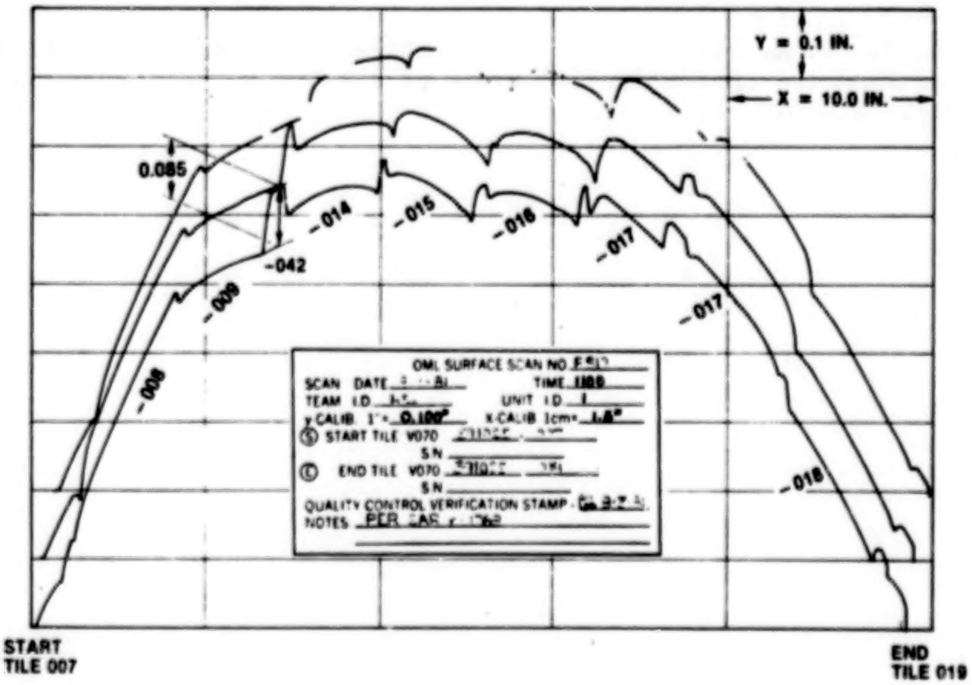

Figure 2.- Profilometer trace on nose landing gear door.

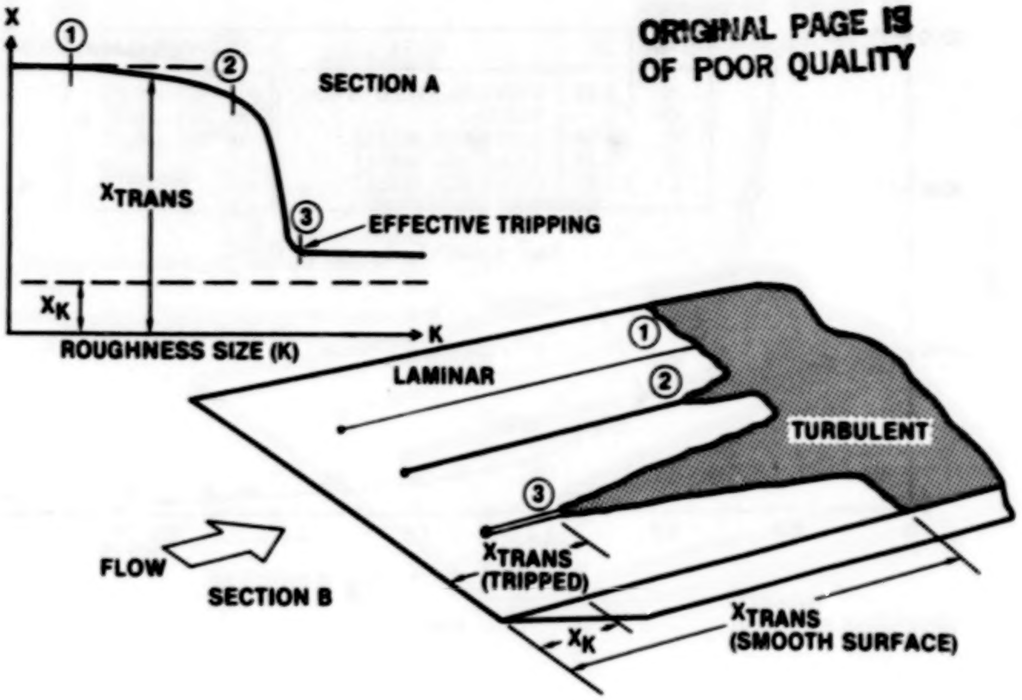
X
①
②
SECTION A
X_{TRANS}
③
EFFECTIVE TRIPPING
X_K
ROUGHNESS SIZE (K)
K
①
LAMINAR
②
TURBULENT
③
X_{TRANS} (TRIPPED)
FLOW
SECTION B
X_K
X_{TRANS} (SMOOTH SURFACE)

Figure 3.- Description of roughness-produced transition.

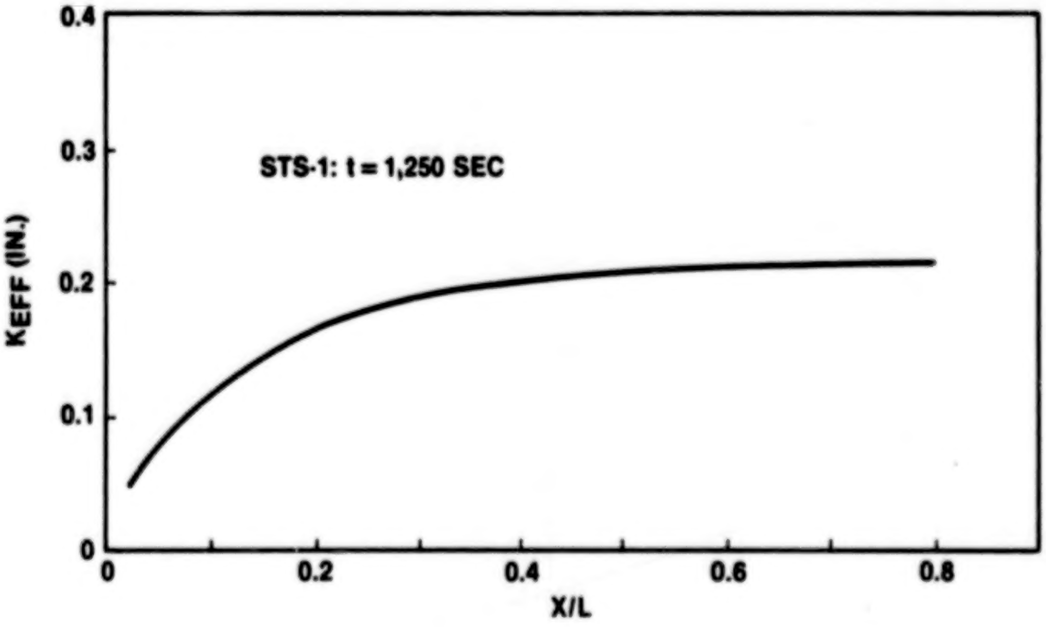

Figure 4.- Typical variation of effective roughness with length.

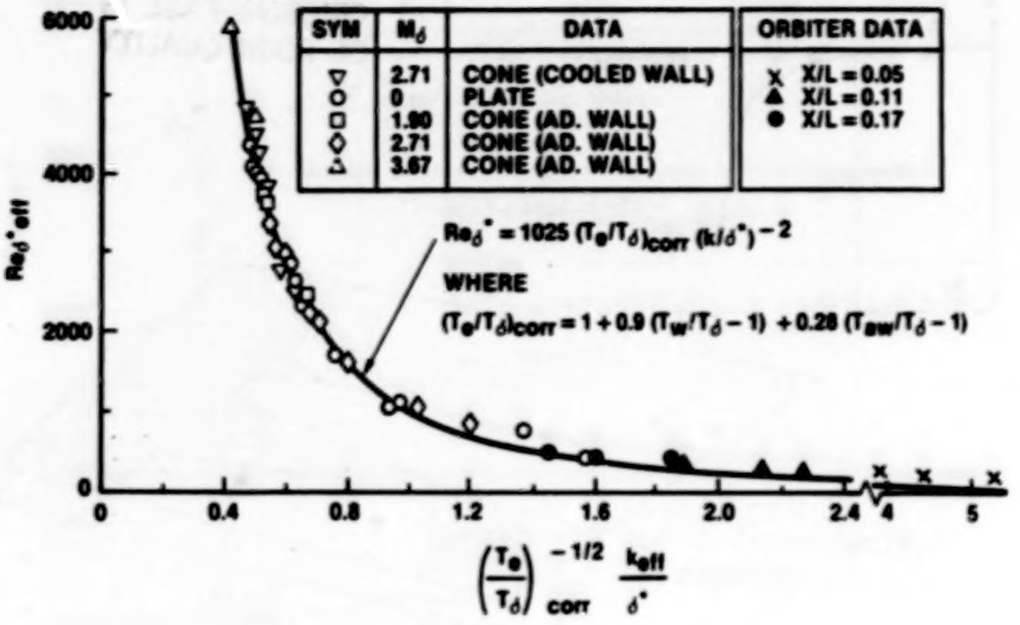

Figure 5.- Composite plot of effective transition data including compressibility and cooling.

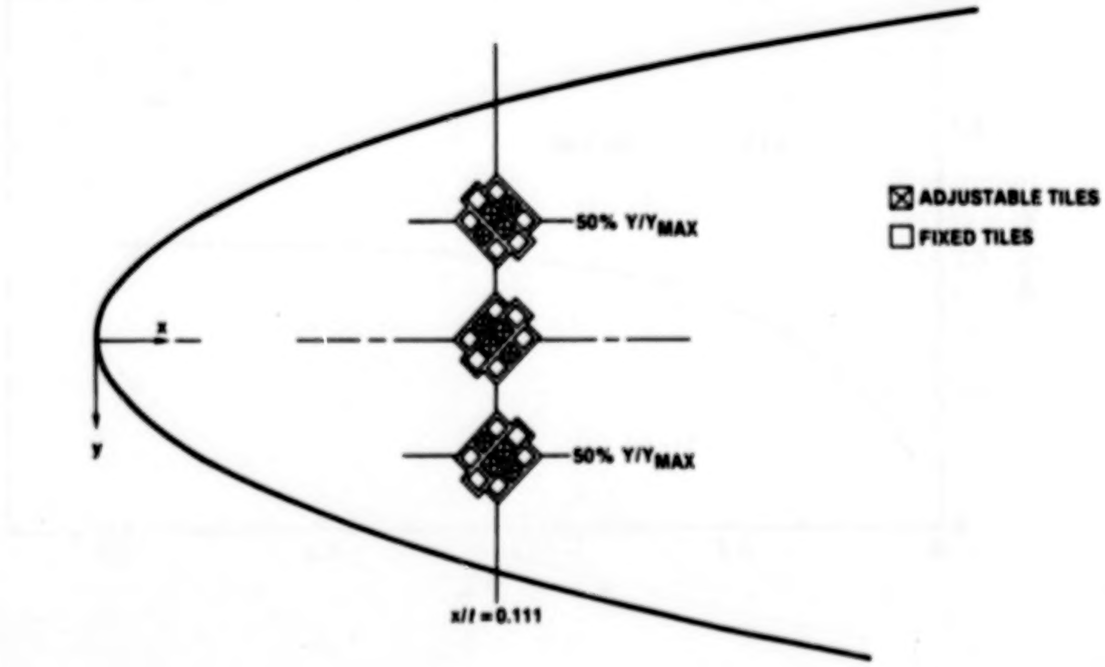
☒ ADJUSTABLE TILES
☐ FIXED TILES
50% Y/Y$_{MAX}$
50% Y/Y$_{MAX}$
x
y
x/l = 0.111

Figure 6.- Tile cluster layout.

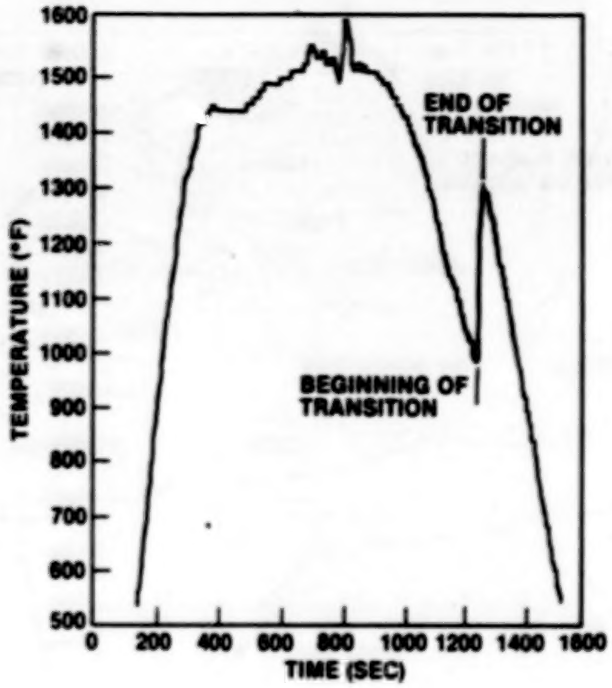

Figure 7.- STS-2 surface temperature history (X/L = 0.30; Y/L = 0.04).

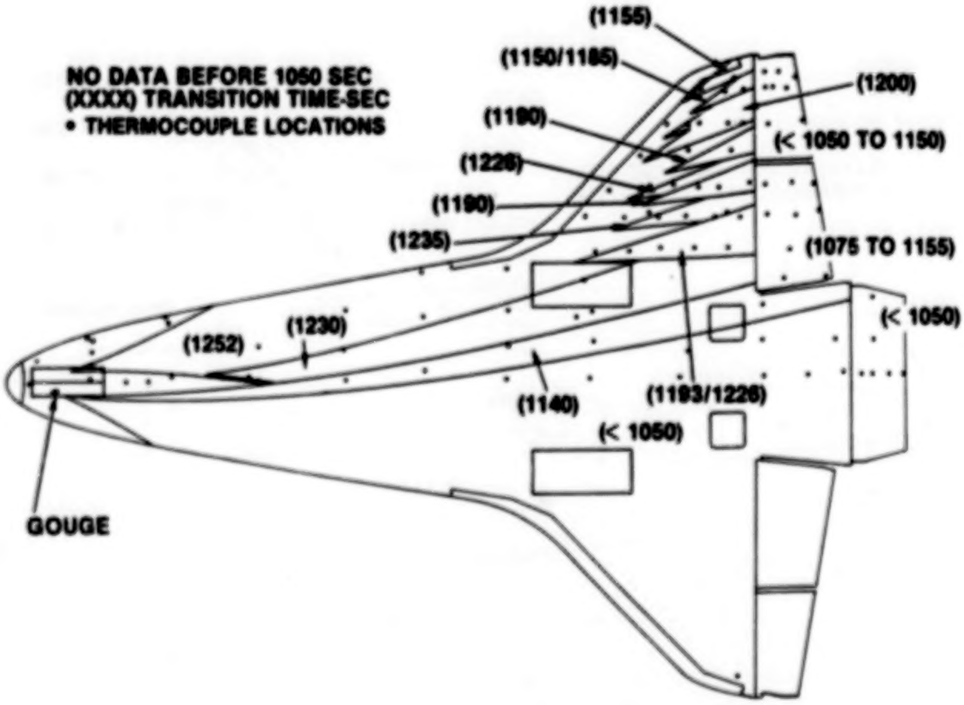
NO DATA BEFORE 1050 SEC
(XXXX) TRANSITION TIME-SEC
• THERMOCOUPLE LOCATIONS
(1155)
(1150/1185)
(1200)
(1190)
(< 1050 TO 1150)
(1226)
(1190)
(1235)
(1075 TO 1155)
(< 1050)
(1252)
(1230)
(1140)
(1193/1226)
(< 1050)
GOUGE

Figure 8.- STS-1 transition map.

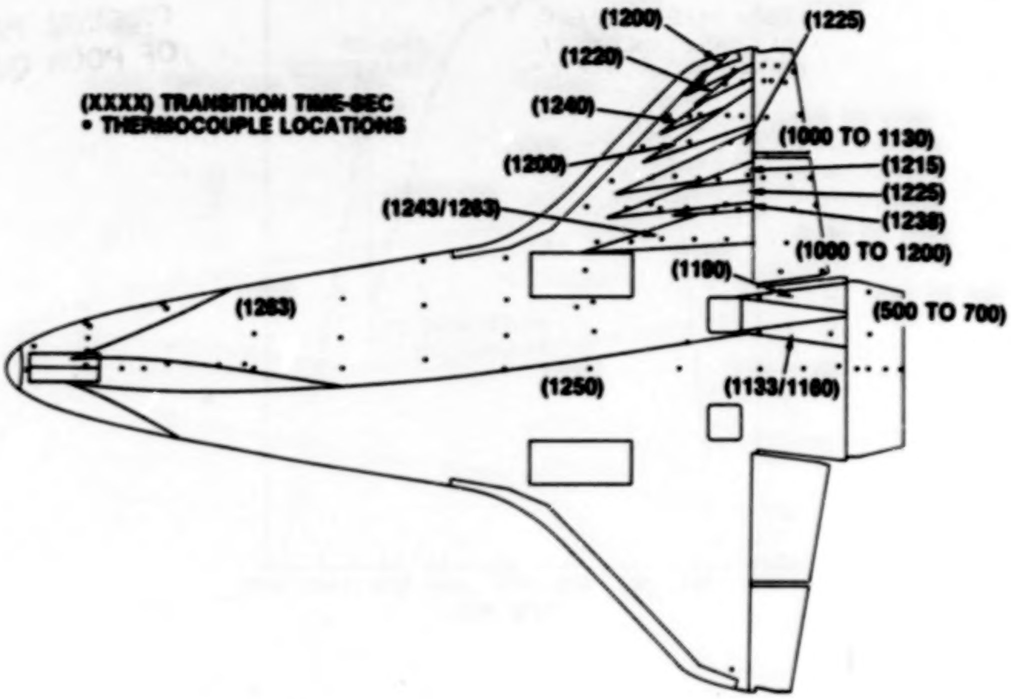
(XXXX) TRANSITION TIME-SEC
• THERMOCOUPLE LOCATIONS
(1200)
(1225)
(1220)
(1240)
(1000 TO 1130)
(1200)
(1215)
(1225)
(1243/1263)
(1238)
(1000 TO 1200)
(1190)
(1263)
(500 TO 700)
(1250)
(1133/1160)

Figure 9.- STS-2 transition map.

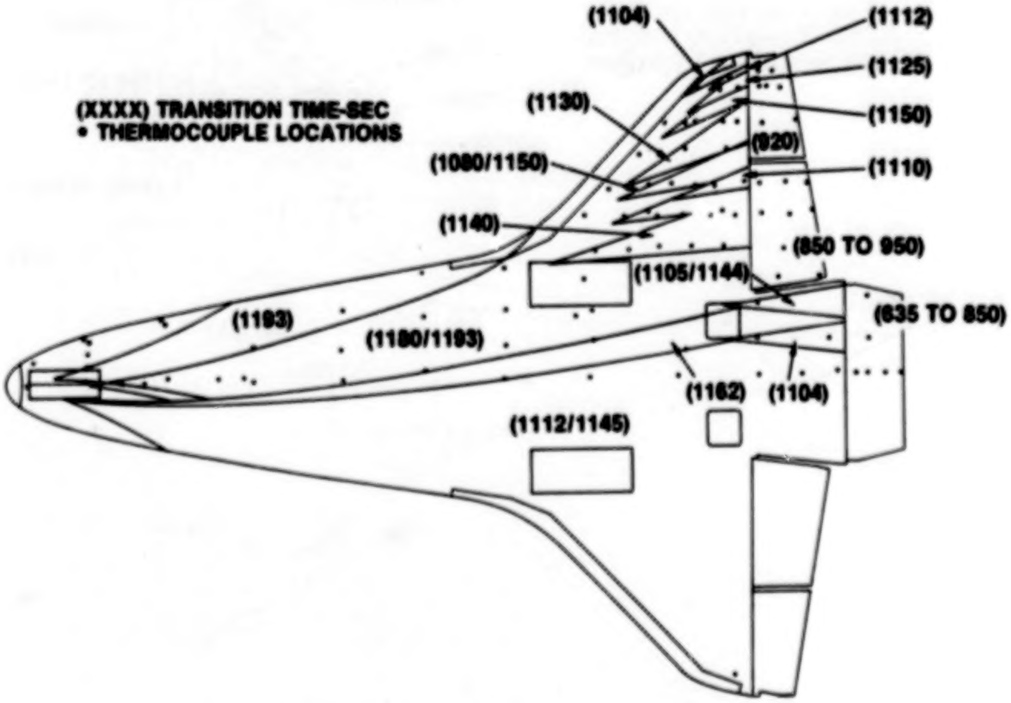
(1104)
(1112)
(1125)
(XXXX) TRANSITION TIME-SEC
• THERMOCOUPLE LOCATIONS
(1130)
(1150)
(920)
(1080/1150)
(1110)
(1140)
(850 TO 950)
(1105/1144)
(1193)
(635 TO 850)
(1180/1193)
(1162)
(1104)
(1112/1145)

Figure 10.- STS-3 transition map.

ORIGINAL PAGE IS
OF POOR QUALITY

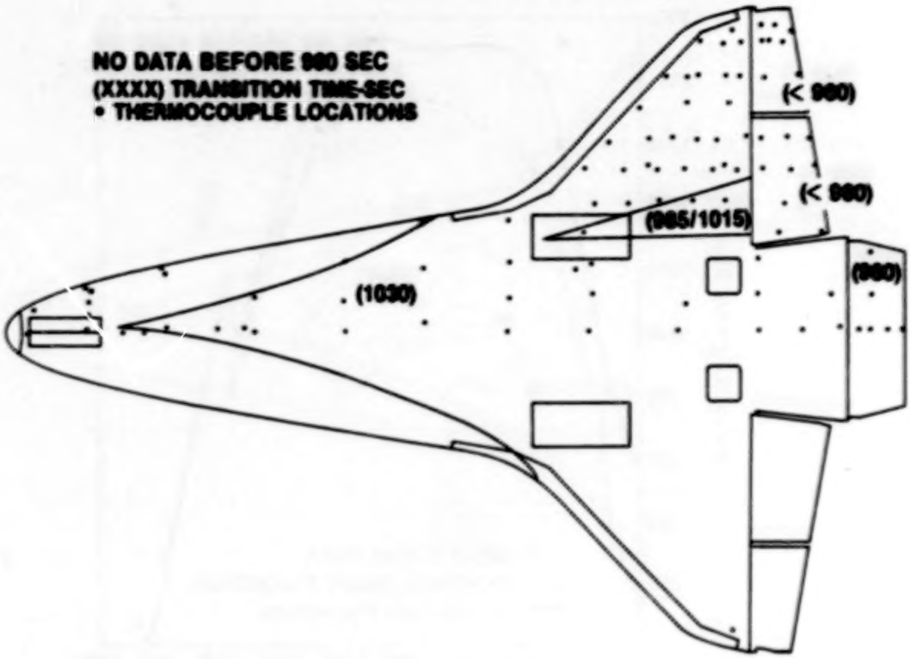
NO DATA BEFORE 980 SEC
(XXXX) TRANSITION TIME-SEC
• THERMOCOUPLE LOCATIONS
(< 980)
(< 980)
(985/1015)
(980)
(1030)

Figure 11.- STS-4 transition map.

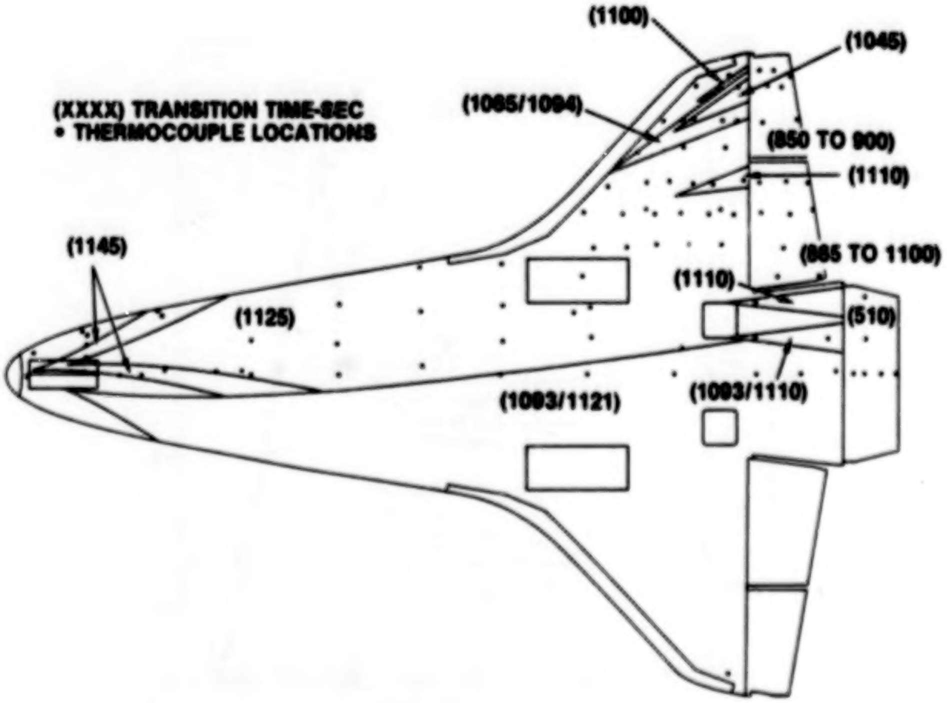
(XXXX) TRANSITION TIME-SEC
• THERMOCOUPLE LOCATIONS
(1100)
(1045)
(1085/1094)
(850 TO 900)
(1110)
(1145)
(865 TO 1100)
(1110)
(1125)
(510)
(1093/1121)
(1093/1110)

Figure 12.- STS-5 transition map.

ORIGINAL PAGE IS
OF POOR QUALITY

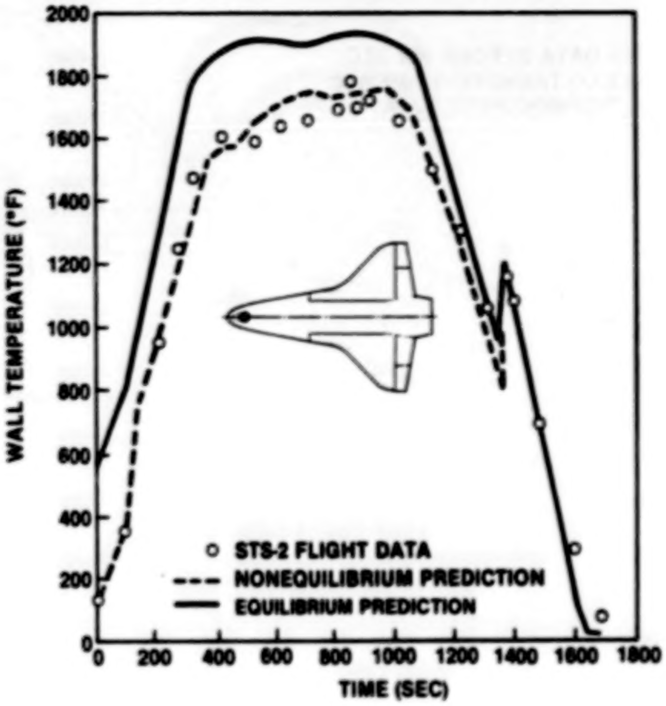

Figure 13.- STS-2 temperature history on fuselage lower-surface centerline at X/L = 0.1.

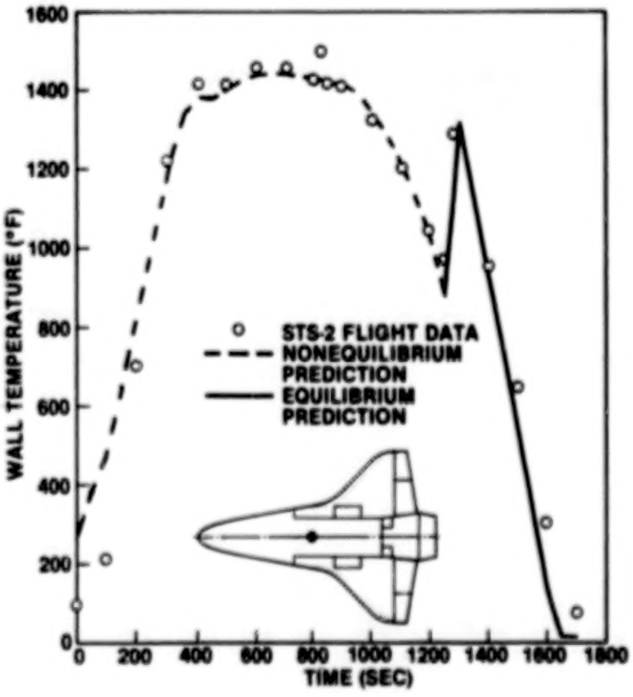

Figure 14.- STS-2 temperature history on fuselage lower-surface centerline at X.L = 0.5.

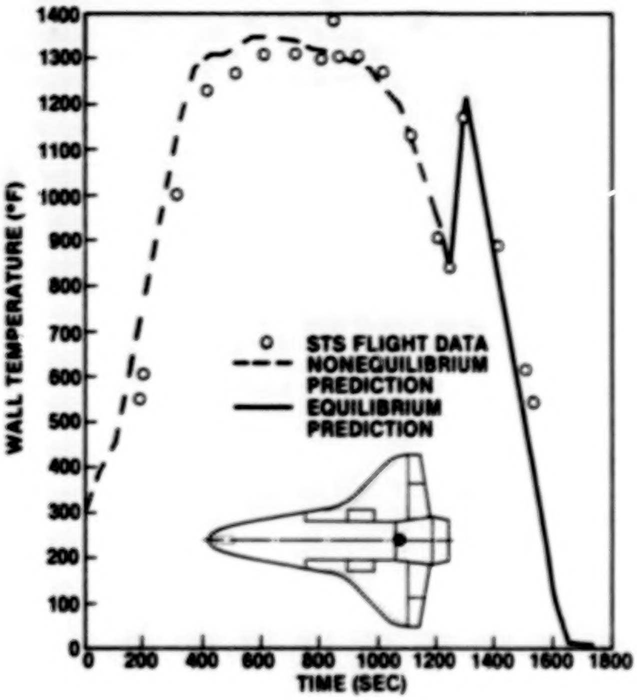

Figure 15.- STS-2 temperature history on fuselage lower-surface centerline at X/L - 0.9.

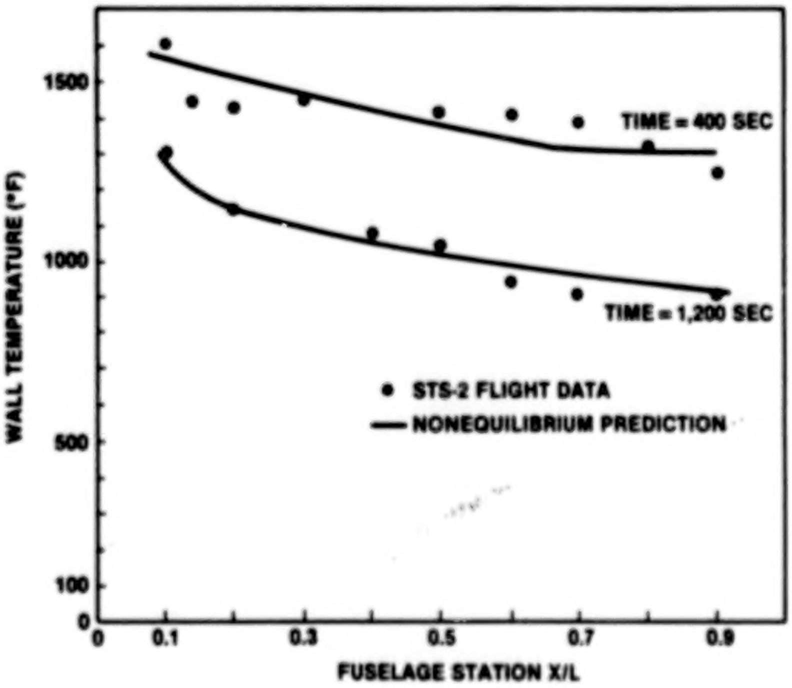

Figure 16.- Temperature distribution on fuselage lower-surface centerline 400 and 1,200 seconds after entry interface.

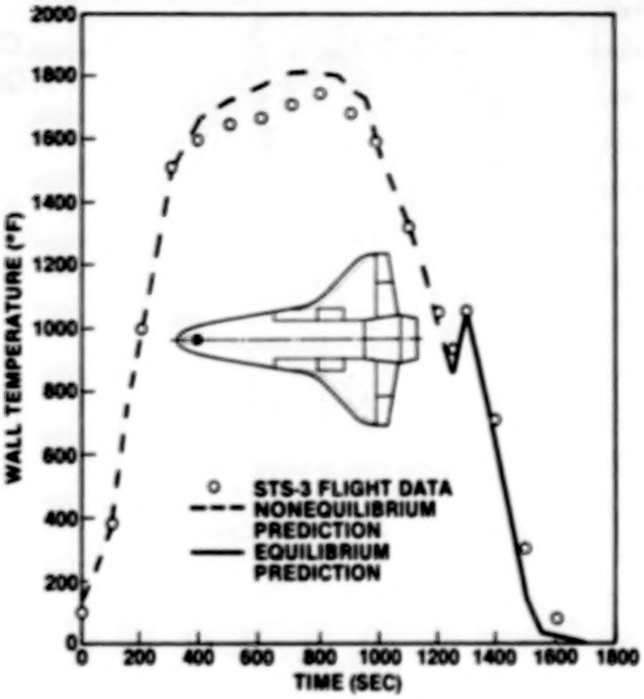

Figure 17.- STS-3 temperature history on fuselage lower-surface centerline at X/L = 0.1.

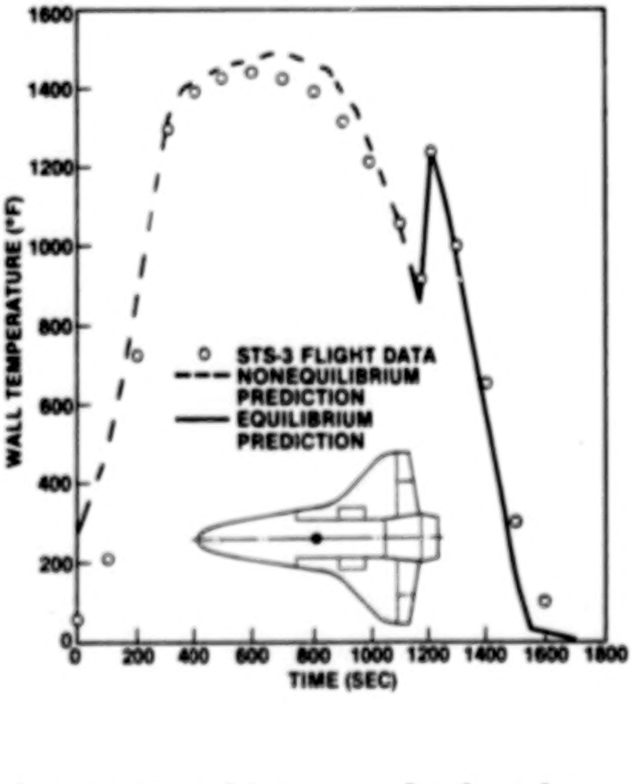

Figure 18.- STS-3 temperature history on fuselage lower-surface centerline at X/L = 0.5.

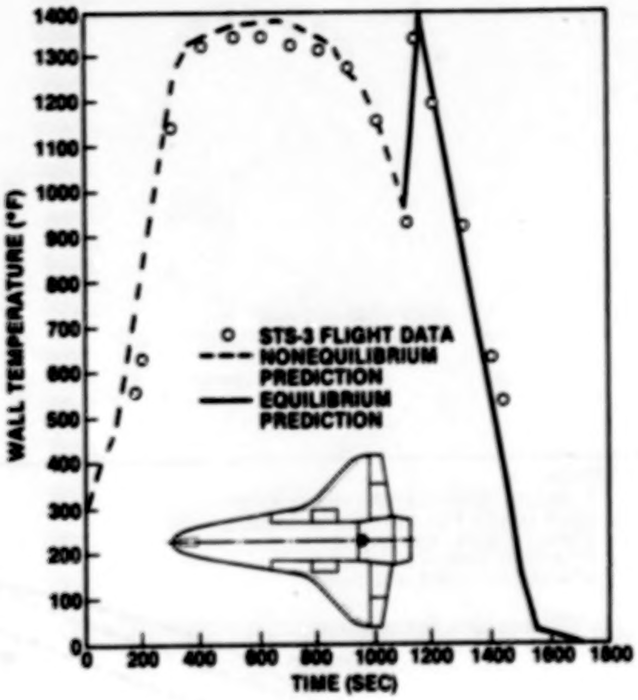

Figure 19.- STS-3 temperature history on fuselage lower-surface centerline at X/L = 0.9.

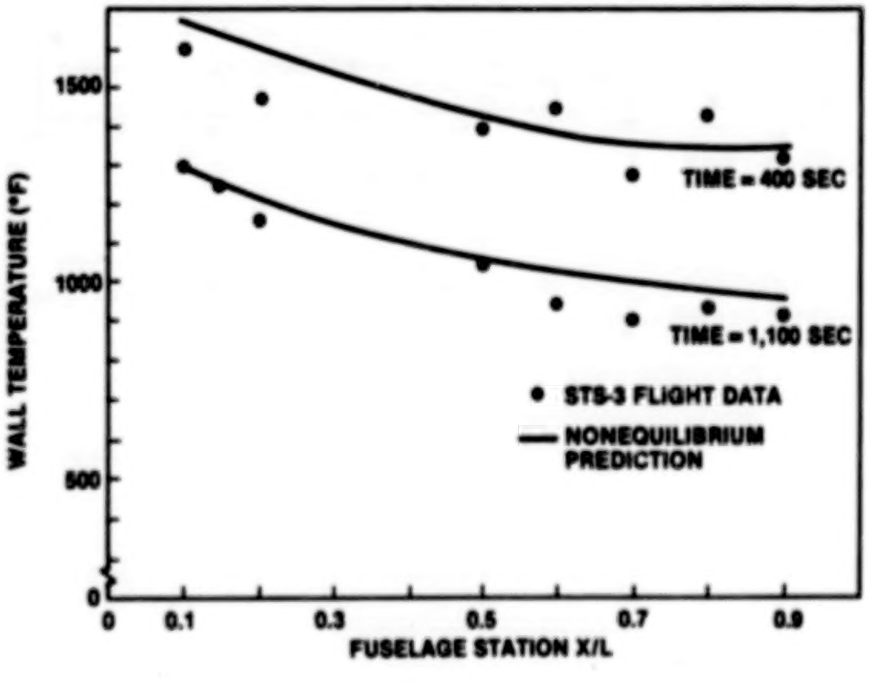

Figure 20.- Temperature distribution on fuselage lower-surface centerline 400 and 1,200 seconds after entry interface.

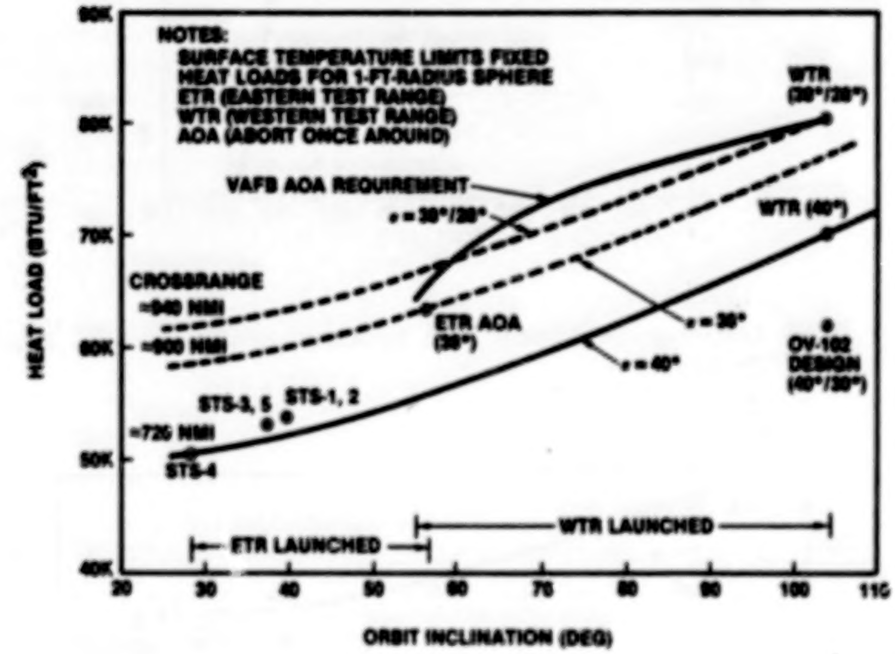

Figure 21.- Stagnation-point heat-load variation with orbit inclination and crossrange.

N84
10151

UNCLAS

N84 10151 D7

VISCOUS SHOCK-LAYER PREDICTIONS OF THREE-DIMENSIONAL NONEQUILIBRIUM FLOWS PAST THE SPACE SHUTTLE AT HIGH ANGLE OF ATTACK

M. D. Kim, S. Swaminathan, and Clark H. Lewis
Aerospace and Ocean Engineering Department
Virginia Polytechnic Institute and State University
Blacksburg, Virginia

SUMMARY

Computational solutions have been obtained for chemically reacting flowfields over the entire windward surface of the Space Shuttle at high angle-of-attack. The recently developed computational method for the Space Shuttle is capable of treating three-dimensional viscous nonequilibrium air flow as well as equilibrium air and perfect gas flows. A general nonorthogonal computational grid system is used to treat the nonaxisymmetric geometry. Boundary conditions take into account noncatalytic wall, equilibrium catalytic wall, and shock and wall slip conditions. The nonequilibrium solutions with noncatalytic wall condition are compared to the fully catalytic wall solutions, the equilibrium air solutions, the perfect gas solutions, and also the Shuttle flight heating and pressure data. The comparisons show good agreements and correlations in most cases.

INTRODUCTION

Recently the nonequilibrium effect on the Shuttle reentry flowfield has been widely investigated to reduce the surface heating by employing a proper surface material. The purpose of the present paper is to accurately predict the three-dimensional nonequilibrium flowfield over the entire Shuttle windward surface and compare the result with the flight data of heating rate and pressure. For a few typical reentry flight conditions, the nonequilibrium solutions were obtained for both noncatalytic and fully catalytic wall conditions, and compared with the corresponding equilibrium and perfect gas solutions. The present numerical scheme was also extended to include the capability to treat the nonequilibrium wall and shock slip conditions.

The present numerical method (SHTNEQ) has been developed based on the two-dimensional nonequilibrium flowfield code by Miner and Lewis (ref. 1) and the three-dimensional perfect gas code by Szema and Lewis (ref. 2). The complete governing equations and the description of the present method are given by Kim, Swaminathan and Lewis (ref. 3). The SHTNEQ method uses a general nonorthogonal computational grid system to treat the nonaxisymmetric Shuttle geometry. Since the three-dimensional viscous shock-layer equations are parabolic in both the streamwise and crossflow directions, the equations are solved by a highly efficient finite-difference scheme developed by Murray and Lewis (ref. 4), which requires much less computing time than PNS or time-dependent methods. The present method can solve both subsonic and supersonic flows and requires the shock shape as initial input data. The shock shapes for the present Shuttle calculations were provided by the inviscid HALIS method of Weilmuenster and Hamilton (ref. 5).

In the later sections, a description of the governing equations and boundary conditions is given, and the thermodynamic properties and chemical reaction model used in the present calculations are also described. It is known that the nonequilibrium real gas effects persist through a wide range of the Shuttle reentry trajectory (altitudes of 122 to 50 km). In the present work, three points along the trajectory of the second Space Shuttle flight (STS-2) are chosen, and the numerical solutions are obtained over the entire windward surface of the body. These freestream conditions are the same as used in ref. 3, and the present paper is an extension of the previous paper by including more calculations with comparisons to additional flight data and also the wall and shock slip effects. The computational results of the surface heating rate and pressure predictions are compared with the STS-2 flight data. The variations of some shock-layer profiles along the body are also presented.

SYMBOLS

C_p	specific heat at constant pressure
FULCAT	nonequilibrium solution with fully catalytic wall
$\underset{\sim}{g}_1$	vector in streamwise (ξ_1) direction
$\underset{\sim}{g}_2$	vector in normal (ξ_2) direction
$\underset{\sim}{g}_3$	vector in circumferential (ξ_3) direction
L	Shuttle body total length, 32.84 m
M_∞	freestream Mach number
NONCAT	nonequilibrium solution with noncatalytic wall
NONEQL	nonequilibrium flow calculation
NSH	shock-layer thickness nondimensionalized by R_n
p	pressure, $p^*/(\rho_\infty U_\infty^2)$
PG	perfect gas solution
PHI	same as ϕ in cylindrical coordinates
PW/PINF	same as p_w/p_∞
QW	surface heating rate due to conduction and diffusion (MW/m^2)
Re_∞	freestream unit Reynolds number, m^{-1}
R_n	dimensional Shuttle nose radius, 62.23 cm (24.5 inches)

SHTNEQ	Shuttle nonequilibrium, the present numerical method
STS	space transportation system
S/RN	surface distance along body nondimensionalized by R_n
T	temperature, T^*/T_{ref}
T_{ref}	dimensional reference temperature, $U_\infty^2/C_{p\infty}$
t	Shuttle entry time from 122 km altitude
U_∞	dimensional freestream velocity
u,v,w	streamwise, normal and circumferential velocity tensor components nondimensionalized by U_∞
U/UINF	streamwise velocity, u^*/U_∞
$\dot{w}_i$	species production term
Y/RN	body-normal distance nondimensionalized by R_n
z,r,ϕ	reference cylindrical coordinates
Z/L	axial distance along body, same as z/L
α	angle of attack, degree
ε	Reynolds number parameter, $[\mu_{ref}/(\rho_\infty U_\infty R_n)]^{1/2}$
μ	viscosity, μ^*/μ_{ref}
μ_{ref}	reference viscosity evaluated at T_{ref}
ξ_1,ξ_2,ξ_3	computational coordinates
ρ	density, ρ^*/ρ_∞

Superscript

*	dimensional quantity

Subscript

i	species i
w	wall value
∞	dimensional freestream value

ANALYSIS

Governing Equations

The governing equations are derived from the steady Navier-Stokes equations for a reacting gas mixture as given by Bird et al. (ref. 6), and they are written in a surface-oriented general nonorthogonal coordinate system (see fig. 1). The ξ_1 coordinate consists of straight lines in the surface-normal direction. At the body surface, the ξ_3 coordinate is chosen to coincide with the ϕ coordinate of the reference cylindrical coordinate system. The coordinate system requires orthogonality only at the body surface. The normal velocity v and normal coordinate ξ_2 are assumed to be the order of ε, and all terms which are of higher order than ε are neglected i the governing equations. The local physical velocity vector is defined as

$$\underline{V} = u\underline{g}_1 + v\underline{g}_2 + w\underline{g}_3$$

where the u, v and w are tensor velocity components in the computational coordinate system. Only laminar flow is considered in the present analysis. The derived nondimensional form of the three-dimensional viscous shock-layer equations for a reacting gas mixture is given in ref. 3.

Boundary Conditions

At the body surface, the slip and temperature-jump boundary conditions can be used if necessary. The nonequilibrium wall slip equations given by Hendricks (ref. 7) have been rewritten for the present coordinate system and chemical model. The calculated Reynolds number parameter ε was less than 0.108 for the present test cases which indicates that the slip effects on the heating rate and surface pressure will be small (see e.g. ref 8), but the slip effects on some shock-layer profiles over the nose region are calculated and presented. The wall temperature is specified by the STS-2 flight thermocouple data. In the present calculations, the wall species concentration is dictated by the noncatalytic or fully catalytic condition, but the boundary condition can easily be extended to include the effects of finite wall catalycity on the recombination of dissociated air. At the low surface temperature of Shuttle, the equilibrium catalytic wall condition can be replaced by the fully catalytic wall condition.

In the present method, shock shape information is necessary as an input which is used for the calculation of the shock-boundary condition. The three-dimensional shock-boundary conditions with slip effects (modified Rankine-Hugoniot jump relations) given by Murray and Lewis (ref. 4) have been extended to include finite-rate chemistry and the nonorthogonal coordinate system. Two-dimensional shock-normal coordinates are defined in the plane which contains both the freestream velocity vector and the vector which is normal to the local shock surface. Then, the freestream velocity vector is written in the shock-normal coordinates, and two-dimensional shock-crossing conditions are calculated in the shock-normal coordinates. The known after-shock quantities are rotated into the three-dimensional computational coordinates.

Thermodynamic and Transport Properties

Multi-component ionizing air is considered to be a mixture of thermally perfect gases, and the thermodynamic and transport properties for each species are calculated using the local temperature. The properties for the gas mixture are then determined in terms of the individual species properties. The enthalpy and specific heat of each species are obtained from the thermodynamic data tabulated by Browne (refs. 9-11). A second-order Lagrangian method is used to interpolate the values at a given temperature. The viscosity of the individual species is calculated from the curve fit relation given by Blottner (ref. 12), and the thermal conductivity of each species is calculated from the Eucken semi-empirical formula using the species viscosity and specific heat. After the viscosity and thermal conductivity of the individual species are calculated, the viscosity and thermal conductivity of the gas mixture are calculated by the method suggested by Armaly and Sutton (refs. 13, 14). In the present work, the diffusion model is limited to binary diffusion with the binary diffusion coefficient specified by the Lewis number of 1.4.

Chemical Reaction Model

It is assumed that the chemical reactions proceed at a finite rate, and the rate of production terms $\dot{w}_i$ of the individual species are included in the energy equation and the species continuity equations. The $\dot{w}_i$ terms are functions of both the temperature and the species concentrations, and they must be rewritten so that the temperature or the species concentrations appear as one of the unknowns as given in ref. 1. In the present calculations, the chemical reaction model and the reaction-rate constants are taken from Blottner (ref. 15). Seven (7) chemical species are considered in the reactions; viz., O, O_2, NO, N, NO^+, N_2, and e^-. The following pure air chemical reactions are used for the present study:

1. $O_2 + M1 \rightleftarrows 2O + M1$
2. $N_2 + M2 \rightleftarrows 2N + M2$
3. $N_2 + N \rightleftarrows 2N + N$
4. $NO + M3 \rightleftarrows N + O + M3$
5. $NO + O \rightleftarrows O_2 + N$
6. $N_2 + O \rightleftarrows NO + N$
7. $N + O \rightleftarrows NO^+ + e^-$

where M1, M2 and M3 are the catalytic third bodies (ref. 15). Since the rate of production terms are for nonequilibrium flows, the present method encounters difficulty in obtaining a converged solution whenever the flow conditions approach equilibrium. The difficulty is severe, particularly at the stagnation point.

Numerical Solution

Davis (ref. 8) presented an implicit finite-difference method to solve the viscous shock-layer equations for axially symmetric flows, and Murray and Lewis (ref. 4) further developed the scheme for three-dimensional flows. In the present work, the method is extended to the chemically reacting three-dimensional flowfield solution in a surface-oriented nonorthogonal coordinate system. Since the viscous shock-layer equations are parabolic in both the streamwise and crossflow directions, the equations are solved by a highly efficient finite-difference scheme. The continuity and normal momentum equations are solved in a coupled form to promote convergence. The shock stand-off distance is evaluated by integrating the continuity equation.

The solution begins on the spherically blunted nose by obtaining an axisymmetric solution in the wind-fixed coordinate system. The axisymmetric solution is rotated into the body-fixed coordinates and is used as the initial profile for the three-dimensional solution. The three-dimensional solution begins in the windward plane and marches around the body obtaining a converged solution at each ξ_3-step. After completing a sweep at a ξ_1-marching station, the procedure then steps downstream in ξ_1 and begins the next ξ_3-sweep. At each point the equations are solved in the following order: (i) species continuity, (ii) ξ_3-momentum, (iii) energy, (iv) ξ_1-momentum, (v) integration of continuity for shock-layer thickness, and (vi) coupled continuity and normal momentum equations.

RESULTS AND DISCUSSION

In order to predict the Shuttle reentry flowfield, three test cases were chosen and the viscous windward flowfield solutions were obtained using various chemical models. For the wide range of the Shuttle reentry conditions (above 50 km altitude) the nonequilibrium effects can occur, and the nonequilibrium effects are largest near the nose of the body and around t = 450 sec on the trajectory (ref. 16). The altitudes selected for the present calculations are 81, 70 and 60 km (t = 250, 460, 630 sec, respectively). Detailed freestream conditions for the three test cases are given in table I. The inviscid input shock shapes for the present calculations have been provided by the HALIS method for an angle-of-attack of 40 deg for both perfect gas and equilibrium air. The inviscid HALIS shock was available only up to z/L = 0.5 or less. The viscous flowfield solutions for perfect gas and equilibrium air have been obtained up to z/L = 0.5 in order to compare with the nonequilibrium solutions. The nonequilibrium solutions, however, were obtained for the entire windward surface up to the body end using an extended shock. The shock extension was done using the STEIN (ref. 17) solution of the shock shape for an angle-of-attack of 25 deg. The extended shock was scaled and smoothed before being used as input data. In order to enhance the accuracy of the nonequilibrium viscous solution, a global iteration has been performed using the viscous output shock as an input.

The nonequilibrium solutions have been obtained for both noncatalytic and fully catalytic wall conditions for the purpose of comparison. The cross-sections of the modified Shuttle orbiter which have been used for the inviscid and viscous solutions are depicted in fig. 2. Presented results include the surface heating rate, surface pressure, shock shapes, a few shock-layer profiles, and finally slip effects over the nose region. The flight heating-rate data obtained from the method by Throckmorton (ref. 18) are used for comparison with the computational results. The flight measurement data of pressure are used for comparison with the present surface-pressure predictions.

Surface Heating Rate

The heating-rate predictions along the windward centerline are compared with each other in fig. 3 for Case 1. The nonequilibrium solution with noncatalytic wall condition agrees well with the flight data for most of the region. The nonequilibrium solution with fully catalytic wall condition shows quite close agreement with the equilibrium air solution. The heating-rate prediction from the perfect gas model is below the equilibrium air solution but well above the noncatalytic wall solution for the entire body. The reason for the local mismatch around z/L = 0.2 is not currently known. At z/L = 0.4, the perfect gas solution is 20% lower than the equilibrium solution and 50% higher than the noncatalytic wall solution. In fact, the surface finite catalytic effect for Case 1 is negligible compared to that for Cases 2 and 3, due to the altitude dependence of the surface catalytic activity (ref. 19). The decrease of the heating after z/L = 0.8 is due to the slope change of the body surface.

For Cases 2 and 3, the general trends of the computed heating rates are similar to the result of Case 1, but the noncatalytic wall solution underpredicts compared to the flight data especially on the nose region and the body-end region as shown in figs. 4 and 5. The discrepancy over those regions may be due to the surface catalytic effect as recently discussed by other investigators (refs. 16, 19 and 20). In fig. 6, the nonequilibrium solution with noncatalytic wall condition along the body is shown for various ϕ-planes, together with the corresponding equilibrium air solution for Case 2. The equilibrium air solution is much higher than the noncatalytic wall solution for all the ϕ-planes. In fig. 6, the surface heating distributions along the body for all the ϕ-planes are shown. The sudden increase of the heating rate at $\phi = 80$ deg and $z/L = 0.5$ is due to the spanwise slope change of the body surface along the body (see fig. 2). At $z/L = 0.6$ and $\phi = 90$ deg, the solution did not converge, due to the severe surface slope change of the wing tip section. The calculated windward spanwise heating rates at two axial stations ($z/L = 0.2$ and $z/L = 0.44$) for Case 2 are shown in fig. 7. The comparisons among the various chemical models show similar trends and correlations for the spanwise heating rate distributions due to the flow expansion around the body. The flight data were available only at the windward centerline ($\phi = 0$ deg), and the data agree well with the noncatalytic wall solution.

Surface Pressure Comparison

In fig. 8 the surface-pressure distribution over the entire Shuttle windward surface is presented together with the available flight data for comparison. The ϕ-planes from 10 deg to 40 deg were omitted on the plot because the results for those planes were almost identical with the result for the windward centerline. The agreement with flight data is good especially on the windward centerline for Cases 2 and 3. In fig. 9 the spanwise surface pressure distributions are shown at two axial stations ($z/L = 0.1$ and $z/L = 0.2$). The present calculation tends to underpredict over the flow expansion region (off the centerline) compared to the flight data (e.g. about 20% underprediction at $\phi = 67$ deg, $z/L = 0.1$). This disagreement may be due to the uncertainty of the flight data. A computation using a smaller ϕ-stepsize may also reduce the discrepancy. The present solution by the SHTNEQ method used ϕ-stepsize of 10 deg around the body, and this stepsize may not be small enough for the noncircular cross section of the Shuttle geometry (see fig. 2). If more ϕ-planes than the present 10 planes were included in the computation, the current relatively large storage requirement and computing time would increase accordingly.

Shock-Layer Thickness

A comparison of the shock-layer thickness distributions along the body at the $\phi = 0$ plane which has been obtained from various chemical models is shown in fig. 10. All the viscous shock shape results except the inviscid shock are from the once globally iterated results. When an inviscid input shock is not very accurate, the output shock shape is, in general, different from the input shock. In such a case, a global iteration is necessary in order to refine the entire flowfield solution. Thus, for the present three test cases, all the presented viscous flowfield solutions are from the first global iteration. The inviscid shock is from the HALIS code and was available only up to $z/L = 0.5$ as mentioned earlier. The inviscid HALIS shock for $\alpha = 40$ deg has been extended by the inviscid shock of $\alpha = 25$ deg from the STEIN method. The extended shock was scaled and smoothed, and then used as the input shock data for the initial calculation (zeroth iteration). When the various viscous shock-layer thicknesses are compared to the inviscid perfect gas shock at $z/L = 0.4$, the viscous perfect gas shock is 86.7%, the nonequilibrium shock is 52.8% and the equilibrium shock is 36.1%. The shock from the fully catalytic wall condition is almost identical to the noncatalytic wall solution.

Comparison of Shock-Layer Profiles

The nonequilibrium flowfield structure of the viscous shock-layer at a few selected axial stations on the windward centerline is depicted for both the noncatalytic and fully catalytic wall conditions in figs. 11-14. The profiles include temperature, tangential velocity and mass fractions of oxygen and nitrogen atoms for Case 2 (t = 460 sec). The temperature and velocity profiles in figs. 11 and 12 show that the viscous effects are dominant across the entire shock-layer, especially on the forward part of the body. At the axial station of $z/L = 0.046$ in the plot of temperature profile, the wall temperature gradient of the fully catalytic wall solution is larger than that of the noncatalytic wall solution, which produced a 34% larger conduction heating rate. At the same station the heating rate due to the mass diffusion was 93% of the conduction heating rate in the fully catalytic wall solution. The diffusive heating in the noncatalytic wall case was, of course, negligib The surface chemical catalycity has negligible effect on the velocity profile as shown in fig. 12. The mass-fraction profiles of oxygen and nitrogen clearly show the effects of the noncatalytic and fully catalytic wall conditions. In the noncatalytic wall case, the oxygen atom concentration at the wall remains almost constant along the body, while the nitrogen atom concentration is reduced downstream due to more rapid recombination.

Slip Effects

The SHTNEQ method has been further extended to include the shock slip and the wall slip conditions. In high altitude freestream conditions, the conventional frozen shock crossing of Rankine-Hugoniot relations for nonequilibrium flows gives poor prediction of the after-shock quantities. It is known that the slip effects on surface-measurable quantities like heating rate and pressure are significant, especially for reentry bodies with a small nose radius at very high altitude. For the Space Shuttle geometry at the test case freestream conditions, however, the calculated Reynolds number parameter ε was less than 0.108 which indicates that the slip effects on the surface-measurable quantities will not be significant (ref. 8). In fig. 15, the shock-slip effects on the temperature profile and mass fraction of oxygen and nitrogen atoms are shown at the stagnation point. The slip temperature at the shock is less than the no-slip temperature by 1500 K. The shock-slip effect on the oxygen mass-fraction distribution across the shock-layer is limited to the region near the bow shock, but for nitrogen the shock-slip effect is propagated all through the shock-layer. Figure 16 shows the wall-slip effects on the surface temperature and axial flow velocity jumps over the nose region for Case 2. The amount of the temperature jump is about 200 K at the stagnation point, and the slip velocity is 0.0056 times the freestream velocity at S/RN = 0.8.

Computing Times

The computing times required for the flowfield computations of all the test cases are listed in table II. The computing times are based on an IBM 370/3081 general purpose computer. The nonequilibrium computations took about one and a half hours CPU time for solving the entire Shuttle windward surface. When an input shock data is not accurate, generally a global iteration is required, thus consuming more computing time than the tabulated one. The computing times for the perfect gas and equilibrium air are for the solution of the first half of the body (up to $z/L = 0.5$). The solution of the perfect gas or equilibrium air flows took relatively small computing times (less than 20% of nonequilibrium case). The axial marching step-sizes are controlled internally in the code considering the number of local iterations taken. A fixed input of 51 or 101 grid points was used in the surface-normal direction and 10 planes were used around the body for the windward surface (10 deg step-size). The leeward surface of the Space Shuttle was not considered, because a solution cannot be obtained by the present method due to strong flow separation. The storage requirement of the present SHTNEQ code is 852 kilo-bites in the IBM 370/3081 computer.

CONCLUSIONS

In general, the computational results of surface heating rate for the three-dimensional nonequilibrium flowfield over the Space Shuttle compare well with the available flight data. The flight heating rate data are higher than the noncatalytic wall solution especially on the nose region and the body end due to the surface finite catalytic effect. The nonequilibrium solution with fully catalytic wall gives quite close agreement with the equilibrium heating rate prediction. The perfect gas solution of surface heating rate is less than the equilibrium solution but higher than the flight data for the entire region. The calculated pressure distribution also shows good agreement with the flight data. The calculated nonequilibrium shock- and wall-slip effects on the heating rate were negligible for the present test cases. The computing times taken for the nonequilibrium calculation are reasonable considering the large size of the computational grid due to the complex Shuttle geometry and the chemical reactions of seven species. Further work is planned to calculate the effects of finite catalytic wall conditions on the three-dimensional nonequilibrium flowfield.

REFERENCES

1. Miner, E. W. and Lewis, C. H.: "Hypersonic Ionizing Air Viscous Shock-Layer Flows over Nonanalytic Blunt Bodies," NASA CR-2550, May 1975.

2. Szema, K. Y. and Lewis, C. H.: "Three-Dimensional Viscous Shock-Layer Flows over Lifting Bodies at High Angles of Attack," AIAA Paper No. 81-1146, June 1981.

3. Kim, M. D., Swaminathan, S., and Lewis, C. H.: "Three-Dimensional Nonequilibrium Viscous Shock-Layer Flow over the Space Shuttle Orbiter," AIAA Paper No. 83-0487, Jan. 1983.

4. Murray, A. L. and Lewis, C. H.: "Hypersonic Three-Dimensional Viscous Shock-Layer Flow over Blunt Bodies," AIAA Journal, Vol. 16, No. 12, pp. 1279-1286, Dec. 1978.

5. Weilmuenster, K. James and Hamilton, H. Harris, II: "A Method for Computation of Inviscid Three-Dimensional Flow over Blunt Bodies Having Large Embedded Subsonic Regions," AIAA Paper No. 81-1203, June 1981.

6. Bird, R. B., Stewart, W. E. and Lightfoot, E. N.: Transport Phenomena, John Wiley and Sons, Inc., 1960.

7. Hendricks, W. L.: "Slip Conditions with Wall Catalysis and Radiation for Multicomponent Nonequilibrium Gas Flow," NASA TM X-64942, June 1974.

8. Davis, R. T.: "Numerical Solution of the Hypersonic Viscous Shock-Layer Equations," AIAA Journal, May 1970, pp. 843-851.

9. Browne, W. G., "Thermodynamic Properties of Some Atoms and Atomic Ions," MSD Engineering Physics TM2, General Electric Co., Philadelphia, PA, 1962.

10. Browne, W. G.: "Thermodynamic Properties of Some Diatomic and Linear Polyatomic Molecules," MSD Engineering Physics TM3, General Electric Co., Philadelphia, PA, 1962.

11. Browne, W. G.: "Thermodynamic Properties of Some Diatoms and Diatomic Ions at High Temperature," MSD Advanced Aerospace Physics TM8, General Electric Co., Philadelphia, PA, May 1962.

12. Blottner, F. G.: "Non-equilibrium Laminar Boundary-Layer Flow of Ionized Air," General Electric Report R64SD56, November 1964.

13. Armaly, B. F. and Sutton, K.: "Viscosity of Multicomponent Partially Ionized Gas Mixtures Associated with Jovian Entry," Aerothermodynamics and Planetary Entry, Progress in Astronautics and Aeronautics, Vol. 77, edited by A. L. Crosbie, AIAA, New York, 1981, pp. 335-350.

14. Armaly, B. F. and Sutton, K.: "Thermal Conductivity of Partially Ionized Gas Mixtures," Thermophysics of Atmospheric Entry, Progress in Astronautics and Aeronautics, Vol. 82, edited by Thomas E. Horton, AIAA, New York, 1982, pp. 53-67.

15. Blottner, F. G., Johnson, M., and Ellis, M.: "Chemically Reacting Viscous Flow Program for Multi-Component Gas Mixtures," Sandia Laboratories Report SC-RR-70-754, Dec. 1971.

16. Rakich, J. V., Steward, D. A., and Lanfranco, M. J.: "Results of a Flight Experiment on the Catalytic Efficiency of the Space Shuttle Heat Shield," AIAA Paper No. 82-0944, June 1982.

17. Marconi, F. and Yaeger, L.: "Development of a Computer Code for Calculating the Steady Super/Hypersonic Inviscid Flow Around Real Configurations." NASA CR-2675, April 1976.

18. Throckmorton, D. A.: "Benchmark Aerodynamic Heat Transfer Data from the First Flight of the Space Shuttle Orbiter," AIAA Paper No. 82-0003, Jan. 1982.

19. Shinn, J. L., Moss, J. N. and Simmonds, A. L.: "Viscous Shock-Layer Heating Analysis for the Shuttle Windward Plane with Surface Finite Catalytic Recombination Rates," AIAA Paper No. 82-0842, June 1982.

20. Scott, C. D. and Derry, S. M.: "Catalytic Recombination and the Space Shuttle Heating," AIAA Paper No. 82-0841, June 1982.

TABLE I. TEST CASE FREESTREAM CONDITIONS

Case No.	t (sec)	Altitude (km)	α (deg)	M_∞	Re_∞ (m^{-1})	U_∞ (km/s)	T_∞ (K)	p_∞ (atm)
1	250	85.74	41.0	26.6	2726.	7.53	199.	3.587E-06
2	460	74.98	40.0	25.5	15686.	7.20	198.	2.142E-05
3	650	71.29	39.4	23.4	25756.	6.73	205.	3.965E-05

TABLE II. COMPUTING TIMES[a] FOR TEST CASES

Flow Model	Case No.	z/L from - to	Grid Size of ξ_1-steps	ξ_2-pts	ξ_3-planes	CPU Time (H:M:S)
Nonequilibrium Noncatalytic	1	0. - 0.93	127	51	10	1:20:34
	2	0. - 0.93	129	51	10	1:50:28
	3	0. - 0.93	142	51	10	1:51:40
Nonequilibrium Fully Catalytic	1	0. - 0.93	123	51	10	1:23:02
	2	0. - 0.93	124	51	10	1:26:53
	3	0. - 0.93	124	51	10	1:27:22
Perfect Gas	1	0. - 0.50	78	101	10	0:07:07
	2	0. - 0.50	78	101	10	0:07:06
	3	0. - 0.50	78	101	10	0:07:05
Equilibrium	1	0. - 0.453	72	101	10	0:08:32
	2	0. - 0.453	72	101	10	0:08:28
	3	0. - 0.453	72	101	10	0:08:27

[a] CPU time on IBM 370/3081, H=OPT2 compiler

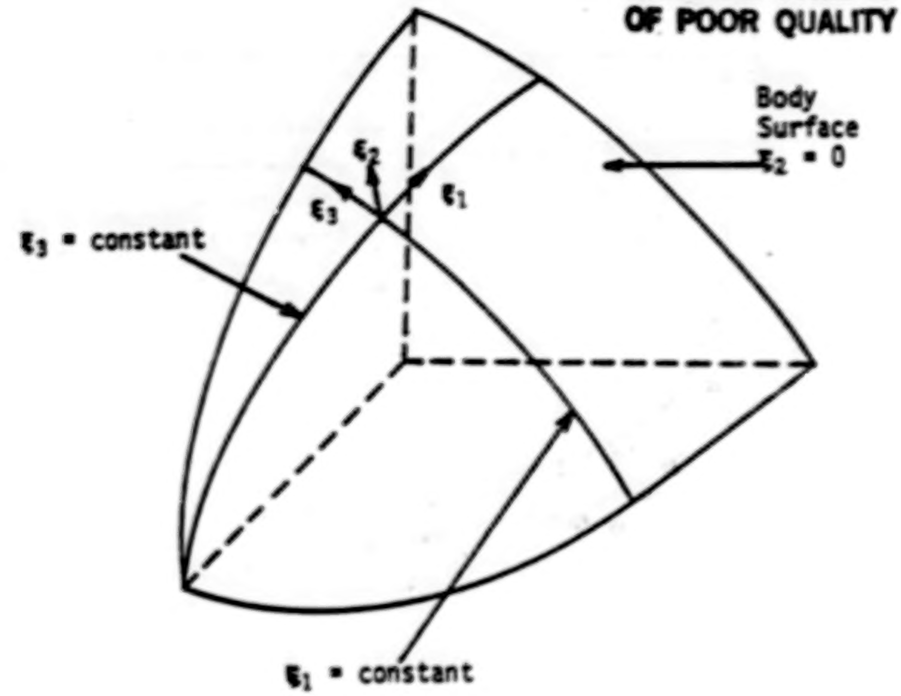
Body
Surface
$\xi_2 = 0$
ξ_2
ξ_1
ξ_3
ξ_3 = constant
ξ_1 = constant

Figure 1.- Body-generator nonorthogonal coordinate system.

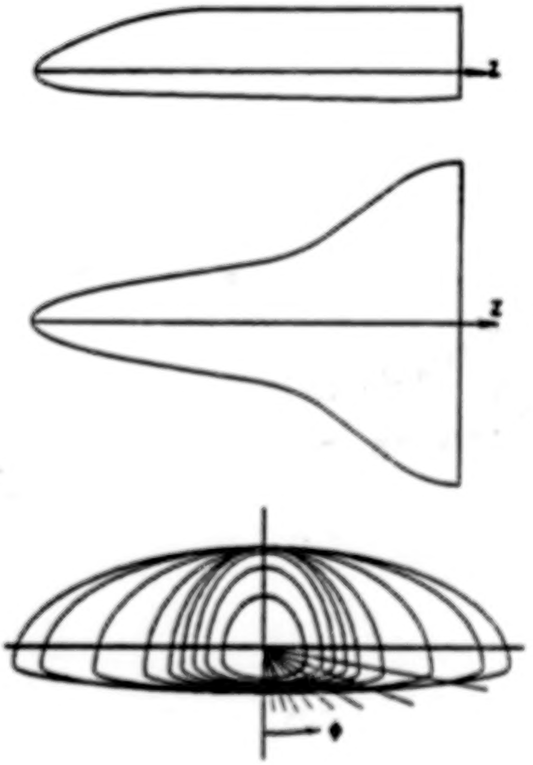

Figure 2.- Cross sections of the modified Shuttle orbiter.

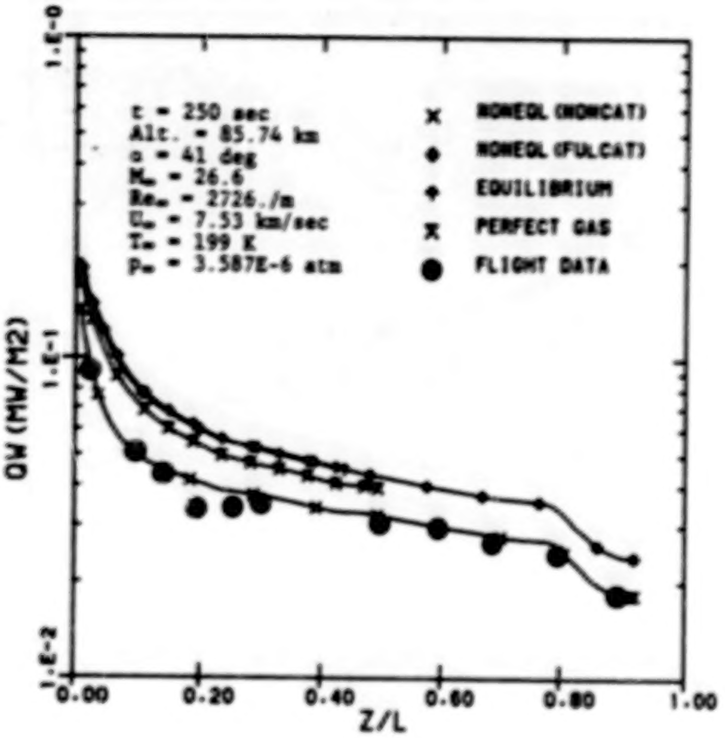

Figure 3.- Comparison of measured and calculated heating rates along the windward centerline of Case 1.

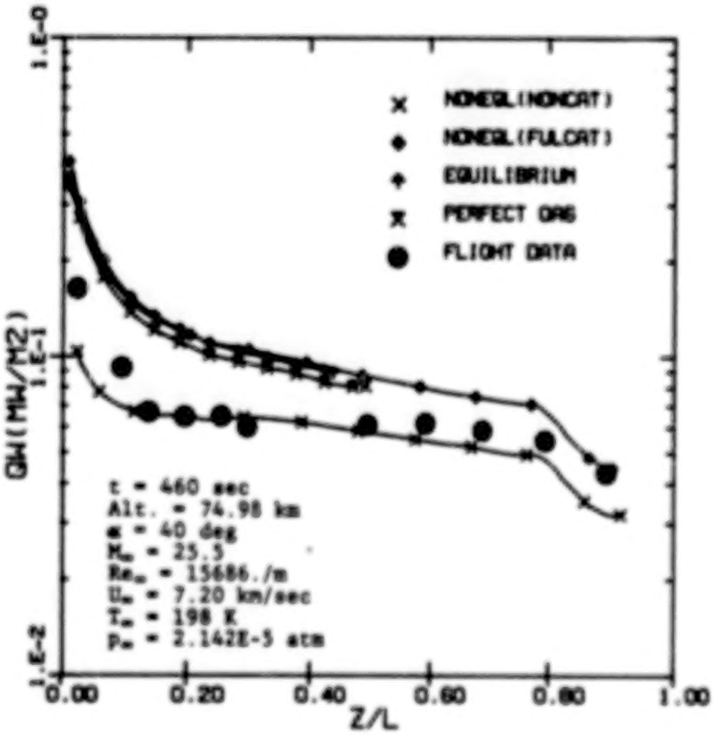

Figure 4.- Comparison of measured and calculated heating rates along the windward centerline of Case 2.

ORIGINAL PAGE IS OF POOR QUALITY

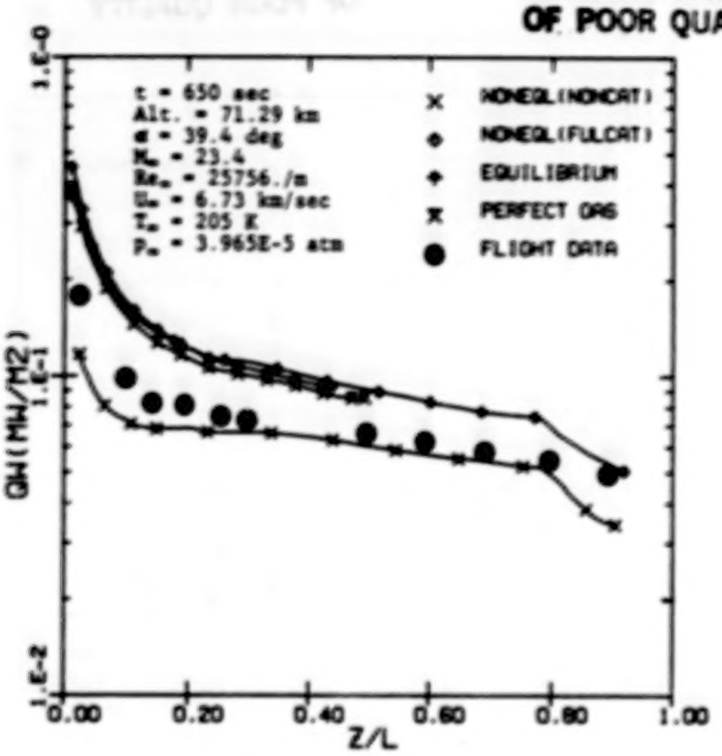

Figure 5.- Comparison of measured and calculated heating rates along the windward centerline of Case 3.

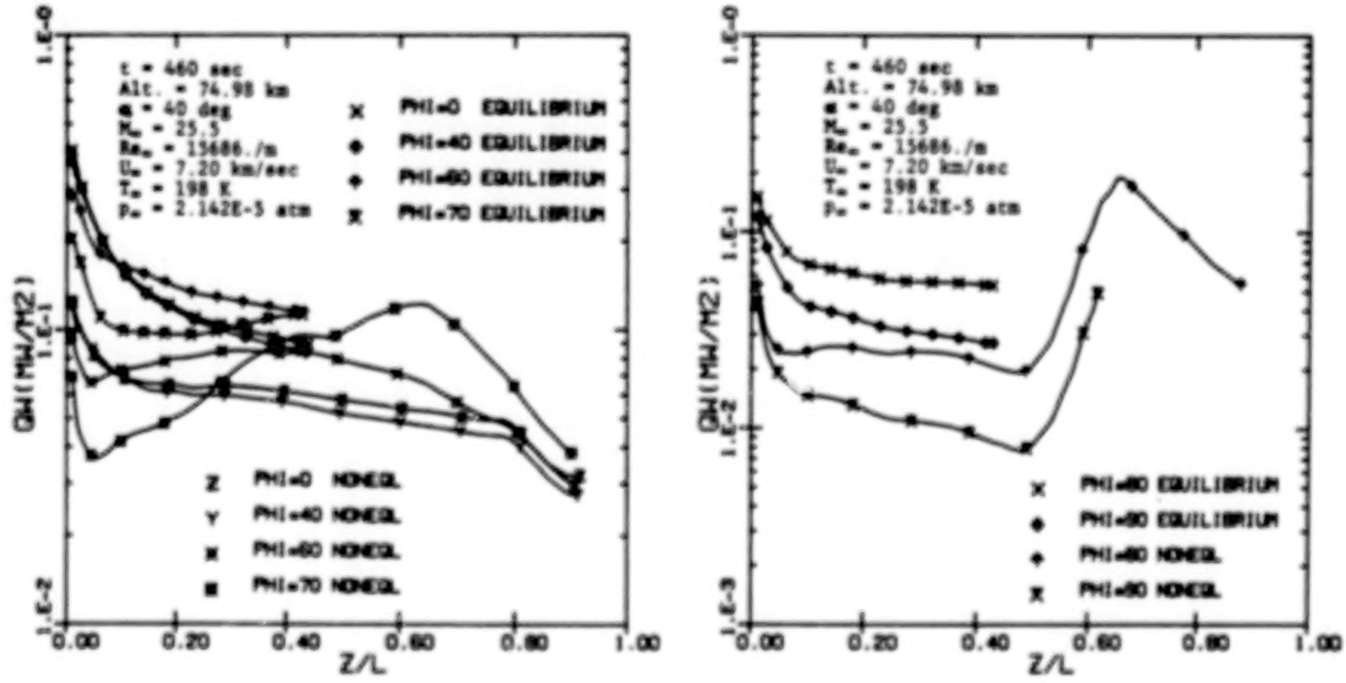

(a) (b)

Figure 6.- Surface heating rate distributions along the body for different ϕ-planes of Case 2.

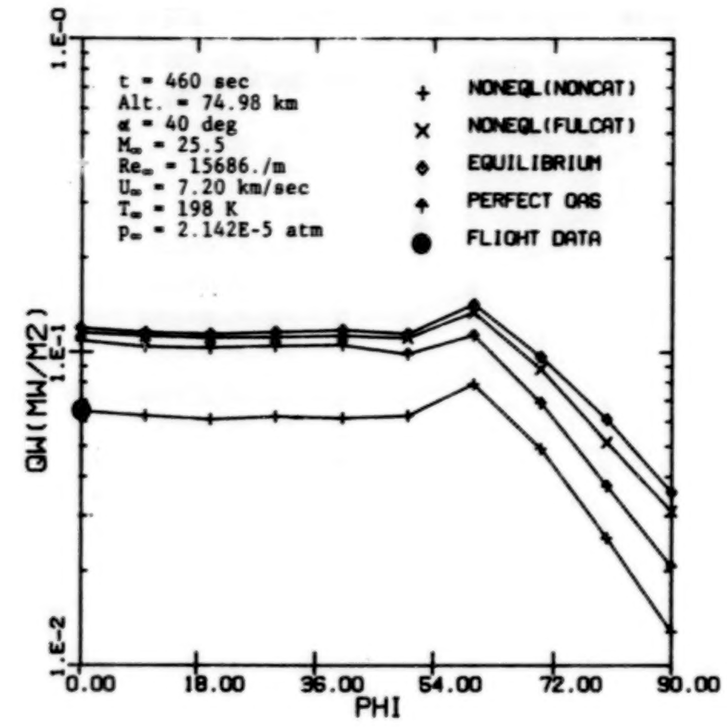

(a) z/L = 0.20.

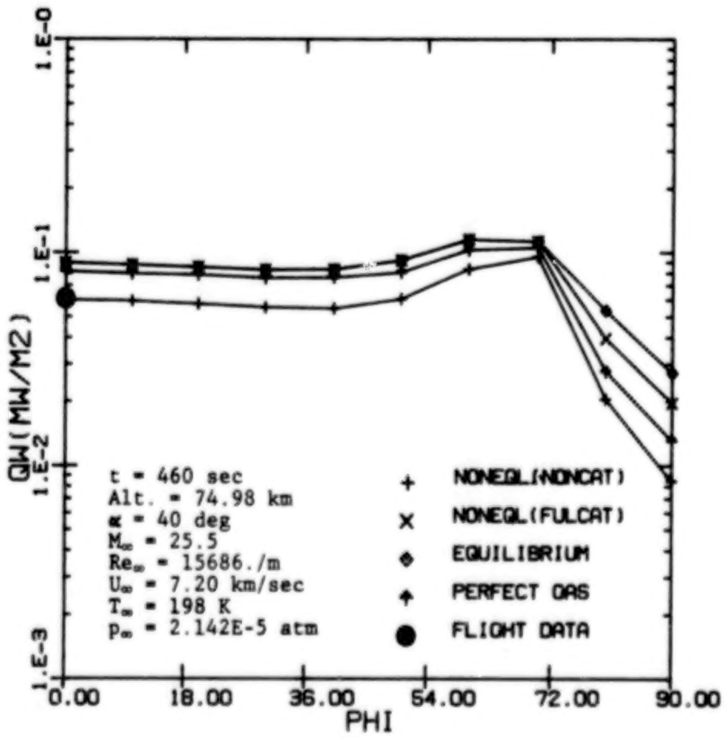

(b) z/L = 0.44.

Figure 7.- Spanwise heating rate comparison for Case 2.

ORIGINAL PAGE IS
OF POOR QUALITY

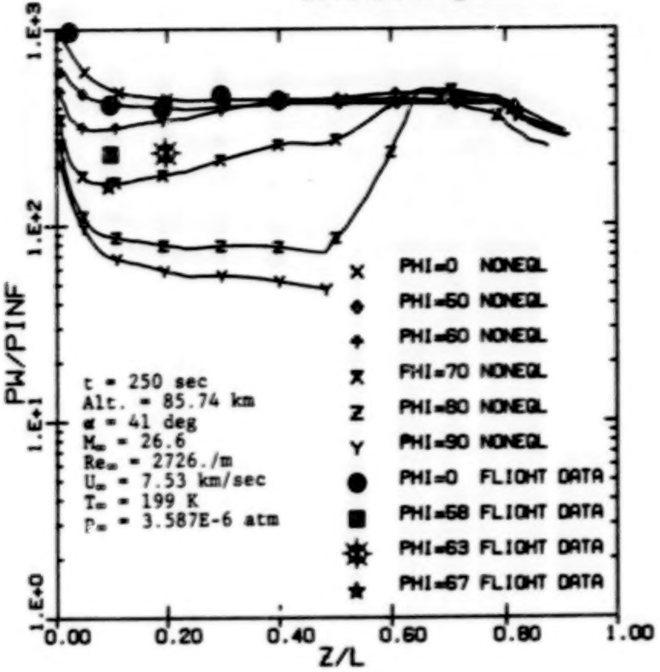

(a) Case 1.

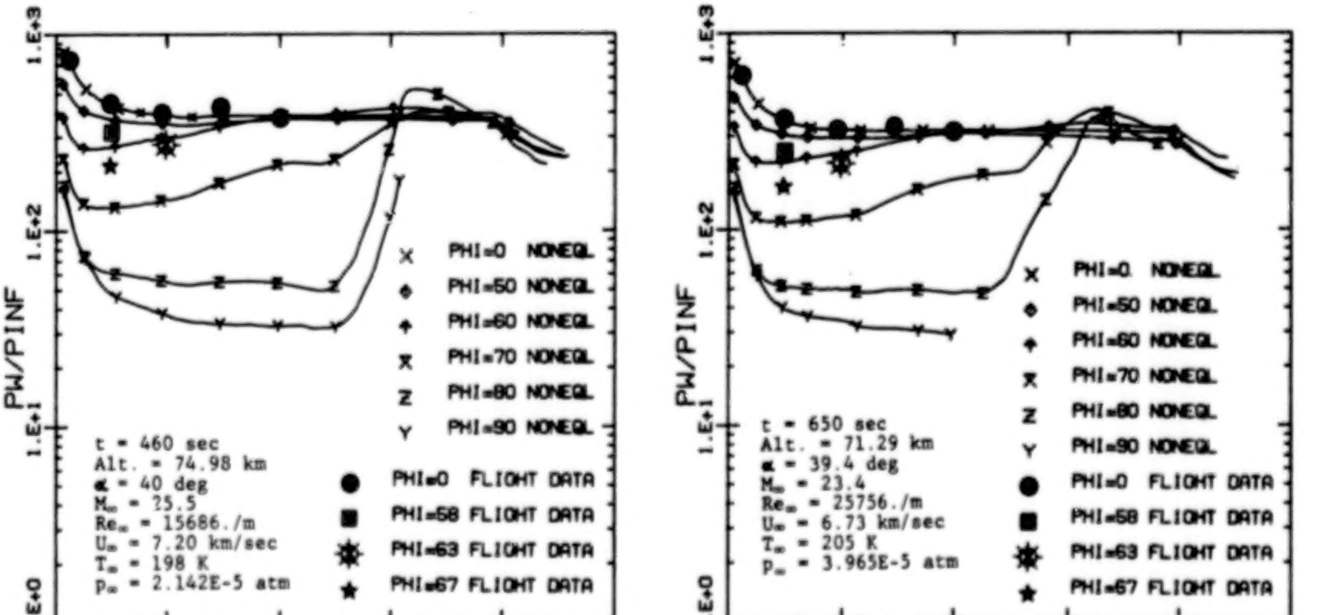

(b) Case 2.

(c) Case 3.

Figure 8.- Comparison of surface pressure distributions along the body.

ORIGINAL PAGE IS
OF POOR QUALITY

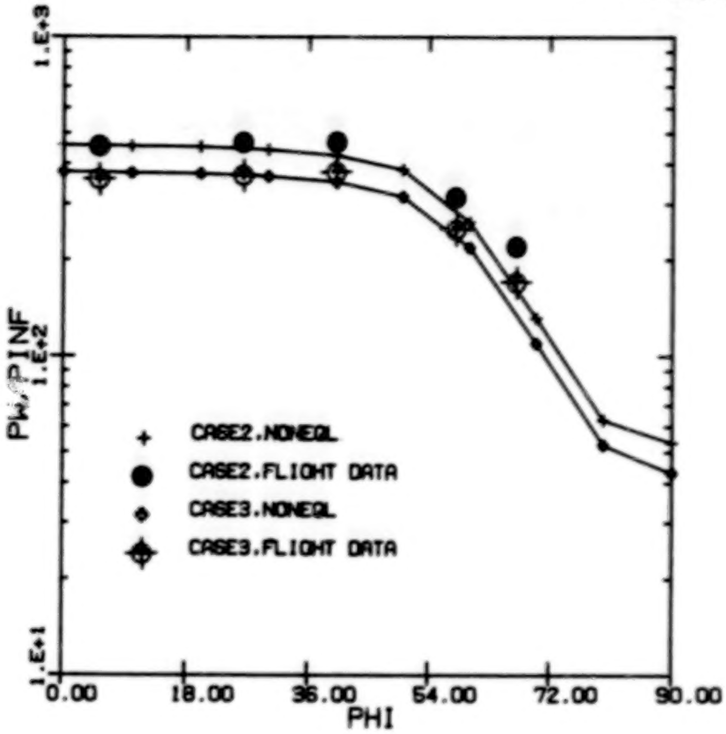

(a) z/L = 0.1.

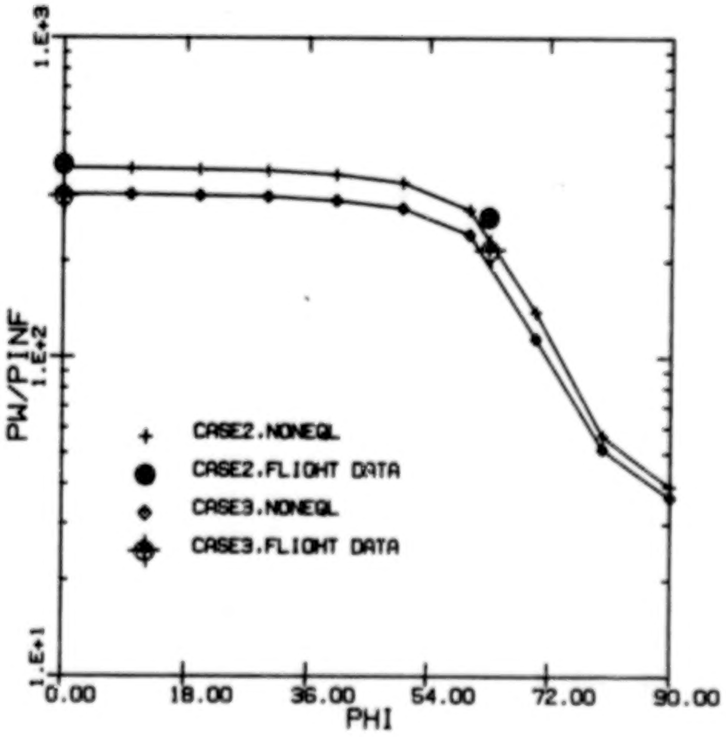

(b) z/L = 0.2.

Figure 9.- Comparison of spanwise surface pressure distributions.

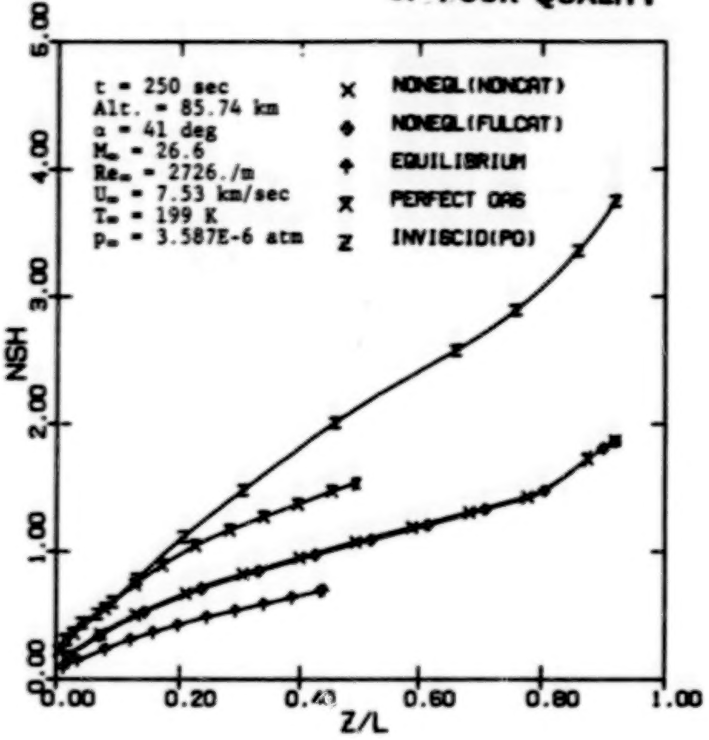

Figure 10.- Comparison of globally iterated shock layer thickness solutions at $\phi = 0$ for Case 1.

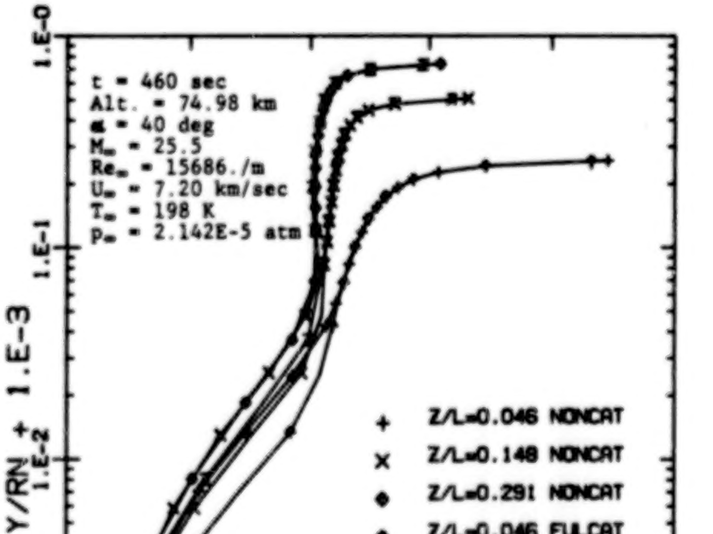

Figure 11.- Shock layer profiles of temperature at various axial body locations along $\phi = 0$ for Case 2.

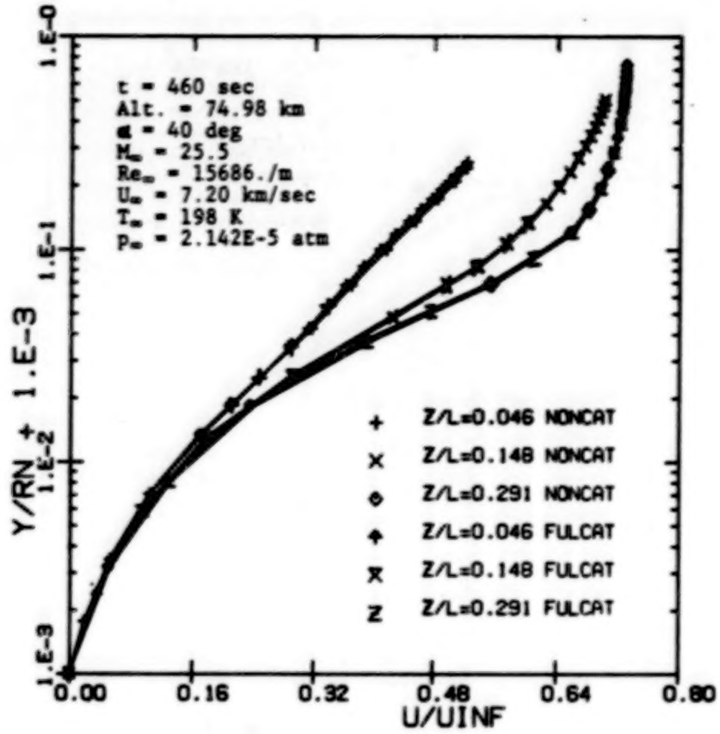

Figure 12.- Shock layer profiles of velocity at various axial body locations along $\phi = 0$ for Case 2.

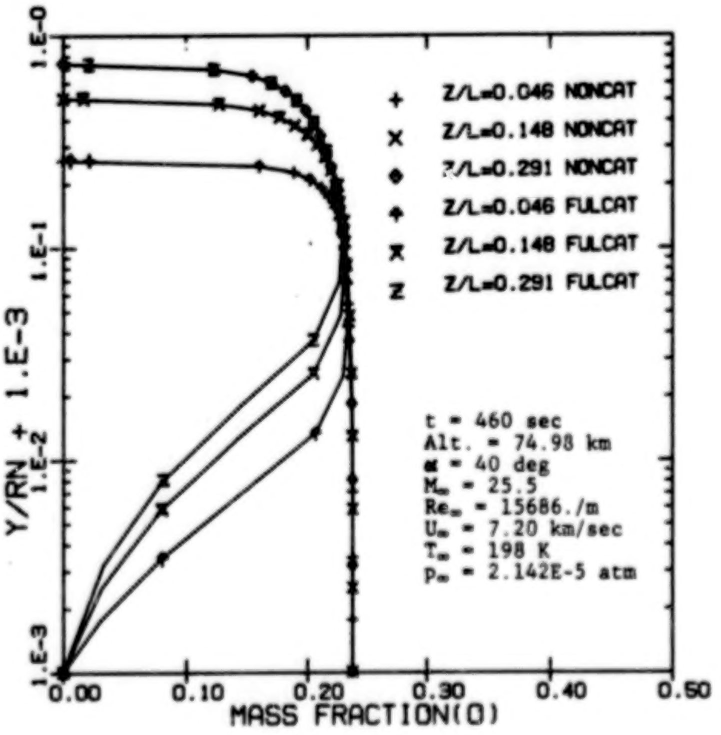

Figure 13.- Shock layer profiles of oxygen mass fraction at various axial body locations along $\phi = 0$ for Case 2.

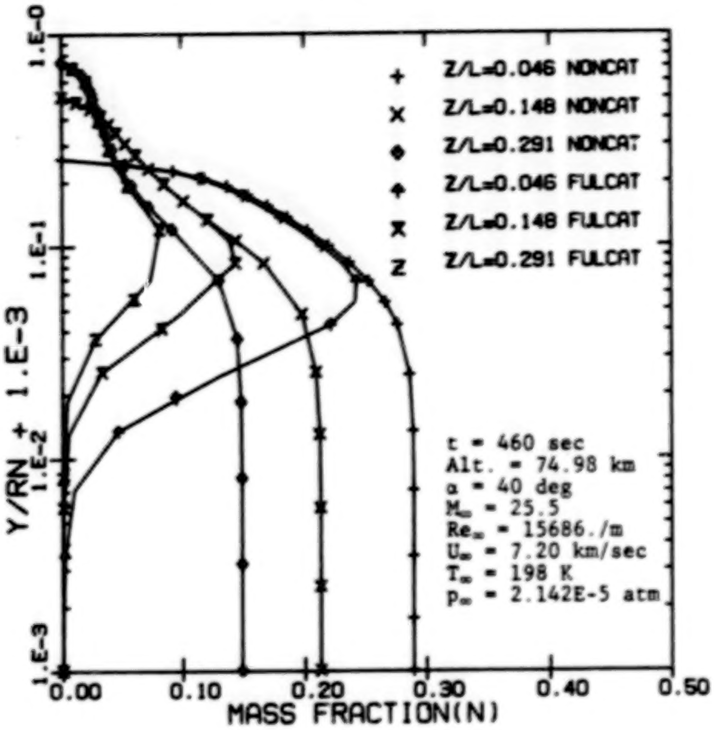

Figure 14.- Shock layer profiles of nitrogen mass fraction at various axial body locations along $\phi = 0$ for Case 2.

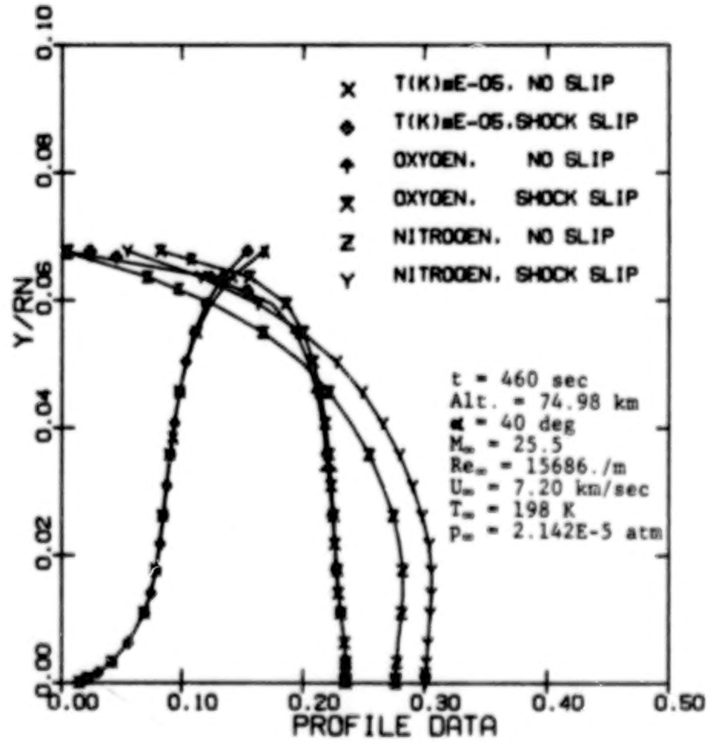

Figure 15.- Shock slip effect on the profile of temperature and mass fraction at stagnation point of Case 2.

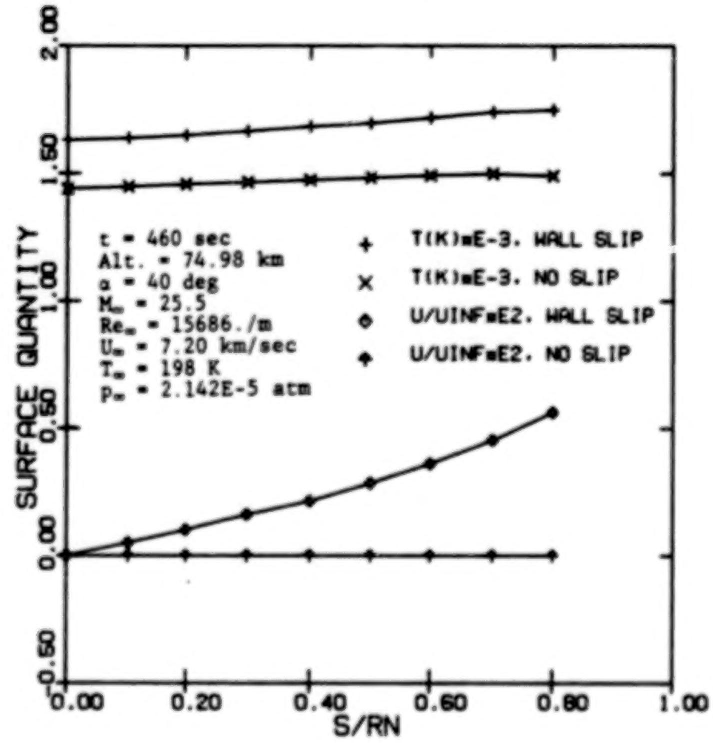

Figure 16.- Wall slip effect on the velocity and temperature jump on the nose region of Case 2.

N84
10152

UNCLAS

N84 10152

DB

CATALYTIC SURFACE EFFECTS ON SPACE SHUTTLE THERMAL PROTECTION SYSTEM DURING EARTH ENTRY OF FLIGHTS STS-2 THROUGH STS-5

David A. Stewart and John V. Rakich
Ames Research Center, Moffett Field, California

and

Martin J. Lanfranco
Informatics, Inc., Palo Alto, California

SUMMARY

This paper describes an on-going "OEX" catalytic surface effects experiment being conducted on the Space Shuttle. The catalytic surface effects experiment was performed on four of the five flights of Columbia. Temperature-time histories and distributions along the midfuselage and wing of the orbiter were used to determine the surface catalytic efficiency of the baseline HRSI. Correlation parameters are shown that allow the comparison of all flight data with predictions from the design trajectory 14414.1. These data show that the catalytic surface efficiency increased and surface emittance decreased as a result of contaminants during the five flights of the Space Shuttle.

INTRODUCTION

The possibility of reduced heating of the Shuttle orbiter during atmosphere entry because of noncatalytic surface effects has generated great interest since the first Shuttle flight, when surface temperature was found to be lower than expected. Noncatalytic surface effects for the Shuttle were previously predicted from computations and arc-tunnel tests (ref. 1) and were later confirmed (ref. 2) by data from flight STS-2. With present experience from the first five Shuttle flights, more definitive conclusions can now be made regarding noncatalytic surface effects.

The catalytic surface effects (CSE) "OEX" experiment was designed to determine if the low catalytic efficiency of the coating on the heat shield tiles would persist at flight conditions. The CSE experiment was conducted on four of the five flights of Columbia. This on-going experiment uses baseline high-temperature reusable surface insulation (HRSI) tiles located along the midfuselage and wing of the orbiter. The HRSI tiles are covered with a reaction cured glass (RCG) coating to provide emittance control and ease of handling (ref. 3). Development flight instrumentation (DFI) was used to measure surface temperature and pressure without impacting the Space Shuttle operations. A catalytic overcoat of black iron cobalt chromia spinal in a polyvinyl acetate binder was sprayed onto selected tiles (ref. 1). Measured surface temperatures obtained from tiles with and without the catalytic overcoat were compared with theoretical predictions using the reacting boundary-layer computation of Rakich and Lanfranco (ref. 2). High-temperature surface properties obtained from ground-test facilities for the RCG glassy surface and catalytic overcoat were used along with individual trajectory data to perform the computational

PAGE 826 INTENTIONALLY BLANK

PRECEDING PAGE BLANK NOT FILMED

analysis to define each flight experiment. Temperature-time histories and distributions along the midfuselage and wing of the orbiter were used to determine the surface catalytic efficiency of the baseline HRSI. This paper describes results (lessons learned) from a collection of flight data obtained from flights STS-2 through STS-5. The data include optical properties and surface temperatures that are used to define the surface catalytic efficiency of the Space Shuttle thermal protection system (TPS). A correlation parameter and a normalized surface temperature are introduced that allow the comparison of all flight data with a prediction obtained from the design trajectory 14414.1.

SYMBOLS

C_H	heat-transfer coefficient
C_p	specific heat
H_w	wall enthalpy
I_r	total enthalpy
k_w	reaction-rate constant
$\bar{L}$	Lewis number
L	orbiter length, 32.77 m
M	Mach number
P	pressure
q	heat flux
R	Reynolds number
T	temperature
t	Earth entry time, from 122 km
V	velocity
X	axial distance from nose of orbiter
Y	spanwise distance from orbiter centerline
α	angle of attack
δ	tile thickness
σ	Stefan-Boltzmann constant
ϵ_{TH}	total hemispherical emittance
ρ	density

ϕ roll angle

θ sweep angle

Subscripts:

e boundary-layer edge

0 stagnation condition

w wall condition

∞ free-stream condition

FLIGHT EXPERIMENT

The catalytic surface effects experiment consisted of two phases. The first phase was completed with STS-5. It used tiles with single surface thermocouple. The tiles were sprayed with a catalytic overcoat; temperatures were compared with those of nearby uncoated tiles. Tile locations for the first phase were at $X/L = 0.15$ and $X/L = 0.4$ for STS-2 and $X/L = 0.3$ and $X/L = 0.4$ for STS-3. Before flight STS-4, tiles located at $X/L = 0.1, 0.15, 0.2, 0.3,$ and 0.4 along the midfuselage were sprayed with the catalytic overcoat; however, no entry heating data were obtained from the flight because of a data system malfunction. Tiles located at $X/L = 0.1, 0.15, 0.2, 0.3,$ and 0.6 along the midfuselage and those at $X/L = 0.76$ and $X/L = 0.82$ along a 60% semispan on the wing were also sprayed with the catalytic overcoat for flight STS-5. For the same flight, a strip, 1.52 m by 0.22 m, along the midfuselage between $X/L = 0.35$ and $X/L = 0.4$ was sprayed with the catalytic overcoat (fig. 1). The catalytic overcoat was sprayed with an air brush to a thickness maintained at approximately 0.005 cm. A plastic sheet masked off the surrounding tiles (fig. 2).

The second phase, which is in the development stage, requires tiles that are constructed with multiple surface thermocouples. The catalytic overcoat will be sprayed onto one of several tiles to define the shape of the heat pulse during Earth entry of the orbiter.

POST-FLIGHT EVALUATION

Flight Photographs

Pre- and post-flight STS-5 photographs of tiles with the catalytic overcoat are shown in figures 3 and 4. The preflight photograph (fig. 3) shows (looking toward the nose) the tiles on the strip and at $X/L = 0.3$ and $X/L = 0.2$. The post-flight photographs (fig. 4) show that the catalytic overcoat on the nose wheel door ($X/L = 0.1$), fuselage ($X/L = 0.6$), and wing ($X/L = 0.76$ and $X/L = 0.82$) of the orbiter remained intact. The catalytic overcoat on the strip was eroded from the corner of two tiles along its edge during flight. However, the major portion of the overcoat remained on the surfaces. A change in color of the RCG surface from black to gray can be observed on the midfuselage and on the wing of the vehicle, indicating possible surface contamination. Visual inspection showed that the color change was not noticeable after STS-3, but it became more pronounced after STS-4 and STS-5. However, a color change was observed on the body flap after earlier flights. Possible sources of contamination are the gap fillers in the nose wheel door and metallic sensors located along the midfuselage between X/L = 0.1 and X/L = 0.2 (fig. 5). Contaminants from these sources have been identified as Fe_2O_3, SiO_2, and Cr_2O_3 (Flowers, O. L., private communication, 1982).

Chemical Analysis

Chemical analyses were conducted on the surface of two tiles removed from locations X/L = 0.138 and X/L = 0.4 on the orbiter after flight STS-5 (Dr. Daniel B. Leiser, private communication, 1983). Analyses of the surfaces were performed using X-ray diffraction (XRD) and a scanning electron microscope with an X-ray fluorescence attachment. The X-ray fluorescense analysis attachment, an energy dispersive X-ray analysis (EDX) unit, was used to obtain qualitative chemical analysis data of the coating surface; a description of the unit is given in ref. 4. Post-flight STS-5 XRD analysis of the RCG coatings showed the presence of cristobalite on the surface. In addition, X-ray fluorescence analysis showed the presence of aluminum, silicon, sodium, and magnesium on the surface of the two tiles. The aluminum, probably in the form of alumina, is attributed to by-products deposited from the burning solid rocket fuel during launch. The other elements are commonly found in sea salt. Sea salt tends to increase the reaction-rate constant because of its effect on ion mobility and viscosity of the borosilicate glass, and alumina decreases the emittance.

Surface Properties

Two important surface properties that determine surface temperature on the heat shield are (1) the reaction-rate constant and (2) total hemispherical emittance. The reaction-rate constants for the RCG coating and catalytic overcoat surfaces were obtained from experiments conducted in the Ames Research Center Aerodynamic Heating Facility. The reaction-rate constant for baseline RCG is shown in figure 6. The reaction-rate constant varied from roughly $k_w = 25$ cm/sec to $k = 100$ cm/sec for most of the area over the midfuselage where the catalytic surface effects experiment was being conducted. For simplicity in the reacting boundary-layer computation the reaction-rate constant was assumed to be constant at $k_w = 100$ cm/sec. After flight STS-2 experiments using a microwave cavity generated nitrogen plasma on pieces of RCG covered tiles showed no change in the reaction-rate constant. Post-flight STS-5 experiment also showed no change in the reaction rate-constant for the RCG coating.

The total hemispherical emittance for both surfaces is plotted in figure 7. The preflight total hemispherical emittance of both surfaces is very similar over the temperature range of interest (figs. 7(a) and 7(b)). Taken at room temperature, the total hemispherical emittance for both surfaces was calculated from spectral, hemispherical reflectance data obtained using a Beckman model DK-IA (wavelength range 0.3 μ to 2.3 μ) and a Willey model 318 (wavelength range 2.0 μ to 15 μ) spectrophotometer, respectively. Spectral hemispherical emittance data for the RCG surfaces are plotted in figure 7(c). Figure 7(d) shows a comparison of the total hemispherical emittance calculated from spectral hemispherical reflectance data and values obtained from arc-jet tests. The arc-jet data were obtained from disks tested in an arc-plasma airstream using measurements of the radiant flux and surface temperature. The radiant heat flux was measured using a radiometer and the surface temperature with a surface thermocouple (platinum-platinum/13% rhodium) and pyrometer (wavelength = $0.9\ \mu$). Post-flight STS-5 total hemispherical emittance calculated from reflectance measurements is shown in figure 7(a). Post-flight STS-5 data were obtained from two tiles removed from the midfuselage at locations $X/L = 0.138$ and $X/L = 0.4$ adjacent to the baseline reference tiles. These data show less than 5% decrease in the total hemispherical emittance of the RCG coating after STS-5.

Computations

The reacting boundary-layer computation uses dynamic pressure, velocity, and angle of attack from the flight trajectory and calculated wall pressure in addition to the above described surface properties, to predict surface temperature on the orbiter TPS during Earth entry. The wall pressure-stagnation pressure ratio was calculated using an inviscid nonequilibrium real-gas solution. Typical pressure ratios are plotted for several locations along the midfuselage of the orbiter for flight STS-3 (fig. 8). Agreement between the flight data and predictions is good for all locations except $X/L = 0.1$ where the prediction was high. The difference in the measured and calculated pressure is attributed either to a local disturbance of the boundary layer or possible leakage of the pressure line from the surface of the tile to the transducer. Boundary-layer calculations of the radiation equilibrium temperature were performed for equilibrium and reacting flows. The calculated heating for STS-3 is shown for two surface locations ($X/L = 0.15$ and $X/L = 0.4$) along the midfuselage of the orbiter (fig. 9). Shown on the figure are the calculated wall pressure histories. The flow is assumed to be laminar in the vicinity of the experiment for the majority of the Earth-entry trajectory, when surface catalytic effects are important. Transition to turbulent flow was assumed to occur late in the Earth entry of the orbiter (~1200 s). The computations show that a reacting flow resulted in a 34-40% reduction in the heat-transfer rate at $X/L = 0.15$ and 25% reduction at $X/L = 0.4$ for a substantial portion of the heating history. The effect of this temperature reduction on heat-shield thickness was evaluated. A one-dimensional model calculation using a modified charring material ablator (CMA) program shows that for reacting flow the tile thickness can be reduced by greater than 22% at $X/L = 0.15$ and greater than 6% at $X/L = 0.4$ and still meet Shuttle design requirements.

RESULTS AND DISCUSSION

Flight data for STS-2 and STS-3 are compared with the computations and shown in figure 10. The surface-temperature distribution along the midfuselage was calculated for equilibrium and reacting flows at an entry time of 650 s. The boundary-layer analysis predicts a discontinuous rise in temperature on the test tile with catalytic overcoat. The temperature rise goes above the equilibrium value because of the sudden release of the energy of dissociation. The agreement between theory and data is good at the forward location $X/L = 0.15$ for STS-2. The low temperature at $X/L = 0.4$ can be attributed to the removal of some of the catalytic overcoat on this tile during STS-2 entry to Earth. Better agreement between flight data and theory was observed on STS-3. Some of the temperature data points are off the centerline and those should be a little higher than those on the centerline. These flight data show that the surface temperatures on the baseline HRSI tiles are consistently below the equilibrium computation (13% to 35%), and the data from the test tiles are above equilibrium.

Data Correlation

To compare data from each flight, a normalized surface temperature and a correlation parameter had to be determined. The normalized surface temperature ($\bar{T}$) was derived from the well-known expression for flat-plate heating with dissociated gas flow (ref. 5):

$$-q_w = C_H\rho_e V_e(I_e - H_w)\left[\frac{(C_{p_f})_{av}}{(C_p)_{av}}(1 - \bar{L}) + \bar{L}\right]^{2/3} \tag{1}$$

and assuming

$$\bar{L} = 1, \quad q = \epsilon_{TH}\sigma T_w^4$$

$$\bar{T} = \frac{T_w}{\left[\frac{\rho_\infty V_\infty^3}{2\sigma}\right]^{1/4}} = \left[\frac{C_H}{\epsilon_{TH}}\frac{\rho_e V_e}{\rho_\infty V_\infty}\right]^{1/4} \tag{2}$$

The hypersonic viscous interaction parameter ($M_\infty/\sqrt{R_\infty}$) was found to be a correlation parameter relating equivalent flight conditions during each trajectory. To illustrate the validity of this parameter, heat-transfer coefficients for equilibrium and reacting flows were calculated for the design trajectory 14414.1 and plotted as a function of the hypersonic, viscous interaction parameter (fig. 11). Calculated values of the heat-transfer coefficient C_H obtained from trajectories STS-2 through STS-5 were compared with values from the design trajectory 14414.1. Excellent agreement was obtained between values obtained from the flight and design trajectories. Since the normalized surface temperature is proportional to C_H, it follows that the flight data also can be directly compared with the design trajectory 14414.1 prediction using the hypersonic viscous interaction parameter.

Normalized surface temperatures for several locations along the midfuselage of the orbiter (X/L = 0.15, X/L = 0.3, and X/L = 0.4) were plotted against the correlation parameter (fig. 12). The predictions included values for equilibrium and reacting flows. Figure 12 shows values of the average surface-temperature rise across the tiles with the catalytic overcoat (short dashed line). In general, good agreement between the flight data and the predictions was obtained. During STS-2, the low temperature measurement at X/L = 0.15 on the baseline RCG coating occurred with a thermocouple that failed a little over halfway through the entry to Earth of the orbiter. The low-temperature measurement for the coated tile at X/L = 0.4 during STS-2 occurred as a result of the loss of some catalytic overcoat.

The correlation parameter for all orbiter flights is plotted as a function of the time of entry to Earth from 121,920 m (fig. 13). Also, angle of attack and roll angle are shown on the figure. These calculated parameters ensure that the flight data are compared at similar flight conditions without large deviations in angle of attack or roll angle. Four cases of laminar flow conditions were chosen to compare normalized surface-temperature distributions along the midfuselage and wing with predictions using the design trajectory 14414.1 (figs. 14 through 16).

Midfuselage Heating

Figures 14(a) through 14(d) show normalized surface temperature as a function of distance along the orbiter midfuselage centerline. Boundary-layer computations are shown for equilibrium and reacting flows. The flight data on figure 14 include off-centerline corrections using the solutions outlined in reference 6. Good agreement between STS-2, STS-3, and the prediction using the reacting flow is shown for all four cases. The flight data from STS-5 appear high for the baseline RCG coating and low for tile surfaces with the catalytic overcoat. The difference between these data cannot all be accounted for by the 5% reduction in the total hemispherical emittance measured after flight STS-5. The difference between the STS-5 data and the prediction is attributed to an increase in k_w for the RCG surface coating. The lower surface-temperature measurements at $X/L = 0.2$ during STS-5 and higher surface-temperature measurements at $X/L = 0.3$ during STS-3 on the tiles with the catalytic overcoat cannot be explained at this time. These data show that the surface catalytic effect on surface temperature decreases with decreasing Mach number and with increasing distance along the midfuselage centerline of the orbiter. In figure 14(b), $M_\infty/\sqrt{R_\infty} = 0.0184$ includes a prediction for a reacting flow and reaction-rate constant that varied with temperature (see fig. 6). The normalized temperature-distribution prediction was in close agreement with the flight data from STS-2 and STS-3 along the midfuselage centerline.

The temperature at $X/L = 0.4$ on STS-5 is lower than the peak overshoot value because of the long (1.5 m) run of catalytic overcoat. However, that temperature is still above equilibrium, which is in agreement with the theory.

The temperature distribution along the midfuselage centerline of the orbiter was calculated using post-flight STS-5 total hemispherical emittance and assuming a reaction-rate constant $k_w = 200$ cm/sec for the RCG glass coating (fig. 15). Included on the figure are computations for equilibrium flow and a reacting flow with $k_w = 100$ cm/sec for the RCG glass coating. All computations were made for test point $M_\infty/\sqrt{R_\infty} = 0.0304$. The calculations using STS-5 post-flight total hemispherical emittance and increased reaction-rate constant during STS-5 agree well with the flight data. A substantial heat reduction below the equilibrium value still occurs at $X/L < 0.2$. However, at $X/L > 0.2$ the reduction in heating to the surface of the tiles is less between the reacting and equilibrium flows.

Wing Heating

To test for possible noncatalytic effects on the windward side of the wing, two tiles along the 60% semispan $(Y/L = 0.60)$ were sprayed with the catalytic overcoat. This test was necessary because of uncertainty as to the origin of streamlines wetting the wing surface. If the streamlines originate at the nose of the Shuttle, the flow should be close to equilibrium because of the large distance from the nose and the results observed at $X/L = 0.6$ along the midfuselage. On the other hand, if the wing streamlines pass through the wing-leading-edge shock, then the flow has greater possibility of being out of equilibrium, and lower noncatalytic heating can occur. Streamlines from wind-tunnel tests suggest the latter possibility.

Because of the difficulty in exactly computing the wing flow field, simple two-dimensional strip theory was used to analyze the wing heating. Cutting the wing at $Y/L =$ constant yields a section shape that can be approximated by a blunted flat plate. For heating computations, the boundary layer is assumed to flow two dimensionally over the plate, starting approximately on the stagnation line on the wing

C-3

leading edge. The surface pressure is approximated with a Newtonian type of pressure distribution. Thus, the wing pressure was approximated by:[1]

$$\frac{P_w}{P_0} = \cos^2(\theta - \theta_0) \tag{3}$$

where, due to the wing sweep, $\theta_0 = 50°$ for $\alpha = 40°$ and P_0 is the normal shock stagnation pressure. The pressure and normalized surface temperature are shown in figure 16. The heating computation included a correction for boundary layer swallowing effects (ref. 2).

The Newtonian pressure approximation is, of course, constant on the flat part of the wing, but agrees reasonably well with the level of flight data, STS-3. The pressure data decrease with distance as the overpressure caused by the blunted leading edge decays toward the flat-plate value.

Figure 16 shows normalized surface-temperature predictions as a function of distance along a 60% semispan located on the wing of the orbiter. The normalized surface temperatures show peaks at $X/L = 0.76$ and 0.81, where the tiles are coated. We note that the data for the coated tiles show a significant rise over the uncoated tiles indicating a significant noncatalytic effect. The theory overpredicts the catalytic overshoot but is in fair agreement with the baseline tiles. As with the centerline data, there seems to be a slight rise in temperature of the baseline tiles for flight STS-5. This tendency has been discussed earlier. In summary, the wing heating is reasonably well predicted by simple two-dimensional strip theory.

CONCLUDING REMARKS

Lessons learned from the catalytic surface effects experiment on four STS Columbia flights flown are listed below.

1. Low surface catalytic efficiency of the RCG-coated baseline tiles results in lower heating during Earth entry for early flights of the orbiter.

2. Decrease in surface temperature on the HRSI because of its catalytic surface efficiency was less with distance along the orbiter midfuselage and Earth entry time.

3. Total hemispherical emittance of RCG coating decreased with number of flights.

4. Results indicate that surface catalytic efficiency (reaction-rate constant) of the RCG coating increased with number of flights.

5. Thermal response predictions can be made from ground-test data, design trajectory, and reacting boundary-layer computation.

---

[1] We note that equation (3) is not applicable at the wing leading edge because wing sweep reduces the pressure there, but it is adequate to start the boundary-layer computation.

6. Correlation parameter and a normalized surface temperature allow the comparison of data from several flights with predictions along the midfuselage and wing from the design trajectory 14414.1.

7. Flight data confirm the noncatalytic surface effects on the wing.

REFERENCES

1. Stewart, D. A.; Rakich, J. V.; and Lanfranco, M. J.: Catalytic Surface Effects Experiment on the Space Shuttle. AIAA Paper 81-1143, Palo Alto, Calif., 1981.

2. Rakich, J. V.; Stewart, D. A.; and Lanfranco, M. J.: Results of a Flight Experiment on the Catalytic Efficiency of the Space Shuttle Heat Shield. AIAA Paper 82-0944, St. Louis, Mo., 1982.

3. Goldstein, H. E.; Leiser, D. B.; and Katvala, V.: Reaction Cured Borosilicate Glass Coating for Low-Density Fibrous Silica Insulation. Borate Glasses, Plenum Corp., New York, 1978, pp. 623-634.

4. Leiser, D. B.; Stewart, D. A.; and Goldstein, H. E.: Chemical and Morphological Changes of Reusable Surface Insulation Coatings as a Function of Convectively Heated Cyclic Testing. NASA TM S-2719, 1972.

5. Dorrance, W. H.: The Dissociated Laminar Boundary Layer. Viscous Hypersonic Flow, McGraw-Hill Book Co., New York, 1962, pp. 69-101.

6. Rakich, J. V.; and Lanfranco, M. J.: Numerical Computation of Space Shuttle Laminar Heating and Surface Streamlines. Journal of Spacecraft and Rockets, vol. 14, no. 5, May 1977, pp. 265-272.

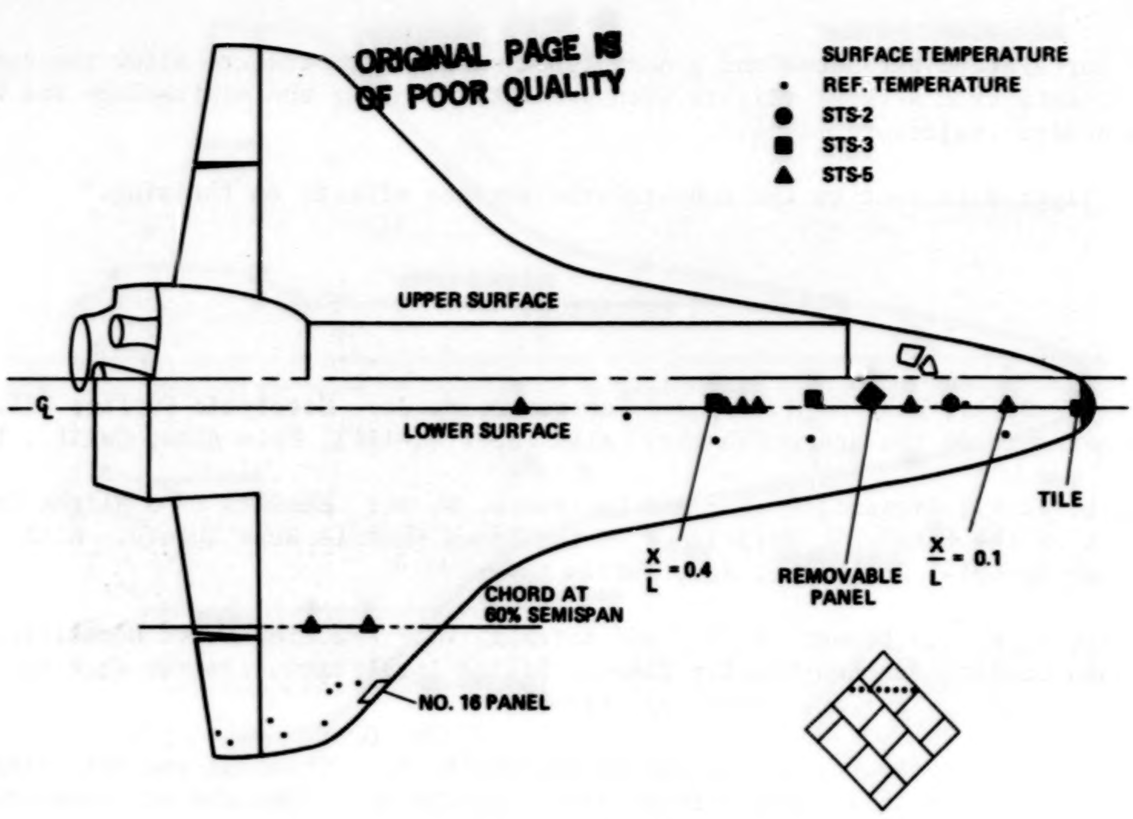
SURFACE TEMPERATURE
• REF. TEMPERATURE
● STS-2
■ STS-3
▲ STS-5
UPPER SURFACE
℄
LOWER SURFACE
TILE
X/L = 0.4
REMOVABLE PANEL
X/L = 0.1
CHORD AT 60% SEMISPAN
NO. 16 PANEL

Figure 1.- Experiment thermocouple locations.

Figure 2.- Catalytic overcoat application.

Figure 3.- Preflight STS-5 photograph of experiment.

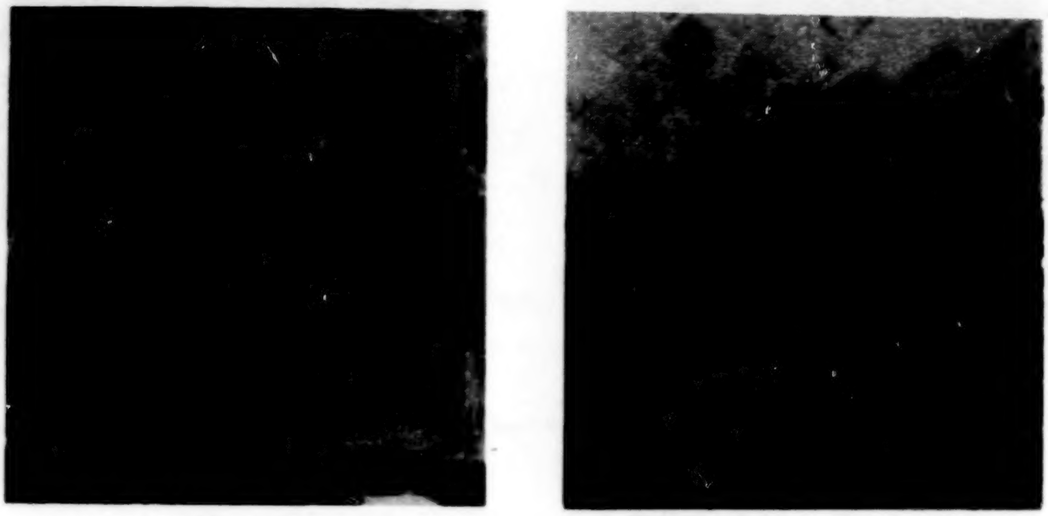

X/L = 0.1 **STRIP, 0.35 ≤ X/L ≤ 0.4**

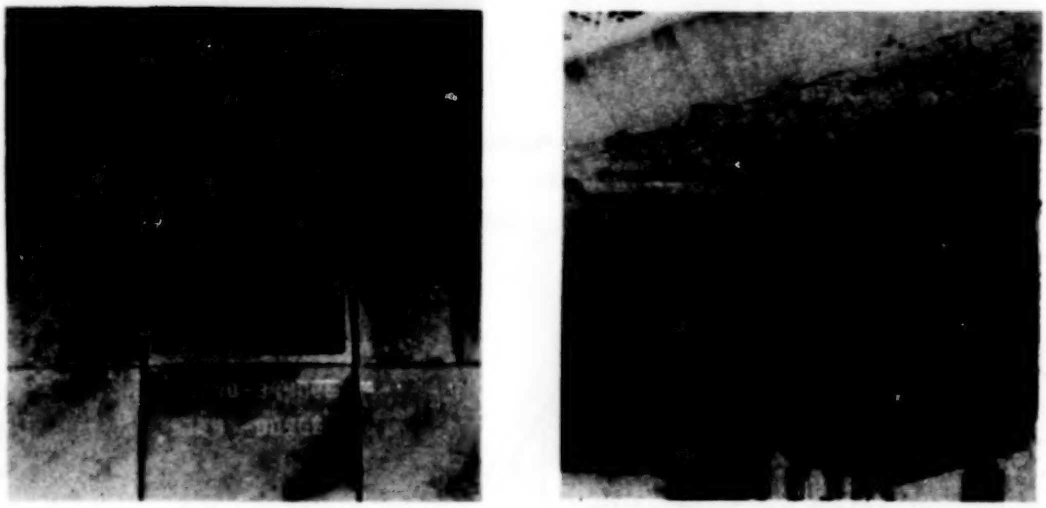

X/L = 0.6 **WING, 60% CHORD**

Figure 4.- Post-flight STS-5 photograph of selected tiles.

GAP FILLERS

SENSORS

Figure 5.- Contamination sources.

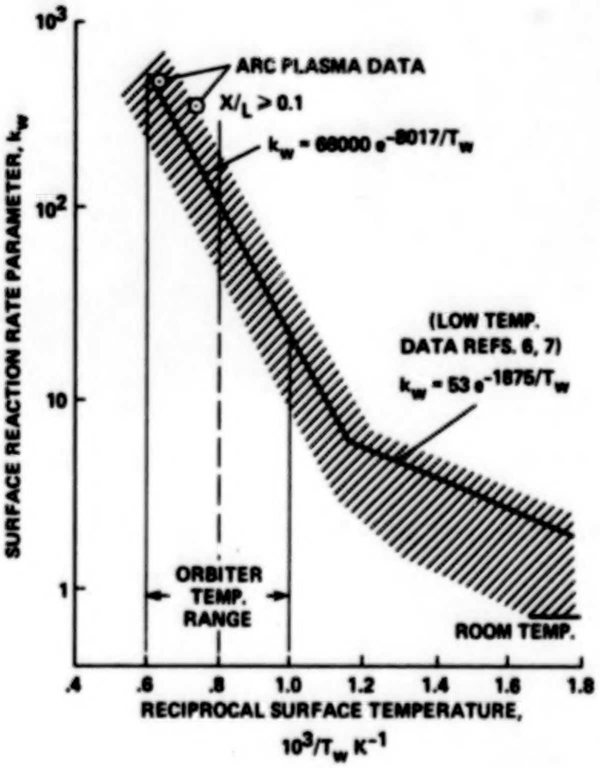

Figure 6.- Initial catalycity of RCG coating.

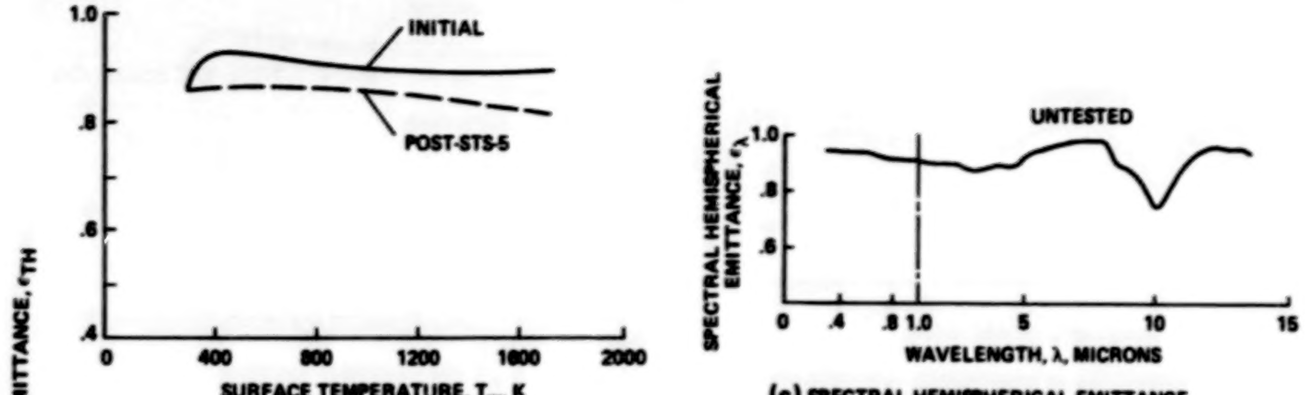

(a) RCG BASELINE COATING

(c) SPECTRAL HEMISPHERICAL EMITTANCE

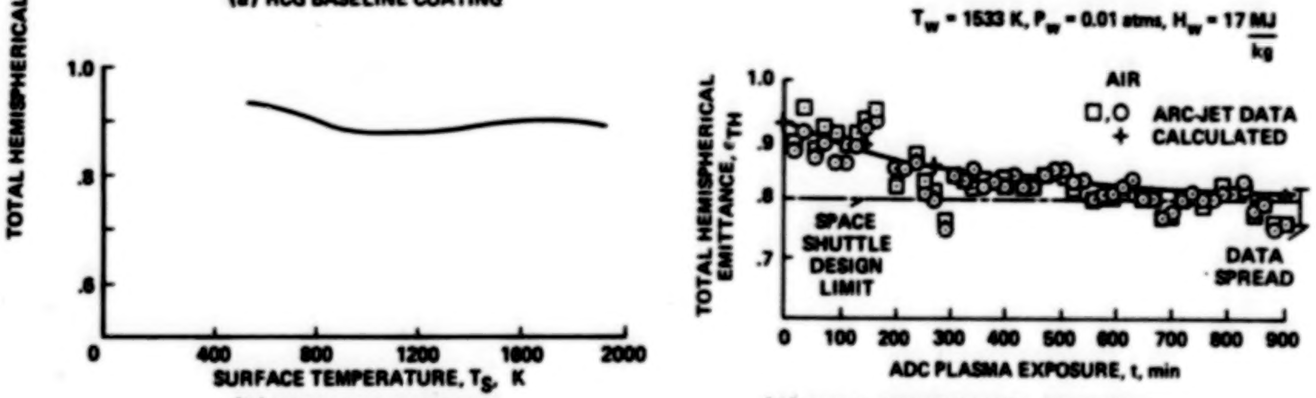

(b) CATALYTIC OVERCOAT

(d) TOTAL HEMISPHERICAL EMITTANCE

Figure 7.- Hemispherical emittance.

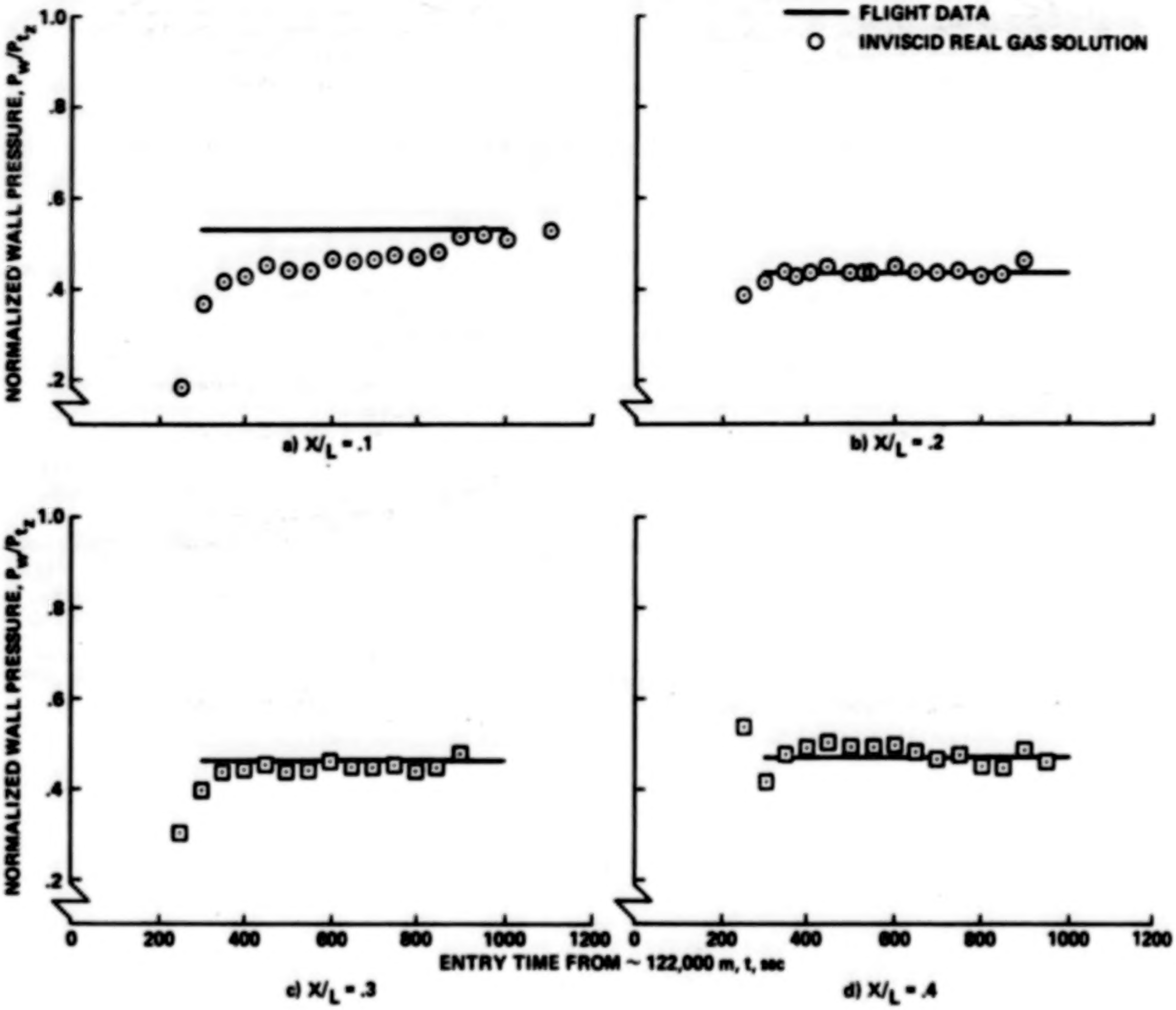

a) $X/_L$ = .1

b) $X/_L$ = .2

c) $X/_L$ = .3

d) $X/_L$ = .4

Figure 8.- Pressure histories for flight STS-3 windward centerline.

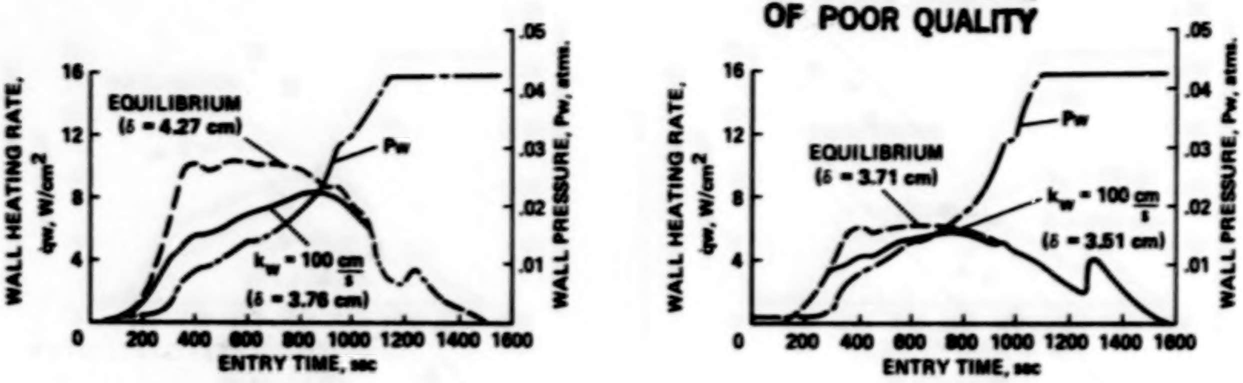

a) $X/_L$ = 0.15

b) $X/_L$ = 0.40

Figure 9.- Calculated STS-3 heating and pressure profiles during entry.

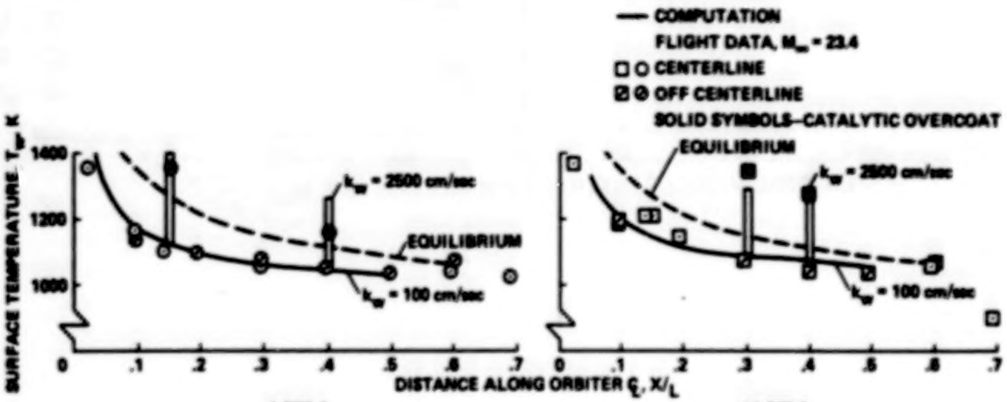

a) STS-2

b) STS-3

Figure 10.- Surface temperature variation on orbiter windward centerline.

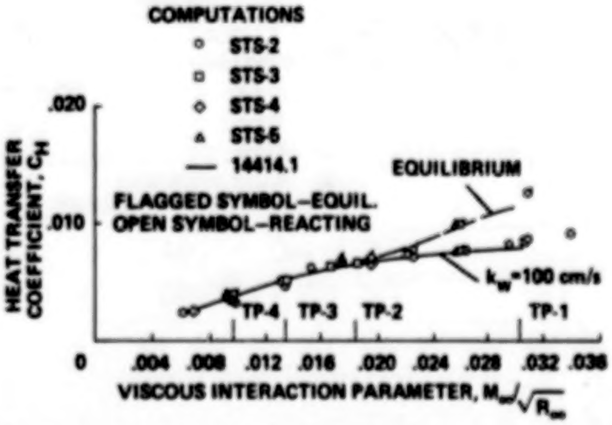

Figure 11.- Correlation of calculated heating transfer coefficients.

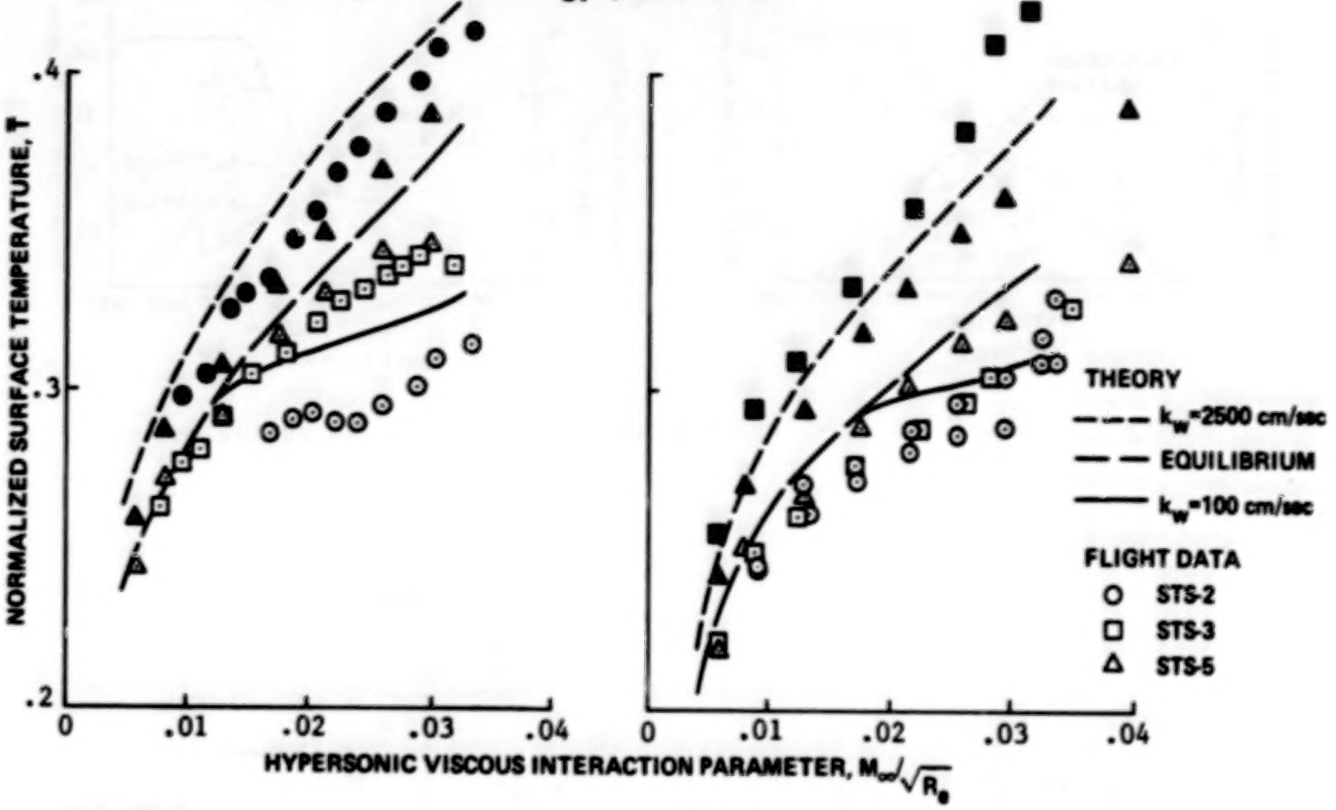

a) $X/_L$=0.15

b) $X/_L$=0.3

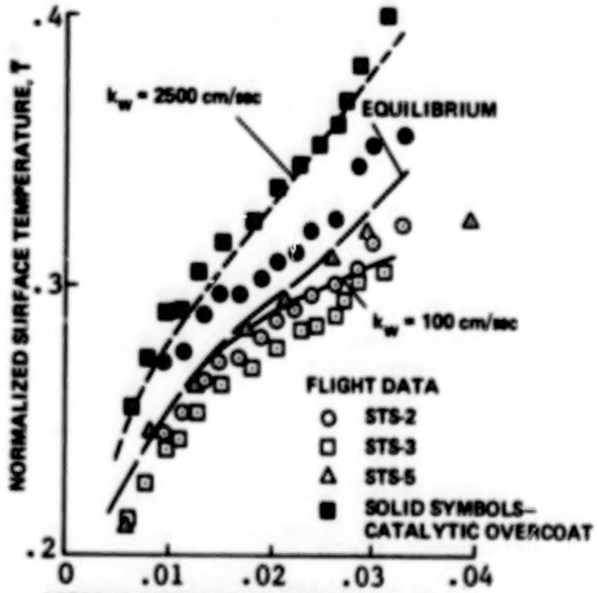

c) $X/_L$=0.4

Figure 12.- Normalized surface temperature as a function of correlation parameter.

ORIGINAL PAGE IS
OF POOR QUALITY

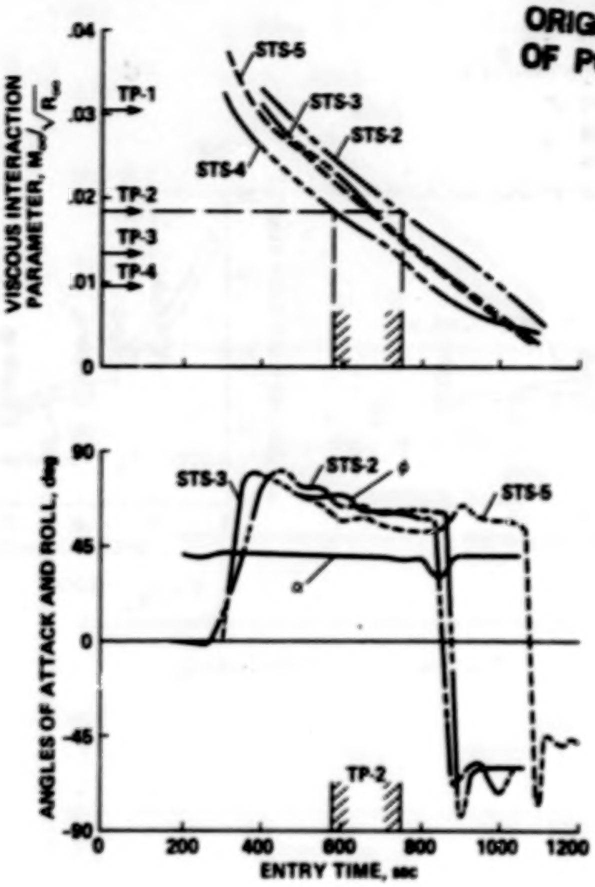

Figure 13.- Flight trajectory parameters.

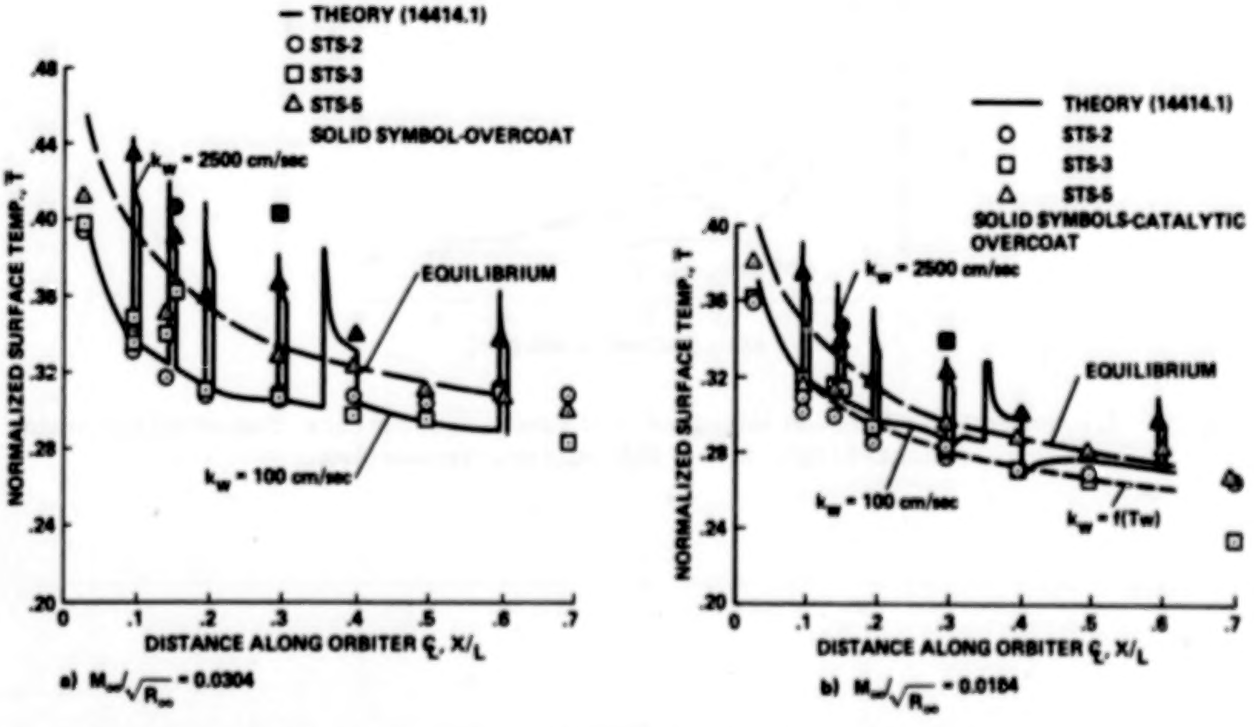

a) $M_\infty/\sqrt{R_\infty} = 0.0304$

b) $M_\infty/\sqrt{R_\infty} = 0.0184$

Figure 14.- Surface temperature distribution along midfuselage centerline.

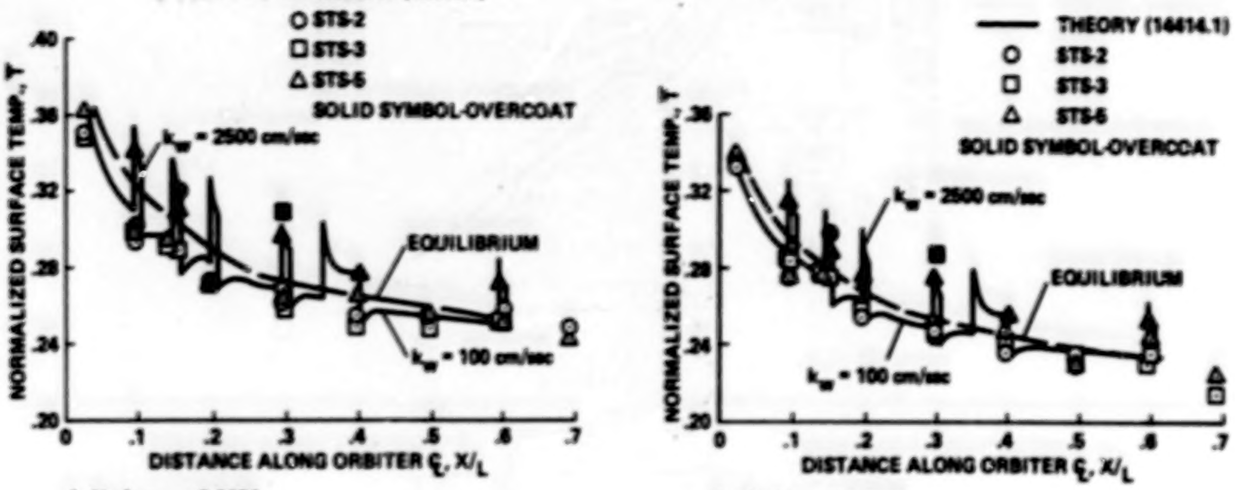

c) $M_\infty/\sqrt{R_\infty}$ = 0.0134

d) $M_\infty/\sqrt{R_\infty}$ = 0.0096

Figure 14.- Concluded.

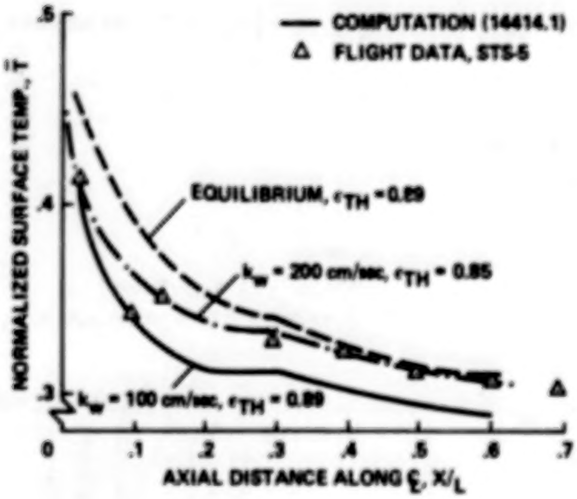

Figure 15.- Comparison between measured and predicted surface temperatures using post-flight STS-5 RCG surface properties.

ORIGINAL PAGE IS
OF POOR QUALITY

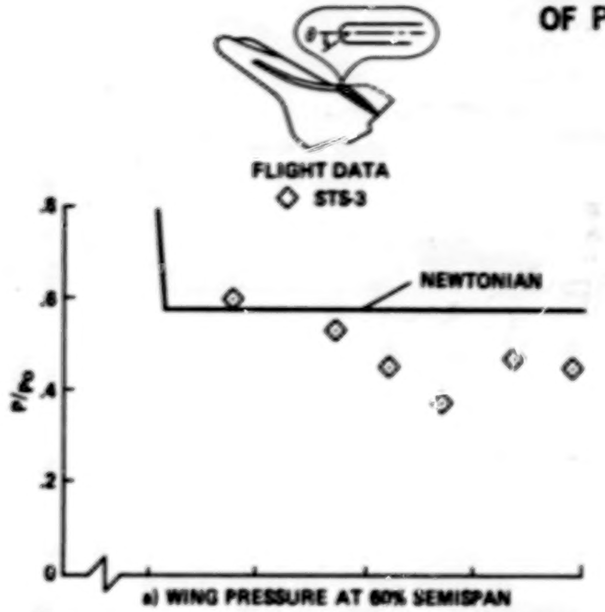

a) WING PRESSURE AT 60% SEMISPAN

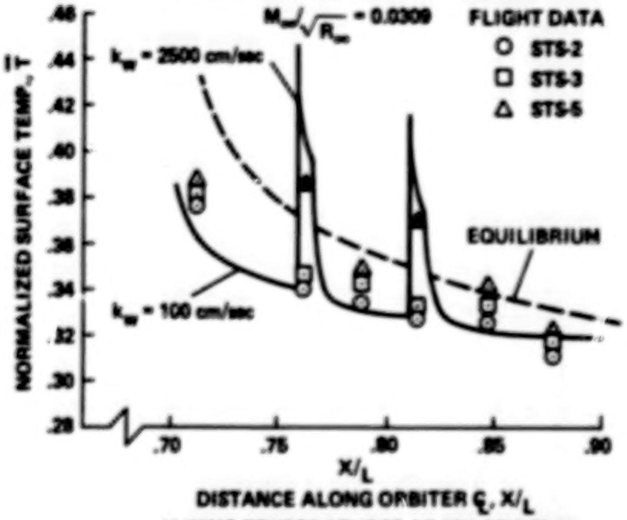

b) WING TEMPERATURES AT 60% SEMISPAN

Figure 16.- Surface pressure and temperature distributions along 60% semispan on orbiter wing.

N84
10153

UNCLAS

N84 10153 D9

ORBITER CATALYTIC/NONCATALYTIC HEAT TRANSFER AS EVIDENCED BY HEATING TO CONTAMINATED SURFACES ON STS-2 AND STS-3

David A. Throckmorton, E. Vincent Zoby, and
H. Harris Hamilton II
NASA Langley Research Center
Hampton, Virginia

SUMMARY

During that portion of Space Shuttle orbiter entry when significant aerodynamic heat transfer occurs, the flow over the vehicle is in chemical nonequilibrium. The parameter which most significantly influences the level of surface heat transfer in such a flow field is the catalytic efficiency of the surface with respect to the recombination of dissociated oxygen atoms. Significant, and instantaneous, changes were observed in the level of heat transfer at several lower-surface centerline locations on STS-2 and STS-3. This phenomenon apparently resulted from a sudden change in the surface catalytic efficiency at these locations due to contamination of the surface by metallic oxides. As a result, data obtained from affected measurements cannot be considered as "benchmark" data with which to attempt to characterize nonequilibrium heat transfer to the orbiter's lower surface centerline.

INTRODUCTION

The design of the thermal protection system (TPS) of the Space Shuttle orbiter was based upon predicted aerothermodynamic environments which were generated assuming that the orbiter flow field was everywhere in chemical equilibrium (ref. 1). Detailed preflight calculations (refs. 2 and 3), however, indicated that significant chemical nonequilibrium would persist over the majority of that portion of orbiter entry when significant aerodynamic heat transfer occurs. The parameter which most significantly influences the level of surface heat transfer in such a flow field is the catalytic efficiency of the TPS surface with respect to the recombination of dissociated oxygen atoms. The catalytic efficiency of the reaction-cured glass (RCG) coating on orbiter TPS tiles was thought to be relatively low based upon arc-tunnel experiment results (ref. 4). Therefore, flight heating rates were expected to be lower than "equilibrium chemistry" predictions as a result of the combination of nonequilibrium chemistry and a non-fully-catalytic TPS surface.

The desire to confirm, in flight, the apparent low catalytic efficiency of the RCG coating and the accompanying benefits of nonequilibrium heat transfer to that surface led to the development of the NASA Ames Research Center's Catalytic Surface Effects (CSE) Experiment (refs. 5 and 6). CSE experiment results were obtained on STS-2, 3, and 5. The STS-2 data (ref. 6) provided graphic evidence that the RCG coating of the orbiter's TPS tiles is indeed

PAGE 846 INTENTIONALLY BLANK

PRECEDING PAGE BLANK NOT FILMED

"noncatalytic." The flight data showed that surface temperatures of the CSE-experiment catalytic-coated tiles were substantially greater than those of the baseline tiles and that, therefore, the surface catalytic efficiency of the baseline tiles is low.

In addition to the CSE experiment, however, an unexpected event occurred during the orbital flight test mission entries which provided further information into the catalytic/noncatalytic nature of orbiter windward-surface heat transfer. This "unplanned experiment" manifested itself in instantaneous, significant changes in measured TPS surface temperatures at affected measurement locations. The phenomenon occurred to varying degrees on both STS-2 and STS-3. It was apparently the result of anomalous deposition of metallic oxides on portions of the lower surface TPS, due to oxidation of upstream acoustic sensor covers (ref. 7). Although occurrence of the phenomenon has been recognized in the literature (refs. 7-10), there has been little analysis of the qualitative information relative to catalytic/noncatalytic heat transfer which is embodied in the resulting data. This paper provides comparisons of the heat transfer to affected measurement locations from mission to mission and to contaminated versus noncontaminated surfaces. Discussion of the implications of these results should aid in assessment of the overall quality of data obtained from these and later flights and corresponding flight-data analyses.

SYMBOLS AND ACRONYMS

CSE	Catalytic Surface Effects
DFI	Development Flight Instrumentation
h	altitude
q	convective heat-transfer rate
q_{ref}	heat-transfer rate to the stagnation point of a 1-foot radius sphere
POPU	push-over/pull-up maneuver
RCG	reaction-cured glass
T	temperature
t	time from entry interface
TPS	thermal protection system
u	velocity
VxxTxxxx	DFI measurement identification number
X/L	nondimensional body length (L = 1295 inches)

α angle of attack

ρ density

FLIGHT DATA

Source

During the orbital flight test missions, the orbiter was equipped with an instrumentation system referred to as the Development Flight Instrumentation (DFI). The DFI was comprised of over 4500 sensors, associated data-handling electronics, and recorder, which provided data to enable post-flight certification of orbiter subsystems design. Included among the DFI were measurements of the aerodynamic surface temperature at 14 locations on the forward fuselage lower surface. These measurements were obtained from thermocouples mounted within the thermal protection system tiles, in thermal contact with the surface coating. (Temperature measurement locations are shown in figure 1, depicted by the planform of the TPS tile which contains the thermocouple.) DFI temperature data were recorded once each second throughout the time period of entry from Earth orbit. The measured surface temperature-time histories were used to determine the surface heat-transfer rates. DFI tape recorder malfunctions on missions STS-1 and STS-4 resulted in the loss of all thermal data during that portion of entry when the vehicle was not in communications contact with the ground. Therefore, no data were obtained at flight Mach numbers above approximately 14 on STS-1 or STS-4. On STS-5, the DFI measurement locations discussed in this paper were coated with the catalytic coating of the Catalytic Surface Effects experiment. Consequently, only data from missions STS-2 and STS-3 are considered herein.

Heat-Transfer Rate Determination

A one-dimensional, transient heat-conduction analysis (ref. 11) was used to determine the convective heating rate to each measurement location. The flight-measured surface temperature data provided a time-dependent boundary condition for the analysis, which assumes an initially uniform temperature throughout the thermal protection system materials. The analysis is a mathematically rigorous simulation of heat conduction within the thermal protection system, and reradiation from its surface, so as to provide a "benchmark" determination of the flight heat-transfer rates.

The reference heating rate used herein is that to the stagnation point of a 1-foot radius sphere in radiation equilibrium at the flight condition. The heat-transfer rate computation was made by the method of reference 12 using the Fay and Riddell (ref. 13) expression for the stagnation-point heat transfer.

Flight Environment Definition

Determination of the vehicle attitude and free-stream flight environment data used herein was accomplished through post-flight reconstruction of the orbiter entry trajectory and definition of the atmosphere along that trajectory at the time of entry. The trajectory reconstruction process (ref. 14) utilizes ground-tracking data and onboard measurements of orbiter inertial attitude, linear and angular accelerations, and angular rates to determine the vehicle's inertial position, velocity, and attitude throughout the entry. Definition of the atmosphere along the trajectory is accomplished (ref. 15) by combining atmospheric profile data obtained from soundings made on the day of entry with atmospheric modeling techniques to infer the free-stream atmospheric properties of pressure, temperature, density,* and winds at the time of entry. The results of the trajectory and atmospheric reconstruction processes are melded together to provide an analytically and physically consistent definition of the free-stream flight environment.

TEMPERATURE "JUMP" ANOMALY

The temperature history measured during STS-2 at the X/L = 0.194 location on the windward centerline (fig. 2) graphically illustrates the temperature "jump" anomaly observed at several locations on the windward centerline on both STS-2 and STS-3. The sudden "jump" in surface temperature was apparently caused by an instantaneous change in the catalytic efficiency of the TPS surface at this location which resulted in increased aerodynamic heat transfer. The change in surface catalytic efficiency apparently resulted from deposition on the surface of oxidation products from upstream, stainless-steel, acoustic sensor covers. Acoustic sensors were located in tiles at X/L = 0.106 and X/L = 0.204 (fig. 1). Post-flight vehicle inspection revealed the oxidation occurrence and deposition of oxidation products downstream of the acoustic sensors. Figure 3 shows the post-flight condition of the acoustic sensor located at X/L = 0.106 (fig. 3(a)), and the trail of contamination left on the downstream TPS surface (fig. 3(b)), after the STS-1 entry. It should be noted that although the surface contamination was observed after STS-1, the potential influence of this contamination on surface heat transfer was not recognized until the temperature "jump" anomaly was observed in the STS-2 data.

Scott and Derry (ref. 7) stated that the oxidation products were iron oxide and nickel oxide. They have postulated that the temperature of the sensor covers reached a value at which they "began to violently react with the oxygen in the flow. The oxide was then carried downstream and was deposited on the tiles. Since iron oxide and nickel oxide are highly catalytic to oxygen and nitrogen recombination, the coating caused increased heating on the contaminated tiles. The oxides may also have catalyzed atom recombination in the gas phase, as well, which would cause an increase in boundary-layer temperature."

---

*For STS-2, free-stream density was determined as described. For STS-3, however, in the altitude range from 185,000-250,000 feet, density data were determined using measured orbiter surface pressure data. Measured surface pressures near the orbiter nose were processed using the methods of reference 16 to derive free-stream dynamic pressure information. Density was then inferred using this dynamic pressure data and the velocity from the reconstructed trajectory.

Table I provides a reference summary of the tile surface condition and observed temperature anomaly response at each of the centerline measurement locations on STS-2 and STS-3. On STS-2, the temperature "jump" phenomenon was observed at centerline measurement locations at $0.194 \leq X/L \leq 0.402$. At the most aft of these locations ($X/L = 0.402$), the STS-2 temperature anomaly response was a temperature decrease as opposed to the increase observed at the other locations. This tile was catalytically coated as part of the CSE experiment. If surface contamination had caused a sudden increase in the catalytic efficiency of the TPS surface upstream of this location, as is suggested by the available evidence, a sudden depletion in the number of dissociated oxygen atoms reaching the location of the catalytic-coated tile would result. Therefore, with suddenly fewer oxygen atoms available for recombination, the sudden temperature decrease which was observed would be expected - not due to local surface contamination, but rather to the residual effect of upstream surface contamination. On STS-3, the temperature "jump" was only observed at the $X/L = 0.194$ and $X/L = 0.285$ measurement locations. Why the phenomenon was not observed at other locations is not fully understood, but it is thought to relate to a progressively increasing level of contamination with each flight. The temperature "jump" anomaly was not observed at locations not on the lower surface centerline.

ANALYSIS

STS-2/3 Trajectory Comparison

Before valid comparisons can be made between heat-transfer data for STS-2 and STS-3, one must understand the comparative relationship of the two entry trajectories. Velocity and atmospheric density data for the two entries are shown in figure 4 for the altitude range of interest for this paper. While density levels were similar for the two entries, the STS-3 entry velocity was slightly greater than for STS-2. Because of the higher entry velocity, the orbiter reached a particular flight condition earlier in time on STS-3 than STS-2. Consequently, time from entry interface is not considered to be an appropriate parameter for correlation of data for the two flights.

The reference heating rate (i.e., that to the stagnation point of a 1-foot radius sphere at the flight condition) variation as a function of altitude is shown in figure 5 for both entries. The reference heating rate levels are comparable at a given altitude, with the maximum difference between the STS-2 and STS-3 reference rates being less than 4 percent of the mean. Vehicle angle of attack was nominally constant at 40 degrees on both STS-2 and STS-3 over the altitude range of interest (fig. 5). Because of these relationships, heat-transfer data compared herein will be shown in dimensional form with STS-2/STS-3 comparisons made as functions of altitude.

Non-Contaminated Surfaces

In order to demonstrate the similarity of the heating environments on STS-2 and STS-3, heat transfer data for two locations which were not subject to contamination are shown in figure 6. The first location (fig. 6 (a)) is on the windward centerline at $X/L = 0.098$, just upstream of the more forward acoustic sensor. The second location (fig. 6 (b)) is at X/L = 0.297, but is 51 inches away from the centerline. For these locations, which were not subject to surface contamination, the levels of heat transfer experienced on STS-3 were approximately the same as were experienced on STS-2. (The small differences observed between the STS-2 and STS-3 heating rate levels are of the same magnitude as the uncertainty of the derived heating rates themselves.)

Contaminated Surfaces

On STS-3, the temperature "jump" anomaly was observed at only two measurement locations. At one of these locations, the aerodynamic surface was that of a baseline tile which had experienced previous entry exposures, and potential contamination, on STS-1 and STS-2. At the second location, the aerodynamic surface was that of a virgin tile with no prior entry exposure or possible contamination. This tile was part of the Tile Gap Heating experiment panel (ref. 17) which was replaced prior to each flight. Discussion of heat transfer to contaminated surfaces will focus on these two locations.

Multiple-Exposure Tile

Heat transfer data from the measurement location at X/L = 0.194 for both STS-2 and STS-3 are shown in figure 7. The tile at this location was "original equipment" and, therefore, subject to prior contamination. On STS-2, the occurrence of the contamination event resulted in a 40 percent step increase in heat transfer at this surface location. On STS-3, the increase was only 25 percent, but the underlying heating rate immediately before the contamination event was higher than for STS-2. Comparing the levels of heat transfer between STS-2 and STS-3 after the contamination events (altitude < 238,000 ft), the STS-3 heating rate level was approximately 18 percent greater than the STS-2 level. This implies a mission-to-mission progressive contamination of the TPS surface with an attendant increase in the surface catalytic efficiency at this location. It is also interesting to note that the STS-2 post-contamination data and STS-3 pre-contamination data (ostensibly equal levels of contamination) correlate well over the entire altitude range considered (fig. 8). It is unfortunate that there are no data from STS-4 to add to this comparison.

Virgin Tile

Heat-transfer data for the tile with no prior exposure history, X/L = 0.285, is shown in figure 9. On STS-2, the heat transfer increase resulting from the contamination event was 40 percent. On STS-3, the step increase was only about 17 percent, but the underlying heating rate immediately before the contamination event was higher than for STS-2. Note that after the contamination event (h < 238,000 ft), the heating rates to this surface were the same on both STS-2 and STS-3. The tile surface at this location was not subject to progressive contamination, as was the multi-mission tile, but was subject to single event contamination on two different entries. Equal levels of contamination would be expected on each entry and, therefore, equal levels of heat transfer following contamination, as are shown in figure 9.

Previously-Catalytic Surface

A somewhat different catalytic surface heating phenomenon has been observed in the flight data from the measurement at X/L = 0.166. The tile containing this measurement was coated on STS-2 with the high-catalytic-efficiency coating of the CSE experiment. Prior to STS-3, the tile was ostensibly cleaned of the coating so as to return the surface to the uncoated "baseline" condition. Data obtained from this measurement on STS-3, however, indicated that the tile surface, after cleaning, remained substantially more catalytic than baseline tile surfaces. This is clearly illustrated in figure 10 where the STS-3 data from this measurement are compared with data from those measurement locations just upstream and downstream of this tile. If the surface catalytic efficiencies at each of these locations were the same, the data from the X/L = 0.166 location would be expected to fall between the values obtained at the other two locations. However, the heat transfer rates observed at this location are always equal to or greater than those observed even at the more upstream location (X/L = 0.140), over the altitude range considered. Why the heating rate to the X/L = 0.166 location "peaks" as it does, at approximately 247,000 feet altitude, is not fully understood. However nonequilibrium viscous shock layer computations have indicated that maximum nonequilibrium effects on surface heat transfer would be expected to occur in this altitude range (refs. 18 and 9).

CONCLUSIONS

The foregoing discussion of the heat transfer results from STS-2 and STS-3 provides strong evidence that portions of the TPS surface on the lower centerline of the orbiter's forward fuselage have been contaminated with materials which have altered the catalytic efficiency of the TPS surface. Specific sources of contamination were the acoustic sensors and the catalytic overcoat of the CSE experiment. As a result, data obtained from affected measurements cannot be considered as "benchmark" data with which to attempt to characterize nonequilibrium heat transfer to the orbiter's lower surface centerline with baseline TPS. Even the first high altitude, high Mach number data obtained on STS-2 are probably biased by contamination which was experienced on STS-1.

Experience with the tile which was catalytically coated on STS-2 and "cleaned" prior to STS-3 indicates that once the coating material is applied and exposed to the entry environment, the catalytic efficiency of that tile surface is apparently permanently altered. The majority of the instrumented tiles on the lower surface centerline were catalytically coated on STS-4 and STS-5. It is, therefore, presumed that the catalytic efficiency of these tile surfaces has been irreversably altered.

Alas, during the orbital flight test missions of the orbiter, not one set of data was obtained for the lower surface centerline with a clean TPS surface of nominal baseline catalytic efficiency. Since the lower surface centerline is the one area which can be adequately modeled by nonequilibrium flow-field and boundary-layer codes, the lack of flight data on a surface of known and uniform thermochemical properties is a significant obstacle to any effort to determine catalytic efficiencies and surface recombination rates using flight data as a "benchmark."

It is proposed that serious consideration be given to replacement of all lower surface centerline tiles, at some future date, with new "virgin" tiles, and that substantially more of these tiles be instrumented. Such a retrofit would also eliminate the acoustic sensors and any other potential contamination source. Future flights with a "clean" lower surface centerline would provide the "benchmark" flight data required to characterize the orbiter's nonequilibrium heating environment--data which were anticipated from the orbital flight tests, but apparently never obtained.

REFERENCES

1. Lee, D. B., and Harthun, M. H.: Aerothermodynamic Entry Environment of the Space Shuttle Orbiter, AIAA Paper 82-0821, June 1982.

2. Rakich, J. V., and Lanfranco, M. J.: Numerical Computation of Space Shuttle Laminar Heating and Surface Streamlines, Journal of Spacecraft and Rockets, Vol. 14, No. 5, May 1977, pp. 265-272.

3. Scott, C. D.: Space Shuttle Laminar Heating with Finite Rate Catalytic Recombination, AIAA Paper 81-1144, June 1981.

4. Scott, C. D.: Catalytic Recombination of Nitrogen and Oxygen on High-Temperature Reusable Surface Insulation, AIAA Paper 80-1477, June 1980.

5. Stewart, D. A., Rakich, J. V., and Lanfranco, M. J.: Catalytic Surface Effects Experiment on the Space Shuttle, AIAA Paper 81-1143, June 1981.

6. Rakich, J. V., Stewart, D. A., and Lanfranco, M. J.: Results of a Flight Experiment on the Catalytic Efficiency of the Space Shuttle Heat Shield, AIAA Paper 82-0944, June 1982.

7. Scott, C. D., and Derry, S. M.: Catalytic Recombination and the Space Shuttle Heating, AIAA Paper 82-0841, June 1982.

8. Zoby, E. V.: Analysis of STS-2 Experimental Heating Rates and Transition Data, AIAA Paper 82-0822, June 1982.

9. Shinn, J. L., Moss, J. N., and Simmonds, A. L.: Viscous-Shock-Layer Heating Analysis for the Shuttle Windward Plane with Surface Finite Catalytic Recombination Rates, AIAA Paper 82-0842, June 1982.

10. Throckmorton, D. A., Hamilton, H. H., II, and Zoby, E. V.: Preliminary Analysis of STS-3 Entry Heat-Transfer Data for the Orbiter Windward Centerline, NASA TM-84500, June 1982.

11. Throckmorton, D. A.: Benchmark Determination of Shuttle Orbiter Entry Aerodynamic Heat-Transfer Data. Journal of Spacecraft and Rockets, Vol. 20, No. 3, May-June 1983.

12. Hamilton, H. H., II: Approximate Method of Calculating Heating Rates at General Three-dimensional Stagnation Points During Atmospheric Entry. NASA TM-84580, November 1982.

13. Fay, J. A., and Riddell, F. R.: Theory of Stagnation Point Heat Transfer in Dissociated Air, Journal of the Aeronautical Sciences, Vol. 25, February 1958, pp. 73-85, 121.

14. Compton, H. R., Findlay, J. T., Kelly, G. M., and Heck, M. L.: Shuttle (STS-1) Entry Trajectory Reconstruction, AIAA Paper 81-2459, November 1981.

15. Price, J. M.: Atmospheric Definition for Shuttle Aerothermodynamic Investigations, Journal of Spacecraft and Rockets, Vol. 20, No. 2, March-April 1983.

16. Siemers, P. M., III, Wolfe, H., and Flanagan, P. F.: Shuttle Entry Air Data System Concepts Applied to Space Shuttle Orbiter Flight Pressure Data to Determine Air Data - STS-1-4, AIAA Paper 83-0118, January 1983.

17. Pitts, W. C.: Flight Measurements of Tile Gap Heating on the Space Shuttle, AIAA Paper 82-0840, June 1982.

18. Gupta, R. N., Moss, J. N., Simmonds, A. L., Shinn, J. L., and Zoby, E. V.: Space Shuttle Heating Analysis with Variation in Angle of Attack and Surface Condition, AIAA Paper 83-0486, January 1983.

TABLE I

MEASUREMENT	X/L	STS-2		STS-3	
		TILE SURFACE CONDITION	TEMPERATURE ANOMALY RESPONSE	TILE SURFACE CONDITION	TEMPERATURE ANOMALY RESPONSE
V09T9341	0.025				
V07T9452	.098				
ACOUSTIC	.106				
V07T9462	.140				
V07T9463	.166	Catalytic			
V07T9464	.194		Discontinuous increase		Discontinuous increase
ACOUSTIC	.204				
V09T9381	.255		Discontinuous increase		
V09T9421	.285	Virgin tile	Discontinuous increase	Virgin tile	Discontinuous increase
V07T9468	.297		Discontinuous increase	Catalytic	
V07T9471	.402	Catalytic	Discontinuous decrease	Catalytic	
V09T9521	.497				

ORIGINAL PAGE IS
OF POOR QUALITY

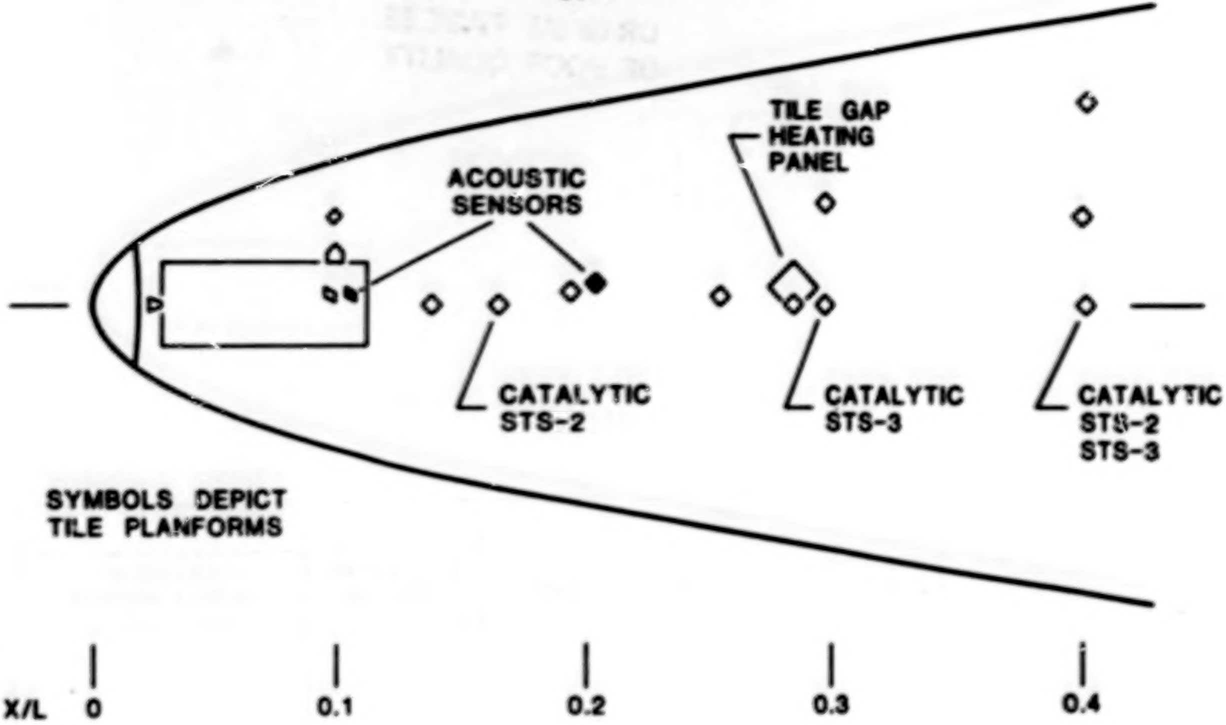
ACOUSTIC
SENSORS
TILE GAP
HEATING
PANEL
CATALYTIC
STS-2
CATALYTIC
STS-3
CATALYTIC
STS-2
STS-3
SYMBOLS DEPICT
TILE PLANFORMS
X/L
0
0.1
0.2
0.3
0.4

Figure 1.- Forward fuselage lower surface temperature measurements.

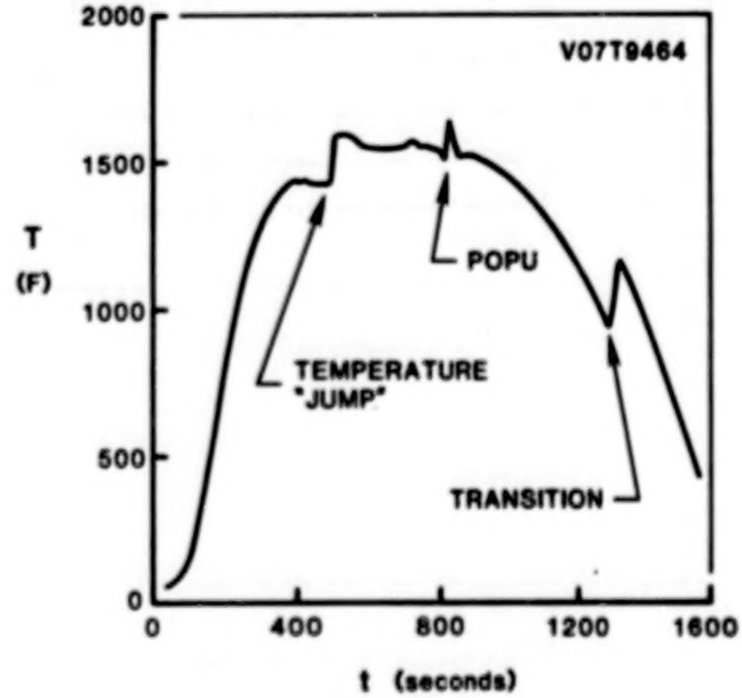

Figure 2.- STS-2 temperature-time history at X/L = 0.194.

(a) Acoustic sensor at X/L = 0.106.

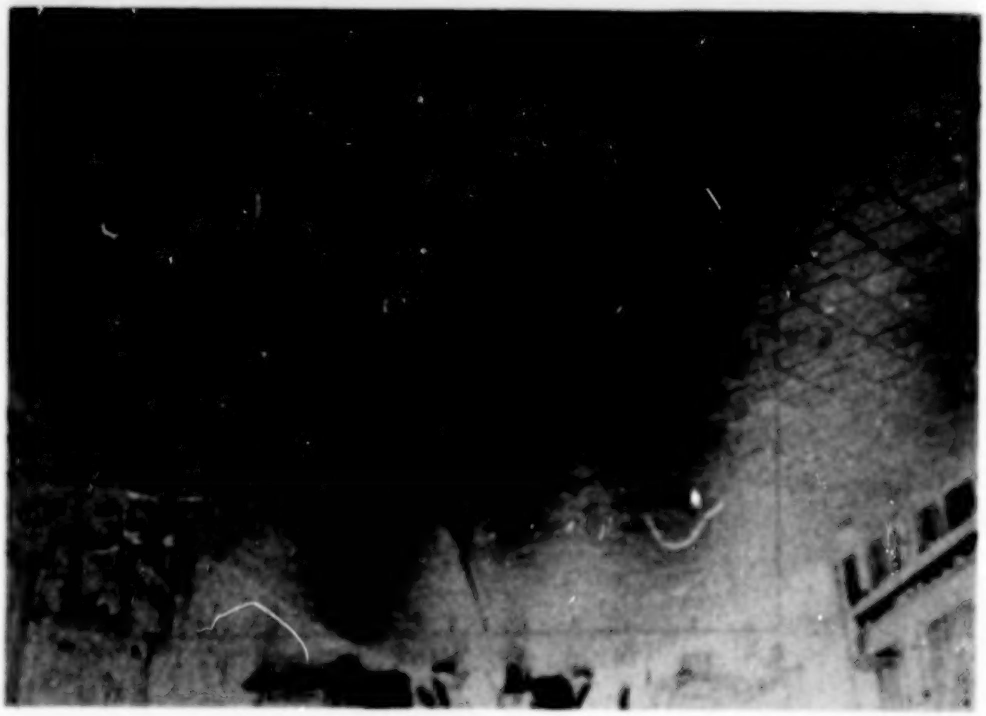

(b) Orbiter lower surface, looking forward.

Figure 3.- STS-1 TPS surface contamination emanating from acoustic sensor.

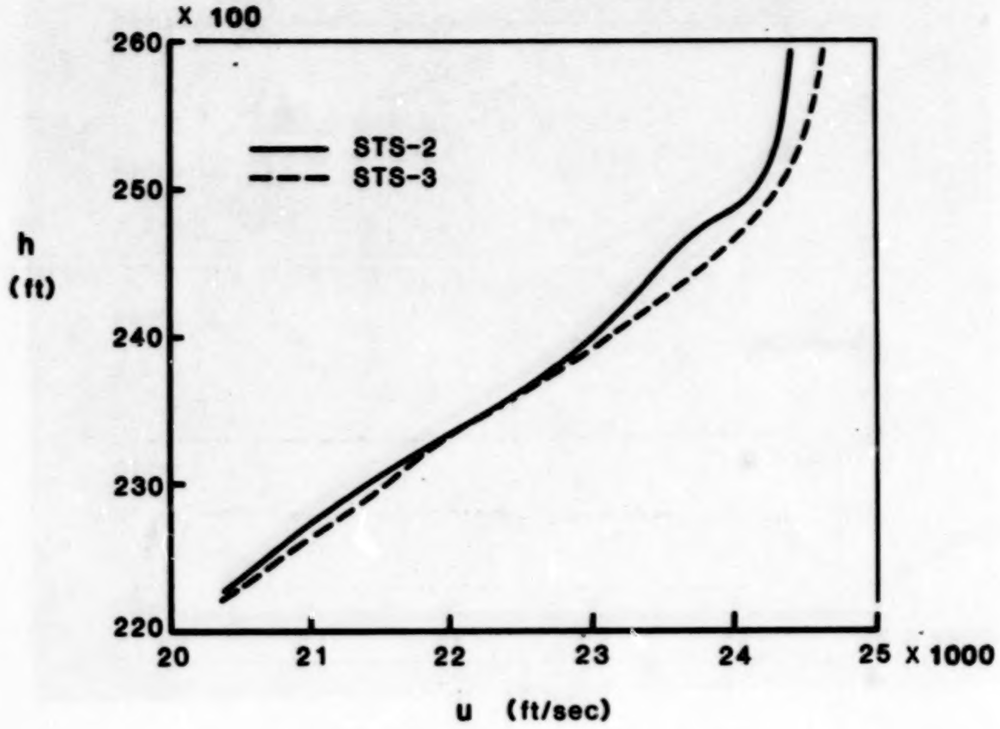

(a) Velocity-altitude.

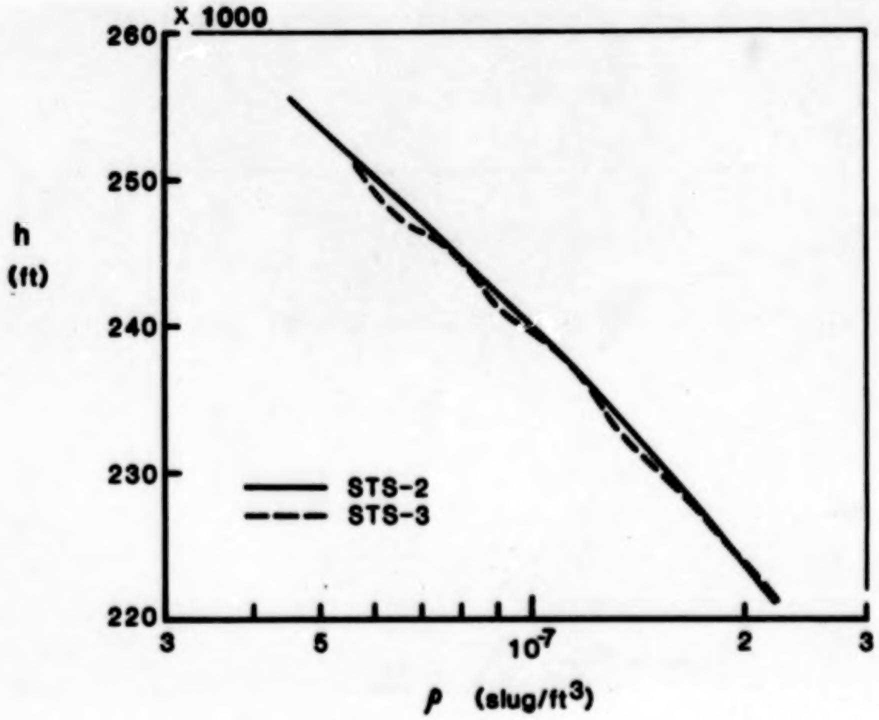

(b) Density-altitude.

Figure 4.- STS-2/STS-3 entry trajectory comparison.

ORIGINAL PAGE IS
OF POOR QUALITY

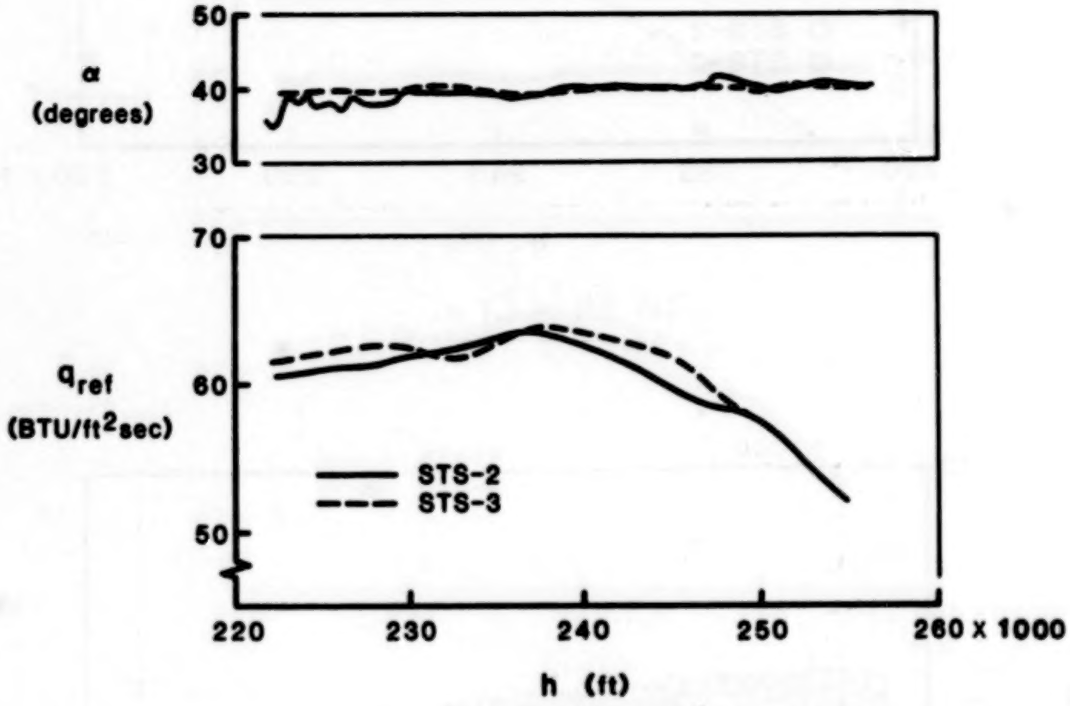

Figure 5.- STS-2/STS-3 angle of attack and reference heating rate comparisons.

ORIGINAL PAGE IS
OF POOR QUALITY

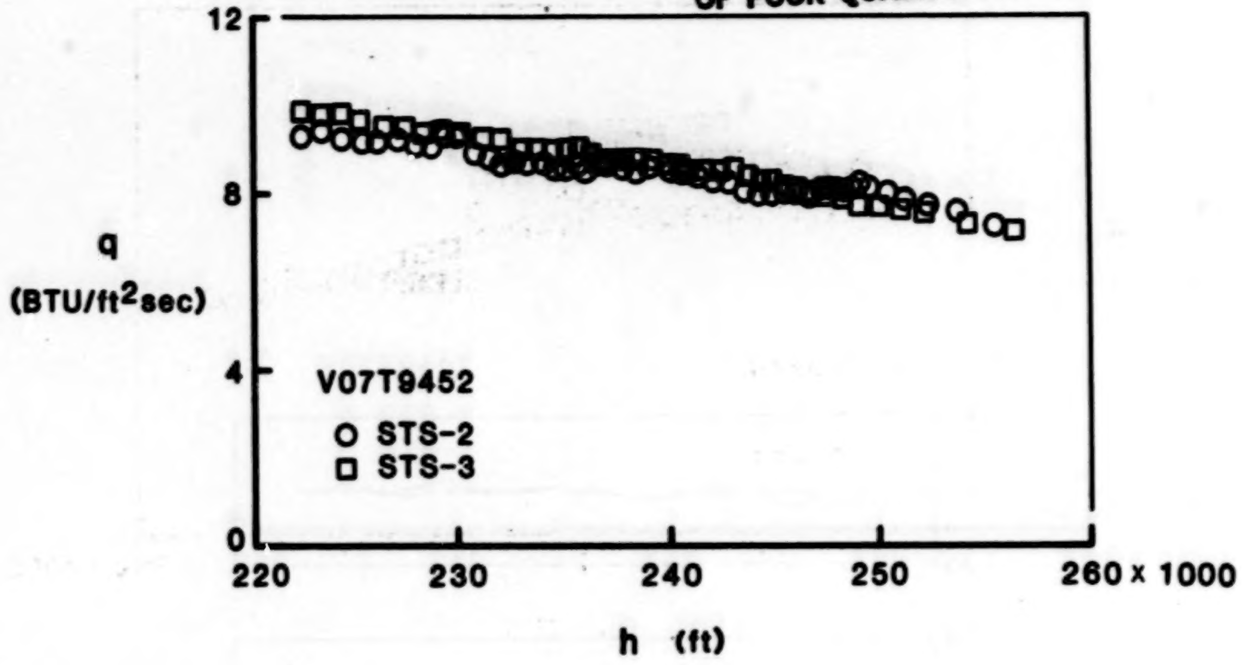

(a) X/L = 0.098.

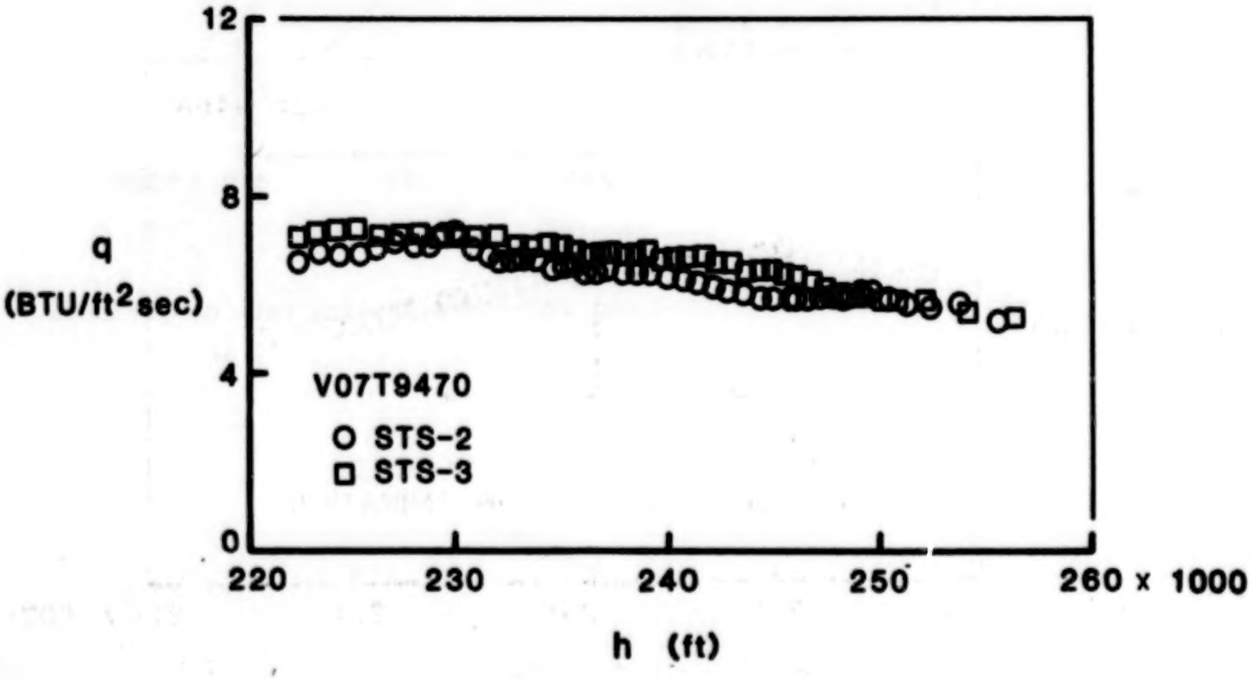

(b) X/L = 0.297, off centerline.

Figure 6.- Heat transfer to noncontaminated surfaces.

ORIGINAL PAGE IS
OF POOR QUALITY

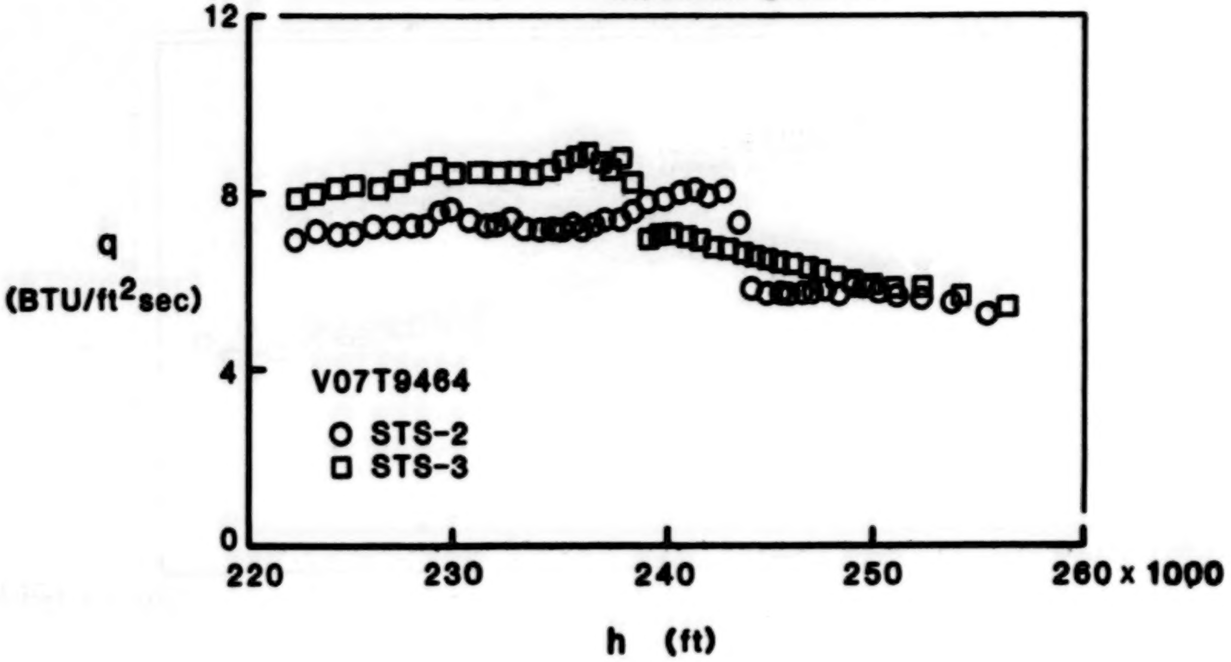

Figure 7.- Heat transfer to "multiple-exposure" tile, X/L = 0.194.

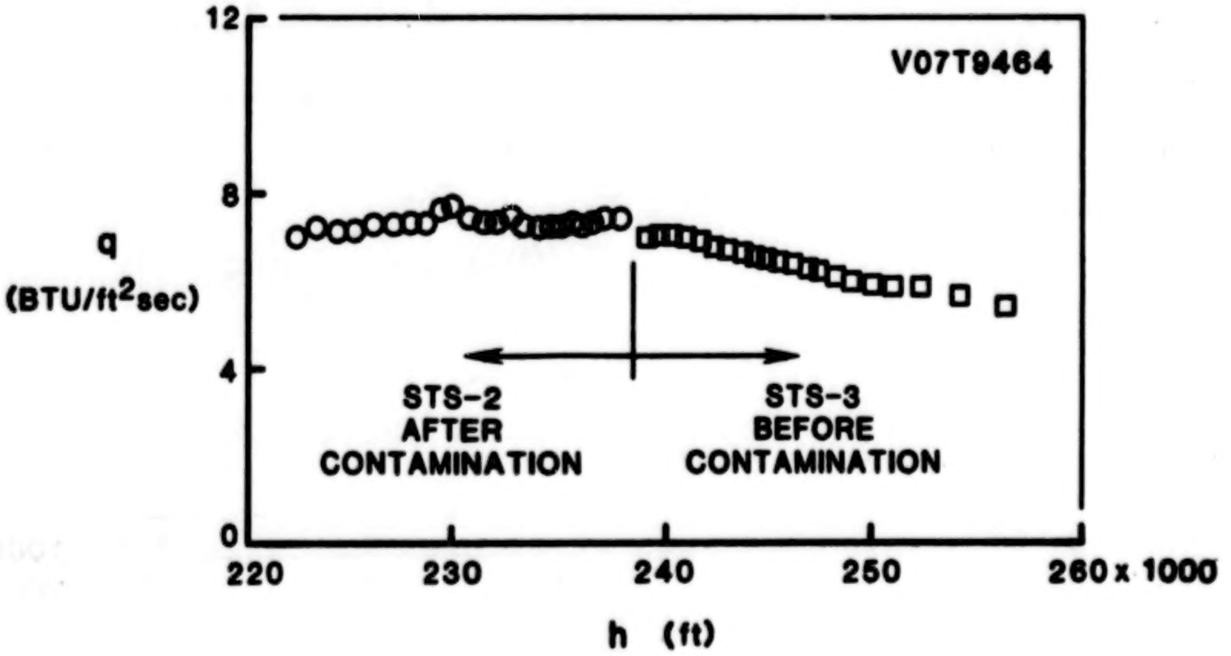

Figure 8.- Heat transfer to "multiple-exposure" tile, X/L = 0.194.

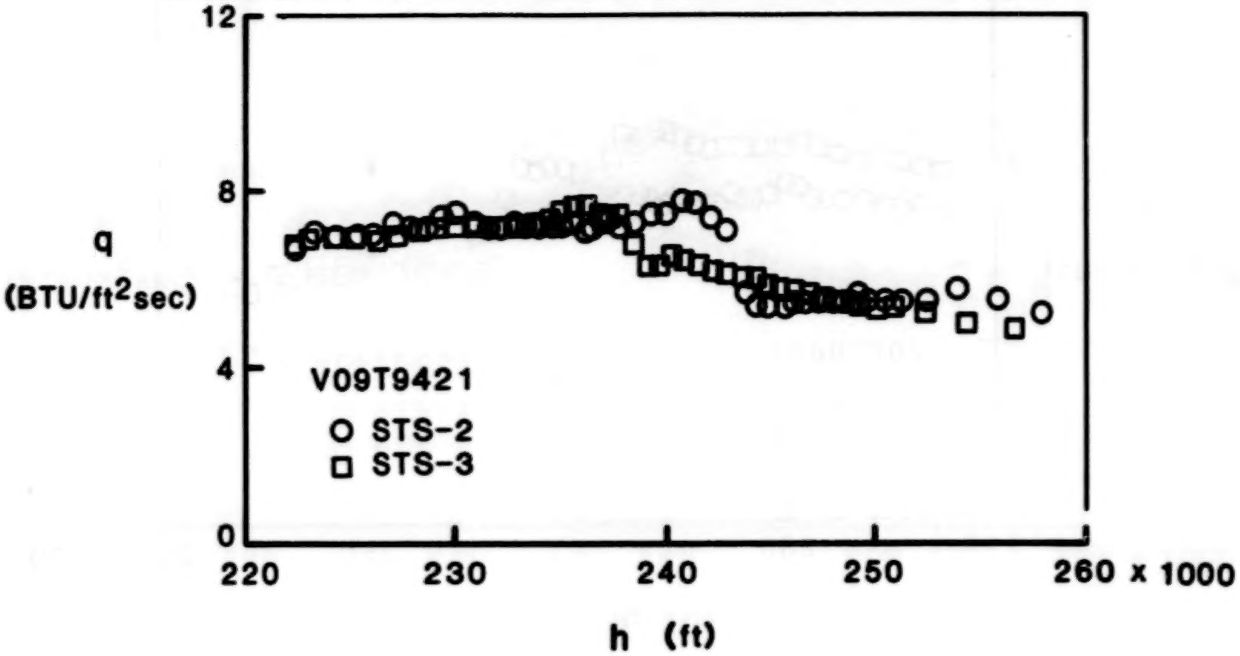

Figure 9.- Heat transfer to "virgin" tile, X/L = 0.285.

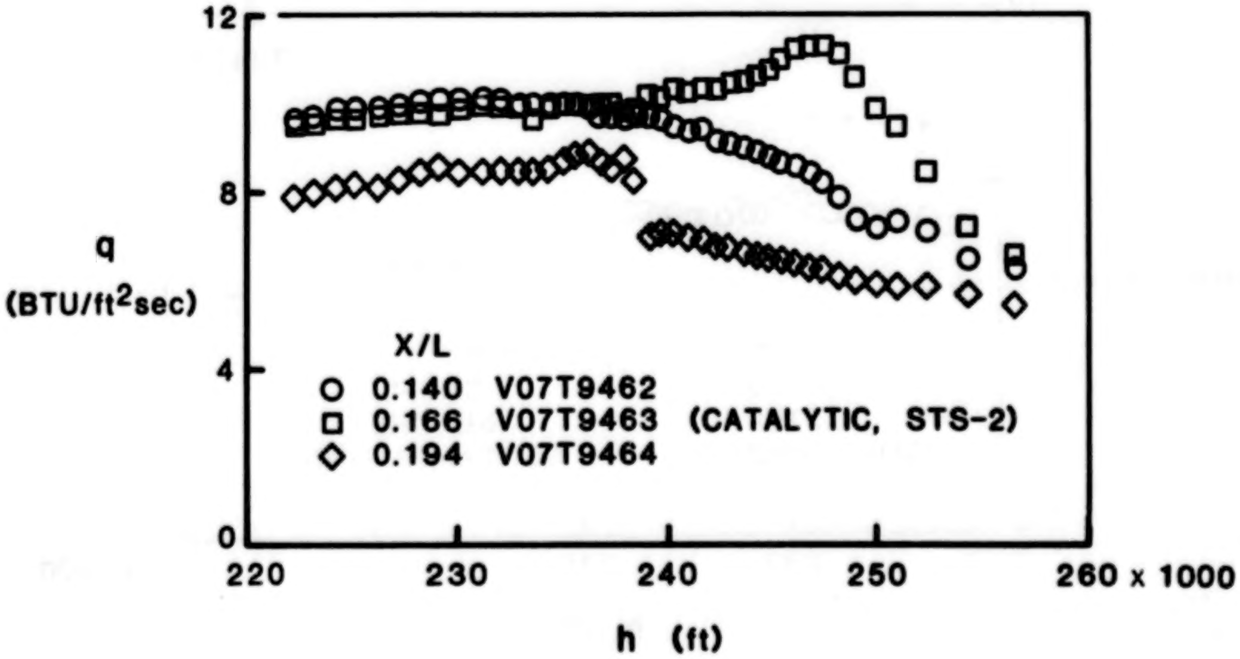

Figure 10.- Heat transfer to "previously-catalytic" tile, X/L = 0.166.

N84
10154

UNCLAS

N84 10154 D10

A REVIEW OF NONEQUILIBRIUM EFFECTS AND SURFACE CATALYSIS ON SHUTTLE HEATING

Carl D. Scott
NASA Johnson Space Center
Houston, Texas

SUMMARY

This paper is a review of the nonequilibrium calculation techniques developed by various authors over the past decade to predict heat fluxes to the windward side of the Space Shuttle orbiter. The results of these techniques are compared with measurements made on the first few flights of the Space Shuttle. The calculations attempt to account for finite rate chemistry in the shock layer around the vehicle and for finite rate catalytic atom recombination on the thermal protection materials. The techniques considered are the axisymmetric viscous shock layer method, three-dimensional (3-D) reacting Euler equation solutions coupled with axisymmetric analog boundary layer method, and a recently developed nonequilibrium 3-D viscous shock layer method.

The comparisons indicate a substantial influence of nonequilibrium chemistry on the heating to the relatively noncatalytic thermal protection tiles of the orbiter. That is, the heat flux is much lower than if the flow were in equilibrium or the tiles were fully catalytic. It is shown that all of the methods agree with the measurements within about 10 to 30%, depending on the location, flight condition, and assumption about the catalytic recombination coefficients. None of the calculations could predict the measurements uniformly over the entire windward centerline for all flight conditions. (Until now the 3-D viscous shock layer calculations have only treated the noncatalytic wall.)

It is noted that for a given flight condition the temperature measured on the orbiter tended to increase from the second flight to the fifth flight. The cause of this increase is not known, but it may be due to contamination of the surface, causing an increase in catalycity, or to a decrease in emittance.

Nitrogen recombination was found to be significant early in the entry especially in areas dominated by normal shock flow such as near the nose. This makes knowing the nitrogen recombination phenomena important. Such phenomena will be of more importance on an aerobraking orbital transfer vehicle which enters the atmosphere at higher velocities.

It is concluded that the nonequilibrium methodologies have significantly enchanced the capability to predict the heat flux for high altitude reentry, but some improvements are still required to improve the current accuracy.

SYMBOLS

ALT	altitude
C	atom mass fraction
f	heat flux adjustment factors defined in eq. (2)
h_T	total enthalpy
k	Boltzmann constant
k_w	catalytic recombination speed
L	length of vehicle
m	mass of atom
P	pressure
q	heat flux
T	temperature
V	velocity
VINF	freestream velocity
X	axial distance from nose
Z	geometric altitude

Greek Symbols

ϵ	emittance
γ	energy transfer catalytic combination coefficient

Subscripts

FC	fully catalytic
N	nitrogen
O	oxygen
w	wall
∞	freestream
ref	reference condition or property

INTRODUCTION

The Space Shuttle orbiter is a hypersonic glide reentry vehicle that spends much of its entry time at relatively tenuous altitudes in which chemical nonequilibrium predominates in the shock layer. Calculations have shown that both dissociation nonequilibrium[1,2] and recombination nonequilibrium exist[1]. The dissociated nonequilibrium exists in the inviscid layer and the recombination nonequilibrium exists in the boundary layer. Verification of these phenomena has not been directly obtained; however, these phenomena are inferred by comparing heat transfer measurements with the reacting flowfield results.

Although measurements of surface temperatures on the high temperature reusable surface insulation (HRSI) tiles have been made at numerous locations on the orbiter, this paper only addresses measurements on or near the windward centerline of the lower fuselage because predictions of local flow conditions are much easier to obtain in this region. The presence of chemical nonequilibrium was made easier to verify because the HRSI tile glass coating (RCG) is relatively noncatalytic with respect to atom recombination and the associated dissociation energy accommodation. Also of great importance in demonstrating the nonequilibrium flow behavior is the catalytic surface effects orbiter flight experiment of Stewart, Rakich, and Lanfranco[3], whose initial results were reported in reference 4. Prior to the flight experiments, predictions of the noncatalytic nature were reported in references 1, 2, and 3 based on flowfield computations and arc jet experiments. Besides the results reported in reference 4 other calculations have been made for the RCG coated tiles and compared with flight measurements. Scott and Derry[5] used the reacting flowfield/boundary layer method of reference 2 with measured energy transfer catalytic recombination coefficients of reference 6 and compared those predictions with flight measurements. Likewise, Shinn, Moss, and Simmonds[7] computed heat fluxes using an axisymmetric reacting viscous shock layer code with the recombination coefficients of reference 6 and showed better agreement with flight measurements. Recently Kim, Swaminathan and Lewis[8] solved the 3-D viscous shock layer equations for the Shuttle geometry, and obtained encouraging results.

This paper critically evaluates the various flowfield predictions, comparing the results of equilibrium and nonequilibrium flowfields coupled with reacting axisymmetric analog boundary layer solutions and the results of viscous shock layer solutions with flight temperature/heat flux measurements near the windward centerline for the Shuttle flights STS-2, 3, and 5.

In the comparisons with flight heat flux measurements there is concern with two basic aspects of the predictions, the flowfield methodology and the surface catalytic recombination phenomena. The first aspect can be subdivided into dynamical and geometrical characteristics, and thermophysical properties and gas phase chemical reaction kinetics. The second aspect can be subdivided into wall recombination rates of the basic thermal protection material, contamination issues, and knowledge gained from the catalytic surface effects experiment. All of these aspects are interrelated and the Shuttle flight does not provide an experiment in which each aspect can be controlled independently. Numerical simulation is capable of single parameter variation, but confirmation of the results is difficult because of flight complexities and unknowns; particularly, there is no measurement of the chemical composition of the flow. This paper considers flowfield chemical composition effects (equilibrium vs nonequilibrium), methods of solution (two-layer approaches and viscous shock layer approaches), and surface catalytic recombination rates, and it touches on possible contamination on the surface. The issues of incomplete chemical energy accommodation of catalytically-formed excited species and subsequent quenching are not explored.

COMPUTATIONAL METHODS AND THEIR APPLICATION

Five computational methods are considered here which are subdivided into applications of those methods, which are further subdivided into particular cases. These cases are summarized in Table 1.

The first two methods are axisymmetric viscous shock layer methods of Moss[9] and Miner and Lewis[10]. The next two are two-layer approaches. Rakich and Lanfranco[2] treated the 3-D reacting inviscid flowfield and used the results for reacting boundary layer edge conditions. Goodrich et al.[11] solved the equilibrium

3-D inviscid case and used their results as edge conditions for equilibrium boundary layer solutions. The fifth method is the 3-D nonequilibrium viscous shock layer method of Kim, Swaminathan and Lewis[8].

Shinn, Moss and Simmonds[7] applied the Moss[9] method with variable wall recombination coefficients to the Shuttle orbiter by approximating the Shuttle geometry with hyperboloids of revolution fitted by Zoby[12]. They presented cases for various times in the orbiter entry and concluded the following. The Shuttle flight data indicates the shock layer flow is appreciably in nonequilibrium down to an altitude of 50 km. Scott's extrapolated recombination rates[6] used in their viscous shock layer calculations result in good agreement with flight data forward, but not aft, on the vehicle. Better agreement aft is obtained if k_{wO} = 100 cm/sec is used. The temperature of the surface during entry is 80 to 200 K less than if it were fully catalytic.

Gupta, Moss, Simmonds and Shinn[13] similarly applied the Moss[9] method with various recombination coefficients and for a range of angle of attack of the orbiter. They found that a ±5° variation in angle of attack does not affect the nonequilibrium heating appreciably at 75 and at 48 km altitudes. The temperature dependence of the oxygen recombination rate is not as steep as an extrapolation of Scott's[6] data indicates. They concluded that a value of k_{wO} = 200 cm/sec seems to yield better agreement with the flight measurement of heat flux at certain locations and flight regimes. A 49% reduction in heating due to nonequilibrium effects was noted in the nose region at X/L = 0.025 and 75 km altitude. Nonequilibrium effects on the heating are not significant below about 65 km even though the flow may not be in equilibrium, indicating that equilibrium boundary layer methods or heating correlations of the type suggested by Rakich et al.[4] may be useful.

The method of Rakich and Lanfranco[2] was applied by Rakich, Stewart and Lanfranco[4] to calibrate the results of an approximate method that uses equilibrium normal shock isentropic boundary layer edge conditions in lieu of the reacting variable entropy edge conditions. This approximate method was then used to infer k_{wO} of the reaction cured glass (RCG)-coated high temperature reusable surface insulation (HRSI) tiles and to infer k_{wO} of the iron-cobalt-chromia spinel (C742) coating used in the catalytic surface effects flight experiment tiles. They inferred that k_{wO} = 80 cm/sec and assumed that $k_{wN} = 0.3\ k_{wO}$ for RCG at T_w of about 1100 K. Their catalytic surface effects experiment demonstrated that the flow is indeed in chemical nonequilibrium. Rakich's method was also used by Scott[5] with temperature dependent recombination coefficients inferred from arc jet measurements.[6,14] He used the reacting boundary layer code BLIMPK developed by Bartlett and Kendall[15] and extended by Tong, Buckingham and Morse[16]. This method resulted in higher heating than measured on the nose of the orbiter, but tended to predict or underpredict the heating on the midbody. These results are presented here for comparison with other results.

Reacting boundary layer calculations were made with equilibrium edge conditions provided by Goodrich et al.[11] along with different wall recombination assumptions. These results are presented here.

Miner and Lewis[10] axisymmetric, reacting viscous shock-layer code was applied with various catalytic wall assumptions and those results are likewise presented here.

The fifth computational method considered herein for nonequilibrium flow calculations applied to the Space Shuttle was presented by Kim, Swaminathan and Lewis[8]. That recent paper addressed the windward side of the Space Shuttle, applying the 3-D nonequilibrium shock layer method with noncatalytic boundary conditions. Their windward centerline results for two points in the STS-2 trajectory are presented here.

MEASUREMENTS OF HEAT FLUX TO SHUTTLE

Surface temperature measurements of several instrumented HRSI tiles, distributed along the lower surface of the orbiter, are considered in this paper. The flights considered are STS-2, 3, and to a limited extent STS-5. Trajectory information was obtained from acceleration measurements on the orbiter and from atmosphere models calibrated by atmospheric soundings. The resulting best estimated trajectories (BET) were obtained from the Johnson Space Center, Mission Planning and Analysis Division. Heat fluxes were inferred from the measured temperatures by computing the corrected radiation equilibrium heat flux

$$q = 1.06\varepsilon\, \sigma T_w^4\, f \qquad (1)$$

The factor 1.06 accounts for the fact that the thermocouples lie about 0.38 mm beneath the surface coating and for conduction in the tile. This factor was obtained from the method of Williams and Curry[17] who inferred heat fluxes from temperatures using an inverse thermal math model formulation*. Over the range of time in the trajectory and temperatures considered in this paper, a correction factor of 1.06 is accurate to within 2 or 3 percent.

When comparing the measurements of one flight with another or when comparing calculations with measurements it is necessary to adjust the heat fluxes to account for differences in freestream conditions. Since the hypersonic stagnation point heating is approximately proportional to $(\rho/\rho_{ref})^{1/2}\,(V/V_{ref})^3$ all points were corrected by the ratio of that factor for the two freestream conditions, i.e.,

$$f = (\rho_\infty / \rho_{\infty ref})^{1/2}\,(V_\infty/V_{\infty ref})^3 \qquad (2)$$

The flight BET and the flight heating rates are used as reference conditions when flight measurements are compared with calculations. The heat fluxes are then presented in absolute units as obtained from equation (1). The factor f is probably accurate to within ±3% as verified by a comparison of calculations using the Miner and Lewis[10] code. All the comparisons were made for an angle of attack of about 40 degrees.

To determine the consistency from flight to flight the bottom centerline heat flux measurements for STS-2, 3, and 5 are compared at three different times in the flights as shown in Figures 1, 2, and 3, respectively. The corresponding freestream conditions are given in Table 2. It is seen that the flight-to-flight repeatability is about 15-30% and the standard deviation about the mean at each X/L is about ±10%. The STS-2 heat fluxes are consistently lower than the other two flights at almost all locations. The reason for this is not understood, but it may be related to a change in catalycity resulting from contamination of the surface or to a change in emittance. The heating rate correction for these cases is no larger than 5% as seen in Table 2. The measurement at $X/L = 0.695$ seems anomalously low and therefore, it may be a bad measurement. The rather large discrepancy in the measurement for STS-2 compared with the other two flights at $X/L = 0.14$ also is not understood.

---

* The author is grateful to S. D. Williams of Lockheed Engineering and Management Services, Co. for calculating the heat flux for this determination.

SHUTTLE CENTERLINE PRESSURES

Pressure measurements during the time of high heating on the orbiter were obtained only during STS-3 and 5. These measurements normalized by $\rho_\infty V_\infty^2$ are presented in figure 4 along with values calculated by three methods. It is seen that the flight-to-flight repeatability is very good at almost all locations. The pressure decreases very rapidly in the forward 10% of the vehicle then remains almost constant from X/L of 0.1 to 0.4, rising slightly at $X/L = 0.8$. The 3-D flowfield calculations of Rakich and Lanfranco[2] and Goodrich et al.[11] agree with the measurements within about 5% except in the vicinity of $X/L = 0.1$ where the calculations are about 23% higher than the measurements. Likewise, the calculations using the Miner and Lewis[10] code agree within about 5% except at $X/L = 0.1$, where the agreement is within about 9%. The large discrepancy at $X/L = 0.1$ may result from an experimental error due to a negative bias of unknown amount[18]. The instrumentation and signal processing of the pressure measurements only result in positive readings. The existence of a negative bias was indicated by a measurement that did not exceed zero until a time later than expected for the flight condition. See reference 18. If the error associated with the negative bias is small, then the calculations appear to be in error at $X/L = 0.1$. Although a direct comparison of the geometries has not been made, it is possible that the geometry descriptions in the flowfield codes do not adequately describe the vehicle as actually built; otherwise these codes do not adequately handle the rapid expansion around the nose, overpredicting the pressure (and heat flux) near $X/L = 0.1$.

HEAT FLUX COMPARISONS

In the following comparisons the author has used the results of others and in some cases has used the method of others to make present calculations. In these cases the author is responsible for any error or misapplication of the method, not the developers of the methods.

Equilibrium and Nonequilibrium - Two Layer Methods

It has been shown in the past that the heat flux predicted by equilibrium calculations and by reacting calculations with a fully catalytic wall are approximately equal. To verify this for the two boundary layer methods cosidered here comparisons are made between equilibrium results of Goodrich et al.[11] and the results obtained using the Rakich and Lanfranco[2] method. The freestream conditions are given in Table 3. In figure 5 the Goodrich equilibrium prediction is compared with two nonequilibrium boundary layer cases with fully catalytic walls. (Fully catalytic here means $\gamma_O = \gamma_N = 1$, vis-a-vis $k_w = \infty$ or $C_{O_w} = C_{N_w} = 0$.) The edge conditions in the latter two cases are Goodrich equilibrium and Rakich and Lanfranco nonequilibrium. Given the same edge conditions it is seen that the equilibrium boundary layer calculation is about 15% lower than the all-nonequilibrium calculation over the entire length of the vehicle. Evidently, the transport of chemical energy by diffusion is more efficient in this case than via conversion of chemical energy to thermal energy which is then transported to the wall via conduction. The opposite result was obtained by Shinn et al.[7] who found the equilibrium viscous shock layer resulted in higher heating than the equilibrium catalytic wall nonequilibrium case.

The comparison of the reacting boundary layer with equilibrium edge conditions versus reacting edge conditions indicates that on the nose there is very little difference between the two cases, whereas on the midfuselage the nonequilibrium edge conditions results in about 15% lower heating. The nonequilibrium edge case with a fully catalytic wall is very close to the all equlibrium calculation aft of $X/L = 0.2$. The latter agreement does not stem from the flow approaching equilibrium downstream because the equilibrium nitrogen atom concentration both at the edge and in boundary layer is greater than the nonequilibrium concentration by a factor of about 1.3 in this case. Moreover, it was shown in reference 1 that the boundary layer is virtually frozen.

A comparison of the axisymmetric reacting viscous shock layer method of Miner and Lewis[10] and the reacting two-layer approach of Rakich and Lanfranco[2] is made in figure 6 where the nonequilibrium boundary layer result for a fully catalytic wall lies above the viscous shock layer results by about 20% on the nose. Agreement improves to within about 11% at $X/L = 0.55$. The effect of edge conditions is about 10% or less everywhere for a fully catalytic wall. The results for a noncatalytic wall are given in figure 7 where it is seen that the boundary layer heat flux is about 30% greater than the viscous shock layer heating on the nose, but improves to about 10% at $X/L = 0.55$. Agreement of the reacting viscous shock layer results and the reacting boundary layer with equilibrium edge conditions is within about 10% everywhere along the body. The equilibrium edge condition results fall below the nonequilibrium results on the nose, but they are very close farther aft.

Attention is now turned to a comparison of the axisymmetric viscous shock layer method of Moss[9] as applied by Shinn et al.[7], and the two-layer method of Rakich and Lanfranco[2] applied here for a lower velocity and altitude situation. It is seen in figure 8a that the axisymmetric nonequilibrium viscous shock-layer with equilibrium catalytic wall (ECW) and the equilibrium viscous shock layer agree quite well (within about 5%). They also agree quite well with the Goodrich[11] equilibrium two-layer result. It is seen that the fully catalytic nonequilibrium two-layer results are greater by about 10-20% which is the same as noted for case 1. Agreement in figure 8b for the noncatalytic case is worse than the two-layer results, being about 20-40% higher than the axisymmetric viscous shock layer results of Shinn et al.[7] and present results using the Miner and Lewis[10] code. The latter results seem to indicate that heat transfer by atom diffusion is more important in the viscous shock layer. This is consistent with the somewhat higher degree of dissociation, especially the nitrogen, associated with the viscous shock layer calculation. The reason for the differences in atom fraction in the two methods is not understood since the reaction rates used in both methods were essentially the same.

The recent 3-D nonequilibrium viscous shock layer results with a noncatalytic wall are also given in figure 8b. The heat flux at $X/L = 0.1$ is closer to the axisymmetric VSL results, but does not decrease as rapidly downstream. In fact, the 3-D results are higher than the two-layer results aft of $X/L = 0.2$. The chemical reaction model[19] in all the methods is virtually the same, (except ions are neglected in the Rakich and Lanfranco method). Therefore, the differences seen are most likely due to differences in the computational method or the geometry.

Comparison of Measured and Calculated Heat Flux

Attention is now turned toward a comparison of the calculated heat flux and the measured values along the lower surface centerline. The comparison is at two times in each of two flights. The particular times were selected to match the velocity and density as closely as practicable to the conditions used in the boundary layer predictions for cases 460 and 650 in Table 3. It was not possible to simultaneously match both velocity and density. The resulting heat fluxes were adjusted for the mismatch by the factor f of equation (2). As mentioned earlier the measured heat fluxes were inferred from the measured temperatures using equation (1) where $\varepsilon = 0.85$.

Several choices of catalytic recombination coefficients were used as wall boundary conditions for the two layer and the axisymmetric shock layer calculations. The energy transfer catalytic recombination coefficients for nitrogen and oxygen recombination on the RCG tile coating are presented in figures 9 and 10, respectively. The coefficients presented are those found in references 6, 7, and 12. In those cases where a catalytic speed k_w was given the recombination coefficient is plotted as a dashed line, the length of which indicates the temperature range over which k_w was used, where

$$q = k_w \sqrt{2\pi m/kT}$$

It is seen in figure 9 that the inferred values of k_{wN} of reference 4 are 0.1 to 0.2 times the values of reference 6. This lack of agreement is not surprising since kw_N was assumed to be 0.3 times k_{wO} in reference 4. The values of k_{wO} (see figure 10) of references 4 and 6 agree within experimental accuracy at the higher temperature range. At lower temperatures $k_{wO} = 80$ cm/sec is about a factor of 1.5 to 8 higher than the extrapolation of reference 6, depending on temperature.

Extrapolating to such a low temperature could be inaccurate, but the extrapolation is generally consistent with other recombination measurements (see figure 6 of reference 4). Since the temperatures measured on the Shuttle fell mostly in the lower temperature range 900-1100 K, the predictions of heat flux using the $k_{wO} = 80$ cm/sec would result in higher heating except on the nose or earlier in time where the nitrogen carries a larger part of the dissociation energy.

A comparison is made in figures 11-14 between the measurements and several calculations for STS-2 and 3 at two times in the trajectories. The measurements are near the bottom centerline of the vehicle except for a few points that are about 1.3 m off the centerline. This comparison between the calculations and the measurements is typical for all times and both flights. In the higher altitude cases (figures 11 and 13) the viscous shock layer methods with the temperature dependent values[6] of γ_O and γ_N yield better agreement for $X/L < 0.3$. The two layer method with $k_{wO} = 80$ cm/sec also agrees with the measurements at $X/L > 0.5$. At the lower altitude (figures 12 and 14) the two-layer methods yield better agreement for $X/L > 0.2$.

In the higher altitude cases (figures 11 and 13), the nonequilibrium axisymmetric viscous shock layer methods with the temperature dependent γ_O and γ_N, yield good agreement at $X/L < 0.3$ and the nonequilibrium two layer method with k_{wO} = 80 cm/sec and k_{wN} = 24 cm/sec yields good agreement for $X/L < 0.5$. For the lower altitude case this two-layer approach yields better agreement for $X/L > 0.2$ than the axisymmetric viscous shock layer methods. The nonequilibrium two-layer method using temperature dependent γ_O and γ_N results are about 30% higher than the measurements on the nose area for all cases presented here, but the agreement improves toward the mid-vehicle and at lower altitude. It is apparent that the two-layer approach predicts higher heat fluxes for given wall boundary conditions than the viscous shock layer approaches. This may be due in part to the VSL having a slightly higher level of dissociation as well as to differences in the flowfield dynamics.

In comparing the 3-D nonequilibrium calculations of Kim, Swaminathan and Lewis[8] with other noncatalytic predictions, one sees that the heat flux does not decrease as rapidly down the vehicle as do the axisymmetric viscous shock layer calculations and the two layer calculations. This indicates a possible influence of geometry and cross flow that is more adequately accounted for in the 3-D viscous shock layer model. In figures 11 and 12 the 3-D viscous shock layer results of reference 8 tend toward better agreement with the measurements than the other calculations aft of $X/L = 0.6$. This 3-D approach should be further investigated with appropriate finite rate recombination coefficients.

The increase in measured heat flux above the calculations on aft half of the vehicle and especially for the later flight may also have other explanations. The increase could be due to increasing recombination rates, but that would be inconsistent with the measurements on the forward part of the vehicle unless the aft is contaminated with a catalytic material. This is possible because the adhesive used to bond tiles to the structure contains various metal oxides, particularly iron oxide which is known to be highly catalytic.

The two-layer methods have been used to calibrate faster and more flexible codes to provide heat fluxes and other properties over a wider range of conditions than for which the two-layer methods were applied. The nonequilibrium results of Rakich and Lanfranco[2] have been used by Rakich, Stewart and Lanfranco[4] and by Scott and Derry[5]. One of the weaknesses of these applications is the inability to properly account for variations in the flowfield chemical composition as parameters such as the angle of attack, freestream density and velocity differ from the few cases available from the 3-D Euler solutions. The axisymmetric shock layer codes have the advantage that they are more flexible in running cases because of their fast computation time. Gupta et al.[13] investigated the influence of small variations in angle of attack on the nonequilibrium heating and found the influence on heat flux to be small. A larger percentage variation was observed for lower velocities. This may be due to greater temperature sensitivity of the level of oxygen dissociation at lower temperatures rising in the lower altitude case. Small changes in the component of velocity normal to the shock wave associated with the change in angle of attack result in temperature changes in a range in which the oxygen dissociation is very sensitive. However, since the general sensitivity of absolute heat flux to angle of attack is small, the approximations made in references 4 and 17 should not be very significant in this regard.

The disadvantage of the axisymmetric viscous shock layer methods is that they are only capable of handling bodies of revolution and they rely on angle of attack simulation via changing the body profile. Cross flow or transverse body curvature is therefore quite limited. Fortunately, for the present work this has not been a strong limitation but it may explain why there is disagreement with measurements on the aft of the vehicle.

The 3-D viscous shock layer approach does away with those approximations, but suffers from the requirement of a shock shape as input (as do the axisymmetric viscous shock layer solutions). The 3-D version has only recently been developed and will require further work to compare with measurements before its adequacy will be known.

The 3-D inviscid solution method coupled with boundary layer solutions requires very much computer time to obtain the inviscid flowfield and requires assumptions about how far into the inviscid flow from the body to go to obtain boundary layer edge conditions. Choosing the boundary layer edge too far into the lower entropy flowfield will result in heating predictions that are too high. This may be the reason that the two-layer methods predicted higher results than the axisymmetric viscous shock layer method for the noncatalytic case at $X/L > 0.02$ and for the fully catalytic case at $0.02 < X/L < 0.2$. The noncatalytic case is more sensitive to the dissociation level which is higher in the flow from the normal shock region.

Inferring catalytic recombination rates from the flight measurements is made difficult for several reasons. First, the flowfield is composed of oxygen and nitrogen atoms in varying amounts according to the vehicle trajectory and location on the vehicle. If one chooses a lower velocity condition where very little nitrogen is dissociated then it may be possible to infer k_{wO}. However, we have seen a flight-to-flight measurement uncertainty of at least 15% and prediction-to-prediction variation of the same magnitude. Heating uncertainties of this magnitude result in k_w uncertainties on the order of a factor of 5 (see reference 13). Therefore, such a procedure should be used with great caution. This illustrates the need for careful ground experiments or great fidelity in the flight heat flux calculations to obtain accurate recombination coefficients. The ground measurements of Scott[6,14], as with any ground measurements, require either precise heat flux calculations and/or a reliable reference surface with which to compare the heating. Even then accurate results are difficult. Fortunately only moderately accurate recombination coefficients are required to calculate reasonably accurate heating rates.

To ascertain the nitrogen recombination coefficients from flight measurements is almost impossible without knowledge of the coefficients for oxygen because the oxygen atom is always an important species in the flow whenever there is any nitrogen dissociated. If the flowfield and k_{wO} were known accurately as a function of T_w then it might be possible to infer k_{wN}.

Heating to Highly Catalytic Tiles

Attention is now turned to the results of the Ames Research Center's catalytic surface effects orbiter experiment[3,4]. Not only did this very significant experiment demonstrate the noncatalytic nature of the RCG coated tiles, but it also may give some clues as to the variation of dissociation in the boundary layer and the wall recombination rates. On STS-2 two tiles were painted with a highly catalytic material, iron-cobalt-chromia spinel (C742), developed by Stewart et al.[3] at the Ames Research Center. The predicted and measured heat fluxes in the vicinity of the two C752-coated tiles on the bottom centerline of the orbiter during STS-2 reentry are given in figures 15 and 16. The measurements were obtained at 475 sec after 122 km altitude was reached. At the forward location near the nose, the two-layer calculation using the method and recombination rates of Rakich et al.[4] yields the best agreement with the measurements. This should be the case because the recombination coefficients were inferred from the measurements at this location and approximate entry time. Also shown is the same calculation but using recombination coefficients obtained from arc jet measurements[6,14]. As see in figure 15, (the forward location), the increase in heat flux on the C742-coated tile is larger for the Rakich recombination rates than for the recombination rates of references 6 and 14, even though the latter rates for C742 are larger. The reason for this behavior is that, due to the higher RCG recombination rates of reference 6, the boundary layer is depleted of atomic nitrogen and oxygen so that when the flow reaches the C742-coated tile there is not as much chemical energy available for transfer to the highly catalytic tile. A similar behavior is seen at $X/L = 0.4$ in figure 16. Since the recombination rates of references 6 and 14 increase with temperature, the upstream edge of the C742-coated tile sees a high heat flux that decreases rapidly because of depletion of atoms in the boundary layer and this lead to further reduction in recombination rate along the tile as the temperature decreases.

The agreement between the axisymmetric viscous shock layer method and the boundary layer method is not very good on the C742-coated tiles. The heat flux drops much more rapidly, possibly because of more rapid depletion of atoms in the boundary layer than the boundary layer method predicts. There also seems to be some sensitivity of the heat flux distribution along the tile to the streamwise nodal spacing used in the calculation.

CONCLUDING REMARKS

This paper has attempted to evaluate the current state-of-the-art nonequilibrium flow tools applied to the Space Shuttle. From this discussion the importance of nonequilibrium phenomena to the Space Shuttle reentry heating has been assessed. Since the inception of the design of the Space Shuttle over fourteen years ago there have been developments in the heat flux prediction methodologies. Initially nonequilibrium and surface catalysis effects were ignored. This led to a design that exceeded the requirements in many areas, but also resulted in an added margin of safety in other areas that proved beneficial.

It was found that the heat fluxes measured on the windward centerline of the orbiter tended to increase from flight to flight. Roughly, a 20% change was noted from STS-2 to 5 at most of the thermocouple locations, indicating changes in surface properties such as emittance or catalycity.

The nonequilibrium heat flux methods that have been developed and the catalycity measurements obtained over the past decade have improved the prediction capability from a 20 to 100% overprediction for an assumed fully catalytic surface material to an accuracy of about 10 to 30% for nearly noncatalytic materials, e.g., the RCG coating on HRSI. These methods are the two-layer inviscid 3-D reacting flowfield coupled with the reacting boundary layer, and the reacting viscous shock layer solutions. The application of these methods may result in less reliance on wind tunnel measurements which cannot simulate the high enthalpy reacting flows associated with orbital reentry. Indeed the calculations are necessary for such a simulation.

As the comparisons of the predictions with the measurements from the Space Shuttle flight tests have shown, we are now in a position of refining the prediction techniques and determining those phenomena that will be of significance for the design of future reentry vehicles such as an aerobraking orbital transfer vehicle (AOTV).

Although nonequilibrium calculation techniques using finite rate catalycity wall boundary conditions has significantly improved the prediction capability, none of the methods yields good agreement uniformly for all locations and freestream conditions. This points to the need for further refinement in these methods. The 3-D viscous approaches in particular should be pursued since the trends of the heating profiles tend to be better than for the other methods.

Nitrogen recombination is seen to be a very important phenomenon, particularly on the nose and elsewhere at the higher velocities. This means that the accuracy of the nitrogen recombination coefficients is important to the heat flux predictions in those areas. Since the AOTV enters the atmosphere at higher speeds and remains at higher altitudes where nonequilibrium flow dominates, the nitrogen gas and surface reactions will be especially important.

REFERENCES

1. Scott, C. D., "Space Shuttle Laminar Heating with Finite-Rate Catalytic Recombination," Thermophysics of Atmospheric Entry, Progress in Astronautics and Aeronautics, Vol. 77, edited by T. E. Horton, AIAA, New York, 1982, pp. 273-289.

2. Rakich, J. V. and Lanfranco, M. J., "Numerical Computation of Space Shuttle Laminar Heating and Surface Streamlines," Journal of Spacecraft and Rockets, Vol. 14, May 1977, pp. 265-272.

3. Stewart, D. A., Rakich, J. V. and Lanfranco, M. J., "Catalytic Surface Effects Experiment on the Space Shuttle," in Thermophysics of Atmospheric Entry, Vol. 82 of Progress in Astronautics and Aeronautics, 1982, T. E. Horton, Editor, pp. 248-272.

4. Rakich, J. V., Stewart, D. A. and Lanfranco, M. J., "Results of a Flight Environment on the Catalytic Efficiency of the Space Shuttle Heat Shield," AIAA Paper 82-0944, AIAA/ASME 3rd Joint Thermophysics, Fluids, Plasma and Heat Transfer Conference, June 7-11, 1982, St. Louis, MO.

5. Scott, C. D. and Derry, S. M., "Catalytic Recombination and the Space Shuttle Heating," AIAA Paper 82-0841, AIAA/ASME 3rd Joint Thermophysics, Fluids, Plasma and Heat Transfer Conference, June 7-11, 1982, St. Louis, MO.

6. Scott, C. D., "Catalytic Recombination of Oxygen and Nitrogen in High Temperature Reusable Surface Insulation," in Aerothermodynamics and Planetary Entry, edited by A. L. Crosbie, Vol. 77 of Progress in Astronautics and Aeronautics, 1981, pp. 192-212.

7. Shinn, J. L., Moss, J. N. and Simmonds, A. L., "Viscous-Shock-Layer Heating Analysis for the Shuttle Windward Plane with Surface Finite Catalytic Recombination Rates," AIAA Paper 82-0842, AIAA/ASME 3rd Joint Thermophysics Fluids, Plasma and Heat Transfer Conference, June 7-11, 1982, St. Louis, MO.

8. Kim, M. D., Swaminathan, S. and Lewis, C. H., "Three-Dimensional Nonequilibrium Viscous Shock Layer Flows Over the Space Shuttle Orbiter," AIAA Paper 83-0487, AIAA 21st Aerospace Sciences Meeting, January 10-18, 1983, Reno, NV.

9. Moss, J. N., "Reacting Viscous Shock-Layer Solutions with Multicomponent Diffusion and Mass Injection," NASA TR R-411, June 1974.

10. Miner, E. W. and Lewis, C. H., "Hypersonic Ionizing Air Viscous Shock-Layer Flows Over Nonanalytical Blunt Bodies," NASA CR-2550, May 1975.

11. Goodrich, W. D., Li, C. P., Houston, C. K., Chin, P. B. and Olmedo, L., "Numerical Computations of Orbiter Flowfields and Laminar Heating Rates," Journal of Spacecraft and Rockets, Vol. 14, May 1977, pp. 257-264.

12. Zoby, E. V., "Analysis of STS-2 Experimental Heating Rates and Transition Data," AIAA/ASME 3rd Joint Thermophysics Fluids, Plasma and Heat Transfer Transfer Conference, June 7-11, 1982, St. Louis, MO.

13. Gupta, R. N., Moss, J. H., Simmonds, A. L., Shinn, J. L. and Zoby, E. V., "Space Shuttle Heating Analysis with Variation in Angle-of-Attack and Surface Condition," AIAA Paper 83-0486, AIAA 21st Aerospace Sciences Meeting, January 10-13, 1983, Reno, NV.

14. Scott, C. D., "Catalytic Recombination of Nitrogen and Oxygen on Iron-Cobalt-Chromia Spinel," AIAA Paper 83-0585, January 1983, Reno, NV.

15. Bartlett, E. P. and Kendall, R. M., "An Analysis of the Coupled Chemically Reacting Boundary Layer and Charring Ablator, Pt. III: Nonsimilar Solution of the Multicomponent Laminar Boundary Layer by an Integral Matrix Method," NASA CR-1062, June 1968.

16. Tong, N., Buckingham, A. C. and Morse, H. L., "Nonequilibrium Chemistry Boundary Layer Integral Matrix Procedure," NASA CR-134039, July 1973.

17. Williams, S. D. and Curry, D. M., "An Analytical and Experimental Study for Surface Heat Flux Determination," Journal of Spacecraft and Rockets, Vol. 14, No. 10, October 1977, pp. 632-637.

18. Bradley P. F. Siemers, P. M., III and Weilmuenster, K. J., "An Evaluation of Space Shuttle Orbiter Forward Fuselage Surface Pressures: Comparison with Wind Tunnel and Theoretical Predictions," AIAA Paper 83-0119, AIAA 21st Aerospace Sciences Meeting, January 10-13, 1983, Reno, NV.

19. Blottner, F. G., "Nonequilibrium Laminar Boundary-Layer Flow of Ionized Air," General Electric Report R64SD56, November 1964.

TABLE 1 - METHODS AND APPLICATIONS PRESENTED IN PLOTS

Application No.	Method	Application	Wall Boundary Condition	Flow Field	Boundary Layer	
					Edge Condition	Chemistry of B.L.
1	Moss[9]	Shinn, et al[7]	Scott[6]	VSL+ Noneq.	N/A	N/A
2	"	"	ECW*	"	"	"
3	"	"	Noncata.	"	"	"
4	"	"	Equilib.	VSL Equilib.	"	"
5	Miner & Lewis[10]	Present	Scott[6]	VSL Reacting	"	"
6	"	"	Fully Cata.	"	"	"
7	"	"	Noncata.	"	"	"
8	Goodrich, et al[11]	Goodrich, et al[11]	Equilib.	3-D Inviscid Equilib.	Equilib.	Equilib.
9	Rakich, et al[2]	Present	Fully Cata.	3-D Inviscid Noneq.	Noneq.	Noneq.
10	"	"	Scott[6]	"	"	"
11	"	"	Noncata.	"	"	"
12	Goodrich, et al[11]	"	Fully cata.	"	Equilib.	"
13	"	"	Scott[6]	"	"	"
14	"	"	Noncata.	"	"	"
15	Rakich, et al[2]	"	Rakich, et al[4]	"	Noneq.	"
16	Kim, et al[14]	Kim,et al	Noncata.	3-D VSL Noneq.	N/A	N/A

* ECW = Equilibrium Catalytic Wall
+ VSL = Viscous Shock-Layer

TABLE 2 - FREESTREAM CONDITIONS[c] FOR CORRESPONDING HEAT FLUX MEASUREMENTS

Flight	time[b] sec	V_∞ km/sec	ρ_∞ kg/m^3	α deg	f[a]	Z km	h_T MJ/kg	$\rho_\infty V_\infty^2$ kPa
STS-2	475	7.16	.412.4	40.37	1,000	74.7	25.6	2.11
	700	6.57	.807.4	39.99	1,000	70.2	21.6	3.49
	1050	4.56	.402-3	40.56	1,000	57.2	10.4	8.35
STS-3	400	7.29	.394-4	40.02	1.033	75.1	26.6	2.09
	700	6.29	.113-3	39.58	1.037	68.2	19.8	4.46
	960	4.58	.417-3	40.72	1.032	57.6	10.5	8.75
STS-5	400	7.17	.408-4	40.05	.998	74.9	25.7	2.09
	700	6.19	.104-3	40.71	.950	61.9	19.2	3.99
	950	4.56	.441-3	39.19	1.046	54.0	10.4	9.16

[a] $f = (\rho/\rho_{ref})^{1/2} \; (V/V_{ref})^3$ Factor used to adjust heat flux relative to STS-2 condition, based on stagnation point theory.

[b] Time from entry interface (Z = 122 km)

[c] Best Estimated Trajectory

TABLE 3 - FREESTREAM CONDITIONS FOR CALCULATIONS

Case No.	1	1	2	460[a]	650[a]
Method	BL	VSL	BL	VSL	VSL
Velocity, km/s	7.62	7.62	6.614	7.20	6.73
Attitude, km	75.0	75.0	68.9	75.0	71.3
Angle-of-Attack, deg	41.4	41.4	40.2	40.0	39.4
Density, kg/m^3	3.795-5	3.974-5	9.28-5	3.81-5	6.83-5
Total Enthalpy, MJ/kg	29.0	29.0	21.8	25.9	22.6
Temperature, K	197.	197.	221.	198.	205.
Stagnation Point Pressure, kPa	2.20	2.31	4.10	1.98	3.09
Nose Radius, m	0.814	1.342	0.814	1.276	1.253
Hyperboloid angle[b], deg	-	42.2	-	40.75	40.20
Lewis No. in Shock Layer					
Present Calculations	-	1.0	-	1.0	1.0
Reference 11	-	1.4	-	1.4	1.4
Reference 16	-	1.4	-	1.4	1.4

[a] These freestream conditions are the same as the one in reference 7 for STS-2 times corresponding to the case number and the same as cases 2 and 3 in reference 8.

[b] Not applicable to 3-D VSL.

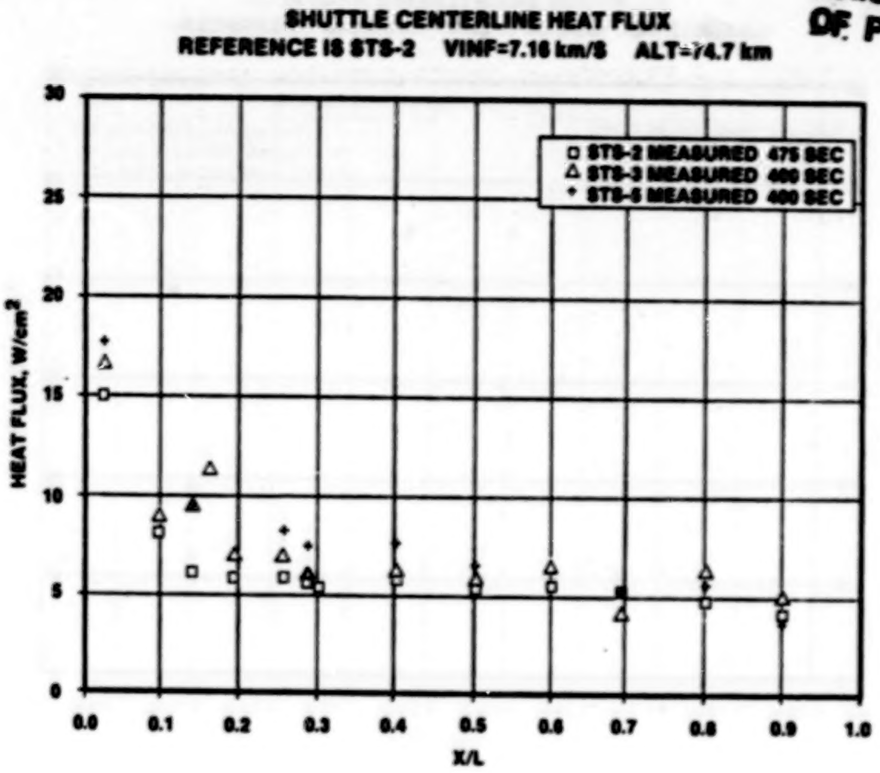

Figure 1.- Measured radiation equilibrium heat fluxes near windward centerline of orbiter. Altitude = 74.7 km.

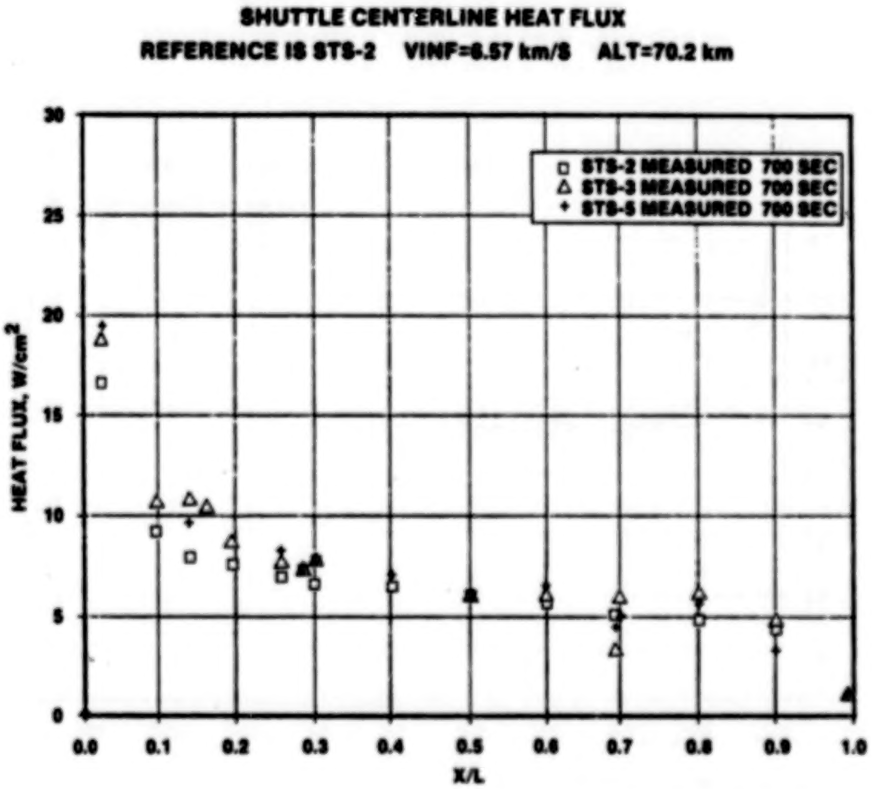

Figure 2.- Measured radiation equilibrium heat fluxes near windward centerline of orbiter. Altitude = 70.2 km.

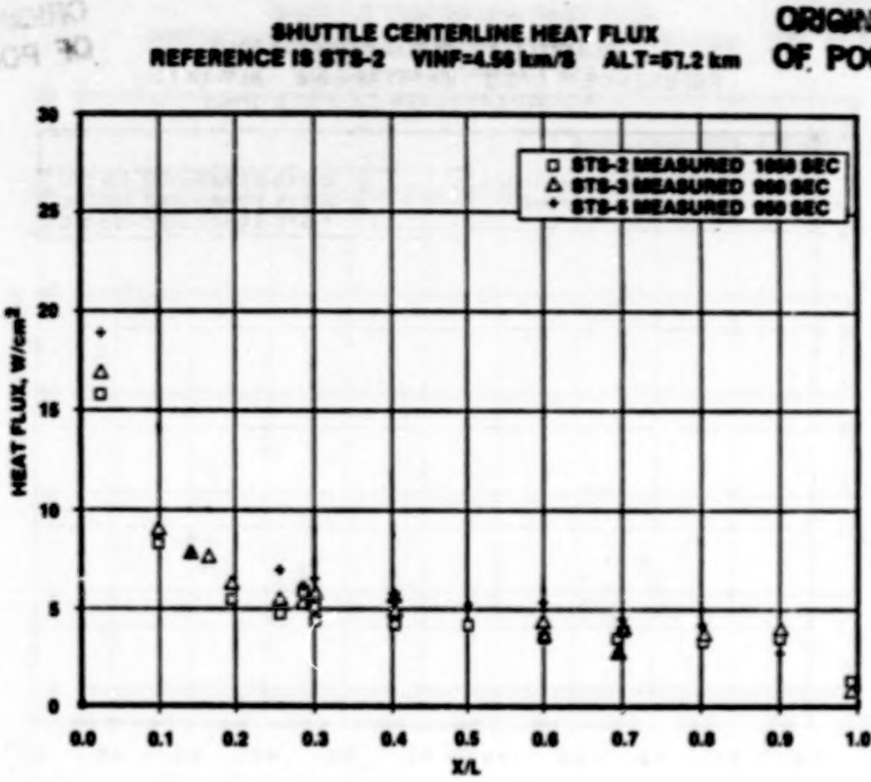

Figure 3.- Measured radiation equilibrium heat fluxes near windward centerline of orbiter. Altitude = 57.2 km.

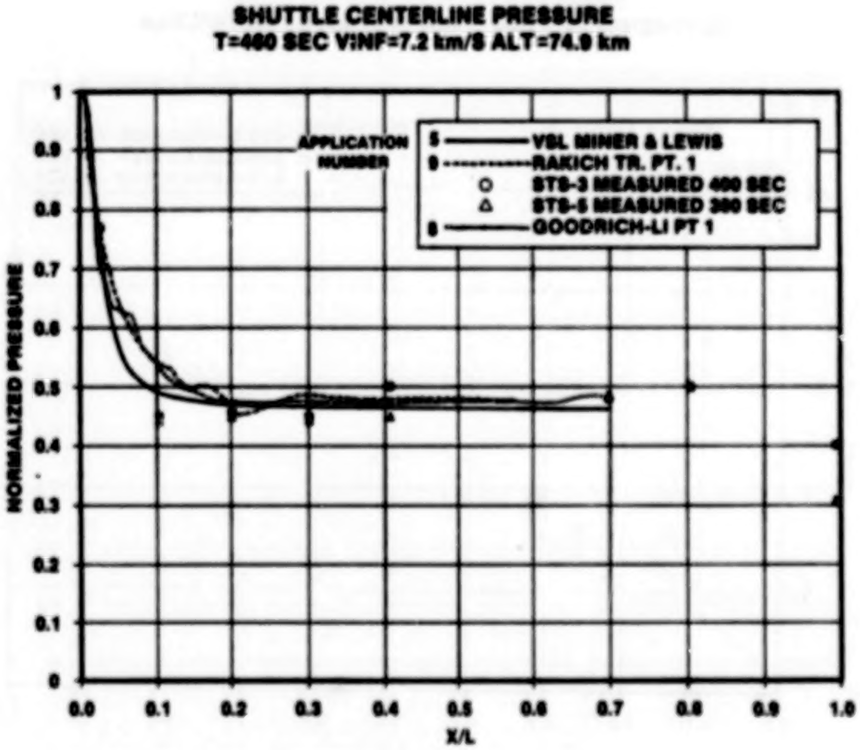

Figure 4.- Measured and calculated pressures on centerline of orbiter.

ORIGINAL PAGE IS
OF POOR QUALITY

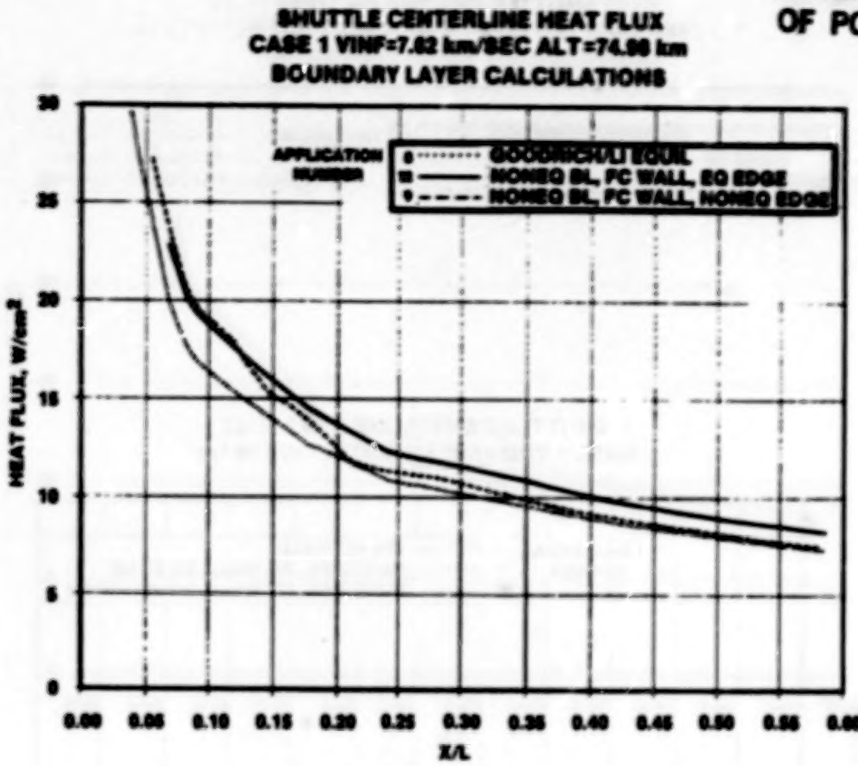

Figure 5.- Comparison of equilibrium and nonequilibrium boundary layer calculations with fully catalytic wall.

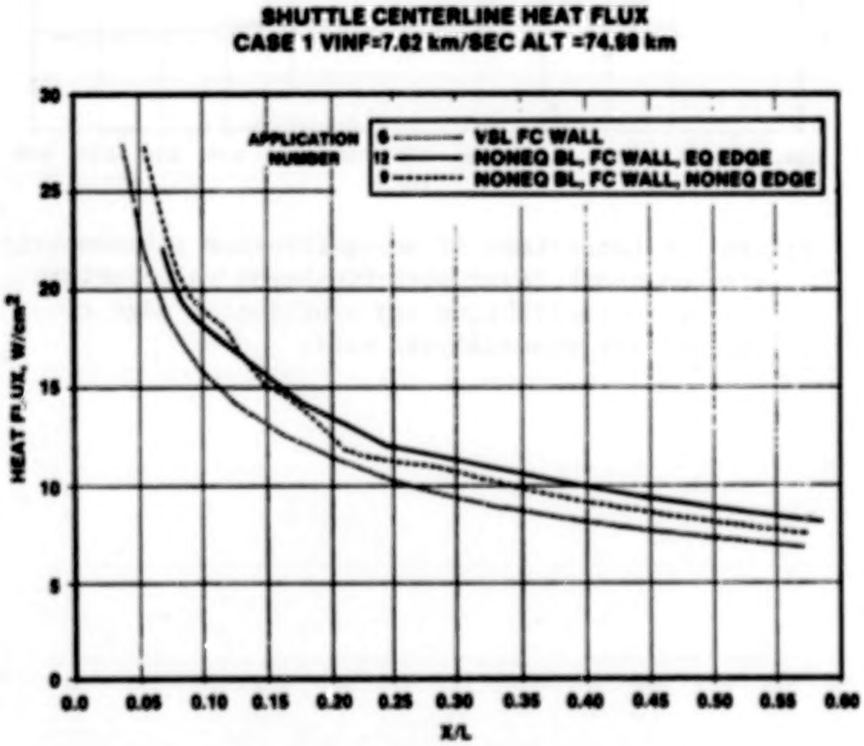

Figure 6.- Comparison of nonequilibrium axisymmetric viscous shock layer and two-layer calculations with fully catalytic wall.

ORIGINAL PAGE IS
OF POOR QUALITY

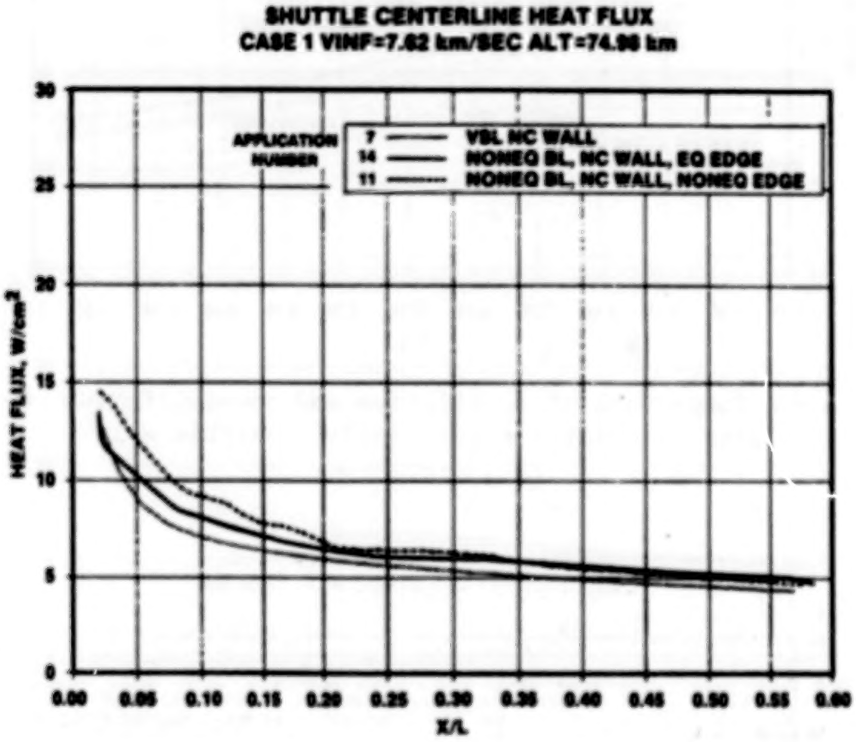

Figure 7.- Comparison of nonequilibrium axisymmetric viscous shock layer with two-layer calculations having nonequilibrium and equilibrium edge conditions for noncatalytic wall.

ORIGINAL PAGE IS
OF POOR QUALITY

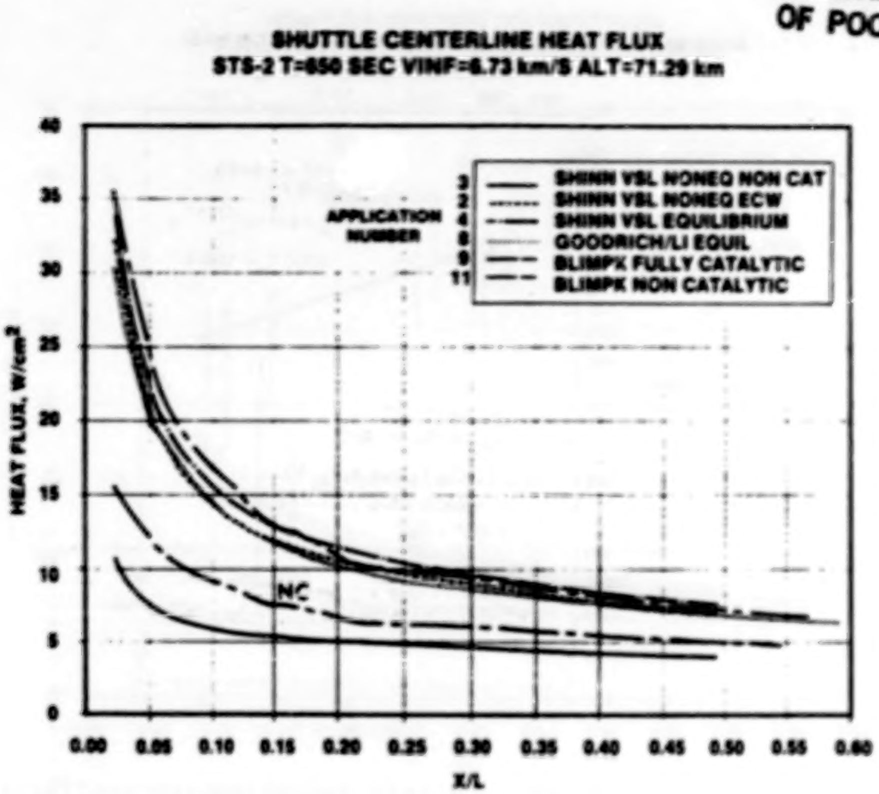

(a) Comparison of axisymmetric viscous shock layer and two-layer calculations for STS-2 650-sec case.

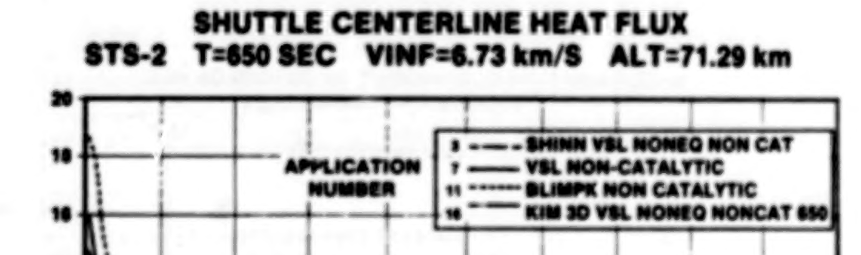

(b) Comparison of nonequilibrium axisymmetric and 3-D viscous shock layer and two-layer calculations with noncatalytic wall.

Figure 8.- Comparison of available prediction methods for Shuttle centerline heat flux.

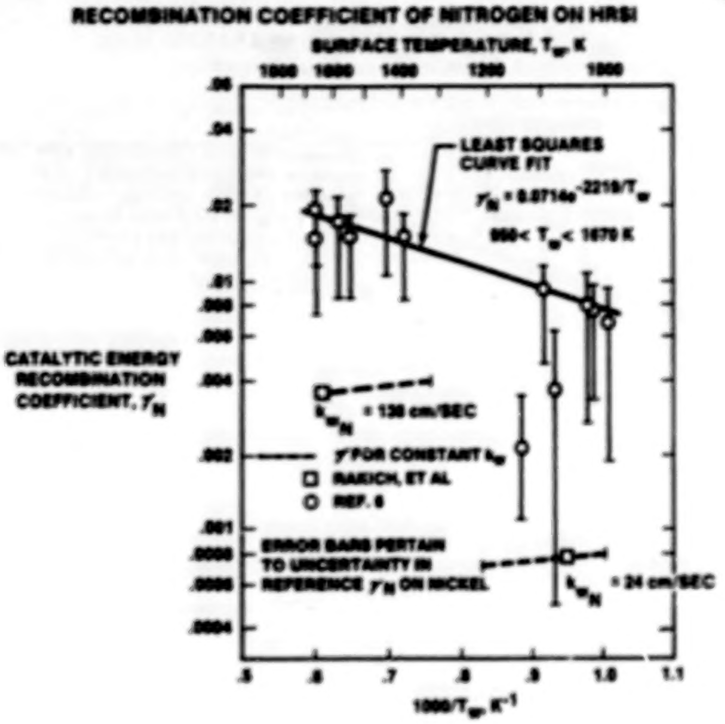

Figure 9.- Energy transfer catalytic recombination coefficient for nitrogen on RCG-coated HRSI.

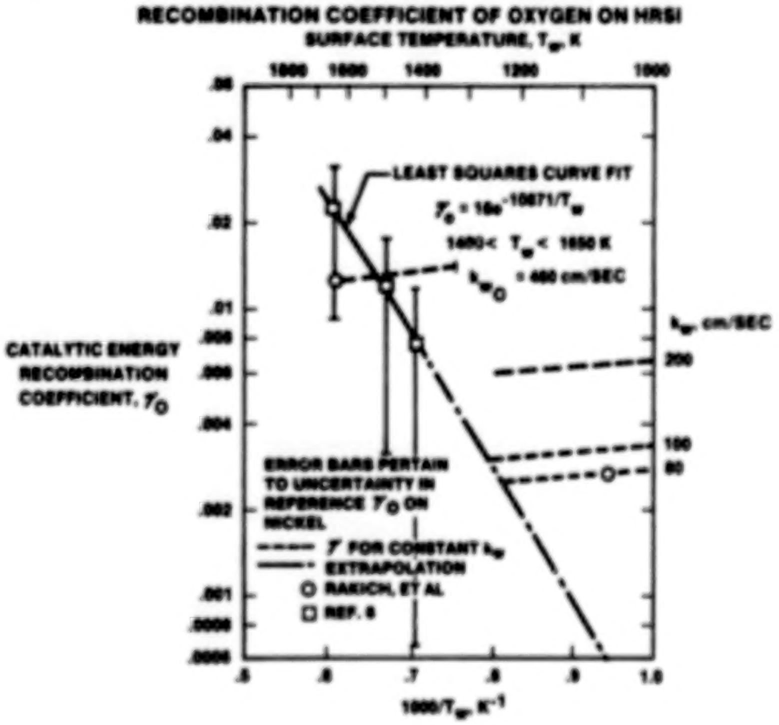

Figure 10.- Energy transfer catalytic recombination coefficient for oxygen on RCG-coated HRSI.

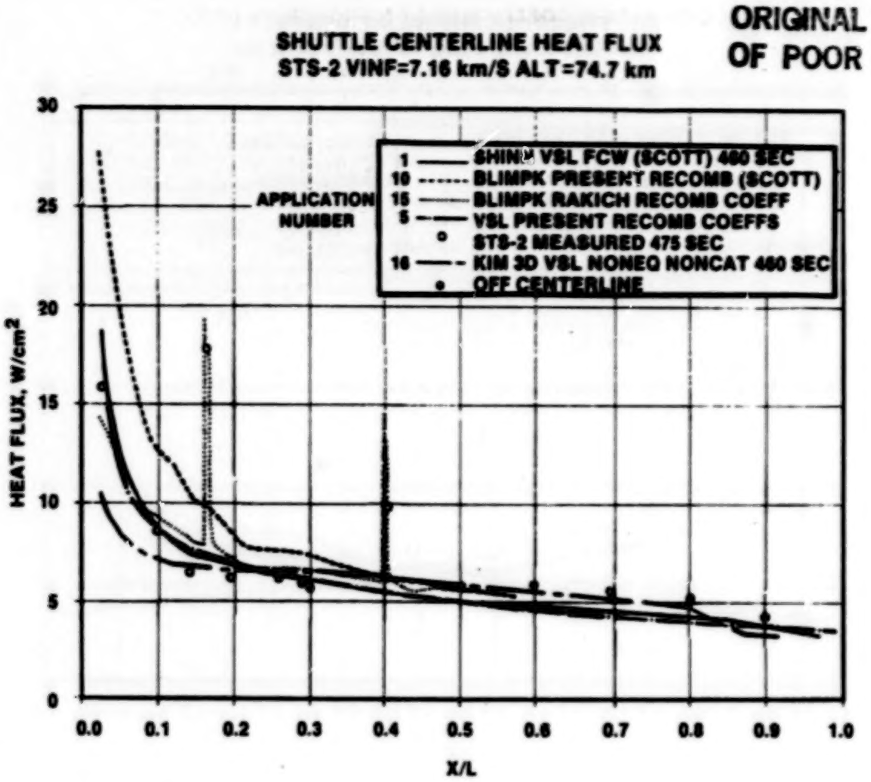

Figure 11.- Comparison of calculated and measured Shuttle heat fluxes for STS-2. t = 475 sec; altitude = 74.7 km.

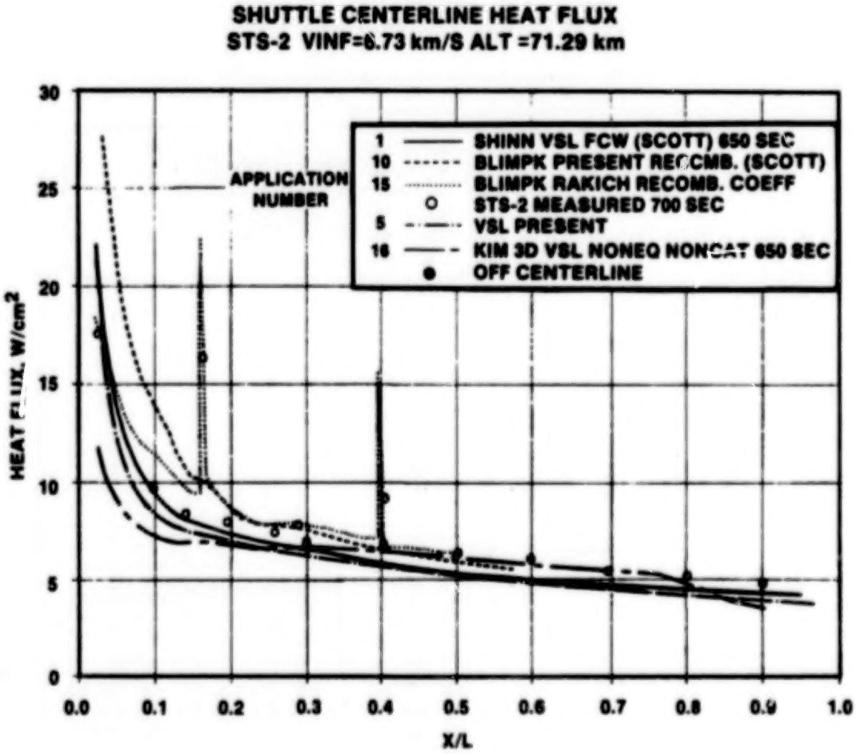

Figure 12.- Comparison of calculated and measured Shuttle heat fluxes for STS-2. t = 475 sec; altitude - 71.29 km.

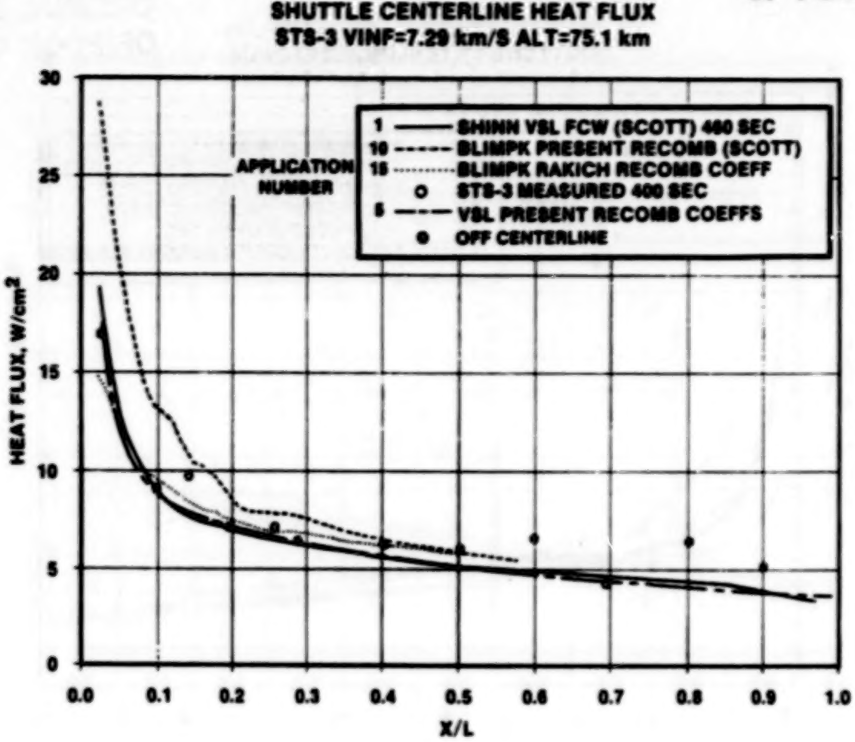

Figure 13.- Comparison of calculated and measured Shuttle heat fluxes for STS-3. t = 400 sec.

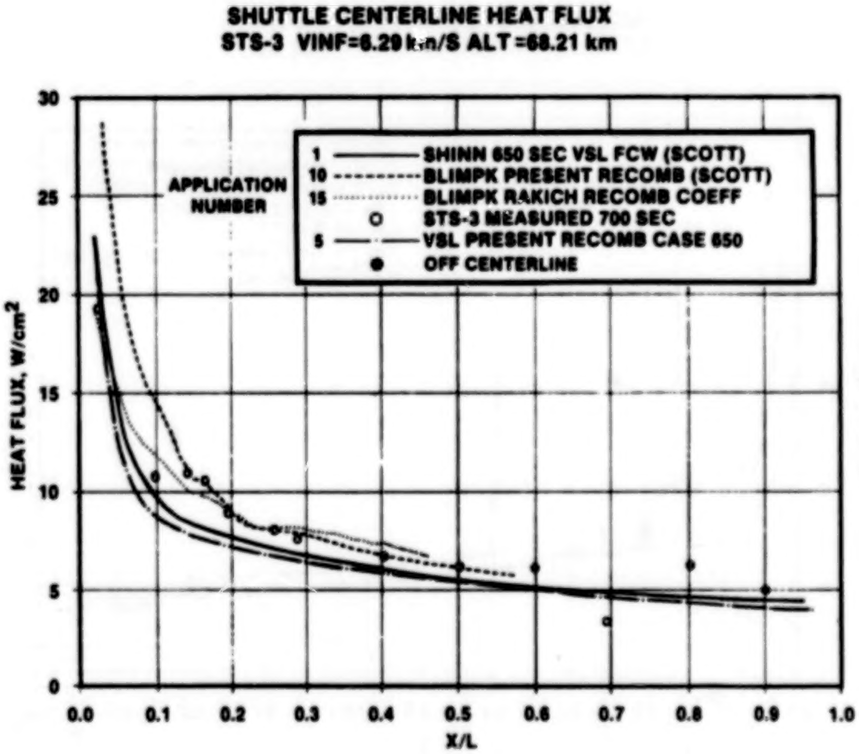

Figure 14.- Comparison of calculated and measured Shuttle heat fluxes for STS-3. t = 700 sec.

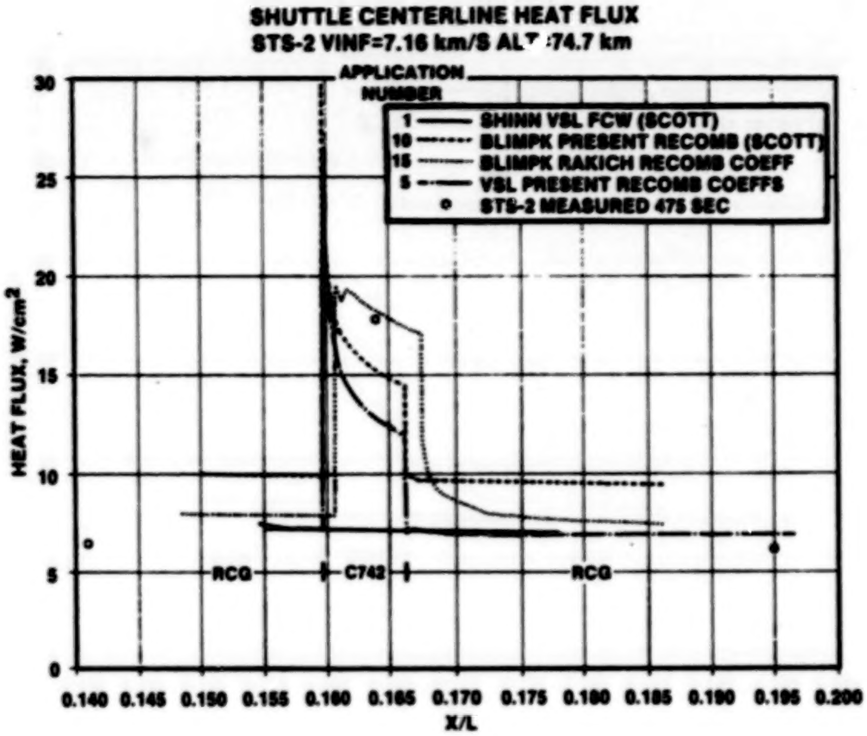

Figure 15.- Heat fluxes on C742-coated tile at X/L = 0.163 for STS-2. t = 650 sec.

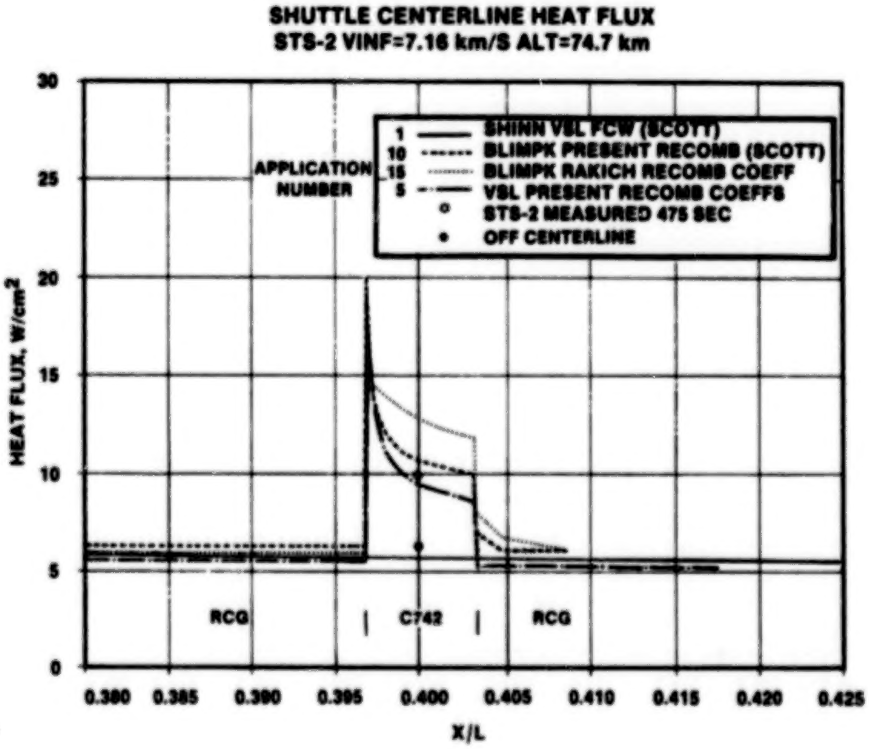

Figure 16.- Heat fluxes on C742-coated tile at X/L = 0.40 for STS-2. t = 650 sec.

N84
10155

UNCLAS

N84 10155

FILLER BAR HEATING DUE TO STEPPED TILES IN THE SHUTTLE ORBITER THERMAL PROTECTION SYSTEM

D. H. Petley, D. M. Smith, C. L. W. Edwards,
A. B. Patten, and H. H. Hamilton II
NASA Langley Research Center
Hampton, Virginia

SUMMARY

An analytical study has been performed to investigate the excessive heating in the tile-to-tile gaps of the Shuttle Orbiter Thermal Protection System (TPS) due to stepped tiles. The excessive heating was evidenced by visible discoloration and charring of the filler bar and strain isolation pad (SIP) that is used in the attachment of tiles to the aluminum substrate. Two tile locations on the Shuttle orbiter were considered, one on the lower surface of the fuselage and one on the lower surface of the wing. The gap heating analysis involved the calculation of external and internal gas pressures and temperatures, internal mass flow rates, and the transient thermal response of the thermal protection system. The results of the analysis are presented for the fuselage and wing location for several step heights. The results of a study to determine the effectiveness of a half-height ceramic fiber gap filler in preventing hot gas flow in the tile gaps are also presented.

INTRODUCTION

The Shuttle Orbiter Vehicle 102 (Columbia) has successfully flown five orbital missions. The Thermal Protection System (TPS) on the orbiter exterior has performed satisfactorily although damage has been observed on random individual tiles after each flight. One of the causes for damage to the TPS has been vertical and lateral relative movement between adjacent tiles that do not have gap filler. This relative movement can cause forward facing steps on the TPS aerodynamic surface and large gaps between the tiles. The combination of forward facing steps and large tile-to-tile gaps has caused higher than expected heating within the gaps during atmospheric entry at random locations on the lower surface of the orbiter resulting in damage to the filler material and the strain isolation pad (SIP). The heat damage has been severe enough in some instances to require tile removal in order to replace the filler material and SIP. Filler material damage was observed on the lower fuselage and the lower surfaces of both wings of the orbiter. These regions are geometrically flat regions so that aerodynamic pressure gradients on the TPS are essentially zero. Tile-to-tile gap fillers were not used in these regions for this reason.

PAGE 890 INTENTIONALLY BLANK

PRECEDING PAGE BLANK NOT FILMED

An analytical study was conducted to determine the magnitude of tile steps and gaps that would cause the observed filler bar damage. This paper describes the techniques used to define the conditions under which damage to the filler bar would occur. There is also a discussion of a possible fix to the problem.

SYMBOLS

A_c	cross sectional area for flow
B	width of flow path
G	conductance for laminar flow between parallel plates
G_1	conductance of gap with full gap filler
G_2	conductance of gap with half-height gap filler
h	tile step height
k	thermal conductivity
K_p	permeability constant
L_t	tile thickness
$\dot{m}$	mass flow rate
M	Mach number
P	pressure
$\dot{q}$	conduction heat flux
Re_c	Reynolds number for base pressure correlation
s	straight line length between points
T	temperature
w	tile-to-tile gap width
X,Y	Shuttle orbiter coordinates
ΔX	longitudinal coordinate measured in the downstream direction from the point of separation
ΔX_{ff}	longitudinal coordinate measured in the upstream direction from a forward facing step

δ	velocity boundary layer thickness
δ^*	boundary layer displacement thickness
δ_{eff}	1.5 δ^* for turbulent flow, δ for laminar flow
Λ	sweep angle of a tile with respect to the local flow
μ	viscosity coefficient
ρ	density

PROBLEM DESCRIPTION

The TPS on the lower fuselage and lower surfaces of the wings (figure 1) consists of silica foam tiles typically 6 x 6 inches square and of variable thickness depending on their location on the orbiter. There is a glass coating containing black pigment on the exterior of the tile to increase the radiative properties of the surface. Radiating heat from the tile surface during entry is a key consideration in the thermal design of the TPS. The tiles are bonded to the aluminum skin of the orbiter through a strain isolation pad (SIP). The SIP is a nylon fiber material that is used to absorb relative movement between the brittle silica tiles and the aluminum substrate. The tiles have gaps between them to allow for differential thermal expansion between the tiles and substrate. The nylon fiber filler bar is directly beneath the tile-to-tile gaps. There is a silicone rubber membrane on the top surface of the filler bar to prevent hot gases from flowing under the tiles. The filler bar is bonded to the aluminum skin but not to the bottom of the tiles. This filler bar material sustained damage on all flights of the Columbia, the first Shuttle.

Post-flight measurements, taken after the first flight around the tiles with damaged filler bar, are shown in table 1. Tile-to-tile steps varied from -0.1 inch to +0.12 inch and tile gaps varied from almost complete closure (0.01 inch) to an opening of 0.13 inch. NASA Johnson Space Flight Center categorized the degree of damage to the filler bar by performing arc jet tests on a TPS panel and duplicating the varying degrees of observed damage. Thermocouples were embedded in the filler bar to record temperatures for each category of damage. The threshold temperature to cause filler bar damage was 970°F causing the RTV rubber membrane to discolor. Temperature exposures above 1375°F caused both the RTV and nylon fiber material to char.

The probable cause of damage to the filler bar is shown in figure 2. A tile with a forward facing step causes a local pressure disturbance in the external boundary layer. The flow tends to stagnate on the forward face directly over the tile-to-tile gap. Similarly, the aft facing step creates a low pressure region as the flow leaves the surface of the stepped tile and reattaches downstream. This combination of pressures around a stepped tile causes flow in the tile gaps that would not exist if all tiles were at the same height. The objective of the analytical study was to define the conditions under which a stepped tile could result in damage to the filler bar. In order to define these conditions, five major phases of study were required:

(1) Definition of the local freestream conditions on the lower surface of the wing and fuselage

(2) Development of a technique for predicting the distribution and magnitude of the pressure disturbance caused by a stepped tile

(3) Predicting the temperature of the gases which enter the tile-to-tile gap from the external boundary layer as a result of the stepped tile

(4) Predicting the pressure distribution around and under the tile and the mass flow rates in the tile gap as a result of the pressure disturbance

(5) Determining the temperature response in the tile gap and in particular the temperature on the filler bar caused by flow in the gaps

ANALYSIS

Two locations, one on the lower surface of the fuselage and one on the lower surface of the left wing, were selected for analysis from the regions where damaged filler bar was observed (figure 3). The location on the fuselage was selected because local flow conditions during entry can be accurately predicted for this position, flight measurements of pressure and temperature are available, and the boundary layer thickness will be large since the point is about 40 feet from the nose of the orbiter. The wing location was selected for the same reasons, except in this case the boundary layer will be relatively thin since the point is about 8 feet aft of the local leading edge. These are 6 inch x 6 inch tiles with thicknesses of 1.41 inches at the fuselage location and 2.25 inches at the wing location.

The pressure and other thermodynamic properties at the edge of the boundary layer at the fuselage location were calculated using a tangent-cone approximation where the half angle of the cone is equal to the local flow deflection angle, (i.e., the local body deflection angle plus the angle of attack). The real gas, axisymmetric, flow-field solution over a cone was obtained using a time-asymptotic numerical procedure with equilibrium thermodynamic properties obtained from reference 1. The tangent-cone approximation has been shown to yield accurate predictions of the local flow on the windward surface of Shuttle-like configurations (reference 2). Local flow conditions on the wing lower surface were calculated assuming two dimensional inviscid flow. The boundary layer calculations on the fuselage were made using a "local infinite swept cylinder" analysis (reference 3) and on the wing using two-dimensional "strip theory."

Pressure Disturbances

The characteristic shape of the pressure disturbance caused by a forward facing step in supersonic flow is shown in figure 4. The step height needed to cause this disturbance is equal to or greater than the boundary layer thickness for laminar flow and equal to or greater than 1.5 times the displacement thickness for turbulent flow. The step causes the boundary layer to separate locally from the body forward of the step. In addition, an oblique shock is formed at the point of separation. The pressure behind the shock is called the plateau pressure, $P_{plateau}$, in figure 4. There is a final peak pressure at the face of the step as the flow stagnates. The figure is a plot of $P_{plateau}/P_{local}$ versus Mach number from test data obtained in the LaRC Unitary Plan Wind Tunnel and experimental results reported in the literature (references 4, 5, and 6). The data are directly applicable to the lower surface of the orbiter since the local Mach number behind the bow shock ranges from 2.5 - 3.75 during the high aerodynamic heating period of entry. The equation for a straight line correlates the data very well as is shown in the figure.

Boundary layer thicknesses varied from 0.87 inch to 4.0 inches at the fuselage location and 0.54 to 1.54 inches at the wing location. Tile step heights considered in the analyses were 0.12 inch maximum in accordance with measured tile steps after the first flight. Therefore, forward facing steps in the tiles were deeply submerged in the boundary layer and do not cause the severe pressure disturbances shown in figure 4. Figure 5 shows experimental data for pressure distribution versus separation distance for various step heights. The face of the step is at $\Delta X_{ff}/\delta^* = 0$ in the figure. The shaded symbols indicate data that is in the range of step height-to-displacement thickness ratios that apply for the filler bar analysis. A significant feature of the plots in figure 5 is the similarity of the curves as step height is decreased. The characteristic shape of the pressure distribution for a large forward facing step ($h/\delta^* = 1.5$) can be used to obtain the pressure distribution for a smaller step height by using the lower portion of the curve starting at the point of separation and scaling the peak pressures as a function of h/δ^*. A correlation technique was developed to obtain pressure disturbance distributions for small step heights at various Mach numbers between 2.35 - 3.85 based on the experimental data previously referenced. Figure 6 shows the result of the correlation technique being applied at $M = 3.85$. The pressure distribution curves are plotted as a function of the nondimensionalized separation distance. The separation point is at $\Delta X/\delta^* = 0$. The lower dashed curve is the correlated pressure curve for the step height that is 1.5 times the displacement thickness of the turbulent boundary layer ($\delta_{eff} = 1.5\ \delta^*$). It has the characteristic shape of a pressure disturbance that has an oblique shock at the separation point shown previously in figure 4. The top dashed curve envelopes the peak pressures for various step heights. For the filler bar analyses, the pressure disturbances were obtained by using the lower dashed curve from the point of separation to an appropriate point and then fairing a distribution to the enveloping curve for the step height of interest. Details of the development of the correlation technique can be found in reference 7.

The effect of sweep angle on the pressure distribution in front of a forward facing step was taken into account using data from reference 8 (figure 7). The forward face of a stepped tile was assumed to be swept 45° with respect to the local flow. Base pressure predictions on the aft facing steps were based on data from reference 9 (figure 8). The exponent, n, in the definition of characteristic length for the Reynolds number was empirically determined to be 0.9 in the reference.

Flow Model

With the pressure disturbances around the top of a stepped tile defined, pressure distributions in the tile gaps, in the SIP and filler bar, and within the silica foam tile can be calculated along with the resulting mass flow rates. Figure 9 is a schematic of a 9-tile array flow model that was developed to analyze the flow around a stepped tile (Tile 9 in figure 9). The tile gaps were modeled as flow passages around the tiles. Boundary conditions at the top of tiles were the calculated pressure disturbances around the stepped tile and a constant pressure, P_{local}, around the other tiles in the array to simulate the zero aerodynamic pressure gradient assumption. Lateral movement of the stepped tile caused by the pressure differences around it were simulated in the flow model because the SIP material is very flexible and allows tile movement. The position of the remainder of the tiles in the array was held constant. Figure 10 shows further detail that was incorporated into the flow model. View A in the figure shows flow passages near the filler bar that were modeled. The flow passages include flow in and out of the bottom of the tile where it is not bonded to the SIP, flow between the tile and filler bar, and flow in and out of the SIP. Flow through the fibrous material of the filler bar was also considered.

The equation that describes flow through porous media,

$$\dot{m} = - \frac{K_p \rho A_c}{\mu} \frac{dP}{ds} \tag{1}$$

is analogous to the steady state heat conduction equation

$$\dot{q} = - k A_c \frac{dT}{ds} \tag{2}$$

The flow in the tile gaps can be described as flow between parallel walls. Mass flow rates between parallel walls for laminar incompressible flow (calculated Reynolds numbers in the tile gaps indicate the flow is laminar to transitional) can be obtained from

$$\dot{m} = - \frac{1}{12} \frac{\rho w^2 A_c}{\mu} \frac{dP}{ds} \tag{3}$$

This equation is also analogous to the equation for steady state heat transfer. By using these analogies, the Martin Interactive Thermal Analyzer System (MITAS) (a general purpose finite difference heat transfer computer program) was used to obtain the pressure and flow distribution around the stepped tile. The flow model, originally developed for a tile loads analysis using ascent conditions, was modified during the study to account for compressibility effects in the tile gap flow. This modification was necessary because pressure differences calculated around the stepped tile were large enough to cause compressible flow. The compressible flow in the tile gaps was modeled assuming internal flow of an ideal gas with constant cross-sectional area and frictional effects (Fanno line flow). Complete details of the modified flow model can be found in reference 7.

Thermal Model

A thermal model representing the region around a stepped tile was developed to determine temperature response to hot gas flow in the tile gaps. The region modeled is shown in figure 11. The model included portions of the two tiles on each side of the gap and the filler bar, SIP, and aluminum substrate at the base of the tiles. It was chosen because the mass flow rates in the tile gap are highest at the corner of the tile where the pressure distribution goes from a high pressure region on the forward face to the low pressure region on the aft face of the stepped tile. The thermal model was limited to this region of the stepped tile to keep the model size within the capacity of MITAS. It was assumed that the temperature of the gas entering the modeled region in the horizontal direction was equal to the temperature of the gas in the gap in the center of the model at the same depth from the surface. This assumption was made because the flow down the gap is much larger than the flow entering the gap in the horizontal direction. The inlet temperature of the gas that entered the tile gap in the vertical direction was assumed to be the integrated average stagnation temperature of the boundary layer air from the tile surface to a point in the boundary layer equal to the tile step height. Convection, conduction, and radiation on the tile sidewalls and top surface were accounted for in the analysis. An energy balance was also maintained on the gas as it flowed through the tile gap.

ANALYSIS RESULTS

Figure 12 is an example of the results from the pressure disturbance calculations. The zero point for atmospheric entry time is taken to be the time at which the orbiter reaches 400,000 feet altitude during entry. Pressure and flow calculations were made at discrete time points with freestream conditions held constant. Flow data for the discrete time points was used in the transient temperature calculations over corresponding time intervals. The curves are terminated at the time when maximum filler bar temperature occurs. The maximum pressure difference across a 0.1 inch stepped tile at the fuselage location was approximately 0.33 psi. Figure 13 is an example of the results obtained from the transient thermal analysis. The result is for a 0.1 inch stepped tile at the fuselage location. The filler bar temperature peaks at 1470°F. It occurs after boundary layer transition (transition is indicated by the rapid rise in inlet gas temperature at 1250 seconds) and after the tile surface temperature has begun to fall. Table 2 shows a summary of peak filler bar temperature results for the fuselage location. Two different tile step heights (0.04 inch and 0.1 inch) were held constant and the tile gap width was allowed to vary. The maximum step size (0.03 inch) and maximum gap width (0.065 inch) that are acceptable during tile installation are also indicated on the figure. Extrapolation of the calculated results to these maximum installation tolerances indicates damage to the filler bar would not occur or at least would be minimized if the tile step height and gap width could be held within the tolerances. Table 3 is a summary of the peak filler bar temperature results at the wing location. Only one gap width (.05 inch) was analyzed. These results also indicate filler bar damage can be minimized by maintaining tile steps and gaps within the specified installation tolerances.

POTENTIAL SOLUTION USING GAP FILLERS

As shown in the analysis, filler bar charring is caused by the flow of hot gases in the tile-to-tile gaps. The rate of hot gas flow in this gap depends on the width of the gap and the size of the forward or rearward facing step at the heated surface. It follows that the filler bar charring problem can be solved by controlling the steps and gaps to within acceptable limits. Since control of steps and gaps in the TPS has been difficult, consideration should be given to installing additional tile gap fillers to reduce hot gas flow.

The suggested solution to the filler bar charring problem is to install gap fillers at all locations where filler bar charring is a problem. The suggested gap filler is different from the gap fillers which have been used previously on the Shuttle orbiter. A sketch of the gap filler design concept is shown in figure 14. The ceramic fiber gap filler would extend up to the height in the gap where the maximum gas temperature and loading due to hot gas flow are within the capability of the gap filler material. The gap filler could be bonded on one side to the tile using a high temperature bonding material (colloidal silica could be used) or it could be bonded at the bottom to the tile or the filler bar using a lower temperature bonding material (RTV could be used). The gap filler would be compressed on installation so that it would remain in contact with the tile side wall when the tiles shift under load. The black glass coating (this coating is 0.02 inches thick with a density of 104 lbm/ft.^3) could be left off of the tile side wall where the side wall is covered by the gap filler yielding a net weight reduction. The black coating would be maintained in the upper part of the gap. One of the design requirements for the Shuttle orbiter is a cold soak condition. The cold soak causes the tile-to-tile gap to close so that a gap filler in these gaps will load the tiles. These cold soak loads could be reduced if necessary by cutting out the lower part of the tile to accommodate a thicker gap filler with a nominal gap still maintained in the upper part of the gap as shown in figure 14.

The thermal performance of a half-height gap filler made of ceramic fiber blanket material was estimated by analysis. The material chosen for this gap filler analysis has a density of 6 lbm/ft^3. The permeability used in the analysis was 3.66×10^{-10} square feet as measured for a pressure of 142 psf (pounds per square foot) and a pressure gradient of 1114 psf per foot. (See table 4 for test results.) This gap filler material has a temperature capability of 2600°F. The adjustment to the model to represent the gap filler was to set the tile-to-tile gap such that the flow resistance of the open gap is equivalent to the flow resistance of an 0.05-inch gap with a half-height ceramic fiber gap filler installed. Based on the gap filler permeability of 3.66×10^{-10} square feet and a gap filler installed in the entire gap the equivalent open gap width is 0.00316 inches:

$$G_1 = G \tag{4}$$

$$\frac{K_p \rho w_{gf} B}{\mu L_t} = \frac{1}{12} \frac{\rho w_{pp}^3 B}{\mu L_t} \tag{5}$$

$$w_{pp} = [12\ K\ w_{gf}]^{1/3} = 0.00316 \text{ inches} \tag{6}$$

The equivalent gap width for the case of a half-height gap is approximated by comparison of flow down the gap:

$$G_2 = G \tag{7}$$

$$\frac{K_p \rho w_{gf} B}{\mu (L_t/2)} = \frac{1}{12} \frac{\rho w_{pp}^3 B}{\mu L_t} \tag{8}$$

$$w_{pp} = [24\ K\ w_{gf}]^{1/3} = 0.00398 \text{ inches} \tag{9}$$

The thermal model was run with an initial gap width of 0.004 inches to represent this half-height gap filler being installed in the 0.05-inch tile-to-tile gap. The wing location with an 0.06-inch tile-to-tile step was chosen for the gap filler analysis. The pressure boundary conditions are the same as for the analysis without the gap filler and are given in figure 15. The temperature results of the gap filler analysis are given in figure 16. The results show that the addition of a half-height ceramic fiber gap filler protected the filler bar such that charring would not occur. The maximum filler bar membrane temperature calculated was only 450°F while 970°F is required to start the charring process. The calculated filler bar temperature for the same conditions and

0.05-inch gap without gap filler was 1747°F. The half-height ceramic fiber gap filler reduced the peak filler bar temperature by 1297°F.

CONCLUSION

An analysis of the entry heating that occurs during entry in the tile-to-tile gap due to uneven tile heights in the Shuttle orbiter TPS has been performed. In order to conduct the analysis, a technique was developed for predicting the local pressure disturbance caused by a stepped tile. In addition, a method was developed for calculating the air flow rates in the tile-to-tile gaps, and for predicting the temperature level of the gas ingested from the boundary layer. A thermal analysis was conducted on the stepped tile configuration to determine the extent of heating on the tile sidewalls, the filler bar, and the SIP due to the hot air flow in the gap. Combinations of tile step heights and tile-to-tile gaps that could cause varying degrees of damage to the filler bar on the lower fuselage and wing were determined. The magnitudes of the predicted step heights and gaps were comparable to the step heights and gaps that were observed in damaged regions after each of the initial flights of the Shuttle. The results indicate that the steps and gaps must be controlled within tight tolerances during tile installation and the tolerances must be maintained in flight. If the tolerances cannot be maintained, tile-to-tile gap filler would be an alternative. Analysis indicated that a half-height, flexible, ceramic fiber blanket gap filler prevents charring of the filler bar. At the present time, the TPS is inspected after each flight for damaged filler bar. If there is sufficient damage, the filler bar is replaced and a rigid temporary gap filler is added.

REFERENCES

1. Tannehill, J. C.; and Mugge, P. H.: Improved Curve Fits for the Thermodynamic Properties of Equilibrium Air Suitable for Numerical Computations Using Time-Dependent or Shock Capturing Methods, Part I - Final Report. NASA CR-2470, October 1974.

2. Adams, John C., Jr.; and Martindale, William R.: Hypersonic Lifting Body Windward Surface Flow-Field Analysis for High Angles of Incidence. AEDC-TR-73-2, February 1973.

3. Hamilton, H. Harris, II: Approximate Method of Predicting Heating on the Windward Side of Space Shuttle Orbiter and Comparisons with Flight Data. AIAA Paper No. 82-0823, June 1982.

4. Zukoski, Edward, E.: Turbulent Boundary-Layer Separation in Front of a Forward-Facing Step. AIAA Journal, Vol. 5, No. 10, pp. 1746-1753, October 1967.

5. Uebelhack, H. I.: Turbulent Flow Separation Ahead of Forward Facing Steps in Supersonic Two-Dimensional and Axisymmetric Flows. Von Karman Institute Technical Note 54, July 1969.

6. Wu, J. M.; Valkili-Dastjerd, A.; Collins, E. G.; Reddy, K. C.; and Moulden, T. H.: Fundamental Studies of Subsonic and Transonic Flow Separation. Part III. Third Phase Summary Report. AEDC-TR-79-48, October 1979.

7. Smith, D. M.; Petley, D. H.; Edwards, C. L. W.; and Patten, A. B.: An Investigation of Gap Heating Due to Stepped Tiles in Zero Gradient Regions of the Shuttle Orbiter Thermal Protection System. AIAA Paper No. 83-0120, January 1983.

8. Lord, Douglas R.; and Czarnecki, K. R.: Aerodynamic Loadings Associated with Swept and Unswept Spoilers on a Flat Plate at Mach Numbers of 1.61 and 2.01. NACA RM L55L12, March 1956.

9. Wu, J. M.; Su, M. W.; and Moulden, T. H.: On the Near Flow Field Generated by the Supersonic Flow Over Rearward Facing Steps. Supersonic Characteristics of Flow Field Over Rearward Facing Steps TLSP: Final Report, AD-736770, Tennessee University, Tullahoma, November 1971.

TABLE 1.- STS-1 POST-FLIGHT MEASUREMENT EXTREMES IN DAMAGED FILLER BAR AREAS

TILE/TILE STEPS	-0.099 TO +0.12 in.
TILE/TILE GAPS	0.010 TO 0.13 in.

CATEGORIZATION OF DAMAGED FILLER BAR

CATEGORY	TEMPERATURE	DAMAGE
1	970 °F	RTV DISCOLORED
2	1100 °F	RTV CHARRED
3	1375 °F	RTV AND FILLER BAR CHARRED

TABLE 2.- PEAK FILLER BAR TEMPERATURES AT FUSELAGE LOCATION

STEP, INCH	INITIAL GAP, INCH	MAX GAP, INCH	PEAK FILLER BAR TEMPERATURE, °F	CATEGORY
0.04	0.05	0.067	970	1
0.10	0.05	0.092	1500	3

INSTALLATION SPECIFICATION: TILE STEP - 0.030 INCH MAX
TILE GAP - 0.065 INCH MAX

TABLE 3.- PEAK FILLER BAR TEMPERATURES AT WING LOCATION

STEP, INCH	INITIAL GAP, INCH	MAX GAP, INCH	PEAK FILLER BAR TEMPERATURE, °F	CATEGORY
0.017 (INSTALL SPEC)	0.05	.063	864	
0.03	0.05	.080	1286	2
0.06	0.05	.103	1747	3

TABLE 4.- PERMEABILITY TEST RESULTS FOR FIBERFRAX 880JH (CARBORUNDUM CO.) CERAMIC FIBER BLANKET

Flow, Std. cu. ft.	P_1, psf	P_2, psf	$\dot{m}$, lbm/sec.	$-\frac{dP}{dx}$, psf/ft.	K_p, ft.^{2}
3.53×10^{-3}	200.5	83.5	4.409E-6	1114	3.66E-10
7.06×10^{-3}	273.4	83.5	8.818E-6	1816	3.57E-10
10.60×10^{-3}	338.3	83.5	1.323E-5	2426	3.40E-10
14.13×10^{-3}	396.8	83.5	1.764E-5	2893	3.24E-10
17.66×10^{-3}	448.3	83.5	2.205E-5	3474	3.14E-10
14.13×10^{-3}	398.5	83.5	1.764E-5	2999	3.21E-10
10.60×10^{-3}	342.5	83.5	1.323E-5	2466	3.31E-10
7.06×10^{-3}	278.5	83.5	8.818E-6	1856	3.45E-10
3.53×10^{-3}	203.3	83.5	4.409E-6	1141	3.54E-10

Sample thickness = 0.093 in.
Sample width = 1.26 in.
Sample length = 1.26 in.
Sample frontal area = 0.1172 in.^{2}
Standard temperature = 70 °F
Standard pressure = 2116 psf

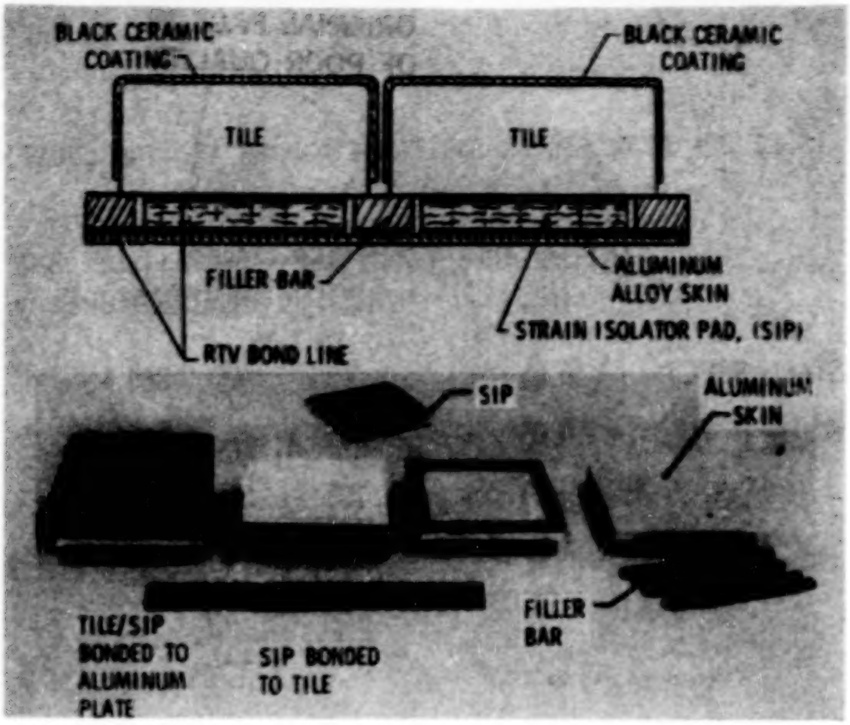
BLACK CERAMIC COATING
BLACK CERAMIC COATING
TILE
TILE
FILLER BAR
ALUMINUM ALLOY SKIN
STRAIN ISOLATOR PAD, (SIP)
RTV BOND LINE
SIP
ALUMINUM SKIN
FILLER BAR
TILE/SIP BONDED TO ALUMINUM PLATE
SIP BONDED TO TILE

Figure 1.- Tile configuration on lower surface of orbiter.

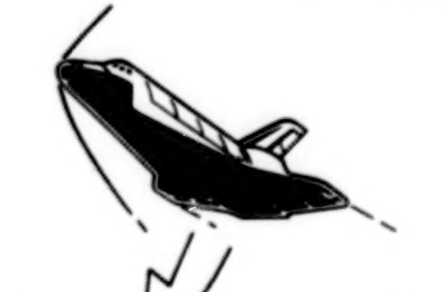
GAP WIDTH
STEP HEIGHT
LOCAL FLOW DIRECTION
P1
P2
Λ
SUBSURFACE FLOW

Figure 2.- Local pressure disturbances caused by a stepped tile.

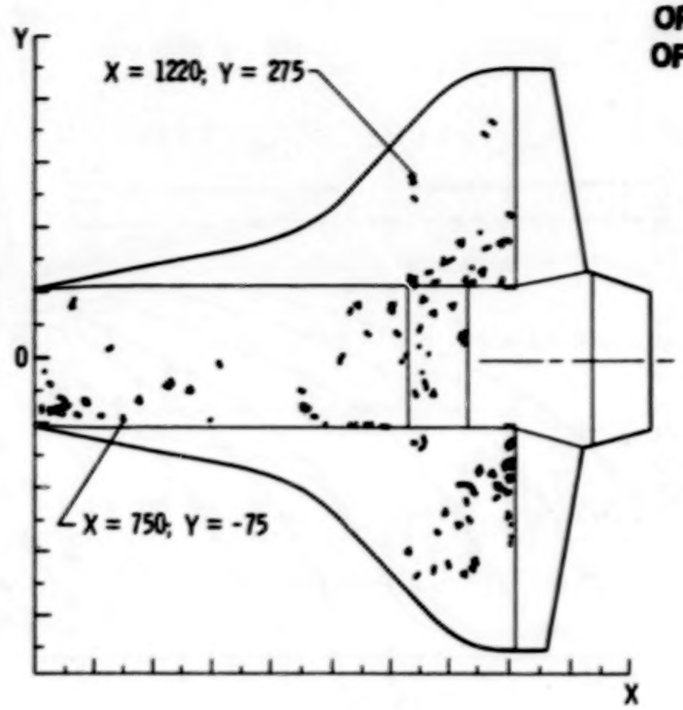
Y
X = 1220; Y = 275
0
X = 750; Y = -75
X

Figure 3.- STS-1 orbiter lower surface - charred filler bar locations for analysis.

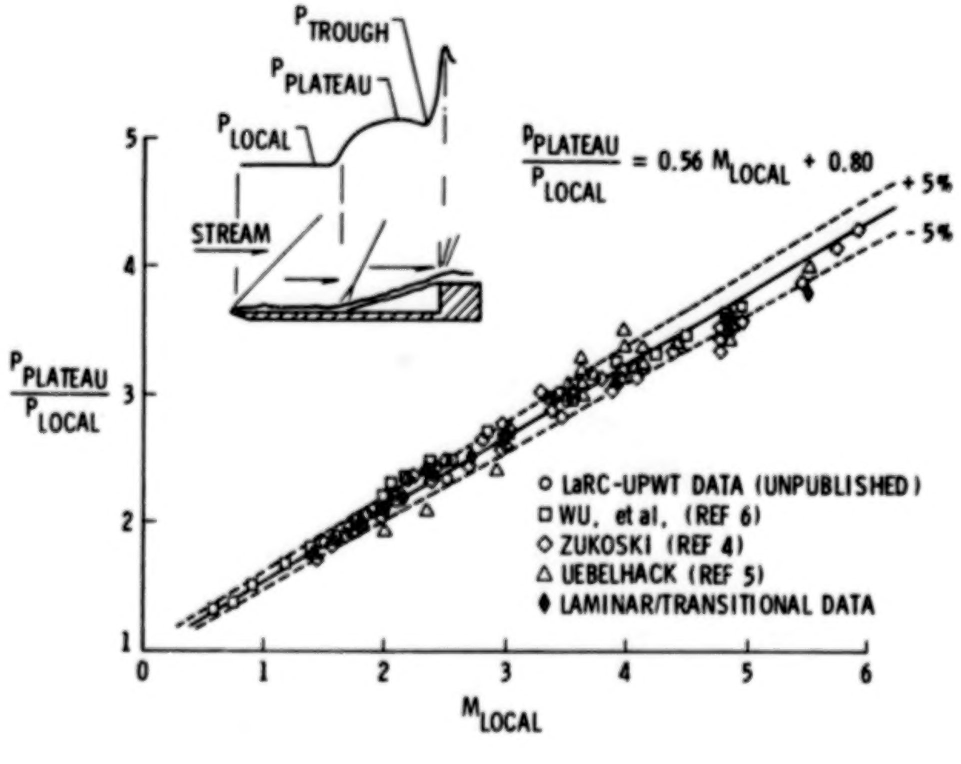

Figure 4.- Plateau pressure correlation.

ORIGINAL PAGE IS OF POOR QUALITY

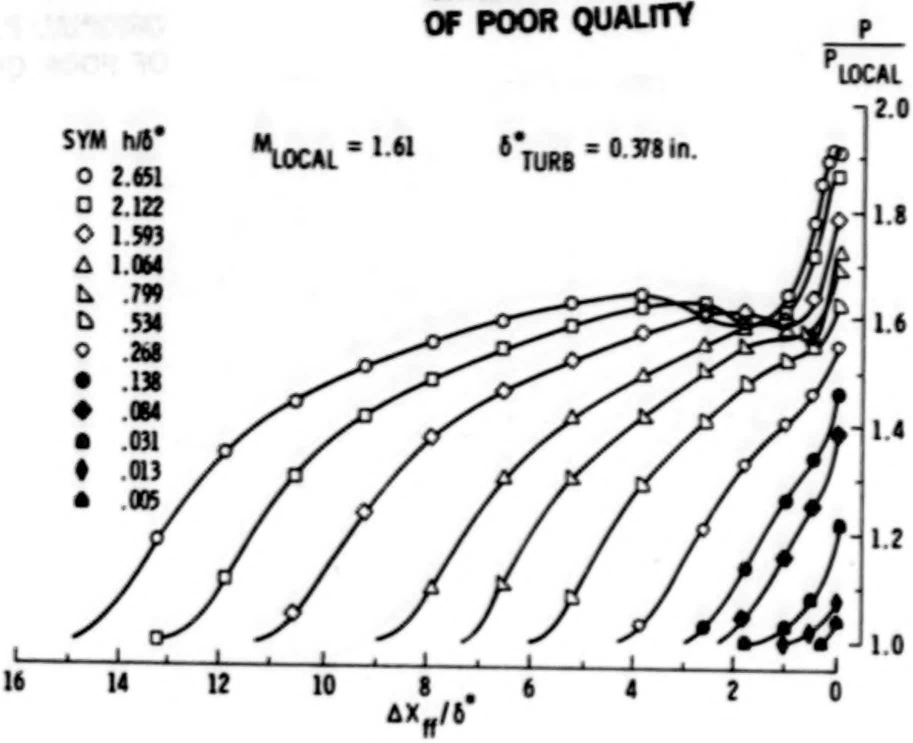

Figure 5.- Experimental pressure data for forward-facing steps.

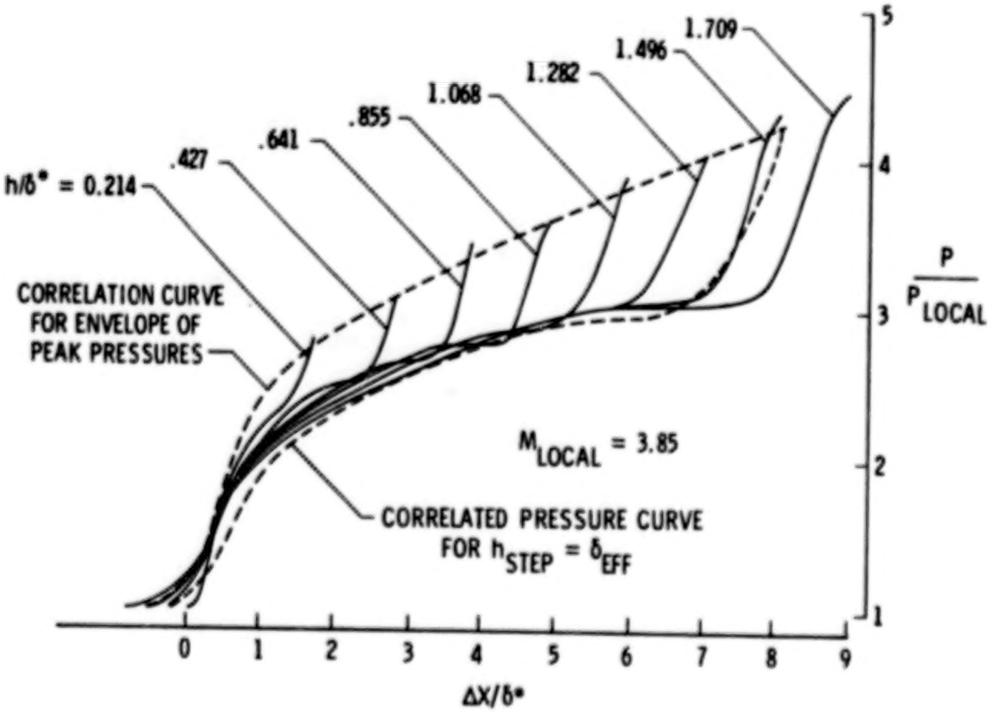

Figure 6.- Comparison of correlation and experimental pressure profile data.

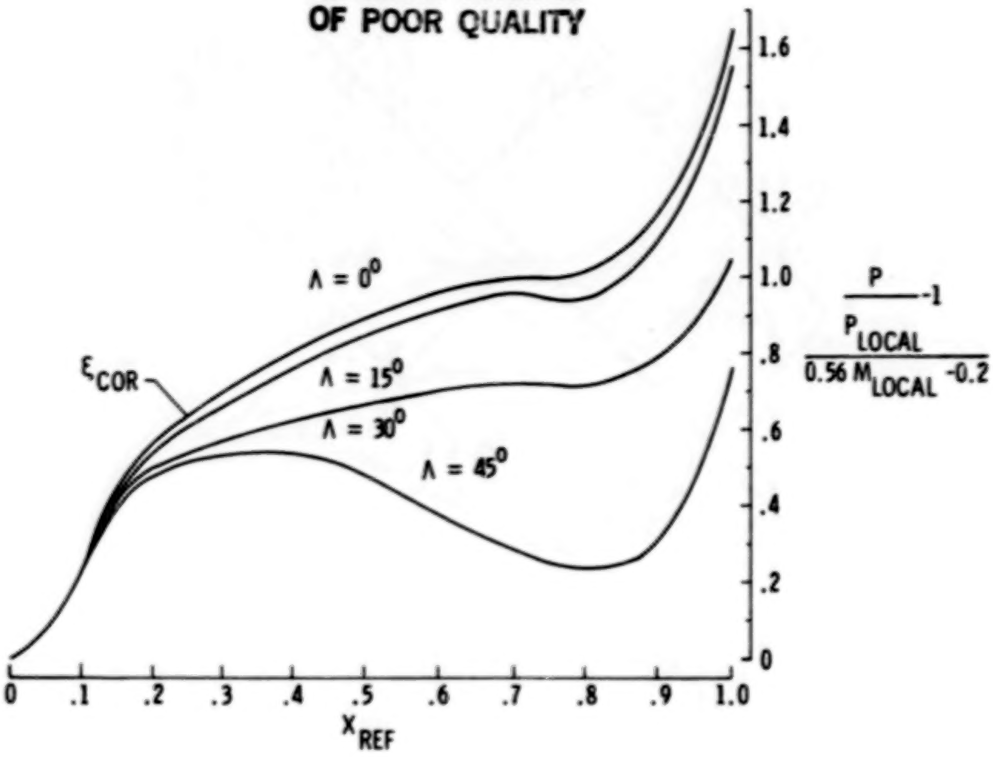

Figure 7.- Pressure distributions ahead of unswept and swept forward facing steps.

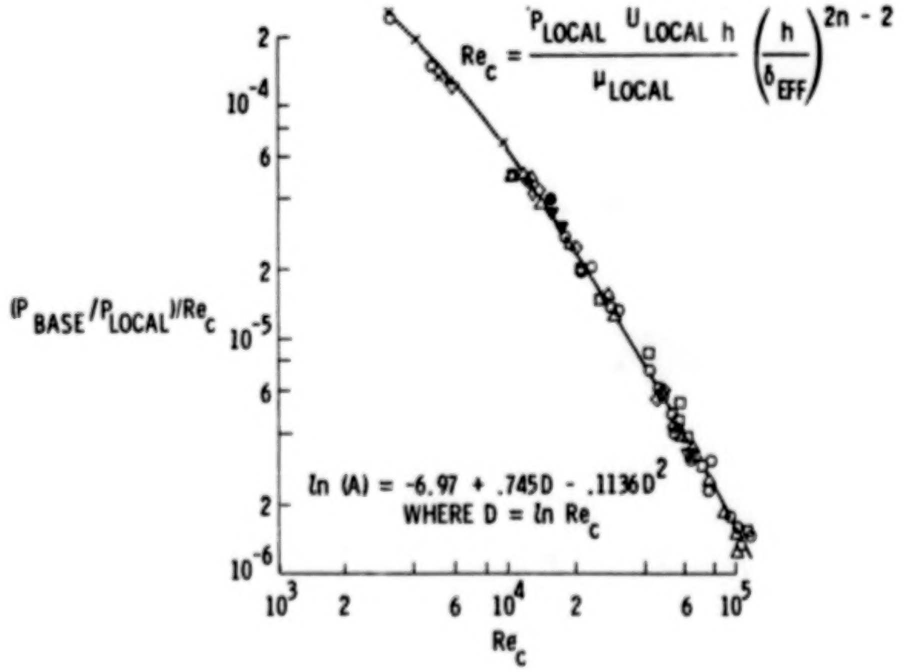

Figure 8.- Base pressure correlation (reference 9).

ORIGINAL PAGE IS
OF POOR QUALITY

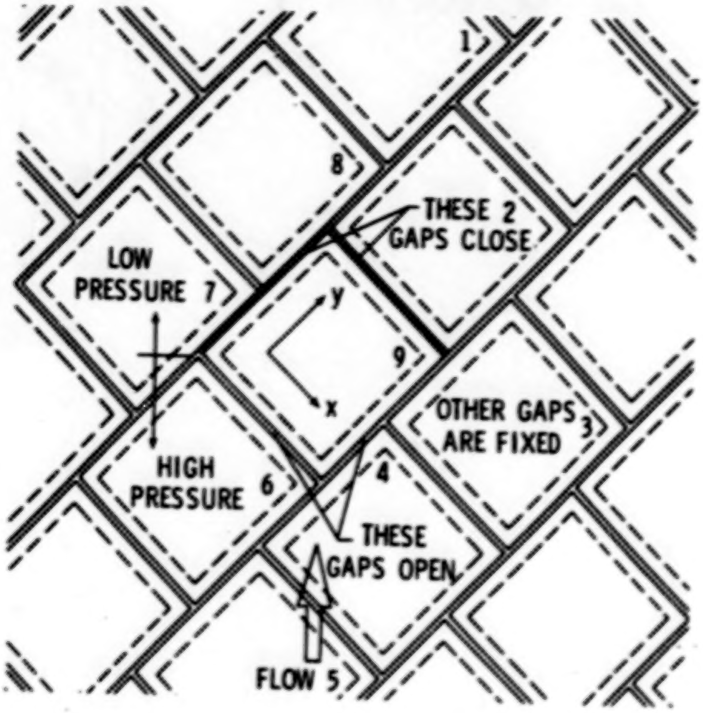
1
8
THESE 2
GAPS CLOSE
LOW
PRESSURE 7
y
9
x
OTHER GAPS
ARE FIXED 3
HIGH
PRESSURE 6
4
THESE
GAPS OPEN
FLOW 5

Figure 9.- Flow model tile array.

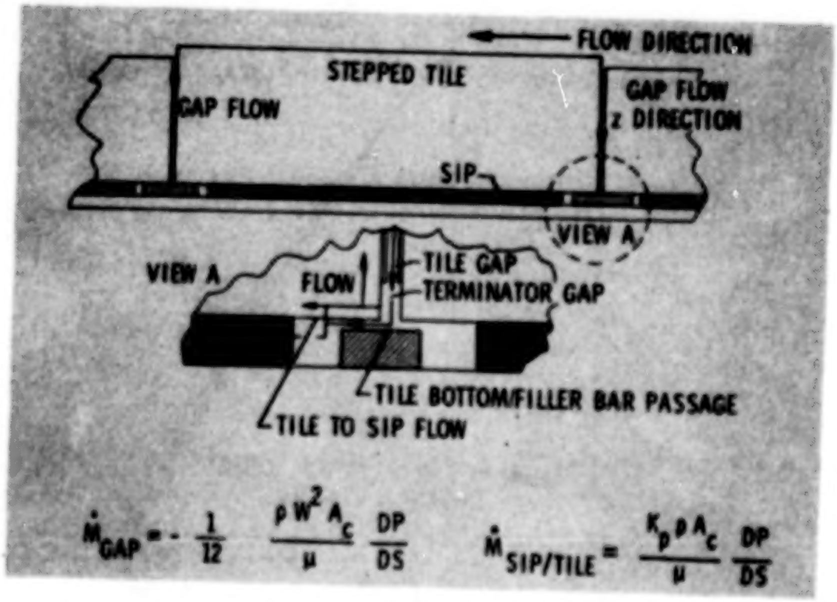
FLOW DIRECTION
STEPPED TILE
GAP FLOW
GAP FLOW
z DIRECTION
SIP
VIEW A
VIEW A
FLOW
TILE GAP
TERMINATOR GAP
TILE BOTTOM/FILLER BAR PASSAGE
TILE TO SIP FLOW

$$\dot{M}_{GAP} = -\frac{1}{12}\ \frac{\rho W^2 A_c}{\mu}\ \frac{DP}{DS} \qquad \dot{M}_{SIP/TILE} = \frac{K_p \rho A_c}{\mu}\ \frac{DP}{DS}$$

Figure 10.- Typical flow paths in Shuttle tile flow model.

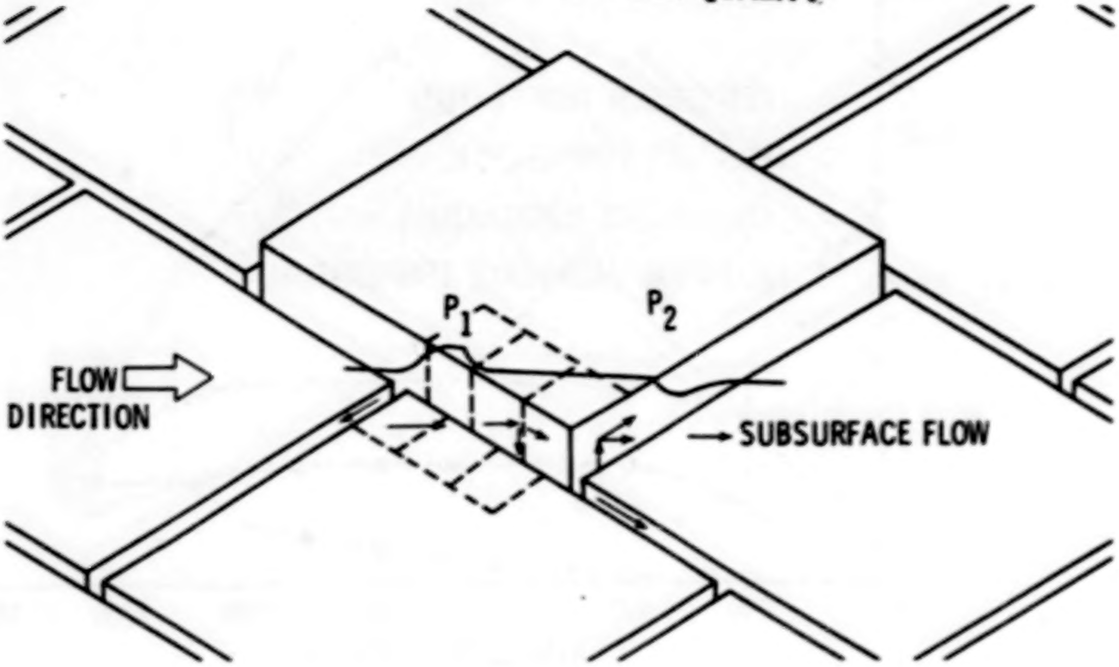
P1
P2
FLOW
DIRECTION
SUBSURFACE FLOW

Figure 11.- Region modeled for thermal analysis.

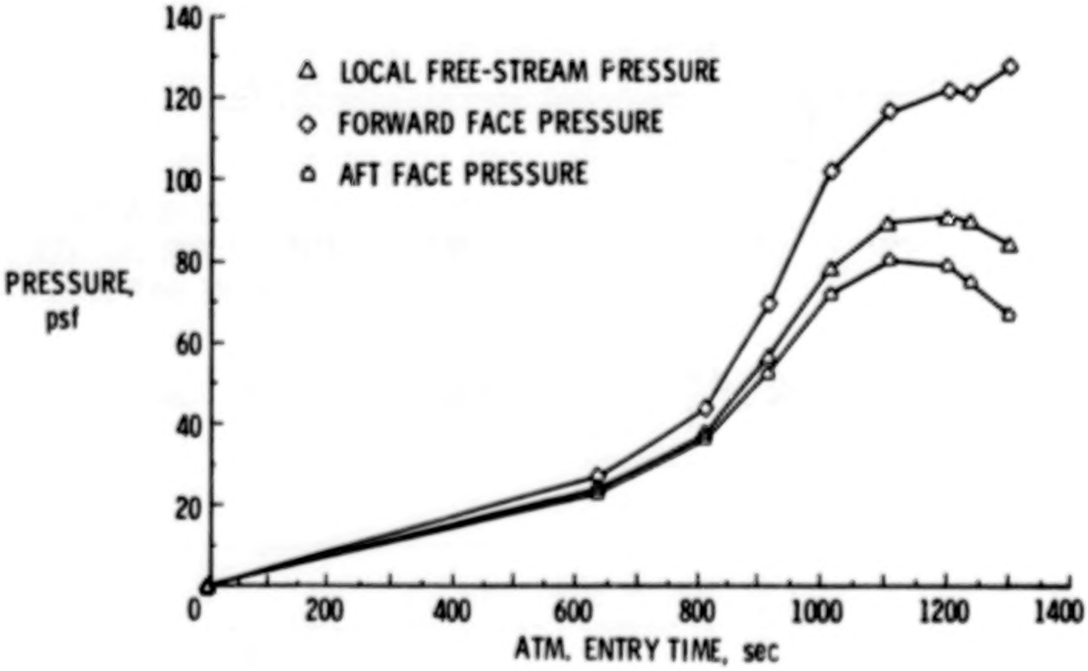

Figure 12.- Pressures at fuselage location, 0.1-inch step.

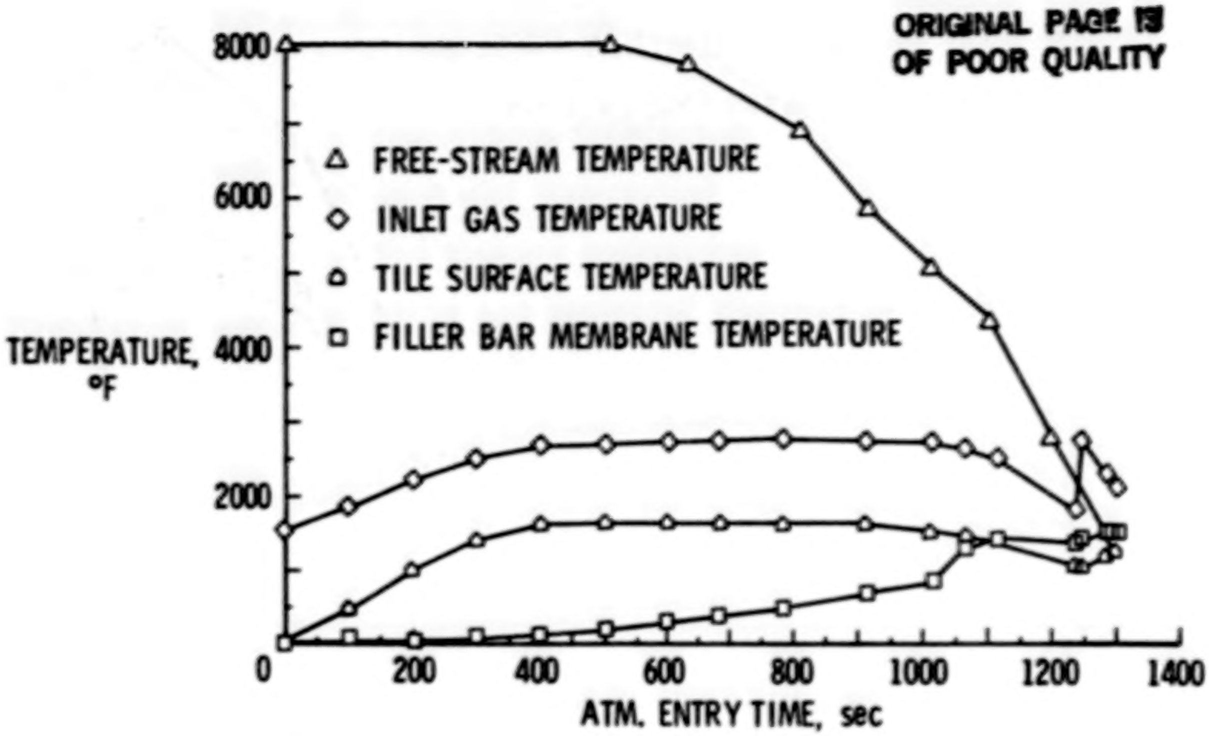

Figure 13.- Gap temperatures at fuselage location, 0.1-inch step.

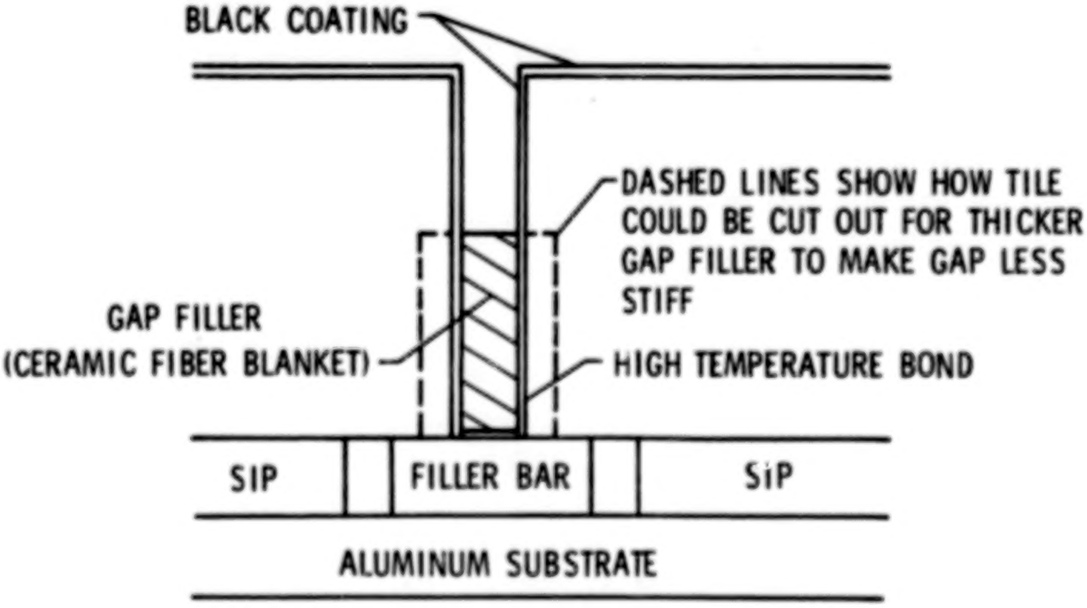
BLACK COATING
DASHED LINES SHOW HOW TILE COULD BE CUT OUT FOR THICKER GAP FILLER TO MAKE GAP LESS STIFF
GAP FILLER (CERAMIC FIBER BLANKET)
HIGH TEMPERATURE BOND
SIP
FILLER BAR
SiP
ALUMINUM SUBSTRATE

Figure 14.- Ceramic fiber gap filler concept.

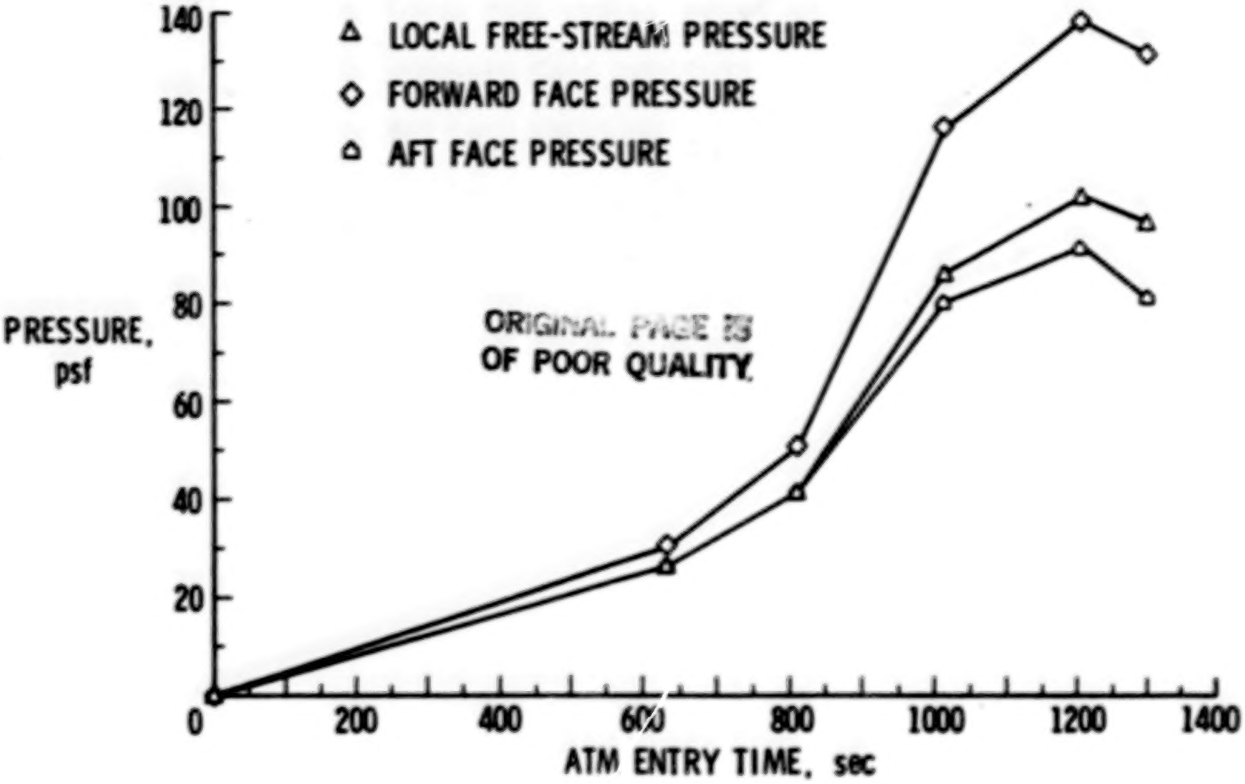

Figure 15.- Pressures at wing location, 0.06-inch step.

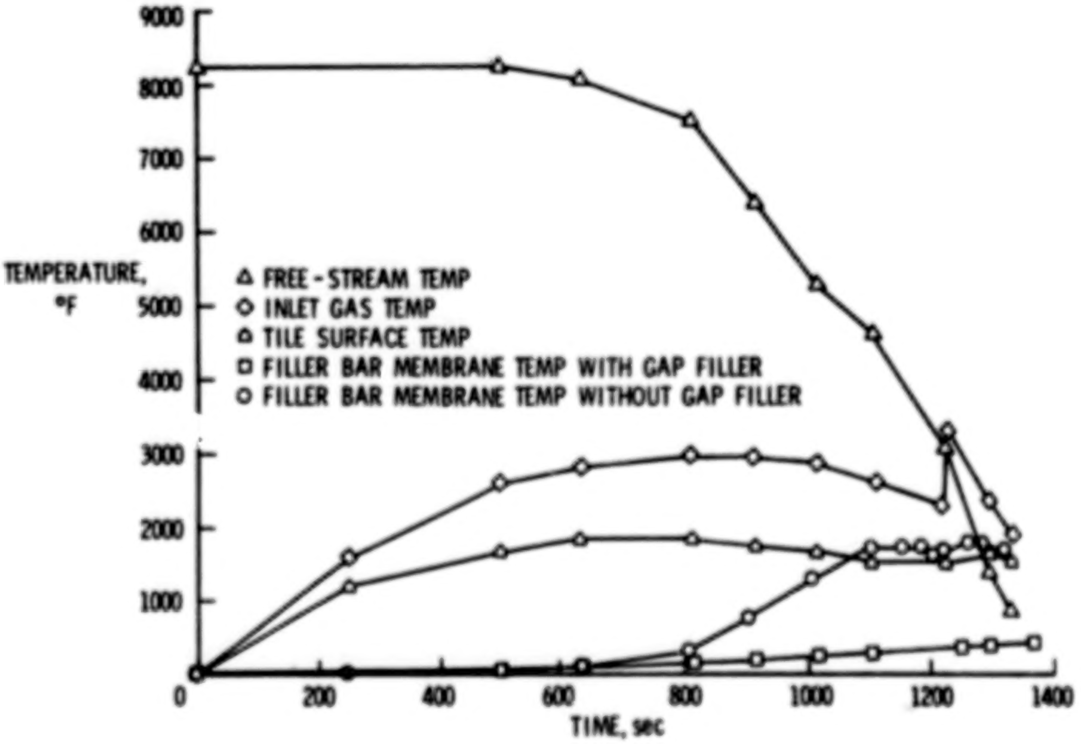

Figure 16.- Gap temperatures at wing location, 0.06-inch step.

N84
10156

UNCLAS

N84 10156

D/2

LEEWARD CENTERLINE AND SIDE FUSELAGE ENTRY HEATING PREDICTIONS FOR THE SPACE SHUTTLE ORBITER

Vernon T. Helms III
NASA Langley Research Center
Hampton, Virginia

SUMMARY

Heat transfer data measured along the leeward centerline and on the side fuselage of the Space Shuttle orbiter during STS-2 and STS-3 are compared with predictions of empirical heating techniques derived from wind-tunnel tests. Steps required to extrapolate an existing leeward centerline theory to flight conditions are described. Generally favorable comparisons from Mach 24 down to approximately Mach 7 for both flights are presented. The side fuselage impingement heating method is currently under development, but some preliminary results are available. The method is briefly described and compared with wind-tunnel and flight measurements. Side heating predictions are given for an STS-3 trajectory point near Mach 10 showing good agreement with flight data. There is evidence of embedded vortices emanating from the side fuselage impingement line which significantly enhance local heating rates at both wind-tunnel and flight conditions.

INTRODUCTION

Heating on top of the Space Shuttle orbiter's vortex-dominated fuselage is a complex function of Mach number, Reynolds number, and angle of attack. The upper fuselage thermal environment is generally characterized in terms of heating to the leeward centerline where heating rates can be relatively high.[1-3] An empirical technique for predicting top centerline heating on the orbiter has been developed and successfully applied to wind-tunnel data covering a large range in Reynolds number and angle of attack at Mach 6 and 10.[4] This method consists of a modified turbulent swept cylinder correlation using an effective local sweep angle that is measured directly from oil-flow patterns on the upper fuselage. A consistent relationship was demonstrated between the axial distribution of measured sweep angles and the distribution of top centerline heating. This report explains how to extrapolate these wind-tunnel sweep angles to account for conditions at flight Reynolds numbers and Mach numbers. Comparisons of leeward centerline heating predictions with flight values are then presented.

The basic concepts for a new technique designed to predict heating along the side fuselage impingement line are also presented here. This method uses the same form of heating equation as the top centerline theory. Furthermore, it makes use of similar assumptions concerning the relationship between surface flow directions and the side fuselage impingement heating distribution. The side fuselage method is derived from oil-flow and phase-change paint wind-tunnel data and supplemented by thermocouple measurements. Although the

PAGE 912 INTENTIONALLY BLANK

PRECEDING PAGE BLANK NOT FILMED

side impingement method is still under development, some promising preliminary comparisons have been made with both wind-tunnel and flight heating rates.

SYMBOLS

AFFDL	Air Force Flight Development Laboratory
C	Chapman-Rubesin coefficient
L	characteristic length of wind-tunnel model or full-scale vehicle as indicated
M	Mach number
OMS	Orbital Maneuvering System
q_c	convective heating rate
q_{c_h}	stagnation heating rate on a sphere with radius equal to average height of orbiter flat side body
q_{c_o}	stagnation heating rate on a scaled one-foot radius sphere in the free stream
q_{c_s}	stagnation heating rate on a sphere with radius equal to that of orbiter top fuselage
Re	Reynolds number, based on L unless otherwise specified
s	cross-sectional surface running length measured from top centerline
STS	Space Transportation System
T	temperature
x	axial length measured from orbiter's nose
℄	centerline
α	angle of attack
α_r	reference α defined in equation (6)
β	bow shock angle measured with respect to free stream direction
δ	flow deflection angle across bow shock
ϵ	surface flow angle and local angle of attack
η	change in sweep angle with respect to angle of attack
η'	change in η with respect to x/L

Λ	effective sweep angle
Λ_r	reference Λ defined in equations (3), (4), and (5)
ν	Prandtl-Meyer turning angle
ϕ	Mach number correction factor
$\overline{\chi}$	hypersonic viscous-interaction parameter = $M^3\sqrt{C}/\sqrt{Re}$ (see reference 5)

Subscripts

D	in equation (1), twice the orbiter upper fuselage radius; in equation (16), twice the average height of orbiter flat side body
ext	extrapolated
f	flight condition
L	quantity based on characteristic length
ℓ	quantity based on local flow properties
max	maximum value
t	wind-tunnel condition
∞	free stream

WIND-TUNNEL DATA

Oil flow patterns used to extrapolate the leeward centerline heating method to flight conditions were obtained on the upper fuselage of a 0.01-scale orbiter model in air in the Langley Research Center's Mach 6 and Mach 10 facilities,[6-8] and also on a 0.006-scale model in the 20-Inch Mach 14 AFFDL wind tunnel at Wright-Patterson Air Force Base.[9] Tests at Mach 6 ranged from 15° to 40° angle of attack at Reynolds numbers of 2.7×10^6, 5.4×10^6, and 7.3×10^6. Oil flows at Mach 10 were run at $\alpha = 15°$ to $45°$ for free-stream Reynolds numbers of 0.59×10^6, 1.19×10^6, and 2.37×10^6. Angles of attack of 15° to 40° at $Re_\infty = 0.280 \times 10^6$ and 0.423×10^6 were used at Mach 14.

The phase-change paint heat transfer, oil flow, and thermocouple measurements used to derive the side fuselage impingement heating method were made on 0.01-scale Shuttle orbiter models in Langley's Mach 6 and Mach 10 tunnels. Tests were conducted for $Re_\infty = 0.59 - 7.3 \times 10^6$ and at angles of attack of 20°, 30°, and 40°. Oil-flow tests were made using an aluminum model. Models for the phase-change paint heating measurements were constructed of a filled epoxy casting compound and a semi-infinite slab solution[10] was assumed during data reduction. The supplemental thermocouple results were drawn from a previously unpublished data base described in reference 4.

FLIGHT DATA

Flight measurements used for comparison with the top centerline and side fuselage heating methods were obtained on STS-2 and STS-3 at the locations shown in figure 1. The top centerline heating rates, measured by calorimeters, were the only data from STS-2 that were used in this report. The convective component of heat transfer for the calorimeters was determined by adding the radiative loss term to the calorimeter value. Heating due to solar radiation was then subtracted for those trajectory points where the instruments were in sunlight. The effect of solar heating was computed by the technique of reference 11. All of the instrument locations for STS-3 were occupied by thermocouples. A one-dimensional, transient-conduction analysis[12] was used to determine convective heating for these instruments with solar radiation heating, once again, computed separately.* A process combining the results of trajectory and atmospheric reconstruction provided information on vehicle attitude and free stream conditions.[13,14]

LEEWARD CENTERLINE HEATING

Review of Theory

The empirical leeward centerline heating method described in reference 4 is embodied in the equation

$$q_c = 0.75\, q_{c_s}\, Re_{\ell,D}^{0.3}\, (0.002975 + 0.003428 \cos\Lambda) \qquad (1)$$

The parameter q_{c_s} is the stagnation heating rate on a sphere with a radius equal to that of the Shuttle's upper fuselage. The Reynolds number is based on twice that radius. Both quantities are defined by local leeside flow properties computed using the flow model shown in figure 2. It was determined that the bow shock angle, β, through which free stream flow is processed must be equal to 2α. The flow deflection angle, δ, depends on M_∞ and β. The Prandtl-Meyer angle, ν, required to expand the flow to the Shuttle's upper fuselage is the sum of δ and α.

A pivitol feature of the theory is the close relationship between axial variations in heating and changes in upper fuselage surface flow directions, Λ, measured from oil flow photographs. The technique used to measure oil-flow patterns is illustrated in figure 3. The angle, ε, between the top centerline and a line drawn tangent to the oil-flow path inflection point is equated with the local angle of attack of flow approaching the top fuselage. The local sweep angle is thus defined as

---

*Heating rates reduced from STS-3 thermocouple data and solar-heating corrections for STS-2 and STS-3 were provided by D. A. Throckmorton, Aerothermodynamics Branch, Space Systems Division, Langley Research Center.

$$\Lambda = 90° - \varepsilon \tag{2}$$

Figure 4 shows two sets of wind-tunnel data where the measured sweep angles and the corresponding values of normalized heating rate are plotted as a function of x/L at two different test conditions. It is readily apparent that sweep angle and top centerline heating vary in an inverse fashion. A more appropriate term for Λ is "effective" sweep angle because, as defined for the purpose of the top centerline method, its value often becomes larger than 90°. Effective sweep angles greater than 90° are generally associated with inboard flow in the vicinity of the leeward centerline or with surface patterns caused by flow circulation ahead of the OMS pods and vertical tail. This is simply a mathematical convenience which allows the theory to penetrate zones on the leeward meridian where heating is influenced by various classes of separated flow patterns.[4] Using this approach, it was demonstrated that the leeward centerline theory is able to cope with the diverse heating environments represented by the wind-tunnel data. As an example, figure 5 shows a comparison of the theory's heating predictions with wind-tunnel data at the two test conditions indicated in figure 4.

Extrapolation to Flight Conditions

The wind-tunnel data base of upper fuselage surface flow directions is presented in figures 6, 7, and 8 where axial distributions of measured sweep angles for Mach numbers of 6, 10, and 14, respectively, are plotted for each angle of attack and Reynolds number combination. The hypersonic viscous-interaction parameter is also given for each test condition since this term is often used to classify the general behavior of leeside separated flow. Sweep angles from $x/L = 0.383$ to 0.731 correspond to axial locations where thermocouples were positioned on the wind-tunnel model. Additional measurements from $x/L = 0.30$ to 0.787 were made to encompass the locations of orbiter flight instrumentation. For a given Mach number, the Reynolds numbers in flight are considerably higher than those in the wind tunnel. Conversely, flight Mach numbers are greater than in the wind-tunnel data for corresponding Reynolds numbers. The ground-to-flight difference in each of these parameters will affect both upper-surface flow patterns and leeward centerline heating. Details of the many complex flow interactions which determine upper fuselage heating and surface flow patterns cannot be directly addressed due to the lack of information concerning the specific nature of leeside flow processes. However, it will be demonstrated that the relatively simple approach described here for extrapolating the leeward centerline heating equation and wind-tunnel sweep angles to flight conditions is able to capture the essential trends of the Reynolds number and Mach number influences on top centerline heating.

The first step toward converting the empirical leeward centerline heating method into a flight prediction technique is to establish a procedure for extrapolating the wind-tunnel sweep angles to their equivalent flight Reynolds number values. The next step is to define a criterion which relates the flight environment at each trajectory point to the proper set of wind-tunnel test conditions in order to duplicate flight trends in leeward centerline heating distributions. A third requirement is to develop a method of correcting for the effects of the differential between flight Mach numbers and the wind-tunnel Mach number from which the flight sweep angle distribution is to be extrapolated. The solution to these three problems will now be investigated.

A Reynolds number correction for the upper fuselage surface flow patterns may be obtained through manipulation of the sweep-angle data base. The data for each Mach number were cross-plotted in a variety of ways in order to reveal the format which optimized the effect of Reynolds number related trends. No easily discernable or consistent Reynolds number trends could be found in the Mach 6 data, which correspond to low values of $\bar{\chi}_\infty$. The mixed trends in the data for figure 6 also suggest that a majority of the Mach 6 sweep angle distributions are relatively independent of Reynolds number. It was concluded that the sweep angles measured over the Reynolds number range indicated in figure 6 require no overall correction for the effect of flight Reynolds number. However, flow angles for the different Mach 6 tests must still be linked to the appropriate range of flight conditions in a manner that is yet to be described. Similarly, sweep angles for the two free stream conditions near Mach 14, where $\bar{\chi}_\infty$ is large, were found to be nearly identical for most test cases. Only the surface flow directions at Mach 10, for intermediate values of $\bar{\chi}_\infty$, were subject to significant variations as a function of Reynolds number. Rough estimates for the range of $\bar{\chi}_\infty$ where wind-tunnel data must be corrected for the effects of flight Reynolds numbers can be offered on the basis of these assessments. The lower bound of this range may be $\bar{\chi}_\infty \approx 0.2$ to 0.3. These numbers are close to the maximum value for the Mach 6 tests but well below the lowest Mach 10 parameter for which, as will be discussed below, there is a strong Reynolds number effect. The upper bound on the range of $\bar{\chi}_\infty$, where Reynolds number corrections are required, is perhaps 1.5 or less. This is based on the observation that the axial sweep angle distribution for $\alpha = 45°$ at $M_\infty = 10.16$ and $\bar{\chi}_\infty = 1.219$ in figure 7 is similar to those at Mach 14 for lower angles of attack in figure 8. These Mach 10 flow patterns are still dependent on Re_∞, but it is suggested that a moderate increase in $\bar{\chi}_\infty$ may dissolve the association with Reynolds number.

The Mach 10 data exhibited very clear Reynolds number relationships by plotting sweep angles at all Reynolds numbers versus angle of attack for each axial location. This is illustrated for $x/L = 0.51$ in figure 9. Linear curve fits are used to indicate general trends of the flow-angle measurements at each of the three Reynolds numbers. Individual data points usually fall within $\pm 10°$ of the corresponding curve fit. An increase in Reynolds number increases the rate of change of the sweep angle as a function of angle of attack. The linear curve fits for each Reynolds number share one common value of sweep angle and angle of attack, denoted by Λ_r and α_r, where local flow directions are independent of Reynolds number. Plots like the one in figure 9 for other axial locations reveal variations in Λ_r and α_r that depend on x/L. The axial dependence of Λ_r is shown in figure 10. In a broad sense, Λ_r is an indication of the average magnitude of sweep angles on the upper fuselage at each axial station. The large values of Λ_r for $0.2 < x/L < 0.34$ are due to the influence of the canopy and the initiation of the leeside vortex flow patterns. The effect of the canopy diminishes with increasing axial length and leeside flow becomes well established beyond $x/L = 0.34$. As a result, Λ_r is nearly constant until reaching $x/L = 0.63$ where it begins to rise again. This is due to the forward extent of surface patterns with reversed flow directions, particularly at large angles of attack and high Reynolds numbers, caused by flow interactions with the blunt forward face of the OMS pods and with the vertical tail. The straight-line segments in figure 10 which approximate Λ_r are defined as follows:

for $0.2 < x/L < 0.34$
$$\Lambda_r = 117.7° - 133.7° (x/L) \tag{3}$$

for $0.34 \leq x/L \leq 0.63$
$$\Lambda_r = 72.0° \tag{4}$$

for $0.63 < x/L < 0.8$
$$\Lambda_r = 1.3° + 112.3° (x/L) \tag{5}$$

Figure 11 shows that α_r varies linearly and decreases with increasing x/L. This is primarily caused by the flow interactions at aft axial stations mentioned above. Effective sweep angles within the resulting surface flow patterns are elevated at high values of α and Re_∞. This forces the point of intersection for the various Reynolds number distributions, like those in figure 9, to lower angles of attack. The linear curve fit for α_r is given by

$$\alpha_r = 40.1° - 29.5° (x/L) \tag{6}$$

The parameters Λ_r and α_r will be used as part of the procedure to correct Mach 10 wind-tunnel sweep angles for the effects of flight Reynolds numbers.

A basic property of the Reynolds number correction for local flow directions is related to the slopes of the linear distributions of Λ vs α. A well-defined Reynolds number relationship develops when the slopes of the linear curve fits for each Reynolds number, $\eta = \Delta\Lambda/\Delta\alpha$, are plotted against x/L as in figure 12. The slope of Λ vs α, η, becomes larger at all axial stations with increasing Reynolds number. Each Reynolds number produces a maximum value of η at $x/L = 0.445$ as also shown by the straight-line curve fits for the data. The rate of change of η with respect to x/L depends on axial location and Reynolds number. This is shown in figure 13 where $\eta' = \Delta\eta/\Delta(x/L)$ is presented as a function of log Re_∞ for locations both fore and aft of $x/L = 0.445$. These terms are defined as follows:

for $x/L < 0.445$
$$\eta' = - 11.059 + 2.542 \log Re_\infty \tag{7}$$

for $x/L > 0.445$
$$\eta' = 15.429 - 3.297 \log Re_\infty \tag{8}$$

The variation of η at $x/L = 0.445$ provides the information which allows extrapolation of the entire Mach 10 sweep angle data base to higher Reynolds numbers corresponding to flight conditions. Figure 14 indicates that the three wind-tunnel data points that are available form a linear function of log Re_∞ which is given as

$$\eta_{max} = -13.332 + 2.424 \log Re_\infty \tag{9}$$

The dispersion of each data point from the linear correlation is quite small. This would appear to confine the error band of the extrapolation to a very narrow range up to Reynolds numbers at least an order of magnitude larger than the wind-tunnel values.

The assessment of Reynolds number effects on sweep angles for the various sets of wind-tunnel data and the extrapolation of the Mach 10 upper fuselage flow patterns to their equivalent flight Reynolds number form described above complete the first step required of applying the empirical leeward-centerline heating method to flight conditions. The second step, which was outlined earlier, involves the definition of a criterion that relates flight conditions to the proper set of wind-tunnel test data. The purpose of this is to insure that general trends in heating predictions will reproduce the axial distributions of flight heating measurements. The most direct way of obtaining this information is to collect heating distributions at various entry trajectory points and observe which of the wind-tunnel tests produce a corresponding inverse variation in sweep angles. Examples of such comparisons are illustrated in figures 15 through 17 for Mach numbers from 24 to approximately 7. Both flights produced nearly the same leeward centerline heating distributions at corresponding trajectory points. However, heating rates measured by calorimeters on STS-2 are higher than the thermocouple-derived heat-transfer rates for STS-3 at similar flight conditions. This point will be discussed later. In each case it is noted that the correct distribution of sweep angles corresponds to a wind-tunnel test for which the free stream Reynolds number is roughly 40 percent of the flight Reynolds number. A study of orbiter leeside heating in reference 15 also found that trends in ground-based heating rates appeared during entry only at flight Reynolds numbers that were considerably higher than in the wind tunnel. Apparently, the wind-tunnel environment more accurately simulates flight flow structures on the upper fuselage at higher Reynolds numbers over a wide Mach number range. For practical purposes, it is sufficient to use the set of wind-tunnel sweep angles for a freestream Reynolds number that is closest to 40 percent of the flight value. This allows nearly complete coverage of the orbiter's entry trajectory instead of having heating predictions at only a few discrete flight conditions. This relationship seems to be independent of either wind-tunnel or flight Mach number, which indicates that the distribution of leeward centerline heating is almost exclusively a function of free stream Reynolds number. According to this criterion, top centerline heating predictions at early entry times for STS-2 and STS-3 should use wind-tunnel sweep angles from the Mach 14 data. Flight heating distributions from $M_\infty = 20$ down to around 10 require the extrapolated Mach 10 Λ's. Trajectory points below this will use the Mach 6 wind-tunnel data.

Heating rates on STS-2 using calorimeters were significantly above the STS-3 thermocouple heating measurements. A general dissatisfaction with the calorimeters' performance on STS-1 and STS-2 resulted in their removal. There is also the unsettled question concerning hot-to-cold wall effects on heating rates measured by calorimeters. It can be expected that the large temperature differential which existed between the relatively cool calorimeters and the surrounding hot surface areas would cause these instruments to register a higher heating rate than was actually present. The thermocouple data do not suffer from this problem. For these reasons, the determination of a Mach number effect on leeward centerline flight heating predictions was based on thermocouple measurements from flight 3.

Heating predictions based on the Reynolds number extrapolation of wind-tunnel sweep angles will be required to obtain the Mach number correction. The following is a step-by-step set of instructions on how to use the Reynolds number correction. Heating predictions for a given trajectory point will make use of sweep angles at the wind-tunnel Reynolds number closest to 40 percent of the flight Reynolds number

$$Re_{\infty,t} \approx 0.4\, Re_{\infty,f} \qquad (10)$$

Calculate η_{max} and η' for both Reynolds numbers. Next determine η at the desired axial location using the expressions

$$\eta_f = \eta_{max,f} - (0.445 - x/L)\eta'_f \qquad (11a)$$

$$\eta_t = \eta_{max,t} - (0.445 - x/L)\eta'_t \qquad (11b)$$

Now compute Λ for each Reynolds number at the desired angle of attack assuming a linear curve fit of Λ vs α, as in figure 9, using the relationships

$$\Lambda_f = \Lambda_r + (\alpha - \alpha_r)\eta_f \qquad (12a)$$

$$\Lambda_t = \Lambda_r + (\alpha - \alpha_r)\eta_t \qquad (12b)$$

The change in sweep angle required to extrapolate the ground-based Λ to the flight Reynolds number is the difference between Λ_f and Λ_t, thus

$$\Lambda_{ext} = \Lambda + (\Lambda_f - \Lambda_t) \qquad (13)$$

where Λ is interpolated for x/L and α from the wind-tunnel data set identified by equation (10). Usually, $\Lambda \neq \Lambda_t$ because the linear distribution containing Λ_t is only meant to be a general representation of the measurements. However, the difference between two such linear representations for a given x/L and α is a direct measure of the effect of changing the Reynolds number. These steps must be repeated for all axial locations where heating predictions are to be made.

The lack of wind-tunnel data at very high Mach numbers precludes the possibility of extracting a Mach number effect on upper fuselage flow directions, and the associated leeward centerline heating, from the available ground tests. As with the criterion relating flight-heating distributions to wind-tunnel surface flow patterns, the effect of flight Mach number on the extrapolated heating prediction must be formulated using a small portion of the entry data. Heating rates at $M_\infty = 14.0$, $Re_\infty = 3.52 \times 10^6$, and $\alpha = 40.9°$ for flight three were chosen at random and plotted in figure 18(a) along with three sets of heating predictions calculated using the MINIVER[16] aerodynamic heating computer program. The highest heating predictions resulted from applying the uncorrected wind-tunnel sweep angles for $M_\infty = 10.34$ and $Re_\infty = 1.19 \times 10^6$ directly to the flight environment. The set of predictions at intermediate heating levels shows the effect of using the Reynolds number extrapolation outlined in equations (10) through (13). The result of this procedure is a predicted heating distribution that displays the general trends of the flight measurements, but the predictions are higher by almost a factor of two. This residual is assumed to be related to the difference between the flight and wind-tunnel Mach numbers. It can be accounted for at the Mach 14 trajectory point by multiplying heating rates for the Reynolds number extrapolation by a Mach number correction factor, ϕ, given as

$$\phi = (M_{\infty,t}/M_{\infty,f})^2 \tag{14}$$

The modified Reynolds-number corrected predictions are in good agreement with the measured heating rates. This factor was proven to yield results that were consistent with flight data at other trajectory points, as shown in figure 18(b) for $M_\infty = 20.0$, $Re_\infty = 1.53 \times 10^6$, and $\alpha = 39.8°$. The corresponding wind-tunnel sweep angles were for $M_\infty = 10.16$ and $Re_\infty = 0.59 \times 10^6$. Three sets of predictions are plotted as before. There is a much larger effect of Mach number at this entry point. But the Mach number correction in equation (14) places the fully corrected predictions very close to the flight data. Figure 18 demonstrates that the wind tunnel to flight difference in both Mach number and Reynolds number is important for predicting the magnitude of flight heat transfer to the orbiter's leeward meridian. By incorporating the Reynolds number extrapolation, the criterion for reproducing the flight heating distribution and the Mach number correction, equation (1) can now be written as

$$q_c = 0.75 q_{c_s} \phi \, Re_{\ell,D}^{0.3} (0.002975 + 0.003428 \cos \Lambda_{ext}) \tag{15}$$

At flight conditions requiring the use of wind-tunnel sweep angles from the Mach 6 or Mach 14 tests, Λ_{ext} is assumed to be equal to Λ.

Comparison of Leeward Centerline Heating Predictions With Flight Data

Figures 19 and 20 present comparisons of leeward centerline heating predictions with entry measurements made at Mach numbers from 24 to 7 during STS-2 and STS-3, respectively. Similar free stream conditions for each trajectory are shown here so that measurements and theory for both flights may be compared. Calorimeter measurements of heating rate on STS-2 are consistently above the thermocouple data of flight 3 by 50 percent to 100 percent or more. The largest differences occur at free stream Mach numbers greater than 20 and less than 10. Heating predictions for the two flights at approximately the same free stream conditions and angle of attack are at about the same level. This indicates that the discrepancy in heating measurements may be due to instrumental effects rather than large variations in the flight environment. The magnitude of predicted heating tends to agree more closely with STS-3 thermocouple measurements. The predicted axial distribution of heating rate is much the same as flight measurements of heating distributions for both entry trajectories. The very large disagreement between theory and flight data below Mach 10 on STS-2 may be another symptom of instrumental effects, as might be the case for $M_\infty > 20$. The comparisons at low Mach numbers for STS-3 are much closer.

Evidence for transition from laminar to turbulent flow can be seen in these comparisons, particularly in the thermocouple data of flight 3. Most of the predicted heating rates, which are turbulent, are higher than measured values by a factor of approximately two for $M_\infty > 20$. This is a clear indication of laminar flow on the upper fuselage at very high Mach numbers.

The theory and flight data rapidly converge for both flights beginning near $M_\infty = 20$. The entire leeward centerline appears to become turbulent within a very short time. However, another study[15] of leeward centerline heating for STS-3 concludes that transition to turbulent flow occurs no earlier than $M_\infty = 18$. This difference may be related to the corrections applied to wind-tunnel sweep angles used for heating predictions in the vicinity of $M_\infty = 20$. It was noted earlier that the high angle of attack, low Reynolds number Mach 10 flow patterns bear a resemblance to the Mach 14 sweep angles for which no Reynolds number correction is required. Perhaps by virtue of their relatively large value of $\overline{\chi}_\infty$, the low Reynolds number Mach 10 flow angles used in the $M_\infty = 20$ heating prediction may require less correction for Reynolds number effects than was imposed by the wind-tunnel extrapolation. If so, predicted heating rates could be higher than those indicated for the Mach 20 STS-3 trajectory point. This would shift the realm of fully turbulent flow to somewhat lower Mach numbers. But if such an influence of the viscous interaction parameter exists, it is not readily apparent in the available wind tunnel data. Even though corrections for this kind of second order effect may be necessary for heating predictions to agree exactly with flight data, the first-order corrections presented here produce favorable comparisons with entry heating measurements.

SIDE FUSELAGE HEATING

Basic Concepts of Theory

An empirical method for predicting side fuselage impingement heating on the Shuttle orbiter is under development. It is based on an analysis of oil-flow patterns and corresponding phase-change paint and thermocouple heating measurements. The side fuselage theory uses the same form of turbulent heating equation as for the wind-tunnel top centerline correlation. The equation as derived for $M_\infty = 10.36$, $Re_\infty = 2.37 \times 10^6$, and $\alpha = 40°$, since these parameters are close to the conditions for which flight comparisons will be made, is

$$q_c = 0.42\, q_{c_h}\, Re_{\ell,D}^{0.3}\,(0.003531 + 0.004069 \cos \Lambda) \tag{16}$$

The factor 0.42 corrects the reference heating rate, q_{c_h}, from the stagnation value on a sphere to that on a sharp-cornered slab of infinite length with a half width equal to the average height of the side fuselage flat surface. Reynolds number and the reference heating rate are based on local flow parameters that are computed using the methods outlined below, and the coefficients are determined by iteration using only a few data points at different values of Re_∞.

The surface oil-flow directions radiating away from the impingement line are also taken to represent angle of attack of flow approaching the side fuselage and, thus, a sweep angle in the same sense as illustrated in figure 3 for the upper body. The axial variation of sweep angle along the impingement location is shown in figure 21 for M_∞ = 10 and α = 40°. Sweep angles on the side fuselage show little change with Reynolds number. They are constant over the forward portion of the impingement line and increase sharply at large values of x/L. The increase in Λ was determined to be a result of an additional expansion of the flow before reaching the fuselage. Both factors contribute to a rapid fall in impingement heating at those locations.

The source of the impinging flow is assumed to be the shear layer which originates along a separation line on the strake's upper surface. It is further assumed that separation-point shear-layer flow properties are proportional to those at the same axial location on the strake's leading edge. Variations in leading-edge flow properties along the strake were accounted for by interpolation of pressure distributions computed by the three-dimensional High Alpha Inviscid Solution (HALIS)[17] computer code.* It was found that pressure increases linearly along the extent of the strake. Another simplifying assumption states that leading edge flow from a given fractional distance along the strake will influence heating at the same fractional distance along the side fuselage impingement line. This model allows the flow to travel downstream as it moves upward and over toward the fuselage.

These procedures were incorporated into the MINIVER computer program. Figure 22 shows an example of a comparison between the theory's side fuselage impingement line heating predictions and phase-change paint measurements for the test condition of M_∞ = 10.36, $Re_\infty = 2.37 \times 10^6$, and α = 40°. The initial rise in heating is due to the increase in pressure along the strake's leading edge combined with the constant Λ's in figure 21. Peak heating occurs just forward of x/L = 0.4 corresponding to the location at which sweep angles begin to increase. Larger sweep angles and the additional expansion of flow beyond this point cause a rapid reduction of impingement heating. The heating predictions are in close agreement with wind-tunnel data over the entire length of the impingement line. Similar comparisons have been obtained for all test conditions at Mach 10 which includes angles of attack from 20° to 40° and free stream Reynolds numbers of 0.59×10^6, 1.19×10^6, and 2.37×10^6.

Comparisons With Flight Data

The effect of Mach number on the heating prediction has not yet been assessed. Therefore, a preliminary comparison with flight data has been limited to the STS-3 trajectory point where M_∞ = 10.37, $Re_\infty = 5.41 \times 10^6$, and α = 38.9°. Flight Mach number and angle of attack are within the range of the wind-tunnel conditions. The flight Reynolds number is larger by over a factor of two. But wind-tunnel sweep angles, as well as the impingement location, showed little change with Reynolds number at a given angle of attack. Values of Λ and impingement location for α = 38.9° were interpolated from the wind-tunnel measurements and applied to the flight prediction. Figure 23 shows the resulting axial distribution of impingement heating rate for the selected flight parameters. The peak heating rate is approximately ten times higher than the average top centerline heating at this same trajectory point.

---

*Existing HALIS flow-field computations were supplied by K. James Weilmuenster, Aerothermodynamics Branch, Space Systems Division, Langley Research Center.

It is difficult for the relatively few instruments on the orbiter's side fuselage to obtain a direct measurement of impingement heating. Figure 24 shows the predicted location of flow impingement in relation to the positions of the side fuselage thermocouples. However, a comparison of the heating prediction shown in figure 23 with flight data can be accomplished as illustrated in figure 25. Cross-sectional measurements of heating at six axial stations are presented along with the predicted impingement heating for each value of x/L. Wind-tunnel measurements indicate that flow impingement moves off of the upper side fuselage near $x/L = 0.65$ for $\alpha = 40°$, so only data for $x/L \leq 0.594$ are used here. The next downstream array of orbiter instruments is at $x/L = 0.696$. The heating distributions superimposed on the data points were taken from wind-tunnel phase-change paint measurements for $M_\infty = 10.36$, $Re_\infty = 2.37 \times 10^6$ at $\alpha = 40°$ and normalized by the predicted impingement heating. The flight heating data generally conform to the trend and magnitude of the projected distributions. This seems to indicate that the impingement heating prediction is near the correct level.

Flight data at $x/L = 0.497$ and $x/L = 0.542$ contain some heating measurements that are approximately 80 and 120 percent above the mean local values, respectively. Figure 26 shows that these pulses of high convective heating are associated with large and erratic excursions in surface temperature which occur at later entry times. Similar temperature fluctuations affect many of the side fuselage thermocouple locations at slightly different times, but these variations are always confined to the high Reynolds number portion of the trajectory. The anomaly at $x/L = 0.497$ is above the impingement line while at $x/L = 0.594$ it is well below the impingement location. Many similar heating "spikes" were observed in the wind-tunnel data for Mach 6 and Mach 10, but only at locations above the impingement line. This is illustrated in figure 27 using one of the Mach 6 test cases for which Reynolds number is the same as for the STS-3 trajectory point. The average increase over local heating associated with these features in the wind tunnel was about 70 percent. The phase-change paint data revealed that the phenomena are highly localized, as indicated by the slender heating profile in figure 27. This same profile was applied to the data in figure 25 using dashed lines in order to distinguish actual flight measurements from normalized wind-tunnel heating.

It is suggested that these elevated local heating rates are caused by embedded vortices which are generated by viscous interactions during the impingement process. Embedded vortices are believed to be caused by boundary-layer cross-flow instabilities.[18] References 19 and 20 are two examples of the many studies on the relation between embedded streamwise vorticity and flow impingement. Figure 28 contains a photograph showing a sequence of uniformly spaced streaks in phase change paint above, and originating from, the impingement location on the orbiter model's side fuselage at a Mach 6 test condition. Each streak is thought to represent a very thin line of vortex impingement which produces locally higher heating, and the magnitude of heating decreases along its length. Side fuselage "streak" heating has also been noted on an early phase B orbiter configuration[21] and on the ASSET entry vehicle.[22] A larger number of streaks were observed in the phase-change paint tests with increasing Reynolds number and higher angles of attack. Streaks were present for all test conditions except $\alpha = 20°$ and 30° for Mach 10.

These trends indicate that side fuselage "streak" heating may well be expected to occur in the entry flight regime containing the selected STS-3 trajectory point. In addition, the changing number of streaks and variations in the spacing between them at different free-stream conditions and angles of attack mean that embedded vortices on the orbiter in flight will move longitudinally on the side fuselage. This motion will cause a number of individual vortices to sweep across a fixed location resulting in intermittent locally higher heating. This could explain the large temperature variations at later entry times shown in figure 26. Very large side fuselage STS-2 heating rates that have been previously documented[23] may also be caused by the onset of embedded vorticity.

CONCLUDING REMARKS

A method has been developed for extrapolating a wind-tunnel-developed empirical heating technique for the Space Shuttle orbiter's leeward centerline to flight conditions. The distribution of heating along the vehicle's leeward meridian was found to be primarily a function of Reynolds number. Axial heating trends in flight correspond to those in the wind tunnel for which the Reynolds number is approximately 40 percent of the flight value. Only those wind-tunnel leeside fuselage flow patterns at intermediate values of $\overline{\chi}_{\infty}$ displayed significant and consistent sensitivity to changes in Reynolds number. The effect of Mach number on heating predictions was determined through limited use of the flight data. Application of the extrapolated heating method to the flight environments of STS-2 and STS-3 produced generally favorable comparisons. It was tentatively concluded that the STS-2 heating measurements were of lower quality than those of STS-3. The theory may provide a somewhat conservative indication for the time of transition from laminar to turbulent flow. Heating predictions afforded by this procedure are adequate for the design of upper fuselage thermal protection systems.

A new technique for computing side fuselage impingement heating was briefly described. This method is derived from the leeward centerline theory. Although still under development, the side fuselage heating method was shown to agree well with wind-tunnel data and with selected STS-3 flight measurements. The comparison with flight data revealed that, as in the wind tunnel, there are areas of locally enhanced heating at side fuselage locations well away from the impingement line. The associated heating rates were approximately 100 percent higher than nearby undisturbed levels. It is suggested that this phenomenon is caused by embedded vortices resulting from viscous interactions that are perhaps related to flow reattachment at free-stream conditions which satisfy critical values of Mach number and Reynolds number at a given angle of attack. The existence of these features will have an impact on thermal protection requirements of future winged entry vehicles which experience flow impingement on the side fuselage.

REFERENCES

1. Whitehead, A. H., Jr., Hefner, J. N., and Rao, D. M., "Lee Surface Vortex Effects Over Configurations in Hypersonic Flow." AIAA Paper No. 72-77, January 1972.

2. Hefner, J. N., "Lee-Surface Heating and Flow Phenomena on Space Shuttle Orbiters at Large Angles of Attack and Hypersonic Speeds." NASA TN D-7088, 1972.

3. Zakkay, V., Miyazawa, M., and Wang, C. R., "Hypersonic Lee Surface Flow Phenomena Over Space Shuttle at Large Angles of Attack at $M_\infty = 6$." NASA CR-132501, 1974.

4. Helms, Vernon T., III, "An Empirical Method for Computing Leeside Centerline Heating on the Space Shuttle Orbiter." AIAA Paper No. 81-1043, June 1981.

5. Bertram, Mitchel H., "Hypersonic Laminar Viscous-Interaction Effects On the Aerodynamics of Two-Dimensional Wedge and Triangular Planform Wings," NASA TN D-3523, August 1966.

6. Goldberg, Theodore J., and Hefner, Jerry N. (Appendix by Emery, James C.), "Starting Phenomena for Hypersonic Inlets With Thick Turbulent Boundary Layers at Mach 6." NASA TN D-6280, 1971.

7. Schaefer, William T., Jr., "Characteristics of Major Active Wind Tunnels at the Langley Research Center." NASA TM X-1130, 1965.

8. Dunavant, James C., and Stone, Howard W., "Effect of Roughness on Heat Transfer to Hemisphere Cylinders at Mach Numbers of 10.4 and 11.4." NASA TN D-3871, 1967.

9. Gregorek, G. M., and Lee, J. D., "Design, Performance and Operational Characteristics of the ARL 20-Inch Hypersonic Wind Tunnel." Report No. ARL 62-392, Aeronautical Research Labs, Wright Patterson Air Force Base, August 1962.

10. Jones, Robert A., and Hunt, James L., "Use of Fusible Temperature Indicators for Obtaining Quantitative Aerodynamic Heat-Transfer Data." NASA TR R-230, February 1966.

11. Throckmorton, D. A., "Influence of Radiant Energy Exchange on the Determination of Convective Heat Transfer Rates to Orbiter Leeside Surfaces During Entry." AIAA Paper No. 82-0824, June 1982.

12. Throckmorton, D. A., "Benchmark Aerodynamic Heat Transfer Data from the First Flight of the Space Shuttle Orbiter." AIAA Paper No. 82-0003, January 1982.

13. Compton, H. R., Findlay, J. T., Kelly, G. M., and Heck, M. L., "Shuttle (STS-1) Entry Trajectory Reconstruction." AIAA Paper No. 81-2459, November 1981.

14. Price, J. M., "Atmospheric Definition for Shuttle Aerothermodynamic Investigations." Journal of Spacecraft and Rockets, Vol. 20, March-April 1983, pp. 133-140.

15. Throckmorton, D. A., and Zoby, E. V., "Orbiter Entry Leeside Heat Transfer Data Analysis." AIAA Paper No. 83-0484, January 1983.

16. Hender, D. R., "A Miniature Version of the JA70 Aerodynamic Heating Computer Program, H800 (MINIVER)." McDonnell Douglas Astronautics Company, MDC G0462, June 1970, Revised January 1972.

17. Weilmuenster, K. James, and Hamilton, H. Harris, II, "A Method for Computation of Inviscid Three-Dimensional Flow Over Blunt Bodies Having Large Embedded Subsonic Regions." AIAA Paper No. 81-1203, 1981.

18. Morkovin, Mark V., "Observations on Streamwise Vortices in Laminar and Turbulent Boundary Layers." NASA CR-159061, April 1979.

19. Seegmiller, H. L., "Surface-Flow Visualization Investigation of a Delta Wing Shuttle Configuration at a Mach Number of 7.4 and Several Reynolds Numbers." NASA TM X-62036, June 1970.

20. Ginoux, J. J., "On Some Properties of Reattaching Laminar and Transitional High Speed Flows." Von Karman Institute, Belgium, Technical Note 53, September 1969.

21. Matthews, R. L., Buchanan, T. D., Martindale, W. R., and Warmbrod, J. D., "Experimental and Theoretical Aerodynamic Heating and Flow Field Analysis of a Space Shuttle Orbiter." NASA TM X-2507, pp. 261-296, February 1972.

22. Pagel, L. L., Beardsley, P. P., and Gaumer, G. R., "ASSET Volume IV Correlative Analysis of Heat Transfer Data." AFFDL-TR-65-31, Volume IX, April 1966.

23. Lee, D. B., and Harthun, M. H., "Aerothermodynamic Entry Environment of the Space Shuttle Orbiter." AIAA Paper No. 82-0821, June 1982.

REFERENCES

1. Cooper, Paul A.; and Holloway, Paul F.: The Shuttle Tile Story. Astronautics and Aeronautics, Vol. 19, No. 1, January 1981, pp. 24-36.

2. Korb, L. J.; and Clancy, H. M.: Shuttle Orbiter Thermal Protection System: A Material and Structural Overview. Material and Process Applications - Land, Sea, Air, Space. Proceedings of the 26th National Symposium and Exhibition, Society for the Advancement of Material and Process Engineering, 1981, pp. 232-249.

3. Sawyer, James Wayne; and Cooper, Paul A.: Fatigue Properties of Shuttle Thermal Protection System. NASA TM-81899, August 1980.

4. Muraca, Ralph J.: Shuttle Tile Environments and Loads. The Shock and Vibration Bulletin, Bulletin 52, Part 2, May 1982, pp. 111-125.

5. Cooper, Paul A.; Miserentino, R.; Sawyer, J. W.; and Leatherwood, J.: Assessment of the Shuttle Orbiter Thermal Protection System Undensified Tiles Under Mission Dynamic Loads. Proceedings of the 23rd Structures, Structural Dynamics and Materials Conference, Part 1, 1982, pp. 32-40.

6. Smith, D. M.; Petley, D. H.; Edwards, C. L. W.; and Patten, A. B.: An Investigation of Gap Heating Due to Stepped Tiles in Zero Pressure Gradient Regions of the Shuttle Orbiter Thermal Protection System. Paper presented at the AIAA 21st Aerospace Sciences Meeting, Reno, NV, January 10-13, 1983.

7. Stein, Manuel; and Stein, Peter: Analysis of Tiles on Nonlinear Foundations and Plate Post-Buckling. Paper presented at the George Washington University/NASA Symposium on Advances and Trends in Structural and Solid Mechanics, October 4-7, 1982.

8. Sawyer, James Wayne: Analysis of Strain Levels in Densified and Undensified Shuttle TPS Tiles. NASA TP-2141, 1983.

9. Housner, J. M.; Giles, G. L.; and Vallas, M.: Dynamic and Static Modeling of the Shuttle Orbiter's Thermal Protection System. The Shock and Vibration Bulletin, Bulletin 52, Part 2, May 1982, pp. 127-145.

C-5

N84
10160

UNCLAS

N84 10160 D16

SHUTTLE TPS THERMAL PERFORMANCE AND ANALYSIS METHODOLOGY

W. E. Neuenschwander, D. U. McBride, and G. A. Armour
Space Transportation and Systems Group
Rockwell International
Downey, California

SUMMARY

Thermal performance of the TPS was approximately as predicted. The only extensive anomalies were filler bar scorching and over-predictions in the high Δp gap heating regions of the orbiter. A technique to predict filler bar scorching has been developed that can aid in defining a solution. Improvement in high Δp gap heating methodology is still under study.

Minor anomalies have also been examined for improvements in modeling techniques and prediction capabilities. These include improved definition of low Δp gap heating, an analytical model for IML convection heat transfer, better modeling of structure, and inclusion of sneak heating.

The limited number of problems related to penetration items that presented themselves during OFT have been resolved expeditiously, and designs have been changed and proved successful within the time frame of that program.

INTRODUCTION

The Space Shuttle orbiter thermal protection system (TPS) is designed to perform at least 100 missions before requiring major refurbishment. This is in contrast to the single-use designs for previous manned spacecraft heatshields such as Apollo. Basically, the protection against severe ascent and entry heating environments is composed of coated carbon panels, silica insulating tiles, and nylon felt blankets. The engineering task is further complicated where the system reaches interfaces with the various mechanical subsystems that are essential for launching, operating, landing, and servicing the vehicle. These interface areas are called TPS penetrations or singularities.

An overview evaluation of TPS thermal performance during the OFT program and of the analysis methodology is presented in this paper. Results of this evaluation will have value in the TPS thermal performance certification for more severe entry missions and TPS design of second-generation Shuttle-type spacecraft. TPS thermal performance assessments are based on postflight inspection results and measured TPS structure and component peak flight temperatures. These are compared with postflight developed analytical temperatures. Assessment of the analysis methodology is based on detailed comparisons of predicted temperature histories with measured data and evaluation of differences. Because their performance during the orbital flight test (OFT) program has not received as much publicity as that given the acreage tiles, the penetrations are granted some emphasis.

Included are the following: a summary description of the Columbia TPS design; thermal performance as evidenced by postflight inspections and development flight instrumentation (DFI) temperatures; and evaluation of thermal analysis methodology. Results are interpreted to reflect potential improvements in TPS thermal performance and analysis methodologies.

ABBREVIATIONS

AFRSI	advanced flexible reusable surface insulation
B/F	body flap
C/M	crew module
DFI	development flight instrumentation
ET	external tank
F/B	filler bar
FRSI	flexible reusable surface insulation
G/F	gap filler
HRSI	high temperature reusable surface insulation
IML	inner mode line
LRSI	low temperature reusable surface insulation
OFT	orbital flight test
OML	outer mold line
OMS	orbiter maneuvering system
OV	orbiter vehicle
PLB	payload bay
RCC	reinforced carbon-carbon
RCS	reaction control system
R/SB	rudder/speed brake
RSI	reusable surface insulation
RTV	room temperature vulcanized
SIP	strain isolation pad
STS	space transportation system

T/B	thermal barrier
TMM	thermal math model
TPS	thermal protection system

SYMBOLS

h	heat transfer film coefficient (Btu/ft^2·hr·^{o}F)
h'	heat transfer film coefficient at time of vent opening (Btu/ft^2·hr·^{o}F)
P	pressure
P'	compartment pressure at time of vent opening
p	local pressure (psf)
p_∞	freestream static pressure (psf)
$\dot{q}$	heat transfer rate (Btu/ft^2·sec)
$\dot{q}_s$	surface heating rate (Btu/ft^2·sec)
$\dot{q}(z)$	tile gap heating rate (Btu/ft^2·sec)
T_A	local air temperature (^{o}F)
T_A'	local air temperature at time of air vent opening (^{o}F)
T_o	initial temperature (^{o}F)
T_{SK}	structural skin temperature (^{o}F)
T_{STR}	structure
T'_{SK}	structural skin temperature at time of air vent opening (^{o}F)
T_t	peak surface temperature with turbulent boundary layer (^{o}R)
$\bar{t}_{s/s}$	equivalent thickness of structure skin and stringers (in.)
V	compartment flow velocity
V'	compartment flow velocity at vent opening
w_1	tile-to-tile gap width (in.)
z	dimension from heated surface (in.)
Δ	tile step dimension relative to adjacent tile (in.)
Δp	pressure difference across the tile
$\Delta\bar{t}$	delta heatsink capability of $\bar{t}_{s/s}$ due to nearby heavier structure (in.)
δ	tile thickness (in.)
ψ	filler bar scorching parameter

TPS GENERAL DESCRIPTION

The OFT vehicle Columbia, Orbiter 102, employs four basic thermal protection materials: reinforced carbon-carbon (RCC), high temperature reusable surface insulation (HRSI) tiles, low temperature reusable surface insulation (LRSI) tiles, and flexible reusable surface insulation (FRSI) blankets. These have been discussed in detail in references 1 through 5. Figure 1 shows the location of the acreage TPS materials on the orbiter and figure 2 shows typical penetrations. The list of the penetrations given in table I shows that the TPS is more complex than just tiles and FRSI blankets even though the penetrations comprise only a fraction of TPS surface area.

The basic TPS was designed to protect the primary structure from exceeding 350°F (the 100-mission temperature limit). The design was developed employing a minimum-weight engineering approach; that is, there was no intentional conservatism in the entry trajectory, heating or thermal analysis methodologies. However, the design was based on a single-orbit type mission that yields higher structure temperatures at the start of entry. This would be the case for a once-around abort, but the TPS was not designed to an abort as is sometimes believed.

Establishment of and design to material temperature limits were of prime importance. These criteria include those for the basic TPS materials illustrated in figure 3, and also cover about 50 other materials predominately used in the penetrations. Typical limits are shown in table II. There are a number of exceptions as illustrated by the following examples. AB312 ceramic fabric, used for gap filler/thermal barrier covers, has a nominal 2000°F limit, but its use is acceptable to 2300°F and 2600°F for ten and one missions, respectively. High-density HRSI (LI-2200) has been certified to 2900°F by arc-jet testing for at least one mission at a worst-case environment predicted in the gap between the elevons and the fuselage. On the other hand, titanium mounting flanges on the reaction control system (RCS) thrusters are limited to as low as 400°F to protect adjacent components.

The TPS and structure were instrumented with thermocouples and other temperature-sensing devices to provide data for thermal performance verification of the TPS for operational missions more severe than OFT missions. Figure 4 shows representative installations of the flight instrumentation plus number and locations of temperature measurements.

Unique designs in the TPS are called penetrations or singularities. These include the hatches and actuated doors, windows, aerodynamic control surfaces, RCS and orbital maneuvering system (OMS) thrusters, main engines, overboard vents and drains, umbilical connections, service access panels, and structural lifting and attach points (see table I). Around them the TPS is comprised of components made from numerous temperature-resistant metals, ceramics, plastics, and elastomers, which have been formed, cast, extruded, woven, and laminated. Penetrations to be discussed are located on the orbiter, as indicated in figure 2. They include the external tank (ET) umbilical door, a payload bay door bare hinge, selected rudder/speed brake components, the aft fuselage stub and body flap, one location in the wing/elevon seal system, primary thrusters in the forward RCS, and the windshield.

FLIGHT TEST RESULTS

OFT Entry Conditions

Example comparisons of surface temperature responses are shown in figure 5 for a lower surface mid fuselage location. These comparisons depict trajectory effects at the time of boundary layer transition to turbulent flow as evidenced by the rapid increase in surface temperature in the 1000- to 1300-second time frame. As shown, the turbulent spike temperatures occur earlier for each successive OFT flight, and the turbulent spike heating rate is indicated to increase as transition time decreases. This general trend is typical for the orbiter lower surfaces.

Acreage TPS

For the most part, the OFT heating environments were rather mild relative to the capability of the TPS. This is illustrated by the STS-2 peak surface temperatures shown by figure 6. STS-4 experienced higher peak turbulent temperatures, as illustrated by figure 5; however, these are not shown because of limited data (not available until about 1000 seconds after the entry interface.) Peak temperatures of the filler bars (F/B), strain isolation pad (SIP), and structure from STS-2 DFI are presented in figure 7. All peak temperatures are noted to be considerably lower than the 100-mission design allowables. These temperatures are typical of those for all flights. A comparison of peak structure temperatures for all flights is presented in figure 8. These temperatures are about the same, ±25°F for all flights, and well below the 350°F, 100-mission allowable.

TPS Penetrations

It is not feasible to discuss flight data from all the instrumented penetrations, so three were chosen for this section as being illustrative. They are an ET door, a payload bay door hinge, and the rudder/speed brake conic seal and structure.

The ET is connected to the orbiter through two umbilical panels located on either side of the lower centerline just behind the aft fuselage bulkhead. Structural attachments, various propellant lines, and a number of electrical connections pass through these panels. During ascent, the ET umbilical doors are held open by latches located at the centerline. After the ET is jettisoned, the doors are closed to protect the umbilical panels. Each door is attached to the fuselage with two bare hinges, which are flush with the outer mold line (OML). The outer surface of the door when closed is covered with HRSI. A thermal barrier, which runs around the periphery of each umbilical well, protects the structure from entry aerodynamic heating and accommodates relative movement between the door and fuselage. Pressure seals between the doors and structure and flow restricters along the door edge tiles complete the local TPS. The ET door/fuselage interface is depicted in figure 9. The doors are made from beryllium for stiffness, reduced weight, and to obviate the need for insulation blankets, which would be exposed to destruction during ascent. Even though the beryllium could tolerate almost twice the temperature, the thermally critical component for the doors is the 550°F HRSI/SIP bondline limit. At this location the thermal barrier consists of an AB312 cover and sleeve with an internal Inconel (International Nickel Company) X-750 knitted wire spring.

Flight temperatures for three DFI are shown in figure 10. It can be seen that the thermal barrier cover temperature neared its long term limit on STS-1 and may have been dropping from a peak above 1600°F on STS-4 when post-blackout data were acquired. The HRSI tile DFI recorded temperatures well below the limit, but this would be expected because it is located in a tile sidewall below the OML. The door remained relatively cool.

The payload bay doors are attached to the fuselage by 13 external hinges on each side. The six forwardmost hinges, which experience the most severe heating, are covered to protect them. The covers are made of Inconel and are designed to permit the doors to open without any restriction on movement. Since the predicted baseline aerodynamic entry heating was sufficiently lower, the remaining external hinges were left unprotected to reduce complexity. The gaps between the doors and fuselage are filled with a silica fiber brush thermal barrier. This protects the door structure and the environmental seal from direct convective heating and also accommodates structural movement (see figure 11).

STS-1 through STS-4 DFI temperatures for the most forward unprotected hinge are presented in figure 12. One DFI is on the forward clevis facing the oncoming flow. Recorded maximums were well over the 1200°F criterion for this instrument on two missions; however, readings were erratic, and poor contact between the sensor and clevis was suspected. Postflight inspection of the sensor indicated that it was attached but the amount of contact area with the clevis could not be determined. Because it was uncertain if the DFI data actually were a true indication of the clevis temperature, authority was issued to remove pins on hinge 7 (maximum temperature) and hinge 9 (lowest stress margin), inspect the dry lubricant (limit 1000°F), and run hardness tests on pin 7. The results indicated no degradation caused by excessive temperature exposure and no loss of strength. In order to eliminate direct stagnation-type heating on the DFI, a piece of filler bar was placed over the sensor for STS-2 and STS-3 and replaced prior to STS-5. The below-limit readings on these flights are more accurate measurements of the clevis temperature. Temperatures at the clevis/fuselage interface remained low and changed little from flight to flight. The hinge lug is exposed to far less aerodynamic heating, and its DFI is located in a cavity between tiles. These facts are reflected in the much lower lug temperatures (compared to the clevis) plotted in figure 12.

As illustrated in figure 13, the vertical tail consists of a fixed structure, the fin, and two moveable surfaces that have the capability of acting together as a rudder or separately as a speed brake. At the hinge line a gap exists to permit movement of the rudder/speed brake with respect to the fin. In addition to external LRSI and HRSI, the structure must be thermally protected by closing the gaps along the hinge line and around the rudder/speed brake perimeter with a system of seals. The most visible element is the Inconel conic seal, which acts as a rub surface for seals attached to the fin trailing edge and the rudder/speed brake leading edge. Other seals are found at the top and bottom of the cone as well as between rotating sectors. Around the perimeter, there are seal requirements in the gaps between the fin and the rudder, along the rudder/speed brake trailing edge, and at the split line between upper and lower panels. The aforementioned seals are made from several combinations of flat metallic springs, insulation-filled ceramic sleeving, graphite blocks, and knitted wire springs.

There are several DFI on the conic seal. Readings from two of them are plotted in figure 14. Both sensors are located on the inner face sheets of the Inconel honeycomb. One is forward near the fin seal, and the other is aft but at the predicted point of maximum interference heating when the rudder/speed brake is closed during entry. Conic seal temperatures stayed well below the 1250°F limit. The gentle rise in the aft sensor DFI data to only about 250°F indicates that it is behind the rudder/speed brake leading edge seal rather than forward of it in the more severely heated position described above. More rapid increases, although to lower levels, are seen for the structure instrument located near the rudder/speed brake trailing edge. This behavior is as expected for metallic surfaces that are directly exposed to a small amount of wake heating when the rudder/speed brake is opened at Mach 10.

TPS Thermal Anomalies

Postflight inspections have shown every flight to have had some local anomalies. Table III identifies the general types of heat protection anomalies that have been observed during inspections. Figure 15 identifies the locations of those that are most significant. Most anomalous conditions are easily detectable by visual inspection of the OML; however, some require removal of access panels and/or more detailed inspections.

Priority attention has been (and is) given to understanding and preventing anomalous conditions that require detailed inspection. Some design changes have already been implemented to alleviate these problems. Certain tile gaps near the wing trailing edge have been filled to reduce air flow into the elevon cove, and the internal insulation has been changed from FRSI to AFRSI. Designs of the edge tiles of the gear and ET doors have been modified to restrict subsurface flow. In some cases, repairs have been made to the existing design. An example of this is in the body flap stub plate tiles.

One anomaly of concern that requires detailed inspection is filler bar (F/B) scorching between lower surface tiles. At several hundred randomly distributed locations, filler bars reached 950°F to greater than 1375°F where 400°F to 500°F were predicted. Filler bar scorching has occurred on every flight. A summary of occurrences and scorch severity is presented by table IV. Some filler bar scorching is known to be caused by structure leakage, e.g., around doors. These can be eliminated by design change or local repairs. Scorching in the general acreage is a probability event depending on certain combinations of tile steps and gaps, heating/boundary layer conditions, and tile-to-filler bar gaps. Eliminating filler bar scorching in the acreage regions is a more complex problem.

Since multiple reflights of scorched filler bars could result in structural damage, degraded ones are repaired after each flight. They are mostly repaired by filling the gap with room temperature vulcanized (RTV) impregnated ceramic fabrics (Ames gap filler). When severely degraded, the filler bars are replaced, and this requires tile removal. The repair effort is relatively simple, but the problem is that many thousands of gaps have to be inspected just to find a few hundred scorches that require repair. This inspection has been required because, until recently, the cause wasn't quantitatively defined and step/gap allowables (criteria) that would preclude filler bar scorching could not be developed.

Continued examination of flight data resulted in identification of a correlation parameter that distinguishes between step/gap combinations that cause scorching and those that do not. The parameter is

$$\psi = (T_t/1000)^{0.5} \, (\Delta^{.5} + w_1^{.83})/\Delta^{.12}\delta^{.5}$$

This parameter correlated a statistically representative sample of scorched filler bar data to within ±20 percent. The lowest value was 0.41 and corresponds to a filler bar temperature of about 950°F which is the threshold of visual detection of a scorch per inspection criteria and NASA JSC plasma-arc test results. The ψ value for 800°F, the 100-mission limit, was identified to be 0.38 from a combination of flight and plasma-arc data. With these analysis results, tile step/gap criteria can be defined that will preclude filler bar scorching.

Unfortunately, implementation of an absolute no-scorch step/gap criteria has only theoretical feasibility. Analysis of data indicates that about 20 percent of scorches were caused (or highly influenced) by aft-facing steps on adjacent tiles. Step/gap criteria involving multiple tiles would be difficult to apply and execute with confidence. Other practicality problems exist. These include the fact that future worst-case trajectory/heating environments are required to define criteria, but are not presently known, and inspection/repair for scorched filler bar is not included in the planned orbiter turnaround schedules. At the time of this writing, the best program solution to this problem is under study.

The body flap is attached to the aft fuselage stub and driven in its trim control function by rotary actuators. In addition to HRSI tiles that cover the exterior of the stub and body flap, there are a number of seals that prevent direct flow and resultant convective heating from passing from the high pressure lower surface to the low pressure wake region. There is the hinge seal, consisting of Inconel 718 panels, which covers the entire width from stub to stub, closing off the lower cove. So-called chain seals block flow around the ends of the stub. The design for thermal barriers between the body flap end tiles and the stub consists of knitted wire springs within AB312 covers. All of the above are or have ceramic cloth components that bear on aluminum heat sinks attached to each end of the fuselage stub. These are known as the rub plates (see figure 16).

A temperature sensor on the left-hand body flap rub plate exhibited a rapid rise to 395°F after communications blackout during STS-1 entry (see figure 17). This behavior was unexpected because the rub plate is heavy. The peak also constituted an overtemperature since the 100-mission aluminum material limit is 350°F. No other overtemperatures were recorded in the area, although the output of another DFI on the upper end of the plate also rose and fell rapidly. Postflight visual inspection of the exterior revealed no particular evidence of overheating. Observed aluminum temperatures were used as drivers in the thermal math model (TMM) along with postflight predicted heating. Stress analysis personnel used output from this work and came to the conclusion that no structural degradation had occurred during STS-1. A later visual inspection revealed gaps between the tiles at the lower, outboard corner of the stub. It was surmised that sneak flow entered at these points, directly heated portions of the rub plate bounded by the hinge and chain seals, and exited at a lower pressure area—perhaps the upper cove. For STS-2, the aforementioned gaps, which were tapered in-depth, were plugged with Ames fillers to preclude the flow.

Again on STS-2, the rub plate DFI rose rapidly and went over temperature to 405°F. Because the shapes of the temperature-versus-time curves were almost identical for both flights, it was evident that the Ames gap fillers installed after STS-1 did not cure the anomaly. Carrier panel tiles were removed from the left-hand stub. As shown in figure 18, a section of charred and missing filler bar was found. The corner of the rub plate adjacent to this section was discolored indicating excessive temperatures. There was also evidence of a forward-facing OML step between these tiles. Prior to STS-3, the missing filler bar was replaced, and nearby pad gap fillers were rebonded. The stepped tile was not refurbished.

Figure 17 reveals that the left-hand rub plate temperature followed a repeat history during STS-3. As noted, a new flow barrier was added along with the pad gap filler, and two lower surface tiles were remade to remove the forward-facing step. Finally, on STS-4, the maximum temperature was what had been expected for a heavy aluminum plate; however, the STS-5 temperature history, while not exceeding the 350°F criteria, looks familiar. More extensive tile changes have been designed to permit use of full-depth pad in place of Ames gap filler, and these are being installed during the modification period.

The elevons provide orbiter flight control in pitch and roll during atmospheric entry flight. They are divided into two segments for each wing, and each segment is supported by three hinges (two fixed and one actuator). The seal system design must permit the required control surface motion and yet prevent the destructive flow of hot plasma from the lower to upper surfaces through the wing/elevon interface. Basic features are shown in figure 19, a section normal to the hinge line. The lower surface is protected by sculptured HRSI with a nominal 0.5-inch gap between wing trailing edge and elevon leading edge tiles. The lower, internal cavity is closed out by primary and redundant seals. Spring-loaded polyimide blocks bearing on aluminum and Inconel rub tubes make up the primary seal while reinforced silicone elastomer sheets form the redundant seal. Together, the aforementioned penetration is known as the elevon lower cove. Also depicted in figure 19 is the closeout to the upper wing-to-elevon cavity, commonly known as flipper doors and rub panels. This TPS is insulated hot structure made from titanium and Inconel on the inboard and outboard elevons, respectively. The wing/elevon seal system takes on its greatest complexity when a chordwise interruption occurs at the inboard and outboard ends of each elevon and at each hinge and actuator.

There have been some temperature-related problems with the elevon lower cove, but none that brought forth safety-of-flight concerns. STS-1 postflight visual inspection of the closeout panel FRSI insulation revealed evidence of spanwise and/or leakage flow within the coves. There were areas of scorching and charring, particularly at the outboard elevons. This is illustrated in figure 20, which is a view looking up with the wing trailing edge and elevon leading edge tiles removed. Physical evidence revealed that flow entered the gap between wing and elevon tiles and exited near the stubs and actuators. After the first flight, the insulation on the closeout panels was changed from FRSI to higher temperature capability AFRSI. In addition, Ames gap fillers were placed between the tiles immediately upstream of the trailing edge tiles and thicker SIP was added to improve seating of these tiles.

Some anomalous behavior of elevon lower cove DFI was noted, but they recorded no overtemperatures. Time-temperature histories of the sensor on the primary seal tube at 90 percent half span are plotted in figure 21. The shapes have more pronounced peaks than would be expected in pure soakback situations. This is ascribed to the direct, low level convective heating that caused the FRSI degradation. The heating is thought to have come about from the spanwise flow mentioned above and from sneak circuit flow under the wing trailing edge tiles. Also note in figure 21 that seal leakage measurements in this region have generally declined. All in all, it would appear that the elevon lower cove seal system on Columbia is currently functioning as designed.

Including the payload bay door bare hinge overtemperatures, which were described earlier as instrumentation installation problems, three anomalous penetrations situations have been discussed. This points out that, considering the hundreds of penetrations and singularities, there were a minimal number of temperature-related discrepancies during the OFT program.

EVALUATION OF THERMAL ANALYSIS METHODOLOGIES

Assessment of analysis methodologies is being performed by comparing analytical results with flight measurements. Discrepancies between flight and calculated temperatures using design methodologies are examined for cause. When a discrepancy appears to result from analytical modeling, the technique is examined for potential improvement. In the case of acreage TPS, the orbiter is surveyed to assess data consistency of discrepancies and modeling improvements. However, for penetrations the analysis is mostly unique to a specific penetration.

Acreage TPS

Nodal TMM's are used for flight temperature predictions. A design model for a 1.0-inch tile would have about 120 LI-900 nodes or about 240 LI-900 nodes for a 3.0-inch tile. Nominal thermophysical property data are used for all TPS and structure materials.

Nodal models of tiles are three-dimensional and include simulation of the SIP and filler bars. Gap heating is applied to the tile sidewalls. For low pressure gradient regions of the orbiter, the gap heating varies with surface heating rate and dimension from the tile surface. For high pressure gradient regions with open gaps (i.e., wing glove, aft chine, forward fuselage, and elevons), the gap heating is also a function of pressure and pressure gradient in direction of the open gap. High pressure gradients are defined as $p^{1/2}\ dp/ds > 1.06\ \text{psf}^{3/2}/\text{inch}$.

The structure is modeled to include the effective thickness of skin, and stringers ($\bar{t}_{s/s}$) and the thermal capacity of nearby heavier structure (i.e., frames). Honeycomb structure is modeled as honeycomb. The structure inner mold line (IML) is assumed to be adiabatic.

The FRSI design nodal models are one-dimensional with nominal thermal property inputs. Structures are modeled as described.

Postflight analyses have been performed using these design methodologies to assess the TPS thermal performance and the adequacy of the analytical models for flight certification. Although there have been some anomalies, the overall TPS thermal performance and analysis adequacy appears acceptable. Peak temperatures of SIP and structure, as measured by the DFI, are well within design allowables. This is illustrated by figure 22, which also shows that calculated temperatures, using actual flight surface heating, are in reasonable agreement with measured data. These temperatures, shown for STS-2, are typical of those for all OFT flights.

Detailed examination of the DFI and analysis data shows some discrepancies not indicated by peak temperatures. Temperature history comparisons are shown by figures 23 through 27. These are rather typical results. Figure 23 illustrates that the high pressure gradient gap heating is quite conservative. Calculated tile sidewall, filler bar, and structure temperatures are all well above the measured. Gap DFI in high Δp regions is very limited. However, at several high Δp locations, surface and structure skin measurements are available. Analysis at these locations shows similar conservative disagreement with structure temperatures.

In low pressure gradient regions, the trend is for the temperature rise rates of SIP and structure to be greater than calculated. But the agreement is reasonably close and the analytical conservatism of the cool down compensates for the rise-rate optimism. Figures 24 and 25 illustrate this observation.

Figure 25 implies another analysis anomaly that also shows up at other orbiter locations: the calculated in-depth reusable surface insulation (RSI) temperatures are conservative but the SIP and structure temperatures are optimistic. This could be interpreted to mean that the low gap heating in the analysis is optimistic; however, figure 25 shows this gap heating to be reasonable until late in the entry (to about 1200 seconds). The LI-900 temperature measurements are suspect. It is speculated that launch vibroacoustics resulted in the thermocouples cavitating the LI-900 such that they were not in contact with LI-900 at the thermocouple junction. That this could happen was evidenced in a vibroacoustic test performed at NASA Langley where thermocouple wires were observed to have cavitated LI-900. Other explanations (e.g., LI-900 conductivity variation with temperature, hot air ingestion at the base of the tile) were considered improbable following analysis.

Examples of thermal response at upper surface locations are presented by figures 26 and 27. Figure 26 shows the thermal response at an LRSI location. The calculated SIP and structure rise rates are slightly lagging measured temperatures. (Note also the contradiction by the LI-900 temperatures.) Figure 27 shows the thermal response at an FRSI location, where again calculated temperatures are lagging measured temperatures. Both the examples show good agreement with peak temperatures and cool down rates. This is typical of upper surface locations with the thinner TPS.

In summary, the acreage TPS design methodologies produce peak temperatures that are conservative and adequate for Eastern Test Range flight certifications. However, this conservatism results from compensating effects of optimistic and conservative thermal modeling techniques.

Modeling improvements are being evaluated to show better agreement with flight data and include structure modeling, low pressure gradient gap heating, and IML convection. Also, the tile models have a finer nodal network of the SIP and filler bar.

The design method of structure modeling was to use an effective structure thickness that included both the skin stringer and $\Delta\bar{t}$. The new method connects $\Delta\bar{t}$ to $\bar{t}_{s/s}$ with a contact resistance to increase the rise rate of the structure skin. Values were empirically established. The value for the lower fuselage is 1.0 Btu/ft^2·hr·°F. For other locations except lower wing, the coefficient is 0.2 Btu/ft^2·hr·°F. At time of this writing, the lower wing modeling is still under study.

A pressure dependent, low pressure gradient gap heating model was developed that improves agreement between flight and analysis data. The model is

$$\dot{q}(z)/q_s = (1.0 + p/20)^{1.4\sqrt{z}} \times (\dot{q}/\dot{q}_s)_{\text{des. extended}}$$

The $1.4\sqrt{Z}$ exponent is truncated at a value of 1.85. The design gap heating and design extended distributions are presented by figure 28. The pressure factor gets to be a large number for higher pressures and thick tiles. Even so, at later entry times when the gap heating is negative, the pressure factor is not large enough to match gap cool down rates.

The orbiter interior is repressurized by air vent air, which has a marked effect on structure temperatures. Air vents open at 2400 fps orbiter ground speed, which is typically about 85,000 feet altitude. From flight and analysis results, hot structure (skin) is cooled and cold structure is heated by the ingested air.

A heat transfer convection model was developed from examination of flight and venting analysis data. The modeling analysis was difficult to accomplish because of lack of direct data. The heating/cooling is a function of three parameters that are dependent on each other and vary with time:

$$\dot{q} = h\ (T_{STR} - T_A)$$

Nonetheless, based on a DFI air temperature measurement and a high density of structure thermocouples at BP1801, a heat transfer model was developed.

$$h = h'\left(\frac{P}{P'}\ \frac{T_A'}{T_A}\ \frac{V}{V'}\right)^{1.6}$$

Air temperature (T_A) is defined to vary linearly with time between compartment air at the time of air vent opening and ambient air temperature at touchdown at the landing site. Air temperature at air vent opening time is approximated as

$$T_A' = T_O + 0.1\ T_{SK}'$$

The film coefficient at air vent opening, h', was empirically defined to be 0.07 Btu/ft^2·hr·°F for IML-insulated structures and 0.10 for uninsulated structures.

Compartment pressure is a function of freestream static pressure, as shown by figure 29. Velocity ratio (V/V') is defined in the same figure for STS-2. Extrapolation of the STS-2 velocity parameter to other trajectories uses the following relationship:

$$V/V' = [\dot{p}_\infty/(\dot{p}_\infty)_{STS-2}]\ (V/V')_{STS-2}$$

This extrapolation technique was used to calculate STS-3 structure temperatures. It showed that the agreement was reasonably good (about the same as the STS-2 data agreements).

Overall, the modeling improvements yield better structure temperature rise rates and peaks. Also, the shaping of the SIP temperature response and peaks are also better; however, in some cases there is very little improvement over results from the design models. This is usually the case for the thinner TPS and locations where $\Delta\bar{t}$ is small compared to the structure skin-stringer thickness.

Assessment of these modeling improvements has been made by comparing analytical and measured temperatures at 47 locations for STS-2 and 25 locations for STS-3. The agreement is quite good for the fuselage, OMS pod, and vertical tail low pressure gradient regions. Modeling of the wing TPS and structure is still under study.

The agreement between analytical and measured temperatures is illustrated by figures 30, 31, and 32 for the fuselage lower surface. Figure 30 is for a forward fuselage location where the IML is insulated. Peak temperatures are in good agreement and the response shapes for the filler bar, SIP, and structure skin are quite acceptable. The deviation between the filler bar temperatures after the peaks is caused by the convective gap cooling being greater than calculated even though the pressure factor in the gap heating model is large. Figures 31 and 32 compare temperatures at an uninsulated location. Again, structure skin and SIP temperatures are in agreement. The calculated filler bar temperature appears to be conservative; however, it is not known if the filler bar thermocouple is located in an open gap.

Temperature comparisons at upper surface locations are shown by figures 33 and 34. The calculated structure temperature on the vertical tail lags the measured temperature by about 10°F, but the peak is good. The OMS pod structure temperature also lags the measured temperature by about 50°F, but the peak is in good agreement. On the OMS pod the calculated cool down rate is greater than measured.

In most cases, the modeling improvements yield better agreement with flight temperatures than the methodology used for design. This is particularly evident in comparison of structure temperatures in regions of high heat load where the tiles are thick. In these regions, such as the lower wing, IML cooling helps to offset a rather significant increase in structure temperature from heat soakback from the tiles.

More modeling improvement analysis is in process. The structural backface of the three-dimensional tile model could use improvement to better account for radiative interchange between the upper and lower wing structure. Even with the modeling improvements described, the lower skin temperature rise rates are optimistic and the cool down conservative. Another area of modeling improvement is with the high pressure gradient gap heating since the design method appears to be very conservative.

Penetrations

The general approach to a penetration thermal analysis required identification of the physical location and configuration, applicable heating and other boundary conditions, and subsystem operating parameters. To physically represent the penetration, the structural and TPS cross-section of the installation was subdivided into a sufficiently fine matrix to represent it as a TMM in the computer thermal analyzer program. Baseline models represented nominal design configurations. Limit case heating and other boundary conditions were also identified and formatted for computer input. These included various combinations of the following:

1. Initial temperatures either prelaunch or pre-entry after specified orbital operation

2. Predicted ascent and entry aerodynamic heating at all OML areas and within the penetration

3. Ascent radiative heating from the booster and main engine plumes, and recirculation convection effects from the latter source

4. Local RCS and OMS engine plume heating during system operation

5. External reradiation or radiation interchange within the penetration and/or internal to the orbiter

6. Miscellaneous system operating parameters (e.g., ablation, internal heat generation, fluid flow, and cabin conditioning)

The complexities of the installations typically dictated the use of two-dimensional TMM's based on the worst case location in each individual penetration rather than more comprehensive models; however, limited three-dimensional models were forced in a few situations, while other cases were simple enough to represent in one dimension.

The basic TPS sizing was accomplished based on minimum insulation thickness requirements for each given orbiter location without regard for special situations such as penetrations and singularities. Further design constraints required the penetrations to be thermally controlled passively and independent of internal systems for cooling. All in all, these ingredients imposed challenging design conditions on these TPS features.

Postflight evaluations consisted of screenings that categorized results as to their criticality. First priority was given to components that exceeded their design temperature limit. Two examples were discussed in previous sections: the payload bay bare hinge and the fuselage stub rub plate and body flap. Second came those that exhibited anomalous readings that were considered problems even though they stayed below criteria. Instances include the wing/elevon lower cove, which was mentioned earlier and will be discussed further in the following, and the RCS installation, which is covered in this section. Because of the limited time and resources, the least attention could be devoted during the flight test program itself to DFI readings that were overpredicted.

The canopy windshields have obvious functional requirements, serving as the pilots view ports during launch, landing, and other operations. There are a total of six windshields with each window assembly consisting of three high temperature glass panes. Figure 35 depicts a sample cross-section. The outer pane of each set is fused silica glass, which serves as a heat shield and is sealed to prevent hot gas plasma from penetrating into the internal structures. The middle window pane is also fused silica and serves as a fail-safe redundant member to either the outer thermal pane or the inner pressure pane. The inner pane is heat-tempered aluminosilicate glass and is the primary pressure containing pane for the cabin atmosphere. All glass surfaces are coated except for those of the thermal (outer) panes. Special HRSI (LI-900) tiles that overhang the outer window frames protect the aluminum canopy structure. The HRSI is bonded to 0.09-inch SIP, which is, in turn, bonded to carrier panels. These assemblies are mechanically attached to the frames. Captive-type gap fillers are installed between the tiles. AB-312 cloth filler, bonded only to the carrier panels, supports the overhanging portions of HRSI. To prevent the inflow of hot plasma during entry and the possible leakage of cabin pressure, thermal barriers and pressure seals were incorporated into the window design. The external thermal barriers are made of woven ceramic fiber. For external pressure seals, fluorocarbon O-rings are used. The crew module windows (redundant and pressure panes) are contained in frames having steel, aluminum, and beryllium components. The crew module window frame is actively cooled by water flowing in pairs of tubes around each window's inboard perimeter. Environmental barriers having rigid and flexible portions are located between the canopy and the crew module. At highly heated windshield locations, insulated heat shields are required to protect the flexible purge barrier. In turn, the crew module wall requires TCS insulation blankets to protect it from radiating surfaces.

Figure 36 shows DFI data and analysis time-temperature histories for a location at the downstream region of the middle windshield. On STS-2, the preflight work substantially overpredicted the bondline DFI early in entry. A comparison between prediction and data at the OML surface indicates a probable cause for the bondline error: the experienced aeroheating did not have an early high load period but did display an unexpected peak. Heating rates were derived from surface DFI data and extrapolated to the window pane surface and the overhanging tile sidewall. These were then used in the baseline TMM. As shown by the solid line in the figure 36 plot, a much improved correlation at the bondline was achieved.

The situation regarding STS-3 was similar. Just as the preflight prediction of aeroheating was better, so was the thermal analysis output. Again, an improved overall match between predicted bondline temperature and data came from using derived heating. Even though the bondline value is slightly undercalculated (<25°F) at its peak and falls less rapidly than the data, the basic validity of the TMM has been demonstrated.

The forward RCS provides attitude control and small velocity increment translation from main engine cutoff during ascent until the entry interface. It includes 16 radiation-cooled thrusters (14 primary and 2 vernier), made predominantly from columbium (disilicide coated except for the injector plates), and fully exposed to aerodynamic heating. Surrounding HRSI tiles of the TPS have been partially replaced by other materials. Insulation-filled metallic plume shields are placed downstream of long scarf (primary -Z and -X and vernier) thrusters. High density (22 pcf) RSI tiles form the TPS in narrow areas between the -Z, ±Y, and -X thrusters. Thermal barriers serve to block gaps between nozzle exits and adjacent TPS from hot boundary layer gases. Other thermal barriers are required between the plume shields and surrounding tiles. Each thruster is housed within a cylindrical titanium container that seals the internal compartment from the exterior environment. The design is complex. There are approximately 20 maximum temperature limits to be observed, many with several variations associated with position, mission phase, or frequency of occurrence. The primary downfiring (-Z) thrusters experience the most severe entry heating. A section through the downstream edge of this installation is shown in figure 37.

A DFI is located on the inside of the plume shield adjacent to the thermal barrier. The recorded sudden rise in entry temperatures on STS-2 was not predicted by the baseline TMM employing postflight nominal aeroheating. This can be seen by comparing the solid curve with the data symbols (filled circles) in figure 38. The response is little different than the STS-1 experience reported in reference 1.

Several revisions were made to the TMM after studying thermal flight data from the region and the postflight inspection reports. First, the as-built configuration (thermal barrier recessed inside the OML and rounded) and expansion characteristics of the plume shield were considered. This exposed additional areas of the sealing surface to direct aeroheating and altered the perturbation and gap heating factors. Second, interpolation between the data from the closest surface DFI was used to estimate actual reference heating. Third, the plume shield DFI itself was added to the TMM at its design location. With the revisions, a much better prediction of STS-4 data was obtained, as indicated by comparing the dashed curve to triangle symbols in figure 38. Peak values are well matched as is the time-temperature history following the peak. The early overprediction is thought to be caused by the shape of the derived aeroheating curve. The forward RCS thruster TPS TMM is considered sound.

Flight data from a DFI in the wing/elevon lower cove was presented earlier (figure 21) along with a description of this penetration area. A series of TMM updates have markedly improved the ability to predict temperatures for future entry environments. Figure 39 shows that the baseline was poor at anticipating both the peak and shape of the recorded data. One of the first changes included correcting the sensor location. Since it was obvious from postflight inspections that direct convective heating was present in the cove, several low percentage values of OML reference heating were applied to appropriate TMM internal sections. This produced predictions that bracketed the data. Although the assumed levels of sneak flow heating were slightly higher than that correlated from ground tests, they seemed quite believable in light of the FRSI degradation in the first OFT flight. Finally, an intermediate level of sneak heating was combined with cooling correlations developed for air flow following the vent opening. As demonstrated by the solid curve in figure 39, the validity of the current TMM is much better.

CONCLUSIONS

Overall, flight data show the TPS design and thermal performance to be quite good and the thermal analysis methodologies adequate. Examination of physical and analytical data has identified some elements of the design and methodologies that could have been better if data had been available on which to base improvements.

LESSONS LEARNED

Results revealed that some technology inadequacies exist. Their identification could benefit future design and analysis of spacecraft heat protection systems.

Low Δp gap heating is a function of pressure level. This wasn't known before STS-2. Ground test facilities did not have the capability to produce data to identify effects of pressure level and theory (engineering methodology) did not identify pressure level as a significant parameter. This knowledge could have affected TPS design. Filler bar scorching is caused by abnormally high rates of gap heating. These high heating rates are pressure-level dependent and the significance of pressure level is amplified with boundary layer disturbances caused by tile steps. If this had been known before the first flight, filler bar scorching would have been expected and step/gap criteria for prevention identified; however, it is most probable that these criteria would have not prevented about 20 percent of the filler bar scorches, and would not have eliminated detailed postflight inspection for the scorched filler bars. As such, it is likely that this ignorance was to the advantage of the STS program in its preflight stage. Now, however, gap heating sensitivities to pressure level and tile step/gap dimensions are all recognized and should be considered in future ground testing of similar TPS configurations. This suggests that consideration should be given to upgrading the flight simulation capability of plasma-arc test facilities.

Other inadequacies relate to the IML convection heat transfer phenomena. Per interpretation of flight data, the governing heat transfer relationships deviate considerably from theoretical expectations. The air temperature and heat transfer coefficients are predominantly influenced by the local structure temperatures (hot and cold) with little remembrance of prior temperature/boundary layer history. Also, the variation of heat transfer film coefficient with air density and flow velocity is considerably more pronounced than expected. These anomalies are quite probably unique to the orbiter's air vent system and structural configuration; therefore, it appears that IML convection cooling is more complex than theory indicates but extrapolation of OFT data to other STS entry environments can be justified. However, applying IML cooling for design of new spacecraft warrants caution.

Thermal analysis prediction capabilities are quite good when the environments are known. Analysis of flight data demonstrates this claim. Absence of flight data is evidenced in attempts to understand discrepancies between flight and analysis results. One example of this is not having adequate instrumentation to measure pressure gradients in high Δp regions of the orbiter. Assessment of high Δp gap heating requires this information. More pressure instrumentation should have been located in high Δp regions of the orbiter. Also, more surface and structure thermocouples should have been placed in areas where local heating environments are difficult to predict (e.g., elevon spill regions and penetrations).

REFERENCES

1. Dotts, R. L.; Battley, H. H.; Hughes, J. T.; and Neuenschwander, W. E.: Space Shuttle Orbiter Reusable Surface Insulation Subsystem Thermal Performance. AIAA Paper 82-0005, Jan. 1982.

2. Curry, D. M.; Cunningham, J. A.; and Frahm, J. R.: Space Shuttle Orbiter Leading Edge Structural Subsystem Thermal Performance. AIAA Paper 82-0004, Jan. 1982.

3. Dotts, R. L.; Smith, J. A.; and Tillian, D. J.: Space Shuttle Orbiter Reusable Surface Insulation Flight Results. Shuttle Performance: Lessons Learned, NASA CP-2283, Part 2, 1983, pp. 949-966.

4. Curry, D. M.; Johnson, D. W.; and Kelly, R. E.: Space Shuttle Orbiter Leading Edge Flight Performance Compared to Design Goals. Shuttle Performance: Lessons Learned, NASA CP-2283, Part 2, 1983, pp. 1065-1082.

5. Cunningham, J. A.; and Haney, J. W., Jr.: Space Shuttle Wing Leading Edge Heating Environment Prediction Derived From Development Flight Data. Shuttle Performance: Lessons Learned, NASA CP-2283, Part 2, 1983, pp. 1083-1110.

ORIGINAL PAGE IS
OF POOR QUALITY

TABLE I.- SUMMARY OF TPS PENETRATIONS

Type	Quantity	Type	Quantity
Actuated doors and hatches		External window assemblies	9
• Landing gear	3		
• Payload bay (segments)	8	Structural element interface areas	4
• Crew hatches	3		
• Structural vents	18		
• Flipper doors	30	Antennas	22
• External tank	2		
• Star tracker	2	Exposed umbilical connectors	87
• Air data probe	2		
		Fixed panels and doors	295
Aero surfaces assemblies		Miscellaneous singularities	
• Elevons	4	• External hinges and latches	36
• Body flap	1		
• Rudder/speed brake (segments)	4	• Hot structure panels	37
		• Attach, hoist, and jack points	315
Engines			
• Main	3	• Vertical tail leading edge	1
• OMS	2		
• RCS	44	• Emergency access releases	3
		• Passive air vents	6
Vents and drains	54	• External light	1

TABLE II.- TYPICAL TPS TEMPERATURE CRITERIA

Material	TPS Elements	Temperature Limit (°F)*
Aluminum (2XXX, 6XXX)	Structure brackets, etc.	350
Beryllium	Heat sinks	1000
Borosilicate glass	HRSI coating	2300
	LRSI coating (low α_s/ε)	1200
Ceramic fabric (AB-312)	Thermal barrier, gap filler, and insulation covers	2000
Ceramic fibers, bulk		
(Dynaflex)	Batt insulation	2600
(Saffil)	Thermal barrier and gap filler	2000
Columbium, coated	Hub seals, nozzles, and flanges	2500
Fluoroelastomer (Viton)	Seals	500
Nickel alloy (Inconel 6XX)	Hot structure, seals, etc.	1400
Nylon (Nomex) felt	Filler bar	800
	FRSI	700
	SIP (for standard size tiles)	550
Polyimide/glass laminate	Isolators, brackets, etc.	600
Silica fibers, rigidized	Standard ($\rho = 9$ pcf) tiles	2300
	High-density ($\rho = 22$ pcf) tiles	2300
Steel (21-6-9)	Vents, brackets, etc.	900
(3XX)		1200
Titanium (6AL-4V)	Hot structure, brackets, etc.	800

*For 100 missions; higher values acceptable for limited missions or by specific tests, lower values specified in some system applications.

TABLE III.- TPS POSTFLIGHT ANOMALY OBSERVATIONS

Item	Location Code**
Tile slumping (overtemperature)*	A
Thermal barrier degradation*	B
Scorched FRSI*	C
Structural overtemperature	D
Tile erosion*	E
Gap filler degradation*	F
Gap filler leakage	G
Burned elevon cove insulation	H
Scorched filler bars	Random on lower surfaces

*Easily detectable by visual inspection of the OML
**Refer to Figure 15

TABLE IV.- SCORCHED FILLER BAR

Flight	Total	CAT. 1	CAT. 2	CAT. 3	Tiles Removed*	Comments
STS-1	614	113	269	232	246	Early trans (gouge) First flight
STS-2	360	130	194	36	47	
STS-3	219	73	117	29	34	
STS-4	478	238	224	16	16	Early trans (PUPO)

*Because of scorched filler bars

CAT. 1: 950 → 1100°F

CAT. 2: 1100 → 1375°F

CAT. 3: > 1375°F

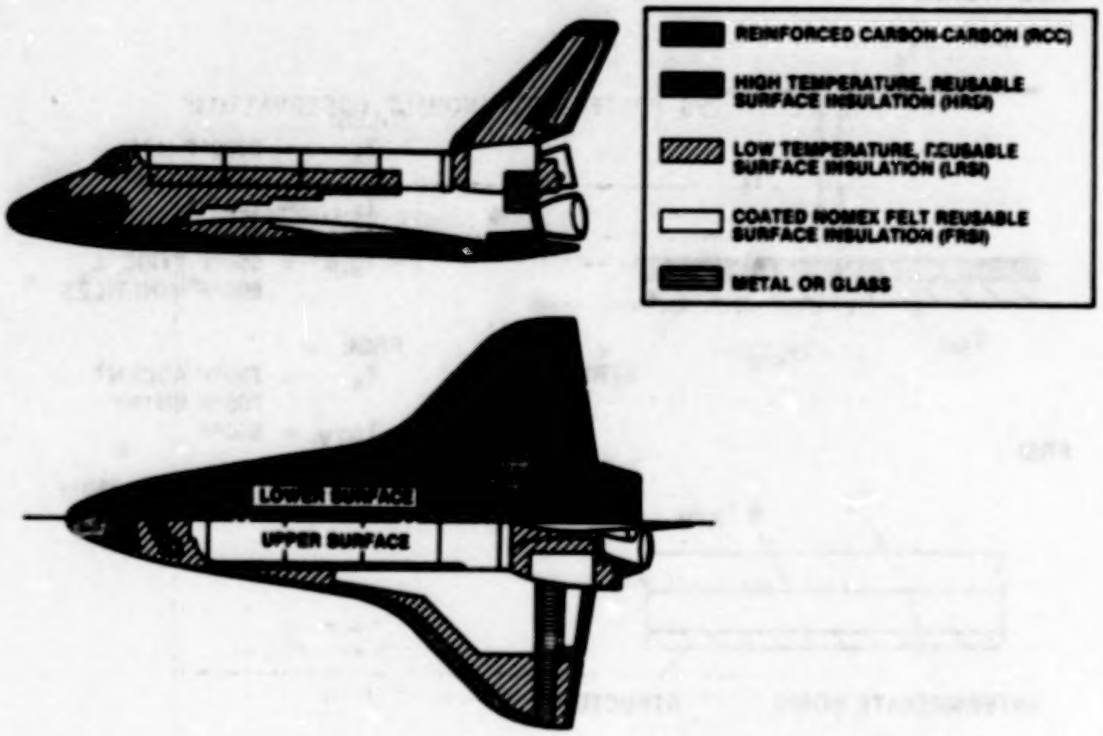
REINFORCED CARBON-CARBON (RCC)
HIGH TEMPERATURE, REUSABLE SURFACE INSULATION (HRSI)
LOW TEMPERATURE, REUSABLE SURFACE INSULATION (LRSI)
COATED NOMEX FELT REUSABLE SURFACE INSULATION (FRSI)
METAL OR GLASS
LOWER SURFACE
UPPER SURFACE

Figure 1.- Thermal protection system (Orbiter 102).

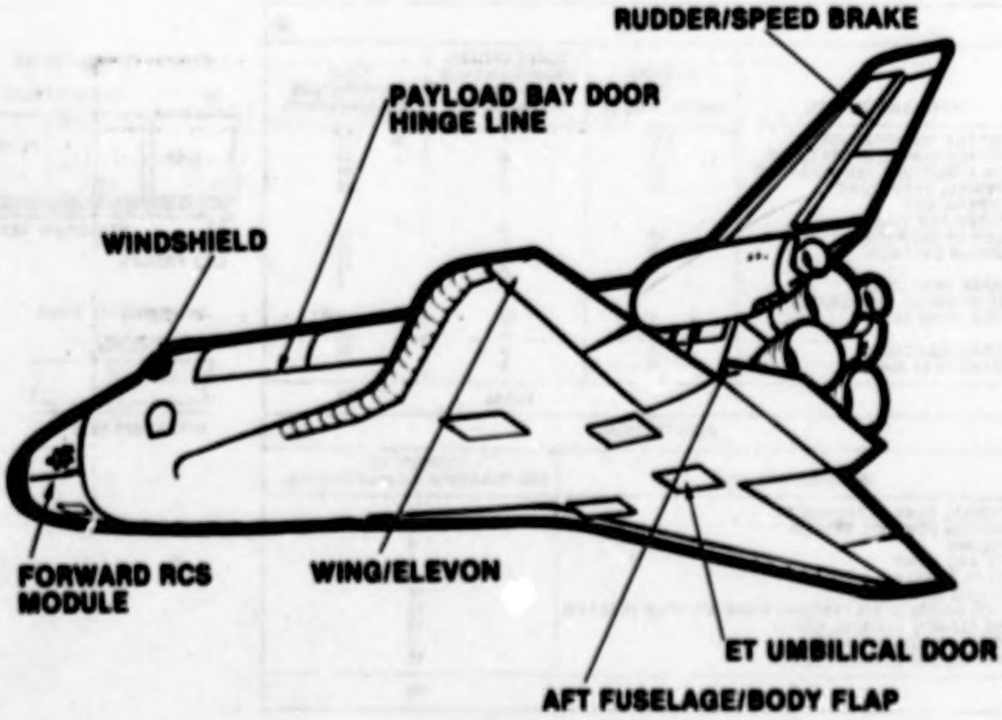
RUDDER/SPEED BRAKE
PAYLOAD BAY DOOR HINGE LINE
WINDSHIELD
FORWARD RCS MODULE
WING/ELEVON
ET UMBILICAL DOOR
AFT FUSELAGE/BODY FLAP

Figure 2.- Typical TPS penetrations.

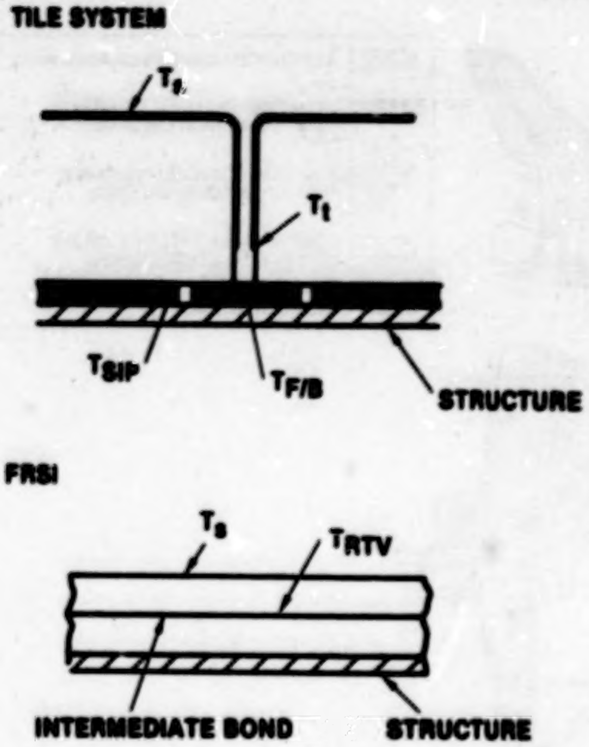
TILE SYSTEM
T_s
T_t
T_{SIP}
$T_{F/B}$
STRUCTURE
FRSI
T_s
T_{RTV}
INTERMEDIATE BOND
STRUCTURE

TILES:
T_s = 2300°F HRSI
1200°F LRSI
T_t = 1050°F
$T_{F/B}$ = 600°F
T_{SIP} = 550°F TYPICAL
600°F MINI TILES

FRSI:
T_s = 750°F ASCENT
700°F ENTRY
T_{RTV} = 550°F

PRIMARY STRUCTURE: 350°F

Figure 3.- 100-mission temperature allowables (acreage).

ACREAGE			
INSTALLATION TYPE	NUMBER OF INSTALLATIONS	TEMPERATURE MEASUREMENTS PER INSTALLATION	TOTAL TEMPERATURE MEASUREMENTS
SURFACE TEMPERATURES	177	1	177
SURFACE/SKIN TEMPERATURES	11	2	22
SKIN STRUCTURE TEMPERATURE	61	1	61
INTERNAL STRUCTURE TEMPERATURE	67	1	67
CENTER-TILE PLUG			
LOWER SURFACE	13	5	65
UPPER SURFACE	2	5	10
	3	4	12
BASE HEAT SHIELD	1	5	5
TILE SIDEWALL TEMPERATURE			
TILE JOINT ARRAY	1	13	13
	5	9	45
TRAILING EDGES	11	5	55
BASE HEAT SHIELD	1	5	5
		TOTAL	537

PENETRATIONS	
INSTALLATION TYPE	NUMBER OF TEMPERATURE MEASUREMENTS
EXTERNAL TANK ATTACHMENT	2
REACTION CONTROL SYSTEM	5
WINDOWS	6
VENT AND DUMP	7
ACCESS PANELS	3
PAYLOAD BAY DOORS	10
OTHER DOORS (MAIN LANDING GEAR, ET, STAR TRACKER)	13
WING ELEVON DYNAMIC SEALS	10
BODY FLAP DYNAMIC SE[illegible]	7
VERTICAL TAIL DYNAMIC [illegible]S	12
TOTAL	80

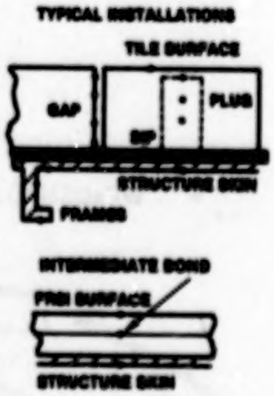
TYPICAL INSTALLATIONS
TILE SURFACE
GAP
SIP
PLUG
STRUCTURE SKIN
FRAMES
INTERMEDIATE BOND
FRSI SURFACE
STRUCTURE SKIN

Figure 4.- Development flight instrumentation.

ORIGINAL PAGE IS
OF POOR QUALITY

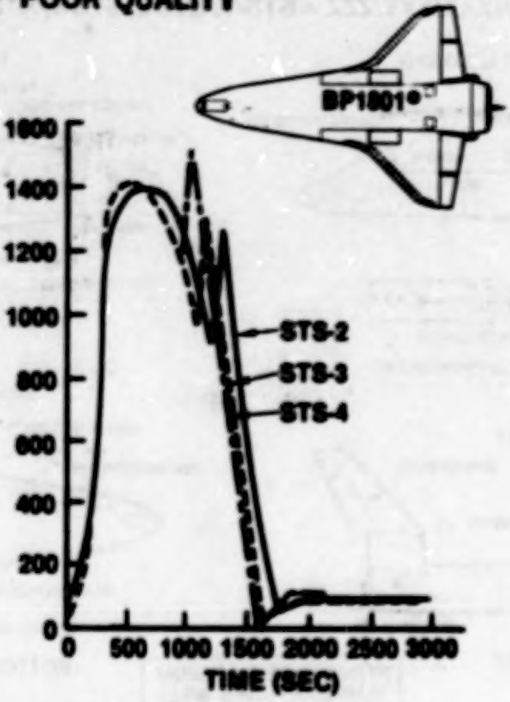

Figure 5.- Representative lower surface temperature response.

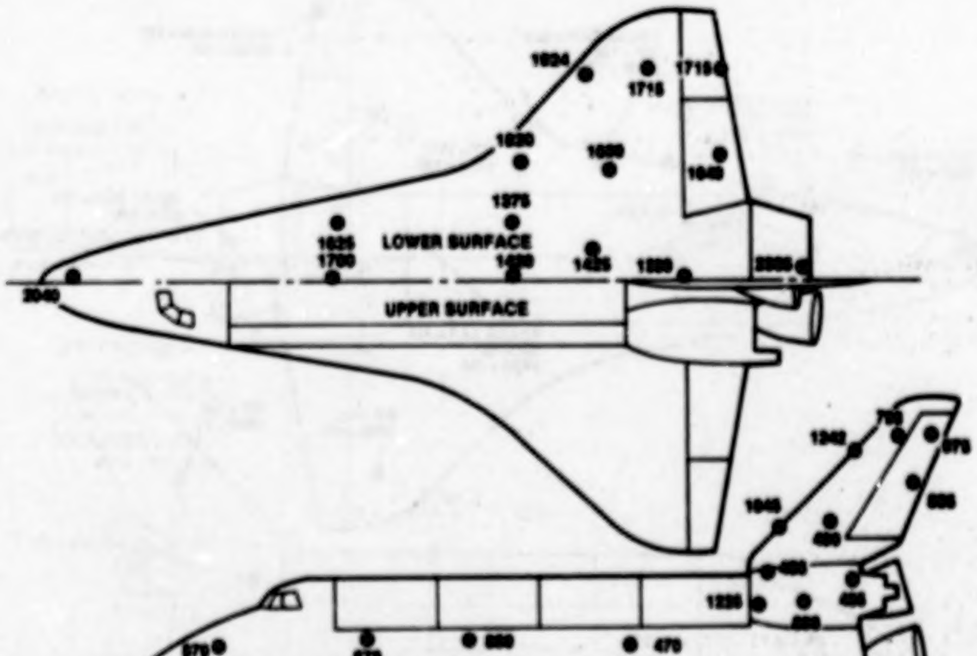
2040
1824
1715
1715
1820
1880
1640
1375
1625
1700
LOWER SURFACE
1420
1425
1380
2000
UPPER SURFACE
750
1242
675
600
1045
400
450
1230
400
650
670
1365
679
600
470

Figure 6.- STS-2 peak surface temperatures (^{o}F).

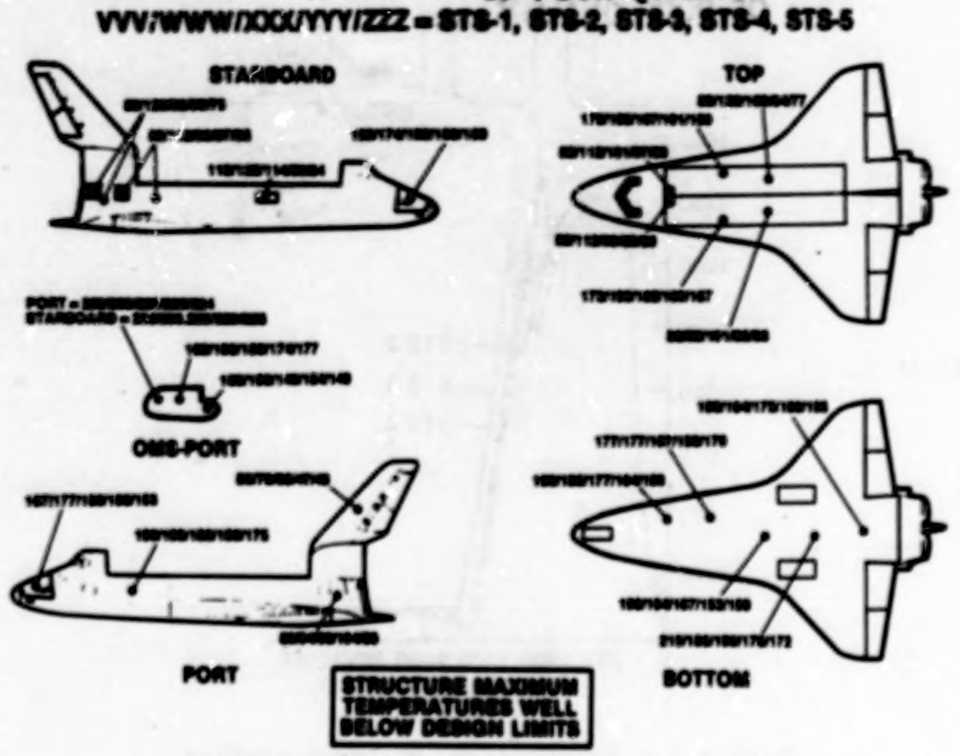
VVV/WWW/XXX/YYY/ZZZ = STS-1, STS-2, STS-3, STS-4, STS-5
STARBOARD
TOP
PORT =
STARBOARD =
OMS-PORT
PORT
BOTTOM
STRUCTURE MAXIMUM TEMPERATURES WELL BELOW DESIGN LIMITS

Figure 7.- STS-2 flight temperatures (°F).

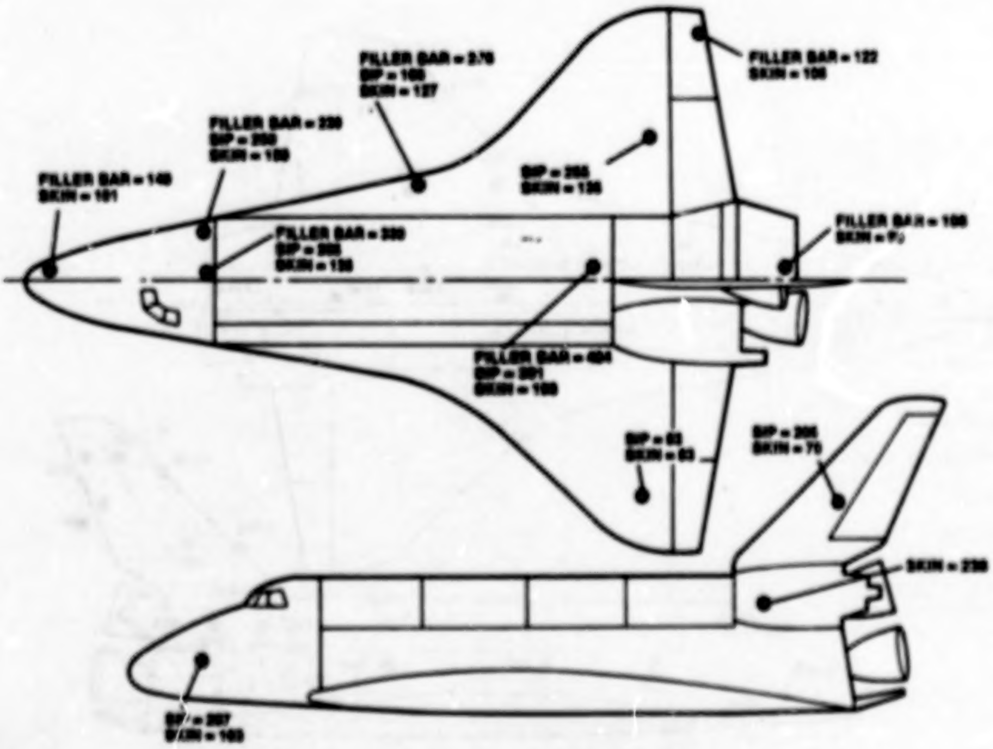
FILLER BAR = 270
SIP = 166
SKIN = 127
FILLER BAR = 122
SKIN = 106
FILLER BAR = 230
SIP = 250
SKIN = 150
FILLER BAR = 140
SKIN = 101
SIP = 255
SKIN = 135
FILLER BAR = 106
SKIN = 91
FILLER BAR = 230
SIP = 255
SKIN = 135
FILLER BAR = 424
SIP = 291
SKIN = 160
SIP = 83
SKIN = 83
SIP = 205
SKIN = 75
SKIN = 230
SIP = 207
SKIN = 103

Figure 8.- Structure maximum temperatures (°F).

ORIGINAL PAGE IS
OF POOR QUALITY

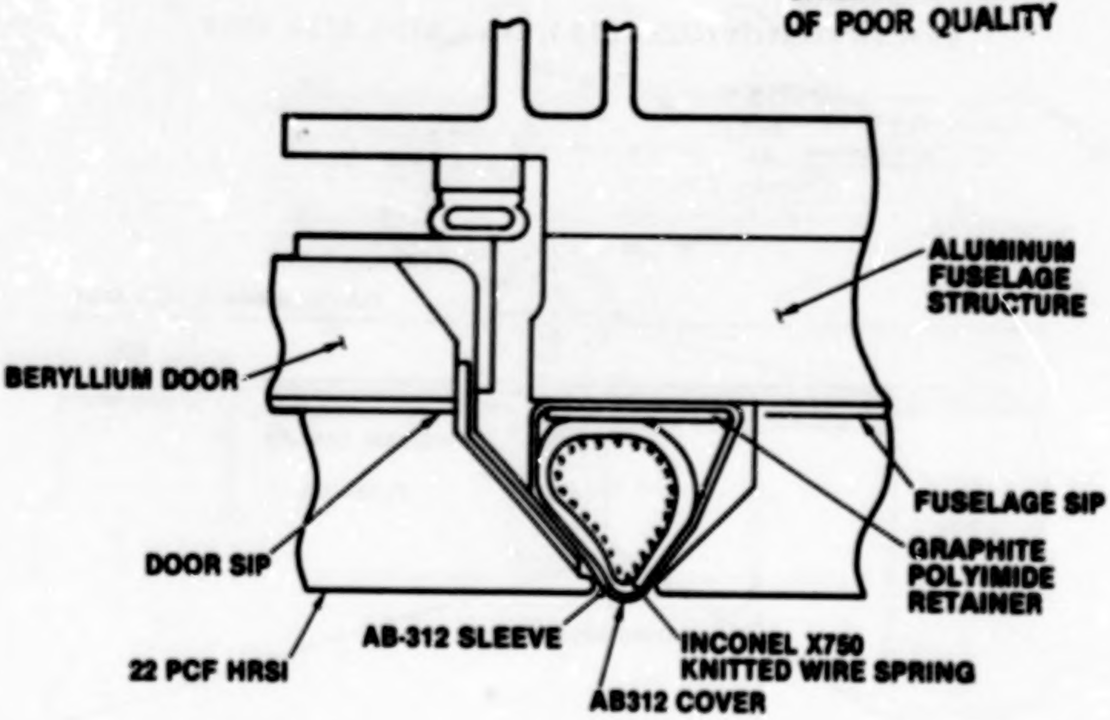
ALUMINUM FUSELAGE STRUCTURE
BERYLLIUM DOOR
FUSELAGE SIP
GRAPHITE POLYIMIDE RETAINER
DOOR SIP
AB-312 SLEEVE
INCONEL X750 KNITTED WIRE SPRING
22 PCF HRSI
AB312 COVER

Figure 9.- ET/orbiter umbilical door.

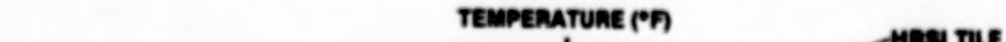

Figure 10.- ET door temperatures.

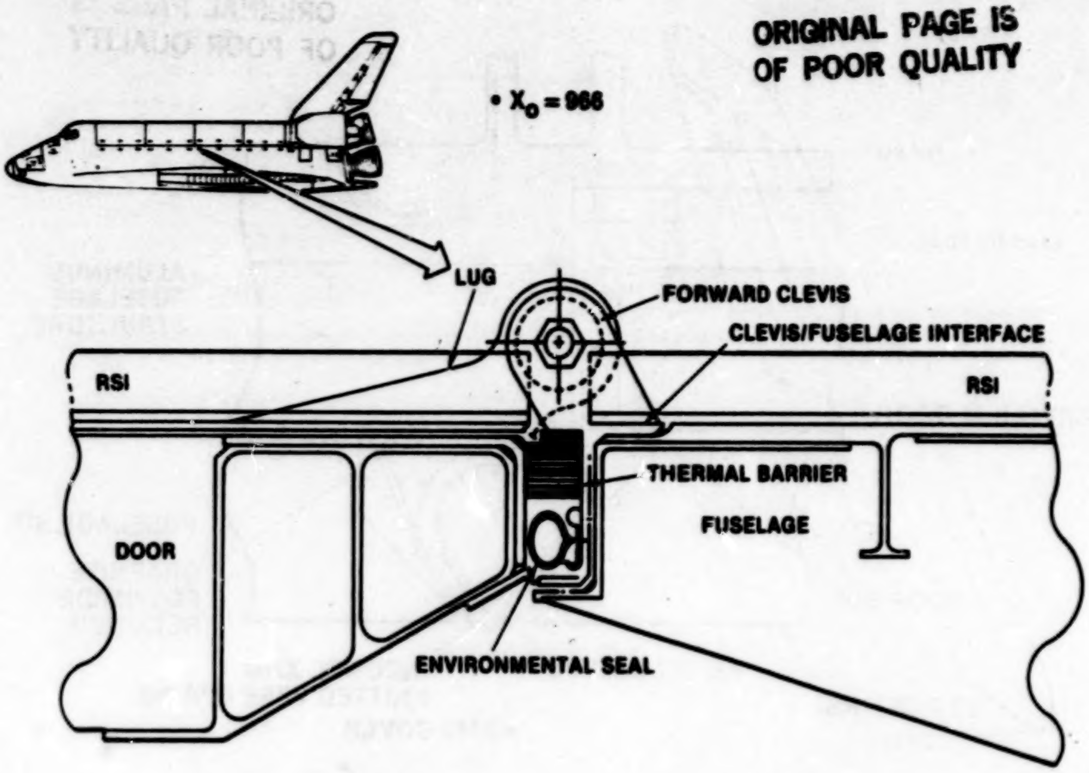
• $X_o = 966$
LUG
FORWARD CLEVIS
CLEVIS/FUSELAGE INTERFACE
RSI
RSI
THERMAL BARRIER
FUSELAGE
DOOR
ENVIRONMENTAL SEAL

Figure 11.- Unprotected PLB door hinge.

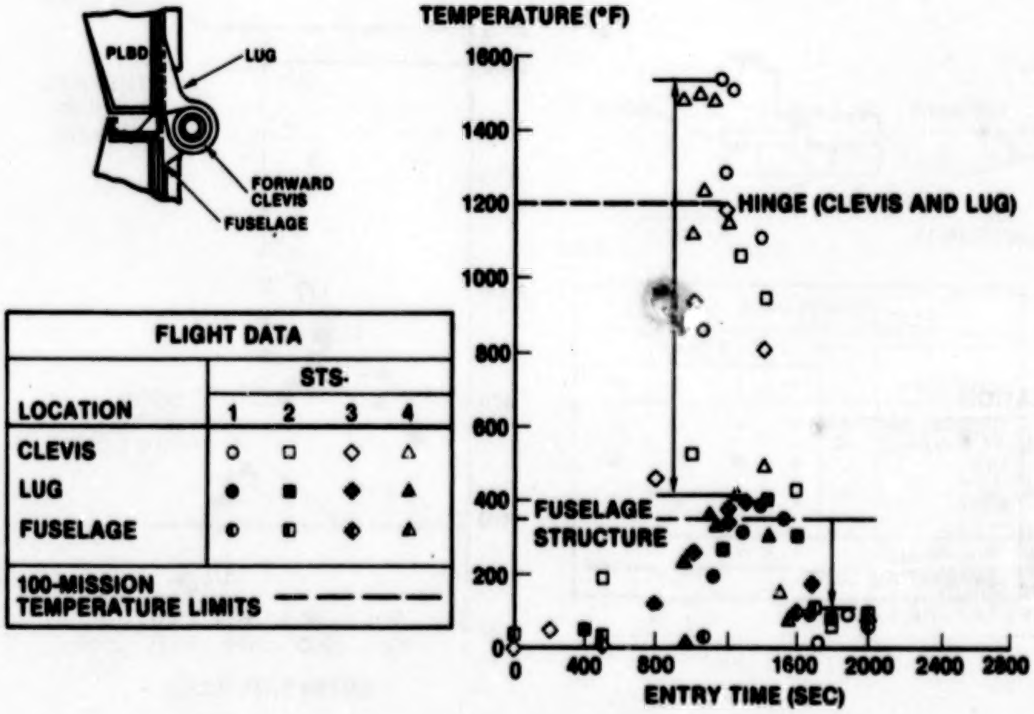

Figure 12.- PLB door bare hinge temperatures.

ORIGINAL PAGE IS
OF POOR QUALITY

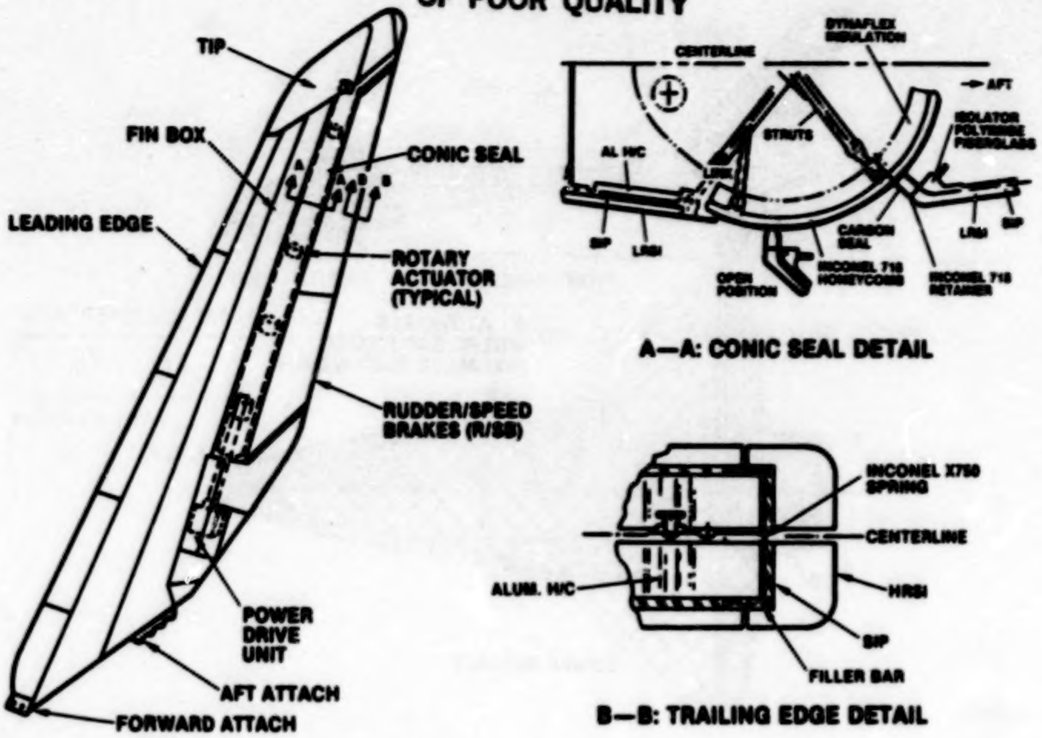
TIP
FIN BOX
CONIC SEAL
LEADING EDGE
A
B
ROTARY ACTUATOR (TYPICAL)
RUDDER/SPEED BRAKES (R/SB)
POWER DRIVE UNIT
AFT ATTACH
FORWARD ATTACH
DYNAFLEX INSULATION
CENTERLINE
AFT
ISOLATOR POLYIMIDE FIBERGLASS
STRUTS
AL H/C
LINK
SIP
LRSI
CARBON SEAL
INCONEL 718 HONEYCOMB
INCONEL 718 RETAINER
OPEN POSITION
LRSI
SIP
INCONEL X750 SPRING
CENTERLINE
ALUM. H/C
HRSI
SIP
FILLER BAR

A—A: CONIC SEAL DETAIL

B—B: TRAILING EDGE DETAIL

Figure 13.- Vertical tail.

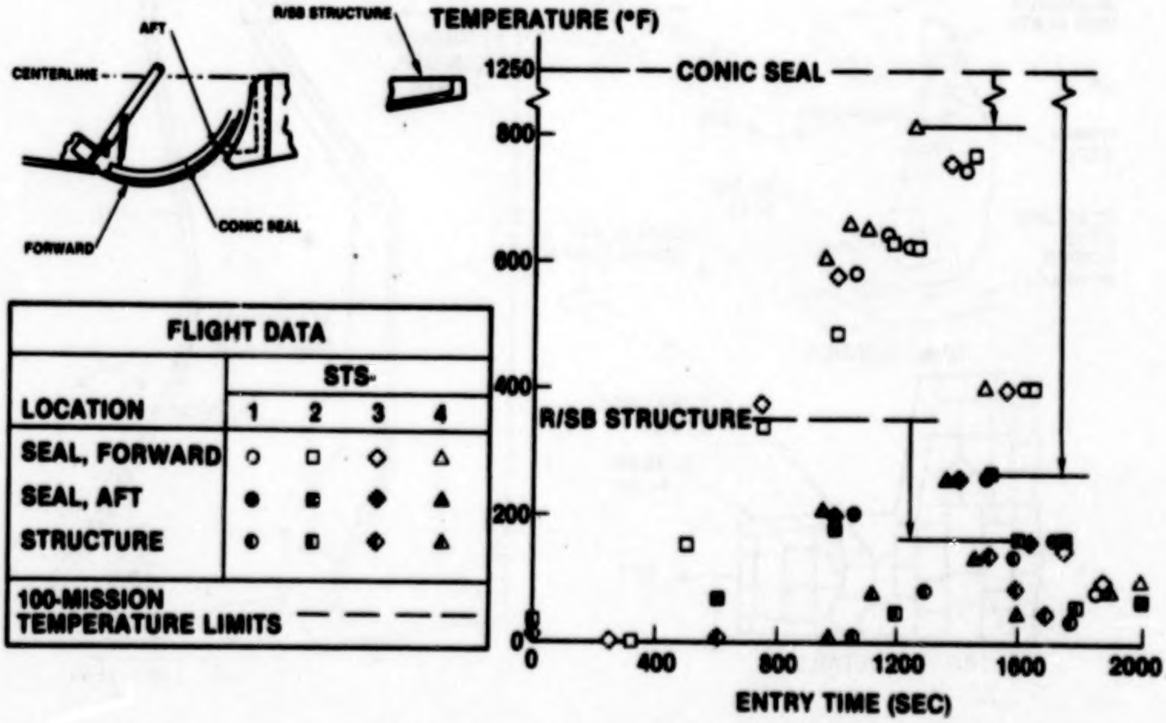

Figure 14.- Conic seal and rudder/speed brake structure temperatures.

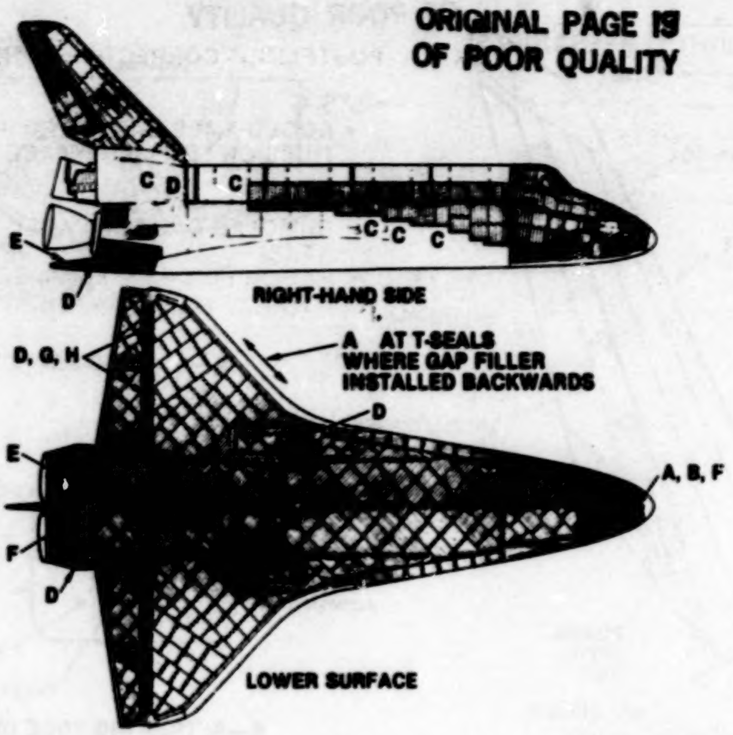
C
D
C
C
C
C
E
D
RIGHT-HAND SIDE
D, G, H
A AT T-SEALS WHERE GAP FILLER INSTALLED BACKWARDS
D
E
A, B, F
F
D
LOWER SURFACE

Figure 15.- Locations of significant TPS degradation.

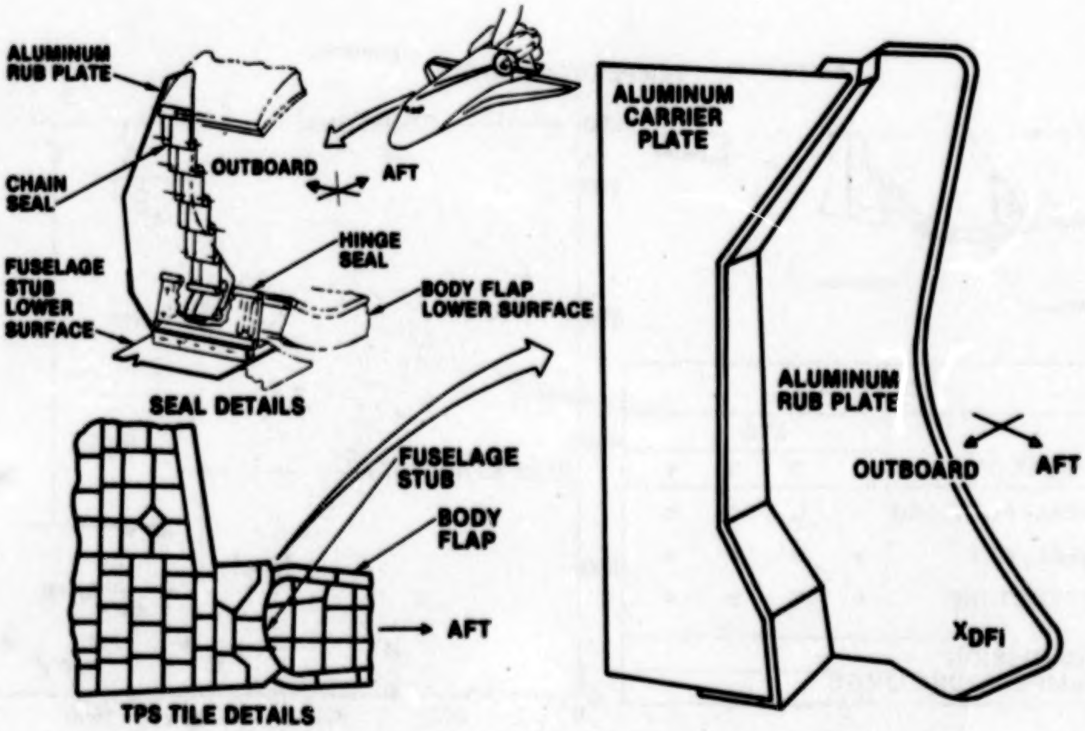
ALUMINUM RUB PLATE
CHAIN SEAL
OUTBOARD
AFT
HINGE SEAL
FUSELAGE STUB LOWER SURFACE
BODY FLAP LOWER SURFACE
SEAL DETAILS
FUSELAGE STUB
BODY FLAP
AFT
TPS TILE DETAILS
ALUMINUM CARRIER PLATE
ALUMINUM RUB PLATE
OUTBOARD
AFT
X_{DFI}

Figure 16.- Stub and body flap.

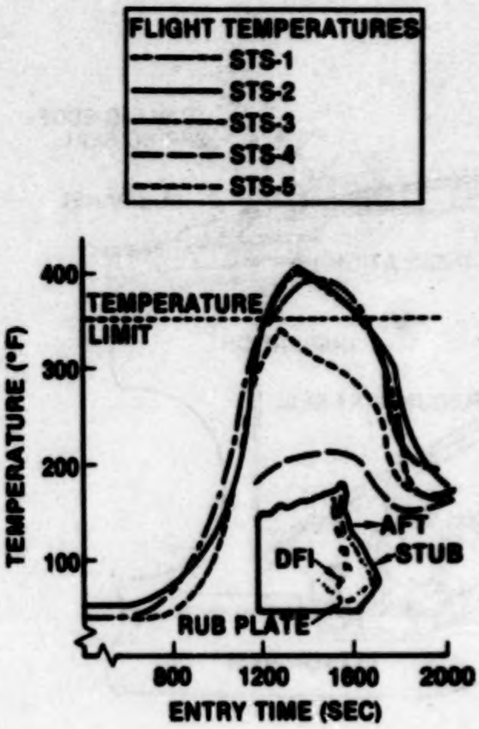

POSTFLIGHT CORRECTIVE ACTIONS

- STS-1
  - ADDED AMES GAP FILLER BETWEEN STUB TILES ON LOWER SURFACE
- STS-2
  - REMOVED CARRIER PANEL TILES (SIDE OF STUB)
  - REPLACED CHARRED/MISSING FILLER BAR
  - PAD GAP FILLER REBONDED
- STS-3
  - REMOVED CARRIER PANEL TILES
  - REMADE TWO LOWER SURFACE TILES TO REMOVE FORWARD-FACING STEP
  - ADDED AB312 ROPE FLOW BARRIER, NEW GAP FILLER AND RTV
- STS-4
  - NONE
- STS-5
  - CARRIER PANELS OFF AWAITING TILE AND GAP FILLER MODIFICATIONS

Figure 17.- Body flap rub plate anomaly.

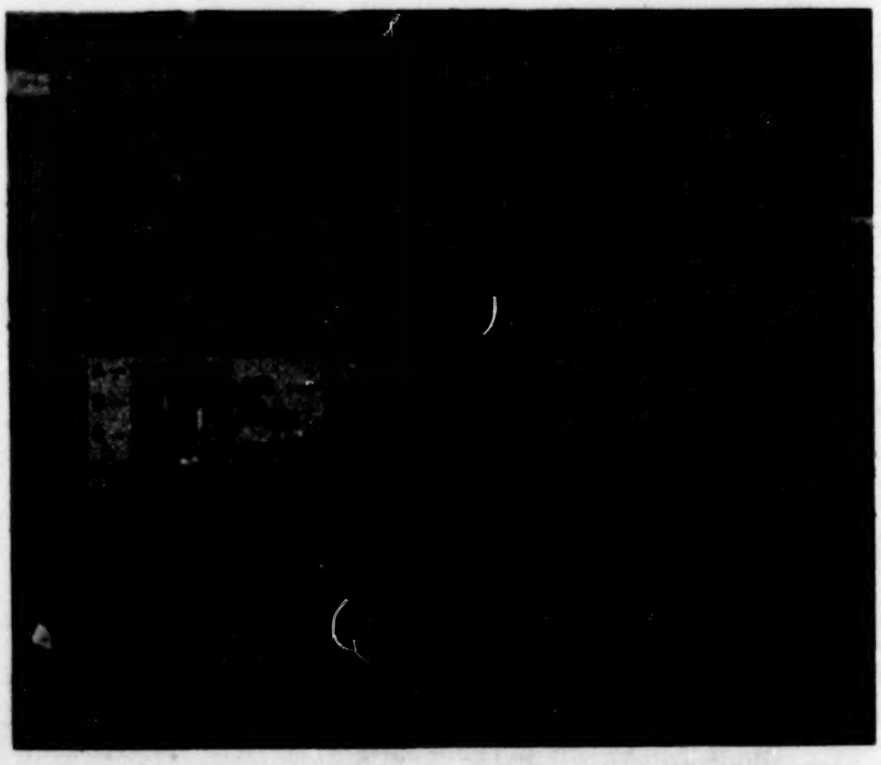

Figure 18.- STS-2 postflight condition of fuselage stub.

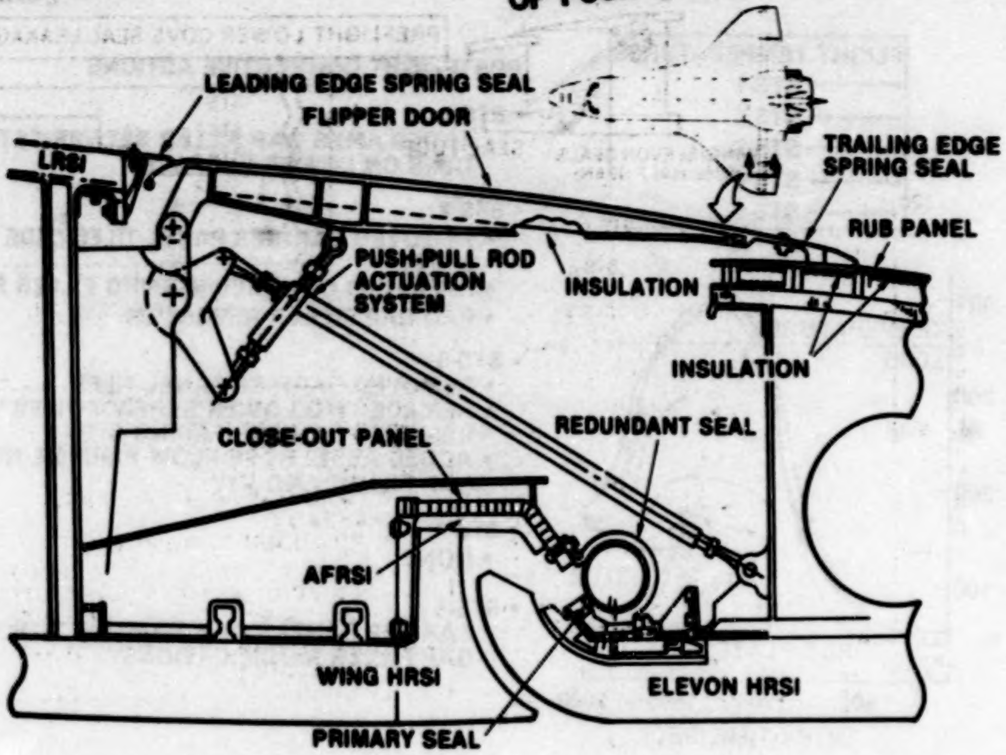
LEADING EDGE SPRING SEAL
FLIPPER DOOR
LRSI
TRAILING EDGE
SPRING SEAL
RUB PANEL
PUSH-PULL ROD
ACTUATION
SYSTEM
INSULATION
INSULATION
REDUNDANT SEAL
CLOSE-OUT PANEL
AFRSI
WING HRSI
ELEVON HRSI
PRIMARY SEAL

Figure 19.- Elevon seal system: design configuration.

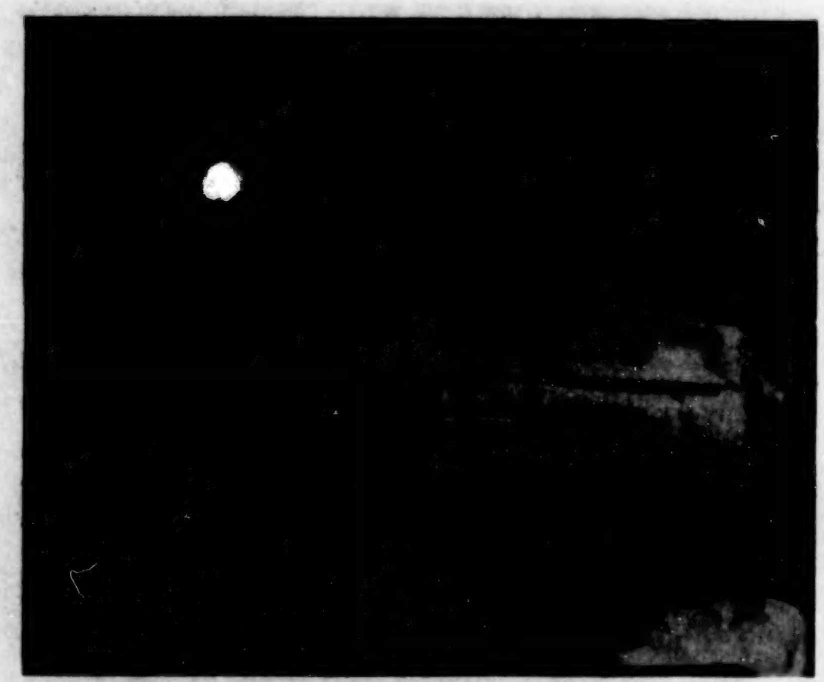

Figure 20.- Elevon lower cove close-out panels after STS-1.

ORIGINAL PAGE IS
OF POOR QUALITY

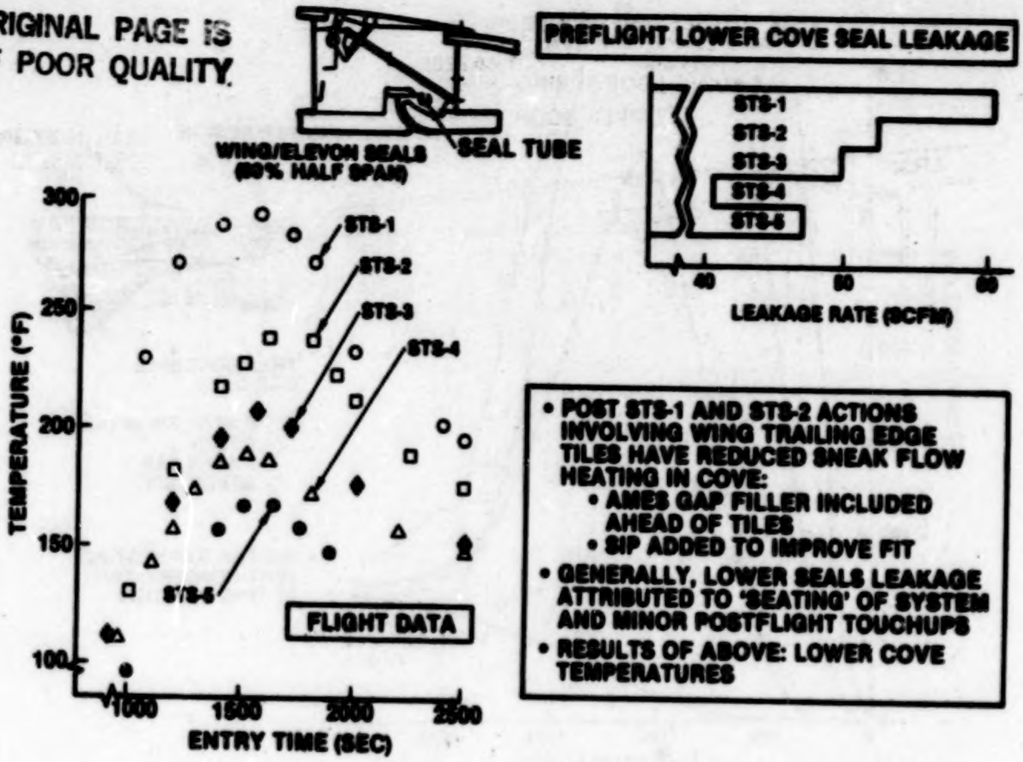

- POST STS-1 AND STS-2 ACTIONS INVOLVING WING TRAILING EDGE TILES HAVE REDUCED SNEAK FLOW HEATING IN COVE:
  - AMES GAP FILLER INCLUDED AHEAD OF TILES
  - SIP ADDED TO IMPROVE FIT
- GENERALLY, LOWER SEALS LEAKAGE ATTRIBUTED TO 'SEATING' OF SYSTEM AND MINOR POSTFLIGHT TOUCHUPS
- RESULTS OF ABOVE: LOWER COVE TEMPERATURES

Figure 21.- Trends in the elevon lower case.

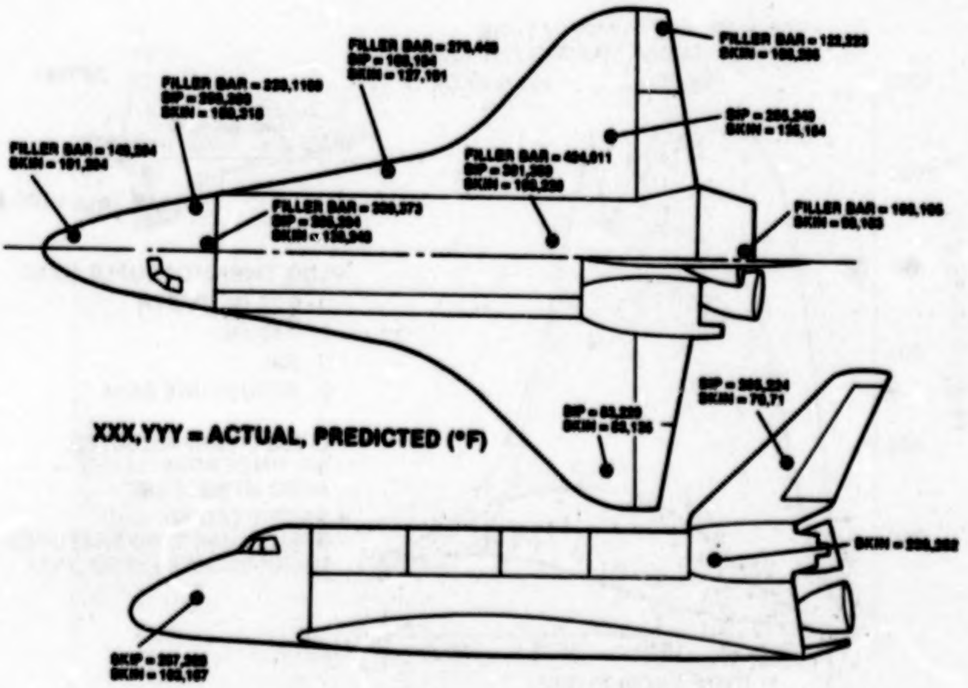
FILLER BAR = 149,284
SKIN = 101,284
FILLER BAR = 229,1169
SIP = 298,369
SKIN = 189,316
FILLER BAR = 279,449
SIP = 168,194
SKIN = 127,161
FILLER BAR = 329,373
SIP = 309,284
SKIN = 139,349
FILLER BAR = 424,011
SIP = 391,369
SKIN = 169,229
FILLER BAR = 129,229
SKIN = 199,286
SIP = 286,249
SKIN = 126,184
FILLER BAR = 169,106
SKIN = 99,163
SIP = 83,229
SKIN = 83,136
SIP = 389,234
SKIN = 79,71
SKIN = 229,282
SKIP = 237,369
SKIN = 103,167
XXX,YYY = ACTUAL, PREDICTED (°F)

Figure 22.- Comparison of STS-2 flight and postflight analysis temperatures.

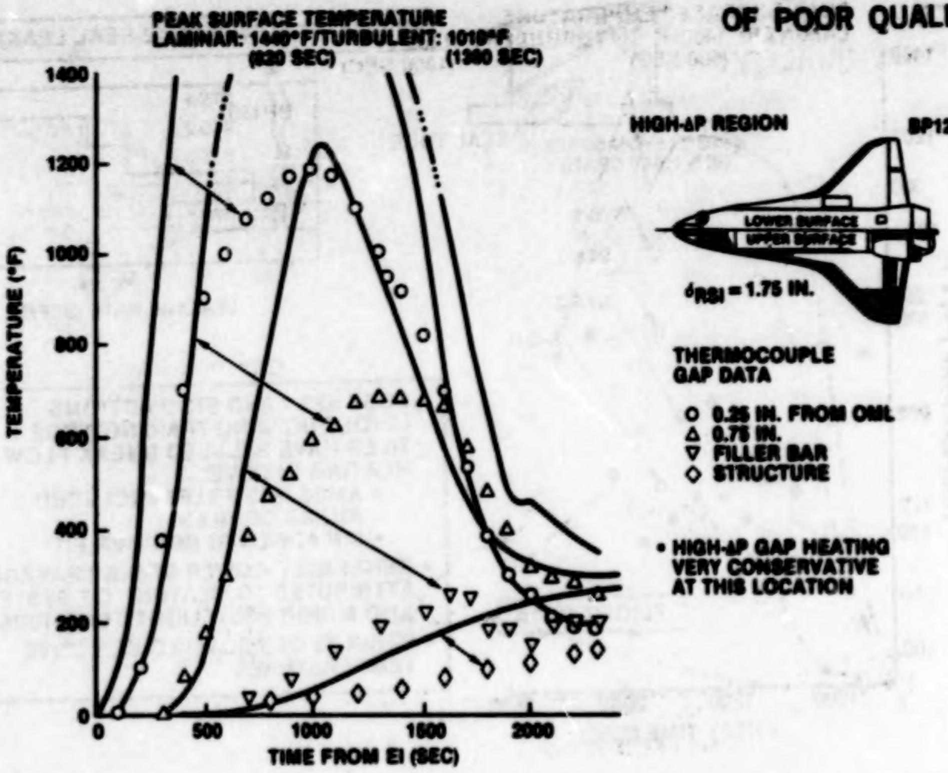

Figure 23.- Comparison of design method with STS-2 flight temperatures (high Δp location).

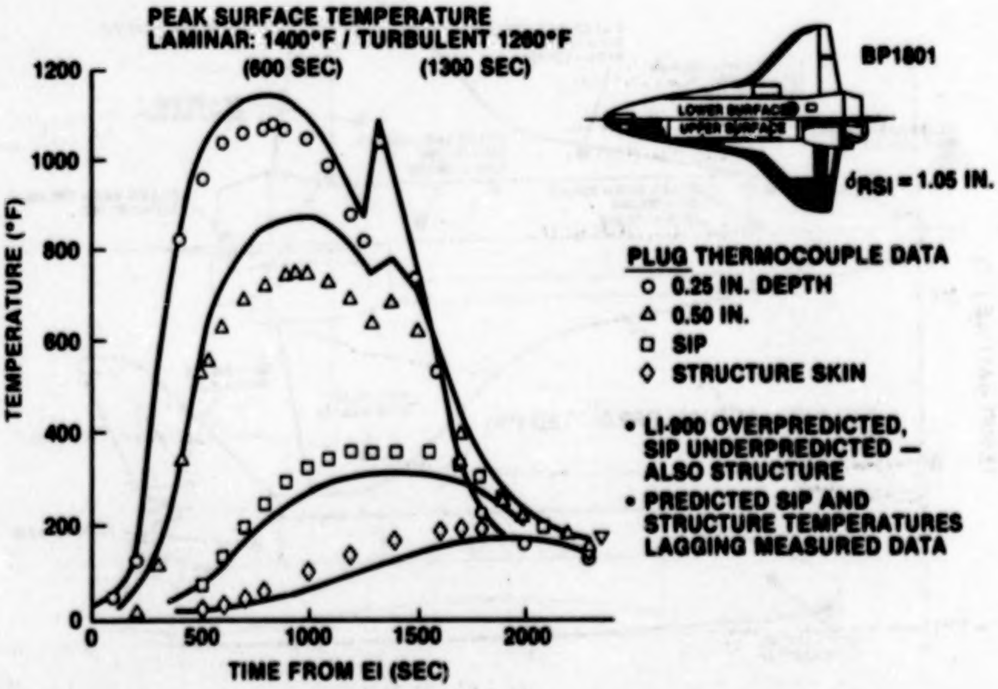

Figure 24.- Comparison of design method with STS-2 flight temperatures (plug thermocouples).

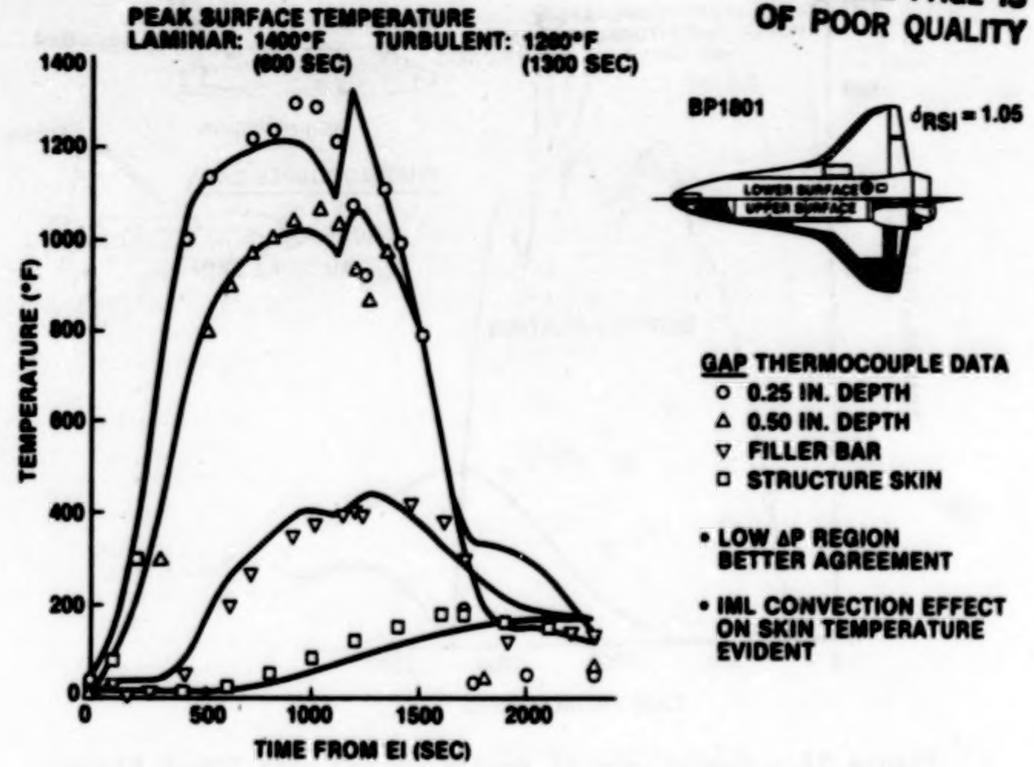

Figure 25.- Comparison of design method with STS-2 flight temperatures (gap thermocouples).

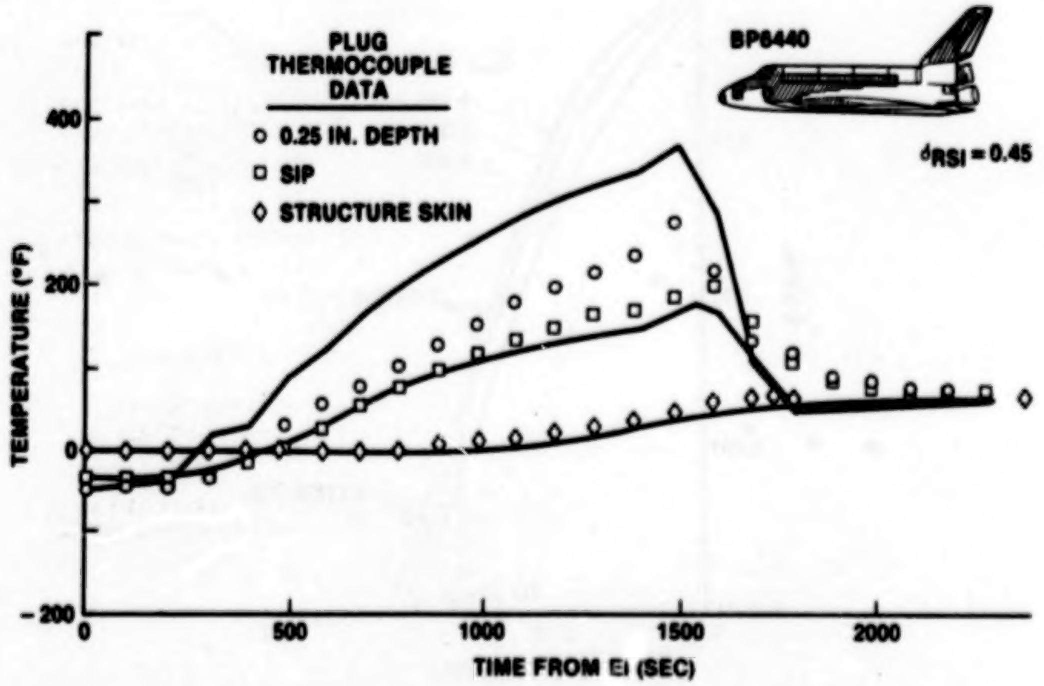

Figure 26.- Comparison of design method with STS-2 flight temperature (LRSI location).

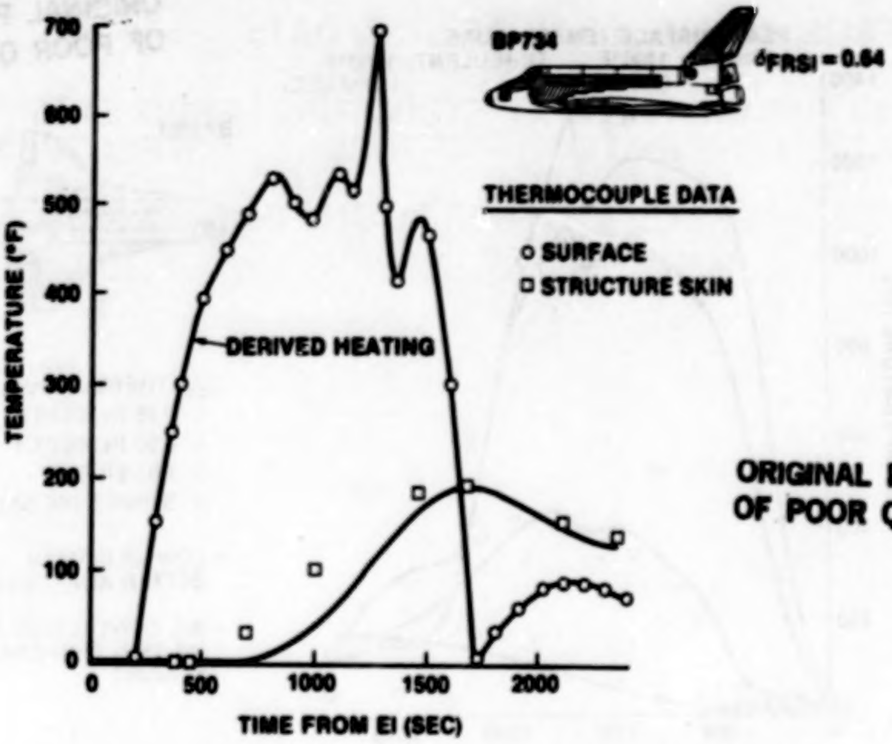

Figure 27.- Comparison of design method with STS-2 flight temperature (FRSI location).

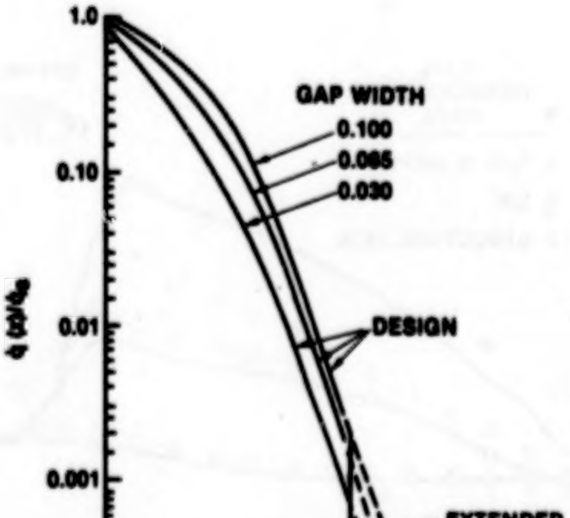

Figure 28.- Low pressure gradient gap heating distribution.

n = 1.6 FROM CORRELATION OF STS-2 DATA

h′ = 0.10 FOR UNINSULATED STRUCTURE } FROM EXAMINATION OF
h′ = 0.07 FOR INSULATED STRUCTURE } STRUCTURE DATA

V/V′ FROM INTERPRETATION OF FLIGHT DATA

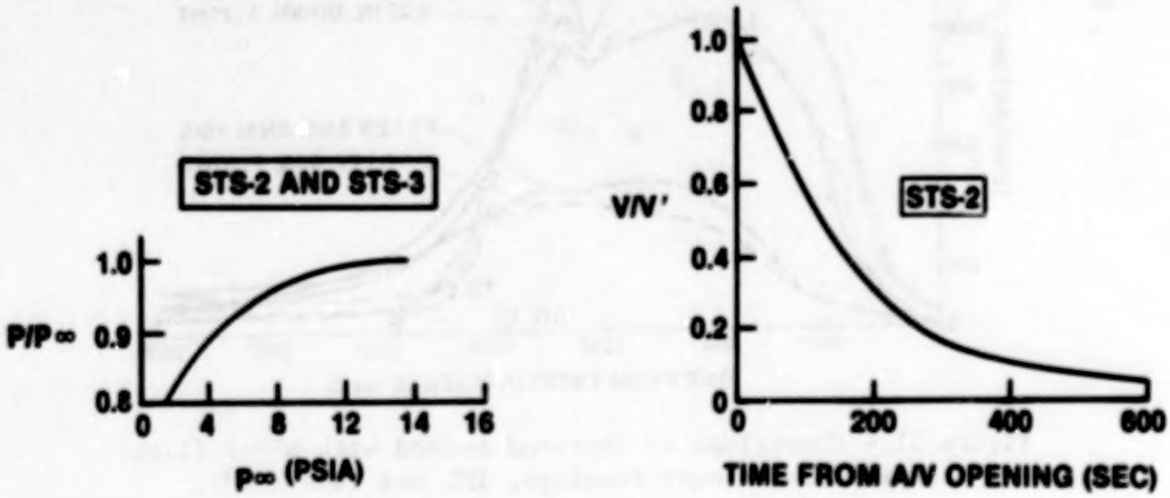

Figure 29.- Preliminary IML convection data.

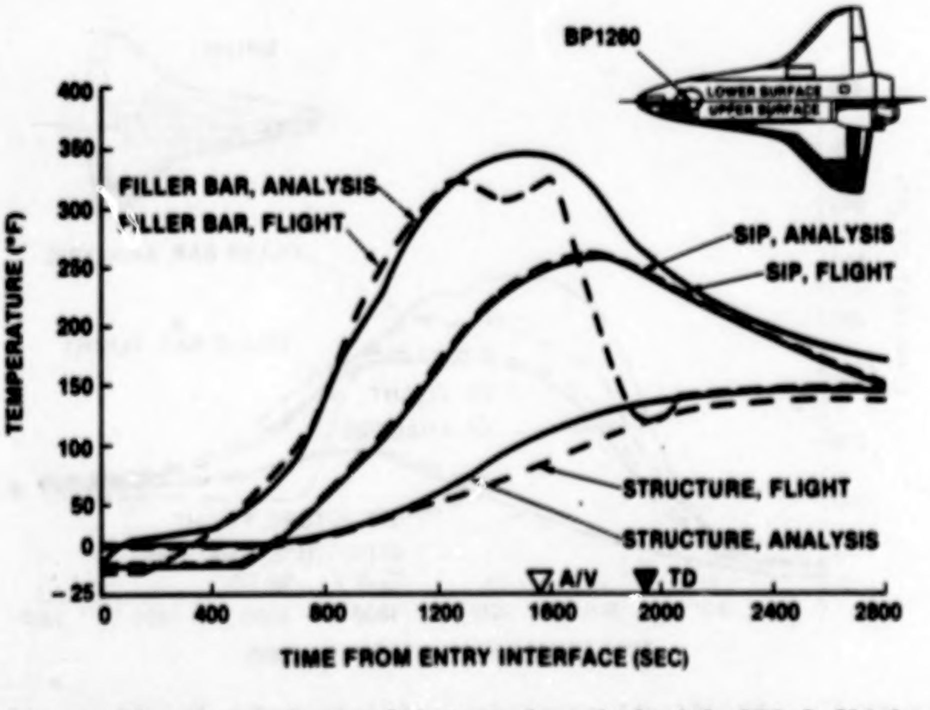

Figure 30.- Comparison of improved method with STS-2 flight temperatures (lower fuselage, IML insulated).

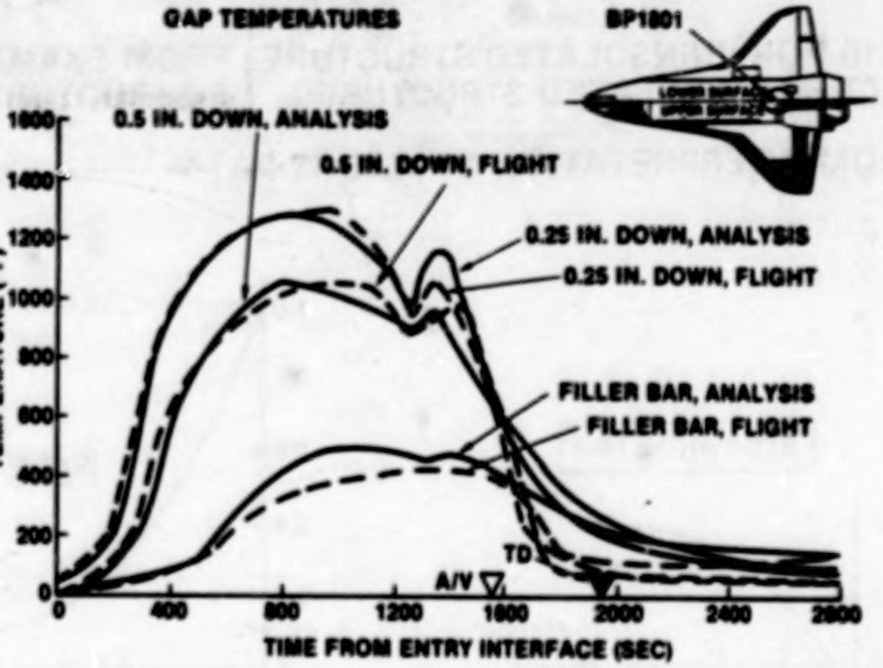

Figure 31.- Comparison of improved method with STS-2 flight temperatures (lower fuselage, IML not insulated).

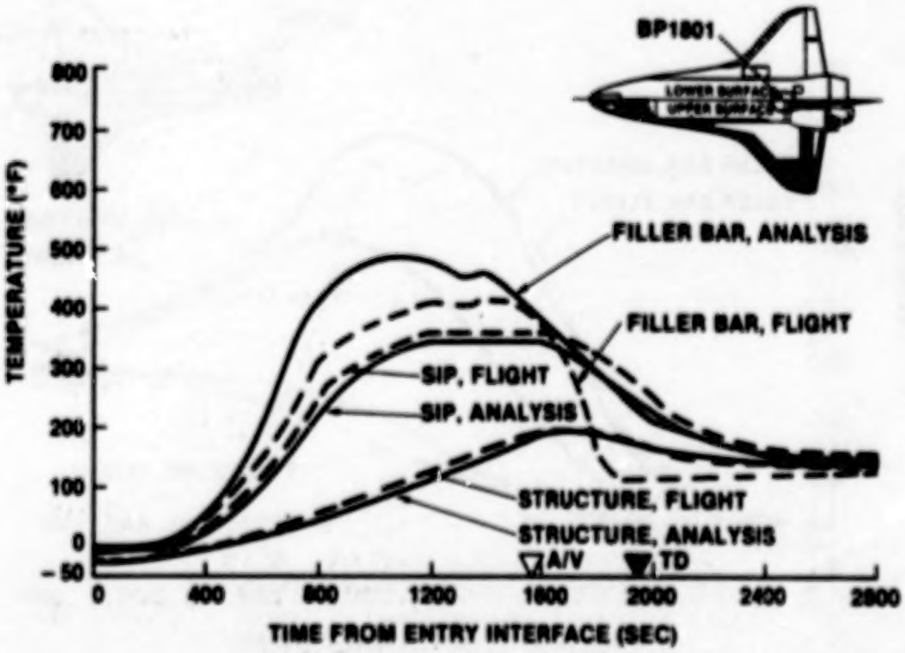

Figure 32.- Additional comparison of improved method with STS-2 flight temperatures (lower fuselage, IML not insulated).

ORIGINAL PAGE IS
OF POOR QUALITY

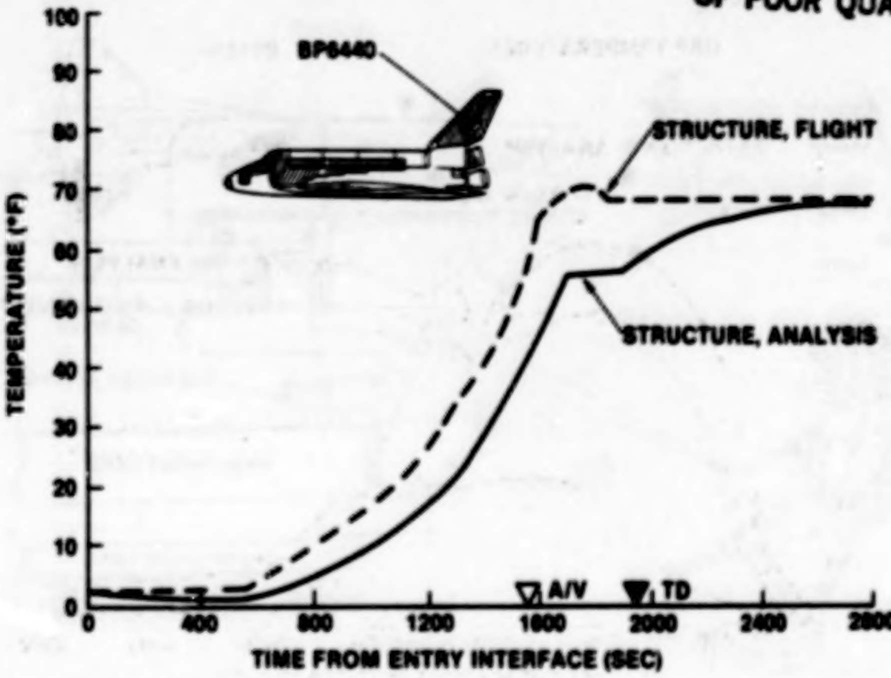

Figure 33.- Comparison of improved method with STS-2 flight temperatures (LRSI location).

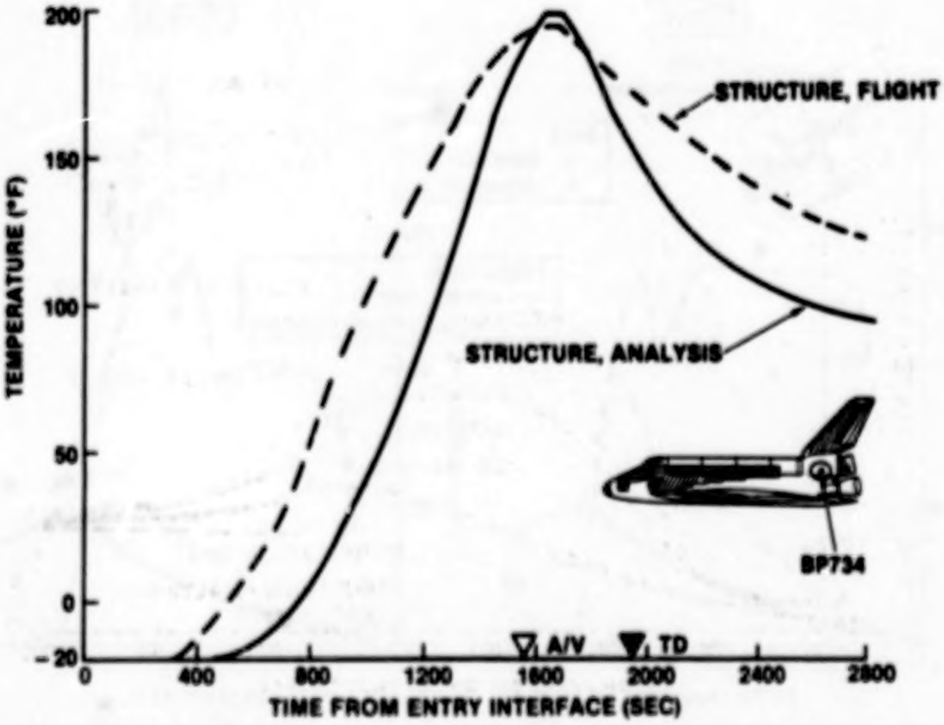

Figure 34.- Comparison of improved method with STS-2 flight temperatures (FRSI location).

ORIGINAL PAGE IS
OF POOR QUALITY

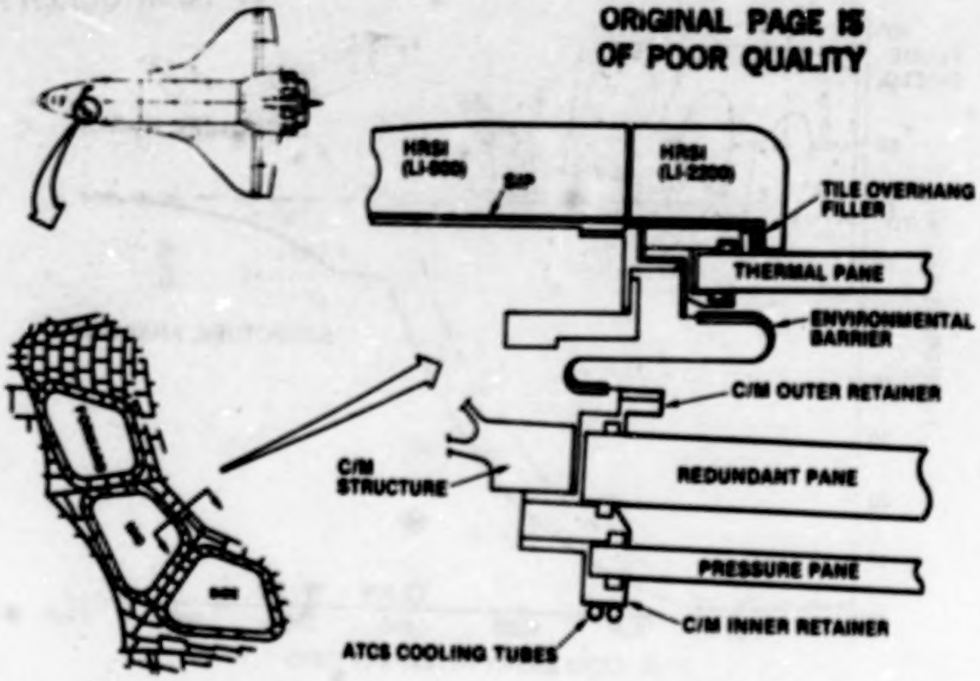
HRSI (LI-900)
SIP
HRSI (LI-2200)
TILE OVERHANG FILLER
THERMAL PANE
ENVIRONMENTAL BARRIER
C/M OUTER RETAINER
C/M STRUCTURE
REDUNDANT PANE
PRESSURE PANE
C/M INNER RETAINER
ATCS COOLING TUBES

Figure 35.- Windshield design configuration.

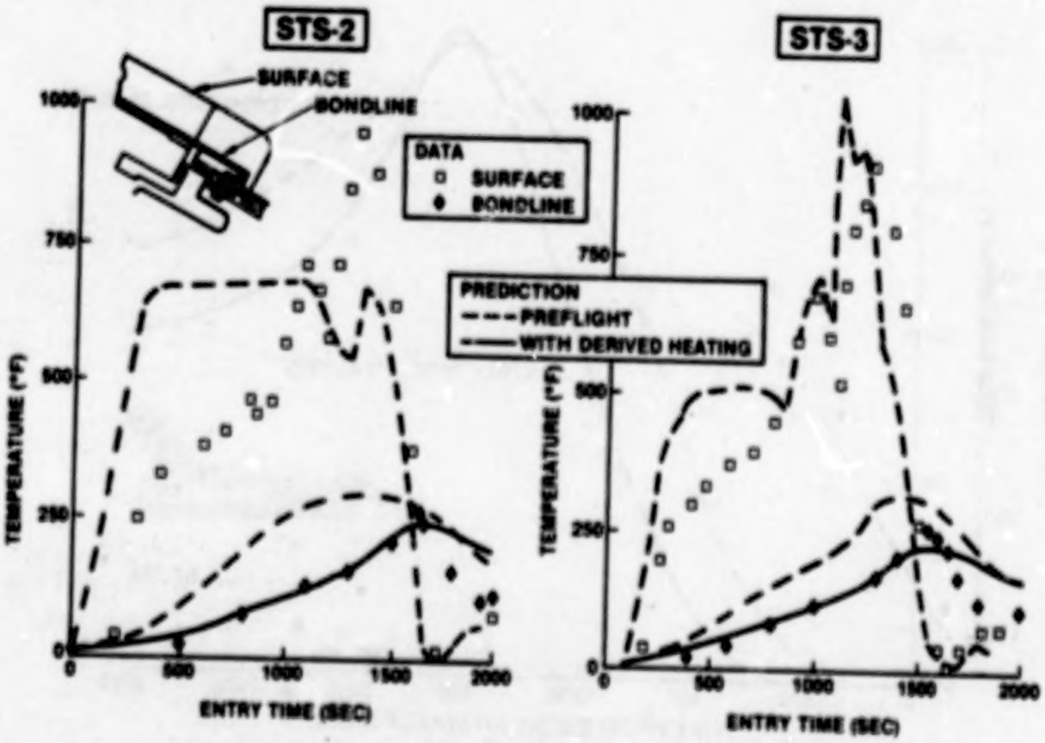

Figure 36.- Windshield modeling improvements.

ORIGINAL PAGE IS
OF POOR QUALITY

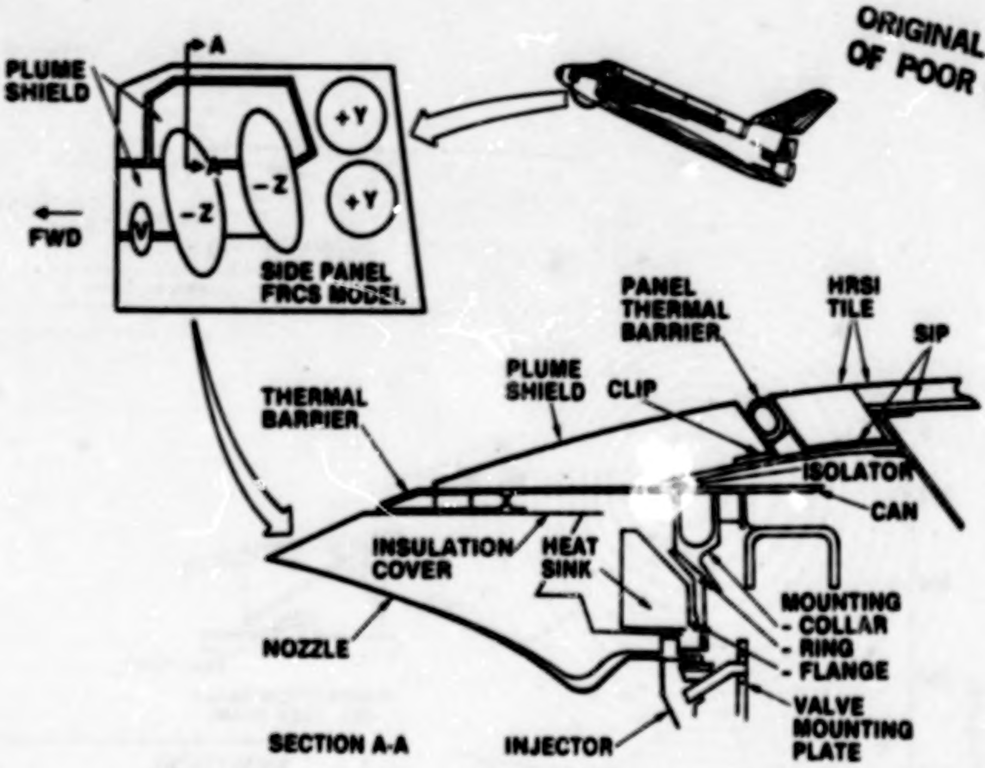

PLUME SHIELD
A
+Y
-Z
-Z
+Y
FWD
SIDE PANEL FRCS MODEL
PANEL THERMAL BARRIER
HRSI TILE
SIP
PLUME SHIELD
CLIP
THERMAL BARRIER
ISOLATOR
CAN
INSULATION COVER
HEAT SINK
MOUNTING
- COLLAR
- RING
- FLANGE
NOZZLE
VALVE MOUNTING PLATE
SECTION A-A
INJECTOR

Figure 37.- FRCS-Z thruster design installation.

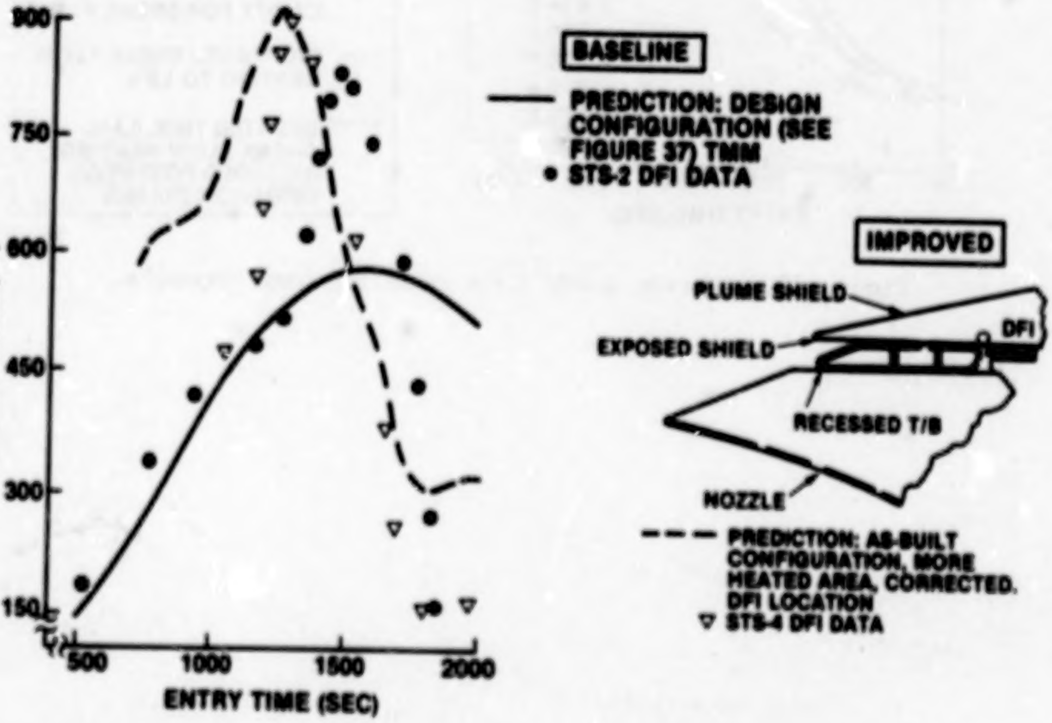

Figure 38.- FRCS thruster modeling improvements.

ORIGINAL PAGE IS
OF POOR QUALITY

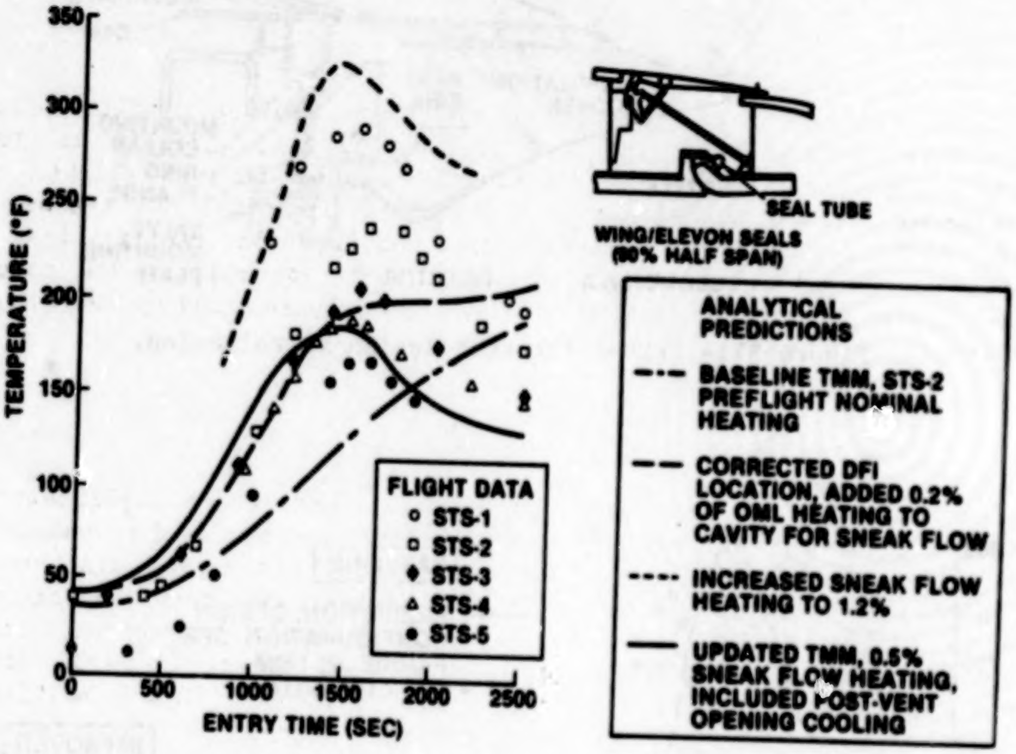

Figure 39.- Elevon lower cove modeling improvements.

N84
10161

UNCLAS

N84 10161 D/7

SPACE SHUTTLE ORBITER
LEADING-EDGE FLIGHT PERFORMANCE COMPARED TO DESIGN GOALS

Donald M. Curry
NASA Johnson Space Center
Houston, Texas

David W. Johnson
Vought Corporation
Dallas, Texas

Robert E. Kelly
Rockwell International
Downey, California

ORIGINAL PAGE IS
OF POOR QUALITY

SUMMARY

Thermo-structural performance of the Space Shuttle orbiter Columbia's leading-edge structural subsystem for the first five (5) flights is compared with the design goals. Lessons learned from these initial flights of the first reusable manned spacecraft are discussed in order to assess design maturity, deficiencies, and modifications required to rectify the design deficiencies. Flight data and post-flight inspections support the conclusion that the leading-edge structural subsystem hardware performance has been outstanding for the initial five (5) flights.

INTRODUCTION

Conception of a new era in man's advantageous utilization and exploitation of space was realized recently with the successful completion of the four development test flights and the initial commercial mission of the Space Shuttle orbiter, Columbia. Unique design and construction of the orbiter to achieve reusability, a feature previously impractical in space vehicles, were attainable with the progressive development of high-technology materials used in the Thermal Protection System (TPS). Multi-mission capability is the key in achieving cost effective access to space for routine manned operations. Assessment of this capability is now possible with the accrued flight data coupled with the information gathered from post-flight inspections conducted after each flight.

Essential to the total system of thermal protection of the orbiter is the leading-edge structural subsystem (LESS), generally defined as those areas of the wing leading edge and the forward fuselage that exceed maximum temperatures of 2300°F during re-entry. Reinforced Carbon-Carbon (RCC) is one of the new generation materials that is indispensable in providing multi-mission capability in this punishing, high-temperature environment while concurrently maintaining the integrity of the aerodynamic surfaces. RCC is a hard carbon structural material possessing reasonable strength throughout the operational temperature range predicted for the orbiter. Thermal shock and thermoelastic stress effects are minimized with the low coefficient of thermal expansion. Oxidation protection, fundamental to the reusability feature of RCC, is provided to the carbon substrate by converting the outer surface to Silicon Carbide (SiC) in a diffusion coating process. Further enhancement of the oxidation protection is provided by post-coating treatments of vacuum impregnation of the laminate with Tetraethyl Orthosilicate (TEOS).

Success of the initial five flights of Columbia implies that the flight environments were appropriately anticipated and the system response accurately predicted. Although verification of the total system capacity in terms of reusability remains unconfirmed, certain parameters can be evaluated from the acquired flight data to provide forecasts necessary for operational viability for the life of the orbiter. Lessons learned during the early stages of this unique, reusable space vehicle can be used to identify not only areas of the orbiter that need attention to achieve maturity but also technology deficiencies on which to concentrate research and development for future space systems.

LESS DESIGN

The orbiter LESS basically consists of the RCC nose cap and seals, the wing leading-edge RCC panels and seals, the associated metal attachments to the supporting structure, the internal insulation systems, and the interface Reusable Surface Insulation (RSI) tiles. Depicted pictorially in Figure 1, the RCC nose cap and wing leading-edge constitutes approximately 420 square feet of external surface area. Additionally, although not included in the original design, pre-flight modification of the region surrounding the forward, external tank attachment was made to include a RCC cover plate, appropriately identified as the arrowhead illustrated in Figure 1.

Figure 1.- Leading-edge structural subsystem.

ORIGINAL PAGE IS
OF POOR QUALITY

Basic design goals and purpose for the LESS are to provide thermo-structural capabilities for the regions of the orbiter that exceed 2300°F. Operational requirements include the retention of the aerodynamic shape of the outer moldlines, the control of the aluminum structure maximum temperature to less than 350°F, and the capability to sustain 100 missions with minimal refurbishment. Interface control between the RCC and the RSI tiles was a significant parameter in the design not only to retain the aerodynamic surface for flight quality but also to preclude damaging the more vulnerable tiles. Serviceability was another issue that dictated the field-break design configuration for access to the attachments and easy removal of the RCC components.

Final design configuration of the RCC nose cap assembly is illustrated in Figure 2, consisting of the dome, five (5) gap seals, and three (3) expansion seals. Functional requirements of the seals are to allow thermal expansion and deflections while simultaneously preventing hot gas influx into the cavity and precluding deflections of the RCC that penetrate into the interface RSI tile envelope. Illustrated pictorially by the representative panel-seal set in Figure 3, the wing leading edge consists of twenty-two (22) similar assemblies on each wing. Gap seals are provided between the panels to serve the same function previously described for the nose cap seals. Optimization of the size of the panels included as significant parameters: structural integrity, producibility in terms of tooling and facility requirements, and weight.

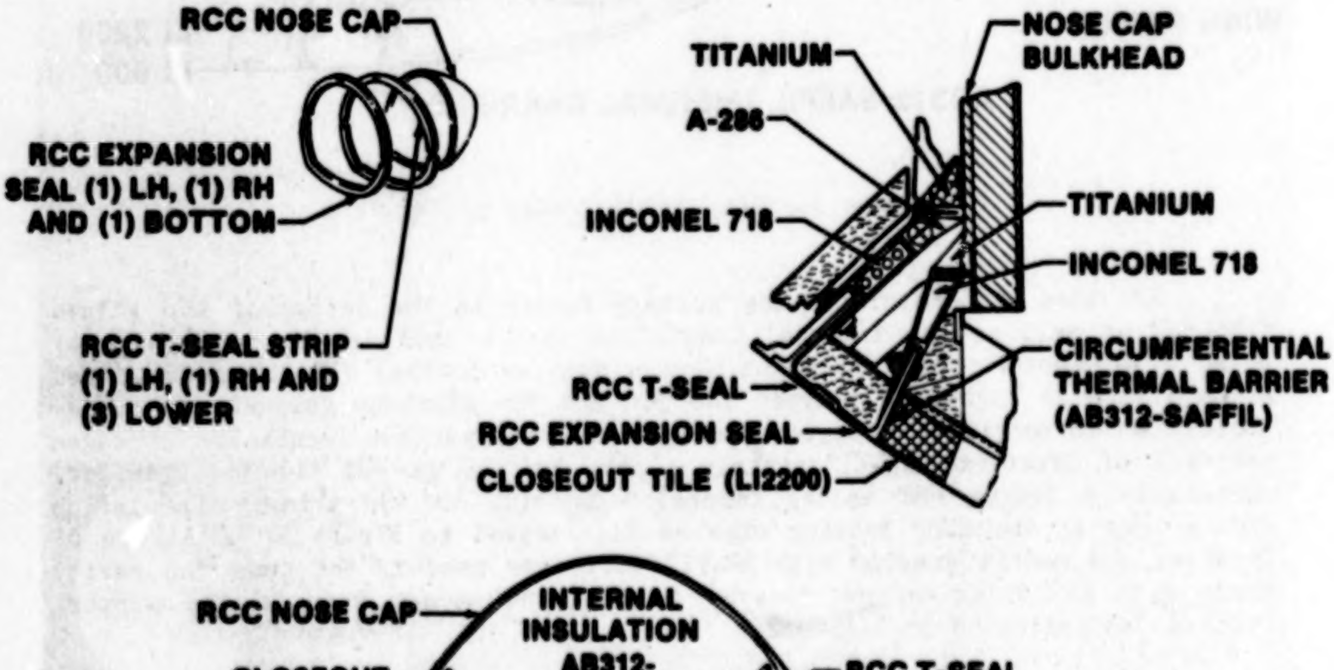
RCC NOSE CAP
RCC EXPANSION SEAL (1) LH, (1) RH AND (1) BOTTOM
RCC T-SEAL STRIP (1) LH, (1) RH AND (3) LOWER
TITANIUM
A-286
INCONEL 718
NOSE CAP BULKHEAD
TITANIUM
INCONEL 718
CIRCUMFERENTIAL THERMAL BARRIER (AB312-SAFFIL)
RCC T-SEAL
RCC EXPANSION SEAL
CLOSEOUT TILE (LI2200)
RCC NOSE CAP
INTERNAL INSULATION AB312-DYNAFLEX
CLOSEOUT TILE (LI2200)
RCC T-SEAL
RCC EXPANSION SEAL
LI2200

Figure 2.- Nose cap system.

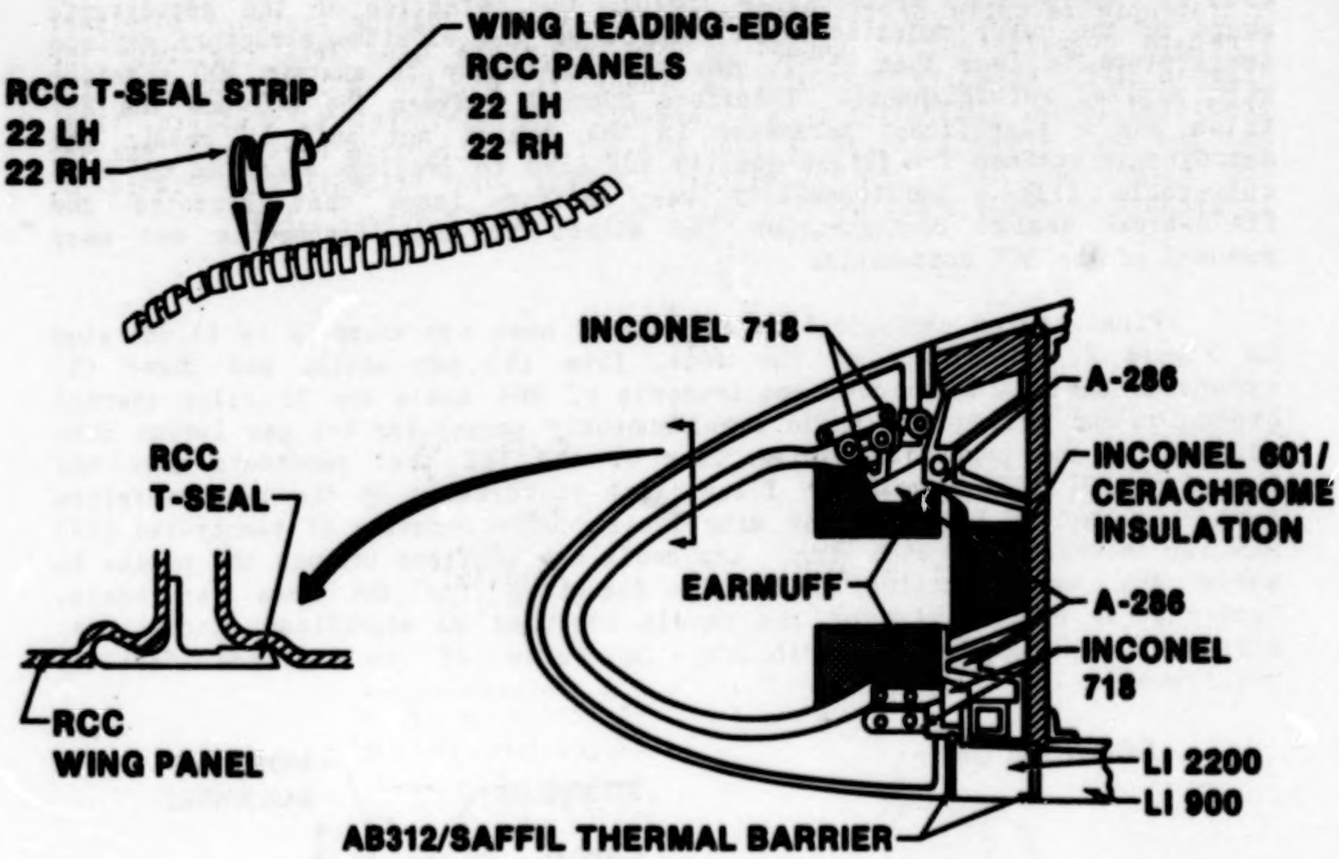
WING LEADING-EDGE
RCC PANELS
22 LH
22 RH
RCC T-SEAL STRIP
22 LH
22 RH
INCONEL 718
A-286
INCONEL 601/
CERACHROME
INSULATION
RCC
T-SEAL
EARMUFF
A-286
INCONEL
718
RCC
WING PANEL
LI 2200
LI 900
AB312/SAFFIL THERMAL BARRIER

Figure 3.- Wing leading-edge system.

Elevated temperature is the primary factor in the design of the attach fittings as well as the internal insulation system used in the protection of those attachments. Heat resistant metals such as Inconel 718 and A-286 steel are utilized to interface between the RCC and the aluminum support structure. Protection is provided these metal components with various insulation packages composed of Dynaflex, AB-312 ceramic cloth, saffil, or RSI tiles. Dynaflex, contained in formed and welded Inconel 601 foil, is the primary insulation system used in the wing leading edge as illustrated in Figure 3. Blankets of Dynaflex and saffil wrapped with AB-312 cloth are used in the nose cap cavity along with RSI tiles on the forward face of the access door in the support bulkhead as indicated in Figure 2.

Thermophysical properties of the RCC material and the hollow shell design promote internal cross radiation from the hot stagnation region to the inherently cooler regions. This characteristic reduces the stagnation region temperatures and the critical lower lug temperatures and minimizes the thermal gradients in the shell. Paradoxically, the insulation used in the cavity to preclude exceeding the maximum temperature limits established for the metal components also retards the cooling rate of the lugs, contributing to the undesirable oxidation rate.

Oxidation rate is the single most important variable parameter in the determination of mission life of RCC parts. Oxidation of the carbon substrate occurs as a result of oxygen penetrating the protective coating through microscopic porosity or fissures inherent in the coating system. Resultant strength degradation [1,2] caused by the substrate mass loss restricts the mission life capacity through the inability of the RCC to sustain the predicted loads. Oxidation rate is a function of temperature, pressure, time, and the type of environment, either radiant or convective heating.[3] Radiant and convective mass loss correlation curves are presented in Figure 4, applicable to the flanges and the outer shell regions respectively.

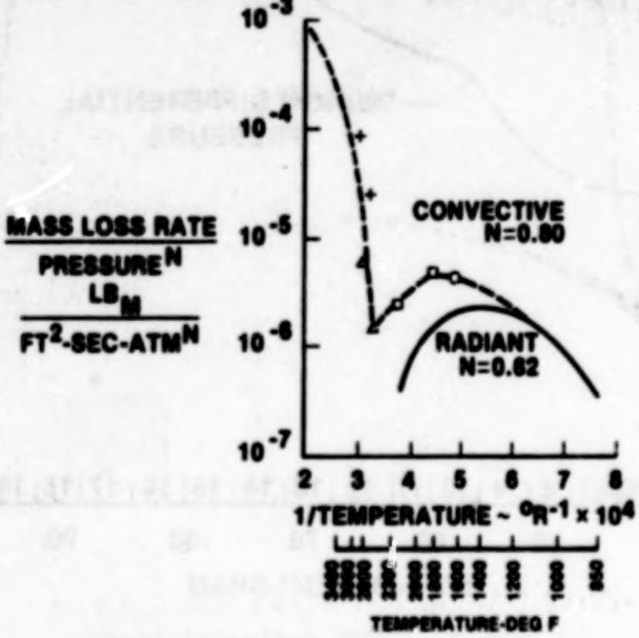

Figure 4.- RCC mass loss correlation.

Thermal analyses were performed on the nose cap and representative wing leading-edge panels to correctly design the temperature sensitive elements as well as to determine the temperature histories at selected locations. Comprehensive two- and three-dimensional thermal math models, developed for the design analysis, were verified in the development and qualification tests and used for flight certification.[4,5]

Structural analyses were performed on the nose cap and wing leading edge with the basic objective to determine the resultant stresses, deflections, and margins of safety for the applied environments. The complex nature of the design coupled with the deterioration of the mechanical properties of RCC with each repeated exposure to oxidation created unusual analytical problems. Detailed finite element structural models were constructed for the nose cap and representative wing leading-edge panels to insure adequate resolution of the issues. Verification of the analytical methodology was achieved in the qualification test program which led to flight certification.[6,7] Additional complexity was introduced with the inherent shape of the parts, the variable stiffness of the support structure, and the interaction of the adjacent parts. Critical stresses had to be determined for each part, dependent upon these parameters and sensitive to the distribution of the applied airloads. Typical spanwise variation in the airloads along the wing span can be observed in Figure 5.

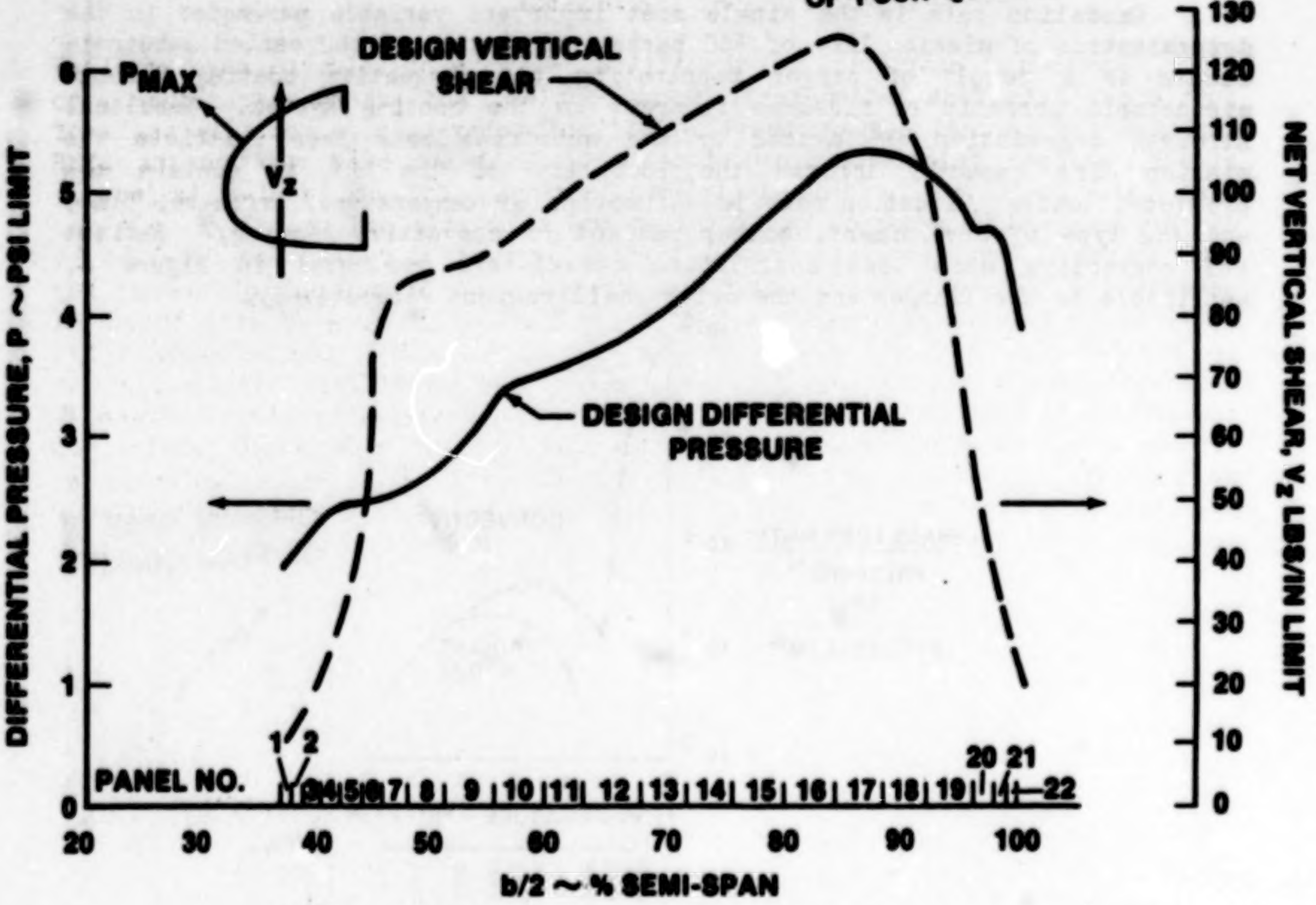

Figure 5.- LESS design airloads.

Thermoelastic stress analyses were also performed on the LESS components at several time cuts in the re-entry trajectory. Thermal-induced stresses in the wing leading edge are minimal with the attachment system providing unconstrained spanwise growth capability, and the thermal gradients are insignificant. However, the nose cap with relatively rigid constraints and high thermal gradients exhibited critical thermoelastic stresses during the initial flights. Coefficient of thermal expansion differences between the RCC and the metal fittings dictated slotted joint designs to eliminate induced stresses. Integrated thermal expansion and combined environment-induced deflections also had to be accurately predicted in order to determine the gap requirements between adjacent parts as well as to avoid RCC to tile interference at the interface joints.

Certification of the LESS for flight was accomplished by analyses verified with development and qualification tests conducted on full-scale hardware. Critical launch and entry conditions were simulated in these tests, cyclically exposing the parts to acoustic, thermal, and airload environments. Comparisons of the predicted versus measured response to the airloads [6,7] and thermal[4] stimuli resulted in approval of the certification process. Structural assessment of the flight performance must integrate the results of ground tests to substantiate any observation or conclusion from the flight data.

FLIGHT PERFORMANCE

Successful completion of the initial flights of Columbia have provided sufficient data from radiometers, thermocouples, and pressure transducers to appraise the thermal performance. STS flight parameters, especially angle of attack, allowed relatively lower total heat load and heat rate on the LESS than that predicted for the design trajectory. STS and design trajectory differences can be assessed by comparing the heat rate and heat load to a one-foot sphere. Peak heat rate varied from 80 percent of design for STS-1 to 96 percent for STS-4; whereas, heat load varied from 84 percent of design for STS-5 to 92 percent of design heat load for STS-2. Radiometer data presented in Figures 6 and 7 for the nose cap and wing leading edge, respectively, indicates good agreement between the predicted and measured temperatures for the RCC shell inner surface. Measured STS flight temperatures for the panel 9 attachment clevis fitting were lower than both the STS and design predictions as indicated in Figure 8. Evaluation of the STS flight data indicates no degradation in the thermal performance of the LESS components, particularly the insulation systems.

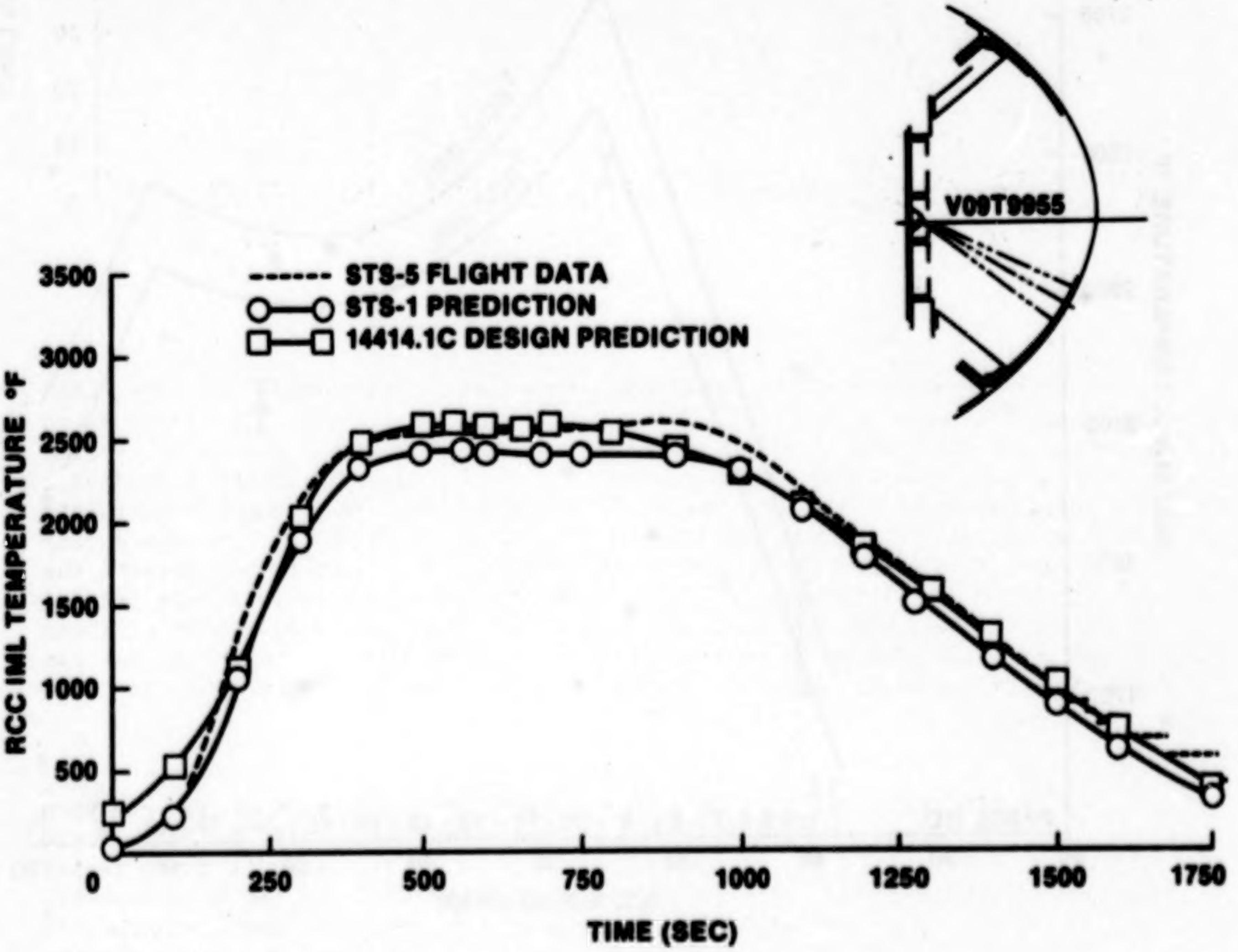

Figure 6.- Nose cap RCC inner moldline (IML) temperature.

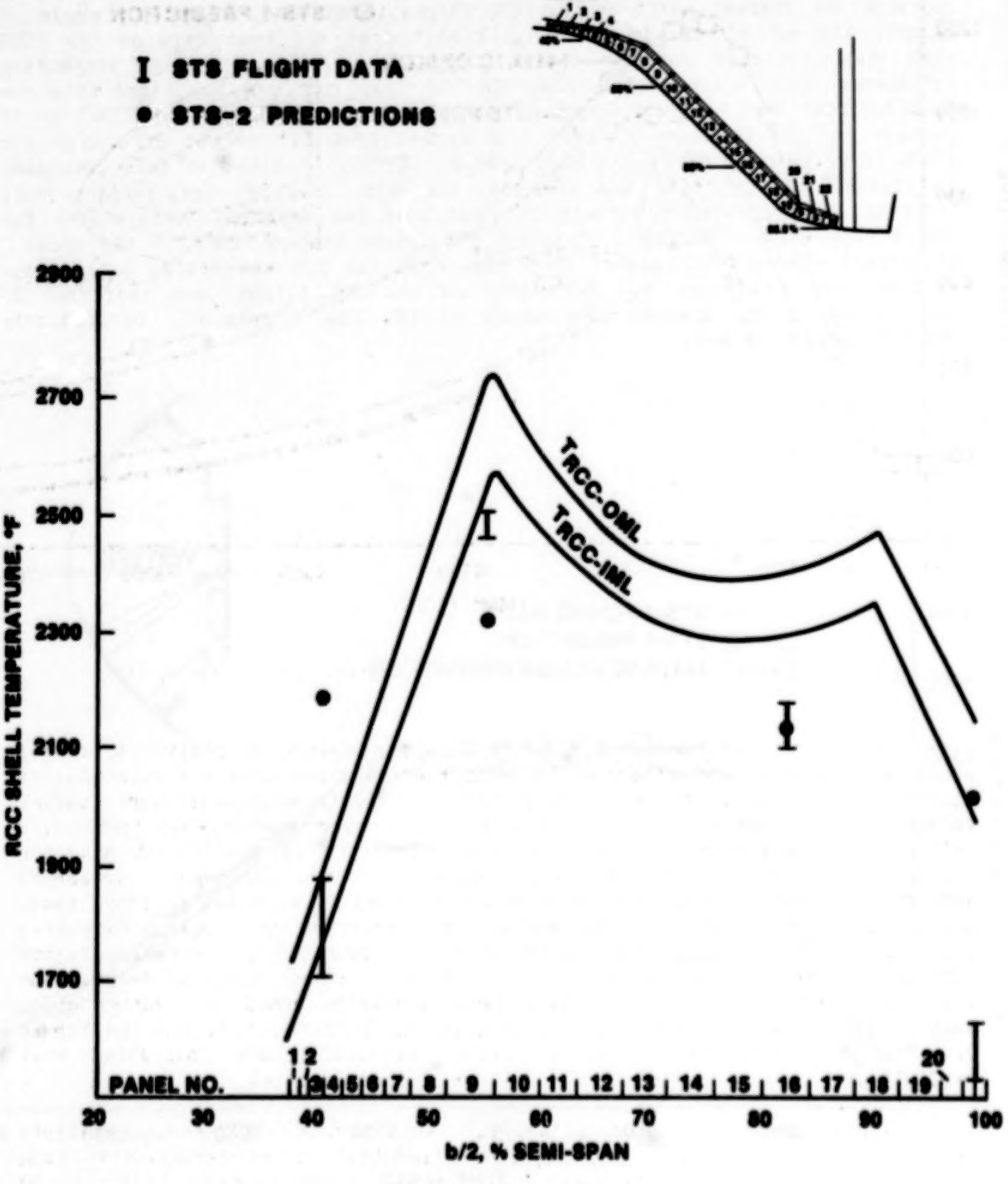

Figure 7.- Wing leading-edge inner moldline (IML) temperatures.

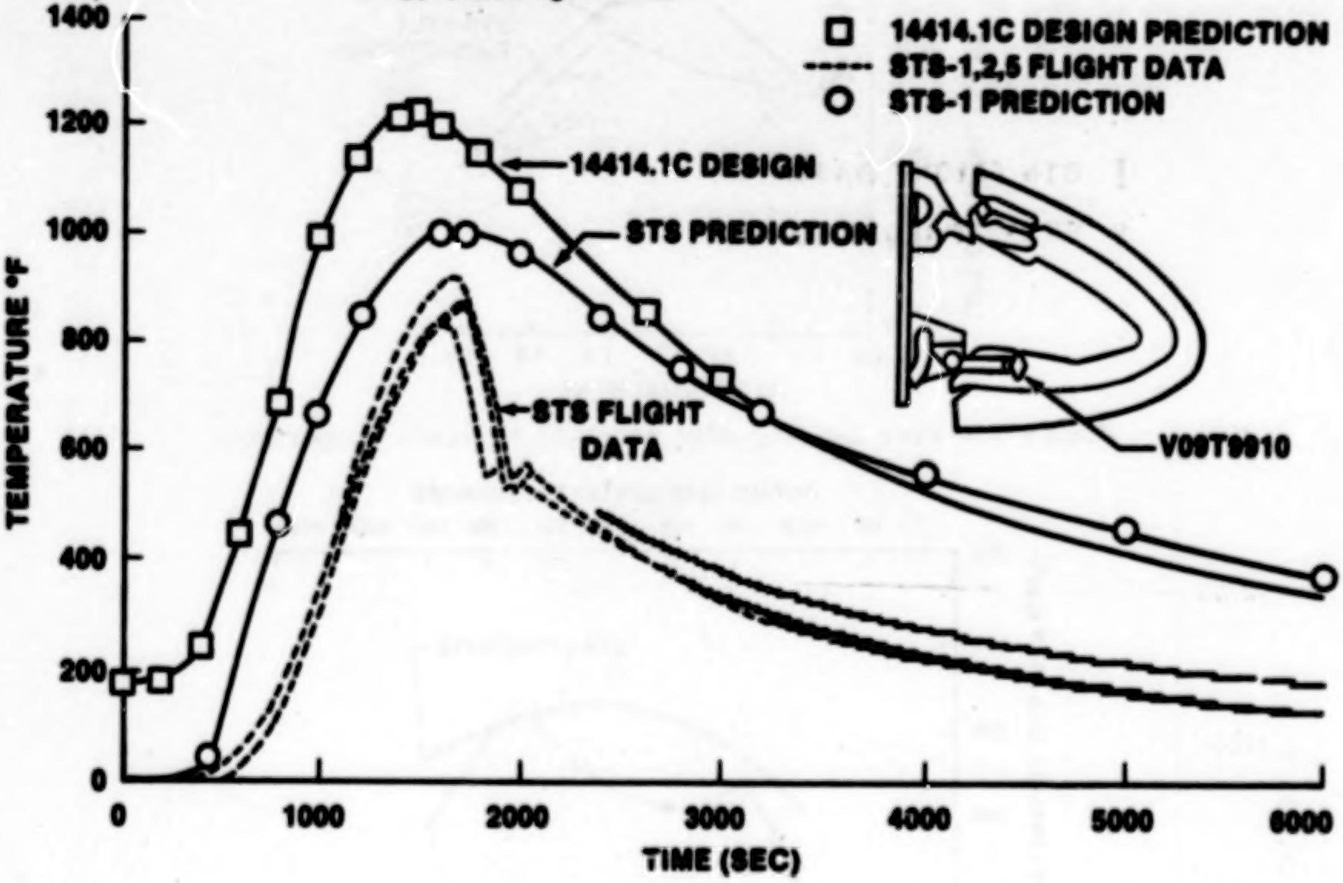

Figure 8.- Wing leading-edge panel-9 lower attach clevis temperature.

Structural performance evaluation requires a more subjective appraisal since the elevated temperature environment precludes the direct acquisition of flight airload data in the critical regions. Strain measurements were limited to special, instrumented attach fittings on the wing leading-edge panel 13, calibrated to determine the magnitude and direction of the flight airloads during ascent. Effective loads are combined external aerodynamic pressures and internal cavity pressures. Load vectors, parallel to the wing front spar, are developed by integrating the differential pressure over the surface area of a panel. Peak ascent loads occur in the maximum dynamic pressure regime coincident with transonic speeds between 1.0 and 1.5 Mach number. Ascent load vectors, developed from flight strain measurements on panel 13, average about eleven (11) percent higher than the anticipated loads as indicated in Figure 9. This is considered to be excellent correlation and indicative that realistic airloads were used in the LESS structural analyses.

Vibroacoustic environments that were used for the LESS design analysis and flight qualification procedures were determined to be conservative from the flight data. Wing leading-edge flight acoustic data present in Figure 10 is comparatively less than the design environment. Impact of this difference is considered negligible at this time but indicative that the critical margins of safety for the RCC lugs are conservative from the vibroacoustic effects perspective.

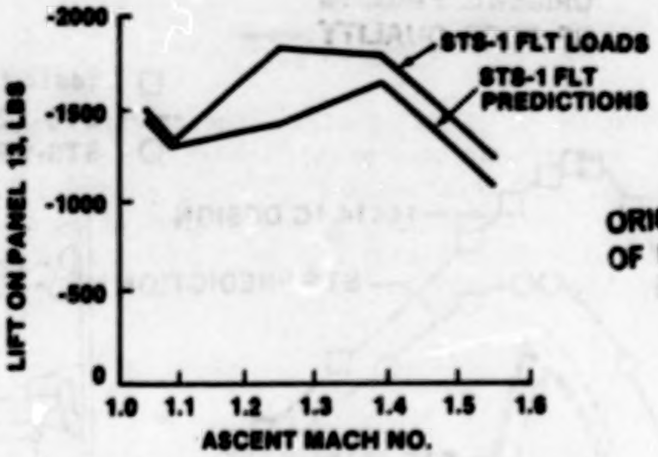

Figure 9.- Wing leading-edge panel-13 airloads comparison.

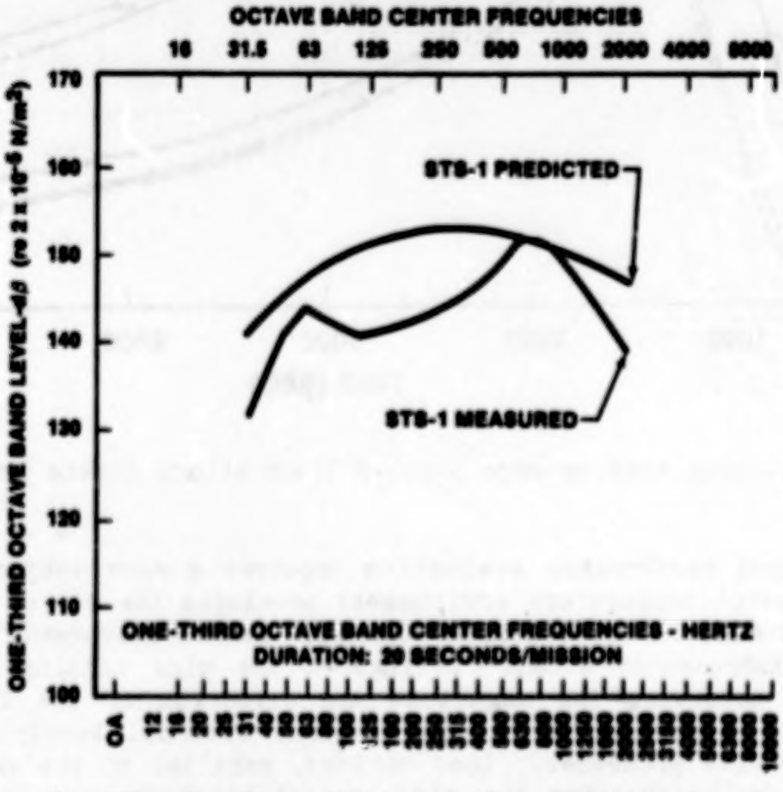

Figure 10.- Wing leading-edge acoustic environment comparison.

General flight performance characteristics can also be deduced from the flight data and the post-flight condition of the parts. Structurally, the leading edge has apparently achieved its purpose of maintaining the aerodynamic shape throughout the flight, inclusive of the elevated temperature regime during atmospheric re-entry. Elasticity of the RCC components can be deduced from the fact that the parts returned to their original shape and position after aerodynamic pressure and thermal-induced distortions. Noticeable markings on the side load restraint pins and on the RCC panel to RCC gap-seal mating surfaces confirm that the parts experience motions and displacement patterns compatible with the analytically predicted response. Although displacement magnitudes cannot be determined, visual inspections have revealed no anomalies and no conditions generating concern for the structural integrity of the leading-edge system.

LESSONS LEARNED

Combined results of LESS design studies and analytical iterations, development tests, qualification tests, and flight tests during the design, development, testing, and evaluation (DDT&E) phase of the Space Shuttle program have not only confirmed basic concept and design sufficiency but also revealed areas of design deficiencies. Modifications have in most cases been adopted to rectify those deficiencies.

Gap heating development tests on LESS interface geometric design concepts revealed a thermal anomaly at the RCC to RSI interface. Hot gas intrusion around the thermal barrier between the RCC and the RSI necessitated a redesign to incorporate a flow stopper. Evidence from STS-1 and STS-2 indicated the continuance of hot gas emanating from the lower interface region and flowing through the LESS cavity as illustrated in Figure 11. Modification of the flow stopper to eliminate this flow-through was incorporated and the effectiveness verified in the subsequent flights as indicated in Figure 12. Heating phenomena at the lower centerline region of the nose cap during STS-5 created a condition in the interface tiles unique to this flight. Hot gas penetration into the gap between two interface tiles caused slumping/melting of the tiles, thermal damage to the gap fillers, filler bars, and flow stoppers, and local melting of the aluminum carrier plate as depicted in Figure 13. Penetration of the hot gas damage into the insulation blankets was minimal, and no evidence of overheating of the nose cap Inconel attachments was found. Gap heating damage in this region during previous flights had been limited to tile slumping and filler bar overheating; therefore, this is assumed to be a problem associated with flow stopper and gap filler mission life.

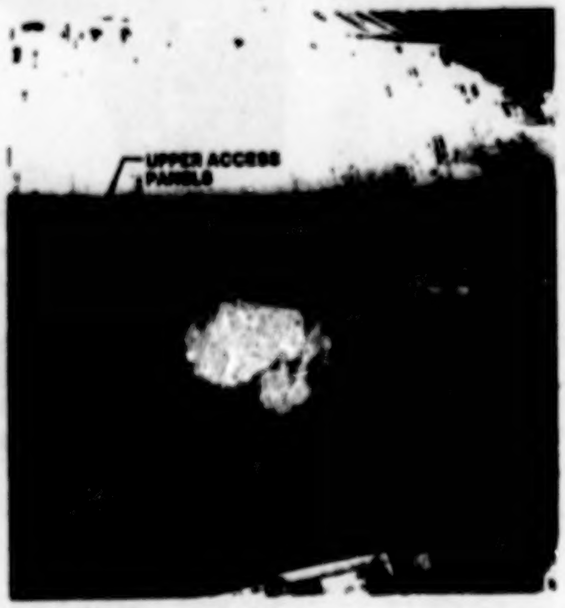

Figure 11.- Wing leading-edge hot gas flow.

ORIGINAL PAGE IS
OF POOR QUALITY

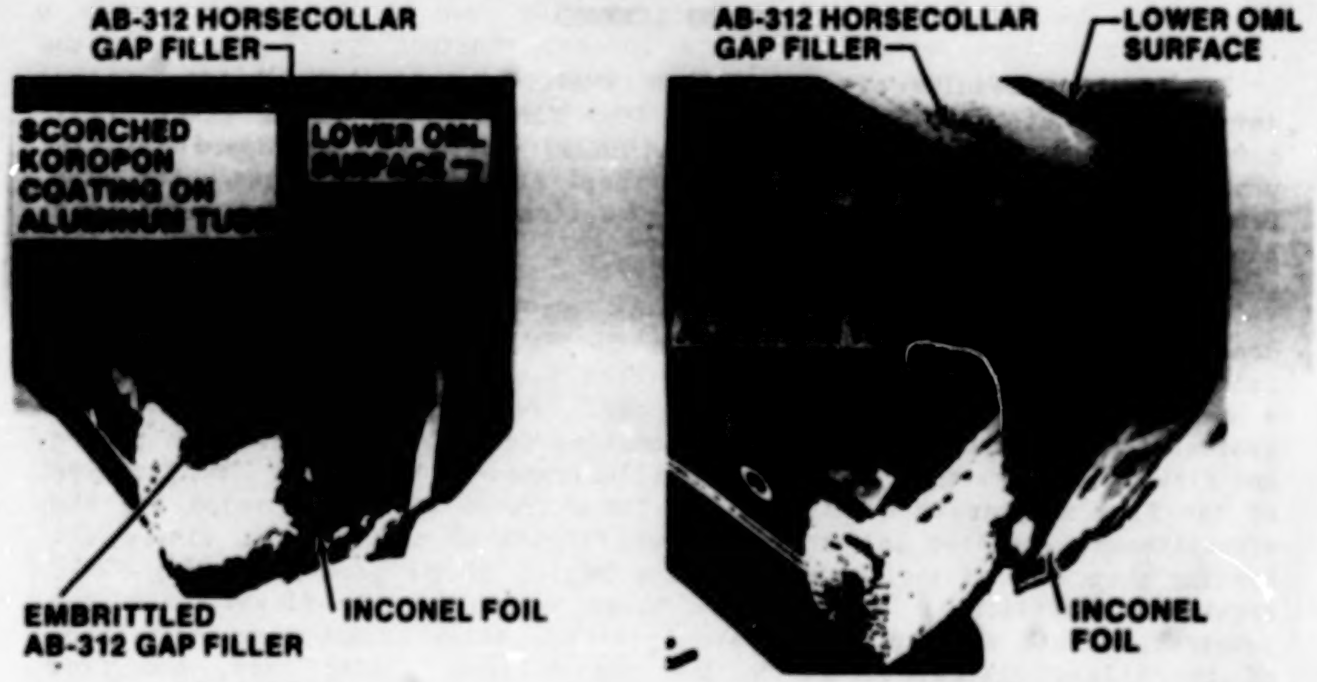
AB-312 HORSECOLLAR GAP FILLER
SCORCHED KOROPON COATING ON ALUMINUM TUBE
LOWER OML SURFACE
EMBRITTLED AB-312 GAP FILLER
INCONEL FOIL
AB-312 HORSECOLLAR GAP FILLER
LOWER OML SURFACE
INCONEL FOIL

POST STS-2

POST STS-3

Figure 12.- Wing leading-edge panel-10 heating effects comparison.

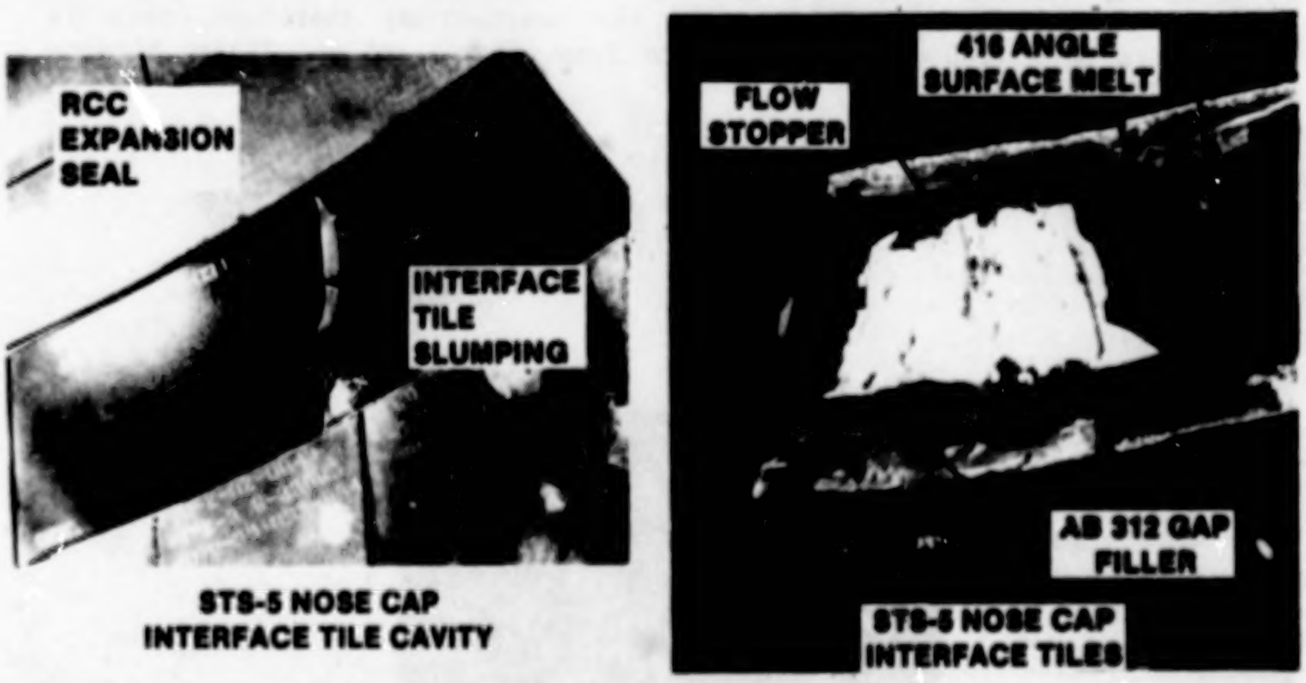
RCC EXPANSION SEAL
INTERFACE TILE SLUMPING
416 ANGLE SURFACE MELT
FLOW STOPPER
AB 312 GAP FILLER

STS-5 NOSE CAP INTERFACE TILE CAVITY

STS-5 NOSE CAP INTERFACE TILES

Figure 13.- Interface tile gap heating.

Cyclic exposure of the wing leading-edge internal insulation system to thermal and acoustic environments in component tests confirmed the reusability capability but also revealed a limited life of about thirty (30) missions. A comparison of the qualification test article after twenty (20) cycles to a typical Columbia insulation package after five (5) flights is presented in Figure 14. Both systems are capable of sustaining additional cycles.

Insulation blankets of AB-312 wrapped Dynaflex used in the nose cap have a higher temperature capacity than the Inconel sheathed Dynaflex used in the wing leading edge; however, it is more susceptible to installation handling damage. Exposure to temperatures in the range of 2300°F causes the AB-312 fabric to become friable. Damaged insulation as a result of handling in the nose cap qualification test article after five (5) cycles is illustrated in Figure 15 and compared to the Columbia insulation after four (4) flights. Inspections of the insulation systems on the Columbia after four (4) flights reveal no deterioration, and the flight data has revealed no thermal performance degradation. Additional life tests will be used in conjunction with continued, scheduled inspection of the flight insulation system to establish the actual life capacity.

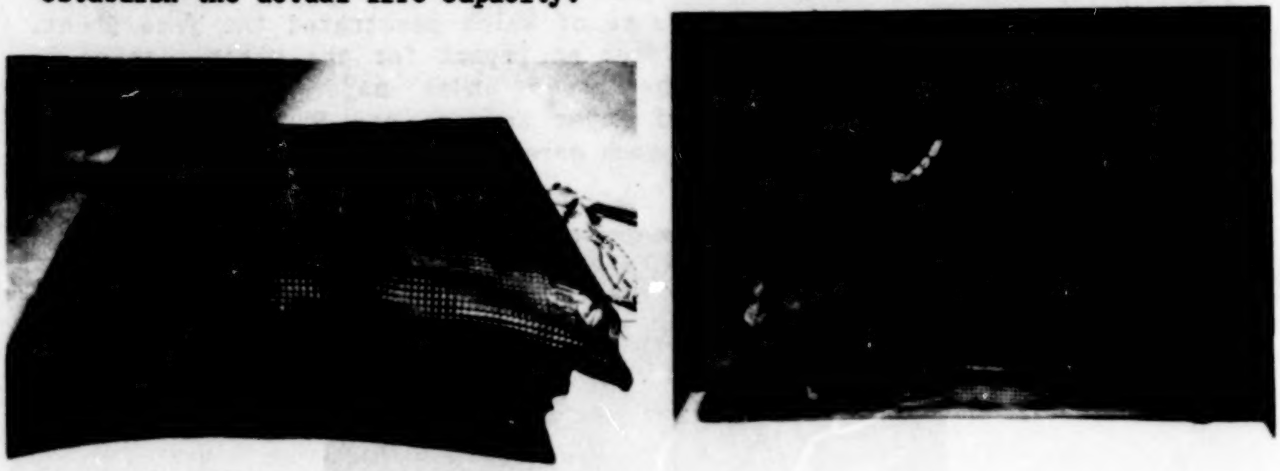

WING LEADING SPAR INSULATION
PHASE B THERMAL TEST
(20 OXIDIZING CYCLES)

STS-5 WING LEADING-EDGE
SPAR INSULATION

Figure 14.- Wing leading-edge insulation system thermal effects comparison.

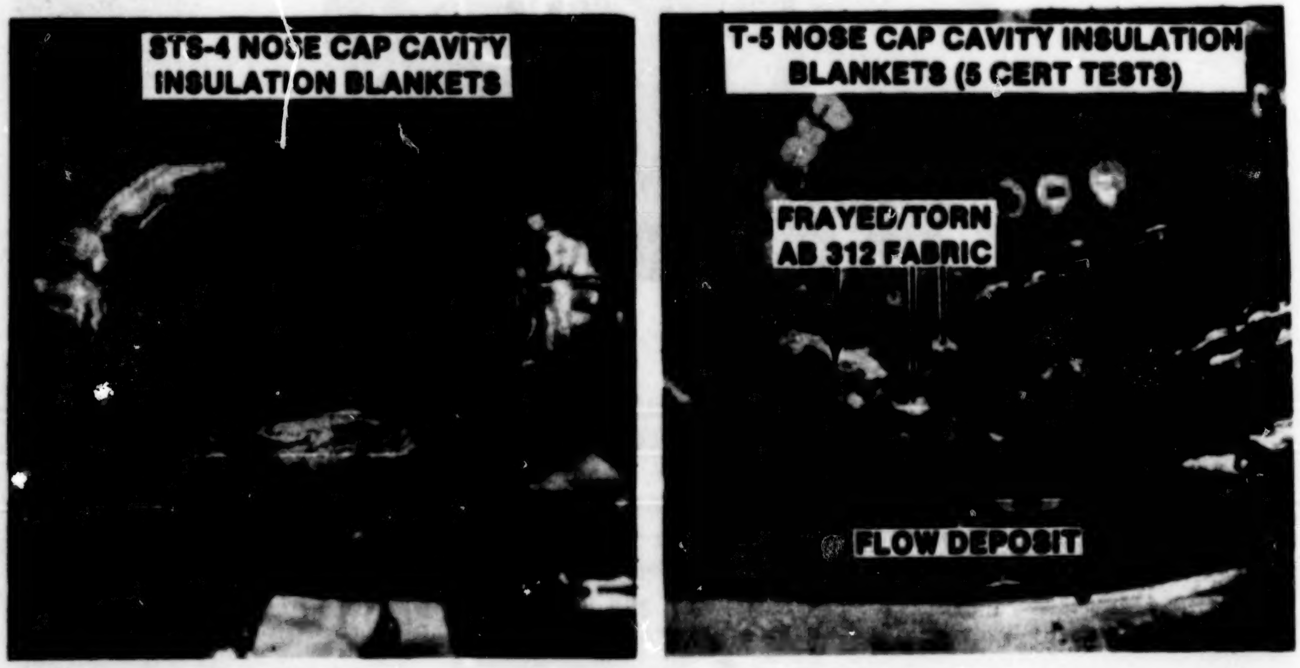
STS-4 NOSE CAP CAVITY
INSULATION BLANKETS
T-5 NOSE CAP CAVITY INSULATION
BLANKETS (5 CERT TESTS)
FRAYED/TORN
AB 312 FABRIC
FLOW DEPOSIT

Figure 15.- Nose cap insulation system thermal effects comparison.

Related to the insulation system is a phenomena occurring on the wing front spar where the Inconel sheathed Dynaflex insulation is attached directly to the aluminum honeycomb spar. Corrosion of the aluminum, appearing as blisters in the Super Koropon paint as illustrated in Figure 16, is assumed to be a result of galvanic activity caused by the contact of dissimilar metals with the source of moisture being the humid air flowing through the LESS vent system. Direct exposure to the salt atmosphere could also be a contributing factor to the corrosion problem. The OV-102 wing front spar is constructed of aluminum honeycomb with face sheet thicknesses ranging from 4 mils to 120 mils that is painted with 1 mil of Super Koropon for corrosion protection. The insulation is contained in 4-mil thick waffled Inconel foil. Corrosion, occurring in discrete areas, created pits in the aluminum 80 to 100 mils in diameter and 1 to 14 mils in depth, some of which penetrated the face sheet. Ramifications of the corrosion range from no impact for the minor pitting to potential structural damage for the areas under major attack. Viable solutions include additional coats of Super Koropon and RTV to the painted aluminum surface, thereby providing a much more tolerant protection system.

TYPICAL
WING SPAR
CORROSION

Figure 16.- Wing front spar corrosion.

Moment constraint fittings, illustrated and compared to the basic design in Figure 17, were retro-fitted to the LESS design on several wing leading-edge panels as a result of a substantial increase in the predicted airloads. Joint tolerances and the design concept required by the temperature environment caused some speculation on the effectiveness of these fittings in reducing the critical RCC stresses. Substantiated by qualification tests and the absence of problems with the flight performance, the moment constraint fitting concept has proven to be an effective design "fix."

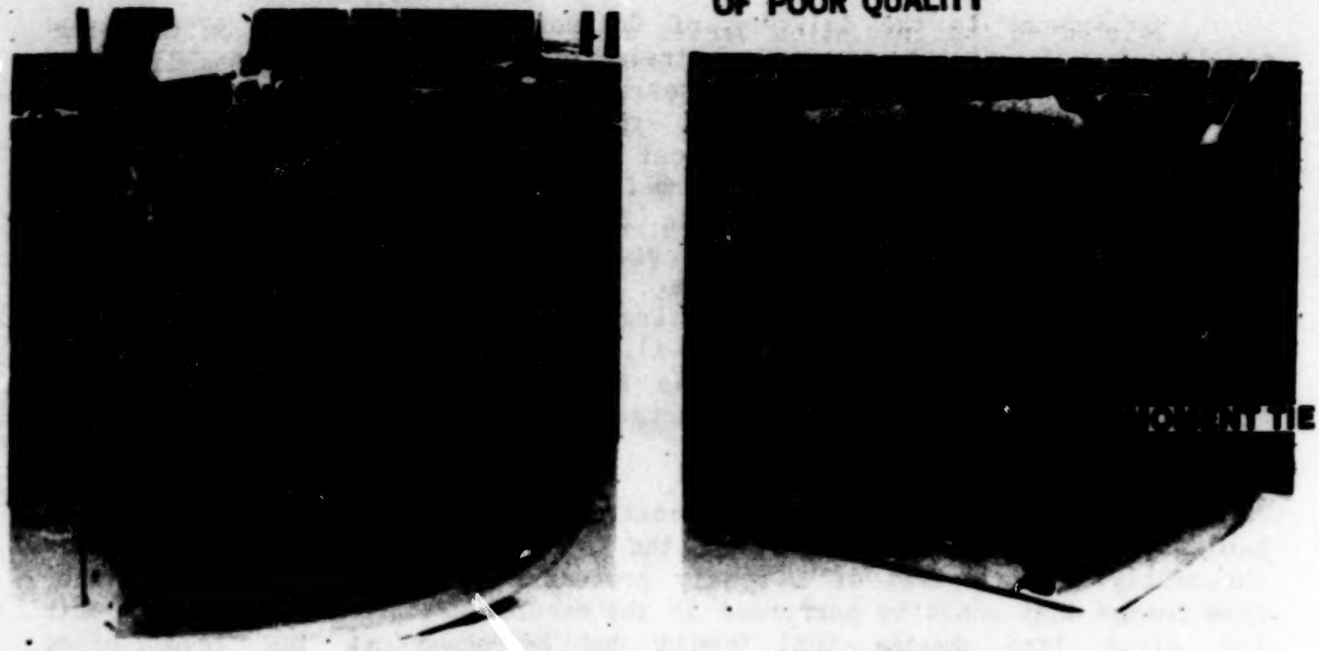

Figure 17.- Wing leading-edge panel attach hardware.

Wing leading-edge RCC panels are cantilevered off the front spar at four points by high-temperature, A-286 steel fittings. Figure 18 shows the general configuration. The initial material selection and sizing for these fittings were driven by expected temperatures (about 1000°F) and large airloads. In addition, producibility required a minimum gage of 100 mils for this very tough material. As the design environments matured and the analysis methods became more refined, peak temperatures dropped below 600°F. This allowed 6AL-4V titanium to be used in lieu of steel. At the same time, the load paths were optimized, resulting in one piece fittings. Producibility gains allowed the minimum gage to drop to 60 mils compared to the 100 mils required in the A-286 steel design. A weight reduction of about 300 pounds per shipset was realized with this change.

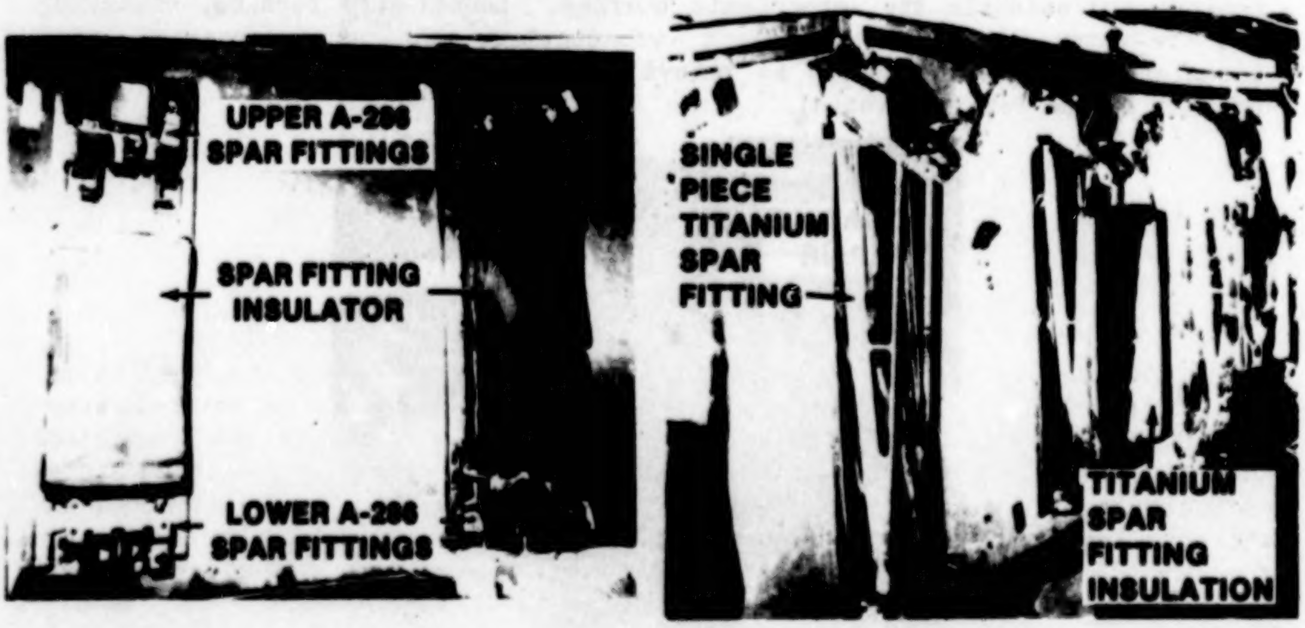
UPPER A-286 SPAR FITTINGS
SPAR FITTING INSULATOR
LOWER A-286 SPAR FITTINGS
SINGLE PIECE TITANIUM SPAR FITTING
TITANIUM SPAR FITTING INSULATION

Figure 18.- Wing leading-edge spar fittings.

Subsequent to the delivery of Columbia, element tests revealed the possibility of getting porous substrate in some areas of the production parts. High porosity in the substrate reduces the effectiveness of the basic Silicon Carbide (SiC) coating and the Tetraethyl Orthosilicate (TEOS) impregnation. Predicated on the local time at temperature history in the autoclave cure cycle, the high porosity is generally restricted to the external surface shell region. The consequence is an increase in the oxidation rate in the porous region and in some cases a reduction in the mission life of the affected parts. Reconciliation of this undesirable feature was achieved with a post-coating treatment of a sodium silicate and graphite fiber surface sealant (Type A). Potential mission life enhancement with the Type A surface sealant has been accomplished on all subsequent vehicles. Rework of the Columbia parts to add the Type A coating has been initiated after STS-5.

Susceptibility of the SiC coating to chipping, primarily ground handling damage on the edges of the RCC parts, necessitates a repair capability. Development of a repair procedure included a repair for major type damage that would be performed at the manufacturer's facility and a repair for minor type damage that could be performed at the launch site. Differentiation between major and minor damage is primarily determined by whether the black carbon substrate is exposed by the coating damage. Although the launch site repair would provide some protection from local oxidation for damage exposing the substrate, limitations have been placed on the procedure restricting it to one flight only. Several major coating repairs were made on the Columbia prior to STS-1, typically pictured in Figure 19. Additional launch site repairs were made subsequent to each of the first three missions. Flight exposure of these repairs has allowed several observations. Performance of the major repairs has been consistent with ground test results in that the repairs have remained intact with no appearance of shrinkage, craze cracking, or any other deleterious anomalies. Assuming congruency with test results, absence of flaws in the repair also suggests that the substrate is adequately protected from oxidation. Durability of the launch site repairs applied to minor damage areas also confirms the validity of this procedure to achieve and maintain the aerodynamic surface. Launch site repairs, utilizing the re-entry thermal environment to complete the cure process, will occasionally require touch-up to remove flaws that developed due to shrinkage or flow of the repair material.

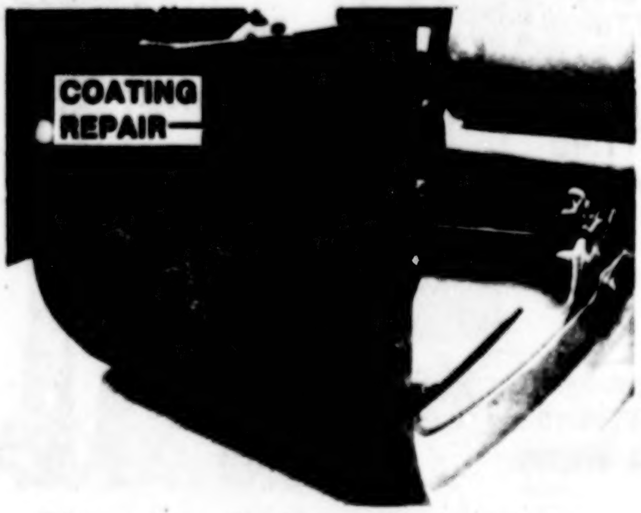

Figure 19.- Typical coating repair.

The RCC arrowhead, illustrated in Figure 20, was a redesign and retro-fit of the original RSI tile design that failed the qualification tests of the explosive separation of the external tank. Configured in two pieces to facilitate installation around the attach mechanism, the RCC arrowhead parts are independently attached to the carrier plate with fasteners countersunk into the outer RCC surface. Design alterations required a rework of the Columbia arrowhead to provide a 45° bias joint instead of the joggle overlap at the interface of the two RCC components. Removal of the flange necessitated a major coating repair which, due to the lack of flight experience of coating repairs, caused a one-flight restriction to be placed on this particular assembly. Performance of the RCC arrowhead during STS-1 was superb, not only surviving the punishing explosive separation but also providing its primary function, along with the internal insulation, of thermal protection of the metal structure. Contrary to pre-flight, pessimistic expectations, the extensive coating repair exhibited no shrinkage or obvious detrimental effects from the initial flight exposure. Approval was therefore granted for an additional mission. In fact, this arrowhead eventually flew three missions prior to being replaced and used as a "guinea pig" to subjectively evaluate the multi-mission capability of an extensive coating repair and the integrity of the substrate around the attach holes. Sections taken in several areas revealed that the substrate around the attach holes looked good, contrary to the condition of the ground test article subsequent to the simulated separation tests. Interface conditions between the substrate and the coating repair were not ideal, but the repair was in excellent condition. The presence of localized mass loss was minimal and could actually have been caused by shrinkage of the repair material rather than oxidation of the substrate.

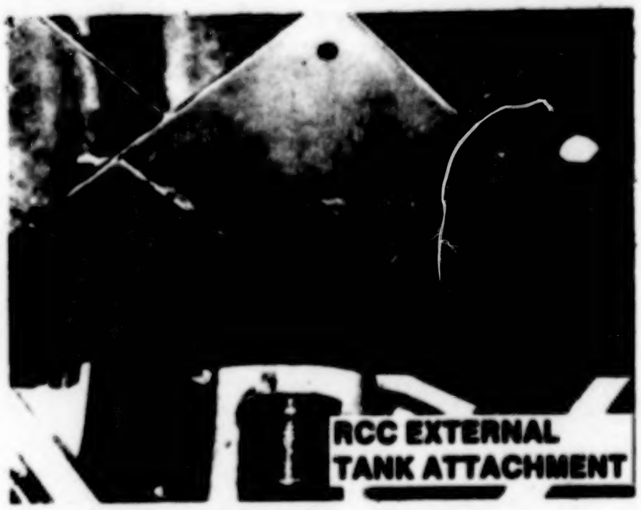

Figure 20.- RCC arrowhead.

CONCLUDING REMARKS

Successful completion of the four (4) development test flights and the initial commercial mission has demonstrated the adequacy of the Orbiter LESS design. Comparisons of measured and predicted temperatures and airloads have verified the analytical models used in the certification of the LESS for operational missions. Post-flight inspections not only confirmed the basic design concepts but also revealed areas of design deficiencies which have been modified to eliminate any potential operational problems. In summary, the LESS hardware performance has been outstanding with no degradation after the initial five (5) flights.

REFERENCES

1. Smith, T. W., Leading Edge Structural Subsystem Mechanical Design Allowables for Material with Improved Coating System, Report No. 221RP00614, Vought Corporation, July 1977.

2. Curry, D. M., Scott, H. C., and Webster, C. N., Material Characteristics of Space Shuttle Reinforced Carbon-Carbon, Proceedings of 24th National SAMPE Symposium, Volume 24, Book 2, 1979, pp. 1524-1539.

3. Curry, D. M., Johansen, K. J., and Stephens, E. W., Reinforced Carbon-Carbon Oxidation Behavior in Convective and Radiative Environments, NASA TP-1284, 1978.

4. Curry, D. M., Cunningham, J. A., and Frahm, J. R., Space Shuttle Orbiter - Leading Edge Structural Subsystem Thermal Performance, AIAA Paper No. 82-0004, 1982.

5. Curry, D. M., Latchem, J. W., and Whisenhunt, G. B., Space Shuttle Orbiter Leading Edge Structural Subsystem Development, AIAA Paper No. 83-0483, 1983.

6. Quirk, W. J., Engineering Analysis Report Nose Cap Systems Phase A (T-5) Airloads Test, Rockwell Report SOD 80-0440, Rockwell International, January 1981.

7. Quirk, W. J., Engineering Analysis Report Wing Leading Edge System (T-35) Phase A Airloads Test, Rockwell Report STS 81-0253, Rockwell International, January 1981.

N84
10162

UNCLAS

N84 10162 D/18

SPACE SHUTTLE WING LEADING EDGE HEATING ENVIRONMENT PREDICTION DERIVED FROM DEVELOPMENT FLIGHT DATA

John A. Cunningham
Joseph W. Haney, Jr.
Space Transportation and Systems Group
Rockwell International
Downey, California

SUMMARY

An analytical program is in progress at Rockwell International to revise wing leading edge heating predictions in order to improve correlation with STS-1 to -5 flight radiometer data. This paper discusses the methods that have been used to improve agreement between prediction and flight and summarizes the aerothermodynamic correlations which, when updated, will be used to analyze future orbiter missions.

INTRODUCTION

The first four flights of the orbiter Columbia (OV-102), termed STS-1 through STS-4, were dedicated to obtaining engineering flight data for system certification that would lead to operational verification of OV-102 and subsequent orbiters. Later in the program it was decided to record Development Flight Instrumentation (DFI) during STS-5, the first operational mission. Since the STS-5 mission fell within the OFT entry envelope, these data have also been included in this study. Prior to STS-1, extensive DFI were defined, designed, and installed on the vehicle. Some of the sensors, such as thermocouples, pressure taps, and associated electronic components, were off-the-shelf items. Others, because of sensitivity or accuracy requirements, flight environment exposure, etc., were designed and fabricated by Rockwell International.

It was necessary to design all DFI so that the function of the component or subsystem parameter measured was not degraded. Because of the Thermal Protection System (TPS) criticality and susceptibility to damage during liftoff acoustics and flight airloads, TPS sensors frequently required a unique engineering approach and, in some cases, ground testing to test sensor function and to insure that the component or subsystem integrity was not impaired.

Wing leading edge heating data were required during the Orbiter Flight Test (OFT) program to validate the technical prediction methods used prior to STS-1 and to provide flight data to modify these methods if necessary. Leading edge data were particularly important because of the uncertainties in scaling from wind tunnel to flight conditions. Standard aerothermodynamic equations fitted to include wind tunnel derived constants had been used to make the initial environment predictions prior to STS-1.

An engineering study of leading edge measurement methods was performed. It was concluded that use of thermocouples to measure the panel inner mold line (IML) temperature would be highly undesirable. It was recommended that a pyrometric device, later termed a radiometer, should be mounted on the leading edge spar and focused on the RCC panel inner mold line (IML) to measure IML temperature.

SYMBOLS

α	angle of attack
γ	specifc heat ratio
Δ	leading edge sweep, geometric
Λ_{EFF}	effective leading edge sweep
q_{LE}	heat rate of leading edge stagnation line
$q_{1'R}$	heat rate to a one foot radius sphere
R	leading edge radius
R_{EFF}	effective leading edge radius
R_{ACT}	actual leading edge radius
C_P	local pressure coefficient
C_{PS}	stagnation pressure coefficient
V_∞	freestream velocity
f	heat flux scale factor
q'	assumed surface heat flux
q_{REF}	preflight surface heat flux

This paper compares typical data obtained during the first five flights, which included the OFT Program STS-1 to -4, to preflight predictions. Using radiometer data, a method was developed to adjust the heat flux levels and leading edge heating distribution to improve agreement between the predictions and radiometer flight data. This was accomplished by performing parametric thermal analyses at RCC panels 9 and 16 thereby establishing the required scaling necessary to insure agreement. The effect of scaling on internal insulation and leading edge spar predicted temperatures was compared to flight data at panel 9 and an investigation performed using other panel 9 DFI to explain what at first appeared to be differences between temperatures predicted using these RCC heating corrections and flight temperatures.

SYSTEM DESCRIPTION

The orbiter wing leading edge is a subsystem of the Thermal Protection System that has been designed to withstand entry heating for as many as 100 Shuttle missions. The leading edge consists of 44 reinforced carbon-carbon (RCC) wing panels, 22 panels per wing (fig. 1). Left-hand and right-hand wing panels are mirror images; however the molded, high-temperature processes used during fabrication require individual panel designs and fabrication tooling.

An RCC T-seal that serves as an aerodynamic transition between adjacent panels is mechanically assembled to the outboard surface of each panel. The T-seal functions primarily as an expansion joint which is designed and fitted to inboard and outboard mating panels. The T-seal prevents boundary layer plasma flow from the windward, high pressure surface into the reduced-pressure internal cavity during entry. Figure 2 is an exploded view of the panel showing the panel assembly of a typical panel/T-seal set and the attachment arrangement for OV-102.

Nickel alloy fittings fasten each panel at two inboard and two outboard locations called field breaks by means of brackets mounted from the wing box forward spar. This arrangement allows easy assembly of the panel to the forward spar and permits removal of panels either singly or in groups. The fittings are shimmed to allow adjustment of the panel, thereby insuring proper alignment and fitup. Cross sections through the panel attachment plane and mid-panel shown on figure 3 provide the attachment arrangement and the other major subsystem assemblies, the spar insulation, and upper and lower access panels.

A spar insulation blanket protects the aluminum wing box structure from the intense radiant heating environment of the RCC cavity during entry (T_{max} = 2600°F). Access panels, as the name implies, provide access to the leading edge cavity to perform inspections with the wing panel on the vehicle and also permit access to the field break bolts for panel removal.

LEADING EDGE INSTRUMENTATION

Early in the Shuttle program, a study was performed to determine possible ways of measuring the entry heat rate to the RCC. One method that would use conventional calorimeters was ruled out because of the extreme thermal environment. A second method considered provided for bonding high-temperature thermocouples (T/C) to the RCC inner mold line. After a critical evaluation of a T/C application, use of thermocuples was discarded for the following reasons.

- The influence of the T/C on RCC panel structural integrity would be very difficult to assess.
- A high-temperature T/C installation required ceramic bonding that would be highly susceptible to failure during the liftoff acoustic environment.

- Thermal ground test experience showed that the T/C junction would rapidly degrade. This degradation occurs at flight temperature levels as a result of T/C junction deterioration in the presence of silicon carbide, the RCC panel coating material.

The only acceptable alternate proved to be a noncontact temperature-measuring device that operates similar to a pyrometer. This device, which was termed a radiometer, could be calibrated to continuously measure RCC panel IML temperatures during the entry.

The radiometer is a thermoelectric device that functions in conjunction with a lens system that collimates incident thermal energy to a thermopile sensor. The sensor millivolt output is calibrated as a known function of source temperature and emittance and, in operation, provides a continuous readout of RCC temperature. The sensor/lens configuration was mounted in a thick-walled copper shroud that had been designed to maintain the radiometer temperature at acceptable levels. Figure 4 shows the assembled radiometer.

Five leading edge radiometers were installed in the OV-102 L/H leading edge to measure RCC temperature in two ranges: 302°F to 2570°F and 410°F to 3000°F. These two ranges were selected by considering the predicted flight temperatures and the desire to achieve maximum accuracy within each range.

The leading edge radiometer installation had to be maintained in a thermal environment that would not exceed its operating temperature range of -250°F to 600°F. This was accomplished by imbedding each device in a 22 PCF (LI 2200) RSI tile which, in turn, was recessed in the Inconel-Dynaflex spar insulation panel. The OV-102 type installation at panel 16 L/H is shown in figure 5.

Five radiometers were installed in four OV-102 L/H wing panels as shown on figure 6. Four of these were selected to measure maximum heating region temperatures at panels 4, 9, 16 and 22. The fifth measured panel 9 leeward surface data so that data at two locations would be available to infer heat flux distribution at panel 9. Table I summarizes the radiometer location plan, identifies sensor number (V09T9909A, etc.), and denotes sensor function.

PREFLIGHT ANALYSIS METHODS

Aerothermodynamic Methods

The wing leading edge of the Shuttle orbiter was aerothermodynamically modeled by first simplifying the design into its basic shape, a swept cylinder. Using this approach the leading edge consisted of a 45-degree swept cylinder with regions of higher sweep at the glove fillet and at the wing tip.

Using this simplified geometric approach allowed the use of the swept cylinder equation:

$$q_{LE}/q_{1'R} = \frac{1}{\sqrt{2}} \cdot \sqrt{\frac{1}{\bar{R}}} \cos^{1.2} \Lambda_{EFF}$$

where

$$\Lambda_{EFF} = \sin^{-1}(\cos\alpha \cdot \sin\Lambda)$$

In reality, the treatment of the leading edge as a cylinder was only applicable at the forwardmost region, since the cylinder region was blended into airfoil sections forming the wing. To account for this change to the leading edge shock shape, wind tunnel test data were correlated to determine the relationship between the actual geometric radius and the effective radius that influences heating. This analysis resulted in the following relationship:

$$\Lambda_R = R_{EFF} = \left(\frac{R_{EFF}}{R_{ACT}}\right) \cdot R_{ACT}$$

where

$$\frac{R_{EFF}}{R_{ACT}} = \mathrm{EXP}\left[f(\alpha) - \cos^{1.3}\Lambda\right]$$

and where

$$f(\alpha) = .18513 - .0240167\alpha + .00280425\alpha^2 - .000024\alpha^3$$

In computing pressure, a simplified approach was again taken to determine the pressure along the stagnation line of the leading edge, so that

$$C_p/C_{PS_{max}} = \cos^2 \Lambda_{EFF}$$

These two approaches were taken to define the environments to the stagnation line of the leading edge away from regions of disturbance (bow shock impingement). This approach was validated through wind tunnel test data.

To transfer from the stagnation line on the RCC to the closeout HRSI tiles on the wing upper and lower surface, a modified Beckwith and Cohen distribution (ref. 1) was utilized to allow for a smooth variation between leading edge and wing.

The prior discussion pertains only to the regions of the wing leading edge outside of the bow shock-leading edge shock interaction (i.e., greater than 55 percent semispan).

Analysis of schlieren data, oil flow patterns, and heat transfer data from wind tunnel tests indicated that the bow and leading edge shock impinged with a resulting third shock and vortex/jet impinging on the wing. The shock pattern was similar to the type V pattern of Edney (ref. 2). The main effects of this disturbance were increased heating at 55 percent semispan on the leading edge, earlier transition on the outboard portions of the wing lower surface, and vortex scrubbing on the outboard wing upper surface.

By using heat transfer data obtained from thin film gage wind tunnel tests and the previously mentioned swept cylinder approach, the effects of shock impingement during wind tunnel conditions were determined.

The importance of scaling the effects of shock impingement from wind tunnel to flight conditions was indicated by the work of Edney and Keyes and Hains (ref. 2 and 3) relative to γ. These works showed that the theoretical calculation of the inviscid shock interaction flow field in connection with empirically derived correlations of the viscous interaction phenomenon caused the interaction to be more severe as the specific heat ratio decreased. Additional analysis by Bertin et al. (ref. 4 and 5) related the pressure changes across the "double-shock" system to shock pattern changes and thereby heat transfer with freestream velocity. These analyses were used to develop a scaling correlation from wind tunnel measured data to anticipated flight conditions.

In addition to scaling the magnitude of the shock impingement heating, the location of the shock interaction as it traveled along the leading edge was correlated with γ and V_∞ and allowed to vary throughout reentry.

The combined effects of scaling the wind tunnel data to flight using the double-shock and traveling-shock procedures resulted in maintaining the maximum level of heating as indicated by direct scaling of the wind tunnel data but moved the peak heating location inboard of the wind tunnel impingement location.

Thermal Analysis Methods

The leading edge radiometers measured RCC IML temperatures directly, and these temperatures could be rapidly compared to OFT preflight IML temperature predictions. However, the primary purpose of the radiometers was to provide temperature data that would be used to calculate OML heat rate histories and heating distributions experienced by the RCC surface during entry. The conversion of IML temperature data to OML heat flux predictions required a detailed thermal analysis of the radiation enclosure formed by the leading edge cavity that consists of the panel IML and the spar insulation surface.

Two dimensional thermal math models (TMM) were developed to convert radiometer temperatures to surface heating. The TMM for panel 16 is shown on figure 7. Except for panel geometry, a second model developed for panel 9 is thermally identical to the panel 16 model. As flight data became available, these models were used to perform analyses using data from the panel 9 radiometers V09T9926A and V09T9927A and the panel 16 radiometer V09T9934A (see table I).

The panel 9 and 16 locations were selected for flight data analyses since panel 9 is in the peak entry heating zone and panel 16 is in the maximum entry airload zone. These two locations are the most critical of the leading edge subsystem. The panel 4 glove and panel 22 wing tip radiometer data are in much less severe heating environments; however, radiometer data at these locations were useful to compare directly to predictions and provided the means to establish temperature/heating trends at these locations. If flight data warranted study at the glove and wing tip environment in greater detail, analyses similar to the panel 9 and 16 data analyses could be performed to establish heat rates at these locations. After examining entry flight data, to conserve time, it was decided to use approximate methods of calculating heat flux at this time since, as will be shown in the next section, the data at these two wing zones were indeed thermally less critical.

OFT FLIGHT DATA

Entry Trajectory Definition

The development flight test program consisted of four orbital missions, STS-1 through STS-4, with launch inclinations varying from 28.5 degrees to 40.5 degrees. All four entry trajectories were quite similar, with the majority of each entry having the orbiter attitude at an angle of attack of 40 degrees to the velocity vector. STS-3 and STS-4 differed slightly from the first two flights in that the flying time was approximately 100 seconds shorter for each flight. As previously noted, DFI were also recorded during the STS-5 first operational mission, and these data have also been included in this study.

Flight Data Overview

Unfortunately, because of a malfunction of the orbiter flight recorder during STS-1 and STS-4, only telemetered down-link data were recorded. Since down-link data can only be transmitted after the blackout period (approximately 950 seconds) while the peak heating plateau extends from 350 to 800 seconds, peak heating data were not available for these flights. Fortunately, however, this problem was avoided during STS-2, -3 and -5 so that a full complement of DFI including leading edge radiometer data was obtained during these flights.

Maximum heating radiometer data from STS-1 and STS-2 are compared to the preflight prediction for panel 9 (V09T9926A), 55 percent semispan, on figure 8 and for panel 16 (V09T9934A), 80 percent semispan, on figure 9. The predicted temperature is seen to be several hundred degrees lower than flight data at panel 9 while data and prediction are in excellent agreement at panel 16. From these comparisons, it could be concluded that predictions using the swept cylinder approach with modifications based on wind tunnel data, such as the panel 16 analysis, were generally validated by flight data. However, at panel 9, which is in the 45 percent to 55 percent semispan bow shock interaction region, the predictions are low. Inspection of the temperature distribution provided by the panel 9 leeward radiometer (V09T9927A) plotted on figure 10 further substantiates this trend.

Panel 4 (40 percent semispan) and panel 22 (98.6 percent semispan) maximum heating radiometer data were compared to prediction by first calculating the surface heat rates at these locations. This comparison was completed for the remainder of the wing by performing similar calculations at panel 9 and panel 16. Maximum heating was then plotted as a function of percent semispan on figure 11. Both the panels 4 and 22 heat rates in the glove and wing tip are substantially overpredicted, as had been expected since the swept cylinder approach is known to be conservative in regions of high sweep.

TECHNICAL DISCUSSION

The five radiometers in the leading edge provided the temperature data that were required to establish leading edge heating. To facilitate analyses, the leading edge was partitioned into three heating zones: 45 degrees swept wing, bow shock impingement or double shock zone, and highly swept wing, which consisted of the wing glove and wing tip. The bow shock impingement zone, panel 9, was of particular interest since it was in the maximum heating zone.

Two of the five radiometers were installed at panel 9. The first radiometer (V09T9926A) monitored peak heating temperature and the second (V09T9927A) was focused on the leeward wing surface. It had been planned to use the data from these two instruments in combination to determine both heat flux level and heat flux distribution for the panel. Other radiometer locations were the highly swept wing glove panel 4 (V09T9909A), the wing tip panel 22 (V09T9940A), and the 45 degree swept wing outboard of the double shock zone at panel 16 (V09T9934A).

The panel 9 peak heating region and panel 16 maximum ascent/entry airload location were selected for study because they are critical to the thermal and structural evaluation of the leading edge subsystem. It was for this reason that math models had been developed to analyze these locations.

Revision of wing heating methods would be as accomplished in two steps.

1. Thermal math models would be used to perform parametric analyses to establish heating levels and heat flux distributions and to improve agreement between RCC predictions and flight data.

2. The amended heating would then be used as the basis to revise aerothermo correlations used to predict leading edge heating rates. These revised correlations would then be employed to perform aerothermo analyses for ETR missions and might also be used to estimate heating for other missions such as WTR missions.

Other DFI that provided spar insulation surface temperature, spar temperature, and attachment temperatures were also used to validate the heating update.

Double Shock Region Analyses

The peak windward heating and leeward radiometer data for panel 9 were compared to predictions on figure 10. This comparison indicated that preflight STS-1 heating methods used to predict RCC temperatures provided the proper heating trend; however, they underpredicted the flight data by approximately 200°F. As a first attempt at correlation, parametric analyses were performed in which heating values were parametrically increased by a multiplier. The multiplying factor f was defined as

$$f = \frac{q'}{q_{REF}}$$

where

$$q = q(\theta, Tw, S)$$

and

θ = Time from entry interface, seconds

Tw = Surface temperature, °F

S = Surface location, inch

RCC temperature was then plotted as a function of the multiplier (f) to compare with flight data.

These curves for both peak heating (V09T9926A) and leeward (V09T9927A) radiometers are plotted on figures 12 and 13. Both plots were found to be linear and indicate peak temperatures from STS-2, -3, and -5 radiometer data can be correlated with a scale factor of 1.32 to 1.37 for both maximum heating and leeward radiometers. A factor of 1.34 was selected to best represent the flight data range for both radiometers.

At this time, another panel 9 shell analysis was performed using STS-1 preflight heating with a multiplier of 1.34. The results of this analysis are compared to flight peak temperature data in table II and on figures 14 and 15.

Table II summarizes RCC panel peak temperature predictions and shows that the scaled surface heating (f = 1.34) provides virtual agreement between predicted and flight maximum temperatures. A more critical comparison is shown by figures 14 and 15, in which radiometer temperature-time data are compared to the revised predictions. The curves show that the correlation between predicted RCC temperature and radiometer data is substantially improved when the 1.34 factor is applied. Radiometer data could not be plotted below the sensor threshold temperature, 500°F on the figures. Correlation with internal temperature measurements, consisting of three insulation surface thermocouples and two structural forward spar measurements, is summarized in table III and figures 16 through 18.

The peak insulation temperatures in table III are seen to exceed flight data, which seems to contradict the requirement to increase surface heating to correlate RCC temperature. After studying the other DFI data at panel 9, a reasonable explanation for this deviation was reached. This explanation is best understood by first examining flight data obtained at the panel 9 outboard attachment, rib station 10.

Analytical predictions for the RS10 panel clevis and spar are compared to STS-2 flight data on figures 19 and 20 respectively. The accuracy of the RS10 attachment math model used for the predictions had been verified with full-scale ground test data obtained at the NASA Johnson Space Center Radiant Heating Test Facility early in the program so that there was a high confidence level in the capability of the models to accurately predict attachment temperatures. However, the test correlation had been performed for a purely conduction/radiation test environment. Removal of leading edge panel 9 after the OFT flights had shown that high-energy air was leaking past the lower access panel thermal barriers into the RCC cavity from the windward surface. High-temperature gas streaks were evident both on the aluminum spar and on the lower spar bracket and the lower attachment clevis. Since the attachment model had been "tuned" to a radiant heating ground test, which did not simulate boundary layer heating or the surface pressure gradients that would lead to gas in-flow and gas streaking that occur during flight, internal convection not included in preflight analyses would be a potential source of deviation between prediction and flight.

In fact, it was concluded that this was the case, and inspection of the panel clevis and spar bracket flight temperature traces for STS-2 clearly show that convection strongly influenced these temperatures. This is most clearly shown on figure 20 by the rapid rise of the spar bracket temperature (V09T9911A) at RS10 that can only be heat transfer from initially hot gas in-flow followed by a spike and rapid reduction that would indicate a reduced inflow gas temperature and bracket cooling. The subsequent reversal and increase of the bracket temperature after touchdown is most likely due to residual heat transfer from the aluminum wing box. Convection is also felt to be present with the panel clevis (V09T9919A) whose temperature is plotted on figure 19. The latter figure indicates that air in-flow produces a net cooling of the clevis.

From the foregoing flight data and consideration of the spanwise pressure gradients in the leading edge, it was further concluded that air flow and convection do occur in the OV-102 leading edge cavity and, therefore, convection may affect the temperatures of subsystem components in the cavity. It is likely, therefore, that spanwise air currents will occur as well as local inflow from the windward high-pressure surface.

With convection present in the panel 9 cavity, it is reasonable to assume that air convection, not accounted for in the insulation temperature predictions, may account for the difference observed between the predicted insulation temperature and flight data shown on figures 16 through 18. In this case, the consistently lower insulation flight temperatures indicate that there is a net cooling of the insulation surface.

Table III shows that the model gives a reasonable correlation of spar average temperature that adds additional confidence to use of surface heating factors to simulate soakback heat loads to the spar. It should be emphasized, however, that the complex construction and heating environment of the wing box are not adequately modeled in the panel 9 TMM and that the spar temperature prediction is considered only an approximation.

45 Degree Swept Wing Analyses

The logic used to develop the surface heating factor for panel 9 was extended to panel 16, which is outside of the wing zone affected by bow shock impingement. Although only a single radiometer (V09T9934A) was located at panel 16, panel 9 data indicated it was reasonable to assume that temperature/heating distributions are the same as predictions.

Comparison of STS-2 radiometer data to the preflight prediction in figure 9 showed excellent agreement, and only minor deviations from preflight predictions were evident. The panel 16 radiometer parameter study (figure 21) showed that heat flux required to correlate flight data was with 2 percent of the preflight prediction. This is considered to verify swept-wing methods outside of the shock interaction zone and no scaling (i.e., f = 1.0) would be required in this wing zone. The maximum temperatures predicted using preflight heating (f = 1.0) are compared to flight data in table IV. Unfortunately, the single insulation surface thermocouple V09T9931A had been lost prior to STS-1 so that a comparison of insulation flight data at panel 16 was not possible.

Highly Swept Wing Analyses

Both panel 4 wing glove radiometer data (V09T9909A) and panel 22 wing tip data (V09T9940A) indicated heat flux levels substantially lower than predicted (see fig. 11). The comparison of temperature history data to flight data plotted on figures 22 and 23 showed that this was true at panel 4 but not true at panel 22 for the following reason. The panel 4 plot on figure 22 clearly shows a peak temperature overprediction of 260°F while the panel 22 prediction is in excellent agreement with data until 900 seconds. At that time, the onset of boundary layer transition that was assumed in the prediction causes a predicted temperature excursion which really doesn't occur in flight. Accordingly, it was concluded that the existing wing tip analysis method is adequate to predict flight heating provided transition is ignored.

Analyses Summary

The results of the foregoing discussion are summarized in table V, which provides temperature comparisons between flight and prediction and scale factors f that, when applied to preflight aerothermo analyses, will improve heating/temperature predictions at the three wing leading edge heating zones considered.

CONCLUDING REMARKS

Leading edge panel thermal math models have been developed and used to establish scale factors that, when used in conjunction with preflight heating, improve the correlation with flight radiometer data. These factors may be used to perform leading edge analyses for the 45-degree swept wing zone, double-shock region, and the two highly swept wing zones. Data from other DFI at panel 9 generally corroborate the revised surface heating approach; however, there is evidence that RCC cavity air convection influences subsystem internal component temperatures. This source of heat transfer is not fully understood at this time and could not be included in this study.

This leading edge heating update will form the basis for revision of aerothermo analysis methods used to predict the leading edge heating environments. These revised methods can then be used to analyze future ETR missions and to estimate environments for other orbiter missions.

REFERENCES

1. Beckwith, J. E., and Cohen, N. B., Application of Similar Solutions to Calculation of Laminar Heat Transfer on Bodies with Yaw and Large Pressure Gradients in High Speed Flow, NASA TN D-625, January 1961.

2. Edney, B., Anomalous Heat Transfer and Pressure Distribution on Blunt Bodies at Hypersonic Speeds in the Presence of an Impinging Shock, Aeronautical Research Institute of Sweden, FFA Report 115, February 1968.

3. Keyes, J. Wayne and Hains, Frank D., Analytical and Experimental Studies of Shock Interference Heating in Hypersonic Flows, NASA TN D-7139, May 1973.

4. Bertin, John J., Graumann, Bruce W., and Goodrich, Winston D., High Velocity and Real-Gas Effects on Weak Two-Dimensional Shock-Interaction Patterns, J. Spacecraft, Vol. 12, No. 3, March 1975.

5. Bertin, John J., Mosso, Stewart J., Bacrette, Daniel W., and Goodrich, Winston D., Engineering Flowfields and Heating Rates for Highly Swept Wind Leading Edges, J . Spacecraft, Vol. 13, No. 9, September 1976.

TABLE I.-OV-102 WING LEADING EDGE RADIOMETERS

Percent Semispan	Panel	Sensor V09TXXXXA	Range, °F	Surface Measured	
				Maximum Heating	Leeward
40	4	9909	410-3000	X	
55	9	9926	410-3000	X	
55	9	9927	302-2570		X
80	16	9934	410-3000	X	
98.6	22	9940	410-3000	X	

TABLE II.-PANEL 9 RCC FLIGHT DATA CORRELATION

RCC IML Location	Sensor V091XXXXA	Maximum Temperature, °F		
		Flight	f= 1.0	f= 1.34
Maximum heating	9926	2490	2262	2475
Leeward	9927	1910	1735	1920

TABLE III.-PANEL 9 INSULATION/SPAR FLIGHT DATA CORRELATION

Component	Sensor V09TXXXXA	Maximum Temperature		
		Flight	f= 1.0	f = 1.34
Insulation				
Lower surface	9922	2010	1986	2180
Center	9918	1835	1930	2100
Upper surface	9923	1750	1860	2040
Spar				
Lower spar cap	9915	290	229	280
Upper spar cap	9911	210	210	250
Average	-	250	220	265

TABLE IV.-PANEL 16 FLIGHT DATA CORRELATION

Component	Sensor V09TXXXXA	Maximum Temperature, °F	
		Flight	f= 1.0
RCC, max heating	9934	2110	2086
Insulation center	9931	___*	1849
Lower spar	9929	248	175

*Data questionable for STS-1 through STS-5

TABLE V.-WING LEADING EDGE RECOMMENDED SCALE FACTORS

Panel	Semispan	Radiometer V09TXXXXA	RCC Maximum Temperature, °F			Recommended Scale Factor, f*
			Preflight	Radiometer	Revised	
4	40%	9909	2070	1800	1800	0.48
9	55%	9926	2260	2480	2500	1.34
9	55%	9927	1760	1910	1925	1.34
16	80%	9934	2100	2110	2100	1.0
22	98.6%	9940	2050	1835	1800	1.0

Note: All temperature are RCC inner mold line

$$*f = \frac{q'}{q_{REF}}$$

$$q = q(\theta, T_w, S)$$

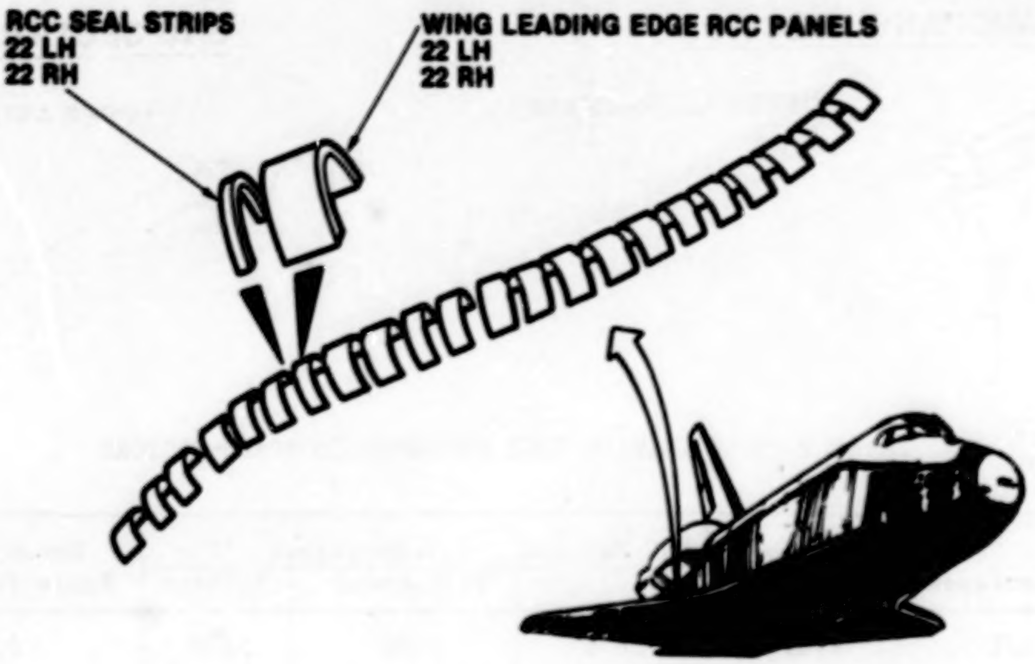
RCC SEAL STRIPS
22 LH
22 RH
WING LEADING EDGE RCC PANELS
22 LH
22 RH

Figure 1.- Shuttle orbiter wing leading edge configuration.

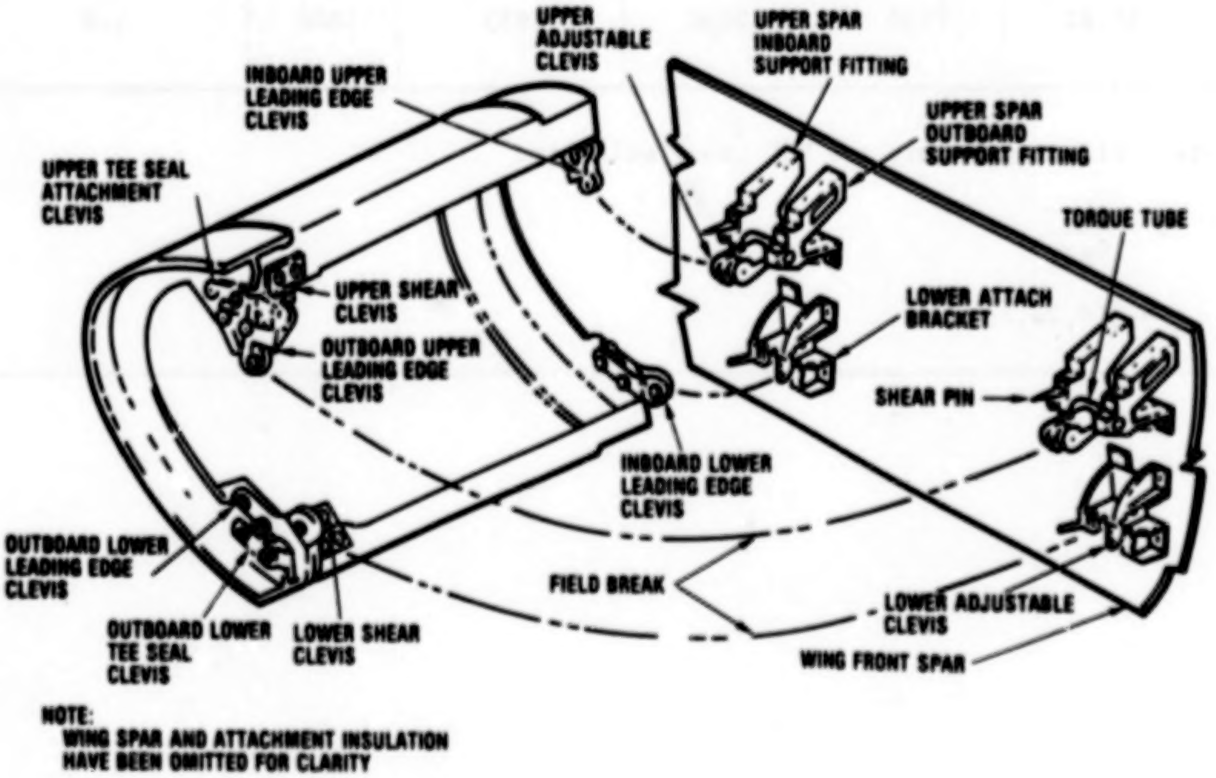
UPPER ADJUSTABLE CLEVIS
UPPER SPAR INBOARD SUPPORT FITTING
INBOARD UPPER LEADING EDGE CLEVIS
UPPER SPAR OUTBOARD SUPPORT FITTING
UPPER TEE SEAL ATTACHMENT CLEVIS
TORQUE TUBE
UPPER SHEAR CLEVIS
LOWER ATTACH BRACKET
OUTBOARD UPPER LEADING EDGE CLEVIS
SHEAR PIN
INBOARD LOWER LEADING EDGE CLEVIS
OUTBOARD LOWER LEADING EDGE CLEVIS
FIELD BREAK
LOWER ADJUSTABLE CLEVIS
OUTBOARD LOWER TEE SEAL CLEVIS
LOWER SHEAR CLEVIS
WING FRONT SPAR
NOTE:
WING SPAR AND ATTACHMENT INSULATION HAVE BEEN OMITTED FOR CLARITY

Figure 2.- Leading edge attachment arrangement.

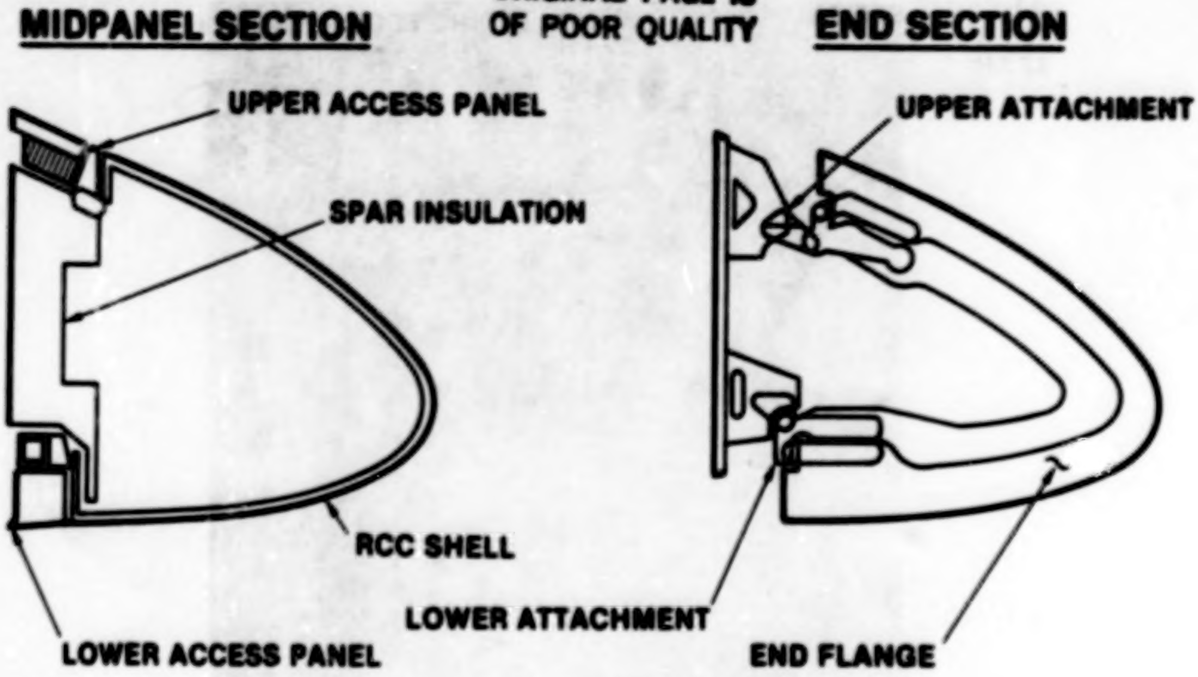
MIDPANEL SECTION
END SECTION
UPPER ACCESS PANEL
SPAR INSULATION
RCC SHELL
LOWER ACCESS PANEL
UPPER ATTACHMENT
LOWER ATTACHMENT
END FLANGE

Figure 3.- Leading edge panel shell and end flange sections.

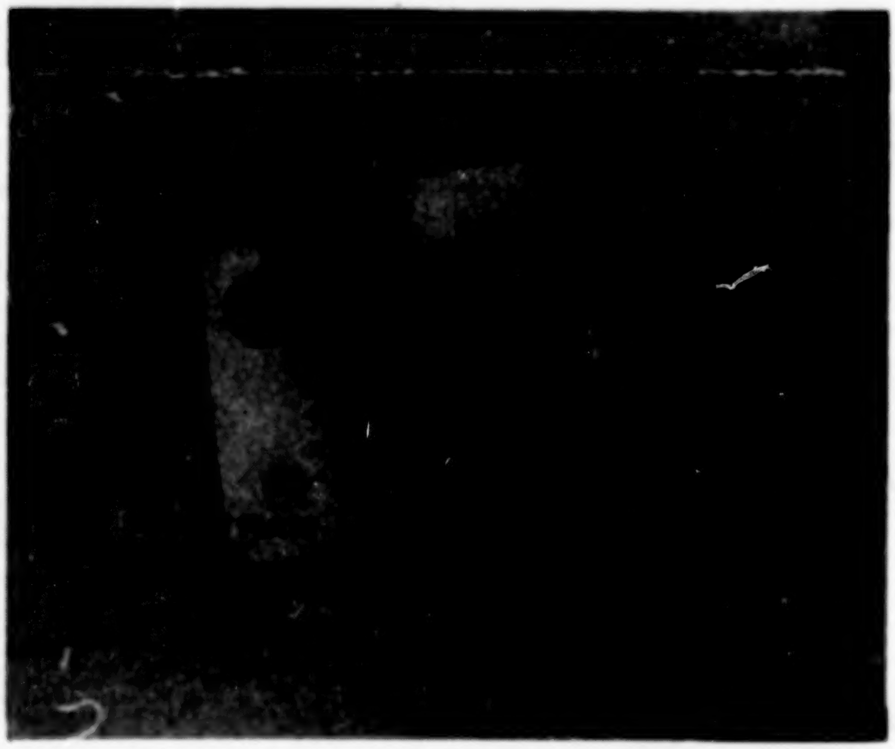

Figure 4.- Radiometer assembly.

SPAR INSULATION

Figure 5.- Panel 16 radiometer installation.

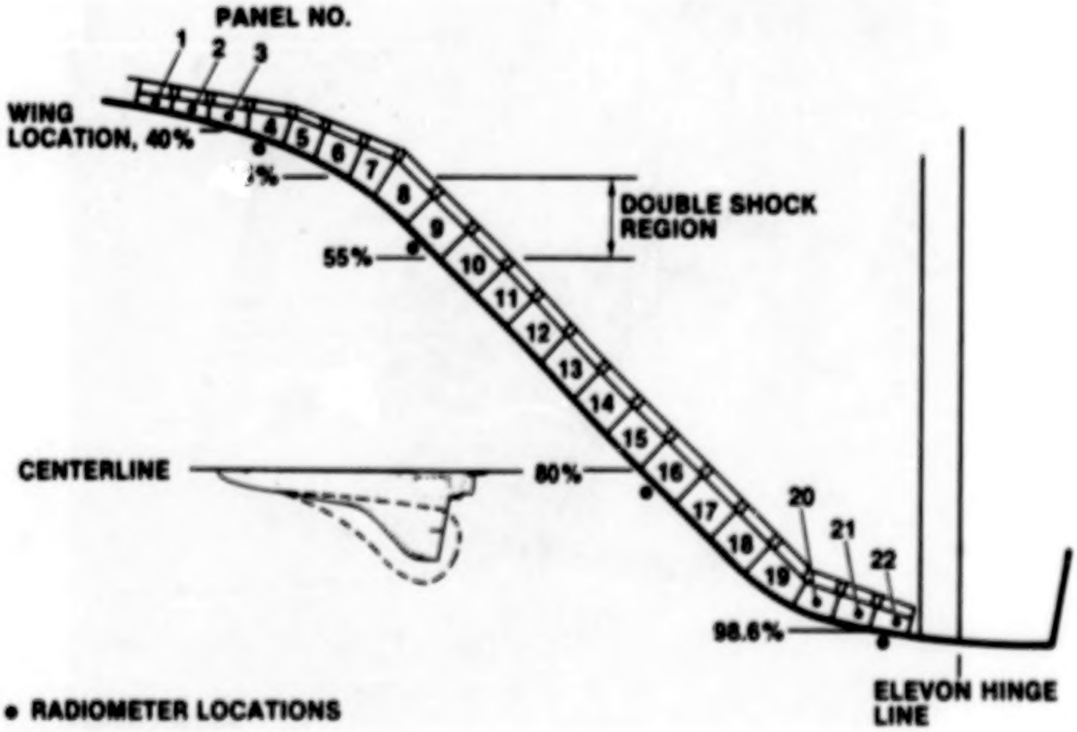
PANEL NO.
1
2
3
4
5
6
7
8
9
10
11
12
13
14
15
16
17
18
19
20
21
22
WING
LOCATION, 40%
%
55%
DOUBLE SHOCK
REGION
CENTERLINE
80%
98.6%
ELEVON HINGE
LINE
● RADIOMETER LOCATIONS

Figure 6.- Orbiter vehicle 102 radiometer locations.

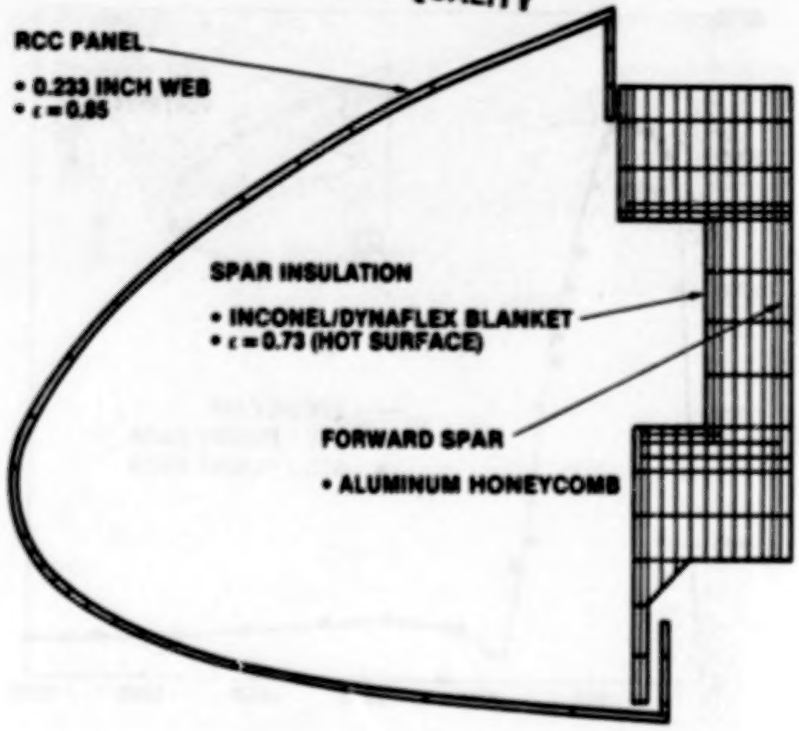
RCC PANEL
• 0.233 INCH WEB
• ε = 0.85
SPAR INSULATION
• INCONEL/DYNAFLEX BLANKET
• ε = 0.73 (HOT SURFACE)
FORWARD SPAR
• ALUMINUM HONEYCOMB

Figure 7.- Panel 61 RCC shell thermal math model.

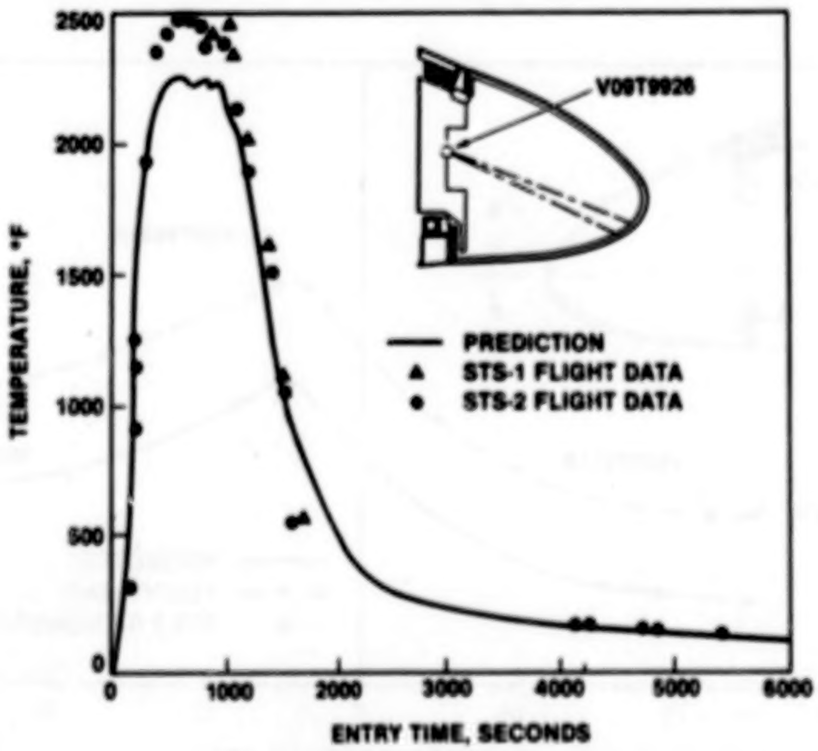

Figure 8.- Panel 9 radiometer V09T9926A data comparison to prediction.

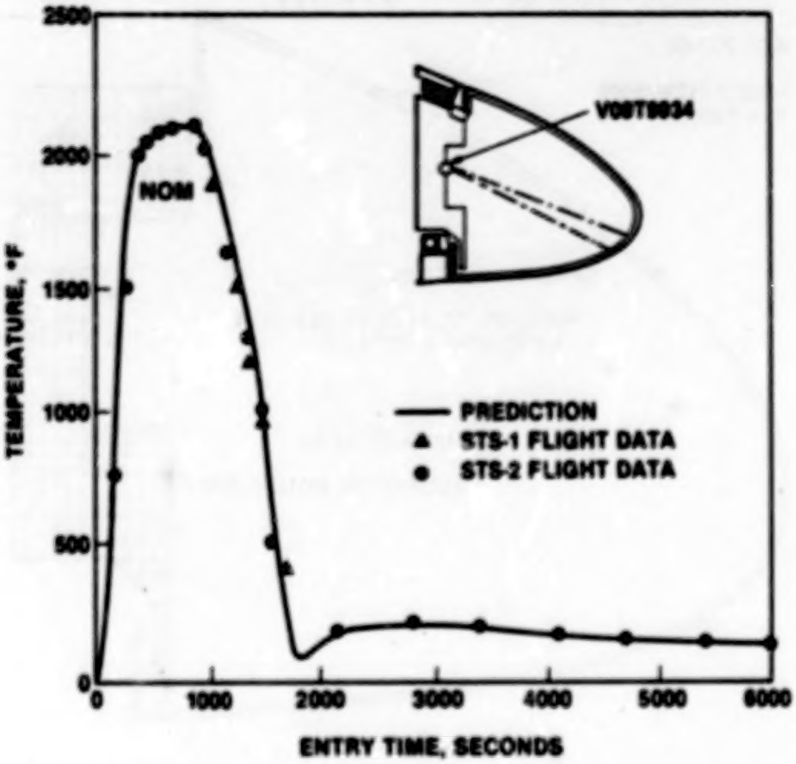

Figure 9.- Panel 16 radiometer V09T9934A data comparison to prediction.

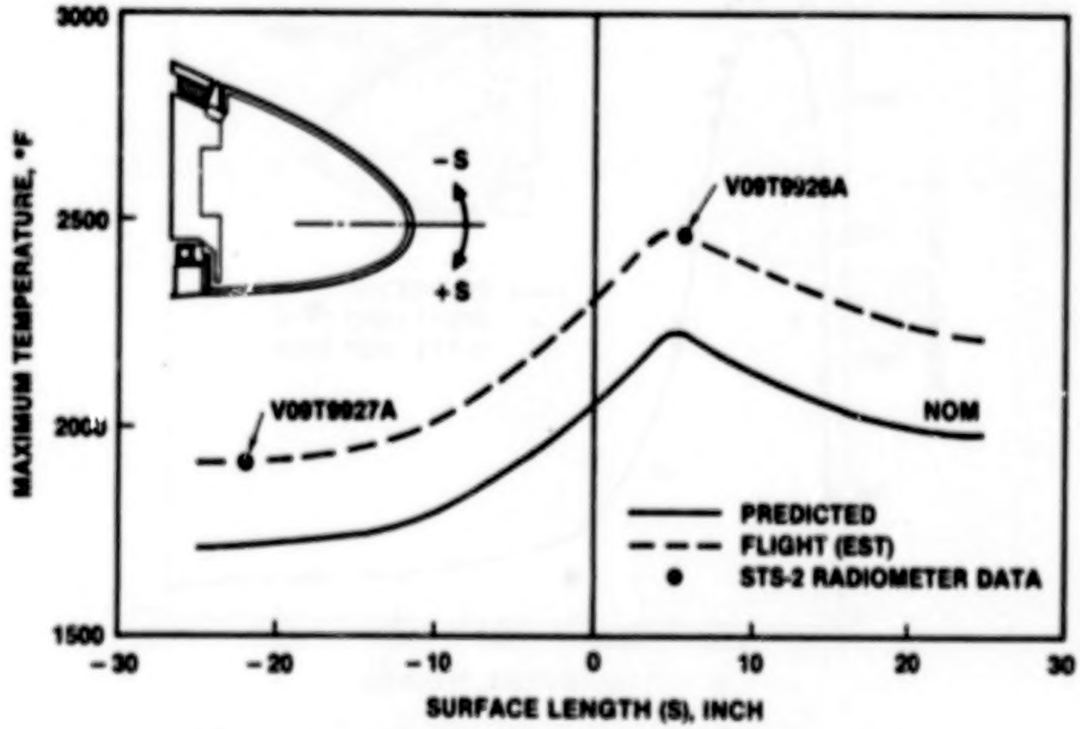

Figure 10.- Panel 9 temperature distribution.

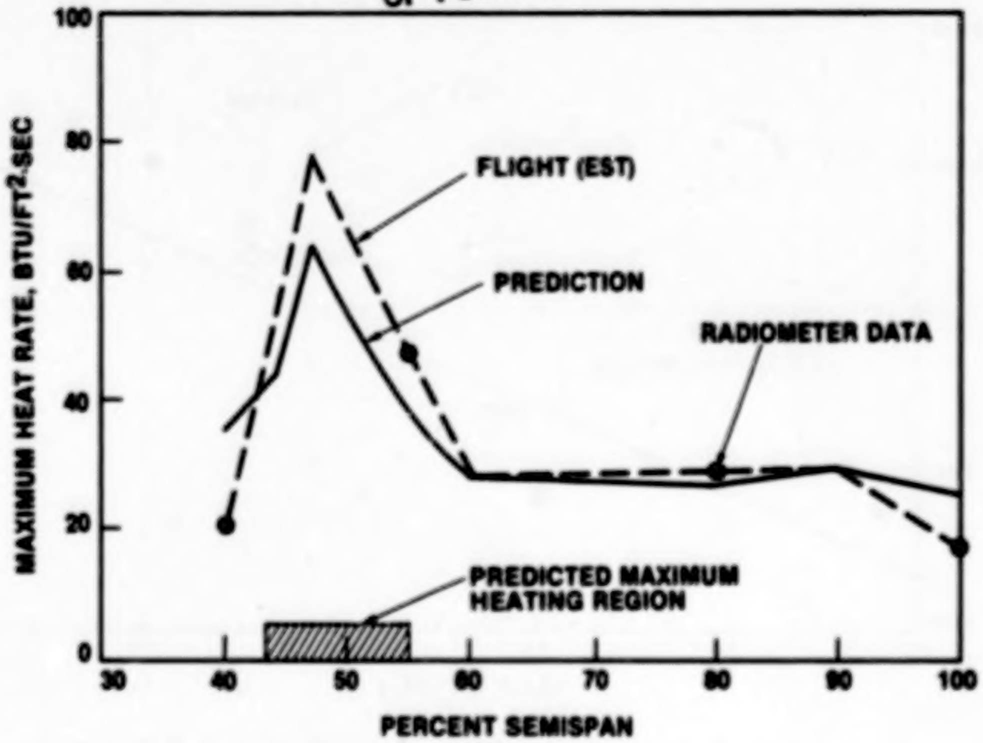

Figure 11.- Spanwise maximum heat rate comparison.

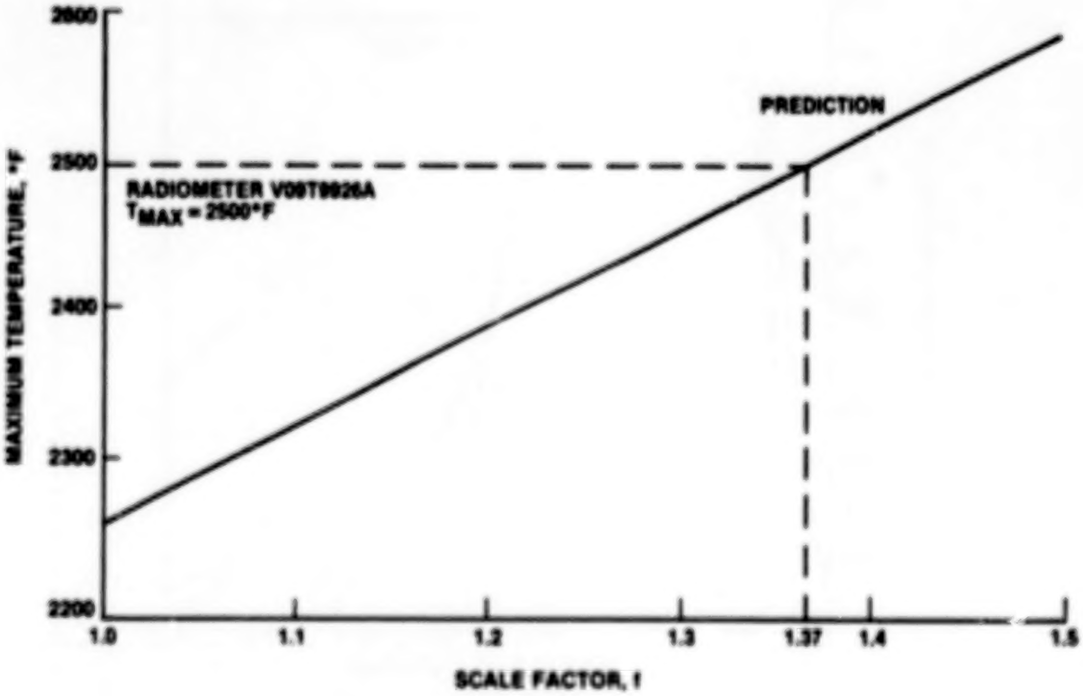

Figure 12.- Parametric scaling of predicted radiometer V09T9926A temperature.

ORIGINAL PAGE IS
OF POOR QUALITY

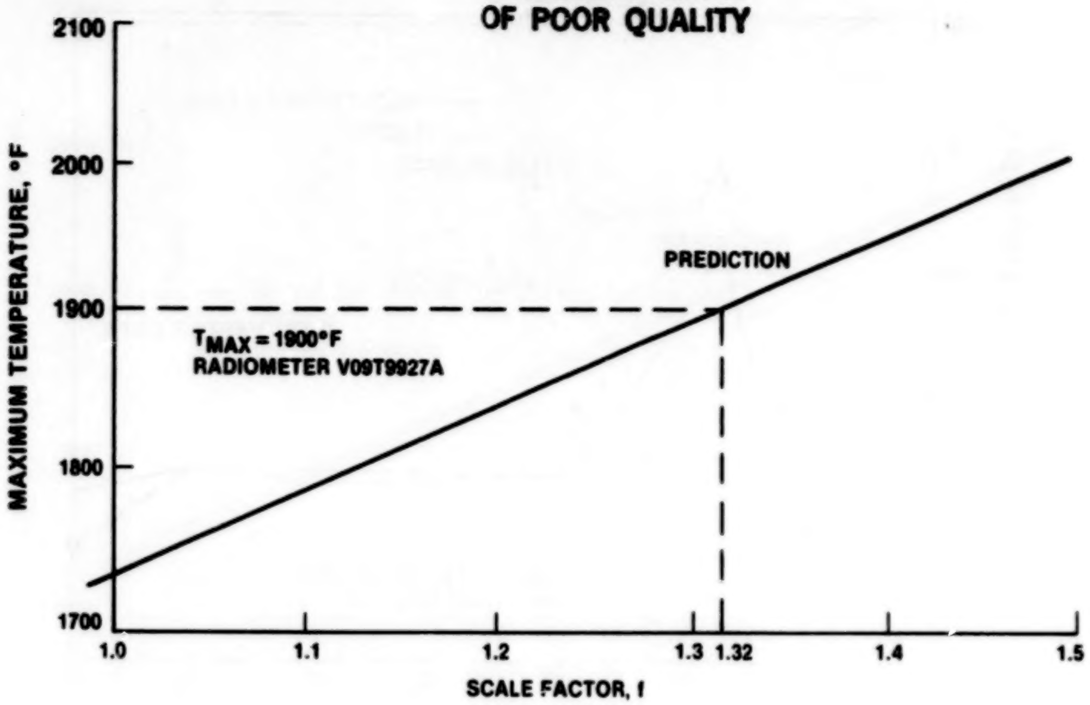

Figure 13.- Parametric scaling of predicted radiometer V09T9927A temperature.

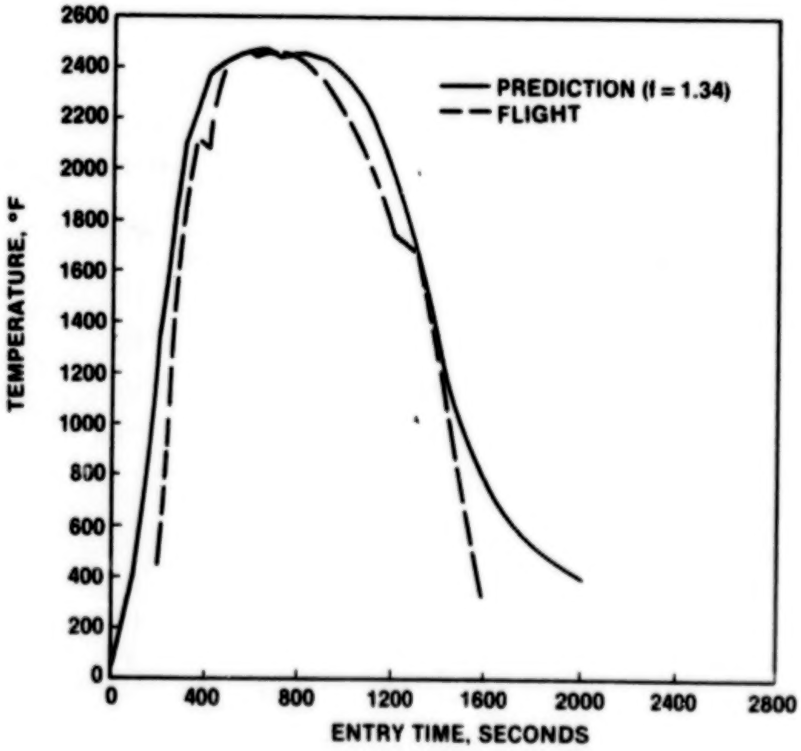

Figure 14.- Panel 9 maximum heating radiometer V09T9926A temperature prediction (f = 1.34).

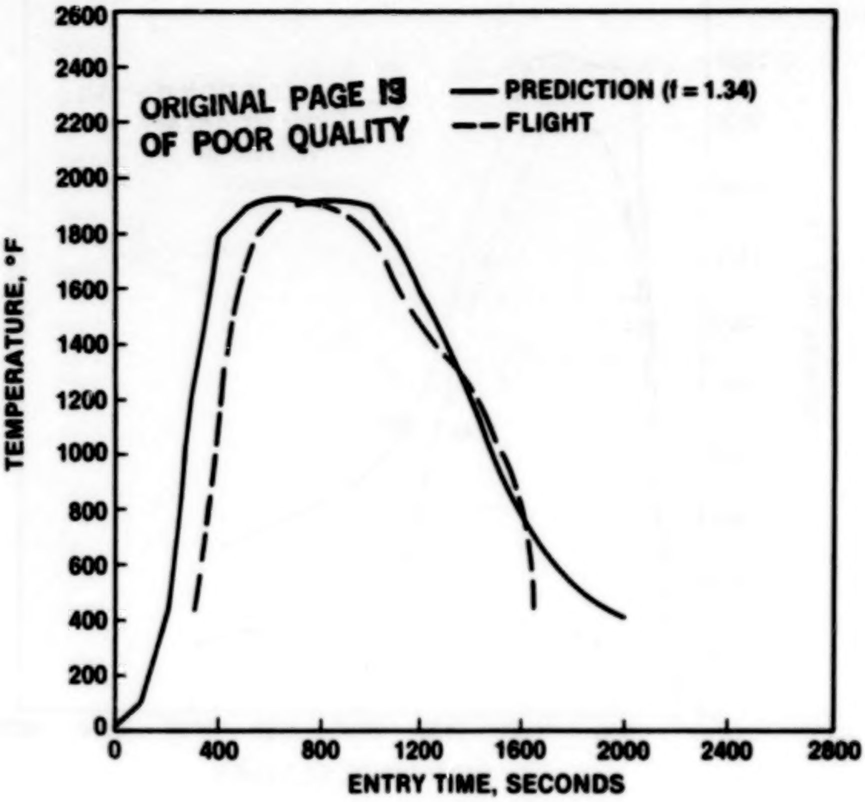

Figure 15.- Panel 9 leeward radiometer V09T9927A temperature prediction (f = 1.34).

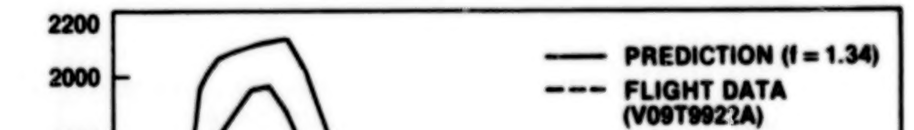

Figure 16.- Panel 9 lower insulation temperature prediction (f = 1.34).

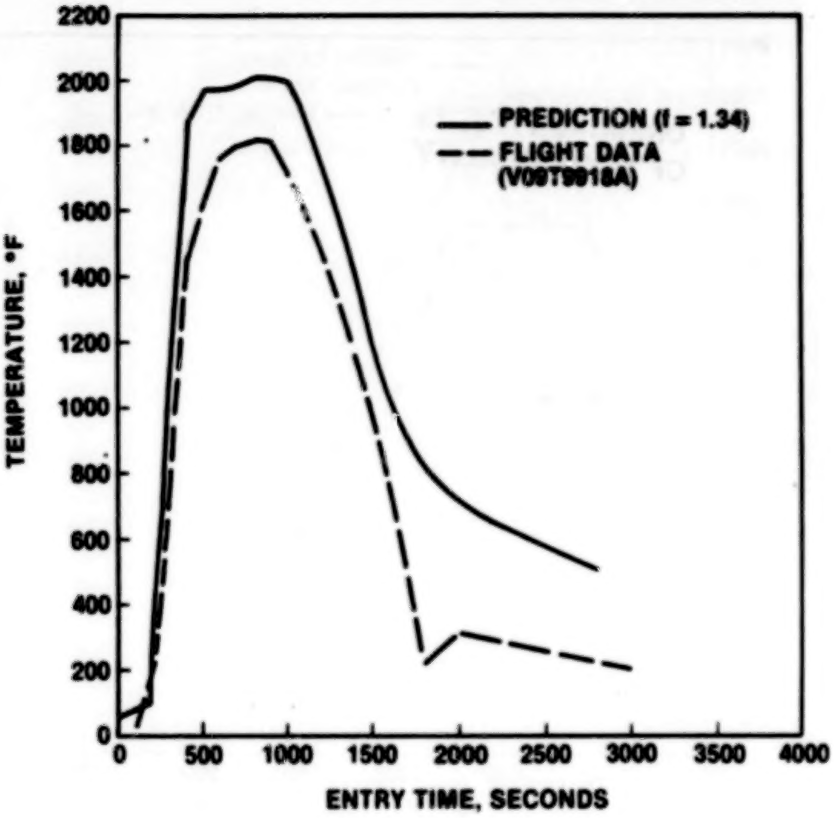

Figure 17.- Panel 9 insulation midplane temperature prediction (f = 1.34).

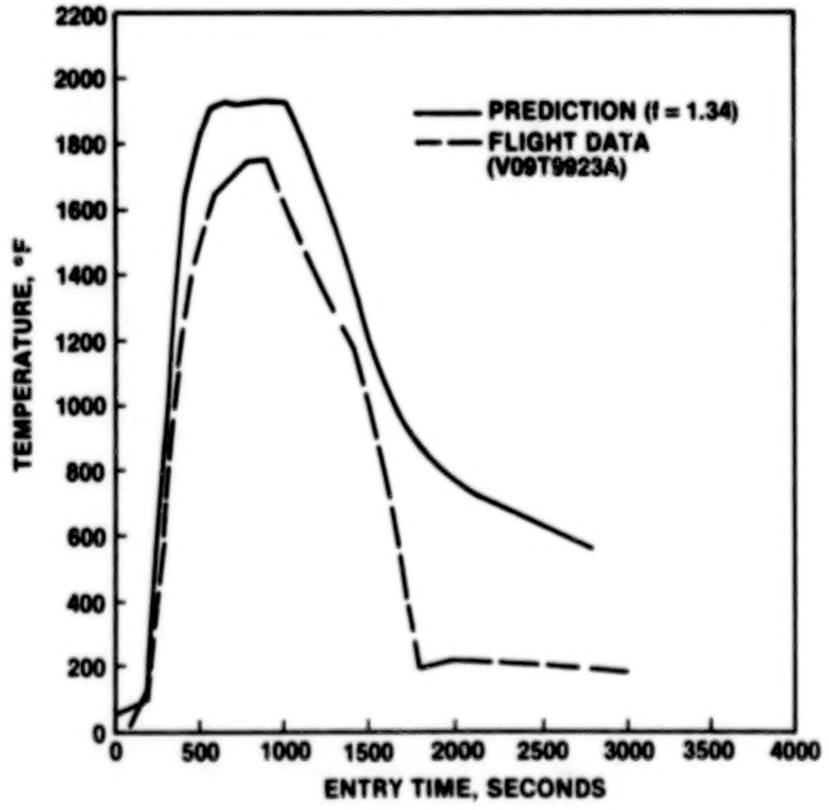

Figure 18.- Panel 9 insulation upper surface temperature prediction (f = 1.34).

ORIGINAL PAGE IS
OF POOR QUALITY

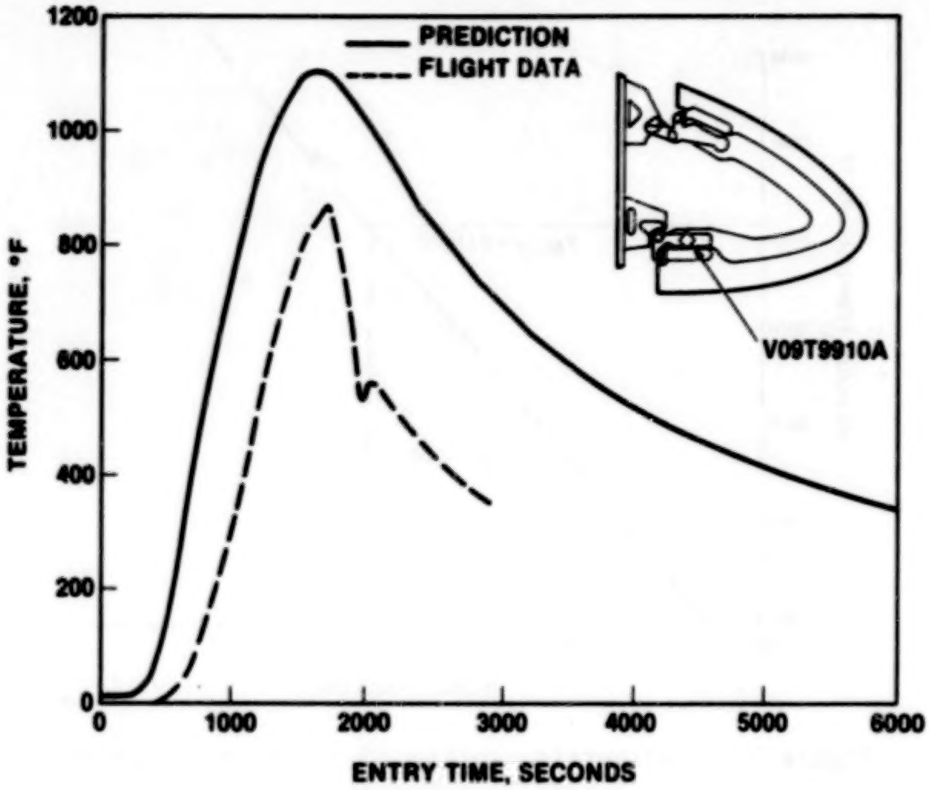

Figure 19.- Rib station 10 lower panel clevis temperature comparison (f = 1.34).

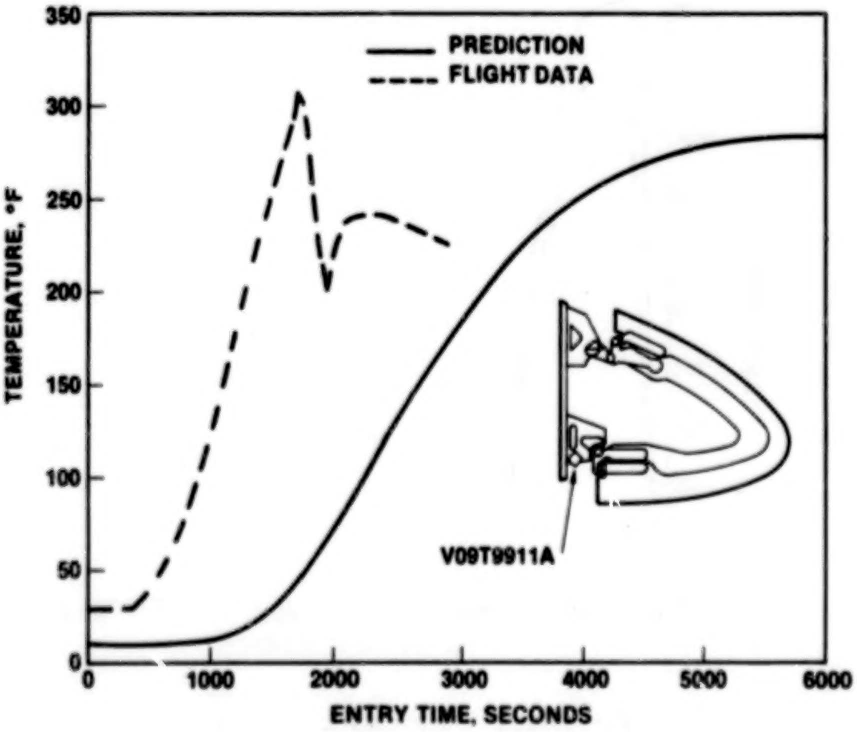

Figure 20.- Rib station 10 lower spar bracket temperature comparison.

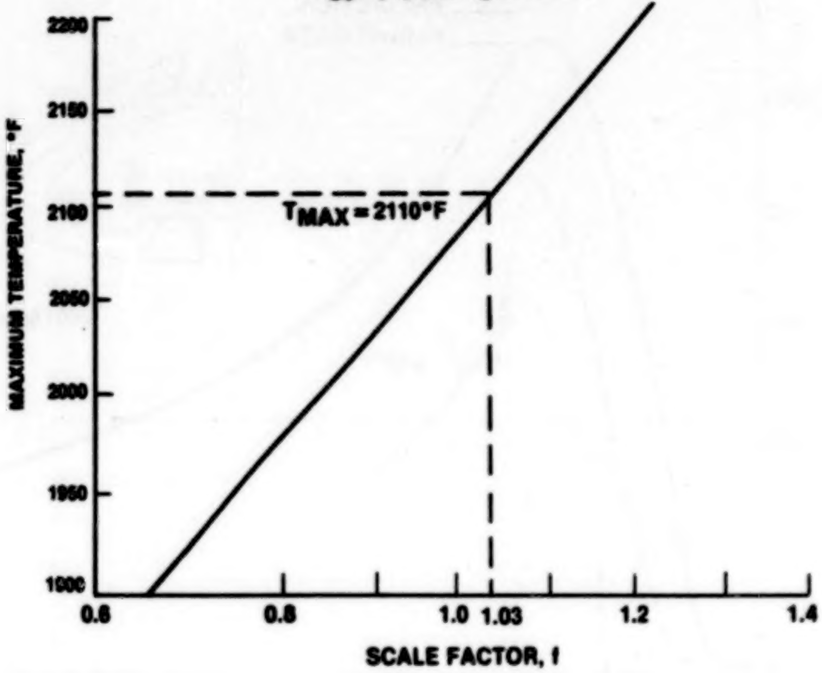

Figure 21.- Parametric scaling of predicted radiometer V09T9934A temperature.

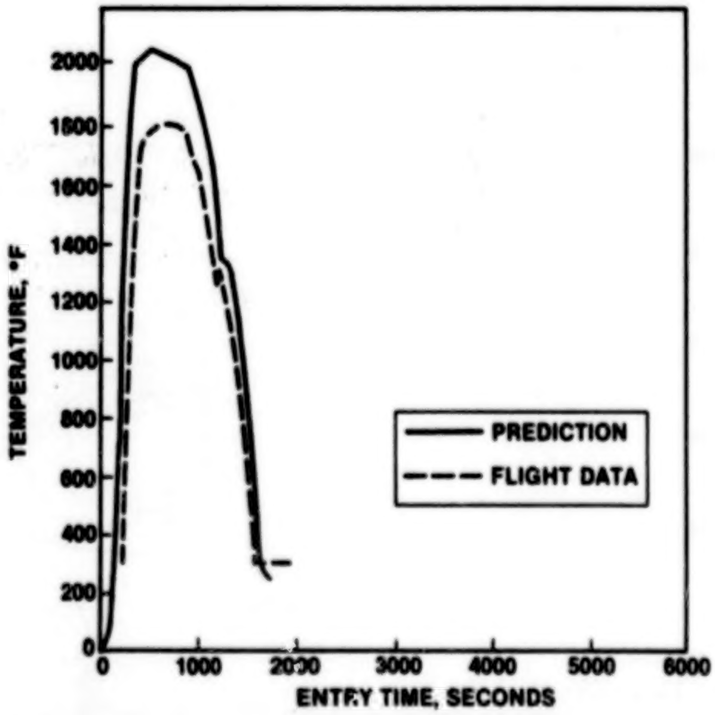

Figure 22.- Panel 4 radiometer V09T9909A data comparison to prediction.

ORIGINAL PAGE IS
OF POOR QUALITY

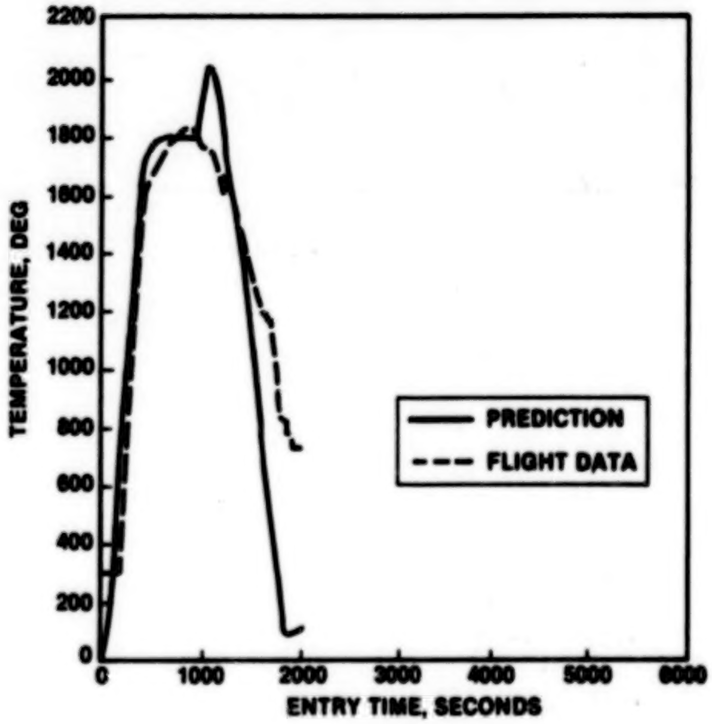

Figure 23.- Panel 22 radiometer V09T9940A data comparison to prediction.

N84
10163

UNCLAS

N84 10163

SUBSONIC LONGITUDINAL PERFORMANCE COEFFICIENT EXTRACTION FROM SHUTTLE FLIGHT DATA -- AN ACCURACY ASSESSMENT FOR DETERMINATION OF DATA BASE UPDATES*

John T. Findlay, G. Mel Kelly, and Judy G. McConnell
Analytical Mechanics Associates, Inc.
Hampton, Virginia

Harold R. Compton
NASA Langley Research Center
Hampton, Virginia

SUMMARY

Longitudinal performance comparisons between flight derived and predicted values are presented for the first five NASA Space Shuttle Columbia flights. Though subsonic comparisons are emphasized, comparisons during the transonic and low supersonic regions of flight are included. Computed air data information based on the remotely sensed atmospheric measurements as well as in situ Orbiter Air Data System (ADS) measurements were incorporated. Each air data source provides for comparisons versus the predicted values from the LaRC data base. Principally, L/D, C_L, and C_D comparisons are presented, though some pitching moment results are included. Similarities in flight conditions and spacecraft configuration during the first five flights are discussed. Contributions from the various elements of the data base are presented and the overall differences observed between the flight and predicted values are discussed in terms of expected variations. A discussion on potential data base updates is presented based on the results from the five flights to date.

INTRODUCTION

The NASA Space Transportation System (STS) entry flights offer aerodynamic researchers unique opportunities to extract aerodynamic coefficients from flight data for comparisons with pre-flight data base values (refs. 1, 2). In this sense, the Space Shuttle is utilized experimentally as a "flying" wind tunnel throughout the entire speed regime. Results from this so-called Aerodynamic Coefficient Measurement Experiment (ACME) have been widely published in the literature, as examples, see references 3, 4, and 5. Though considerable subsonic analyses have been performed by aerodynamicists throughout the aerospace community, some of the results of which are reported in references 6 and 7, most of the published results have emphasized comparisons in the supersonic/hypersonic regime. Here, flight determinations are potentially limited by the accuracy of the remotely sensed atmospheric density, ρ , and the requirement to translate same in time and over rather large global areas to conform to the spacecraft ground track and vertical profile. The third (STS-3) and fifth (STS-5) flights permitted an alternative in situ density determination. These

---

*This work was performed under NASA Contract NAS1-16087.

PAGE 110 INTENTIONALLY BLANK

PRECEDING PAGE BLANK NOT FILMED

in situ ρ determinations were obtained by processing the Development Flight Instrumentation (DFI) fuselage pressure measurements (ref. 8).

In the subsonic regime, alternate air data are always available. Air data can be computed based on remotely measured atmospheric information or obtained directly from the Orbiter Air Data System (ADS). Use of both sources is assumed herein. Discussions are presented which summarize the use of both and quantify the differences which one could expect since both sources result in different flight extraction and predicts generation. One must consider the actual flight/data base comparisons obtained based on both sources in terms of the expected pre-flight data base accuracy, the so-called variations (refs. 9, 10) based on aerodynamicists' consensus. Also, subsonic data base prediction becomes more complex in that additional elements of the overall model are introduced, e.g., rudder, speed brakes, gear effects, and ground effects. Refer to figure 1 for a schematic of the actual control surface configuration of the Orbiter vehicle. The expected contributions from the various elements of the data base are presented and discussed in view of the flight differences. Repeatability in terms of flight conditions and spacecraft configuration across flights is investigated. Such results provide a precursor analysis to enhance more rigorous flight extraction for data base update determinations, i.e., for control surface effectiveness, stability, and performance determinations using regression methods.

DISCUSSION OF AIR DATA SOURCES

The necessary air data information required to extract flight coefficients and enable determination of predicted values can be computed from the measured atmospheric parameters or obtained from the ADS directly. The first method has conventionally been utilized at Langley Research Center (LaRC). Though some of the ADS parameters have been utilized for wind evaluation/estimation in generating the LaRC results as discussed later, direct use of the ADS angle of attack (α), Mach, and dynamic pressure (q) permits independent flight determinations and predicts generation.

Throughout the region investigated herein, conservatively below Mach ~2.5, complete air data are available from the ADS. These data are derived using pressure measurements from the ADS, which consists of two side probes deployed at Mach ~3.5. Each probe is configured with three pressure orifices, each orifice instrumented to provide redundant pressure measurements. Four static ports are also available on each side. These data are processed on/board using a reduced set of calibration coefficients to provide operational air data (except for sideslip angle, β) for spacecraft flight control. Though these on/board ADS parameters are available from the Operational Instrumentation (OI), researchers are able to utilize postflight results which incorporate more rigorous calibrations. These include updates based on Shuttle experience and further analysis of the data obtained during the Approach and Landing Test (ALT) flights for which nose-boom measurements provided additional calibration information. Use of the sensed air data for flight extraction and predicts generation is straightforward. The majority of investigators throughout the community have utilized and recommended use of the ADS in a similar manner.

Use of the remotely measured atmospheric data is discussed next. Subsonically, remote atmospheric measurements available from rawinsonde soundings are more optimally located (time and spatial) and ambient parameters should be more accurate considering the correspondingly lower altitude regions. These measured atmospheres are assembled as Langley Atmospheric Information Retrieval System (LAIRS) files as discussed in reference 11. Reference 12 discusses the merging of these data with the inertially reconstructed trajectory (BET) to obtain the air relative parameters.

Of considerable importance throughout this region are the winds encountered. Figure 2 depicts the drastically different wind environments for the various flights to date. Uncertainties in the available wind measurements, both magnitude and direction, contribute almost entirely to the flight determination uncertainties. The winds are utilized directly to compute the necessary air data parameters: α , β , and air relative velocity, V_A. The latter is used in conjunction with the measured ρ to compute the dynamic pressure. In view of this direct dependence, alternate source data (jimsphere measurements) and information from the postflight calibrated ADS data have been utilized extensively at LaRC to evaluate the remotely measured winds as discussed in reference 13. Basically, atmospheric independent algorithms have been developed which estimate winds using 1) α and β in a deterministic sense to derive winds on a point by point basis, or 2) α , β , and the true air speed, V_T , to obtain wind profiles at break point altitudes with a batch smoother. Evaluations above Mach 1 have not been successful since the uncertainties in the wind estimates increase dramatically with Mach number when constant uncertainties in the ADS parameters are assumed. It is noted that the actual winds incorporated for STS-3 and STS-4 were batch winds in lieu of the measured data. This replacement was somewhat arbitrary for STS-4, but wind measurement problems on STS-3 left no alternative as discussed in reference 13.

FLIGHT EXTRACTION DIFFERENCES

Flight determined aerodynamic coefficients based on the computed (LaRC) and measured (ADS) air data are discussed. In both instances the flight values are computed utilizing the same measured spacecraft rates, accelerations, and mass properties. The measured accelerations and rates are obtained from the accurate Inertial Measurement Unit (IMU) data. For example, the acceleration information is accurate to 1 mg and the angular rates are accurate to 0.01 deg/sec for the nominal 1 sec time homogeneous data. Mass properties are obtained post-flight as time histories. For all intents and purposes, the mass and inertias can be considered accurate to 1 percent or better. An important concern is the knowledge of the spacecraft center-of-gravity (c.g.) required to compute the moment coefficients. A sensitivity to reasonable c.g. errors is discussed later in terms of the resultant effect on the pitching moment, C_m .

Body axis coefficients, normal (C_N) and axial (C_A), are determined directly from the accelerometry and dynamic pressure. The LaRC q utilizes the inertial velocity from the reconstructed trajectory, the measured/evaluated winds, and, of course, the measured ρ . Stability axis coefficients, lift (C_L) and drag (C_D), are obtained by transforming the body axis coefficients through the angle-of-attack. The latter is computed from the inertial orientation of the spacecraft and the orientation of the air relative velocity vector, V_A , which requires knowledge of the wind magnitude and heading. Thus, the influence of the winds are twofold as they affect both q and attitude. For the ADS, the α and q are directly available. The q affects the computed body axis coefficients directly, which then are rotated through the ADS α for stability axis computations. Clearly, differences in the flight extracted coefficients from the two sources can be expected dependent on the observed differences between the α and q.

Figures A1(a) through A1(e) in the attached Appendix present plots of the flight conditions (α, M, and q) for both air data sources for the first five Shuttle flights. They are plotted versus the BET altitude which is utilized as common to both. These data are shown as composite plots for all five flights as figure 3 (LaRC) and figure 4 (ADS) in this paper. These data are plotted from the Aerodynamic Best Estimate Trajectory (AEROBET) files generated using the particular air data source. Reference 14 discusses the contents of these data files. Figures A2(a) through A2(e) show expanded plots of α and q versus Mach number from both sources for STS-1 through STS-5, respectively. Mach number from both sources is seen to be multi-valued in some regions. Though Mach number doesn't affect the flight extraction per se, any differences versus Mach number are most relevant for predicts generation as discussed later. Except for STS-4 and 5, there are noticeable differences between the two sources near Mach 1. Clearly the most pronounced differences occur for STS-2 and STS-3. Readers will recall from figure 2 that the winds encountered during these missions were considerably larger than those occurring on the other flights. Also, the profiles exhibited extremely large gradients, particularly for STS-3 in the vicinity of 10 and 55 kft. The measured winds which were utilized for STS-2 were never sufficiently substantiated using the estimation algorithms, at least in the vicinity of $h \sim 24$ kft and $h \sim 50$ kft (Mach ~ 1). Though estimated winds were incorporated for STS-3 as discussed, large differences in both the winds and dynamic pressure resulted when either the deterministic (α, β) or batch (α, β, V_T) algorithms were employed. This suggests an inconsistency between the attitude angles and true air speed which ostensibly depends on the actual environs. Indeed, an inconsistency among these parameters and the sensed Mach and q is suggested. Though the true air speed is utilized in the batch wind algorithm, it is recognized that this is a derived quantity based on the calibrated Mach number and derived ambient temperature. For STS-1, 4 and 5, this has not been indicative of a problem. However, true air speed/attitude inconsistencies were noticeable for STS-2 and pronounced for STS-3. In any event, one must be impressed with the performance of the ADS, recognizing that the in situ nature of these data might well represent the best air data available. It is noted that Mach and q differences could be a manifestation of ambient atmospheric measurement errors from the rawinsonde data.

The differences shown in the attached Appendix are of some concern. Referring back to either figures 3 or 4 for discussion purposes, considerable repeatability of flight conditions is evident, most noticeably above Mach 1.1 ($h \sim 55$ kft). One can sense the development of a flight data base permitting multiple opportunities for data base update determinations. For example, the total spread in α is essentially less than 2 degrees, with dynamic pressure within ± 25 psf about some average curve. These results are somewhat misleading in terms of α since some α differences between the two air data sources for any one flight are approximately the same magnitude as the total spread across flights. A trend exists in this interval as well. The computed α tends to be somewhat higher in the interval though there are exceptions. Additional analysis is required to further substantiate both sources though, as stated, wind estimation or evaluation at these altitudes is improbable. Below Mach 1 the variation in flight conditions is seen to be considerable, particularly for the STS-2 flight below 20 kft. Again, significant air data parameter differences are observed in some instances in the subsonic region as well. More repeatable conditions will result after additional flights but these will be selected cases restricted to very narrow intervals. For example, conditions at 20 kft (Mach ~ 0.6) for the five flights suggest reasonably similar conditions for regression purposes.

Though the figures presented in the Appendix best show the actual difference signatures for each flight, it is of interest to summarize these differences statistically. Table I shows the actual difference statistics for α and q for the two sources as these differences relate directly to the flight extraction accuracy. Data presented in this table were generated for three different Mach intervals as shown. It can be seen that mean differences (μ) in α are generally less than 0.2 degree for the five flights, the LaRC values being slightly larger on average in all instances. Standard deviations (σ) of these differences vary between 0.2 and 0.5 degrees. Locally, differences in excess of 1 degree are seen to occur in the figures. Dynamic pressure differences, tabulated as percentage differences, are less than 1 percent (μ) in most instances though as much as 3 percent occurs for STS-3. Differences of nearly 20 percent occur, though generally the differences locally are less than 10 percent as evidenced by the computed σ for each flight which varies between 1.3 and 4.4 percent. These differences can relate to ~ 2 (±3) percent differences in L/D and C_L. Mean differences in C_D are somewhat less though random differences exceed 5 percent. Peak differences for each performance coefficient can exceed 10 percent locally.

DATA BASE PREDICTION DIFFERENCES

A LaRC version of the Orbiter aerodynamic data base (ref. 15) has been utilized throughout. This data base, though vintage 1978, is essentially representative of the final pre-operational data base (ref. 16). Some six updates have occurred and thus it is difficult to quantify the differences in terms of actual percentage changes. More recent versions utilized revised fairings of some of the longitudinal performance data in the Mach interval from 1.2 to 2. These revised fairings were the result of correlating (fitting) various wind tunnel data sets such that the implied variations were reduced. Another update which resulted was the inclusion of theoretical body flap effects (in the presence of the ground) on longitudinal performance and trim characteristics. Beyond these changes, it is understood that most of the changes were for Mach numbers above that interval considered herein. Any lateral directional updates which have evolved would, of course, have no influence on the results presented.

The complete data base model provides for effects due to Mach, $\bar{V}_\infty$ (in the hypersonic regime), control surface deflections, reaction jet (RCS) contributions, and air relative attitude angles, α and β. Ground effects and landing gear contributions are also modelled. Control surface deflections and RCS activity are obtained from the OI recorded data. Figure 5 presents a composite plot of the longitudinal control surface deflections versus the BET altitude for the five Shuttle flights. Plotted are the elevator (δ_E), body flap (δ_{BF}), and speed brake (δ_{SBA}) deflections, the latter with respect to the aerodynamic reference line and not about the hinge line of the swept tail configuration. The aerodynamic reference line is utilized for both speed brake and rudder for consistency with the data base as modelled. Figure 5 suggests reasonable repeatability of spacecraft configuration above 50 kft which should permit multiple opportunities for data base update determination studies. Evident below this altitude are the ample opportunities for control surface effectiveness studies. The control surface deflections are plotted individually for each flight in the attached Appendix. These data are plotted versus the Mach number from both sources as figures A3(a) through A3(e) for STS-1 through STS-5, respectively. Keeping in mind that the control surface deflections are the same versus time and/or altitude, differences shown thereon merely reflect the Mach number differences. Lateral control surface deflections (δ_A, δ_{RA}) as well as side-slip and vehicle roll angle (with respect to the air relative velocity vector) are included in the Appendix for each flight as figures A4(a) through A4(e). The β curves basically reflect the differences between the computed and ADS values though the Mach number differences contribute to the difference signature. Differences in any of the other parameters only reflect the slightly different Mach number from the two air data sources. These figures are included in the Appendix for information only. These parameters have no influence on the longitudinal performance parameters considered in this paper.

Since the data base is Mach and α dependent, the predicts from all elements of the data base will vary when either the ADS or computed air data are utilized. Angle-of-attack differences have been shown previously. Mach number differences need be quantified. The LaRC AEROBETs utilize the LAIRS temperature profile to compute the speed-of-sound. This, in conjunction with the inertial velocity and measured/evaluated winds, permits Mach determinations. Differences between the measured (ADS) and computed Mach numbers are ~0.01 (±0.03) with local differences of ~0.1. Again, these differences can be seen in the attached Appendix. Mach differences, in conjunction with the α differences previously discussed, can result in prediction differences comparable to the flight extracted differences.

FLIGHT/DATA BASE COMPARISONS

Performance Overview

An assessment of Shuttle performance between Mach 2 and landing is presented as Figures 6 through 10 for STS-1 through STS-5, respectively. These data were generated based on the LaRC AEROBETs as typical, i.e., the computed air data parameters were employed. Shown on each figure are the flight (○) and predicted (△) performance coefficients; L/D, C_L, and C_D. Variations (V) are also shown thereon as indicated. These variations are a representative estimate of the pre-flight accuracy of the data base. Though more detailed flight/data base comparisons are later presented, it is shown on these figures that the flight C_L agrees with the data base values to well within one variation above Mach 1. Flight L/D essentially is within one variation of that predicted over the same interval, indicating slightly more performance than predicted. Flight computed drag for all five flights agrees within one variation of the predicted values over a more restrictive Mach interval, namely, above M ~1.4.

Pitching moment comparisons are presented as Figure 11. Five strip charts are presented, one for each flight. These figures show results with respect to the best available flight c.g. and include thereon flight (○), predicts (△), and variations (V). This figure is concluded by showing the composite five flight pitching moment comparisons. Plotted are percentage errors ((flight - predicts)/flight) referenced to a c.g. of 65 percent of the body length, the reference c.g. utilized in the data base. As shown, the differences in terms of percentage are considerable, indicative of misprediction of either longitudinal control surface effectiveness or basic pitching moment. Even the suggested mean differences are large and, it is felt, not consistent with (reasonable) expected flight c.g. errors. For example, a one inch $X_{c.g.}$ location error should contribute approximately 5 percent as a mean error. Similarly, a one inch $Z_{c.g.}$ error would relate to only ~ 2 percent. Since some of the differences shown could reflect the vintage data base utilized no further C_m analysis was performed. Thus, the influence of the Flight Assessment Deltas (FADS) (ref. 6) on C_m has not been investigated. In this interval the FADS do include a basic C_{m_0} prediction update and a ground effects update. The C_{m_0} correction (0.0075) for the 65 percent reference c.g. is in the direction to reduce the mean differences shown below Mach 0.75.

As indicated, the data base predicted results are comprised of the contributions from many elements of the model. Figures 12 and 13 show the expected contributions to the total predicted lift and drag, respectively. The LaRC AEROBET parameters were utilized to generate these typical results which are presented as information. Shown thereon are: basic aerodynamic effects (assuming undeflected controls except for the speed brakes which are assumed in this configuration to be deflected 25 degrees); incrementals due to elevator, body flap, and speed brakes; and gear and ground effects. All are plotted as a ratio to the total predicted coefficient to show, in essence, the percentage contribution of each to the total predicted value. An additional item modelled, i.e., the flexible airframe contribution, is sufficiently small and, as such, is not shown.

These figures are presented for completeness to, perhaps, identify sources for the actual flight/data base differences next discussed. In general, above Mach 1.2 almost all of the predicts are determined by the basic airframe characteristics which are, of course, Mach and α dependent. Below Mach 1, expected control surface contributions become very significant. Specifically, the lift contribution from the elevators varies between 20 and 60 percent dependent upon the different deflections for the various flights. It is observed that the expected body flap contribution to the predicted lift can be as much as 20 percent with an expected reduction due to speed brakes of a similar magnitude. No predictable lift increment is modelled for the deployed landing gear configuration. Control surface contributions to the predicted drag are: 10 to 20 percent from the elevators; generally less than 10 percent from the body flap; and as much as 30 percent from the speed brakes. The negative drag increment shown due to the speed brakes is for deflections less than 25 degrees, the presumed undeflected controls configuration. The expected incremental drag due to the landing gear is approximately 20 percent. Incrementals indicated for the ground effects show that the expected lift contribution is approximately twice that for drag. Readers are advised that the BET altitude accuracy is approximately 5 ft at touchdown. As such, the BET altitude is of questionable accuracy in the required altitude/span (h/b) computation for predicted ground effects based on the extreme sensitivity to this parameter. The last strip chart presents an estimate of prediction errors for an α error of 1 degree. These partials, C_{L_α} and C_{D_α}, are numerically derived based on a 1 degree perturbation in α from the nominal.

Flight/Data Base Performance Comparisons

Figures 14 and 15 show performance comparisons in terms of percentage differences. These composite plots utilize both the LaRC (figure 14) and ADS (figure 15) air data parameters. Figure 14 is, of course, the percentage difference equivalent of those differences seen in figures 6-10, respectively. For more detailed investigations, figures A5(a) through A5(e) are included in the Appendix of this paper. These

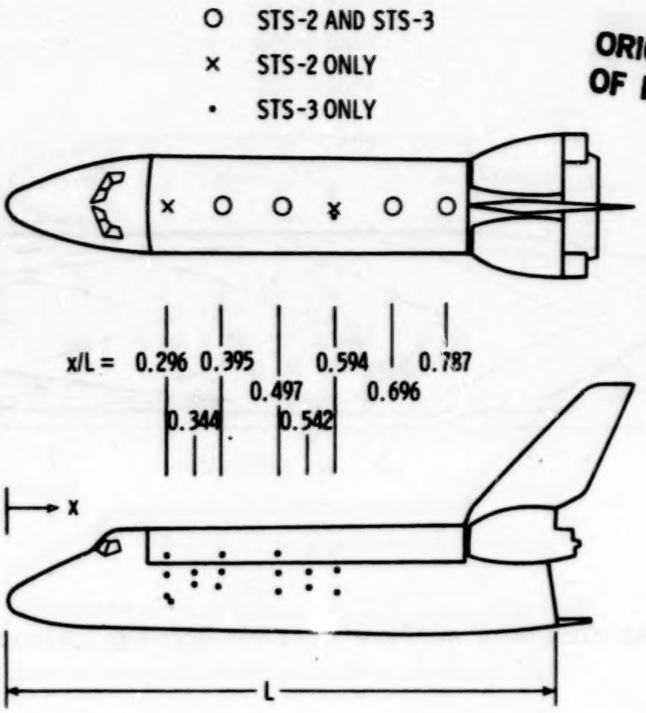
○ STS-2 AND STS-3
× STS-2 ONLY
• STS-3 ONLY
x/L = 0.296 0.395 0.594 0.787
0.497 0.696
0.344 0.542
x
L

Figure 1.- Locations of entry heating rate measurements on Shuttle orbiter's fuselage.

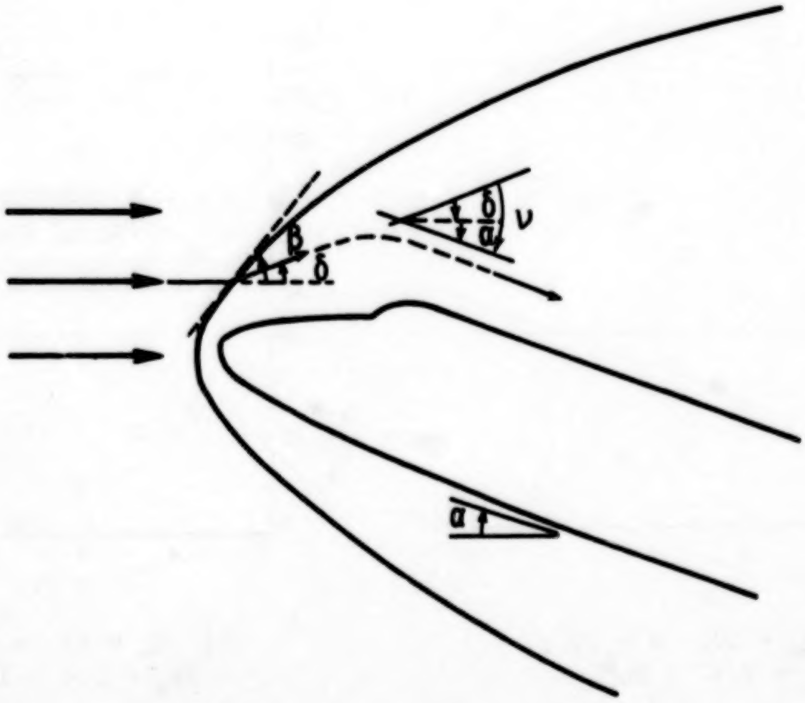

Figure 2.- Flow field model used to compute local leeside properties for leeward centerline heating theory.

C-4

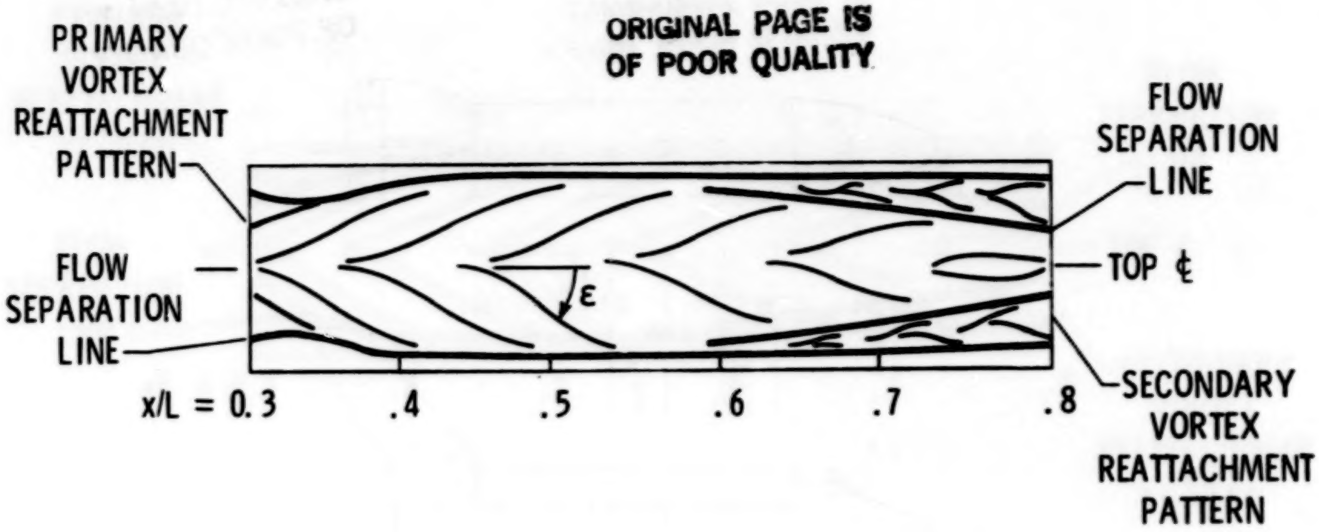
PRIMARY VORTEX REATTACHMENT PATTERN
FLOW SEPARATION LINE
FLOW SEPARATION LINE
ε
TOP ℄
SECONDARY VORTEX REATTACHMENT PATTERN
x/L = 0.3
.4
.5
.6
.7
.8

Figure 3.- Upper fuselage surface pattern showing measurement of flow angle.

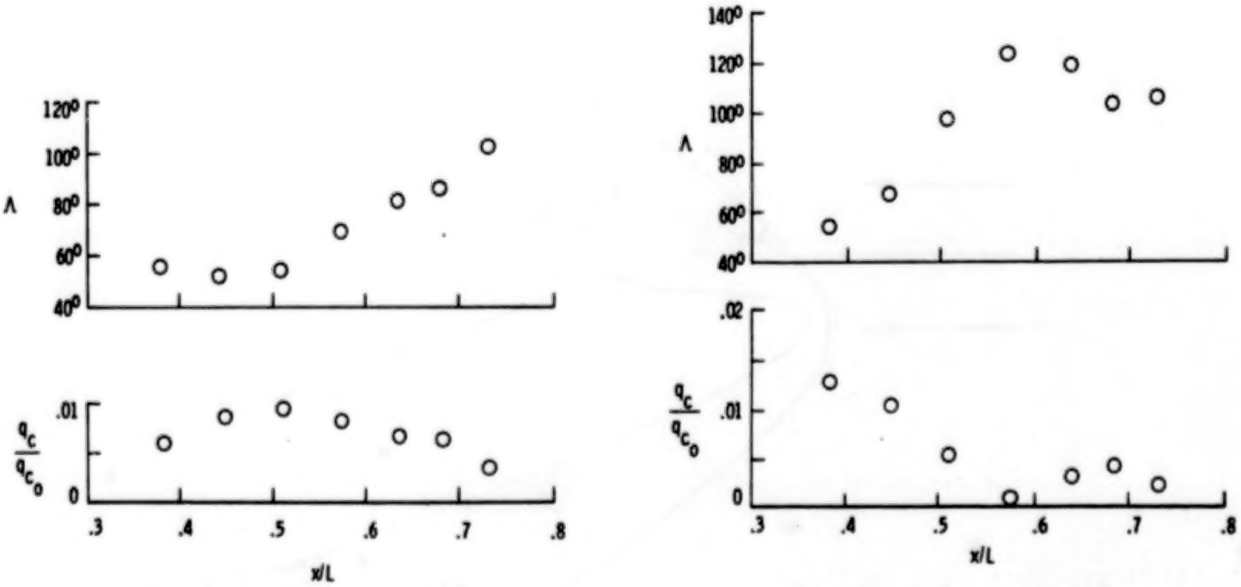

(a) $M_\infty = 10$; $\alpha = 20^\circ$; $Re_\infty = 2.37 \times 10^6$.

(b) $M_\infty = 6$; $\alpha = 30^\circ$; $Re_\infty = 5.4 \times 10^6$.

Figure 4.- Illustration of the inverse relation between effective sweep angle and leeward centerline heating rate.

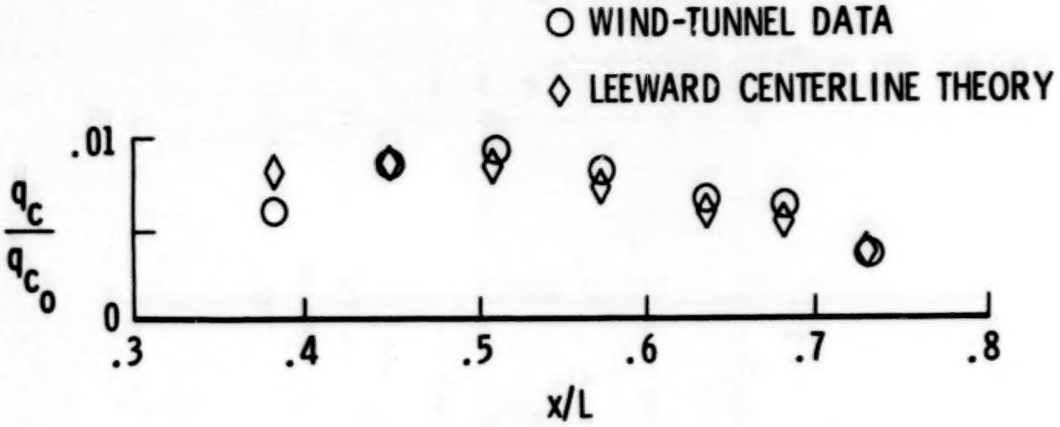

(a) $M_\infty = 10$; $\alpha = 20^\circ$; $Re_\infty = 2.37 \times 10^6$.

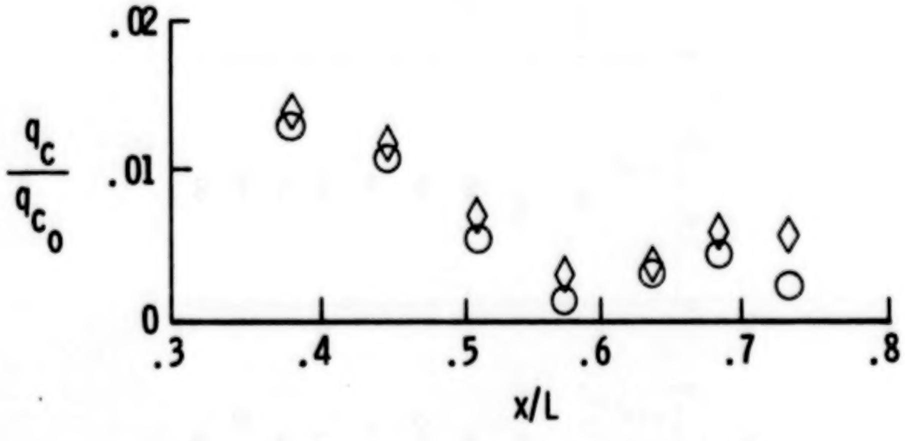

(b) $M_\infty = 6$; $\alpha = 30^\circ$; $Re_\infty = 5.4 \times 10^6$.

Figure 5.- Representative comparisons of leeward centerline heating predictions with wind tunnel data.

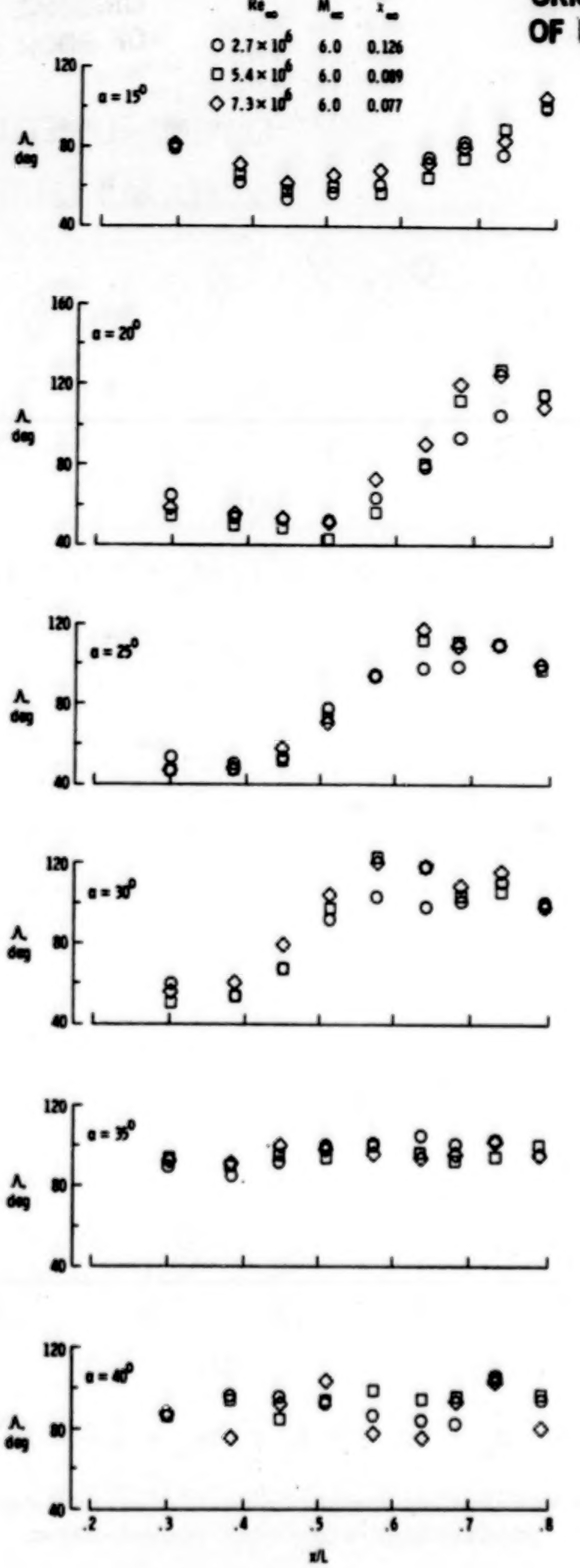

Figure 6.- Effective sweep angles measured from Mach 6 oil flow patterns.

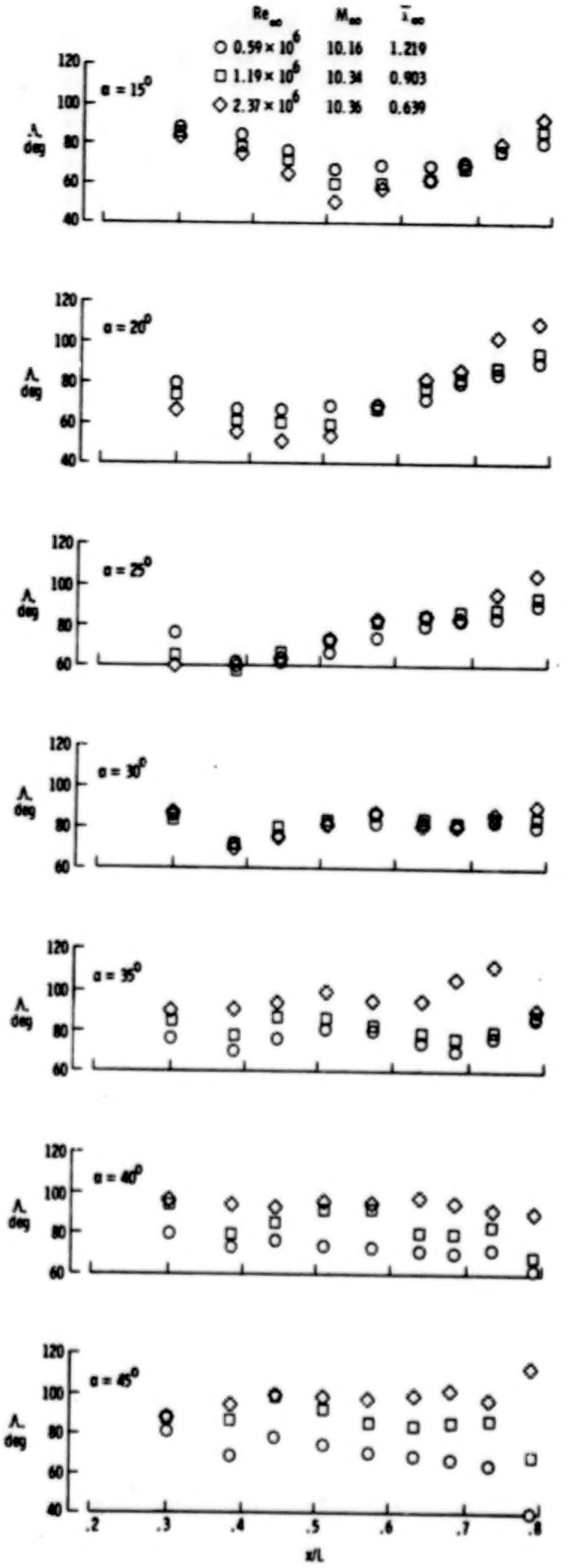

Figure 7.- Effective sweep angles measured from Mach 10 oil flow patterns.

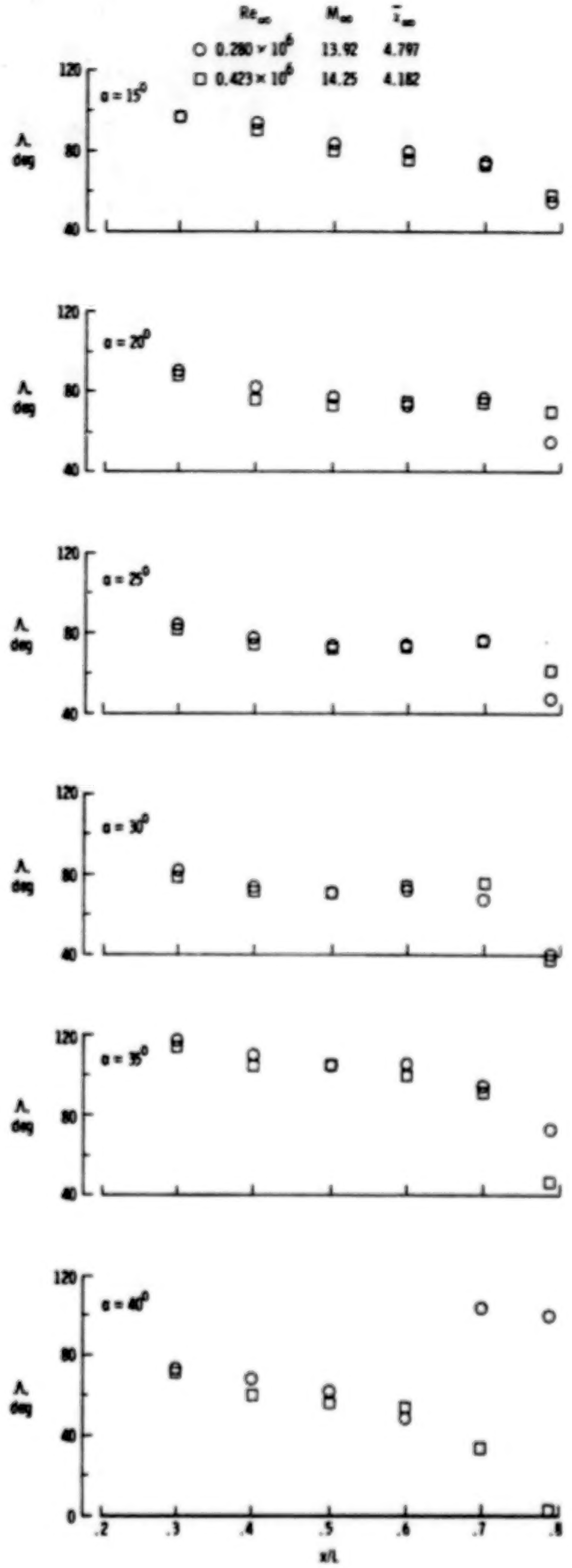

Figure 8.- Effective sweep angles measured from Mach 14 oil flow patterns.

ORIGINAL PAGE IS
OF POOR QUALITY

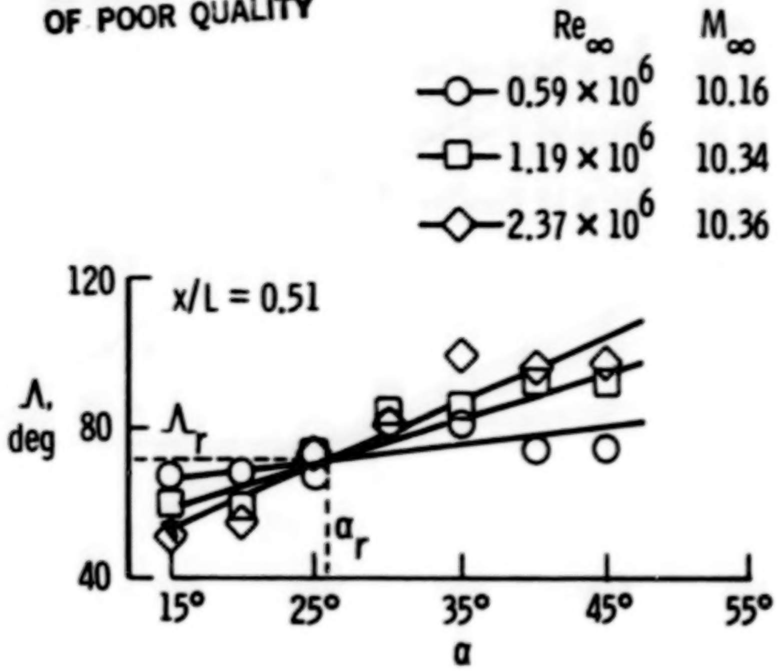

Figure 9.- Illustration of Reynolds number effect on Mach 10 wind tunnel sweep angles.

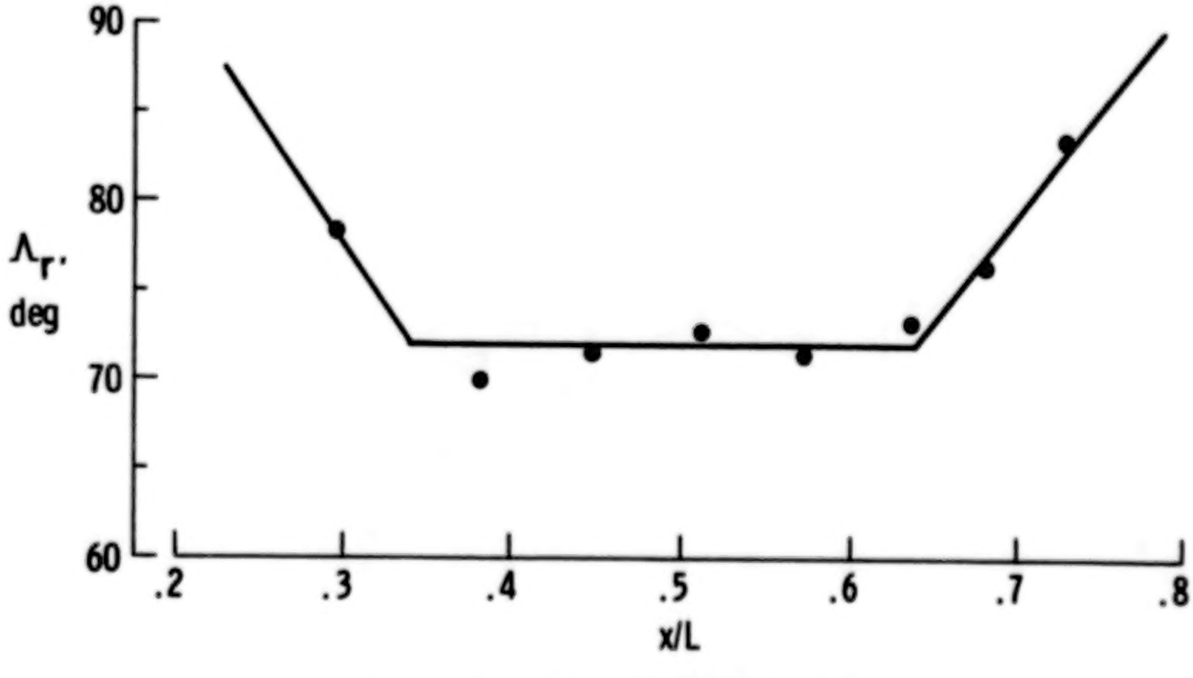

Figure 10.- Axial dependence of Λ_r.

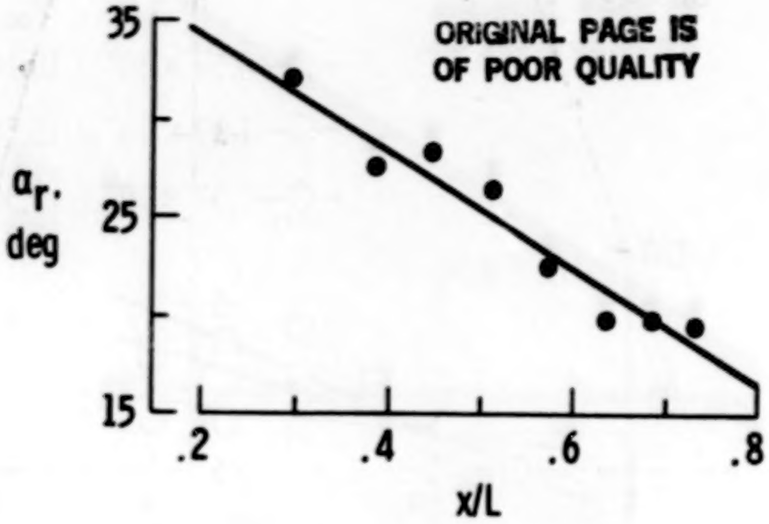

ORIGINAL PAGE IS OF POOR QUALITY

Figure 11.- Axial dependence of α_r.

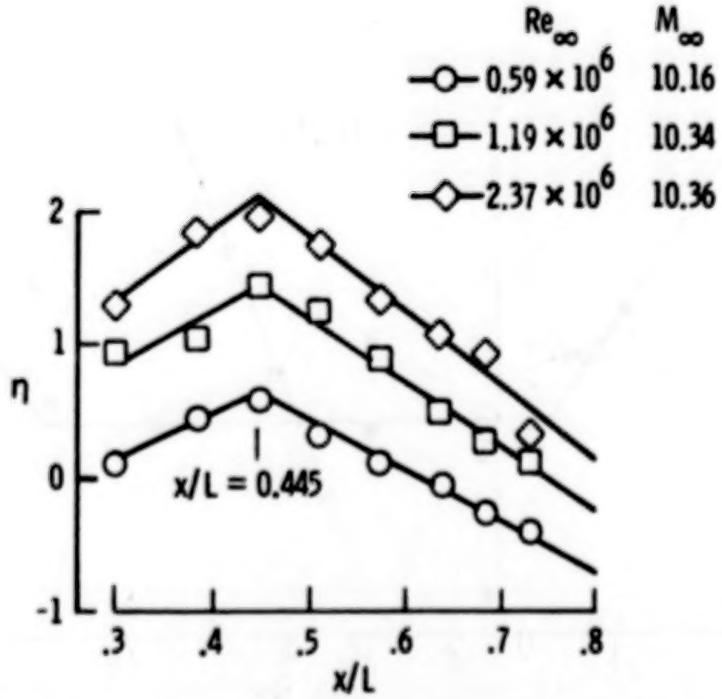

Figure 12.- Slope of Λ vs α as a function of Reynolds number and x/L.

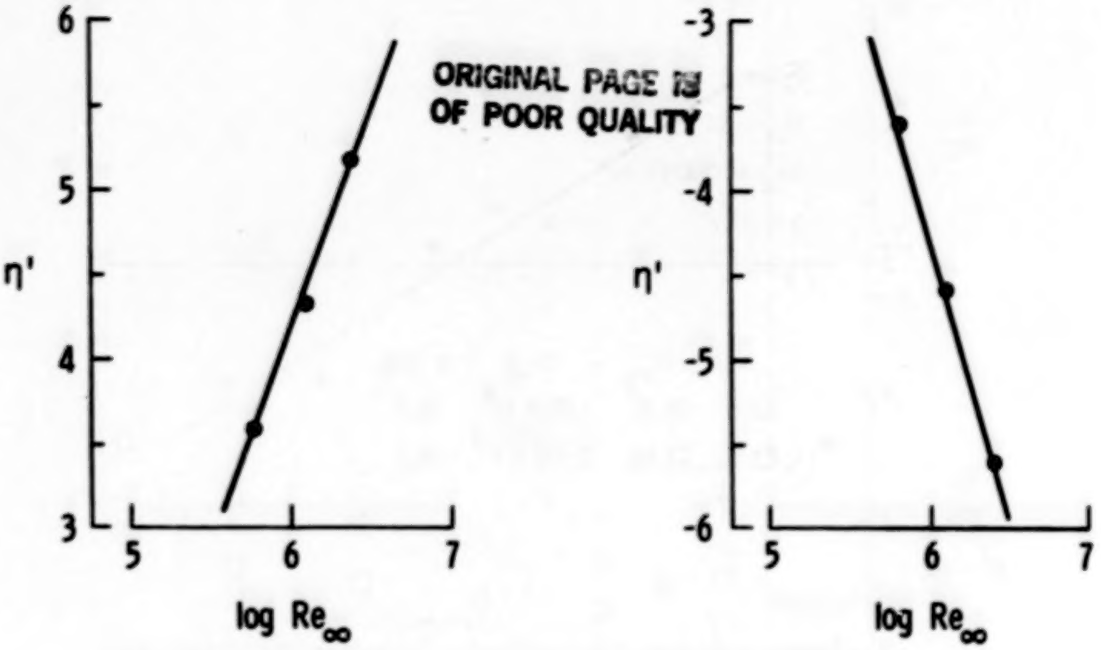

(a) $x/L < 0.445$. (b) $x/L > 0.445$.

Figure 13.- Rate of change of η with respect to Reynolds number.

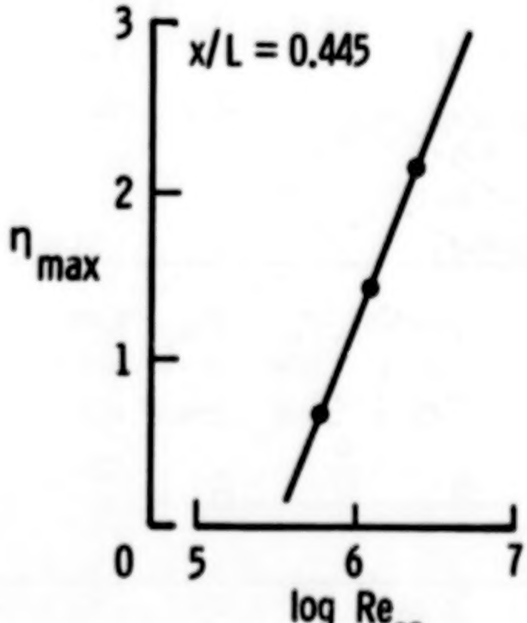

Figure 14.- Extrapolation of η at $x/L = 0.445$ in terms of Reynolds number.

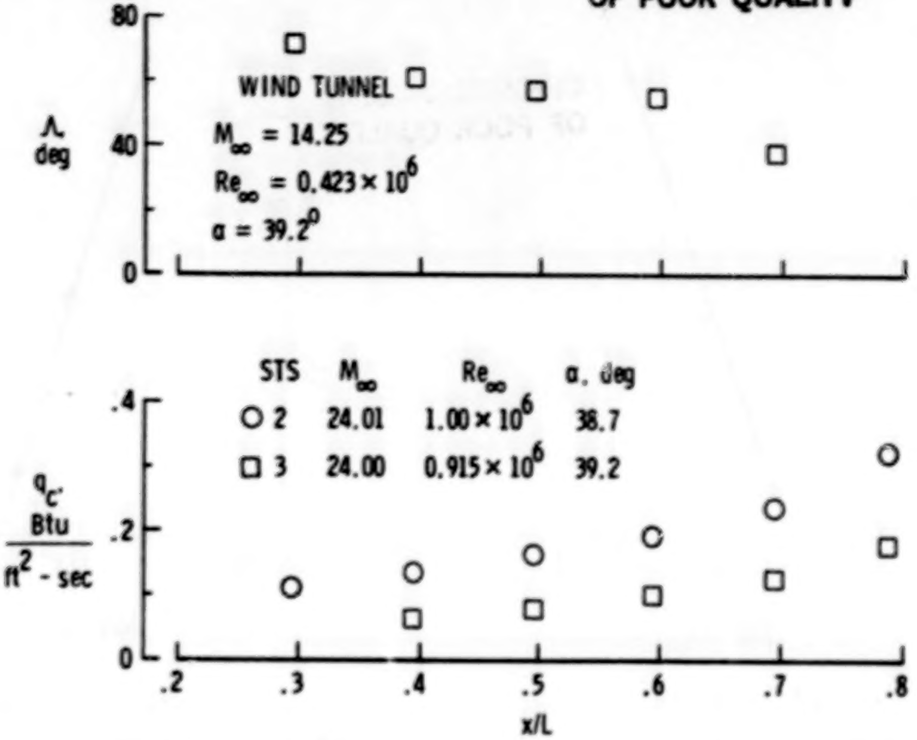

Figure 15.- Comparison of flight leeward centerline heating distributions near M_∞ = 24 with wind tunnel effective sweep angle variations.

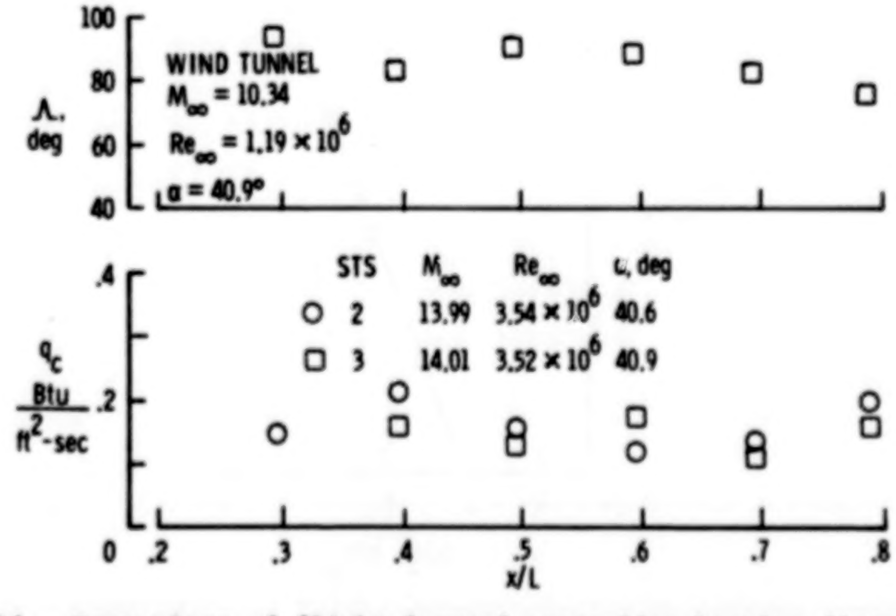

Figure 16.- Comparison of flight leeward centerline heating distributions near M_∞ = 14 with wind tunnel effective sweep angle variations.

ORIGINAL PAGE IS
OF POOR QUALITY

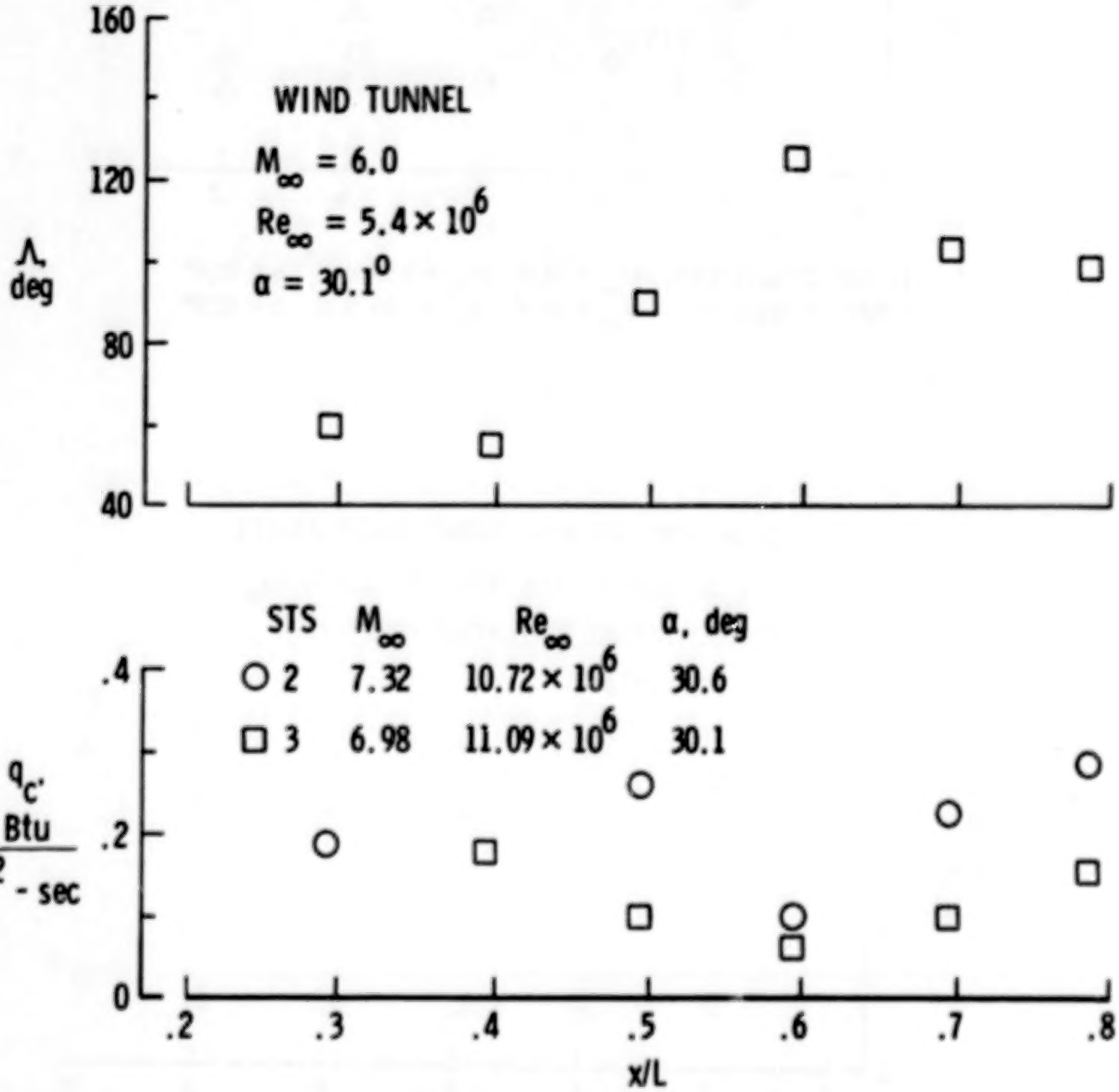

Figure 17.- Comparison of flight leeward centerline heating distributions near $M_\infty = 7$ with wind tunnel effective sweep angle variations.

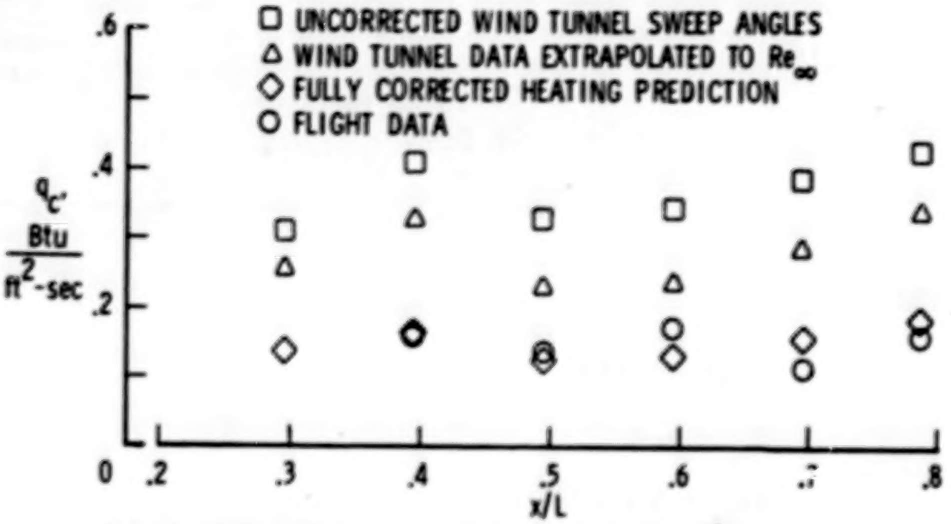

FLIGHT CONDITIONS: $M_\infty = 14.01$, $Re_\infty = 3.52 \times 10^6$, $\alpha = 40.9°$
TUNNEL CONDITIONS: $M_\infty = 10.34$, $Re_\infty = 1.19 \times 10^6$, $\alpha = 40.9°$

(a)

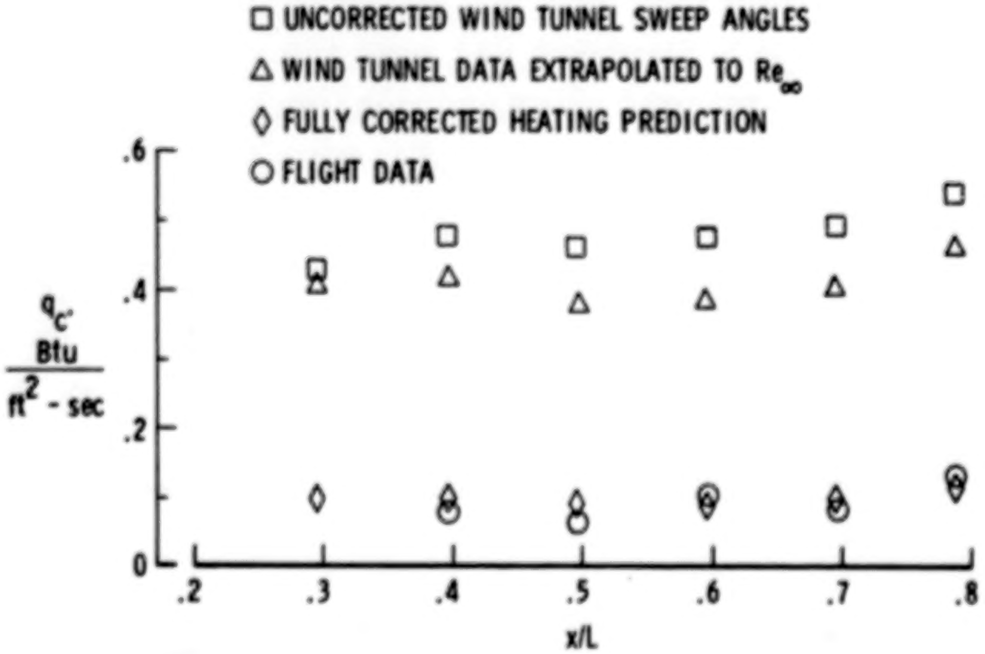

Flight conditions: $M_\infty = 20.00$, $Re_\infty = 1.53 \times 10^6$, $\alpha = 39.8^0$
Tunnel conditions: $M_\infty = 10.16$, $Re_\infty = 0.59 \times 10^6$, $\alpha = 39.8^0$

(b)

Figure 18.- Comparison of flight leeward centerline heating rates with predictions in various stages of correction for the effects of Mach number and Reynolds number.

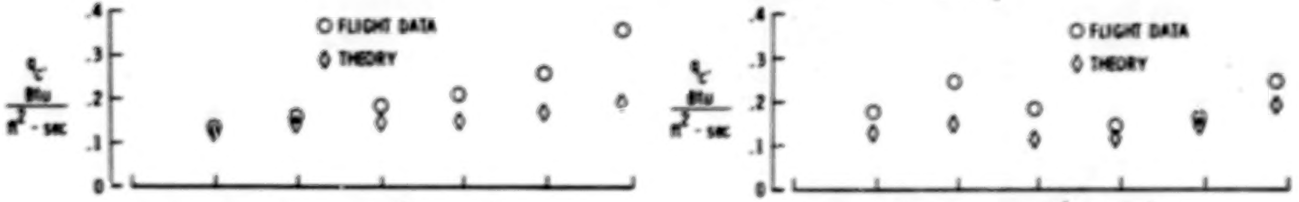

(a) $M_\infty = 24.01$, $Re_\infty = 1.00 \times 10^6$, $\alpha = 38.7^\circ$

(g) $M_\infty = 13.99$, $Re_\infty = 3.54 \times 10^6$, $\alpha = 40.6^\circ$

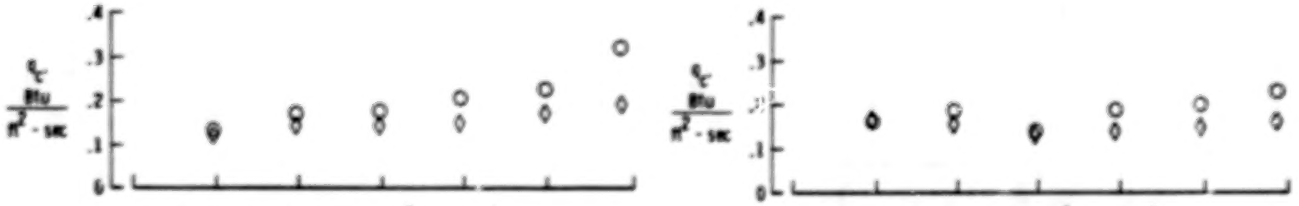

(b) $M_\infty = 22.01$, $Re_\infty = 1.27 \times 10^6$, $\alpha = 38.0^\circ$

(h) $M_\infty = 11.93$, $Re_\infty = 5.04 \times 10^6$, $\alpha = 38.3^\circ$

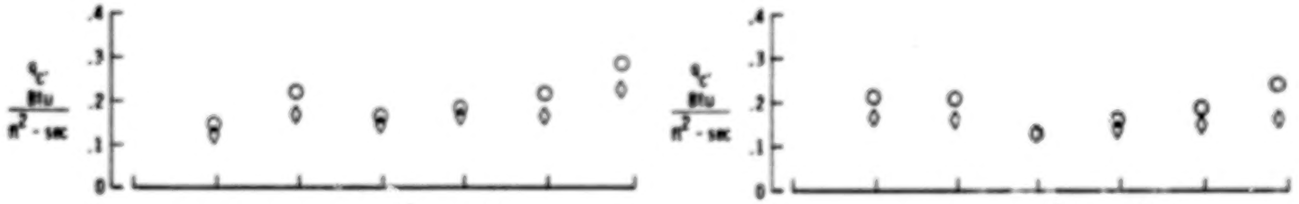

(c) $M_\infty = 20.02$, $Re_\infty = 1.55 \times 10^6$, $\alpha = 45.0^\circ$

(i) $M_\infty = 10.8$, $Re_\infty = 5.4 \times 10^6$, $\alpha = 38.5^\circ$

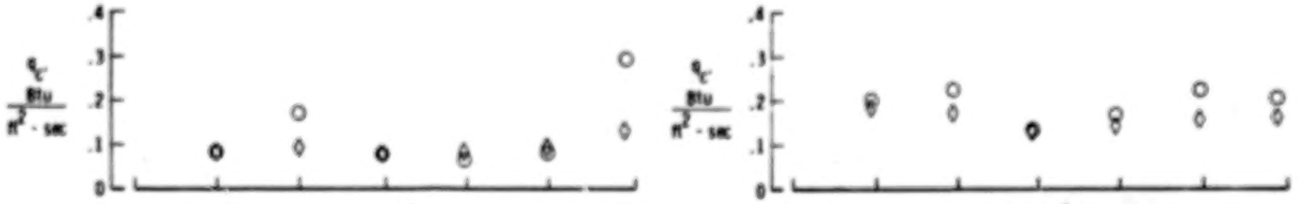

(d) $M_\infty = 17.99$, $Re_\infty = 1.91 \times 10^6$, $\alpha = 41.2^\circ$

(j) $M_\infty = 10.00$, $Re_\infty = 6.24 \times 10^6$, $\alpha = 37.6^\circ$

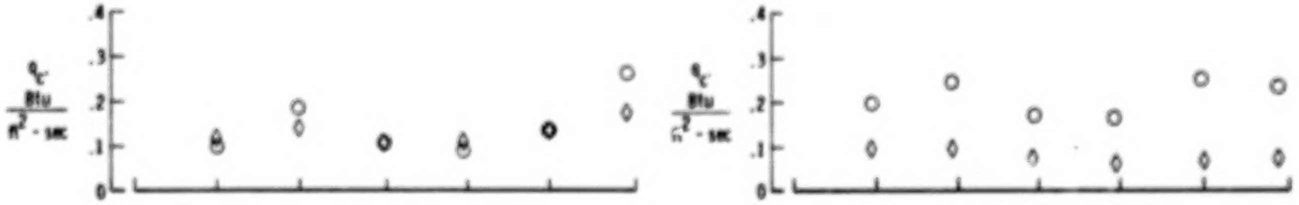

(e) $M_\infty = 16.6$, $Re_\infty = 2.40 \times 10^6$, $\alpha = 40.4^\circ$

(k) $M_\infty = 9.4$, $Re_\infty = 7.29 \times 10^6$, $\alpha = 36.0^\circ$

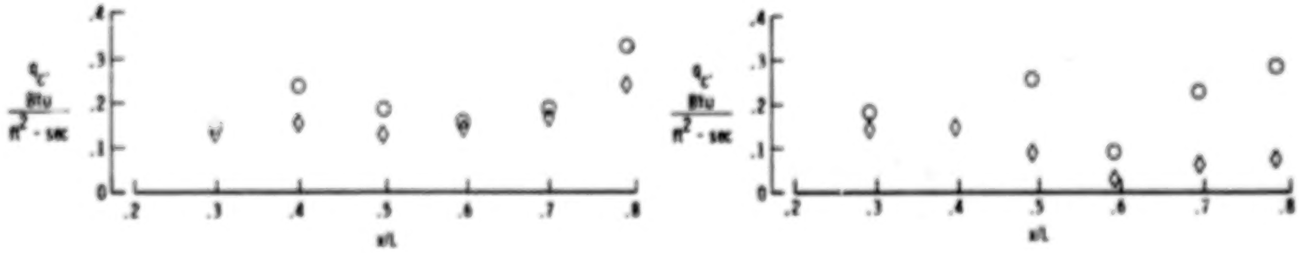

Figure 19.- Comparison of leeward centerline heating predictions with STS-2 flight data.

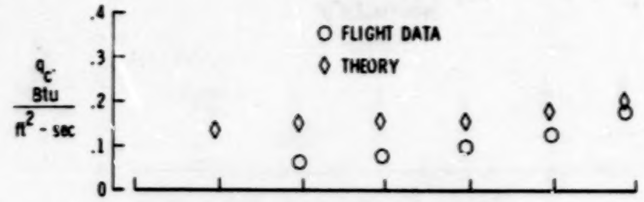

(a) M_∞ = 24.00, Re_∞ = 0.915 × 10^6, α = 39.2°

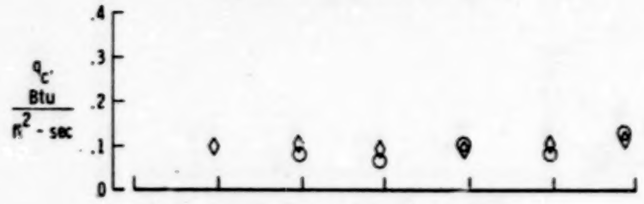

(b) M_∞ = 20.00, Re_∞ = 1.53 × 10^6, α = 39.8°

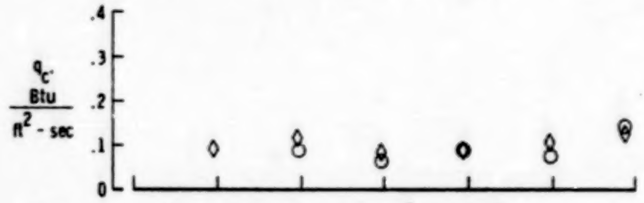

(c) M_∞ = 18.00, Re_∞ = 2.07 × 10^6, α = 39.3°

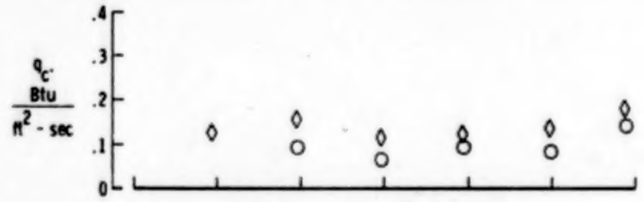

(d) M_∞ = 16.00, Re_∞ = 2.55 × 10^6, α = 40.5°

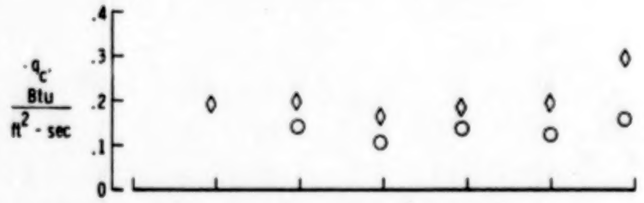

(e) M_∞ = 15.14, Re_∞ = 2.71 × 10^6, α = 43.1°

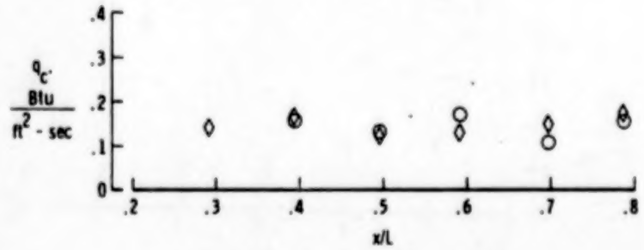

(f) M_∞ = 14.01, Re_∞ = 3.52 × 10^6, α = 40.9°

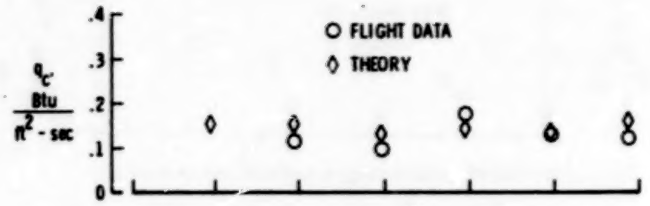

(g) M_∞ = 10.37, Re_∞ = 5.41 × 10^6, α = 38.9°

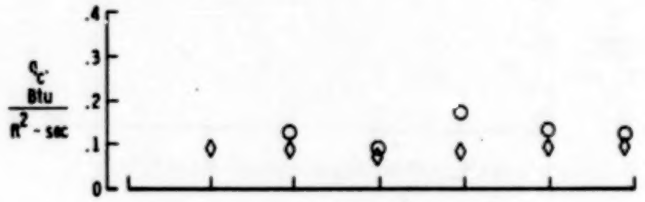

(h) M_∞ = 9.03, Re_∞ = 7.32 × 10^6, α = 35.1°

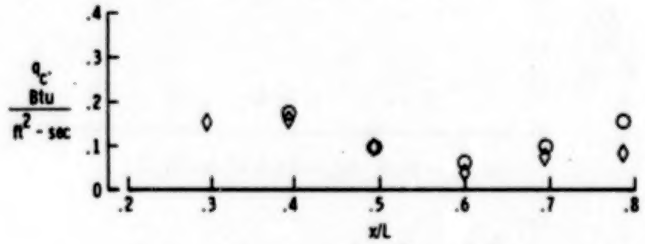

(i) M_∞ = 6.98, Re_∞ = 11.09 × 10^6, α = 30.1°

Figure 20.- Comparison of leeward centerline heating predictions with STS-3 flight data.

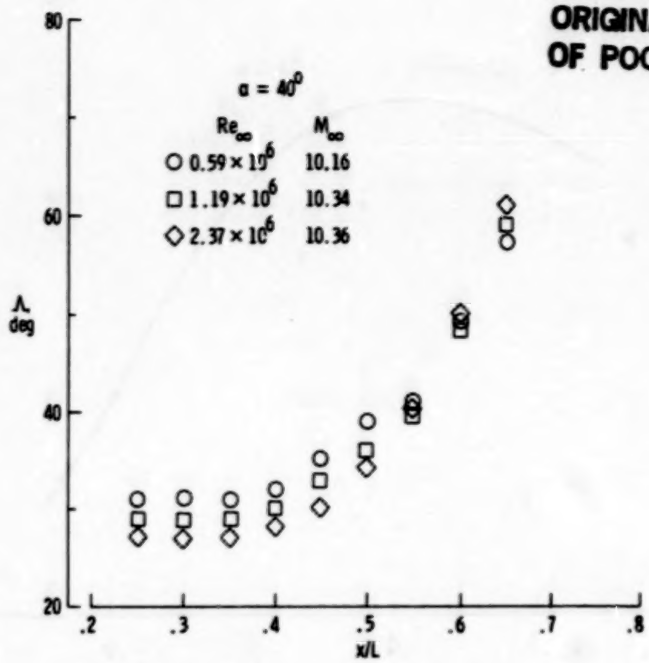

Figure 21.- Effective sweep angles resulting from side fuselage impingement.

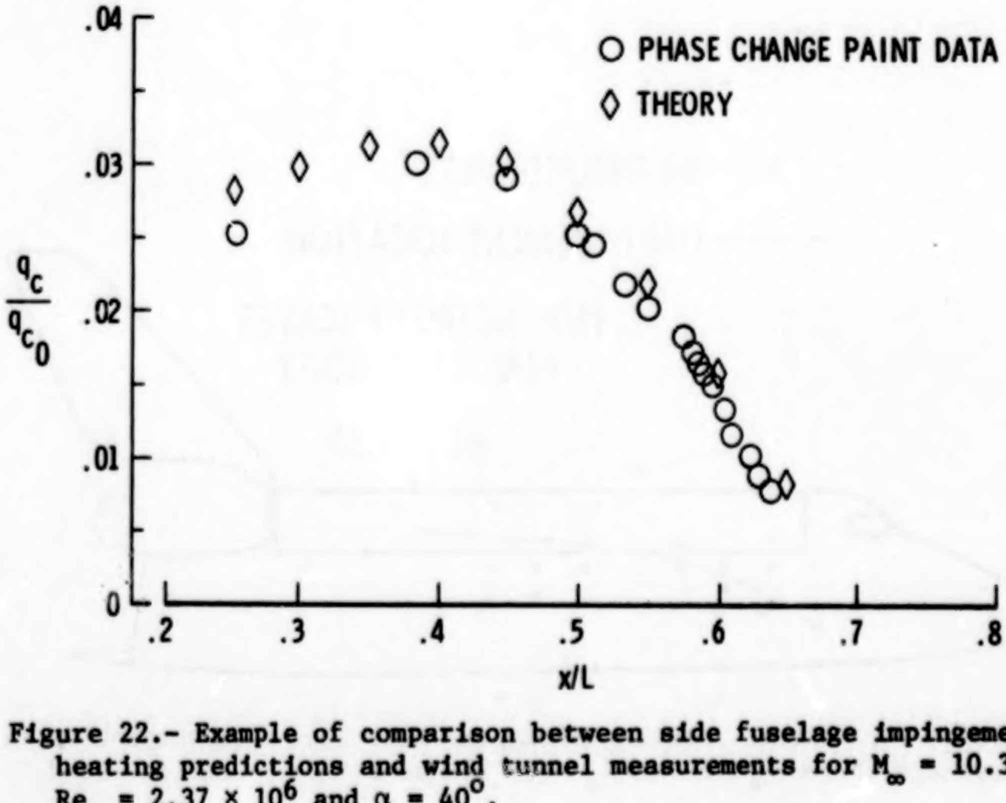

Figure 22.- Example of comparison between side fuselage impingement heating predictions and wind tunnel measurements for $M_\infty = 10.36$, $Re_\infty = 2.37 \times 10^6$ and $\alpha = 40^\circ$.

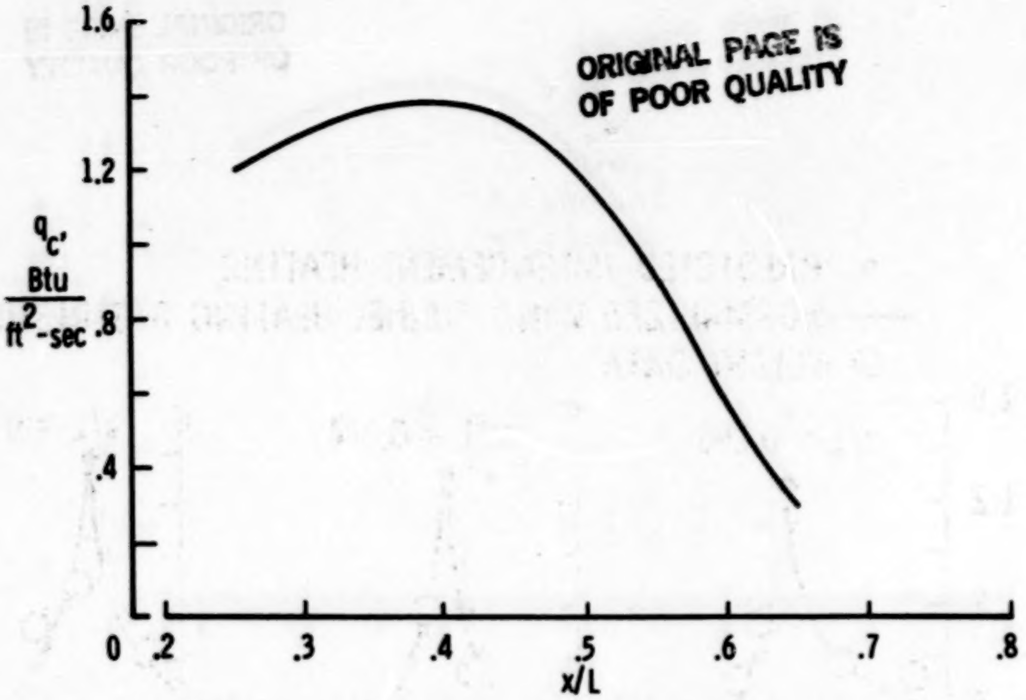

Figure 23.- Predicted side fuselage impingement heating for STS-3 at $M_\infty = 10.37$, $Re_\infty = 5.4 \times 10^6$, and $\alpha = 38.9^\circ$.

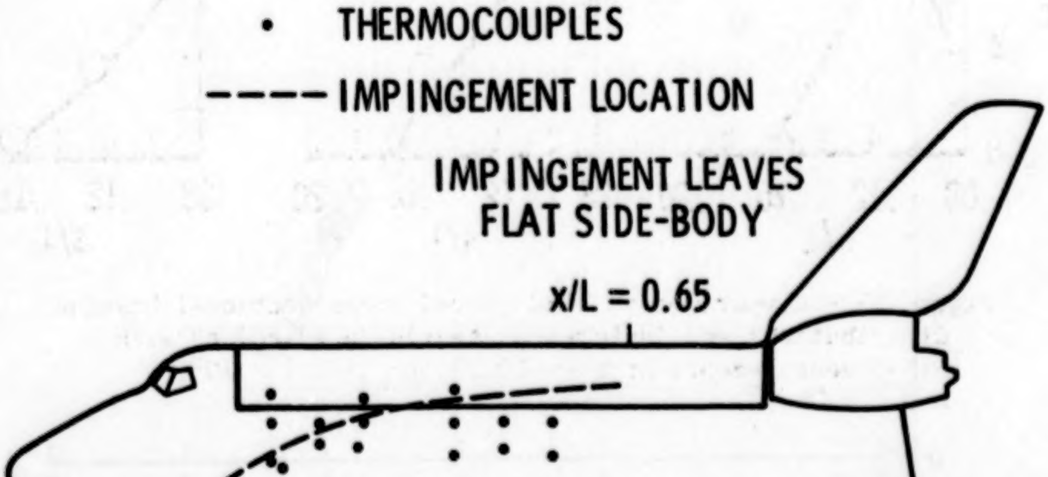
• THERMOCOUPLES
---- IMPINGEMENT LOCATION
IMPINGEMENT LEAVES
FLAT SIDE-BODY
x/L = 0.65

Figure 24.- Predicted location of impingement line with respect to side fuselage thermocouples at $M_\infty = 10.37$ and $\alpha = 38.9^\circ$ during STS-3.

ORIGINAL PAGE IS
OF POOR QUALITY

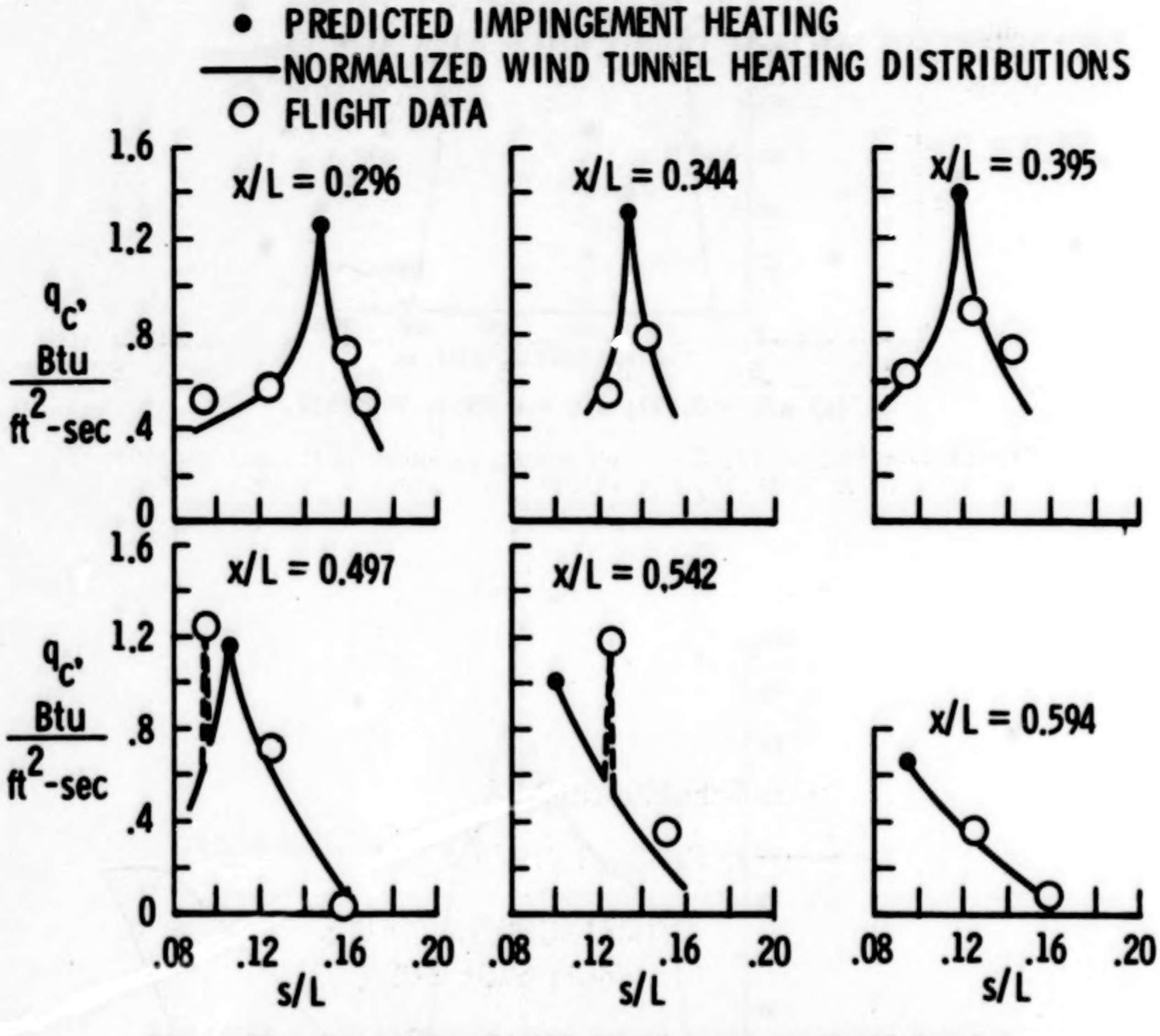

Figure 25.- Comparison of wind tunnel cross-sectional heating distributions and impingement heating predictions with STS-3 measurements at $M_\infty = 10.37$, $Re_\infty = 5.4 \times 10^6$, and $\alpha = 38.9^\circ$.

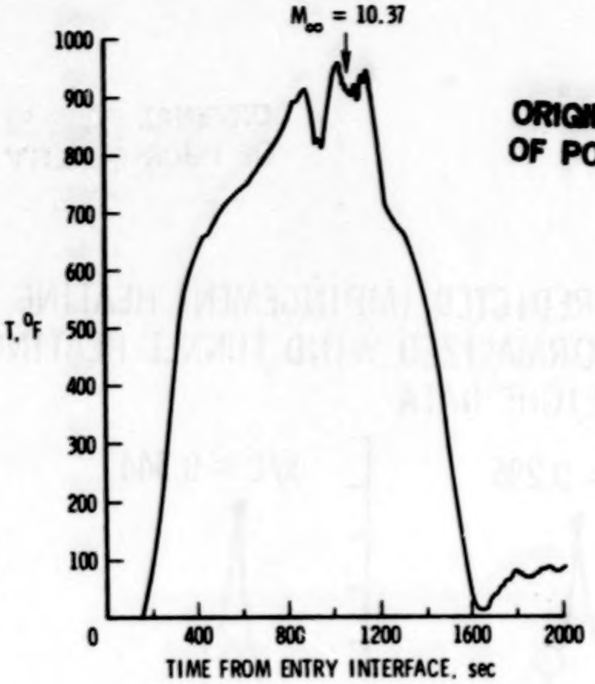

(a) x/L = 0.497; s/L = 0.0950; V07T9924.

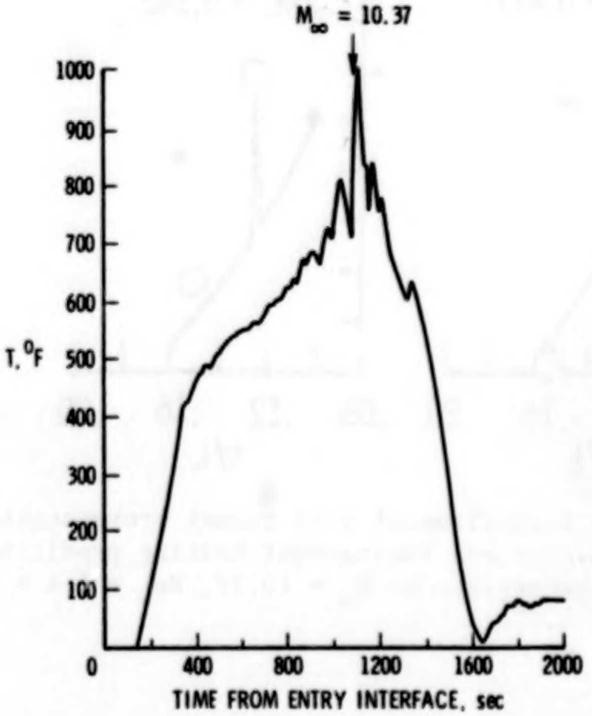

(b) x/L = 0.542; s/L = 0.1248; V07T9905.

Figure 26.- STS-3 side fuselage temperature time histories showing temperature fluctuations for entry times near M_∞ = 10.37.

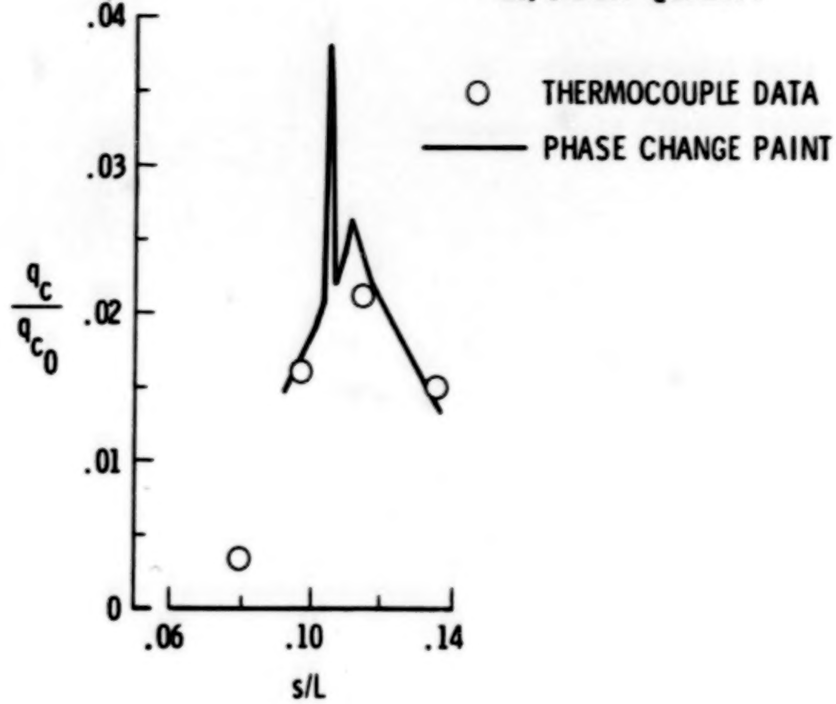

Figure 27.- Example of heating spike in wind tunnel data for $M_\infty = 6$, $Re_\infty = 5.4 \times 10^6$, and $\alpha = 40^\circ$ at $x/L = 0.447$.

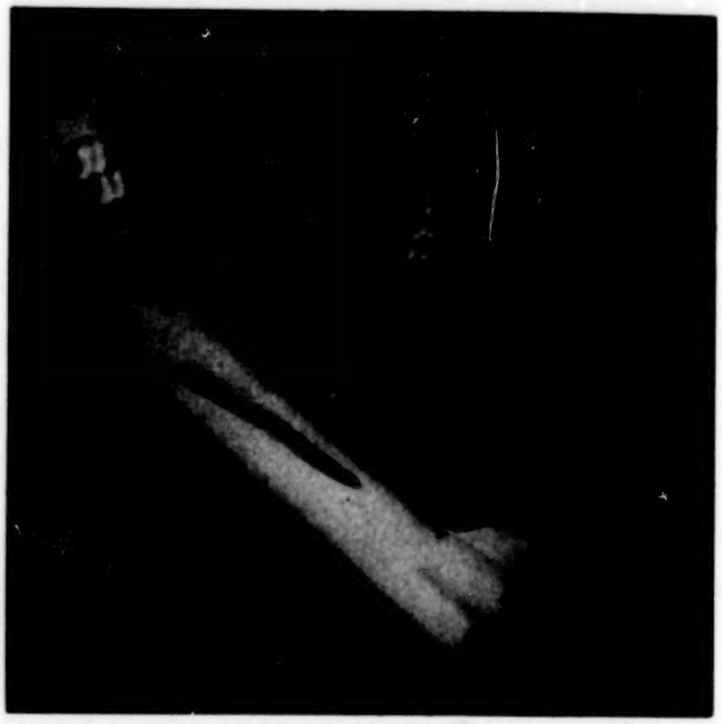

Figure 28.- Pattern of "streak" heating in phase change paint test at $M_\infty = 6$, $Re_\infty = 5.4 \times 10^6$, and $\alpha = 40^\circ$.

N84
10157

UNCLAS

N84 10157 D13

SPACE SHUTTLE ORBITER REUSABLE SURFACE INSULATION FLIGHT RESULTS

Robert L. Dotts, James A. Smith, and Donald J. Tillian
NASA Johnson Space Center
Houston, Texas

SUMMARY

The first five flights of the orbiter Columbia have provided the initial data required to certify the operational performance of the reusable surface insulation (RSI) thermal protection system (TPS). This paper discusses the flight performance characteristics of the RSI TPS. This discussion will be based primarily on postflight inspections and postflight interpretation of the flight instrumentation. TPS modifications of the future orbiters (OV-099, 103, and subs) will also be discussed.

INTRODUCTION

The orbiter thermal protection system (TPS) must protect the primary vehicle structure and other subsystems from the severe aerothermodynamic conditions associated with entry into the Earth's atmosphere. In order to minimize design and development costs, the orbiter vehicle utilized standard aluminum fabrication techniques with the exception of the cargo bay doors and orbiter maneuvering system pods in which the lightweight graphite-epoxy structure was used. Use of these structural materials which have relatively low temperature capability (<350°F) necessitated the design and development of lightweight, thermally efficient thermal protection materials.

A major constraint on the use of conventional TPS materials (such as the ablators or metallic systems that existed in the late 1960's) was the requirement for 100-mission reuse in the oxidizing entry environment at temperatures exceeding 2000°F. Based on these unique requirements, the most promising class of materials at the time was the ceramics; this class is virtually insensitive to the deteriorating effects of oxidation. After considerable development activity, the rigidified silica TPS evolved, which possessed a stable chemical structure along with the unique thermal properties required for a minimum weight TPS.

Five successful flights of the orbiter Columbia have provided the initial data to verify the thermal performance, structural integrity, and reusability of the tile TPS. Overall, the silica tile TPS has performed remarkedly well after multiple exposures to severe natural environmental conditions as well as the induced thermal and load environments. There have been some minor localized areas of the orbiter in which heating exceeded expectations; however, these areas have been amenable to design corrections, and vehicle turnaround has not been adversely affected. The amount of TPS refurbishment activities between flights is approaching the

PAGE 948 INTENTIONALLY BLANK

PRECEDING PAGE BLANK NOT FILMED

level of effort required to meet operational vehicle turnaround timetables.

This paper will provide a brief description of the design characteristics of the TPS tile system, a summary of the design goals and requirements, the principal findings of the flight test program, and future TPS changes.

SYSTEM DESCRIPTION

The reusable ceramic tile TPS has evolved after more than a decade of dedicated development activity by both governmental and industrial organizations. This unique TPS material, which is used on ~70% of the external surface of the orbiter Columbia, is manufactured in two forms. The lower density form (termed LI-900) has a nominal density of 9 lb/ft^3, the higher density form (termed LI-2200) has a nominal density of 22 lb/ft^3. These materials are fabricated in the form of tiles covered with an external borosilicate glass coating. Two types of coatings are used on the LI-900 tiles. A black version with good high-temperature emittance is used on the lower surface of the orbiter, and a white version with low solar absorptance for orbital thermal control purposes is used on the upper surfaces of the orbiter. The tiles are then bonded to a strain isolation pad (SIP), and then the SIP is bonded to the orbiter structure. Figure 1 shows the installed tile/SIP configuration. The other reusable surface insulation material (termed flexible reusable surface insulation (FRSI)) is the simplest TPS material on the orbiter and consists of a needled nylon felt material that is coated with a thin silicone elastomer film. Locations of the various thermal protection materials that are applied to the orbiter Columbia structure are shown in figure 2. The material characteristics and detailed descriptions of the design applications have been presented in references 1-3.

DESIGN REQUIREMENTS

The application of the relatively brittle silica tiles for the orbiter TPS necessitated innovative design approaches. The key factor of the design was the requirement to operate satisfactorily for 100 missions with minimal maintenance or refurbishment.

The TPS is designed for the entry thermal environments that encompass mission parameters such as the orbit inclination, vehicle entry angle of attack, attitude, size of payload (e.g., total entry weight), and downrange and crossrange emissions. The TPS design mission is known as mission 3A normal-nominal ascent, single-orbit polar mission, and mission 3B entry. The design trajectory for this mission (14414.1c) was used to initially size the orbiter TPS and resultant outer mold line. Figure 3 illustrates the predicted maximum temperature distributions on the surface of the orbiter during the entry phase of the design mission. Figure 4 compares the design entry mission maximum reference heating rate and heat load with the STS-1 thru -5 mission reference values. As can be seen, the STS-1 thru -5 missions were ~10-15% lower than the design mission in heat load and ~5-30% lower in maximum heating rate. Later missions are planned to verify the design mission capability.

The RSI tile is an excellent thermal insulation and is designed to reradiate a majority of the entry heat back to space. To perform its intended thermal function, the TPS must also sustain the other induced environments such as the launch vibroacoustics and structural deflections, on-orbit cold soak, and exposure to the natural environments of wind and rain.

To insure that each tile maintains its structural integrity and attachment to the vehicle structure, the vehicle loads were defined, then the detailed loading mechanisms which induce critical stresses in the tiles were identified, followed by detailed stress analyses which predicted the flight margins for each tile. The various sources of tile stresses, the stress analysis methodology, descriptions of the various structural integrity tests and verification activities are described in reference 4.

FLIGHT TEST PROGRAM RESULTS

Five successful flights of the orbiter Columbia have provided significant thermal-structural performance data as well as reuse characteristics of the silica-tile thermal protection system. The primary trajectory parameters (i.e., altitude, velocity, and vehicle angle of attack) during the five flights have been relatively similar with the exception of control surface deflections. The flight data is available in the form of thermal responses from the development flight instrumentation and from observations during the detailed postflight inspections conducted at the landing sites and at the Kennedy Space Center (KSC).

THERMAL PERFORMANCE

Thermal performance data was obtained during each of the five flights of the orbiter Columbia. Complete entry data was obtained only during STS-2, -3, and -5 due to recorder malfunctions during the STS-1 and -4 flights. Partial data was obtained during the STS-1 and -4 flights by data transmission to a ground station after the entry blackout period. The basic TPS thermal response data is obtained primarily from thermocouples located on the tile surfaces, at various depths in the tile, at various locations on the tile sidewalls, and at numerous locations on the orbiter structure.

Sufficient data has been acquired to describe the primary aerothermodynamic characteristics of the orbiter configuration for the conditions under which it has been flown. In general, transition effects have occurred later than expected. The surface temperature distributions and magnitudes that occurred during entry were within expected ranges. However, there were some localized areas where surface temperatures exceeded the design thermal limits of the TPS materials. Figure 5 shows an area of FRSI that experienced overtemperature conditions on the aft side of the OMS Pod. Figure 6 shows an area of FRSI that experienced overtemperature conditions on the side of the payload bay doors.

Gap heating in a number of locations was more severe than predicted. The excessive gap heating resulted in some cases of tile sidewall shrinkage, filler bar overtemperature (charring), and in one case, localized severe structural temperature gradients. Extensive test programs were undertaken at JSC to reproduce the filler bar charring observed during the flights and to demonstrate that the vehicle corrections (i.e., partial gap filler installations) would perform satisfactorily. Refined numerical solutions as discussed in reference 5 were also conducted to understand the complex physical phenomena that were involved.

Heating levels on the lower forward fuselage were ~200-300°F lower than predicted. This is attributed to the noncatalytic characteristic of the coated tiles. With the lower surface energy input into the tiles on the lower surface, the structural temperatures responded accordingly. In addition, an internal structure convective cooling phenomenon was observed. This effect started late in the entry (Mach = 2.5) when the orbiter vent doors opened. In some areas, the effect suppressed the structural temperature response by as much as 20°F. Peak surface temperatures for STS-2, -3, and -5 are shown in figures 7-9. Structural temperature rise data from all five flights are shown in figures 10-12. In general, consistent performance has been observed. When surface temperature is used as an input factor in math models, good agreement between flight data and analyses is obtained as shown in figures 13-15.

STRUCTURAL PERFORMANCE

The structural integrity of the tile and its attachment system has been excellent during the flight test program. None of the critical black tiles on the lower surface of the orbiter has been lost. Some undensified OMS pod tiles were lost (figure 16) during STS-1. This was due to improper machining operations performed during operations at KSC just prior to STS-1. There was also a loss of some undensified tiles during STS-3 on the upper forward fuselage area (figure 17) and upper body flap (figure 18), which was determined to be due to excessive use of the tile rewaterproofing material. In general, however, it can be said that the strength integrity of the tile and its attachment system has been adequate for the induced environments experienced to date.

MOISTURE

Early in the TPS development, prevention of moisture entrapment and/or moisture absorption after exposure to the natural environment at the launch site was recognized as a particularly difficult problem. After extensive development efforts, the best exterior water repellant material was selected for use on the orbiter. During the STS-2 thru -5 flights, this material has shown marginal performance in view of the loss of portions of tiles due to moisture absorption during STS-2, loss of undensified tiles on the upper surfaces of the vehicle during STS-3 due to the effects of the water repellant material solvent, and excessive moisture absorption prior to the STS-4 launch.

TILE DAMAGE AND REMOVAL EXPERIENCE

The numbers and causes for removal of tiles that have occurred during the turnaround activities at KSC are shown in table 1. The number of tiles requiring removal between succeeding flights is declining and is less than the levels projected for the operational program. The majority of the tiles that have been damaged during the ascent phase by various debris sources have shown no adverse degradation of their thermal performance. Most of the tile damage has been readily repairable by means of ceramic filler agents or silica slurry materials that are brushed on. The flight data to date indicates that these repairs have multimission life capabilities.

TPS CHANGES FOR FUTURE ORBITERS

During the fabrication of the orbiter Columbia, considerable difficulty was experienced in the installation of the thin, relatively fragile, white tiles, particularly on the front of the highly curved OMS pods. This led to use of a relatively new TPS material called flexible insulation (FI) on the OV-099 OMS pods instead of the white tile used on the Columbia. The FI, flexible silica cloth insulation blanket development is discussed in reference 6.

Virtually all the white tile will be replaced with FI blankets on the OV-103 and 104 orbiters. The higher heating on the sides of the fuselage and on the OMS pods noted during the OFT program was factored into the FI thickness design for OV-103 and OV-104. This should allow the OV-103 and OV-104 orbiters to fly the hotter western test range (WTR) missions.

Another change incorporated in the OV-103 and OV-104 design was use of another relatively new TPS material, called fiber reinforced composite insulation (FRCI-12), instead of the high-density LI-2200 tile. Reference 7 describes the development of this lightweight high-strength tile material.

CONCLUDING REMARKS

The thermal/structural performance of the reusable surface insulation TPS during the first five flights has been better than our most optimistic projections. The structural attachment of the critical black tiles on the lower surface has been excellent, and no adverse degradation of the tiles or the attachment system has occurred. There have been localized overtemperature conditions experienced on the upper surface which have necessitated minor repairs to the TPS during the ground turnaround operations. Also, excessive gap heating conditions occurred in a number of gaps on the lower surface and required minor turnaround refurbishment. However, all of these problems areas have been amenable to either design corrections or turnaround repairs, and satisfactory performance is expected during the operational flights. Tile refurbishment and replacement have been at the levels of effort projected for the operational flights. The advanced TPS materials that will be used on future orbiters should upgrade TPS performance to the levels required for the WTR missions as well as lower the amount of refurbishment activities required between flights.

REFERENCES

1. Korb, L. J., and Clancy, H. M., Space Shuttle Orbiter Thermal Protection System: A Material and Structural Overview, Material and Process Applications - Land, Sea, Air, Space; Proceedings of the 26th National Symposium and Exhibition, Society for the Advancement of Material Process Engineering, Los Angeles, CA, April 1981, pp. 232-249.

2. Dotts, R. L., Battley, H. H., Hughes, T. J., and Neuenschwander, W. E., Space Shuttle Orbiter-Reusable Surface Insulation Subsystem Thermal Performance, AIAA Paper No. 82-0005 , January 1982.

3. Dotts, R. L., Tillian, D. L., and Smith, J. A., Space Shuttle Orbiter-Reusable Surface Insulation Flight Performance, Proceedings of the AIAA/ASME/ASCE/AMS 23rd Structures, Structural Dynamics and Materials Conference, May 1982, pp. 16-22.

4. Moser, T. L., and Schneider, W. C., Strength Integrity of the Space Orbiter Tiles, AIAA Paper No. 81-2469, November 1981.

5. Smith, D. M., Petley, D. N., Edwards, C. L. W., and Patten, A. B., An Investigation of Gap Heating Due to Stepped Tiles in Zero Pressure Gradient Regions of the Shuttle Orbiter Thermal Protection System. AIAA Paper No. 83-0120, January 1983.

6. Goldstein, H. E., Leiser, D., Larson, H., and Sawko, P., Improved Thermal Protection System for the Space Shuttle Orbiter, Paper presented at the AIAA/ASME/ASCE/AMS 23rd Structures, Structural Dynamics and Materials Conference, New Orleans, LA, May 10-12, 1982.

7. Leiser, D. B., Smith, M., and Goldstein, H. E., Developments in Fibrous Refractory Composite Insulation. Ceramic Bulletin, Vol. 60, No. 11, November 1981, pp. 1201-1204.

ORIGINAL PAGE IS
OF POOR QUALITY

TABLE 1.- POSTFLIGHT TPS TILE REMOVAL SUMMARY

		POST STS-1	POST STS-2	POST STS-3	POST STS-4	POST STS-5**
RELATE TO OPERATIONAL TURN-AROUND	INFLIGHT DAMAGED	247	109	113	122	119
	LOOSE (DETECTED BY EXCESSIVE STEP)	158	18	15	3	6
	SCORCHED FILLER BAR	246	47	39	36	10
	GROUND DAMAGED	55	13	41	44	36
	FAILED PULL TEST AFTER RE-INSTALLATION	17	7	0	5	1
	SUB TOTALS	723	194	208	210	172
OFT UNIQUE	INSTRUMENTATION REWORK	73	13	3	4	0
	FLIGHT EXPERIMENTS	20	11	11	2	0
	ENGR. MODIFICATIONS	52	17	0	12	215
	ASSESS FOR STRUCTURAL EVAL/ REWORK	72	8	22	17	34
	ENGR. EVALUATIONS	* 22	21	18	26	14
	MISCELLANEOUS	59	5	2	3	0
	DENSIFICATION OF TILES NOT DENSIFIED PRIOR TO STS-1	526	202	783	0	1239
	TOTALS	***1547	471	1047	274	1674

*NOTE 1 - MANY INCLUDED IN MISC CATEGORY FOR POST STS-1 TURNAROUND

**NOTE 2 - AS OF 2/7/83, TURNAROUND ACTIVITY NOT COMPLETE

***NOTE 3 - DOES NOT INCLUDE THE 379 TILES THAT REQUIRED REINSTALLATION AS A RESULT OF THE N_2O_4 SPILL THAT OCCURRED JUST PRIOR TO STS-2

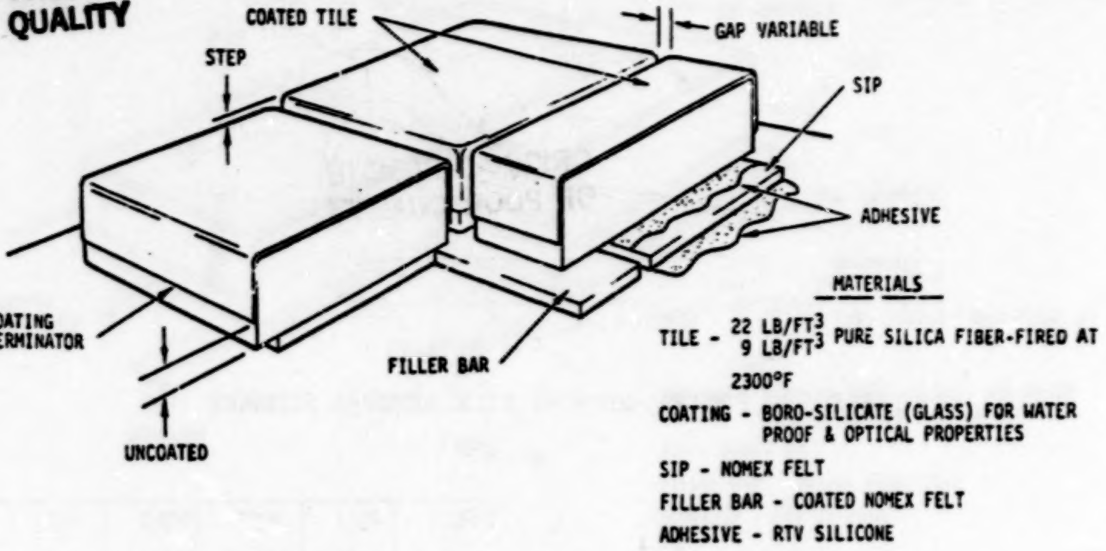
COATED TILE
GAP VARIABLE
STEP
SIP
ADHESIVE
COATING TERMINATOR
FILLER BAR
UNCOATED
MATERIALS
TILE - 22 LB/FT^3 / 9 LB/FT^3 PURE SILICA FIBER-FIRED AT 2300°F
COATING - BORO-SILICATE (GLASS) FOR WATER PROOF & OPTICAL PROPERTIES
SIP - NOMEX FELT
FILLER BAR - COATED NOMEX FELT
ADHESIVE - RTV SILICONE

Figure 1.- Tile system configuration.

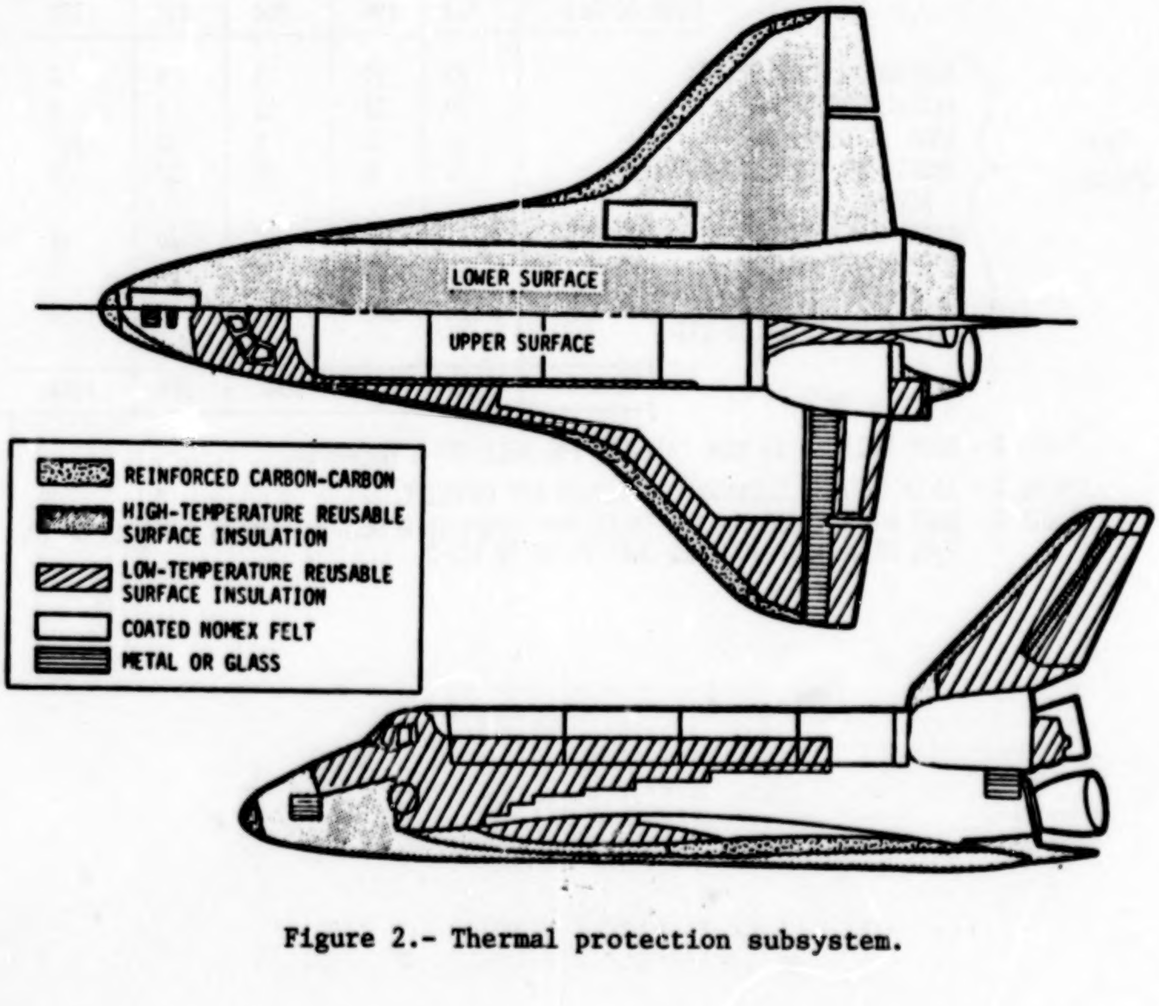
LOWER SURFACE
UPPER SURFACE
REINFORCED CARBON-CARBON
HIGH-TEMPERATURE REUSABLE SURFACE INSULATION
LOW-TEMPERATURE REUSABLE SURFACE INSULATION
COATED NOMEX FELT
METAL OR GLASS

Figure 2.- Thermal protection subsystem.

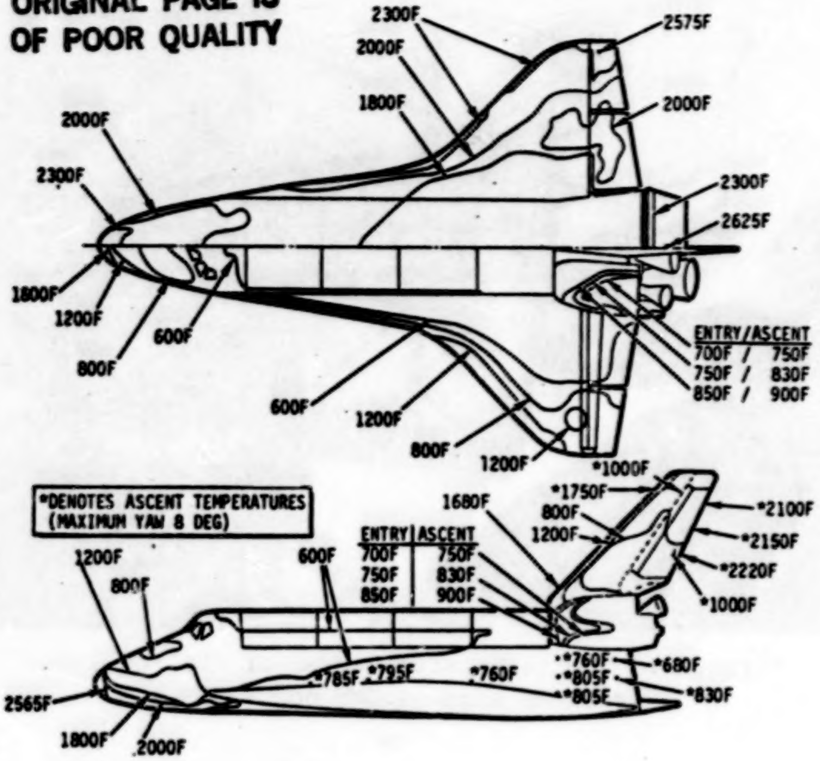
2300F
2575F
2000F
1800F
2000F
2000F
2300F
2300F
2625F
1800F
1200F
600F
800F
ENTRY/ASCENT
700F / 750F
750F / 830F
850F / 900F
600F
1200F
800F
1200F
*1000F
*DENOTES ASCENT TEMPERATURES
(MAXIMUM YAW 8 DEG)
1680F
*1750F
800F
1200F
*2100F
*2150F
*2220F
*1000F
ENTRY ASCENT
700F 750F
750F 830F
850F 900F
600F
1200F
800F
*785F
*795F
*760F
*760F
*805F
*805F
*680F
*830F
2565F
1800F
2000F

Figure 3.- Orbiter design entry isotherms.

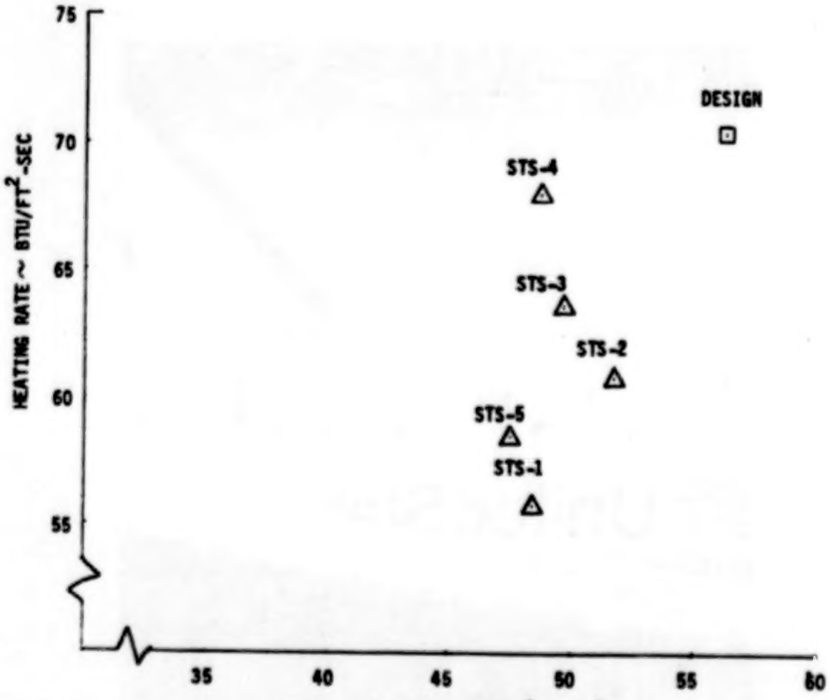

Figure 4.- Comparison of reference heating conditions (design versus STS-1 thru STS-5).

ORIGINAL PAGE IS
OF POOR QUALITY

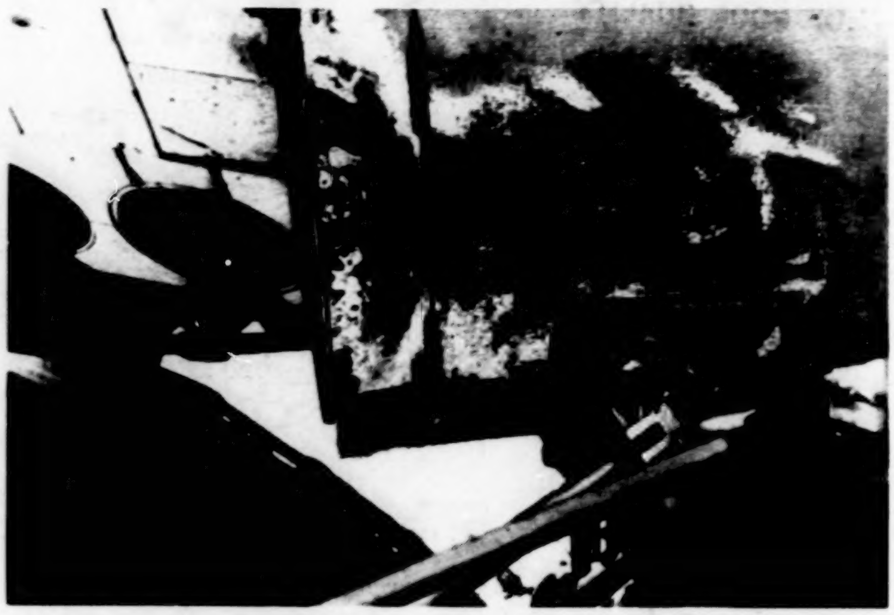

Figure 5.- Overtemperature areas of FRSI on lower trailing edge of OMS pod - STS-1.

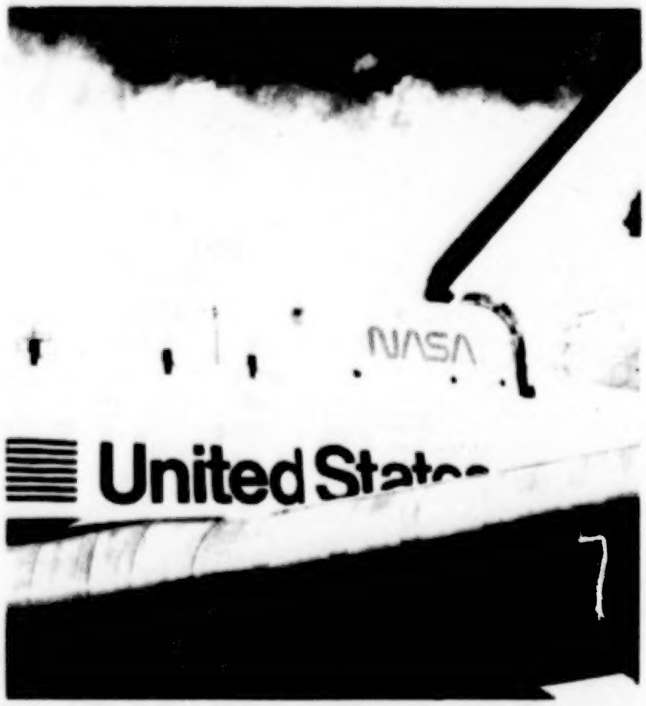

Figure 6.- Overtemperature areas of FRSI on payload bay door - STS-1.

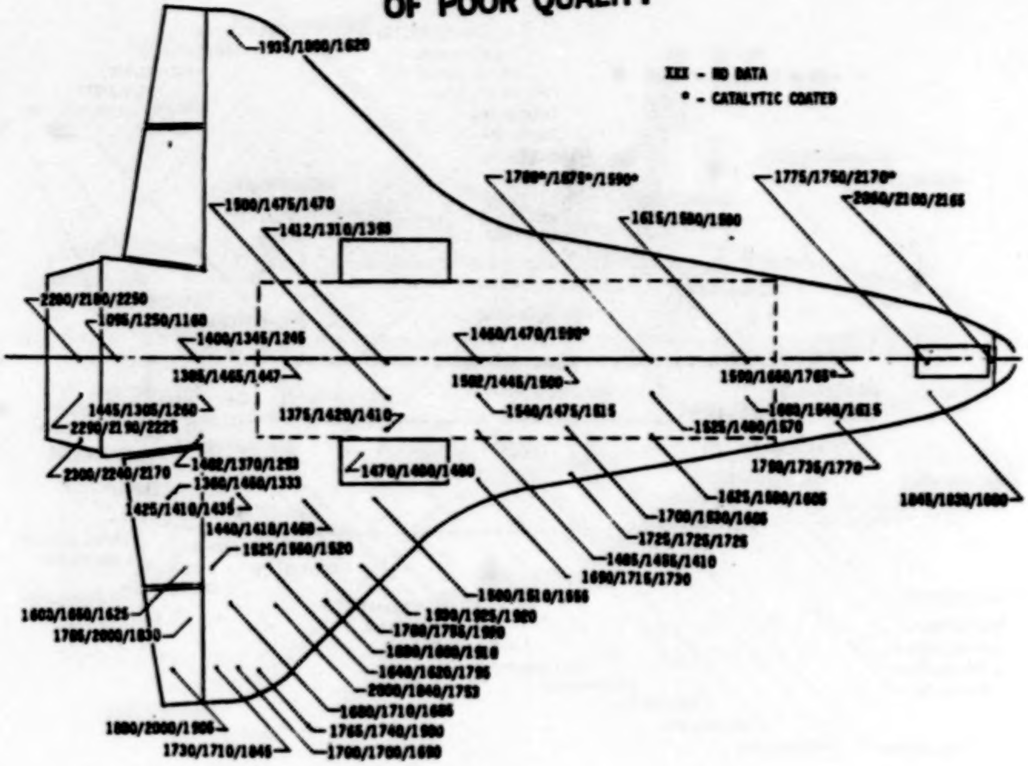
XXX - NO DATA
* - CATALYTIC COATED
1935/1900/1620
1700*/1675*/1590*
1775/1750/2170*
2060/2100/2165
1500/1475/1470
1412/1310/1360
1615/1590/1600
2200/2100/2250
1095/1250/1160
1400/1345/1245
1460/1470/1590*
1385/1465/1447
1502/1445/1500
1590/1660/1765*
1445/1305/1260
1375/1420/1410
1540/1475/1615
1525/1490/1570
1660/1540/1615
2290/2190/2225
1790/1735/1770
2300/2240/2170
1402/1370/1293
1470/1400/1400
1625/1560/1605
1845/1830/1680
1360/1460/1333
1425/1410/1435
1700/1630/1605
1440/1410/1460
1725/1725/1725
1625/1560/1520
1405/1455/1410
1690/1715/1730
1500/1510/1655
1603/1650/1625
1990/1925/1920
1785/2000/1830
1700/1795/1900
1690/1600/1910
1640/1620/1795
2000/1840/1753
1680/1710/1685
1890/2000/1905
1765/1740/1900
1730/1710/1845
1700/1700/1690

Figure 7.- Orbiter TPS peak surface temperatures, STS-2/STS-3/STS-5.

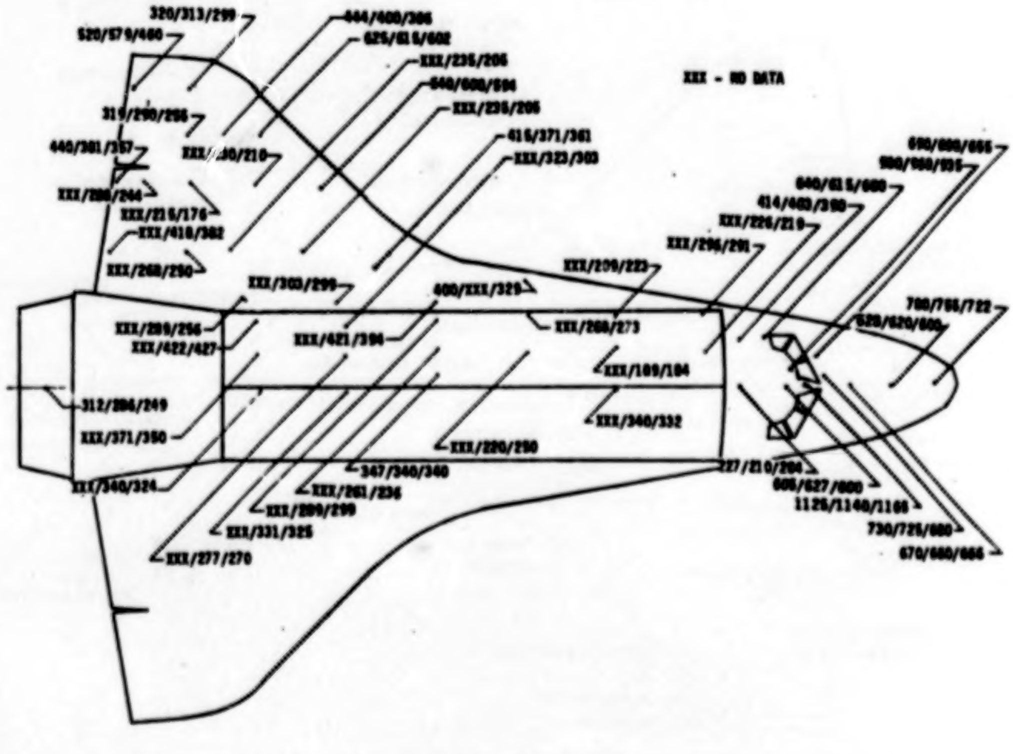
XXX - NO DATA
320/313/299
520/579/460
444/400/306
625/615/602
XXX/235/205
640/600/594
319/290/256
XXX/235/205
415/371/361
440/381/357
XXX/230/210
XXX/323/303
690/690/655
900/960/935
XXX/286/244
640/615/600
414/403/390
XXX/215/176
XXX/226/219
XXX/410/382
XXX/296/291
XXX/268/290
XXX/303/299
400/XXX/329
XXX/209/223
XXX/299/256
XXX/421/394
XXX/268/273
700/755/722
XXX/422/427
620/620/600
XXX/109/104
312/286/249
XXX/340/332
XXX/371/350
XXX/220/250
347/340/340
227/210/204
XXX/340/324
XXX/261/236
605/627/600
XXX/290/299
1125/1140/1168
XXX/331/325
730/725/680
XXX/277/270
670/680/666

Figure 8.- Orbiter TPS peak surface temperatures, STS-2/STS-3/STS-5.

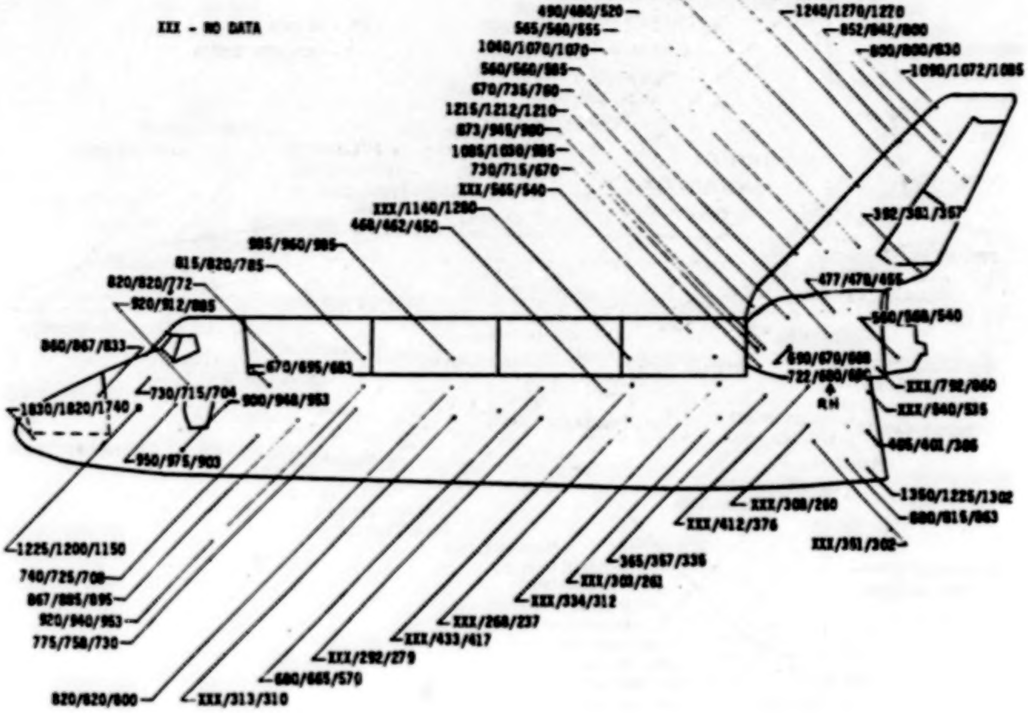
XXX - NO DATA
1160/1200/1190
490/480/520
565/560/555
1060/1070/1070
560/560/585
670/735/760
1215/1212/1210
873/945/900
1085/1030/985
730/715/670
XXX/565/540
XXX/1140/1280
460/462/450
985/960/985
815/820/785
820/820/772
920/912/885
860/867/833
1830/1820/1740
730/715/704
900/940/953
670/695/683
950/975/903
715/733/705
1240/1270/1270
852/842/800
800/800/830
1090/1072/1085
392/381/357
477/470/455
560/560/540
690/670/668
722/680/686
RH
XXX/792/860
XXX/840/535
405/401/386
1350/1225/1302
880/815/863
XXX/351/302
XXX/308/280
XXX/412/376
365/357/336
XXX/300/261
XXX/334/312
XXX/268/237
XXX/433/417
XXX/292/279
680/665/570
XXX/313/310
820/820/800
1225/1200/1150
740/725/708
867/885/895
920/940/953
775/758/730

Figure 9.- Orbiter TPS peak surface temperatures, STS-2/STS-3/STS-5.

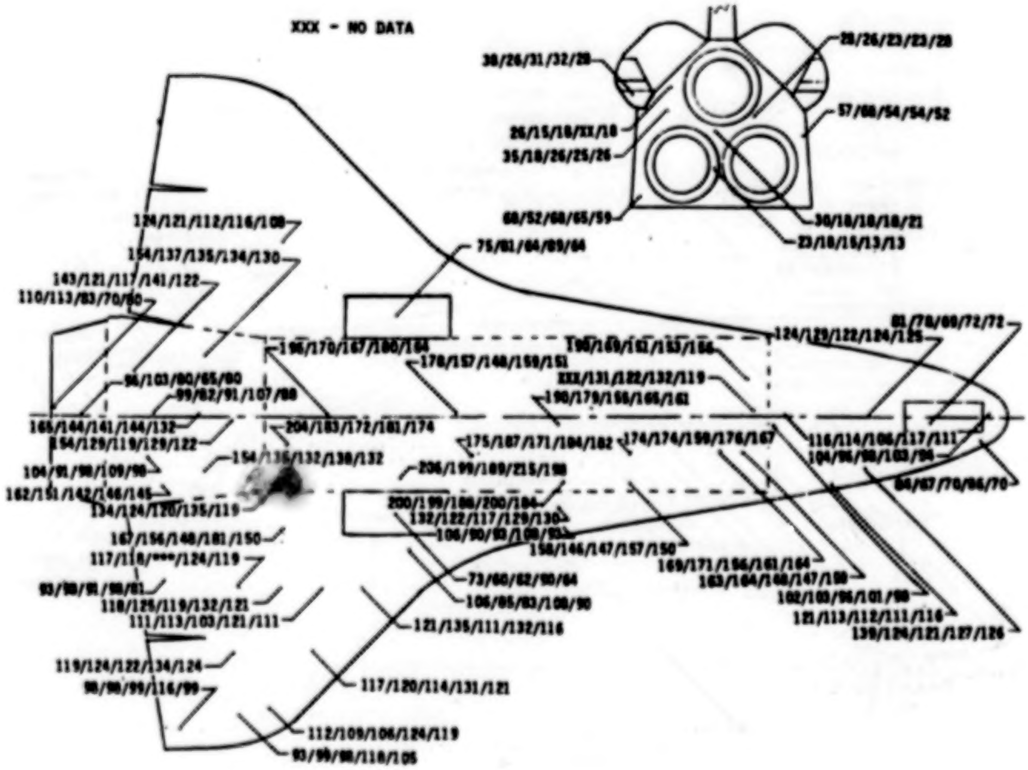
XXX - NO DATA
38/26/31/32/28
26/15/18/XX/18
35/18/26/25/26
68/52/68/65/59
28/26/23/23/28
57/60/54/54/52
30/18/18/18/21
23/18/15/13/13
75/81/84/89/84
124/121/112/116/108
154/137/135/134/130
143/121/117/141/122
110/113/83/70/80
98/103/80/65/80
99/82/91/107/88
165/144/141/144/132
154/129/119/129/122
104/91/98/109/98
162/151/142/146/145
134/124/120/135/119
167/156/148/181/150
117/118/***/124/119
93/90/91/98/81
118/125/119/132/121
111/113/103/121/111
119/124/122/134/124
98/98/99/116/99
112/109/106/124/119
93/99/98/118/105
117/120/114/131/121
121/135/111/132/116
106/85/83/108/90
73/60/62/90/64
106/90/93/108/93
132/122/117/129/130
200/199/188/200/184
206/199/189/215/198
154/135/132/138/132
204/183/172/181/174
196/170/167/180/184
178/157/148/159/151
175/187/171/184/182
174/174/159/176/167
190/179/166/165/161
190/169/151/153/156
XXX/131/122/132/119
158/146/147/157/150
169/171/156/161/164
163/164/148/147/190
102/103/96/101/98
121/113/112/111/116
139/124/121/127/126
124/129/122/124/125
81/78/69/72/72
116/114/106/117/111
104/96/98/103/96
84/67/70/86/70

Figure 10.- Structural temperature rise resulting from entry heating (STS-1 thru STS-5).

ORIGINAL PAGE IS OF POOR QUALITY

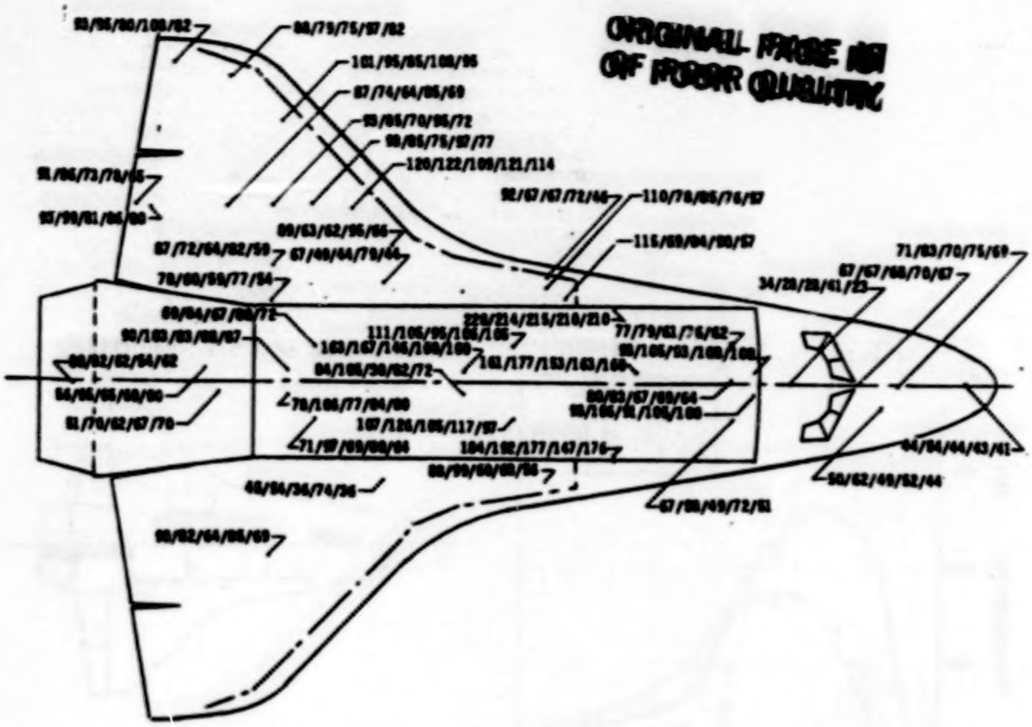
93/95/90/100/82
88/79/75/97/82
101/95/85/108/95
87/74/64/85/69
95/85/70/95/72
98/85/75/97/77
120/122/109/121/114
91/86/73/76/85
95/90/81/86/80
89/63/62/95/66
87/72/64/82/59
67/49/64/79/64
78/80/59/77/54
89/84/67/80/72
90/103/83/88/87
80/82/82/84/82
84/86/85/80/80
81/70/82/87/70
111/106/95/108/106
163/167/146/109/169
228/214/215/210/210
161/177/153/163/168
84/105/30/82/72
78/106/77/84/80
107/126/105/117/97
71/97/89/88/84
104/192/177/147/176
88/99/80/82/86
48/84/36/74/36
98/82/84/85/69
92/67/67/72/46
110/78/85/76/97
115/89/84/90/97
77/79/81/76/82
93/105/93/108/108
80/83/67/89/64
93/106/91/105/100
71/83/70/75/69
67/67/88/70/67
34/20/28/41/23
84/84/44/43/41
50/62/49/52/44
67/80/49/72/51

Figure 11.- Structural temperature rise resulting from entry heating (STS-1 thru STS-5).

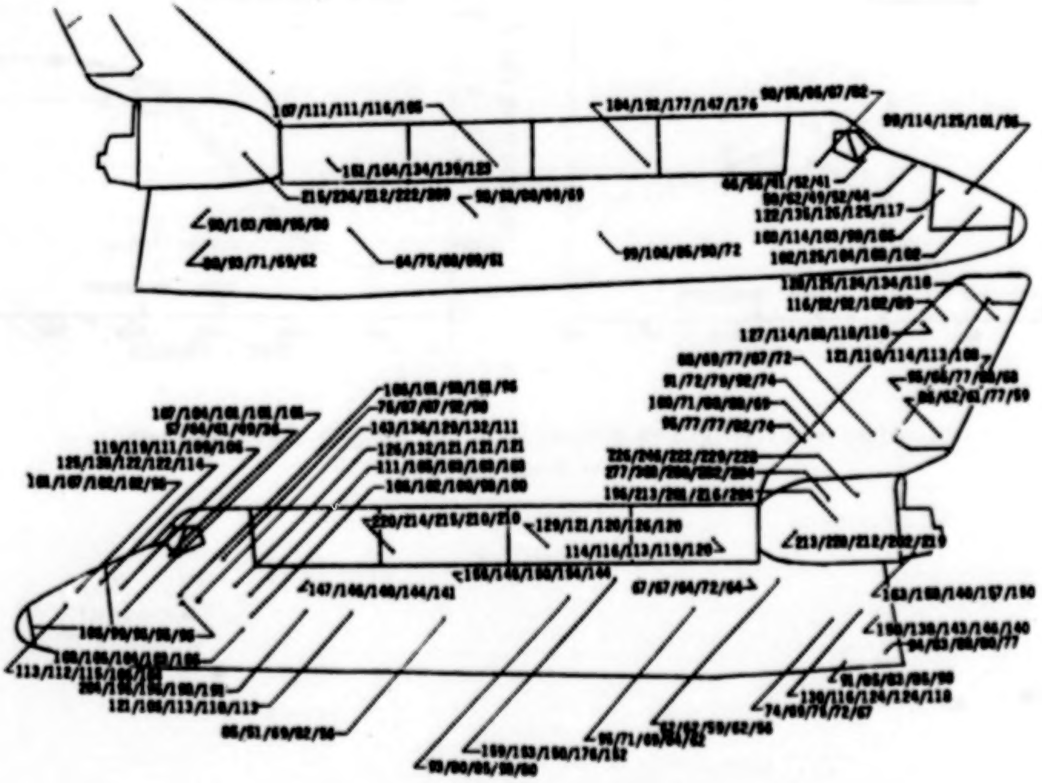
107/111/111/116/106
104/192/177/147/176
90/95/86/87/82
99/114/125/101/95
151/164/134/139/123
215/236/212/222/209
90/93/80/89/69
46/56/41/52/41
50/62/49/52/44
122/136/126/125/117
108/114/103/98/105
102/125/104/109/102
90/103/88/95/80
88/93/71/69/62
84/75/88/89/81
99/106/85/90/72
130/125/134/134/118
116/92/92/102/89
127/114/108/110/118
121/110/114/113/108
88/69/77/87/72
91/72/79/92/74
100/71/80/88/69
96/77/77/82/76
95/86/77/88/88
86/82/81/77/59
106/101/99/101/96
75/87/87/92/90
107/104/101/101/105
97/84/81/69/36
143/136/129/132/111
119/110/111/109/106
126/132/121/121/121
125/128/122/122/114
111/105/103/103/103
101/107/102/102/96
106/102/100/98/100
226/246/222/220/228
277/260/280/282/284
196/213/201/216/200
220/214/215/210/210
129/121/120/126/120
114/116/113/119/120
213/220/212/202/219
158/148/150/154/144
147/146/140/144/141
67/67/84/72/84
163/158/146/157/150
105/99/95/98/95
190/138/143/146/140
84/83/88/80/77
108/105/104/103/105
113/112/115/106/105
204/195/198/188/191
121/105/113/118/113
91/85/83/85/90
130/116/124/124/118
74/85/76/72/67
85/51/69/82/56
52/62/59/62/56
95/71/85/84/82
159/153/150/176/152
93/90/95/98/90

Figure 12.- Structural temperature rise resulting from entry heating (STS-1 thru STS-5).

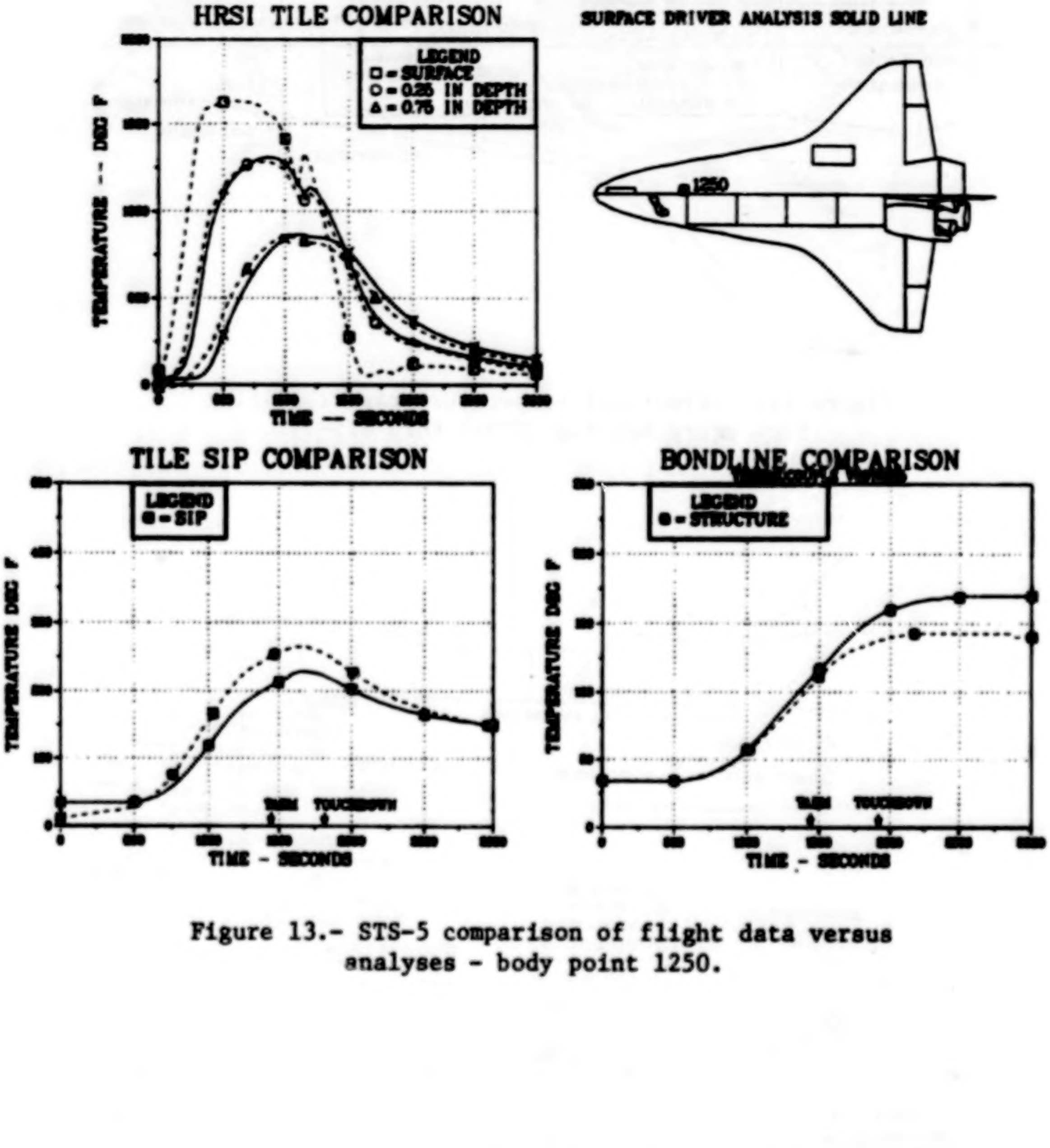

Figure 13.- STS-5 comparison of flight data versus analyses - body point 1250.

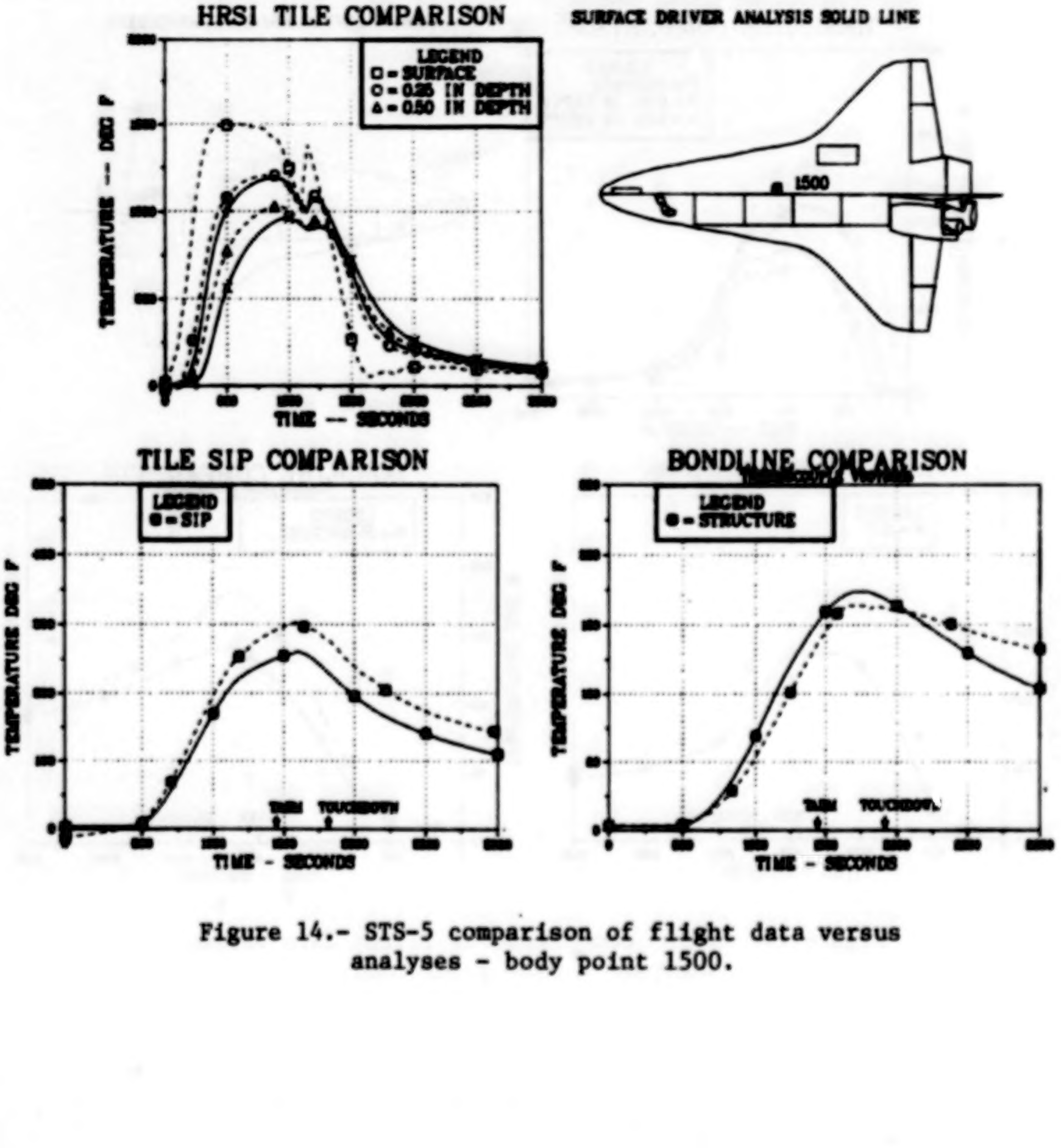

Figure 14.- STS-5 comparison of flight data versus analyses - body point 1500.

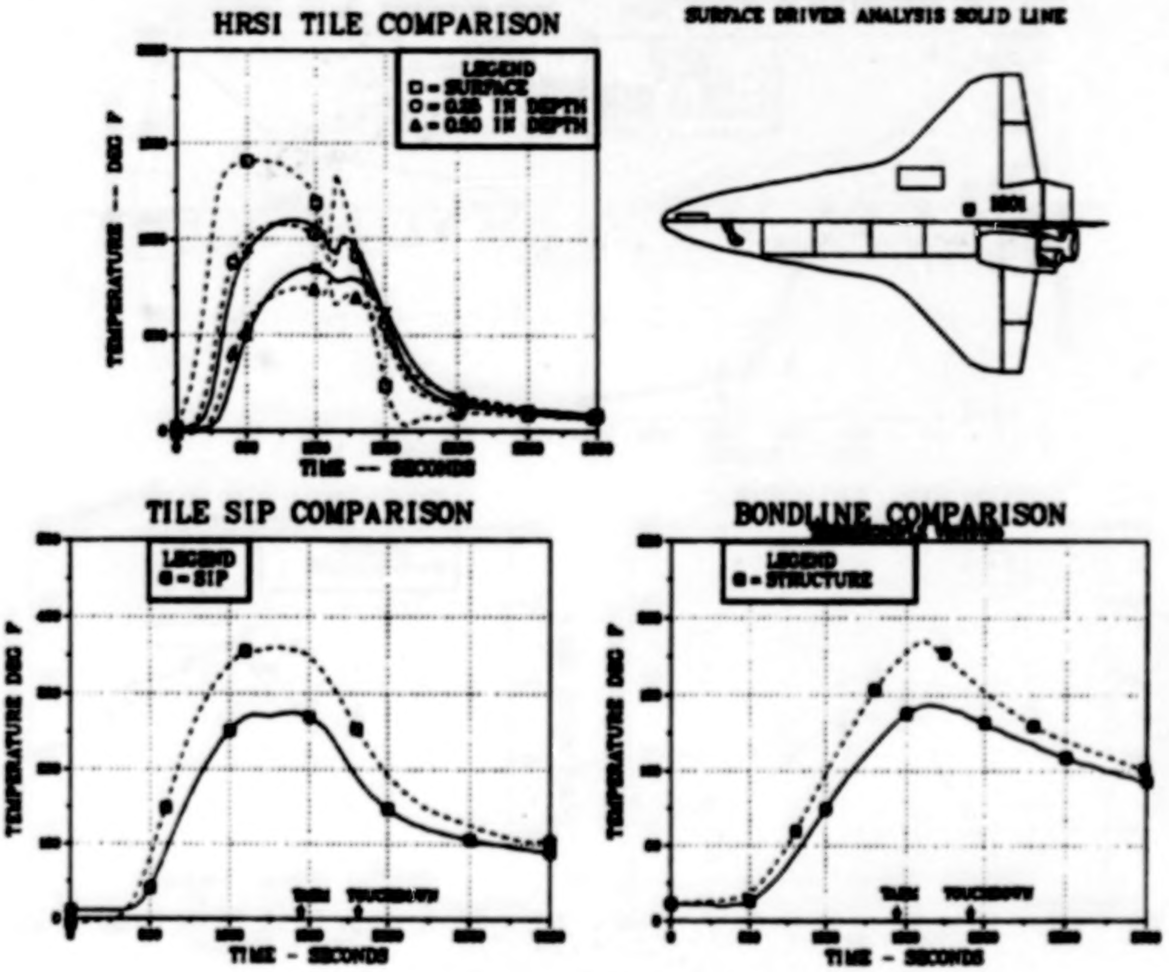

Figure 15.- STS-5 comparison of flight data versus analyses - body point 1801.

ORIGINAL PAGE IS
OF POOR QUALITY

Figure 16.- Loss of diced LRSI tiles on OMS pod - STS-1.

Figure 17.- Loss of nondensified tiles on forward fuselage area - STS-3.

ORIGINAL PAGE IS
OF POOR QUALITY

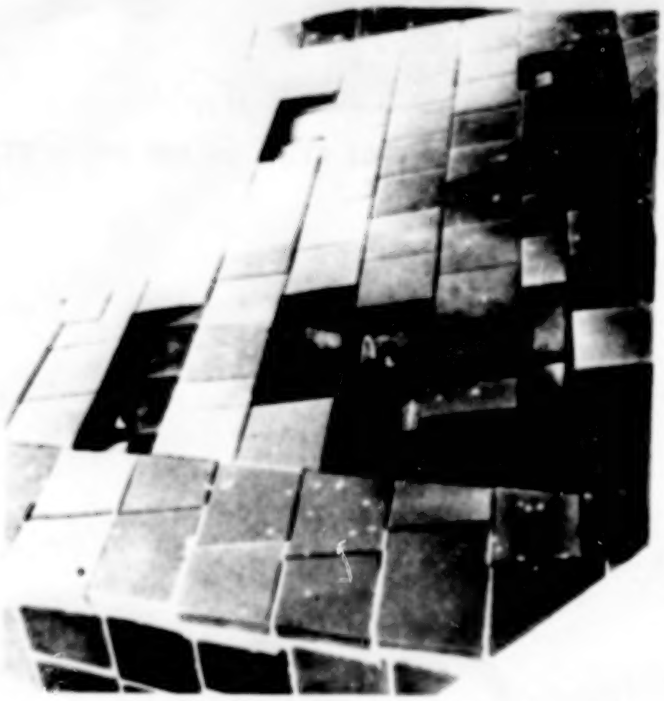

Figure 18.- Loss of nondensified tiles on upper surface of body flap - STS-3.

N84
10158

UNCLAS

N84 10158 D14

LESSONS LEARNED FROM THE DEVELOPMENT AND MANUFACTURE OF CERAMIC REUSABLE SURFACE INSULATION MATERIALS FOR THE SPACE SHUTTLE ORBITERS

Ronald P. Banas, Donald R. Elgin, Edward R. Cordia,
Kenneth N. Nickel, Edward R. Gzowski, and Lawrence Aguilar
Lockheed Missiles & Space Company, Inc.
Sunnyvale, California

SUMMARY

Three ceramic, reusable surface insulation materials and two borosilicate glass coatings were used in the fabrication of tiles for the Space Shuttle orbiters. Approximately 77,000 tiles have been made from these materials for the first three orbiters, Columbia, Challenger and Discovery. Lessons learned in the development, scale-up to production and manufacturing phases of these materials will benefit future production of ceramic reusable surface insulation materials.

INTRODUCTION

The landing of Columbia after STS-5 on 11 November 1982 demonstrated the reality of a truly "reusable" thermal protection system. The concept of a non-ablating, rigid, reusable, ceramic insulation material was identified by a Lockheed patent disclosure in December 1960. It was recommended as a TPS for Lifting Reentry Vehicles by Lockheed in 1964 (ref. 1) and was pursued as a low level research and development effort during the early 1960's. A concentrated development effort was started in 1968 (refs. 2, 3, 4 and 5) to parallel the NASA Phase B studies that defined some early Space Shuttle configurations (ref. 6). Many lessons were learned during each phase of the evolution from laboratory development to an initial production facility in 1971 (refs. 7 and 8), and finally to the full production facility (refs. 9 and 10), which produced a shipset of tiles for the orbiter Columbia.

Lessons learned during the development and scale-up to production of three rigid, ceramic, Reusable Surface Insulation (RSI) materials and two borosilicate glass coatings will be discussed. However, the main emphasis will be on the significant lessons learned from the following manufacturing phases in the full production facility:

1. Processing of raw materials into tile blanks and coating slurries

2. Programming and machining of tiles using numerical controlled milling machines

3. Preparing and spraying tiles with the two coatings

4. Controlling material shrinkage during the high-temperature (2100-2275°F) coating glazing cycles

5. Measuring the tiles before coating and after coating glazing

6. Loading tiles into polyurethane array frames, shimming the tiles to the proper tile-to-tile gap width and machining the inner-mold-line of all tiles in an array

The RSI materials include LI-900 (Lockheed insulation at a density of 9 lb/ft^3), an all-silica material developed by Lockheed Missiles & Space Company Inc. (LMSC) in 1972. A predecessor, LI-1500, (a 15 lb/ft^3 density all-silica material) was developed by LMSC in 1962 (ref. 1). It was the lowest weight prime material for Lockheed's reusable lifting reentry vehicle studies (ref. 11) from 1962 until 1971 when LI-900 was developed (ref. 12). LI-2200, a 22 lb/ft^3 density all-silica material, was patented by NASA ARC (ref. 13) and scaled up to production by LMSC in 1977. FRCI-12 (Fibrous Refractory Composite Insulation at a density of 12 lb/ft^3) is a composite fiber RSI material. During design, development, test, and evaluation of Columbia, the need for improved thermal protection tiles was recognized. Stronger, less dense tiles more resistant to impact damage were desired. A ceramic tile material with these characteristics, in addition to the other required properties, was invented by the NASA ARC (ref. 14) and scaled up to production size billets by LMSC (ref. 15). This material, FRCI, composed of a blend of silica fibers and aluminum borosilicate fibers, is an outgrowth of LI-900 and LI-2200 technologies and basic research of high temperature materials.

The two borosilicate coatings are Class 1 and Class 2. The Class 1 (0036C) coating (ref. 16) is white and has a ratio of solar absorptance to total hemispherical emittance between 0.2 and 0.4 from -170°F to 135°F, and an emittance ≥ 0.7 at 1200°F. The Class 2 or Reaction Cured Glass (RCG) coating (ref. 17) is black, and has a total hemispherical emittance ≥ 0.8 at 2300°F and a ratio of solar absorptance to total hemispherical emittance between 0.7 and 1.1 from 170°F to 250°F. It is used on LI-900 tiles that experience surface temperatures from 1200°F to 2300°F and all LI-2200 and FRCI-12 tiles.

LI-900 was scaled up to production in 1975 and the first production billet for Columbia was fabricated in September 1976. LI-2200 was implemented as a pilot plant operation to produce about 100 tiles per orbiter in October 1977. After the final tile deliveries were made for Columbia and Challenger, about 3000 tiles per orbiter were made from LI-2200.

The pilot plant operation for FRCI-12 started in January 1979 under a contract from NASA ARC (ref. 15). Facility modification and the scale-up to production billet sizes started in October 1979. The first FRCI-12 production billet for Discovery (OV-103) was produced in October 1981. About 2700 FRCI-12 tiles are scheduled for installation on Discovery and Atlantis (OV-104). The processing parameters involved in the production of these materials are described in reference 18.

LIST OF SYMBOLS AND ABBREVIATIONS

APT	Applied Programmed Tool, a computer language used to drive numerically controlled milling machines
ARC	Ames Research Center
ATA	Array tile assembly, which consists of a polyurethane array frame loaded with tiles. Tile IML's are cut in the frame. The ATA is used as a shipping container and for tile installation on the orbiter.
Billet	A finished piece of LI-900, LI-2200 or FRCI-12
Breather Area	The uncoated area on the sides of the tile that starts at the coating terminator line and extends to the tile IML. The breather area allows air to vent out during ascent to preclude a loss of coating.
CADAM	Lockheed Computer Aided Design and Manufacturing system
CAD/CAM	Computer Aided Design/Computer Aided Manufacturing
CATIA	A Computer-Graphics Aided Three-Dimensional Interactive Application system developed by Dassault Aircraft in France
Class 1 Coating	White coating used for temperatures of 1200°F or less
Class 2 Coating	Black RCG coating used for temperatures between 1200° and 2300°F
Class 1 Tile	LI-900 covered on the OML and sides with a white borosilicate coating
Class 2 Tile	LI-900 covered on the OML and side with a black borosilicate coating (Class 2 coating)
Class 4 Tile	LI-2200 covered on the OML and sides with a black borosilicate coating (Class 2 coating)
Dry Density	The density of an LI-900, LI-2200 or FRCI-12 billet prior to exposure to the sintering cycle
FRCI	Fibrous Refractory Composite Insulation

FRCI-12	**A rigid, composite fiber insulation made of 78% silica fibers, 22% Nextel fibers with 3% by weight of silicon carbide at an average density of 12.5 lb/ft^3**
FRSI	**Felt Reusable Surface Insulation**
GHP	**Guarded Hot Plate**
IML	**Inner Mold Line**
IP	**In-plane direction which is perpendicular to the through-the-thickness direction**
LI-2200	**A rigid, all-silica fibrous insulation with about 2% by weight of silicon carbide at an average density of 22 lb/ft^3**
LI-900	**A rigid, all-silica fibrous insulation with an average density of 8.75 lb/ft^3**
LMSC	**Lockheed Missiles & Space Co. Inc.**
MD	**Master Dimension**
MDI	**Master Dimensions Intersections**
Mylars	**Tile section cuts put on flexible heavy gauge plastic by Rockwell or LMSC and used by LMSC inspectors to measure the sides of complex tiles**
NC	**Numerical Control**
Nested Tile	**A tile that is individually measured for planform dimensions and has its IML cut while being held in a polyurethane nest**
Nextel 312®	**Aluminum borosilicate fiber; a product of Minnesota Mining and Manufacturing Co.**
OML	**Outer Mold Line; experiences aerodynamic heating during ascent and reentry**
0036B	**The original Class 1 coating; a dual layer coating consisting of porous optically adjusted subcoat and fused glass topcoat**
0036C	**The present Class 1 coating; a single layer system that meets the optical property requirements**
0050	**The original Class 2 coating; a fused silica subcoat and a topcoat of 7930 frit at 8% B$_2$O$_3$ with a silicon carbide emittance agent**

PTX Lot	A blend of 20 Manville silica fiber lots
RCC	Reinforced Carbon Carbon
RCG	Reaction Cured Glass (the Class 2 coating)
RSI	Reusable Surface Insulation
STS	Space Transportation System
Terminator or Witness Line	The line that is put on the sides of most tiles to define the extent of the coating down the sides
TPS	Thermal Protection System
TTT	Through-the-thickness direction; also, the pressing direction during the casting operation

RSI LOCATIONS ON COLUMBIA

Over 30,800 RSI tiles were installed on Columbia by Rockwell. About 18,500 of the 23,400 tiles made by LMSC were HRSI, which is either LI-900 or LI-2200 with the Class 2 coating. The remaining 6000 tiles were LRSI, which is LI-900 with the Class 1 coating. The locations of the HRSI and LRSI tiles are shown in figure 1 along with the location of the RCC and FRSI. More details on the composition of these materials and the installation procedures used for all Orbiter TPS materials can be found in references 19 and 20.

LI-900 PROCESS DESCRIPTION

Materials

The principal component in LI-900 is all-amorphous silica fibers with an average diameter of 1.2 to 1.4 microns and lengths to 1/4 inch. During development, a major goal was to obtain a stable material that resists devitrification at elevated temperatures. This was accomplished in an extensive development program with the fiber supplier, Manville Corporation. The final product, Q-fiber, is amorphous silica with greater than 99.7 percent purity. These fibers retain their amorphous structure when exposed to a temperature environment of 2500°F for extended periods. The LI-900 system contains a colloidal silica binder that requires extensive treatment to obtain the purity required for high-temperature morphological stability.

Material Pretreatment

During the development of LI-900, certain pretreatment procedures were developed to improve uniformity and processability of the constituent materials. Maintaining uniform shrinkage characteristics was difficult early in the development of the process. This was overcome by heat-treating the fiber before processing it into billets. In addition, unfiberized glass called "shot", if not removed, causes high density, devitrified inclusions in the sintered material. To eliminate the "shot", the fiber is slurried with deionized water and passed through a hydro-cyclone cleaner (fig. 2). The cleaned fiber slurry is transferred into a centrifugal extractor to remove excess water and to form a fiber "cake", in preparation for final drying. Also, silica fiber lots received from Manville exhibit variable fiber characteristics that cause variations in billet densities. A blend of 20 Manville lots, called a PTX lot, was developed to reduce this variability (fig. 3).

LI-900 Fabrication

The LI-900 process flow is shown in figure 4. LI-900 billets are cast in two sizes, 15 x 15 x 6.5 inches and 10 x 20 x 7.3 inches. The operation is performed in an automated casting line. Preweighed amounts of fiber are loaded into twenty-six hoppers on a carousel that automatically positions and empties the hoppers sequentially. Originally, 4.9 lbs of fiber were used for each casting. Later development resulted in a change to 5.2 lbs of fiber along with a reduced water to fiber ratio (fig. 5). These changes, plus others to be described later, resulted in improved density distribution within the billets. The fiber and a pre-determined quantity of water are combined in a tank containing a low shear mixer that uniformly disperses the fiber with minimum chopping. At the conclusion of the timed mix cycle, the slurry is automatically transferred into a casting mold positioned directly below the mixing tank.

Entrapped air bubbles are removed from the slurry prior to compressing the billet to its final cast size. This is accomplished by a combination of vibration and stirring. Care must be exercised during this operation to maintain a homogeneous dispersion of the fiber. Water is removed and the casting is compressed to a specified height in the volume adjustment operation. Concurrently, a vacuum is applied to the bottom of the mold to remove a specified quantity of water. At this stage, the standard billet contains 5.2 lbs fiber and approximately 24 lbs of water. The next step in the casting operation is the dispersion of a colloidal silica binder in the compressed casting at the weight adjustment station. The binder solution components are automatically mixed and dispensed through metering pumps. The solution is dumped on top of the compressed billet and a vacuum is applied to the bottom of the casting mold. The residual water in the billet is displaced by the binder that is dispersed throughout the casting to a specified solids concentration. Upon removal from the mold, the wet billet is weighed to provide a check that all steps of the casting operation were performed correctly. The current method, described above, is an improvement over the original method which excluded the void reduction and vacuum water withdrawal (fig. 6).

Since maintaining a uniform distribution of the colloidal silica binder in the casting is important to maintain uniform physical properties, a gelling agent is used to set the binder and prevent it from migrating during drying. The billets are dried using either a conventional oven or a microwave dryer. They are weighed after drying to assure that the specified amount of water is removed prior to sintering. Originally, the castings received a first and second sintering with an additional binder addition between sinterings (fig. 5). Later development resulted in a single sintering combined with the change from 4.9 to 5.2 lbs of fiber. The result is an improvement in billet density distribution and an increase in yield.

An additional improvement in average billet density was obtained with the implementation of a fiber compact shrinkage test. A correlation between billet density and sintering schedule was developed for each PTX lot (fig. 7). This allows adjustment of the sintering schedule to accommodate the PTX lot shrinkage characteristics which influence the billet density.

Originally, the dried castings were sintered in specially designed 3-zone tunnel kilns at a peak temperature of 2350°F. These kilns were used from 1975 to 1982. Early in 1982, the sintering operations were transferred to elevator kilns. Six side heating is utilized in these kilns compared to five side heating in the previous kilns (fig. 6). This improves the strength distribution within the billets. The sintering schedule is adjusted to produce billets with an average density of 8.8 lb/ft^3 by adjusting the sintering time to accommodate the PTX lot shrinkage variations.

LI-2200 PROCESS DESCRIPTION

Materials

LI-2200 is composed of amorphous silica (Q-fiber) and a small amount of silicon carbide powder which provides additional thermal protection if the material is exposed to excessive temperatures due to coating loss at the tile outer surface. With LI-2200, the fiber heat-treatment is omitted, and only the hydro-cyclone cleaning is performed. Until January 1981, the fiber cleaning was performed by an air bubbling procedure which was less efficient and less reproducible than the present procedure.

LI-2200 Fabrication

The LI-2200 process flow is shown in figure 8. The billets are cast in a specially designed, manually operated casting tower in a 14.4 x 14.4 x 8 inch size. The mixing process differs from LI-900 in that the preweighed fibers are combined with water, SiC, and ammonium hydroxide into a V-blender equipped with an intensifier bar. Since LI-2200 requires a significantly higher casting density than LI-900, the slurry requires some chopping action to obtain the necessary fiber packing. After the blended slurry is transferred into the casting tower and sealed, void elimination is accomplished by applying a high vacuum to the slurry prior to billet formation. The billet is formed by removing part of the water by gravity drain, compressing the slurry to a final thickness, and then extracting additional water with vacuum.

The billets are dried in a batch oven at 450°F for 16 hours. The dry density of the LI-2200 is approximately 13 lb/ft^3. Originally, this was the final operation before sintering. However, the billets sometimes exhibited cracks after sintering. An additional drying at 1000°F for 12 hours was developed and implemented in September 1981 to eliminate this problem.

The LI-2200 is sintered in elevator kilns. The sintering schedule is similar to that used for LI-900, except that the peak temperature is 2420°F. The soak time at peak temperature is adjusted to maintain final densities within a 22 ±2 lb/ft^3 density range. Originally, the soak times were based on fiber chemistry. A more accurate method, based on fiber compact shrinkage, was developed and implemented in June 1981.

FRCI-12 PROCESS DESCRIPTION

Materials

FRCI-12 is a composite fiber material containing amorphous silica (Q-fiber®) and aluminum borosilicate fibers (Nextel 312®, a product of Minnesota Mining and Manufacturing Company) in a fused fiber matrix. Silicon carbide powder is added for additional thermal protection as it is in LI-2200. The bulk silica and Nextel fibers are heat treated at 2200°F and 2000°F respectively to stabilize and standardize fiber properties. Hydro-cyclone cleaning is performed on the silica fibers to remove particulate contaminants, followed by drying.

Fabrication

The FRCI-12 process flow is shown in figure 9. Silica and Nextel fibers are intermixed and cast into billets using a multi-stage, wet-slurry blending process and automated casting equipment. Castings are dried using a combination of microwave and convection-air ovens to achieve optimum drying rates. Dry castings are sintered in elevator kilns using microprocessor controllers to achieve uniform, repeatable heating to the optimum sintering temperature (approximately 2400°F). The optimum sintering temperature varies as a function of FRCI composition and desired final density.

FRCI can be fabricated with a range of compositions and densities to allow tailoring the material to a specific application. An FRCI formulation with a density of 12 pounds per cubic foot and a silica to Nextel fiber ratio of 78/22, identified as FRCI-12, was developed to replace LI-2200. Other FRCI materials with densities of 8 lb/ft^3 and 20 lb/ft^3 have been produced. FRCI-12 tiles were substituted for approximately 2764 LI-2200 tiles on the third orbiter, Discovery. Substituting FRCI-12 for LI-2200 saves approximately 870 pounds of weight per orbiter due to the lower density of FRCI-12. Also the tensile strength design value is increased by 50 percent, and the susceptibility to coating impact damage is reduced by eliminating residual tensile strain in the coating due to a better match in coefficient of thermal expansion between FRCI and tile coating materials.

Development of full-scale manufacturing processes for FRCI-12 required considerable effort by many individuals within NASA, Rockwell International, and LMSC from October 1979 through October 1981. Several important lessons were learned during this development about the inter-relationships between processing and fundamental material properties. The development effort was complicated by the requirement to produce a tile material to meet all the existing requirements of the baseline material, while also providing improvements of significant importance to warrant replacement of proven materials.

The first significant FRCI problem was encountered during initial scale-up work on the NAS2-10134 contract. Nextel fibers did not readily disperse when blended with silica fibers in the full-scale mixing equipment. Clumps of undispersed Nextel fibers, which varied from 1/8 to 1/2 inches in length and were present in the sintered FRCI-12 material, caused unacceptable coating discontinuities on finished tiles. The original laboratory method called for wetting the Nextel fibers prior to introduction into a small lab-scale V-blender containing silica fibers. This lab-scale equipment and procedure produced an acceptable mixture of the two fibers in lab-size castings. However, when the same procedure was used in full-scale production equipment, the Nextel fibers did not disperse and Nextel clumps occurred in the finished material. An interim dispersion method, only marginally acceptable, was devised for the pilot plant operation conducted under NAS2-10134. Nextel fiber was preblended in water in a lab-size V-blender to break up Nextel clumps, mixed with an equal amount of silica fiber in the same blender to prevent reaggregation of the Nextel into clumps, and then blended with the remaining silica fiber in the full-scale blender to produce a slurry with suitable characteristics for casting. This interim dispersion method reduced the number and size of clumps in the finished material, but the method was not considered suitable for full-scale production due to the need for considerable coating touch-up. A high-speed, high-shear blender was substituted for the small V-blender for preblending operations in the final production process. As shown in figure 10, use of the high-shear mixer for preblending Nextel fibers totally eliminated Nextel clumps in finished tiles (ref. 21).

The second significant problem was encountered during characterization testing of the pilot-plant material. The apparent[1] thermal conductivity of the pilot-plant FRCI-12 was higher than the LI-900 base line value. Rockwell's criterion for substitution of any material for LI-900 or LI-2200 was that the thermal response must be equal to or lower than that of LI-900. A guarded hot plate (GHP) apparatus is normally used to characterize the thermal conductivity of a material. Measurements can be obtained over a wide range of temperatures and pressures to establish design values. However, the ±18% uncertainty band associated with GHP data makes comparative measurements on different specimens, with minor variations in thermal conductivity, uncertain. Comparative measurements are more easily accommodated with the instrumented tile method (ref. 23) shown in figure 11. Tiles fabricated from different materials can be tested side-by-side in a radiant heating environment at reduced pressures. Either steady-state or transient heating conditions can be simulated. This method yields more reliable comparative results than the GHP method which is limited to testing one material at a time. Apparent thermal conductivity values for laboratory FRCI-12 were much lower than the pilot-plant FRCI-12, but still higher than LI-900, indicating that some key parameter(s) must have been inadvertently varied during scale-up. An investigation of the effects of various compositional and processing variables on FRCI-12 properties showed that apparent thermal conductivity can be affected by several factors, the most important being density change during the billet sintering cycle (ref. 24). Pilot-plant FRCI-12 experienced a density change of 5.5 lb/ft^3 during sintering, whereas laboratory material experienced a change of 4 lb/ft^3. Full-scale production FRCI-12, which has acceptable apparent thermal conductivity (ref. 25), experiences only a 2 lb/ft^3 density change. Reducing the density change during sintering was accomplished by use of the high dry density concept, producing castings with increased fiber content (i.e. more fibers per unit volume) and sintering at a lower temperature for a shorter time (fig. 12). Reducing the time/temperature profile during sintering caused a reduction in average tensile strength of the material compared with pilot-plant material. However, use of six-sided heating in the kiln in place of the five-sided heating resulted in a more uniform strength distribution within the billets and provided design tensile strength values nearly equal to the pilot plant values by lowering the deviation.

Another significant development problem was encountered when attempts to achieve FRCI-8 (8 lb/ft^3) thermal conductivity equivalent to LI-900 were unsuccessful. Minimizing the change in density during sintering was not sufficient to produce FRCI-8 with acceptable thermal conductivity. A combination with other, less significant, thermal conductivity "drivers" was necessary. Experiments showed that reducing the Nextel fiber concentration in the material formulation and reducing the size of the silicon carbide particles in the material, provided the additional reduction in thermal conductivity that was required (ref. 26). Pilot-plant FRCI-8 experienced a change in density during sintering of 2.5 lb/ft^3, has a silica to Nextel fiber ratio of 78/22, and contained 320 mesh silicon carbide particles. Full-scale FRCI-8, which has acceptable thermal conductivity, experiences only a 1.5 lb/ft^3 change in density, has a silica to Nextel fiber ratio of 85/15, and contains 600 mesh silicon carbide particles. Reducing the change in density during sintering was accomplished by producing castings with higher dry density and sintering at a lower temperature for a shorter time (fig. 13). Reducing the time/temperature profile during sintering and reducing the concentration of Nextel fibers in the formulation resulted in lower average strength for the full-scale material compared with the pilot-plant FRCI-8. However, use of six side heating in the kiln instead of five side heating, and increasing the heat-up rate to the sintering temperature (to minimize shrinkage during heat-up and maximize time above the critical fiber bonding temperature of 2350°F) resulted in a more uniform strength distribution within the billets and provided design allowable strength values nearly equal to pilot plant values.

---

[1] For porous materials, the term apparent thermal conductivity is used to denote heat transfer within the material by solid conduction, gas conduction and radiation (ref. 22).

TILE PROCESS FLOW

The sequence of operations performed after the insulation material is cut into cubes is shown in figure 14. After the tiles are machined, they are heat cleaned to remove organic contaminants, masked to allow an uncoated breather space area along the lower perimeter adjacent to the IML, sprayed with Class 1 or Class 2 coating and sintered at 2100 to 2250°F in an Ipsen tunnel-hearth roller kiln. After vacuum waterproofing with a methyl trimethoxy silane (Dow Corning DC 6070), the tile identification number is painted on the OML and the tiles are checked dimensionally as required prior to the IML cuts.

The tile IML cut is performed either individually, which is called a "nested" tile, or on a group of tiles simultaneously in an array frame, which is known as an ATA.

The dimensions of a nested tile are checked as required prior to the IML cut. The dimensions of the ATA tiles are checked by their ability to fit into a premeasured polyurethane array frame with the required tile-to-tile gaps, which are generally 0.045 ±0.016 inch on the lower wings and fuselage and 0.055 ±0.016 inch on the upper wings, fuselage and vertical fin.

ENGINEERING

Engineering Data Flow

Engineering data, which is used to define the tile and array frame geometries, is received from Rockwell in the form of engineering assembly drawings, tile bounding plane data and inner/outer mold line data (fig. 15). Only 115 of the 23,400 tiles that Lockheed made for OV-102 are defined by conventional engineering drawings. The mold line data can be represented by points (X, Y, Z coordinates) and corresponding normal vectors (MDI data), and recorded on a magnetic tape and/or contained as surface definitions described in the Master Dimensions Specification Book, Document No. MD-V70, Rockwell International. The MDI data are transformed from an orbiter coordinate system to a local tile/array coordinate system that is compatible with the APT language. These transformed data are stored in a geometry file that is accessed by the NC programmer for use in preparing the part program to machine tiles.

A tile machining drawing is used to determine the proper tile shrinkage compensation factor (see Tile Measurement and Shimming Methods section) to include in the tile part program.

The geometry file, which contains the tile boundary planes and the OML and IML surfaces, is also used to write the NC part program to machine the array frame. LMSC fabricated 739 array frames for Columbia. Product Assurance Inspection Standards are also prepared for use in inspection of the tiles on the Cordax measuring machines.

Master Dimension Refinements

Almost 18,500 of the 23,400 tiles LMSC made for OV-102 were MDI tiles, which are defined in a grid of X, Y, Z coordinates and corresponding normal vectors. The remaining tiles are the more complex MD tiles, which have their geometries defined in the Master Dimensions Specifications book. Substantial refinements have occurred in the procedures used to define the 4900 MD tiles. Originally, hand calculators or personal computers were used to calculate points to approximate complex surfaces, tile and array corner points, Product Assurance Inspection Standards, and points to check the accuracy of inspection aids (mylars) furnished by Rockwell (table I). Surfaces which could not be analytically defined were approximated by calculating points and passing a curve through these points.

Software, in the form of APT and FORTRAN computer programs, is now being used to calculate tile and array corner points and to provide accurate blank sizes. Additional software and a CAD/CAM system are both used to develop and check the accuracy of complex surfaces. This same CAD/CAM system is used to provide mylars to check hard-to-inspect tiles, reducing the time required for tile inspection. The accuracy of certain Rockwell furnished mylars is checked at LMSC using the CAD/CAM system if a discrepancy is noted during the inspection process.

Mylars were seldom used for Columbia tiles. However, for Challenger and Discovery, mylars were used extensively for hard-to-measure tiles. For example, 123 complex hinge cover tiles, which contain conical surfaces, ruled surfaces and through holes, were recently delivered for Discovery ahead of schedule. This success was due to a joint LMSC-RI effort to make 28 mylars that were used to inspect these tiles.

NC Programming Refinements

Initially, an attempt was made to automate tile programming by using a cut package to program each family of tiles (table II). Each minor difference in tile geometry required a different cut package which was inefficient and often difficult to use. Limited knowledge of the unusual and complex surfaces involved made the programming task very difficult and time consuming. Programmers experienced many failures before being able to visualize a tile, working from just the master dimensions data. It required 90 NC programmers working for ten months, using more than 160 hours per week of Univac 1108 computer time. An interactive graphics system was not available to program tiles.

Tiles with planar sides were programmed as planar surfaces. This resulted in corner shrinkage when the tile coating was glazed (see Tile Shrinkage section). One cutting tool was used to machine most tiles. Since no coating terminator line was machined on complex tiles, problems were encountered when these tiles were masked for spraying and a high rejection occurred for tiles with insufficient breather area (fig. 16). The use of different fixtures to locate different size blanks on the three Danley Corp. NC machines caused a relatively high percentage of tiles to be scrapped due to operator error in locating the blank.

Programming and tile machining are now more efficient due to knowledge and experience gained over the life of the program. About 6000 tool tries were required to develop the proper part programs for the tiles on Columbia. About 1400 tool tries were required in connection with design changes on Challenger and about 600 tool tries as a result of design changes were required on Discovery. Planar sides are now programmed as cylinders with 900-inch radii to reduce tile corner shrinkage. About 30 electroplated diamond tools ranging in diameter from 1/8 to 2 inches were designed during the first year of production and are now used to reduce machining time. A coating terminator line is now added to most complex tiles to facilitate coating spraying and reduce the number of tiles scrapped or reworked due to incorrect breather area. The same fixture is also used on the NC mills to locate all blanks, regardless of size. This change has greatly decreased the number of tiles scrapped because of operator error in locating the blank on the bed of the NC machine.

Interactive Graphics

The recent use of an interactive graphics system (CATIA) to program the redesign of specific complex tiles has demonstrated that this method of programming reduces the number of tool tries required before an acceptable part can be made. The NC programmer has the ability to replay the cutter motion on the graphics system terminal and correct any errors observed prior to machining the first tool try.

The expanded use of an interactive graphics system for the redesign of the more complex HRSI tiles would markedly reduce both the cost and time required to manufacture these tiles (fig. 17). An example of how this system would work follows. A three dimensional engineering model of a given tile is constructed on the system. The tile model can be rotated on the terminal scope, showing all facets and all surface intersections. The model is then accessed, the cutter motion is added, the cutter motion is replayed to check for and correct errors, and then a tape is produced and sent to the machine shop for a tool try. Any errors encountered during the tool try can be easily corrected using the same engineering model. However, as the NC programmer becomes more proficient with the 3-D model, this sequence should minimize the number of tool tries. In addition, Product Assurance can access the same engineering model and extract the attributes necessary to inspect the tile.

BOROSILICATE COATINGS

Class 1 Coating

Development of the Class 1 (white) coating was a significant challenge because of the stringent optical property and weight requirements. The optical property requirements are a ratio of solar absorptance to total hemispherical emittance between 0.2 and 0.4, to achieve low temperatures while on orbit, and an emittance of 0.7 at 1200°F to allow maximum re-radiation of the convective heating energy during reentry (fig. 18). An intensive development program was successful in producing a dual layer coating that was started in production in October 1977. This coating (0036B) consisted of a fused, water-impervious topcoat of clear glass plus zinc oxide, over a porous subcoat that contained aluminum oxide for high reflectance and silicon carbide for high emittance. The subcoat required drying at 1300°F prior to spraying the topcoat. After both layers were applied, glazing at 2100°F was required to produce a water-impervious, dual layer coating.

In mid 1978, effort was directed toward combining the dual layers while retaining both the optical properties and the water imperviousness. A single layer coating (0036C) was successfully developed, qualified and implemented into production in early 1978. During this period, the maximum coating weight requirement was increased from 0.09 to 0.12 lb/ft^2 to alleviate a coating cracking problem which was unavoidable with a 0.008 inch thick coating. This coating was successfully applied to about 5700 tiles for orbiter 102. For Challenger, OV-099, the maximum coating weight requirement was increased to 0.17 lb/ft^2. While in production for OV-102, a major water imperviousness problem affected the Class 1 coating. A three month investigation revealed that the cause was large frit particle size that precluded complete fusion (ref. 27). A complete particle size distribution requirement was determined and imposed on the frit supplier, Corning Glass Works. Particle size controls were also instituted for the coating slurry (fig. 19) to assure complete fusion during the 2100°F coating glazing cycle.

Class 2 Coating

The Class 2 (Gray) coating (0050), developed in 1974 (fig. 20), was a dual layer system that contained Corning 7930 frit with a boria content of 8% and a silicon carbide emittance agent. Because of a high coating residual tensile strain (values of 200-300 microinches per inch), crack propagation was not inhibited. This coating was replaced in June 1976 with a NASA ARC-patented Reaction Cured Glass (RCG) coating. The RCG coating is a single layer system that meets all the optical property requirements and also has lower coating residual tensile strains. It was implemented into production in May 1976 and was used on 195 tiles that were installed on the lower mid-fuselage of the Enterprise, which was used for all the subsonic aerodynamic tests at the NASA Dryden Flight Research Center. Subsequently (ref. 28), the RCG coating was shown to be susceptible to both coating impact damage and crack propagation. However, this susceptibility is probably common to any thin glass coating; RCG is a single layer coating system that was easy to scale up to a production operation and which proved to be repairable when damage occurred.

The Class 2 frit used in the RCG coating also encountered a particle size anomaly in January 1976 when the coating process was transferred to LMSC from NASA ARC (ref. 29). Examples of coating anomalies that are caused by too many fines (particle size less than 1 micron) are shown on the left side of figure 19. Within 3 months after the implementation of both the Class 1 and Class 2 coatings into the production facility, both frits and slurries were controlled by full particle size distribution requirements (ref. 30).

Universal Patch

Rigidized fibrous insulation is subject to casting voids and to scratches and gouges during handling. The initial method for filling these voids was to fill them with cured silica slip for Class 1 coated tiles and with RCG coating for Class 2 coated tiles. This process required multiple fill and drying cycles. Also, there was concern that the dense fills could vibrate loose, and further enlarge the voids.

A universal patch material was developed that has a density approximately equal to that of the tile, is applicable to both silica and FRCI tiles, is compatible with the coating glazing cycle, is capable of repairing tile edges and corners, and is easily and rapidly applied. Existing, approved Shuttle materials which are used to compound the patch material are silica fibers, colloidal silica, acrylate solution, deionized water, and a combination of fuchsin and methyline blue dyes. The slurry is simply placed into a void at twice the void volume, and flattened with a teflon spatula. After patching, the tile is dried at 1200°F for 8 minutes, and is then ready for coating. Full patch cure occurs during coating glazing. Excellent bonding of patch to tile has been demonstrated, and no crystallization occurs from exposure to a temperature of 2300°F for 15 hours. The scrap rate for damaged tiles was significantly reduced after this procedure was introduced into production.

Tile Coating Application

Class 1 and Class 2 borosilicate glass coatings are applied to tile blanks by spray application of a slurry. Tile blanks are set up on holding fixtures, masked to provide a breather space near the IML surface, and patched as necessary to cover surface deformities. Class 1 tiles are seal-coated with a suspension of colloidal silica in water and dried prior to application of the coating. Class 2 tiles are wetted with alcohol prior to application of the coating.

The amount of slurry applied to each tile is controlled by maintaining slurry viscosity, line pressure, and the number of coats within predetermined limits. The coating weight is determined "wet" and a conversion factor is applied to calculate "dry" weight. Coating weights are between 0.07 and 0.17 lb/ft^2 for Class 1 tiles and between 0.09 and 0.17 lb/ft^2 for Class 2 tiles. The corresponding coating thicknesses are 6 to 15 mils for Class 1 tiles and 8 to 15 mils for Class 2 tiles.

Several significant problems with the coating process were encountered during production of tiles for Columbia. One problem involved robot sprayers, which were initially used in 1977 to coat the less complex tiles. The first 3000 to 4000 tiles, primarily Class 2, that were coated using the robots had excessively high reject and/or rework rates for coating deficiencies such as runs, non-uniformity and excess or insufficient coating thickness. Extensive experimentation with adjustments and programming of the robots indicated that the following problems could not be resolved with the existent capabilities of these first generation robots.

1. They were unable to accommodate minor variations in viscosity typically encountered with production batches of slurry.

2. There was no capability to change the speed of the robot from that used during the programming (teaching) phase.

3. Robots used twice as much slurry as manual spraying (i.e. only 45 tiles per 5 gallon batch were sprayed compared to as many as 80-100 tiles per batch for manual spraying).

4. The cassette tapes used to control the robots were not interchangeable between robots so each robot had to be taught (programmed) individually.

5. Dirt on the tape heads caused unplanned and uncontrollable motion in the robots.

6. There was no feedback loop in the system during the production spraying phase that could change the speed or the rate at which the slurry was being sprayed.

It was found that experienced coating technicians could accommodate the variations in tile geometry and slurry viscosity and provide a yield in excess of 95% for this operation (fig. 21). Use of robots was discontinued for spraying production tiles in March 1979. Current, more sophisticated robots, with advanced technology such as control by floppy disk or computer, and active feedback loops, could probably handle the mechanical problems. However, the ability to distinguish subtle changes in slurry viscosity and apply in-process corrections still appears to be handled best by skilled operators. A qualified sprayer can adjust the spraying speed to overcome any subtle changes in viscosity and can also touch up the tile as required at any time in the spraying sequence.

Another significant problem was high rejection rate for coating weight discrepancies. Coating weights were initially determined after glazing. Excess or insufficient coating caused the tile to be scrapped. A method of determining the coating weight while still "wet" was developed. The "wet weight" is determined by the operator and corrections are made if necessary before the coating dries. Underweight tiles receive an extra coat of slurry and overweight tiles are stripped and recoated (fig. 22). Another problem was changes in slurry viscosity with time. Slurry viscosity degraded with time to the point where it was too "thin" to be sprayed without running and sagging. Investigation showed that trace amounts of iron contamination were introduced by processing equipment at the frit manufacturer's production facility. The iron oxidized with time in the made-up slurry at LMSC, destabilizing the particle suspension. A heat treating procedure at 1000°F was used initially to oxidize the iron before making the coating slurries. Later, the source of the iron contamination at the manufacturer was identified and eliminated.

Another significant problem was wide variation in tile shrinkage rate and degree of coating fusion. Investigation showed that a narrow and repeatable temperature range is required to provide the desired dimensional tolerances and uniform degree of fusion. The degree of fusion not only affects appearance, but also water imperviousness. The original glazing kilns (stage tunnel kilns) were not capable of holding the desired temperature tolerances. Tunnel hearth roller kilns (Ipsen Inc.) were obtained that maintain temperatures within ±10°F between 2100 and 2300°F. Tile glazing problems were virtually eliminated by using these kilns.

Tile Waterproofing

Initially, the tiles were rendered hydrophobic (waterproof) by immersion in a hexamethyl - disilazane silicone/freon solution. Tile weight gain was about 1.0 percent. Several hundred grams of freon solvent evaporated from each tile during thermal exposure. The process provided good water imperviousness, but left a dark, carbonaceous residue when heated to between 800° and 1000°F, resulting in an increase in the ratio of solar absorptance to hemispherical emittance to above the 0.4 specification limit.

The present method involves release of a trimethoxysilane vapor into a vacuum chamber containing the tiles. The tile weight gain is only 0.1 percent. Also, the material sublimes in a char-free condition, and no change in optical properties is encountered.

Tile Shrinkage

During the development of LI-900, dimensional control had not been identified as a problem since little was known about tile gap heating, and the tile dimensional tolerances were not defined. Tile shrinkage and warpage were not fully understood and the significant factors that influence tile behavior during the glazing cycle were not known.

In 1976 a series of test programs led to the realization that tile shrinkage could be correlated to a single factor, tile thickness, if all other parameters were held constant. This knowledge was aided by the utilization of precision Bendix Cordax machines, which provide accurate, repeatable measurement data for each tile. This enabled Lockheed engineers to develop a clear and complete picture of tile dimensional changes during glazing.

The initial results showed that tile length or width changes were related to the glazed tile thickness. A best-fit, least-squares logarithmic equation was developed using the available data. Reference 31 describes the details of this activity.

A plot of the basic offset equation, which reflects the use of the Richmond III glass melt, is shown in figure 23. Notice that the curve crosses the dashed line of zero shrinkage at a sintered tile thickness of 2.1 inch. This means that "thin" tiles experience a net shrinkage, while thick tiles "grow" due to addition of the coating on the sides.

The basic offset equation was used for most of the 15,000 NC tile part programs that Lockheed wrote for OV-102. These programs are relatively expensive software and are not easily changed. After a new glass melt, Waterville 1, was put into use, it was discovered that tiles made from the new glass melt fibers did not shrink the same as tiles from the original Richmond III glass melt. Therefore, another test program was conducted and a new offset equation was developed.

A plot of this new equation is shown in figure 23. Waterville 1 tiles shrink more than Richmond III tiles. The difference is significant when compared to the allowable side tolerance of ±.008 inch. Since it was not cost-effective to revise the NC part programs to correct for the increased shrinkage of the new melt, it was decided to continue using the existing NC software and to apply an offset correction at the time the tile is machined. Figure 23 shows the offset for a given glazed tile thickness. A table of tile machining offsets was developed and implemented by entering a letter code on the IBM travel card that accompanies each tile. New software was written which allowed the NC machine to "read" the letter code and apply the corresponding offset to each tile side during machining.

As new glass melts were introduced into the manufacturing process, test programs were conducted to develop the appropriate offset tables (ref. 31). To date, seven melts have been used for all orbiters and an eighth melt is being processed. Approximately 110,000 tiles have been made from these melts to date.

TPS tiles were originally machined with planar vertical sides. Subsequent shrinkage investigations revealed that special offsets were necessary to control shrinkage during coating glazing (fig. 24). These special offsets are classified into three categories: planar, which is the type of shrinkage discussed above, side-slope and radius-type compensation. The planar type shrinkage, which is the largest of the three, accommodates planform shrinkage during the glazing cycle. The side-slope and radius compensations are smaller in magnitude and accommodate distortion shrinkages. The side-slope distortion occurs because the OML edge shrinks more than the base of the tile. Radius compensation is necessary because the corners shrink more than the middle side of the tile. All adjustments are made in an equal and opposite sense and constitute typical adjustments made to NC machine part programs.

The solution to the side slope distortion problem was simple and economical. Since the original part programs used the coating terminator line as the drive path, a conically shaped tool having the same diameter at the tip as the cylindrical tool was designed (fig. 26). The cone angle was designed to give optimum offset to a majority of tiles that were manufactured by LMSC. With the same diameter at the tip as the cylindrical tool, the same part programs could be used with no changes.

The radius type compensation is made by simply machining a cylinder through a point at the center of the tile side. This results in more material left at the corners to accommodate the "pillow" type distortion.

During the early stages of Columbia tile delivery, simple (square-flat) tiles were manufactured. When more complicated tiles were fabricated, dimensional problems occurred. Tiles whose sides were not parallel or normal to each other (i.e., tiles with a wrap-around OML) had a high dimensional rejection rate. An investigation revealed that the shrinkage normal to the in-plane direction, which is defined as the through-the-thickness direction, is about three times larger than the in-plane shrinkage (fig. 27). The in-plane direction usually denotes a plane that is parallel to the orbiter surface. The shrinkage and distortion of these surfaces follow a complex relationship. Since the numerically controlled machines have limitations in application of automatic offsets to only the in-plane direction, which usually lies parallel to the machine bed, no letter offset method exists to adjust the part programs. As a result, a fixed offset is used in the NC part program for through-the-thickness shrinkage corrections. For example, all elevon cove tiles receive a fixed through-the-thickness offset for a specific silica glass melt. Wraparound and step tiles are treated in a similar manner (fig. 27).

Tile Measurement and Shimming Methods

Most of the OV-102 tiles had to be measured and verified for planform dimensional conformance prior to loading into array frames to machine the IML (fig. 14). Consequently, an automated system to measure tiles was implemented. Two Cordax measuring devices were programmed to automatically summon the inspection standards from a host computer, locate the tile on the machine bed and automatically determine the acceptability of the tile by using a series of 6 to 12 predetermined touch points on the tile sides, and 5 touch points on the OML surface.

The average time to measure a tile using a Cordax machine is 5 to 15 minutes. Another device, the "maxi-measure" (fig. 28) was developed to reduce the load on the Cordax measurement machines. This device consists of two parallel plates that measure the maximum dimension of tiles with parallel sides. The average measurement time for the "maxi-measure" device is less than one minute.

After about 70% of the tiles were fabricated for OV-102 the "load-and-go" concept was implemented to reduce the time required to dimensionally inspect tiles and to increase the rate of ATA deliveries to Rockwell. As shown in figure 29, the concept consists of an initial measurement of the array frames with aluminum templates or by probe on a large bed NC mill. The tiles are then loaded into the frame and shimmed to the proper gaps. If the proper tile-to-tile gaps are obtained, the IML's of all tiles in the array are cut as a group on one of the two large bed NC mills. The ATA's are then shipped to Rockwell. The advantages of the "load-and-go" concept are:

1. The number of tiles that must be checked for planform dimensions is greatly reduced.

2. Tile planform dimensional outages greater than ±.015 inch per side are allowed but the proper tile-to-tile gaps are maintained, and the overall array dimensions are to print.

3. ATA's that did not shim to the minimum tile-to-tile gap were reworked by refiring an entire row of oversized tiles to reduce their planform dimensions (Fig. 30).

4. If the ATA cannot be shimmed to the maximum tile-to-tile gap selected, tiles are remade to allow the ATA to shim properly.

For OV-102, about 3600 tiles were shipped to Rockwell in 170 ATA's using the "load-and-go" concept. For OV-099, which was the first shipset to use the "load-and-go" concept for all AFA's, 3,200 tiles were shipped as nested tiles and 20,500 tiles were loaded into 745 ATA's under the "load-and-go" concept. For Orbiters 103 and 104, which have about 18,200 LMSC tiles, about 2,100 tiles are nested and 15,800 tiles will be loaded into 535 arrays under the "load-and-go" concept.

Material Physical Properties

LMSC has had responsibility for material characterization tests of all the ceramic RSI materials. Rockwell has had responsibility for performing the systems tests on all RSI materials including RCC and FRSI. Figure 31 shows typical average room temperature physical properties developed by LMSC for

LI-900, LI-2200 and FRCI-12. More detailed data along with values at both elevated and cryogenic temperatures can be obtained in reference 19.

CONCLUDING REMARKS

This paper has presented a multitude of lessons learned in the development and scale-up to production of three ceramic RSI materials and two borosilicate coatings that were used in the manufacture of tiles for the first three orbiters: Columbia (late 1976 to early 1979), Challenger (April 1979 to March 1982), and Discovery (March 1982 to present). These improved methods, which are summarized in Table III, are presently being used in the fabrication of tiles for Atlantis, the fourth orbiter.

The effectiveness of the lessons learned is revealed in the overall tile yields: 48% for about 23,400 tiles for Columbia, 81% for about 23,800 tiles for Challenger and 88% for about 18,200 tiles for Discovery. With the deletion of certain planform measurements of nested tiles on 1 February 1983 as a result of an expanded process control program, the overall yield on Atlantis tiles is expected to be about 90%. While some of the increase in yield can be attributed to modified requirements, the majority of the yield increase is due to the improved methods discussed herein, primarily the addition of coating terminator lines on most tiles, the addition of homing devices on the NC mills, the reliance on real time process control for coating weight, and the "load-and-go" concept.

Experience since the start of production in October 1976 has shown that ceramic fiber reusable surface insulations still retain some "art" in their fabrication processes as opposed to all "science". Consequently, making a consistent, repeatable product requires good process control and all changes to the process must be thoroughly evaluated prior to implementation and tightly controlled after implementation.

Another lesson that has been illustrated through the development of LI-900 (ref. 12), LI-2200 (ref. 13) and FRCI-12 (ref. 15) is that the RSI materials can be "tailored" to the application as with fiber-reinforced composites. This "tailoring" is also evidenced in the recent advanced studies of FRCI using ratios of Nextel to silica of up to 80/20 (ref. 32). Hence, these families of RSI materials offer the designer a very flexible design concept.

Finally, if LMSC were to introduce a new, man-rated ceramic RSI material into production for an advanced Shuttle or Orbital Transfer Vehicle, the minimum changes that would be introduced are:

- Vacuum degassing of casting slurries
- Addition of silicon carbide particles to the billets for emittance retention of the RSI in the event of coating loss during entry
- Use of an interactive graphics system like CATIA or CADAM for the design of tile geometries and to provide an automated method to write NC part programs
- Implementation of real-time process control in critical manufacturing areas

- Consideration of different coating and tile concepts if rewaterproofing is required after every flight (i.e., tiles with larger planform dimensions and fewer if any material shrinkage problems in the absence of a coating glazing cycle)

REFERENCES

1. Thermal Protection Concepts for Lifting Entry Vehicles. Lockheed Missiles & Space Co. Report 6-62-64-5, May 5, 1964.

2. Hammitt, R. L.: Lightweight Insulation, LI-15, Test Summary. Lockheed Missiles and Space Co., LMSC-685434, Code 9999, Apr. 26, 1968.

3. Rusert, E. L.: Development of a Rigidized Surface Insulative Thermal Protection System for Shuttle Orbiter, Final Report. NASA CR-114973, Feb. 15, 1971.

4. Banas, R. P.; Kural, M. H.; Deruntz, J. A.; Burns, A. B.; Chinn, A. J.; Lambert, R.; Ritz, J. R.; Vanwest, B.; and Woneis, J. T.: Space Shuttle Thermal Protection System Development. Lockheed Report LMSC-D152738, Lockheed Missiles and Space Co., Space Systems Division, Jan. 17, 1972.

5. LI-1500 Heat Shield, Independent Development Program C548. Lockheed Missiles and Space Co. Report LMSC-D153908, Dec. 24, 1971.

6. Space Shuttle Concepts. Final Report for NAS8-26362, Lockheed Missiles and Space Co. Report LMSC-D153024, Mar. 15, 1972.

7. Development and Design Application of Rigidized Surface Insulation Thermal Protection Systems. Lockheed Missiles and Space Co. Report LMSC-D282673, Dec. 30, 1972.

8. A Proposal for Space Shuttle Orbiter High-Temperature Reusable Surface Insulation. Lockheed Missiles and Space Company Report LMSC-D336595, Mar. 14, 1973.

9. Forsberg, K.: Producing the High-Temperature Reusable Surface Insulation for the Thermal Protection System of the Space Shuttle. Presented at XIVe Congress International Aeronautique, Paris, France, June 1979.

10. Burns, A. Bruce and McCarter, C. R.: Manufacture of Reusable Surface Insulation (RSI) for the Space Shuttle Orbiter. Presented at the 1980 SAE Aerospace Congress & Exposition, Oct. 15, 1980.

11. Banas, R. P.; Dolton, T. A.; Housten, S. J.; and Wilson, R. G.: Lifting Entry Vehicle Thermal Protection Review. Proceedings of Thermodynamics and Thermophysics of Space Flight. Palo Alto, California, 1970, pp. 239-276.

12. Improvement of Reusable Surface Insulation Material. Final Report for NAS9-12137. Lockheed Missiles and Space Co. Report LMSC-D266204, Mar. 1, 1972.

13. Goldstein, H. E., Smith, Marnell and Leiser, Daniel: Silica Reusable Surface Insulation. United States Patent 3,952,083, Apr. 20, 1976.

14. Leiser, Daniel B., Goldstein, Howard, E. and Smith, Marnell: Fibrous Refractory Composite Insulation. United States Patent 4,148,962, Apr. 10, 1979 (FRCI-12).

15. Banas, R. P. and Cordia E. R.: Advanced High-Temperature Insulation Material For Reentry Heat Shield Applications. Presented at 4th Annual Conference On Composites and Advanced Materials, Ceramic - Metal Systems Division - American Ceramic Society, Jan. 1980.

16. Wheeler, W. H., Garofalini, S. H. and Beasley, R. M.: Development of an Unusual Coating System for the Space Shuttle Orbiters. Paper presented at American Ceramic Society Meeting in Cincinnati, Ohio, May 4, 1976.

17. Goldstein, H. E., Leiser, D. B. and Katvala, V. W.: Reaction Cured Glass and Glass Coatings. United States Patent No. 4,093,771, June 6, 1978.

18. Banas, R. P., Gzowski, E. R. and Larsen, W. T.: Processing Aspects of the Space Shuttle Orbiter's Ceramic Reusable Surface Insulation. Proceedings of the 7th Conference on Composites and Advanced Materials, Ceramic-Metal Systems Division - American Ceramic Society, Cocoa Beach, Fla. Jan. 16-21, 1983.

19. Korb, L. J. and Clancy, H. M.: Shuttle Orbiter Thermal Protection System: A Material And Structural Overview. Presented at the 26th National Symposium Society for the Advancement of Materials and Processes Engineering, Paper No. STS 81-0219, Apr. 28-30 1981.

20. Dotts, R. L., Battley, H. H., Hughes, J. T. and Neuenschwander, W. E.: Space Shuttle Orbiter - Reusable Surface Insulation (RSI) Flight Performance. AIAA paper No. 82-0788-CP, May 1982.

21. Holmquist, G. R. and Cordia E. R.: Advances in Reusable Surface Insulation for Space Shuttle Application. MATERIALS 1980 - Proceedings of the 12th National SAMPE Technical Conference, Volume 12. Society for Advancement of Materials and Processes Engineering, Oct. 1980.

22. Banas, R. P. and Cunnington Jr., G. R.: Determination of Effective Thermal Conductivity for the Space Shuttle Orbiter's Reusable Surface Insulation (RSI). AIAA Paper No. 74-730, Thermophysics & Heat Transfer Conference, Boston, Ma., July 1974.

23. Williams, S. D. and Curry, D. M.: Nonlinear Least Squares - An Aid to Thermal Property Determination. NASA TM X-58092, June 1972.

24. Holmquist G. R., Cordia E. R. and Tomer, R. S.: Effects of Composition and Processing on Thermal Performance of a Rigidized Fibrous Ceramics Insulation Material. Ceramic Engineering and Science Proceedings - 5th Annual Conference on Composites and Advanced Materials, Volume 2, American Ceramic Society, July 1981.

25. Elgin, D. and Schirle, J.: Thermal Performance of a Fibrous Refractory Composite Insulation (FRCI). Presented at 5th Annual Conference on Composites and Advanced Materials. American Ceramic Society. Merritt Island, Florida. Jan. 18-22, 1981.

26. Tomer, R. S. and Cordia, E. R.: Development of an Improved Lightweight Insulation Material for the Space Shuttle Orbiter's Thermal Protection System, Ceramic Engineering and Science Proceedings - 6th Annual Conference on Composites and Advanced Materials, Volume 3, American Ceramic Society, pp. 601-611, Sept. 1982.

27. Tanabe, T. M. Izu, Y. D.: Influence of Particle Size Distribution on Ceramic Coating Characteristics. Presented at 32nd Pacific Boast Regional Meeting of American Ceramic Society, Seattle, Washington, Oct. 24-26, 1979.

28. Dotts, R. L., Smith, J. A., and Tillian, D. J.: Space Shuttle Orbiter Reusable Surface Insulation Flight Results. Shuttle Performance: Lessons Learned, NASA CP-2283, Part 2, 1983, pp. 949-966.

29. Creedon, J. F., Banas, R. P. and Stern, P.: Results of Lockheed Missiles & Space Co. Studies of NASA/ARC Reaction Cured Glass Coating for the Space Shuttle Orbiter. Presented at American Ceramic Society's 29th Pacific Coast Meeting under Ceramic-Metal Systems Division, San Francisco, Ca.,Nov. 2, 1976.

30. Nakano, H. N. and Izu, Y. D.: Significance of Particle Size Distribution on Refractory Frit Sintering. Presented at 12th Annual Meeting of Fine Particle Society - Powder and Bulk Solids Conference, Rosemont, Illinois, May 12-14, 1981.

31. Fitchett, B. T.: Dimensional Control of Space Shuttle Tiles during Manufacture. Proceedings of the 7th Conference on Composites and Advanced Materials, Ceramic - Metal Systems Division, American Ceramic Society, Cocoa Beach, Fla.,Jan. 16-21, 1983.

32. Leiser, D. L., Smith, M., Stewart, D. and Goldstein, H.: Thermal and Mechanical Properties of Advanced High-Temperature Ceramic Composite Insulation. Proceedings of the 7th Conference on Composites and Advanced Materials, Ceramic - Metal Systems Division - American Ceramic Society, Cocoa Beach, Fla.,Jan. 16-21, 1983.

TABLE I.- MASTER DIMENSIONS REFINEMENTS

ORIGINAL METHOD	IMPROVED METHOD
• HAND CALCULATION OF TILE CORNER POINTS & PA STANDARDS.	• MD DEVELOPED SOFTWARE TO CALCULATE CORNER POINTS & PA STANDARDS.
• HAND CALCULATION OF BLANK SIZES.	• SOFTWARE DEVELOPED TO PROVIDE BLANK SIZES.
• APPROXIMATION OF COMPLEX SURFACES.	• CAD/CAM DEVELOPMENT & CHECK OF COMPLEX SURFACES.
• PRODUCT ASSURANCE POINTS FOR HARD-TO-INSPECT TILES.	• CAD/CAM DEVELOPED MYLARS TO INSPECT COMPLEX TILES.
• HAND CALCULATION OF POINTS TO CHECK ROCKWELL MYLARS.	• CAD/CAM CHECK OF ROCKWELL MYLARS.

TABLE II.- NC PROGRAMMING REFINEMENTS

ORIGINAL METHOD	IMPROVED METHOD
• CRUDE CUT PACKAGES TO PROGRAM TILE FAMILIES.	• OPTIMIZED CUT PACKAGES TO FACILITATE PROGRAMMING & REDUCE COMPUTER RUN TIME.
• ONE INCH DIAMETER CUTTER USED FOR MOST MACHINING.	• ABOUT 30 CUTTER GEOMETRIES WERE USED TO REDUCE MACHINE TIME
• NO COATING LINE ON COMPLEX TILES.	• COATING TERMINATOR LINE ADDED TO COMPLEX TILES REDUCED SCRAP.
• SEPARATE FIXTURES FOR DIFFERENT BLANK SIZES.	• SAME FIXTURE FOR ALL BLANKS REDUCED SCRAP.
• PLANAR SIDES PROGRAMMED AS PLANAR SURFACES.	• PLANAR SIDES PROGRAMMED AS CYLINDERS TO REDUCE CORNER SHRINKAGE.
• LIMITED KNOWLEDGE OF COMPLEX SURFACES.	• EXPERIENCE REDUCED PROGRAMMING & MACHINING TIME.
• LIMITED USE OF CAD/CAM SYSTEM TO PROGRAM TILES.	• CAD/CAM SYSTEM SHOULD REDUCE TOOL TRIES.
• NO CHECK FOR REFERENCE POINT	• HOMING DEVICES INSTALLED ON N/C MILLS ASSURE PROPER REFERENCE POINT

TABLE III.- A SUMMARY OF LESSONS LEARNED

1. FIBER PREPARATION METHODS
    - A 20 blend of Manville silica fibers provides better material uniformity.
    - Use of a hydro-cyclone removes unwanted glass shot from the silica fiber lots.
    - Dual stage agitation of Nextel fibers eliminates fiber clumping in FRCI-12 billets.
2. BILLET CASTING AND SINTERING METHODS
    - Precursor silica fiber lot compact tests allow better prediction of production billet sintering requirements.
    - Elimination of an intermediate billet sintering cycle for LI-900 was successfully accomplished.
    - Implementation of void reduction and vacuum assisted casting procedures minimize voids in LI-900 billets.
    - Implementation of six-side heating for LI-900 and FRCI-12 during the sintering cycle improved the strength distribution within billets.
    - Vacuum degassing of slurries for LI-2200 and FRCI-12 prior to casting eliminates voids in the billets.
    - The high dry-density concept for FRCI-12 and FRCI-8 was successfully used to tailor the apparent thermal conductivity.
3. ENGINEERING DATA AND NUMERICAL CONTROL PROGRAMMING REFINEMENTS
    - Experience with the data has led to many refinements in the tile part programs that have made tile fabrication more efficient.
    - Addition of various software tools reduced the requirement to hand calculate various master dimension surfaces.
    - The use of interactive graphics methods for tile design and NC part programming would reduce the number of tool tries and improve efficiency.
    - Use of CADAM to generate mylars for use as tile dimensional inspection tools eliminates the need to supply computerized tile dimensional data for hard-to-measure tiles.
4. TILE FABRICATION
    - The addition of homing devices on the NC mills provided assurance that tiles were being cut correctly.
    - Design changes to the cutting tools improved the consistency of the tile-to-tile gaps in the delivered tiles.
    - An understanding of fiber shrinkage characteristics for LI-900, LI-2200 and FRCI-12 led to the implementation of tile machining offsets that resulted in tiles that meet the dimensional requirements.
    - Implementation of letter offsets on the IBM tile travel cards with appropriate changes in the NC hardware and software provided an efficient method to modify tile machining offsets.
    - Recognition of the anisotropic shrinkage characteristics of LI-900, LI-2200 and FRCI-12 further improved the tile dimensional yield.
5. COATINGS AND THEIR APPLICATION
    - Use of a universal patch compound prior to coating spraying eliminated irregular surfaces and craters in the glazed coatings.
    - Man is a more efficient tile sprayer than robots.
    - Control of particle size for glass frits and coating slurries eliminated most coating anomalies.
    - Real time process control of coating weight in the manufacturing area eliminated tiles scrapped for coating weight.
    - The propensity for cracks in the Class 1 coating was resolved by increasing the maximum coating weight to 0.17 $lb/_{ft}2$, making it consistent with the Class 2 coating.
6. TILE MEASUREMENT AND SHIMMING
    - Introduction of the "maxi-measure" and Cordax apparatus yielded accurate dimensional data.
    - The "Load-and-Go" concept minimized tiles being scrapped for planform dimensional anomalies, while preserving dimensional control at the array level.
    - Introduction of a second glazing operation, to shrink tiles, eliminated tiles scrapped for an oversize condition.
    - Use of mylars for complex or hard-to-measure tiles for Challenger greatly improved the determination of acceptability compared to the "whip-and-fit" criterion used for Columbia's complex tiles.

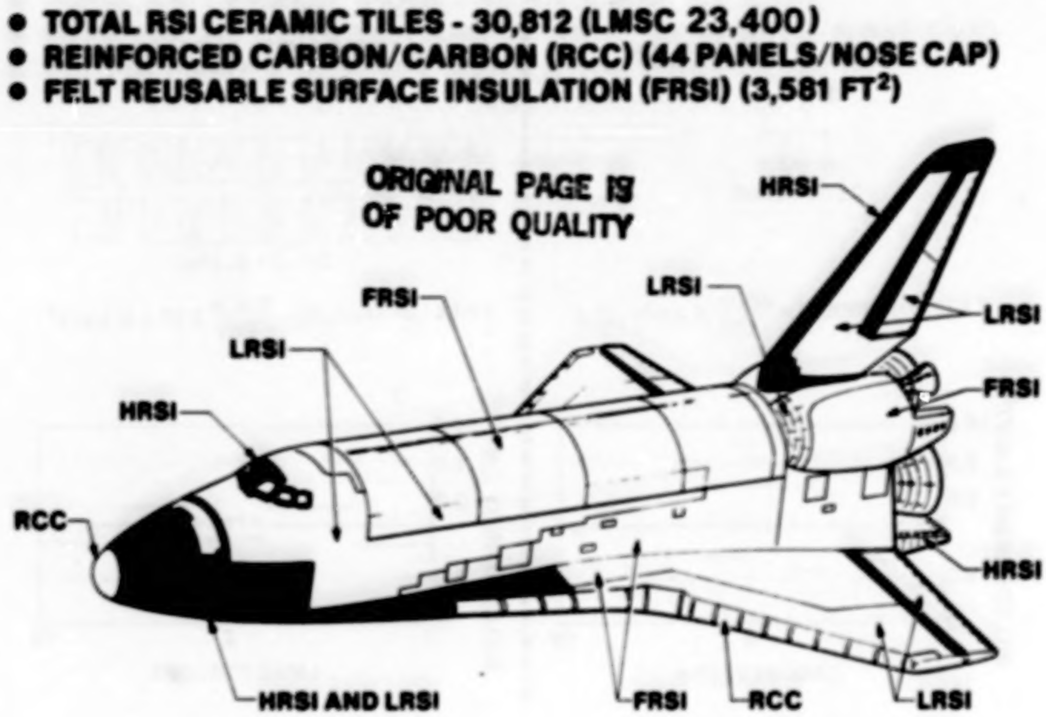
• TOTAL RSI CERAMIC TILES - 30,812 (LMSC 23,400)
• REINFORCED CARBON/CARBON (RCC) (44 PANELS/NOSE CAP)
• FELT REUSABLE SURFACE INSULATION (FRSI) (3,581 FT²)
HRSI
LRSI
FRSI
LRSI
LRSI
FRSI
HRSI
RCC
HRSI
HRSI AND LRSI
FRSI
RCC
LRSI

Figure 1.- TPS locations on Columbia (OV-102).

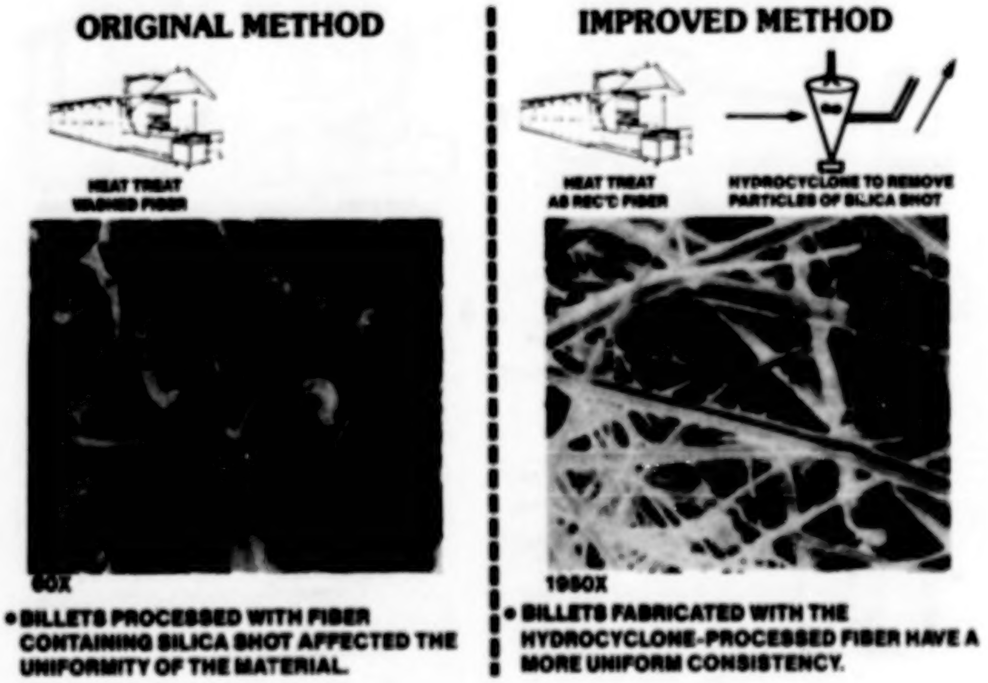
ORIGINAL METHOD
IMPROVED METHOD
HEAT TREAT
WASHED FIBER
HEAT TREAT
AS REC'D FIBER
HYDROCYCLONE TO REMOVE
PARTICLES OF SILICA SHOT
60X
1950X
• BILLETS PROCESSED WITH FIBER CONTAINING SILICA SHOT AFFECTED THE UNIFORMITY OF THE MATERIAL.
• BILLETS FABRICATED WITH THE HYDROCYCLONE-PROCESSED FIBER HAVE A MORE UNIFORM CONSISTENCY.

Figure 2.- Pretreatment of silica fibers for LI-900.

ORIGINAL PAGE IS
OF POOR QUALITY

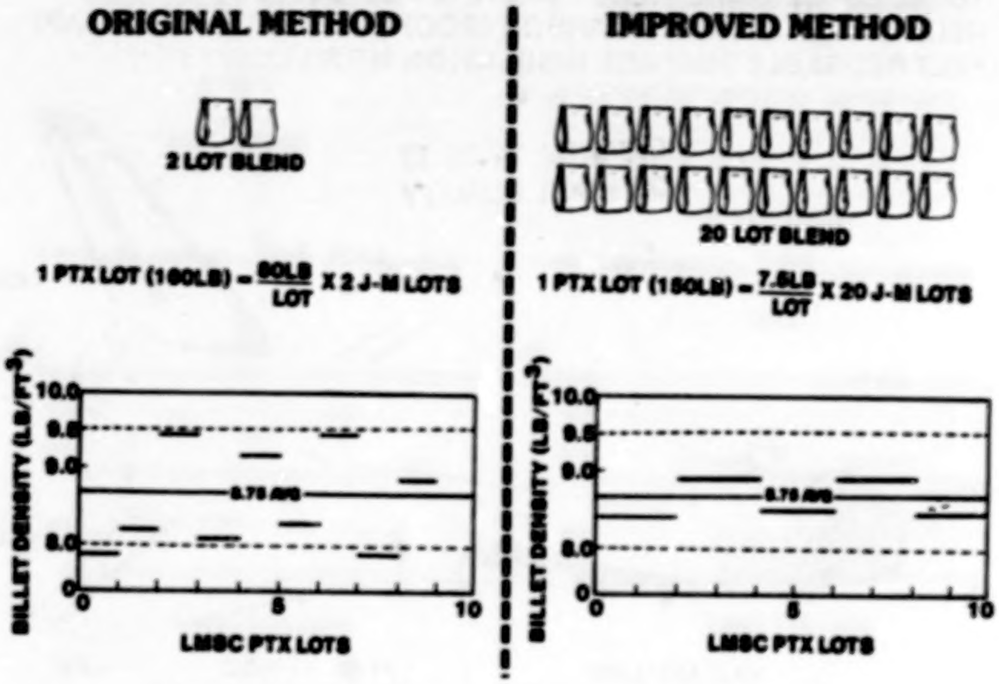

Figure 3.- Blending J-M fiber lots for LI-900.

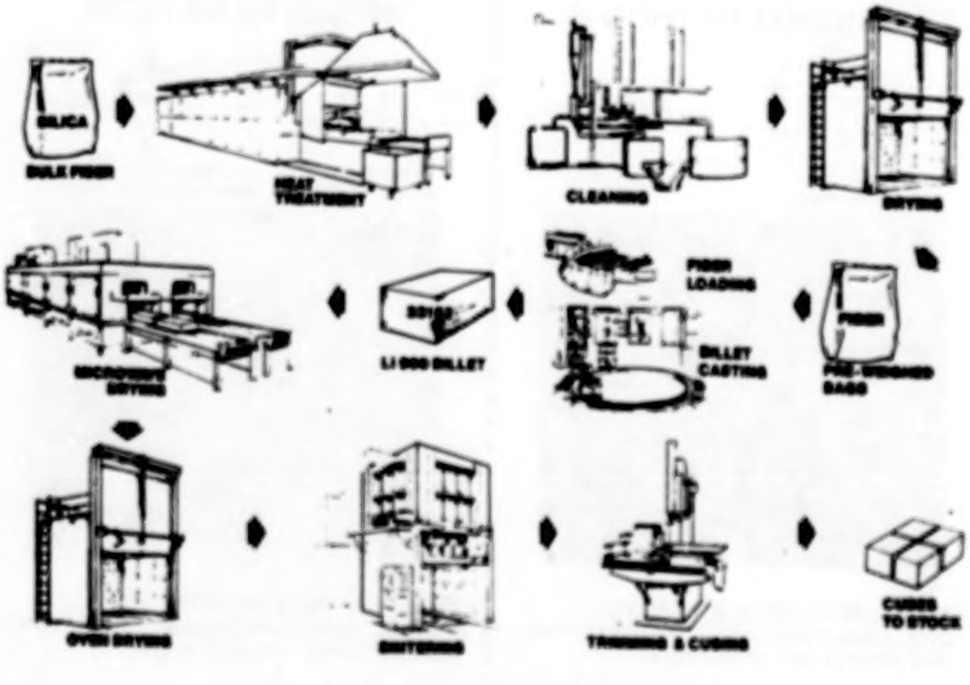
SILICA
BULK FIBER
HEAT TREATMENT
CLEANING
DRYING
MICROWAVE DRYING
LI 900 BILLET
FIBER LOADING
BILLET CASTING
FIBER
PRE-WEIGHED BAGS
OVEN DRYING
SINTERING
TRIMMING & CUBING
CUBES TO STOCK

Figure 4.- LI-900 process flow.

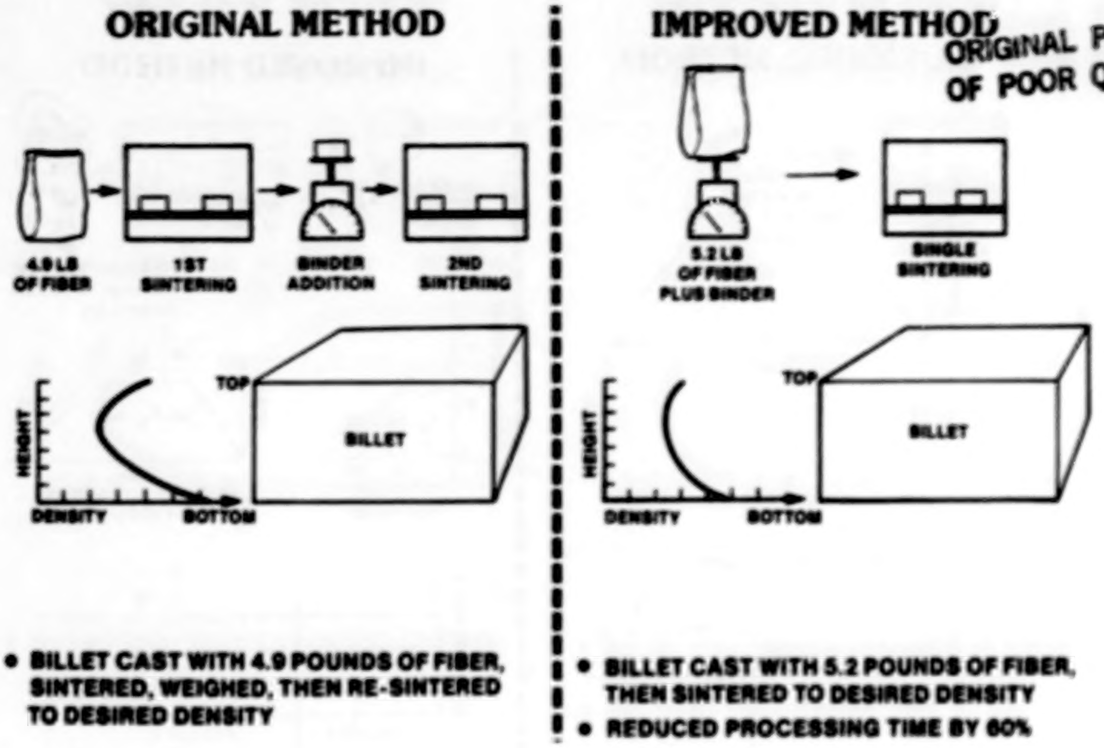
ORIGINAL METHOD
4.9 LB OF FIBER
1ST SINTERING
BINDER ADDITION
2ND SINTERING
HEIGHT
DENSITY
TOP
BOTTOM
BILLET
IMPROVED METHOD
5.2 LB OF FIBER PLUS BINDER
SINGLE SINTERING
HEIGHT
DENSITY
TOP
BOTTOM
BILLET

- BILLET CAST WITH 4.9 POUNDS OF FIBER, SINTERED, WEIGHED, THEN RE-SINTERED TO DESIRED DENSITY

- BILLET CAST WITH 5.2 POUNDS OF FIBER, THEN SINTERED TO DESIRED DENSITY
- REDUCED PROCESSING TIME BY 60%

Figure 5.- Changes in LI-900 casting and sintering procedures.

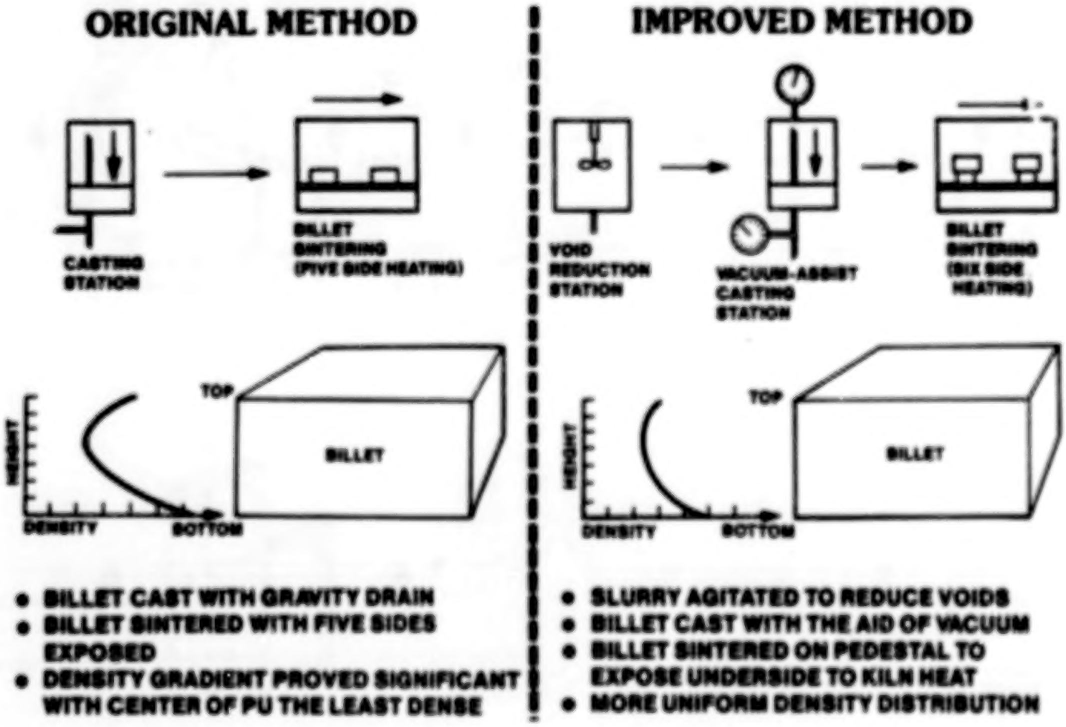
ORIGINAL METHOD
CASTING STATION
BILLET SINTERING (FIVE SIDE HEATING)
HEIGHT
DENSITY
TOP
BOTTOM
BILLET
IMPROVED METHOD
VOID REDUCTION STATION
VACUUM-ASSIST CASTING STATION
BILLET SINTERING (SIX SIDE HEATING)
HEIGHT
DENSITY
TOP
BOTTOM
BILLET

- BILLET CAST WITH GRAVITY DRAIN
- BILLET SINTERED WITH FIVE SIDES EXPOSED
- DENSITY GRADIENT PROVED SIGNIFICANT WITH CENTER OF PU THE LEAST DENSE

- SLURRY AGITATED TO REDUCE VOIDS
- BILLET CAST WITH THE AID OF VACUUM
- BILLET SINTERED ON PEDESTAL TO EXPOSE UNDERSIDE TO KILN HEAT
- MORE UNIFORM DENSITY DISTRIBUTION

Figure 6.- LI-900 void reduction and vacuum assisted casting methods.

ORIGINAL PAGE IS
OF POOR QUALITY

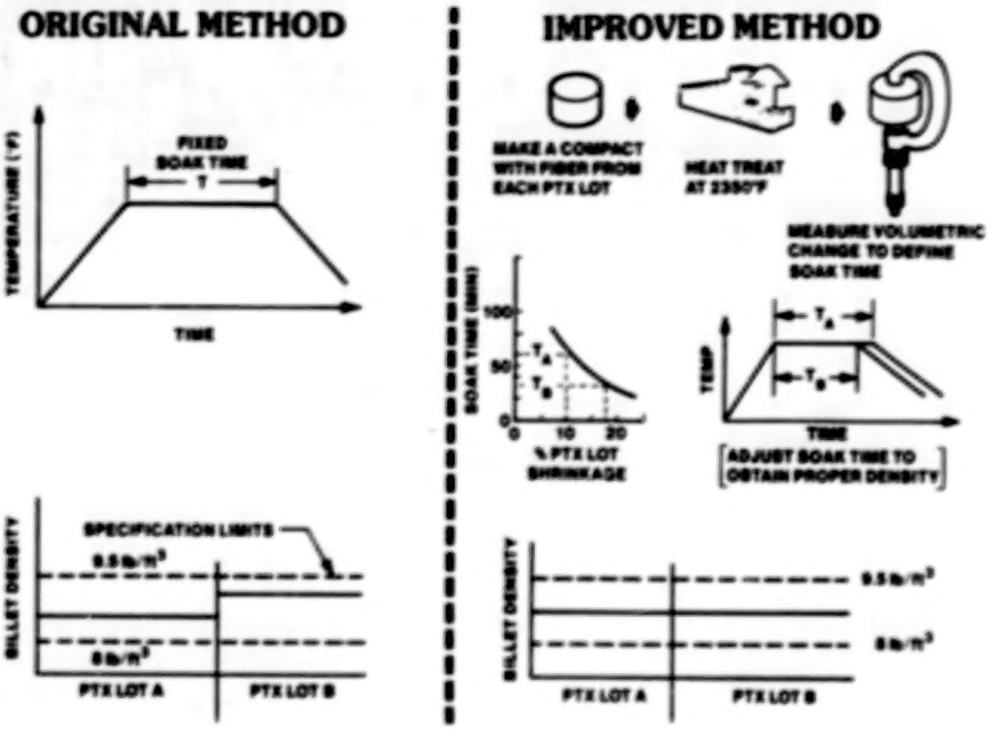
ORIGINAL METHOD
IMPROVED METHOD
FIXED
SOAK TIME
T
TEMPERATURE (°F)
TIME
MAKE A COMPACT
WITH FIBER FROM
EACH PTX LOT
HEAT TREAT
AT 2350°F
MEASURE VOLUMETRIC
CHANGE TO DEFINE
SOAK TIME
SOAK TIME (MIN)
100
50
0
T_A
T_B
10
20
% PTX LOT
SHRINKAGE
TEMP
TIME
ADJUST SOAK TIME TO
OBTAIN PROPER DENSITY
SPECIFICATION LIMITS
9.5 lb/ft³
8 lb/ft³
BILLET DENSITY
PTX LOT A
PTX LOT B

Figure 7.- Silica fiber compact test for LI-900.

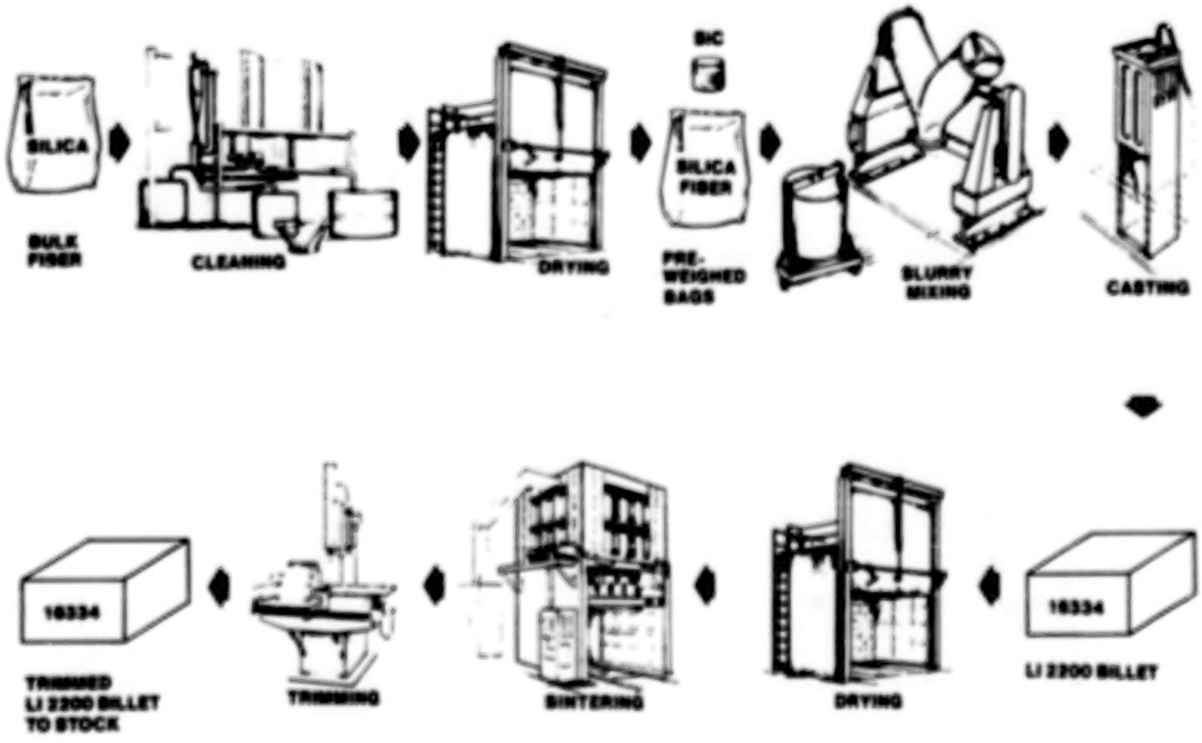
SILICA
BULK
FIBER
CLEANING
DRYING
SiC
SILICA
FIBER
PRE-
WEIGHED
BAGS
SLURRY
MIXING
CASTING
16334
TRIMMED
LI 2200 BILLET
TO STOCK
TRIMMING
SINTERING
DRYING
16334
LI 2200 BILLET

Figure 8.- LI-2200 process flow.

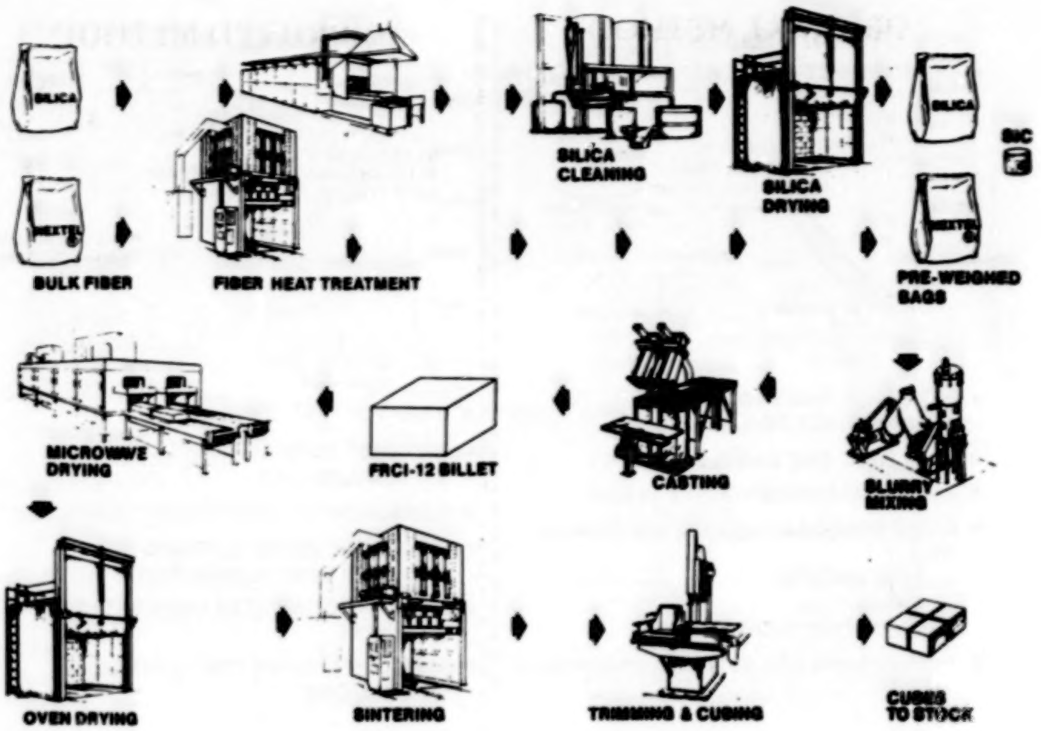
SILICA
NEXTEL
BULK FIBER
FIBER HEAT TREATMENT
SILICA CLEANING
SILICA DRYING
SILICA
SIC
NEXTEL
PRE-WEIGHED BAGS
MICROWAVE DRYING
FRCI-12 BILLET
CASTING
SLURRY MIXING
OVEN DRYING
SINTERING
TRIMMING & CUBING
CUBES TO STOCK

Figure 9.- FRCI-12 process flow.

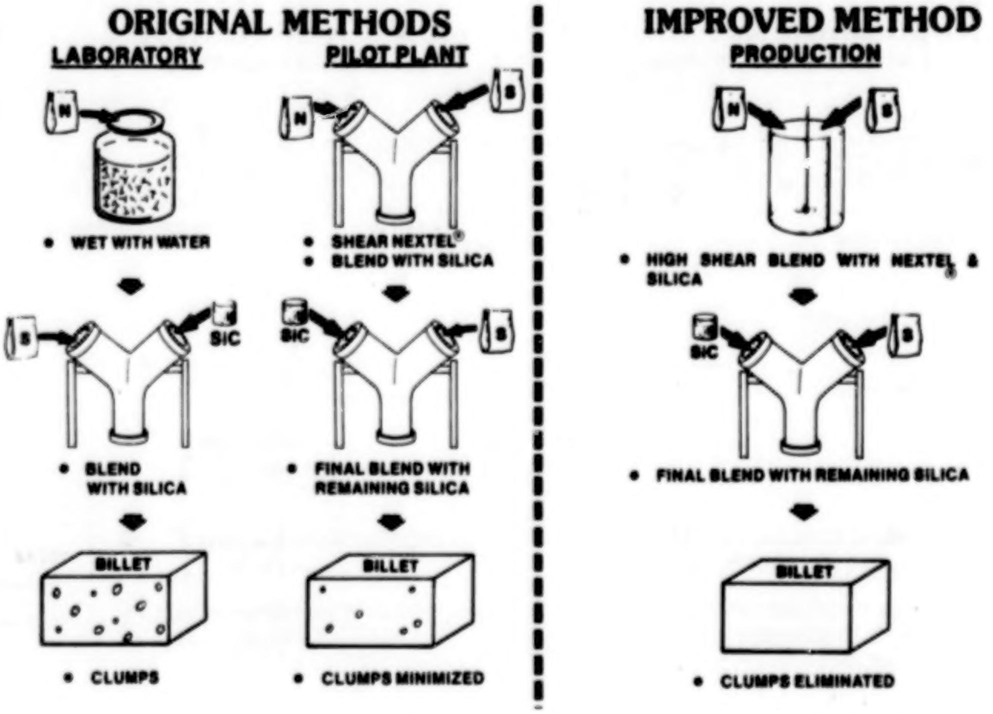
ORIGINAL METHODS
LABORATORY
PILOT PLANT
IMPROVED METHOD
PRODUCTION
N
S
• WET WITH WATER
• SHEAR NEXTEL®
• BLEND WITH SILICA
• HIGH SHEAR BLEND WITH NEXTEL® & SILICA
S
SIC
• BLEND WITH SILICA
• FINAL BLEND WITH REMAINING SILICA
• FINAL BLEND WITH REMAINING SILICA
BILLET
• CLUMPS
• CLUMPS MINIMIZED
• CLUMPS ELIMINATED

Figure 10.- Nextel dispersion methods for FRCI-12.

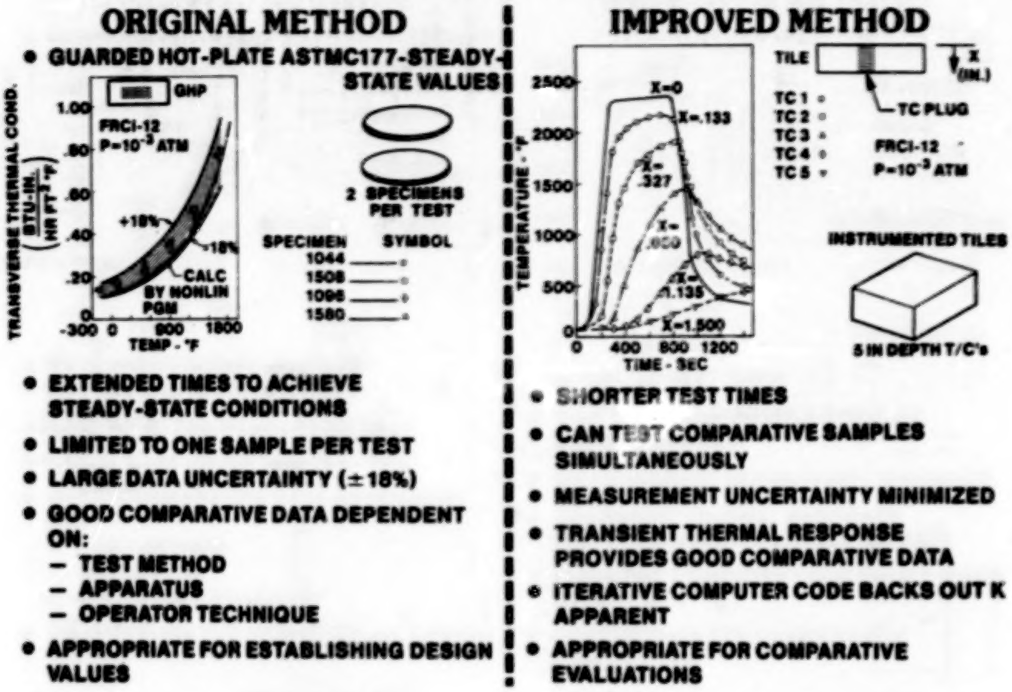

ORIGINAL METHOD

- GUARDED HOT-PLATE ASTMC177-STEADY-STATE VALUES
- EXTENDED TIMES TO ACHIEVE STEADY-STATE CONDITIONS
- LIMITED TO ONE SAMPLE PER TEST
- LARGE DATA UNCERTAINTY (±18%)
- GOOD COMPARATIVE DATA DEPENDENT ON:
  - TEST METHOD
  - APPARATUS
  - OPERATOR TECHNIQUE
- APPROPRIATE FOR ESTABLISHING DESIGN VALUES

IMPROVED METHOD

- SHORTER TEST TIMES
- CAN TEST COMPARATIVE SAMPLES SIMULTANEOUSLY
- MEASUREMENT UNCERTAINTY MINIMIZED
- TRANSIENT THERMAL RESPONSE PROVIDES GOOD COMPARATIVE DATA
- ITERATIVE COMPUTER CODE BACKS OUT K APPARENT
- APPROPRIATE FOR COMPARATIVE EVALUATIONS

Figure 11.- Thermal performance evaluation methods.

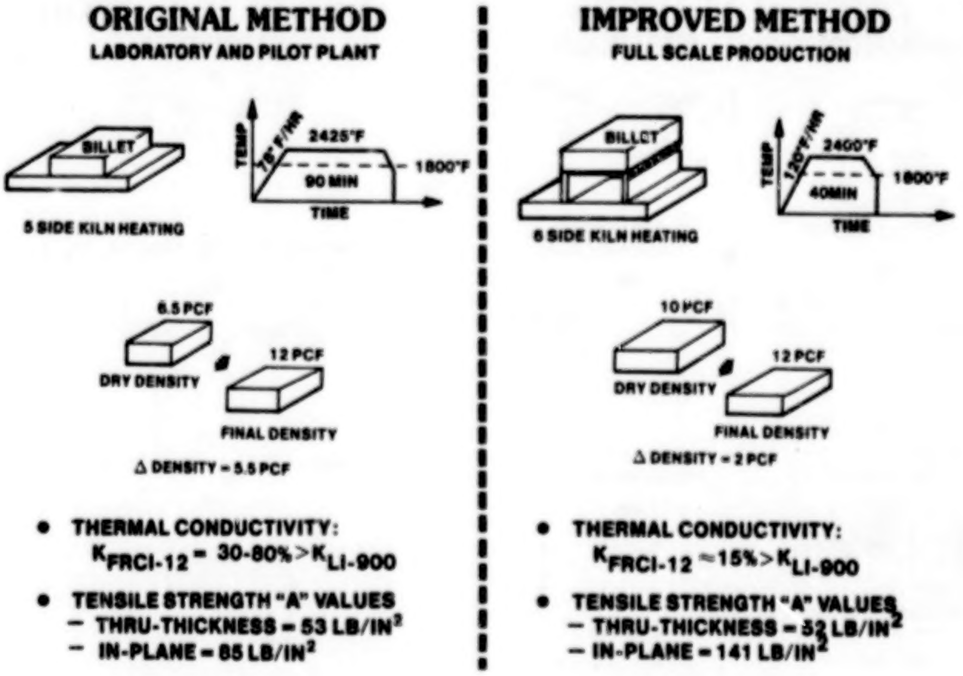
ORIGINAL METHOD
LABORATORY AND PILOT PLANT
BILLET
5 SIDE KILN HEATING
TEMP
75°F/HR
2425°F
90 MIN
1800°F
TIME
6.5 PCF
DRY DENSITY
12 PCF
FINAL DENSITY
Δ DENSITY = 5.5 PCF
IMPROVED METHOD
FULL SCALE PRODUCTION
BILLET
6 SIDE KILN HEATING
TEMP
120°F/HR
2400°F
40MIN
1800°F
TIME
10 PCF
DRY DENSITY
12 PCF
FINAL DENSITY
Δ DENSITY = 2 PCF

ORIGINAL METHOD

- THERMAL CONDUCTIVITY: $K_{FRCI-12} = 30\text{-}80\% > K_{LI-900}$
- TENSILE STRENGTH "A" VALUES
  - THRU-THICKNESS = 53 LB/IN²
  - IN-PLANE = 85 LB/IN²

IMPROVED METHOD

- THERMAL CONDUCTIVITY: $K_{FRCI-12} \approx 15\% > K_{LI-900}$
- TENSILE STRENGTH "A" VALUES
  - THRU-THICKNESS = 52 LB/IN²
  - IN-PLANE = 141 LB/IN²

Figure 12.- High dry density concept for FRCI-12.

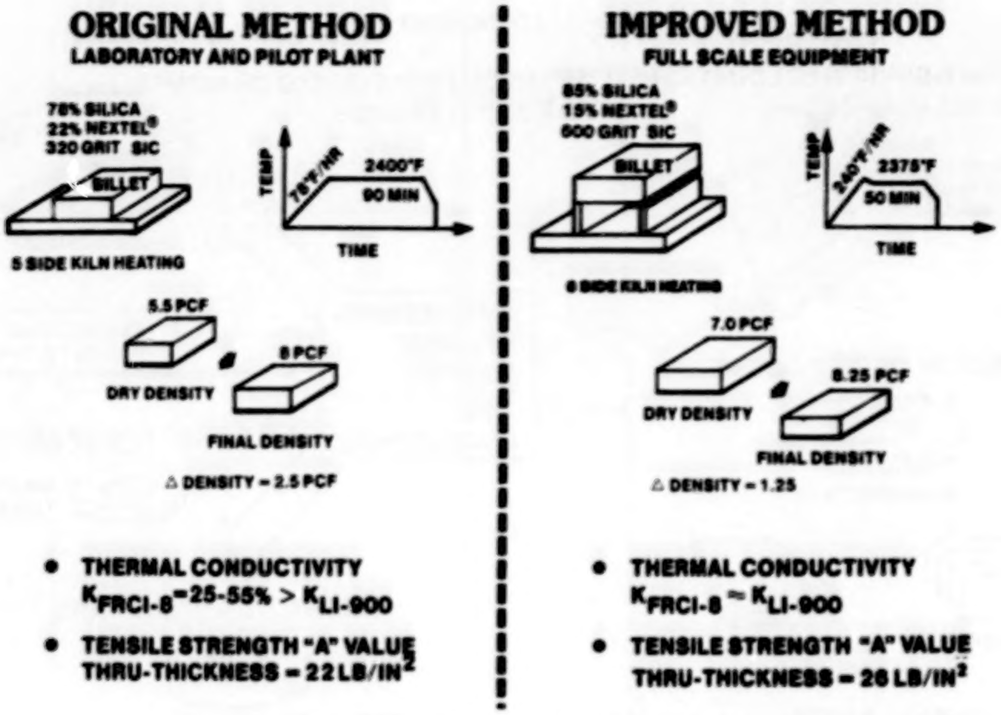
ORIGINAL METHOD
LABORATORY AND PILOT PLANT
78% SILICA
22% NEXTEL®
320 GRIT SIC
BILLET
5 SIDE KILN HEATING
TEMP
75°F/HR
2400°F
90 MIN
TIME
5.5 PCF
DRY DENSITY
8 PCF
FINAL DENSITY
△ DENSITY = 2.5 PCF
• THERMAL CONDUCTIVITY
K FRCI-8 = 25-55% > K LI-900
• TENSILE STRENGTH "A" VALUE
THRU-THICKNESS = 22 LB/IN²
IMPROVED METHOD
FULL SCALE EQUIPMENT
85% SILICA
15% NEXTEL®
600 GRIT SIC
BILLET
6 SIDE KILN HEATING
TEMP
240°F/HR
2375°F
50 MIN
TIME
7.0 PCF
DRY DENSITY
8.25 PCF
FINAL DENSITY
△ DENSITY = 1.25
• THERMAL CONDUCTIVITY
K FRCI-8 ≈ K LI-900
• TENSILE STRENGTH "A" VALUE
THRU-THICKNESS = 26 LB/IN²

Figure 13.- FRCI-8 high dry density concept.

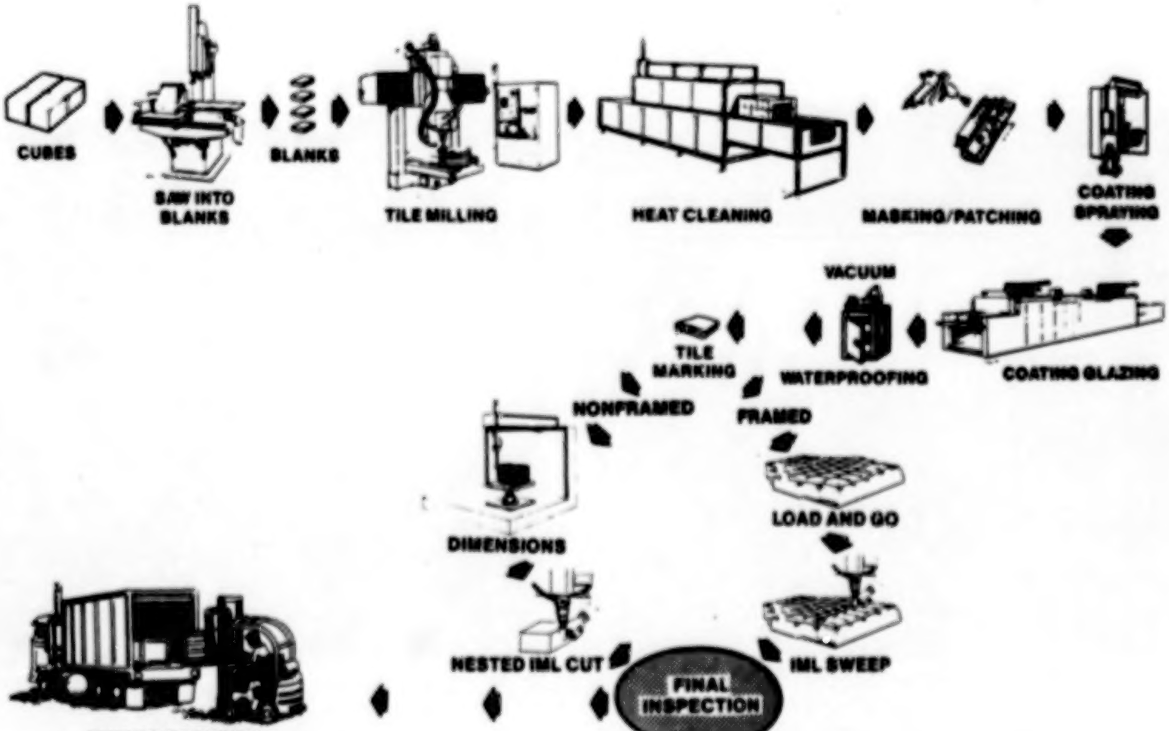
CUBES
SAW INTO BLANKS
BLANKS
TILE MILLING
HEAT CLEANING
MASKING/PATCHING
COATING SPRAYING
COATING GLAZING
VACUUM
WATERPROOFING
TILE MARKING
NONFRAMED
FRAMED
LOAD AND GO
DIMENSIONS
IML SWEEP
NESTED IML CUT
FINAL INSPECTION
SHIP TO ROCKWELL

Figure 14.- The tile process flow.

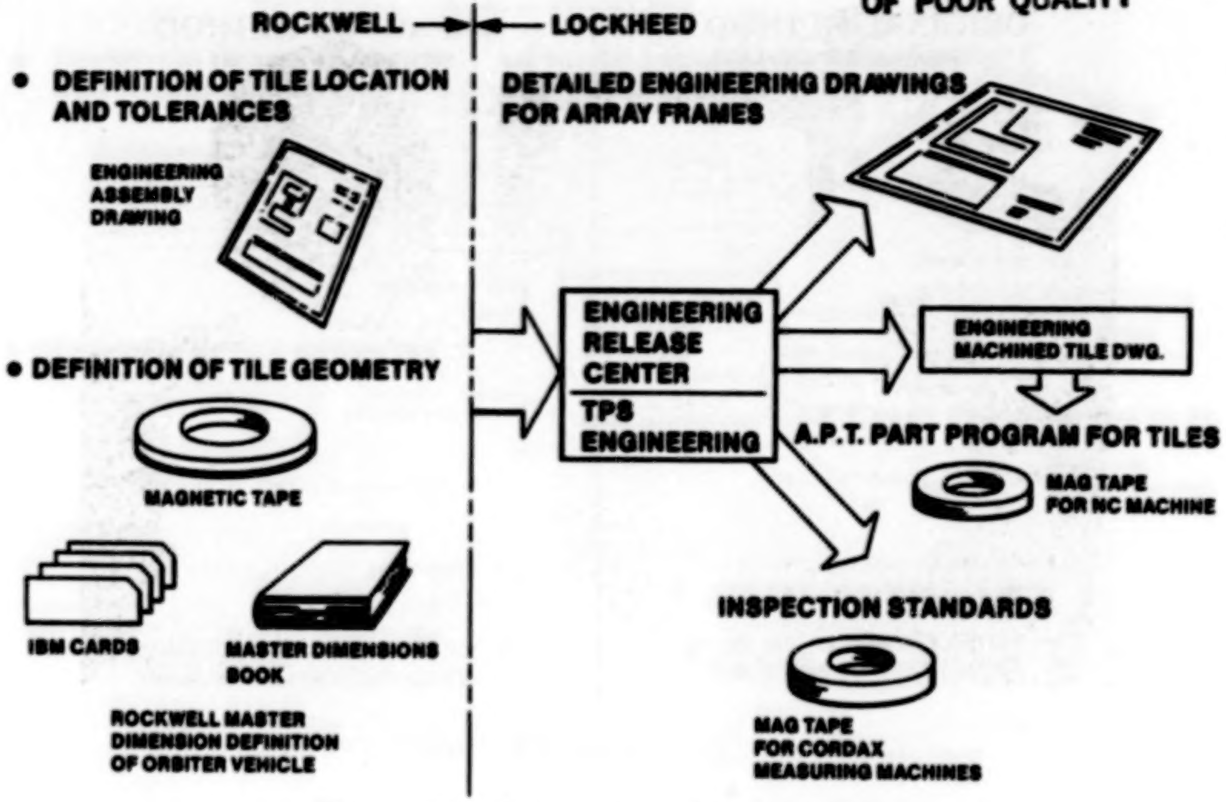
ROCKWELL
LOCKHEED
• DEFINITION OF TILE LOCATION AND TOLERANCES
ENGINEERING ASSEMBLY DRAWING
• DEFINITION OF TILE GEOMETRY
MAGNETIC TAPE
IBM CARDS
MASTER DIMENSIONS BOOK
ROCKWELL MASTER DIMENSION DEFINITION OF ORBITER VEHICLE
DETAILED ENGINEERING DRAWINGS FOR ARRAY FRAMES
ENGINEERING RELEASE CENTER
TPS ENGINEERING
ENGINEERING MACHINED TILE DWG.
A.P.T. PART PROGRAM FOR TILES
MAG TAPE FOR NC MACHINE
INSPECTION STANDARDS
MAG TAPE FOR CORDAX MEASURING MACHINES

Figure 15.- The engineering data flow.

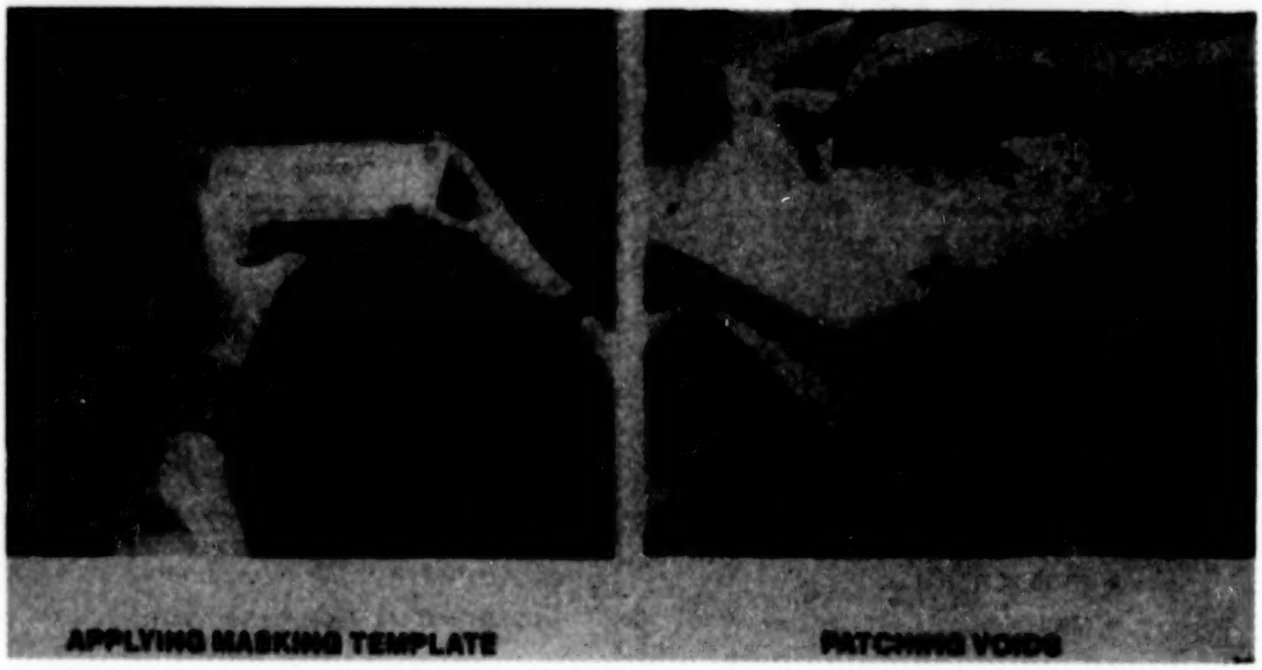
APPLYING MASKING TEMPLATE

PATCHING VOIDS

Figure 16.- Examples of complex tiles without coating terminator lines.

ORIGINAL PAGE IS
OF POOR QUALITY

Figure 17.- An interactive graphics method showing a Shuttle infrared leeside temperature sensing tile.

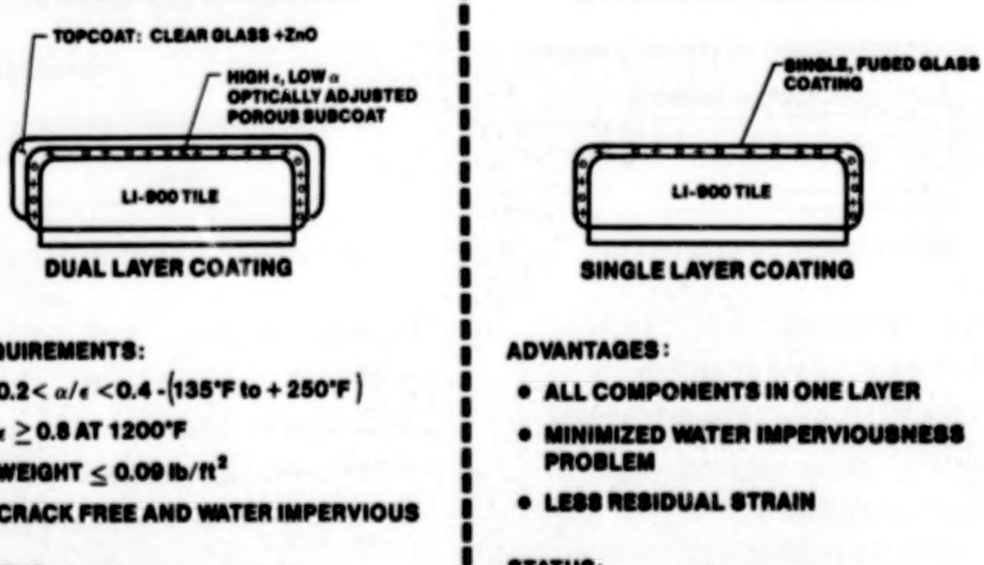
TOPCOAT: CLEAR GLASS +ZnO
HIGH ε, LOW α
OPTICALLY ADJUSTED
POROUS SUBCOAT
LI-900 TILE
DUAL LAYER COATING
SINGLE, FUSED GLASS
COATING
LI-900 TILE
SINGLE LAYER COATING

ORIGINAL COATING

REQUIREMENTS:

- $0.2 < \alpha/\epsilon < 0.4$ -(135°F to + 250°F)
- $\epsilon \geq 0.8$ AT 1200°F
- WEIGHT ≤ 0.09 lb/ft^2
- CRACK FREE AND WATER IMPERVIOUS

STATUS:

- PRODUCTION START IN OCT. 1977
- THIN COATING CRACKED EASILY

IMPROVED COATING

ADVANTAGES:

- ALL COMPONENTS IN ONE LAYER
- MINIMIZED WATER IMPERVIOUSNESS PROBLEM
- LESS RESIDUAL STRAIN

STATUS:

- USED ON COLUMBIA AT 0.12 lb/ft^2
- USED ON CHALLENGER AT 0.17 lb/ft^2

Figure 18.- Class 1 coating optimization.

ORIGINAL PAGE IS
OF POOR QUALITY

ORIGINAL METHOD

- COATING ANOMALIES

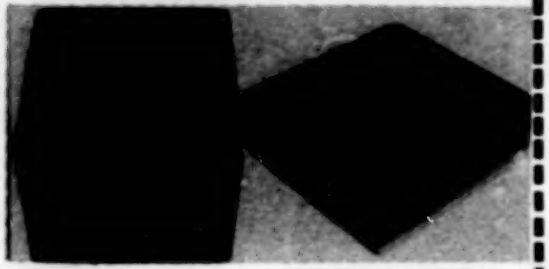
"MUD CRACKING"
"ONION SKINNING"

STATUS:

- NO CLASS 1 FRIT SIZE CONTROL OTHER THAN 90% THROUGH 325 MESH AND A 50% POINT REQUIREMENT
- USE OF SLURRY IMMEDIATELY AFTER PREPARATION ELIMINATED VISCOSITY VARIATIONS
- NO CLASS 2 FRIT SIZE CONTROL OTHER THAN A 50% POINT REQUIREMENT

IMPROVED METHOD

- DEFINED FULL PARTICLE SIZE DISTRIBUTION FOR CL.1/CL. 2 FRITS AND SLURRIES

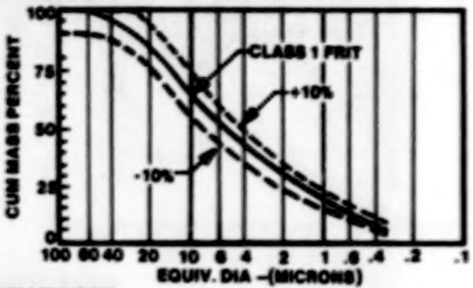

ADVANTAGES:

- SLURRY VISCOSITY CONTROL IS IMPROVED
- SPRAYING CHARACTERISTICS ARE MORE UNIFORM
- COATING CRACKS DURING GLAZING ARE ELIMINATED
- FUSION OF CLASS 1 AND CLASS 2 COATINGS IS ASSURED

Figure 19.- Effect of glass frit particle size effects on glazed coatings.

ORIGINAL COATING

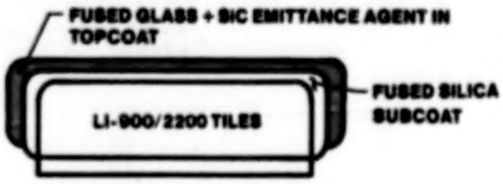
FUSED GLASS + SiC EMITTANCE AGENT IN TOPCOAT
LI-900/2200 TILES
FUSED SILICA SUBCOAT

DUAL LAYER COATING (0050)

CHARACTERISTICS:

- EMITTANCE ≥ 0.8 AT 2300°F
- HIGH RESIDUAL TENSILE STRAINS (200-300$\mu\epsilon$)
  - HIGH CRACK PROPAGATION
- GLAZED AT 2500°F
- FOAMED DURING EXPOSURE TO PLASMA TESTS

IMPROVED COATING

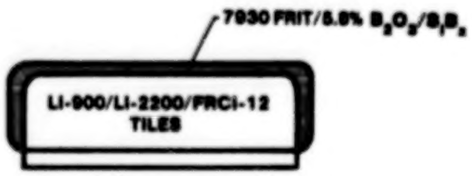
7930 FRIT/5.5% B_2O_3/SiB_4
LI-900/LI-2200/FRCI-12 TILES

SINGLE LAYER COATING (RCG)

CHARACTERISTICS:

- WEIGHT ≤0.17 lb/ft^2
- GLAZED AT 2200°F
- EMITTANCE ≥0.8 AT 2300°F
- LOW RESIDUAL TENSILE STRAINS (50-100$\mu\epsilon$)
  - MINIMAL CRACK PROPAGATION
- REUSABLE TO 2300°F
- GOOD FOR SINGLE EXPOSURE TO 2700°F

Figure 20.- Class 2 coating optimization.

ORIGINAL PAGE IS
OF POOR QUALITY

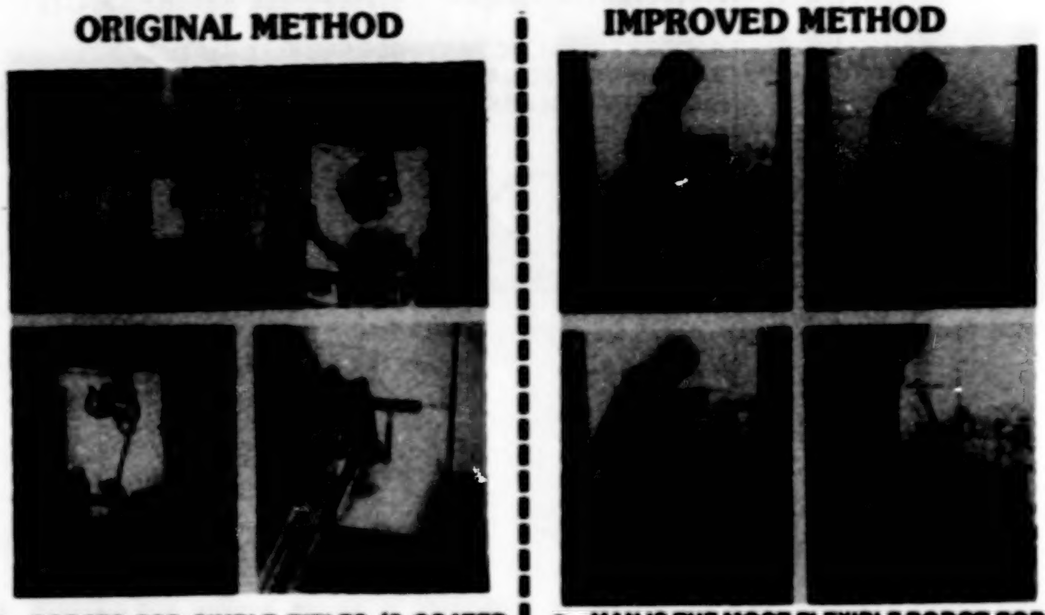

ORIGINAL METHOD

- ROBOTS FOR SIMPLE TITLES (5 COATED SURFACES)
- MAN FOR COMPLEX TITLES (UP TO 20 SURFACES)

IMPROVED METHOD

- MAN IS THE MOST FLEXIBLE ROBOT FOR ALL TILES

Figure 21.- Methods of spraying class 1 and class 2 tiles.

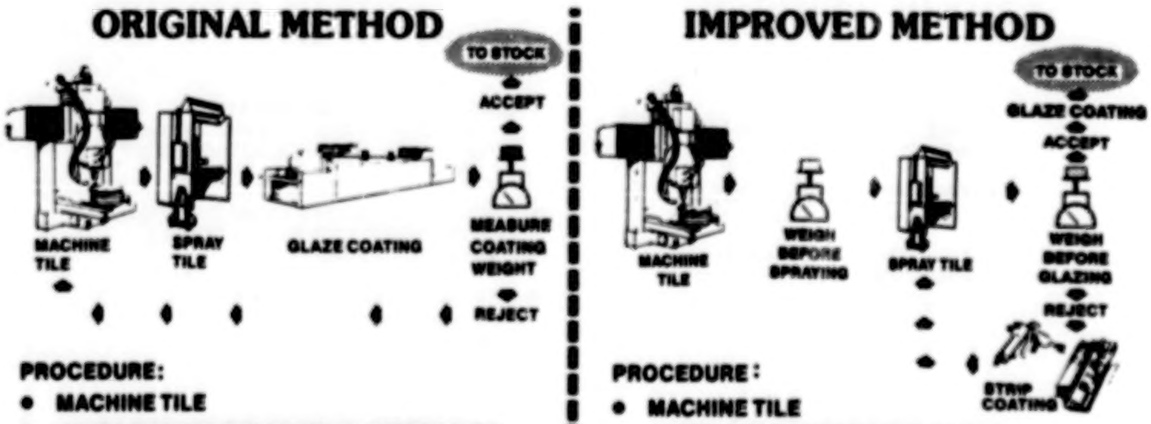
TO STOCK
ACCEPT
MACHINE TILE
SPRAY TILE
GLAZE COATING
MEASURE COATING WEIGHT
REJECT
TO STOCK
GLAZE COATING
ACCEPT
MACHINE TILE
WEIGH BEFORE SPRAYING
SPRAY TILE
WEIGH BEFORE GLAZING
REJECT
STRIP COATING

ORIGINAL METHOD

PROCEDURE:

- MACHINE TILE
- WEIGH BEFORE SPRAYING IN INSPECTION
- WEIGH AFTER COATING GLAZING IN INSPECTION
- SCRAP TILES FOR LOW OR HIGH COATING WEIGHT
- MACHINE NEW TILE

DISADVANTAGES:

- TILES SCRAPPED FOR HIGH/LOW COATING WEIGHT
- TIME LOST TO REMACHINE TILES

IMPROVED METHOD

PROCEDURE:

- MACHINE TILE
- WEIGH BEFORE SPRAYING IN MFG
- WEIGH BEFORE GLAZING IN MFG
- STRIP COATING FROM LOW/HIGH WT. TILES
- RESPRAY SAME TILE

ADVANTAGES:

- ELIMINATES:
  - TILES SCRAPPED FOR COATING WEIGHT
  - MACHINING NEW TILES
  - QUALITY ASSURANCE WEIGHT CHECKS
- SUBSTITUTES IN PROCESS COATING WEIGHT CHECK

Figure 22.- Methods to control coating weight.

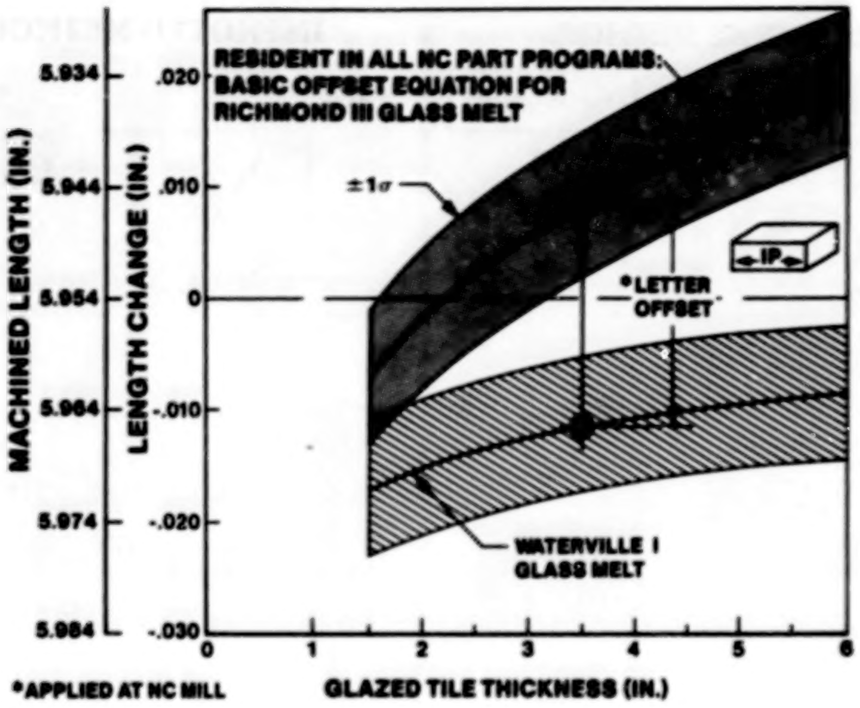

Figure 23.- In-plane machining offsets for LI-900.

- ALL ENGINEERING DEFINITION IS BASED ON COMPUTER (MASTER DIMENSION) DATA
- EACH TILE HAS UNIQUE PART PROGRAM FOR NC MACHINING
- ALL MANUFACTURING AND INSPECTION OPERATIONS ARE CONTROLLED BY ONE IBM CARD PER TILE
- DIMENSIONAL REQUIREMENT ± 0.016-INCH (LENGTH & WIDTH) AND ± 0.010-INCH (THICKNESS) FOR MOST TILES
- EACH TILE REQUIRES COMPENSATION FOR MATERIAL SHRINKAGE DURING COATING GLAZING
- SHRINKAGE VARIES WITH
  - GLASS MELT
  - TILE THICKNESS
  - TILE PLANFORM

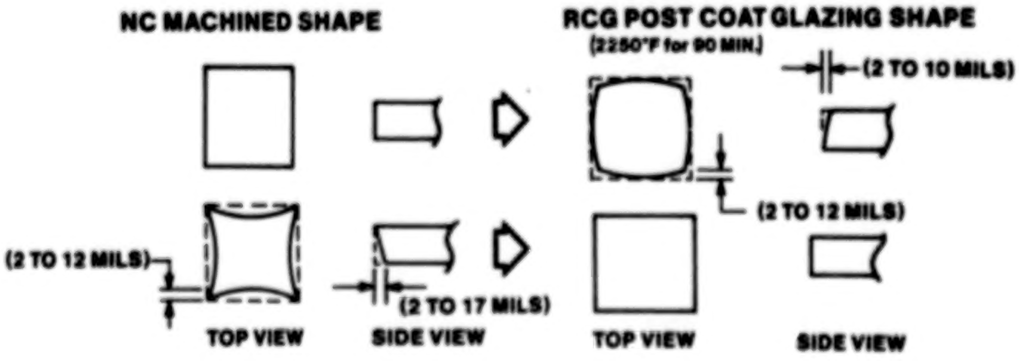
NC MACHINED SHAPE
RCG POST COAT GLAZING SHAPE
(2250°F for 90 MIN.)
(2 TO 10 MILS)
(2 TO 12 MILS)
(2 TO 12 MILS)
(2 TO 17 MILS)
TOP VIEW
SIDE VIEW
TOP VIEW
SIDE VIEW

Figure 24.- Tile fabrication requirements.

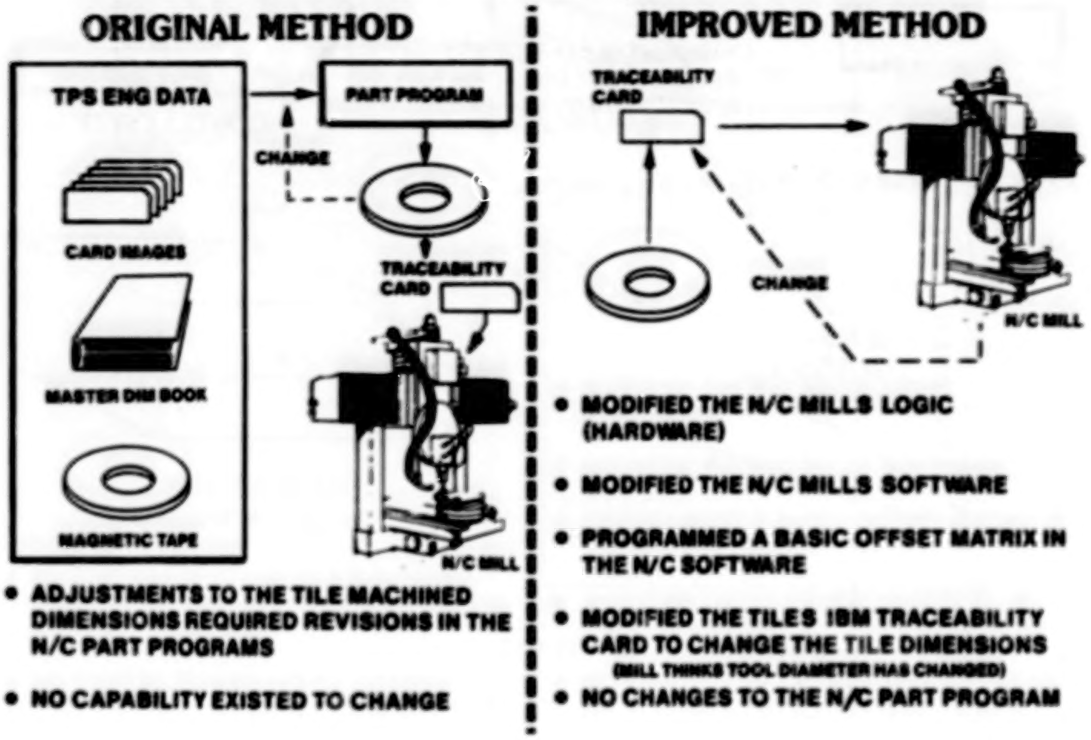
ORIGINAL METHOD
TPS ENG DATA
PART PROGRAM
CHANGE
CARD IMAGES
TRACEABILITY CARD
MASTER DIM BOOK
MAGNETIC TAPE
N/C MILL
IMPROVED METHOD
TRACEABILITY CARD
CHANGE
N/C MILL

- ADJUSTMENTS TO THE TILE MACHINED DIMENSIONS REQUIRED REVISIONS IN THE N/C PART PROGRAMS
- NO CAPABILITY EXISTED TO CHANGE

- MODIFIED THE N/C MILLS LOGIC (HARDWARE)
- MODIFIED THE N/C MILLS SOFTWARE
- PROGRAMMED A BASIC OFFSET MATRIX IN THE N/C SOFTWARE
- MODIFIED THE TILES IBM TRACEABILITY CARD TO CHANGE THE TILE DIMENSIONS (MILL THINKS TOOL DIAMETER HAS CHANGED)
- NO CHANGES TO THE N/C PART PROGRAM

Figure 25.- Implementation aspects of tile machining letter offsets.

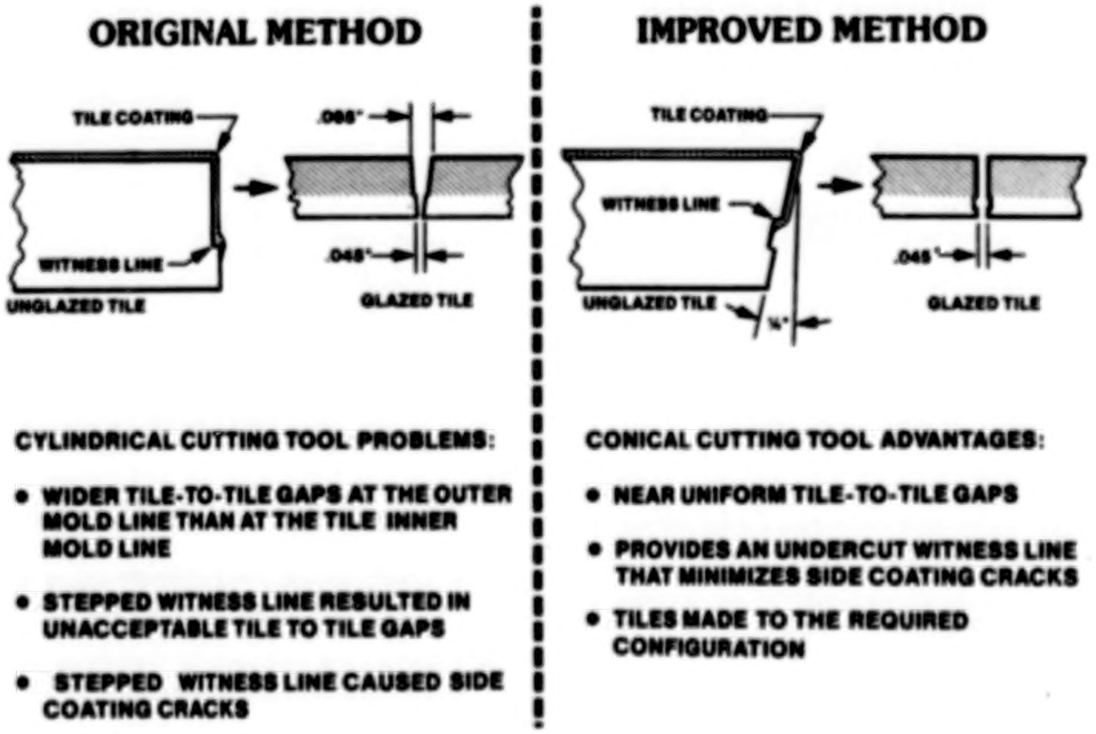
ORIGINAL METHOD
TILE COATING
.068"
WITNESS LINE
.045"
UNGLAZED TILE
GLAZED TILE
IMPROVED METHOD
TILE COATING
WITNESS LINE
.045"
UNGLAZED TILE
¼"
GLAZED TILE

CYLINDRICAL CUTTING TOOL PROBLEMS:

- WIDER TILE-TO-TILE GAPS AT THE OUTER MOLD LINE THAN AT THE TILE INNER MOLD LINE
- STEPPED WITNESS LINE RESULTED IN UNACCEPTABLE TILE TO TILE GAPS
- STEPPED WITNESS LINE CAUSED SIDE COATING CRACKS

CONICAL CUTTING TOOL ADVANTAGES:

- NEAR UNIFORM TILE-TO-TILE GAPS
- PROVIDES AN UNDERCUT WITNESS LINE THAT MINIMIZES SIDE COATING CRACKS
- TILES MADE TO THE REQUIRED CONFIGURATION

Figure 26.- Cutting tool configuration changes.

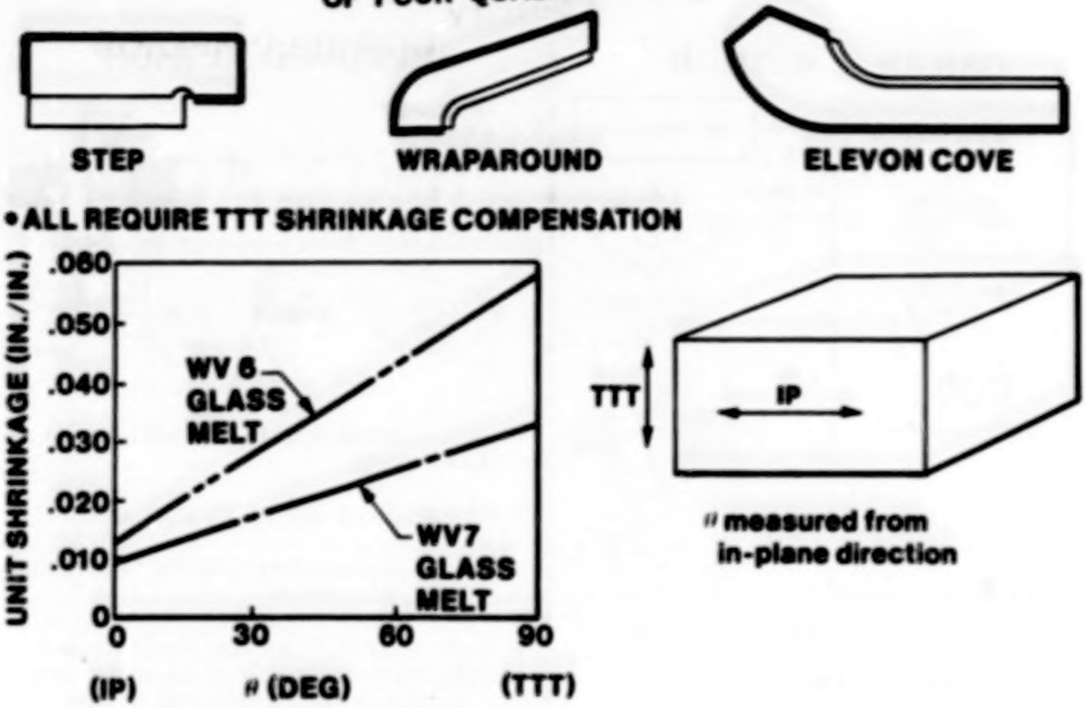

- ALL REQUIRE TTT SHRINKAGE COMPENSATION
- ALL "FIXES" CONTAINED IN NC PART PROGRAMS

Figure 27.- LI-900 tile shrinkage in the through-the-thickness direction.

ORIGINAL METHOD | **IMPROVED METHOD**

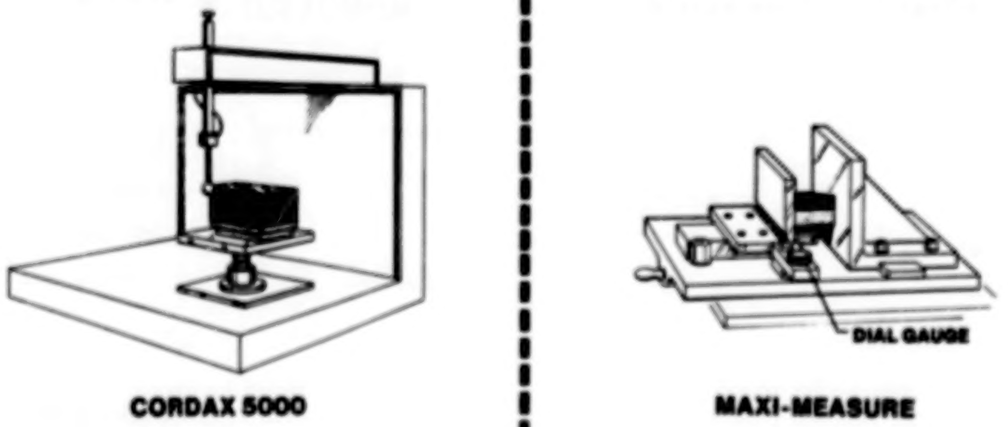

- USED TO MEASURE ALL TILES BEFORE LOADING INTO ARRAY FRAMES
- ONLY DISCRETE POINTS ARE MEASURED ON TILE SIDE

- MEASURES THE SHIMMED DIMENSIONS
- ALLOWS MORE EFFICIENT MEASUREMENT OF TILES WITH PARALLEL SIDES
- CORDAX OR MYLARS ARE USED FOR TILES WITH NON-PARALLEL SIDES

Figure 28.- Tile measurement methods.

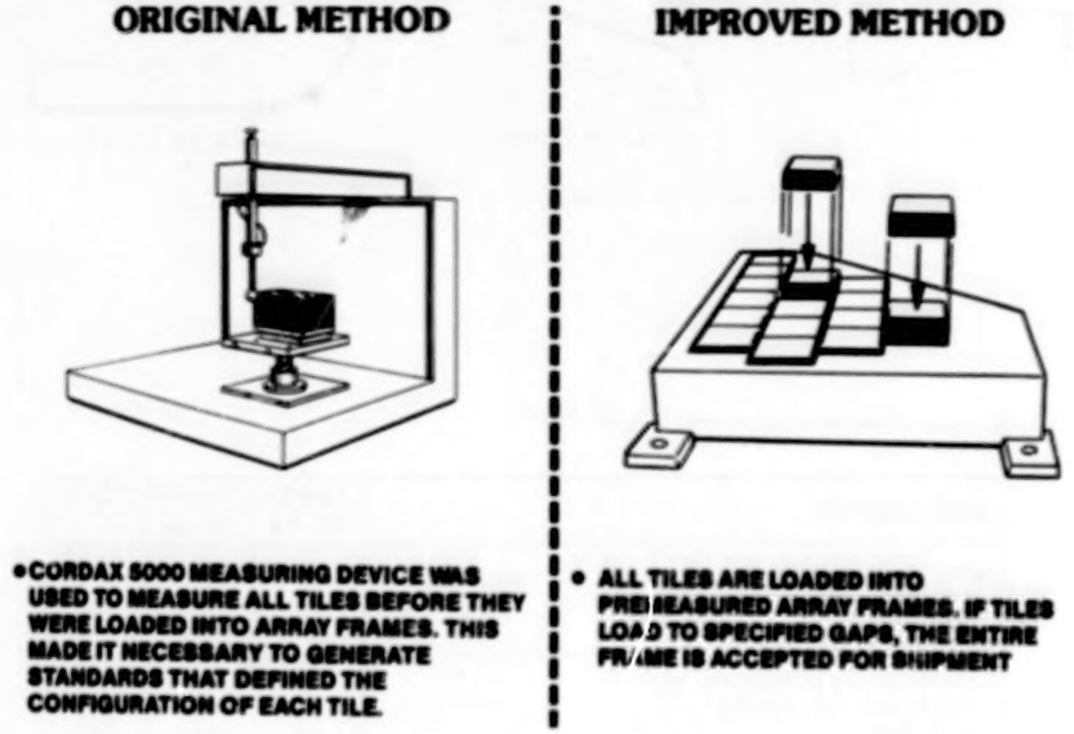

ORIGINAL METHOD

- CORDAX 5000 MEASURING DEVICE WAS USED TO MEASURE ALL TILES BEFORE THEY WERE LOADED INTO ARRAY FRAMES. THIS MADE IT NECESSARY TO GENERATE STANDARDS THAT DEFINED THE CONFIGURATION OF EACH TILE.

IMPROVED METHOD

- ALL TILES ARE LOADED INTO PREMEASURED ARRAY FRAMES. IF TILES LOAD TO SPECIFIED GAPS, THE ENTIRE FRAME IS ACCEPTED FOR SHIPMENT

Figure 29.- The load and go concept.

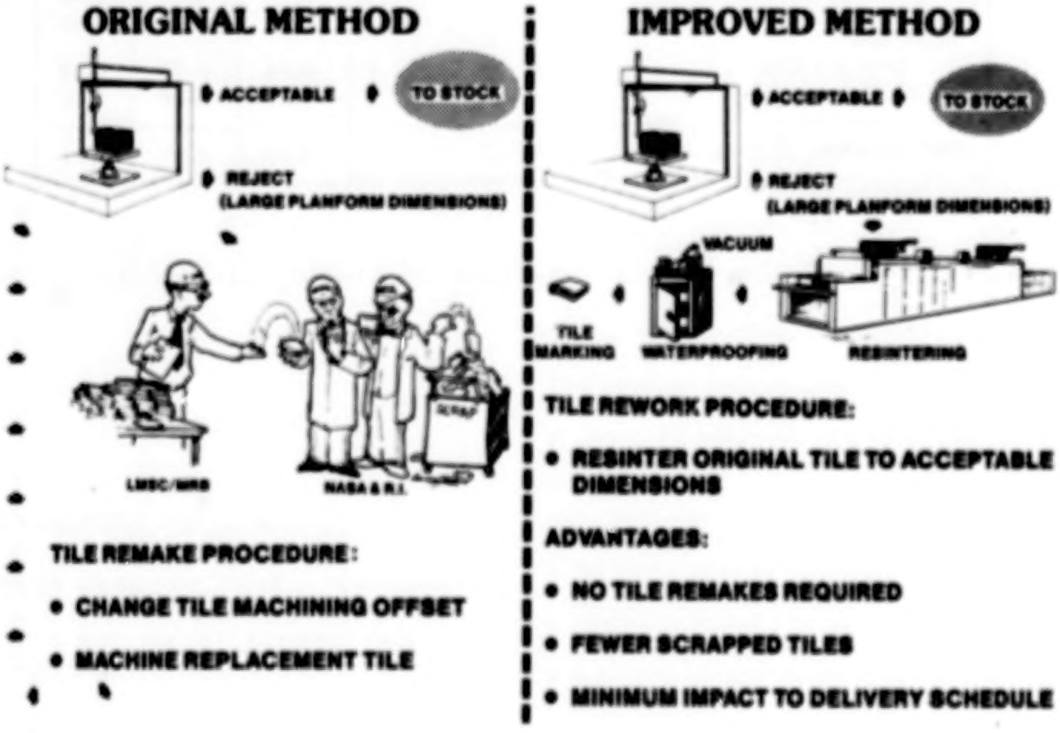

ORIGINAL METHOD

ACCEPTABLE
TO STOCK
REJECT
(LARGE PLANFORM DIMENSIONS)
SCRAP
LMSC/MRB
NASA & R.I.

TILE REMAKE PROCEDURE:

- CHANGE TILE MACHINING OFFSET
- MACHINE REPLACEMENT TILE

IMPROVED METHOD

ACCEPTABLE
TO STOCK
REJECT
(LARGE PLANFORM DIMENSIONS)
VACUUM
TILE MARKING
WATERPROOFING
RESINTERING

TILE REWORK PROCEDURE:

- RESINTER ORIGINAL TILE TO ACCEPTABLE DIMENSIONS

ADVANTAGES:

- NO TILE REMAKES REQUIRED
- FEWER SCRAPPED TILES
- MINIMUM IMPACT TO DELIVERY SCHEDULE

Figure 30.- A second sintering to shrink oversize tiles.

ORIGINAL PAGE IS
OF POOR QUALITY

DENSITY (lb/ft³)	LI-900	LI-2200	FRCI-12
	8.0-9.5	20-24	11.9-13.5
TENSILE STRENGTH* (lb/in²)			
THRU-THE-THICKNESS	24	73	81
IN-PLANE	67	180	257
COMPRESSIVE STRENGTH* (lb/in²)			
THRU-THE-THICKNESS	28	130	132
IN-PLANE	70	230	265
THERMAL EXPANSION* (in/in - °F)			
THRU-THE-THICKNESS	4×10^{-7}	4×10^{-7}	7×10^{-7}
IN-PLANE	4×10^{-7}	4×10^{-7}	7×10^{-7}
APPARENT THERMAL CONDUCTIVITY* (BTU-in/ft² hr - °F)			
THRU-THE-THICKNESS			
70°F @ 10^{-4} ATM	0.10	0.22	0.13
1000°F @ 10^{-4} ATM	0.28	0.41	0.34
IN-PLANE			
70°F @ 1 ATM	0.44	0.73	0.53
1000°F @ 1 ATM	1.08	1.25	1.13
SPECIFIC HEAT* (BTU/lb - °F)	0.17	0.17	0.17

*AVERAGE VALUE

Figure 31.- Typical physical properties of LI-900, LI-2200 and FRCI-12.

N84
10159

UNCLAS

N84 10159 D15

LIFE CONSIDERATIONS OF THE SHUTTLE ORBITER DENSIFIED-TILE THERMAL PROTECTION SYSTEM

Paul A. Cooper and James Wayne Sawyer
NASA Langley Research Center
Hampton, Virginia

SUMMARY

The Shuttle orbiter thermal protection system (TPS) incorporates ceramic reusable surface insulation tiles bonded to the orbiter substructure through a strain isolation pad. Densification of the bonding surface of the tiles increases the static strength of the tiles. The densification process does not, however, necessarily lead to an equivalent increase in fatigue strength. Investigation of the expected lifetime of densified-tile TPS under both sinusoidal loading and random loading simulating flight conditions indicates that the strain isolation pads are the weakest components of the TPS under fatigue loading. The felt pads loosen under repetitive loading and, in highly loaded regions, could possibly cause excessive step heights between tiles causing burning of the protective insulation between tiles. A method of improving the operational lifetime of the TPS by using a strain isolation pad with increased stiffness is presented as is the consequence of the effect of increased stiffness on the tile inplane strains and transverse stresses.

INTRODUCTION

The thermal protection system (TPS) on the windward surface of the orbiter consists of ceramic tiles bonded to strain isolator pads (SIP), which are in turn bonded to the orbiter aluminum substructure as shown in the schematic of Figure 1. To prevent premature failure of the TPS at the interface of the SIP and the tile due to stress concentrations caused by the localized transfer of load through the SIP, the faying surface of the tiles was strengthened by a surface densification process. The greater static strength achieved by the surface densification does not fully translate into an equivalent increase in fatigue strength (ref. 1 and 2). Fatigue failure of the densified TPS takes the form of excessive elongation through the thickness of the SIP. On the other hand, fatigue failure of TPS with undensified tiles involves complete separation at the SIP/tile interface (see ref. 3). Fatigue failure of densified TPS is relatively benign when compared with fatigue failure of undensified TPS since a tile beginning to loosen can be identified and replaced during postflight maintenance.

Although the fatigue failure mode of densified tiles is relatively forgiving, tiles which loosen can cause problems in three ways. First, hot gas may be allowed to penetrate between tiles to the filler bar protecting the substructure. Second, chipping of the protective coating of neighboring tiles may occur. Third, disruption of the airflow could prematurely trip the boundary layer causing turbulent flow which would lead to an increase in downstream heating. This paper reviews results of tests to evaluate the fatigue characteristics of densified TPS and introduces a possible method of increasing the operational lifetime of the TPS if required.

DESCRIPTION OF TPS

A schematic of a typical tile/SIP assembly is shown in Figure 1. The tile is composed of compacted 1.5-micron-diameter silica fibers bonded together by colloidal silica fused during a high-temperature sintering process. Two types of tiles are used on the windward surface of the orbiter, a 9 lb/ft^3 tile designated LI-900 and a higher strength 22 lb/ft^3 tile designated LI-2200. The tiles are coated on five sides with reaction-cured glass (RCG) consisting of silica, boron oxide, and silicon tetraboride to provide an abrasion-resistant watertight surface. The remaining uncoated side of the tile is densified by the application of a ceramic slurry at the surface which fills the voids between fibers and provides a strengthened bonding surface for the SIP. A photomicrograph of the densified region is given in Figure 2 and shows the colloidal silica particles situated between the silica fibers. Most densification material remains within 0.10 in. of the bonding surface as shown in the second photomicrograph of Figure 2 with the larger particles occurring at the surface and with the particle size and number of particles decreasing gradually toward the interior of the tile.

The SIP is bonded to the tile and the aluminum substructure of the orbiter using an elastomeric room temperature vulcanizing (RTV) silicone adhesive. The SIP is a felt pad of nylon fibers compacted by passing a barbed needle normal to the pad surface in a sewing machine like process. The compacting process provides tensile strength and extensional stiffness in the pad thickness direction and provides a load transfer path between the substructure and the tile. A photomicrograph of the SIP is given in Figure 3 and shows a region of transverse fibers produced by the needling process. The RTV adhesive transfer coat is also shown in Figure 3. This coat is bonded to the densified surface of the tile. A filler bar is bonded to the aluminum substructure between tiles to provide thermal protection for the substructure. A

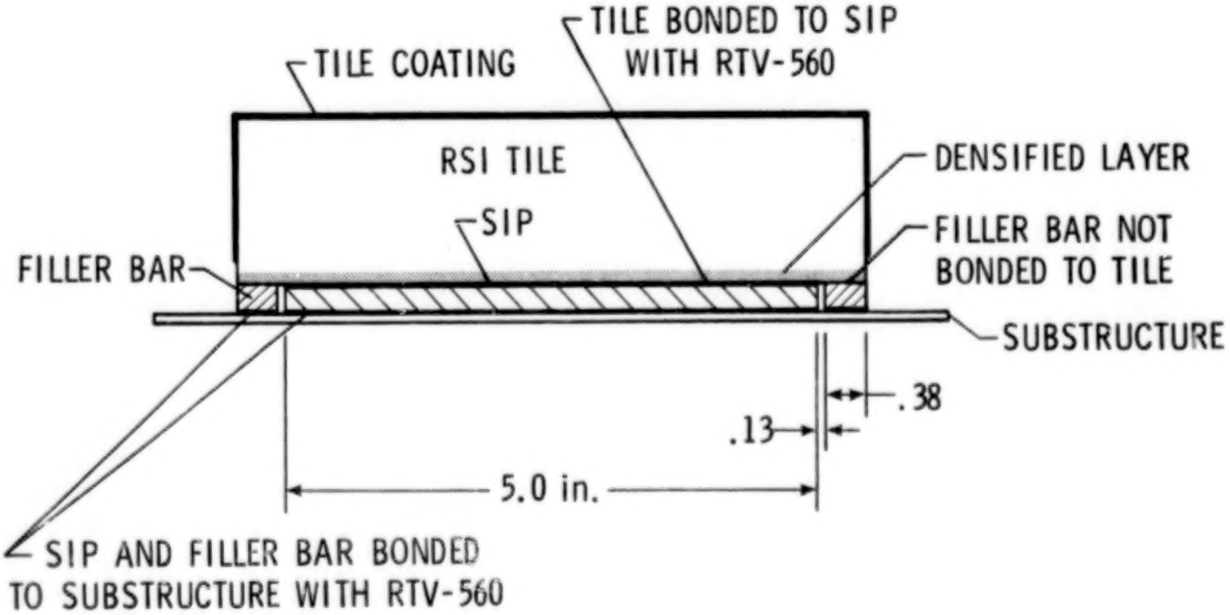

Figure 1.- Schematic of ceramic TPS.

more complete description of the TPS is provided in references 1 and 2. Two types of SIP are used most often on the orbiter and are identified by their thickness in inches, 0.160 SIP and 0.090 SIP. The 0.090 SIP is formed by the same procedure as the 0.160 SIP but is more highly compacted by an increased amount of needling which results in a higher strength and stiffness.

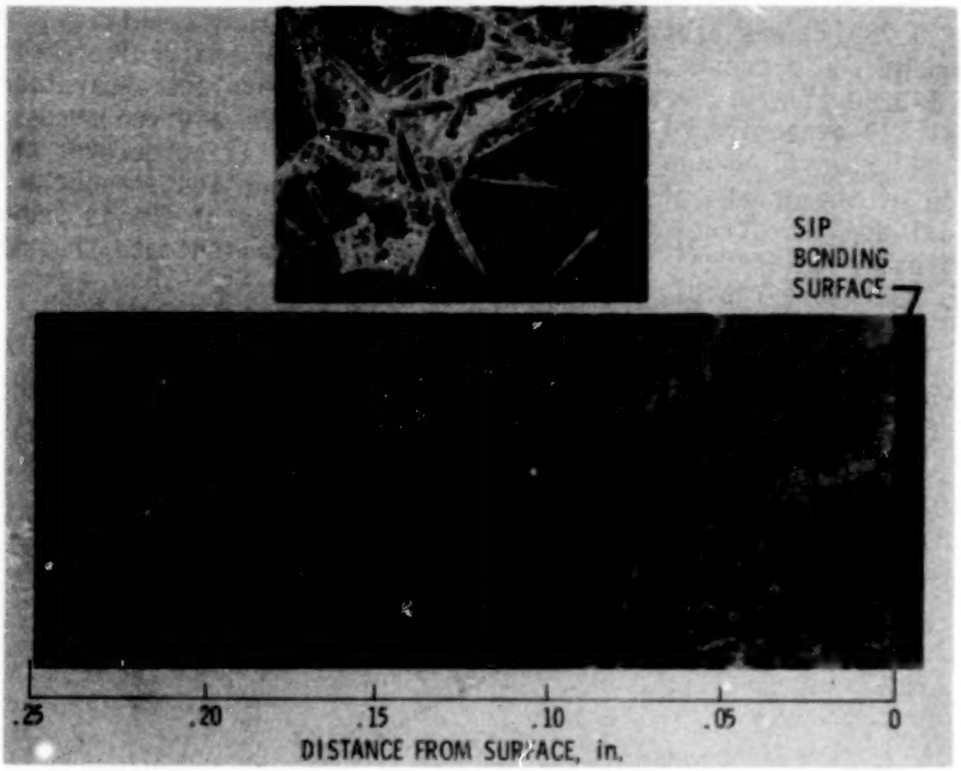
SIP
BONDING
SURFACE
.25
.20
.15
.10
.05
0
DISTANCE FROM SURFACE, in.

Figure 2.- Photomicrograph of densified region of tile.

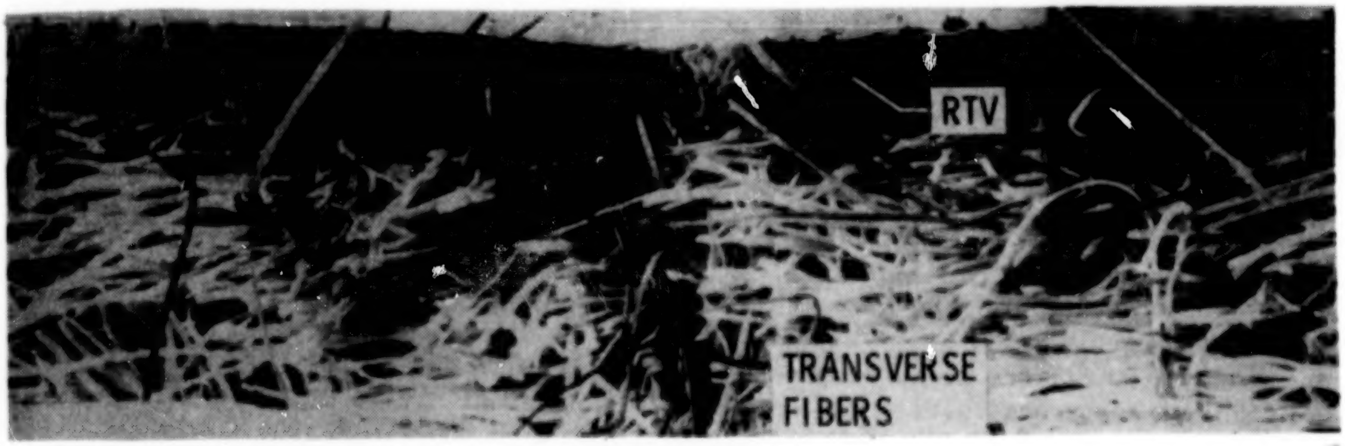
RTV
TRANSVERSE
FIBERS

Figure 3.- Photomicrograph of strain isolation pad cross section.

SINUSOIDAL FATIGUE BEHAVIOR

A series of fatigue characterization tests of densified LI-900 tile/0.160 SIP and densified LI-2200 tile/0.090 SIP specimens were performed with results reported in reference 3. The 2.25-in.-diameter specimens were tested under repeated fully reversed sinusoidal loads applied at 1 Hz with results as shown in Figure 4. The lower strength LI-900 tile/0.160 SIP failed under cyclic loads by SIP extension when a total travel of 0.25 in. was arbitrarily selected as a failure condition. A total travel of this amount would constitute excessive looseness on the orbiter. The higher strength LI-2200 tile/0.090 SIP specimens failed by complete separation of the SIP before a total SIP extension of 0.25 in. was reached. For a given stress level, the stronger TPS had several orders-of-magnitude increase in lifetime over the weaker TPS. A comparison of the growth of the SIP during the fatigue tests under a fully reversed sinusoidal applied stress of 12 psi for the two types of TPS is shown in Figure 5. The stress displacement curves shown in the figure indicate that the 0.160 SIP loosens much more rapidly than the 0.090 SIP.

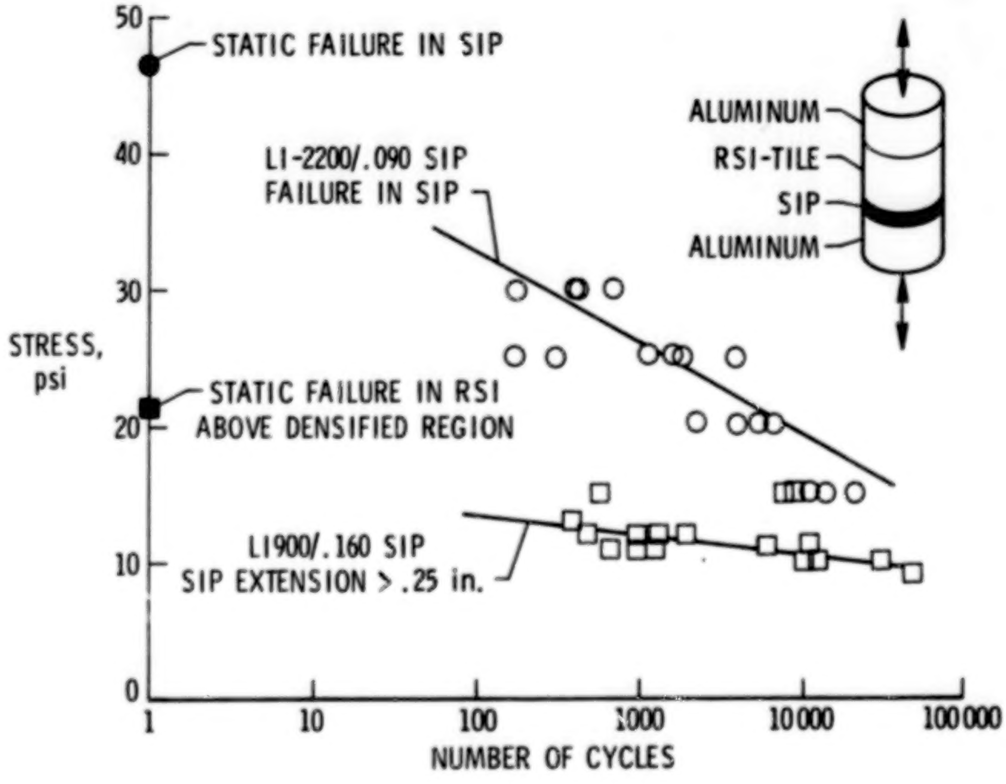

Figure 4.- Fatigue of densified TPS subject to fully reversed sinusoidal loads (R = -1).

Figure 6 shows the measured growth of the 0.160 SIP during the fatigue test for various applied stress levels and indicates the number of cycles at which total displacement is equal to the assumed failure criteria of 0.25 in. As the number of cycles increases, the SIP transverse fibers continue to stretch and unravel resulting in an increase in total specimen travel and a continual loosening of the tile. The growth rate increases nearly exponentially as the growth increases.

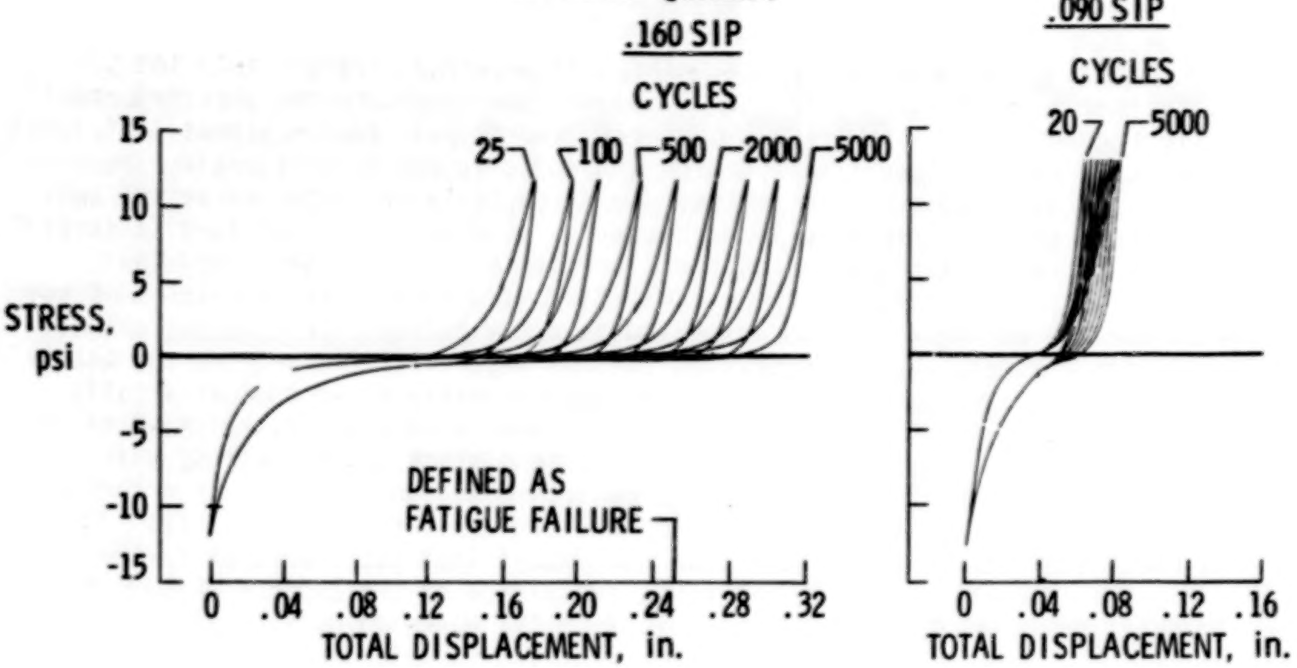

Figure 5.- SIP extension under fatigue loading.

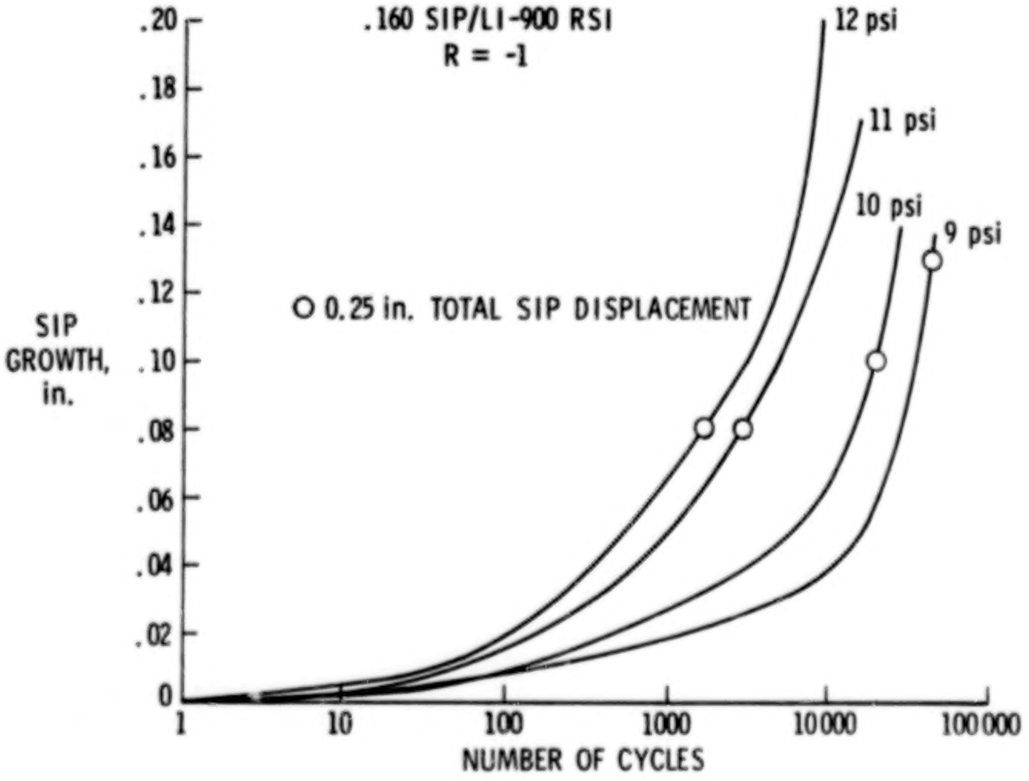

Figure 6.- Measured growth of SIP displacement under sinusoidal fatigue loading.

RANDOM DYNAMIC LOAD FATIGUE TEST

A sinusoidal load condition, while helpful in providing insight into the expected fatigue behavior of the TPS, is a severe load condition not expected under actual flight conditions. The tiles experience a variety of random vibrational loads during ascent. These include: main engine and solid rocket motor ignition overpressures during liftoff, substructure motions due to engine vibrations and aerodynamic loadings, direct acoustic pressure loads caused by boundary layer noise, differential pressures due to shock passages, aerodynamic gradients and gust loads, and tile buffeting due to vortex shedding from a connecting structure. The critical load conditions on the TPS during ascent are expected to occur between the time the orbiter reaches transonic speeds (approximately 40 seconds after liftoff) and the time the orbiter experiences maximum dynamic pressure (approximately 65 seconds after liftoff). During this critical time, the TPS on the lower wing and midfuselage surfaces experiences loads caused by substructure deformation, shock passage aerodynamic gradients, which can cause a net tensile force and moment on the tiles, and random acoustic loads transmitted to the tiles from the orbiter base structure (ref. 4). Prior to the first flight, a series of random dynamic load tests were performed on undensified tiles to obtain a more realistic evaluation of the expected behavior of the TPS under simulated flight load conditions in the windward surface wing and midfuselage region. Results of those tests are reported in reference 5. After completion of those tests and before the initial flight, a densified tile was tested using the same test procedure and fixtures but under slightly higher load conditions since many densified tiles were expected to be subjected to load levels higher than those experienced by undensified tiles.

Test Setup

A schematic of the load application fixture is shown in Figure 7. The fixture consists of a thin aluminum plate riveted to five thick-walled aluminum tubes. The fixture was designed so that after the tile/SIP test specimen is bonded to the plate, the plate can be deformed to a shape typical of the substructure deformations expected in the orbiter skin in either the wing or midfuselage region. The plate is deformed by bolting the tubes to a rigid base plate with shims under alternate tubes as required for the region of interest. The shims cause the thin plate to deform to an approximate sine wave with the peak-to-peak amplitude given by the shim thickness and the half wavelength governed by the tube spacing.

The fixture surface on which the specimen is bonded is first chemically etched, sprayed with a protective primer, and vacuum baked to remove all volatiles. The specimen is bonded to the test fixture with the tile diagonals parallel to the edge of the test fixture as shown in Figure 7. The tile is located on the test fixture so that one corner of the SIP is over the centerline of one of the tubes. A circular aluminum thin disk is bonded to the top of the tile using epoxy adhesive to provide a load attachment point for application of a steady tensile load and moment which simulate the effect of a steady aerodynamic gradient. The attachment point at the center of the disk is located 0.5 in. from the center of the tile measured along a tile diagonal perpendicular to the tube axes. To apply a random dynamic load to the specimen, the fixture, with the specimen in place and shims installed to simulate substructure deformations at a wing location, is bolted to the drive head of a 30,000 lb electromagnetic shaker. A schematic of the test setup is shown in Figure 8.

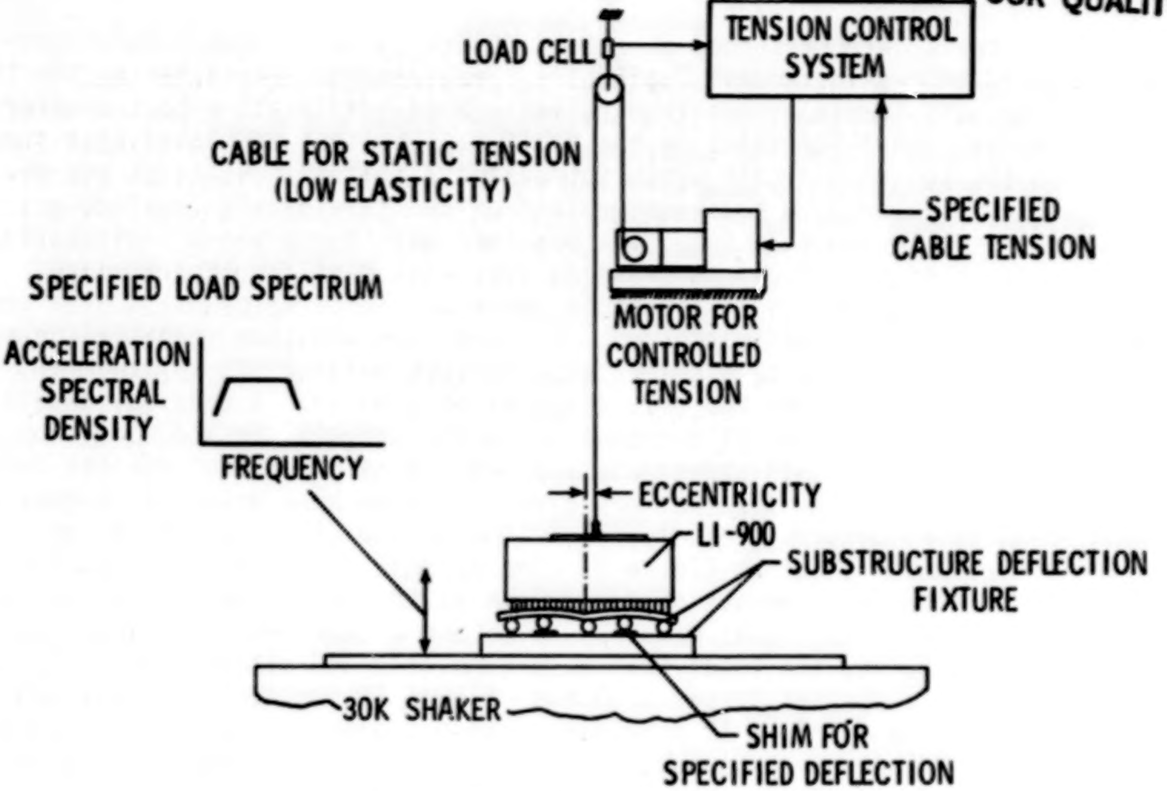
LOAD CELL
TENSION CONTROL SYSTEM
CABLE FOR STATIC TENSION (LOW ELASTICITY)
SPECIFIED CABLE TENSION
SPECIFIED LOAD SPECTRUM
ACCELERATION SPECTRAL DENSITY
FREQUENCY
MOTOR FOR CONTROLLED TENSION
ECCENTRICITY
LI-900
SUBSTRUCTURE DEFLECTION FIXTURE
30K SHAKER
SHIM FOR SPECIFIED DEFLECTION

Figure 7.- Random dynamic fatigue test fixture.

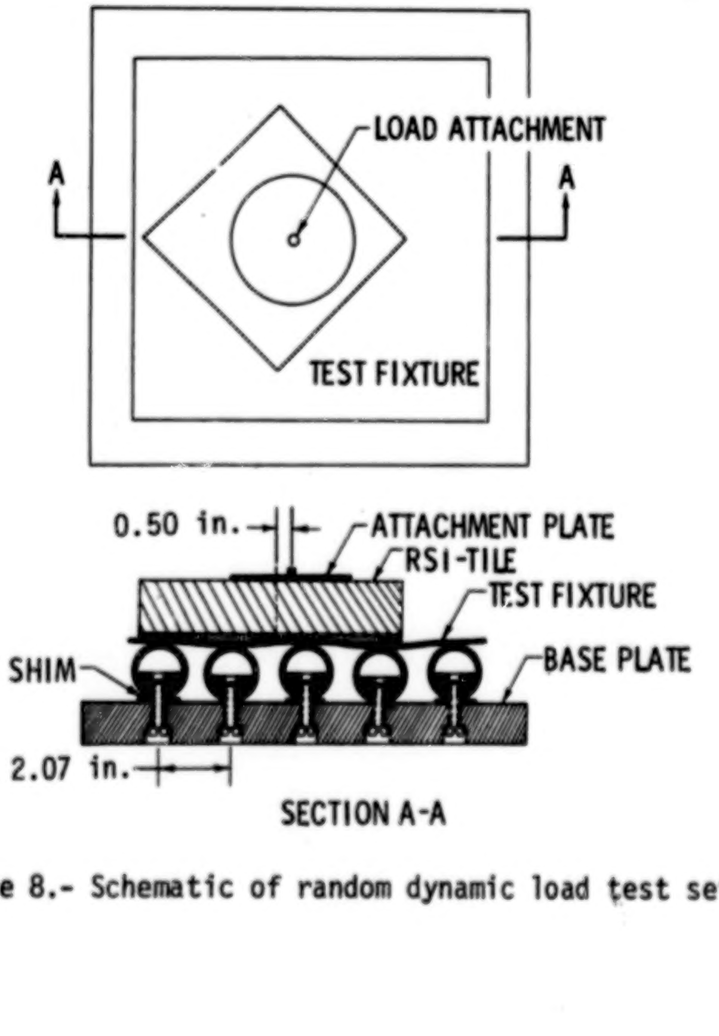
LOAD ATTACHMENT
A
A
TEST FIXTURE
0.50 in.
ATTACHMENT PLATE
RSI-TILE
TEST FIXTURE
SHIM
BASE PLATE
2.07 in.
SECTION A-A

Figure 8.- Schematic of random dynamic load test setup.

Test Program

A series of tests were performed on a 2-in. thick by 6-in. square densified-LI-900 tile bonded to a 5-in. square 0.160 SIP. The specimen, installed on the thin plate with filler bars in place, was first given a bond verification test similar to that given actual densified tiles on the orbiter. The test consisted of a steady load applied to the top of the tile which introduced a uniform tensile stress of 10 psi on the SIP followed by a compressive load of the same stress level to bring the tile back to its equilibrium position. The specimen was then given a 5-psi uniform tension stress followed by a 5-psi compression test with displacement response recorded to establish the stress displacement characteristics which existed before the random dynamic load test was performed. The specimen was then installed on the base plate using shims to provide a static substructure deflection amplitude of 0.015 in. with a half wavelength along the tile diagonal of 2.07 in. A tensile force of 50 lb displaced 1/2 in. from the tile center along the diagonal in the direction which causes the most severe SIP stress was applied and held constant for the duration of the dynamic test. The specimen was given a random base drive of 30 grms with the driving frequencies occurring mainly between 60 Hz and 250 Hz using the power spectral density distribution shown in Figure 9. The dynamic test was conducted for a total of 2.5 hours with measurements of SIP growth at the most highly stressed corner taken every 1/2 hour with all loads removed. With one ascent mission assumed equal to 25 seconds of test time, the total test time simulated 360 ascent missions (100-mission lifetime with a scatter factor of 3.6). Figure 10 contains a photograph of the actual test setup, and Figure 11 provides a closeup view of the test specimen showing the installed instrumentation used to obtain dynamic response information. On completion of the dynamic test, the specimen was again given a 5-psi static tension and compression test with load displacement measurements taken. Finally, the specimen was given a tensile test-to-failure to determine its residual strength.

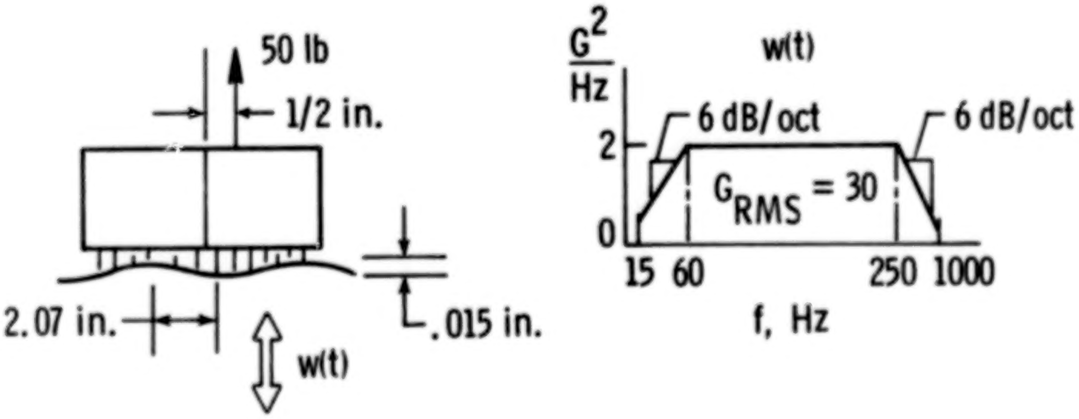

Figure 9.- Test loads applied on densified TPS.

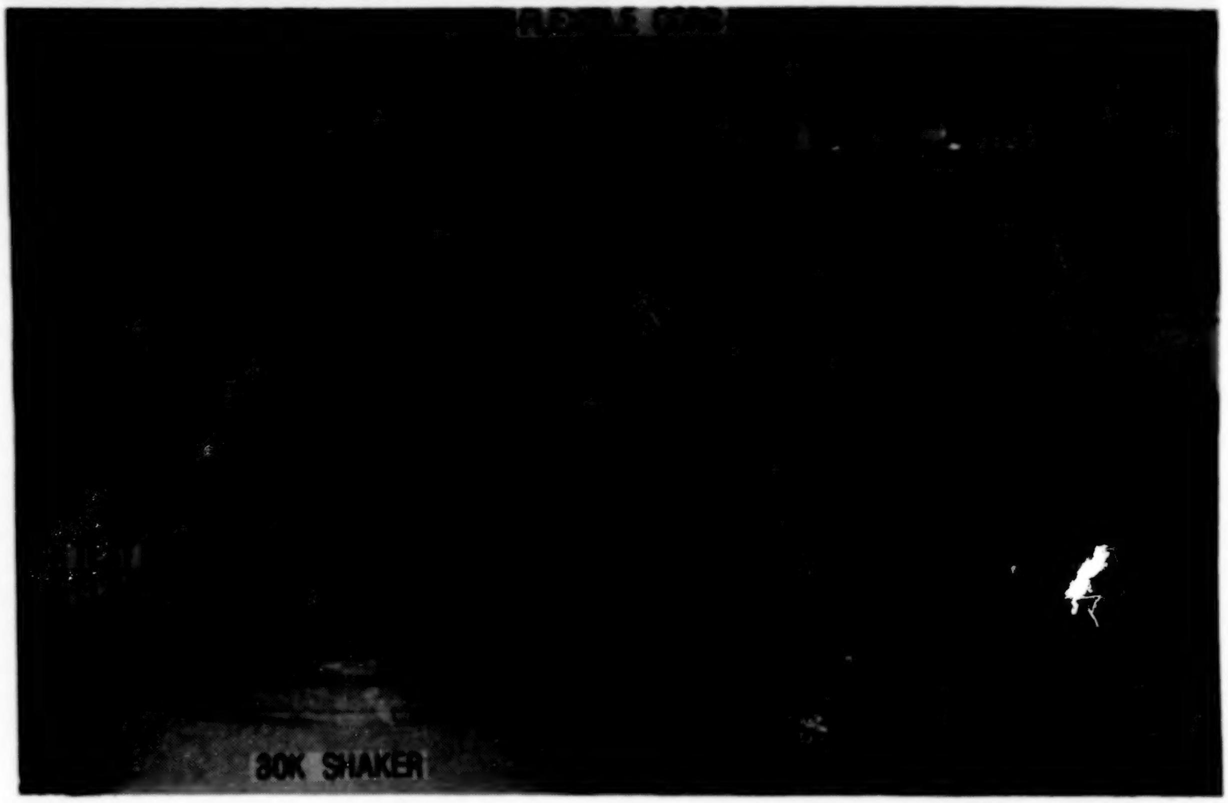

Figure 10.- Photograph of laboratory test setup for dynamic testing of densified TPS.

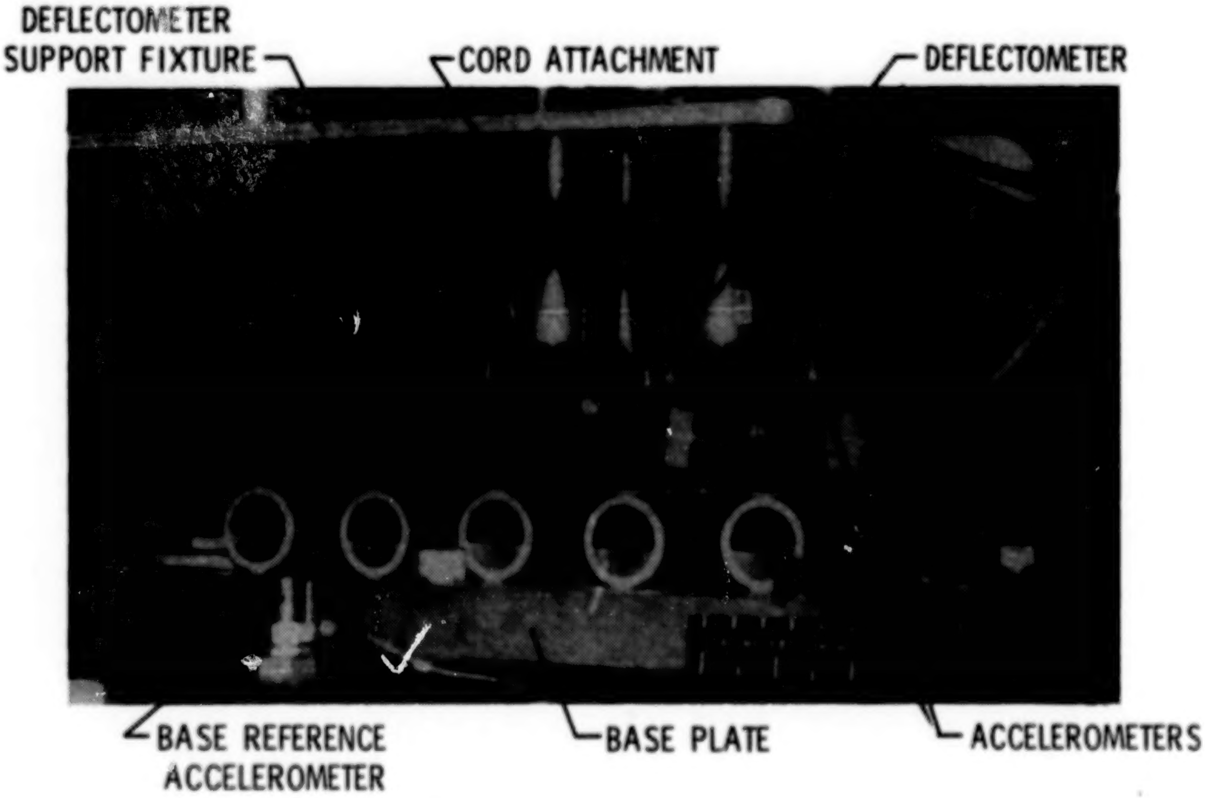
DEFLECTOMETER SUPPORT FIXTURE
CORD ATTACHMENT
DEFLECTOMETER
BASE REFERENCE ACCELEROMETER
BASE PLATE
ACCELEROMETERS

Figure 11.- Photograph of test specimen and fixture.

ORIGINAL PAGE IS
OF POOR QUALITY

Test Results

Figure 12 contains a picture of the tile after completion of the dynamic load test and before the final test-to-failure. The top plate shown in the figure replaces the load attachment disk used during the dynamic test so that the larger tensile loads required to fail the system can be applied. The figure also contains a plot of the development of permanent growth of the SIP at the highest stressed corner as the dynamic test progressed. By the conclusion of the test, the SIP had a permanent extension at this corner equal to the initial thickness of the SIP (i.e., 100-percent increase in thickness). Figure 13 presents a comparison of the applied stress vs. displacement measured during the ±5-psi static uniform load tests

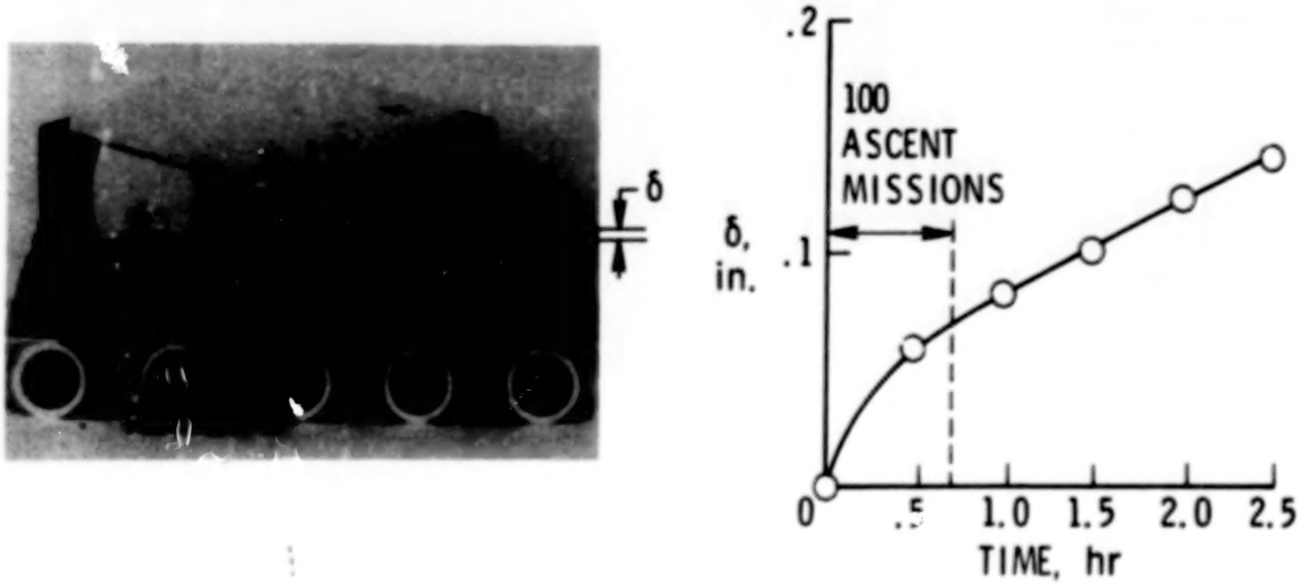

Figure 12.- Permanent growth of SIP subjected to random dynamic loads.

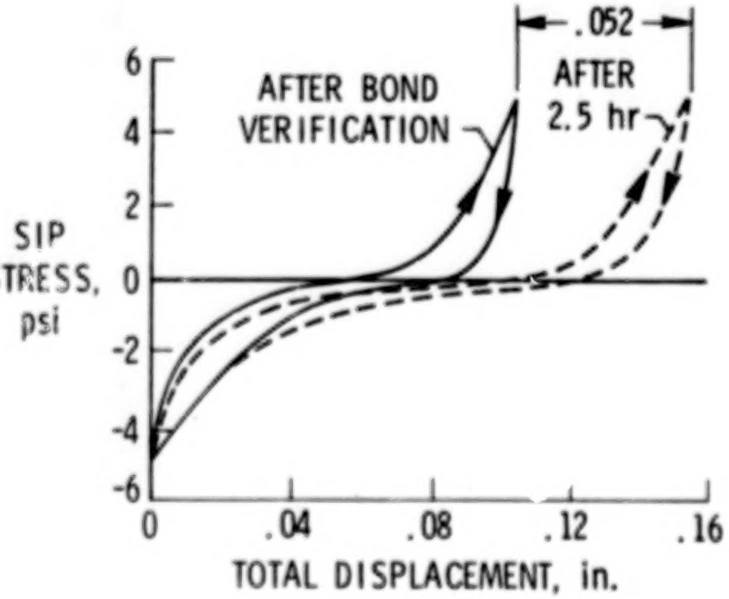

Figure 13.- Loosening of TPS due to multimission random dynamic loading.

performed before and after the dynamic test. The peak-to-peak measurement of 0.052 in. is an indication of the degree to which the SIP has loosened. The tile failed during the final test-to-failure in the parent undensified region at an ultimate static load of 422 lb. This failure load was 70 percent greater than the original bond verification load.

If the load spectrum does represent actual flight conditions, the test data indicate that excessive SIP growth may occur within the operational lifetime of the orbiter. This mode of failure under random loading is benign if corrective action is taken during ground maintenance between flights; however, if loose tiles are not eventually replaced, several unacceptable consequences as discussed in the introduction might result. One of these consequences, that of filler bar burning, has been analyzed, and a maximum growth criterion for prevention of this condition is discussed in the next section.

FILLER BAR BURNING

Table 1 gives a history of tile removal for various causes after each of the first four flights. Tile loosening does not seem to be a developing problem this early in the orbiter lifetime; however, there does seem to be a persistence of incidents of filler bar burning from flight to flight. An indication of the effect of the tile gap and step on filler bar burning is provided in reference 6. The reference contains the results of a study to investigate the cause of the excessive

TABLE 1.- TILE REMOVAL HISTORY FOR OV-102 AFTER FOUR FLIGHTS

	STS-1	STS-2	STS-3	STS-4
TOTAL NO. OF TILES REMOVED	1547	4[illegible]1	1047	271
REMOVED FOR DENSIFICATION (NO STRUCTURAL ISSUE)	526	202	783*	0
REMOVED FOR LOOSENESS	170	18	15	3
REMOVED FOR EXCESSIVELY BURNT FILLER BAR	246	47	39	36
OCCURENCES OF BURNT FILLER BAR NOT SEVERE ENOUGH TO REMOVE	614	360	219	502+

*PRIMARILY WHITE TILES (NONCRITICAL) IN FORWARD FUSELAGE REGION

+PROBABLY DUE TO HIGHER HEATING RATE DURING ENTRY heating observed in the tile-to-tile gaps of the orbiter. A flow model was developed in the referenced study to determine the pressure loading and flow rates in the gap during entry. A thermal model of adjacent tiles, the tile-to-tile gap and step, filler bar, and SIP was used to predict temperature distributions throughout the system. Tests have shown that temperatures greater than 1375°F will cause charring of the RTV and filler bar to a degree which requires replacement of the filler bar. The computed temperature distributions at a wing location where a 0.06 in. step is assumed are shown for various locations in a gap in Figure 14. The peak filler bar temperature calculated for the assumed step is 1750°F. A similar study for a 0.03-in. step yields a maximum filler bar temperature of 1290°F. Thus, from a linear interpolation between these two conditions, the critical temperature for filler bar burning is reached under the flow conditions of the study when a step between tiles of 0.034 in. exists.

Results of the random dynamic load test shown in Figure 12 indicate that a permanent SIP extension of 0.034 in. would occur under the simulated loads well before the 100-mission flight desired lifetime has been completed. One could conservatively estimate that this extension coupled with the increased loosening of the SIP shown in Figure 13 would cause a step of the order of 0.04 in. assuming the neighboring tile was under compression or at least remained unextended. Thus, if the assumed load simulation used in the random dynamic load tests is realistic and the thermal predictions of reference 6 are an accurate evaluation of actual conditions, increased incidence of burned filler bar can be expected during the lifetime of the orbiter.

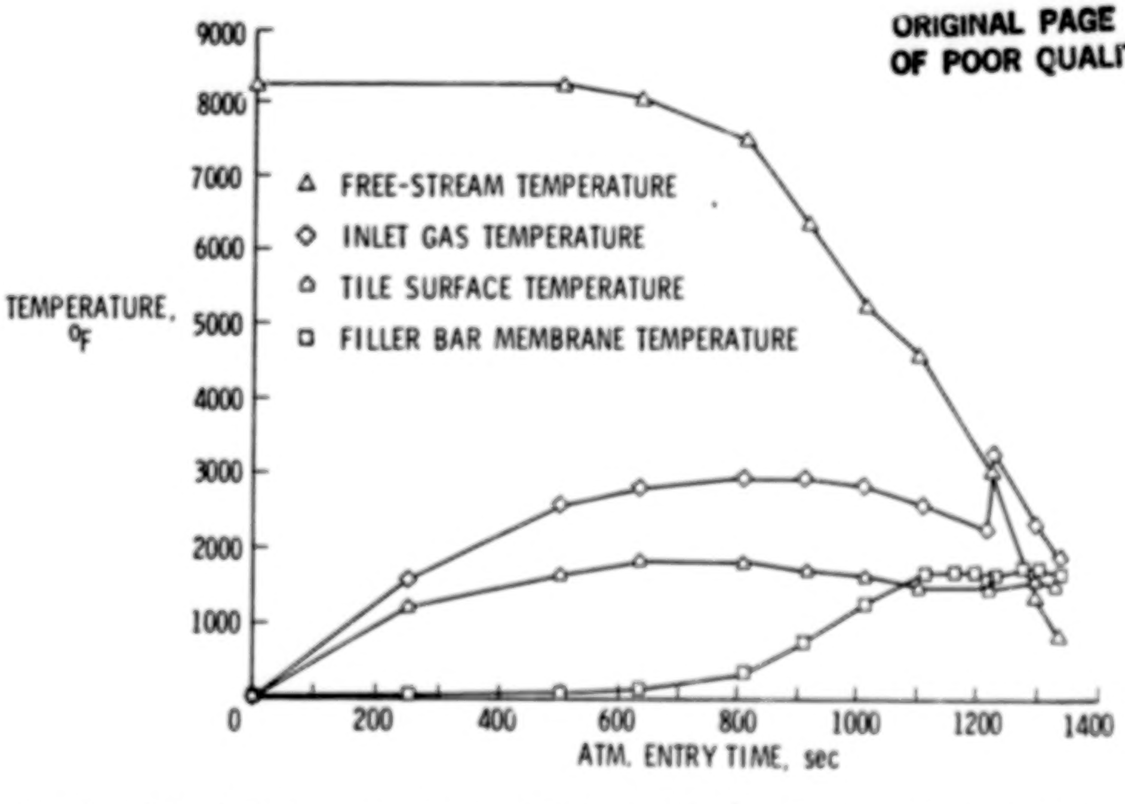

Figure 14.- Calculated temperature of tile and filler bar at wing location during reentry, Step = 0.06 in., ref. 6.

METHOD FOR EXTENDING SIP LIFETIME

Several possible methods can be used to reduce the incidence of filler bar burning and loosening of tiles. Currently, gap fillers are placed in the gaps between tiles where filler bar burning occurs. The gap fillers prevent hot gas influx between tiles and reduce the dynamic response of the tiles to external stimulations. Another possible method is to bond the tiles to the filler bar, thus reducing the nominal stress in the SIP by providing an increased support area for the applied loads. A third method, which will be discussed here, is the replacement of the 0.160 SIP with a SIP of the same thickness but with stiffness and strength properties equal to those of the 0.090 SIP. Replacement with a stiffer SIP is suggested since, as shown in Figures 4 and 5, the 0.090 SIP has at least an order-of-magnitude greater lifetime than the 0.160 SIP for a given stress level. A SIP of this type could be fabricated by starting with a pad thicker than the pad used to form the 0.160 SIP and reducing it to the desired 0.160 thickness when it is needled to the same degree as the 0.090 SIP. Replacement of the standard SIP over the entire windward surface of the orbiter with a stiffer SIP of this type would cause an increase in orbiter dry weight of approximately 300 lb. There is a limitation to the allowable increase in stiffening of the SIP beyond which it begins to fail in its function as an effective strain isolator for densified tiles. An analysis and test program was performed to determine this limitation.

Limitation of SIP Stiffness for Inplane Strains

An analysis was developed and reported in reference 7 to evaluate the inplane strains transmitted through the SIP to the densified region and the top coating of a tile caused by the combined effect of substructure inplane and normal deformations. The problem was treated as a deep stiff beam (including the effects of transverse shear) on a soft elastic nonlinear foundation which resists both transverse extension and shearing. The analysis requires a knowledge of the extensional modulus of the densified region of the tile. To find the modulus, a series of four-point beam bending tests were performed using small beam specimens fabricated from tile material and densified on the loading surfaces. The beams were treated as sandwich structures with an assumed densified region thickness of 0.10 in. Results from these tests, including an evaluation of the inplane failure strain of the densified region, are presented in reference 8.

Using the analysis and the experimentally determined modulus of the densified region, a study was made of the maximum inplane strains in densified tiles of various thicknesses ranging from 0.25 in. to 2.0 in. The tiles were subjected to an inplane substructure strain equal to the yield strain of the aluminum plus the unconstrained thermal strain caused by a rise in substructure temperature of 280°F. In addition, the tiles were subjected to a tensile load of 250 lb offset from the tile center by 0.5 in. This combined load condition is greater than any actual condition expected on the orbiter tiles. Results of the study for a standard 0.160 SIP and a SIP with ten times the stiffness of the standard SIP are shown in Figure 15. Only for the thinnest tiles does the maximum strain in the densified region and the top coating approach the inplane failure strain. Thus, a considerable increase in SIP stiffness can be tolerated without compromising the inplane integrity of the tiles. A 0.090 SIP has approximately three times the stiffness of 0.160 SIP. This is well within the acceptable stiffness range to function properly as an isolator of inplane strains.

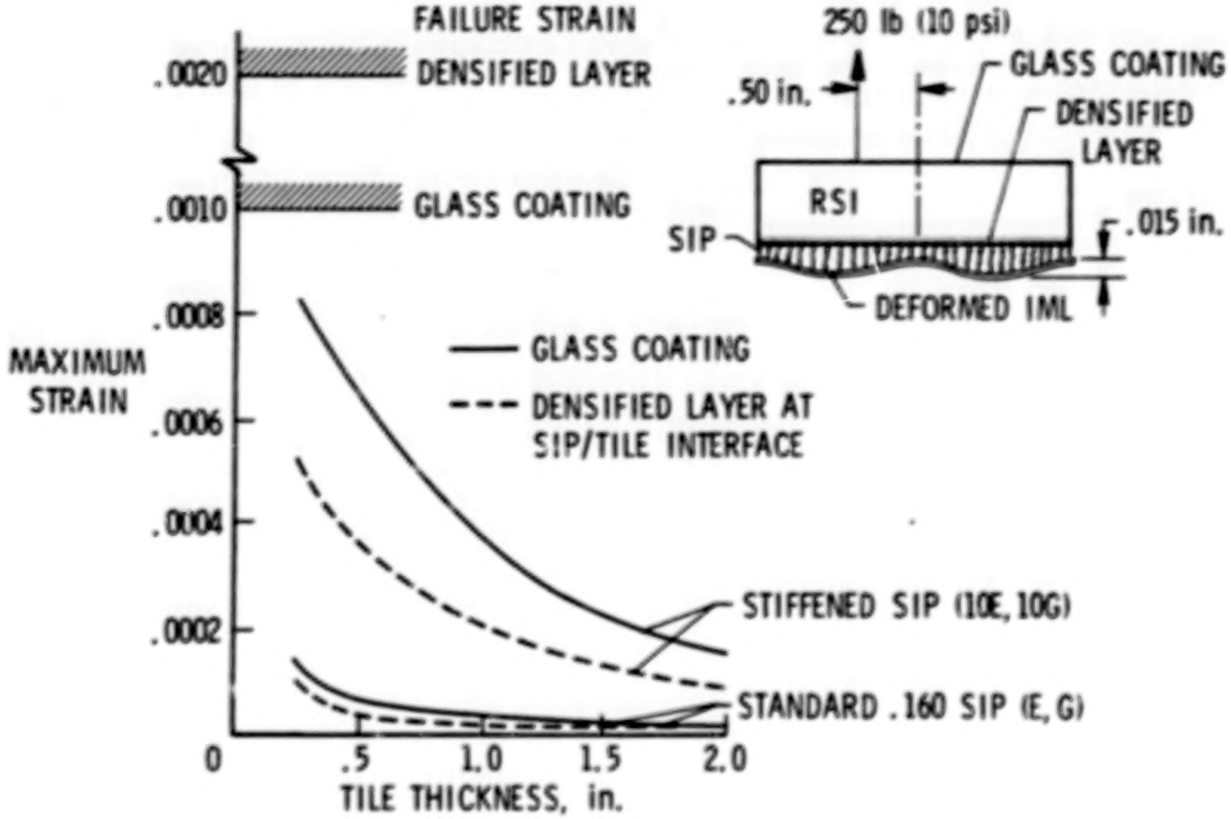

Figure 15.- Effect of SIP stiffness on tile inplane strains for a range of tile thicknesses.

Limitation of SIP Stiffness for Transverse Stress

A SIP with a higher stiffness will increase the stress in the direction normal to the plane of the pad (transverse stress) in the region of the SIP/tile interface when substructure deformations are applied. To evaluate the effect of a stiffer SIP on the transverse stress at the SIP/tile interface, the stresses were computed using an analysis described in reference 9 for a standard 0.160 SIP and a 0.160-in. thick SIP with stiffness properties equal to that of a 0.090 SIP. A comparison of results for typical high-load conditions expected on orbiter tiles is shown in Figure 16. Use of the stiffer SIP causes approximately a 50-percent increase in the maximum stress at the SIP/tile interface for the load conditions considered. At the higher applied load levels shown in the figure, the computed stress in the SIP approaches the failure stress of the tile material so that tile strength in regions of high substructure deformations becomes the limiting factor for determining the maximum permissible increase in SIP stiffness. However, the stress computation shown is most likely conservative in that the maximum stress occurs at the boundary of the SIP, and the computations do not account for the relaxation of stress at SIP boundaries observed in laboratory tests.

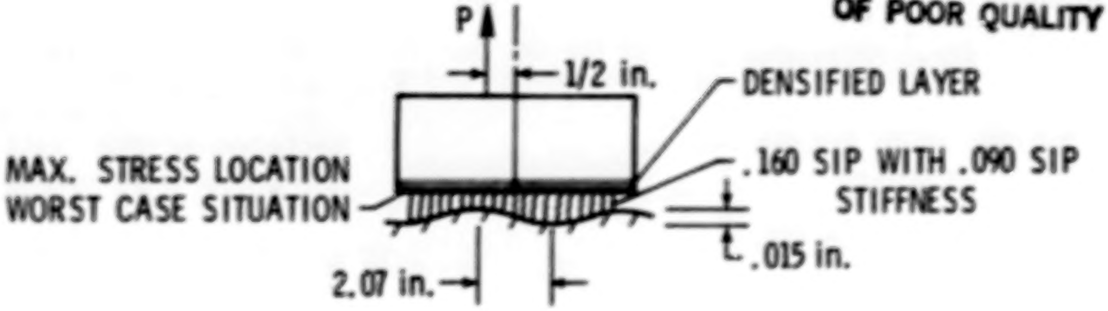

P, lb	$\sigma_{max\ ttt}$ STANDARD SIP, psi	$\sigma_{max\ ttt}$ STIFF SIP, psi	INCREASE, %
100	10.1	14.9	48
125	11.5	17.2	49
150	13.0	19.3	49

AV $\sigma_{failure}$ IN PARENT MATERIAL ≈ 21 psi

Figure 16.- Comparison of maximum SIP transverse stresses at tile/SIP interface for standard and stiff SIP.

CONCLUDING REMARKS

Sinusoidal fatigue tests of the ceramic TPS on the windward surface of the Shuttle orbiter indicate that the failure mode of the TPS is an excessive extension of the SIP which is a relatively benign failure mode and can be corrected during ground maintenance by replacement of the offending TPS. Random dynamic tests of the TPS simulating expected flight conditions during ascent indicate that the tiles might loosen sufficiently during the operational lifetime of the orbiter to cause burning of the filler bar in highly loaded regions. Sinusoidal tests indicate that a stiffer SIP can have an order-of-magnitude increase in fatigue lifetime. A method of improving the operational lifetime of the TPS by using a SIP with increased stiffness is presented as is the consequence of the effect of increased stiffness on the in-plane strains and transverse stresses. Results indicate that a stiffer SIP can be used to increase the TPS lifetime without compromising the structural integrity of the TPS except in regions with very thin tiles and possibly in regions with very high substructure deformations and applied loads.

figures show the flight/data base performance comparisons for each flight individually using both air data sources, LaRC (○) and ADS (□). The variations are shown thereon as the dashed lines. Tables II and III present the difference statistics (μ, σ) for each flight for the LaRC and ADS, respectively. Ensemble results for all five flights are also included thereon.

Comparison of figure 14 and figure 15 indicates the ADS results are more consistent in the differences across flights, particularly above Mach 1.1. This suggests, in view of the similarity in flight conditions, configuration, and expected contribution from same in this interval as shown in figures 12 and 13, that the ADS represents the best source for air data. However, neither air data source results in significant flight/data base discrepancies in this interval. Below Mach 1 the LaRC results show both STS-2 ($0.7 < \text{Mach} < 1.0$) and STS-3 ($0.5 < \text{Mach} < 0.7$) as potential outliers. Problems with winds for these flights have already been discussed. The ADS results, as stated, have the advantage of being based on in situ measurements. However, required calibrations to obtain air data parameters could conceivably introduce some systematic error in the process. This is only proposed as a possibility and is certainly not suggested in the results.

Detailed inspection of the expanded plots in the Appendix shows regions of comparable flight/data base differences for both air data sources. The biggest discrepancy for STS-1 is seen to be essentially a bias difference in all three performance parameters above Mach 1. The differences relate to the average α and $\bar{q}$ differences from the two sources (see table I). Near landing there are some sizable (~10 percent) lift and L/D differences suggested by the two sources. Figure A5(b) shows comparable agreement below Mach 0.7 for STS-2. Sizable differences occur near Mach 1 and in the vicinity of landing. Use of the ADS data indicates a large misprediction of the ground effects, particularly for C_L. Some similarities between the two sources for STS-3 can be seen in figure A5(c) though in very restricted regions, e.g., C_D differences below Mach 0.6. The differences observed for L/D and C_L between Mach 0.5 and 0.8 are most significant. These differences are the result of both the $\bar{q}$ and α differences shown in figure A2(c). Again, bias is seen in the lift and drag differences above Mach 1, on the order of 5 percent for both parameters. STS-4 and STS-5 differences shown in figures A5(d) and A5(e) show the results throughout are virtually independent of air data source to within a very few percent, differences near Mach 1 being the exception. For these flights the ADS $\bar{q}$ appears to have been linearly extrapolated between Mach 0.95 and 1.15.

In general the flight derived lift agrees with the predicted values to well within 1 variation throughout the Mach region investigated, with noted exceptions as discussed for STS-2 and STS-3. Drag is generally overpredicted by one variation below Mach 0.7 Exceptions are noted in the immediate vicinity of touchdown. Predictions due to ground effects are very sensitive to altitude and even for reasonable BET altitude errors, (~ 5 ft), are difficult to quantify.

DATA BASE UPDATE DISCUSSION

With only five flights to date it is felt that rigorous data base updates are premature. Rigorous updates herein imply refinements to all elements of the data base as modelled, i.e., Mach and α dependence for the basic aerodynamic characteristics, control surface incrementals, and gear and ground effects. More flights will enable development of a larger flight data base and permit more comprehensive updates.

C-6

Based on current results, simple predicts adjustments are plausible. However, throughout much of the region investigated herein, different results were obtained dependent upon the air data source utilized. Comparison of the results shown in figure 14 and 15 would indicate that the measured (ADS) air data would best serve for data base updates. If both sources are considered equally viable, the results of this paper can be interpreted as an error analysis defining accuracies of flight extraction, predicts generation, and resultant flight/data base update determinations. In that sense, it is relevant to focus on those regions wherein similar prediction deficiencies are noted independent of air data sources.

Table IV shows ensemble statistics for all five flights for the two air data sources. Below Mach 0.8 an approximate 10 percent overpredicted drag coefficient is independently suggested. This amount is essentially that decrement resulting from application of the FADS of reference 6. Therein, the functional form of the drag correction below Mach 0.6 is a constant drag decrement plus a constant and linear term when $h/b < 0.45$ for ground effect refinements. This total adjustment to the predicted drag will increase the predicted L/D and reduce the flight/data base discrepancies observed for that performance parameter as well. The results from table IV suggest that, beyond the noted plausible C_D correction below Mach 0.8, other predict refinements are questionable. In general, lift corrections would be small and perhaps not statistically significant, albeit dependent on the particular air data source utilized. The FADS do include some predicted lift changes which, when applied to the LaRC data base with ADS air data over the interval $0 < \text{Mach} < 2$, essentially remove the small mean error but only reduce the random error by 0.6 percent.

CONCLUSIONS

Flight derived and predicted longitudinal performance based on two independent air data sources vary on the order of 2 (±3) percent, with local differences in excess of 10 percent. Consequently, use of either air data source as the reference results in different flight/data base comparisons. More consistent flight/data base comparisons across flights were observed when the ADS parameters were adopted. In particular, STS-2 and STS-3 results exhibited the largest departures when the computed air data parameters were employed. Large winds were encountered during these two missions. Though estimation/evaluation of these winds versus some of the ADS parameters was performed, uncertainties in these winds would affect the resultant flight/data base comparisons. If both air data sources are considered equally viable, the results presented suggest statistically significant C_L prediction refinements are questionable for the Mach interval investigated. The FADS C_D decrement of ~ 10 percent below Mach 0.6 is substantiated independent of air data source. This decrement increases the predicted L/D and consequently improves comparisons of that parameter with the flight derived performance.

REFERENCES

1. Compton, H.R.; Blanchard, R.C.; and Walberg, G.D.: An Experiment for Shuttle Aerodynamic Force Coefficient Determinations from Inflight Dynamical and Atmospheric Measurements. AIAA Paper No. 78-795, 1978.

2. Jones, J.J.: OEX - Use of the Shuttle Orbiter as a Research Vehicle. AIAA Paper No. 81-2512, 1981.

3. Compton, H.R.; Scallion, W.I.; Suit, W.T.; and Schiess, J.R: Shuttle Entry Performance and Stability and Control Derivatives Extraction From Flight Measurement Data. AIAA Paper No. 82-1317, 1982.

4. Young, J.C.; Perez, L.F.; Romere, P.O.; and Kanipe, D.B.: Space Shuttle Entry Aerodynamic Comparisons of Flight 1 and 2 With Preflight Predictions. AIAA Paper No. 82-0565, 1982.

5. Findlay, J.T.; and Compton, H.R.: On the Flight Derived/Aerodynamic Data Base Performance Comparisons For the NASA Space Shuttle Entries During the Hypersonic Regime. AIAA Paper No. 83-0115, 1983.

6. Underwood, J.M., compiler: STS-4B Deltas Flight Assessment Package - Orbiter Aerodynamics. NASA JSC Report No.-18745, December 1982.

7. Kirsten, P.W.; and Richardson, D.F.: Predicted and Flight Test Results of the Performance and Stability and Control of the Space Shuttle from Reentry to Landing. Paper presented at the AGARD/Flight Mechanics Panel Ground/Flight Test Techniques and Correlation Meeting, Cesme, Turkey, October 11-15, 1982.

8. Siemers, P.M. III; Wolf, H.; and Flanagan, P.F.: Shuttle Entry Air Data System Concepts Applied to Space Shuttle Orbiter Flight Pressure Data to Determine Air Data - STS 1-4. AIAA Paper No. 83-0118, 1983.

9. Young, J.C.; and Underwood, J.M.: The Development of Aerodynamic Uncertainties For the Space Shuttle Orbiter. AIAA Paper No. 82-0563,1982.

10. Gamble, J.D.; and Young, J.C.: The Development and Applicaton of Aerodynamic Uncertainties for Space Shuttle Orbiter. AIAA Paper No. 82-1335, 1982.

11. Price, J.M.; and Blanchard, R.C.: Determination of Atmospheric Properties for STS-1 Aerothermodynamic Investigations. AIAA Paper No. 81-2430, 1981.

12. Findlay, J.T.; Kelly, G.M.; and Heck, M.L.: Reconstruction of the 1st Space Shuttle (STS-1) Entry Trajectory. NASA CR-3561, 1982.

13. Kelly, G.M.; Findlay, J.T.; and Compton, H.R.: Wind Estimation Using Air Data Probe Measurements to Evaluate Meteorological Measurements Made During Space Shuttle Entries. AIAA Paper No. 82-1333, 1982.

14. Findlay, J.T.; Kelly, G.M.; and McConnell, J.G.: An AEROdynamic Best Estimate Trajectory File (AEROBET) for NASA Langley Research Center Shuttle Investigations. AMA Report No. 82-9, March 1982.

15. Aerodynamic Design Data Book. Vol. I - Orbiter Vehicle, SD72-SH-0060-1L, Rockwell International, Oct. 1978.

16. Aerodynamic Design Data Book. Vol. I - Orbiter Vehicle, SD72-SH-0060-1L-6, Rockwell International, April 1982.

TABLE I.-AIR DATA PARAMETER DIFFERENCES, LaRC - ADS

Flight	0<Mach<1				0<Mach<2				1<Mach<2			
	Δα (degrees)		Δq (percent)		Δα (degrees)		Δq (percent)		Δα (degrees)		Δq (percent)	
	μ	σ	μ	σ	μ	σ	μ	σ	μ	σ	μ	σ
STS-1	0.2	0.2	1.4	1.4	0.2	0.2	1.6	1.6	0.1	0.2	2.4	1.8
STS-2	<0.1	0.4	0.2	3.5	0.1	0.4	-0.1	3.8	0.1	0.3	-0.8	4.4
STS-3	0.2	0.5	1.0	2.5	0.2	0.4	1.6	2.9	0.1	0.3	3.1	3.1
STS-4	0.1	0.2	<0.1	1.3	<0.1	0.2	0.2	1.5	<0.1	0.1	0.5	2.0
STS-5	0.1	0.3	0.7	2.5	0.1	0.3	0.7	2.4	-0.1	0.2	0.6	2.0

ORIGINAL PAGE IS
OF POOR QUALITY

TABLE II.-FLIGHT/DATA BASE PERFORMANCE DIFFERENCE STATISTICS, LaRC AEROBETS

Flight	0 < Mach < 1						0 < Mach < 2						1 < Mach < 2					
	$\Delta L/D$ (percent)		ΔC_L (percent)		ΔC_D (percent)		$\Delta L/D$ (percent)		ΔC_L (percent)		ΔC_D (percent)		$\Delta L/D$ (percent)		ΔC_L (percent)		ΔC_D (percent)	
	μ	σ	μ	σ	μ	σ	μ	σ	μ	σ	μ	σ	μ	σ	μ	σ	μ	σ
STS-1	6.1	4.6	-5.2	3.2	-12.2	4.7	5.3	4.5	-4.9	3.0	-10.9	5.0	2.8	3.0	-3.5	1.8	-6.5	3.3
STS-2	6.6	5.7	-0.7	6.1	- 8.0	6.2	5.8	5.6	-0.5	5.4	- 6.9	6.0	3.2	4.6	0.1	2.1	-3.3	3.9
STS-3	2.7	7.6	-5.2	11.2	- 8.1	7.4	2.6	6.7	-4.8	9.6	- 7.6	6.5	2.1	3.3	-4.0	2.0	-6.3	3.0
STS-4	6.0	4.8	-2.5	3.7	- 9.3	5.5	5.2	4.6	-2.3	3.3	- 8.1	5.3	3.0	2.9	-1.3	1.3	-4.5	2.8
STS-5	5.3	5.4	-3.8	5.6	- 9.8	5.2	4.7	5.1	-2.9	5.0	- 8.2	5.5	3.1	3.6	-0.7	1.7	-4.1	3.8
All	5.5	5.8	-3.4	6.7	- 9.5	6.0	4.8	5.4	-3.0	5.9	- 8.3	5.8	2.8	3.6	-2.0	2.4	-5.1	3.6

TABLE III.-FLIGHT/DATA BASE PERFORMANCE DIFFERENCE STATISTICS, ADS AEROBETS

Flight	0 < Mach < 1						0 < Mach < 2						1 < Mach < 2					
	$\Delta L/D$ (percent)		ΔC_L (percent)		ΔC_D (percent)		$\Delta L/D$ (percent)		ΔC_L (percent)		ΔC_D (percent)		$\Delta L/D$ (percent)		ΔC_L (percent)		ΔC_D (percent)	
	μ	σ	μ	σ	μ	σ	μ	σ	μ	σ	μ	σ	μ	σ	μ	σ	μ	σ
STS-1	7.7	6.0	-1.2	4.1	-10.0	6.2	6.8	5.6	-0.8	3.8	-8.5	6.3	3.9	2.4	0.6	1.6	-3.4	3.0
STS-2	6.5	5.2	0.6	5.5	- 6.5	6.3	6.0	4.9	0.8	4.9	-5.7	5.8	4.1	2.9	1.4	1.8	-2.8	2.7
STS-3	6.3	5.6	<0.1	5.4	- 6.9	6.4	5.3	5.1	0.2	4.7	-5.7	6.0	2.8	2.3	0.8	1.8	-2.2	2.8
STS-4	7.0	4.7	-0.9	4.6	- 8.7	5.0	6.0	4.6	-0.8	4.1	-7.4	5.2	3.6	3.1	-0.4	2.2	-4.3	4.5
STS-5	6.2	4.2	-1.5	4.2	- 8.3	4.0	5.3	4.1	-1.2	3.8	-6.9	4.7	2.8	2.9	-0.4	2.5	-3.5	4.6
All	6.7	5.2	-0.8	4.9	- 8.2	5.9	5.9	4.9	-0.5	4.3	-7.0	5.8	3.5	2.8	0.2	2.2	-3.5	3.8

TABLE IV.-ENSEMBLE FLIGHT/DATA BASE DIFFERENCE STATISTICS FOR MACH SUB-INTERVALS

	$\Delta L/D$ (percent)				ΔC_L (percent)				ΔC_D (percent)			
	LaRC		ADS		LaRC		ADS		LaRC		ADS	
Mach Region	μ	σ	μ	σ	μ	σ	μ	σ	μ	σ	μ	σ
0.2 to 0.4	8.2	4.9	7.6	4.6	-0.1	5.3	-0.2	6.7	- 9.1	4.9	- 8.5	4.7
0.4 to 0.6	3.7	5.7	6.9	4.6	-6.2	6.3	-2.9	4.5	-10.5	5.0	-10.7	4.3
0.6 to 0.8	8.8	4.3	9.8	3.5	-0.7	6.6	1.8	3.0	-10.4	5.7	- 9.0	4.7
0.8 to 1.0	3.8	5.9	2.5	5.2	-2.4	5.6	0.4	4.5	- 6.7	7.7	- 2.4	6.3
1.0 to 1.2	5.9	4.6	7.1	2.2	-1.6	2.9	-0.9	2.6	- 8.2	4.5	- 8.7	4.0
1.2 to 1.4	4.0	2.5	4.4	0.9	-2.4	1.6	-0.2	1.4	- 6.7	3.0	- 4.8	1.0
1.4 to 1.6	2.6	1.2	3.2	1.9	-0.5	1.7	1.4	1.6	- 3.2	1.6	- 1.8	1.3
1.6 to 1.8	0.9	1.4	1.8	1.0	-1.6	1.8	1.7	1.2	- 2.6	1.5	- 0.1	0.8
1.8 to 2.0	-0.8	1.1	0.1	1.1	-4.2	2.0	-1.6	1.5	- 3.3	1.3	- 1.6	0.7

ORIGINAL PAGE IS
OF POOR QUALITY

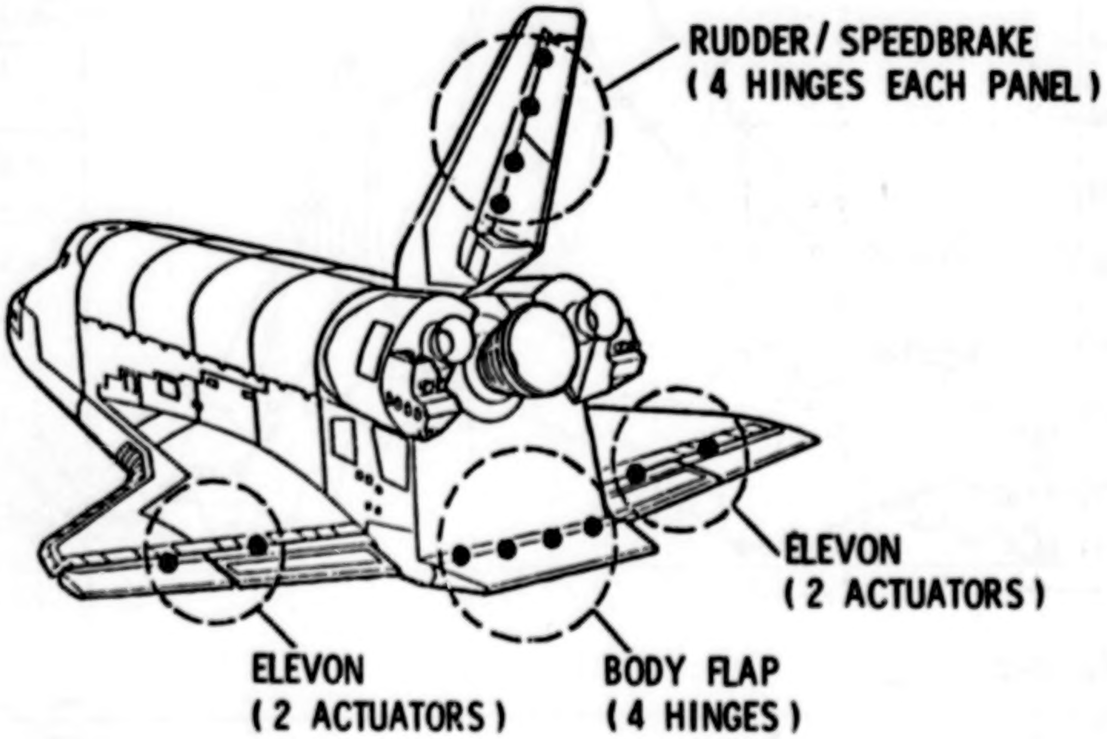
RUDDER / SPEEDBRAKE
(4 HINGES EACH PANEL)
ELEVON
(2 ACTUATORS)
ELEVON
(2 ACTUATORS)
BODY FLAP
(4 HINGES)

Figure 1.- Schematic of Orbiter control surface configuration.

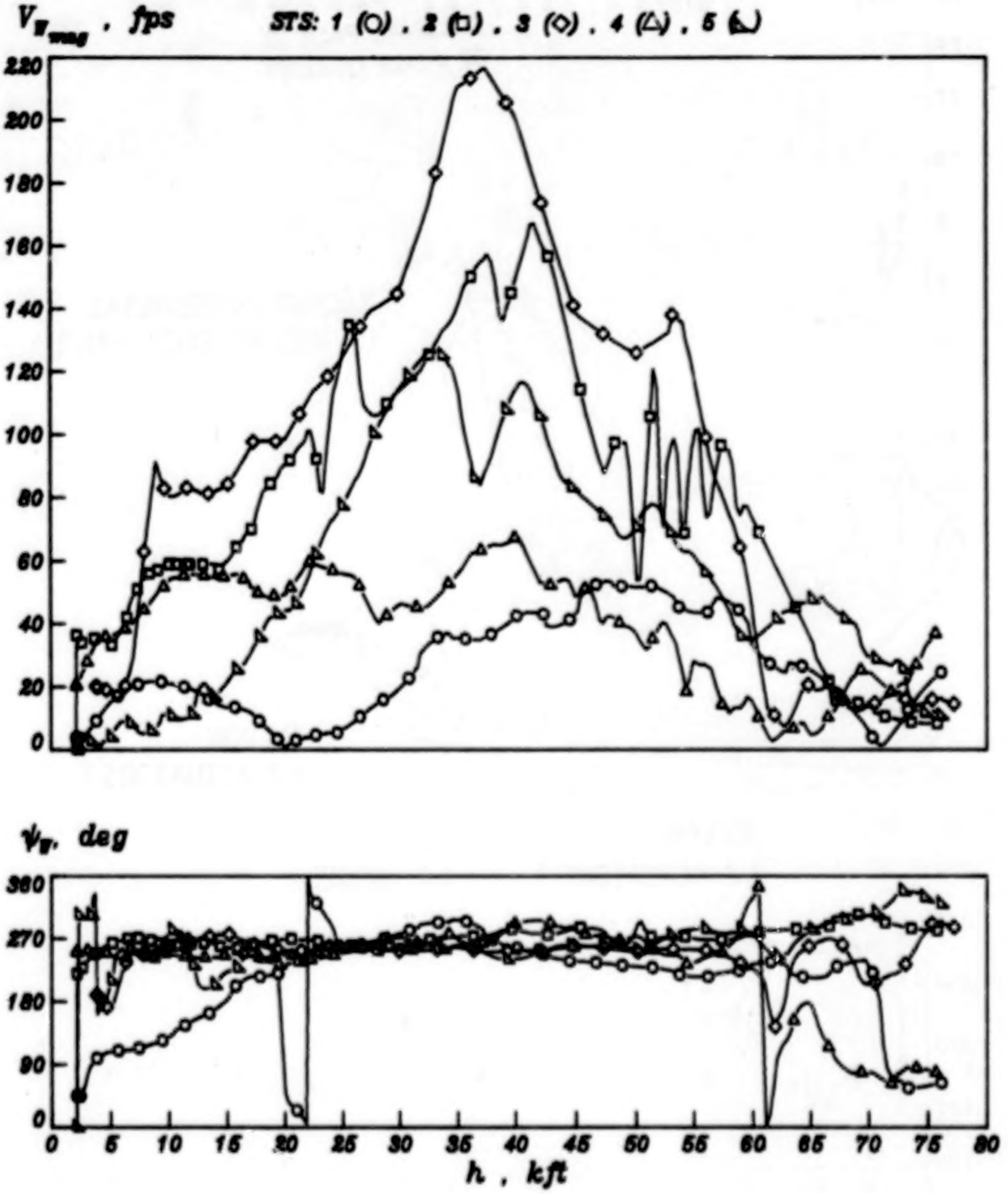

Figure 2.- Wind profiles over lower altitude region.

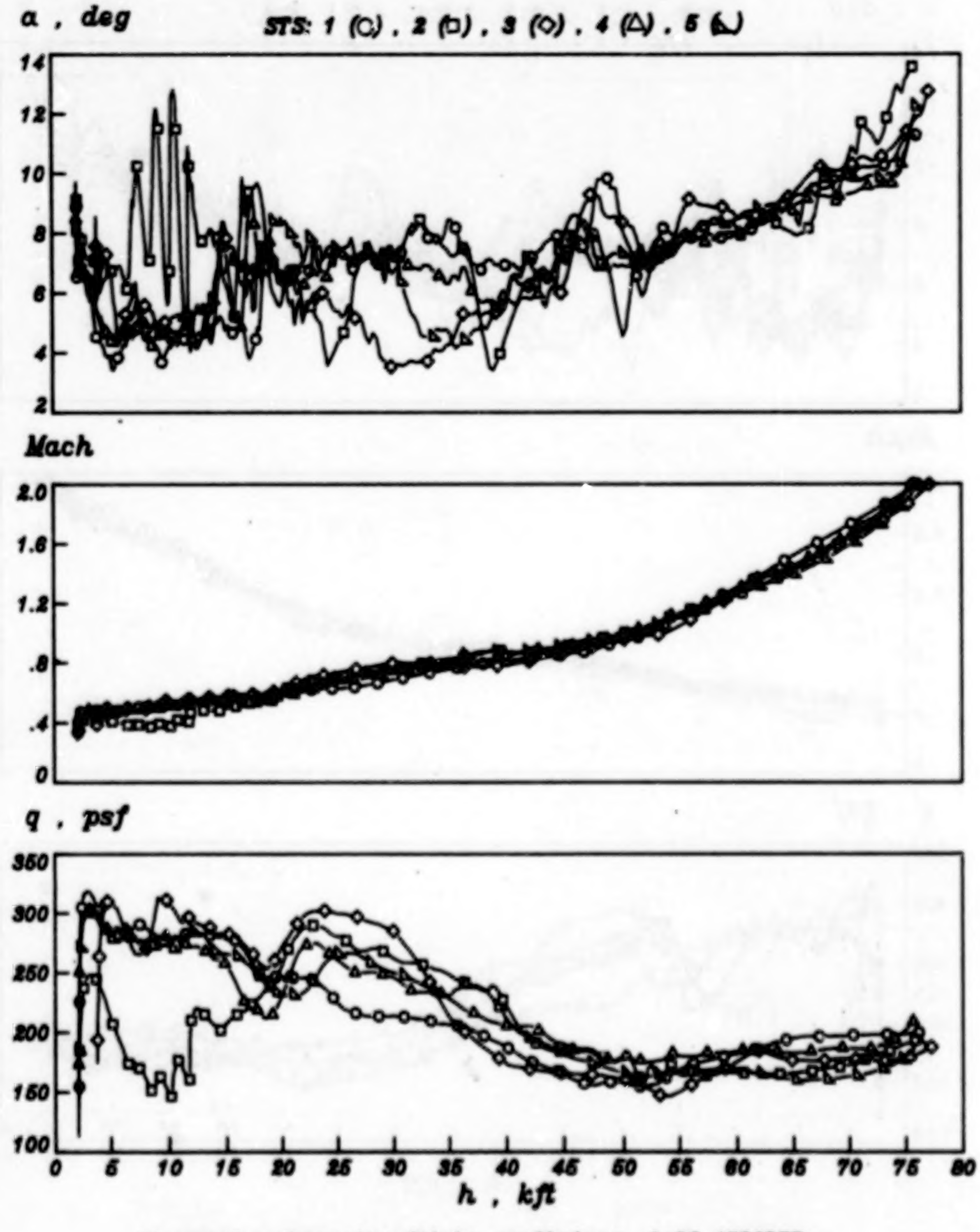

Figure 3.- Composite flight conditions, LaRC AEROBETs.

ORIGINAL PAGE IS
OF POOR QUALITY

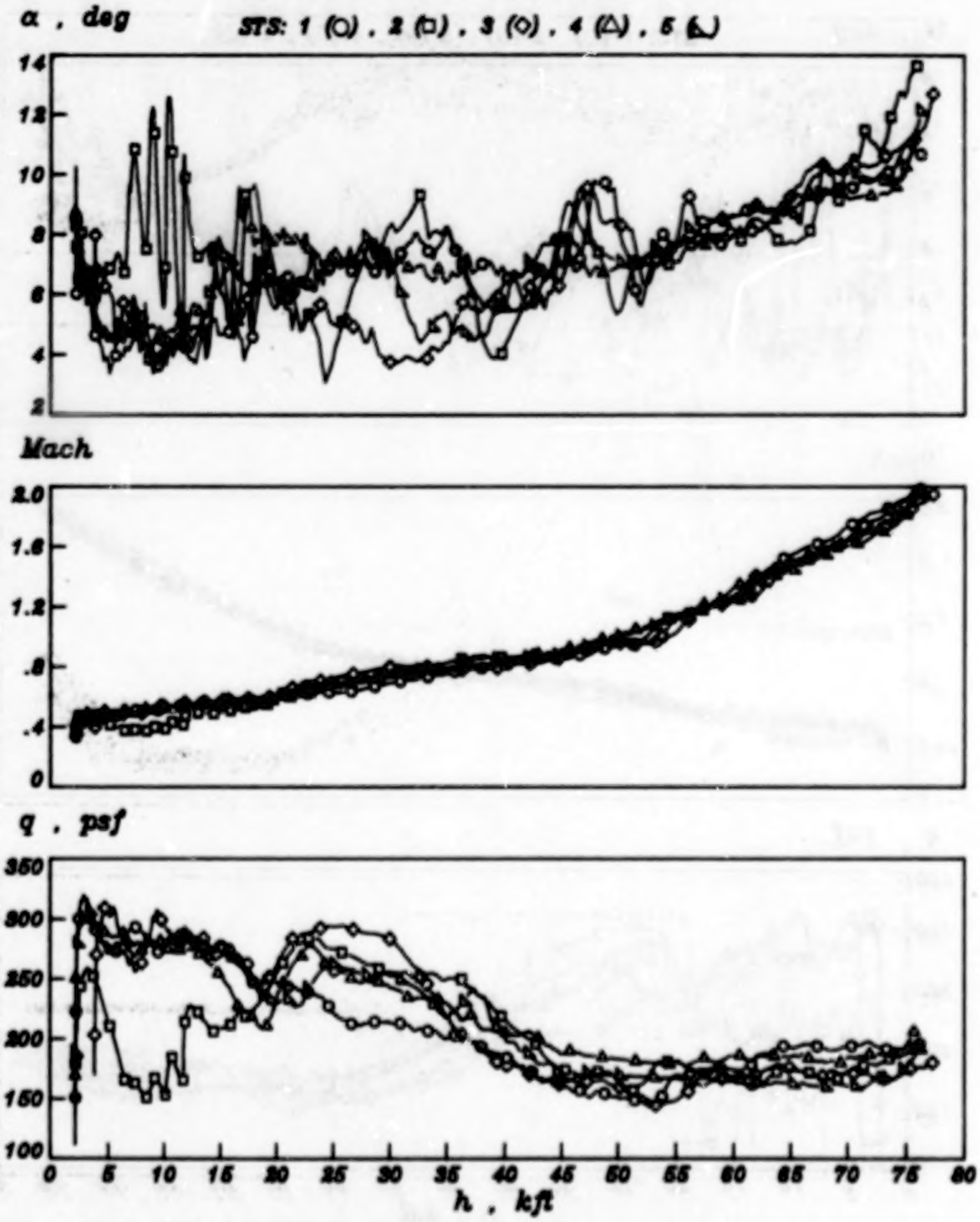

Figure 4.- Composite flight conditions, ADS AEROBETs.

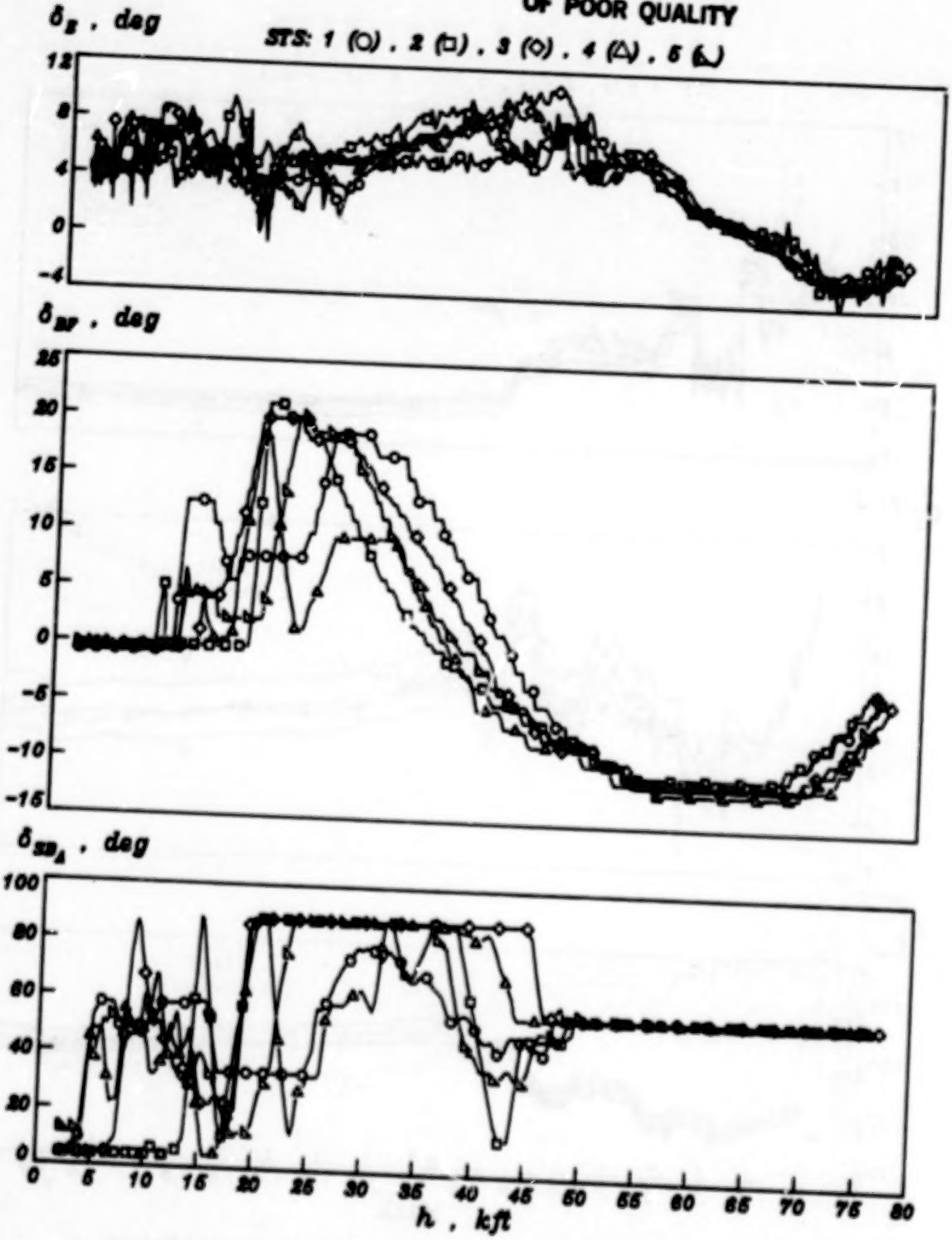

Figure 5.- Composite of control surface deflections versus h.

ORIGINAL PAGE IS
OF POOR QUALITY

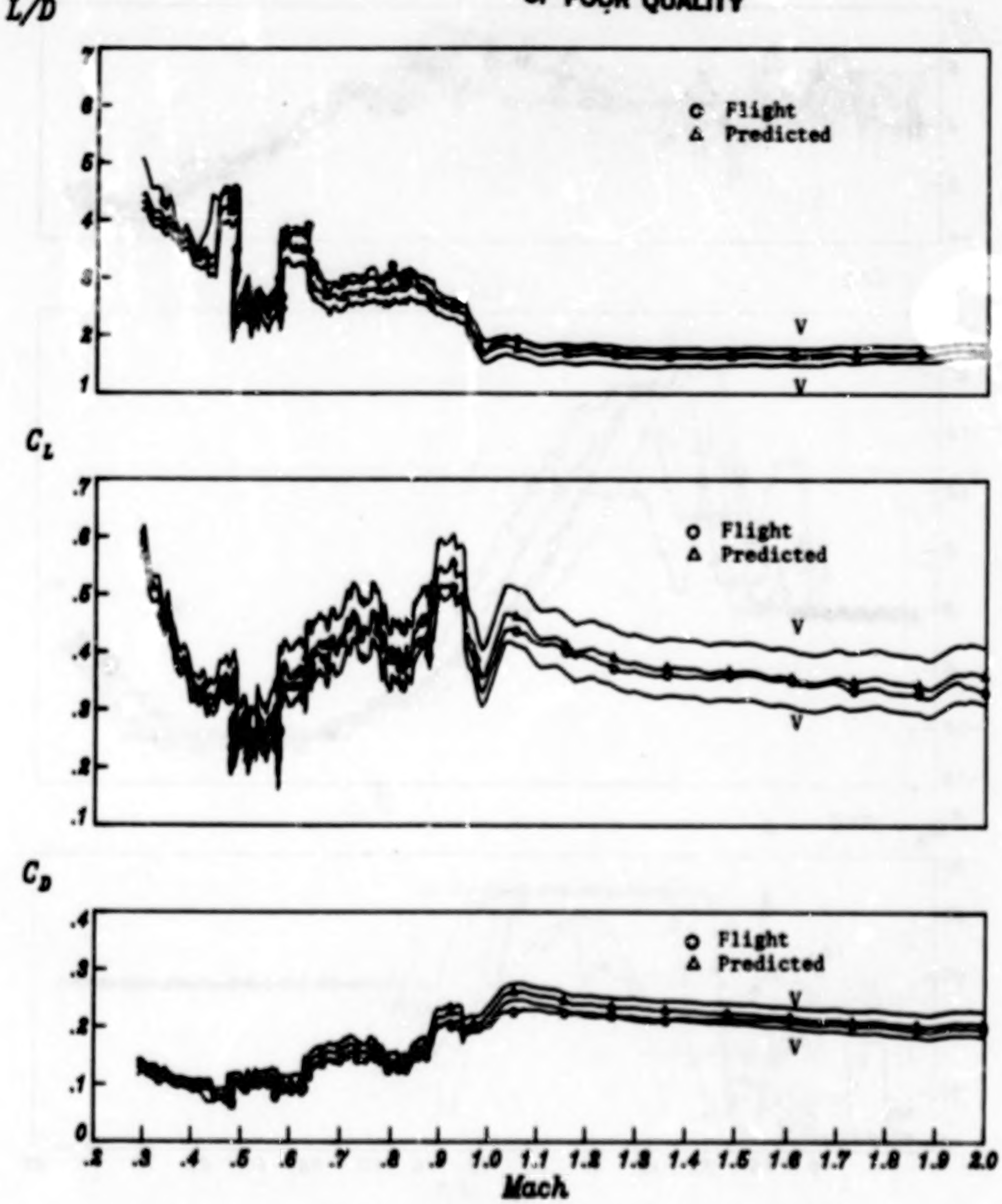

Figure 6.- STS-1 longitudinal performance for LaRC AEROBET.

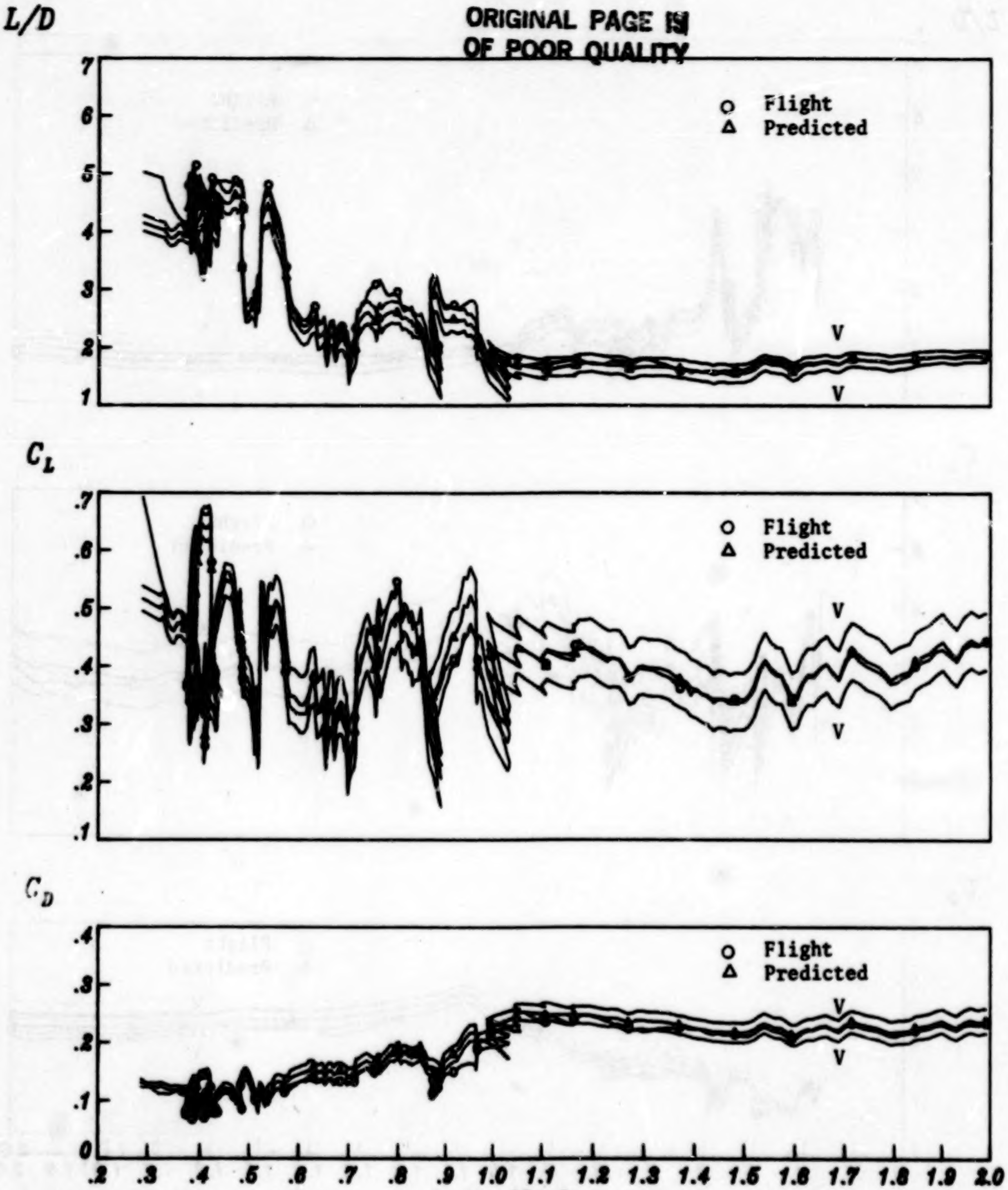

Figure 7.- STS-2 longitudinal performance for LaRC AEROBET.

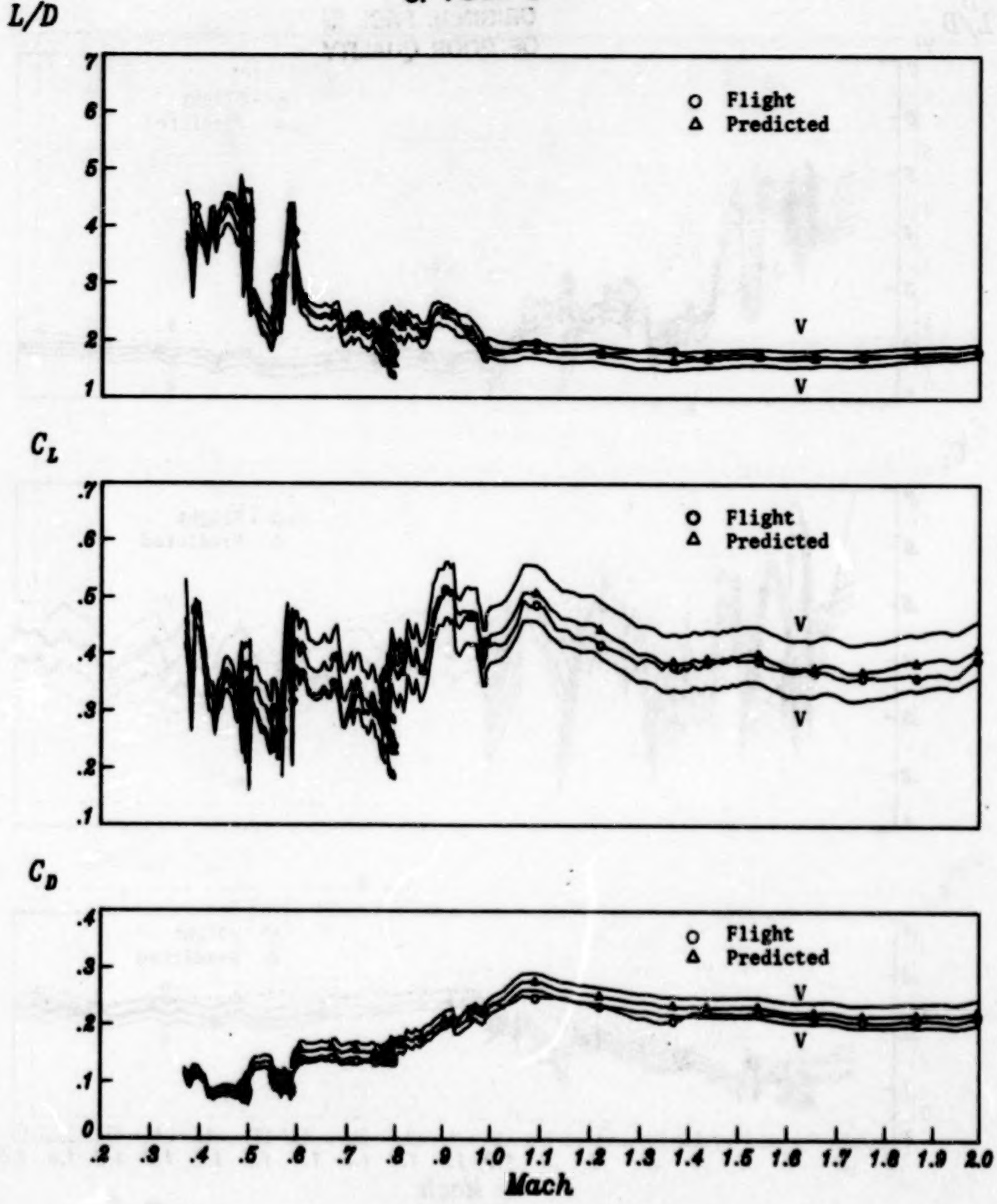

Figure 8.- STS-3 longitudinal performance for LaRC AEROBET.

ORIGINAL PAGE IS
OF POOR QUALITY

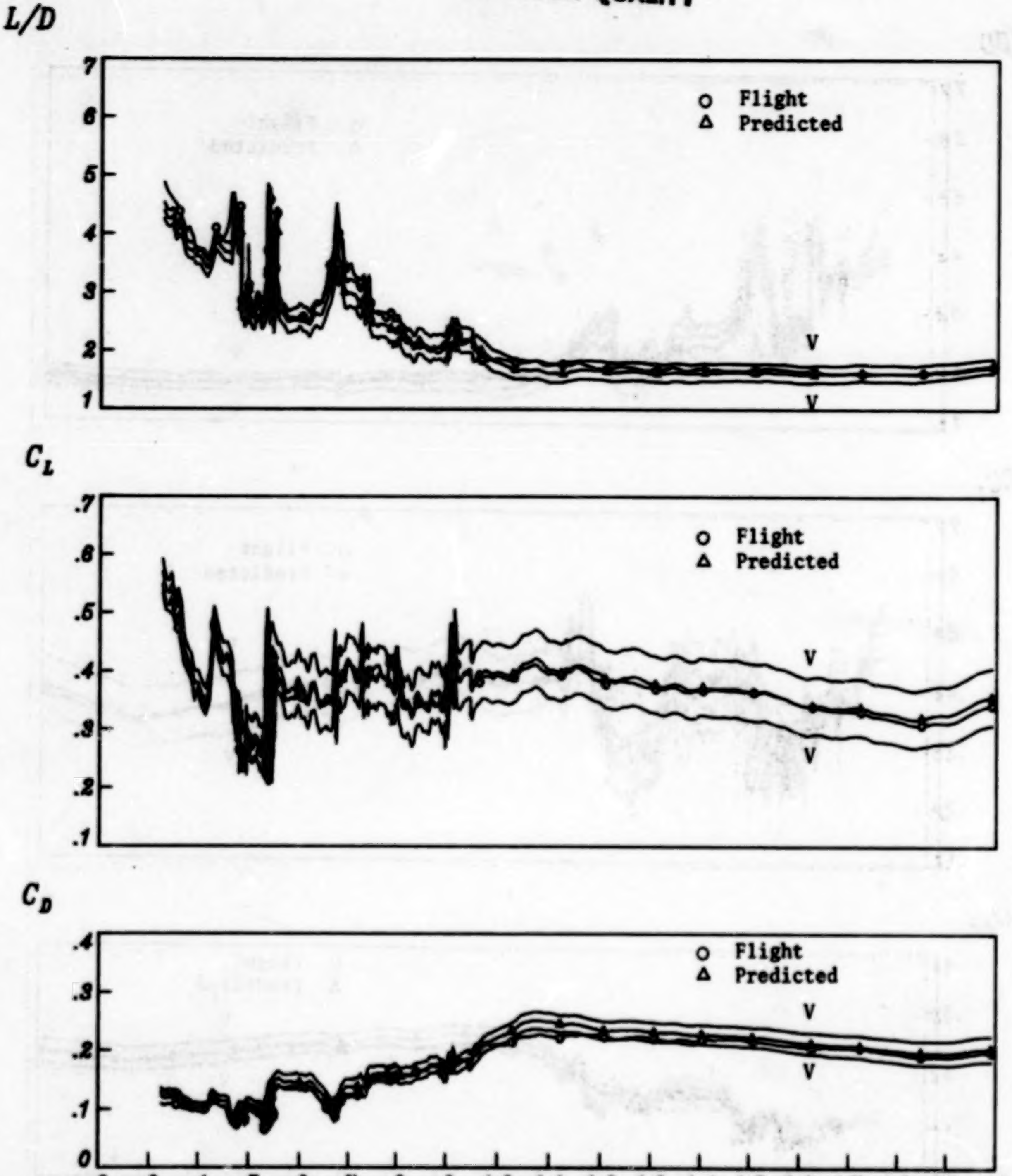

Figure 9.- STS-4 longitudinal performance for LaRC AEROBET.

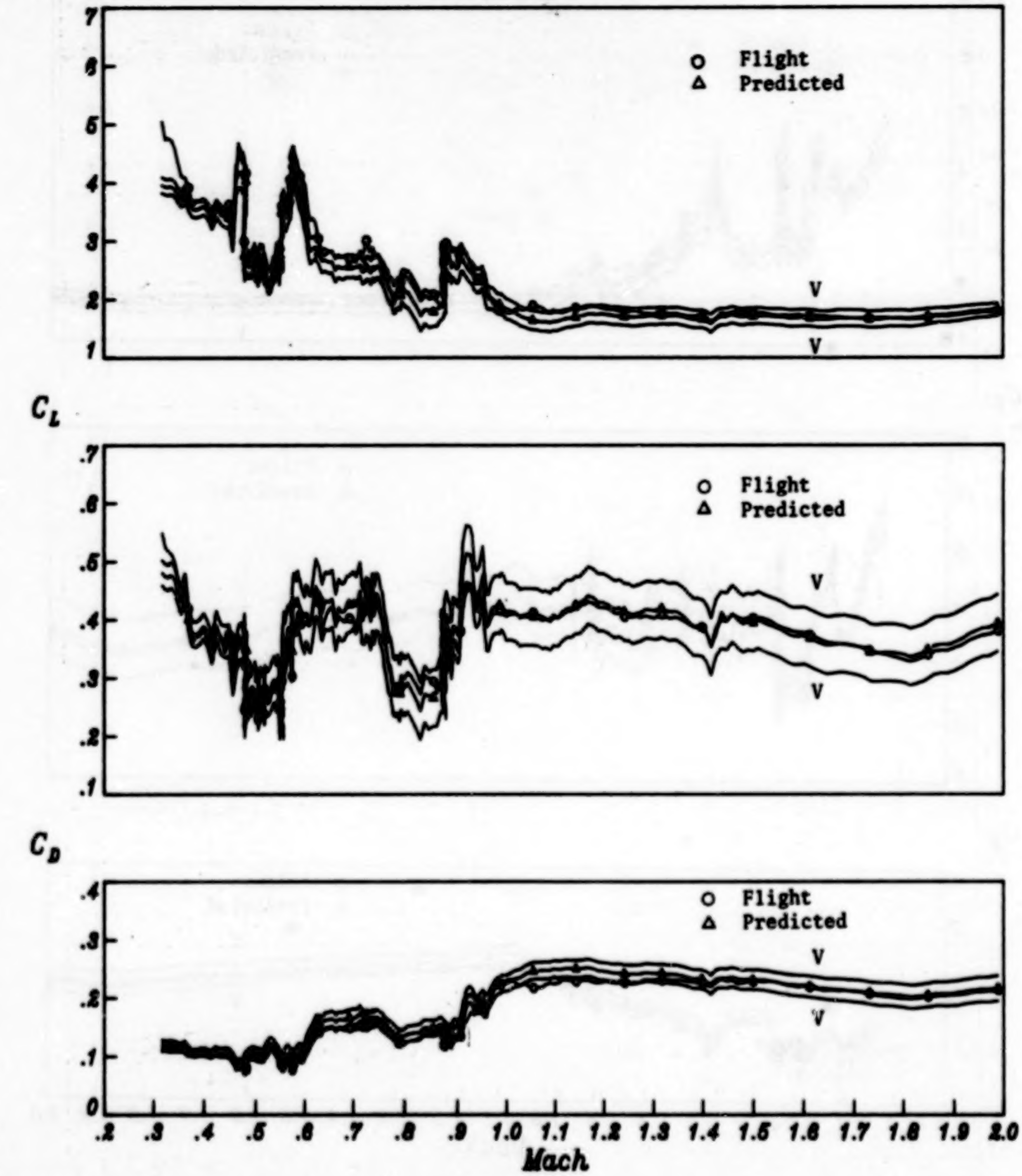

Figure 10.- STS-5 longitudinal performance for LaRC AEROBET.

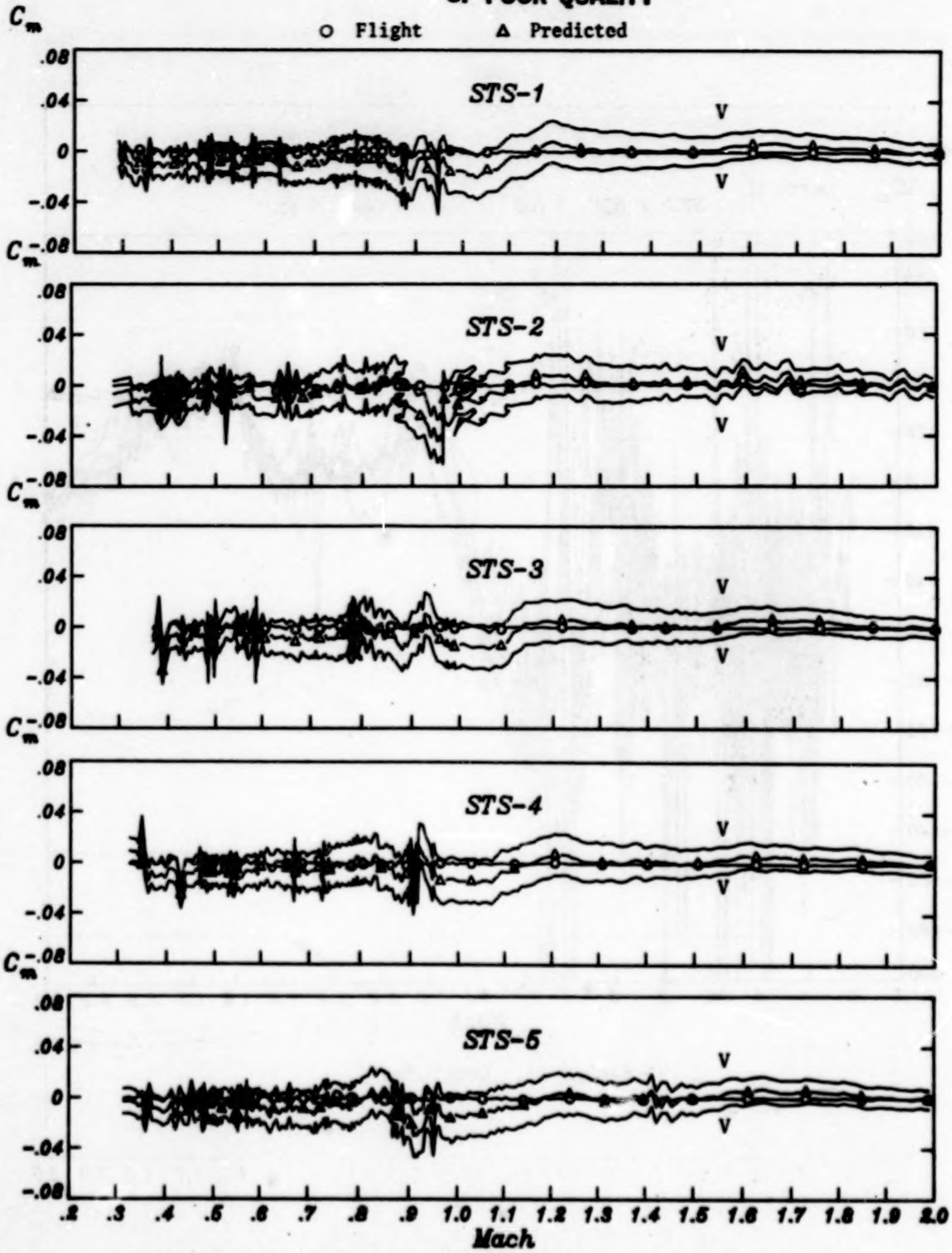

Figure 11.- Pitching moment comparisons for LaRC AEROBETs.

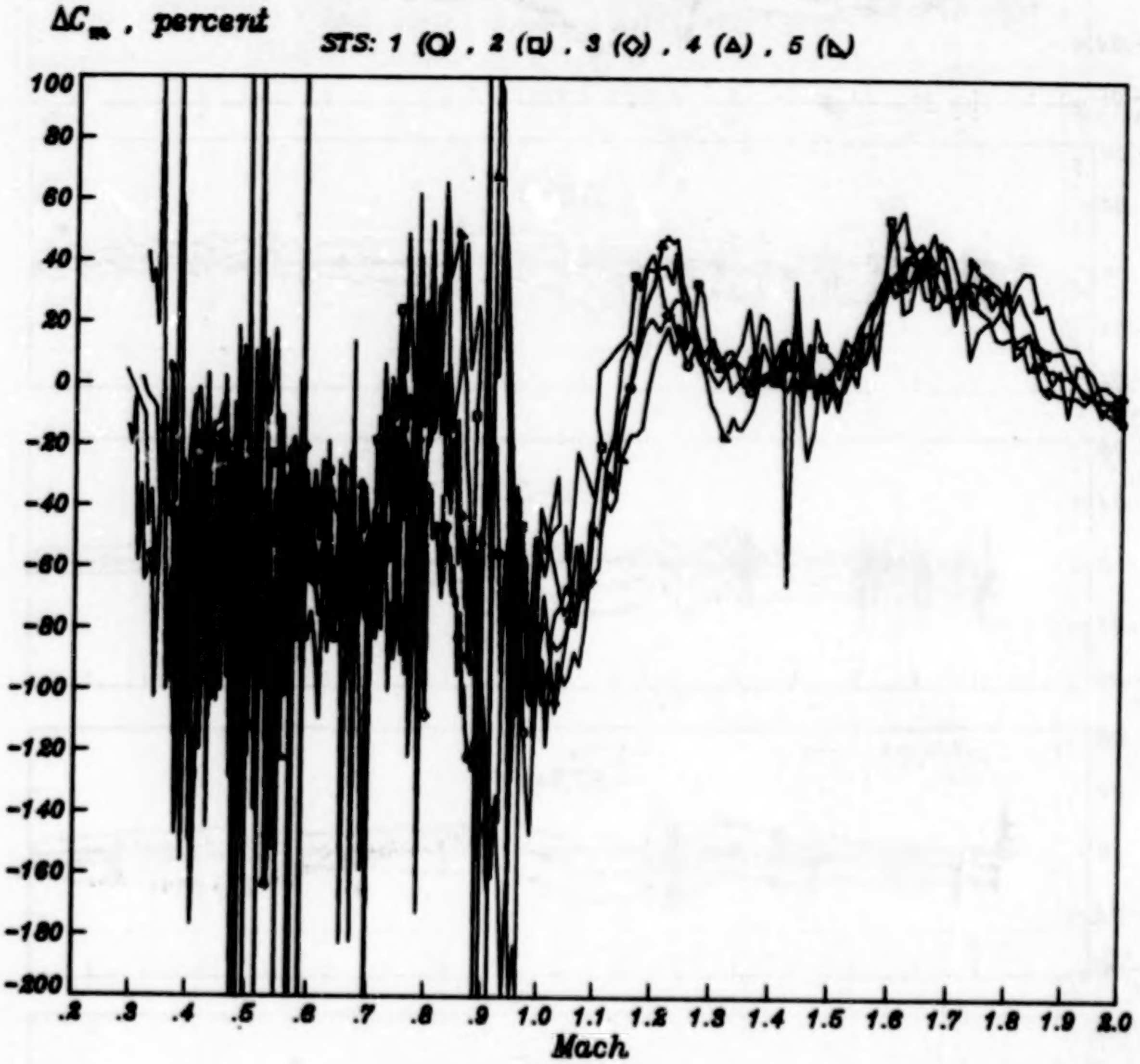

Figure 11.- Concluded.

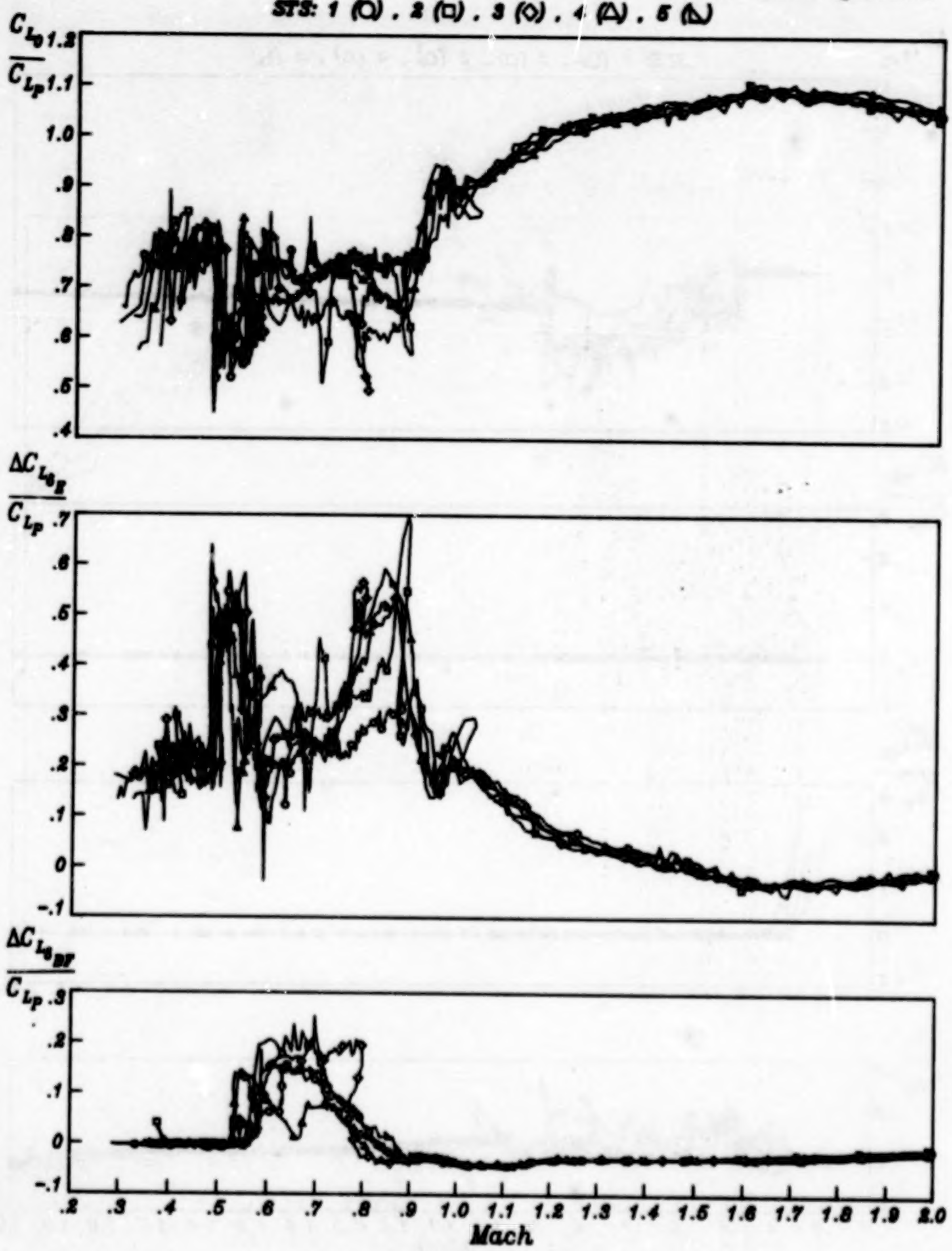

Figure 12.- Predicted C_L contributions.

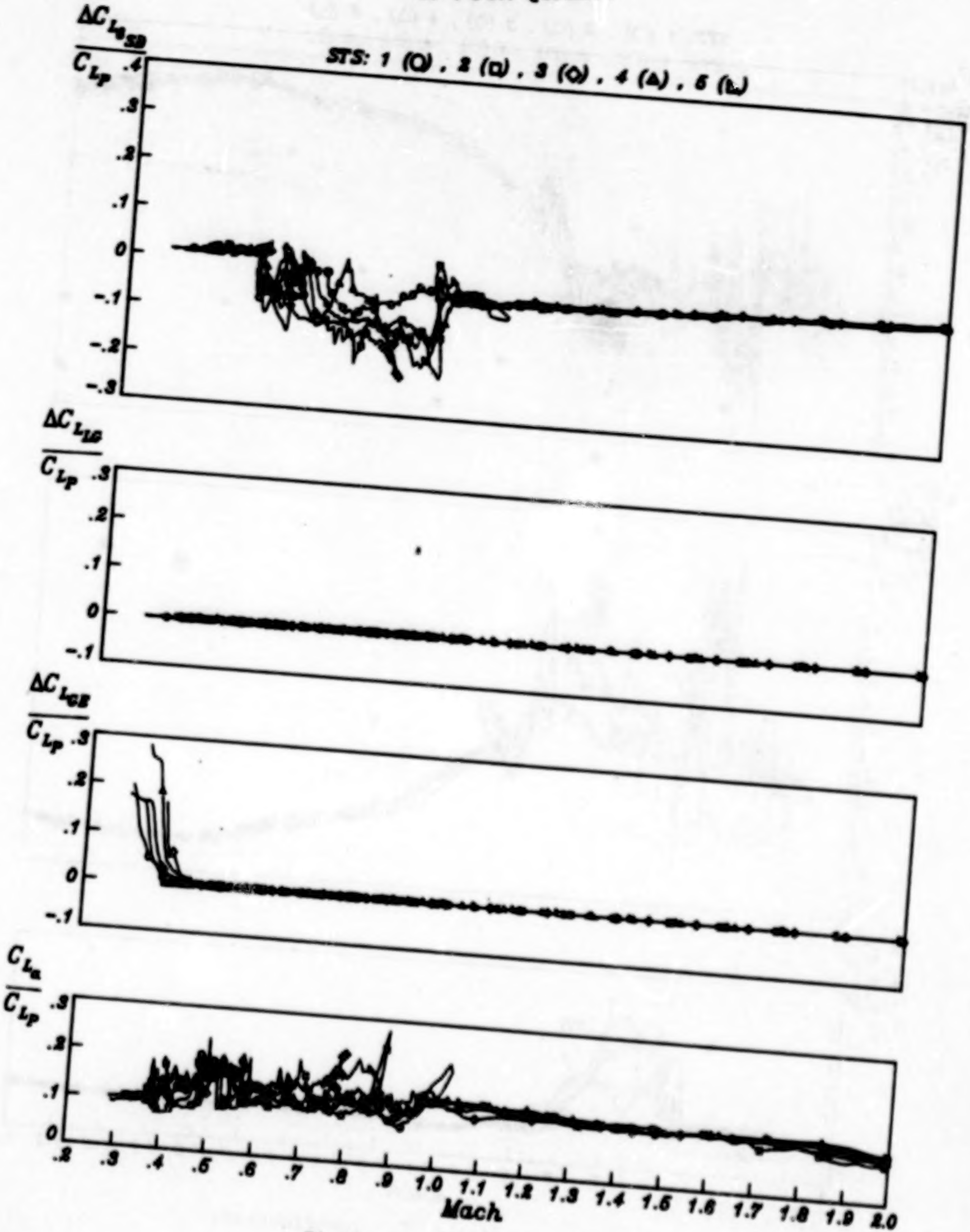

Figure 12.- Concluded.

ORIGINAL PAGE IS
OF POOR QUALITY

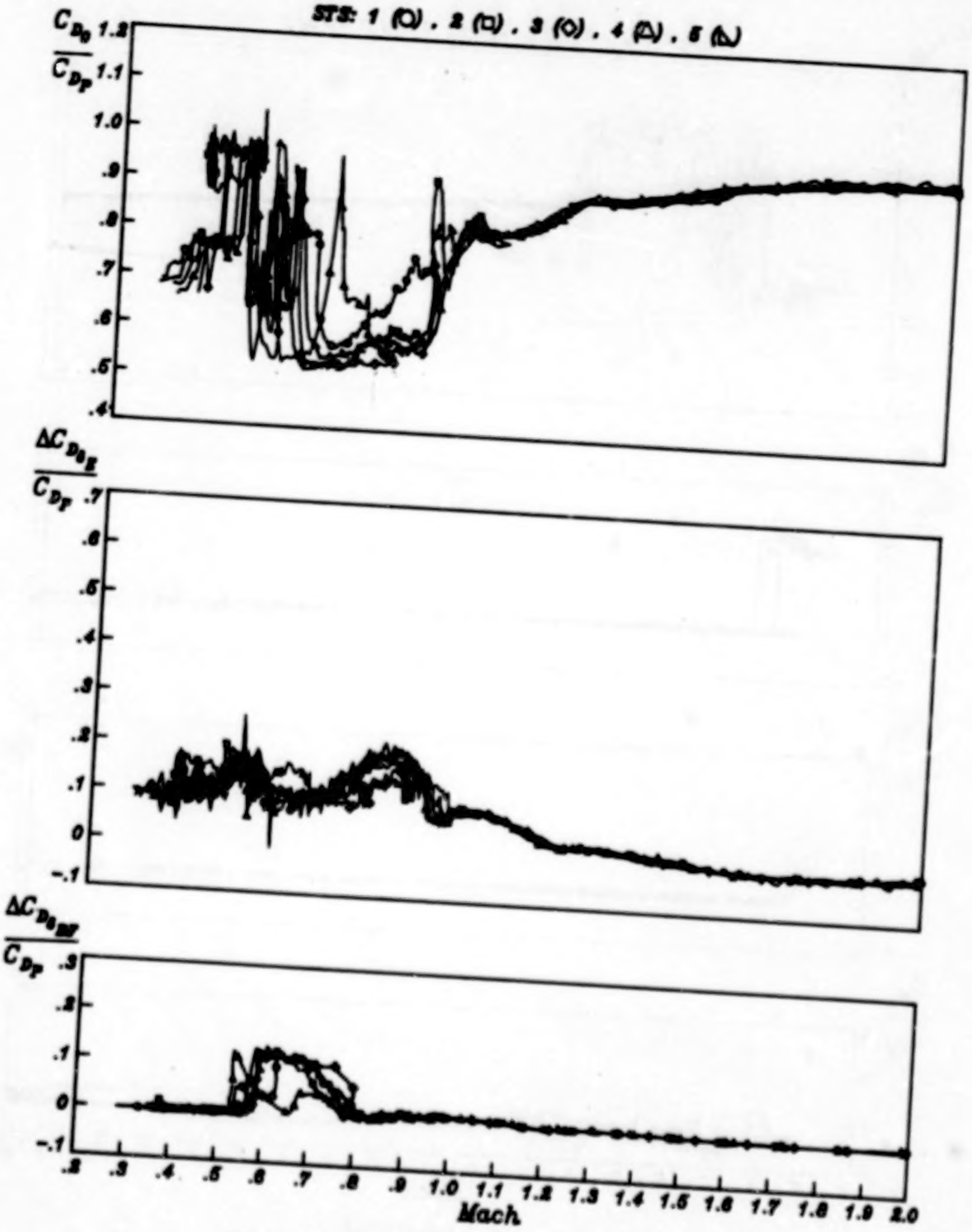

Figure 13.- Predicted C_D contributions.

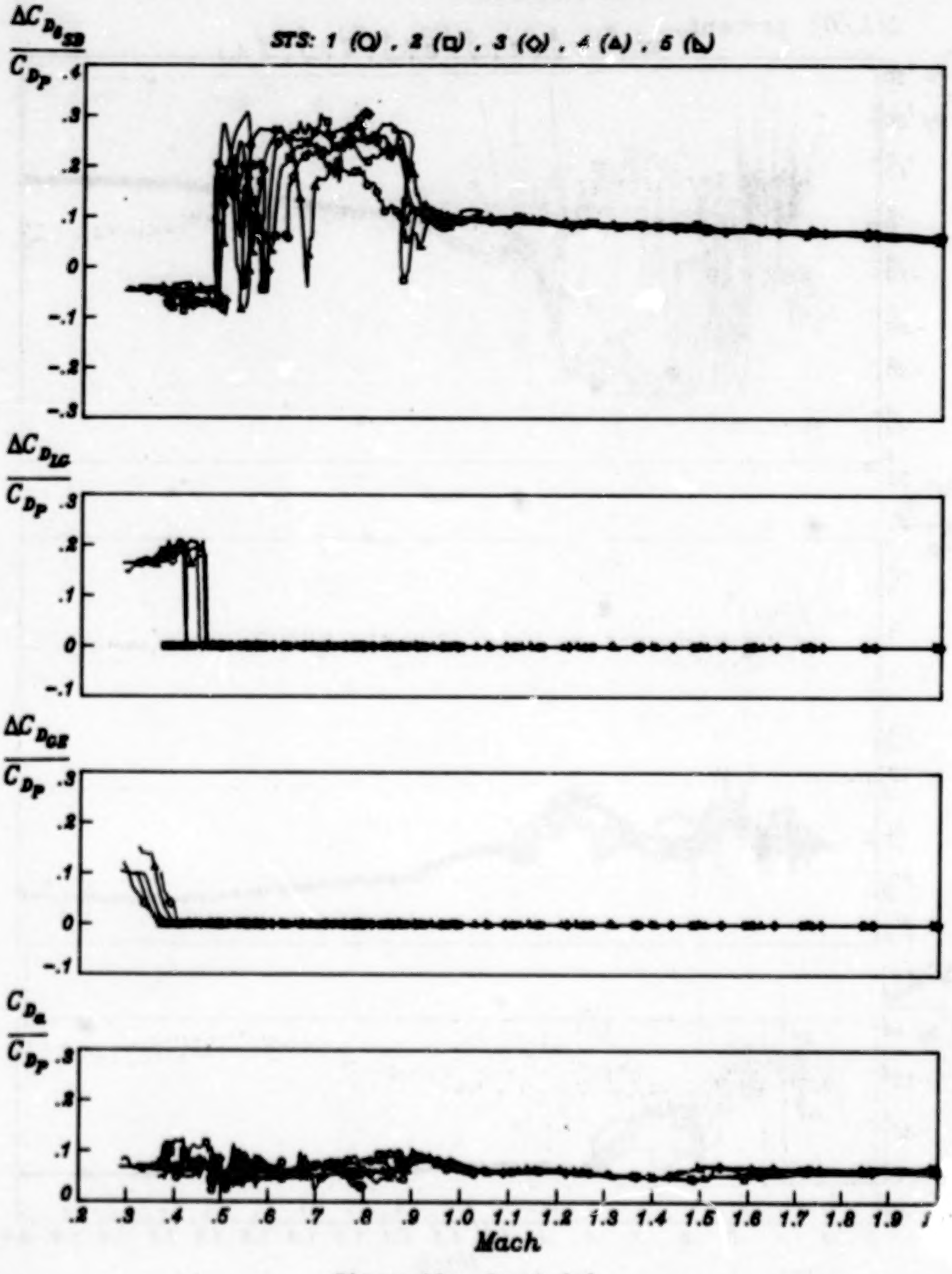

Figure 13.- Concluded.

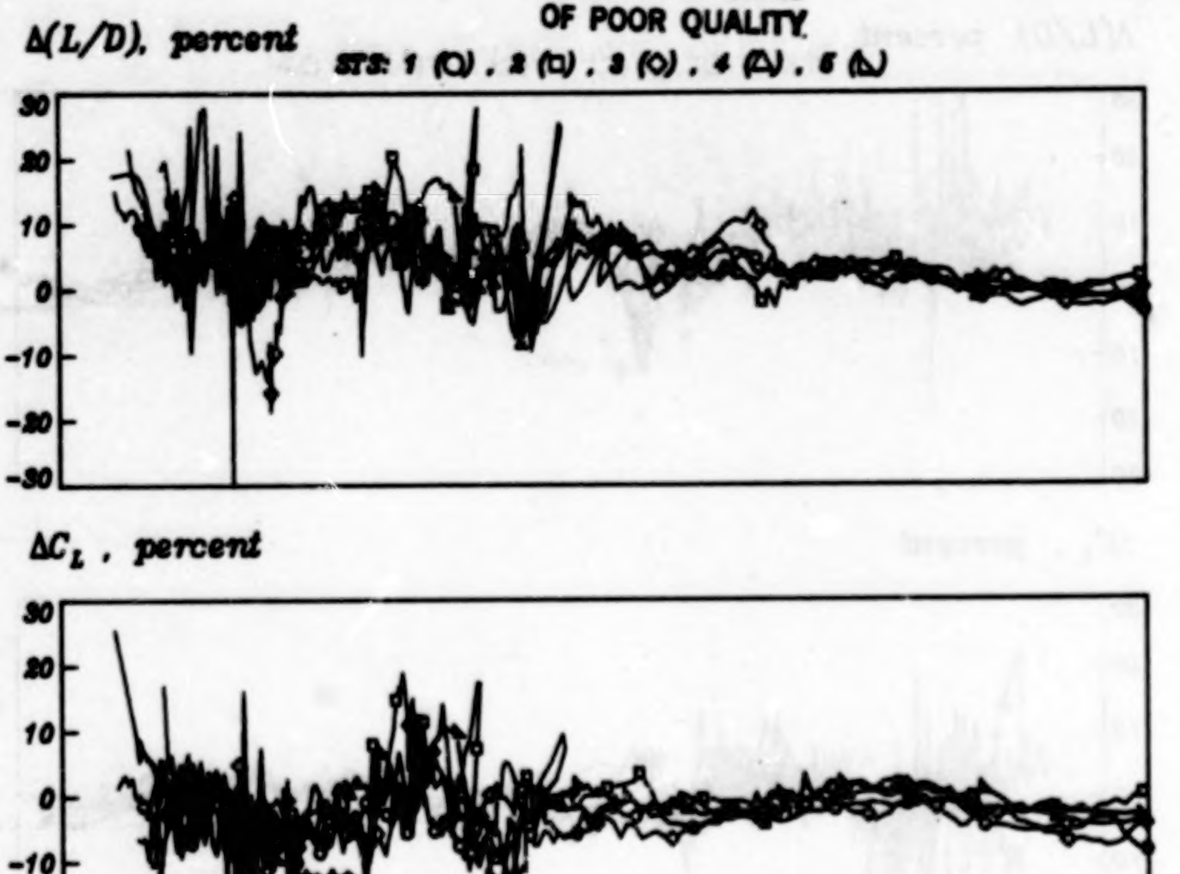

Figure 14.- Flight/data base comparisons for LaRC AEROBETs.

ORIGINAL PAGE IS
OF POOR QUALITY

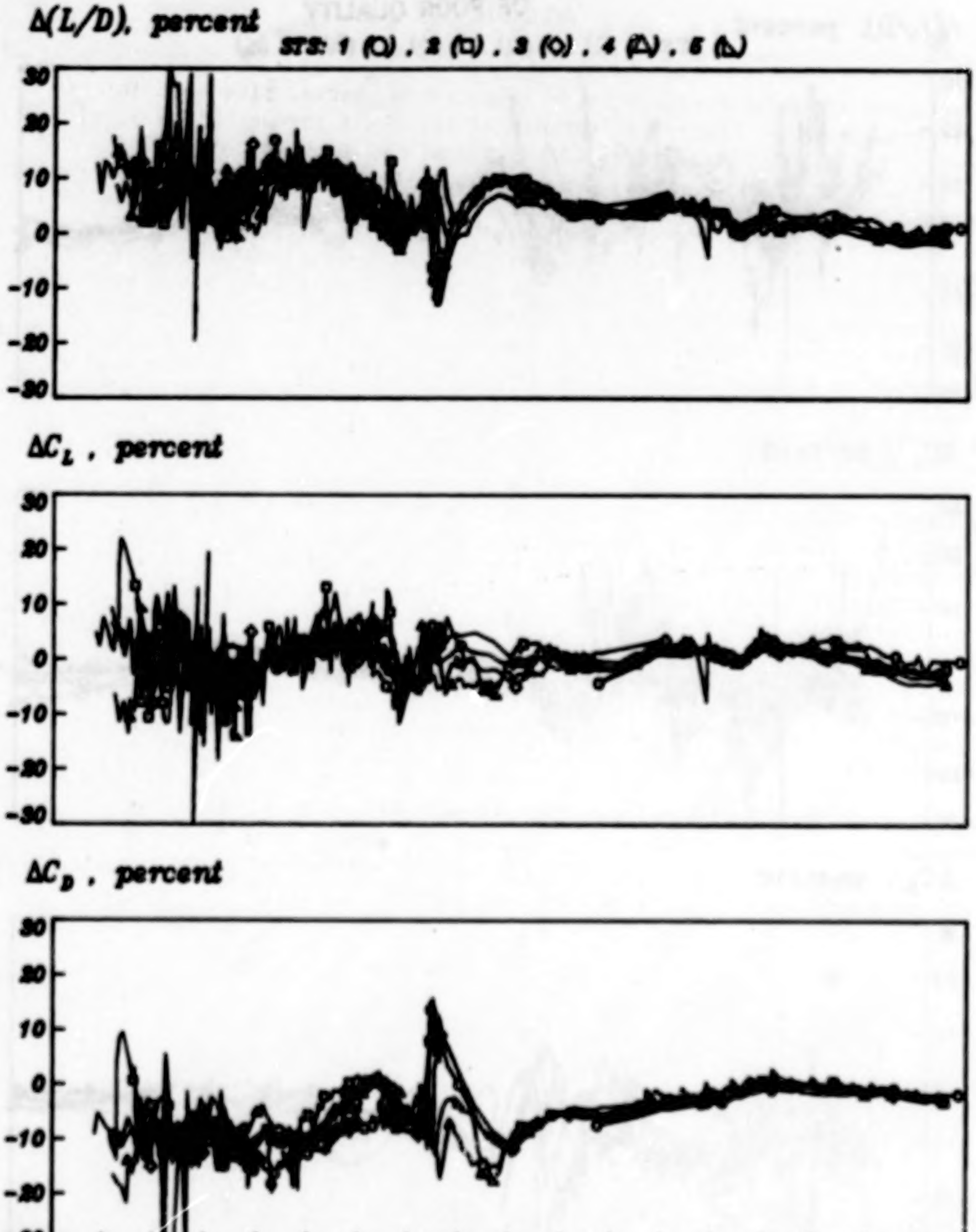

Figure 15.- Flight/data base comparisons for ADS AEROBETs.

APPENDIX

The attached Appendix presents twenty-five strip charts, five each for the Shuttle flights to date. Figures A1 through A5 are STS-1 through STS-5 results, respectively. The first five figures, A1(a) through A1(e), present LaRC (○) and ADS (□) flight conditions (α, Mach, and q) versus the BET altitude. These same data were presented as composite plots in figures 3 and 4 of the paper. Figures A2(a) through A2(e) show expanded plots of these very important differenses in α and q versus Mach number for the two sources. Longitudinal control surface deflections are presented as figures A3(a) through A3(e) for STS-1 through STS-5, respectively. Visible differences on these plots are a manifestation of the Mach number differences between the two sources. These deflection histories would be common plotted versus time and altitude since the BET altitude is utilized with both air data sources. Figures A2(a) through A2(e) and A3(a) through A3(e) exemplify the reasons that each air data source can result in differences in both the flight extracted and predicted performance computations.

For completeness, lateral directional parameters are included as figures A4(a) through A4(e) for the five flights. Included thereon are plots of β, σ, aileron and rudder deflections (about the aerodynamic reference line). The β curve principally shows the differences in the sideslip from the two air data sources, though each is plotted versus the respective Mach number which will contribute somewhat to the difference signature. Roll, aileron and rudder differences are entirely a manifestation of the Mach number differences. These data can be utilized by investigators for other post-flight analyses. There is no predicted influence of these lateral parameters on the longitudinal performance discussed in this paper, nor do the results of this paper suggest that there should be.

Finally, the last five pages, A5(a) through A5(e), are the resultant flight/data base differences obtained for each flight utilizing both air data sources. These data were also presented in the paper as composite plots (see figures 14 and 15) and represent the major import of the analysis presented.

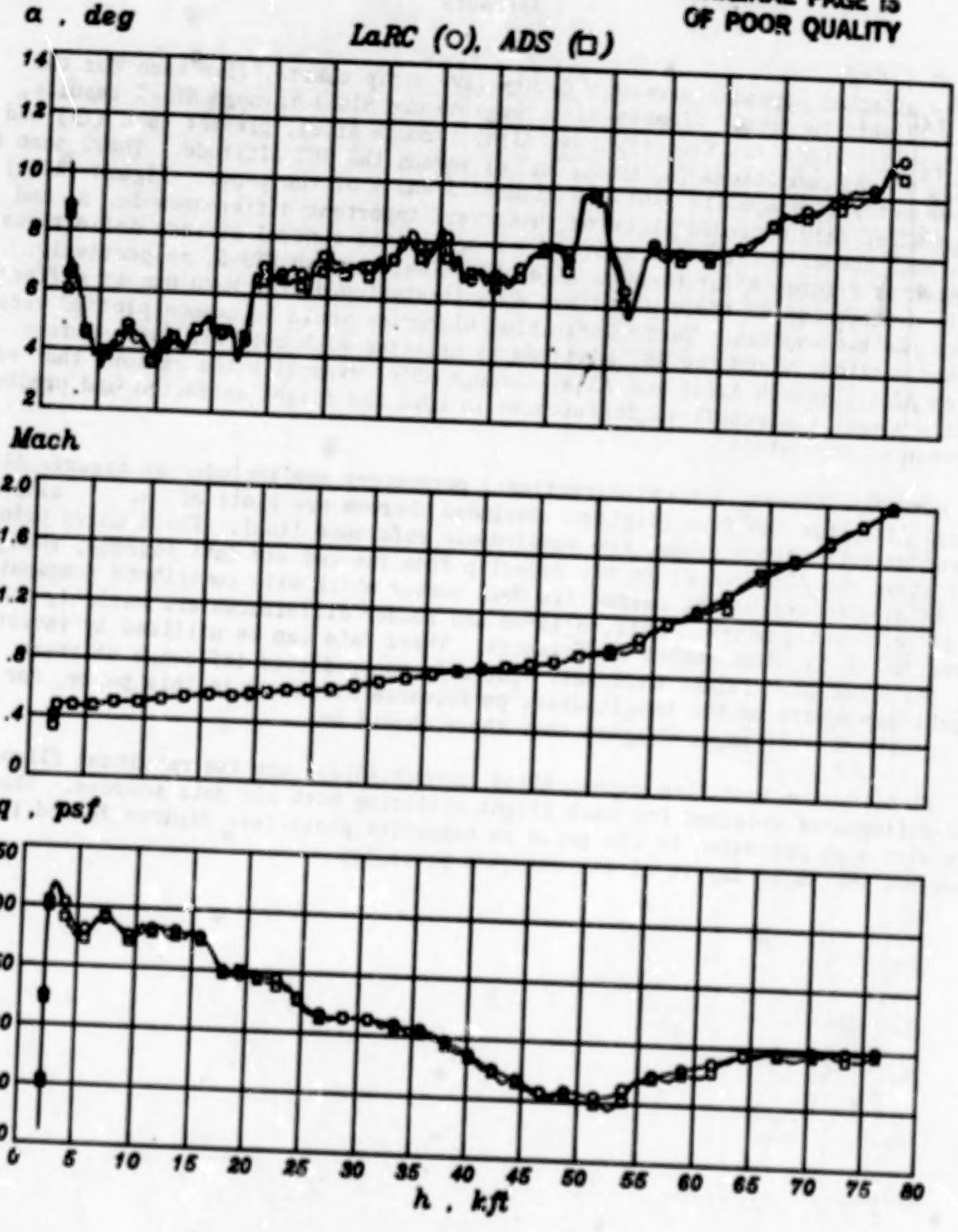

Figure A1(a).- STS-1 flight conditions.

**ORIGINAL PAGE IS
OF POOR QUALITY**

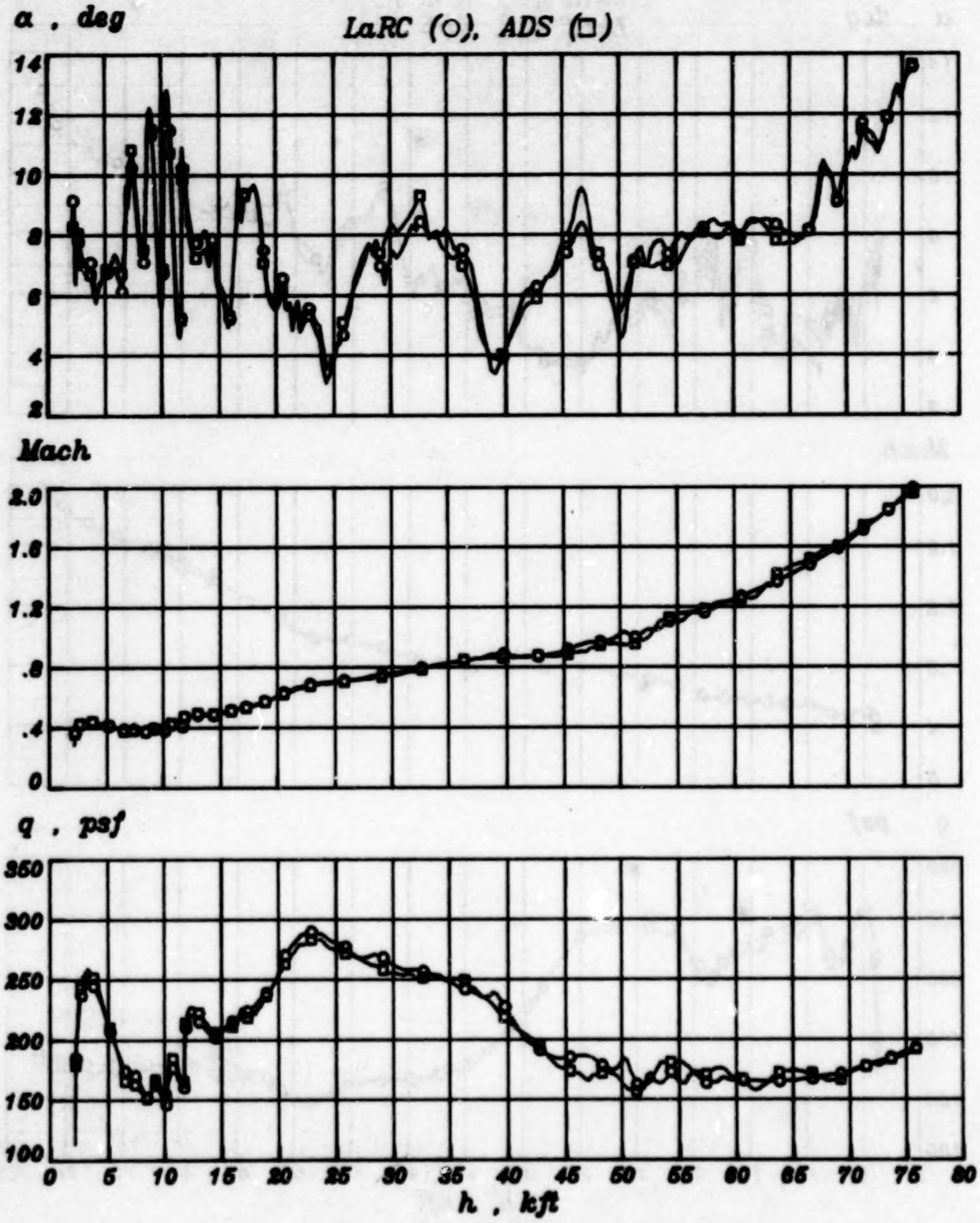

Figure A1(b).- STS-2 flight conditions.

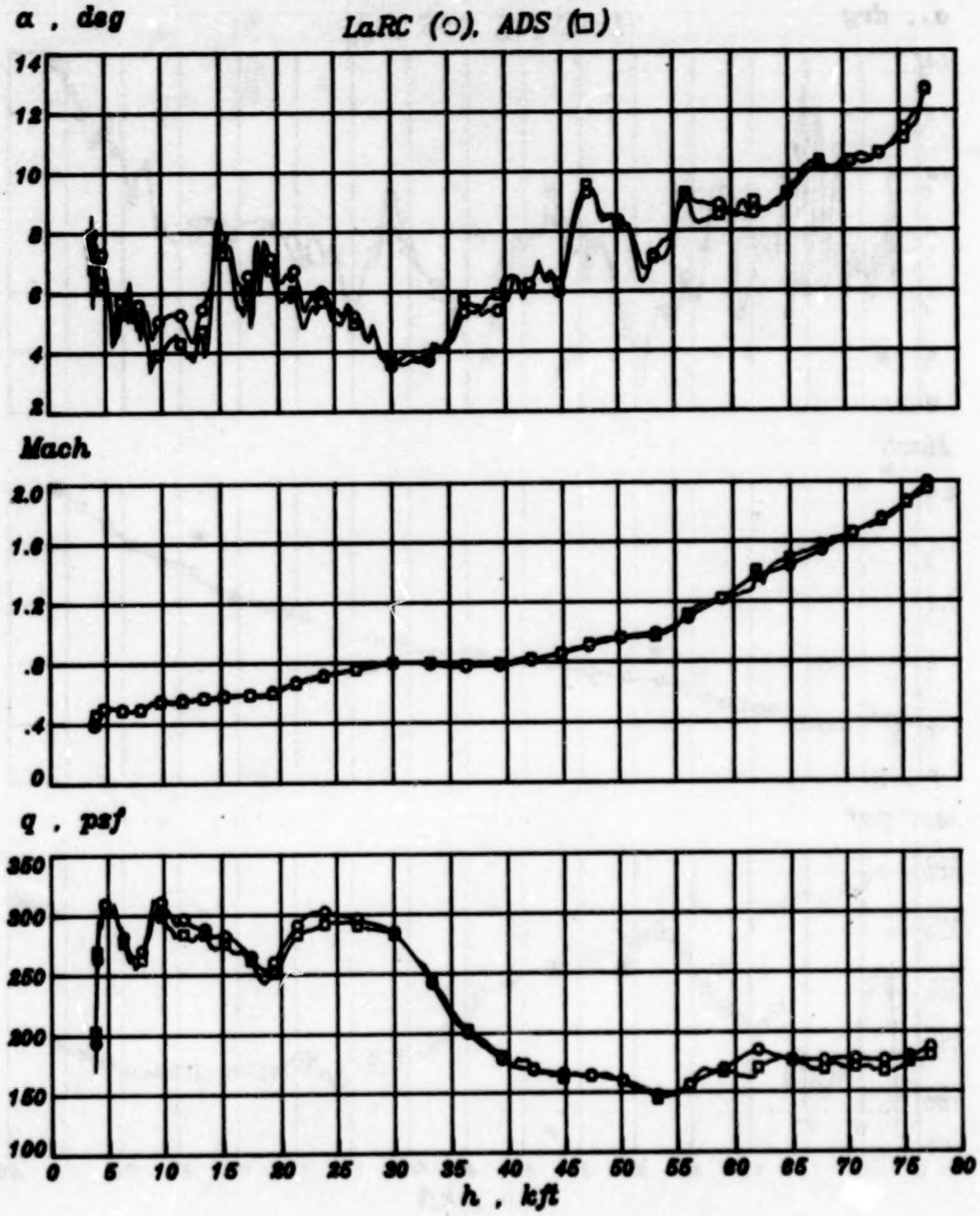

Figure A1(c).- STS-3 flight conditions.

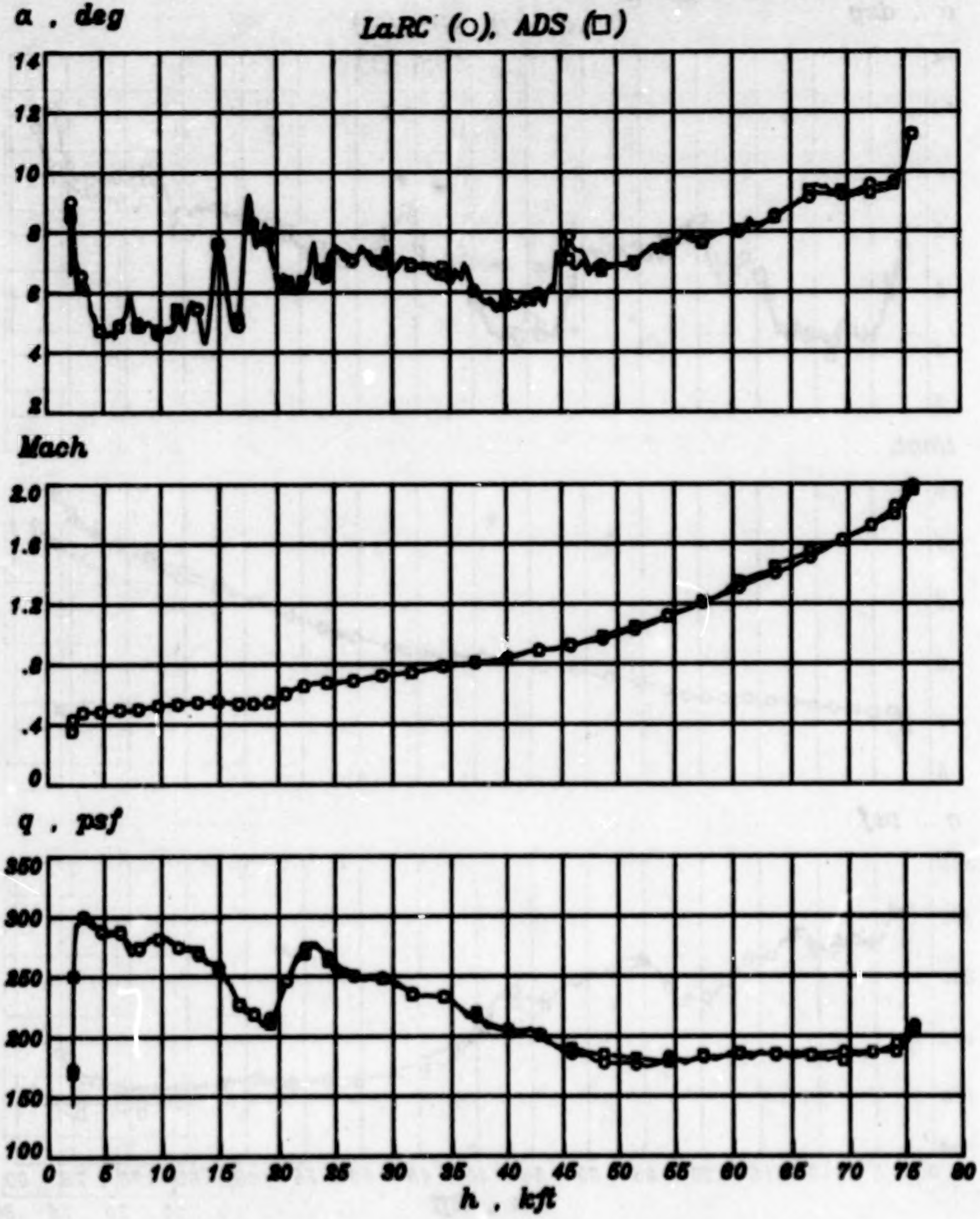

Figure A1(d).- STS-4 flight conditions.

ORIGINAL PAGE IS OF POOR QUALITY

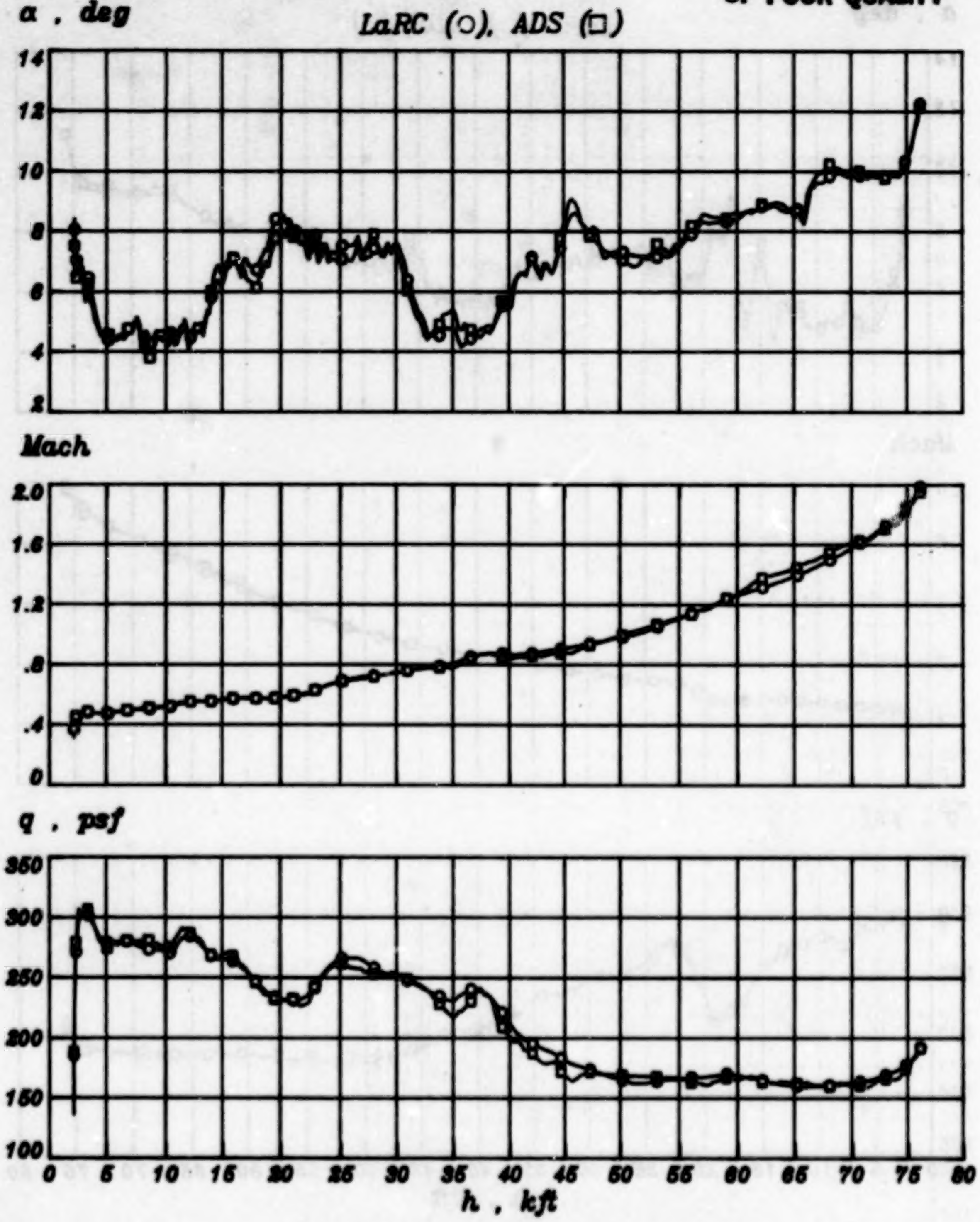

Figure A1(e).- STS-5 flight conditions.

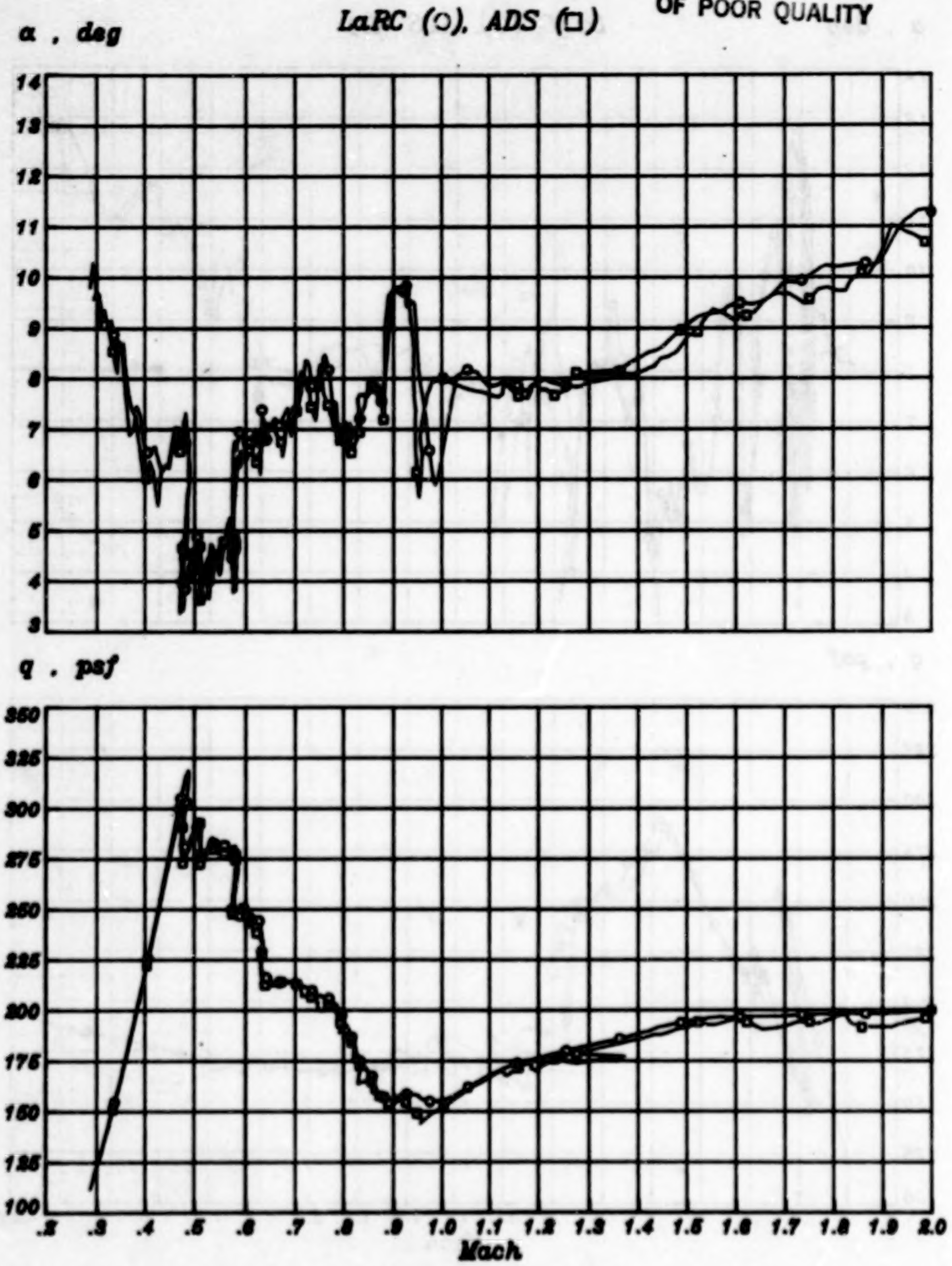

Figure A2(a).- STS-1 flight conditions versus Mach number.

ORIGINAL PAGE IS
OF POOR QUALITY

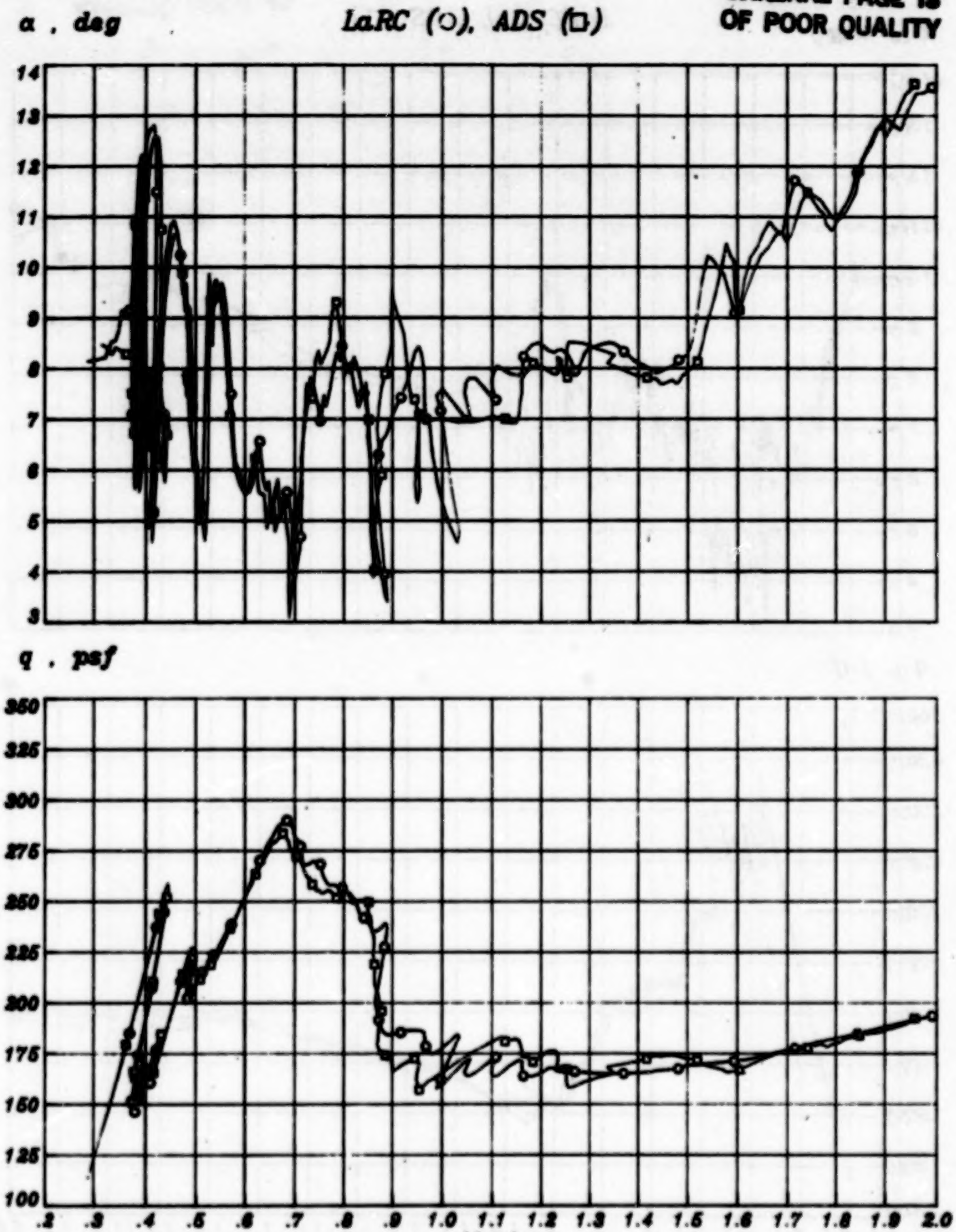

Figure A2(b).- STS-2 flight conditions versus Mach number.

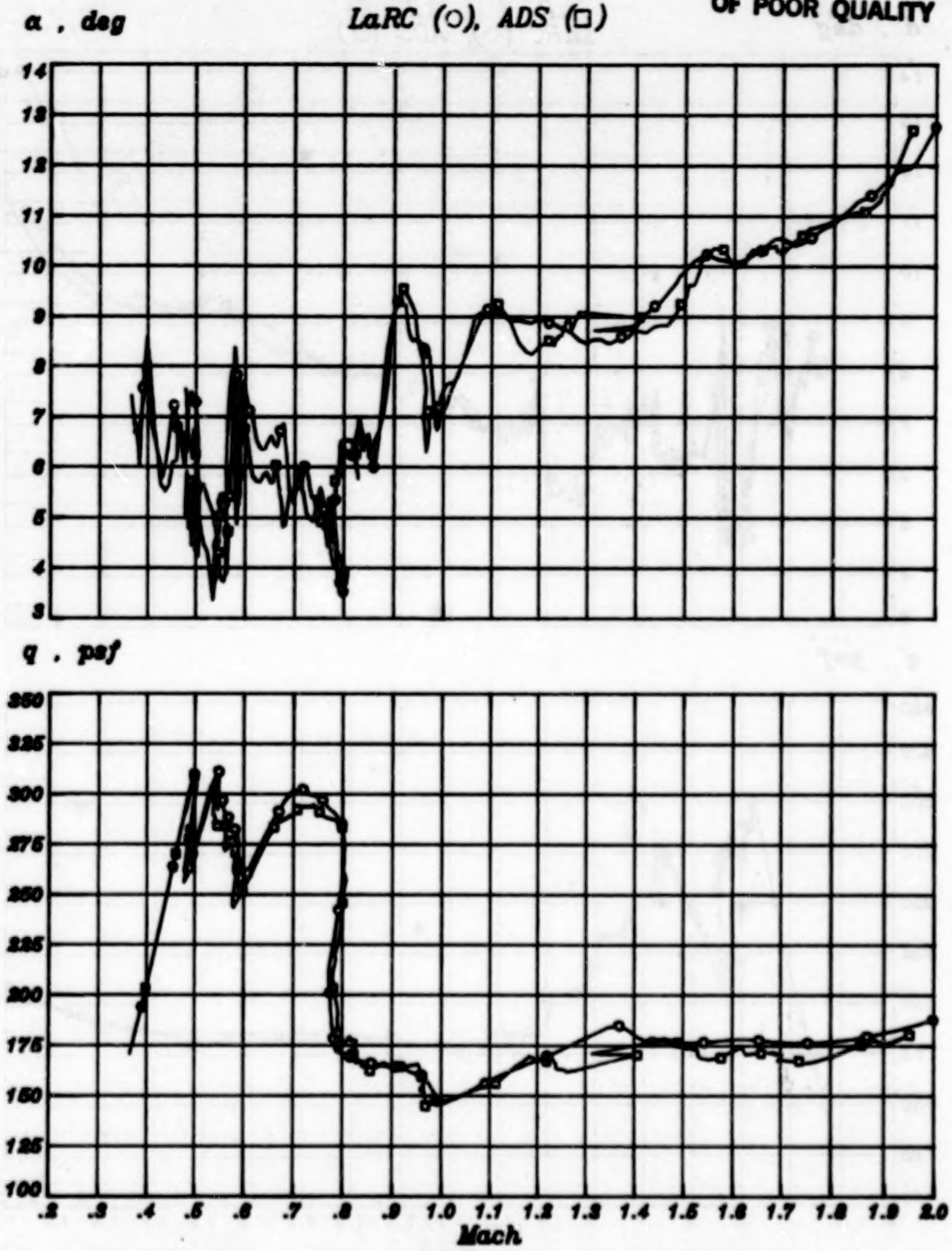

Figure A2(c).- STS-3 flight conditions versus Mach number.

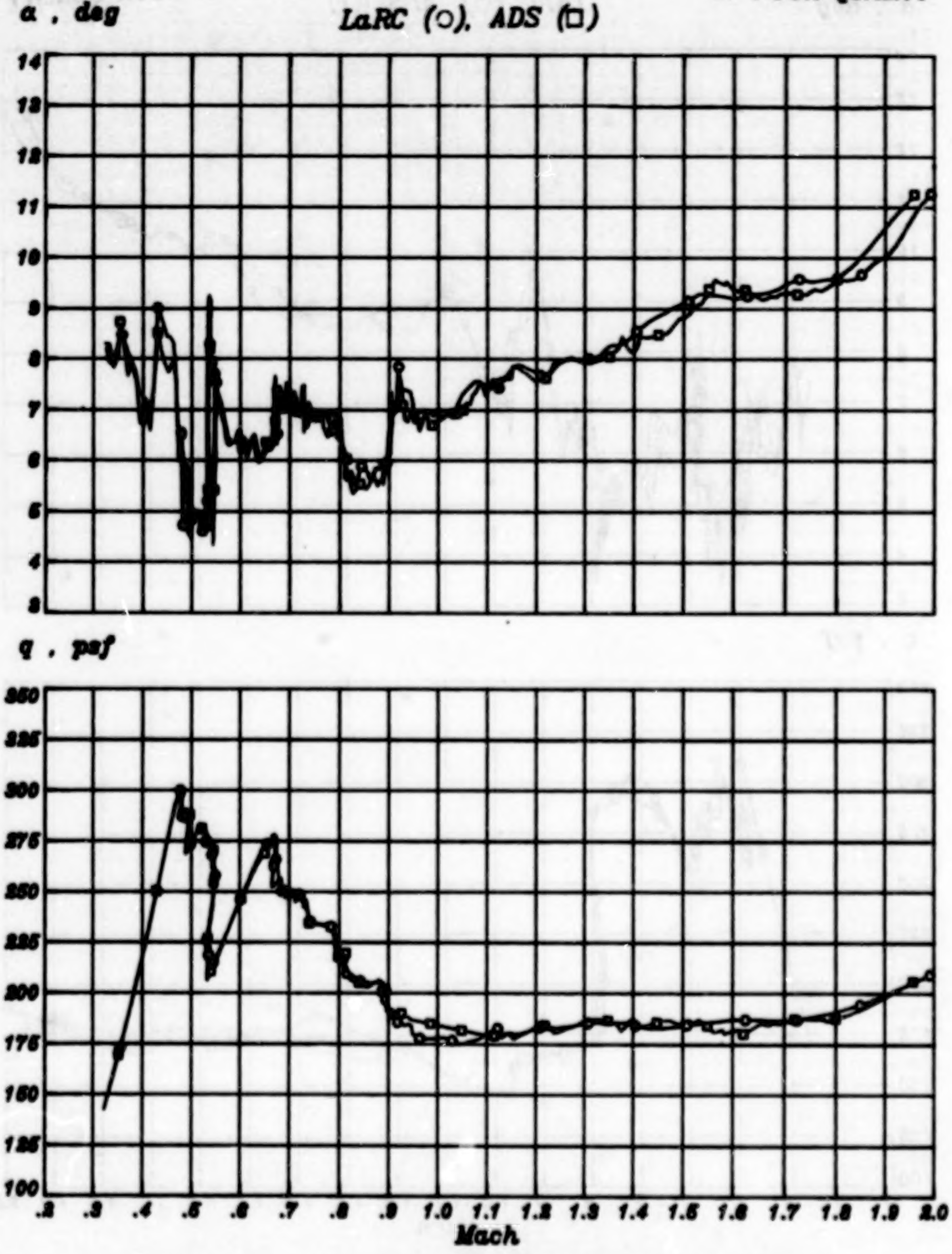

Figure A2(d).- STS-4 flight conditions versus Mach number.

ORIGINAL PAGE IS OF POOR QUALITY

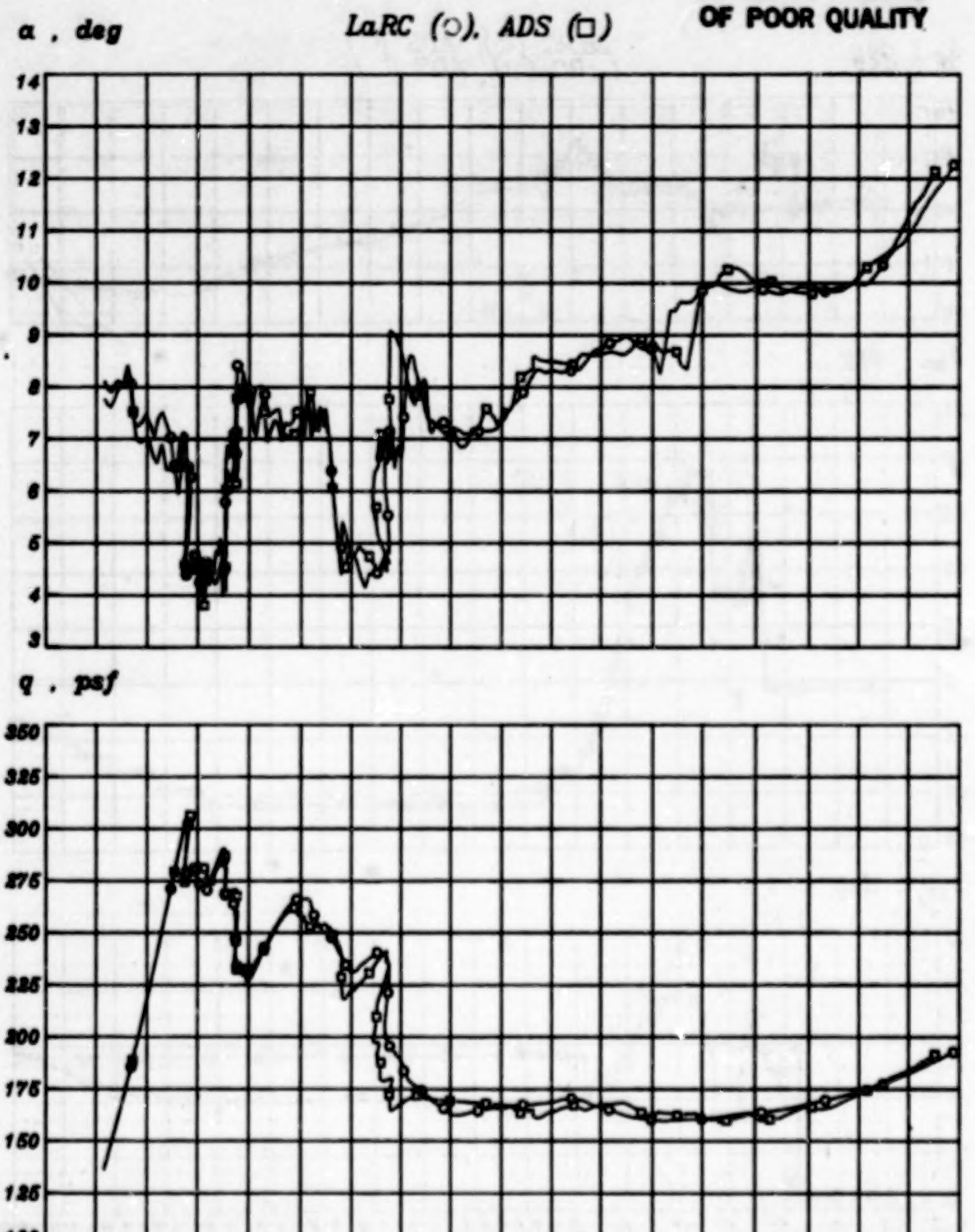

Figure A2(e).- STS-5 flight conditions versus Mach number.

ORIGINAL PAGE IS
OF POOR QUALITY

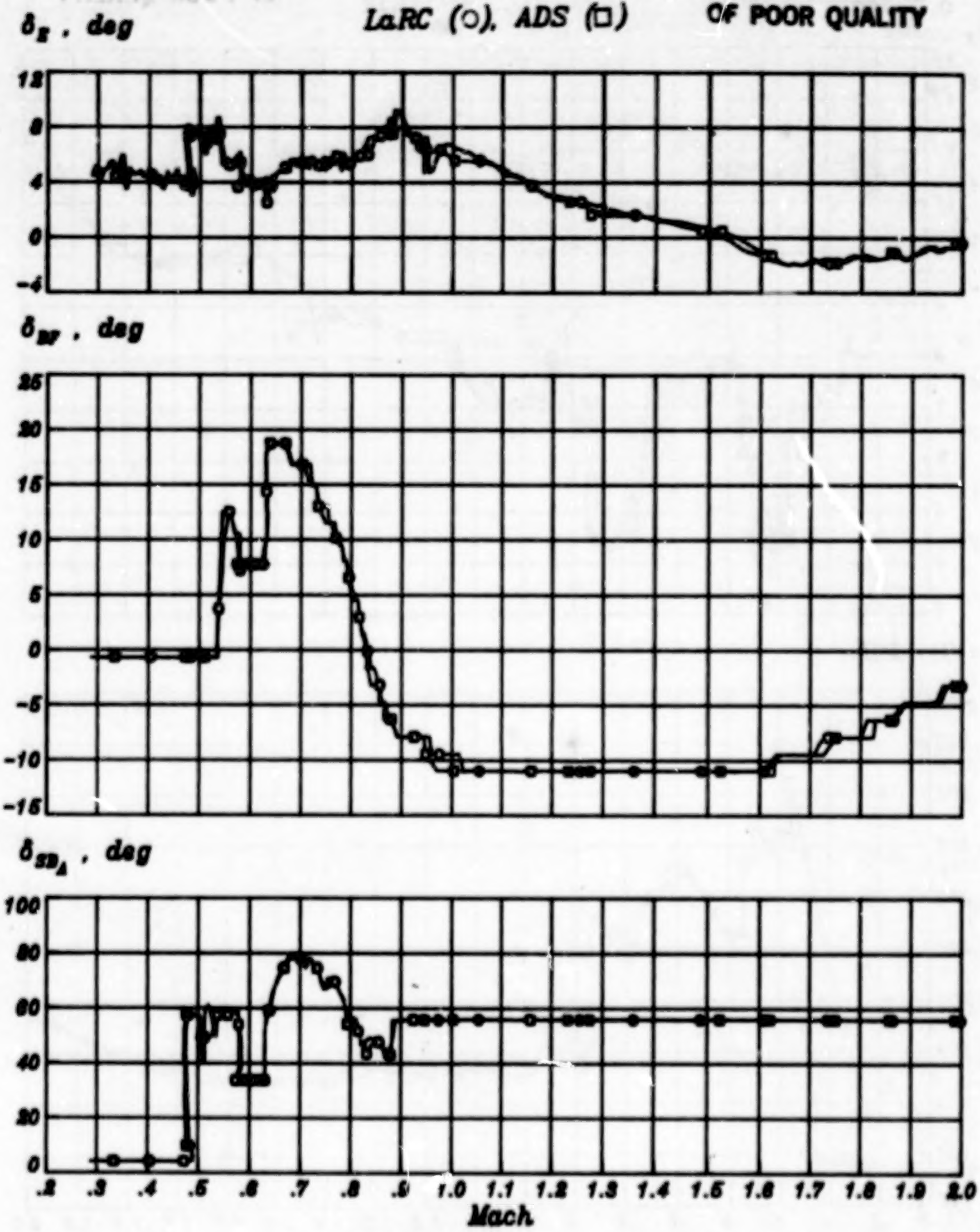

Figure A3(a).- STS-1 control surface deflections versus Mach number.

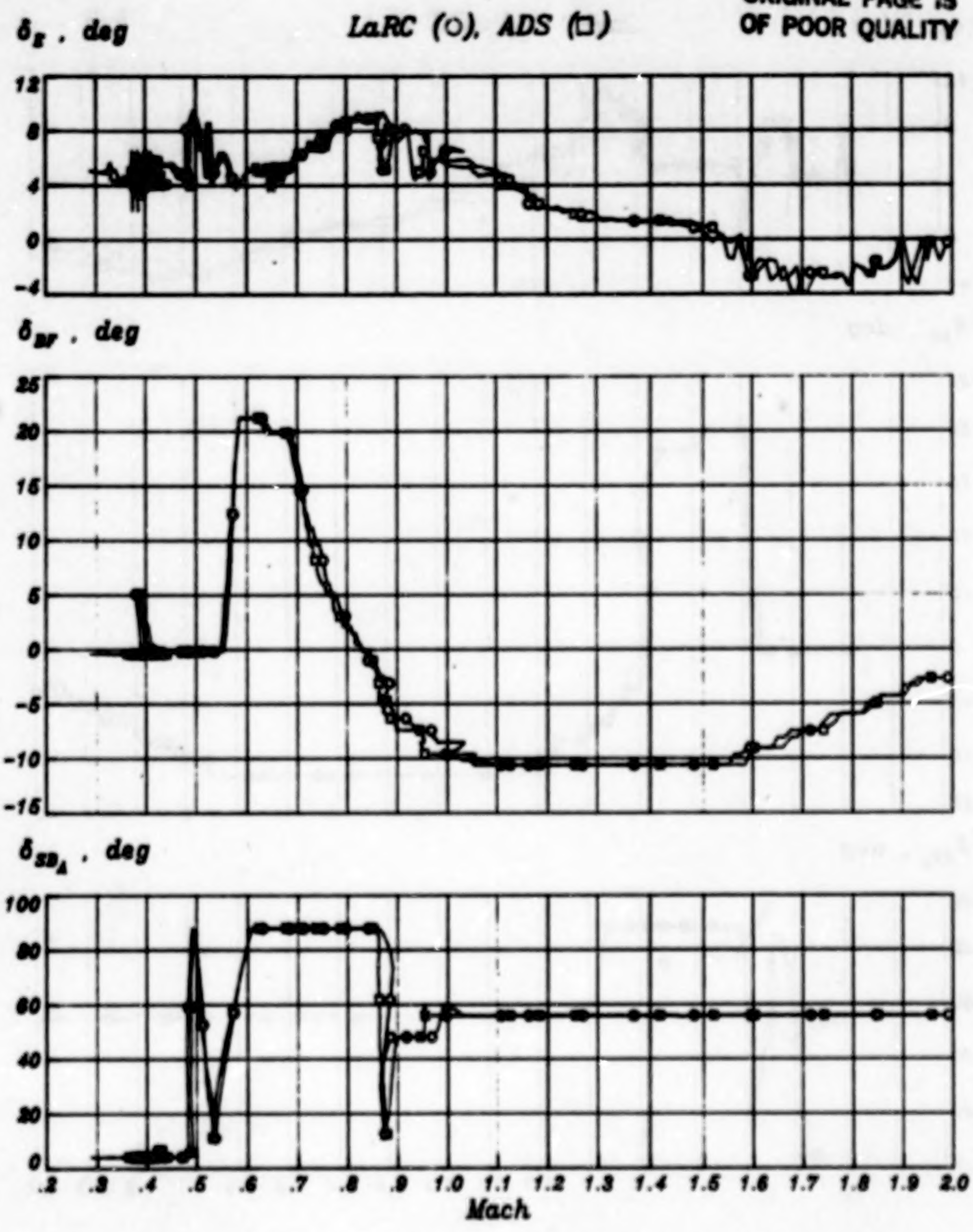

Figure A3(b).- STS-2 control surface deflections versus Mach number.

ORIGINAL PAGE IS
OF POOR QUALITY

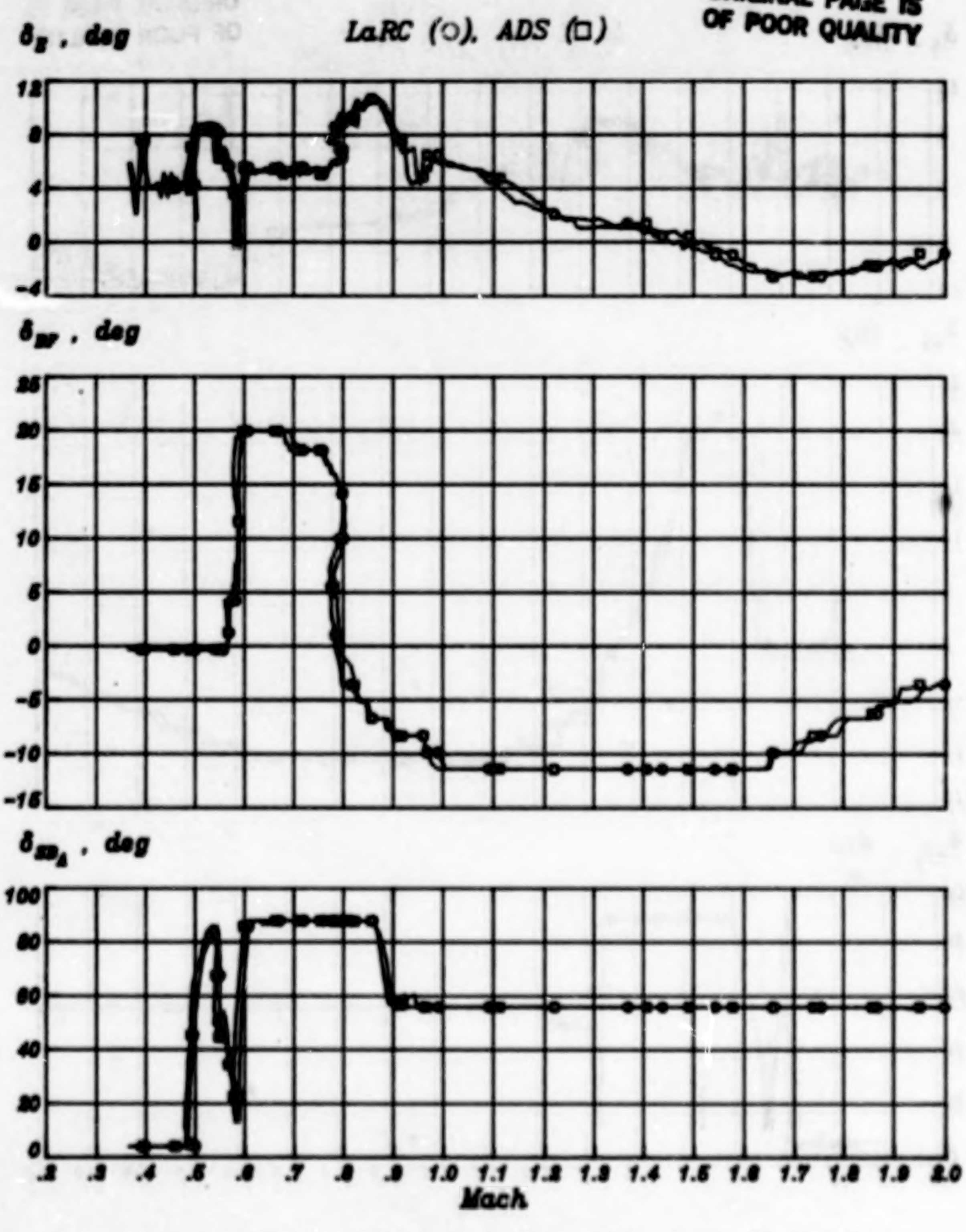

Figure A3(c).- STS-3 control surface deflections versus Mach number.

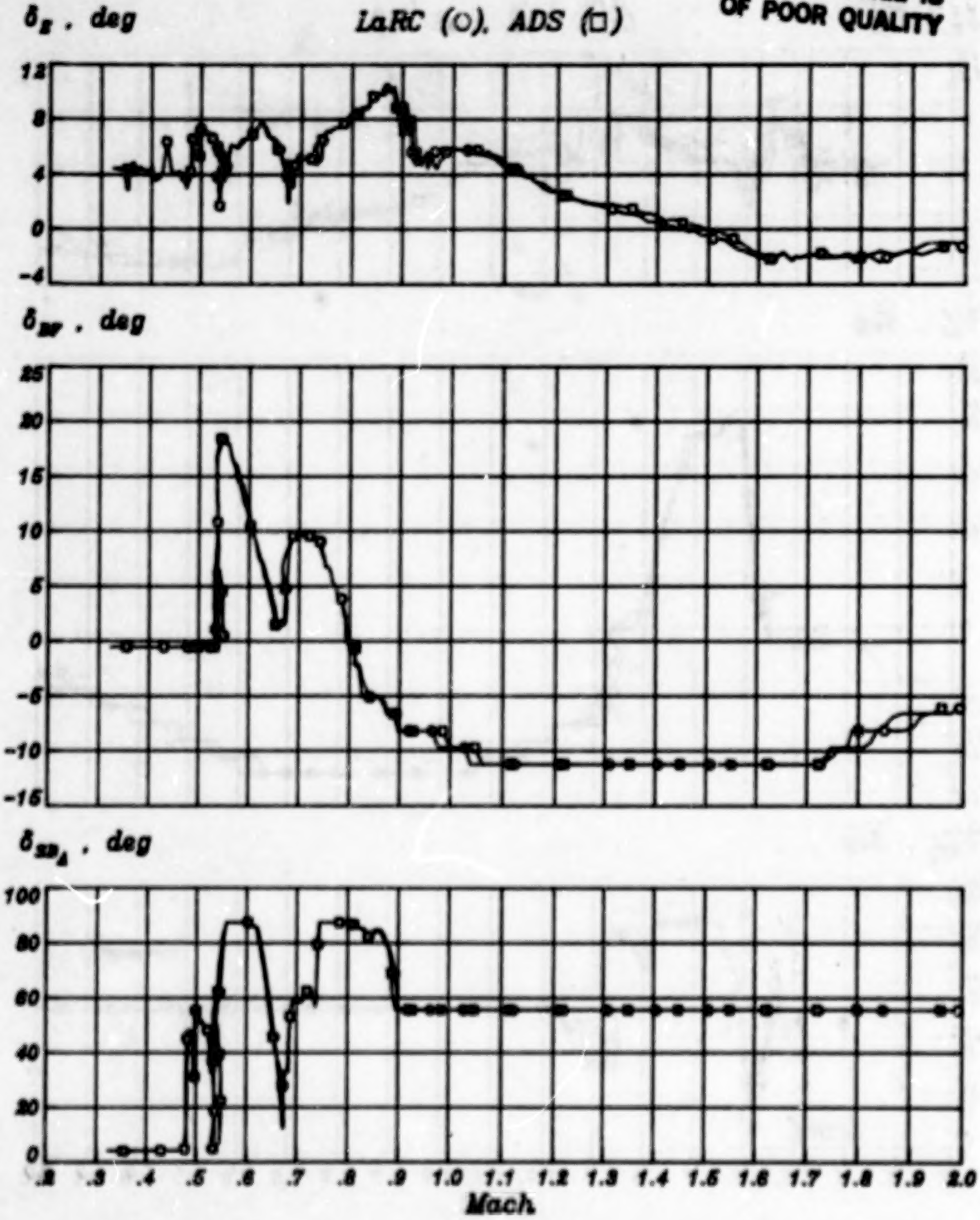

Figure A3(d).- STS-4 control surface deflections versus Mach number.

ORIGINAL PAGE IS
OF POOR QUALITY

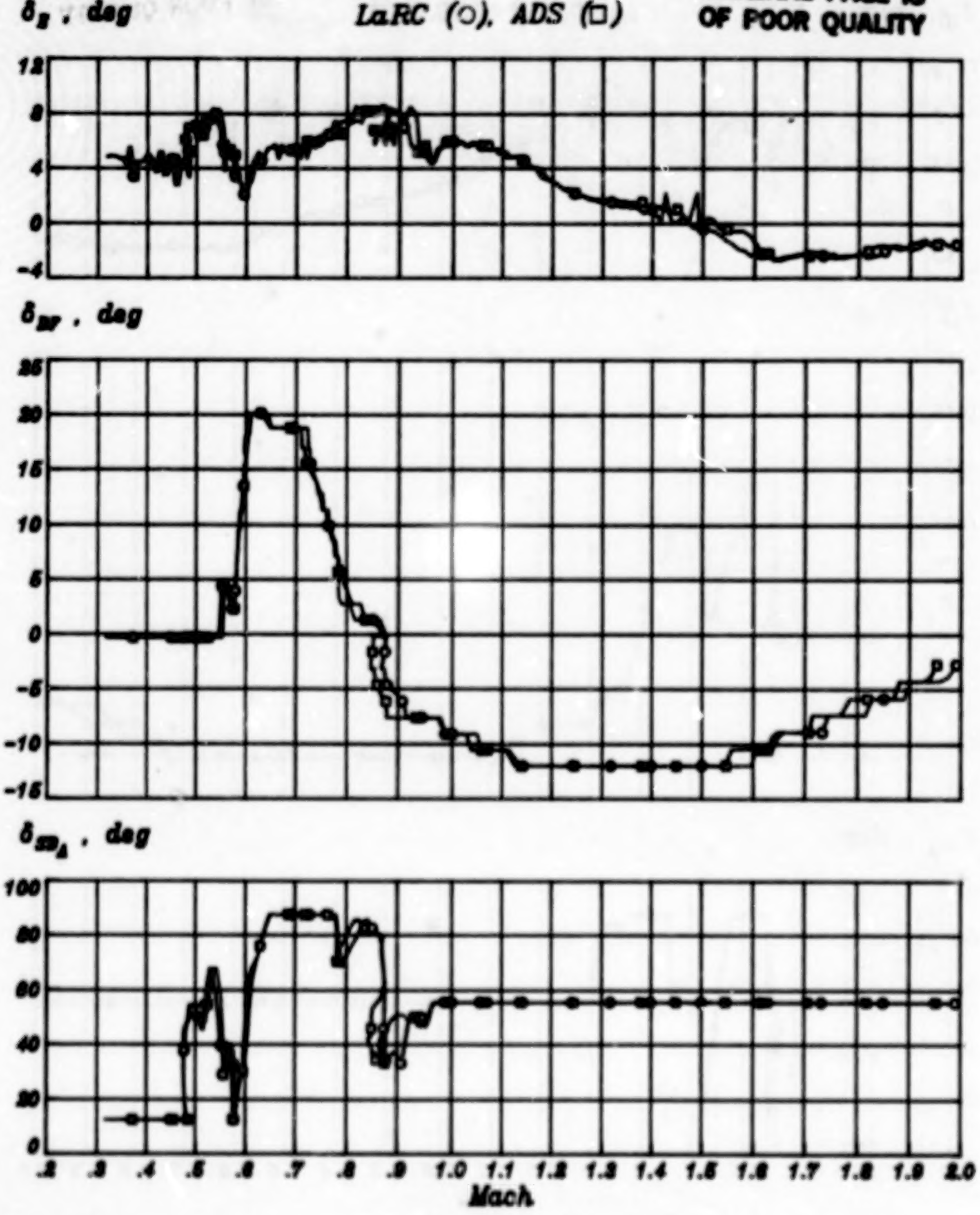

Figure A3(e).- STS-5 control surface deflections versus Mach number.

ORIGINAL PAGE IS
OF POOR QUALITY

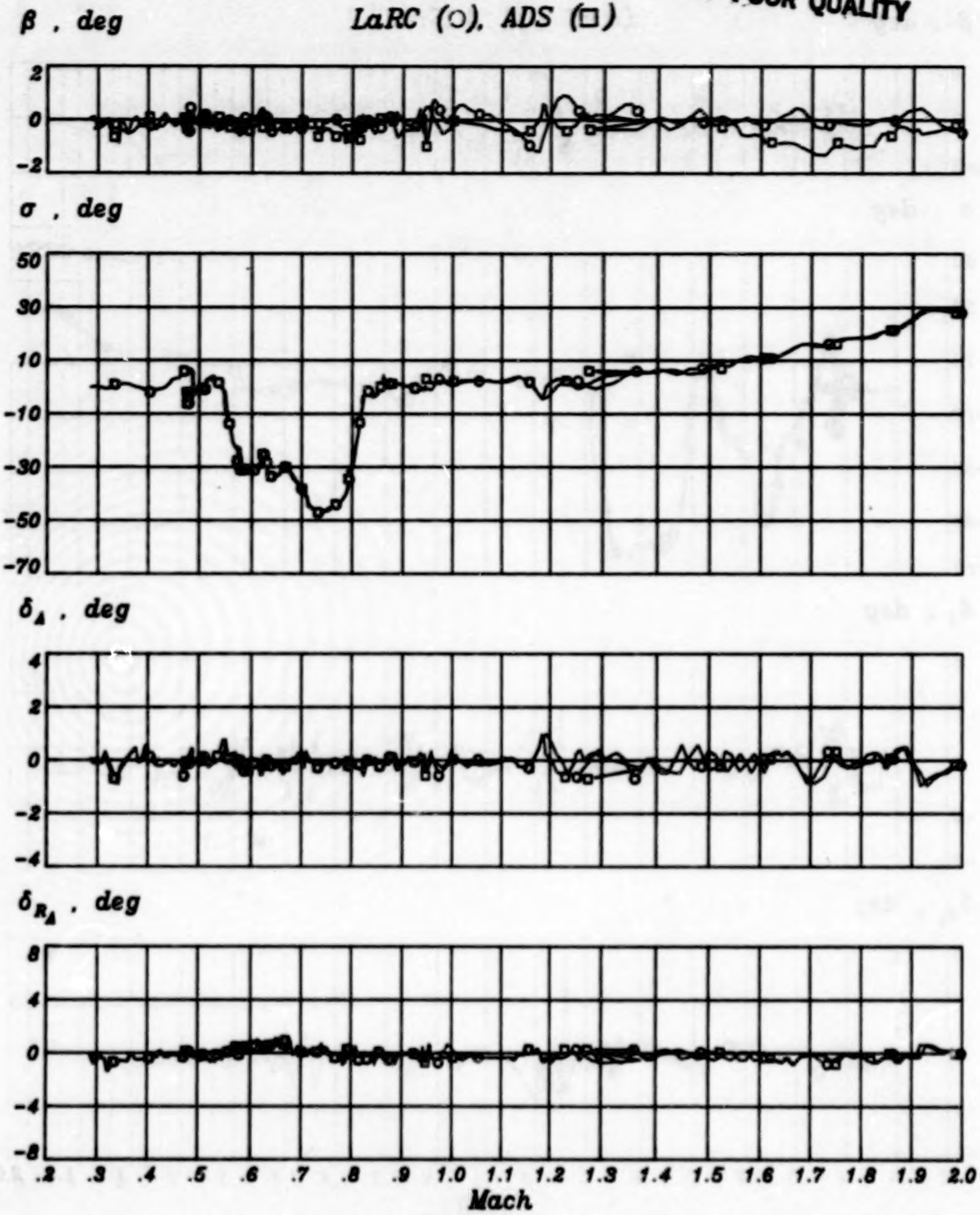

Figure A4(a).- STS-1 lateral directional parameters versus Mach number.

ORIGINAL PAGE IS
OF POOR QUALITY

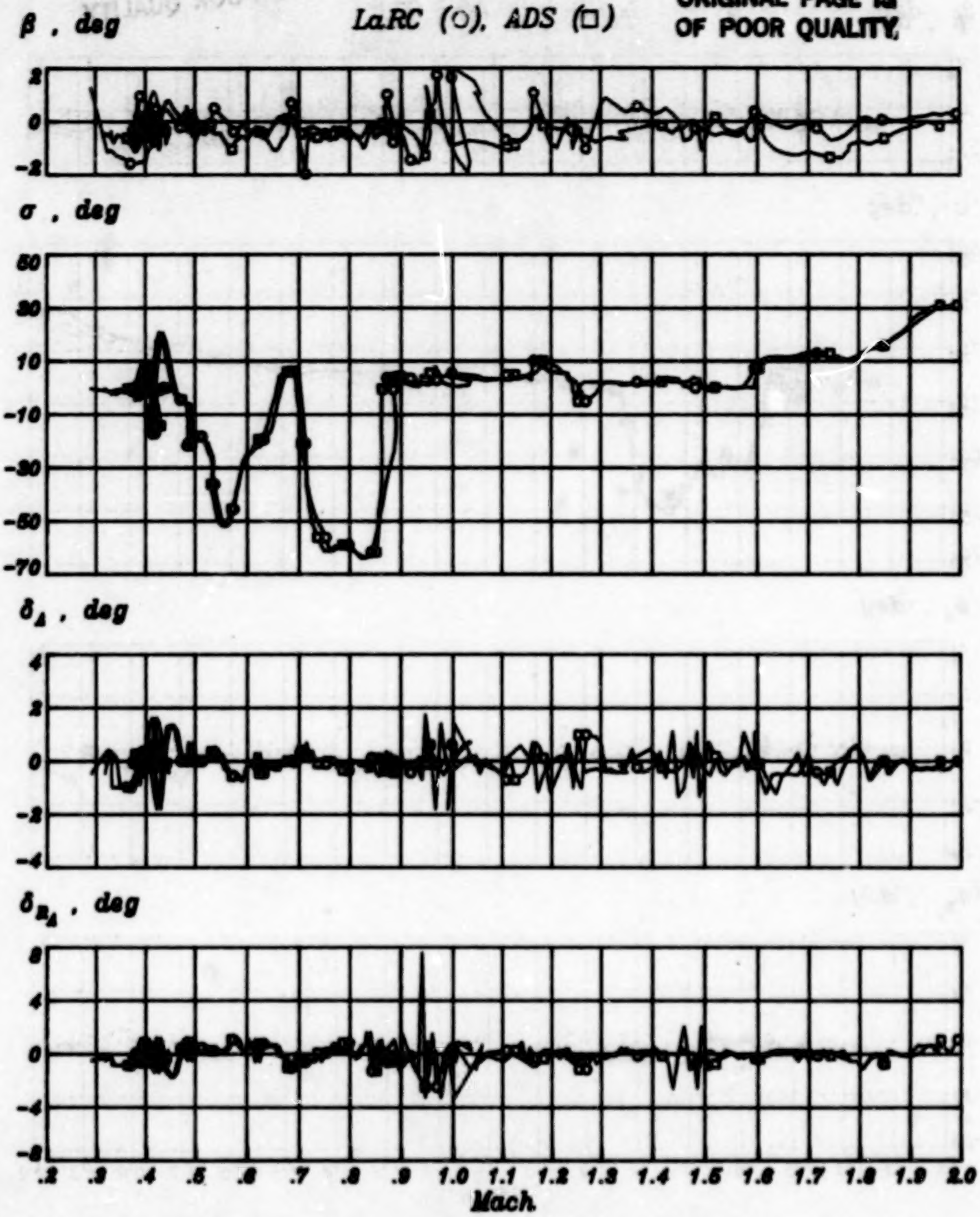

Figure A4(b).- STS-2 lateral directional parameters versus Mach number.

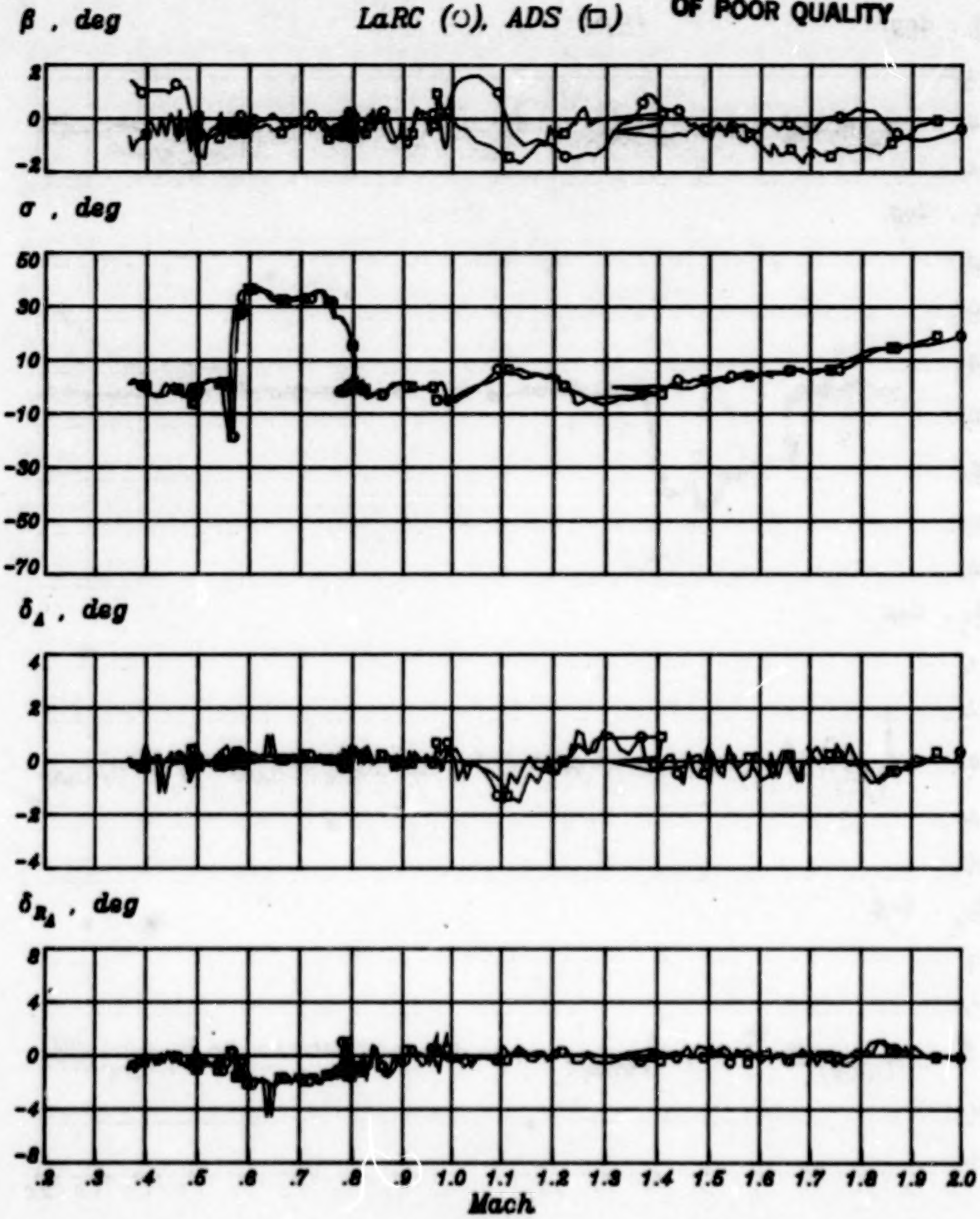

Figure A4(c).- STS-3 lateral directional parameters versus Mach number.

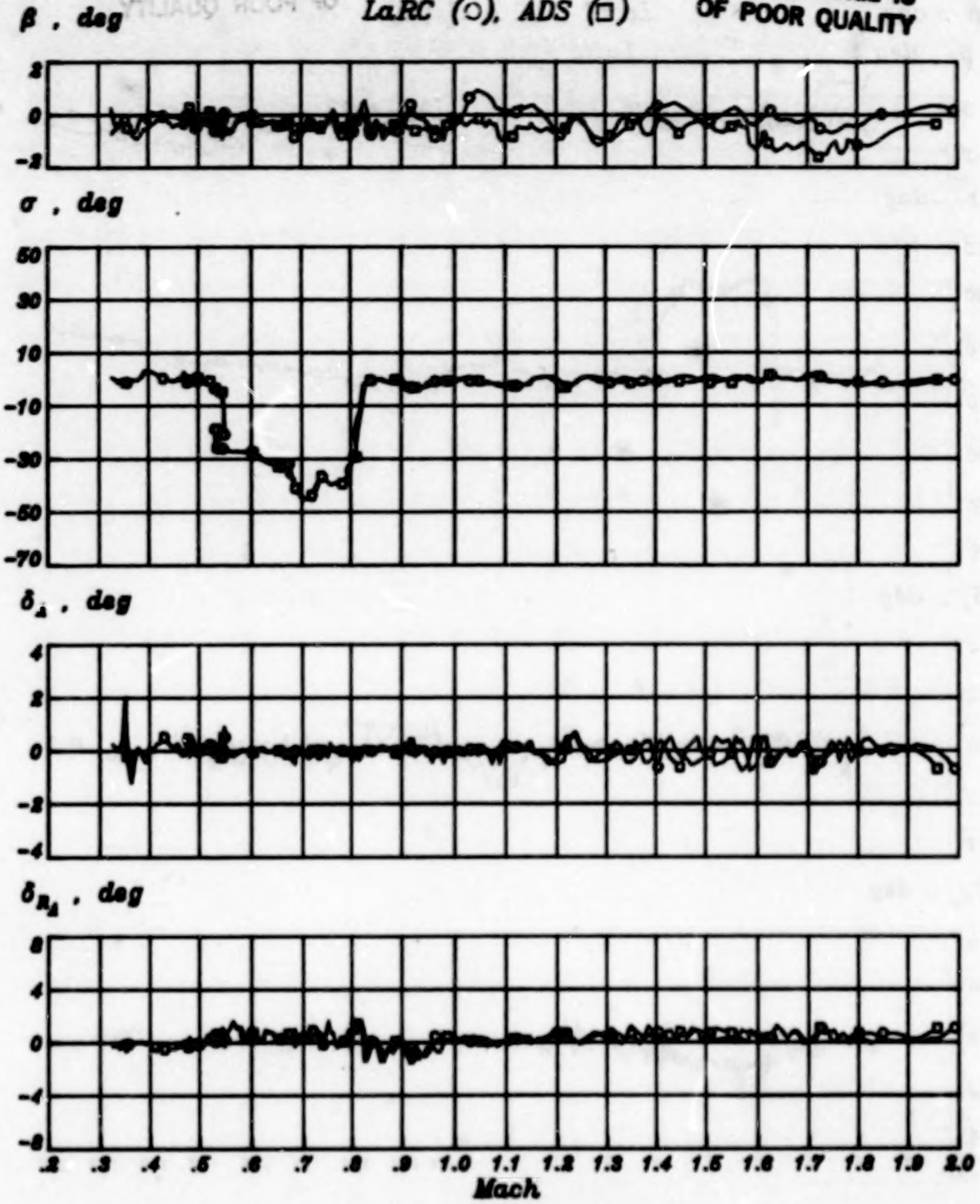

Figure A4(d).- STS-4 lateral directional parameters versus Mach number.

ORIGINAL PAGE IS
OF POOR QUALITY

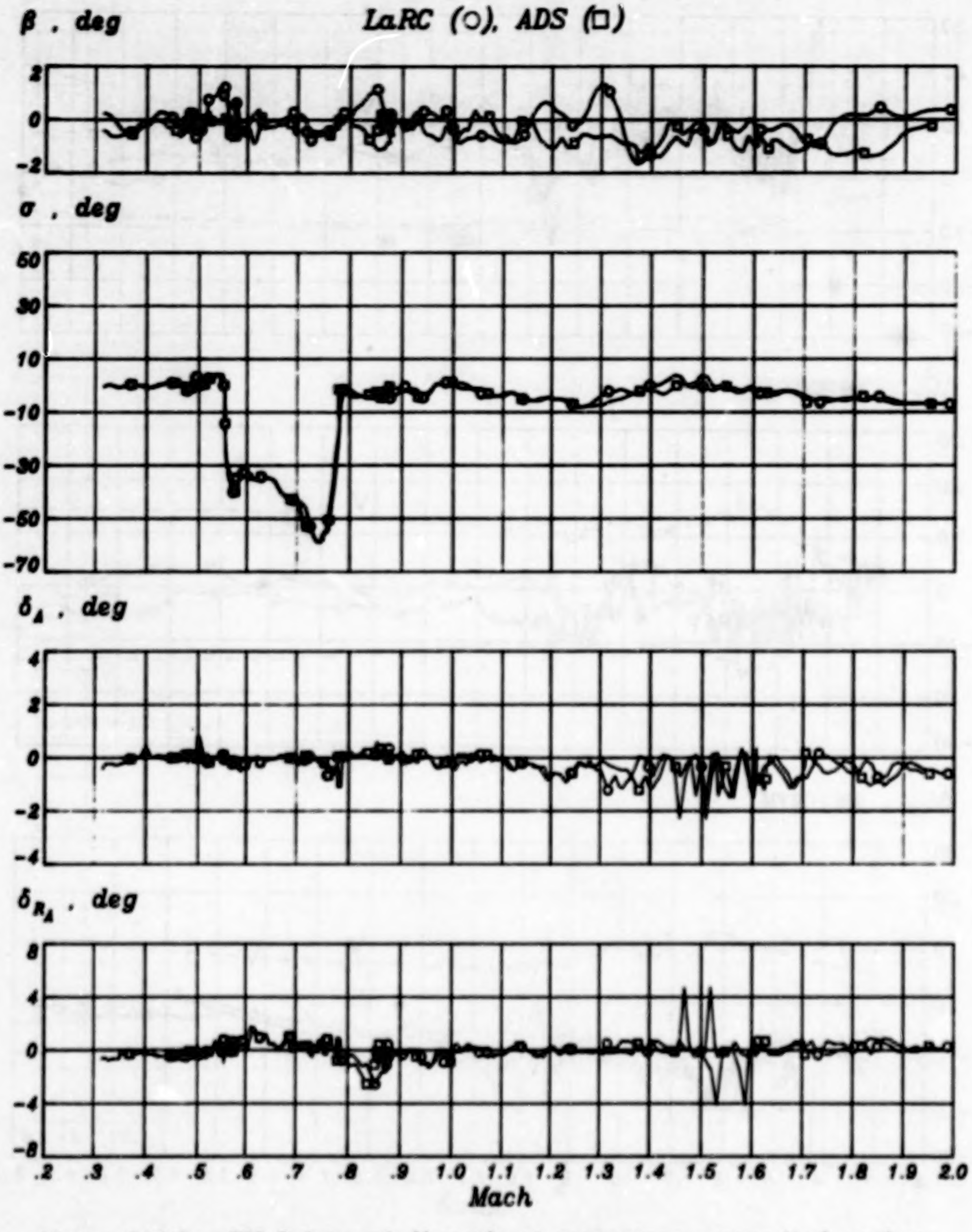

Figure A4(e).- STS-5 lateral directional parameters versus Mach number.

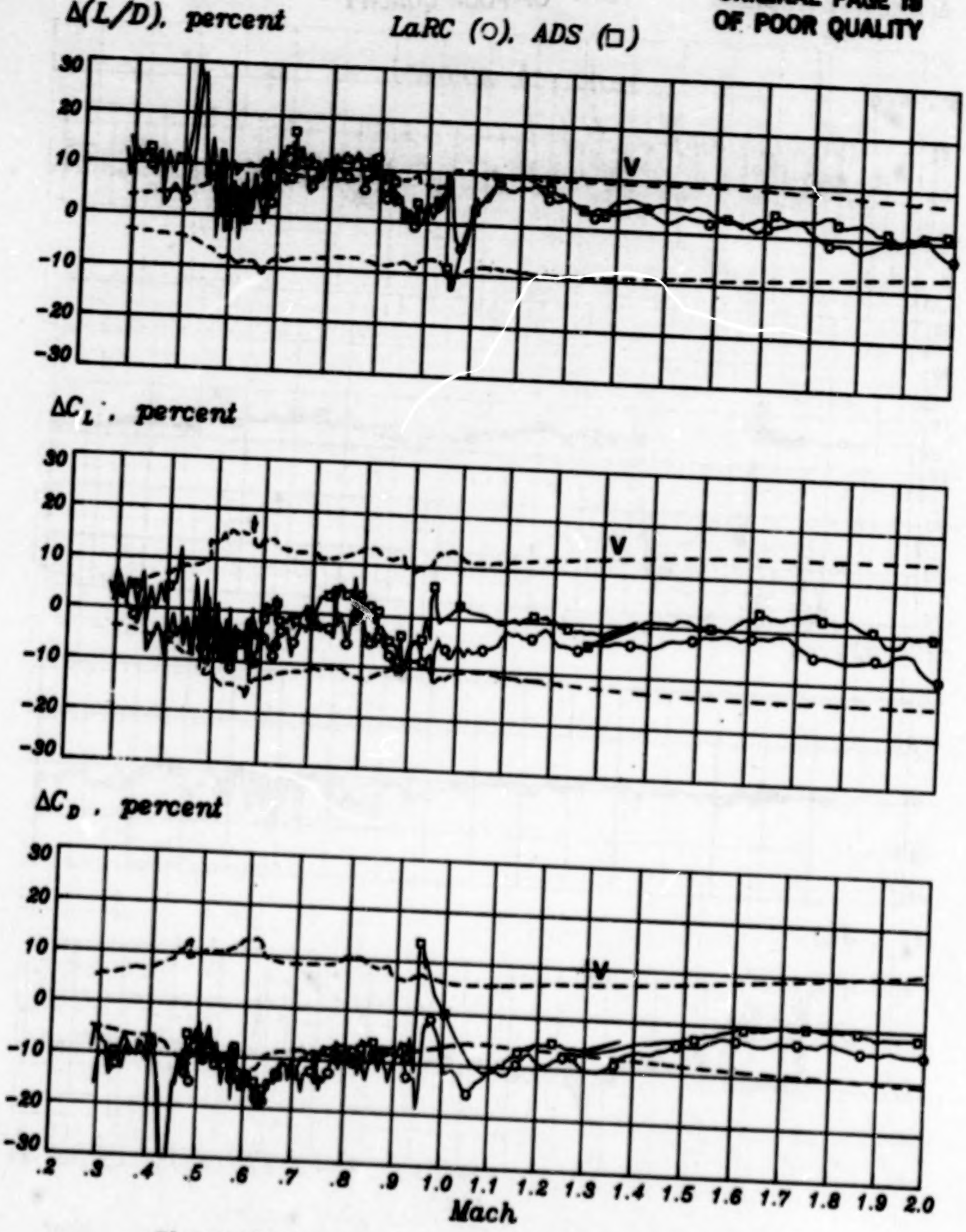

Figure A5(a).- STS-1 flight/data base comparisons.

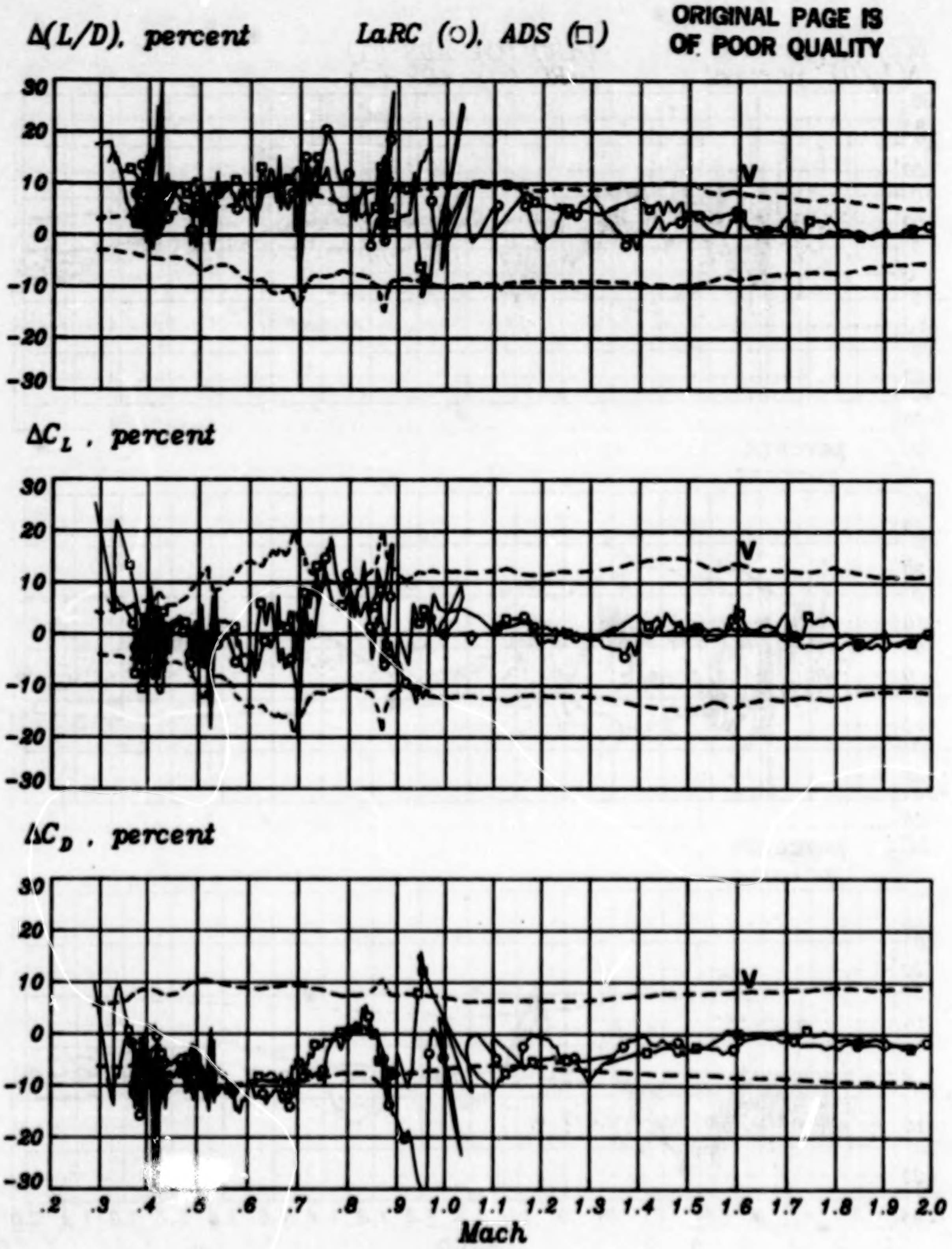

Figure A5(b).- STS-2 flight/data base comparisons.

ORIGINAL PAGE IS
OF POOR QUALITY

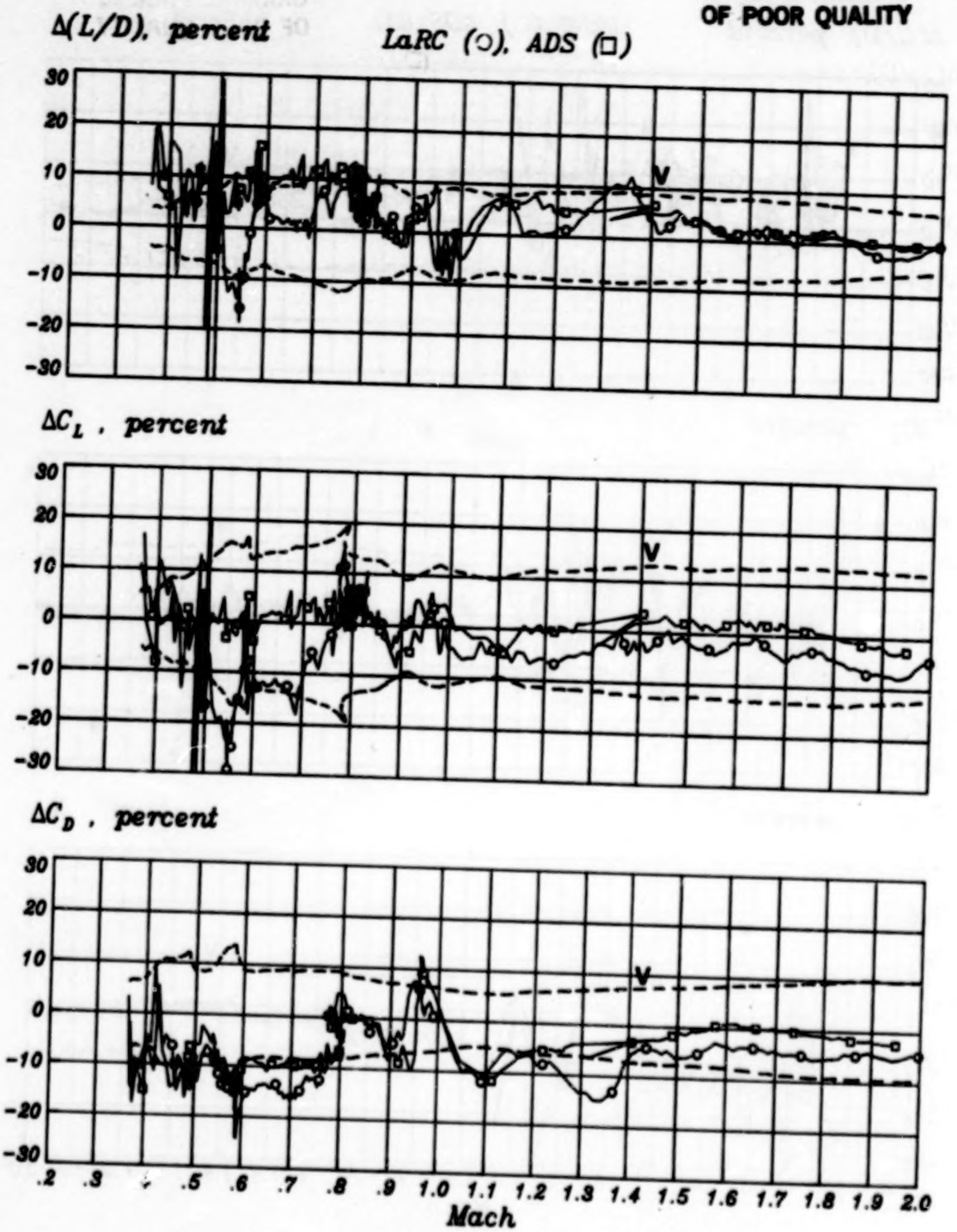

Figure A5(c).- STS-3 flight/data base comparisons.

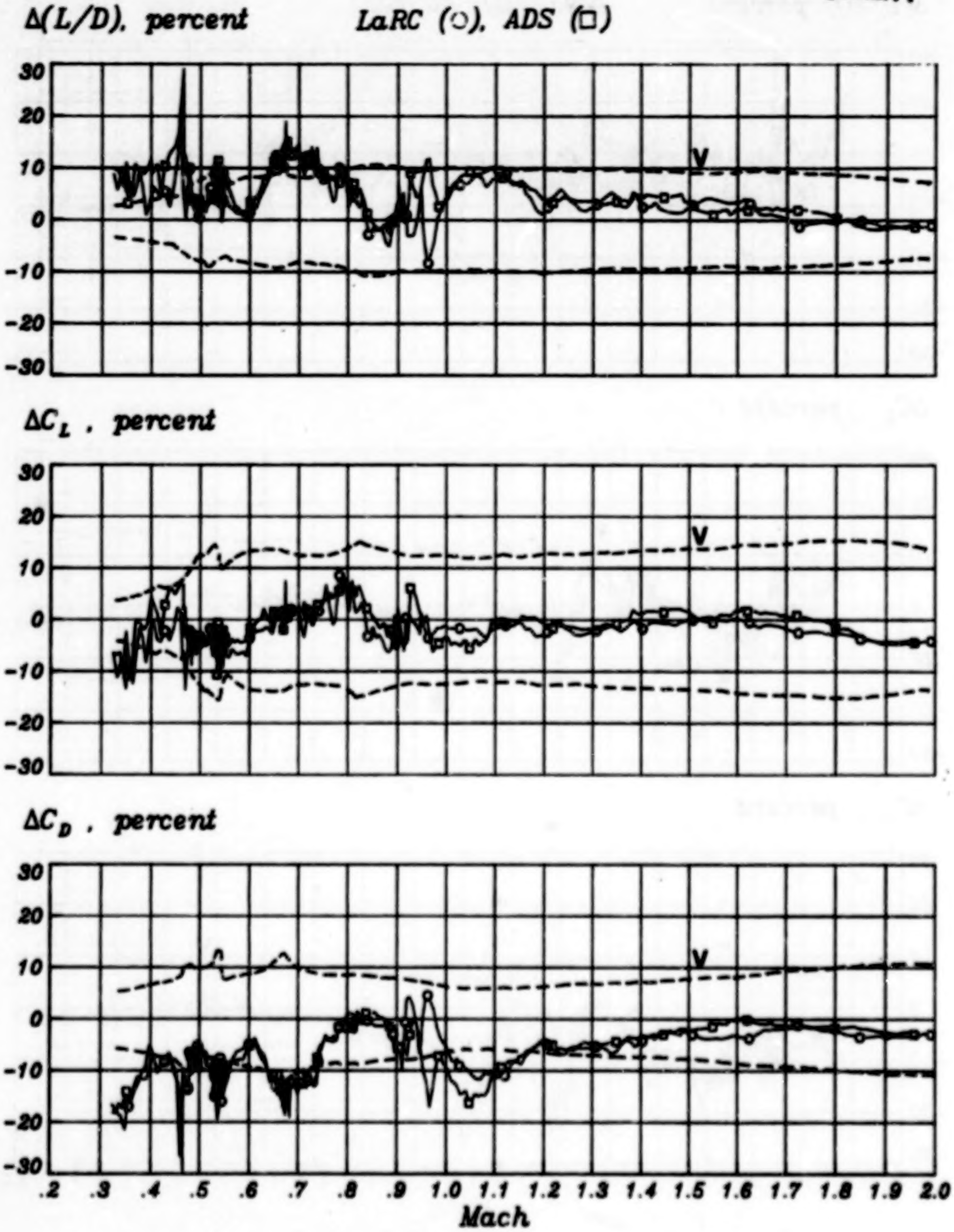

Figure A5(d).- STS-4 flight/data base comparisons.

ORIGINAL PAGE IS
OF POOR QUALITY

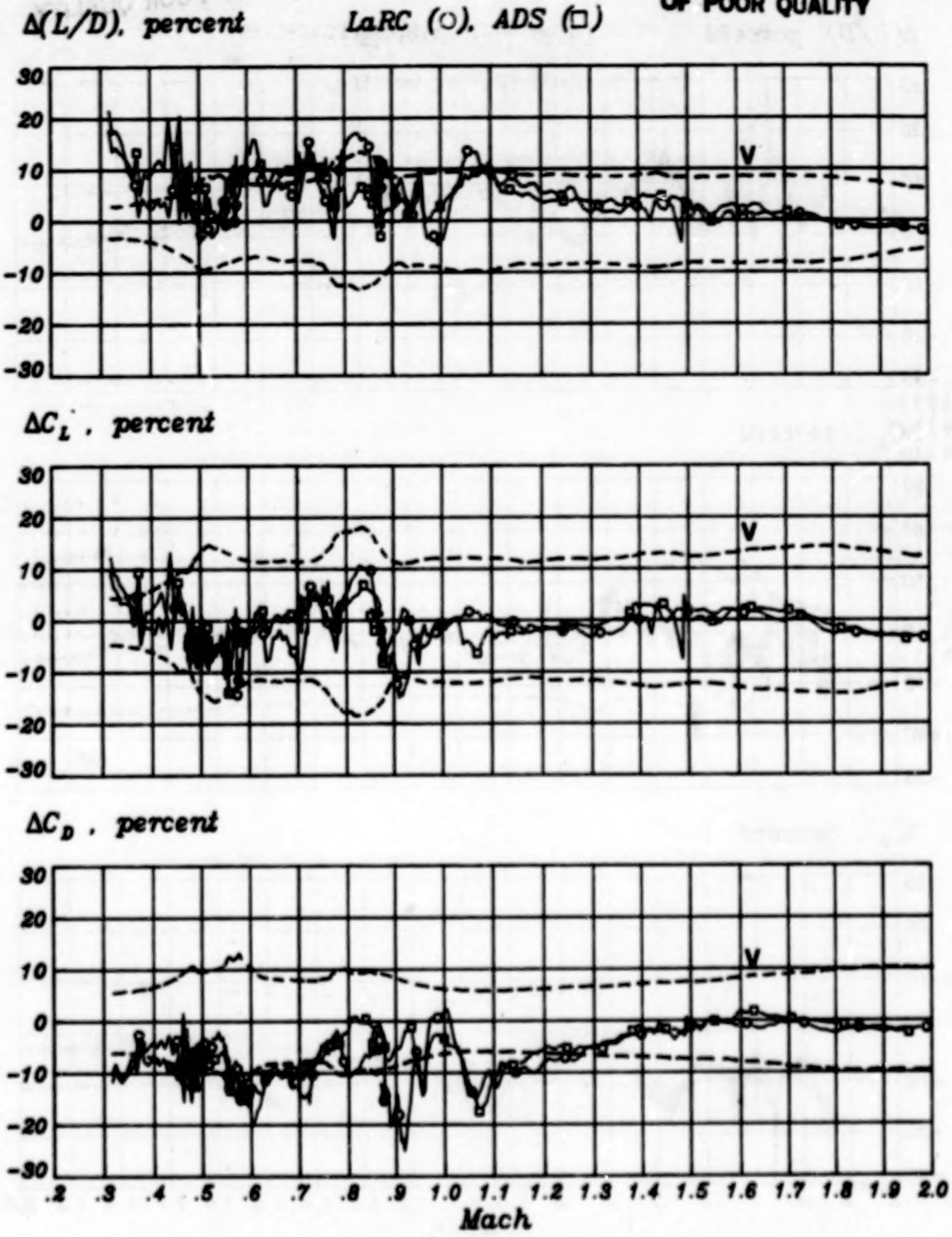

Figure A5(e).- STS-5 flight/data base comparisons.

N84
10164

UNCLAS

N84 10164 D20

THE DEVELOPMENT OF AERODYNAMIC UNCERTAINTIES FOR THE SPACE SHUTTLE ORBITER

James C. Young and Jimmy M. Underwood
NASA Johnson Space Center
Houston, Texas

ABSTRACT

The Shuttle Program development schedule and the management decision to perform an orbital, manned mission on the first launch resulted in a requirement to develop realistic aerodynamic uncertainties for the preflight aerodynamic predictions.

This paper addresses the methodology in developing two types of aerodynamic uncertainties. One involves the ability to reproduce aerodynamic results between various wind tunnel tests. The second addresses the differences between preflight aerodynamic predictions and flight results derived from analysis of past aircraft programs. Both types of uncertainties for pitching moment, lateral-directional stability, rudder power, and aileron power are presented.

In addition, the application of uncertainties to flight control design and flight test planning is briefly reviewed.

NOMENCLATURE

b	Span, inches
$\bar{c}$	Mean aerodynamic chord, inches
$C_{\ell_{\delta_a}}$	Aileron roll derivative, per degree
C_{ℓ_β}	Dihedral stability, per degree
$C_{\ell_{\delta_r}}$	Rudder roll derivative, per degree
C_m	Pitching moment coefficient
$C_{n_{\delta_a}}$	Aileron yaw derivative, per degree
C_{n_β}	Directional stability, per degree
$C_{n_{\delta_r}}$	Rudder yaw derivative, per degree
L_B	Body length, inches

Mach	Mach number
MRC	Moment reference center, fuselage station X_o = 1077 inches
$\bar{q}$	Dynamic pressure, psf
S	Reference area, sq. ft.
α	Angle of attack, deg
β	Angle of sideslip, deg
δ_a	Aileron deflection angle, deg
δ_r	Rudder deflection angle, deg
Δ	Wind tunnel - ADDB difference

ADDB	Aerodynamic Design Data Book
AEDC	Arnold Engineering and Development Center
AFFTC	Air Force Flight Test Center
ARC	Ames Research Center
Calspan	Calspan Corporation
DFRF	Dryden Flight Research Facility
FCS	Flight Control System
HST	Hypersonic Shock Tunnel
HSWT	High Speed Wind Tunnel
JSC	Johnson Space Center
LaRC	Langley Research Center
LTV	Ling-Temco-Vought
NASA	National Aeronautics and Space Administration
NSWC	Naval Surface Weapons Center
RI	Rockwell International
TWT	Transonic Plan Wind Tunnel
UPWT	Unitary Plan Wind Tunnel
16T	16-Foot Transonic

INTRODUCTION

Two management policy decisions made during the initial development planning for Shuttle had a significant impact on the approach to aerodynamic design and verification. In order to meet a compressed development schedule, a decision was made to concurrently design the FCS and conduct aerodynamic verification wind tunnel testing. Realizing the predicted aerodynamics were likely to change during the aerodynamic verification process, the FCS was designed to be insensitive to "reasonable" changes in the aerodynamic characteristics. As a result of this approach, the aerodynamicists were required to provide uncertainties on the preflight aerodynamics. The uncertainties used in the FCS design were defined as tolerances, which are the minimum error that is expected in the preflight aerodynamics.

Secondly, the decision to perform an orbital, manned mission on the first launch highlighted the aerodynamicists' problems. This decision raised the general question of how to maximize the mission safety without the benefit of either a graduated flight test program (as used by the aircraft industry) or an initial unmanned flight concept (as used by the early space program). The consequence of this decision on the development of an aerodynamic data base resulted in the problem of how to provide an estimate of maximum possible errors in the preflight predicted aerodynamics, especially in previously uncharted flight regimes. However, the estimated errors must not be so great as to completely invalidate the FCS design. Thus, a set of "worst case" aerodynamic uncertainties, defined as variations, was developed. As part of the first flight certification, variations, combined with other system uncertainties, were used to "stress" the flight control system through a multitude of simulations. As a consequence, the initial entry was flown at a center of gravity and with FCS gains which maximized the aerodynamic margins thereby maximizing mission safety for these systems.

This paper briefly addresses the development of the nominal preflight aerodynamics and details the methodology for establishing tolerances and variations.

PREFLIGHT PREDICTIONS

One of the largest wind tunnel programs in history has been conducted[1] for the development of the Space Shuttle. The Orbiter (fig. 1) alone has been tested over 27,000 occupancy hours to determine the performance and stability and control characteristics. This extensive wind tunnel program provided the foundation for the formulation and development of the ADDB[2]. The ADDB is the result of the combined efforts of the prime contractor and several NASA centers and consists of a digitized set of tables developed from the engineering analysis and fairing of all valid experimental data, complemented by empirical and theoretical data, and extrapolated to flight conditions where appropriate. Thus, the ADDB represents the "best estimate" of the preflight aerodynamics.

TOLERANCE DEVELOPMENT

Since the wind tunnel data base is the foundation for the preflight predictions, it is reasonable to assume that the minimum error that could be expected (i.e. tolerances) would be the ability to reproduce experimental results between various tests. Therefore, repeat tests were performed using various facilities, different models, and on occasion, different test organizations. Although the individual causes for any differences were not specifically identified, it is felt the total difference is representative of what may be expected for wind tunnel test repeatability.

As an illustration of the mechanics of this procedure, consider pitching moment coefficient, where repeat tests were plotted along with ADDB estimates, as typically shown in figures 2, 3, and 4. From figure 2, it can be seen that a 0.05-scale model, model 39-0, was tested in both ARC 11 x 11-Foot Facility and in the LaRC 16-Foot Transonic Facility. Similarly, a 0.015-scale model, model 44-0, was tested in three facilities: 1) the LTV 4 x 4; 2) the LaRC 8-Foot Tunnel; and 3) the ARC 11 x 11-Foot Facility. In addition, the 0.02-scale model, model 105-0, was tested in the LaRC 16T tunnel. With all these potential sources of differences, a peak-to-peak repeatability in C_m of approximately 0.006 was realized. This repeatability represents the combined error sources of the following: 1) the same model in several tunnels (tunnel-to-tunnel repeatability); 2) different models in the same tunnel (model-to-model repeatability); and 3) different test organizations (testing technique differences). This also includes any Reynolds number and blockage effects.

From this type of basic plot, the difference between the wind tunnel results and the ADDB at various angles of attack were plotted versus Mach number, as illustrated in figure 5. Tolerances (wind tunnel uncertainties) were obtained by fairing a curve through these data points using engineering judgement. The nominal angle of attack (fig. 6) was given a high weighting in the fairing process.

Aerodynamic tolerances for lateral-directional stability (ΔC_{n_β}, ΔC_{ℓ_β}) are presented in figures 7 and 8, while tolerances for rudder power ($\Delta C_{n_{\delta_r}}$, $\Delta C_{\ell_{\delta_r}}$) are shown in figures 9 and 10. Aileron power $\Delta C_{n_{\delta_a}}$, $\Delta C_{\ell_{\delta_a}}$) tolerances are presented in figures 11 and 12. Table 1 presents the facilities and models used in this evaluation.

VARIATIONS DEVELOPMENT

It was felt the most reasonable approach to the development of variations would be to analyze the wind tunnel to flight test differences of past aircraft programs. Unfortunately, the verification of preflight predicted aerodynamics was not a major objective of most of the earlier flight test programs. This severely limited the amount of data available for conducting flight test to wind tunnel comparisons. The flight data base was further limited by restricting the comparison to those vehicles which were geometrically similar to the Orbiter. Those vehicles chosen as applicable to Orbiter are presented in table 2. Also presented are geometric factors and other considerations pertinent to the vehicle configuration choices.

Variations were established by fairing the differences between the flight and predicted aerodynamics as a function of Mach number. The selections of the configurations and the fairing process are very subjective in nature. For this reason, a team of aerodynamicists from AFFTC, NASA-DFRF, NASA-JSC, and RI was formed to conduct the analysis and reach a concensus on variations.

The team's flight-to-predicted correlation and their recommended variation fairings are presented as a function of Mach number for C_m, figure 13; C_{n_β}, figure 14; C_{ℓ_β}, figure 15; $C_{n_{\delta_r}}$, figure 16; $C_{\ell_{\delta_r}}$, figure 17; $C_{n_{\delta_a}}$, figure 18; and $C_{\ell_{\delta_a}}$, figure 19. These figures were taken in part from reference 3.

As can be seen from the flight correlation figures, the flight data is limited to the lower supersonic speeds. In Mach regimes where flight data was unavailable, variations were obtained by multiplying the tolerances by a safety factor, usually 1.5.

Comparison of tolerances and variations at the lower Mach numbers indicate, as one might expect, that tolerances are less than variations.

A more detailed development of variations is found in reference 3. These recommended variations were modified primarily to facilitate computerization and included in the aerodynamic design data base, reference 2.

CONCLUDING REMARKS

Requirements of the Shuttle Program resulted in the development of the first comprehensive set of uncertainties in predicting preflight aerodynamics. In the process of the uncertainties development, a systematic wind tunnel study has been performed which demonstrates the need for testing multiple models/facilities when precise preflight aerodynamic predictions are needed.

The application of these uncertainties resulted in a desensitization of the flight control system to aerodynamics, thus providing increased confidence in the safety aspects of conducting a manned orbital mission on the first launch of the Orbiter.

ACKNOWLEDGEMENTS

The development of variations and wind tunnel uncertainties was a team effort in every sense of the word. Space does not permit recognizing everyone who participated in this effort but the authors, as representatives of the Shuttle program, would like to recognize key government and contractor personnel.

Special thanks to James P. Arrington, Bernard Spencer, Jr. and George M. Ware of LaRC; Joseph Cleary and Lee Jorgensen of ARC; and Paul O. Romere of JSC for their effort in the development of wind tunnel uncertainties.

The difficult task of establishing variations was accomplished by a team composed of Joe Weil of DFRF; Paul W. Kirsten of AFFTC;and Dave Tymms of JSC.

Don C. Schlosser ably represented Rockwell International in both endeavors.

REFERENCES

1. Whitnah, A. M. and Hillje, E. R.: Space Shuttle Wind Tunnel Program Summary, AIAA-82-0562, March 1982.

2. Aerodynamic Design Data Book. Vol. I - Orbiter Vehicle. NASA CR-160903, Nov. 1980. (Rockwell Rept. No. SD72-SH-0060-1M.)

3. Weil, Joseph; Powers, Bruce G.: Correlation of Predicted and Flight Derived Stability Derivatives with Particular Application to Tailless Delta Wing Configurations, NASA TM-81361.

TABLE 1.- WIND TUNNEL TESTS USED FOR UNCERTAINTY EVALUATION

TEST ID	FACILITY	MODEL NO.	MODEL SCALE	Re_c ($x10^6$)	BLOCKAGE (%)
Transonic					
1. OA145A	ARC 11x11 FT	39-0	0.05	5.9, 9.9, 17.8	1.09
2. OA270A	LaRC 16T	39-0	0.05	7.9	.65
3. OA270B	LaRC 16T	105-0	0.02	3.1	.10
4. LA70	CALSPAN 8 FT	44-0	0.015	2.1, 2.7, 4.7	.18
5. LA76	LTV 4x4 HSWT	44-0	0.015	4.5, 5.3, 5.9	.74
6. LA77	ARC 11x11 FT	44-0	0.015	4.7	.10
7. LA111	LaRC 8 FT TWT	44-0	0.015	4.1	.24
8. LA115	LaRC 8 FT TWT	44-0	0.015	2.5	.24
Supersonic					
9. OA145B	ARC 9x7 FT	39-0	0.05	3.0, 6.9, 8.9	
10. OA145C	ARC 8x7 FT	39-0	0.05	2.0, 5.0, 6.4, 7.9	
11. OA209	AEDC A	105-0	0.02	3.4, 7.7, 10.4	
12. LA63A	LaRC UPWT-1	44-0	0.015	1.2	
13. LA63B	LaRC UPWT-2	44-0	0.015	1.2	
14. LA75	LaRC UPWT-2	44-0	0.015	1.2	
(5.) LA76	LTV 4x4 HSWT	44-0	0.015	4.5	
15. LA101	LaRC UPWT-1	44-0	0.015	1.2	
16. LA110	LaRC UPWT-1	44-0	0.015	1.2	
17. LA114	LaRC UPWT-2	44-0	0.015	1.2	
18. LA125	LaRC UPWT-2	105-0	0.02	1.6	

TABLE 2.- ORBITER CORRELATION APPLICABILITY (ref.3)

AIRCRAFT	GEOMETRIC FACTORS					REMARKS
	WING PLANFORM	WING FLAP LONG. CONTROL	WING ELEVON LATERAL CONTROL	SINGLE VERTICAL TAIL	LARGE FCS	
XB-70	✓	✓	✓			GOOD PRED. BASE, M RANGE CANARD, LIMITED α RANGE
YF-12	✓	✓	✓			GOOD M RANGE, LIMITED α RANGE
X-15				✓	✓	WIDE α M RANGE
TACT$_{\Lambda=58^{\circ}}$	✓			✓	✓	ONLY LIMITED DATA CURRENTLY AVAILABLE
HP115	✓	✓	✓	✓		LOW SPEED DATA ONLY
B-58	✓	✓	✓	✓		GOOD PREDICTIVE BASE, M RANGE
YF-16 F-8SCW				✓		SOURCE OF RUDDER CONTROL DATA

*SEE REFERENCE 3 FOR AIRCRAFT IDENTIFICATION

GEOMETRY	COMPONENT	
	WING	VERTICAL TAIL
AREA	2690 FT² (249.9092 m²)	413.25 FT² (38.3922 m²)
SPAN	936.68 (23.8425)	315.72 (8.0193)
ASPECT RATIO	2.265	1.675
TAPER RATIO	0.2	0.404
SWEEP (LE)	81/45 DEG	45 DEG
DIHEDRAL	3.5	— —
INCIDENCE	0.5 DEG	— —
MAC	474.81 (12.0602)	199.81 (5.0752)

NOTE: UNLESS OTHERWISE NOTED, ALL DIMENSIONS ARE IN INCHES (METERS)

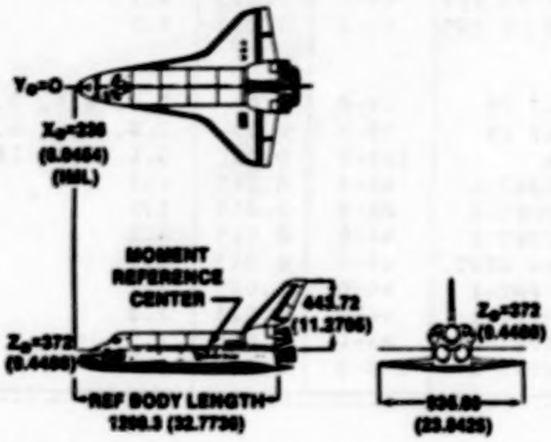
Y0=0
X0=238
(6.0452)
(IML)
MOMENT
REFERENCE
CENTER
443.72
(11.2705)
Z0=372
(9.4488)
REF BODY LENGTH
1290.3 (32.7736)
Z0=372
(9.4488)
936.68
(23.8425)

Figure 1.- Space Shuttle Orbiter geometry.

SYM.	DATA SOURCE	FACILITY	MODEL	SCALE	ORGANIZATION
○	OA145A	ARC 11 x 11	20-0	0.050	RI
□	LA78	LTV 4 x 4	44-0	0.015	LaRC
◇	OA270A	LaRC 16T	20-0	0.050	RI
△	OA270B	LaRC 16T	105-0	0.020	RI
▽	LA77	ARC 11 x 11	44-0	0.015	LaRC
★	LA115	LaRC 8 TWT	44-0	0.015	LaRC
—	AERODYNAMIC DATA BOOK				

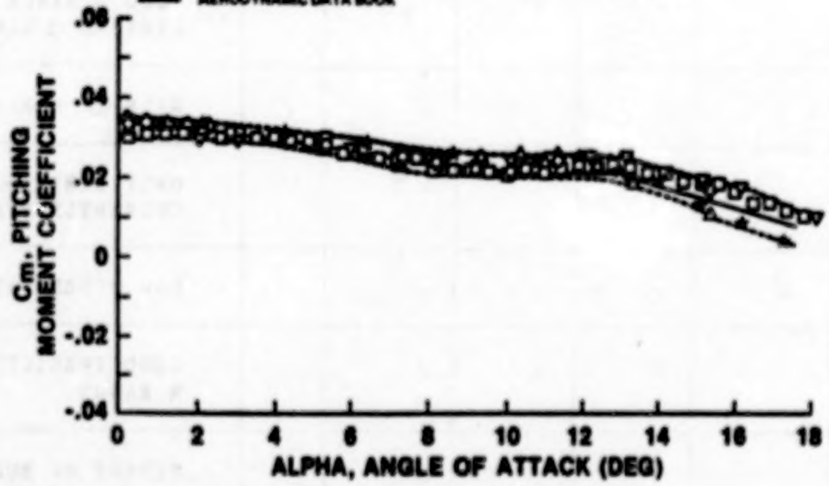

Figure 2.- Pitching moment, Mach 0.6.

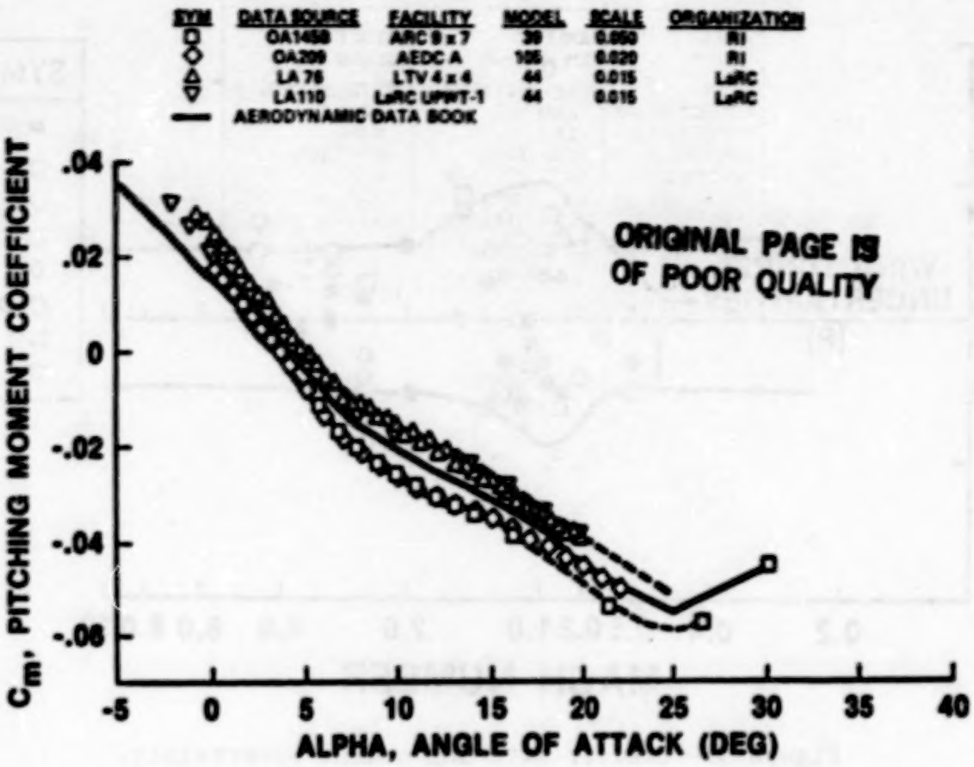

Figure 3.- Pitching moment, Mach 2.0.

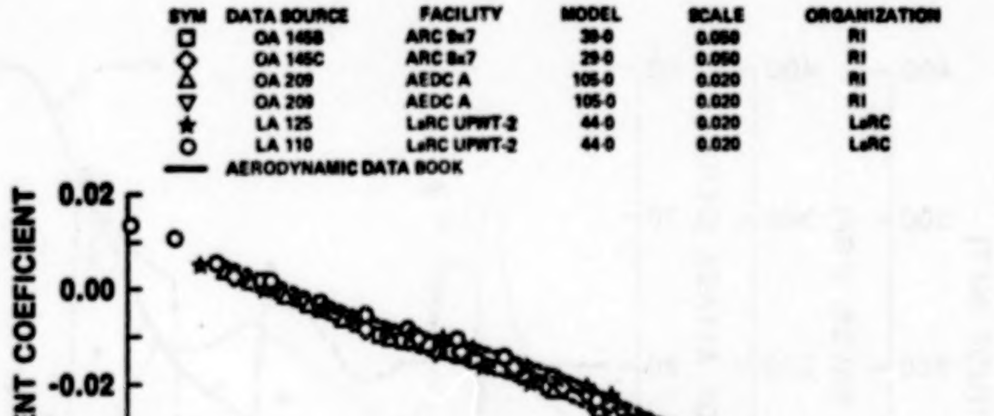

Figure 4.- Pitching moment, Mach 2.5.

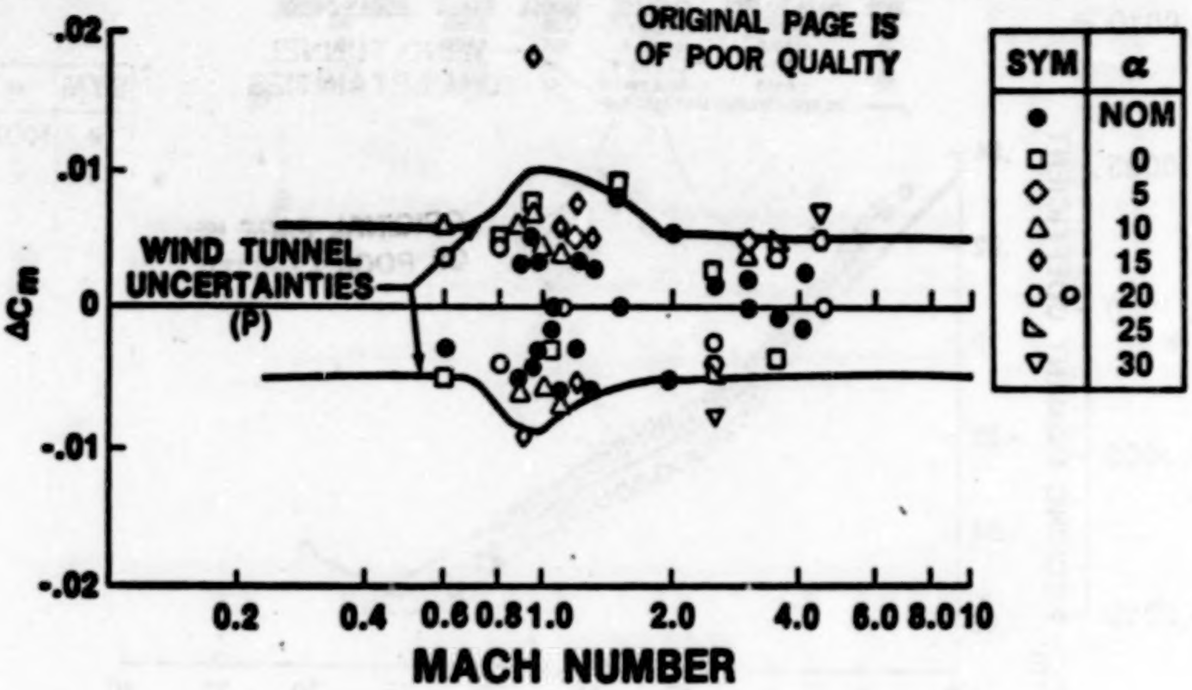

Figure 5.- Orbiter pitching moment uncertainty.

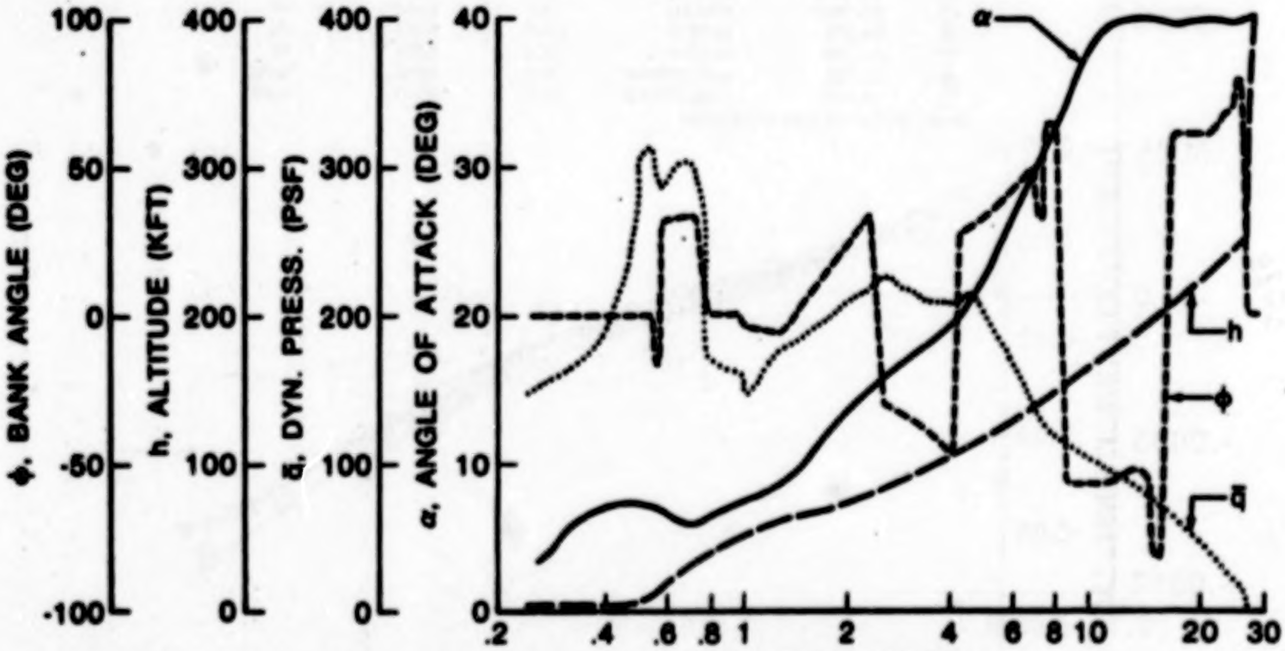

Figure 6.- Typical Orbiter entry trajectory.

ORIGINAL PAGE IS
OF POOR QUALITY

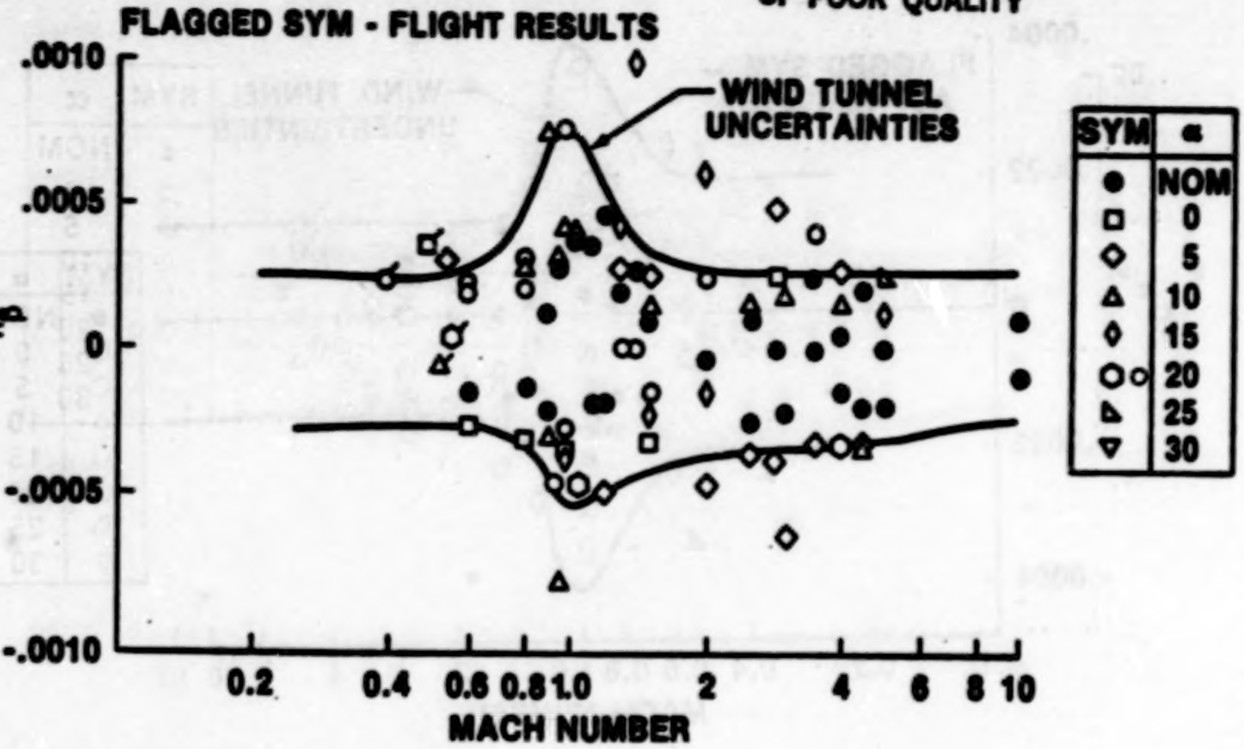

Figure 7.- Orbiter directional stability uncertainty.

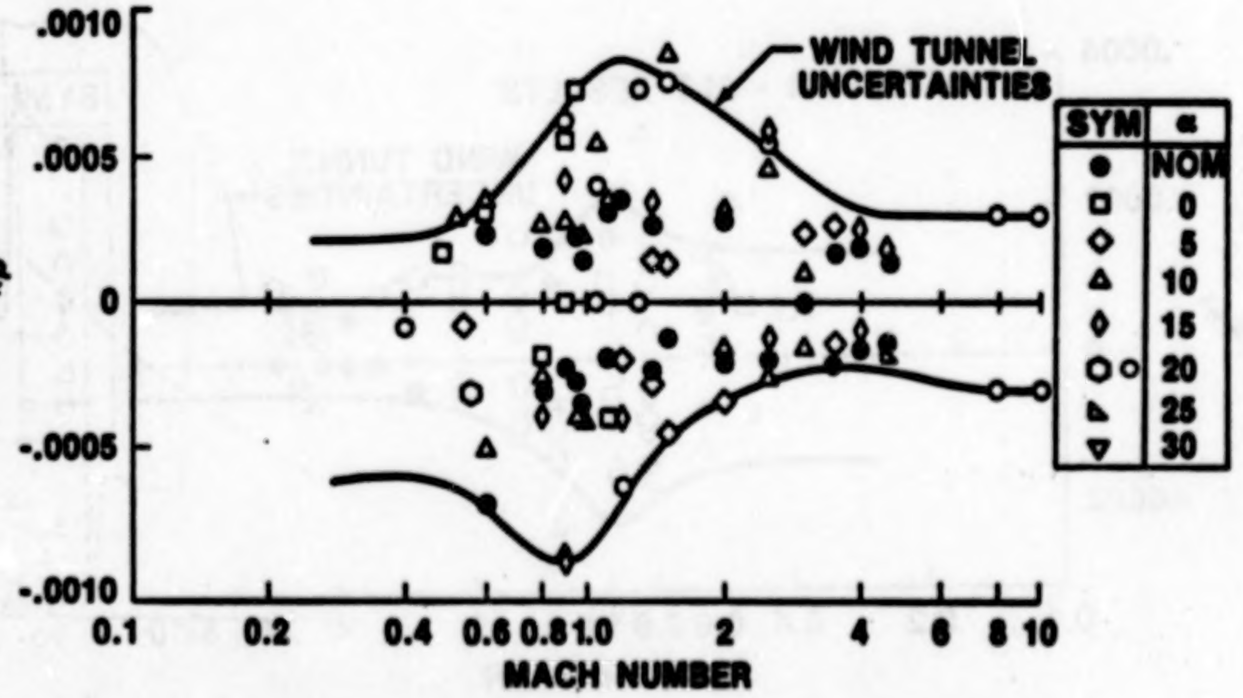

Figure 8.- Orbiter dihedral stability uncertainty.

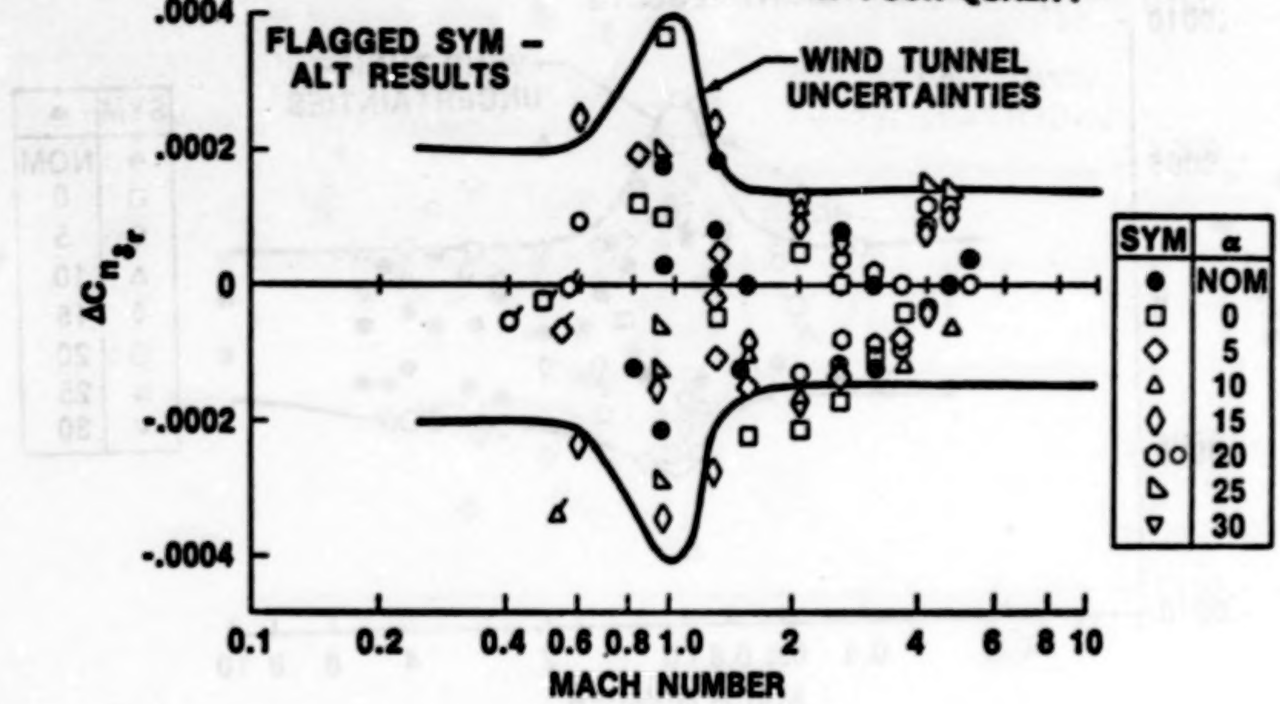

Figure 9.- Orbiter rudder yaw derivatives uncertainty.

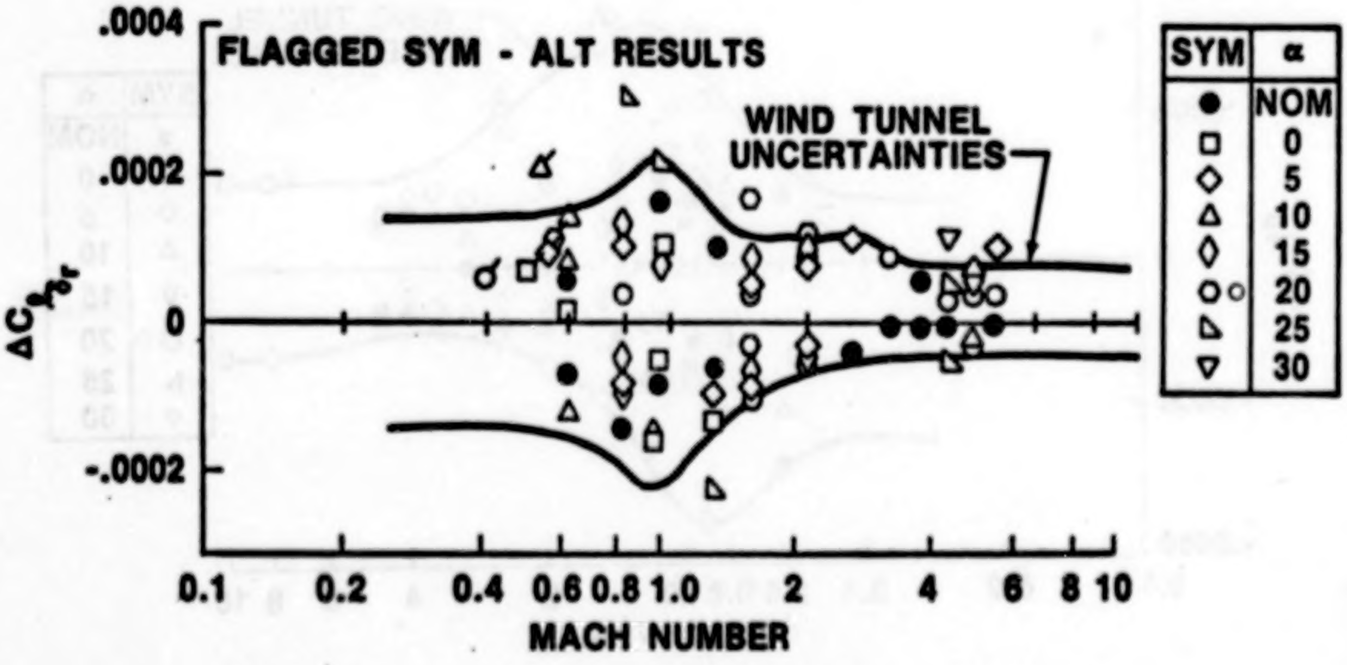

Figure 10.- Orbiter rudder roll derivatives uncertainty.

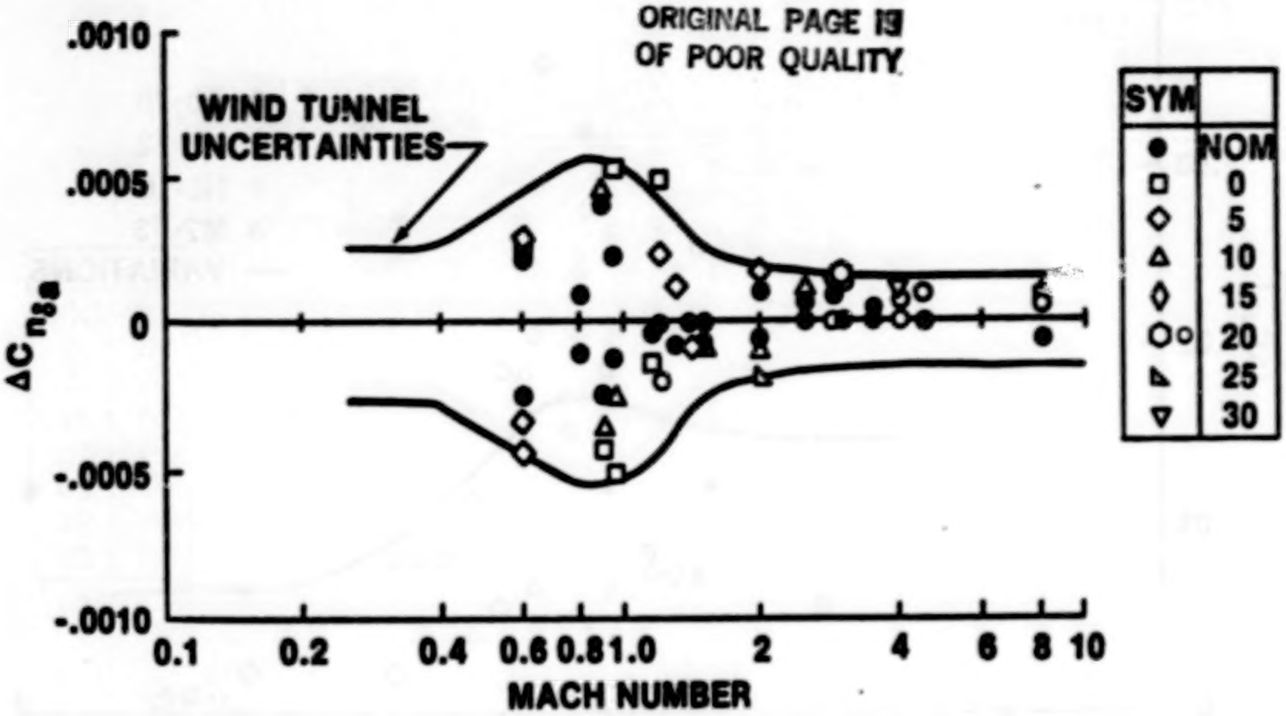

Figure 11.- Orbiter aileron yaw derivatives uncertainty.

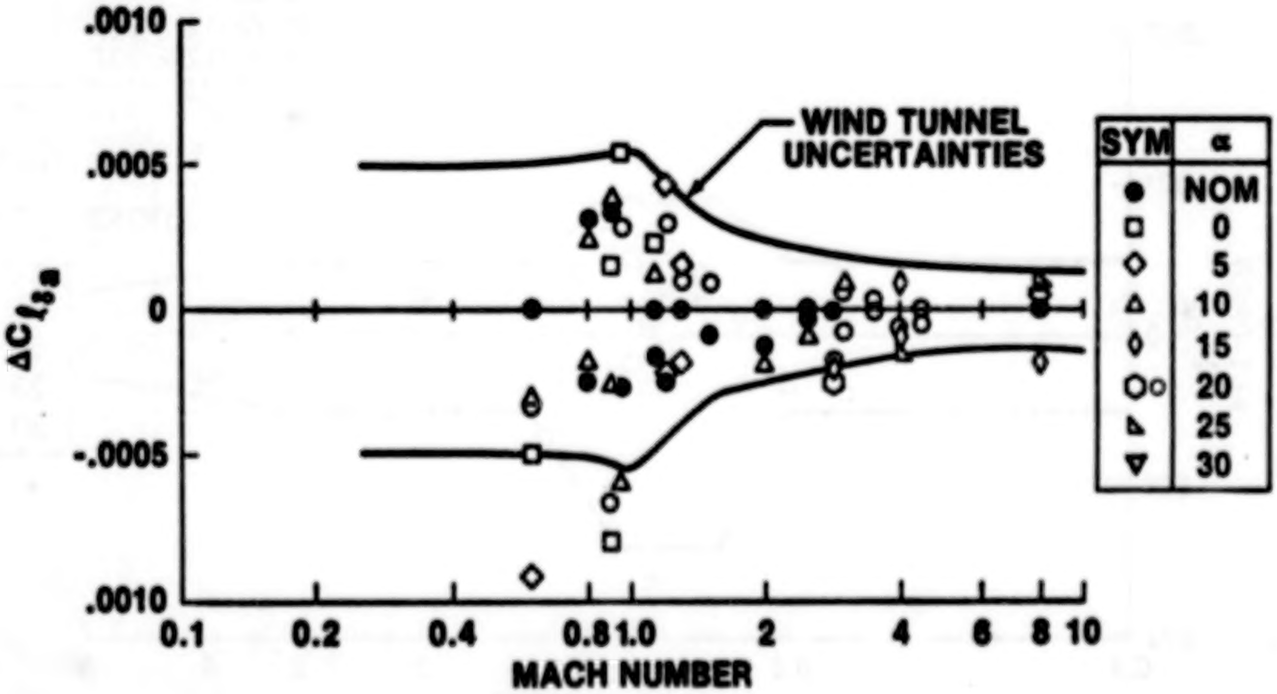

Figure 12.- Orbiter aileron roll derivatives uncertainty.

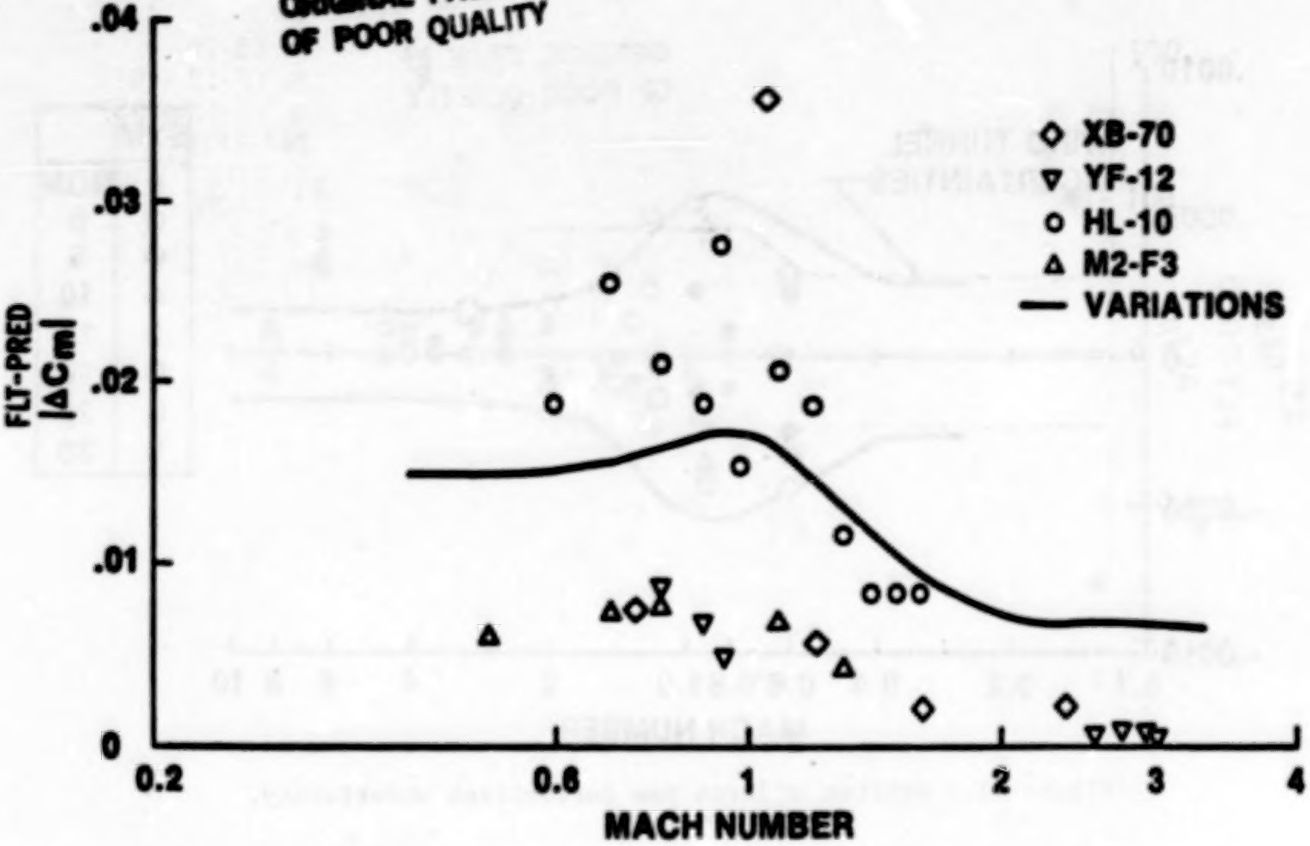

Figure 13.- Correlation of flight and predicted pitching moment.

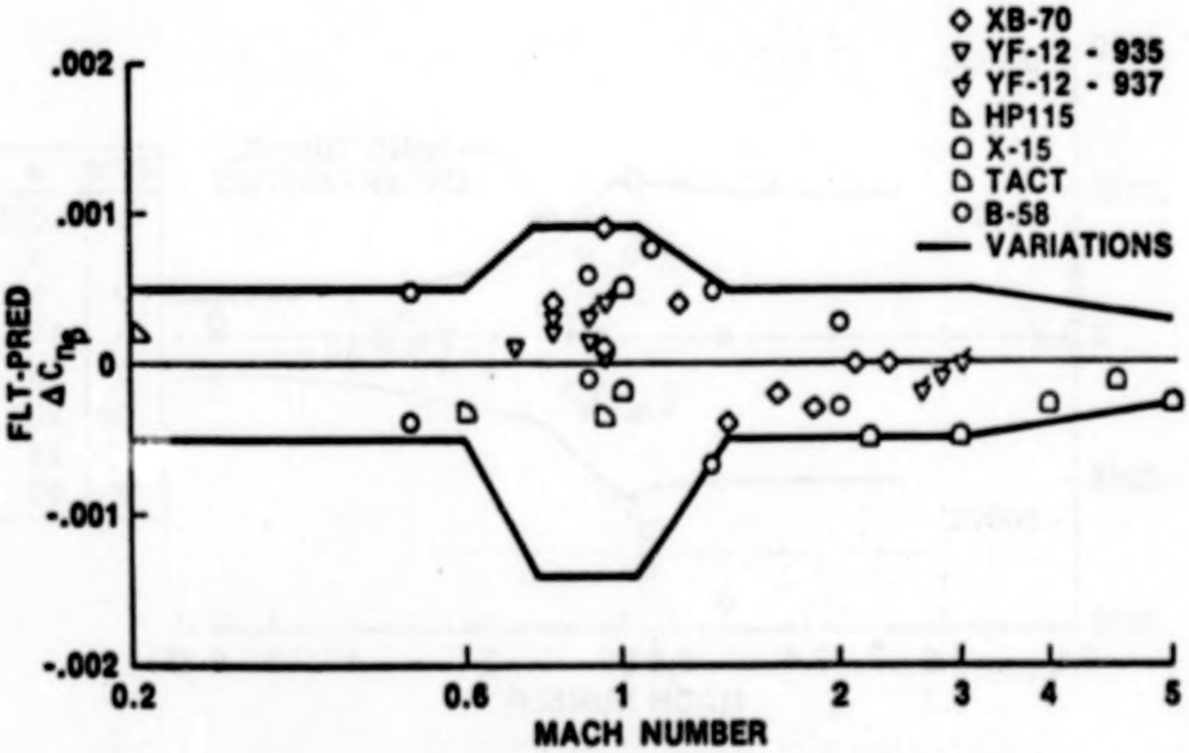

Figure 14.- Correlation of flight and predicted directional stability.

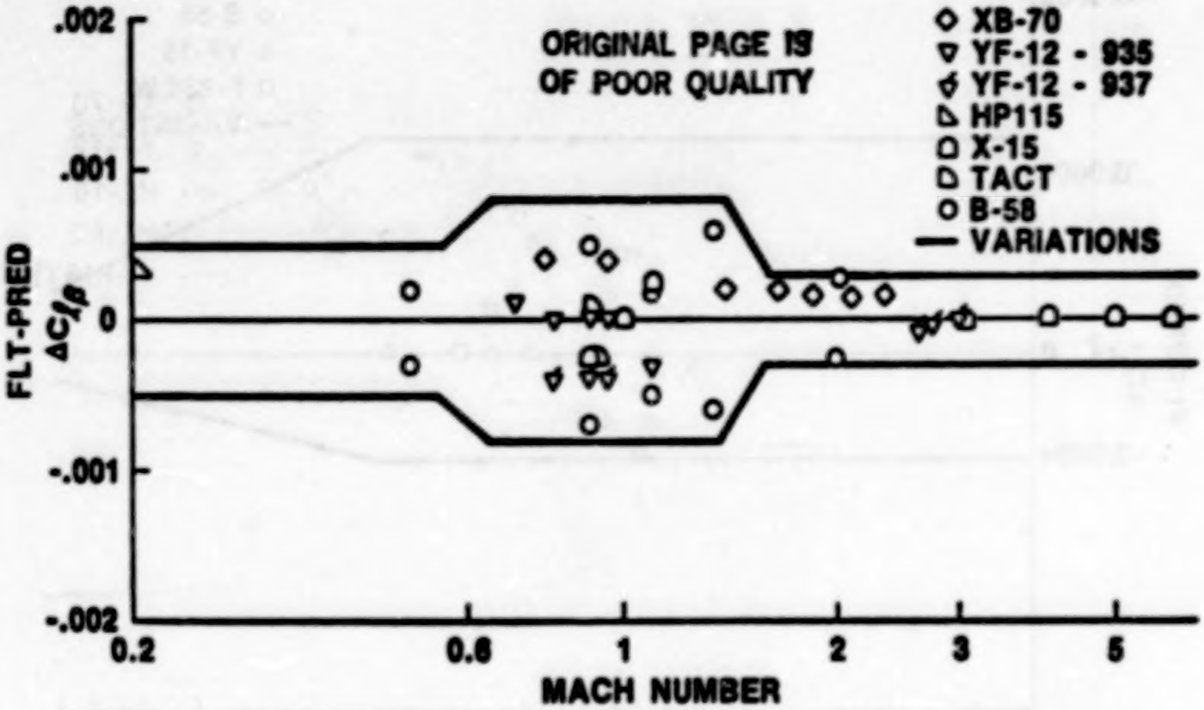

Figure 15.- Correlation of flight and predicted dihedral stability.

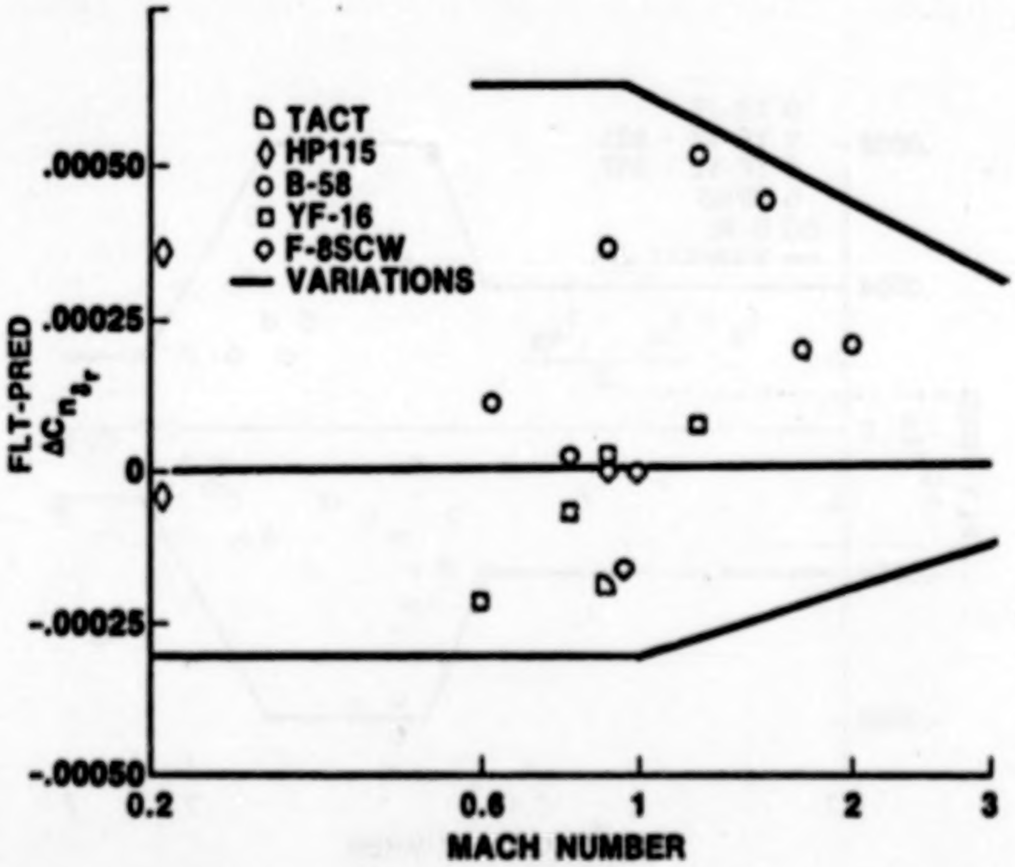

Figure 16.- Correlation of flight and predicted rudder yaw derivatives.

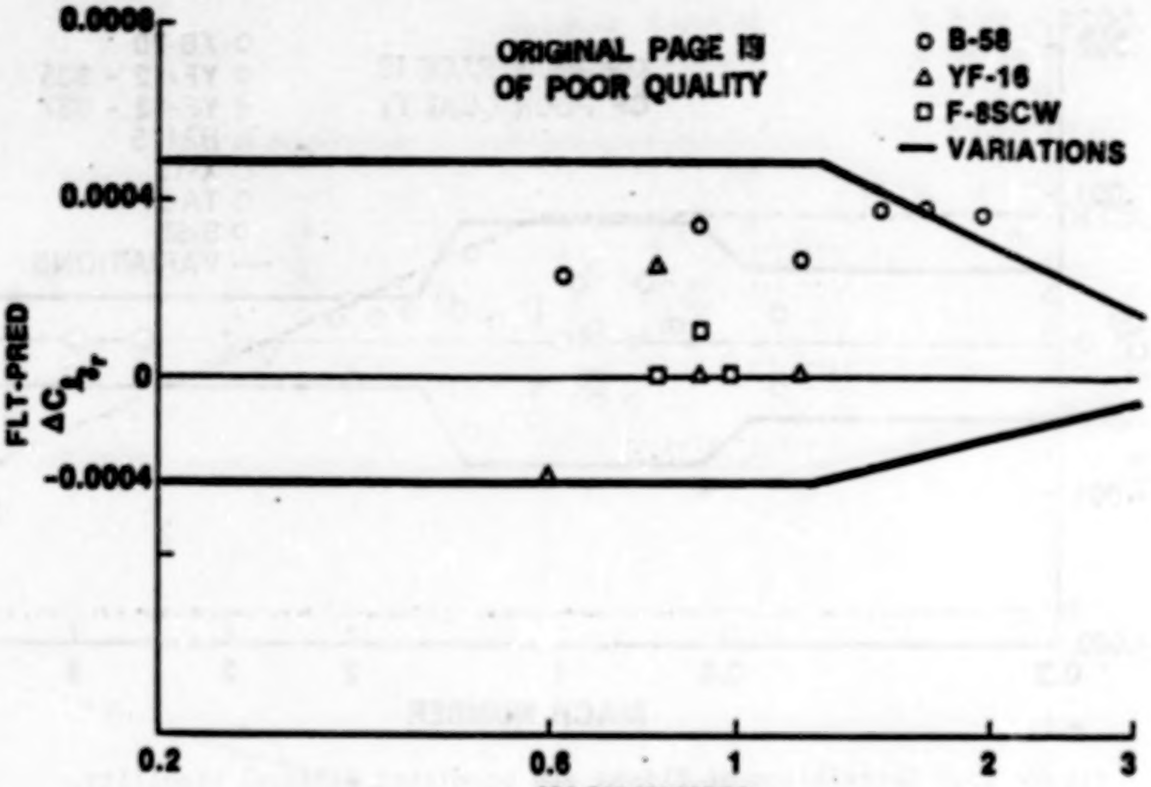

Figure 17.- Correlation of flight and predicted rudder roll derivatives.

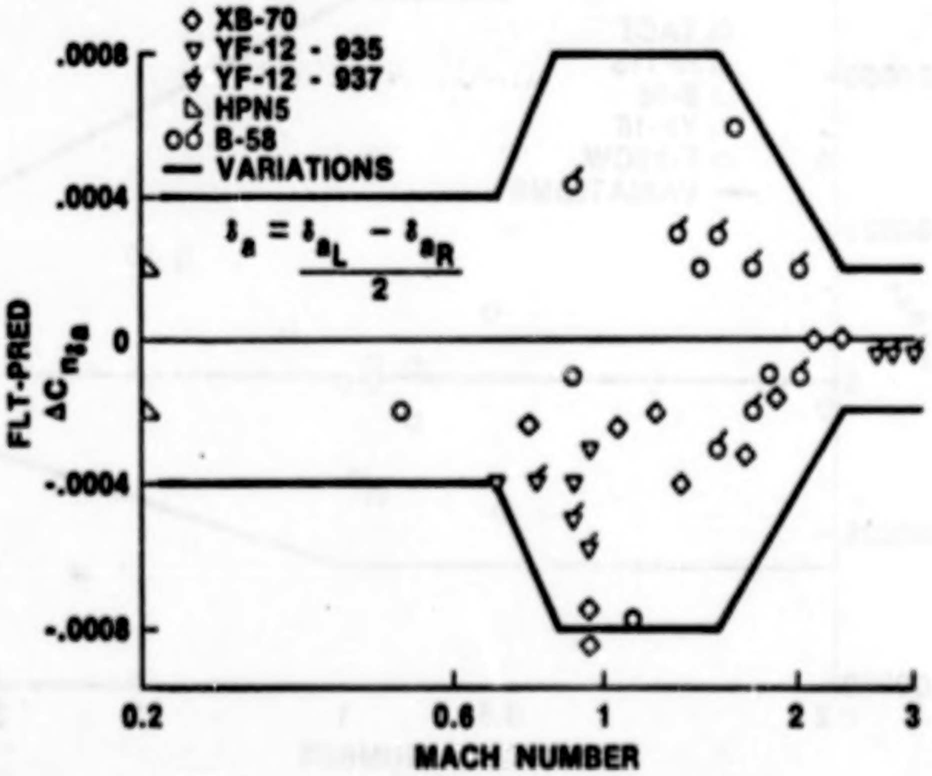

Figure 18.- Correlation of flight and predicted aileron yaw derivatives.

ORIGINAL PAGE IS
OF POOR QUALITY

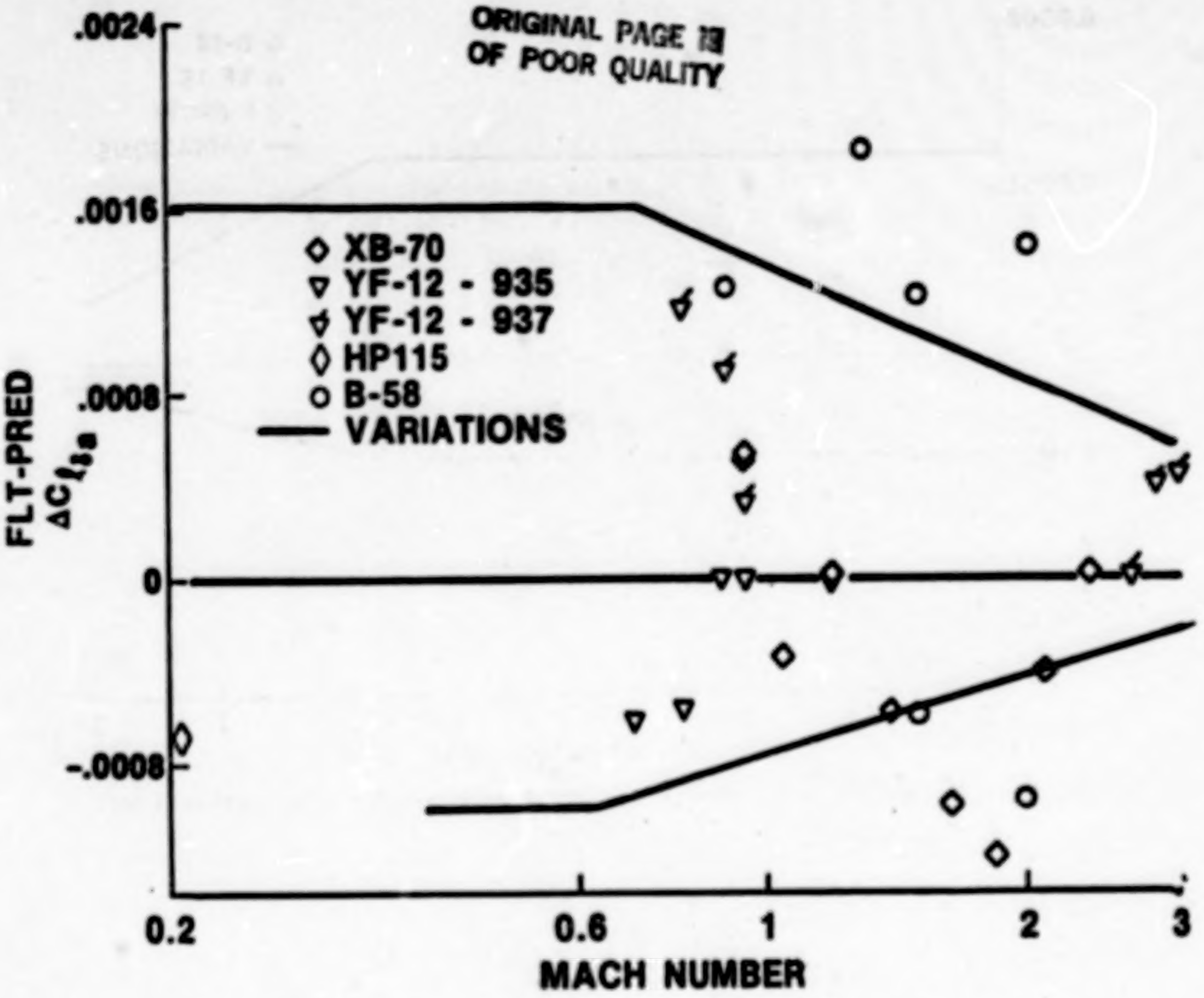

Figure 19.- Correlation of flight and predicted aileron roll derivative.

N84
10165

UNCLAS

N84 10165 D21

THE CALIBRATION AND FLIGHT TEST PERFORMANCE OF THE SPACE SHUTTLE ORBITER AIR DATA SYSTEM

Alden S. Dean and Arthur L. Mena

Space Transportation and Systems Group
Rockwell International
Downey, California

SUMMARY

The Space Shuttle air data system (ADS) is used by the guidance, navigation and control system (GN&C) to guide the vehicle to a safe landing. In addition, postflight aerodynamic analysis requires a precise knowledge of flight conditions. Since the orbiter is essentially an unpowered vehicle, the conventional methods of obtaining the ADS calibration were not available; therefore, the calibration was derived using a unique and extensive wind tunnel test program. This test program included subsonic tests with a 0.36-scale orbiter model, transonic and supersonic tests with a smaller 0.2-scale model, and numerous ADS probe-alone tests. The wind tunnel calibration was further refined with subsonic results from the approach and landing test (ALT) program, thus producing the ADS calibration for the orbital flight test (OFT) program.

The calibration of the Space Shuttle ADS and its performance during flight are discussed in this paper. A brief description of the system is followed by a discussion of the calibration methodology, and then by a review of the wind tunnel and flight test programs. Finally, the flight results are presented, including an evaluation of the system performance for on-board systems use and a description of the calibration refinements developed to provide the best possible air data for postflight analysis work.

INTRODUCTION

The Space Shuttle orbiter is a unique vehicle. Its primary mission is to deliver payloads to near-earth orbit and return, landing like a conventional aircraft. Upon entry, the orbiter must maintain its stability and control over an extensive flight regime. During a typical flight, the Mach number may vary from 27 at entry to 0.25 at landing, with the angle of attack ranging from 40 to 0 degrees. Since the vehicle is unpowered, accurate air data is crucial to enable it to make a safe landing.

In many ways, the Space Shuttle orbiter ADS is a typical ADS. It uses two fuselage-mounted probes to measure local flow conditions. Freestream conditions, such as Mach number, angle of attack, and altitude are computed using previously derived calibration algorithms. The freestream conditions are used by the GN&C system and are also displayed to the crew. In addition, air data is used extensively during postflight aerodynamic analysis of the Shuttle.

PAGE 1186 INTENTIONALLY BLANK

PRECEDING PAGE BLANK NOT FILMED

Since the orbiter is an unpowered air vehicle, the traditional ADS flight calibration methods, e.g., pacer aircraft and tower-fly-by are not possible; therefore, an extremely comprehensive wind tunnel test program was developed to obtain the necessary data to derive the calibration. The wind tunnel data were merged with data obtained during the ALT program to produce an on-board calibration for OFT and a more accurate calibration for postflight aerodynamic analysis. Results from the OFT program indicated that the on-board (general purpose computer [GPC]) calibration easily met the specified requirements. These results were also used in an extensive effort to refine the postflight calibration in order to provide the best possible data for postflight aerodynamic analysis.

ADS DESCRIPTION

A sketch of the orbiter ADS probes illustrating their location on the orbiter nose is shown in figure 1. There are two probes, one on either side of the vehicle. They are secured to rotating doors that allow them to be stowed (and thus protected) during ascent, orbit, and reentry. After reentry, the probes are deployed when the orbiter has slowed to approximately Mach 3.5. Each probe includes a semispherical head with three pressure ports, as seen in figure 1. The center port (P_C) gives an indication of total pressure and senses local total pressure when the probe is aligned with the local flow field. The upper and lower ports (P_U and P_L) are sensitive to local flow angle. In addition, several static pressure ports (P_M) are located aft on the probe shaft, and a total temperature sensor is located at the rear.

The probes are connected to four air data transducer assemblies (ADTA), redundant pairs per side, through pneumatic lines. The ADTA house sensitive pressure transducers that convert the probe-measured pressures to electrical signals. Using the ADS calibrations, the GPC processes the ADTA signals to provide the basic air data parameters: static pressure, total pressure, and angle of attack (also total temperature). From these basic parameters, Mach number, dynamic pressure, pressure altitude, equivalent airspeed, and true airspeed are computed.

ADS CALIBRATION DESCRIPTION

The ADS calibration relates a set of conditions that cannot be measured directly during flight (i.e., Mach number, angle of attack, and altitude) to a set of parameters that can be measured (i.e., probe total, static, upper and lower pressures, and total temperature). In the wind tunnel, specific freestream conditions (i.e., static and total pressure, angle of attack, and sideslip) are known to a relatively high degree of accuracy. During a wind tunnel test these conditions are held constant, while the probe pressures are carefully measured and recorded.

The development of the ADS calibration involved deriving a set of calibration parameters that relate the freestream conditions to the probe-measured conditions, using the wind tunnel derived data base (later merged with flight results). From the freestream conditions, the various air data parameters (Mach number, altitude, etc.) can be computed using basic aerodynamic equations. A flow chart illustrating the ADS calibration and showing how the above freestream parameters are computed is presented in figure 2.

Since the probe measurements are affected by the presence of the orbiter, it is not possible to measure freestream static and total pressure (P_∞ and P_{T_∞}) directly. Thus the error, or decrement from the actual value, was put in nondimensional form and designated CPSD and CPTD. Freestream angle of attack also cannot be measured directly; therefore, a pressure parameter (RAX) was developed to provide an indication of angle of attack. The equations describing these parameters are presented below with typical calibration curves shown in figure 3.

- Static pressure decrement

$$\mathrm{CPSD} = \frac{P_M - P_\infty}{P_C - P_M}$$

- Total pressure decrement

$$\mathrm{CPTD} = \frac{P_C - P_{T_\infty}}{P_C - P_M}$$

- Angle-of-attack parameter

$$\mathrm{RAX} = \frac{P_L - P_U}{P_C - 1/2(P_L+P_U)}$$

Note that CPSD and CPTD relate freestream static and total pressure to P_M and P_C, respectively, while RAX has a fairly linear relationship with angle of attack and exhibits good sensitivity. The wind tunnel data were used to derive a set of polynomial equations of the type shown below, which describe angle of attack as a function of RAX, and CPSD and CPTD as functions of angle of attack.

$$Y(X) = A0 + A1(X) + A2(X)^2 + A3(X)^3 + A4(X)^4$$

where

$$Y(X) = \alpha_{ORB}(\mathrm{RAX})$$
$$\mathrm{CPSD}(\alpha_{ORB})$$
$$\mathrm{CPTD}(\alpha_{ORB})$$

These equations are at a constant Mach number with a linear interpolation used between Mach numbers. For the on-board calibration, software storage restrictions limited the equations to fourth order, with the entire calibration utilizing 196 coefficients. On the other hand, the postflight calibration had no restrictions and thus resulted in a more complex calibration with over 600 coefficients.

Using these equations, the freestream values of static and total pressure are computed. Finally, using P_∞ and P_{T_∞}, the various air data parameters are computed (i.e., Mach number, pressure altitude, dynamic pressure, and equivalent airspeed). Note that since the ADS calibration parameters (RAX, CPSD, and CPTD) are modeled as functions of Mach number it is necessary to make an initial guess at the Mach number and use the equations to converge on the actual value.

SYSTEM REQUIREMENTS

Since air data is used extensively in the orbiter GN&C system, the ADS requirements are based on the GN&C requirements. These are shown in table I. The orbiter flight control system divides the atmospheric portion of the Shuttle flight into three parts: entry, terminal area energy management (TAEM), and approach and landing (A/L). Each area has specific requirements for air data parameters such as Mach number, altitude, and angle of attack, as shown in table I. It should be noted that these are specified system requirements. Postflight analysis accuracy needs are more stringent; hence, much effort was expended to provide postflight air data that is as accurate as the system will allow.

WIND TUNNEL TEST PROGRAM

Most aircraft ADS's have the advantage of being calibrated during flight. Standard techniques involve flying the aircraft at a constant altitude past a known ground station or paced by another aircraft with a known ADS. Since these techniques were not available to the orbiter air vehicle, the limited flight calibration must be supplemented by wind tunnel tests that cover flight envelope extremes not encompassed by the flight test program. Consequently, the orbiter ADS wind tunnel calibration program was necessarily comprehensive.

The wind tunnel program was divided into two distinct parts: tests with the probes mounted on an orbiter model to relate probe response to orbiter freestream conditions, and probe-alone tests to evaluate the probe response to local flow field conditions. The extent of the wind tunnel test program is shown in tables II and III.

The initial ADS calibration wind tunnel tests, with the probes mounted on the orbiter, were performed in order to derive an ADS calibration for Orbiter 101 for use during ALT. Since Orbiter 101 was unpowered, it would not exceed subsonic velocities; hence, the Orbiter 101 ADS calibration was limited to the Mach range of 0.25 to 0.7. Data at Mach 0.25 were obtained using a 0.36-scale orbiter model, complete with scaled air data probes. The model was large enough that the ADS side probes could be accurately simulated; however, because of its size, it could only be tested in the Ames Research Center (ARC) 40 by 80-Foot Wind Tunnel. Because of this, only low speed (Mach = 0.25) data could be obtained.

In order to obtain data at the higher Mach numbers, a much smaller model was used. It was determined that the 0.2 scale was the minimum practical probe size for valid simulation; however, this resulted in probe models that were too small to be completely simulated and an orbiter model that was too large for the available high speed facilities. Therefore, a compromise had to be made. It was decided to divide the four probe pressures between the left and right probe models. Thus, P_C and P_M were placed on one probe, with P_U and P_L on the other. The orbiter model size was reduced by eliminating the portion of the vehicle aft of fuselage station 670, and replacing it with a boattail fairing. The resulting model was still too large, so the scale was reduced to 0.1; hence, the high speed data (Mach > 0.25) were obtained using two 0.2-scale probe models on a 0.1-scale orbiter forebody-only model.

The validity of using a forebody-only model was substantiated by testing a complete orbiter 0.03-scale model with flush pressure taps bracketing the probe location. Wing-on and wing-off comparisons showed essentially no influence at these pressure ports.

For later verification tests, a 0.1-scale probe was developed with a single pressure tap for measuring static pressure; thus, to determine the static pressure parameter, this probe was tested in conjunction with a 0.2-scale probe that measured the total pressure.

ALT PROGRAM

The ALT program was conducted at the Dryden Flight Research Center, Edwards Air Force Base, in August, September, and October, 1977. The program consisted of five air launches from the Boeing 747 Shuttle carrier aircraft, three with a large tailcone fairing closing off the fuselage base and the last two without the fairing, thus simulating the operational configuration. The tailcone-on flights allowed about 5 minutes of free flight time. Less than half that time was available with the tailcone removed.

The ADS was calibrated during ALT using the flight test probe (FTP) as a reference. The FTP was a conventional noseboom, which was mounted on the orbiter nose. It measured stagnation pressure through a total pressure head, static pressure through pressure ports on the barrel of the probe, and both angles of attack and sideslip with vanes. During ALT, the air data from FTP were also used by the backup flight control system (BFCS). There was no FTP installed for the OFT program.

OFT PROGRAM

The OFT program consisted of four flights launched from the Kennedy Space Center in 1981 and 1982. These flights were designated as test flights and the orbiter carried a wide variety of instruments designed to accurately measure its performance. Much of the analysis performed on these flights, and the analysis on the data gathered by the flight test instrumentation, required an accurate source of air data; thus, the ADS provided air data for the on-board systems and air data for postflight analysis. The latter required air data parameters that were more accurate than those provided to the on-board systems.

During OFT, the accuracy of the ADS parameters was judged by comparison with alternate data sources. Since these alternate sources are also subject to errors, differences are not necessarily a measure of the ADS inaccuracy; however, if it is assumed that the alternate data errors are random, any consistent bias error would indicate an actual error in the ADS calibration. The alternate sources available for the OFT flight program include a best estimated trajectory (BET) generated by TRW, another BET generated by the Langley Research Center (LaRC), and a trajectory based on phototheodolite tracking, generated by the Air Force Flight Test Center (AFFTC). The primary cause of inaccuracy in these sources is that the parameters are corrected for measured (jimsphere) winds, which differ in time and location from the actual winds. Of course, the ADS experiences the actual winds.

The OFT program had two primary ADS test objectives: verification of the on-board GPC function, and refinement of the postflight ADS calibration for the generation of high quality air data parameter time histories for postflight aerodynamic analysis.

GPC RESULTS

The GPC air data parameters supplied to the on-board, flight control, guidance, and navigation systems differ from the postflight derived parameters in several regards. On-board (GPC) parameters are provided at 1 sample per second, whereas the postflight parameters are derived from transducer output pressures at 12 1/2 samples per second. The on-board calibration algorithms are simplified in order to conform to the software limitation of 196 calibration coefficients, as compared with approximately 600 coefficients used in the postflight calibration. In addition, the on-board system employs a rate limiting function to avoid air data discontinuities in the Mach jump regions (Mach 1.4 and again near 1.0). Each of these differences can contribute to loss of accuracy.

Another possible error source is the on-board mechanization of the calibration. The system begins with the previous Mach number (initially an assumed Mach number) to enter the calibration equations, but does not iterate with a corrected Mach number. Prior to STS-1, it was analytically shown that the rate of change of Mach number, and/or the calibration coefficients, was low enough to preclude a significant error. This analysis has been verified by flight results.

Results from STS-1 through STS-4 have shown that the GPC functioned satisfactorily and produced air data parameters well within the system accuracy requirements. Figures 4, 5, and 6 show the GPC output dynamic pressure, angle of attack, and Mach number for STS-4 compared with the ADS parameters. The latter have been refined, as described in the following section, and are considered the best source of air data. These figures show the flight region from approximately Mach 2.5 to landing gear deployment. The maximum difference in dynamic pressure (about 9 psf) is approximately 4 percent, while the system accuracy requirement is 10 percent. Similarly, the maximum difference in angle of attack is approximately 0.85 degree as compared to the requirement of ±2.0 degrees, and the maximum difference in Mach number is -0.063 compared with a requirement of ±0.15 (±10 percent). The other air data parameters show similar differences. Comparisons using data from STS-4 are shown in the figures; however, results from the other flights are similar.

The maximum differences between the ADS parameters and the LaRC BET data are shown in table I along with the system accuracy requirements. Only those parameters that have a specified requirement are presented. The table shows that the accuracy achieved by the on-board GPC calibration is well within the system requirements.

SUBSONIC POSTFLIGHT CALIBRATION

The subsonic postflight calibration was based on ALT flight results because the FTP provided an accurate reference data source. Using limited data, initial analysis efforts showed that there were distinct differences between wind tunnel and flight-derived calibrations. The wind tunnel static pressure calibration coefficient (CPSD) was somewhat lower than that indicated by flight. The total pressure calibration coefficient (CPTD) showed differences at low angles of attack, and the angle-of-attack parameter (RAX) showed a bias of approximately 1/2 degree. These differences were applied to produce an initial flight calibration. Additional analysis indicated that this initial calibration could be refined further.

A multiple linear regression technique was adapted for the refinement effort. This is a least-squares technique used to derive a relation between one parameter and several independent variables. In addition to this sophisticated analysis tool, a computer program was developed that was capable of processing a very large quantity of data. The regression analysis was applied to angle-of-attack, static pressure, and total pressure.

The angle-of-attack analysis showed a dependence on α, α^2, and pitch rate. The derived correction took the following form.

$$\alpha_{CORR} = \alpha_{ADS} - \Delta\alpha$$

$$\Delta\alpha = 0.2476 - 0.5853(QTERM) - 0.1033\alpha_{ADS} + 0.00697\alpha_{ADS}^2$$

$$(QTERM) = qr/V_T$$

This correction reduced the three-sigma dispersion in angle of attack from about 3/4 degree to a little more than 1/2 degree. This is illustrated in figures 7 and 8, which show the ADS angle of attack with and without the correction plotted against the FTP-measured angle of attack. Figure 9 shows the correction (with zero pitch rate) plotted as a function of angle of attack. It should be noted that the practical limit for accuracy of flight test determined angle of attack is probably between 1/4 and 1/2 degree.

The static pressure analysis began with determining the dependence of the calibration parameter, CPSD, on angle of attack, Mach number, and pitch rate. The pitch rate dependence was shown to be insignificant, so the analysis continued using Mach number and various powers of angle of attack. The final correction was made consistent with the basic calibration equation, i.e., a polynomial equation with CPSD as a function of Mach number and a fourth order function of angle of attack, as follows:

$$\begin{aligned} \mathrm{CPSD_{CORR}} &= \mathrm{CPSD} - \Delta\mathrm{CPSD} \\ \Delta\mathrm{CPSD} &= -4.843 \times 10^{-2} + 5.293 \times 10^{-2}\,(M_{ADS}) \\ &\quad + 7.612 \times 10^{-3}\,(\alpha_{ADS}) - 1.933 \times 10^{-3}\,(\alpha_{ADS})^2 \\ &\quad + 1.758 \times 10^{-4}\,(\alpha_{ADS})^3 - 4.783 \times 10^{-6}\,(\alpha_{ADS})^4 \end{aligned}$$

This correction reduced the three-sigma dispersion in CPSD from ±0.04947 to ±0.0168. The significance in the equivalent airspeed uncertainty was to reduce the static pressure contribution to the uncertainty from about 4 knots to 1.4 knots. Figure 10 shows the ADS calibration coefficient with no corrections plotted against that derived from the FTP. Figure 11 shows the ADS coefficient with corrections applied.

Total pressure was found to be the largest contributor to the equivalent airspeed uncertainty. The total pressure analysis followed the same steps as the static pressure and culminated in a calibration parameter (CPTD) correction in the same format as the basic calibration equation.

$$\begin{aligned} \mathrm{CPTD_{CORR}} &= \mathrm{CPTD} - \Delta\mathrm{CPTD} \\ \mathrm{CPTD} &= 4.1242 \times 10^{-2} + 6.2598 \times 10^{-2}\,(M_{ADS}) \\ &\quad - 8.3247 \times 10^{-3}\,(\alpha_{ADS}) - 1.5937 \times 10^{-3}\,(\alpha_{ADS})^2 \\ &\quad + 2.4879 \times 10^{-4}\,(\alpha_{ADS})^3 - 8.0762 \times 10^{-6}\,(\alpha_{ADS})^4 \end{aligned}$$

This correction reduced the three-sigma dispersion in CPTD from ±0.0652 to ±0.01686. In terms of equivalent airspeed, it reduced the uncertainty from about 6 knots to about 1.5 knots. The ADS total pressure calibration coefficient is plotted against that derived from the FTP before corrections were applied, as shown in figure 12, and after corrections were applied, as shown in figure 13. The differences between the wind tunnel and flight-derived calibrations are shown in figures 14, 15, and 16. These figures show the ALT flight data with both the wind tunnel and flight-derived calibrations superimposed.

These corrections were applied to the STS flight data in the trajectory range from Mach 0.6 to landing gear deployment. Prior to correction, the maximum differences in equivalent airspeed were about 10 knots when compared to the LaRC BET and about 6 knots when compared to the AFFTC data. After the corrections were applied, these differences were reduced to about 6 knots for the LaRC BET and about 2 knots for the AFFTC data. Considering that the alternate sources are subject to wind uncertainties, the corrected ADS equivalent airspeed is considered the most accurate. Figures 17 and 18 show an example of these comparisons. Figure 17 compares the ADS equivalent airspeed with the LaRC BET before corrections, and figure 18 shows the same comparison after corrections.

TRANSONIC AND SUPERSONIC POSTFLIGHT CALIBRATIONS

The transonic and supersonic postflight calibrations were based entirely on wind tunnel results. This calibration proved to be adequate for on-board use, but in order to provide the best possible air data for postflight analysis, some improvement appeared appropriate.

In the transonic range, the measured static pressure experiences a rapid change at two points: Mach 1.4 and near Mach 1.0. The rapid fluctuations are shown in figure 19. This figure shows a time history of the ADS static pressure calibration coefficient compared with the coefficient derived using the freestream static pressure, as provided by the LaRC BET. This example is for STS-2 and is typical of all the flights. The results of the system not precisely following the rapid changes are discontinuities in the static pressure history. This is also reflected in other parameters. For example, figure 20 shows the effect on Mach number for STS-4. As a first approach to removing the discontinuities, a simple linear interpolation was used; however, other aerodynamic analysis results indicated that this method could be improved upon.

An attempt was made to derive a calibration correction from the three alternate sources of air data for all four flights; however, no consistent error pattern could be determined.

As used by the alternate data sources, the meterological-measured static pressure (Rawinsonde) is considered an accurate measure of static pressure. In fact, it is considered more accurate than is possible with any conventional air vehicle ADS, particularly within the ADS altitude range. Consequently, it was a logical step to resolve the discontinuities in the ADS static pressure, by simply substituting the meteorological static pressure for the ADS-determined static pressure. This was done with the static pressure from the LaRC BET.

At higher Mach numbers (2.5 to 3.5), all four flights showed a consistent negative bias in static pressure when compared with either the LaRC BET or the TRW BET, although the magnitude differed between flights and between sources. An example from STS-4 is shown in figure 21. This bias was also resolved by substituting the static pressure from the LaRC BET.

CONCLUSIONS

The calibration of the Space Shuttle orbiter ADS was a unique program to derive an accurate system calibration without the benefit of an extensive flight calibration program. The bulk of the calibration was derived from an extensive wind tunnel test program and was combined with a limited amount of flight test results. From the comprehensive wind tunnel test program, angle of attack, static pressure, and total pressure calibrations were developed and proved to be sufficiently accurate to meet the specified requirements.

Further refinements were developed from the flight programs to produce the best possible air data parameters for postflight analysis work. From Mach 3.5 to Mach 0.6, the meterological static pressure was substituted for that derived by the ADS. From Mach 0.6 to landing gear deployment, corrections derived from a regression analysis technique were applied to angle of attack, static pressure, and total pressure. The entire ADS Mach number range is illustrated in figures 22 and 23, which show an example of Mach number from the refined ADS (STS-4), compared with that from the LaRC BET. The differences are small and cannot be considered a measure of accuracy since there is some uncertainty associated with the reference source.

To date, there has been no requirement to isolate the effects of ground proximity on the ADS parameters, although it is known that there is a significant effect, particularly in angle of attack. Current analysis work has shown that the angle of attack derived from the inertial measurement unit (IMU) has been adequate.

In general, the final air data parameters are considered an accurate representation of the actual trajectories flown and are suitable for use in postflight data analysis.

SYMBOLS AND ABBREVIATIONS

ADS	air data system
ADTA	air data transducer assembly
AFFTC	Air Force Flight Test Center
ALT	approach and landing test
ARC	Ames Research Center
A/L	approach and landing
BFCS	backup flight control system
CPSD	static pressure decrement coefficient
CPTD	total pressure decrement coefficient
FTP	flight test probe
GN&C	guidance, navigation, and control
GPC	general purpose computer
IMU	inertial measurement unit
LaRC	Langley Research Center
LeRC	Lewis Research Center
OFT	orbital flight test
P_C	probe center pressure
P_L	probe lower pressure

P_M	probe-measured static pressure
P_U	probe upper pressure
P_∞	freestream static pressure
P_{T_∞}	freestream total pressure
q	pitch rate (deg/sec)
r	distance from the center-of-gravity to the ADS probe (ft)
RAX	angle-of-attack parameter
TAEM	terminal area energy management
Ve	equivalent airspeed (knots)
V_T	true airspeed (ft/sec)

BIBLIOGRAPHY

Orbiter Air Data System Substantiation Report. Rockwell International, Space Transportation and Systems Group, SD 75-SH-0038, Rev B, Dec. 1978.

Aerodynamic Design Data Book Volume 1, Orbiter Vehicle. Rockwell International, Space Transportation and Systems Group, SD72-SH-0060-1M, Nov. 1980.

ORIGINAL PAGE IS
OF POOR QUALITY

TABLE I.-ADS PARAMETER PERFORMANCE

Air Data Parameter	Units	Flight Phase Utilization	System Requirement		Most Stringent Subsystem Requirement	Maximum Difference With LaRC BET
			Range	Accuracy (3σ)		
Altitude	ft	TAEM	10K to 100K	±10%	Navigation	±4%
Dynamic pressure	psf	(TAEM)/(A/L)	90 to 375	±10%	G&C	±7%
Mach number	dim	TAEM A/L	0.6 to 2.5 0.25 to 0.6	±10% ±5%	Guidance FCS	±6% ±3%
True airspeed	fps	TAEM A/L	600 to 2500 250 to 600	±10% ±5%	FCS Guidance	±6% ±3%
Equivalent airspeed	KTS	(TAEM)/(A/L)	160 to 335	±5%	Crew	±4%
Angle of attack	deg	(TAEM)/(A/L)	-4 to +20	±2°	G&C	±1°

ORIGINAL PAGE IS
OF POOR QUALITY

TABLE II.-WIND TUNNEL PROGRAM (AIR DATA PROBE CALIBRATION)
ORBITER MODEL TESTS

Test	Model Scale		Mach Range	Facility	Purpose
	Orbiter	Probe			
OA-22	0.03	None	0.6 → 1.5	ARC 11x11, 9x7	Pressure survey
OA-143	0.03	None	0.25	Rockwell NAAL	Pressure survey
OA-100	0.36	0.36*	0.25	ARC 40x80	Development
OA-164	0.36	0.36*	0.25	ARC 40x80	Development
OA-174	0.36	0.36	0.25	ARC 40x80	Verification
OA-161A,B,C	0.03	None	0.6 → 3.5	ARC 11x11, 9x7, 8x7	Pressure and local survey
OA-220	0.10 (forebody)	0.20*	0.3 → 1.1	ARC 14x14	Transonic-scaled probes
OA-224	0.10 (forebody)	0.20	0.2 → 1.3	LaRC 16-ft transonic	Verification
OA-228	0.10 (forebody)	0.20	0.25	Rockwell NAAL	Static pressure comparison
OA-237	0.10 (forebody)	0.10, 0.20	0.25	ARC 40x80	Scale and blockage
OA-232	0.10 (forebody)	0.10, 0.20	0.2 → 1.3	AEDC 16T	Scale and blockage
OA-221B,C	0.10 (forebody)	0.20	1.5 → 3.5	ARC 9x7, 8x7	Development
OA-234	0.10 (forebody)	0.10, 0.20	2.0 → 3.5	LaRC 10x10	Verification
OA-238	0.10 (forebody)	0.10	0.25	Rockwell NAAL	Scaled probes
OA-231B,C	0.10 (forebody)	0.10, 0.20	1.5 → 3.5	ARC 9x7, 8x7	Verification
Other tests:					
OA-236	(ARC Rosemount NAAL tunnel calibration probes)		0.25	Rockwell NAAL	Facilities calibration comparison

*Also nose probe

TABLE III.-WIND TUNNEL PROGRAM (PROBE-ALONE TESTS)

Test	Probe Scale	Mach Range	Facility	Purpose
OA-501	Full	0.2 → 0.95	Rosemount	Preliminary development
OA-502	Full	1.5 → 3.50	AEDC D	Preliminary development
OA-503*	0.36	0.15 → 0.30	Rosemount	Scale development
OA-504	Full	0.20 → 0.95	Rosemount	Development
OA-505	Full	0.80 → 1.50	AEDC IT	Development
OA-506	Full	1.50 → 3.50	AEDC D	Development
OA-507	0.36	0.20 → 0.95	Rosemount	Scale development
OA-508	0.36 & full	0.20 → 0.95	Rosemount	Verification
OA-509	0.20	0.20 → 0.95	Rosemount	Scale development
OA-510	0.20	0.80 → 1.50	AEDC IT	Scale development
OA-511	Full	0.20 → 0.95	Rosemount	Verification
OA-512	Full	1.50 → 3.50	AEDC D	Verification
OA-513	Full	0.80 → 1.50	AEDC IT	Development
OA-514	Full	1.50 → 3.50	AEDC D	Development
OA-515	0.20	1.50 → 3.50	AEDC D	Scale
OA-516	Full	1.50 → 3.50	AEDC D	Verification
OA-517	Full	0.20 → 0.95	Rosemount	Verification (qualification)
OA-518	0.10	0.20 → 0.95	Rosemount	Verification
OA-519	0.10	0.80 → 1.50	AEDC IT	Verification
OA-520*	0.36 noseboom	0.20 → 0.95	Rosemount	Verification

*Includes noseboom tests.

Note: Not in chronological order.

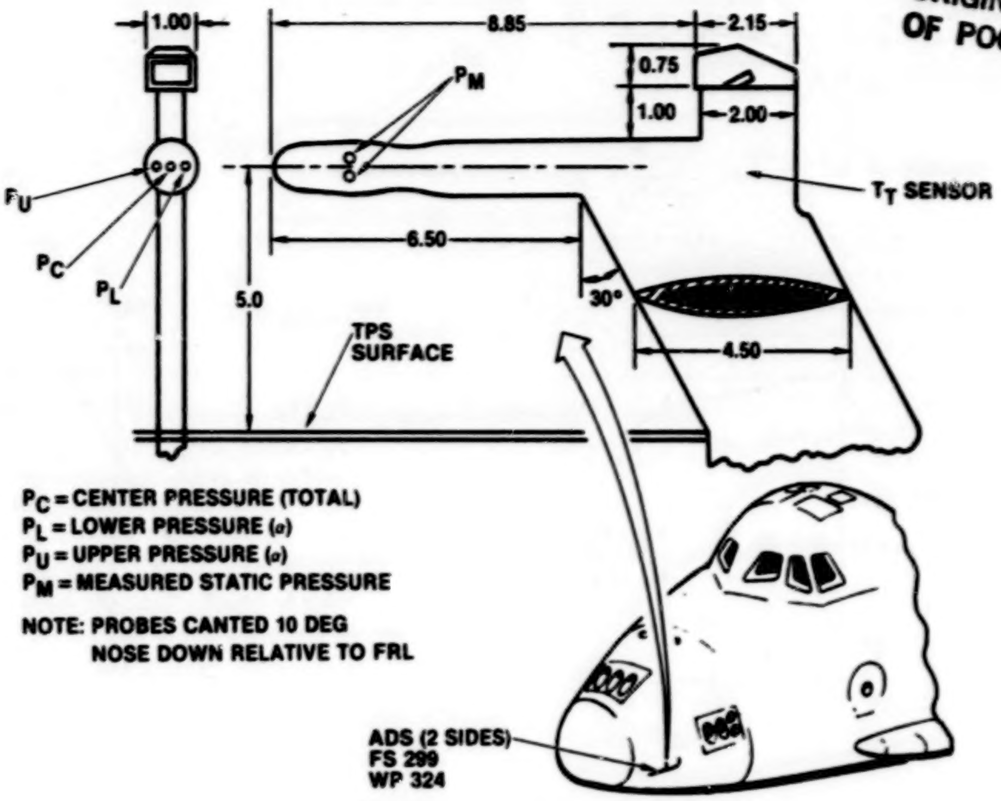
1.00
8.85
2.15
0.75
1.00
2.00
P_M
P_U
P_C
P_L
T_T SENSOR
6.50
5.0
30°
4.50
TPS SURFACE
P_C = CENTER PRESSURE (TOTAL)
P_L = LOWER PRESSURE (α)
P_U = UPPER PRESSURE (α)
P_M = MEASURED STATIC PRESSURE
NOTE: PROBES CANTED 10 DEG
NOSE DOWN RELATIVE TO FRL
ADS (2 SIDES)
FS 299
WP 324

Figure 1.- ADS probe.

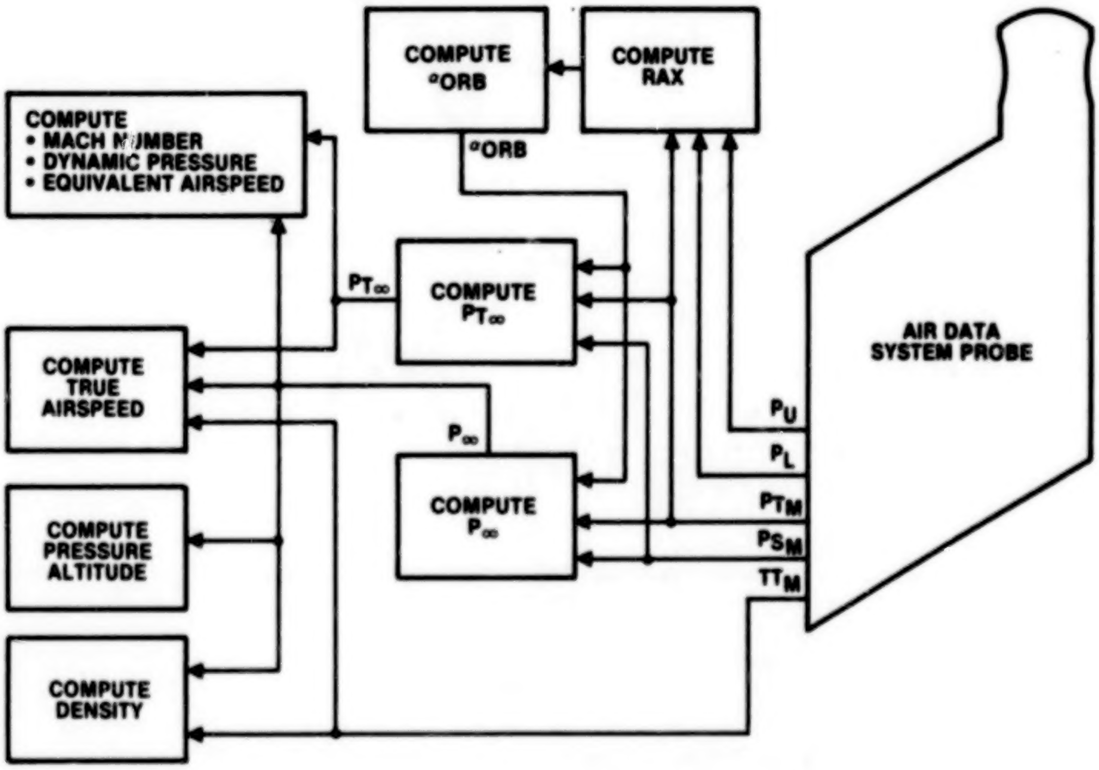
COMPUTE α_{ORB}
COMPUTE RAX
COMPUTE
• MACH NUMBER
• DYNAMIC PRESSURE
• EQUIVALENT AIRSPEED
α_{ORB}
$P_{T\infty}$
COMPUTE $P_{T\infty}$
COMPUTE TRUE AIRSPEED
P_∞
COMPUTE P_∞
COMPUTE PRESSURE ALTITUDE
COMPUTE DENSITY
AIR DATA SYSTEM PROBE
P_U
P_L
P_{T_M}
P_{S_M}
T_{T_M}

Figure 2.- ADS logic program.

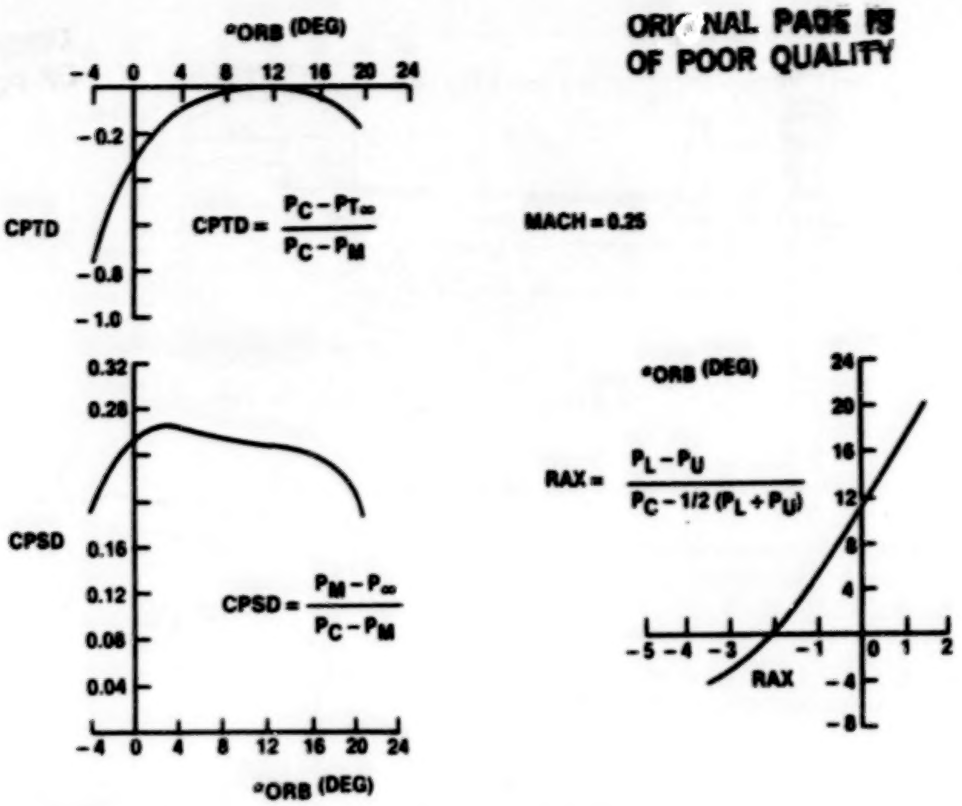

Figure 3.- Typical ADS calibration curves.

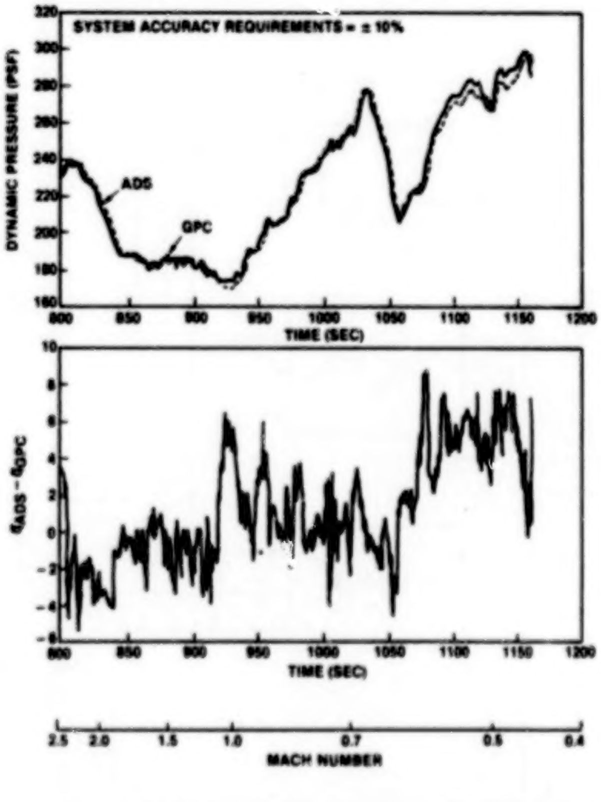

Figure 4.- STS-4 dynamic pressure comparison -
GPC and refined ADS calibration.

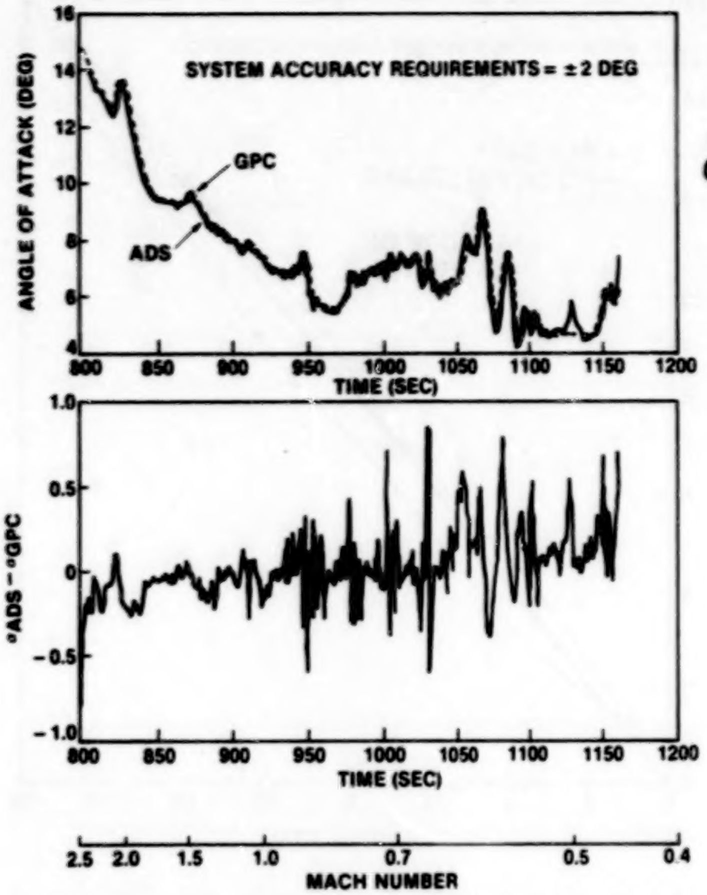

Figure 5.- STS-4 angle-of-attack comparison - GPC and refined ADS calibration.

ORIGINAL PAGE IS OF POOR QUALITY

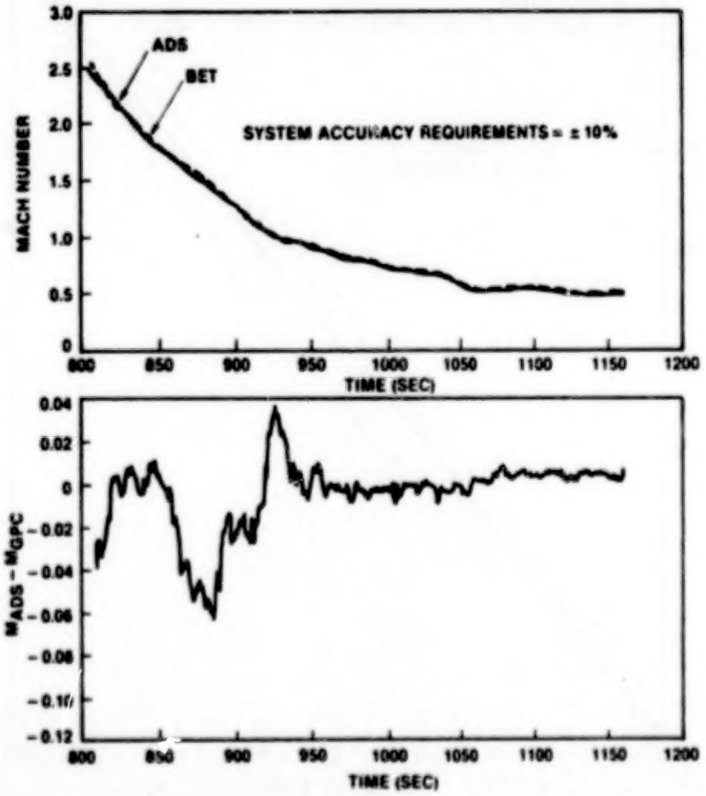

Figure 6.- STS-4 Mach number comparison - GPC and refined ADS calibration.

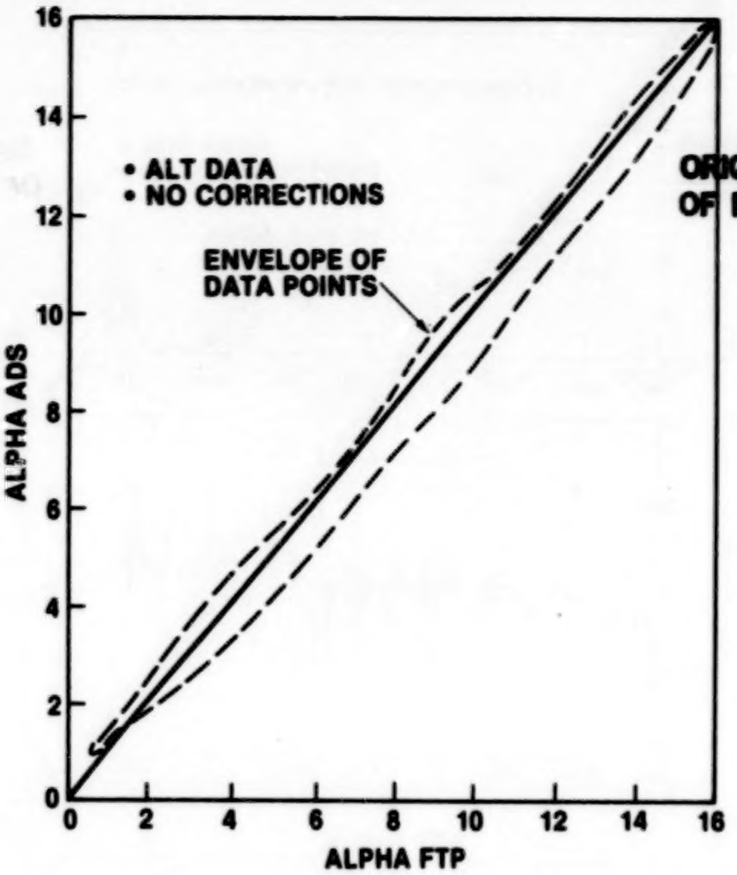

ORIGINAL PAGE IS OF POOR QUALITY

Figure 7.- Angle-of-attack comparison - ADS and FTP (no corrections).

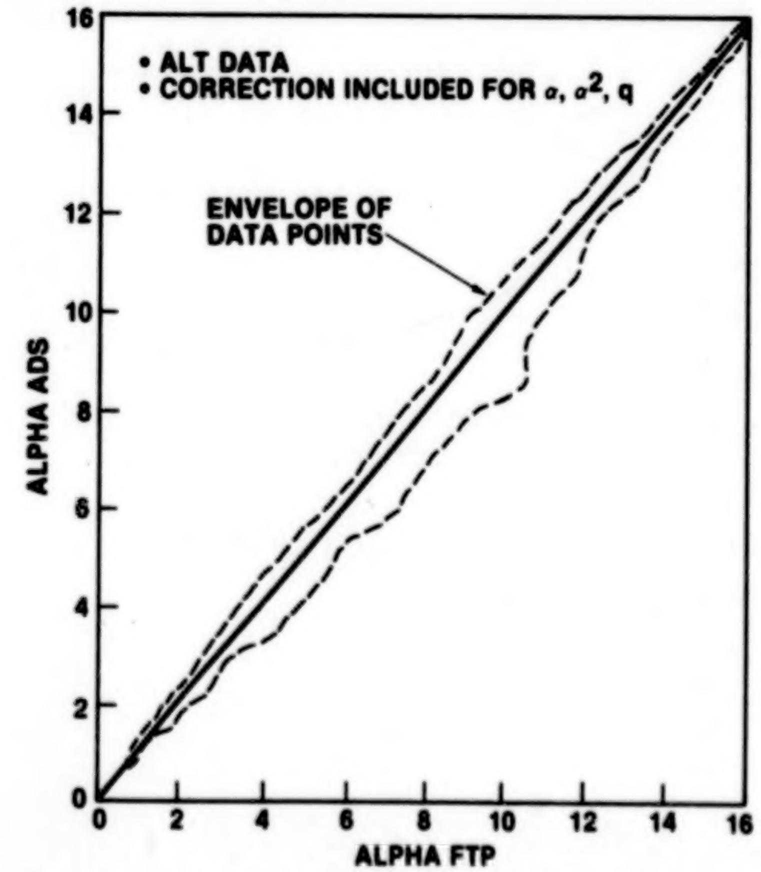

Figure 8.- Angle-of-attack comparison - ADS and FTP (corrections included).

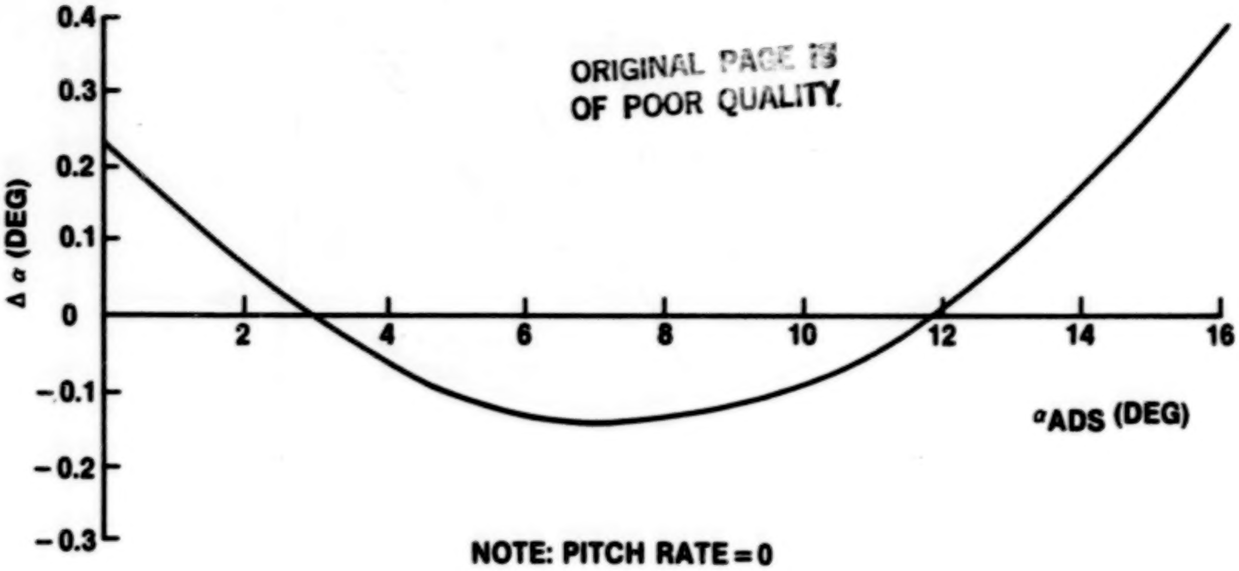

NOTE: PITCH RATE = 0

Figure 9.- Subsonic angle-of-attack correction.

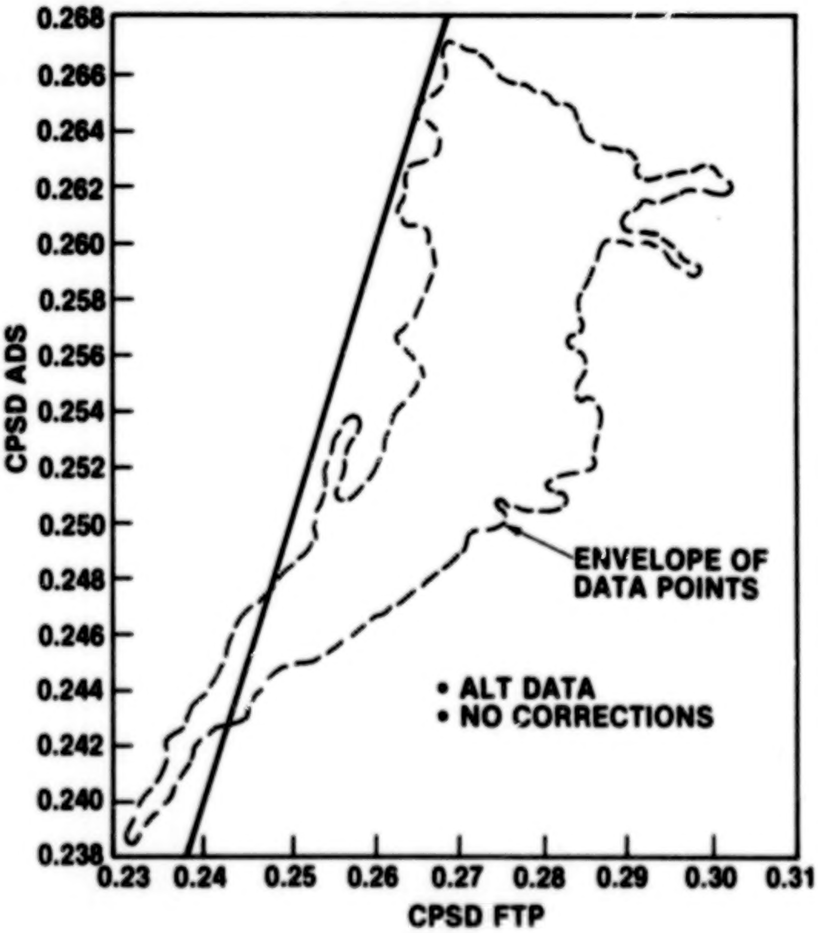

Figure 10.- Static pressure calibration coefficient comparison - ADS and FTP (no corrections).

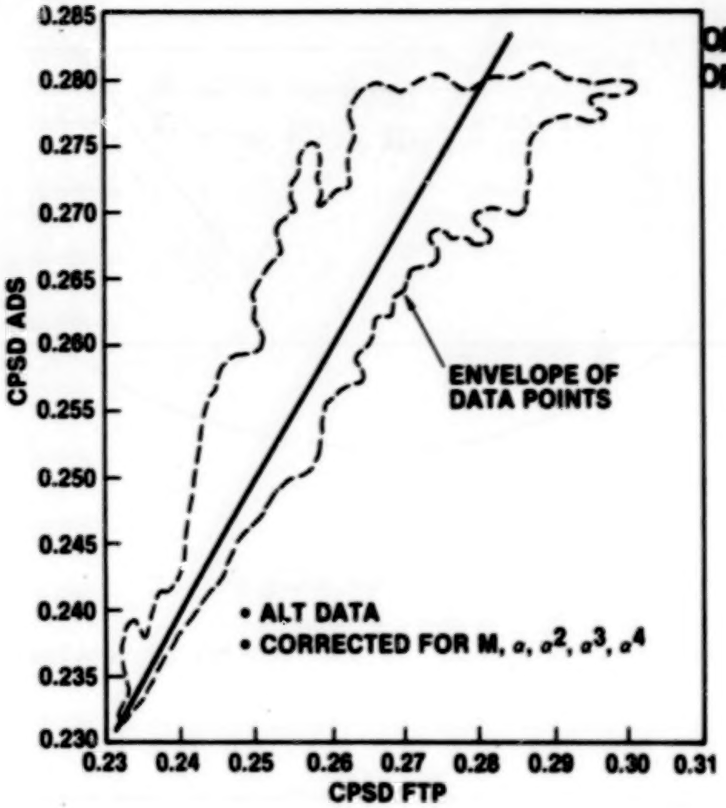

Figure 11.- Static pressure calibration coefficient comparison - ADS and FTP (including corrections).

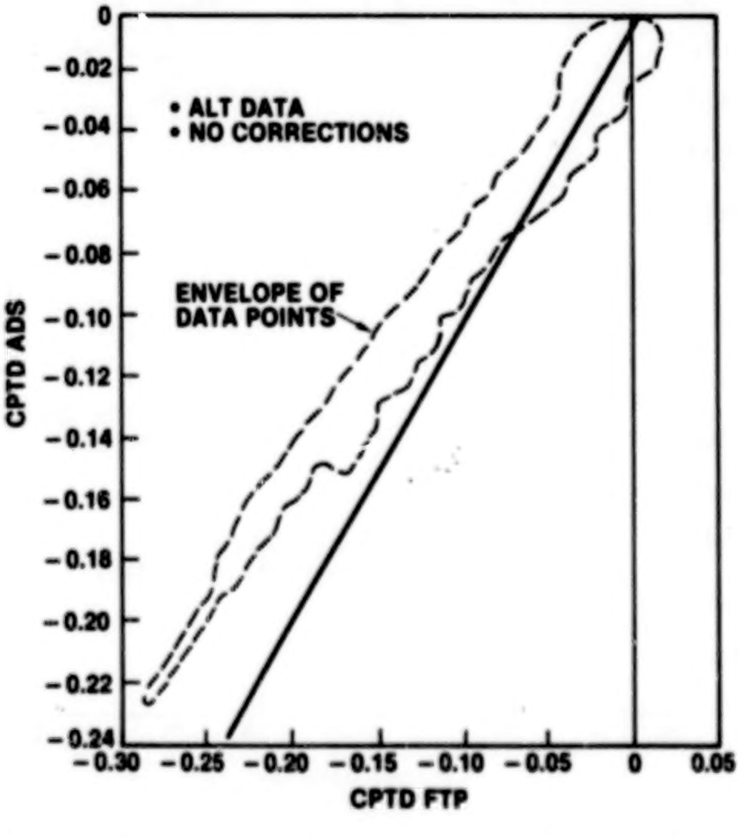

Figure 12.- Total pressure calibration coefficient comparison - ADS and FTP (no corrections).

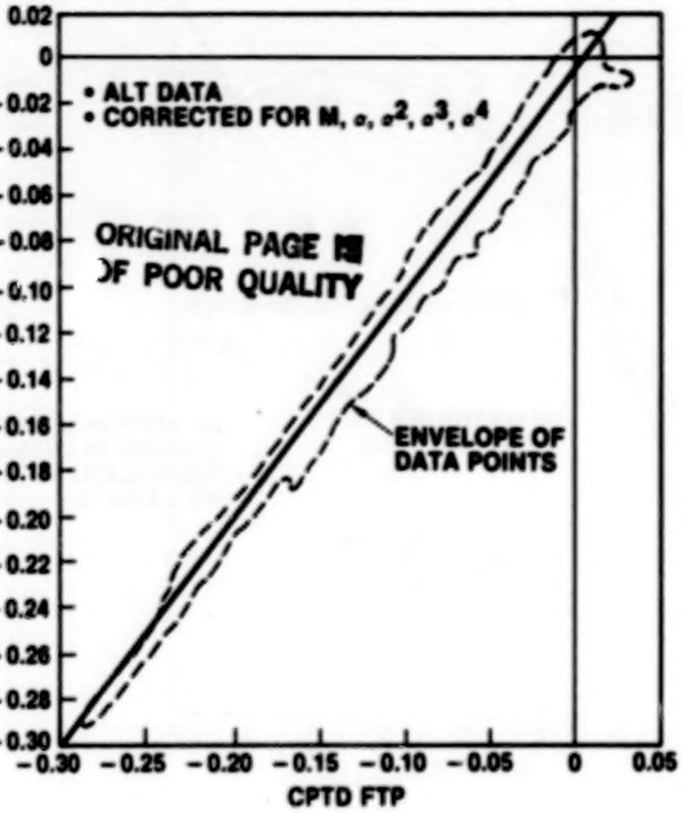

ORIGINAL PAGE IS OF POOR QUALITY

Figure 13.- Total pressure calibration coefficient comparison - ADS and FTP (including corrections).

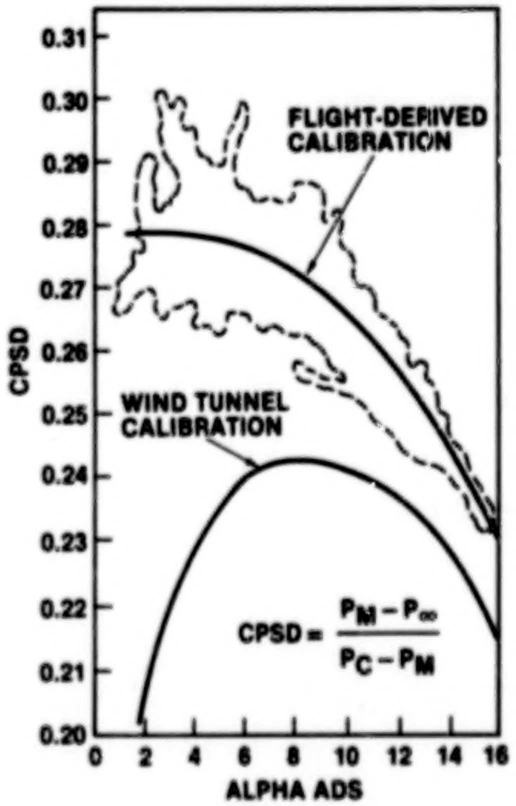

AT APPROACH SPEED (α ≈ 4), THE CHANGE IN CPSD OF ≈ 0.05 IS EQUIVALENT TO AN AIR SPEED OF 4 KNOTS.

Figure 14.- Comparison of wind-tunnel and flight-derived static pressure calibrations (ALT flight data).

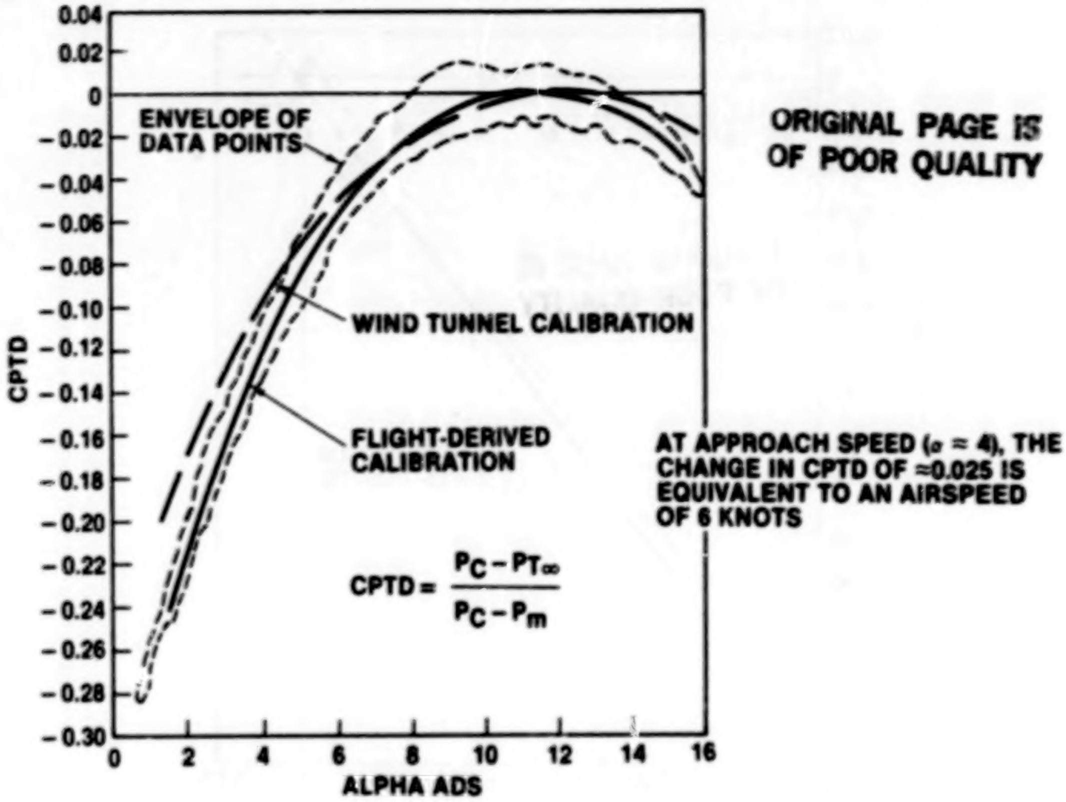

Figure 15.- Comparison of wind-tunnel and flight-derived total pressure calibration (ALT flight data).

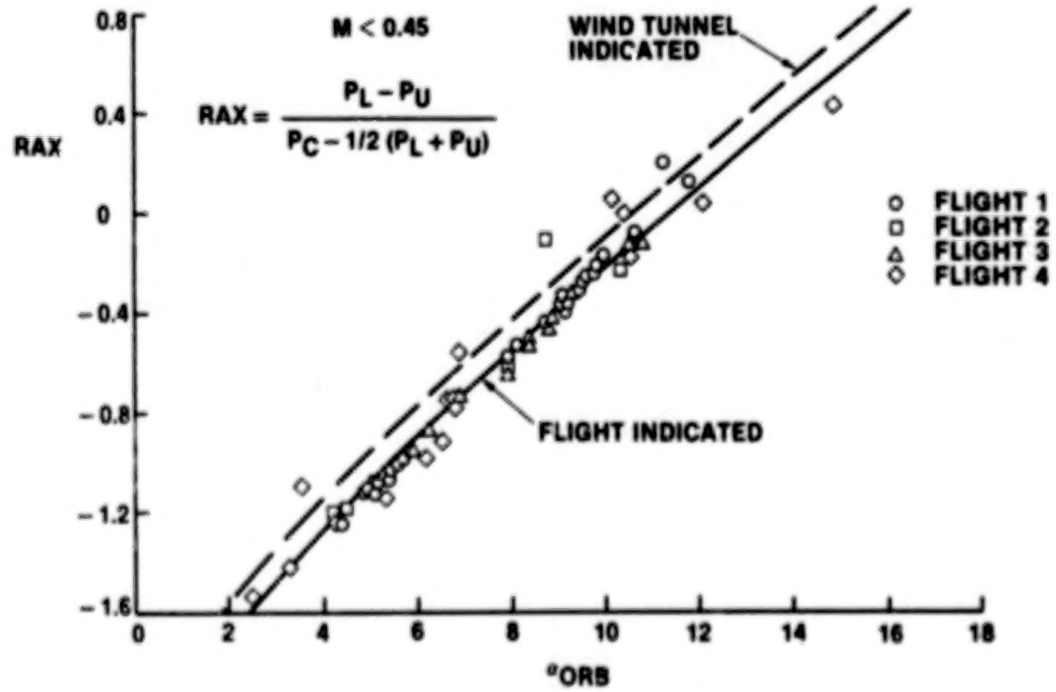

Figure 16.- Comparison of the angle-of-attack calibration and ALT results.

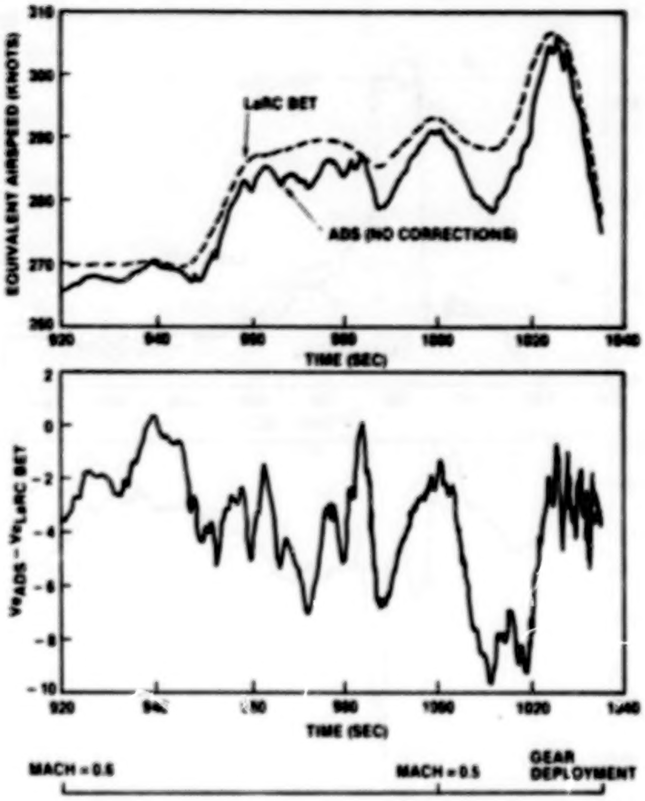

Figure 17.- STS-1 equivalent airspeed comparison - ADS and LaRC BET (no corrections).

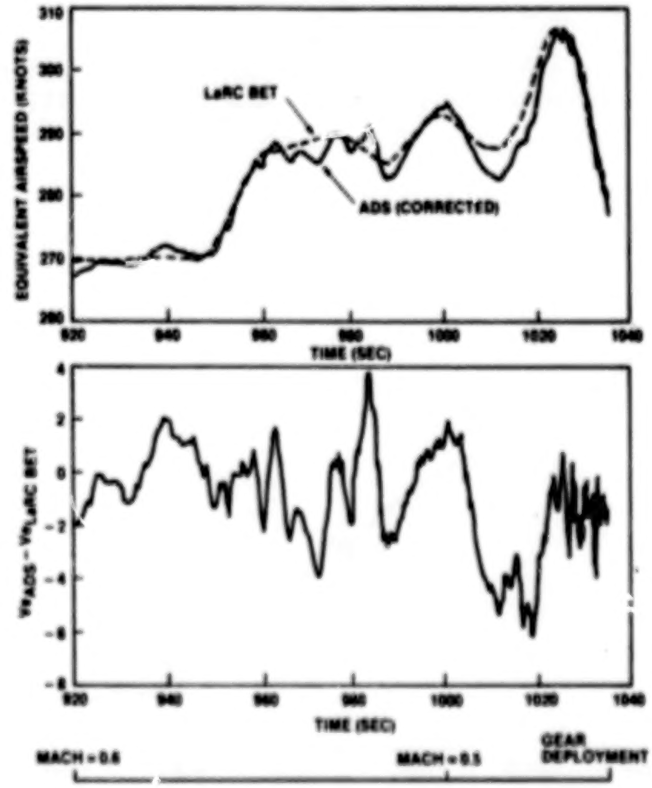

Figure 18.- STS-1 equivalent airspeed comparison - ADS and LaRC BET (including corrections).

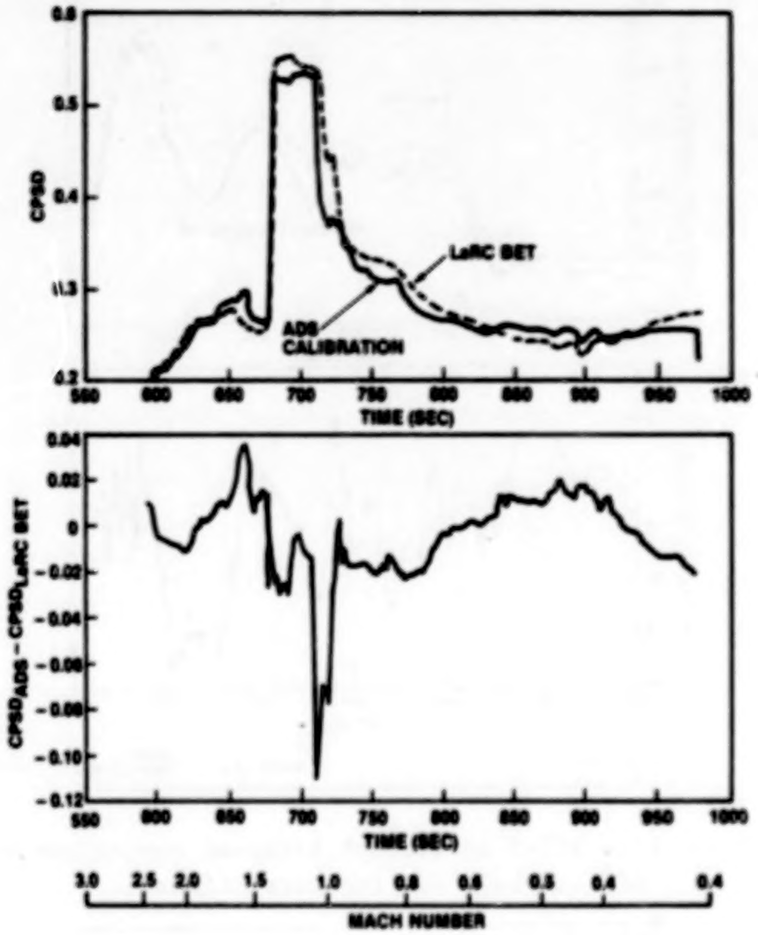

Figure 19.- STS-2 transonic static pressure calibration coefficient comparison - ADS and LaRC BET.

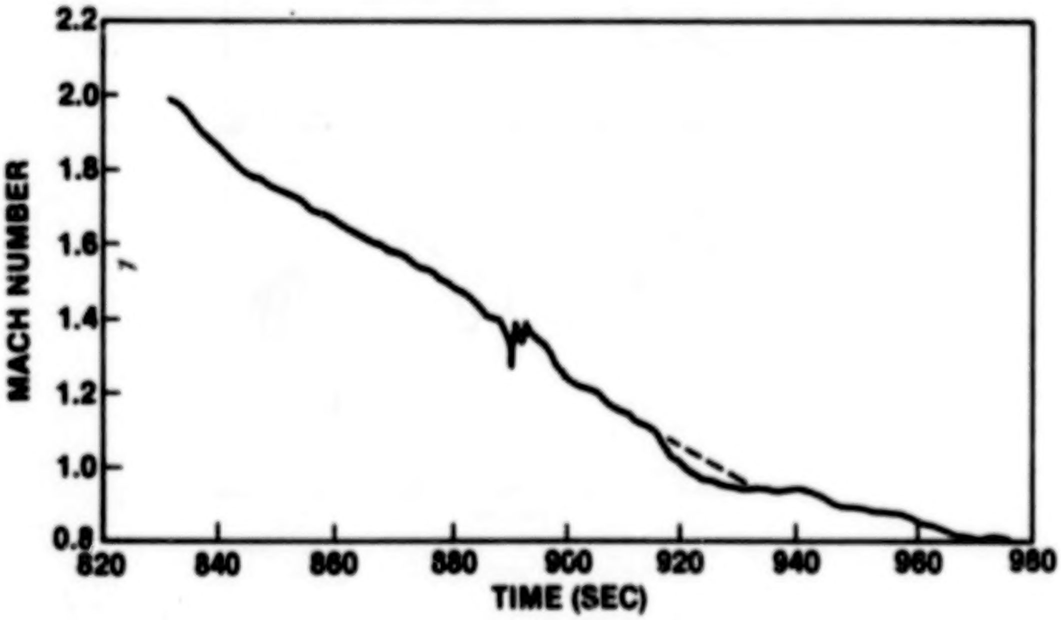

Figure 20.- STS-4 transonic ADS Mach number showing discontinuities.

ORIGINAL PAGE IS
OF POOR QUALITY

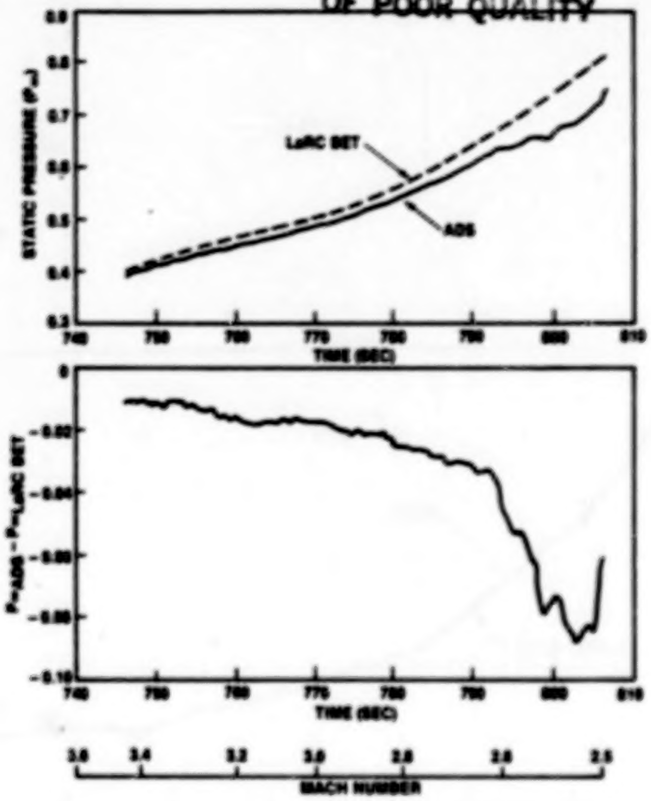

Figure 21.- STS-4 supersonic static pressure comparison - ADS and LaRC BET.

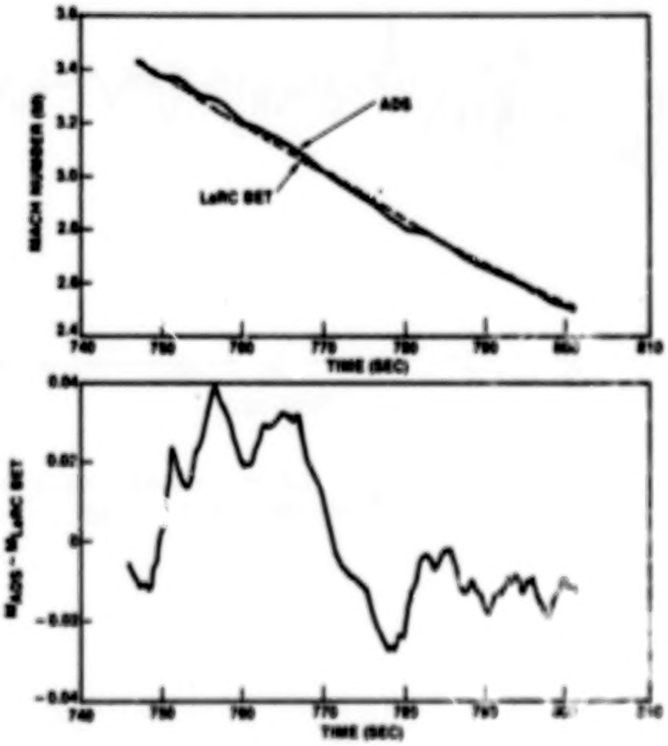

Figure 22.- STS-4 supersonic Mach number comparison - refined ADS and LaRC BET.

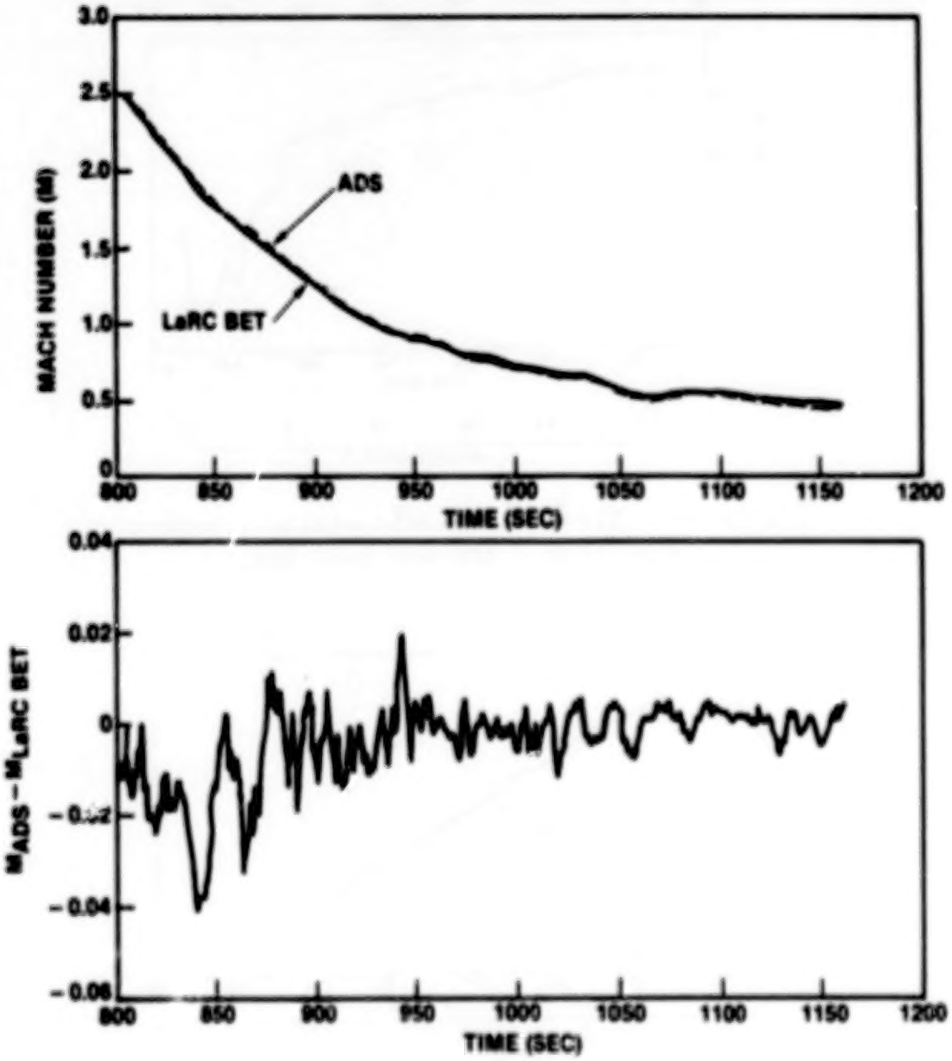

Figure 23.- STS-4 transonic and supersonic Mach number comparison - refined ADS and LaRC BET.

N84
10166

UNCLAS

N84 10166 D22

COMPILING THE SPACE SHUTTLE WIND TUNNEL DATA BASE: AN EXERCISE IN TECHNICAL AND MANAGERIAL INNOVATIONS*

N. Dale Kemp
Michoud Engineering Office
Military and Public Electronic Systems
Chrysler Corporation
New Orleans, Lousiana

ABSTRACT

Engineers evaluating Space Shuttle flight data and performance results are using a massive data base of wind tunnel test data. This data base is the result of years of extensive highly coordinated effort by NASA managers, NASA centers and contractors.

A wind tunnel test data base of the magnitude attained is a major accomplishment. It exists because of lessons learned from the Apollo program.

The Apollo program spawned an automated wind tunnel data analysis system called SADSAC developed by the Chrysler Space Division. An improved version of this system renamed DATAMAN was used by Chrysler to document analyzed wind tunnel data and data bank the test data in standardized formats.

These analysis documents, associated computer graphics and standard formatted data were disseminated nationwide to the Shuttle technical community. These outputs became the basis for substantiating and certifying the flight worthiness of the Space Shuttle and for improving future designs.

As an aid to future programs this paper documents the lessons learned in compiling the massive wind tunnel test data base for developing the Space Shuttle. In particular, innovative managerial and technical concepts evolved in the course of conceiving and developing this successful DATAMAN system and the methods and organization for applying the system are presented.

INTRODUCTION

Background

As early as 1970, farsighted NASA engineers of the Space Shuttle Aerothermodynamic Test Data panel resolved that regarding wind tunnel test data, circumstances of the Apollo program would not be repeated.

***The work reported here was performed for NASA Johnson Space Center, Houston, Texas, under contracts NAS9-13247 and NAS9-16283.**

C-7

As the Apollo program progressed to flight status, engineers substantiating flight data were hindered because of lack of corroborating wind tunnel data. This lack was not because data had not been acquired.

Extensive wind tunnel data had been acquired over the life of the program at a great expenditure of effort and money. The documentation and preservation of the test data, however, were not as extensive as the test program.

Changing Perceptions

Perceptions or attitudes regarding the value of documenting test data analyses evolved because of increased complexities, technical and managerial. Launch, reentry, cruise, and landing design conditions dictated a wind tunnel test program unparalleled in complexity and in data quantities. Engineers perceived the need for revamping the traditional approach of applying test results today and documenting tomorrow - or the day after that - or never.

Changing Circumstances

Performing the Space Shuttle engineering analyses were NASA and contractor personnel from coast to coast. Clearly, it was mandatory that a means be provided for accurately communicating and sharing the extensive wind tunnel data base that was to be the basis of a nationwide engineering development effort.

Purpose

For the Space Shuttle program, the engineers comprising the Aerothermodynamic Test Data panel proposed that all test data acquired would be collected at a central point, that these data would be put in standard forms for preserving and communicating these data to the technical elements of the Shuttle community, and that basic analyses of all tests would be performed, the results documented and disseminated as referenceable reports, and the data be put on file for ready accessing.

For the Space Shuttle they determined to be able to substantiate and certify the aerodynamic design data on the basis of documented and available wind tunnel data. For the Space Shuttle a comprehensive data base of both ground-based facility test results and flight measurements would be preserved as a basis for improving future designs. The objective was to obtain optimum benefits from the wind tunnel test program.

Current Applications

That these goals were attained is evidenced by ongoing flight data analysis work. Currently flight evaluation work is extensively referencing the wind tunnel test data base. The aerodynamic design data base (ADDB) is a synthesis of hundreds of wind tunnel test results, all of which are documented and referenceable.

Data for over 527 Phase C/D wind tunnel tests are in a data bank available to Shuttle design team members. These data are documented and the reports disseminated to the technical community. These wind tunnel test data have been preserved, documented and made widely available at a modest cost.

How did NASA manage to achieve those goals - and achieve them at a modest cost? That is the answer - they "managed" it.

COMPILING AND DOCUMENTING THE WIND TUNNEL TEST DATA BASE

The wind tunnel test data base is the product of highly coordinated efforts of NASA engineers, NASA and contractor test centers, and contractor engineers all working in the context of a system. A key factor in the success of the system is the innovative management approach implemented by NASA in directing these combined efforts. These NASA management concepts are discussed.

A particular innovation was the concept of a focal point for documenting and disseminating test data analyses. Chrysler Corporation's Data Management Services unit, selected as the focal point, also contributed advanced technical and managerial techniques to the effort.

A particularly innovative and advanced concept is the DATAMAN system, the computer system developed and used by Chrysler for automated data handling and computer graphics. This system is discussed, as are the organization and methods developed to perform the data documentation process. A brief description of some of the contributions of the data management operation to the Shuttle design effort and an evaluation of cost effectiveness are presented.

The managerial contributions of both NASA and Chrysler provided the essential environment which encouraged technical innovation. These management approaches are described as a prelude to the technical descriptions.

MANAGEMENT CONCEPTS

NASA Data Base Concepts

Major factors in the successful development of the wind tunnel test data base were the management concepts adopted by NASA. A principal concept was that of mutual interchange of all data acquired. Another was the commitment of documenting data analyses and disseminating data analysis reports to the technical community. Formatting all data to standards and preserving the data in a central data base were also key developments. These concepts were the outgrowth of deliberations of a central body of managers and engineers, the Aerothermodynamic Test Panel.

Aerothermodynamic Test Panel

The Aerothermodynamic Test Panel was established as a coordination and liaison body. Its role was to pull together and provide central direction to the diverse and multi-faceted efforts of NASA centers, the many wind tunnel complexes, the major contractors, and the engineers and managers of these entities in the pursuit of test data for supporting the aerothermodynamic design of the Space Shuttle.

The Aerothermodynamic Test Panel adopted the concept of developing a wind tunnel test data base, and assumed responsibility for achieving it. A commitment was made by all parties involved to cooperate to achieve a data base. A pivotal innovation was the decision to fully interchange all wind tunnel test data acquired.

Data Interchange

Each NASA center agreed to make all Shuttle data acquired in its facilities immediately available to a data center. Accordingly, these data would be converted to standard formats and displays and distributed to all parties involved in the Shuttle design and development.

For Phase B, all contractors participating in the Space Shuttle development were to make all wind tunnel data acquired at government expense available to NASA. These data were then made available to all NASA centers and participating contractors. Thus, the Shuttle development benefitted from a rich cross-fertilization of data uniformly available to all.

Similarly, for Phase C/D, all data were communal property of the Shuttle design and development team. The principals, Rockwell, the prime contractor, and NASA Centers (Ames, Johnson, Langley and Marshall) were provided uniformly all wind tunnel test data available. These participants were enabled to simultaneously and uniformly view wind tunnel data transformed to standardized analysis formats.

CENTRAL DATA BASE MANAGER

The Aerothermodynamic Test Panel selected Chrysler as the wind tunnel test data base documentation manager. Chrysler was selected on the basis of its development of an advanced computer-aided design system for analyzing wind tunnel test data.

The mission of the documentation manager was to be the wind tunnel test data acquisition/documentation/dissemination focal point. Chrysler was to establish standard data formats and presentation formats were established to accomplish a systematic and orderly dissemination of wind tunnel test data. Chrysler was assigned responsibilities for converting Shuttle data into the standard formats, compiling a data bank, analyzing and documenting the results, and making the data and documents available to the Shuttle design team.

For Phase B the panel assumed responsibility for ensuring cooperation of NASA centers and of participating contractors with the data base documentation manager. NASA/MSFC was the contracting agency, with Mr. C. Dale Andrews the COR. For the Phase C/D program, the data documentation contractor continued under NASA/JSC cognizance with Mr. W. C. Moseley, Jr., the COR. Figure 1 shows the relationship of the wind tunnel test program participants and the data base documentation manager.

In performing these responsibilities, the Chrysler unit continued the development of a unique system for data base management. The system is comprised of a committed engineering design team, highly advanced software systems and excellent hardware facilities, all operating in accordance with innovative management philosophies in applying advanced technical concepts.

Benefits of the NASA Management Approach

These concepts reaped many benefits for NASA. Principally, these were results of high volume data handling capability at low unit cost, benefits usually associated with mass production. It is rare that terms associated with economies of scale are applied to engineering projects. There are definite reasons, however.

The combination of the data pool, standard formatting and a central manager resulted in a synergistic high-volume data operation employing large-scale data systems operated by teams of specialists. The result was an extremely efficient data handling process with the attendant high productivity and cost effectiveness of high automated systems.

To acquire the benefits of a highly specialized organization and to develop efficient automation, the data documentation manager, Chrysler Data Management Services unit, had to be equally adept in innovating and applying advanced technical and management concepts.

Chrysler Management Precepts

The management concepts of the contractor can be put in a word: service. By Chrysler's definition, service has four aspects. These are: integrity, timeliness, usefulness, and cost efficiency.

The precepts are more than words. Their observance is mandatory because to violate any one would be to jeopardize the entire undertaking.

Foremost is concern for data integrity. Each NASA center is rightfully protective of its data to prevent misuse. Likewise, the user contractor is properly concerned about being provided compromised data. Accordingly, protecting data integrity is uppermost.

Timeliness is essential in terms of both schedule and usefulness. Hence, the data base service must speed up the user's work, not slow it down.

Usefulness is just that. The service must be an aid, not a hindrance, to the one being served. The man using the data base must perceive the data base as an improvement or an assist to his work.

Cost efficiency is reducing data analysis documentation costs and increasing productivity of the individual engineer.

Automation was perceived by Chrysler as central to attaining all aspects of the service philosophy. Accordingly, Chrysler concentrated its effort in two areas: developing a highly automated computer system for converting massive quantities of wind tunnel test data into a usable data base, and developing an organization to apply the system.

Translating these precepts into a working system and a functioning organization required extensive conceptual innovations in both computer software and engineering operations.

TECHNICAL CONCEPTS

Automated System

The Chrysler service philosophy is designed into an automated system called DATAMAN. A highly integrated computer aided design/computer aided graphics system, DATAMAN embodies unique technical concepts which continue to be state of the art.

The DATAMAN system is a pioneer in the computer aided process of converting wind tunnel data into report ready graphics. The system was initiated in 1966 as the System for Automatic Design for Static Aerodynamic Characteristics (SADSAC) under the auspices of the Saturn IB Apollo program. After the system was selected for the data base management role, the name was changed to DATAMAN to reflect the expanded role.

The DATAMAN system is fully integrated whereby all data manipulation programs and all computer graphics programs operate under a single unified system. Other design features characterize the DATAMAN system. These features and their particular contribution to the capabilities of the DATAMAN system are discussed in the following sections.

The Dataset - Key to the Unified System

The individual computational and graphics programs are unified by means of standardized data format. Communication between the generalized programs of the system is achieved through the "dataset."

The dataset is a packet of test data and associated descriptive information. It includes dimensional data required to initialize and index the system controls. The dataset contains all information and data required for program execution when accompanied by specific user instructions.

Communication between programs is accomplished when a program produces a dataset as output. That same dataset is then read as input by another program. Hence, information is communicated via the dataset.

Interface problems of data transfer between programs are eliminated. Once data are entered into the system, they can be automatically accessed for any application - computational or plotting.

Aerodynamic Data Orientation

The dataset concept is generalized in that the system is indifferent as to what data are incorporated into the dataset. Descriptions of the data and names of the variables are assigned by the user. However, the dataset structure is designed to accommodate aerodynamic related data.

Three dataset forms exist to accommodate three basic forms of aerodynamic data; force and moment data, distributed loads data, and pressure (or heat transfer) field data. This organization of the dataset is depicted in figure 2.

The dataset forms vary essentially in arraying of the variables. Force and moment datasets are bivariately arrayed, corresponding to the basic aerodynamic forcing functions, aircraft attitude and velocity. The same forcing functions apply to the loads and pressure datasets except these assume additional dimensions. Airloads datasets are trivariate - section loads distributed along a fuselage, wing, or panel axis. Pressure datasets are arrayed along an axis, as are distributed loads, and also around the body or panel.

Relationships between the aerodynamic datasets are such that integrating a pressure dataset produces a distributed loads dataset. Integrating a loads dataset results in a force and moment aero data set.

Recall that though the datasets do take the form of velocity-attitude driven vectors with up to 10 coefficients included (for the force and moment datasets), the dataset is generalized. The variables can be any systematically varying set of parameters or parameter matrix whose identities are assigned by the user.

Also, means are provided for manipulating these large sets or data matrices to conform one set to another, transpose or do arithmetic operations, or plot the data. These means provide for flexibility and versatility in doing a variety of tasks on large data blocks. Also, it is a very efficient means of handling significant data quantities because these means are in the context of an integrated system.

Integrated Subsystems

Major elements of the automated system consist of four interrelated subsystems. These subsystems are a program executive, a data handling system, a plotting system, and a file management system. These constitute an integrated system. A schematic arrangement of the integrated system is shown in figure 3.

These subsystems provide the framework for all functions required for a system. The executive system provides the user command and control over operations of the other systems. Within the other subsystems reside an array of callable modular programs for performing certain tasks.

Modularity

These modular programs provide the considerable flexibility of the system and greatly facilitate the addition of capability. This is because each modular program does only a specific task - a specific module for a specific requirement.

What this means is a given task can be programmed into a specific module. Only the specialized code would be required as the existing file management programs can be used to call and store the data. Existing listing and plotting routines can be used to display results. Modularity makes the system easily adaptable to many different applications that arise.

Similarly, the user applies modules selectively to process data as required. The modular programs of the force and moment data system are listed in figure 4. Note the array of categories of programs. Arithmetic, matrix handling, interpolation, and statistical are some of the generalized programs. Programs for specific tasks include those for flow field and air data systems applications. This list illustrates the versatility of the system.

With modularity,the task of data analysis becomes a "decomposition problem" - breaking the job down into a series of discrete basic arithmetic tasks. And doing the job in stepwise fashion enables the user to list or plot intermediate results for checking accuracy.

Also, because these modular functions are highly automated, they are easily set up or modified. Thus the modularity and automation of the system provide for low cost but flexible and versatile capability.

Automated Systems

Operation of the integrated subsystems is automated to a high degree. The design concept is to relieve the user of all repetitive burdens possible in favor of automated operation. Also, the system is designed to be transparent to the user.

The modularity enables the high degree of automation. As each module is restricted to specific tasks, automating these functions is simplified. Accordingly, applying the automated modules is simplified.

For computations (for example, say, interpolation) the user calls the interpolation program at the executive level. The only information required of the user is to name the identifier of the dataset to be interpolated and supply an identifier for the resultant output dataset and the values of the new variable arrays.

Similarly, for plotting, selecting a particular plot module calls for a particular preprogrammed plot format. The only user information required is the identifier of the input dataset. Plots will be generated automatically for all the variables in the dataset on self-scaled grids, a single frame on the page, with the axes labelled by the variable names imbedded in the dataset.

Options can be introduced by the user to custom tailor his plot to his particular needs. These include designated grid increments and ranges, frame layout, custom axes labels and plot titling.

The preprogrammed highly automated features of the system contribute significantly to the labor saving attributes of the system.

Data File Subsystem

File management functions are automated so that all output data of a program module are filed automatically for retrieval. Similarly, automated fetch operations are integral to each modular program for data input.

A key feature of the system is that data once on file are not altered. . For a computation operation, data from the file are read into core but the data on the file remain. Operations on the data in core result in a different valued output dataset which is written out onto the file adjacent to the original input dataset.

Thus the input dataset and the output dataset coexist on the file and are available for comparison or checking. This feature provides an audit trail and is invaluable for verifying the accuracy of the analysis.

The file management system relies extensively on random accessing techniques. A file directory of data identifiers and the corresponding absolute address enables the efficient storage of large variable length data files.

Additionally, two other design features characterize the operation of the DATAMAN system. One is a heavy reliance on default mode of operations, the other, a no-fatal-error operation feature.

Default Mode Operation

Wind tunnel test data are very individual by nature. No means of preprogramming a data analysis algorithm is known that is universally applicable to any and all wind tunnel test data.

However, a generalized program with a number of options can do very well in satisfying the various analysis requirements. The DATAMAN system is extensively optioned, and the options are exercised generally by default.

This means that the program is designed to perform as many tasks as possible and the user must exercise an option to stop an operation. The bias is deliberate and is to encourage the user to get the most out of the system, trading off computer resources for man effort to increase the productivity of the engineer.

No-Fatal-Error

The system is designed to operate with minimum fatal errors. In the event of a nominal data error, missing data, data out of range, or an improper instruction, the system generally will make note of the discrepancy and continue.

The objective is to acquire for the user a complete run-through of his task and acquire a complete set of diagnostics and error messages. To stop a run at each incident, for large data volume runs, is not conducive to obtaining timely results.

With no-fatal-errors, a job runs to completion and the user with the aid of diagnostic messages debugs his setup and resumes processing. This feature contributes to the productivity, the throughput, of the system in a large data volume environment.

System Benefits

These subsystems and system features are designed with the service concepts - data integrity, timeliness, usefulness, cost efficiency - uppermost. How these subsystems and some other design features serve these precepts is described below.

Data Integrity

All program operations are under engineer control through the program executive. Data manipulations and graphics are done only on engineer command.

No potential runaway "black box" functions are permitted. All data manipulations are discrete one step operations.

Verification is attained by automatically preserving results of all data manipulations on the file. These results are accessible for reading or plotting for visual verification. Thus, there is an audit trail which enables the engineer or manager to review or check data manipulations step by step.

Data Timeliness

The system is designed with throughput as a major criterion to accomplish timeliness. Throughput is the result of a highly interrelated system.

Interrelatedness means that, for all functions (input, operations, storage and retrieval, output), the output of one function is, through automation, the input of another. This automation feature enables large jobs comprised of successive tasks to be set up and run with minimum elapsed time.

Data Usefulness

Data to be meaningful must be completely identified. All elements of identification must be associated with the data - proper nomenclature, source and reference characteristics (lengths, areas, moment references).

The dataset provides for associating identifying information with a collection of test data for a given configuration. The association is accomplished at the time of data entry. From initial input, all identifying data descriptions and names automatically appear on all outputs (plots or tabulations). Thus all output is completely identified for proper application.

Productive and Cost Efficient Process

The dataset also provides for the system interrelatedness. This enables the productive throughput capability. The dataset contains all matrix dimensional information required to initialize a program for operating.

Each data manipulation program generates initializing data and imbeds it into the output where it initializes the next successive program. Thus, one program is enabled to communicate to another without user intervention, thereby achieving the highly productive labor-saving automated system operation.

Heavy reliance on default operating modes is another system feature. The default mode enables fast job setup and execution with a minimum of input, and attendant labor saving. Another key system design concept in achieving maximum throughput and high productivity is the no-fatal-error concept.

The system is designed to continue operating to completion when errors are detected. This is to overcome time consuming consequences of jobs terminating because of sequential failures. Thus an engineer is enabled to evaluate the entire job in a single pass, saving considerable time and effort.

The labor saving automated systems not only increase engineering productivity, but contribute significantly to compressing engineering schedules. Thus the productivity increases extend far beyond the cost savings of reduced manhours alone.

Need for Right Methods

The DATAMAN computer system has demonstrated well its considerable power and versatility and the capability to handle high volumes of data efficiently and quickly. However, as with any tool, it needs to be used properly.

It has been stated that the DATAMAN operation is a mix of men, machines, and methods. The DATAMAN system is the machine. To be effective the machine must be used by the right men using the right methods.

OPERATIONAL CONCEPTS

Best Use of the System

To realize the benefits of the DATAMAN system it must be used in a way to exploit its capabilities. Hence, the means of using the system have been designed with the same care and attention to detail as with developing the system. The operational concepts and the resulting functional organization are described below.

Operating Strategies

The Chrysler service philosophy is embodied into the operational cycle in terms of operating strategies and practices. The same philosophy is carried over into the organization which conducts operations.

To apply the precepts of integrity, timeliness, usefulness, and cost efficiency to the operations, a disciplined and organized function is required. That means simply that the work must be done in a methodical, systematic manner. The DATAMAN strategy is to consider the wind tunnel data analysis and documentation task as a process, as in manufacturing operations.

As a process, systematic organized methods can be applied to execution. The types of controls associated with process operations can be used to monitor the performance, quality and costs aspects of an engineering operation.

The application of the process concept to the task of wind tunnel data analysis documentation is the basis for the method of operations. Also, it provides the rationale for developing the functional organization and the management systems for controlling the process.

Process Concept

Process is a term usually applied to procedural manufacturing or chemical operations. Engineering analysis, on the other hand, is a series of heuristic free association activities of analysis and synthesis.

These free association activities remain in the DATAMAN process. But these creative activities are implemented by using the computer system as a multipurpose tool to automatically perform the drudge work of data handling and data graphics.

In doing the work, there are certain procedures performed that are common to all tests, regardless of the diversity of the test. This collection or sequence of common procedures becomes the process and is defined as series of distinct steps, or stages. In this context the analysis is equivalent to a manufacturing process; the work is done in well defined stages. At each stage, as the analysis becomes more complete, it takes on "value." As the work progresses through the system you have "value added" until you acquire the completed product.

Accordingly, the test data analysis process has distinct steps, each of which has an output. And the output is input to the next procedure in the sequence. Work is done on the input to increase its value. These procedures, or production activities, of the DATAMAN process and the corresponding work-in-process outputs are shown in figure 5.

The process is essentially a systematic procedure for bringing together the necessary inputs and activities required to convert wind tunnel test data to a documented analysis. This is the DATAMAN system which, though flexible, requires a high degree of discipline and methodology, which are brought about through organization.

ORGANIZATION

To systematically process wind tunnel test data into documented engineering analyses requires an organized and disciplined effort. The organization corresponds to the process functions in that the specific organizational elements are responsible for specific production phases.

Thus, the operating elements have well defined task assignments and are staffed with the corresponding specific skills. The organization is comprised of three operating elements: field engineering liaison, engineering data operations and computer systems.

Liaison is responsible for the preparatory and preprocessing phases. This includes all customer interface. This involves data coming into the organization and output going to the customer.

Engineering operations is responsible for the production phase. Operations performs the hands-on task of running data through the system to generate computer analyses and graphics. Operations also does the documentation and data banking.

Computer systems is a support function. Computer systems is responsible for all interface with the computer facility. It provides the systems for the line units: the preprocessing system for liaison to convert test data into standard formats, and the analysis system for operations to generate the applications data. Computer systems also supports the data base systems and the project management systems.

Details of the functions of the three operating units are presented in the following sections. The organizational elements and the corresponding production responsibilities are illustrated in figure 6.

OPERATIONS

The operation will be described in terms of the activities and the contributing functional organization. The outputs of each of these activities will be defined.

Quality assurance is an important element of any producing operation. And so it is in the DATAMAN operation. These quality control procedures will be detailed.

Also, tracking and monitoring systems and procedures are employed extensively to maintain schedules and control costs. These will be presented.

The relationships of the tasks, the outputs, and the quality assurance measures are shown in the network chart of figure 7. From this chart it is seen that the liaison unit begins the process by the planning and preparation activity.

Preparations

Liaison begins preparations at the time a test is scheduled. Test data and analysis requirements come through liaison which is also responsible for compiling test data information and developing analysis and graphics requirements. With these inputs liaison also develops the test data reformat specifications.

Preprocessing

Liaison, using the preprocessor computer system, converts the test data from the facility format into a standard DATAMAN format. Liaison forwards the standard formatted data and the analysis execution instructions to engineering operations for continued processing.

Computer Systems Support

Two data handling systems comprise the production systems. These are the preprocessor, the system which converts test facility data tapes into standard DATAMAN formatted tapes, and the DATAMAN system, which is the integrated data analysis system. Computer systems works hand in hand with liaison and operations to keep these systems in a high state of readiness in anticipating and preparing the ongoing test data handling requirements.

Computer systems maintains the systems to keep them current with the ongoing host facility upgrades and improvements. Additionally, with a commitment to automation there is always room for improvement - ways to save engineer time, save machine time, or improve the turnaround. So systems programmers have a continual challenge to improve the system in terms of capability, cost reduction or productivity.

Preliminary Analysis

Taking the reformatted test data tape and the analysis instructions, engineering operations conducts operations for producing the required data analysis and computer graphics. Operations engineers do the hands-on job of running the test data through the DATAMAN system.

Much of the work is checking. Analyzing the computer system diagnostic messages to make certain that good runs have been made and carefully evaluating the graphics and tabular data to make certain that the data results are valid and conform to customer specifications are part of this function.

When data results vary from plan, operations revises the analysis instruction set to correct the variance. For significant discrepancies, operations consults with liaison and the customer for direction before modifying the program instructions.

The operations engineer iterates the job to refine it to achieve the analysis and plot specifications. When satisfied that the analysis results and graphics are as specified, operations sends the output to liaison for review and forwarding to the customer.

Final Analysis

Frequently the data will not behave as the customer planned, or the customer discovers something about the data that requires different treatment or additional analysis.

This is standard operating procedure and is anticipated. The changes the customer desires are incorporated into the analysis instruction set and the job is recycled. The instruction setup is very flexible. Changes can be handled as rework or as add-on.

Operations will iterate the analysis/review cycle to satisfy the analysis and presentation requirements. Final confirmation is supplied by the customer.

Documentation Phase

Liaison is responsible for collecting the customer documentation input. Much of that comes from pretest documents - test plans, objectives, model information. The test engineer supplies commentary on test particulars. Standard facility descriptions are utilized.

Operations compiles the report, produces final computer graphics, complete with plot indexes, and integrates these and the liaison input into report format. Editing, final typing, and proofreading are all performed by operations.

Documentation Control

Report numbers are assigned by operations. Two report numbers are assigned. One is the internal document number. The other number is the contractor report number supplied by NASA. The reports are logged by STIF and listed in the STAR system by the contractor report number.

Document Distribution

Report copies are sent to designated members of the Shuttle design team. Participating NASA centers and the prime contractor are provided all documents for master files.

Reports are also sent to assigned NASA and contractor personnel according to the particular application of the data. For example, reports on orbiter heating data and ascent vehicle stability and control data will have different distributions. Distribution lists are provided by the contracting officer's representative (COR) who provides overall control of the distribution.

STIF is provided a master for further distribution on microfiche. Also, limited quantitites of reports are maintained locally for emergency distribution, again at the direction of the COR.

Data Bank

All the data are archived. Test data go into the data bank. Report material, masters, and notes go into archives.

Once the data are in the system they are always available for ongoing applications. All the test data and analysis data are maintained on magnetic tape. The data are easily accessed long after the analysis is completed. These are accessible for new applications, to compare to other tests, or to review the analysis.

Operations maintains the data bank. The data bank is always in a state of flux. It requires updating for new test data. It also requires periodic maintenance to validate current files and insure backup files. Tape library records are continually updated to reflect current data bank contents.

Test-in-Process Status Reports

Operations issues monthly processing status reports so that all involved always know the status of any tests - whether they are still in process or whether they are completed and in the data bank. Once the data enters the system, everyone is continuously made aware of its status.

Data File Contents Reports

After a test is documented, it is recorded in the Data File Contents Report. This report lists all tests and corresponding documents for completed tests.

These two documents, the Test-in-Process Status Report and the Data File Contents Report, are distributed throughout the Shuttle community. These reports provide current information on all Space Shuttle wind tunnel tests that have been conducted, the test particulars and the status and availability of the data.

These report contents are illustrated in figure 8.

Quality Assurance

As a test-in-process moves through liaison to operations, then back to liaison, quality reviews are made at each interface. Every time a work-in-process package is handed over to the next production phase, a quality review is made.

In-process quality checks result in minimized rework. Also, it is more efficient to inspect the work while it's evolving with reduced risk of overlooking a discrepancy.

Initial Quality Review

The first quality review occurs at the first interface between liaison and operations. Before liaison releases reformatted data, the liaison engineer carefully compares the reformatted data to insure an accurate translation and to insure compliance with the run collation specification. Also, he confirms that the analysis instruction set is consistent with data as collated. On completion, the output is released to operations as certified input.

In case of a discrepancy, a data discrepancy report is issued. This is a quality control document that becomes a permanent record of that test file.

Second Quality Review

As operations produce analysis data and presentation plots, they thoroughly review them for engineering accuracy and compliance with customer requirements. When satisfied, they release them to liaison for a final review and relay to the customer.

Documentation Quality Check

The final quality review is conducted at the documentation interface. As final analysis and graphics are produced, they are incorporated into a data report.

Before publication a double review is performed. The document is reviewed by both engineering operations and liaison, once before the report is sent to be printed and once after the report is printed. The review before printing is to insure compliance with customer specifications and compliance with sound engineering practice. The after-printing review is to insure that the report was printed "as prepared" and to insure legibility.

Tracking and Monitoring Work-in-Process

Tracking and monitoring a test in the documentation process is done using a test status log system. The summary status conditions are reported monthly by milestones. Costs are tracked and collected according to function and task.

Test Status Log

For each test a history is maintained detailing significant events in the processing life, good or bad. Dates of milestone events are recorded.

An automated status system develops a comprehensive status history report for all tests in the system. Also, it provides a milestone summary for all tests. This information is provided to the Shuttle community for data availability awareness.

Milestone Summary Report

The tests are categorized by milestone status in the processing cycle. A typical status summary report is shown in figure 9. Progress of a test is tracked by monitoring its movement from one milestone status to another.

Test status fluctuates between active and inactive as holds develop for inputs or for response to outputs. Status condition is evaluated by comparing the movement of a test status to planned norms which allow for holds.

It is difficult to establish norms as all tests are different. But expectations can be established for tests of similar complexity. Therefore, for each test an expected complexity level is established. The complexity level establishes the planning cycle norms and the budget plan for that test.

Cost Collection

Cost tracking comes from a companion system to the status monitoring system. Liaison is responsible for initiating all management controls. Tracking begins at the time a test is scheduled. At that time the test is assigned a test ID, a unique two-character identifier, which is imbedded in the label of every dataset.

The identifier preserves uniqueness for dataset names in the data file and prevents wrong data from being accessed. Liaison maintains a master log of ID's assigned and those to be assigned. The master log is prepared in advance, with ID preassigned to facilities and assigned as tests are scheduled at the facility.

Work Breakdown Structure

The work activities, the tasks that are performed by liaison and operations and the support provided by computer systems, have been described. These activities define the work breakdown structure.

The WBS task is related to a particular test through the test ID. The combination of WBS number and the test ID as a charge number is the basis for a cost collection system. The charge number associates the test being worked on with the kind of work being done. Daily time charges are compiled, collected and reported to provide cost analysis data for the work-in-process.

Task and Support Work

The WBS is two-tiered. One tier is for measuring effort expended on a specific test. The other tier is for measuring work expended in support.

Task effort is defined as work on a specifically identifiable test or task. Support effort is the myriad of activities from coordination meetings to logging data tapes to archiving accumulated test files.

Data base management tasks (maintaining the data base and servicing access requests) are also classified as support tasks, as are the test status reporting and project reporting tasks, the standard station-keeping chores that attend an organized activity.

Additionally, the automated DATAMAN systems require support personnel and support effort to maintain the systems. Support effort is also utilized to add new capability to meet user needs or improve efficiency.

The process operation also requires a highly coordinated stream of inputs. These coordination tasks with the various data sources are support activities.

The WBS is further divided into subtasks. Manhour expenditures are collected by function (liaison, operations, or programming) and by level (task or support, including the specific subtask). The WBS subtask matrices for task and support levels are shown in figure 10.

Cost Control

Cost control is aided by awareness of the distribution of manhour expenditures. Also, this knowledge provides guidance in determining need for improved or additional automation. A third contribution of the cost collection system to management is that cost data provide essential forecasting and planning information.

Similarly, computer resource costs are compiled according to task activity and test ID. Knowing the manhours and computer resources expended provides a basis for controlling current expenditures and forecasting future costs.

Knowing what test or what task is consuming manhours or computer time enables the manager to spot opportunities for improvement, either in personnel or procedures or in systems.

These management tools, in conjunction with the automated DATAMAN systems and systematic operations, have enabled Chrysler to provide a highly productive, low-cost data analysis service in behalf of the Space Shuttle.

These contributions to the Space Shuttle design effort will be examined in detail in a following section. But one more vital element in the production process will be detailed and that element is the computer facility.

COMPUTER FACILITIES

Capable computer facilities and facility operations are essential to successful data management services. The NASA Slidell Computer Complex is the capable facility utilized by DATAMAN services.

Management Philosophy

A fundamental reason why the Slidell Computer Complex is termed capable is the resident NASA management and their management philosophy. The management philosophy, in a word, is service.

Because of their particular circumstances as a satellite center servicing the remote sites of Michoud and the Mississippi Test Facility, the NASA management clearly perceives its primary duty as providing service. The service philosophy is manifested equally in the two major operating elements, excellent facilities and effective operators.

Computer Equipment

UNIVAC 1100 series mainframes are the CPU systems used for data base operations. These systems have been continuously upgraded beginning with the advanced 1108 (Exec 8) system in 1970 to the current top line system 1100/82.

Graphics

The computer graphics device in use at the Slidell center is the Information International FR-80 system. Coupled with the FR-80, which produces fiche, is the Xerox 970 copier, which produces hard copy from fiche.

The combined capacity of the FR-80/Xerox is measured in tens of thousands of frames daily. This is adequate for data base operations.

Peripherals

Careful management attention to seemingly mundane incidentals contributes significantly to facility efficiency. Two of these lesser items which contribute are peripheral systems.

One peripheral provides for automated job instructions. The other provides automated plot tape labels and instructions, including those for multi-reel files.

These peripherals, long in use at SCC, effectively automate the job control operation and overcome a production bottleneck that continues to plague many computer sites.

Facility Operations

The NASA management influences facility operations in quality day-to-day service and fast response priority service in emergency situations.

Management enforced high performance standards imposed on contractor operations provide the right climate for service oriented data base operations. Rapid NASA management attention is directed to the rare operations breakdown. Similarly, priorities are readily granted on proper justification for unusual or schedule-critical situations.

The efficiency of the SCC computer facility is attested to by the fact that no significant delays in providing data base services have ever been attributed to lack of computer support. This record has been established while the facility simultaneously supported data reduction for Skylab operations, External Tank development, Shuttle engine test programs, and Shuttle flights.

In addition to an efficient facility, another key factor is the support of the resident NASA management. These gentlemen collectively and unstintingly have seen to it that the DATAMAN operation received proper support and that this was done in a highly responsible, uncompromising manner.

EVALUATING DATAMAN OPERATIONS PERFORMANCE

Automated data systems, a skilled, integrated organization using systematic procedures, constitute the DATAMAN operation. How effectively did these elements function? What was accomplished and how well was it accomplished?

Recalling the Mission

The primary mission of the DATAMAN operation was to document and disseminate wind tunnel test data analyses. To act as a central clearing house for all wind tunnel test data, to conform the data to standard formats and to make it available to the Shuttle team were other aspects of the mission.

As the high volume DATAMAN system capabilities became known, secondary responsibilities developed. These were special considerations, usually schedule critical tasks where the special system capabilities were sorely needed. These activities were reduced, however, in 1977 because of budget constraints.

Performance can be measured in terms of shear output volume. Another performance indicator would be productivity; that is, what was accomplished with resources available. Also to be answered is how well the system responded to the varied demands of the design effort.

These performance parameters are provided below.

Data Documentation Results

Since January 1973, DATAMAN has handled over 527 NASA series number tests. These correspond to a total of 57,800 wind tunnel occupancy hours (through 1979), conducted by the prime contractor and by NASA in independent tests.

For these tests over 800 data analysis reports will be published, considering the work-in-process. These reports will involve approximately 500,000 pages. Additionally, 348 special request studies were conducted and these results documented. The total documents then will exceed 1148.

In addition to documented analyses another output was provided the Shuttle community. This was the advance data releases, principally preliminary data plots. The purpose of these preliminary plots was twofold, one, for timeliness, to make the data readily available to the user for advance applications, and the second to involve the user in evaluating the data, for data integrity. Over three million preliminary evaluation plots were delivered.

These significant output volumes, taken at face value, affirm the overall effectiveness of the Chrysler data management operation. An indicator of the system productivity is a comparison of the task load and the corresponding manning. This comparison is presented in the following section.

Task Loading

Task frequency, the number of new tasks submitted per month for handling, was highly irregular but increasing through 1976. The average task input frequency during this period exceeded 12 per month, and for three quarters of 1976 it averaged 15 per month.

The corresponding manning level for this period averaged 23. Task frequency and man levels are shown in figure 11. The task load per man then averages out to be a new task every two months per man. The implication is that with the system, a man completes a task every two months. This is a rough but reasonable indicator that the system is cost effective.

The inference is that a man analyzes a wind tunnel test, produces preliminary data plots, then final data plots, and documents and publishes the results - in two months. That same man is also performing the liaison, system maintenance and data bank station-keeping duties.

System Versatility

Volume and productivity are not the only factors, however, in evaluating system performance. The Shuttle aerothermodynamic test program involved a variety of aerodynamic and thermodynamic tests for a variety of configurations. The ability to handle the wide range of conditions encountered is a measure of system effectiveness.

Aerodynamic tests were conducted for every Shuttle configuration (ascent, external tank, SRB, orbiter entry, landing and mated carrier). These configurations were exposed to a host of perturbations - separation, proximity, component loads, pressure loads, probes, boundary layer rakes, air data system devices, blowing RCS jets, exhaust plumes, flaps, and flexible and rigid controls.

For aerothermoheating, similar tests were performed on the ascent vehicle, external tank, and SRB, both separated and in proximity. The tests included interstage heating, orbiter entry, base heating, and hot jet tests, pressure distribution tests, and obtained pressure distributions for wings, panels, flaps, control surfaces, nozzles, tail cones, external tank, and interstage.

All of these varied kinds of data were handled with the DATAMAN system. The capability of the system to contend with the array of configurations, the varied and extensive types of data and equally varied and extensive applications demonstrates that the DATAMAN system is exceedingly versatile.

The demonstrated performance verifies that the concept of the generalized dataset, a means of organizing any systematically varying collection of data, and the generalized modular data handling subprograms are sound concepts that work exceedingly well, and they work in a most challenging number of situations.

Special Applications

As the wind tunnel test program matured, the test configurations became very involved and complex. Extensive pressure measurements involved thermocouple layouts, instrumented panels, multiple-balance models, and separation/proximity tests.

Essentially, large quantities of data were being taken. Schedules were tight, resources were scarce and available manpower resources of the prime contractor and supporting NASA centers were being taxed to analyze and apply the data within the tight program schedules.

DATAMAN operations was authorized by NASA in mid-1973 to assist the prime and support groups by applying the automated data systems to perform special data applications tasks. The need was so great and the DATAMAN system capability so useful that by 1977 the special task load was larger than the test load.

Examining the list of special applications reveals the range of DATAMAN involvement. Virtually all the design areas using wind tunnel test data benefitted. These areas were the aerodynamic analyses, aerodynamic loads, aerothermodynamic analysis, air data systems, aero design data book development, RCS studies, and local flow. An extensive but not exhaustive list of various applications is compiled in figure 12.

The list shows the applications of the DATAMAN system, but it does not show the time frame or schedule considerations. Several, if not most, of the applications were in response to extremely time constrained situations in support of critical program milestone schedules.

At the end of 1977, budget factors caused a reduction in the level of special support. Funding constraints forced a choice between continuing a very effective and valuable contribution to the ongoing design effort at a high level but jeopardizing the continuation of the mainline test data analysis documentation and data base effort. The analyses documentation and data bank service were the priority choice. As a result, the special request support was severely reduced.

Special applications contributed significantly to the Shuttle design effort. These contributions were pervasive extending to virtually every design area which utilized wind tunnel data. A few samples are given to illustrate the range of application.

Aerodynamic Analysis

A typical data bank application is illustrated by the comparison curves of wing/elevon coefficients for various tunnel entries shown in figure 13(a). Datasets containing outboard hinge moment coefficients for four different tests of similar configurations have been retrieved from the data bank for operations.

These coefficients have been interpolated to common Mach, pitch, sideslip, and control surface deflection conditions. The results have been comparison plotted for evaluation.

These presentations enable the design engineer to quickly assess the relative data merits and expedite the analysis.

Thermodynamic Analysis

A data presentation method for quickly assessing interference heating effects is illustrated in figure 13(b).

Heating distributions are presented for

1) ET alone

2) ET in the presence of the orbiter and SRB's

3) Theoretical heating for the ET alone at the given test conditions

4) Interference to undisturbed heating ratios, h_i/h_u, for test to theory and for test to test.

Note that these data are a mix of measured rates and theory base computed rates.

The heating rates for undisturbed ET are presented with the rates for the ET in the presence of the orbiter. Also presented is the computed ratio of the interference data and undisturbed (h_i, h_u).

Localized areas of high heating can be quickly identified by scanning the h_i/h_u display. Thus, design engineers, after rapidly identifiying potential problem areas with the aid of the displays, are enabled to concentrate effort on solving the problems.

Pressure Load Integrations

Computed delta pressure increments across a rudder panel presented in figure 13(c) show the chordwise aerodynamic loads on a rudder panel.

These load distributions provide first order estimates for design applications.

Integrated panel pressures are integrated to produce local loads. The distributed elevon panel load variation with angle of attack is presented in figure 13(d).

The Mach number crossplot of the same elevon distributed load is presented in figure 13(e).

These two presentations of local loads enable the designer to rapidly determine potentially critical load conditions.

Wing pressures are integrated to obtain wing panel forces and moments. Figure 13(f) shows a wing root normal shear force carpet plotted for a pitch-sideslip matrix.

This matrix display visualizes component forces enabling the designer to rapidly assess the data for critical wing loads.

Demonstrated Utility

These selected samples indicate the ability of the system to handle applications of a wide range. The versatility is extremely useful in fast response, schedule-critical situations.

The system is demonstrably versatile. It is capable of very high volume operations. It contributes significantly to increasing engineering productivity.

A complete assessment of the DATAMAN contributions must include consideration of cost. What did it cost to provide these contributions, and was it worth the candle?

COST PERFORMANCE

What has it cost to analyze and document the wind tunnel test data and to provide the data bank services? For perspective, an equally important question is how much it has cost to acquire the data being analyzed and documented. Accordingly, data analysis and documentation costs are presented relative to data acquisition costs.

Assessments of input over output provide direct cost parameters. DATAMAN manhours and contract costs are the input. Data reports are the output. The distribution of manhours for the various production tasks provides insight on the productivity of the system. Therefore, an analysis of the manpower utilized is presented.

The cost data presented substantiate the claims made for the DATAMAN operation; it is an efficient system, and it does provide a low-cost means of data transfer.

Wind Tunnel Test Program Cost Estimates

Estimates for contractor model fabrication and estimated tunnel occupancy costs are $73.3 million through 1979 (reference 2). The total occupancy hours are 57,800 for tests processed by the DATAMAN system. These hours reflect 21,600 occupancy hours logged by NASA in independent efforts. No cost estimates are available for the NASA independent effort.

Note that the cost estimates are partial costs only. No manpower costs are included for model design nor for test planning or test conducting. Neither are any NASA manpower costs included.

Baseline Reference Costs

Model costs and occupancy hours, though they do not reflect total test program costs, are reasonably well behaved parameters for planning and estimating purposes. Accordingly, cost ratios of data analysis documentation costs show that every contractor dollar expended for model fabrication and tunnel occupancy required an additional 10 cents to be expended for data analysis documentation, or about one dollar for data analysis documentation for every $10 the contractor expended for model fabrication and wind tunnel occupancy (through 1979).

The corresponding manhour factor for data analysis documentation (the number of manhours required per tunnel occupancy hour) is five. For every wind tunnel occupancy hour, five manhours were required to place the test analysis documentation in the hands of the technical community.

These factors are for purposes of perspective. Perhaps a more reliable indicator would be in terms of the output; namely, the data analysis, corresponding documentation and the data bank services.

Input Over Output Factors

The total projected number of NASA series number tests to be handled exceeds 527. These, in turn, resulted or will result in approximately 800 data report volumes. Additionally, 348 special analysis tasks have also been performed and documented.

Average contract costs for these 1148 documents were $7,700 per document for the period 1973-1983. In terms of manhours, approximately 275 manhours, or about 1-3/4 man months, were required per report document.

Note that these cost parameters include not only the production costs of the data analyses, production of graphics, documentation and distribution, but included also the field liaison support and the computer programming support. Also provided for the same cost were ancillary services which included the extensive cataloging, status reporting and data base management functions. File releases of data reports, data base tapes and preliminary plot packages were also continuing activities in moving analysis data from wind tunnel to user. The costs reported include all these services.

Note that these are contract costs. Facility costs are not included. These include computer services and occupancy costs. Occupancy costs are office and utility costs. Occupancy also includes printing services of a government printing office field shop.

The distribution of costs between the data graphics production documentation and data base management activities can be seen in the WBS breakdown presented in the following section.

WBS Manhour Distributions

Manhour allocations between the various WBS functions are shown in figure 14. These allocations show where the 275 manhours were expended to analyze and document the average wind tunnel test.

The spread of effort between the production activities shows that the principal effort is data operations. Note the relatively low effort required for documentation. This is because the output of the automated data operations effort, the computer graphics and computer-generated plot indexes and legends, is incorporated directly into the document.

Note also the division of effort between two categories, task effort and support effort. The data base management functions and the status reporting functions are support only. The production functions also involve support, however.

The highly automated, highly specialized process requires expenditures of effort to maintain the automated systems and to coordinate the work flow to prevent bottlenecks in a high volume operation. These costs are compiled and identified as support costs. The hours identified as task are those expended directly on moving data through the system and out the door.

ORIGINAL PAGE IS
OF POOR QUALITY

Just how effective, then, is the DATAMAN system if it requires such support? The answer is, very.

What might appear to be buzzwords or cliches are words that accurately describe a throughput oriented process using a highly automated analysis system.

The result is a high quality product that is delivered in a timely manner, a very useful product which saves money. A conservative estimate places the savings in a range of 2-4 over alternate techniques.

SUMMARY

The wind tunnel test data analysis documentation effort has contributed significantly to the development of the Space Shuttle. The technical design and development of the Space Shuttle has been materially enhanced by the ready availability of documented wind tunnel test analysis data. Additionally, the DATAMAN operation has aided the Space Shuttle design team through timely deliveries of special data analysis to support schedule-critical program milestones.

Summarized in the following sections are the major highlights of the wind tunnel test data base effort and advancements and contributions, management and technical, realized as a result of the DATAMAN systems and operations.

NASA Management Developments

NASA centers exhibited a high degree of cooperation in participative interchange of the data via the data base. The NASA centers also benefitted by the unprecedented ready uniform availability of useful data.

NASA managers also demonstrated uncommon leadership in keeping the data base function an independent and thereby viable operation. Correspondingly, the contractor operating on service based principles provided a beneficial highly responsive service.

Technical Developments

Attaining the data base was the result of a significant number of conceptual technical innovations.

Central to the data base service is the advanced computer-aided design/graphics DATAMAN system. The conceptual design of the system and the high degree of system integration remain unduplicated.

The engineering productivity increases realized because of the system capabilities resulted in an unprecedented availability of analyzed test data to the design team (unprecedented in terms of both schedule and volume).

Organizational Developments

The very productive automated DATAMAN system enabled the analysis of wind tunnel test data at an unprecedented rate and volume. Adopting high volume production methods to utilize the system capacity resulted in an engineering analysis organization resembling a production organization.

Similarly, production-type management controls and systems and procedures enhanced operating effectiveness and abilities to operate in fast turnaround schedule-critical modes.

Data Awareness

Another result of the data base system was continuously available awareness of the existence and availability of the wind tunnel test data acquired. This information enhanced (optimized) the overall usefulness of the test data.

Data Availability

The most important result of the data base function is that the data were readily available and accessible by the Shuttle design team. Adhering to the original concepts, the test facilities consistently provided to DATAMAN operations timely test data for interchanging.

The DATAMAN operation in turn rapidly converted these data from the variety of facilities, for an array of different kinds of tests and configurations, into standardized formats and displays. These displayed data were uniformly available simultaneously to all Shuttle design participants. Thus, the data base service provided an unprecedented channel of communication for the interchange of data.

The DATAMAN capability was also utilized to provide special data operations for expediting design applications of the data. These special operations contributed significantly in attaining program milestones on a time critical schedule.

Lessons Learned

The lessons learned in compiling the Space Shuttle wind tunnel test data base can be summarized as follows:

1) The centralized data base function, responsive to both prime contractor and NASA, has successfully provided the following benefits to the success of the Space Shuttle design:

   - full and free interchange of data between all participating in Space Shuttle development

   - uniform availability of analyzed test data in a referenceable document for all Shuttle design team members

- standardized formats for enhanced usefulness of test data from over 44 facilities
- guaranteed preservation of test data for flight certification and future design applications.
- enhanced Shuttle design team through special data studies to support schedule-critical program milestones
- benefits accruing from a unified data base (i.e., extensive data retrieval, special data handling and data visualization, test-to-test comparisons, and extended test data analyses)
- complete awareness of total wind tunnel program through management information regarding test status and data

2) Maintaining the data base function as an independent entity (reporting to NASA, not a subordinate prime contractor activity) resulted in the following organizational benefits:

- single purpose mission which enhanced certainty of achieving goals of a complete data base
- high degree of responsiveness to all data users
- high visibility of test data status for improved management and control

3) Centralizing the data base function with the resultant large data volumes has provided the following technical benefits:

- impetus for developing the large-scale highly efficient data handling system (DATAMAN)
- significant cost savings because of efficient systems and economies of scale
- productivity improvements not only in the analysis of wind tunnel test data but corresponding improvements in application of test data

CONCLUSION

In conclusion, the revolutionary productivity increases in data delivery brought about by the automated DATAMAN system and the DATAMAN organization have not only significantly contributed to the successful design of the Space Shuttle, but have provided a means of low-cost data transfer which is applicable and beneficial to any wind tunnel test activity.

This has also resulted in an unprecedented accumulation of ground based facility data by which to verify the vehicle flight characteristics. Also, all the wind tunnel test data, acquired at considerable expense, are available to the technical community as a basis for improved and future designs.

When embarking on the development of the next aerodynamic systems, one question that must be asked is, "Which procedures used on the Shuttle program should be done again?" One of the answers should be the wind tunnel test data analysis/documentation, the DATAMAN system. That should be done again.

ORIGINAL PAGE IS
OF POOR QUALITY

REFERENCES

1. Kemp, N. Dale; Dave, Lynn M.; and Glynn, James L., Jr.: SADSAC Aerothermodynamic Data Management System Manual. DMS-TM-1001, Chrysler Space Division, February 1973.

2. Whitnak, A. M.; and Hillje, E. R.: Space Shuttle Wind Tunnel Testing Program. AIAA Paper Number 82-0562, March 1982.

3. Phase C Aerothermodynamics Data Base Quarterly Data File Contents Report. DMS-DFR-2094, Data Management Services, Chrysler Corporation, Huntsville Electronics Division, Michoud Engineering Office, January/March 1983.

4. Quarterly Task Status History Report. Data Management Services, Chrysler Corporation, Huntsville Electronics Division, Michoud Engineering Office, January/March 1983.

5. Daileda, J. J.: Results of Tests Using a 0.02-Scale Model (89-OTS) of the Space Shuttle Integrated Vehicle in the AEDC 16-Foot Transonic Propulsion Wind Tunnel. NASA CR-160489, April 1981.

6. Dye, W. H.; and Nutt, K. W.: Results of an Investigation of the Space Shuttle Integrated Vehicle Aerodynamic Heating Characteristics Obtained Using the 0.0175-Scale Model 60-OTS in AEDC Tunnel A During Tests IH41B. NASA CR-151069, September 1977.

7. Rudder/Speedbrake Hinge Moments for Pressure Data of Tests OA145A, B, C and OA101. Report Number SPRT9F-3, Data Management Services, Chrysler Corporation, Huntsville Electronics Division, Michoud Engineering Office, April 1981.

8. Elevon and Flipper Door Hinge Moments From Pressure Data of Test OA270A. Report Number SPRT9K, Data Management Services, Chrysler Corporation, Huntsville Electronics Division, Michoud Engineering Office, June 1981.

9. IA135 Pressure Integration 60R Wing and Vertical Tail Loads. Report Number SPRTXH, Data Mangement Services, Chrysler Corporation, Huntsville Electronics Division, Michoud Engineering Office, June 1977.

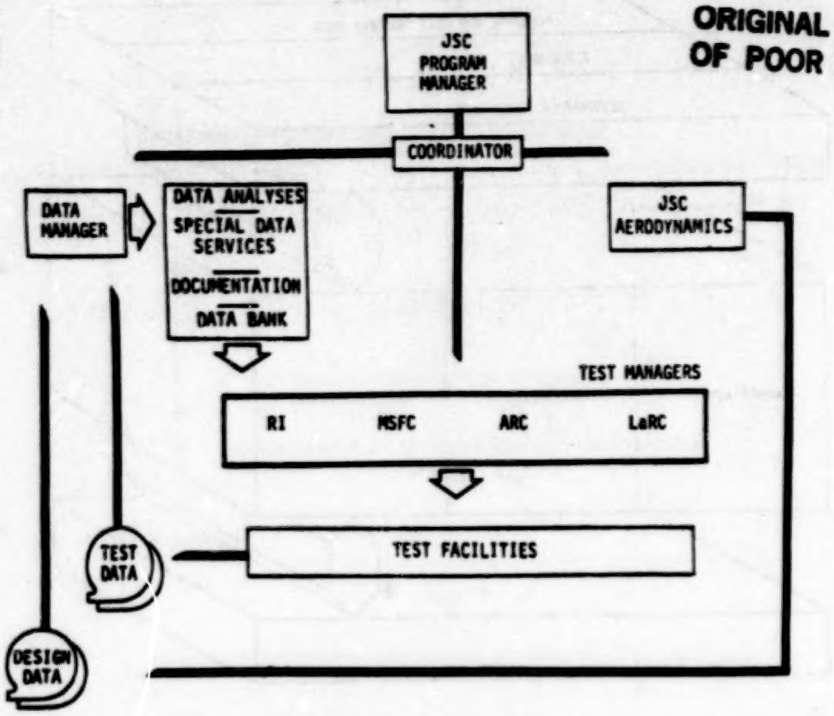

Figure 1.- Chrysler as the data analysis documentation manager services the Space Shuttle design team under the direction of JSC.

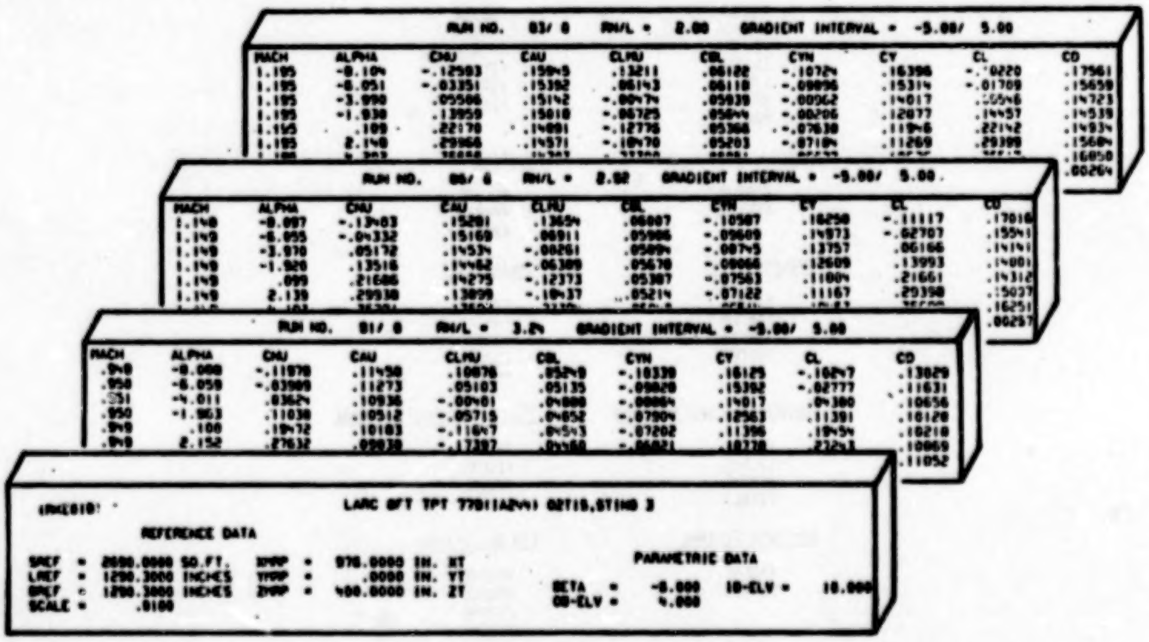

```
                    RUN NO.   03/ 0    RN/L =   2.00    GRADIENT INTERVAL =  -5.00/  5.00
MACH    ALPHA     CNU       CAU       CLMU      CBL       CYN       CY        CL        CD
1.195   -8.104    -.12593   .15945    .13211    .06122    -.10724   .16398    -.'0220   .17561
1.195   -6.051    -.03351   .15392    .06143    .06110    -.09896   .15314    -.01709   .15659
1.195   -3.990    .05506    .15142    -.00474   .05939    -.08962   .14017    .:0546    .14723
1.195   -1.930    .13959    .15010    -.06725   .05644    -.08206   .12077    .14457    .14539
1.155     .109    .22170    .14891    -.12776   .05366    -.07630   .11946    .22142    .14934
1.195    2.140    .29966    .14571    -.18470   .05203    -.07104   .11269    .29399    .15604
                                                                                        .16050
                                                                                        .00264
```

```
                    RUN NO.   08/ 0    RN/L =   2.92    GRADIENT INTERVAL =  -5.00/  5.00
MACH    ALPHA     CNU       CAU       CLMU      CBL       CYN       CY        CL        CD
1.148   -8.097    -.13403   .15281    .13654    .06007    -.10587   .16250    -.11117   .17016
1.149   -6.055    -.04332   .15169    .08911    .05986    -.09609   .14973    -.02707   .15541
1.149   -3.970    .05172    .14534    -.00261   .05894    -.08745   .13757    .06166    .14141
1.149   -1.920    .13516    .14462    -.06309   .05670    -.08066   .12609    .13993    .14001
1.149     .099    .21686    .14275    -.12373   .05387    -.07563   .11004    .21661    .14312
1.149    2.139    .29930    .13899    -.18437   .05214    -.07122   .11167    .29390    .15037
                                                                                        .16251
                                                                                        .00257
```

```
                    RUN NO.   01/ 0    RN/L =   3.24    GRADIENT INTERVAL =  -5.00/  5.00
MACH    ALPHA     CNU       CAU       CLMU      CBL       CYN       CY        CL        CD
 .940   -8.080    -.11970   .11450    .10076    .05249    -.10330   .16125    -.10247   .13029
 .950   -6.059    -.03909   .11273    .05103    .05135    -.09820   .15392    -.02777   .11631
 .951   -4.011    .03624    .10936    -.00401   .04880    -.08864   .14017    .04300    .10656
 .950   -1.963    .11030    .10512    -.05715   .04652    -.07904   .12563    .11391    .10120
 .949     .100    .19472    .10183    -.11647   .04543    -.07202   .11396    .19454    .10210
 .949    2.152    .27632    .09938    -.17397   .04460    -.06821   .10278    .27243    .10069
                                                                                        .11052
```

```
(RKE010)                     LARC 8FT TPT 7701(A2W4) O2T15,STING 3

          REFERENCE DATA

SREF  =  2690.0000 SQ.FT.   XMRP  =   976.0000 IN. XT
LREF  =  1290.3000 INCHES   YMRP  =      .0000 IN. YT          PARAMETRIC DATA
BREF  =  1290.3000 INCHES   ZMRP  =   400.0000 IN. ZT
SCALE =      .0100                                       BETA   =    -0.000   IB-ELV =    10.000
                                                         OB-ELV =     4.000
```

Figure 2.- The dataset is a collection of wind tunnel runs for the same configuration. Associated with the data are supplied identifying descriptive information and dimensional data to complete the packet.

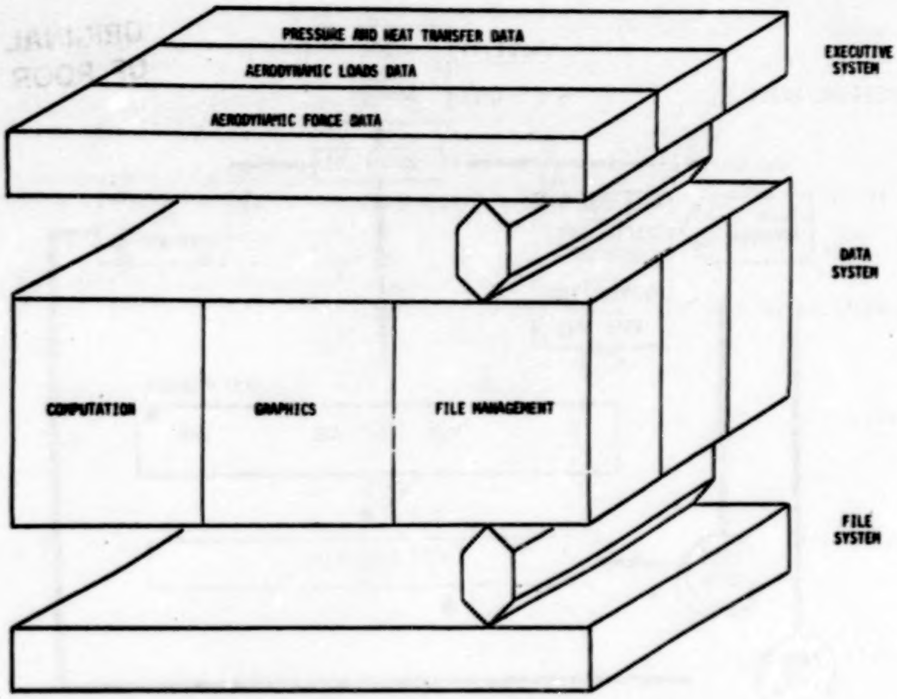
PRESSURE AND HEAT TRANSFER DATA
AERODYNAMIC LOADS DATA
AERODYNAMIC FORCE DATA
EXECUTIVE SYSTEM
DATA SYSTEM
COMPUTATION
GRAPHICS
FILE MANAGEMENT
FILE SYSTEM

Figure 3.- The DATAMAN system is an integrated system consisting of a system executive, data systems, and a file management system. It is also a unified system for processing aerodynamic pressure or heat transfer data, aerodynamic loads, and aerodynamic force data.

Arithmetic Operations

FCOMBN
FCOMPR
FCOMPT
FDERIV
FDSIGN
FPARAM
FRATIO

Matrix Operations

FADJON
FADVAR
FPSWCH
FSTACK
FSWTCH
FTRANS

Edit

FCDMOD
FCELIM

Utility

FDSDAT
FPPCON
FPUNCH

Interpolation

FANTRP
FINTRP
FPNTRP
FSNTRP

Statistical

FPOLYN
FMSTAT
FREGRS
FSIGMA
FSTATS

Aerodynamic Applications

FAXIAL
FSCALE
FCAXIS
FXTRCT

Flow Field Applications

FBLAYR
FLOCAL
FPRCAL
FPROBE

Air Data Systems

FADSAA
FBENCH

I/O Operations

FCDATB
FCDATD
FCDUMP
FCLIST
FCUPDT

Figure 4.- The modular programs of the FORCE DATA SYSTEM illustrate the range of capability and versatility of the system.

	Activity	**Result**
ENGINEERING ANALYSIS	o Planning	o Collation Plan o Analysis Specifications
DATA ENTRY	o Data Initialization o Analysis System Input	o Formatted Data Tape
DATA ANALYSIS OPERATIONS	o Engineering Analysis o Computer Graphics	o Preliminary Analysis Data o Preliminary Data Plots
ANALYSIS EVALUATION	o Inhouse Review o Customer Review	o Confirmed Analysis Data o Confirmed Data Plots
DOCUMENTATION	o Compiling/Editing o Publication/Distribution	o Engineering Report
DATA BASE MANAGEMENT	o Data Base o Document Archives	o Retrievable Data Files o Data Bank Contents Report o Status Reports

Figure 5.- The data analysis documentation operations is a systematic production process of well defined activities and outputs.

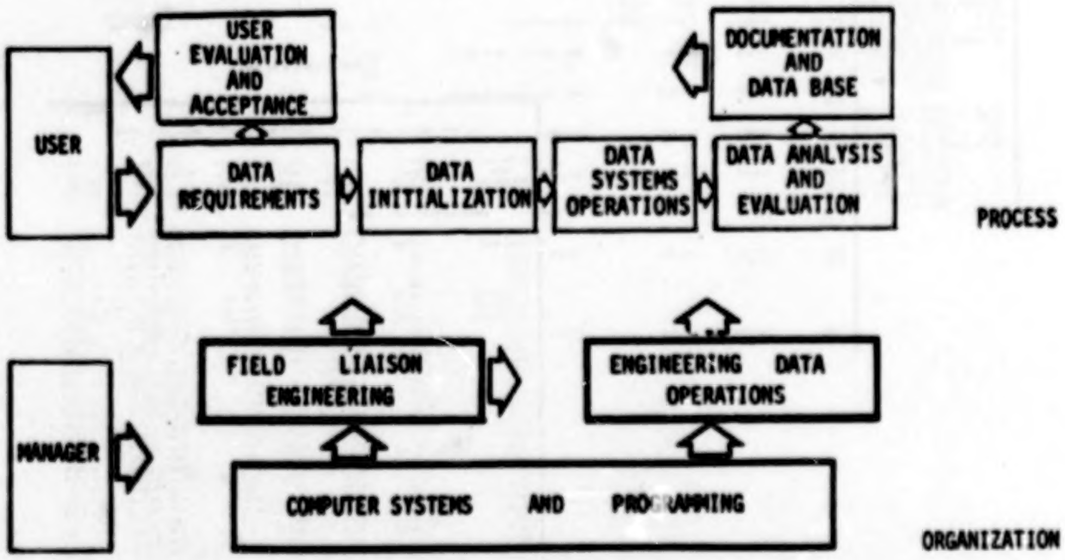
USER
USER EVALUATION AND ACCEPTANCE
DOCUMENTATION AND DATA BASE
DATA REQUIREMENTS
DATA INITIALIZATION
DATA SYSTEMS OPERATIONS
DATA ANALYSIS AND EVALUATION
PROCESS
MANAGER
FIELD LIAISON ENGINEERING
ENGINEERING DATA OPERATIONS
COMPUTER SYSTEMS AND PROGRAMMING
ORGANIZATION

Figure 6.- The DATAMAN organization parallels the analysis production process.

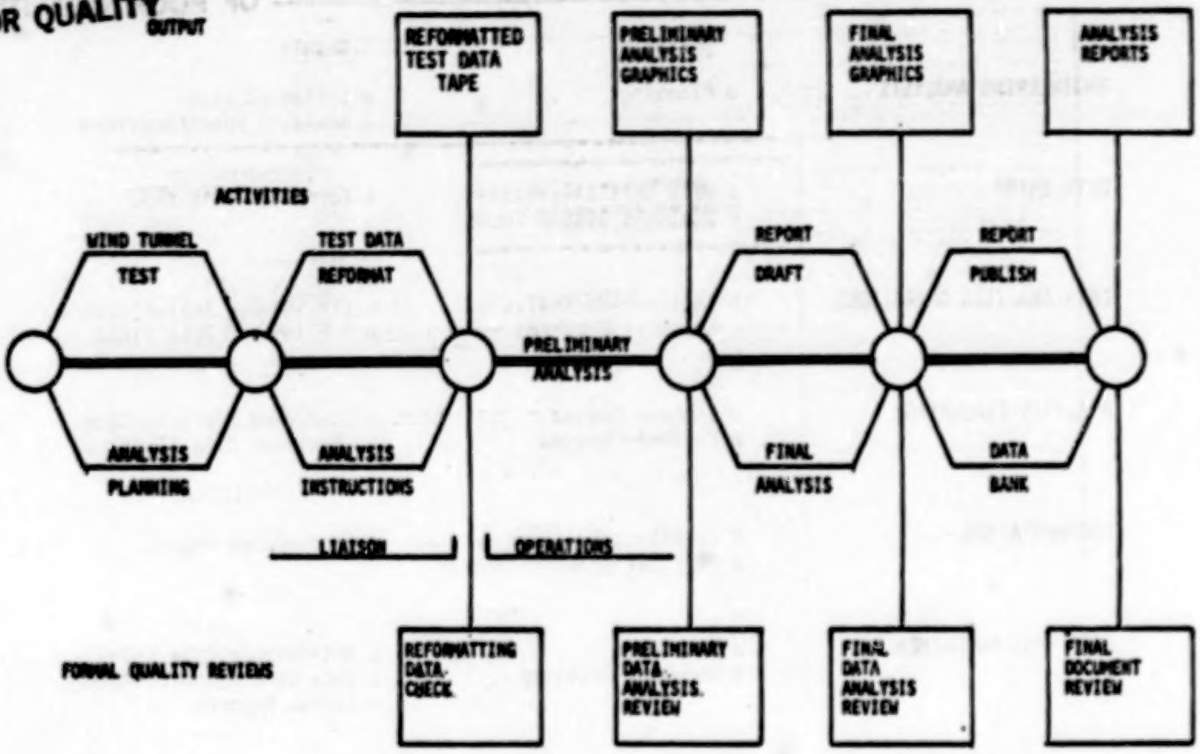
OUTPUT
REFORMATTED TEST DATA TAPE
PRELIMINARY ANALYSIS GRAPHICS
FINAL ANALYSIS GRAPHICS
ANALYSIS REPORTS
ACTIVITIES
WIND TUNNEL TEST
TEST DATA REFORMAT
PRELIMINARY ANALYSIS
REPORT DRAFT
REPORT PUBLISH
ANALYSIS PLANNING
ANALYSIS INSTRUCTIONS
FINAL ANALYSIS
DATA BANK
LIAISON
OPERATIONS
FORMAL QUALITY REVIEWS
REFORMATTING DATA CHECK
PRELIMINARY DATA ANALYSIS REVIEW
FINAL DATA ANALYSIS REVIEW
FINAL DOCUMENT REVIEW

Figure 7.- The network chart shows the relationships of the data analysis and documentation activities to the operational elements.

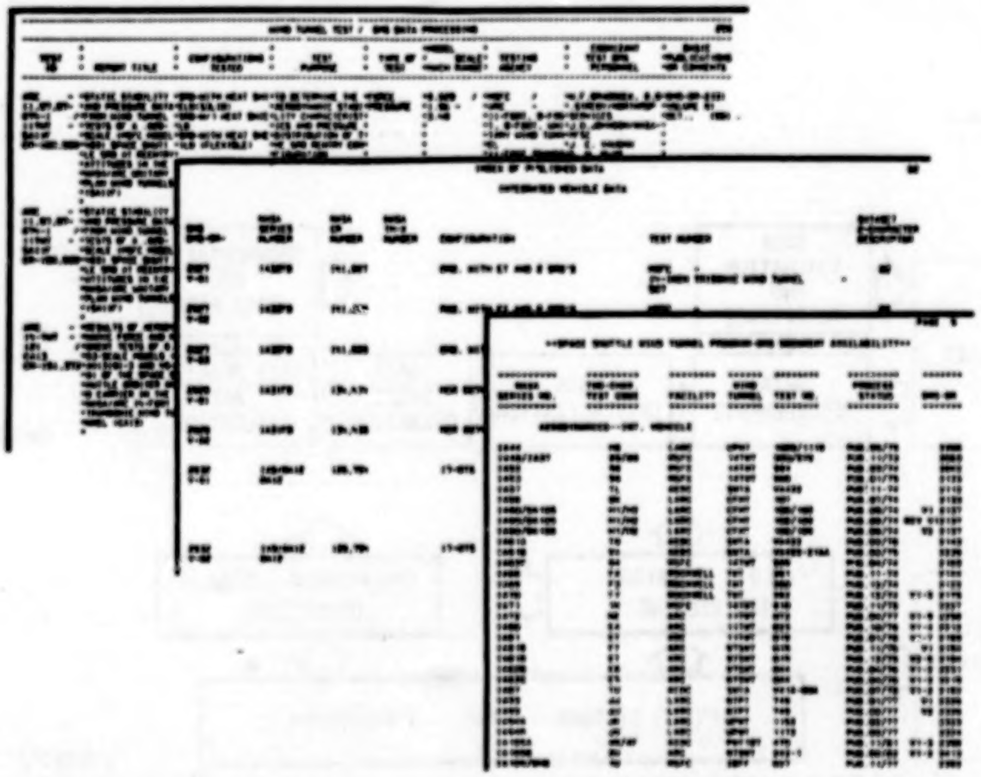

Figure 8.- The Shuttle technical community is continually made aware of data available by data bank contents reports. (From Ref. 3.)

ORIGINAL PAGE IS
OF POOR QUALITY

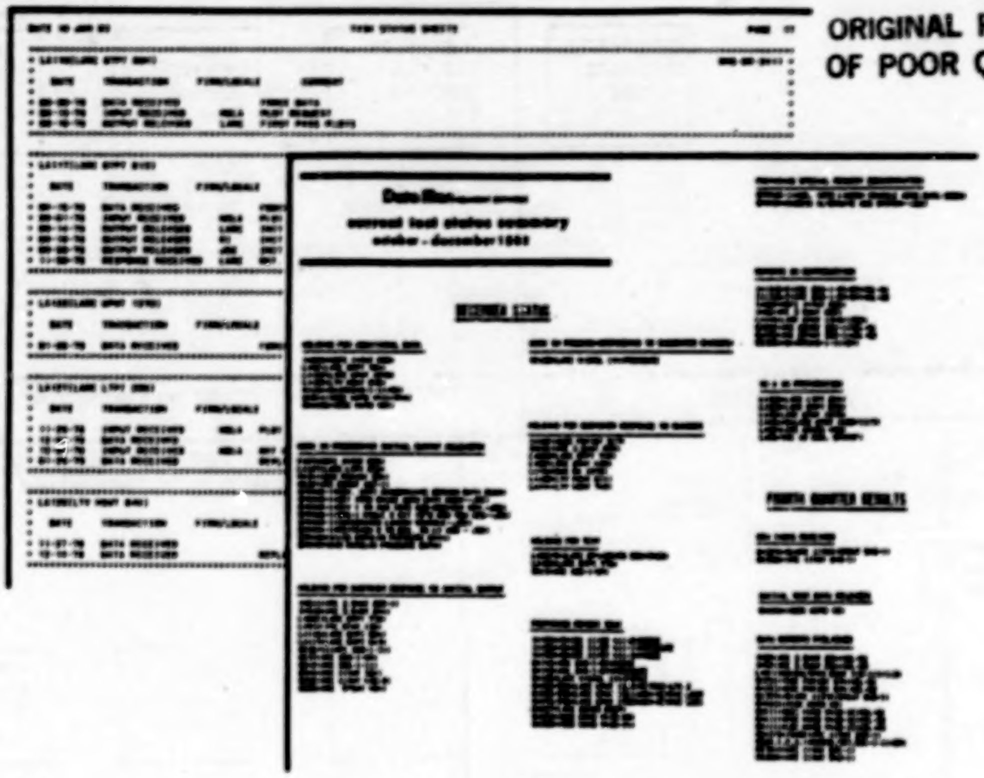

Figure 9.- Work-in-process status is communicated regularly to the Shuttle design team. (From Ref. 4.)

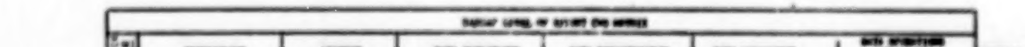
SUPPORT EFFORT
TASK EFFORT

Figure 10.- Manpower applications are tracked and collected by function and task for cost control and forecasting.

ORIGINAL PAGE IS
OF POOR QUALITY

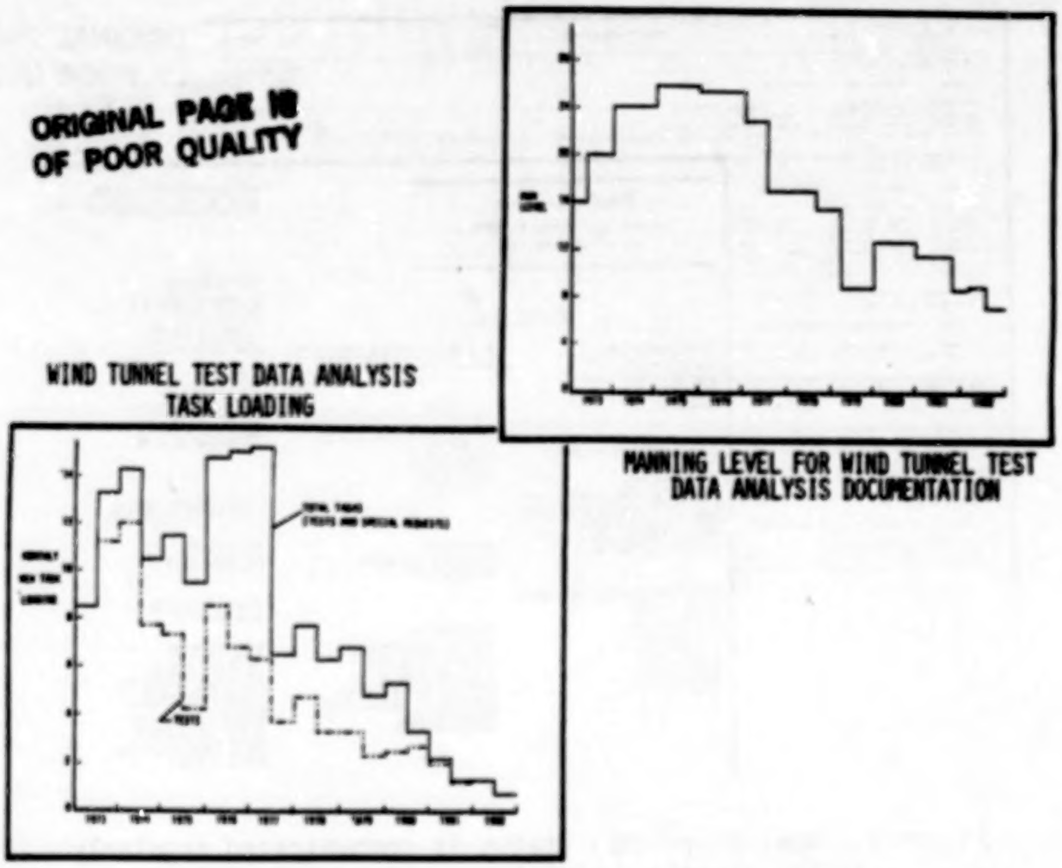
WIND TUNNEL TEST DATA ANALYSIS
TASK LOADING

MANNING LEVEL FOR WIND TUNNEL TEST
DATA ANALYSIS DOCUMENTATION

Figure 11.- Comparing manning level to task loading provides indicator of DATAMAN productivity.

AERODYNAMIC ANALYSIS

- o Test to Test Comparisons
- o Control Surface Effectiveness
- o Derivatives
- o Control Surface Interactions
- o Ground Height Increments
- o Power Increments
- o Hysteresis Displays
- o Post-test Blockage and Tare Corrections

PRESSURE LOAD INTEGRATIONS

- o Control Surface Hinge Movements
- o Protuberance Loads
- o Vehicle Component Loads
- o Nozzle Loads
- o Tailcone Loads
- o Input to NARSLAG Program

THERMODYNAMIC ANALYSIS

- o Development of Analysis Techniques
- o Test-to-Test Comparisons
- o Comparison to Theoretical
- o Mirror-Image Calculations
- o Special Displays

AIR DATA SYSTEMS

- o Algorithm Development
- o FTP Data Analysis Techniques
- o Parametric Analysis of Flush Mounted Ports
- o Composite ADS Test Databases

DESIGN DATA APPLICATIONS

- o Substantiation and Applications
- o Total and Component Coefficient Calculations
- o Update Comparisons
- o Pre-test Predictions

SPECIAL

- o Statistical Error Analysis of RCS
- o RCS Interaction Incrementing
- o Mini-Probe Calibration
- o Protuberance Flow Field Survey

MISCELLANEOUS

- o Punched card inputs to NASA programs
- o Data Tape Inputs to ADAP II
- o Data Tape Inputs to JSC/Structures
- o Data File/Data Base Releases
- o Inputs to NASA Technical Reports
- o Microfiche Documentation

Figure 12.- The DATAMAN operation provided high priority special design applications support to almost every activity using wind tunnel data.

ORIGINAL PAGE IS
OF POOR QUALITY

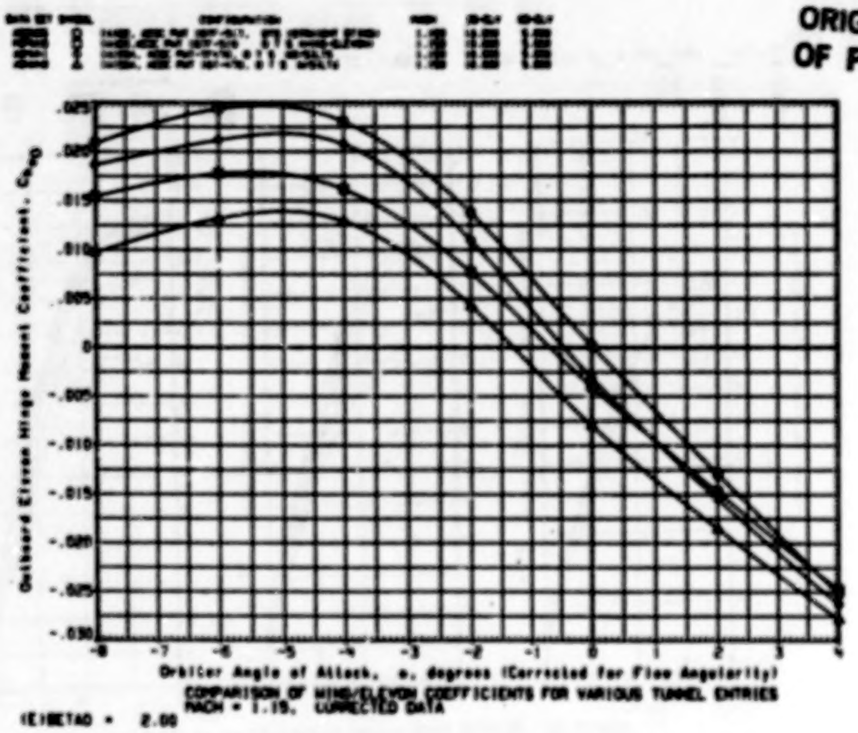

(a) Retrieved data of four tests adjusted to common conditions for comparing data for tunnel effects. (From Ref. 5.)

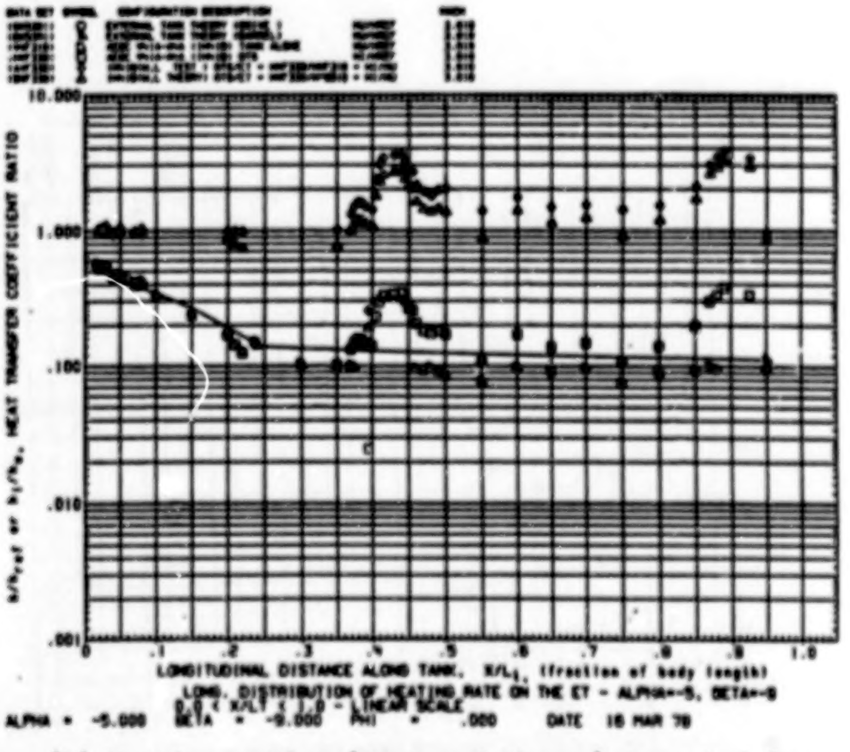

(b) Heating ratios (test and theory) computed for rapid identification of interference heating problems. (From Ref. 6.)

Figure 13.- Special applications of DATAMAN which contributed to Shuttle design effort.

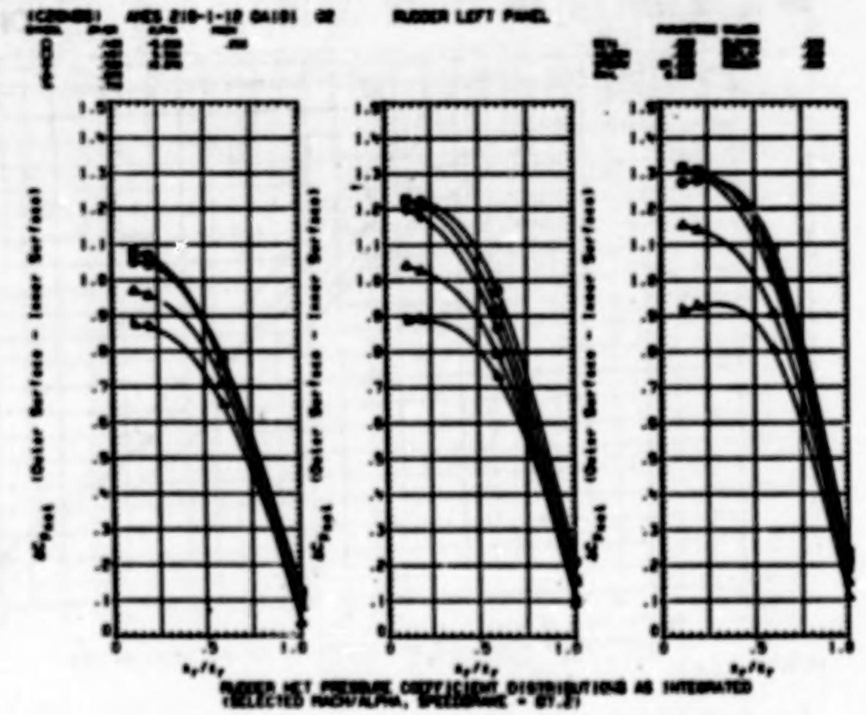

(c) Delta pressure calculations provide rapid estimates of airload distributions. (From Ref. 7.)

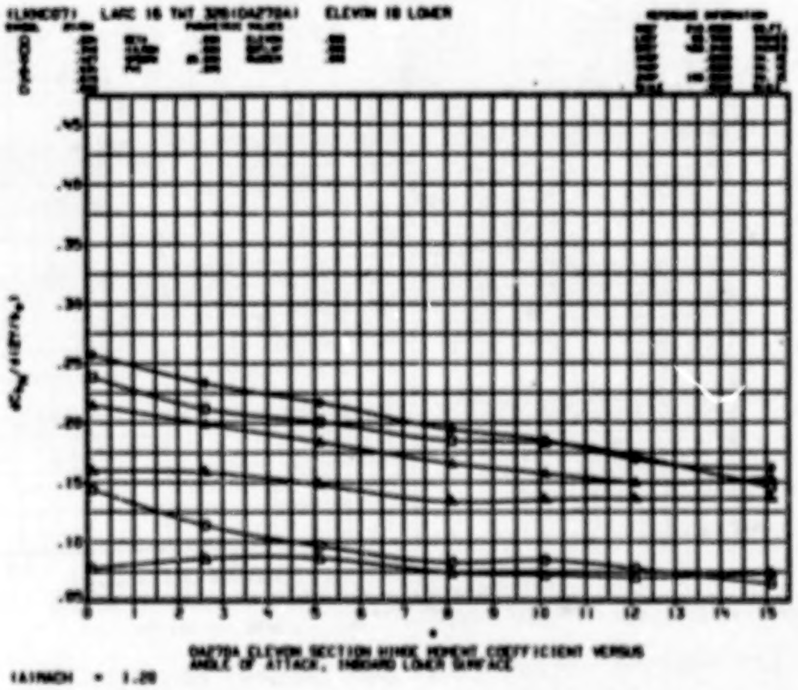

(d) Local distributed loads developed from pressure and displayed for evaluation. (From Ref. 8.)

Figure 13.- Continued.

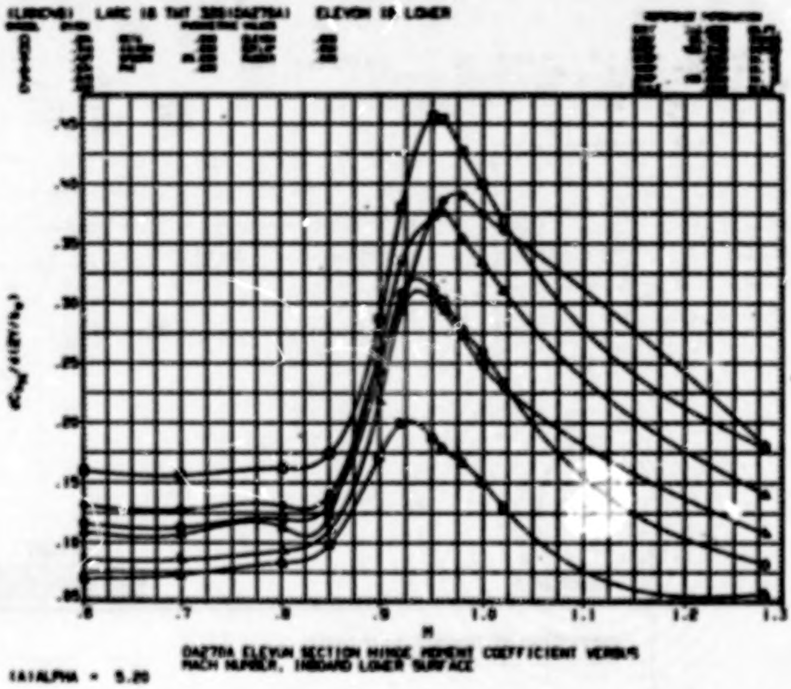

(e) The same distributed loads crossplotted with Mach to ascertain potentially critical conditions. (From Ref. 8.)

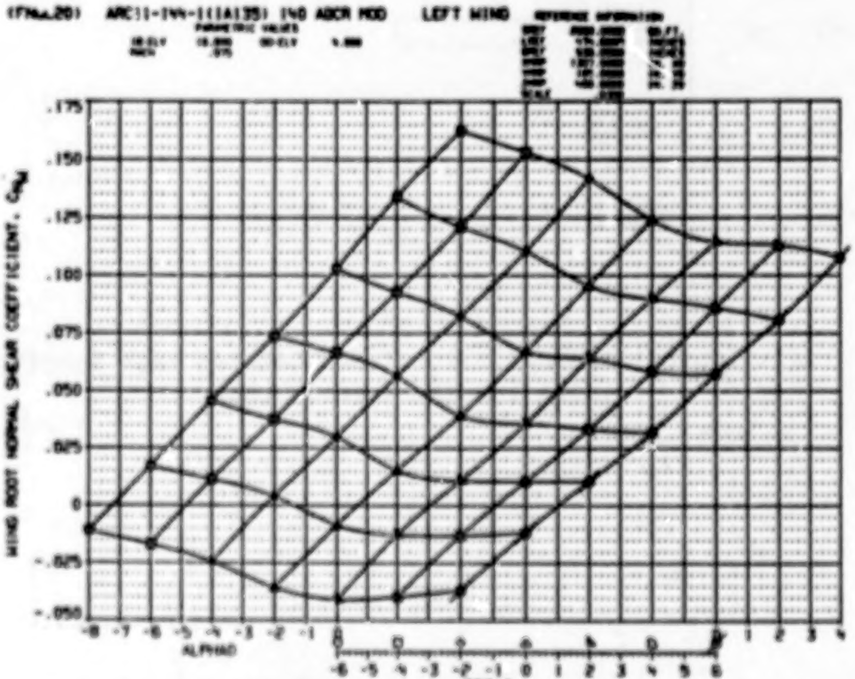

(f) Wing forces developed from pressure integrations carpet displayed to visualize the wing loads in the pitch-sideslip matrix. (From Ref. 9.)

Figure 13.- Concluded.

ORIGINAL PAGE IS
OF POOR QUALITY

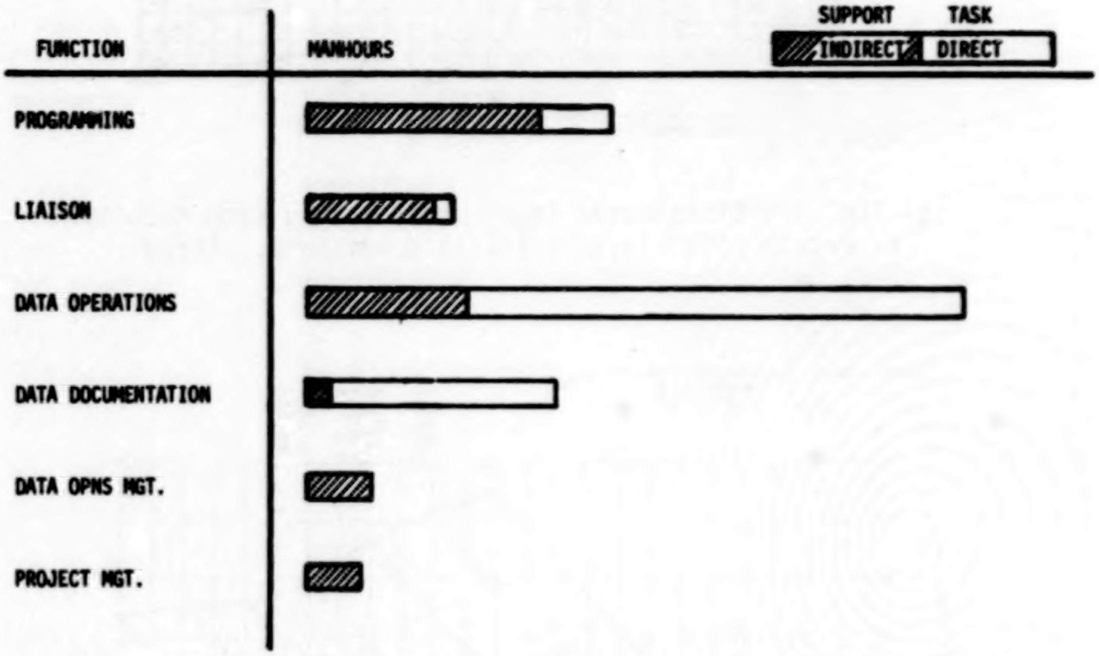

Figure 14.- Typical manhour allocations between task functions are shown for the average test.

N84
10167

UNCLAS

N84 10167 D23

SHUTTLE FLIGHT PRESSURE INSTRUMENTATION:
EXPERIENCE AND LESSONS FOR THE FUTURE

P. M. Siemers III and P. F. Bradley
NASA Langley Research Center
Hampton, Virginia

H. Wolf and P. F. Flanagan
Analytical Mechanics Associates, Incorporated
Hampton, Virginia

K. J. Weilmuenster and F. A. Kern
NASA Langley Research Center
Hampton, Virginia

SUMMARY

Flight data obtained from the Space Transportation System orbiter entries are processed and analyzed to assess the accuracy and performance of the Development Flight Instrumentation (DFI) pressure measurement system. Selected pressure measurements are compared with available wind tunnel and computational data and are further used to perform air data analyses using the Shuttle Entry Air Data System (SEADS) computation technique. The results are compared to air data from other sources. These comparisons isolate and demonstrate the effects of the various limitations of the DFI pressure measurement system. The effects of these limitations on orbiter performance analyses are addressed, and instrumentation modifications are recommended to improve the accuracy of similar flight data systems in the future.

INTRODUCTION

During the first five flights of the Space Transportation System (STS), the orbiter (OV-102) was instrumented to provide the flight data required to evaluate and interpret its performance and thereby verify the vehicle's flight worthiness and mission capability. This instrumentation system, designated Development Flight Instrumentation (DFI), included approximately 4500 measurements of which 200 were surface-pressure measurements intended to assist in the refinement of aerodynamic loads and performance characteristics predictions. It is the primary purpose of this study to evaluate the performance of this DFI pressure measurement system. This evaluation is based on a comparison of flight data obtained from the forward fuselage DFI with wind tunnel and computational data as well as results obtained from postflight analyses incorporating other entry flight data relative to vehicle attitude and state.

The basis for much of the evaluation and recommendations of this study is the experience gained in the development of the Shuttle Entry Air Data System (SEADS) (ref. 1). The SEADS is a new concept in air data systems and consists of an array of flush orifices installed in the nose and forward fuselage of the orbiter. The SEADS will provide research quality air data from Mach 30 to touchdown. The transducers for the SEADS are identical to similarly ranged

DFI transducers and have been rigorously calibrated to provide pressure data to a greater accuracy than available from the DFI. The design of the SEADS and the calibration of the transducers provided generic data applicable to the DFI transducers and pressure data system in general.

In addition, the DFI data have provided the opportunity to verify (in a restricted manner because of the lack of nose cap orifices) the SEADS pressure model incorporated in the data-reduction algorithm. The available data near the nose have been used to predict angle of attack and free-stream dynamic pressure. The results of this SEADS/DFI analysis are compared to other sources of such air data.

This evaluation of the DFI has resulted in a number of recommendations which would enhance the accuracy and usefulness of future flight data systems.

DATA AVAILABILITY

The wind tunnel data were obtained in various ground research facilities using different models. The wind tunnel data range spans the reentry Mach number range from hypersonic ($M = 10.0$) to subsonic ($M = 0.25$) for three different forward fuselage models (0.02 - scale, 0.04 - scale, and 0.10 - scale) (ref. 2). The wind tunnel models were instrumented to duplicate locations of selected orbiter surface DFI pressures as shown in figures 1-3. The computational data were obtained from a solution of the three-dimensional Euler equations about a modified orbiter geometry using the HALIS (ref. 3) computer code for the continuum flow regime at hypersonic Mach numbers. The computational data were also selected to match flight conditions and locations corresponding to these selected DFI pressure sensors. The flight data used in this study are limited to the orifices located in the forward fuselage region because of the limitation of the wind tunnel and computational data (figs. 1-3). Although flight data were measured by the DFI sensors during the orbiter's first five flights, during STS-1 and STS-4 the DFI recorder malfunctioned, thereby restricting the data to those obtained from telemetry after blackout. This limited data to Mach numbers of 13 and below. In addition, due to a power constraint, only a restricted amount of pressure data was available from STS-2. A complete set of data was, however, obtained during STS-3 and -5, which allowed an analysis of the pressure data as well as behavior of the data system. Where comparisons could be performed, pressure data from all flights displayed a high degree of consistency.

DFI FLIGHT DATA ASSESSMENT

As noted in references 2, 4, 5, and 6, several shortcomings in the DFI pressure measurement and data system have been identified that could have a significant effect on the interpretation and application of the flight data. These potential error sources are:

1. Tile Steps and Gaps
2. Port Leakage

3. Transducer Calibration
4. Data System
5. Measurement Location and Range

These error sources have been evaluated and are discussed to quantify DFI pressure uncertainty. This study has resulted in recommendations which could, if incorporated into the DFI or other flight data systems, greatly enhance the accuracy and applicability of the data.

Tile Steps and Gaps

The DFI pressure orifices are generally located near the center of the thermal protection system tile. The orifice penetrates the tile, its bonding material, and the orbiter's aluminum skin (ref. 7). Each instrumented tile is surrounded by other tiles which are separated from one another by a thermal expansion gap. In addition, due to the flexibility of the TPS tile system, steps exist between adjacent tiles. Attempts to quantify the effects of steps and gaps were not entirely successful because of their unpredictability and sensitivity to the thermal environment. Based on the analyses which have been done, the error induced by steps and gaps is below the resolution of the DFI system.

Port Leakage

Port leaks generally occur in the joint at the strain isolation pad (SIP) between the TPS tile and the aluminum skin. These leaks are generally caused when tiles are pull-tested for bond strength and the seal is damaged. Leaks are categorized by the loss of a gas in cm^3/min. Standards for the orifice installation specify a leak rate of over 80 cm^3/min to be unacceptable. A comparison of data obtained during STS-2 for two transducers located symmetrically on either side of the fuselage is shown in figure 4. One of the orifices (V07P9115) was leaking in excess of 200 cm^3/min, while the other (V07P9114) was leaking less than 20 cm^3/min in tests completed prior to the flight. In spite of the leak rate difference, the data from the two transducers are in close agreement. Further evidence that tile leakage is a minor factor in measurement accuracy is shown in figure 5 for the port V07P9871. During STS-1, this orifice was covered by a blank tile, but when the flight data are compared to ground-based data as shown in figure 5, the agreement is no better or worse than any other comparisons.

Subsequent to flight 1, the tile at port V07P9871 was replaced with a properly drilled tile. A comparison of the residuals on a common data arc obtained from STS-1 and STS-3, respectively, was made. While certain differences appear, their magnitude is small and well within the error band derived from other pressure measurements.

Additionally, tests conducted at Rockwell International confirmed that the absence of a pressure port tube through the tile introduced a pressure differential of less than 0.3 psf across the tile. This differential is below the resolution of the DFI data system.

It is concluded that the porosity of the orbiter TPS (gaps) allows bleeding of surface pressure to the sensor, and even if the orifice leaks, the effects on the final data are insignificant given the uncertainties in the existing DFI system.

Transducer Calibration

It is the authors' experience that careful calibration of pressure transducers is essential to maximize measurement capability and to obtain accurate, high-resolution flight data. Although the DFI transducers were calibrated individually and their sensitivity determined for three different temperatures, the calibration data for transducers of similar range were averaged, and a universal calibration curve was established. While such a procedure does not use the full capability of the transducers, it is consistent with the 8-bit data system used in the DFI. In contrast, the SEADS calibration program was designed to take advantage of the full capability of the transducers and account for the environmental conditions of temperature, random vibration, acceleration, and mechanical shock. The results of this calibration showed that the performance characteristics were different enough from transducer to transducer to require detailed individual transducer performance characterization.

Forty-nine pressure transducers, identical except for range to existing DFI transducers, were calibrated at the Langley Research Center in support of SEADS. Of these 49 transducers, seven failed or failed to meet specifications and were, therefore, rejected and not included in this study. Analysis of the calibration data from the 42 acceptable transducers clearly demonstrates the need for detailed performance characterization. Although the transducers met procurement specifications, performance differences within tolerance limits are significant. The output of the transducers at a constant temperature and essentially zero pressure (0.001 psia) bias had a distribution (fig. 6) ranging from -2 to +3.5 percent of full scale. The sensitivity distribution for a constant temperature (fig. 7) has a range of -1.5 to + 1.25 percent of the average sensitivity for the sample. These data establish the requirement for individual characterization of each transducer included in the system, as well as a requirement on the data system to handle negative voltages. Individual transducer response characteristics, although highly repeatable, are not linear. As a result, simple linear transfer function modeling cannot be used in the analysis of flight data without introducing a significant loss of measurement accuracy.

Linear and second-order least-squares analyses were used to assess transducer nonlinearity and hysteresis at a constant temperature. The distribution of the data (fig. 8) indicates a variation from 0 to 0.5 percent of full scale with approximately 75 percent of this variation due to nonlinearity alone. Repeatability of these data was better than 0.02 percent of full scale, demonstrating that a higher order transfer function will significantly improve pressure measurement accuracy.

Temperature affects both the sensitivity and the zero-pressure output (bias) of the transducers. While the SEADS transducers were calibrated at five temperatures between -79°C and 113°C, figure 9 shows the distribution in the thermal zero-pressure coefficient considering only the end and midpoint temperatures as was done for the DFI transducers. The coefficient is shown to vary from nearly 0 to 0.05 percent full scale per degree centigrade. In addition, figures 10 and 11 show that while transducer sensitivity is only slightly affected by temperature (0 to 0.011 percent per degree centigrade), the zero-pressure (bias) dependence on temperature is not only nonlinear but also significantly different in character for each transducer. These results substantiate the need for a thorough temperature calibration.

On the basis of these calibration results, it is concluded that the error in the DFI transducers could be as large as 5.0 percent of full scale. To reduce this error and obtain the maximum accuracy (0.1 percent of full scale), it is necessary to obtain in-flight measurements of transducer temperature and zero-pressure bias as well as the accomplishment of a thorough calibration of each transducer and the use of the individual calibration curves corrected for temperature in data reduction.

Analysis of the random vibration test data over a 20- to 2000-hertz range at 22.6 g rms level, performed primarily to insure transducer survivability, resulted in an output noise level of 10 millivolts. Detailed calibration pre- and postshock and thermal cycle should be obtained to characterize flight-to-flight repeatability. (The majority of the transducer failures occurred during the random vibration and shock calibration tests thereby demonstrating the importance of such tests.) The static acceleration tests at 2 g and 5 g for a 5-minute duration showed an output change of approximately 0.010 millivolts. To avoid this error source, transverse mounting of transducers is best although not critical.

Measurements of the transducer output noise level under zero-pressure load indicated an rms noise level of 5 to 10 millivolts generated by the transducer's 20-KHz carrier frequency. Although the noise is indistinguishable within the resolution of the DFI data system, any improvement in resolution would dictate the need for output filters in the system to minimize the effects of this high-frequency noise.

Five transducers were recalibrated after a period of approximately 2 years. Four of the transducers changed sensitivity less than 0.1 percent. The zero-pressure output showed changes between -0.6 percent to +0.5 percent of full scale. In general, the nonlinearity and hysteresis changed less than 0.1 percent of full scale. These data illustrate the stability of these transducers over long periods of time.

Data System

Data rate and resolution are critical to the accurate interpretation of data such as that obtained during the flight of the STS. Data resolution is dependent on the ability of the measurement sensor to detect small changes in the measured value and on the data system's capability to process these data at a comparable resolution.

The DFI data system digitizes the analog output of the transducer. The nominal output range is 0 to 5 volts, whereas both calibration and flight data show that negative voltages occur at 0 or low pressures. Such negative biases are, therefore, not read, and their omission compromises the accuracy of the data. An 8-bit pulse-code modulator (PCM) is used, and the data are recorded at a rate of 1 sample per second. The resulting resolution of the DFI pressure data is approximately 11.25 psf for the 0-20 psia transducers, 8.44 psf for the 0-15 psia transducers, 0.586 psf for the 0-150 psf transducers, and 0.293 psf for the 0-75 psf transducers. Studies[4,6] have shown that the DFI data rate and resolution introduce uncertainties into the flight data restricting the ability to verify the performance of the flight system through flight and ground-based data correlations. To resolve such shortcomings, a more thorough analysis of the problem to be solved is mandatory when specifying system resolution and response. The orbiter experiment program (OEX), designed to provide highly accurate, research quality data, uses a 12-bit PCM system and data rates between 2 and 150 samples per second depending on the data type.

The incorporation of high resolution into a data system complicates the overall design because of the system's new sensitivity to electromagnetic interference (EMI) and electronic noise. EMI effects must be minimized by using shielded components, particularly shielded cable, as in the Forward Fuselage Support System for OEX. In a typical pressure system, the transducer is a source of noise; therefore, the transducer design must consider the data resolution requirement. The inclusion of integrated filter circuits in the transducer is desirable, but as in the case of the SEADS transducers, these filter circuit requirements were not defined prior to manufacture. Circuits designed based on component tests were incorporated into the data system's PCM slave. In addition, the increased system resolution results in an increased sensitivity within the data system to supply voltage and temperature, both of which must then be monitored for postflight data correction. Finally, in general, the data system should retain a flexibility to be modified as a result of end-to-end system level tests.

Measurement Location and Range

As noted by Scallion (ref. 5) and Siemers (ref. 6), the number of pressure orifices in the DFI is quite small, and considerable judgment must be exercised in the interpretation of the data. A review of the basic flow field phenomena associated with a complex vehicle such as the Space Shuttle orbiter, which incorporates both a reaction control system and aerodynamic control surfaces, indicates that the spatial distribution, limited number, and limited range of the measurements severely restrict analysis of the flight system. This conclusion has been confirmed by an inability to isolate specific flow phenomena such as control surface flow separation, RCS/control surface interaction, and the cause of lofting on ascent based on available flight data. An inability to resolve these problems from the flight data indicates that a substantially more elaborate measurement system would be required to isolate and define the flow field phenomena involved. Even though many of the flow field phenomena were predicted (allowing the proper location of pressure orifice and ranging of the transducers), some were not. Therefore, the measurement system must retain a flexibility which will allow the addition of new orifices, the relocation of others, and the change-out of transducers not of the proper operational range. In his study of Reaction Control System performance, Scallion (ref. 5) observed that "about half of the transducer pressure ranges were exceeded (the gages became saturated)." This gage saturation severely limited the thoroughness of the analysis. Because of saturation, a limited DFI transducer change-out was accomplished at two locations in an attempt to better understand the pressure distributions relative to ascent lofting. Many times, however, the inclusion of a high-range transducer will result in an unacceptable decrease in data resolution at lower pressures. Under these circumstances, it would be necessary to incorporate dual transducers at these pressure ports. This design will provide the capability to obtain the data over the entire pressure range with good resolution. Such a dual system as incorporated in SEADS would have considerably enhanced much of the DFI data.

DFI FLIGHT DATA COMPARISONS

In spite of the shortcomings thus far described, useful results were obtained from the pressure data analyses performed. One objective of the evaluation of the STS-1-5 pressure data was to define flight pressure distributions for comparison with wind tunnel and computational data and to identify inconsistencies, if any. These comparisons contribute both to the validation of the orbiter's design and the demonstration of its flight worthiness, as well as provide a valuable data base for evaluating ground-based research capabilities. In addition, these comparisons determine the need for improvements in existing capabilities or requirements for new capabilities. Typical results from selected ports from STS-3 and -5 are shown in figures 12 through 16. Symbol identification is given in Table 1.

Data from the pressure port nearest the nose on the lower surface are shown in figures 12 and 13. This orifice has two transducers collocated at the same port with two different pressure ranges. The 0 to 15 psi transducer (V07P9100) data are shown in figure 12. Its data resolution for the 8-bit data system is 8.44 psf. For regions in the upper atmosphere, where pressure levels are low, the transducer output appears extremely noisy, but this is in actuality only a function of the resolution of the data system. Data below Mach 10 are much smoother. Both the wind tunnel and the HALIS data for this location match the flight data well, within the error band of the flight data. Where angle-of-attack excursions (aeromaneuvers) are noted in the flight pressure data, corresponding ground-based information gives similar nondimensional pressure levels. This can be noted in this and other figures for Mach 15 (HALIS) during STS-3.

The other transducer located at this same port has a 0 to 150 psf range (V07P9451). Its data resolution is 0.586 psf, and due to its location near the stagnation point and its shortened data range, the transducer is saturated shortly after the orbiter comes out of blackout. This transducer, with much better data resolution, gives a smoother set of flight data in the upper atmosphere, as evidenced in the STS-3 plot. The HALIS calculations matched well in the hypersonic region and predicted the correct pressure level at Mach 15 during the STS-3 aeromaneuver. In this and other plots, both the wind tunnel and HALIS data follow the shape of the flight data curves. For this transducer, however, the ground-based data are slightly higher than the flight data.

Figures 14 through 16 show comparisons of typical flight data with ground-based data. All of these DFI ports have 0 to 150 psf transducers which provide good data resolution. All of the ground-based data are well within the flight data error band. Saturation of these transducers occurs around Mach 1.5 for each flight. This array of transducers is an excellent example of the calibration/bias uncertainties. The V07P9453 and V07P9461 transducers have unknown negative biases. For V07P9453, the flight data are consistently lower than the ground-based data for all three flights indicating that a bias correction could result in better agreement among data sources. The data obtained for V07P9461 are slightly higher than ground-based data. A bias correction would not help the agreement. This is an indication that the bias may be only slightly negative and may be a function of temperature. This slight disagreement could also be caused by the use of the "universal" calibration curve. The V07P9457 transducer has a positive bias which is subtracted from the flight data presented. Even though subtraction of the on-orbit bias lowered the flight data and provided good agreement with the ground-based data, the flight data are still slightly above ground-based results indicating possible temperature variation of the bias.

A review of the data presented in this paper and in references 1 and 2 reveals that, in spite of the many uncertainties in the flight data due to the limitation of the measurement/data system, the agreement is generally good between the flight and ground-based data. Generally, the ground-based data match the shape of the flight data, and observed biases are within the expected DFI measurement system error bands. Confidence in the data base could be improved with the incorporation of an improved measurement/data system.

AIR DATA PARAMETER EXTRACTION FROM DFI PRESSURES

Another objective, only partially attainable due to data limitations and the nonoptimal location of the DFI orifices for this purpose, was a test of the capability of the SEADS method to extract typical air data from DFI pressures. The method used for this purpose is an adaptation of the SEADS flight data computational technique described in detail in references 6 and 8. The basic SEADS technique derives vehicle attitude and free-stream dynamic pressure from the nose region pressure distribution.

For Shuttle orbiter flights STS-1-5, DFI pressure measurements were available at the ports shown in figures 1-3. Only three orifices were considered far enough forward to furnish reliable data representable by the SEADS pressure model. Some of the farther aft orifices on the bottom of the fuselage were considered and were determined to degrade the analysis accuracy. The data from the top orifice was suspect due to possible flow separation at high angles of attack (α), and then the transducer saturated at lower angles (and altitudes), furnishing no useful pressure data for this study. This analysis has thus been restricted to the front fuselage orifices located on the bottom, (P_b), and port side, (P_p). Since no orifice was located on the forward starboard side, the sideslip angle (β) was not obtained. The two pressures, P_b and P_p, permit the solution for only two state variables: angle of attack (α) and free-stream dynamic pressure (q_∞). These physical limitations of the DFI result in the introduction of two simplifying assumptions, neglecting sideslip angle and ambient pressure.

Again, since the DFI recorder did not operate during the STS-1 and STS-4 missions and the complete DFI system was not activated during STS-2, only STS-3 and STS-5 have provided complete sets of data for this part of the study.

The first try (using no external data sources) at obtaining α and q_∞ is shown in figures 17 and 18. This analysis was terminated at approximately $M = 3$, where the low-range transducer P_b saturates. It is seen that the trend of trajectory determined α (labeled BET) was followed well with an error of approximately 2° to 3°. The importance of a high-resolution data system is also obvious in the flight data as the data scatter increases greatly below $M = 10$ where P_b makes a transition from the 0-1 psi to the 0-15 psi transducer.

Because of the limitations imposed by lack of pressure orifices in the nose region, the angle of attack derived from using the SEADS algorithm with the DFI pressures may be questioned when compared to α derived from trajectory or navigation data. Nevertheless, the trends in α are modeled well, and the dynamic pressure is predicted quite accurately. Analysis indicates that distinct improvements in this SEADS method will result when pressure distributions on the nose cap are available.

Comparisons of the final SEADS/DFI derived q_∞ from STS-3 and STS-5 with other sources of q_∞ show that in the hypersonic flight regime the SEADS/DFI - q_∞ agrees with the G & C - q but differs from the Best Estimate Trajectory (BET)-q_∞ by a small, though percentagewise, significant amount. Additional analysis by LaRC (refs. 9, 10), JSC, and Rockwell International has shown that the BET-q_∞ in this region leads to values of the aerodynamic coefficients at variance with their predicted values. While resolution of this discrepancy must await a Shuttle orbiter flight with SEADS onboard, the SEADS/DFI derived value has been accepted as representative in the hypersonic region and has been included in the LaRC BET in this region for STS-3 and -5.

RECOMMENDATIONS

Although significant results have thus far been obtained as a result of the analyses conducted using the DFI pressure data from STS-1 through STS-5, these results are severely limited because of the limitations which have been shown to exist in the DFI. Design of future pressure measurement systems for flight system performance evaluations should incorporate the following improvements.

1. Design the data system to provide the data accuracy, resolution, and frequency required to evaluate the flow field phenomena of interest as well as accepting the bias or other idiosyncrasies of the measurement system.

2. Proper selection of number and location of measurements is dependent on available ground data base.

3. Proper ranging of transducers based on predicted pressure-field analysis and available ground data base is necessary.

4. Measurement system should be of a design to allow changes resulting from preflight end-to-end system tests as well as initial flight tests to improve the quantity or quality of the data.

5. Component temperature monitoring and calibration based on nominal temperature profiles are required. Since the response to temperature variation is highly nonlinear, calibration should be performed throughout the expected temperature range.

6. Individual calibration curves of all transducers in the system should be used. "Family" calibrations are not adequate.

7. Transducer biases, both positive and negative, should be accommodated in the data system.

8. In situ reference values (for example, on-orbit pressure zeros, supply voltage, and temperature) should be used in data reduction.

SUMMARY AND CONCLUSIONS

Pressure data obtained from the Space Shuttle orbiter's Development Flight Instrumentation in the forward fuselage region during the STS-1 through -5 reentries have been compared to wind tunnel and computational data. Ground-based data across the speed range matched the flight data within the uncertainty calculated for the DFI system. An analysis of the DFI data system and the calibration procedures associated with the in-flight behavior of the transducers has provided a better understanding of the DFI system and explained differences between the ground-based data and the flight data.

As a result of the analyses presented, certain conclusions are noted here. Agreement between ground-based and flight data, although good, is limited by the resolution of the flight data system and the preflight calibration of the transducers. Improved data system resolution and more thorough transducer calibration could reduce the uncertainty from 5 percent to 0.1 percent full scale. More pressure measurements and transducers of different ranges (more applicable to the reentry environment) are needed onboard the orbiter for accurate pressure modeling. Orifice leakage and tile steps and gaps are not important to the response and accuracy of the DFI flight pressure data given the resolution and quality of the system. Both the wind tunnel tests completed on the forward fuselage models and the HALIS computer program predict in-flight forward fuselage pressure distributions well. Both ground-based techniques can be used confidently, although HALIS data are currently restricted to the windward surface. The technique developed for SEADS to derive accurate air data parameters from forward fuselage pressures has been demonstrated with the DFI data.

REFERENCES

1. Siemers, P. M., III: Shuttle Entry Air Data System. Paper presented at the 1978 Air Data Systems Conference, Colorado Springs, Colorado, May 3, 1978.

2. Bradley, P. F., Siemers, P. M., III, and Pruett, C. D.: Comparison of Forward Fuselage Space Shuttle Orbiter Flight Pressure Data to Wind-Tunnel and Analytical Results in the Hypersonic Mach Number Range. AIAA Paper 81-2477, November 1981.

3. Weilmuenster, K. James, and Hamilton, H. Harris II: A Method for Computation of Inviscid Three-Dimensional Flow Over Blunt Bodies Having Large Embedded Subsonic Regions. AIAA Paper 81-1203, June 1981.

4. Bradley, P. F., Siemers, P. M., III, and Weilmuenster, K. J.: An Evaluation of Space Shuttle Orbiter Forward Fuselage Surface Pressures: Comparison With Wind Tunnel and Theoretical Predictions. AIAA Paper 83-0119, January 1983.

5. Scallion, W. I., Compton, H. R., Suit, W. T., Powell, R. W., Blackstock, T. A., and Bates, B. L.: Space Shuttle Third Flight (STS-3) Entry RCS Analysis. AIAA Paper 83-0116, January 1983.

6. Siemers, P. M., III, Wolf, H., and Flanagan, P. F.: Shuttle Entry Air Data System Concepts Applied to Space Shuttle Orbiter Flight Pressure Data to Determine Air Data STS 1-4. AIAA Paper 83-0018, January 1983.

7. Stoddard, L. W., and Draper, H. L.: Development and Testing of Development Flight Instrumentation for the Space Shuttle Thermal Protection System. Proceedings of the 24th International Instrumentation Symposium, Part 2, Instrumentation Society of America, 1978, pp. 663-672.

8. Pruett, C. D., Wolf, H., Siemers, P. M., III, and Heck, M. L.: An Innovative Air Data System for the Space Shuttle Orbiter: Data Analysis Technique. AIAA Paper 81-2455, November 1981.

9. Compton, H. R., Scallion, W. I., Suit, W. T., and Schiess, J. R.: Shuttle Entry Performance and Stability and Control Derivative Extraction From Flight Measurement Data. AIAA Paper 82-1317, August 1982.

10. Findlay, J. T., and Compton, H. R.: On the Flight Derived/Aerodynamic Data Base Performance Comparisons for the NASA Space Shuttle Entries During the Hypersonic Regime. AIAA Paper 83-0115, January 1983.

TABLE 1

SYMBOL IDENTIFICATION FOR DATA PLOTS

——— FLIGHT DATA

HALIS

- ◣ Mach 20.
- ● Mach 18.
- ▲ Mach 15.3
- ■ Mach 10.

WIND TUNNEL

- ○ Mach 10.
- □ Mach 6.
- ◇ Mach 4.63
- △ Mach 3.5
- ◺ Mach 2.96
- ▷ Mach 2.3
- ⌂ Mach 2.
- ♢ Mach 1.5

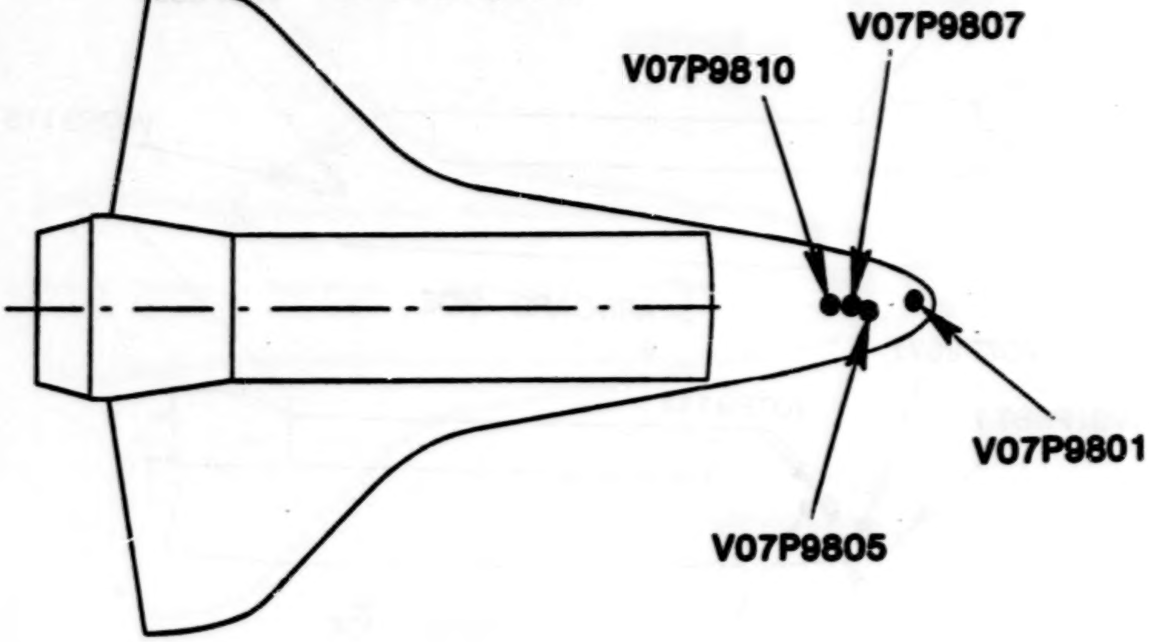
V07P9807
V07P9810
V07P9801
V07P9805

Figure 1.- Upper surface DFI pressures.

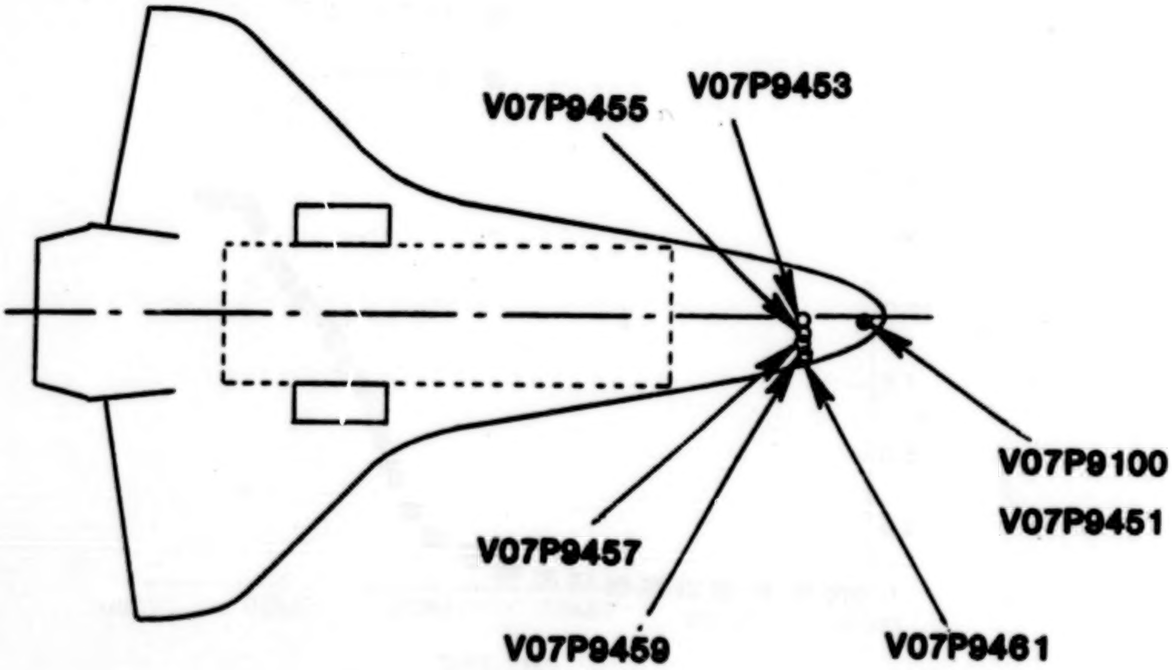
V07P9453
V07P9455
V07P9100
V07P9451
V07P9457
V07P9459
V07P9461

Figure 2.- Lower surface DFI pressures.

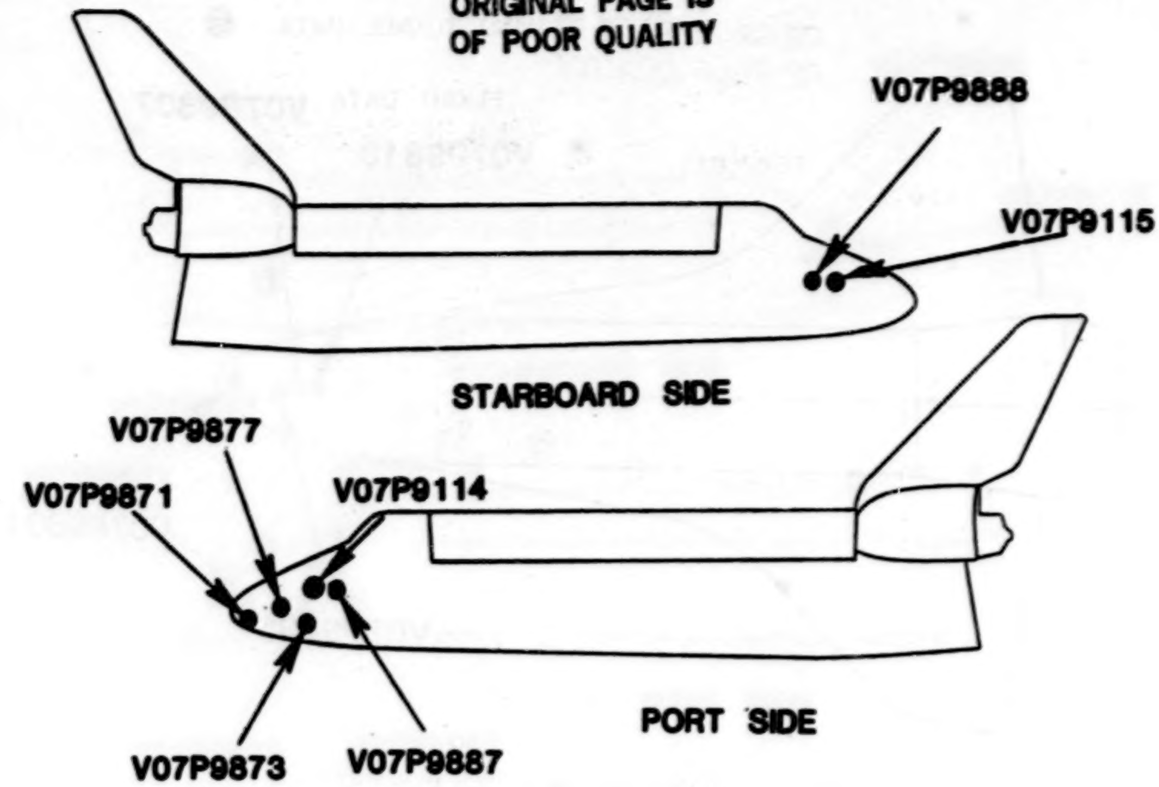
V07P9888
V07P9115
STARBOARD SIDE
V07P9877
V07P9871
V07P9114
V07P9873
V07P9887
PORT SIDE

Figure 3.- Port and starboard DFI pressures.

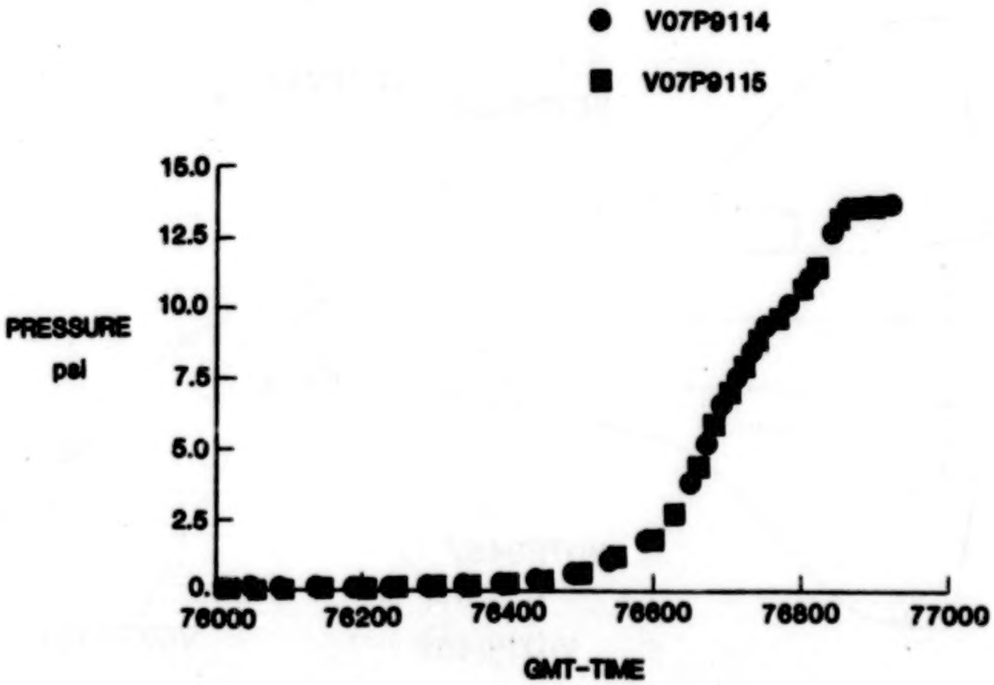

Figure 4.- STS-2 pressure data for V07P9114 and V07P9115.

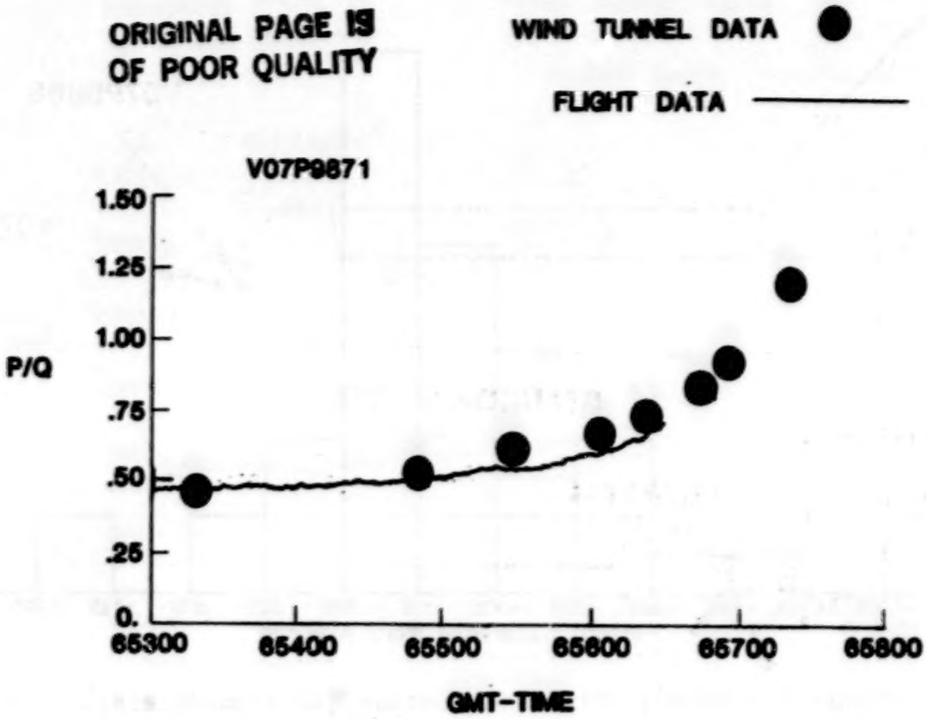

Figure 5.- STS-1 pressure data for V07P9871 compared to wind tunnel results.

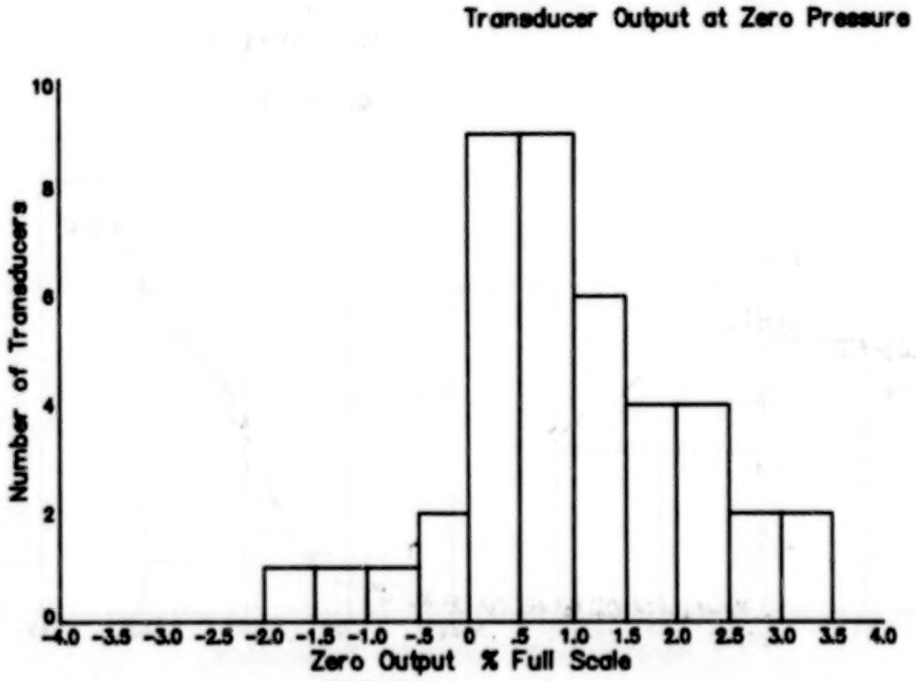

Figure 6.- Zero balance distribution (41 transducers).

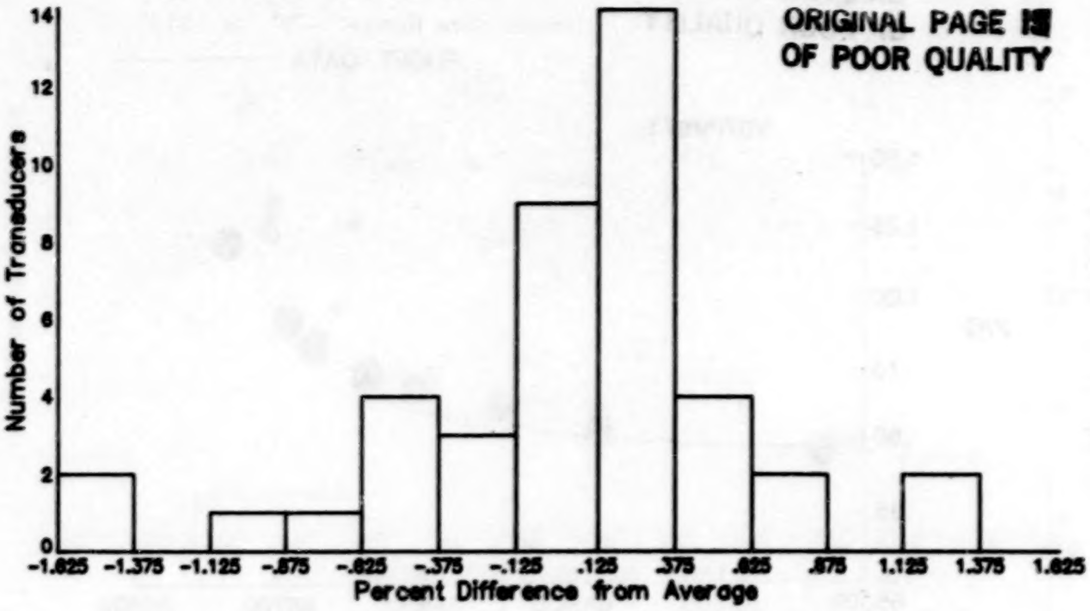

Figure 7.- Sensitivity distribution (42 transducers).

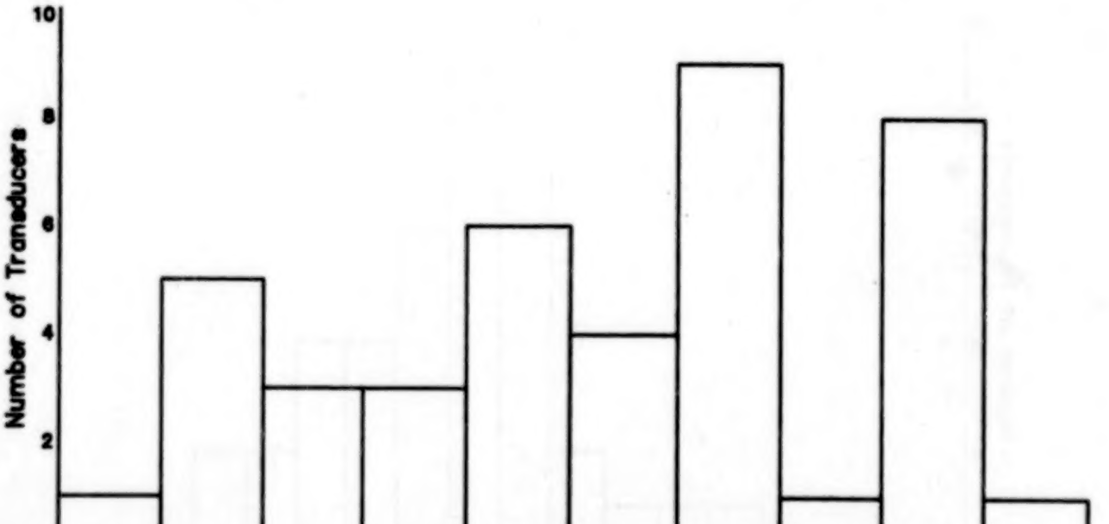

Figure 8.- Nonlinearity and hysteresis distribution (41 transducers).

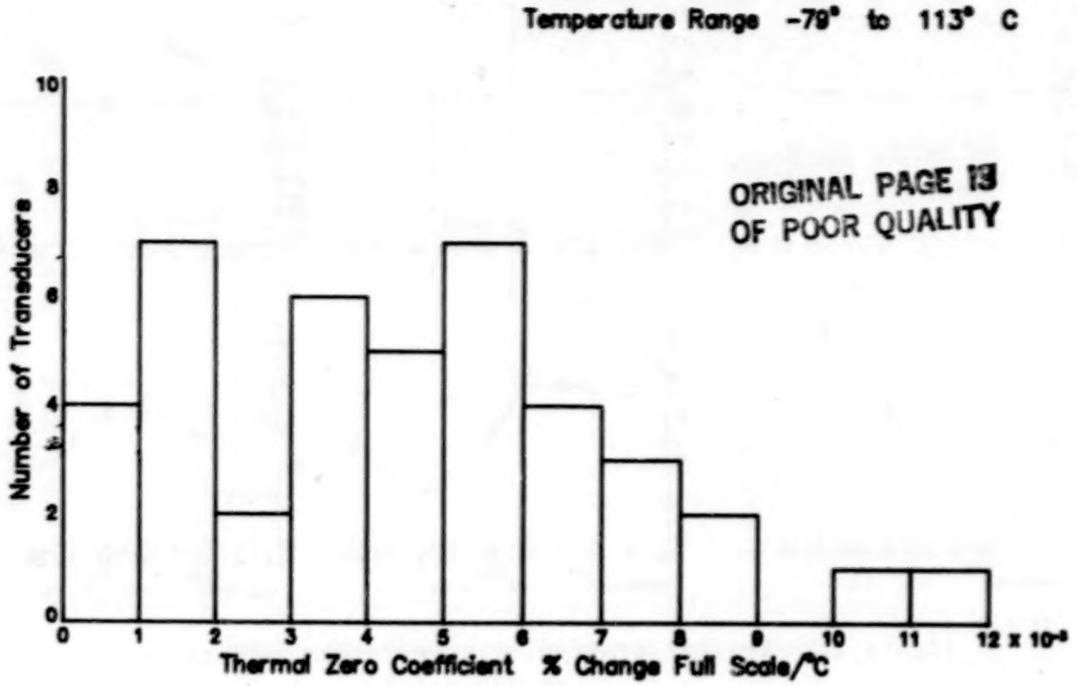

Figure 9.- Thermal zero-coefficient distribution (42 transducers).

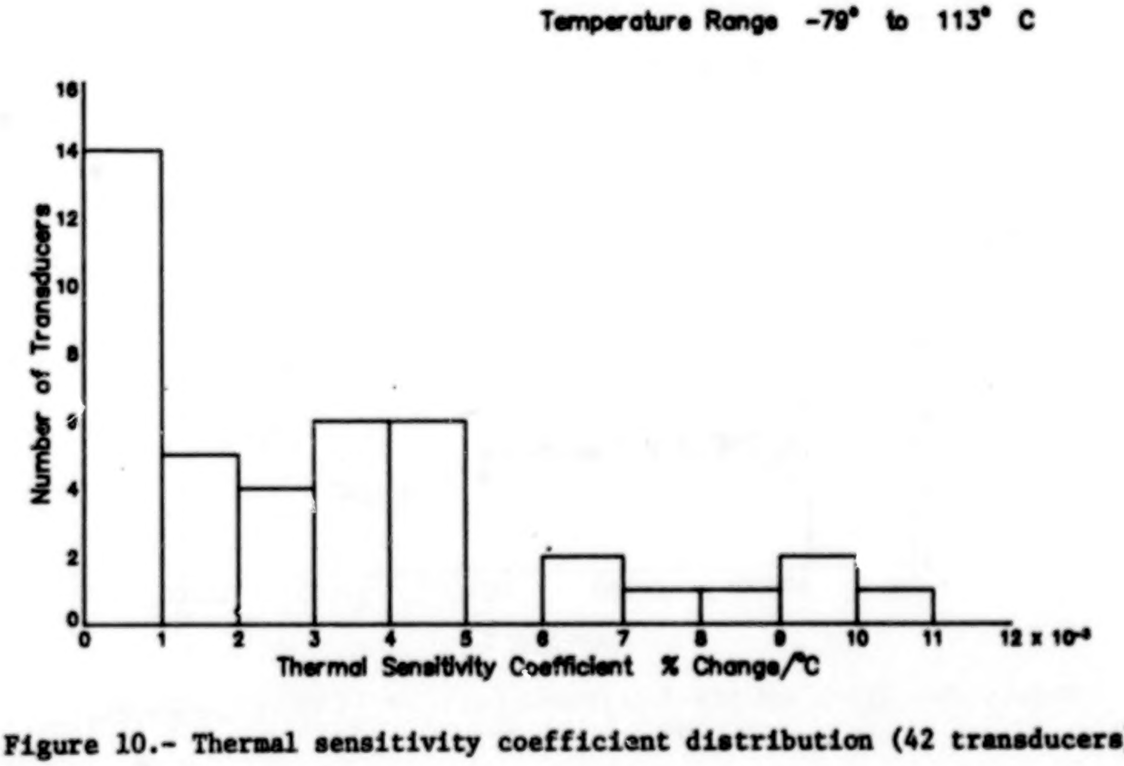

Figure 10.- Thermal sensitivity coefficient distribution (42 transducers).

ORIGINAL PAGE IS OF POOR QUALITY

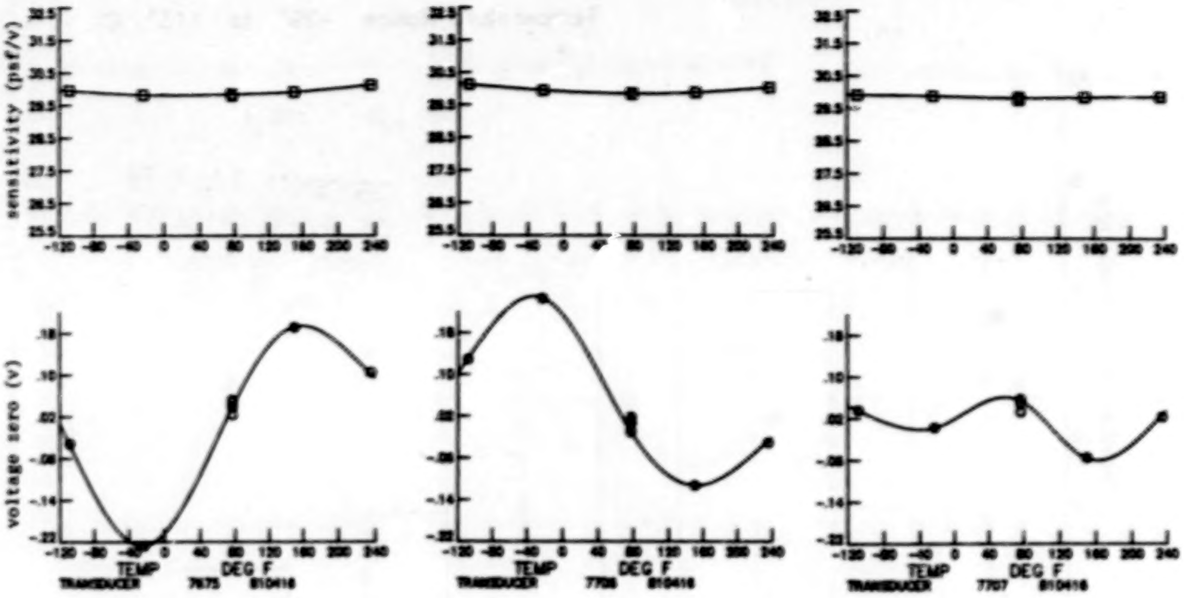

Figure 11.- Typical transducer temperature variations. (See table 1.)

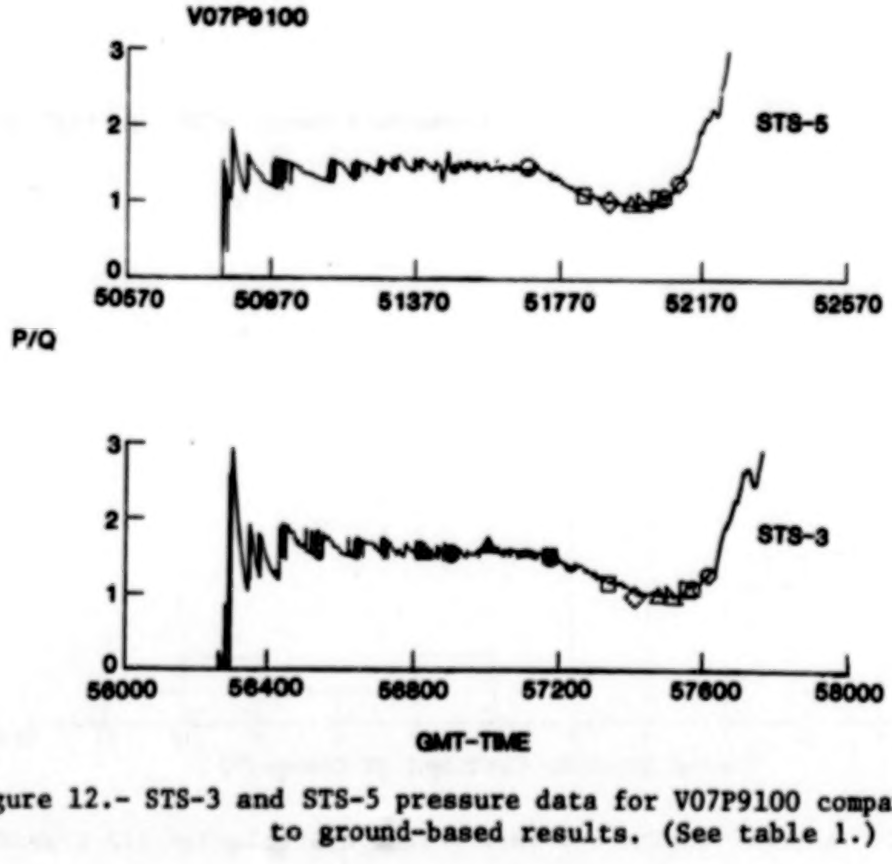

Figure 12.- STS-3 and STS-5 pressure data for V07P9100 compared to ground-based results. (See table 1.)

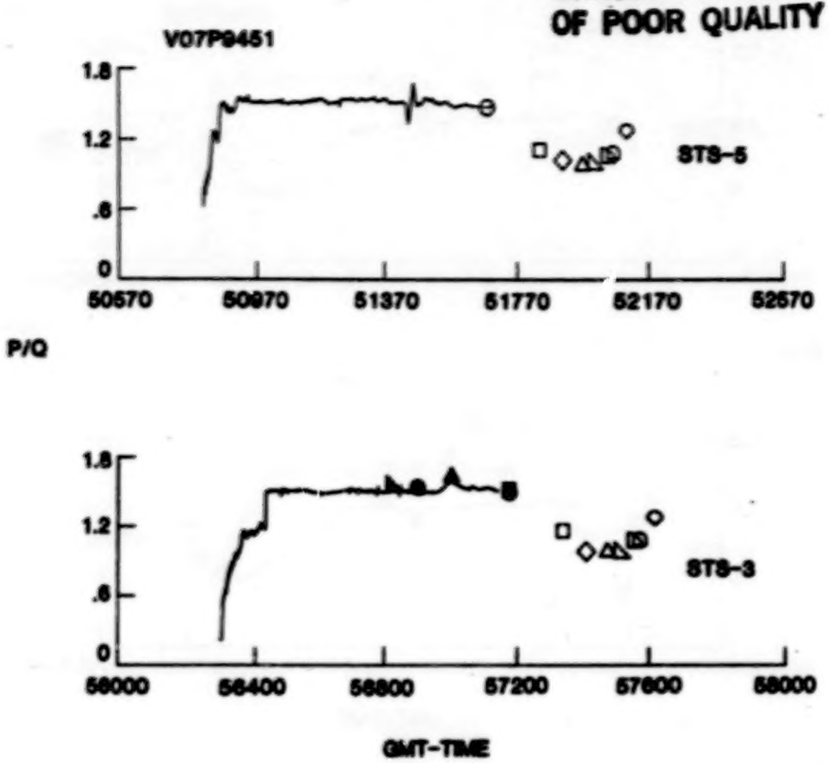

Figure 13.- STS-3 and STS-5 pressure data for V07P9451 compared to ground-based results. (See table 1.)

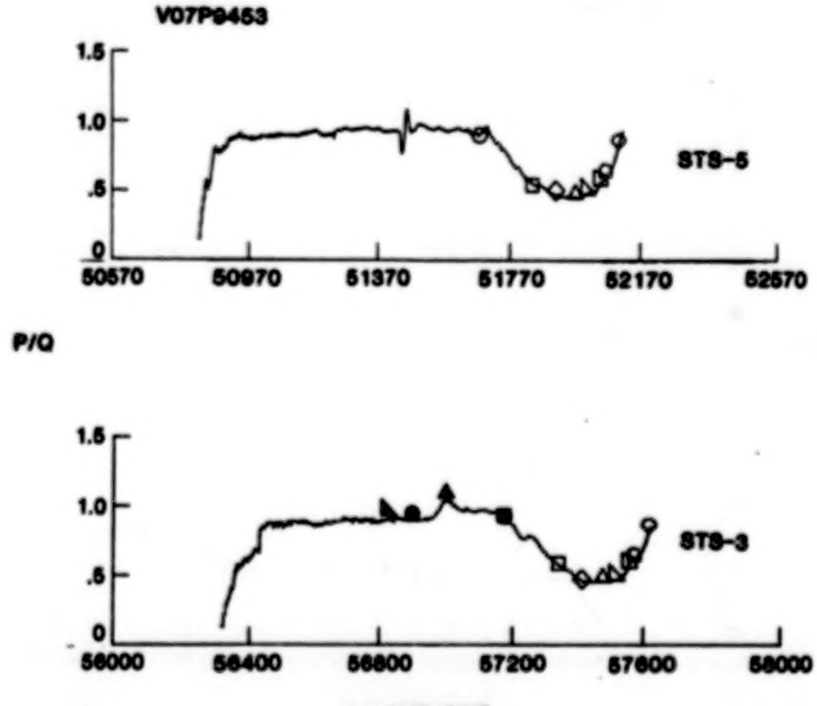

Figure 14.- STS-3 and STS-5 pressure data for V07P9453 compared to ground-based results. (See table 1.)

ORIGINAL PAGE IS
OF POOR QUALITY

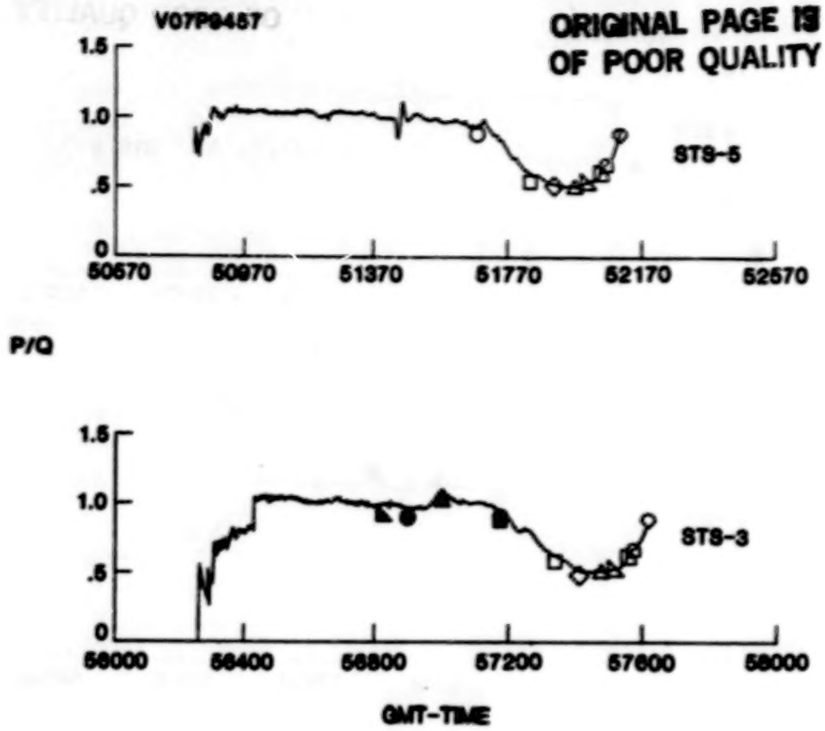

Figure 15.- STS-3 and STS-5 pressure data for V07P9457 compared to ground-based results. (See table 1.)

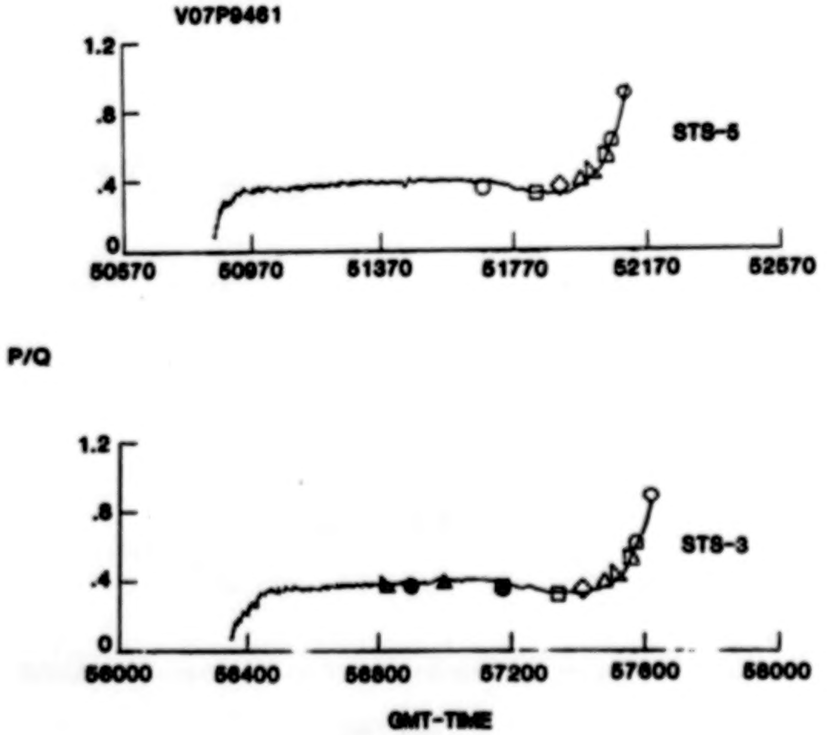

Figure 16.- STS-3 and STS-5 pressure data for V07P9461 compared to ground-based results. (See table 1.)

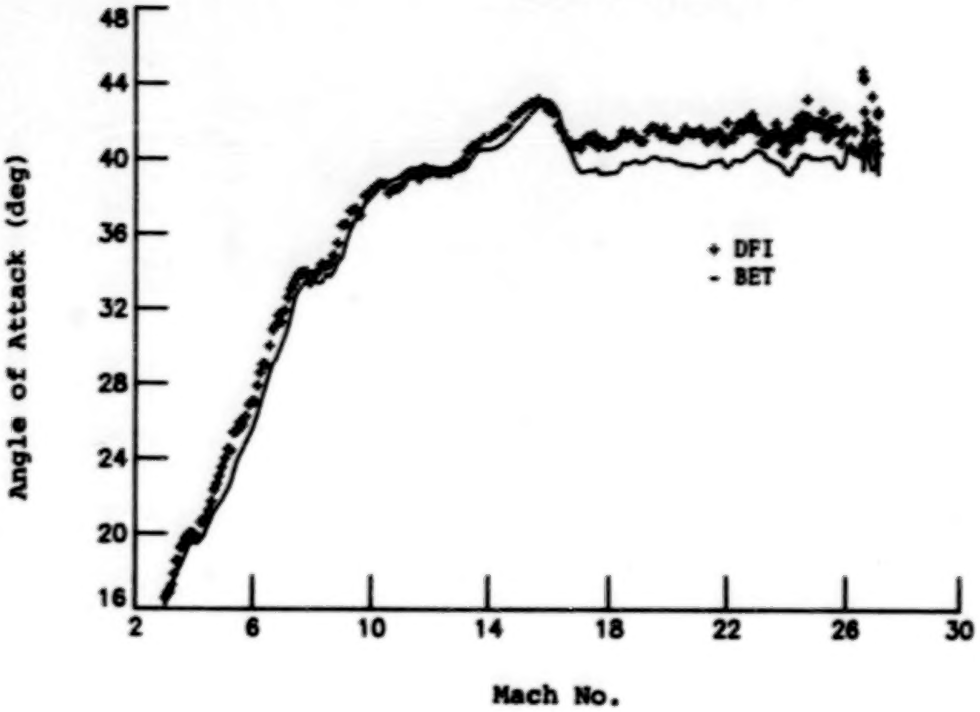

Figure 17.- STS-3 DFI/SEADS derived angle of attack.

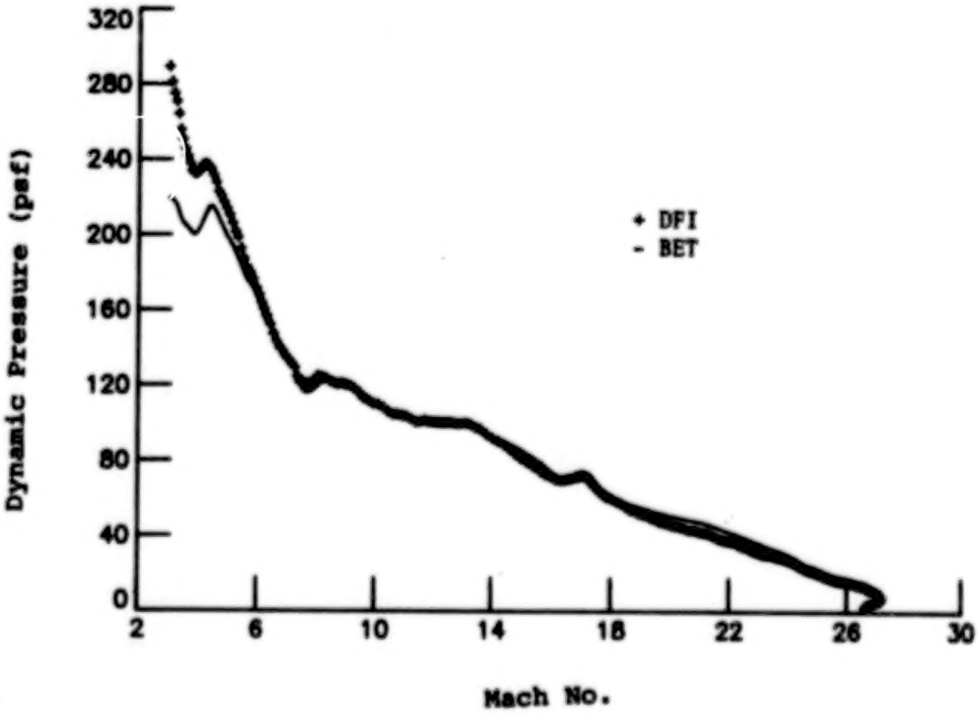

Figure 18.- STS-3 DFI/SEADS derived dynamic pressure.

N84
10168

UNCLAS

A COMPARISON OF MEASURED AND THEORETICAL PREDICTIONS FOR STS ASCENT AND ENTRY SONIC BOOMS

Frank Garcia, Jr.
NASA Johnson Space Center
Houston, Texas

Jess H. Jones
NASA Marshall Space Flight Center
Huntsville, Alabama

Herbert R. Henderson
NASA Langley Research Center
Hampton, Virginia

Summary

Sonic boom measurements have been obtained during the flights of STS-1 through 5. During STS-1, 2, and 4, entry sonic boom measurements were obtained and ascent measurements were made on STS-5. The objectives of this measurement program were (1) to define the sonic boom characteristics of the Space Transportation System (STS), (2) provide a realistic assessment of the validity of existing theoretical prediction techniques, and (3) to establish a level of confidence for predicting future STS configuration sonic boom environments. Detail evaluation and reporting of the results of this program are in progress. This paper will address only the significant results, mainly those data obtained during the entry of STS-1 at Edwards Air Force Base (EAFB), and the ascent of STS-5 from Kennedy Space Center (KSC).

The theoretical prediction technique employed in this analysis is the so called "Thomas Program." This prediction technique is a semi-empirical method that required definition of the near field signatures, detailed trajectory characteristics, and the prevailing meteorological characteristics as an input. This analytical procedure then extrapolates the near field signatures from the flight altitude to an altitude consistent with each measurement location. Predictions of the sonic boom characteristics, i.e. arrival time, overpressure level, duration, etc., are then compared to the measured values at each location. The comparison between measured data and theoretical estimates for both the STS-1 entry and STS-5 ascent conditions showed very good agreement.

INTRODUCTION

No fully theoretical methods are available for calculating the sonic boom overpressure generated by a blunt vehicle with detached shock wave maneuvering at high Mach numbers and high angles of attack. Therefore, sonic boom estimates for Space Shuttle launch vehicles must be based on currently available semi-empirical techniques which were developed based on a large data base from supersonic aircraft flight data and wind tunnel model measurements (Refs. 1 and 2). With these techniques, near field pressure signatures measured in wind tunnels are extrapolated to the far field in a real atmosphere under actual flight conditions. In order to extend the range of conditions for which these techniques are valid, measurements were conducted in the early 1970's using the Apollo launch vehicle configurations as test vehicles. Results from both of these flights are reported in References 3 and 4 and agreement between predicted and flight results was good. This agreement provided some level of confidence on the ability of semi-empirical techniques

PRECEDING PAGE BLANK NOT FILMED

PAGE 1276 INTENTIONALLY BLANK

to predict Space Shuttle sonic boom overpressure levels during ascent. These predicted levels are presently baselined as required by law in the Space Shuttle Program Environmental Impact Statement (Ref. 5).

This paper presents results based on flight pressure signature generated during entry of STS-1 (Orbiter Columbia) at Edwards Air Force Base and ascent of STS-5 from Kennedy Space Center. The STS-1 Orbiter Columbia sonic boom signatures were measured under the descent ground track from near the California coast to Edwards Air Force Base at flight conditions of M = 5.87 to M = 1.23. The STS-5 ascent sonic boom signatures were measured by microphones placed aboard a ship located near the ascent focal zone approximately 71.67 kilometers (km) east of Cape Canaveral, Florida and were generated at a flight Mach number of 3.57. These pressure signatures were recorded on analog magnetic tape and were analyzed using standard data analysis principles. These measured results, i.e. peak sonic boom overpressure levels, are then compared with estimates based on wind tunnel data of Refs. 6 and 7 using the best estimate of trajectory (BET) post flight data along with the appropriate measured meteorological data using the extrapolation procedure of Ref. 1.

ANALYSIS METHOD AND PRESSURE INSTRUMENTATION

The theoretical prediction technique employed in this analysis is the so called "Thomas Program". This prediction technique is a semi-empirical method that requires definition of the near field signatures, detailed trajectory characteristics and the prevailing meteorological characteristics as an input. The near field signatures define the vehicle configuration in terms of shape, Mach number, and altitude; i.e. angle of attack, roll angle. This analytical procedure then extrapolates the near field signature, using the best estimate of trajectory (BET) post flight data as well as the meteorological data acquired in the vicinity of the measurements, from the flight altitude to an altitude consistent with each measurement location. The details of this technique are described fully in Ref. 1.

An integral part of this prediction method is, of course, the near field signatures. These signatures, in effect, define the source characteristics of the vehicle under consideration. These near field signatures have been acquired through wind tunnel testing for both the STS Orbiter entry conditions as well as the Shuttle ascent conditions. These data are contained in Ref. 6 and 7. For the STS ascent configuration, the effect of the exhaust plumes (Space Shuttle Main Engine and Solid Rocket Booster) is significant and this "plume effect" was modeled and is included in these near field signatures characteristics. Post flight trajectory data for both ascent and reentry was used in the theoretical analysis and was based on the best estimate of trajectory (BET) data. A detailed description of the BET data used is presented in Refs. 8 and 9.

Meteorological data was acquired for STS-1 entry from Rawinsonde observations near the ground track (station 2) which was located 93 km from the landing site. These observations were taken approximately 3 hours before and during STS-1 landing on April 14, 1981. Measured values of temperature, wind direction, and speed as a function of altitude were obtained. These results are given in detail in Ref. 8. Balloon data were obtained up to an altitude of about 28,062 meters. Atmospheric data above 28,062 meters are based on a Global Reference Atmosphere obtained from the National Weather Service.

For the STS-5 ascent conditions, Rawinsonde and Rocketsonde observations were taken at the Cape Canaveral Air Force Station, FL along with local climatological data (surface temperature, relative humidity, surface wind and direction) obtained from the Shuttle landing facility at the Kennedy Space Center, FL and station No. 2 (USAF- LCU ship) positioned approximately 71.67 km downrange from the launch site. These atmospheric soundings were taken at 52 hrs., 25 hrs., 13 hrs., 5 hrs., 1.5 hrs., and 1 hr. before liftoff on November 11, 1982. Measured values of windspeed and direction, temperature, dewpoint, and pressure were merged together from Rawinsonde, Rocketsonde, and surface data to give a sounding profile for altitude from the surface to approximately 36576 meters. A detailed description of these results are provided in Ref. 9.

The sonic boom data acquisition system utilized for the Space Shuttle STS-1 reentry and STS-5 ascent sonic boom pressure measurement program is commercially available and is similar to that used in measurements of aircraft sonic boom signatures (Ref. 10) and for measurements taken during the Apollo 16 and 17 sonic boom measurement programs (Refs. 11 and 12). These systems consist of pressure transducers, Dynagages (oscillator detector circuits), signal conditioning amplifiers, FM magnetic tape recorders, and satellite time code receivers. Specifically, the pressure transducer is a commercially available condenser microphone with a high frequency response to 10 kH_z when used with the model DG-605 Dynagage system, with the low-end frequency response of approximately -5dB at 0.01 Hz. A photograph of a typical data acquisition system is shown in Fig. 1.

Fig. 2 depicts a block diagram of a typical instrumentation system for sonic boom data acquisition. Typically, each measurement station recorded six channels of overpressure data, a time code signal, and voice annotation. The output of the microphones was routed through appropriate signal conditioning amplifiers which allowed various sensitivities to be obtained for a range of preselected levels. This is a precaution necessary to allow for uncertainty in the prediction method or anomalous overpressure levels caused by unusual atmospheric, vehicle maneuvering or other focusing conditions.

STS-1 ENTRY CONFIGURATION AND MEASUREMENT DESCRIPTION

The STS-1 Orbiter Columbia was launched from the Kennedy Space Center, Florida on April 12, 1981, at an inclination of 40.3°. The mission had a duration of 2½ days, and the Orbiter Columbia reentered the earth's atmosphere over the mid-Pacific Ocean between Guam and Hawaii. The Columbia landed on the dry lake bed at EAFB approximately 81.49 km downrange of the reentry interface which occurred at an altitude of 121920 m.

A schematic of the STS-1 Orbiter Columbia (descent configuration) whose sonic boom levels were measured during entry is shown in Fig. 3. The Orbiter Columbia is a lifting vehicle capable of maneuvering and landing much like an airplane by using its control surfaces which are augmented by a reaction control system. As such, during its atmospheric flight, it is capable of flying at angles of attack as high as 40 degrees and rolling about the velocity vector to ±70 degrees. Columbia has an overall length of 32.7 meters and had a gross weight at entry interface (121 951.2 meters altitude) of 90 720 kg during the STS-1 mission.

Sonic boom measurements were made at eleven stations (locations) along the reentry ground track and are shown in Fig. 4. In order to define these locations, a pre-flight STS-1 sonic boom analysis was performed based on the final pre-flight predicted STS-1 Operational Flight Profile for a nominal entry into EAFB. This analysis defined the theoretically desired locations for the eleven sonic boom stations, shown in Fig. 4., by a circled number (0-10) and located near the entry ground track shown as a dashed line. The predicted overpressure levels at those locations were used to set the six signal conditioning amplifiers at each station. Selection of the recommended measurement station locations was based on several considerations. Since the primary objective of the sonic boom measurement program is to verify the theoretical technique used to predict sonic boom overpressures (Ref. 1) the station locations were distributed across the flight Mach number range for which wind-tunnel-measured pressure signatures exist in order to verify the near field data base. Consequently, the layout of the measurement stations on this flight was designed primarily to confirm the longitudinal trend of overpressure level with Mach number and secondarily, the lateral trend of overpressure with Mach number in the area of expected high overpressures. The majority of the station locations was selected to capture overpressure in the region of maximum predicted overpressure level which occurs in the immediate vicinity of the EAFB lake bed. This selection criteria also has the advantage of locating the measurement stations in the part of the entry ground track least affected by atmosphere and trajectory dispersions, thus maximizing the probability of obtaining useful data.

STS-1 ORBITER ENTRY RESULTS AND DISCUSSION

Six measurement channels were made at each station location. Five were located in the ground plane and one was placed at a simulated ear-level position; i.e. 1.5 meter elevation. Each of the six measurement channels were ranged differently (calibrated) in anticipation of the possible variation of levels about the nominal or predicted level. In the discussion that is to follow, only the primary ground level measurement (channel 1) and the ear level position measurement (channel 5) will be presented. All measurement stations were near the nominal or predicted level and consequently, these channels provide the most sensitive and better quality measurement.

Selected sonic boom signatures (instantaneous pressure time history) for Orbiter entry at Edwards are presented in Fig. 5a through 5h. These results are plotted for a .8 second time period and are given in Newton/(meter)^2, (N/m^2) for each of the eleven measurement stations. The energy arriving at a given ground location, originates at a specific region along the flight path; i.e. Mach number. For stations which are located generally below the flight path, the Mach number at which the energy originates, decreases as the Orbiter approaches the landing site. With decreasing Mach number, the decrease in the duration of the sonic boom signatures are to be expected. This is evident in Fig. 5a through 5h when comparing station 0 with station 10; i.e. Mach 5.9 with Mach 1.23. Also evident in these figures is the effect of the difference in arrival time between the incident and reflected pressure; i.e. delay time's at the ear level measurement.

All measurements were inspected for any other type of signal events for a period of 2 minutes before and after the sonic boom arrival time of the signatures presented in Fig. 5a through 5h. Only measurements at stations #4 (Camron Canyon) and station #9 (North Edwards) show the effect of a small reflected wave arriving after the primary sonic boom wave. Analysis indicate that these waves (Fig. 6 is presented as an example) are due to reflections from near-by hills rather than from the direct propagation of energy from a different region along the flight path. The peak positive and negative sonic boom levels and the duration for each location are summarized in Table I.

Detailed analysis of the rise time of each signature at each measurement station has also been conducted. A typical example of the rise time is presented in Fig. 7 for a 50 millisecond time internal for both the ground plane measurement and the ear level position measurements for station 7.

The distinct difference in arrival time between the incident and ground reflected wave is clearly evident; i.e., the reflected wave is delayed in time from the incident wave, i.e., delay time, δ. Because the ground plane and ear level position measurements were located at slightly different positions with respect to the sonic boom wave front, the arrival times at these positions were slightly different, as can be seen. For consistency, the sonic boom arrival times at each location are determined using the ground plane measurement (channel 1) and are also summarized in Table I.

Estimates of the ground reflection factor can be made with the aid of the ground plane and ear level measurements. Under simplifying assumptions of a plane wave front that is uniform over these two positions and because the incident wave (at the ear level position) is separated in time from the reflected wave, reasonable estimates are possible. It can be shown, that if the ground plane measurements are divided by the ear level measurement and if the results are restricted to the time internal diving when only the incident wave is present (in the ear level measurement) then the result will provide reasonable estimates of the reflection factor; i.e., R_f. This operation was performed at each measurement station and the results are also presented in Table I. A typical example for station 7 is presented in Fig. 8. The ear level measurement had to be shifted in time before the ratio was performed to account for the slightly different arrival time at the ground plane and ear level location. The reflection factor estimates were obtained by averaging the reflection factor time signal over the latter position of the signals, see Fig. 8.

The duration of the Orbiter entry sonic boom signatures are quite long. They range from 375 milliseconds at M = 1.23 to 700 milliseconds at M = 5.87. Because of these long durations, the predominant energy of these signatures occur at frequencies well below the normal hearing range of the human auditory system. Spectral analysis of the STS-1 reentry signatures have been performed and typical results are presented in Fig. 9 through 11.

When performing spectral analysis of transient signals, such as the sonic boom signature, energy spectral density (ESD) functions should be used instead of power spectral density (PSD) functions normally employed in analyzing stationary random signals. The spectral analysis results presented are typical of those at the other locations. In Fig. 9 and 10, this analysis is presented for a maximum frequency range of 2500 Hz. The rapid decay of energy with increasing frequency is clearly evident in these results. Also, the effect of the ear level microphone (channel 5 in Fig. 10) elevation is clearly evident. This height introduces additional lobing in the frequency spectrum. The analysis bandwidth resolutions in these spectra is 1.22 Hz.

Fig. 11 is presented in order to show in more detail, the characteristics of the lower frequency portion of the spectra; i.e. below 100 Hz. The analysis bandwidth here is .244 Hz. The low frequency character of the STS-1 sonic boom signatures is clearly evident with the peak frequency slightly over 2 Hz and the characteristic 6 dB/octave roll off of these type of signals.

The sonic boom signatures for all ground plane measurements are delineated in Fig. 12 in "iso-time history" format. The complete character of the STS-1 Orbiter entry sonic boom time histories is vividly illustrated.

As indicated earlier, the technique described in Ref. 1 was used to extrapolate the near field overpressure signature from flight conditions to the ground level. The process of identifying both the initial near field signature and the trajectory state, which correspond to the ground overpressure measurements recorded at a given station, is iterative in nature. It consisted of a search on both the trajectory state and its corresponding field signature which were systematically varied until the conditions of the ground wave intersection point and the station location are matched. Table II is a summary of the results of this search and shows for each station the pertinent trajectory conditions, signature ray angle, and the measured and predicted overpressures. As can be seen, the comparison between the measured and predicted levels are good. The predicted overpressure distributions as a function of lateral distance from the ground track for two selected Mach numbers are shown in Fig. 13 and 14 along with the measured results. Again, the comparisons are good. Complete description of these STS-1 results are contained in Ref. 8.

STS-5 ASCENT CONFIGURATION AND MEASUREMENT DESCRIPTION

A schematic of the STS-5 launch vehicle (ascent configuration) whose sonic boom levels were measured during ascent is shown in Fig. 15. The launch vehicle consists of an orbiter, an external tank, and a booster made up of two solid rocket motors. The solid rocket motors burn in parallel with the orbiter main propulsion engines and are separated from the oribiter/external tank and burnout (~ 48000 meters altitude). Thereafter the orbiter main propulsion engines continue to burn until the orbiter is injected into the required ascent trajectory. The launch vehicle configuration consists not only of the elements depicted in Fig. 15 but also of the exhaust plumes generated by the orbiter propulsion system and the solid rocket motors. These exhaust plumes have a significant effect on the ascent sonic boom characteristics. The STS-5 vehicle was launch on November 11, 1982 from launch pad 39-A at Kennedy Space Center on a five day mission with subsequent orbiter landing at the EAFB dry lake bed in California. The launch vehicle has an overall length of 56.3 meters and had a gross liftoff weight of 2036422 kg.

Nine measurement stations were planned to be acquired during ascent of STS-5. The pre-flight location for these measurements was determined by a procedure similar to that described for the STS-1 entry measurements. The data acquisition system was to be deployed aboard ships at these locations. These measurement locations were selected primarily to acquire sonic boom overpressure characteristics in the STS-5 ascent focal zones from near the ground track out to lateral cut-off.

At the time of launch, due to the high sea state conditions off-shore and the restricted ship size only ship number 2 could be deployed to its preplanned location and consequently only data at this station was obtained.

STS-5 ASCENT RESULTS AND DISCUSSION

As indicated above, data was acquired only at one station location during STS-5 ascent; i.e., station 2. For this ascent configuration, no ear level measurements were made, consequently all channels for ship number 2 location were placed in simulated ground plane position.

Ship number 2 was located 71.67 km down range and the sonic boom energy which arrived at this position was generated at a flight ascent Mach number of 3.57 and a flight altitude of 34086 meters.

The ship location, along with the predicted ground overpressure at M = 3.57, is shown in Fig. 16. The detail signature characteristics recorded at ship number 2 position is presented in Fig. 17. The measured positive peak overpressure level is 175.2 N/m^2 psf. As can be seen, this signature exhibits multiple peaks and it has the long slow recovery in the expansion part of the waveform which is associated with launch vehicles with large exhaust plumes. The multiple peaks are consistent with the ascent signature obtained in the focal region during ascent of Apollo 17 (Ref. 12) and is typical of that associated with sonic boom near focal zones in general. The third peak in the signature (Fig. 17) is believed to be caused by energy arriving at this location that originated earlier during the flight than the energy which caused the initial peak. Because of the acceleration and curvature effects of an ascending vehicle, the sonic boom wavefront tends to become folded, thus generating the multiple peaks (see Ref. 13). In general, with increasing downrange distance from the focus, the separation between the first and third peak will tend to increase. The separation between first and third peak is only 1.3 sec, which is another indication that ship number 2 was very near the STS-5 ascent focal zone. The exact nature of the third peak is under further study to verify these observations. It is not clear as to the origin of the second peak and it is also under further study. However, because of the folded nature of the wavefront in this region it is probably associated with dispersion of the energy from the nearby focus or an overhead focus.

Ascent (launch vehicle) signatures do not have the classical N-wave type of signature typically associated with fighter aircraft or the Shuttle Orbiter configuration, for example. This long duration waveform and its slow recovery is a direct result of the effect of Space Shuttle's exhaust plumes. The N-wave type signature results from bodies (vehicle) with distinct termination from front to rear, which is not the case for launch vehicles. However, the first initial rise time is consistent with N-wave type signatures.

Using the extrapolation method of Ref. 1 with the BET post flight data and the measured meteorological data, the predicted sonic boom overpressure level at ship number 2 is 148.4 N/m^2. This compares favorably with the 175.2 N/m^2 level that was measured. The initial portion of the predicted waveform is also shown in Fig. 17, and as can be seen, the comparison is very good. Complete description of these STS-5 results are presented in Ref. 9.

CONCLUDING REMARKS

This paper presents sonic boom pressure signatures recorded during the entry of the STS-1 Orbiter Columbia and ascent of the STS-5 Space Shuttle. During STS-1 entry, peak overpressure levels were recorded at eleven measurement stations and they ranged in level from 33.16 N/m^2 to 114.91 N/m^2. Predicted peak levels and duration of the positive portion of the N-waves using a semi-empirical technique correlated well with the measured data. Analysis of signature characteristics showed that the ground reflection factor varied from 1.83 to 2.09. A reflection factor of 1.9 was used for predictions. The frequency analysis of the STS-1 signatures showed that the peak frequency of the orbiter during entry is on the order of 2 Hz.

Also, comparison of sonic boom levels predicted and measured at one station location during ascent of the STS-5 Space Shuttle Mission was presented. A peak overpressure level of 175.2 N/m^2 was measured during ascent generated from an altitude of 34086 meters at $M = 3.57$. In addition to this initial peak, two other peaks of lower intensity were also observed. The signature was not a simple N-wave in shape, however, it exhibited a rapid rise time and number of intermediate shocks which are associated with the near focus boom region resulting from the curved, accelerating flight profile of the STS-5 launch vehicle. The predicted overpressure level of the sonic boom signature utilizing semi-empirical techniques correlated well with the measurement. Follow-on work will include detailed signature analysis of the measured data and further study of the origin of the additional peaks.

REFERENCES

1. Thomas, C. L.: Extrapolation of Sonic Boom Pressure Signatures by the Waveform Parameter Method. NASA TN D-6832, June 1972.

2. Hayes, W. D., Haefeli, R. C., and Kulsrud, H.: Sonic Boom Propagation in a Stratified Atmosphere, with Computer Program Rept. No. 116, Aeronautical Research Associates of Princeton, Inc., Dec. 1968.

3. Hick, Raymond M., Mendoza, Joel P., and Garcia, Frank: A Wind Tunnel-Flight Correlation of Apollo 15 Sonic Boom. NASA TM X-62111, January 28, 1972.

4. Garcia, Frank, Hicks, Raymond M., and Mendoza, Joel P.: A Wind Tunnel-Flight Correlation of Apollo 16 Sonic Boom. NASA TM X-62073, Feb. 5, 1973.

5. Malklin, M. S.: Environmental Impact Statement for the Space Shuttle Program. NASA Headquarters, NASA TM 82278, 1978.

6. Mendoza, Joel P.: Wind Tunnel Pressure Signatures for a .0041-Scale Model of the Space Shuttle Orbiter. NASA TM X-62432, May 1975.

7. Ashby, George C.: Near-Field Sonic Pressure Signatures for the Space Shuttle Launch and Orbiter Vehicles at Mach 6. NASA Technical Report 1405, April 1979.

8. Garcia, Frank, Jones, J. H., and Henderson, Herbert R.: Preliminary Sonic Boom Correlation of Predicted and Measured Levels for STS-1 Entry. NASA TM-85242, Feb. 1982.

9. Garcia, Frank, Jones, J. H., and Henderson, Herbert R.: Preliminary Sonic Boom Correlations of Predicted and Measured Levels for STS-5 Launch. NASA TM 58253, April 1983.

10. Proceedings of the Sonic Boom Symposium. Journal of the Acoustical Society of America, Vol. 39, No. 5, May 1966, pp S1-S80.

11. Henderson, Herbert R., and Hilton, David A.: Sonic Boom Ground Pressure Measurements from the Launch and Reentry of Apollo 16. NASA TN D-7606, 1974.

12. Henderson, Herbert R., and Hilton, David A.: Sonic Boom Measurements in the Focus Region During the Ascent of Apollo 17. NASA TN D-7806, 1974.

13. Holloway, Paul F., Wilhold, Gilbert A., Jones, Jess H., Garcia, Frank, Hicks, Raymond M.: Shuttle Sonic Boom - Technology and Prediction, AIAA paper No. 73-1039, Oct. 1973.

TABLE I

STS-1 SONIC BOOM OVERPRESSURE CHARACTERISTICS

MEASUREMENT LOCATION		PEAK OVERPRESSURE LEVEL		TOTAL TIME DURATION (SEC)	RISE TIME (MSEC)	BOOM ARRIVAL TIME GMT (H:M:S)	REFLECTED SIGNAL DELAY (MSEC)	REFLECTION FACTOR
STATION NO.	CHANNEL NO.	POSITIVE (N/m^2)	NEGATIVE (N/m^2)					
0	1	33.16	27.39	.693	4.4	18:13:28:432	8.6	1.84
	5	34.33	31.85	.700	4.2			
1	1	58.41	54.58	.583	5.0	18:14:47:579	8.6	1.87
	5	61.77	57.9	.588	5.0			
2	1	44.53	41.18	.530	4.0	18:15:08:729	9.0	2.27- 2.32
	5	38.30	38.3	.538	4.0			
3	1	54.58	53.98	.525	4.4	18:15:29:283	8.2	2.09
	5	50.75	56.98	.531	4.2			
4	1	76.61	73.74	.491	4.8	18:15:54:266	8.6	2.00
	5	68.47	67.03	≈.497	4.6			
5	1	75.17	72.78	.40[illegible]	≈4.4	18:16:20:651	8.0	1.98
	5	75.17	74.21	≈.414	≈4.4			
6	1	114.91	105.82	.394	4.0	18:16:33:797	8.0	*
	5	86.18	90.01	.406	-			
7	1	93.85	84.75	.380	≈4.0	18:16:54:366	7.2	1.85
	5	101.03	90.97	.393	-			
8	1	86.66	79.00	.376	5.0	18:17:11:449	5.4	1.98
	5	81.40	Clipped	Clipped	5.0			
9	1	108.21	90.49	.375	3.6	18:17:08:634	5.4	1.90
	5	94.32	89.54	.380	2.8			
10	1	89.04	83.31	.375	1.8-3.2	18:17:17:103	5.8	1.83
	5	79.48	105.82	.380	≈1.8			

* Channel 5 very noisy.

ORIGINAL PAGE IS
OF POOR QUALITY

TABLE II

COMPARISON OF PREDICTED AND MEASURED OVERPRESSURE LEVELS

STATION	FLIGHT TIME FROM ENTRY INTERFACE (SEC)	MACH NUMBER	ALTITUDE (m)	RAY* ANGLE (DEG)	RAY TRAVEL TIME (SEC)	PREDICTED ΔP (N/m^2)	RECORDED ΔP (N/m^2)
0	1334	5.87	39337	-8.5°	129.7	35.91	33.16
1	1431	3.94	32876	-11	111.5	48.26	58.41
2	1462	3.41	30401	-2	101.3	55.88	44.53
3	1491	2.97	27899	+10	92.1	54.44	54.58
4	1527	2.39	24953	+2	82.6	71.58	76.61
5	1556	1.98	23054	-4	79.4	87.48	78.04
6	1573	1.76	21552	-4	75.1	92.65	114.91
7	1596	1.45	19447	0	73.0	92.98	93.85
8	1596	1.45	19447	-36	90.6	75.17	86.66
9	1600	1.40	19103	+30	83.9	80.63	108.21
10	1616	1.23	17770	-6	76.5	87.43	89.04

*Positive left of groundtrack

ORIGINAL PAGE IS
OF POOR QUALITY

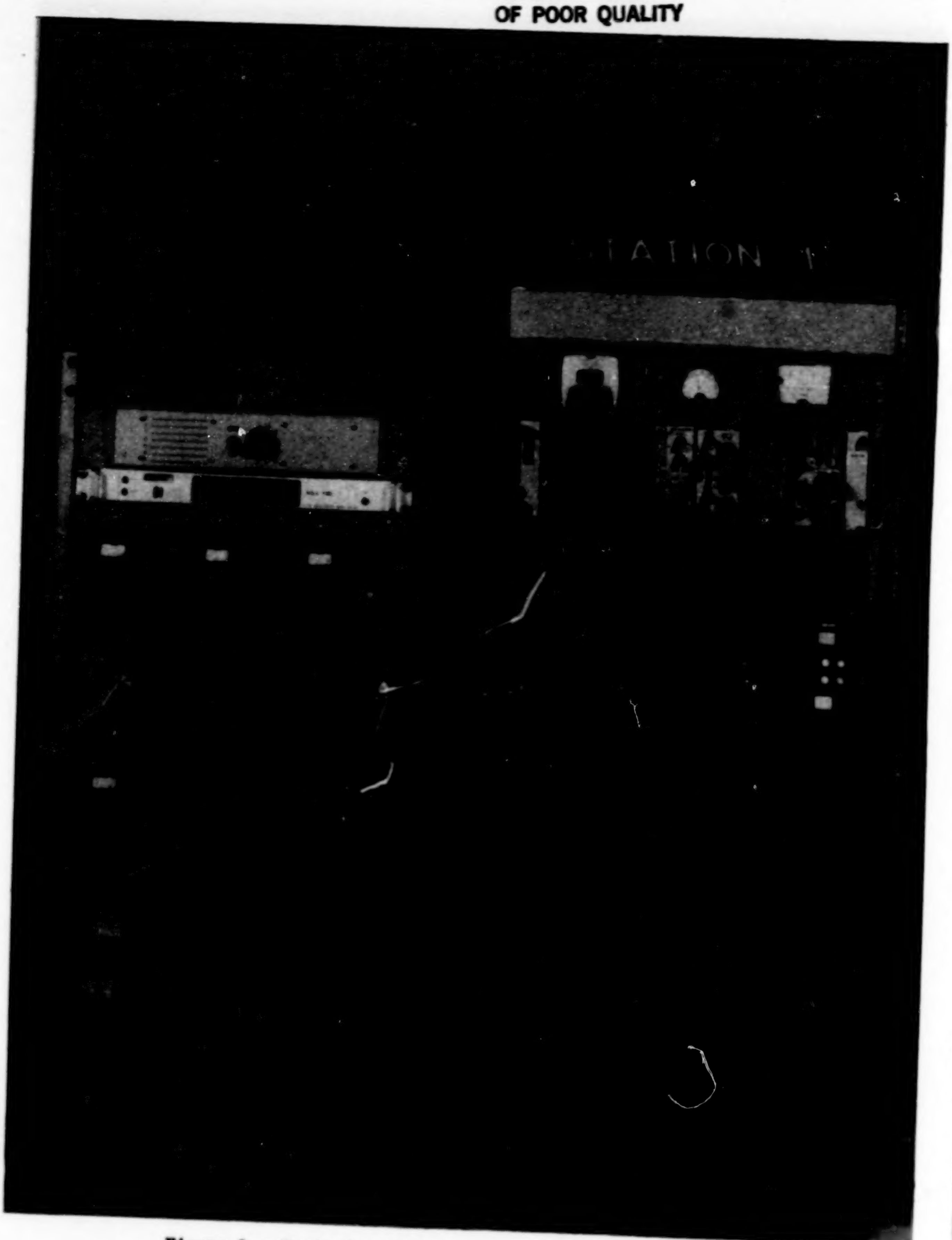

Figure 1.- Typical sonic boom data acquisition system.

ORIGINAL PAGE IS
OF POOR QUALITY

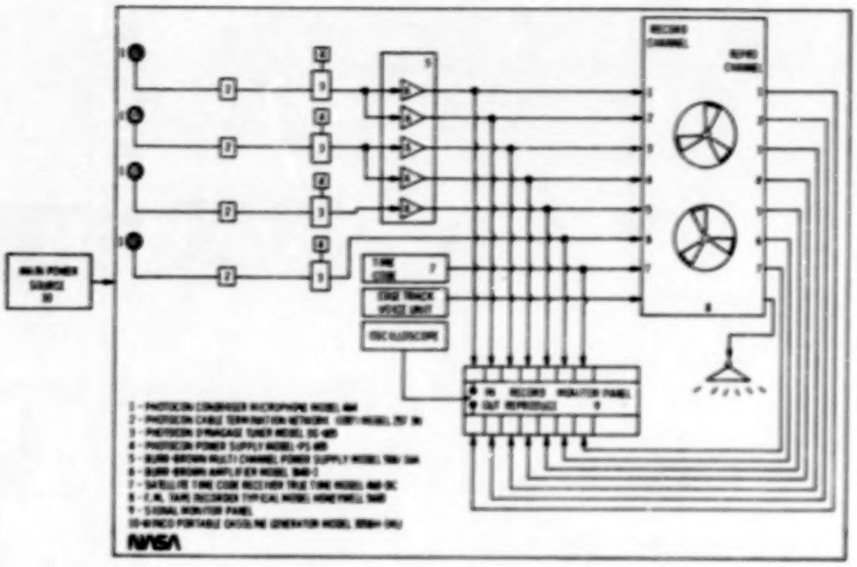
RECORD CHANNEL
REPRO CHANNEL
MAIN POWER SOURCE 10
TIME CODE 7
OSCILLOSCOPE
RECORD MONITOR PANEL
NASA

Figure 2.- Block diagram showing typical sonic boom data acquisition system.

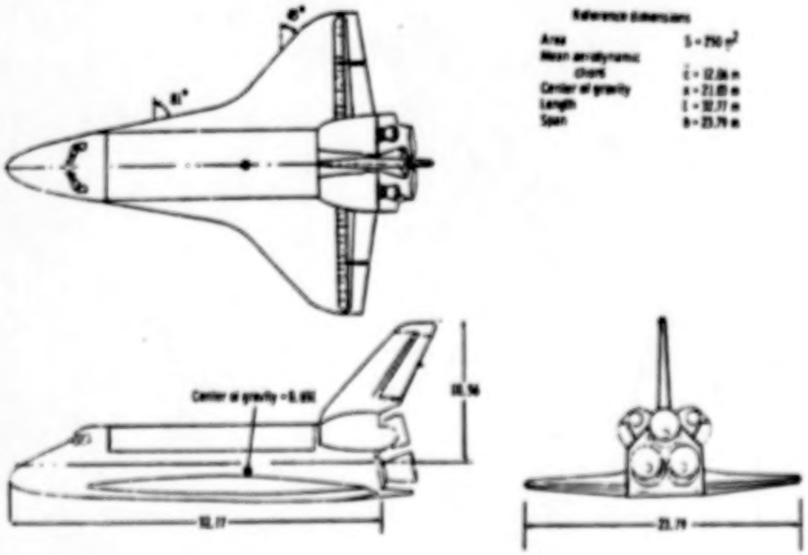
Reference dimensions
Area S = 250 m²
Mean aerodynamic chord c̄ = 12.06 m
Center of gravity x = 21.03 m
Length l = 32.77 m
Span b = 23.79 m
45°
81°
32.77
23.79

Figure 3.- Schematic of orbiter configuration.

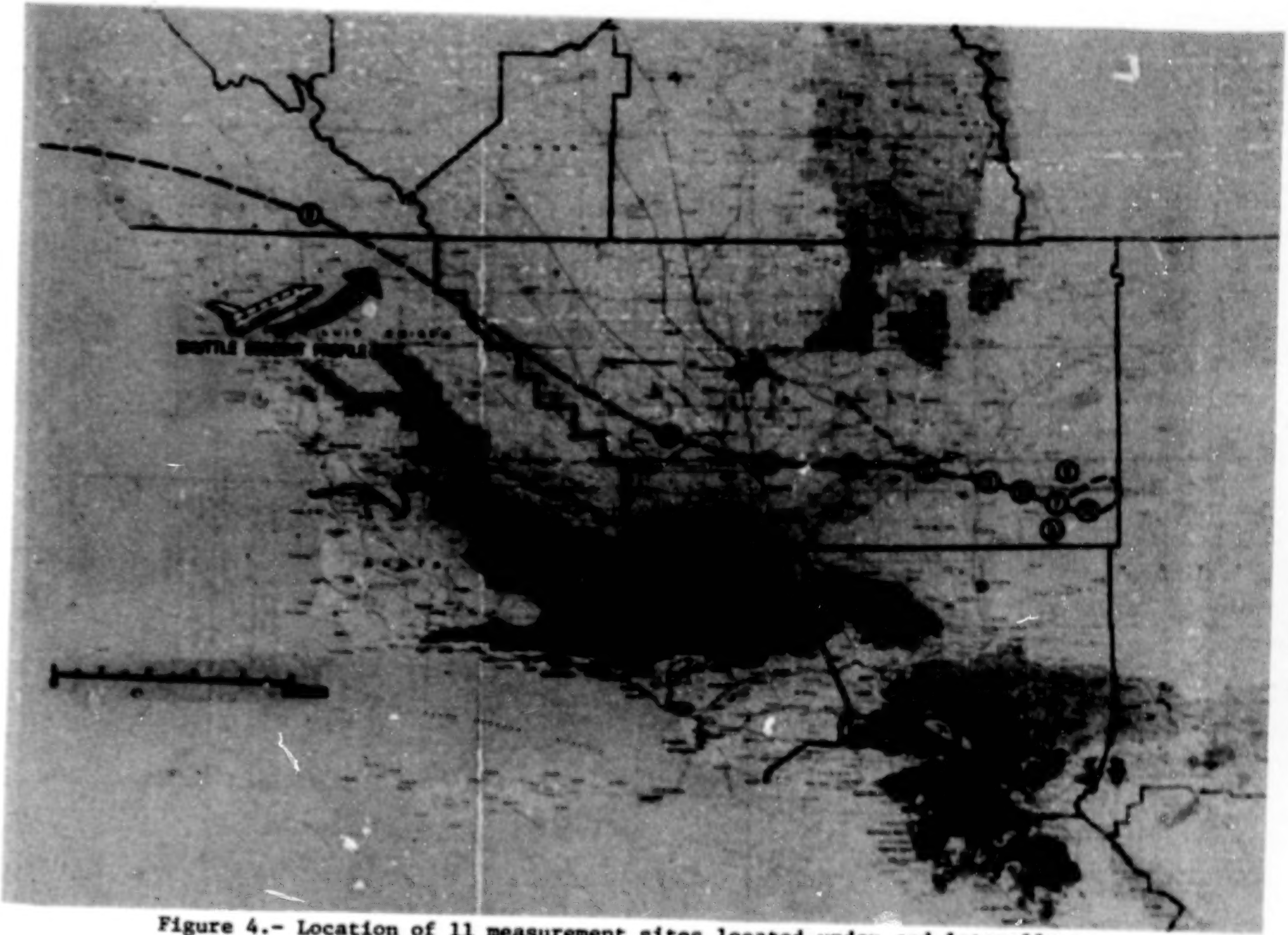

Figure 4.- Location of 11 measurement sites located under and laterally to the STS-1 reentry track into Edwards Air Force Base, CA.

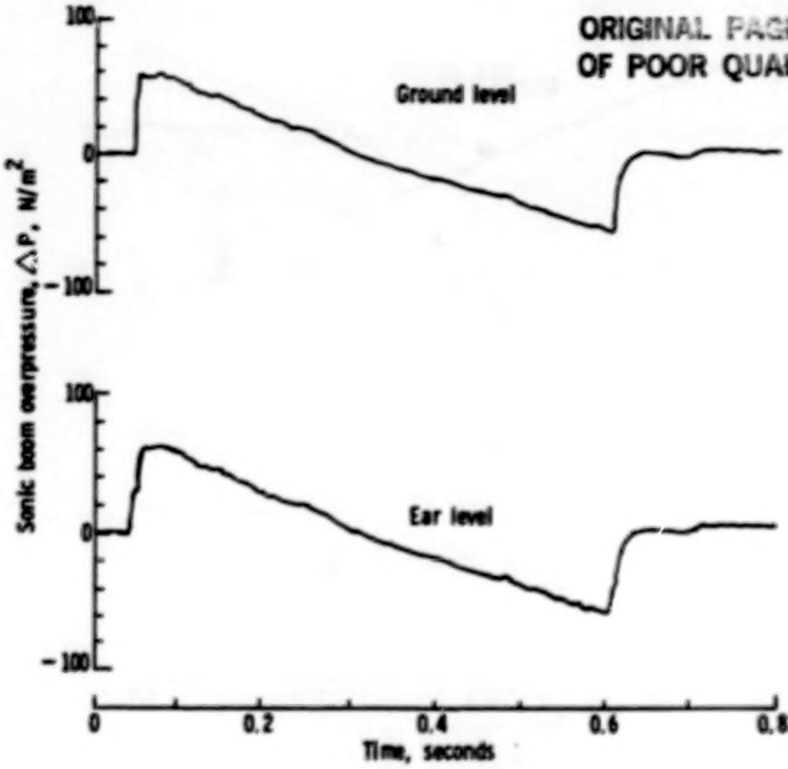

(a) Station 1.

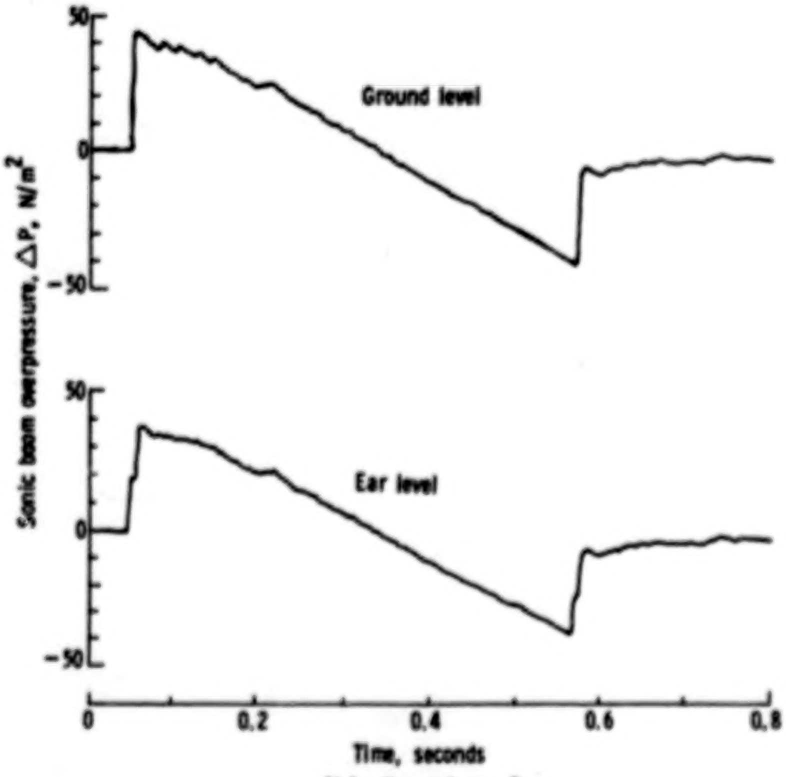

(b) Station 2.

Figure 5.- Sonic boom signatures measured during reentry of STS-1 as recorded at stations 1 through 7 and station 10.

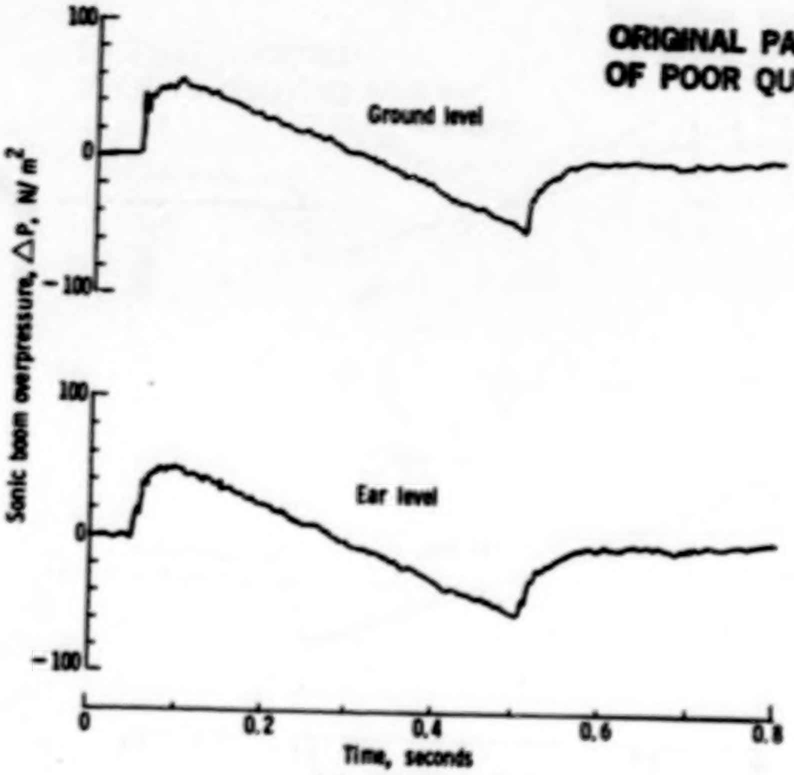

(c) Station 3.

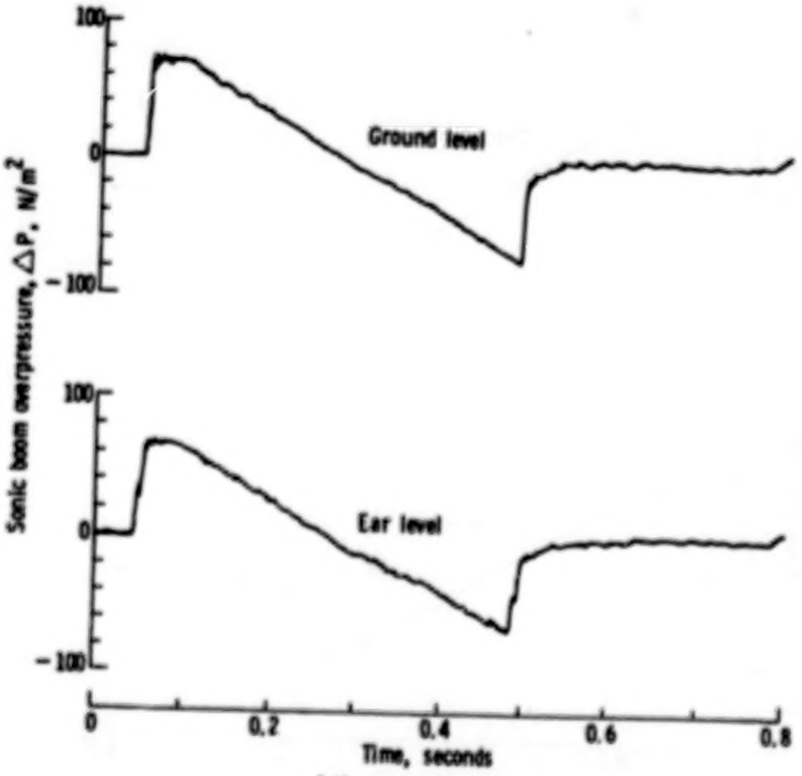

(d) Station 4.

Figure 5.- Continued.

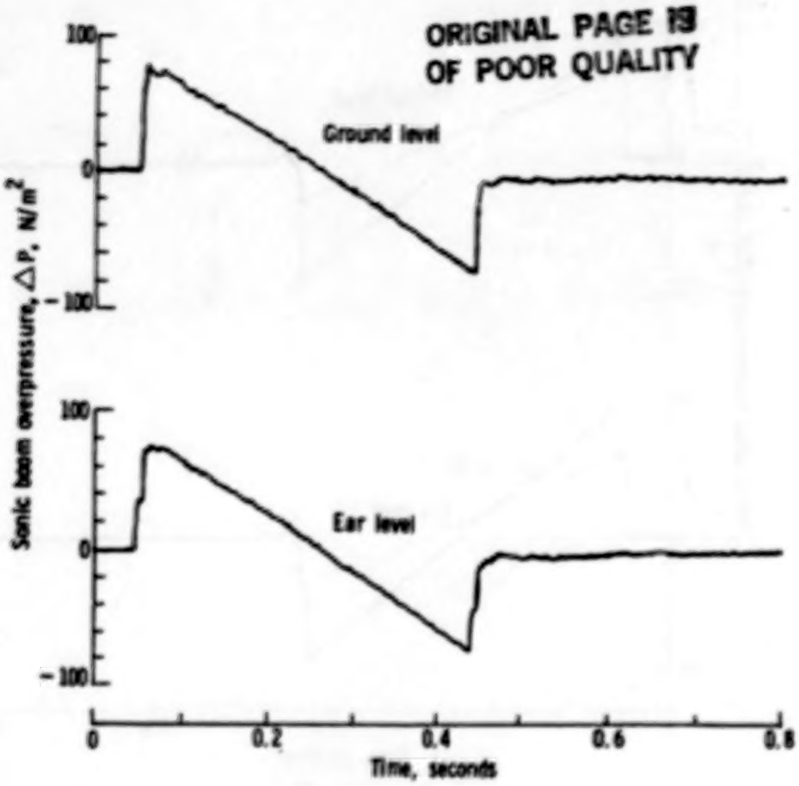

(e) Station 5.

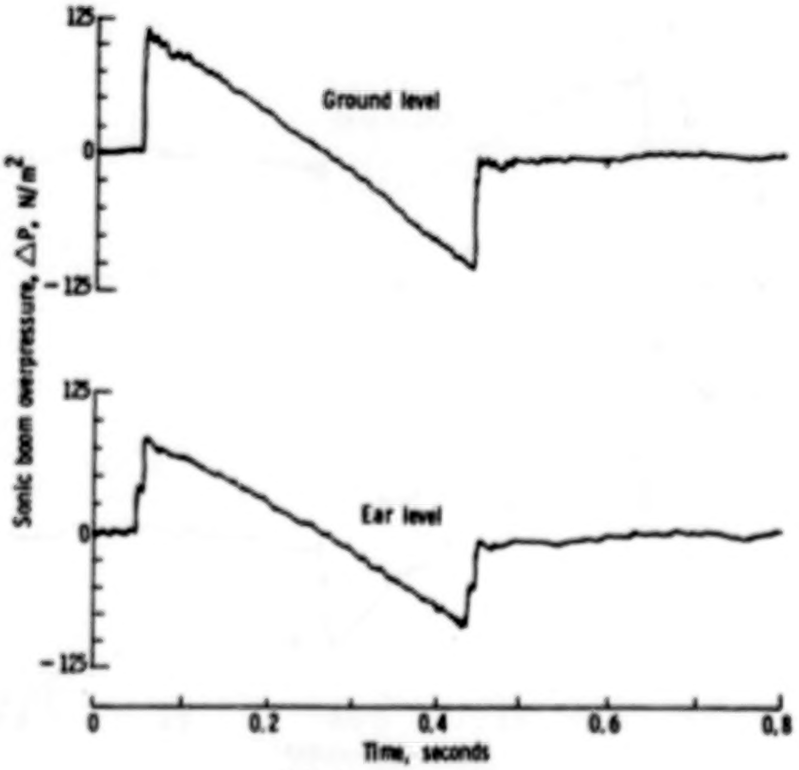

(f) Station 6.

Figure 5.- Continued.

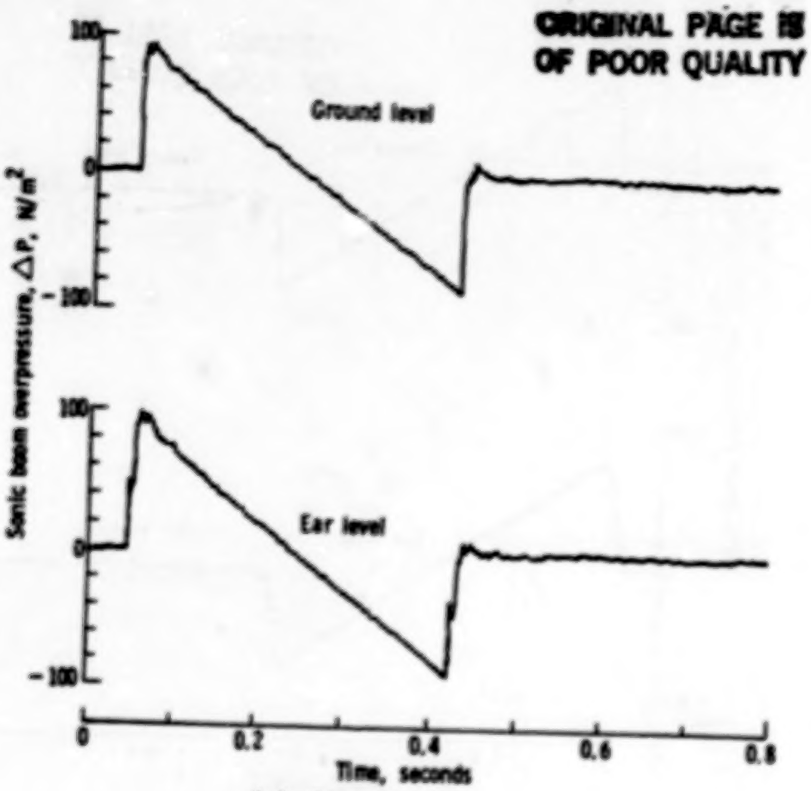

(g) Station 7.

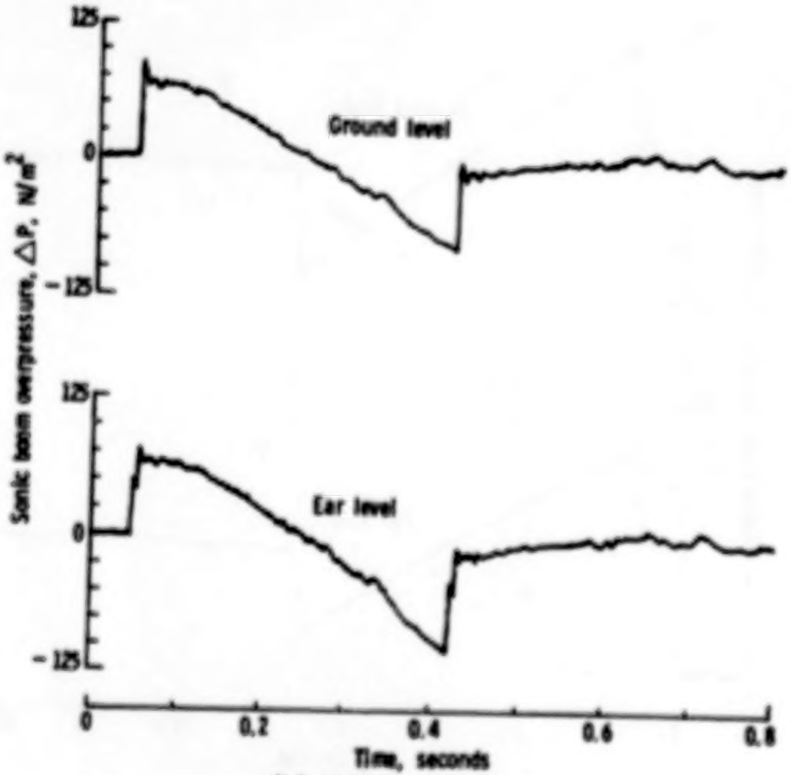

(h) Station 10.

Figure 5.- Concluded.

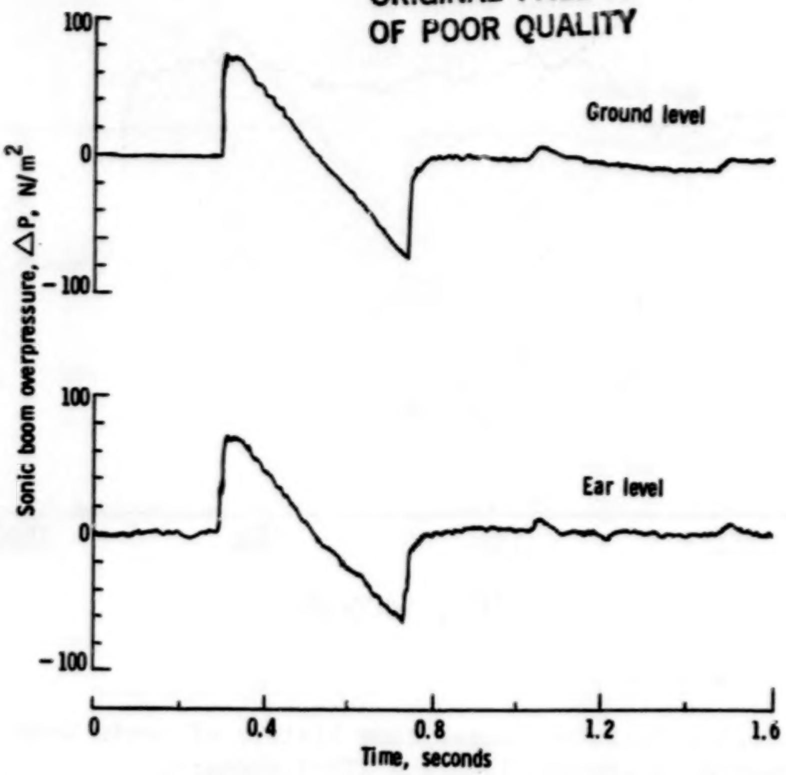

Figure 6.- Measured sonic boom signature showing reflected waves as recorded at station 4 during STS-1 reentry.

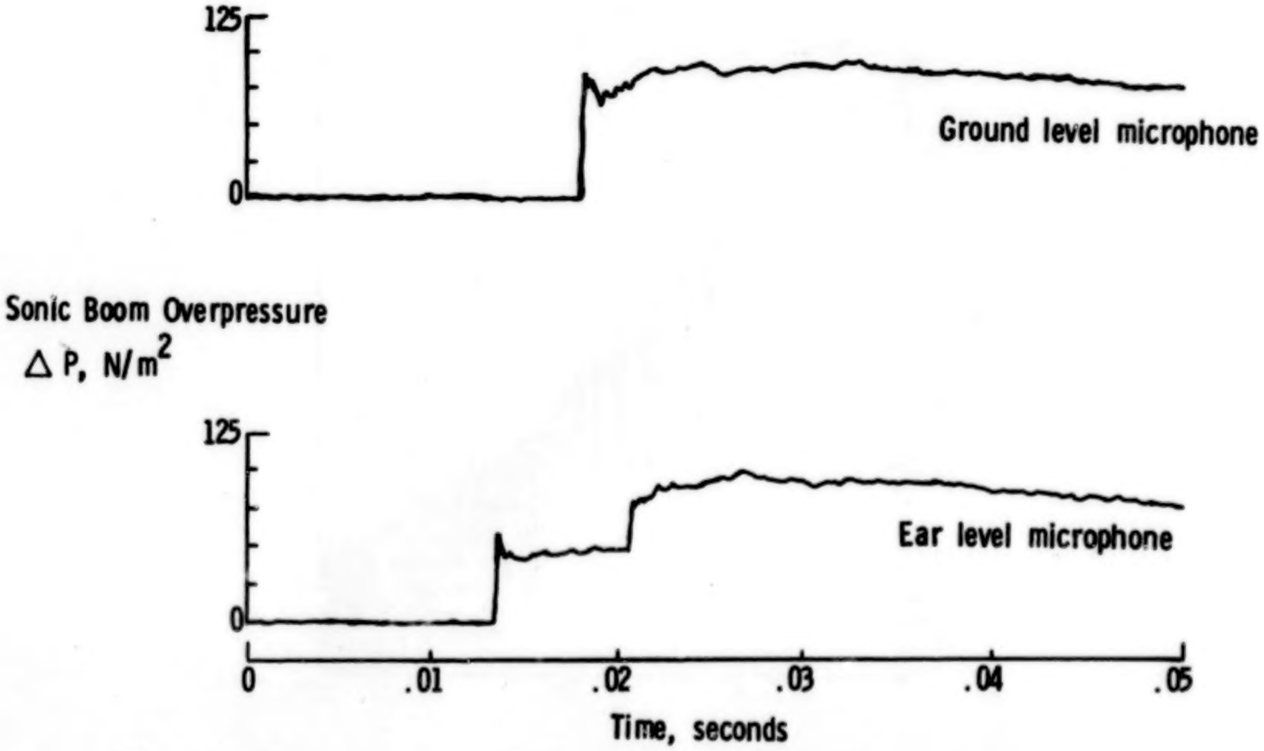

Figure 7.- Measured sonic boom signatures from station 7 during STS-1 reentry showing details of bow shock-wave rise time.

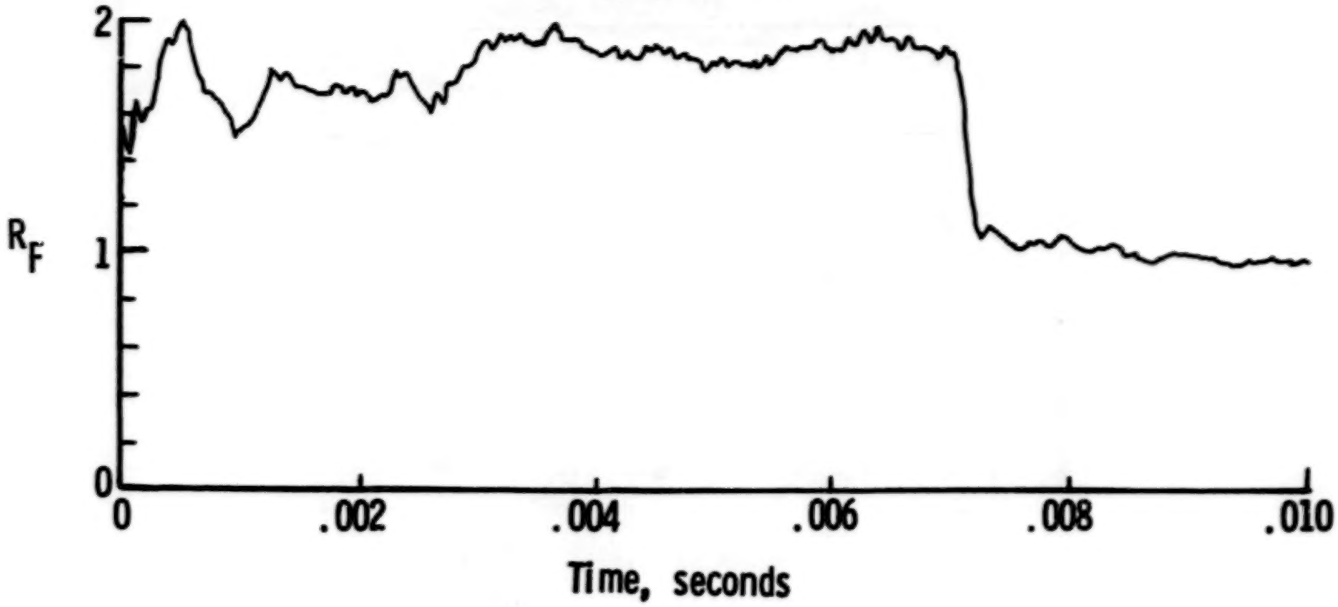

Figure 8.- Typical reflection factor time history of sonic boom signature measured at station 7 during STS-1 reentry.

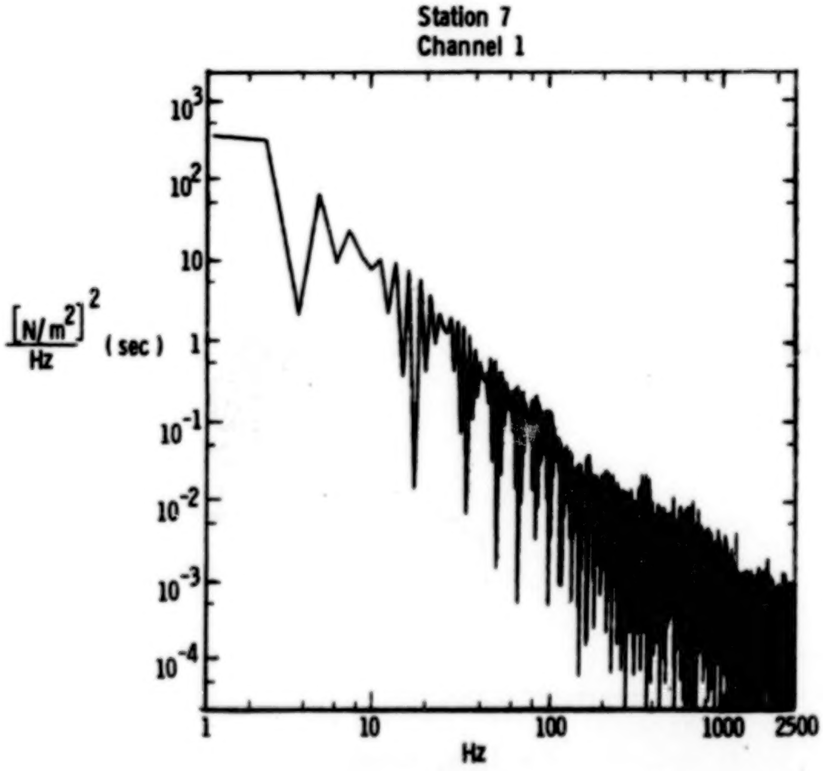

Figure 9.- Energy spectral density analysis from station 7 ground level microphone during STS-1 reentry.

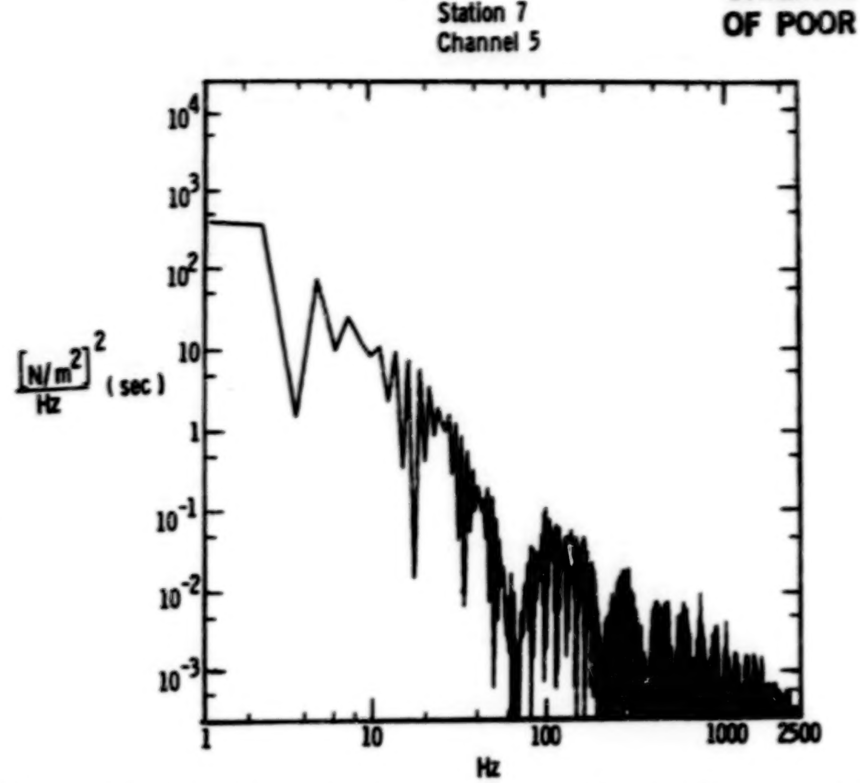

Figure 10.- Energy spectral density analysis from station 7 ear level microphone during STS-1 reentry.

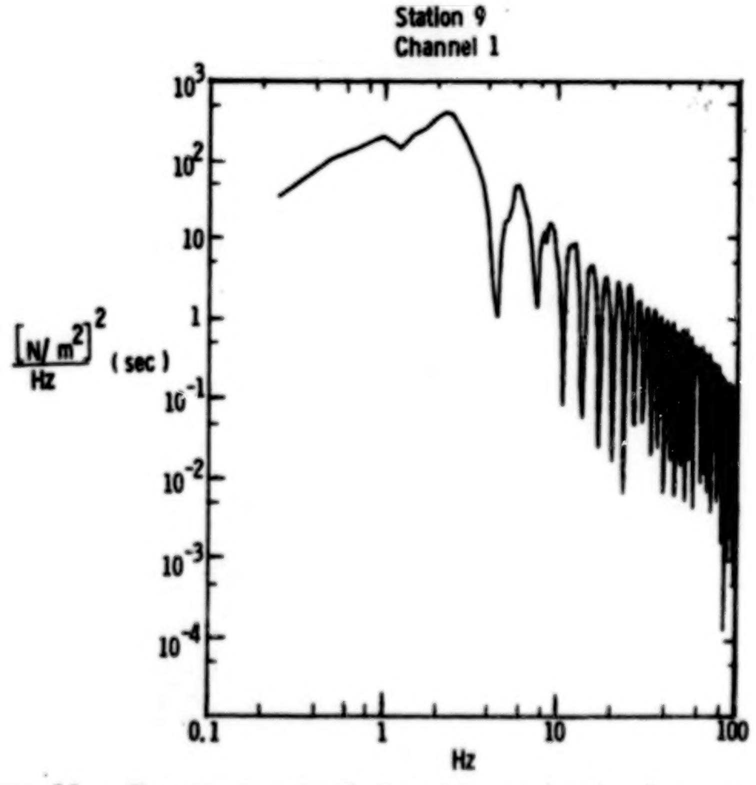

Figure 11.- Energy spectral density analysis from station 9 ground level microphone during STS-1 reentry.

ORIGINAL PAGE IS
OF POOR QUALITY

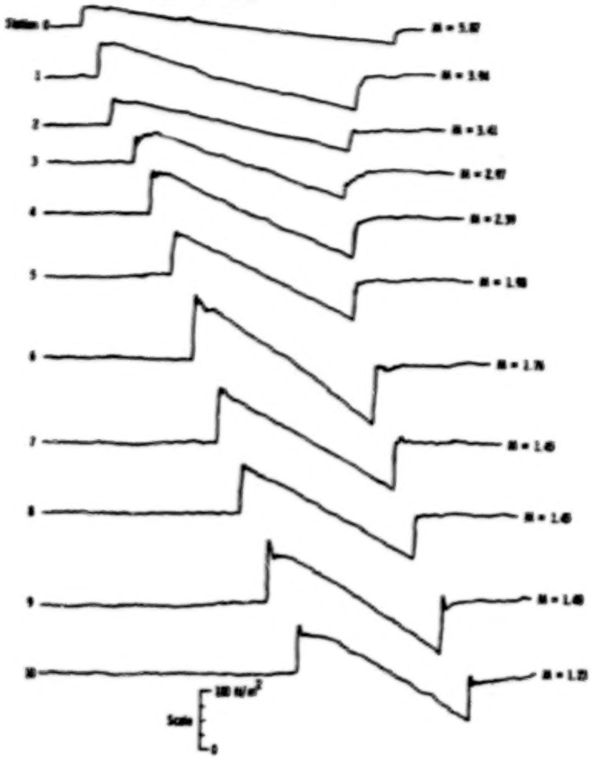

Figure 12.- Measured sonic boom signatures recorded at 11 measurement sites located under and laterally to the STS-1 reentry ground track.

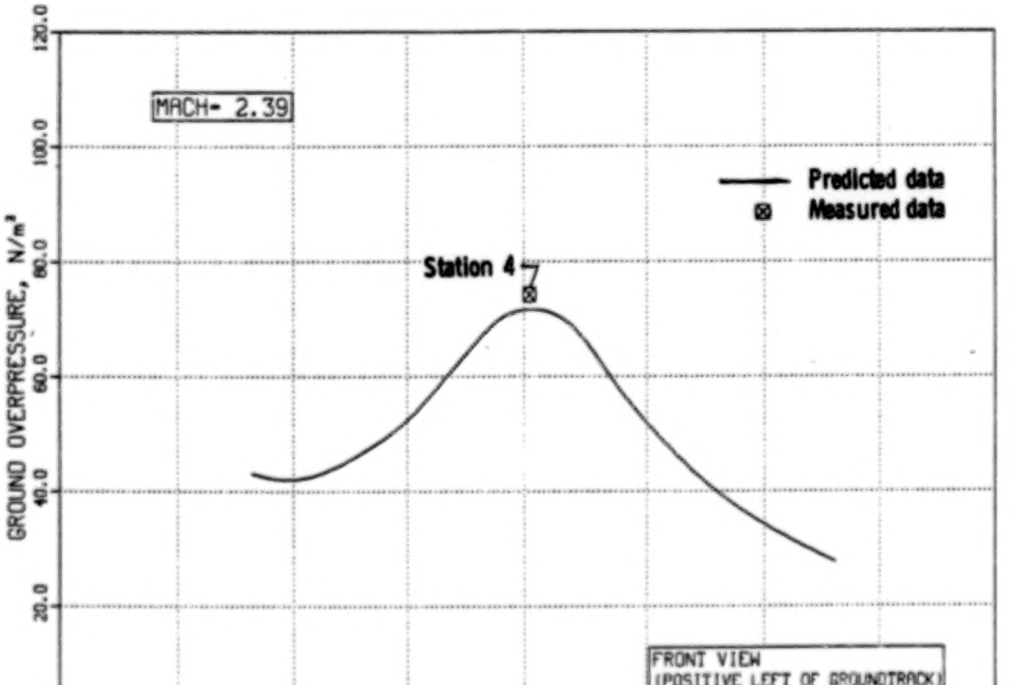

Figure 13.- Predicted and measured overpressure distribution for station 4 during STS-1 reentry.

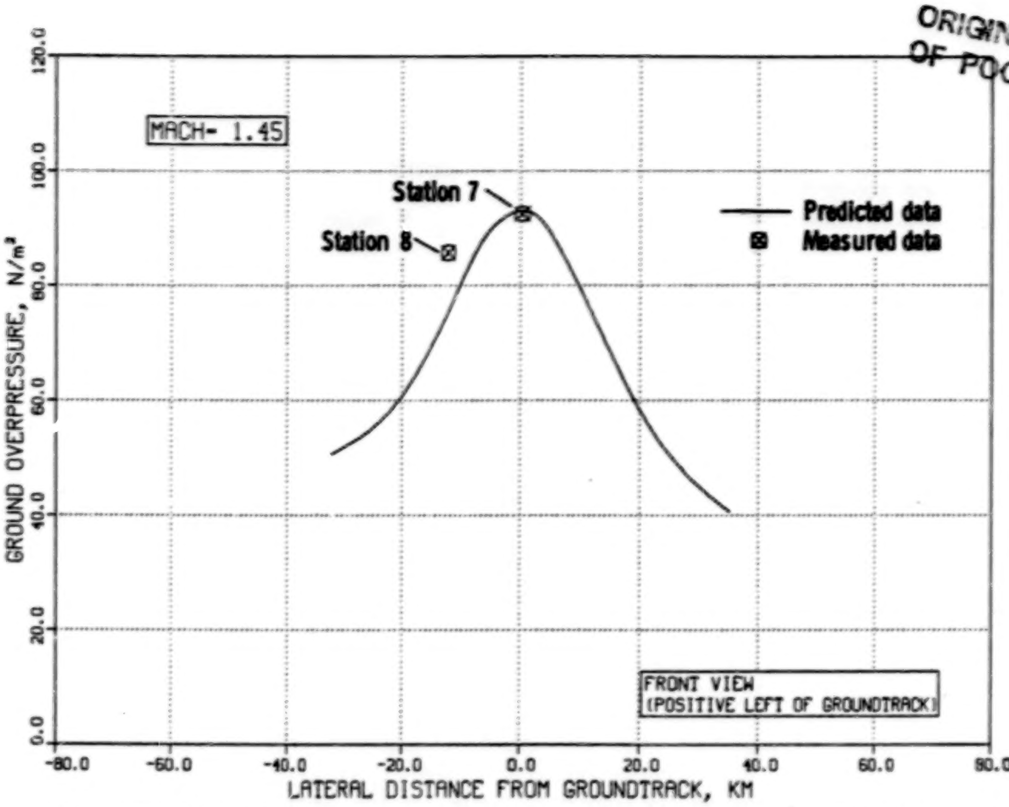

Figure 14.- Predicted and measured overpressure distribution for stations 7 and 8 during STS-1 reentry.

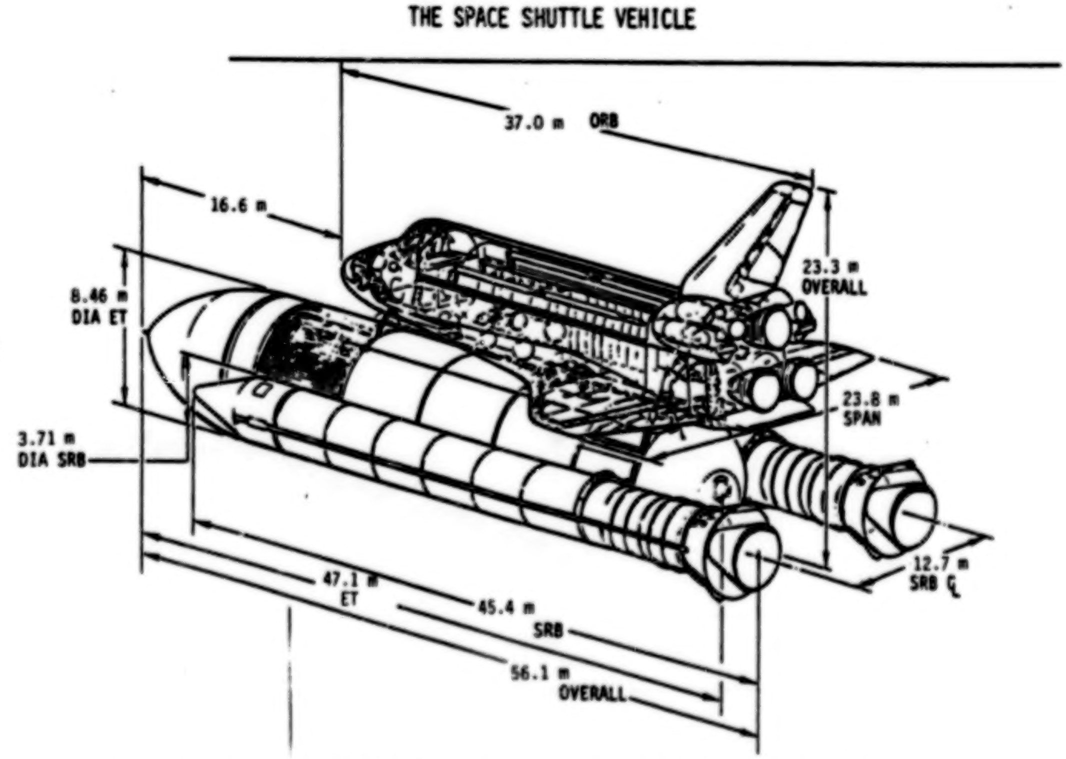
THE SPACE SHUTTLE VEHICLE
37.0 m ORB
16.6 m
8.46 m DIA ET
3.71 m DIA SRB
23.3 m OVERALL
23.8 m SPAN
12.7 m SRB ℄
47.1 m ET
45.4 m SRB
56.1 m OVERALL

Figure 15.- Schematic of Space Shuttle launch vehicle.

ORIGINAL PAGE IS
OF POOR QUALITY

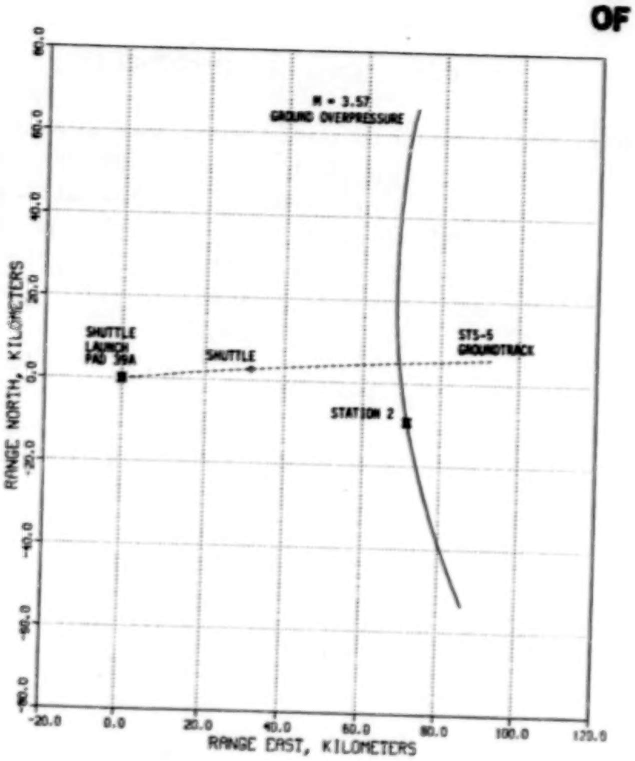
80.0
60.0
40.0
20.0
0.0
-20.0
-40.0
-60.0
-80.0
RANGE NORTH, KILOMETERS
M = 3.57
GROUND OVERPRESSURE
SHUTTLE
LAUNCH
PAD 39A
SHUTTLE
STS-5
GROUNDTRACK
STATION 2
-20.0
0.0
20.0
40.0
60.0
80.0
100.0
120.0
RANGE EAST, KILOMETERS

Figure 16.- Ground overpressure line at M = 3.57 which intersects station 2, STS-5 ascent.

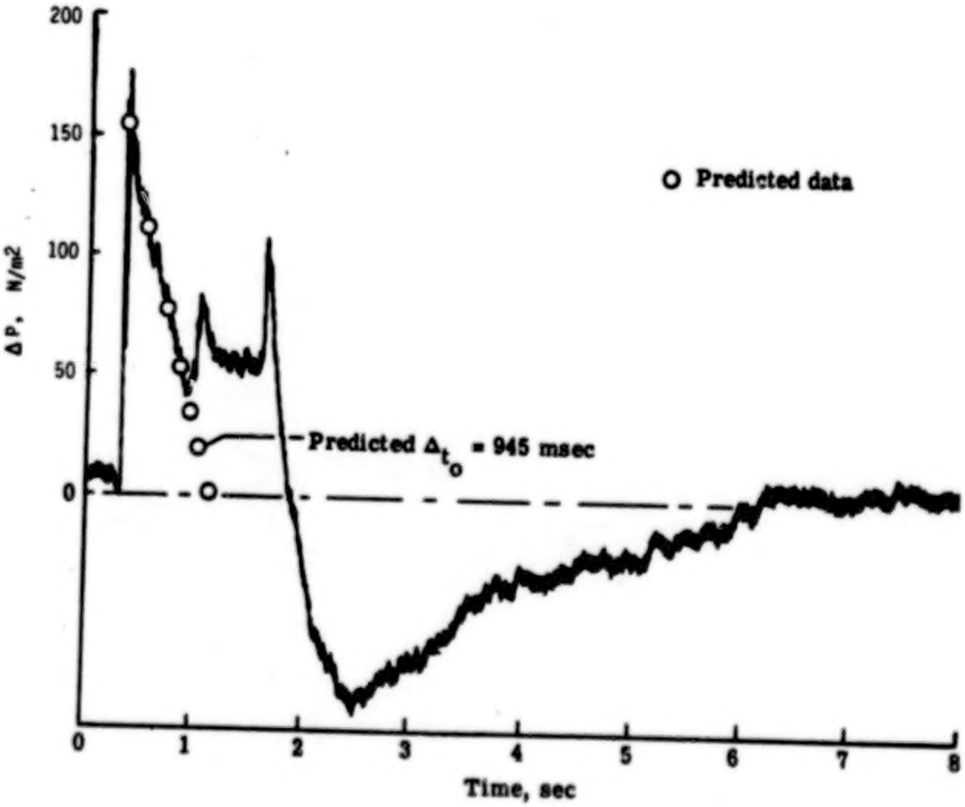

Figure 17.- Overpressure signature measured during the ascent of STS-5.

SUMMARY SESSION: INTRODUCTION

The final afternoon of the Shuttle conference was devoted to overviews and summaries. The session opened with an invited paper by Mr. Robert G. Hoey of the Air Force Flight Test Center. Mr. Hoey is Chief of the Office of Advanced Manned Vehicles, and his office conducted an examination of the flight data that paralleled and frequently supplemented the NASA study. Because the pilots' reactions to the vehicle flying qualities were not discussed in the contributed papers, Major Steven R. Nagel of the Astronaut Office at Johnson Space Center was invited to present that office's viewpoint, particularly for the approach and landing phase when the vehicle is flown manually. The third and final invited paper was by Dr. Milton A. Silveira, Assistant to the Deputy Administrator, NASA Headquarters, who presented remarks concerning the Shuttle Orbital Flight Test program from a NASA and Project Office management perspective.

In the final wrap-up to the meeting, the chairpersons of the technical sessions were asked to prepare comments on significant results presented at the conference. This session was taped, and the comments were transcribed and are included here. The chairpersons and their sessions were:

Ascent Aerodynamics I - Mr. T. E. Surber of Rockwell International, Space Division

Ascent Aerodynamics II - Mr. B. B. Roberts of Johnson Space Center

Entry Aerodynamics I - Mr. J. C. Young of Johnson Space Center

Entry Aerodynamics II - Mr. D. C. Schlosser of Rockwell International, Space Division

Guidance, Navigation, and Control - Dr. K. J. Cox of Johnson Space Center

Aerothermal Environment I - Mrs. D. B. Lee of Johnson Space Center

Aerothermal Environment II - Dr. J. Bertin of the University of Texas at Austin (Dr. Bertin was unable to attend this summary session; his co-chairman, Mr. E. V. Zoby of Langley Research Center, spoke for him.)

Thermal Protection - Mr. H. E. Goldstein of Ames Research Center

Measurements and Data - Mr. E. R. Hillje of Johnson Space Center

N84
10169

UNCLAS

N84 10169 D25

AFFTC OVERVIEW OF ORBITER-REENTRY FLIGHT-TEST RESULTS

Robert G. Hoey
Air Force Flight Test Center
Edwards Air Force Base, California

INTRODUCTION

The Air Force Flight Test Center (AFFTC) has been participating in the flight testing of the Space Shuttle since 1976. We were tasked by Space Division to conduct an independent assessment of the reentry and landing capabilities of the Orbiter with respect to Department of Defense (DOD) missions. This activity is on-going and reports have been published after each flight. AFFTC participation in this conference is not directly related to the DOD assessment activity, however, and the views presented by myself and other AFFTC authors discuss the technical aspects of testing and the technology emanating from these tests. Our views should not be construed as representing official Air Force or Space Division position or policy but rather the technical views of the "testers".

ABBREVIATIONS AND SYMBOLS

AFFTC	Air Force Flight Test Center
ASSET	Aerothermodynamic Structural Systems Environmental Test Program
C_{m_o}	basic pitching moment coefficient
DOD	Department of Defense
L/D	lift-to-drag ratio
MMLE	Modified Maximum Likelihood Estimator
NASA	National Aeronautics and Space Administration
OMS	Orbital Maneuvering System
PRIME	Precision Recovery Including Maneuvering Entry Program
PTI	Programmed Test Input
STS-1,2,3,4,5	Space Transportation System flights 1, 2, 3, 4, and 5

BACKGROUND

The Air Force has been interested in hypersonic flight and maneuvering reentry for many years, primarily spearheaded by efforts of the Air Force Flight Dynamics Laboratory (now Air Force Wright Aeronautical Laboratory) (Figure 1). In the late

PAGE 1302 INTENTIONALLY BLANK

PRECEDING PAGE BLANK NOT FILMED

1950's, the X-15 program was initiated by a joint DOD/NASA team, funded primarily by the Air Force. This program has been recognized as the most successful of all of the X-series research aircraft, breaking new ground in many areas of hypersonic flight and lifting reentry. The follow-on program, the X-20A DynaSoar, was cancelled before flight but resulted in many development activities which were technology advances: for example, a triply redundant, self-adaptive, fly-by-wire flight control system. The Air Force Aerothermodynamic Structural Systems Environmental Test (ASSET) and Precision Recovery Including Maneuvering Entry (PRIME) programs, both small, unmanned lifting reentry shapes, were flown in 1963 and 1966, respectively. These tests successfully demonstrated both radiative/metallic and ablative thermal protection system concepts. The lifting body programs (M-2, HL-10, X-24A) explored transonic aerodynamics and landing characteristics of low lift-to-drag ratio (L/D) reentry configurations. The Air Force X-24B, the last of the X-series rocket-powered research vehicles, was representative of high hypersonic L/D configurations and performed the first hard-surface runway landing for vehicles of this class.

The many years of preparation represented by these programs have produced prediction techniques for the design of lifting reentry vehicles. The Space Shuttle Orbiter represents the culmination of all of this activity combined with the technology from the "capsule" programs. During this conference you have heard how well these prediction techniques worked. Some were accurate, some too conservative, and some non-conservative.

This paper touches on flight test results from most of the technical disciplines and attempts to relate them to each other with regard to the design of future lifting reentry vehicles. Performance (i.e., aerodynamic lift and drag), stability and control, aerodynamic heating and thermal protection, and unpowered approach and landing are the technical areas where we think major technology advances are being made.

PERFORMANCE

The L/D of the Orbiter was predicted very well over most of the Mach range (Figure 2). Although all entries have followed a 40 degree angle of attack profile, transient pushover-pullup maneuvers have produced accurate trends with angle of attack. The subsonic L/D was underpredicted somewhat due to a conservative estimate of the effects of tile surface roughness on drag. Since aerodynamic L/D is the prime measure of reentry maneuvering capability, the Orbiter guidance and energy management control laws have worked well and entry trajectories have been very close to nominal. Although the ratio of lift to drag was well predicted, the magnitude of the normal force coefficient C_N, which is the prime contributor to both lift and drag at high angle of attack, was overpredicted as shown on the right side of Figure 3. The cause of this discrepancy is not well understood at this time and efforts to resolve the differences are hampered by a lack of accurate, onboard measurements of dynamic pressure at the high Mach numbers M. In addition, abrupt changes in measured accelerations (up to 19 percent over a one second time period) have been recorded which do not appear to correspond to flow changes over the vehicle. Changes in atmospheric density are currently considered the most likely cause for these anomalies and, if random in nature, could be an important design consideration for future vehicles and guidance concepts.

A significant discrepancy in pitch trim predictions has been observed on all flights (Figure 4). Elevon pulses, bodyflap sweeps, and pushover-pullup maneuvers have isolated the individual pitching moment contributions from the elevon, bodyflap, and angle of attack and determined that they are all close to predictions. The trim prediction error has thus been isolated to C_{m_o}. Recent theoretical computations by personnel at the Arnold Engineering Development Center have attributed the discrepancy to real gas effects. The magnitude of the correction is quite large and portrays the heavy reliance that must be placed on theoretical and computational aerodynamic models for the design of future reentry vehicles. Had this information been available sooner the nose ramp angle on the Orbiter could have been reduced slightly which would have brought the bodyflap and elevon back to the desired faired position. The result would have been lower temperatures in both the nose ramp area and the control surfaces.

STABILITY AND CONTROL

Stability and control derivatives have been extracted from flight test maneuvers performed over most of the current reentry flight envelope. For the most part the derivatives are close to predictions, although small discrepancies are seen in nearly all of the derivatives. A notable exception is the prediction of yaw jet interaction effects during the initial phase of reentry (Figure 5). The jet interaction effects in roll were much smaller than predicted at the low dynamic pressures $\bar{q}$. The consequence of this prediction error is shown on Figure 6. A rather large, slow, lateral-directional oscillation occurred on the first bank maneuver of the STS-1 entry. A momentary sideslip angle of over 4 degrees was reached during the oscillation compared to a prediction of about 1 degree. This prediction discrepancy was again a result of inadequate ground test facilities to accurately duplicate the simultaneous high Mach number, low density, rocket-firing environment. Orbiter flight test data currently being obtained should be invaluable in improving our ability to predict jet interaction effects in the future.

The long dashed lines on Figure 5 also portray the use of derivative predicted data uncertainties as used in the development of the Orbiter flight control system. A considerable amount of effort was expended early in the program to establish appropriate uncertainty bounds around each derivative prediction. These uncertainties were based on three factors: (1) differences between wind tunnels, (2) differences between prediction and flight test results for a variety of aircraft, and (3) judgment regarding the validity of extrapolations in Mach number. The Orbiter control system was designed to accommodate individual uncertainties in the derivatives as shown by the dashed lines as well as certain logical combinations of uncertainties representing worst-case conditions. The effort was well worth the time expended. All of the derivative prediction discrepancies have been within the variation bounds except for the case shown in Figure 5. As a result, the flight control system has been adequate for safe reentry and landing approaches in either the automatic or manual modes in spite of prediction errors.

AEROTHERMODYNAMICS AND THERMAL PROTECTION

The lower surface or windward side of the Orbiter has experienced a less severe heating environment than expected (Figure 7). Three factors have combined to create this situation. The laminar heating during the early portion of the entry has been less than predicted, especially on the forward portion of the vehicle. The transition from laminar to turbulent flow has occurred later in the entry than expected which has also produced lower temperatures and a lower total heat load. After the vehicle passes through Mach 2.5, vent doors open on the side of the fuselage to equalize the pressure in the payload bay and other internal compartments. The flow of cold air into the vehicle as well as over the outside surface was not accounted for in the conservative heating models used in the design process. This atmospheric cooling effect is quite significant and causes internal structural temperatures to peak earlier and at lower values than anticipated. The combination of these three effects has alleviated concern over the overall adequacy of the lower surface design although several localized problems remain (tile gap heating, for example). The repeatability of these three effects needs to be considered. The reduced laminar heating appears to be repeatable. The transition from laminar to turbulent flow has been consistently later than expected but somewhat different for each flight. The mechanism for controlling flow transition needs to be better understood before a future design could confidently count on late transition in sizing the thermal protection. Carefully controlled testing of boundary layer transition phenomena on the Orbiter could be very beneficial to the design community. The atmospheric cooling effect has been, and should be, highly repeatable. The next generation of entry vehicles might well be equipped, not only with vent doors, but with air scoops and internal baffling to effectively utilize the three to five minutes of free cooling provided by the atmosphere while descending below 80,000 feet.

The heating on the upper surface, or lee side, of the Orbiter has been poorly predicted (Figure 8). This was not entirely unexpected since theory is essentially non-existent for complex shapes and wind tunnels cannot simultanously duplicate the flow conditions of Mach and Reynolds number. Several localized areas have experienced higher heating than predicted, in particular the Orbital Maneuvering System (OMS) pod, side of the fuselage and payload bay door. Wind tunnel data predicted that a vortex impingement would occur on the OMS pod abruptly as the angle of attack decreased through 30 degrees. Flight test results to date indicate an increase in heating starting at about 37 degrees angle of attack and building to considerably higher levels at lower angles of attack. The heating patterns and trends are reasonably repeatable from flight to flight and aerothermodynamic math models for the OMS pod and several other upper surface locations are currently being revised using the available flight test data base. Here again, additional testing of the Orbiter is required to thoroughly understand the factors which influence upper surface heating and to establish better tools for predictions on future vehicles.

FLIGHT TESTING TECHNIQUES

Aerodynamic flight testing of the Orbiter during entry successfully utilized aircraft dynamic testing techniques. (See fig. 9.) Slow pushover-pullups were performed to sweep a range of angles of attack while the vehicle remained essentially in trimmed flight. This maneuver and the corresponding analysis program has been used successfully on rocket powered glide vehicles for many years producing lift, drag, and longitudinal trim data as a function of angle of attack for a particular Mach number.

Programmed Test Inputs (PTIs) were sharp control pulses designed to momentarily upset the trimmed equilibrium condition. The instrumentation then recorded the manner in which the inherent stability and the control system returned the vehicle to equilibrium flight. These maneuvers are similar to the stick pulses used in aircraft dynamic stability testing. The Modified Maximum Likelihood Estimator (MMLE) analysis program has been in use for several years. It produces a set of values for the vehicle stability and control derivatives for each PTI test maneuver. The bodyflap sweep was used to isolate the bodyflap effectiveness derivative and thus establish the overall pitch trim capability of the Orbiter.

The data from pushover-pullup and bodyflap sweep maneuvers were analyzed by an entirely new technique for the dynamic testing of the aerothermodynamic environment. Using the trajectory data and the angle of attack time history as inputs, the new program adjusts the heating model until the output temperature time history matches the thermocouple readings as shown on Figure 10(a). The flight-adjusted heating model is compared with the wind tunnel data in Figure 10(b). Excellent results of heating variation with angle of attack have been obtained for lower surface locations. Nonlinear heating variations, such as on the OMS pod, have also been successfully identified but with lower confidence. Thermal math models for various critical locations are being updated with these flight test results. It is hoped that the aerothermodynamic flight testing techniques which were developed for the Space Shuttle program will form the basis for a whole new flight test discipline which will be applicable to any hypersonic aircraft or reentry vehicle.

UNPOWERED LANDINGS

A piloting technique for landing a low L/D glide vehicle was developed in the late 1950's and early 1960's and was successfully applied to lakebed landings of the X-15 research aircraft. As confidence was gained in the ability to successfully control gliding energy, spot landings were attempted with a fair degree of success. In 1970 a short research program was conducted by AFFTC using an F-111A which successfully demonstrated a technique for accomplishing night and instrument approaches. Several hooded low L/D approaches were flown from Mach 2 down to 1500 feet altitude where a visual flare and landing were completed. Typical landing patterns for the X-15, X-24B, and Space Shuttle Orbiter are shown in Figure 11. The approach and landing technique were the same for each. An overhead, high altitude, circular pattern was flown followed by a high speed final approach (approximately 300 knots). A flare maneuver to essentially horizontal, decelerating flight was initiated at about 1500 feet altitude. The landing gear was extended during or after flare and touchdown occurred between 160 and 200 knots. Notice the similarity in the final approach glide slope between the three vehicles which is indicative of the similarity in subsonic L/D. Notice also that as the landing technique evolved toward improved landing accuracy, the geometry of the pattern was altered to include a longer final approach. This results from the necessity to establish a stabilized energy level at the flare point in order to properly control the touchdown point and stopping point.

Additional refinements to this landing technique are still being made, such as improvements in the ability to compensate for upper altitude winds; however, the basic technique for accomplishing unpowered, low L/D landings has proven to be effective and practical.

CONCLUDING REMARKS

The Space Shuttle test program has been highly successful by any standard of measure. The vehicle was designed to fly in an environment which was largely uncharted. Many design prediction tools were verified (see fig. 12), including a general verification of lifting entry design methods and confirmation of reusable thermal protection system technology. Aircraft flight testing techniques were successfully applied and new aerothermodynamic flight testing techniques were successfully demonstrated.

Many of the design prediction tools were found wanting, as shown in figure 13, but the application of a conservative design philosophy allowed the test program to proceed safely. For example, hypersonic pitch trim and normal force coefficients were not well predicted. Jet interaction effects at low dynamic pressure were also mispredicted. Aerodynamic heating on the lower (windward) surface was generally lower than predictions while heating on local areas of the upper (leeward) surface was higher than expected. It appears that future designers will have to rely more heavily on theory and computational aerodynamics (or even empirical methods based on flight test) to supplement the wind tunnels for the hypersonic environment. (See fig. 14.)

The five-flight test program of the Orbiter has opened the door to several technological advances which could significantly impact the design of future hypersonic vehicles. It is essential that the necessary test data be gathered on future Space Shuttle Orbiter reentries to insure that this new technology is properly developed.

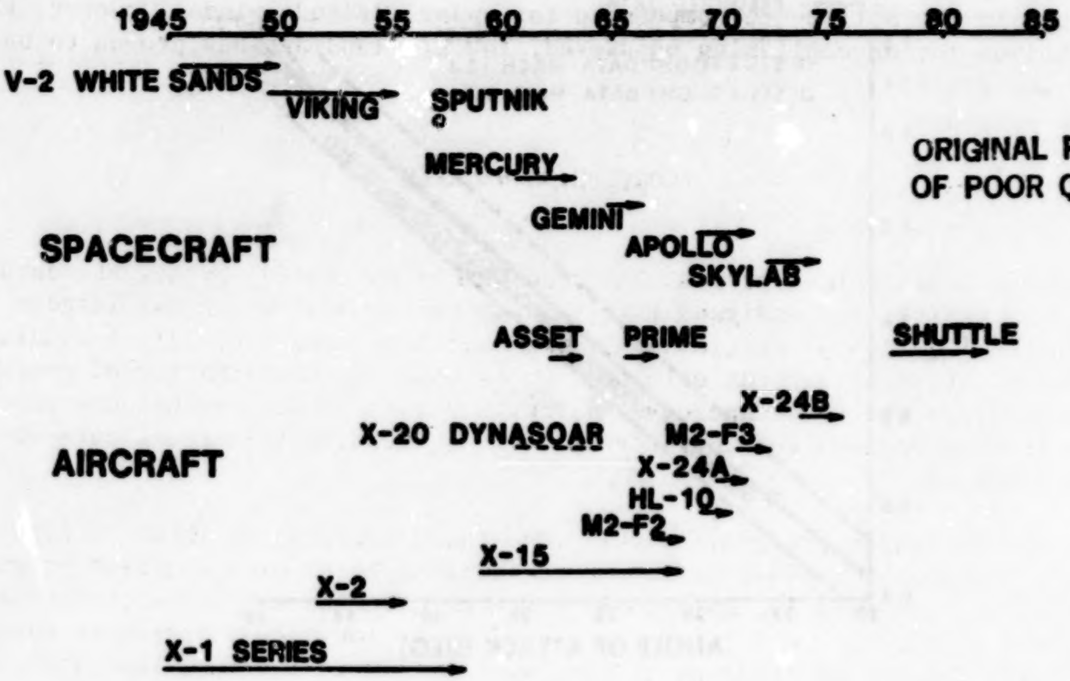
1945
50
55
60
65
70
75
80
85
V-2 WHITE SANDS
VIKING
SPUTNIK
MERCURY
GEMINI
APOLLO
SKYLAB
SPACECRAFT
ASSET
PRIME
SHUTTLE
X-24B
X-20 DYNASOAR
M2-F3
AIRCRAFT
X-24A
HL-10
M2-F2
X-15
X-2
X-1 SERIES

Figure 1.- Chronology of spacecraft/aircraft development.

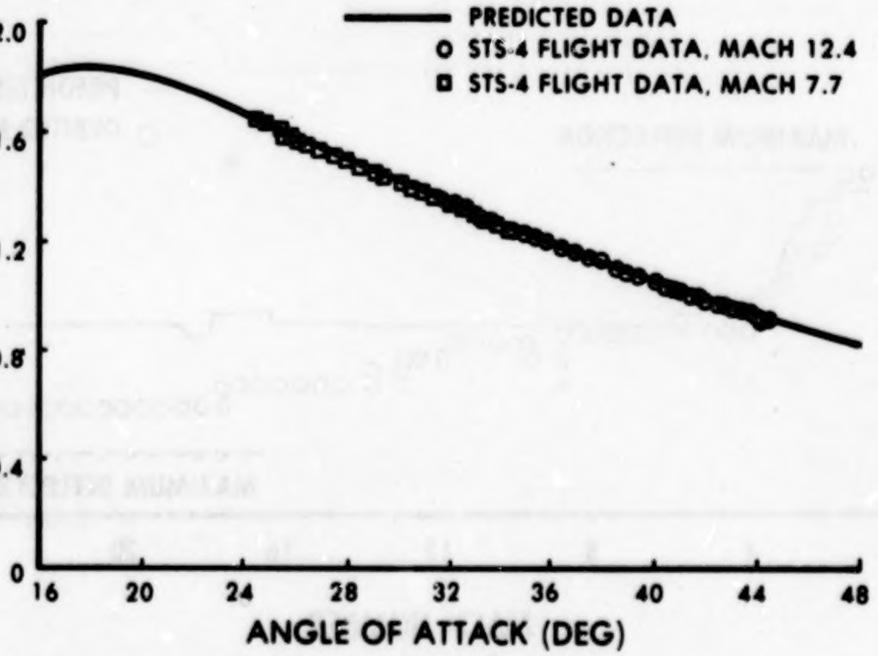

Figure 2.- Hypersonic lift-to-drag ratio data.

C-8

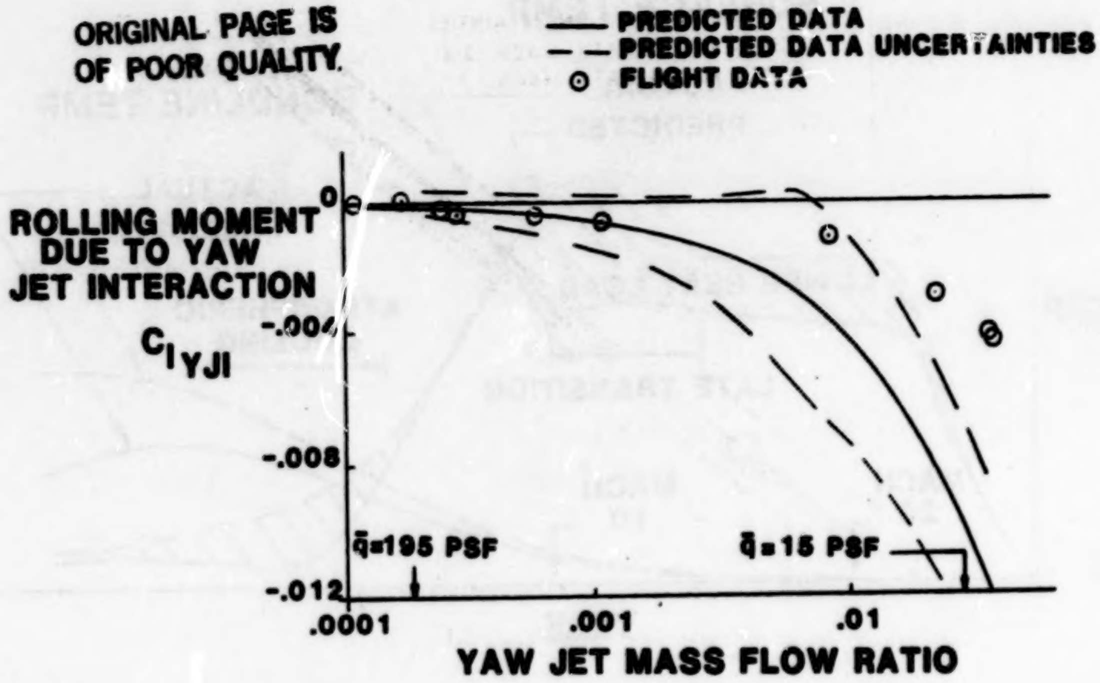

Figure 5.- Yaw jet/aerodynamic interaction.

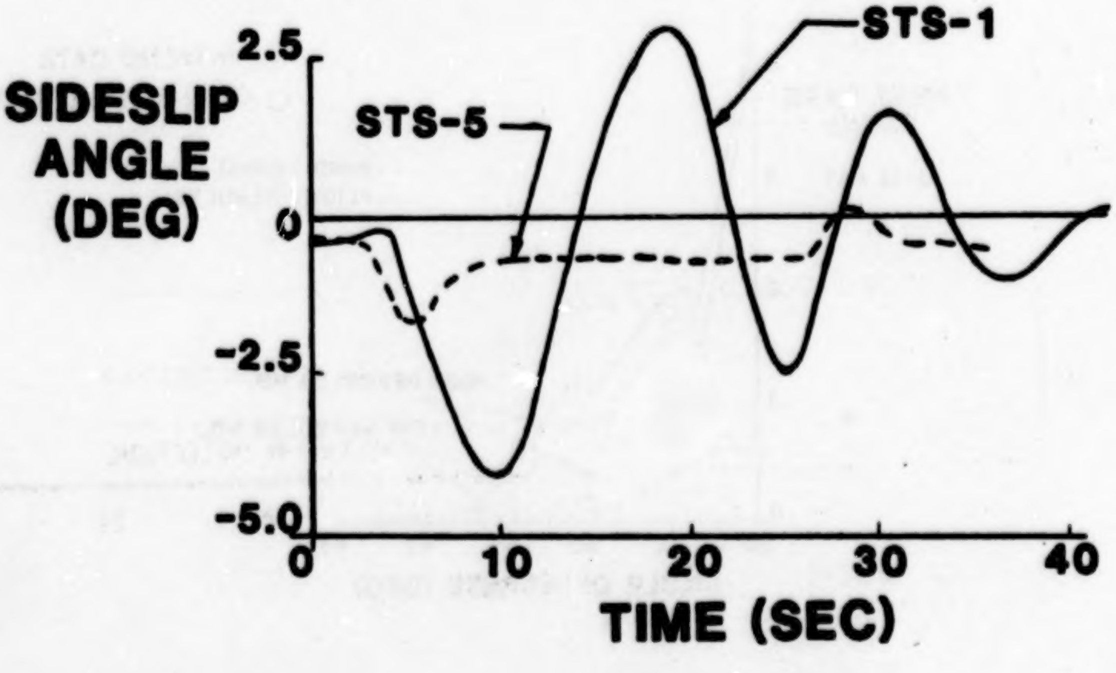

Figure 6.- First bank maneuver (auto).

ORIGINAL PAGE IS
OF POOR QUALITY

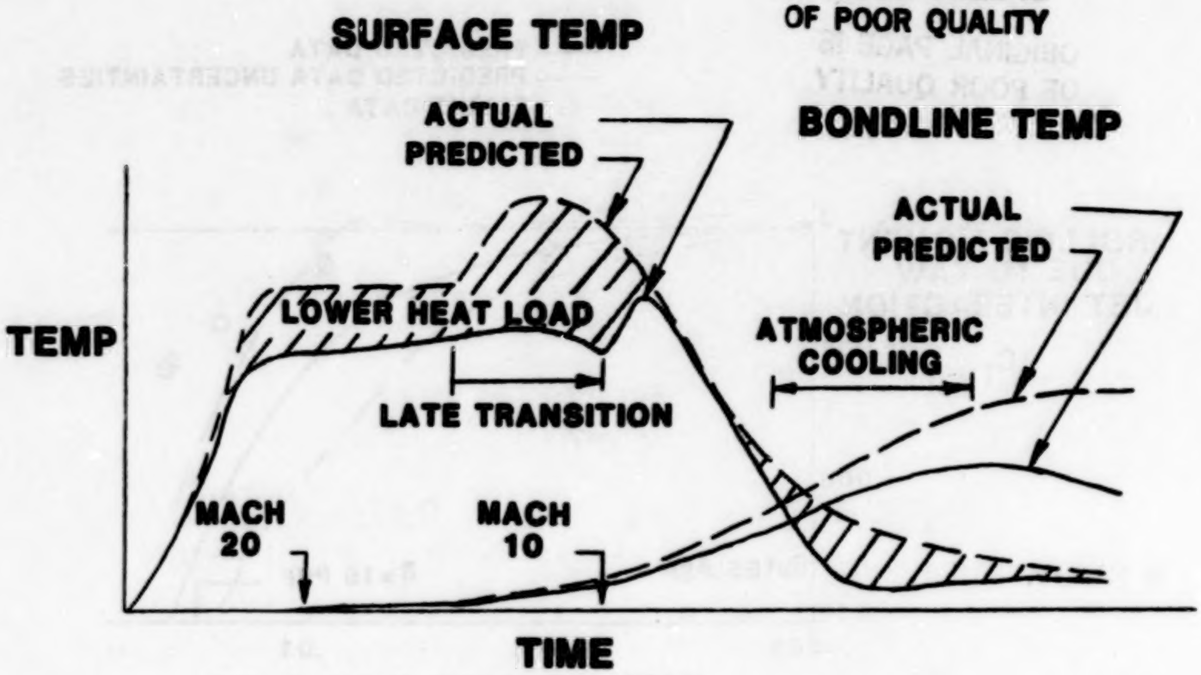
SURFACE TEMP
ACTUAL
PREDICTED
BONDLINE TEMP
ACTUAL
PREDICTED
TEMP
LOWER HEAT LOAD
LATE TRANSITION
ATMOSPHERIC
COOLING
MACH
20
MACH
10
TIME

Figure 7.- Generalized lower surface heating results.

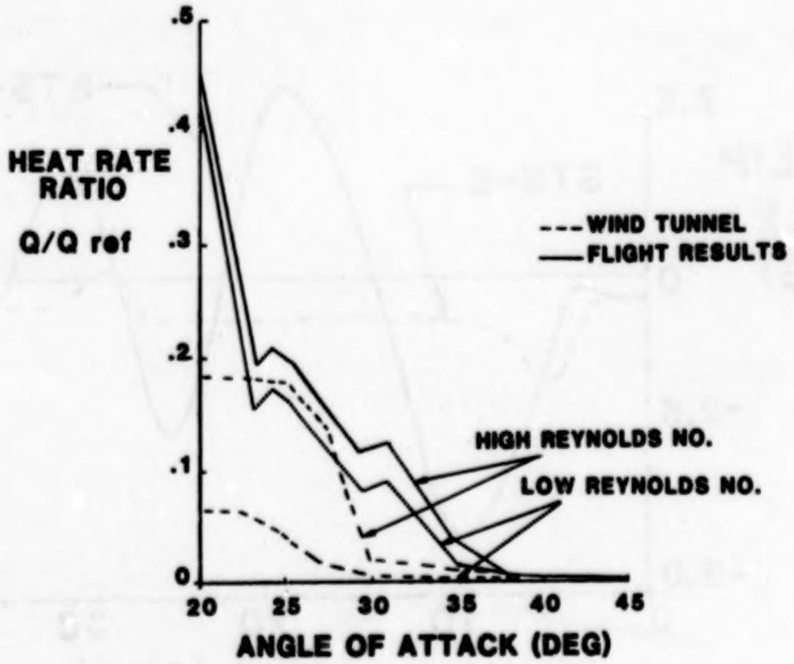

Figure 8.- OMS pod heating.

MANEUVER	DATA OUTPUT
● SLOW PUSHOVER-PULLUP	LIFT, DRAG VARIATION WITH ANGLE OF ATTACK NEW AEROTHERMODYNAMIC ANALYSIS
● PROGRAMMED TEST INPUTS (CONTROL PULSES)	STABILITY AND CONTROL DERIVATIVES
● BODY FLAP SWEEPS	BODY FLAP/ELEVON EFFECTIVENESS NEW AEROTHERMODYNAMIC ANALYSIS

Figure 9.- Successful application of aircraft dynamic testing techniques.

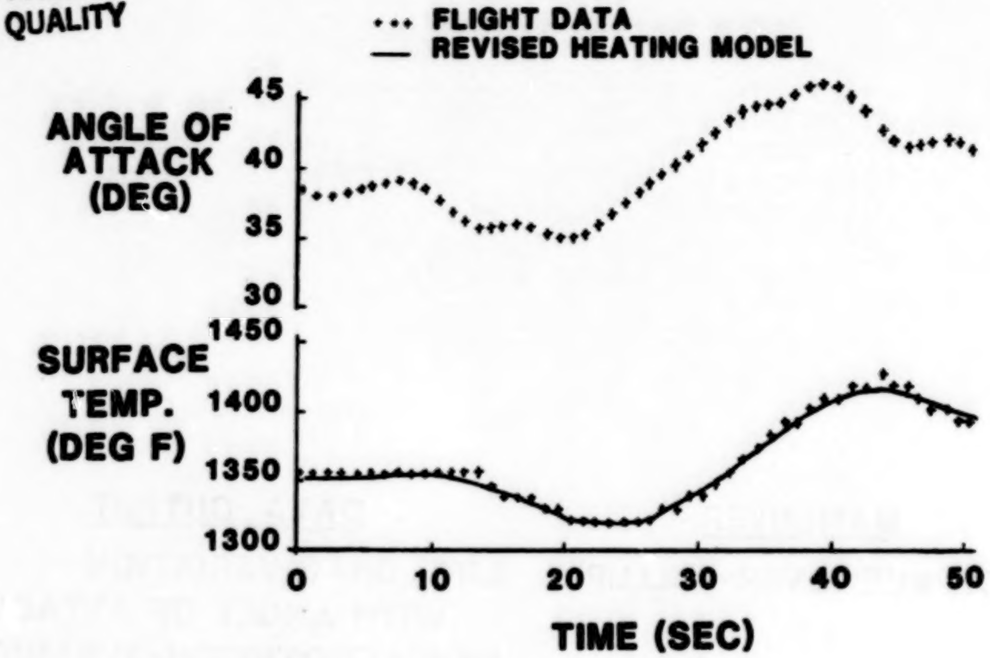

(a) Dynamic test maneuver for aerothermodynamics.

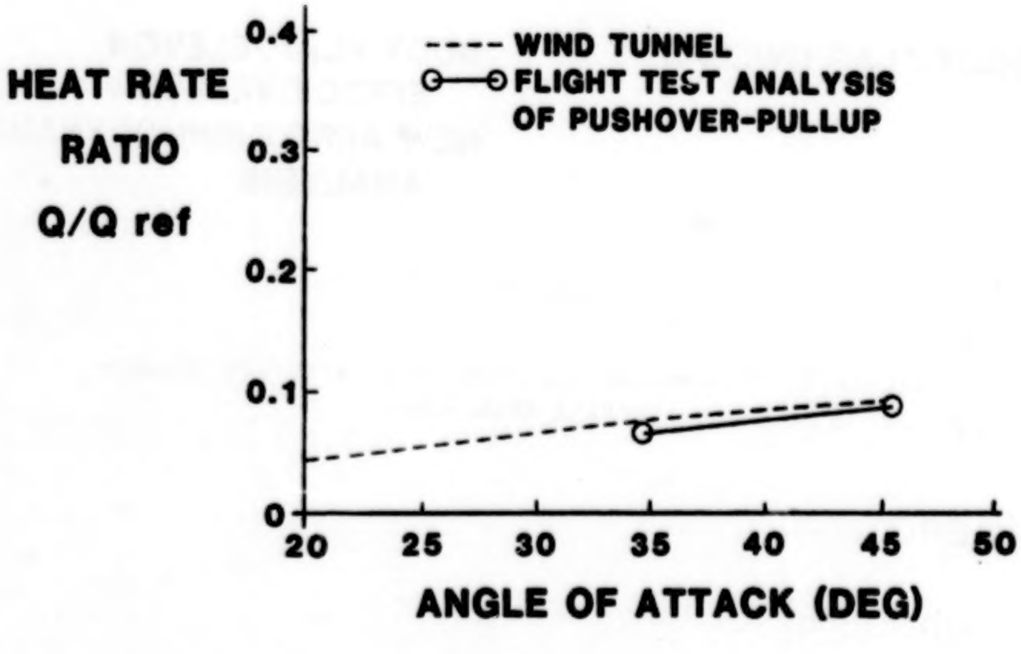

(b) Aerothermodynamic results from dynamic maneuver analysis.

Figure 10.- Dynamic testing of aerothermodynamic environment. Aft lower centerline.

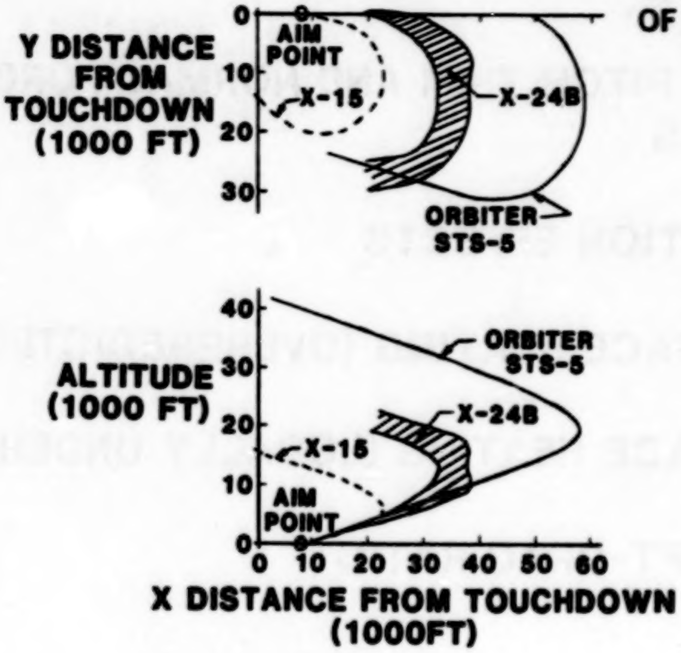

Figure 11.- Low L/D landing patterns.

- **OVERALL LIFTING ENTRY DESIGN METHODOLOGY**
- **REUSABLE THERMAL PROTECTION SYSTEM TECHNOLOGY**
- **APPLICATION OF AIRCRAFT TEST TECHNIQUES**
- **AEROTHERMODYNAMIC FLIGHT TEST METHODS**
- **UNPOWERED, LOW L/D LANDING TECHNIQUES**

Figure 12.- Lessons learned. Design prediction methods verified.

- HYPERSONIC PITCH TRIM AND NORMAL FORCE COEFFICIENTS
- JET INTERACTION EFFECTS
- LOWER SURFACE HEATING (OVERPREDICTED)
- UPPER SURFACE HEATING (LOCALLY UNDERPREDICTED)
- SUBSONIC LIFT-DRAG RATIO

Figure 13.- Lessons learned. Design prediction discrepancies.

- FUTURE HEAVIER RELIANCE ON

  THEORY
  COMPUTATIONAL AERODYNAMICS
  EMPIRICAL FLIGHT TEST RESULTS

  TO SUPPLEMENT WIND TUNNEL PREDICTIONS

- SIGNIFICANT TECHNOLOGY BENEFIT TO BE DERIVED FROM CONTINUED ORBITER REENTRY TESTING

Figure 14.- Concluding remarks.

N84
10170

UNCLAS

N84 10170 D26

FLYING THE ORBITER IN THE APPROACH/LANDING PHASE

Steven R. Nagel
Johnson Space Center
Houston, Texas

INTRODUCTION

The Columbia has completed a spectacularly successful four flight Orbital Flight Test program as well as the first operational mission in which two satellites were deployed. As we await the first launch of the next Orbiter, Challenger, it is an appropriate time to reflect upon some of the accomplishments of these five flights as well as areas of desired improvements. John Young's description of the Orbiter as a "fantastic flying machine" is an accurate representation of the opinions of all the crew members who have flown on the Columbia to date. It is unprecedented that a vehicle so complex as the Shuttle could have reached such a state of maturity in so few missions. This maturity is reflected not only in terms of basic performance during dynamic flight phases, but also in the outstanding performance of individual spacecraft systems. Certainly, one purpose of this paper is to extend to you, the designers and developers, the heartfelt thanks of the crew members who are very pleased to have the opportunity to fly your Space Shuttle. When attempting to describe how the Shuttle flies, one should look at the phase where most of the "hands on" activity has occurred. Appreciably more CSS time has been logged during entry and particularly in the approach and landing phase than any other segment of the mission profile. The discussion that follows, therefore, will outline this phase in some detail including pilot comments, techniques, crew displays and landing aids. Some problem areas related to landing the Orbiter will be discussed, as well as possible solutions.

ABBREVIATIONS AND SYMBOLS

A/L	Approach and Landing	SES	Shuttle Engineering Simulator
CG	Center of Gravity	STA	Shuttle Training Aircraft
CRT	Cathode Ray Tube	STS	Space Transportation System
CSS	Control Stick Steering	TAEM	Terminal Area Energy Management
FCS	Flight Control System		
HAC	Heading Alignment Circle	γ	Flight Path Angle
HSD	Horizontal Situation Display	$C_{L_{\delta e}}$	Change in lift coefficient with elevator deflection
HUD	Heads Up Display		
IGS	Inner Glide Slope	C_{L_α}	Change in lift coefficient with angle of attack
KEAS	Knots Equivalent Air Speed		
OGS	Outer Glide Slope		
PAPI	Precision Approach Path Indicator		
RHC	Rotational Hand Controller		

N84 10170

SETTING UP THE APPROACH

The entry is a progression of events designed to place the Orbiter in a position from which a safe landing can be made. It does this without violating thermal, dynamic pressure, or acceleration constraints for those trajectories within a given dispersion band. Guidance modes for the overall entry fall into three phases:

- Entry Guidance
- TAEM Guidance
- Approach/Landing Guidance

The purpose of Entry Guidance is to deliver the Orbiter to the TAEM interface conditions which are relative velocity of 2500 ft/sec, altitude of approximately 82,000 ft, range of approximately 52 NM, and heading within a few degrees of that required to fly to the tangency point of the appropriate HAC.

TAEM guidance is divided into four subphases as depicted in figure 1. At the end of TAEM the Orbiter is established on the outer glide slope (OGS), on runway centerline and on airspeed.

Approach and Landing (A/L) guidance begins with termination of the TAEM phase and ends when the Orbiter completes rollout. The phases of A/L guidance are depicted in figure 2.

FLYING THE APPROACH

To a large extent the landing point and even quality of touchdown depend upon flight conditions at the preflare point where the Orbiter is transitioned from the OGS to the inner glide slope (IGS). If airspeed, flight path angle, and position are very close to nominal, the end result will likely be a satisfactory touchdown at the desired point. On the other hand, if dispersions of appreciable magnitude exist at preflare, the landing may be salvaged but will probably not occur at the desired point. To assist the crew member in achieving the planned trajectory, several displays and landing aids are available both inside the cockpit and on the ground.

In the cockpit are three types of displays: dedicated, CRT, and the HUD. Dedicated displays are those meters that give classic flight parameters such as airspeed, altitude, angle-of-attack, etc., as well as the attitude and heading indicators. Steering needles on the attitude indicator reflect guidance commands to remain on or correct to the proper trajectory. See figure 3.

The only CRT display that might be used during the approach and landing phase is the Horizontal Situation Display (figure 4). The HSD presents a horizontal depiction of the Orbiter's flight path relative to the HAC and final approach. Its real usefulness is for flying around the HAC, but the HSD may also be used on the OGS, especially if weather is present.

The HUD will be flown for the first time in Challenger and represents a significant improvement to the task of flying or monitoring the final approach and landing (figure 5). All flight critical information is presented on the HUD combining glass so the crew member does not have to go "heads down" during the approach. Additionally, the HUD has a velocity vector which depicts the real time flight path of the Orbiter, thus making the results of any correction to glide path or azimuth immediately apparent. Declutter modes allow certain symbology to be removed from the HUD when not required.

Using these onboard displays the crew member can fly the entire approach by satisfying guidance commands (i.e. centering the needles). Prudence dictates that one also crosscheck the "raw" data - flight conditions and position relative to glide path and runway centerline. And of course, even though we completely trust the onboard indications, it never hurts to take a look out the window.

To assist in the problem of visually acquiring the OGS and IGS, three aids have been placed on the ground: aim point markings, PAPI's, and the Ball-Bar. Markings have been placed at the ground intersection points for the OGS (figure 6). The standard OGS aim point is a rectangle located 7500 ft from the runway threshold while the high wind OGS aim point is a triangle placed 1000 ft closer. When on the OGS the Orbiter is on a collision course with the appropriate aim point until preflare. As a matter of fact, the velocity vector in the HUD (-ȯ-) should overlay this aim point while on the OGS.

Of course, just aiming at the proper point on the ground does not assure the correct flight path angle (normally 19°). To provide a visual aid for gamma (γ) Precision Approach Path Indicator (PAPI) lights are installed at the aim points (figure 7). Each light has a split beam the upper half of which is white and the lower half red. The four lights are set at 22°, 20°, 18°, and 16° elevation respectively. Thus, when one flies down a 19° γ glide path he will see two white lights and two red lights. Likewise, three red and one white light indicate that at that moment the Orbiter is on a 17° γ glide path, and so on.

After many attempts at visual aids for flying the 1 1/2° γ IGS, the Ball-Bar was developed (figure 8 .) The Ball-Bar is so straight forward and simple one would wonder how it belongs in the Space Program. Placed beside the runway and 2200 ft from the threshold, the Bar is an array of six groups of red lights, all set two feet above the ground. In front of the Bar 500 ft is the Ball, a cluster of three white lights on a pole 15 ft tall. A line drawn from the Bar through the Ball subtends an angle of 1.5° from the horizontal. Thus, when the pilot flies the Orbiter to line up the Ball and Bar, he is on the proper IGS - and it works extremely well.

PILOT COMMENTS AND PROBLEM AREAS

The first five Shuttle missions have had varying amounts of manual flying on the HAC and final approach. All landings thus far have been manual. During STS-1 and 5 the commanders were in CSS from approximately 35,000 ft all the way to touchdown. On STS-2, 3, and 4 there were varying mixtures of AUTO and CSS through this phase depending upon the test objectives for each particular mission.

In general, the pilot assessments of the Orbiter subsonic handling qualities are quite favorable. "Smooth, crisp, and precise" are terms that have been used to describe the FCS. Although it is a rate command system, the rate deadbands are so tight that the FCS behaves almost as an attitude hold system. Most pilots have stated that the Orbiter is tighter and more responsive than the Shuttle Training Aircraft (STA/Gulfstream II). The only slight exception to this statement might be with regard to the speedbrake which has rather slow response and poor anticipation for speed control when in AUTO. Many pilots use the technique of manually setting the speedbrake until close to the desired airspeed, then allowing AUTO to assume vernier control.

Along with all the good things that may be said about the Orbiter, there are a couple of areas in which problems may arise sooner or later. Those two areas are the last key events of any mission - landing and stopping.

The Orbiter is not a straightforward and easy airplane to land for at least two reasons. Conventional aircraft exhibit positive speed stability such that for landing the pilot is continually applying increasing aft stick to "hold the airplane off" during the final flare. The Orbiter, with its very tight rate command system, will essentially hold attitude with the RHC in detent. Thus, in landing the Orbiter, one makes short, pulse inputs for fine corrections in the flare, as opposed to increasing back pressure. Additionally, the Orbiter is a large delta wing airplane with an unusually high ratio of elevon area to total wing area (the elevons comprise more than 15% of the total wing area). The well known result is that a pitch command in one direction results in an initial translation in the opposite direction due to the $C_{L_{\delta e}}$ effect until the aircraft rotates enough for $C_{L_{\alpha}}$ to produce the desired response (figure 9.) The bottom line is that any large RHC deflections just above the runway are taboo. All this works very well for a good setup with no gust upsets or other unforseen occurrences. Given off nominal conditions, however, the pilot may have to increase the magnitude of RHC inputs and the result may well be a hard landing. After main gear touchdown the nose gear is lowered to the runway, nominally at 180 KEAS. On STS-3 during the derotation, a pitch instability was discovered. Subsequent analysis confirmed the existence of this instability with weight on main wheels, low pitch attitudes, and forward C. G.'s. Several candidate modifications to the CSS pitch axis for slapdown/rollout were examined in the Shuttle Engineering Simulator (SES). One of the simplest proposals turned out to be the most satisfactory; switching the CSS flight control configuration to the AUTO loop gains at weight on main gear resulted in a very tight, well damped pitch axis.

Once on the runway and derotated, the final objective is to bring the Orbiter safely to a stop. Original design requirements called for touchdown speeds in the neighborhood of 150 KEAS. With several years of weight growth in the design, however, landing speeds have increased drastically. For example, the reference touchdown speed for STS-6 end of mission is 185 KEAS and abort touchdown speed is 205 KEAS. Although they have been improved, the brakes and tires are marginal for heavyweight aborts into short runways.

POSSIBLE SOLUTIONS

Considering first the stopping problem, there are several candidate solutions, some of which are more reasonable than others.

1. Lengthen the short runways
2. Install a drag chute in the Orbiter
3. Install runway barriers
4. Improve brakes, tires, axles
5. Optimize pilot braking technique
6. Develop a closed loop speedbrake logic to reduce landing dispersions

The last three options on this list show some promise and number 6 in particular is interesting. Presently the speedbrake closes at 4000 ft, 2500 ft, or 1000 ft altitude, depending upon energy, and remains closed until touchdown. The "smart" speedbrake logic proposes to control velocity versus x distance from the runway to cross the runway threshold at a given delta above reference touchdown speed. For a nominal landing this delta would be +25 KEAS whereas for an abort it would be +5 KEAS. The result, for example at Dakar, would be a touchdown 2000 ft down the runway at 15 KEAS below nominal touchdown speed.

Orbiter landing handling qualities remain a concern. Several proposed modifications to the CSS pitch axis for landing are presently undergoing evaluation in various engineering simulators. It remains to be seen if any one of these candidate FCS changes is sufficiently better than the baseline system to warrant incorporation. As stated before, to a great extent, the problems close to the runway are related to the physical configuration of a delta wing with large elevons. One way to alleviate this problem is to incorporate active canards. Canards could produce benefits to the Orbiter in many different areas, a few of which are:

1. Active canards for pitch control could eliminate the adverse $C_{L\delta e}$ effect and thus solve the landing longitudinal control problem.

2. With active canards the elevons could be deflected down during landing to serve also as flaps. The decreased touchdown speeds would solve the stopping problem and save the expense of frequent brake refurbishment.

3. Canards would increase L/D, thereby permitting a shallower steep glideslope and decreased pilot workload.

4. By reducing landing speeds and controlling pitchover, canards could reduce the large negative lift loads on the gear and tires resulting from up elevons at nose gear touchdown.

5. After derotation the negative angle of attack provides desirable aerodynamic braking but also imposes large loads on the gear and tires. With reduced landing speeds provided by canards, the nose gear could be extended to alleviate this gear load problem.

CONCLUSION

The Shuttle has continued to impress all of us with its capabilities and performance throughout the envelope. It enters the operational phase backed by many years of development and testing as well as a successful four flight test program. Future flights will see implementation of new elements and design features as the program moves towards even better performance. Along with these changes will come unforeseen problems that will be solved as have those in the past. But one thing is certain - the Shuttle concept is a sound one and will allow us to attain a routine presence in space.

BIBLIOGRAPHY

"GNC ENT 2102 GN and C Entry Operations Guidance and Navigation," Advanced Training Series, NASA Johnson Space Center, April 1982.

Mattingly, Thomas K.; and Hartsfield, Henry W., Jr.: Space Shuttle Progress Report. The Society of Experimental Test Pilots 1982 Report to the Aerospace Profession 26th Symposium Proceedings. September 1982, pp. 267-285.

Stegall, H.: "Altitude Rate Response of Shuttle During Landing Approach and Proposed Handling Quality Candidate," NASA TM EH 23A08-04, Jan. 20, 1983.

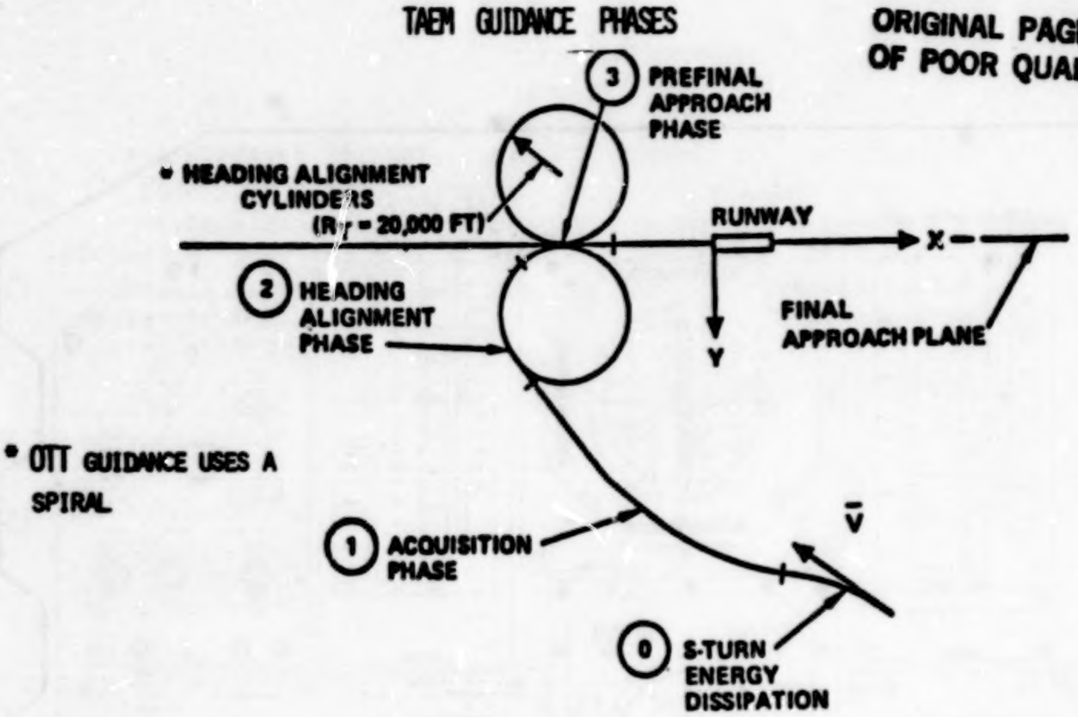
TAEM GUIDANCE PHASES
3 PREFINAL APPROACH PHASE
* HEADING ALIGNMENT CYLINDERS
(R = 20,000 FT)
RUNWAY
X
Y
2 HEADING ALIGNMENT PHASE
FINAL APPROACH PLANE
* OTT GUIDANCE USES A SPIRAL
1 ACQUISITION PHASE
V̄
0 S-TURN ENERGY DISSIPATION

Figure 1

APPROACH AND LANDING PHASE

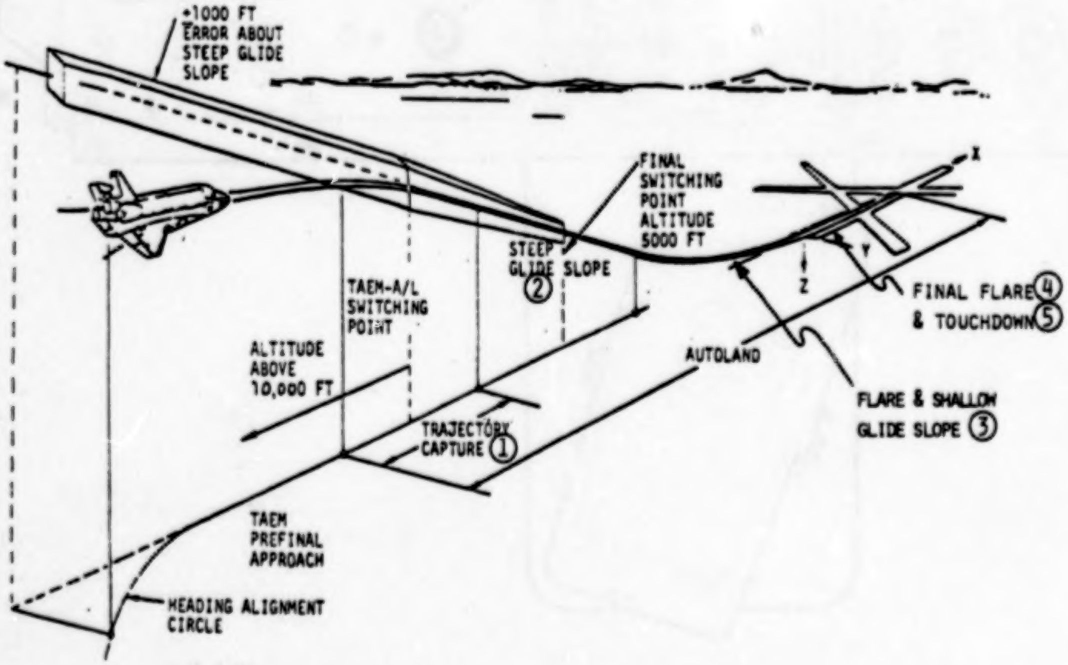
+1000 FT ERROR ABOUT STEEP GLIDE SLOPE
FINAL SWITCHING POINT ALTITUDE 5000 FT
X
Y
Z
STEEP GLIDE SLOPE ②
TAEM-A/L SWITCHING POINT
FINAL FLARE ④
& TOUCHDOWN ⑤
ALTITUDE ABOVE 10,000 FT
AUTOLAND
FLARE & SHALLOW GLIDE SLOPE ③
TRAJECTORY CAPTURE ①
TAEM PREFINAL APPROACH
HEADING ALIGNMENT CIRCLE

Figure 2

ORIGINAL PAGE IS
OF POOR QUALITY

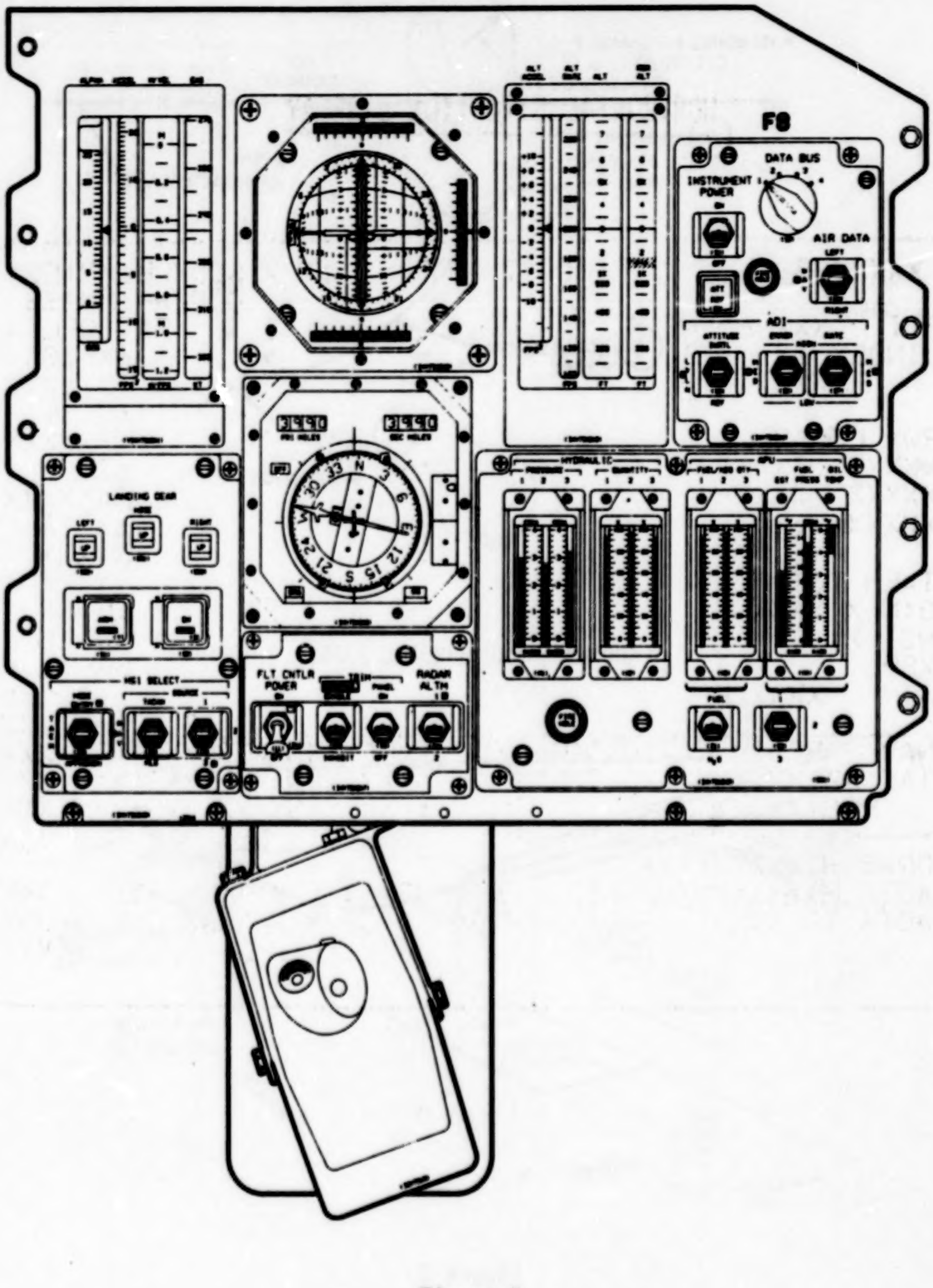
F8
DATA BUS
INSTRUMENT POWER
AIR DATA
LEFT
RIGHT
ADI
HYDRAULIC
APU
LANDING GEAR
LEFT
NOSE
RIGHT
HSI SELECT
FLT CNTLR POWER
TRIM
RADAR ALTM
FUEL
N
3
6
E
12
15
S
21
24
W
30
33

Figure 3

HORIZONTAL SITUATION DISPLAY

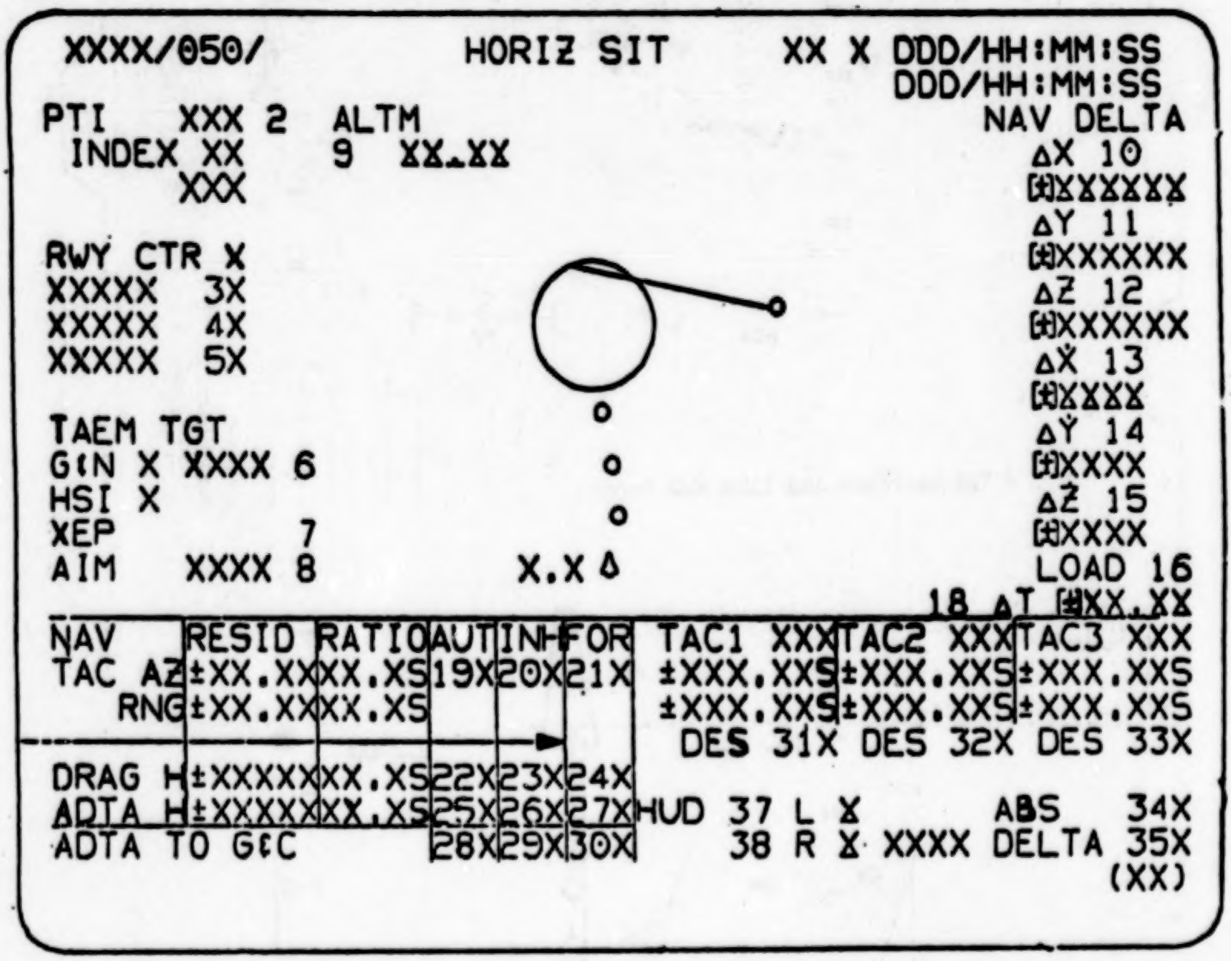

```
 XXXX/050/            HORIZ SIT      XX X DDD/HH:MM:SS
                                          DDD/HH:MM:SS
PTI    XXX 2  ALTM                            NAV DELTA
 INDEX XX     9  XX.XX                          ΔX 10
       XXX                                     ±XXXXXX
                                                ΔY 11
RWY CTR X                                      ±XXXXXX
XXXXX  3X                                       ΔZ 12
XXXXX  4X                                      ±XXXXXX
XXXXX  5X                                       ΔẊ 13
                                               ±XXXX
TAEM TGT                                        ΔẎ 14
G&N X XXXX 6                                   ±XXXX
HSI X                                           ΔŻ 15
XEP         7                                  ±XXXX
AIM   XXXX 8              X.X Δ                 LOAD 16
                                         18 ΔT ±XX.XX
NAV    RESID  RATIO AUT INH FOR  TAC1  XXX TAC2  XXX TAC3  XXX
TAC AZ ±XX.XX XX.XS 19X 20X 21X  ±XXX.XXS ±XXX.XXS ±XXX.XXS
   RNG ±XX.XX XX.XS              ±XXX.XXS ±XXX.XXS ±XXX.XXS
                                  DES 31X DES 32X DES 33X
DRAG H ±XXXXX XX.XS 22X 23X 24X
ADTA H ±XXXXX XX.XS 25X 26X 27X HUD 37 L X         ABS  34X
ADTA TO G&C         28X 29X 30X     38 R X XXXX DELTA  35X
                                                      (XX)
```

Figure 4

ORIGINAL PAGE IS
OF POOR QUALITY

HUD FORMAT

S-turn, acquisition, and heading alignment phase

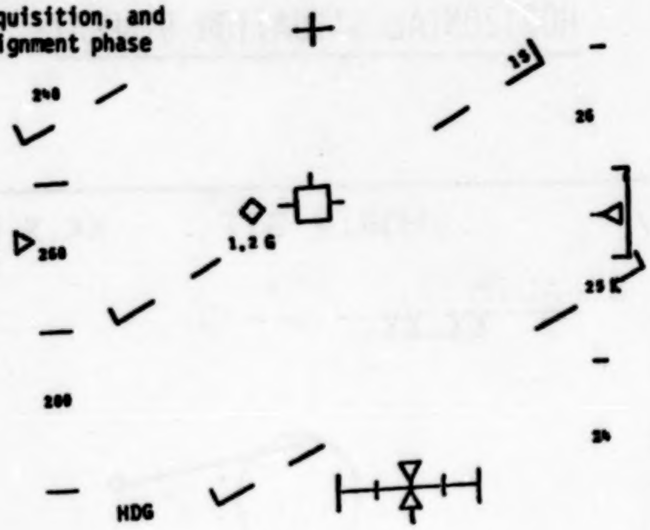
15
240
26
1,2 G
250
25 K
260
24
HDG

The approach and land HUD format

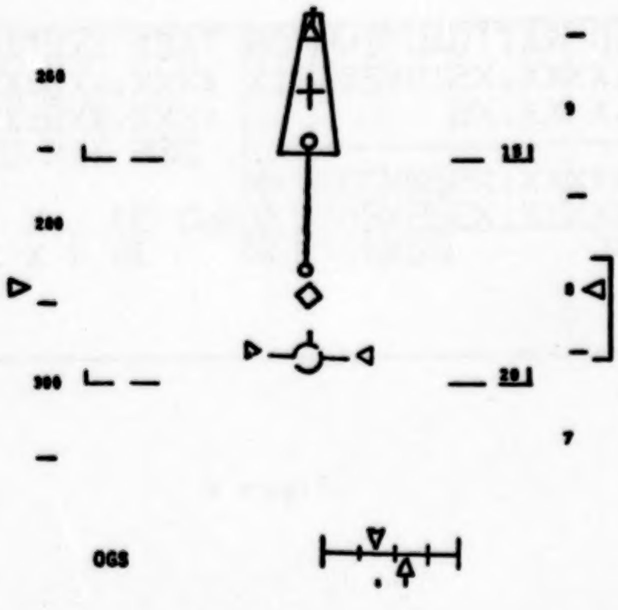
280
9
15
290
8
300
20
7
OGS

Figure 5

AIM POINTS

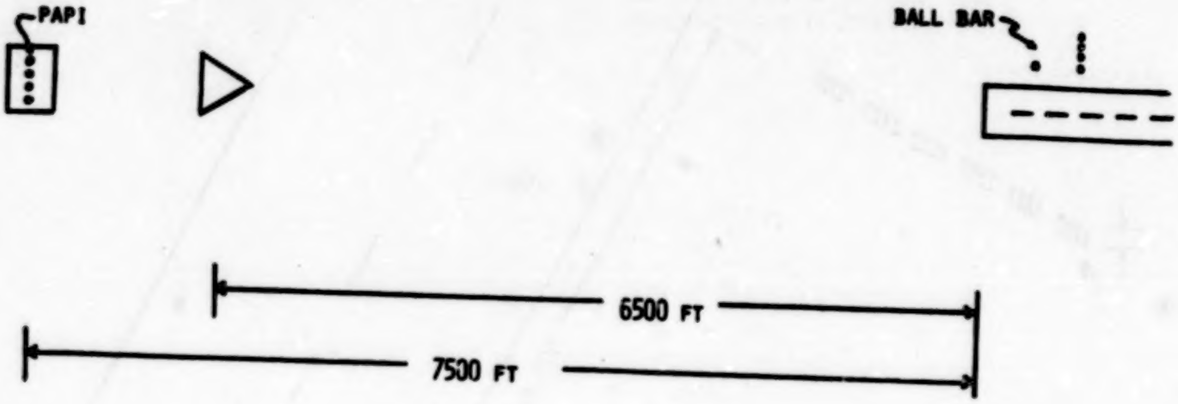
PAPI
BALL BAR
6500 FT
7500 FT

Figure 6

PRECISION APPROACH PATH INDICATOR LIGHTS
(PAPI)

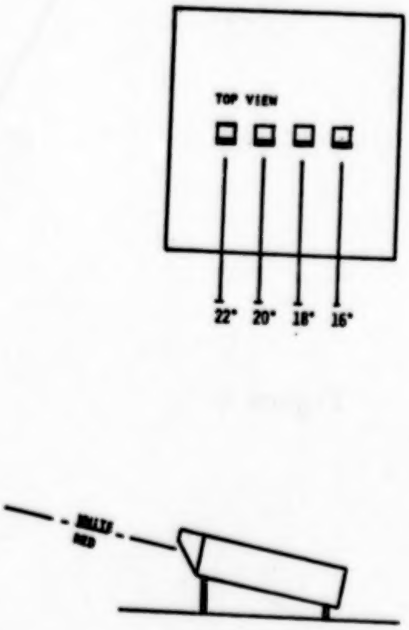
TOP VIEW
22°
20°
18°
16°
WHITE
RED

Figure 7

ORIGINAL PAGE IS
OF POOR QUALITY

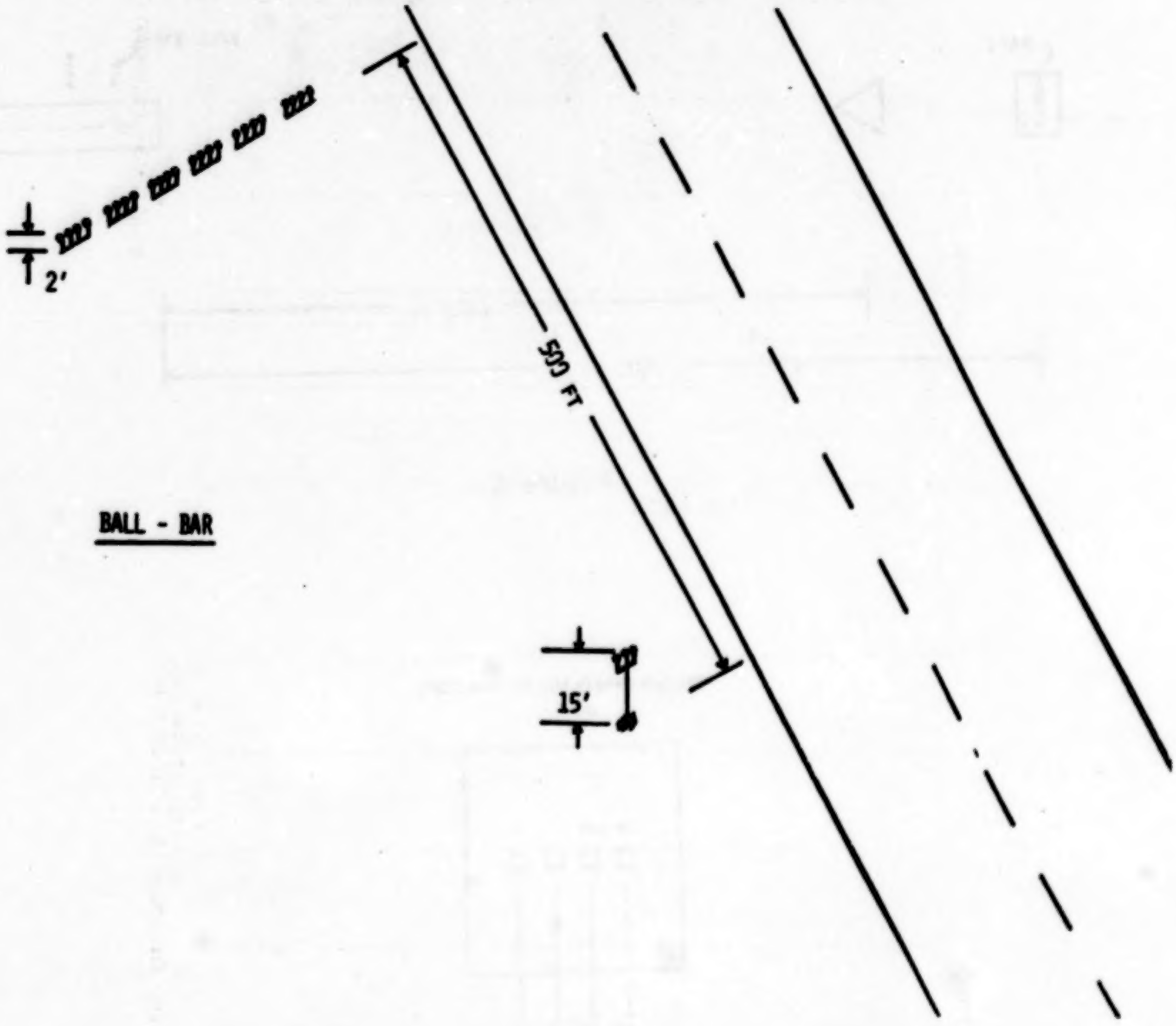

2'
BALL - BAR
500 FT
15'

Figure 8

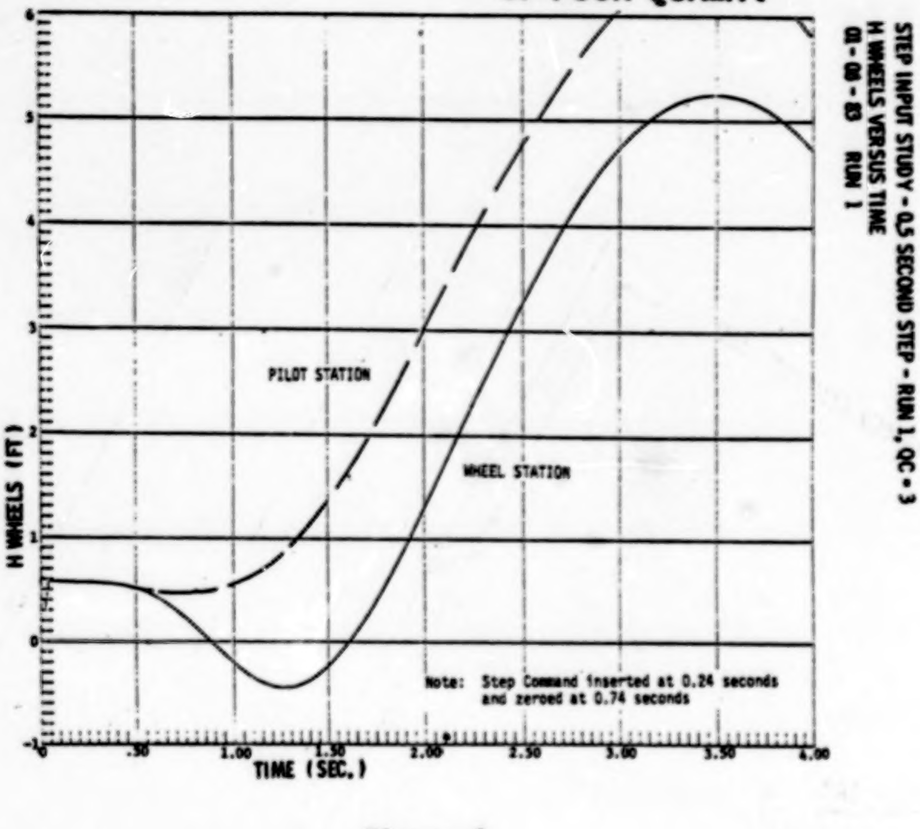

STEP INPUT STUDY - 0.5 SECOND STEP - RUN 1, QC = 3
H WHEELS VERSUS TIME
01 - 06 - 83 RUN 1

Note: Step Command inserted at 0.24 seconds and zeroed at 0.74 seconds

Figure 9

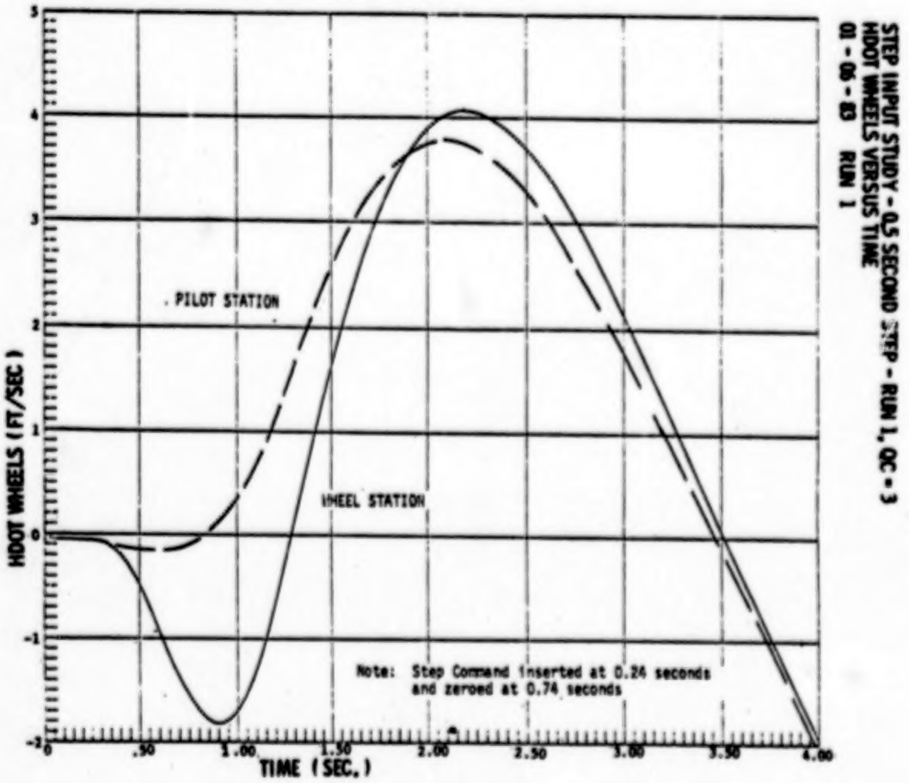

STEP INPUT STUDY - 0.5 SECOND STEP - RUN 1, QC = 3
HDOT WHEELS VERSUS TIME
01 - 06 - 83 RUN 1

Note: Step Command inserted at 0.24 seconds and zeroed at 0.74 seconds

Figure 10

omit 27
TO
END

THE BEGINNING OF A NEW AERODYNAMIC RESEARCH PROGRAM

Milton A. Silveira
Office of Administration
NASA Headquarters
Washington, DC

It's a great pleasure to be here today, particularly after waiting something like 14 years to attend this conference. It's great to see that the initial predictions we made on the vehicle really came true and that we didn't have any more problems than those few we have heard about during the last three days of this conference.

To me, it is still very, very exciting to see the Space Shuttle orbiter land. Particularly if you consider the things that we accomplished on that first flight, seeing the vehicle come back for the first time and make the landing as it did was a very, very thrilling thing. When John Young got out of the airplane, he was jumping all around the place. John was so elated at how the airplane flew and how he flew it back into Edwards that he was just hopping around. He was really elated with it.

Major accomplishments were made on the design of the Space Shuttle (figure 1). Initially, as you know, we looked at a vehicle that had air breathing engines to be able to give us additional ranging capability after entry. Later in the program we decided we were going to use a gliding entry all the way from retrofire down to the airfield. We accomplished that. That's a major accomplishment. We also selected to go to a digital fly-by-wire control-configured flight system. This was in the time period of 1972 to 1974, which was before anybody had committed to a fly-by-wire system; and in particular, it was before anybody even considered a digital flight control system. As you know, because of the step we took in that area, we were able to tolerate very, very large discrepancies in aero data. The idea of using tolerances and variations on aerodynamic coefficients in designing an airplane was a brand new thing as far as the Shuttle was concerned. There were very few airplanes you could design using as wide a boundary on the aerodynamic parameters as we used in designing the Space Shuttle. The vehicle went from a regime of Mach 28 all the way down to landing. When you consider aileron reversals and everything else that the control system must handle, it was a big accomplishment to be able to predict the aerodynamics on the vehicle and build a flight control system to handle them. Of course, the vehicle is statically unstable. That was a hard thing to get John Young to accept--that we were going to have an unstable vehicle to fly.

With the low L/D vehicle there was an argument between whether we needed air breathing engines for go-around purposes at landing or not. We were able to keep the weight down on the vehicle by keeping a very small wing. One of the stories we had early in the program (at least Max Faget was saying) was that the easiest way to get to the point you wanted was ballistically. Now all you need is a little L/D to make a smooth landing at the end point. The way we are able to manage the energy all the way down the flight trajectory is a little different too. We were able to use the speedbrake to modulate the L/D. I think, as Steve Nagel indicated in his talk, it acts just like a throttle. We demonstrated this with many airplane flights. We used the 990 at Ames and we used the Dash 80 airplane at Boeing to prove the concept that this was an acceptable way to fly an airplane. We still use the RCS system to augment us through areas where we have certain stability problems. I will talk a little more about that later.

PAGE 1330 INTENTIONALLY BLANK

PRECEDING PAGE BLANK NOT FILMED

One thing I missed listing on the figure is the accomplishments we really made in the aerothermodynamic area. I think when we first started the vehicle program a lot of people were insisting that it would be necessary to design the heat shield for turbulent heating all the way down. The idea of designing it for laminar then transition was too great a risk. As you know, we did that and we got away with it. And we understood that problem well enough to trust it on the first flight.

Of course, one of the major goals of the Shuttle program at the present time is to become operational (figure 2). As a result, you are going to find a great deal of reluctance in the program to do anything that's not aimed at getting the vehicle to be an operational vehicle. If it interferes or slows down the flight program at the present, it's just a lot of nuisance as far as the program manager is concerned. But I think the things we have to look at are ways that we can continue to use the Space Shuttle as a research airplane.

Back in the early days of NACA and NASA, we used to go out and build the X-series airplanes just to explore flight boundaries and get data to be able to design other airplanes. Here we have an airplane that traverses a very, very large regime of aerodynamic flight. We need to understand and look at the ways we can use the airplane to get additional data. The reason we were able to design this vehicle and make it work--the reason you people could do it--is that you had a very, very high state of technology at the time that we built the airplane. We need to keep the technology going. We need to keep understanding aerodynamics so that when we come up to build our next vehicle we know what we have to do. Now, of course, some of the attempts at that, like the OEX program (figure 3), again have suffered from the requirements of making the vehicle operational in the first place. We are going to continue to push to get the OEX experiments and to get additional OEX experiments put in the program and go fly just to develop technology. That's part of NASA's charter. We particularly need to look at those areas of research (and these will be the easiest ones to sell right now) where we can help the vehicle become more operational. I was talking to Bob Hoey about how we need to understand the reaction control system better and how it interacts with the primary system so that maybe in certain regimes we could stop using it. As a result, not using the propellant of that system during that time period means we can use the additional payload or have additional weight that we can use for some other reason. But, I think that, lastly, we need to look at those things either by air-launched vehicles off the orbiter or by using whatever other method you may think of to use the vehicle as a basic research tool and continue to keep our state of the art in aerodynamic technology ahead of anybody else.

It's a great pleasure to be here, and I want to congratulate you people again for the tremendous job you did in making the Shuttle possible.

WHAT HAVE BEEN THE MAJOR ACCOMPLISHMENTS?

GLIDE ENTRY FROM ORBIT TO AN AIRFIELD

DIGITAL FLY-BY-WIRE CONTROL-CONFIGURED FLIGHT CONTROL SYSTEM

AERODYNAMIC FLIGHT REGIME FROM MACH-28 DOWN

STATIC AERODYNAMICALLY UNSTABLE VEHICLE

LOW L/D AIRPLANE

L/D MODULATION USING SPEED BRAKE

REACTION CONTROL SYSTEM AUGMENTATION

Figure 1

THE MAJOR GOAL OF THE SPACE SHUTTLE PROGRAM

TO BECOME OPERATIONAL

Figure 2

HOW CAN WE USE THE SPACE SHUTTLE FOR RESEARCH

OEX PROGRAM

RESEARCH TO MAKE THE SHUTTLE A BETTER VEHICLE

BASIC RESEARCH USING THE VEHICLE FLIGHT REGIME

Figure 3

ASCENT AERODYNAMICS I & II

Tru E. Surber and Barney B. Roberts

Surber: One area that we would like to have more attention directed to is plume base flow technology since it can provide the insight required for preflight analysis of plume effects. The definition of plume simulation parameters through a base flow technology program is of primary importance in the wind tunnel prediction of plume affected flight loads. In the area of flight test results, a considerable effort has been expended to provide instrumentation to define the aerodynamic effects. The OFT flight program has defined the basic aerodynamic characteristics; however, it is an acknowledged requirement that future flights should provide detailed pressure distributions to support wing load analysis. The loft anomaly which was observed on the first flight has now been identified as a consequence of plume effects and channel flow. A physical description of the flight flowfield has been advanced and the data base has been adjusted to reflect the flight data. The aerodynamic data analysis from subsequent flight has confirmed the adjustments made to the aerodyanmic data base and the loft phenomena has been properly accounted for in the data base. Finally, techniques have been discussed for assessment of ascent aerodynamic characteristics which will require additional algorithms to define fitting loads and strut loads to reduce the time for day-of-launch analysis.

Roberts: In the areas of attachment-induced air loads on the vehicle, techniques have been developed to correctly model and test the localized static and dynamic loads. In the area of separation aerodynamics, techniques to promote efficient wind-tunnel data acquisition and data organization have been developed. These techniques should greatly reduce the test time in the wind tunnel. Techniques have been developed using these data-organization schemes to increase confidence in the data and provide methods for data interpolation. It looks like momentum ratio has been identified as a suitable jet interaction parameter for the booster separation motors. On the subject of launch vehicle debris, it looks as though (although this was a critical problem at first) that all safety-of-flight hazards have been completely eliminated. Since some significant and minor damage issues are still around and apparently will always be present, we should never relax our awareness of this problem. The ascent data system has proved quite useful in measurement of real winds and in verification of the BET, and it has been shown to be accurate for Mach numbers less than 2. Venting models in use today show excellent correlation with the flight data when the flight pressures are input rather than wind-tunnel estimates. Again, we have a problem with launch vehicle plume simulation and with not getting the correct pressures on the fuselage.

In the area of ignition overpressure, it appears as though some advances have been made in both test techniques and in scaling parameters, and it has been shown that excellent flight predictions can now be made. The one bottom line or key point throughout all our ascent papers has been plume simulation, and it is indeed a critical parameter for aerodynamic testing. We feel that the state of the art has been advanced significantly; however, some deficiencies still remain. Taking a look back on where we started, which was pretty much from zero, we don't feel too bad about that; but it is still deficient. We feel that a technology program should be revisited to complete this Empirical science, and remember again, from the papers you heard, the rocket plumes have affected loads, performance, and venting.

ENTRY AERODYNAMICS I & II

James C. Young and Donald C. Schlosser

Young: The papers in the Entry Aerodynamic Session indicate that the state-of-the-art technology in the early 70's was adequate to produce excellent preflight estimates in the aerodynamics below hypersonic speeds, particularly below Mach 10. It appears recent advances in computation aerodynamics that the deficiencies of the 70's are being attacked and have promise of being corrected. Another key point, if precise preflight aerodynamic estimates are required for future vehicles, is multiple wind-tunnel facility entries combined with careful analysis, since it has been shown beyond any reasonable doubt that you can get different answers from different facilities. Therefore, you have to understand the spread of facility data to really get precise aerodynamics. One of the great things, I think, that has been accomplished in the Shuttle program is the creation of an industrial/government team. We had engineers with various vested interests coming together and really producing, in my estimation, the best technical product that could be done within the nation. That is sort of the general comment, and I'll ask Don if he has any specific comments.

Schlosser: For those that did not attend the second session, I think Doug Cook put together a very good outline showing that the flight test program has really just begun and was not over at the termination of Flight 4. We have 12 more flights to go. They are all planned to explore the areas where we have shown minor differences from our preflight predictions. The area of hypersonic aerodynamics was pointed out as an area that we missed. I don't really think we missed it. Back in the 1970-1975 time period there were people at Langley doing real gas calculations. They predicted a pitching moment of the order of magnitude by which we erred. We did not know how to account for it, since we were not confident in the magnitude of the real gas effect, so we opted not to include it in the basic data. The real gas magnitude was accounted for in the uncertainties. These uncertainties are not symmetrical at high altitude (high Mach number, or high viscous interaction region). A positive bias was included in the variation to account for the real gas effect. At the higher altitudes, the uncertainties adequately covered the flight results except in the Mach 10 to 15 region. I think that was due to the way we modeled the Aerodynamic Data Book, i.e., the manner in which we transitioned from altitude data (presented from 600,000 to 300,000 ft) into the viscous interaction parameter tables that are presented for values of 0.08 to 0.005 into Mach number tables from Mach 20 on down. When exiting the viscous interaction tables at 0.005, the Mach number could be 19 or 13. Therefore, the Aerodynamic Data Book included constant values in the Mach tables between 10 and 20 so that there were no discontinuities in the data as transition from viscous interaction tables to the Mach tables occurred. In so doing, I think we missed the onset of the real gas effects due to a modeling technique. A new edition of the Data Book, that we are going to label as the Operational Data Book, will be released toward the end of this year and will contain certain updates based on the first six flights. We are looking at a different math model which will eliminate the current problem.

PRECEDING PAGE BLANK NOT FILMED

GUIDANCE, NAVIGATION, AND CONTROL

Kenneth J. Cox

First of all, I want to comment on what was presented and also what was not presented that had significance. The ascent GN&C presentation was primarily oriented around control. In the entry area there were presentations on flight control, and flight control testing and validation. The idea of tolerances and variations and how they were used by the flight control designers in their testing was addressed, as well as the entry flight control system design. These presentations were concerned with the orbiter rigid-body characteristics. There were presentations on entry flight control from a structural interaction standpoint and on approach and landing characteristics. Entry and its associated technology disciplines were the areas that were chiefly emphasized at this conference. Guidance and navigation were not covered. An attempt was made to obtain papers in G&N, but the AIAA had a prior conference where excellent G&N papers were given. The general previous conference comment was that performance was relatively good, and that there were no significant problems in the guidance and navigation area. I would remind you that on-orbit flight control was not covered at this conference. This is appropriate in that the flight data available today is immature with regard to many of the flight control interactions that occur when the payload doors are open and a remote manipulator is used to grab and deploy heavy payloads. Furthermore, future missions will require retrieval operations, and flight experience on our ability to do retrieval does not exist. We have all of the dynamics of orbit flight control/structural interaction to contend with. These things are in front of us and it is anticipated that we will find operational problems. A comment which follows along the theme Milt Silveira mentioned is as follows: It is felt that one of the significant things in the Shuttle Program is that we used a single avionics configuration to do the booster function, the spacecraft function, and airplane function, and this represents a major integration accomplishment compared to what was done prior to this time.

I would not like to cover the specific things that came out of the presentations in terms of lessons learned. For ascent, there was discussion of the lofting performance deviation, which has been well covered throughout this conference. Multiple technical disciplines were involved in the resolution of this problem. Also, in ascent, the integrated flight results for the second stage show consistently that the SSME compliance tends to bias the trim when the main engines are thrusting. Entry flight control, as was brought out, did perform well and had extensive testing with regard to uncertainties. I would say the approach to aero variations and the flight testing would appear to be good. The transition maneuver from flying like a spacecraft with RCS jets to an aircraft using aero surfaces has design importance, especially when accomplished under uncertainties. For a nominal set of aerodynamics, the point of switching from a spacecraft to an airplane flying design can be easily set, but given all the uncertainties, selecting the switch point is a difficult design task. I would say that in the area of firing jets in the atmosphere (the RCS/aero interaction) we would recommend applying uncertainties earlier from a flight control standpoint. Considerable information was received on RCS aero uncertainties, but it was late in the design cycle. It should be pointed out that the whole problem of flight control analog filtering, digital filtering, how do you avoid aliasing, etc., is very important. Hewitt Phillips made some inputs early in the problem with regard to hammering effects of digital inputs to the actuators, and those inputs were considered in the filter design. Another comment along the line of what Milt Silveira said was that highly augmented digital flight control requires early emphasis on

PRECEDING PAGE BLANK NOT FILMED

integration across technical disciplines. You cannot start early enough, I think, between the aero, the structures, and the flight control when you have this type of augmented design. It is flight-crucial, it has to work, and early integration is extremely important. For entry, the general system trades that were made between rigid-body design, which is set primarily by flight control/aero considerations, and flight control/structural interactions appear to have been reasonable. The basic flight control design that evolved turns out to be a simple design, but it did require gain scheduling techniques. There was no such thing as a single set of flight control gains and flight control filters that would accommodate the entire dynamic regime. For future designs, it is felt that continued reliance upon some form of gain/filtering scheduling is required. I want to say for Jim Young's benefit that from a flight control standpoint, the levels of aero variations (this is totally in hindsight, given the OFT series) were about right. I honestly believe they were not over-conservative or under-conservative.

Another item that has not been dwelt upon is that entry atmospheric abort represents a new class of designs. What is being discussed is what happens to flight control in a RTLS abort when you kick off the solids, turn off the main engine, and there you are, a glider coming back. The concerns we are continuing to encounter is that there is no flight data for abort. In addition, heavy payloads (not yet flown) do impact flight control stability margins, and one of the issues which I submit is a dilemma: What technology approach should be taken to update the initial aero data in the abort region given that flight test information exists in everything but the abort region? Now one can take a viewpoint that says no flight data exists in the RTLS abort region, therefore, whatever was used prior to STS-1 remains in the program forever. I don't know to what degree, in an aerodynamic sense, one can say I learned something in nominal entry and there is a way to correlate that to the abort region.

Another item is that payload dynamic interactions with regard to entry flight control are important. The design aspects associated with these interactions, including the mounting characteristics, need early emphasis. Analysis of nonlinear design characteristics was one of our payload-induced problems. The IUS/TDRSS flight STS-6 has a nonlinear coulomb damper that required us to design the entry flight control dynamics to limit cycles criteria rather than stability. A question that must be answered is, "What is the amplitude of the limit cycle; how do we know propellant impacts; and how do we know it doesn't affect the crew?"

Approach and landing have already been mentioned, but for future designs, wind estimation biasing should be included so that if there are well-known winds on the way down, we would react earlier. There has been prior discussion on the speedbrake logic and the performance improvements by Steve. Handling qualities, especially pilot-induced oscillations, are important and there are improvement studies presently ongoing. Finally, on the slapdown design with two main wheels on the ground and the nose wheel up, we did not cover all of the dynamics work that should have been done at an early stage. When the nose pitched up on the STS-3, we found some sensitivities in the design which will be corrected through software, but should have been better understood earlier.

In summary, while this was not covered in a conference paper, I want to mention that in the Orbiter Program we conducted an open/closed dynamic stability ground test. This was strongly recommended by the Air Force and also through discussions with General Dynamics and Grumman. This test involved the orbiter with wheels on ground (soft tires or soft support system). The excitation signals were transmitted through the digital software filters and the actual flight equipment to drive the elevons. Then the sensors would pick up the vehicle structural oscillations and feed back through the flight control system. Many valuable items were identified. It was truly an integrated dynamics test involving control, software, structures, sensors, and actuators, and I would suggest that this approach represents a valuable lesson learned. For future designs using a highly augmented system with digital control, I would recommend this test. Finally, in the payloads dynamics interactions area, I previously mentioned the IUS soft cradle design issue. Two weeks ago it was identified that a payload with liquid slosh (Centaur) causes the second-stage ascent to be unstable, and we are working this problem at present. Finally, I want to discuss ALT issues. I have asked myself: (1) was it worth it, and (2) can ALT be avoided for the next program. It is definitely felt to be worthwhile for the Shuttle Program. The issue is, can technology work be done between now and the second-generation orbiter so that the expense of a future ALT program can be avoided. This question is left as a challenge to the technology disciplines.

AEROTHERMAL ENVIRONMENT I

Dorothy B. Lee

This has been a fun and very informative conference. I do think that Langley deserves a compliment for this excellent, successful conference. Each of the papers, not only in my session but all of them, illustrated exceptional technical competence. I am proud of them; many have contributed to advancing the state of the art. All can take pride in having played a major role in history through your contributions made to the Shuttle program. There are some highlights that I want to point out. Terry Greenwood and his colleagues at Remtech and Lockheed have contributed immeasureably to future predictions of plume heating with the development of the very complex two-phase plume flow-field calculations which was coupled with the Monte Carlo radiation code. This is evident in the good agreement of the flight measured base heating environment with the preflight predictions. The Shuttle experience taught the necessity of including the combustion of ET TPS out-gassing with the basic plume radiation model. While the ET TPS is unique to the Shuttle program, it does alert the technical community to the necessity of considering TPS effects on the plume radiation model predictions. The three-engine-cluster convective plume environment added another data point to the experience in the plume world. The work of Jim Hodge, Paul Phillips, and Kevin Hertzler have shown the merits of conducting the push-over/pull-up maneuvers in order to extrapolate the wind-tunnel data for entries at angles of attack and Reynolds numbers beyond the wind-tunnel capabilities. In Joe Haney's paper, several points were brought out that are significant. First of all, with our design philosophy, the flight data supports the use of wind-tunnel data for hypersonic design environments. The use of simple geometric theories on the orbiter lower surfaces, and the direct application of wind-tunnel data to the leeward surfaces for non-vortex flow, are good approaches for the design heating predictions. In regions strongly influenced by vortex scrubbing, the wind-tunnel data underpredict the flight data. This needs to be resolved for future programs, either with flow-field development or extensive flight data analysis. For example, a thorough investigation of the various phenomena associated with the observed rapid temperature increase, as pointed out in Joe's paper, at the scale Reynolds number of 2 million corresponding to 3.9 million for a full-length orbiter could be undertaken.

The last two papers dealt with boundary-layer transition extensively. Boundary-layer transition has been a nemesis throughout history, and especially throughout the Shuttle program. It prompted many meetings and many discussions. It imposed almost unreasonable constraints on manufacturing; but in the long run, these constraints may have saved much of the orbiter TPS localized heating problems. Winston Goodrich made several interesting observations. Transition occurs over most of the centerline for a narrow range of relatively low free-stream Mach numbers (i.e., transition starts around a free-stream Mach number of 10 and is complete around a Mach number of 7). The values of free-stream Reynolds number at transition onset and completion are approximately the same for each of the flights, with the exception of STS-1. While the wind-tunnel conditions provided a reasonable test environment, the transition locations appear to be more sensitive to Reynolds number for flight data than for wind-tunnel data aft of the forward 15 percent of the vehicle. The favorable pressure gradient for the forward 15 percent of the orbiter seems to overshadow the TPS roughness. This suggests that orbiter roughness in this forward region is not as effective a boundary-layer trip as the same roughness located downstream. Aft of the 40 percent station, wind-tunnel noise is apparently the dominant factor. Surface roughness dominates transition at both flight and wind-tunnel conditions between the 15 and 40 percent stations where the wind-tunnel and flight data are in good agreement. The

PRECEDING PAGE BLANK NOT FILMED

rapid forward movement of transition is indicative of a rough surface. Thus, we still do not know the orbiter smooth-body transition for flight.

In contrast to Winston's conclusions, Mark Harthun's paper concludes that single roughness element transition is appropriate for analytically predicting transition. But I want to point out that Harthun, et al., recognized in the beginning that the wind tunnel was expected to provide a conservative transition value due to free-stream turbulence in the tunnel and that transition during flight would be induced by surface roughness. A single roughness site on the nose landing gear door was found to trip the boundary layer on 4 of the 5 flights. An analytical method that predicts the effective roughness size was formulated by Rockwell, scaled from wind tunnel to entry flight conditions, and inferred an average value of approximately 113 to 130 mills, if I remember correctly. An engineering method to predict nonequilibrium boundary-layer heating, which was formulated by Rockwell, provides good agreement with flight-test data during times of significant heating. The application of correlations of boundary-layer transition and catalytic recombination in predicting heating to the orbiter for a high-crossrange mission, indicates that the TPS on the windward surfaces has the capability to successfully perform this mission. Our current motto is "go for it."

AEROTHERMAL ENVIRONMENT II

E. Vincent Zoby

Several papers in this session discussed various computational techniques and resulting comparisons with the Shuttle heating data. The 3-D viscous-shock-layer code, presented in a paper by Kim, gives the opportunity for the first time to compute the heating environment over the entire Shuttle surface. This method avoids the typical inviscid-viscous matching problems that some of the other existing techniques encounter. However, as with any new method, there are some outstanding questions which still need to be resolved. One point that John Bertin made on Kim's paper is the role of perfect-gas heating predictions in approximating the overall heating levels along the Shuttle surface. The point is that industry cannot exercise codes frequently that have long run times and large storage. The perfect-gas results can account for some of the heating reduction in a nonequilibrium environment.

Dave Stewart presented additional results from the Catalytic Tile Experiment which further demonstrate the reduced heating level to the baseline tiles. Obviously, many of the advanced configurations for any future mission will apparently try to take advantage of this particular concept. The centerline heating was noted by David to increase slightly with each flight. What he attributed this result to was possible alumina contamination which would lower the surface emissivity, thus causing increased heating. A somewhat different approach was presented by David Throckmorton when he looked at the experimental STS-2, STS-3 data. In that paper, David suggested that the melting of the acoustic sensors and the subsequent downstream deposition of the material on the surface apparently caused increased surface reaction rates and thus increased heating. In the paper, Dave also provided some information to imply that the cleaning of coated tiles may leave residual effects in the surface so that at some time during the entry, the supposedly cleaned tiles may give the same indication as the catalytic tiles.

Another very interesting paper, I thought, was given by Carl Scott. Carl showed comparison of several of the existing computational methods--those that have been used to compare with the Shuttle data. One of the important things that Carl demonstrated was that when we look at the differences in these methods, and there are several of them, we are only seeing 20- to 30-percent discrepancies in the results. When you consider each of these methods, with their own strong points and deficiencies, the overall differences of 20 to 30 percent are really remarkable. Harris Hamilton made a comment from the floor that one day we should get together and talk about these computational methods--the strong points and the weak points--and that in itself may be worthwhile. Dennis Petley's paper was interesting in that it provided a means to consider how the filler bars were charred during entry and that we have at least some understanding--some hypothesis--for the charring of these filler bars. Vernon Helms' paper on the upper surface heating presented an approximate method which seems to do a very good job in comparison with the heating levels and trends of the upper surface heating rates. We have heard so much about the fact that this is a very difficult area to predict heating levels. However, it seems that this particular technique is doing a fairly good job. Possibly an extrapolation of that technique to different free-stream conditions and to other angle-of-attack conditions may be an interesting test of that particular technique.

If there are a few minutes, I would like to comment on some of the conclusions of the speakers themselves. I felt that a few of them were notable. When you look at our computational ability for such a reentry vehicle like the Shuttle, you find that our detailed codes--our benchmark codes--are really still in an evolving state, and we are still discussing the best approach. The Shuttle has been designed and the Shuttle is flying. Well, maybe, hopefully, from this experience we can learn so that when we go to the AOTV-type application we won't have such large gaps in our computational abilities. Another point that was made (and I think that a lot of us here would like to see it enacted) is that we really don't have any flight data along the windward centerline free of contamination, whatever it may be, and I think that just from a research flight point of view we would like to see that data. We can then use ground-test results and compare then with the flight-test results to characterize the surface material.

THERMAL PROTECTION

Howard E. Goldstein

The papers presented here were the culmination of 12 years of work required to make the first reusable heat shield system operational. When the original Shuttle heat shield was proposed, there were a great many questions as to whether it ever could be built and, if built, whether it would really work. The RSI thermal protection system overall thermal performance as described by Bob Dotts is very acceptable. On the windward surfaces, the heating rates were a little lower than expected. There were various minor anomalies (particularly, burned filler bars). Papers in this session discussed the anomalies and presented correlations to describe the aerodynamic heating effects that caused the anomalies. On the leeward side, the heating was not as accurately predicted, but, in general, the TPS performed well. On the OMS pods and on the sides of the fuselage were hot spots that will require some changes in the TPS system on future vehicles, but nothing that in any way endangers the vehicle. Among the findings was that the tile system, which we know is very fragile, was very forgiving of damage. There were literally thousands of minor discrepancies before flight and some significant impact damage during flight or during launch. But, in all cases, the system came through with flying colors. The issues that remain according to Dotts are primarily lifetime and turnaround concerns. These issues are being addressed by NASA and the contractors and will, in time, be worked out. Rewaterproofing between flights and the burned filler bars are significant problems.

Ron Banas of Lockheed Missiles and Space Company (LMSC) described over 30 problems that occurred in the development of the tile system. He showed that LMSC had progressed from a tile yield of about 40 percent to a yield of about 80 percent, and they have now reached the point at which no further problems are expected in manufacturing for future vehicles. They have also implemented some of the new second-generation materials, such as FRCI, which will save approximately a thousand pounds on orbiter 103.

Paul Cooper of Langley discussed a problem with the strain isolation system that has been significant to the Shuttle TPS for the last several years. He indicated the possible adverse consequences of the long-term changes in strain isolation pad properties. While there is no significant safety risk, this problem could require refurbishment of future vehicles.

The TPS thermal performance calculation methodology was described in great detail by Ed Schlesinger of Rockwell in a paper whose first author was Cotton Neuenschwander of Rockwell. They were able to demonstrate that the heat-transfer theories originally used for the Shuttle were somewhat in error, although not enough to create any problem for future flights, however. These first flights have provided invaluable data to update those calculation techniques. They also described some of the problems involved in calculating the heating in the gaps, around the seals, and in the elevon cove, and they described some fixes that could be used to correct the heating problems that were found.

Don Curry of NASA JSC described the leading-edge subsystem and pointed out that subsurface oxidation, which had been observed early in the program, was a significant issue with respect to the life of the RCC subsystem. He also described some unexpected problems with corrosion of metallic parts of the system. He showed that, in general, the system had worked very well, as was expected. The heating environment on the leading edge showed some discrepancies between what had been predicted and the flight data. In some locations, particularly the nose cap, the heating rate was underpredicted. At other locations along the leading edge, heating rates were overpredicted. In general, none of these differences are a significant problem with respect to the lifetime of the leading-edge system.

The conclusions that one can draw from this series of papers are that the development of the Shuttle TPS system had been successful, that we have a system that is viable, and that the system will provide for an operational Shuttle in the foreseeable future. We also have a system on which significant improvements can be made in the future. All in all, it was an excellent session that presented a very comprehensive review of the first 2 years of the Shuttle's life.

Question: Can you make a prediction on the thermal protection systems for the second generation of orbiters? Answer: Generically, I think the thermal protection systems are going to be very similar. The reusable surface insulation and the carbon carbon have proven themselves. It's obvious, however, that new, more durable versions of these materials are necessary, and they are being developed. There is no reason to expect a fundamental change as a result of what we have learned here. There was nothing in the data presented that was so surprising to indicate any requirement to go to a hot structure or to an all-metal vehicle.

Comment by Val Derugian of Boeing: It seems to me from what I have seen in the papers that the trouble occurred where the flow could get into the system or into the gaps between the tiles. An effort could be made in the future to try and simulate this problem in ground facilities so that these effects don't show up. It's very hard, of course, to guess when they will occur, but additional sealing (as Don Curry has shown) or additional protection so that the flow cannot get through has shown to be very effective. We have seen similar effects on the ASSET flight, for instance, so these phenomena are known. To me, it seems that they can be simulated in ground facilities, in plasma jets for instance, or even in the wind tunnels. I think special attention should be given to the damage that actual flow can make, because we very often feel that if we can heat it in the laboratory and the structure withstands the heat, then everything is fine. This is not so, because the flow can be very damaging.

Answer: I believe that the seals and flow stoppers were the components of the TPS system which produced the most surprises. I certainly think testing in ground test facilities will be very helpful in the future to study these effects to develop new vehicles. As Milt Silveira pointed out in his presentation, we now have the world's largest test-bed in the Shuttle. It would be very foolish if we didn't take full advantage of this test-bed over the next several years to study these kinds of problems along with many others.

MEASUREMENTS AND ANALYSIS

Ernest R. Hillje

The first paper in the measurement and analysis section was on subsonic longitudinal performance coefficient extraction and had to do with different air data inputs and their effect on this type of assessment. John Findlay told us about how his analysis used two separate sources of air data (the Langley trajectory reconstruction and the orbiter air data system) to assess orbiter subsonic entry performance. These sets of data essentially involved meteorology BET type of data, and he mentioned that one of the more important items in those sets of data was to have some good wind data. If both sources of data are considered viable, then the results suggest that significant C_L prediction refinements are questionable. The drag-coefficient decrement of 10 percent below the predicted value at Mach numbers below 0.6 was substantiated by his analysis and proven to be independent of the air data source. This decrement increased the predicted L/D so that data showed better agreement with flight data.

The second paper was given by Jim Young, and it went into the development of aerodynamic uncertainties for the Space Shuttle orbiter. Jim showed how, early in the program, there was a necessity to find two types of aero uncertainties, and he discussed the rationale of what went into these two sets of uncertainties. One was a minimum preflight error called "tolerances" defined to allow the flight control systems design to be desensitized to the aerodynamics. The other set that bounded the aero uncertainties was a worst-case set which was still a reasonable set and was called "variations". This latter set was defined to stress flight control systems through simulations and thus insure flight safety. Jim pointed out that the philosophical approach that was used for the orbiter uncertainties could be used also for future programs.

The third paper was on the orbiter air data system, and Leonard Gaines detailed the extensive wind-tunnel test program that went into that system. There were a tremendous number of design changes in the vehicle that made it impossible to do a conventional calibration. For instance, the RCS ports were opened up after the aero data system was essentially defined, and that threw the calibrations off that were presently available. It negated those, and it was like starting over from scratch. There was a tremendous wind-tunnel testing analysis and calibration formulation that went into the orbiter air data system to make it perform the way it did. Leonard also mentioned the ALT flight data which was not used to verify the calibration, but was actually used to correct it, and he showed that the final calibration results were well within the user requirements and that the system performed as advertised.

Dale Kemp told us about how his Chrysler organization developed the Space Shuttle aerodynamic data base, where he took wind-tunnel data from facilities all around the country, both NASA and private, and put the data into standard form. They put it in the form of magnetic tapes, plots, graphs, and that type of thing which enabled the analysis engineers to work with the data very quickly and have some impact on the design of the Shuttle and to come up with the type of testing that was needed for the next segment of the program. He pointed out the importance of organizing and recalling in an orderly manner large amounts of wind-tunnel data. The system was devised to allow an analysis engineer to have some input into the configuration design in a timely manner. The system also allowed for quick recall of any and all data that was in the system. It was helpful with early documentation and the data was disseminated to the appropriate people. If it were not for this system, the Shuttle program would probably still be sorting and analyzing the wind-tunnel data.

The fifth presentation by Paul Siemers was on analysis of some of the flight instrumentation on the Shuttle on the nose (I think it was mostly the nose area) on the sides and some of the things he learned from analyzing these data. The DFI pressure instrumentation was reviewed by Paul. His obvious interest is the SEADS systems and the two (DFI and SEADS) are, I guess, relatively compatible. He used the SEADS flow-field algorithms to help analyze this data, and he concluded that the accuracy could be improved by instrumentation and data acquisition procedures more amenable to the user community. The detailed results of this study should be considered for future systems. Paul evidently has already considered the related pressure data in his SEADS system.

The last paper was on sonic boom by Frank Garcia. He compared measured and theoretical data for both ascent and entry. He told us about how they set up the measurement stations along the flight path for both ascent and entry. He compared the measurements of the flight overpressures with theory and confirmed the ability to predict sonic-boom characteristics for the Shuttle. Work is continuing, particularly on the ascent portion of this flight.

My two general comments from this session and the other sessions are, and this probably sounds like old hat to a lot of people who keep saying that "I keep telling people things and they don't do anything about it," but the first thing I want to say is, in any program, early communications with all of the disciplines involved is very important. That is, most of the reported results, at least in my session, would benefit tremendously from a good systems integration effort. That word, systems integration, seems to get tossed around a lot, and a lot of people don't really know what it means. It means, essentially, making sure one hand knows what the other hand is doing, and I don't think we do enough of it. The second general comment I want to make is that there seems to be two schools of thought: one is coming from the research people and the other comes from the program people. It seems like there should be a better way to serve both areas. The research people want better data, more accurate data, more data, and more measurements. The program people are constrained by budgets, and they just can't do this type of thing. Sometimes the two groups don't understand each other. I would suggest that someone, whether it be at NASA Headquarters or somewhere else, should be working on a mechanism for the research to continue on the Space Shuttle program. The research people should be looking into funding and putting more effort into using program vehicles such as the Shuttle. I was in the back room preparing this and didn't hear Milton Silveira speak, but from one of the comments he made, he probably already said what I just said.

APPENDIX A

AEROELASTIC CHARACTERISTICS OF THE SPACE SHUTTLE EXTERNAL TANK CABLE TRAYS*†

L. E. Ericsson and J. P. Reding
Lockheed Missiles & Space Co., Inc.
Sunnyvale, California

Abstract

A study of the cable trays on the space shuttle external tank has shown that they are subject to high velocity crossflow, which causes flow separation. Preliminary aeroelastic analysis showed that the flow separation could endanger the structural integrity of the cable trays. A systematic experimental test program incorporating static and dynamic tests provided the information needed for a more definitive aeroelastic analysis, which is described in the present paper. The results of the analysis show that even when considering structural and geometric changes in the cable tray design since the initial analysis, the end result is the same; i.e., the structural integrity of the cable trays can not be ensured. Consequently, various aerodynamic fixes were investigated to alleviate or possibly eliminate the adverse separated flow effects. The one selected for the first flights consists of a 20° flow ramp that shields the cable trays from direct high velocity crossflow.

Nomenclature

A	amplitude parameter, Eq. (7b)
c	2-D chord length
c_0	delta wing root chord
f	frequency
h	cross sectional height of cable tray (Fig. 3)
Δh	gap size (Fig. 3)
l	sectional lift, coefficient $c_l = l/(\rho V^2/2)c$
ℓ	length of ground plane (Fig. 3)
M	Mach number
m_p	sectional pitching moment, coefficient $c_m = m_p/(\rho V^2/2)c^2$
n	sectional normal force, coefficient $c_n = n/(\rho V^2/2)c$
q	pitch rate
r	corner radius
t	time
Δt	time lag
V	crossflow velocity
x	chord wise coordinate
α	angle of attack
Δ	increment and amplitude
ζ_0	structural damping, fraction of critical
$\zeta_a + \zeta_s$	aerodynamic damping, fraction of critical
θ	perturbation in pitch or torsion
λ	disturbance wave length
ν	kinematic viscosity of air
ξ	dimensionless x-coordinate, $\xi = x/c$
ζ_{sp}	effect of separation point movement, Eq. (12)
ζ_w	Karman-Sears wake lag parameter, Eq. (12)
ρ	air density
τ	dimensionless time, $\tau = Vt/c$
ϕ	phase angle, $\phi = \omega\Delta t$
$\omega, \bar{\omega}$	oscillation frequency, $\bar{\omega} = \omega c/V$

Subscripts

a	attached flow
COMP	computed
L	linear range termination
MAX	maximum
s	separated flow
sp	separation point
tot	total
u	upstream
w	wake
0	value at $\bar{\omega}^2 \ll 1$
∞	freestream axial flow conditions

Superscript

*	circulation-induced, c_l^* in Eq. (13)

Derivative Symbols

$C_{m\alpha} = \partial C_m/\partial\alpha$

$\dot{\alpha} = \partial\alpha/\partial t : \ddot{\theta} = \partial^2\alpha/\partial t^2$

$C_{mq} = \partial C_m/\partial(\frac{c\dot{\theta}}{V})$

$C_{m\dot{\alpha}} = \partial C_m/\partial(\frac{c\dot{\alpha}}{V})$

$C_{m\dot{\theta}} = C_{mq} + C_{m\dot{\alpha}}$

$\overline{C_{m\dot{\theta}}}$ = integrated mean value

Introduction

Of the various cable trays present on the main space shuttle booster, the hydrogen-oxygen (HO) tank (Fig. 1), the LO_2 cable tray was of special concern because of its low margin of safety. The rectangular cross-section of the cable tray (Fig. 2) causes the crossflow over it to separate. The initial analysis[1] was made neglecting the presence of a pipe and the external tank (ground plane) surface (Fig. 2a). The later design with its added heat protection material brought the ground plane surface much closer (Fig. 2b), and its presence could no longer be neglected. Consequently, static and dynamic tests[2-4] were performed in a more or less two-dimensional flow arrangement (Fig. 3). The static test was performed only for a nominal sharp cornered cable tray configuration (Fig. 4a), but in the dynamic test a series of configurations (Fig. 4b) were investigated to define with the needed details the unsteady aerodynamics to be used in the final aeroelastic analysis.

---

* The paper is based upon results obtained in work done under contract to Martin-Marietta Corporation, Michoud Operations, New Orleans, La 70189, with Mr. D. B. Schwartz as the Contract Coordinator.

†Paper not presented at conference.

ORIGINAL PAGE IS
OF POOR QUALITY

Analytic Approach

Because of the problem of dynamic scaling[5], it was essential that the dynamic test data[6] could be predicted using static experimental results[7]. Figure 5 shows that the dynamic results of Models 1 and 2 in Fig. 4b could be predicted rather well. Using the experimental dynamic results for Model 2 (Fig. 4b) gave an aeroelastic stability boundary which was in remarkably good agreement with the preliminary (old) prediction of Ref. 1 (Fig. 6). However, the main concern was the analytic treatment of the nonlinear aerodynamics introduced by the severe ground plane interference experienced by the new cable tray geometry (Fig. 2b). Of particular importance was the determination of possible hysteresis effects associated with the discontinuous change of cable tray characteristics at transonic crossflow velocities[2], as they would generate nonlinear frequency effects[8-10]. The comparison between predicted[4] and measured[3] nonlinear dynamic characteristics showed no nonlinear frequency effect (Fig. 7). The hysteresis effect is inversely proportional to the frequency for the measured dynamic stability parameter, i.e. the linear measure of energy dissipation per cycle[8-10]. Thus, the results in Fig. 7 prove that no hysteresis was present, and that the developed analytic method for prediction of rigid body dynamics[4] was sufficiently accurate. This was a necessary prerequisite for the extension of the analysis to predict the aeroelastic characteristics of the space shuttle cable trays.

Aeroelastic Analysis

If the geometry had been the only change between the old and the new cable tray configurations (Figs. 2a and b, respectively) the new aeroelastic cable tray characteristics could be computed utilizing the new sectional aerodynamics in the old aeroelastic analysis[1]. However, the new cable tray design had a load carrying lid, which increased the structural stiffness by an order of magnitude. As a result, the application of the unsteady cross-sectional aerodynamics, which had been obtained at low reduced frequencies, to the elastic cable tray with its very much higher reduced frequencies presented a dynamic scaling problem.

Dynamic Scaling

Complete dynamic simulation of, for example, the LO_2 cable tray in a subscale test is for all practical purposes impossible. What one is concerned with, rather, is the two-dimensional unsteady aerodynamics of the cable tray cross-section in presence of the E.T. surface. These cross-sectional unsteady aerodynamic characteristics will be used to obtain the full scale aeroelastic characteristics of the cable tray, in the manner described in Ref. 1.

The use of dynamic derivatives builds upon the concept of linearity in a manner similar to what is the case for static derivatives. The static aerodynamic characteristics of an airfoil vary linearly with angle of attack up to a certain angle $\alpha = \alpha_L$, where beginning flow separation causes deviations and the characteristics become nonlinear. For $\alpha < \alpha_L$ the static aerodynamics are described completely by the derivatives, e.g. $c_{n\alpha}$ and $c_{m\alpha}$. For perturbations in pitch, θ, around $\alpha = \alpha_0$ one has

$$\left.\begin{aligned} c_n &= c_n(\alpha_0) + c_{n\alpha}\theta \\ c_m &= c_m(\alpha_0) + c_{m\alpha}\theta \end{aligned}\right\} \quad (1)$$

provided that $|\alpha_0 + \theta| < \alpha_L$

Extending the linear concept to the dynamic case of a pitching airfoil one writes

$$\left.\begin{aligned} c_n &= c_n(\alpha_0) + c_{n\alpha}\theta + c_{n\dot\theta}\frac{c\dot\theta}{V} + c_{n\ddot\theta}\frac{c^2\ddot\theta}{V^2} \\ c_m &= c_m(\alpha_0) + c_{m\alpha}\theta + c_{m\dot\theta}\frac{c\dot\theta}{V} + c_{m\ddot\theta}\frac{c^2\ddot\theta}{V^2} \end{aligned}\right\} \quad (2)$$

where θ, $c\dot\theta/V$ and $c^2\ddot\theta/V^2$ are measured in radians.

The aerodynamic inertia or acceleration terms, $c_{n\ddot\theta}\frac{c^2\ddot\theta}{V^2}$ and $c_{m\ddot\theta}\frac{c^2\ddot\theta}{V^2}$, are negligible compared to their structural counterparts. It is only the damping terms, $c_{n\dot\theta}\frac{c\dot\theta}{V}$ and $c_{m\dot\theta}\frac{c\dot\theta}{V}$, that are of concern. The contributions caused by non-zero pitch rate, $\dot\theta \neq 0$, can be written

$$\left.\begin{aligned} \Delta c_n(\dot\theta) &= c_n(\dot\theta) - c_n(0) \\ \Delta c_m(\dot\theta) &= c_m(\dot\theta) - c_m(0) \end{aligned}\right\} \quad (3)$$

These damping terms also have linear branches. In the case of a steadily increasing pitch rate, as in the pitch-up maneuver of an aircraft, one obtains a situation that is a direct extension of the static case. Thus, the linear characteristics prevail as long as[#]

$$\left|\alpha_0 + \theta + \frac{c\dot\theta}{V}\right| < \alpha_L \quad (4)$$

However, in the case of an airfoil that describes pitch oscillations around $\alpha = \alpha_0$, i.e., when

---

[#] This is a conservative value, as dynamic effects extend the linear branch beyond $\alpha = \alpha_L$ (Ref. 11)

$$\left.\begin{aligned}\theta &= \Delta\theta\sin\omega t\\ \frac{c\dot\theta}{V} &= \frac{c\omega}{V}\Delta\theta\cos\omega t\end{aligned}\right\} \qquad (5)$$

one finds that the magnitude of $c\dot\theta/V$ is

$$\left|\frac{c\dot\theta}{V}\right| = \bar\omega\Delta\theta \qquad (6)$$

That is, $|c\dot\theta/V|$ is determined by two parameters, the pitch amplitude $\Delta\theta$ and the reduced frequency $\bar\omega$. How the two together affect airfoil characteristics, in attached and separated flow has been described extensively in Refs. 11-14. These results will be used to delineate the applicability of the dynamic derivative concept.

For the case of attached flow, i.e. when Eq. (4) is satisfied, one is only concerned with the effect of the reduced frequency $\bar\omega$. More specifically, one wants to know to what extent the magnitude of $\bar\omega$ affects the applicability of $c_{n\dot\theta}$ and $c_{m\dot\theta}$. The only contributions to $c_{n\dot\theta}$ and $c_{m\dot\theta}$ that are sensitive to the magnitude of $\bar\omega$ come from the circulation terms. Reference 14 gives the following expression for the circulation lift[*]

$$c_l^*(t) = c_l(\alpha_o) + c_{l\alpha}\bar\lambda\Delta\theta\sin(\omega t - \varphi_w) \qquad (7a)$$

$$\bar\lambda = \begin{cases}1 & ; \ \bar\omega < 0.16\\ 0.675\left[1-(10\bar\omega)^{-1/2}\right] & ; \ \bar\omega \geq 0.16\end{cases} \qquad (7b)$$

$$\varphi_w = \begin{cases}1.5\bar\omega & ; \ \bar\omega < 0.16\\ 14^\circ & ; \ \bar\omega \geq 0.16\end{cases} \qquad (7c)$$

Expanding Eq. (7a) one obtains

$$\begin{aligned}c_l^*(t) = {} & c_l(\alpha_o) + \left[c_{l\alpha}\bar\lambda\cos\varphi\right]\theta(t)\\ & - \left[c_{l\alpha}\bar\lambda\frac{\sin\varphi}{\bar\omega}\right]\frac{c\dot\theta(t)}{V}\end{aligned} \qquad (8)$$

which in turn gives

$$\partial c_l^*/\partial\left(\frac{c\dot\theta}{V}\right) = -c_{l\alpha}\bar\lambda\frac{\sin\varphi}{\bar\omega} \qquad (9)$$

With the definitions in Eqs. (7b) and (7c) Eq. (9) gives

$$\frac{\partial c_l^*}{\partial\left(\frac{c\dot\theta}{V}\right)} = -1.5\,c_{l\alpha}\begin{cases}1 & : \ \bar\omega < 0.16\\ 0.675\left[\text{[illegible]}\left(1-\frac{1}{\sqrt{10\bar\omega}}\right)\right] & : \ \bar\omega \geq 0.16\end{cases} \qquad (10)$$

Equation (10) shows that the value of $c_{n\dot\theta}$ and $c_{m\dot\theta}$ measured at an arbitrary frequency below $\bar\omega = 0.16$ applies to the complete frequency range $\bar\omega < 0.16$. However, when applied to higher frequencies, $\bar\omega > 0.16$, measured attached flow derivatives would overestimate the contribution of the circulation lift.

It was shown in Ref. 13 that the phase lag limit, $\varphi_w = 14^\circ$, existing for attached flow, Eq. (7c), does not apply in the case of dynamic stall, and the circulation lift can be expressed as follows

$$\left.\begin{aligned}c_{l_s}^*(t) &= c_{l\alpha_s}\alpha_i(t)\\ \alpha_i(t) &= \alpha_o + \Delta\theta\sin(\omega t - \varphi_{tot})\\ \varphi_{tot} &= \bar\omega\Delta\tau\end{aligned}\right\} \qquad (11)$$

where $\Delta\tau$ is

$$\left.\begin{aligned}\Delta\tau &= \xi_w + \xi_{sp}\\ \xi_w &= 1.5\\ \xi_{sp} &= \begin{cases}0.75 & \text{Turbulent Stall}\\ 3.0 & \text{Laminar Stall}\end{cases}\end{aligned}\right\} \qquad (12)$$

Again, with $\theta = \Delta\theta\sin\omega t$, expanding Eq. (11) gives

$$c_{l_{\dot\theta_s}} = \partial c_{l_s}^*(t)/\partial\left(\frac{c\dot\theta}{V}\right) = -c_{l\alpha_s}\frac{\sin(\bar\omega\Delta\tau)}{\bar\omega} \qquad (13)$$

---

[*] An analogous expression is obtained for the circulation effect on the pitching moment.

For low reduced frequencies, as in the case of the dynamic tests,[6] Eq. (13) takes the following form

$$\left(c_{l_{\dot{\theta}_s}}\right)_0 = -c_{l\alpha_s}\Delta\tau \tag{14}$$

Combining Eqs. (13) and (14) gives

$$c_{l_{\dot{\theta}_s}} = \left(c_{l_{\dot{\theta}_s}}\right)_0 \frac{\sin(\bar{\omega}\Delta\tau)}{\bar{\omega}\Delta\tau} \tag{15}$$

Equation (15) implies that

$$\frac{c_{m_{\dot{\theta}_s}}}{\left(c_{m_{\dot{\theta}_s}}\right)_0} = \frac{c_{n_{\dot{\theta}_s}}}{\left(c_{n_{\dot{\theta}_s}}\right)_0} = \frac{\sin(\bar{\omega}\Delta\tau)}{\bar{\omega}\Delta\tau} \tag{16}$$

Equation (16) shows that applying the derivative measured at low frequency, $\bar{\omega}^2 \ll 1$, at $\bar{\omega}\ \Delta\tau = 1$ would overestimate the separated flow effect on the pitch damping by less than 20 percent.

In equations(12) through (14) the aerodynamic derivative $c_{l\alpha_s}$ is obtained from static measurements. There is, of course, an upper limit in frequency for which this quasi-steady approach will be applicable, on which the expressions in Eqs. (15) and (16) are based. In the axisymmetric separated flow case encountered for the Saturn-Apollo launch vehicle (Ref. 15 and Fig. 8) it can be assumed that when the separation distance between escape rocket and Apollo command module is large, so that no communication upstream from the command module affects the wake shape, the situation is analogous to that for a sinusoidal gust[16]. That is, the only consideration for the applicability of quasi-steady principles, i.e., use of static derivatives in a dynamic analysis, is that the wave length of the unsteady wake (or gust) is long compared to the extent of the responding body, e.g., the Apollo command module. A minimum requirement for this is (See Fig. 8)

$$c_T < \lambda/4 \tag{17}$$

That is

$$\frac{\omega c_T}{V} < \frac{\pi}{2} \tag{18}$$

ORIGINAL PAGE IS
OF POOR QUALITY

When the distance between wake generator, e.g., the escape rocket, and the submerged body, e.g., the command module, is below a critical value, the wake reattachment conditions on the submerged body start to affect the wake formation at the upstream wake-generating body[17]. In this case one has to consider how the flow field effective time lag $\Delta\tau$ affects the wake in the unsteady case. That is, when does the phase lag φ_{tot} start to change the wake structure such that the static aerodynamic load distribution and associated lumped load derivative can not be realized in the dynamic case. One minimum requirement for the application of static data is that the upstream communication effect, the modulation of the wake geometry, is of the same sense as in the static case. This would require that

$$\omega\Delta t_u < \pi \tag{19}$$

where

$$\Delta t_u = \frac{c_T}{\bar{V}_u} \tag{20}$$

That is, Eq. (20) becomes

$$\bar{\omega} < \pi\bar{V}_u/V \tag{21}$$

where $\bar{\omega} = \omega c_T/V$.

Experimental results for wakes[18] indicates that the upstream convection will take place at a Mach number $M_U \geq 0.4$. Thus, for the subsonic and transonic flow conditions existing in the case of the cable trays one would have

$$\bar{V}_u/V > 0.4 \tag{22}$$

and Eq. (21) becomes

$$\bar{\omega} < 0.4\,\pi \tag{23}$$

When considering the cable tray, the characteristic length is c rather than c_T (See Fig. 8), and the quasi-steady gust criterion, Eq. (18), becomes

$$\bar{\omega} < 0.5\,\pi \tag{24}$$

which is not far from the criterion for quasi-steadiness expressed in Eq. (23). If the upstream communication in the wake occurred through acoustic radiation rather than through convection, one would for the subsonic and transonic flow conditions of concern get

$$\bar{V}_u/V \geq 1 \tag{22a}$$

and Eq. (23) would become

$$\bar{\omega} \leq \pi \tag{23a}$$

Thus, one finds that the criterion for quasi-steadiness used in past aeroelastic analyses of launch vehicles[5,8,19-21] still holds. That is, for the present aeroelastic analysis of the space shuttle cable trays the criterion for application of quasi-steady principles, on which Eq. (16) is founded, is expressed by Eq. (24).

In addition to this consideration for $\bar{\omega}$, expressed by Eq. (24), one also has to take a closer look at ϕ_{tot}. In the case of attached flow $\phi_{tot} = \phi_w$ and does not exceed 14°, Eq. (7c). That this limit on ϕ_{tot} does not apply in the case of dynamic stall has been shown recently[13] (Fig. 9). The predictions are far off the experimental results.[22] In Fig. 9b the ϕ_w limit was removed, that is $\phi_w = 1.5\bar{\omega} = 61^{\circ}$ was used. It can be seen that this provided excellent agreement for the "upstroke" position of the loop below stall, where $\phi_{tot} = \phi_w$. The deviation above stall between prediction and experiment can be explained when considering amplitude modulation effects, as is discussed in Ref. 13. The point to be made here is that the results in Fig. 9 prove that the phase lag can be as large as $\phi_{tot} = 61^{\circ}$. The question is: How large can ϕ_{tot} be?

Experimental results for flow separation off the sharp leading edge of a delta wing[23] indicate that there might be an upper limit for ϕ_{tot} (Fig. 10). Figure 10a shows that the phase lag of the leading edge vortex location (height) above the delta wing[#] is linearly dependent upon the distance from apex, but nonlinearly dependent upon the frequency. The nonlinear frequency effect is shown more clearly in Fig. 10b illustrating how the experimental data trend is mathematically of the form given by Eq. (7c). It is apparent, however, that for separated flow the maximum phase angle is substantially higher than the 14° limit of Eq. (7c). The results in Fig. 10 give

$$\frac{\partial \phi_{tot}}{\partial\left(\frac{x}{c_o}\right)} = \begin{cases} 46^{\circ} & : \bar{\omega} = 1.13 \\ 66^{\circ} & : \bar{\omega} = 3.40 \end{cases} \qquad (25)$$

The data trend in Fig. 10b indicates that the maximum phase lag that could be obtained on the delta wing, at $x/c_o = 1$, is $\phi_{tot} = 66^{\circ}$.

The flow mechanisms leading to the phase lag saturation are very different in the attached flow case, Eq. (7c), and the delta wing leading edge separation just discussed. The results do suggest, however, that a phase lag limit is likely to exist also for the present case of interest, the separated flow past the cable tray cross-section. Whatever this phase lag saturation limit is, one can state as a fact, at least for the flow processes that have been identified to affect the cable tray dynamics, that the aeroelastic analysis will give a conservative result if one assumes $\phi_{tot} \leq \pi/2$. That is, the low frequency dynamic derivative, $(c_{m\dot{\theta}_s})_0$, measured in the dynamic test[6] will be used as follows to provide the derivative, $c_{m\dot{\theta}_s}$, needed in the aeroelastic analysis.

$$\frac{c_{m\dot{\theta}_s}}{\left(c_{m\dot{\theta}_s}\right)_o} = \begin{cases} \dfrac{\sin(\bar{\omega}\Delta\tau)}{\bar{\omega}\Delta\tau} & : \bar{\omega}\Delta\tau < \dfrac{\pi}{2} \\ (\bar{\omega}\Delta\tau)^{-1} & : \bar{\omega}\Delta\tau \geq \dfrac{\pi}{2} \end{cases} \qquad (26)$$

Aeroelastic Characteristics of the Final Cable Tray Design

Because of the very high frequency computed for the revised structural characteristics[24], Eq. (26) reduces to the following for oscillations of the current cable trays:

$$c_{m\dot{\theta}_s} \Big/ \left(c_{m\dot{\theta}_s}\right)_0 = 1 \Big/ (\bar{\omega}\Delta\tau) \qquad (27)$$

where subscript zero designates the damping derivative measured in the dynamic test[6]. At $M < M_a$, $\Delta\tau$ is given as follows[4] for the cable trays with sharp edged and rounded corners, models 3 and 4 in Fig. 4.

$$\text{Model 3.} \quad \Delta\tau = 1.88 \qquad (28a)$$

Model 4

$$\Delta\tau = \begin{cases} 1.88 + 1.2\,M & : M \leq 0.3 \\ 3.08\,(1.27-M) & : 0.3 < M < 0.66 \\ 1.88 & : 0.66 \leq M < M_a \end{cases} \qquad (28b)$$

For the continuous aerodynamics, $M < M_a$, $(c_{m\dot{\theta}_s})_0$ for the two trays is obtained from Ref. 6. Figure 11 demonstrates that the LO_2 cable tray is aeroelastically stable for $M < M_a$, even if the structural damping reaches the minimum level of 0.1%. (Ref. 25).

For the discontinuous aerodynamics at $M = 0.7$ and $M = 0.92$ (Ref. 2) the time lag $\Delta\tau$ is defined in the following manner[4]

$$\left.\begin{aligned} M = 0.7:&\ \Delta\tau = 1.88 + \frac{V}{\bar{V}_\infty} = 4.38 \\ M = 0.92:&\ \Delta\tau = 2 + M = 2.92 \end{aligned}\right\} \qquad (29)$$

[#] And probably also of the local vortex-induced aerodynamic loads.

ORIGINAL PAGE IS
OF POOR QUALITY

Using the measured damping derivatives[6] and the scaling relationships given by Eqs. (27) and (29) gives the aeroelastic stability characteristics shown in Fig. 12. The results indicate that for the guaranteed value of $\zeta_0 = 0.1\%$ (Ref. 25) the limit cycle amplitudes are $\Delta\theta_{LIM} > 3^0$ and $\Delta\theta_{LIM} = 2.1^0$ for $M = 0.7$ and $M = 0.92$ respectively. If the structural damping is one order of magnitude larger, $\zeta_0 = 1\%$, the limit cycle amplitudes decrease to 0.55 and 0.70 degrees respectively. The highest structural damping value that can be expected according to limited shake tests* is $\zeta_0 = 0.01$.

Without any available experimental data that truly represents the LH_2 or SRB cable trays, one has to decide to what extent the experimental results for the LO_2 tray can be used to determine the aeroelastic stability characteristics of the other cable trays. In regard to the LH_2 cable tray, three-dimensional flow effects add to the difficulty of using two-dimensional aerodynamic characteristics obtained with the wrong cross-section (Fig. 13), and no meaningful aeroelastic prediction can be made. In regard to the SRB tray, however, the LO_2 tray aerodynamics should apply. If one neglects the effect of the forward indentation on the topside flow, which may be somewhat unconservative, the LO_2 cable tray aerodynamics can be applied directly to the SRB cable tray (See Fig. 13). In using the structural characteristics[26] one has to correct for the structural coupling between tangential and torsional degrees of freedom[5]. For the first torsion mode the results in Fig. 14 are obtained, showing the rather substantial limit cycle amplitude $\Delta\theta_{LIM} \approx 1.2^0$ for one percent structural damping both at $M = M_\infty = 0.7$ and $M = M_\infty = 0.92$.

Even for the maximum value of structural damping, $\zeta_0 = 0.01$, the limit cycle amplitudes computed for the LO_2 and SRB cable trays exceed the structural capability. Consequently, the final analysis gives the same end result as the initial one[1], i.e. an aerodynamic fix, such as the investigated 20° flow ramp[2,6], is needed to assure the structural integrity of the LO_2 and SRB cable trays. Now as before[1], the results for the LH_2 cable tray are inclusive, and the flow ramp has to be applied in the inflow regions of the LH_2 cable tray until more definitive results are obtained from currently planned analytic and experimental efforts. Until then the space shuttle continues to carry the same protective crossflow ramps as in the first flight[1] (Fig. 15).

Conclusions

An analysis of the aeroelastic stability of the Space Shuttle Cable Trays has produced results that can be summarized as follows:

- Using the c_m-and c_n-discontinuities defined by static test data the measured nonlinear damping characteristics of the LO_2 cable tray cross-section can be predicted by the developed analytic means.
- A careful look at the dynamic scaling shows how to apply the low frequency cross-sectional dynamic test data to obtain a conservative estimate of the aeroelastic stability of high frequency deflection modes of the LO_2 cable tray.
- Using conservative assumptions the dynamic test data for the LO_2 cable tray section have been used to determine the aeroelastic stability of the SRB cable tray.
- The analysis confirms the need for the flow ramps now installed on the space shuttle launch vehicle to assure the structural integrity of the cable trays.

Acknowledgement

The authors want to acknowledge that significant contributions to the presented analysis were made by the participants in the ET Protuberance Airloads Committee Meetings, in particular by W. Dahm and G. A. Wilhold, NASA MSFC.

References

1. Ericsson, L. E. and Reding, J. P., "Aeroelastic Stability of Space Shuttle Protuberances", AIAA Paper No. 81-1672, Aug. 1981.

2. Reding, J. P. and Ericsson, L. E., "Analysis of Static and Dynamic Wind Tunnel Tests of the Space Shuttle Cable Trays", AIAA Paper No. 81-1878, Aug. 1981.

3. LaBerge, J. G. and Orlik-Rückemann, K. J., "Dynamic Wind Tunnel Tests of The Simulated Shuttle External Tank Cable Trays", AIAA Paper No 81-1879, Aug. 1981.

4. Ericsson, L. E. and Reding, J. P., "Separated Flow Dynamics of the Space Shuttle Cable Trays", AIAA Paper No. 81-1880, Aug. 1981.

5. Ericsson, L. E. and Reding, J. P., "Aeroelastic Analysis of the Space Shuttle External Tank Cable Trays", Final Technical Report, Contract ASO-751485, LMSC D766543, April 1981, Lockheed Missiles & Space Company, Inc., Sunnyvale, California.

6. LaBerge, J. G., "Dynamic Wind Tunnel Tests of the Shuttle External Tank Cable Trays at Subsonic Speeds", LTR-UA-55, NRC, Canada, Feb. 1981.

7. Michna, P. J. and Parker, D. R., "Test Results from the Pressure Test of a .12 Scale Model of the External Tank LO_2 Cable Tray and GO_2 Pressure Line and a .1575 Scale Model of the aft ET/SRB Cable Tray in the MSFC 14 Inch Trisonic Wind Tunnel Test No. TWT 661", Report MMC-ET-SE05-89, May 1980, Martin-Marietta Corporation, Michoud Operations, New Orleans, Louisiana.

8. Ericsson, L. E. and Reding, J. P., "Dynamics of Separated Flow Over Blunt Bodies", NASA CR-76912, Dec. 1965.

9. Ericsson, L. E., "Separated Flow Effects on the Static and Dynamic Stability of Blunt Nosed Cylinder Flare Bodies", NASA CR 76919, Dec. 1965.

10. Ericsson, L. E., "Unsteady Aerodynamics of Separating and Reattaching Flow on Bodies of Revolution" Recent Research on Unsteady Boundary Layers, Vol. 1, IUTAM Symposium, Laval University, Quebec, May, 24-28, 1971, pp. 481-512.

---

* Hansen, L. L., Private Communication of unpublished Shake Test Results for the Space Shuttle Cable Trays, April, 1980.

11. Ericsson, L. E. and Reding, J. P., "Dynamic Sta Analysis in Light of Recent Numerical and Experimental Results", J. Aircraft, Vol. 13, No. 4, April, 1976, pp. 248-255.

12. Ericsson, L. E. and Reding, J. P., "Quasi-Stead and Transient Dynamic Stall Characteristics', Paper 24, AGARD CP-204, Feb. 1977.

13. Ericsson, L. E. and Reding, J. P., "Dynamic Stall at High Frequency and Large Amplitudes", J. Aircraft, Vol. 17, No. 3, March 1980, pp. 136-142.

14. Ericsson, L. E. and Reding, J. P., "Unsteady Airfoil Stall, Review and Extension", Journal of Aircraft, Vol. 8, Aug. 1971, pp. 609-616.

15. Ericsson, L. E. and Reding, J. P., "Analysis of Flow Seapration Effects on the Dynamics of a Large Space Booster", J. Spacecraft and Rockets, Vol. 2 No. 4, July-Aug. 1965, pp. 481-490.

16. Ericsson, L. E., Reding, J. P., and Guenther, R. A., "Elastic Launch Vehicle Response to Sinusoidal Gusts", J. Spacecraft and Rockets, Vol. 10, No. 4, April 1973, pp. 244-258.

17. Ericsson, L. E., Reding, J. P., and Guenther, R. A., "Analytic Difficulties in Predicting Dynamic Effects of Separated Flow", J. Spacecraft and Rockets, Vol. 8, No. 8, Aug. 1971, pp. 872-878.

18. Ericsson, L. E. and Reding, J. P., "Transonic Sting Interference", J. Spacecraft and Rockets, Vol. 17, No. 2, March-April 1980, pp. 140-144.

19. Ericsson, L. E., "Aeroelastic Instability Caused by Slender Payloads", J. Spacecraft and Rockets, Vol. 4, No. 1, Jan. 1967, pp. 65-73.

20. Reding, J. P. and Ericsson, L. E., "Aeroelastic Stability of the 747/Orbiter", Jour of Aircraft, Vol. 14, No. 10, Oct. 1977, pp. 988-993.

21. Reding, J. P. and Ericsson, L. E., "Effects of Flow Separation On Shuttle Longitudinal Dynamics and Aeroelastic Stability", J. Spacecraft and Rockets, Vol. 14, No. 7, Dec. 1977, pp. 711-718.

22. Liiva, J., Davenport, F. J., Gray, L., and Walton, I. C., "Two-Dimensional Tests of Airfoils Oscillating Near Stall", USA AVLABS TR 68-13, April 1968.

23. Maltby, R. L., Engler, P. B. and Keating, R. F. A., with addendum by Moss, G. F., "Some Exploratory Measurements of Leading-Edge Vortex Positions on a Delta Wing Oscillating in Heave", R & M 3176, Aer. Res. Council, Great Britain, July 1963.

24. Schwartz, D. B., "Modal Frequencies and Damping Characteristics of ET Cable Trays (LH_2 & LO_2)", Martin-Marietta Aerospace, Michoud Operations, New Orleans, Louisiana, 20 March 1980.

25. Crema, L. B., Castellani, A., and Nappi, A., "Damping Effects in Joints and Experimental Tests on Riveted Specimens", Paper 12, AGARD-CP-277, Oct. 1979.

26. Schwartz, D. B., "Computed Structural Characteristics for the SRB Cable Tray", Martin-Marietta Aerospace, Michoud Operations, New Orleans, Louisiana, 21 April, 1980.

ORIGINAL PAGE IS
OF POOR QUALITY

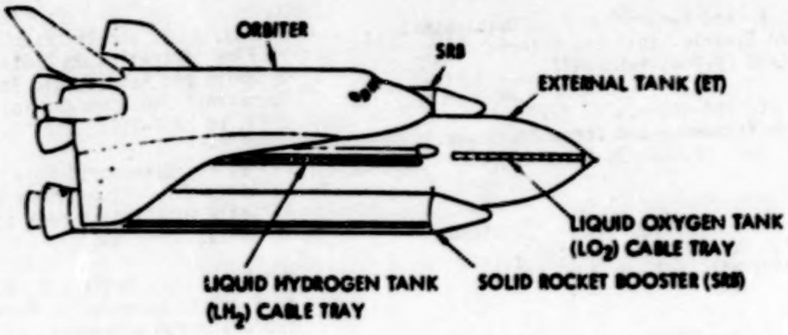
ORBITER
SRB
EXTERNAL TANK (ET)
LIQUID OXYGEN TANK
(LO_2) CABLE TRAY
LIQUID HYDROGEN TANK
(LH_2) CABLE TRAY
SOLID ROCKET BOOSTER (SRB)

Fig. 1. Space Shuttle Booster

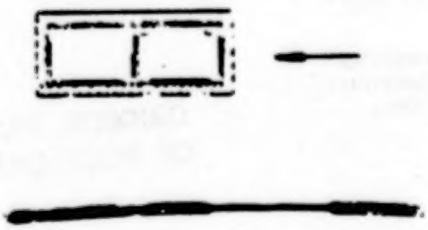

a. Old Configuration

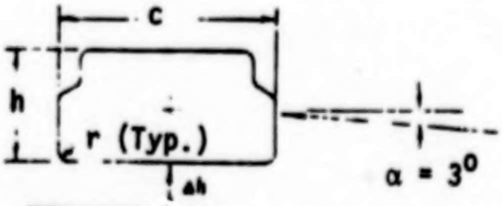
C
T
h
r (Typ.)
Δh
α = 3°

b. New Configuration

Fig. 2. Cable Tray Geometries

MSFC STATIC TEST

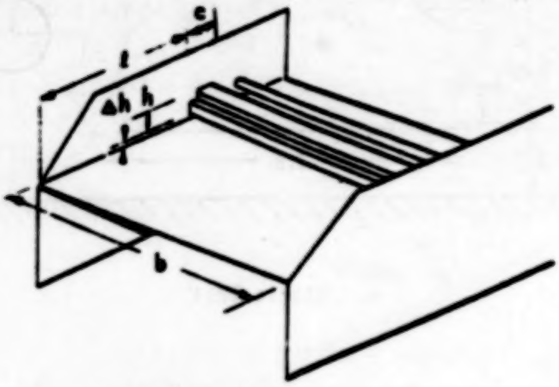

$c = 1.032$ IN. (LO_2)
$c = 1.284$ IN. (SRB)
$h/c = 0.488$
$\Delta h/h = 0.55,\ 1.4$
$b/c = 5.814$
$\ell/c = 0.783$
$M = 0.5 \le M \le 1.46$
$0.6 \times 10^6\ R_e < 0.8 \times 10^6$

NAE DYNAMIC TEST

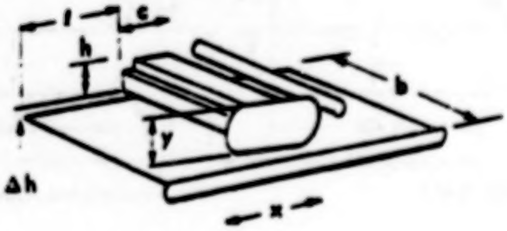

$c = 1.968$ IN.
$h/c = 0.5$
$\Delta h/h = 0.55,\ 1.4$
$b/c = 2.4,\ 3.2$
$\ell/c = 2.25$
$x/c = 1.3$
$y/h = 1.4$
$M = 0.21 \le M \le 0.92$
$0.25 \times 10^6 < R_e < 0.8 \times 10^6$

Fig. 3. Wind Tunnel Test Setups

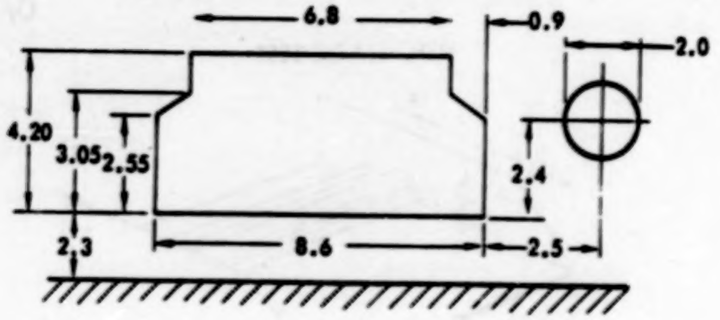
6.8
0.9
2.0
4.20
3.05
2.55
2.4
2.3
8.6
2.5

a. Static Test

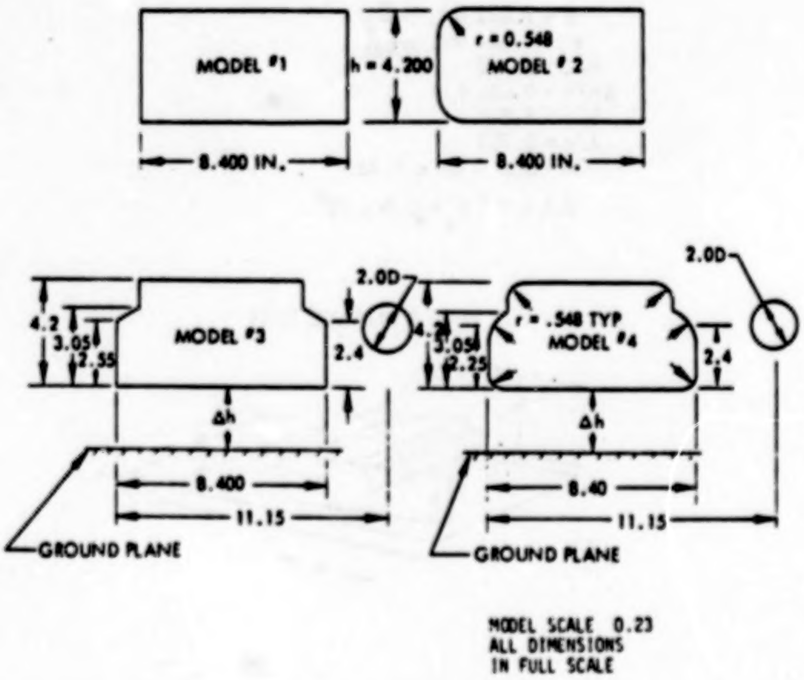
MODEL #1
h = 4.200
r = 0.548
MODEL # 2
8.400 IN.
8.400 IN.
2.0D
4.2
3.05
2.55
MODEL #3
2.4
Δh
8.400
11.15
GROUND PLANE
2.0D
4.2
3.05
2.25
r = .548 TYP
MODEL #4
2.4
Δh
8.40
11.15
GROUND PLANE
MODEL SCALE 0.23
ALL DIMENSIONS
IN FULL SCALE

b. Dynamic Test

Fig. 4. Tested Cable Tray Geometries

ORIGINAL PAGE IS
OF POOR QUALITY

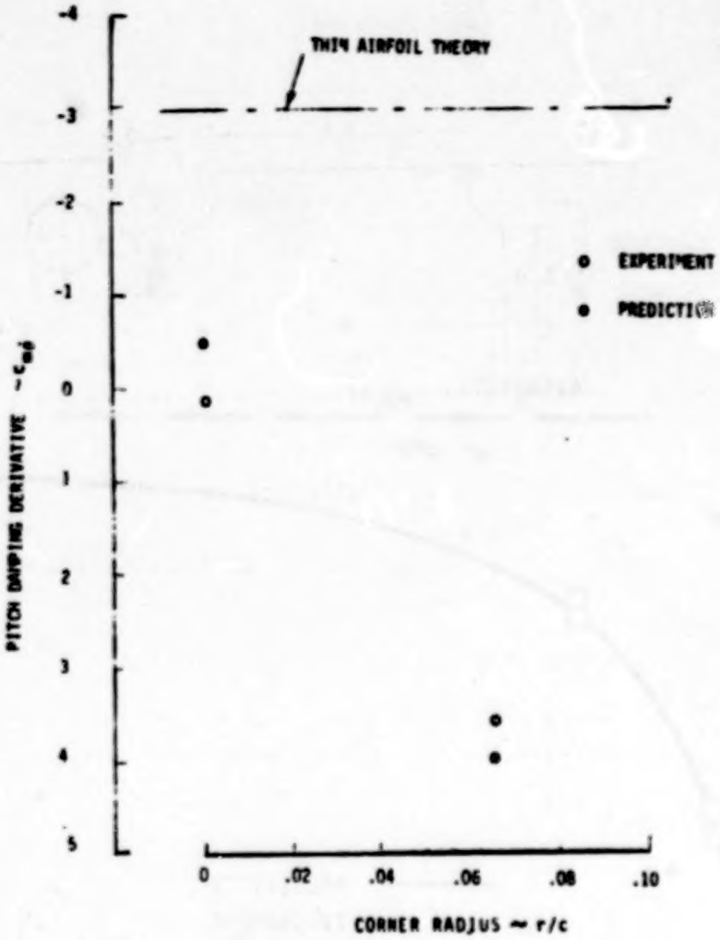

Fig. 5. Comparison Between Predicted and Measured Pitch Damping of a Rectangular Cross-section

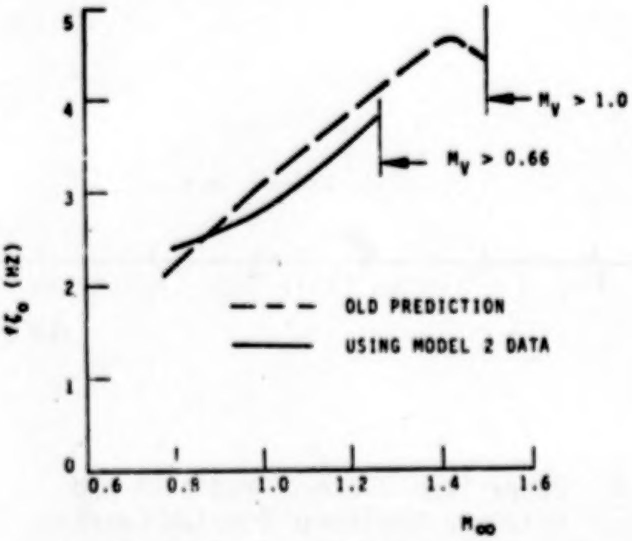

Fig. 6. Comparison Between Aeroelastic Stability Boundaries

ORIGINAL PAGE IS OF POOR QUALITY

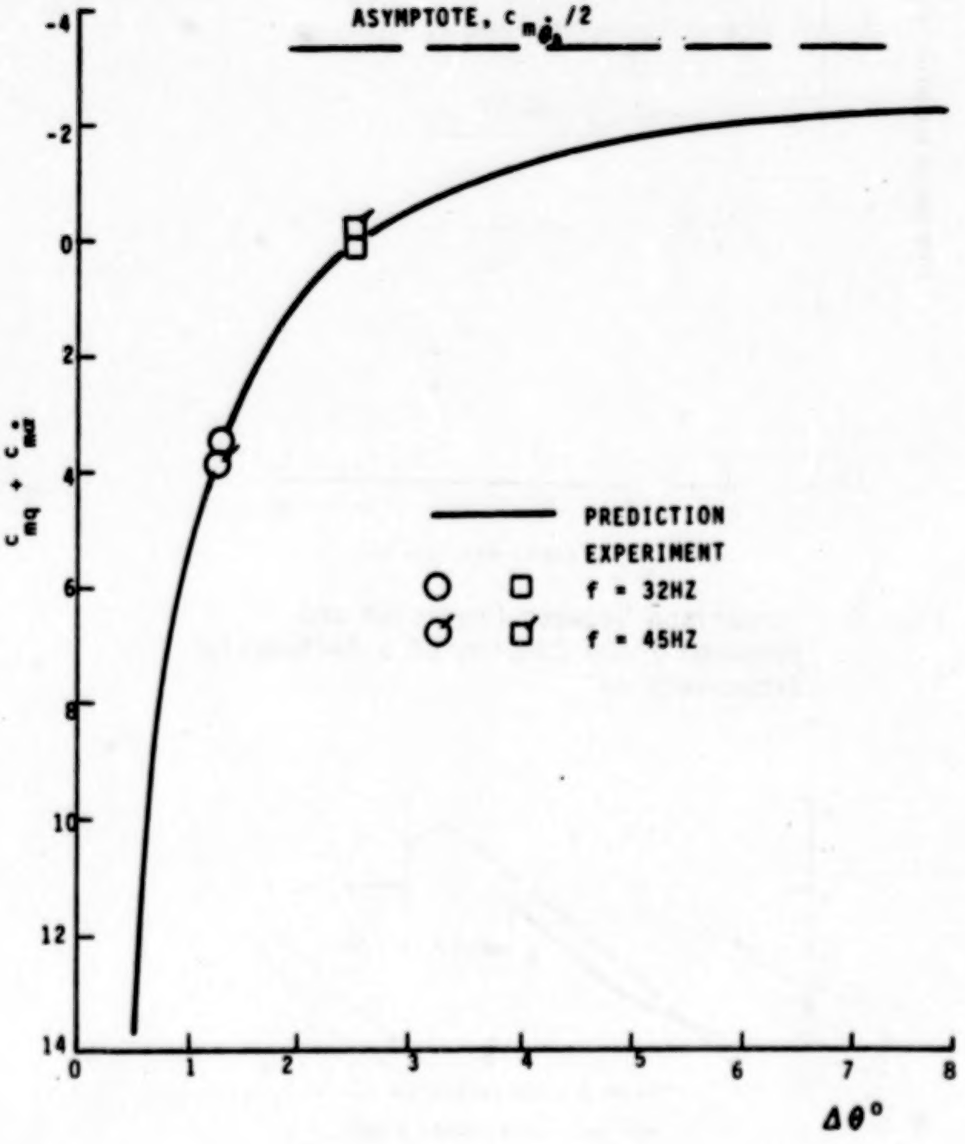

Fig. 7. Comparison Between Predicted and Measured Nonlinear Damping Characteristics for the LO_2 Cable Tray, M = 0.92

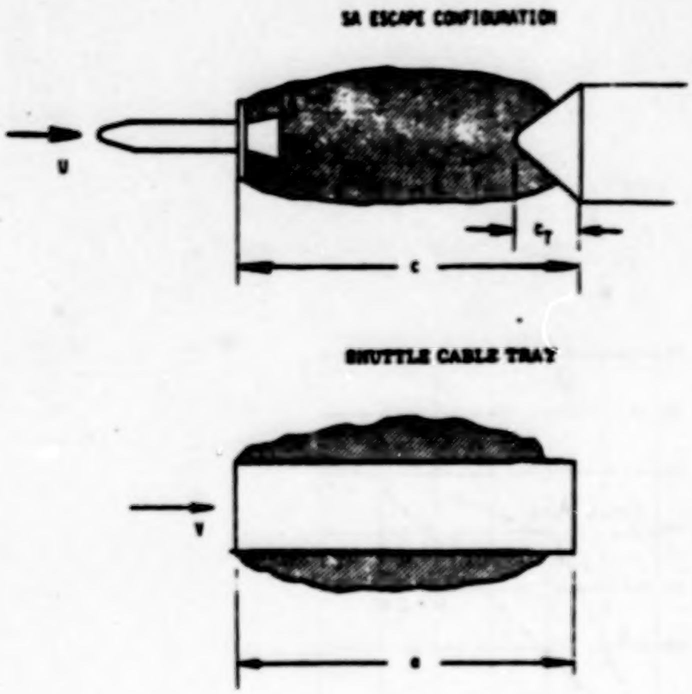
SA ESCAPE CONFIGURATION
U
c_T
c
SHUTTLE CABLE TRAY
V
c

Fig. 8. Frequency-wave Length Restrictions for Quasi-Steady Methodology

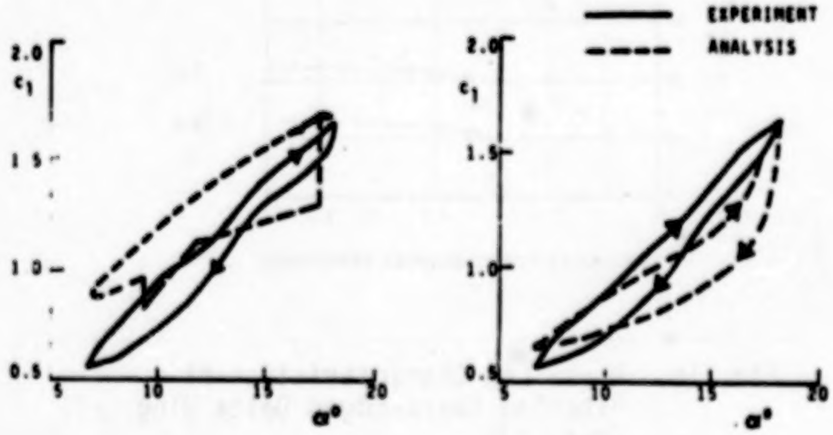

a. Old Method

b. New Method

Fig. 9. Phase Lag Characteristics of Dynamic Lift Stall

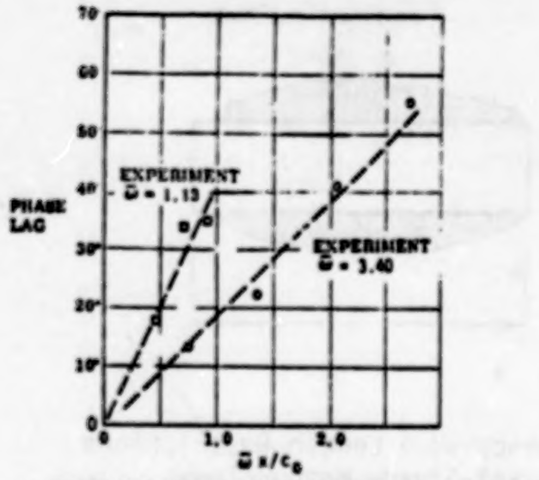

a. PHASE LAG VERSUS LOCAL FREQUENCY PARAMETER

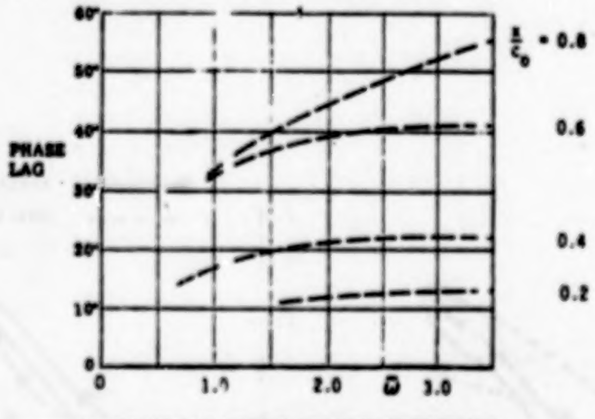

b. PHASE LAG VERSUS REDUCED FREQUENCY

Fig. 10. Phase Lag Characteristics of a Pitching Sharp-Edged Delta Wing (Ref. 23).

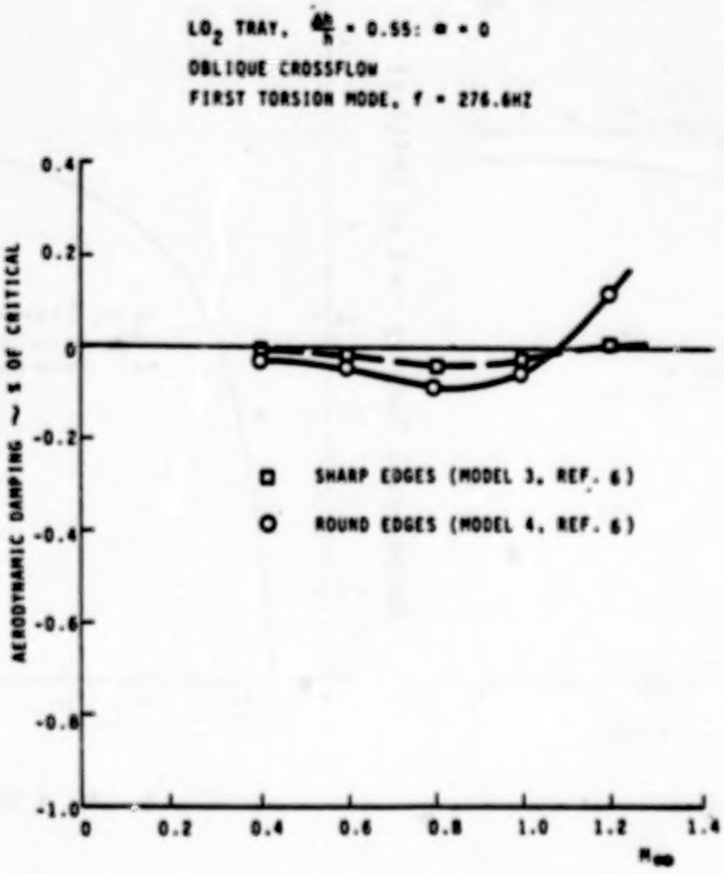

Fig. 11. Linear Aeroelastic Torsional Characteristics of the LO$_2$ Cable Tray at $M < M_a$.

ORIGINAL PAGE IS
OF POOR QUALITY

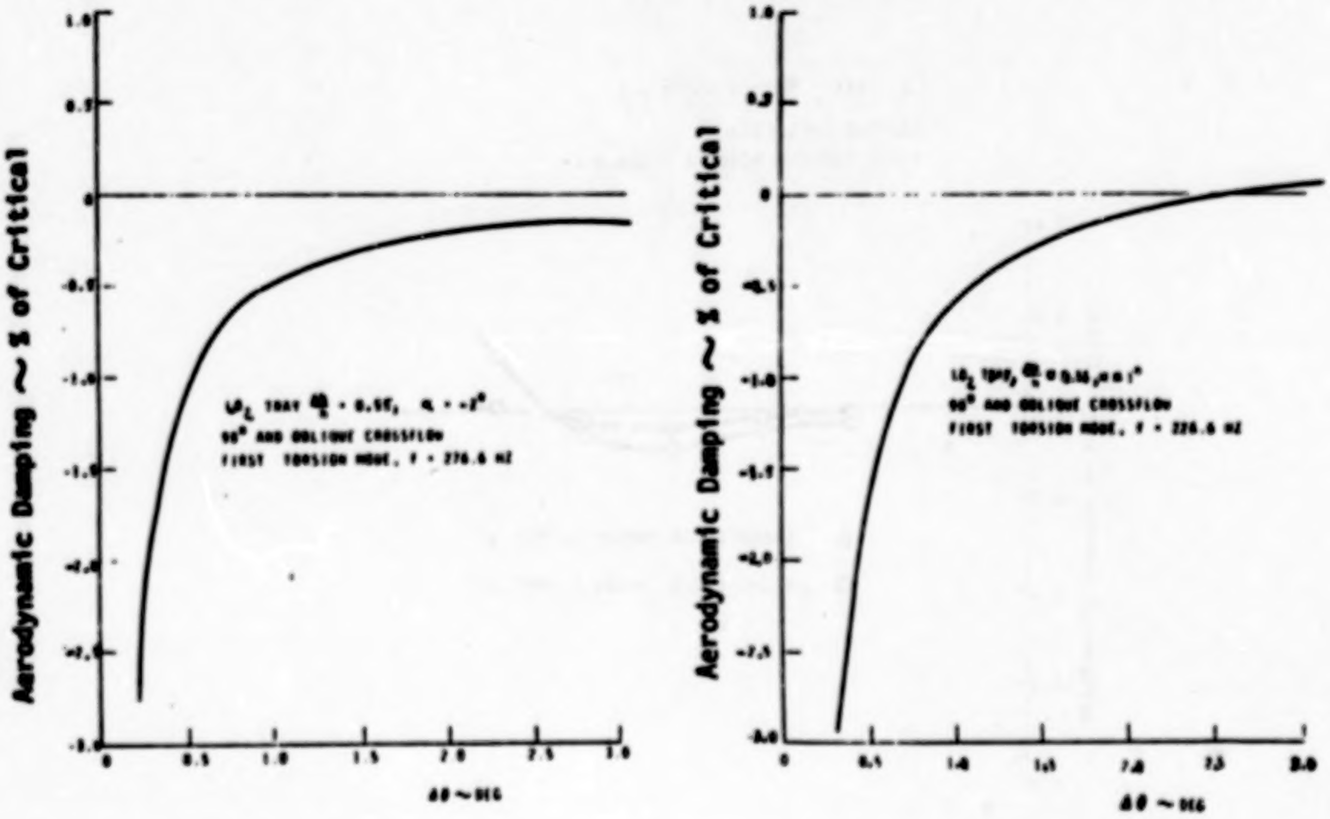

a. M = 0.7

b. M = 0.92

Fig. 12. Nonlinear Aeroelastic Torsional Characteristics of the LO_2 Cable Tray at M = 0.7 and M = 0.92.

ORIGINAL PAGE IS
OF POOR QUALITY

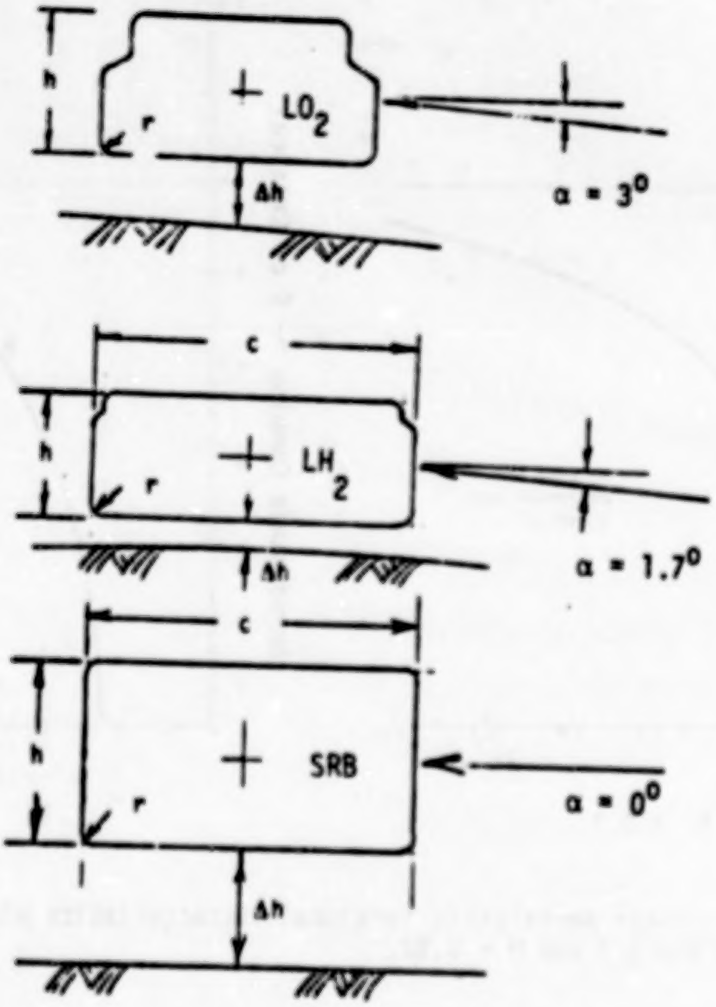
h
r
LO_2
Δh
α = 3°
c
h
r
LH_2
Δh
α = 1.7°
c
h
SRB
r
α = 0°
Δh

Fig. 13. Current Cable Tray Geometries

ORIGINAL PAGE IS
OF POOR QUALITY

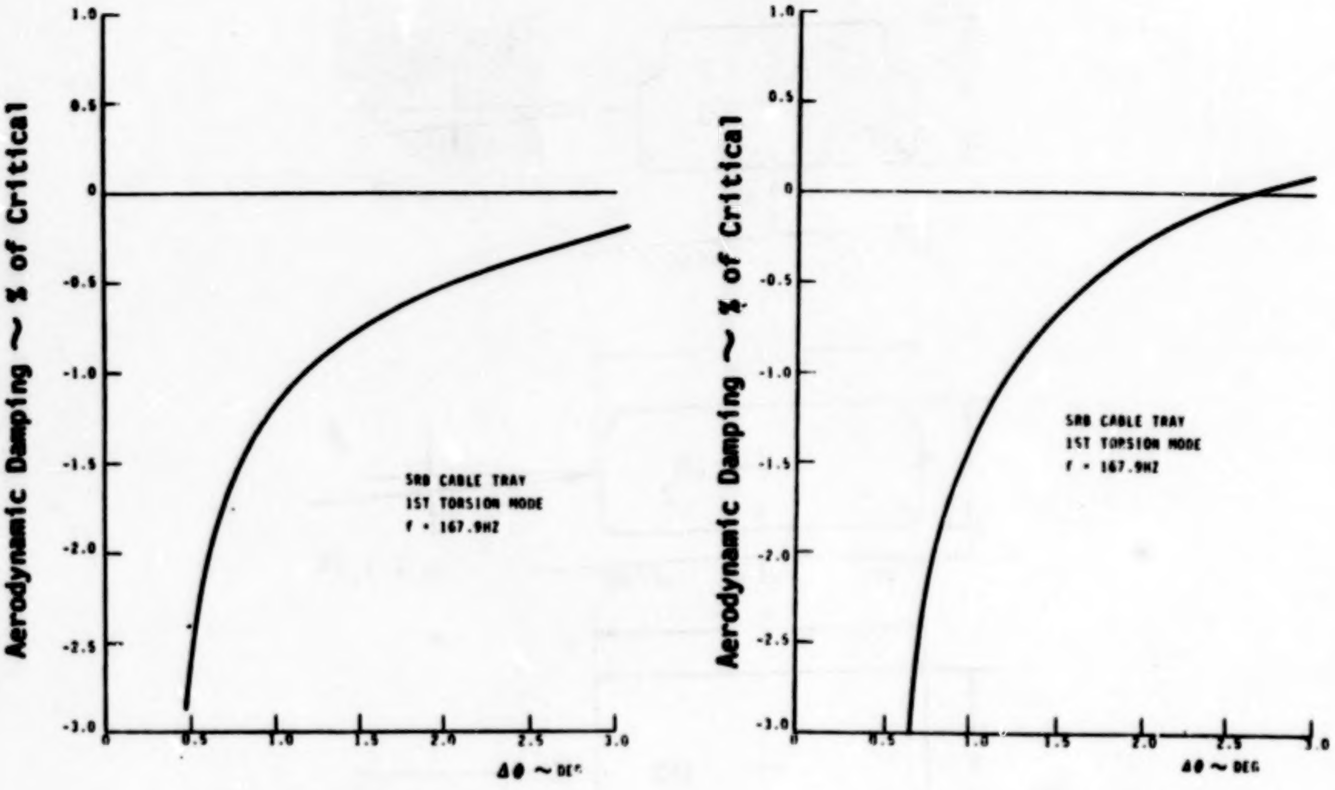

a. M = 0.7

b. M = 0.92

Fig. 14. Nonlinear Aeroelastic Torsional Characteristics of the SRB Cable Tray at M = 0.7 and M = 0.92.

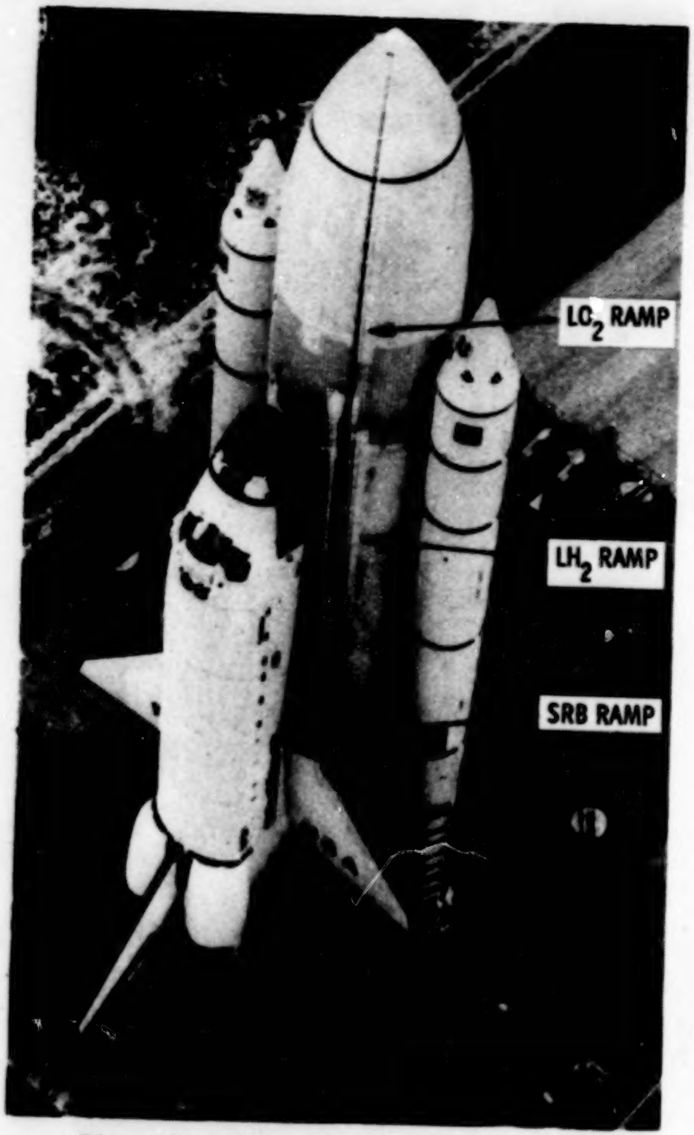
LO$_2$ RAMP
LH$_2$ RAMP
SRB RAMP

Fig. 15. Columbia Booster

APPENDIX B

SHUTTLE CARRIER AERODYNAMICS*

Albert H. Eldridge
Boeing Commercial Airplane Company, 747 Division
Seattle, Washington

SUMMARY

Some interesting aerodynamics problems encountered in configuring the shuttle carrier aircraft (SCA) are described. Predictably, they centered around the interactions between the wake of the shuttle orbiter vehicle and the vertical tail of the carrier. Steps in the evolution of the external configuration are briefly described, along with the experimental and theoretical aerodynamics studies that prompted them.

Directional stability was the strongest driver. This was degraded by the shuttle vehicle and by its support system.

The SCA emerged as an effective and successful vehicle for ferrying the shuttle, and it served the earlier purposes of the air launch and landing tests (ALT) well. These included those lively flights without the tail-cone fairing on the shuttle orbiter. The combined SCA and shuttle vehicles are shown during an ALT flight made in 1977 in figure 1.

Among the lessons learned from (or perhaps really reaffirmed by) this satisfying program have been:

- o We must always design to achieve orderly airflows (usually attached) and benign vortex shedding from all external surfaces.
- o The great value of carefully planned and executed small scale wind tunnel model testing, both as a tool to explore airplane configuration change effects and as a base from which to predict the full scale performance and flight characteristics.
- o That subcritical potential flow panel analysis methods can, at reasonable cost and effort, provide guidance and the basis for understanding the major aerodynamic design refinement problems. They can be used to help resolve these problems and to provide assurance of the aerodynamic suitability of the final design.

It should be emphasized that the views and opinions expressed in this paper are those of the author. They do not necessarily reflect a position, view or policy of The Boeing Company.

PRECEDING PAGE BLANK NOT FILMED

---

*Paper not presented at conference.

SYMBOLS

ALT	air launch and landing tests
FQF	ferry qualification flight
SCA	shuttle carrier aircraft
C	chord length
CA-xx	designation of SCA aerodynamic wind tunnel test
CAS	calibrated air speed
C_D	drag coefficient
c.g.	center of gravity
C_L	lift coefficient
C_m	pitching moment coefficient
C_n	yawing moment coefficient
C_{n_β}	slope, $\partial C_n/\partial \beta$
C_p	pressure coefficient
$f(\alpha)$	function of angle of attack
i_s	incidence angle of the shuttle vehicle relative to the carrier aircraft body axis
M	Mach number
MAC	mean aerodynamic chord length
R_e	Reynolds number
X/C	nondimensional chordwise distance
α_w	wing reference angle of attack
β	sideslip angle
Δ	an increment
δ_R	rudder deflection angle
η	fraction of wing semi-span

MAJOR IMPACTS OF THE SHUTTLE VEHICLE

The study leading to the present shuttle carrier aircraft's (SCA) configuration began in 1973. Initial requirements were for the aircraft to be operable as a freighter and, with the installation of quick-change kits, to carry the shuttle orbiter for ferriage and for air launch and landing tests (ALT) and to ferry the shuttle's external fuel tank. Fuel tank ferrying was deemed feasible but more exacting than carrying the shuttle itself and was soon set aside. A serious attempt was made to resurrect the tank ferry later, but by then the cost and schedule impact would have been severe. We will review the effects of designing the SCA for ferrying the shuttle only.

Heavy external payloads may be carried most efficiently with their centers of gravity (c.g.) located within the fore and aft c.g. range of the carrier aircraft. This is likely to minimize mounting tare and ballast weights. Other considerations may prevail, however. Some of the primary impacts of the large external payload exemplified by the shuttle vehicle are diagrammed in figure 2.

The payload must be supported. Payload and supports have aerodynamic impacts, both direct and indirect. All six aerodynamic force and moment components together with control powers may be affected. Lift induced downwash and sidewash flows and dynamic energy losses affect the performance of the carrier aircraft stabilizing surfaces, while wake unsteadiness caused by vortex shedding may excite structural responses.

In the case of the SCA ferry configuration, the shuttle vehicle's major impacts were direct weight added, drag increase and reduced directional stability. Directional stability considerations largely dictated the final configuration choice. Figures 3 through 6 show some early lift, pitch, drag and directional stability data measured on low speed wind tunnel models. The large drag impact was to be expected from basic considerations (wetted area). Effects on pitch stability were manageable, but the near zero sideslip stiffness derivative C_{n_β} was unacceptable.

SCA CONFIGURATION CHOICES

The expedient resolution of the directional stability problem on the SCA consisted of moving the shuttle vehicle aft, raising its incidence angle to 4-1/4 degrees (it was later lowered to 3 degrees) and replacing the streamlined support struts with cylindrical ones. This was not enough, and after many wind tunnel tests and much soul searching, the addition of vertical stabilizing fins to the tips of the horizontal stabilizers won out over fin tip extensions supplemented by ventral vertical surfaces. Figures 7, 8 and 9 illustrate essential features of the configuration evolution.

Some considerations weighed included:

1. Moving the shuttle vehicle aft. With its midrange c.g. located some 21.8 inches behind the aft limit of the SCA, approximately 8,300 lbs. of forward ballast was needed to balance the carrier modification structure and a 155,000 lb. shuttle vehicle. Clearance between the vertical stabilizer of the SCA and the shuttle during air launch was reduced to a low but comfortable value. This restored about 20% of the directional stability lost with the shuttle installed, while drag was reduced slightly.

2. Increasing the shuttle incidence angle from 0 to 4-1/4 degrees. This was always a trade between drag and $C_{n\beta}$. As the shuttle vehicle was rotated nose up, its wake moved lower with respect to the fin of the SCA and adverse sidewash and dynamic pressure influences on the fin dwindled. On the other hand, the shuttle then generated more of the lift that sustained the mated configurations and induced drag was degraded because the span of the shuttle vehicle is much less than the 747's span. In those early days, range capability seemed adequate and 117 nautical miles was traded away for the recovery of about 20% of the loss in $C_{n\beta}$ caused by the shuttle at takeoff conditions.

3. Cylindrical shuttle support struts. Side forces generated by the streamlin upright support struts originally conceived for carrying the shuttle gave direct and sidewash-induced destabilizing yawing moments. Drag was low with these supports. Proponents of a low cost, structurally simple support system strongly favored cylindrical struts. Counter arguments included the risk of vibration, noise and local structural fatigue damage caused by vortex shedding and wake turbulence from the cylindrical struts. Eventually, the issue was decided in favor of the simple cylindrical struts because range was still not a primary concern; fears for vibration were not quantifiable; and the most pressing current problem was seen as the directional stability one.

Later, after absorbing cruise drag increases seen in high speed wind tunnel tests of models having greater configuration fidelity and from shuttle vehicle drag updates, partial support system fairings (figure 10) were developed and tested. These established a cruise drag reduction potential of 37 counts (6-1/2%). This was worth 185 nautical miles range increase, but the fairings were rejected on the grounds of cost and kit change complexity. At this time, however, it was agreed that the shuttle incidence would be reduced to 3 degrees and a small diameter forward strut, dedicated to ferriage, was adopted. This improved the range by 90 nautical miles.

Rejection of the faired strut concepts in 1975 led to an interesting development problem immediately following the first flight of the SCA with its ALT struts installed. Vibration and noise made their unwanted presence felt, and (local) structural fatigue became a primary concern. This is addressed later.

THEORETICAL AERODYNAMIC CHARACTERISTICS

Potential flow analyses were made using a subcritical flow panel method. Valuable insights into the mutual interactions of the SCA and the shuttle vehicle were obtained in this way. Detailed pressure distributions were studied for local high velocities likely to lead to strong shocks in the flow field and for strong positive pressure gradients which could separate the flow. Overall and component forces and moments derived were helpful in identifying fundamental interferences and how they varied with configuration changes.

A configuration paneling arrangement is shown in figure 11. Both pitch and yaw effects were studied with similar modelings.

Mutual Interferences

Lift distribution. As shown in figure 3, the overall lift with the shuttle vehicle installed on the SCA was practically the same as that of the SCA or 747 aircraft alone. Some differences stand out at extreme angles of attack. It is also fair to say that basic pitching moments were not greatly affected.

Hidden behind this picture of small change, however, are powerful interferences. For example, SCA wing spanwise lift distributions are shown in figure 12 for various shuttle incidence angles relative to the SCA body. Lift over the inboard half of the SCA wing is greatly reduced by the flow field around the shuttle wing. Likewise, though not illustrated, the shuttle wing's lift was reduced by the interference of the SCA wing's flow field. Figure 13 shows the large shuttle influence on the SCA's wing root chordwise loading. These interactions exerted a considerable influence on the wing flight loads.

Body pressures. Flow in the channel formed between the bodies of the two vehicles was greatly affected by their close proximity. Figures 14 and 15 show, respectively, the pressures calculated along the top of the SCA fuselage and the bottom of the shuttle body. Though large positive (adverse) pressure gradients are present, no evidence of flow separation was detected during flow visualization testing. However, no claims could be entertained for a high critical Mach number for this vehicle.

Drag. Interference drag, defined as

$$C_{D_{\substack{SCA\,+\\SHUTTLE}}} - \left[C_{D_{SCA}} + C_{D_{SHUTTLE}}\right]_{ISOLATED}$$

is plotted against angle of attack in figure 16. Agreement with the drag change measured in the low speed wind tunnel, after adjustment for the estimated shuttle support system drag, is excellent. Integrated drags, not shown here, reveal that the SCA's wing and body pressure drags increased (at cruise C_L's) with the shuttle installed; the shuttle body and wing drags actually became negative. The shuttle's cylindrical cross section supports were not represented in the potential flow analysis.

Directional stability. Predicted effects of the shuttle vehicle on the directional stability are shown in figure 17 for a Mach number of 0.6 at six degrees angle of attack. The slope C_{n_β} was approximately halved for the shuttle incidence angle of five degrees illustrated. The degradation measured in the wind tunnel was considerably greater than predicted, possibly due to the combined effects of the viscous wake of the orbiter and its support strut system on the vertical tail of the SCA. These effects could not, of course, be modeled in the analysis.

Conclusions

Theoretical inviscid flow analyses provided an understanding of the large interactions between the shuttle vehicle and the SCA on which it is carried. Effects of major configuration changes were studied and fundamental influences, as distinct from possible viscous or shock interactions, were identified. Probabilities of the latter two could be assessed by inspection of the detailed pressure distributions, of which the flows in the channel between the two aircraft were the most critical. The analyses were a valuable complement to wind tunnel model testing and were, of course, considerably less expensive to perform. Great improvements have been effected in computing capability and costs since these studies were made in 1974, and analytical configuration trade studies should be strongly encouraged in all future development programs. It is believed that the predictable volume and lifting pressure field interactions dominate the aerodynamic interferences on all realistic configurations. Viscous and real flow compressibility effects are still not wholly amenable to analysis. These must be determined by the traditional, carefully controlled wind tunnel testing procedures on small scale models. It is interesting to note that a total of 2,593 hours of wind tunnel occupancy was devoted to the determination of aerodynamics parameters, air loads, flutter and vibration characteristics for the shuttle carrier aircraft and its payload.

PREDICTING THE FULL SCALE AERODYNAMIC CHARACTERISTICS

In principle, methods for predicting the aerodynamic parameters are similar for performance, stability and control characteristics. Small scale model test measurements are corrected for wind tunnel wall, flow distortion, blockage and mount system effects. Calculated elastic, Reynolds number, power and surface roughness/excrescence effects are then added. Finally, trim increments derived from model testing are included where appropriate. In some cases, power effects may be measured on models. This was not necessary for the SCA.

For the shuttle carrier aircraft, we were fortunate in having a flight tested data base for the 747. This was exploited to minimize uncertainties in the final predicted values for the combined vehicles. In essence, model testing was used to establish increments which were adjusted and then added to the known values for the 747 alone. The typical process is illustrated in figure 18.

This procedure was highly successful. Some examples and comments follow in the next section.

FLIGHT TEST RESULTS

Aerodynamic characteristics, especially those affecting flight operations, performance and flying characteristics were, for the most part, essentially as predicted using the techniques described earlier. Lift, drag, control power and controls-fixed damping (both pitch and yaw) were as forecast or slightly better. Predicted air minimum control speed was confirmed. Only the yaw damper performance was measurably less than expected, and this could have been due to excessive free play in the lower rudder which was observed to be close to 0.5 degree.

Support Strut Fairings

The SCA was first flown with ALT shuttle support struts and stabilizing tip fins on the horizontal tail on December 16, 1976. The configuration is shown in the aerial photograph, figure 19. The aircraft handled well, but excessive noise and vibration were reported. Vibration was especially severe at the front strut location in the upper deck cabin. Uncomfortable vibrations were experienced in the main cabin near the aft strut attachments. Interior acoustic and vibration data were measured and sonic fatigue life assessments made for skin panels and stringers. It was determined that fairings were required to reduce the aerodynamic excitation associated with vortex shedding and turbulence in the wake of the cylindrical struts and the massive external end fittings to which they were attached. After about 13.5 hours total flying time, the hastily constructed fairings pictured in figures 20 and 21 were installed and subsequent acoustic/vibration measurements were used to confirm that the structural fatigue problem had been resolved. The aircraft was still noisy, but that was merely a slight inconvenience. More details may be found in reference 1.

The temporary fairings deteriorated rapidly during the aircraft's ALT flights, and at the time of the ferry qualification flight (FQF) tests (for which the forward support struts were, as mentioned earlier, reconfigured), the strut fairings had been rebuilt and were as shown in figures 22 and 23. Everything went well, except that an annoying high frequency pipe organ note was at first produced. This was eliminated when a small leak path through the front strut fairings was sealed and the crude front fairings seen at the forward strut attach points, figure 23, were installed. Close examination of the front struts will reveal a spirally wrapped cable, which is taped over. This was to break up and soften the excitation effects of vortex shedding. Both spiral cables and the fairings have become necessary permanent features of the configuration.

Lateral/Directional Stability

Sideslip maneuvers were performed with the shuttle in the ferry configuration at a number of airspeeds, two test altitudes and with both flaps up and flaps 10, a takeoff flap. Sideslip releases were performed to evaluate the Dutch roll characteristics. Conclusions drawn were that the directional stability and Dutch roll damping/frequency characteristics with yaw dampers off were essentially as predicted. The sideslip angle/rudder deflection relationship in cruise at 16,150 feet pressure altitude and 250 knots CAS is shown in figure 24. This indicates a slightly larger rudder power than forecast, probably due to a reduced shuttle wake energy loss at full scale than on the wind tunnel models. That wake is known to be centered around a line one third of the way up the SCA fin.

Drag and Performance

Drag with flaps down was within 1% of the predicted full scale values. With flaps up, the drags ranged between 1-1/2% and 4-1/2% less than predicted. Miles flown per pound of fuel averaged 6% better than predicted for long range cruise conditions. It seems probable that the strut fairings were largely responsible for bringing the drag down. Credit must also be given to the engines, which, though not new, performed better than expected in terms of specific fuel consumption.

A typical comparison between predicted and measured cruise drag is shown in figure 25. Some difference in polar shape is evident, which could be due to errors in predicting the effects of aeroelasticity and Reynolds number changes on this complex configuration.

Conclusions

The noise, vibration and local structural fatigue impacts of the unsteady airflow from the cylindrical shuttle support struts should be noted. It is concluded that good aerodynamic fairings are not only desirable but essential. Assurance of an orderly, stable flow regime with minimal pressure fluctuations is required for good performance, for satisfactory sound levels and to provide for an acceptable fatigue life/structure weight relationship in the regions potentially subject to aerodynamic excitation.

The methods used for predicting the full scale lift, drag, stability and control force/moment coefficients were sound and reliable. Use of all available flight data for the basic 747 aircraft provided an excellent base to which model test and theoretical increments could be added.

LESSONS LEARNED

First, it was proven that an existing transport aircraft could be converted to become a successful carrier of outsized payloads external to its body. The shuttle carrier aircraft does its job of ferrying the orbiter vehicles well. It could be adapted for air ferrying of other bulky payloads, for which the major requirements would be that they not exceed the weight or the overall body dimensions of the shuttle, that they be aerodynamically faired for ferrying and that they fit on the shuttle support system.

Once again, the merits of designing to maintain an orderly, steady flow of air around all external components of the configuration were reaffirmed. It must be strongly re-emphasized that lightweight structures are greatly susceptible to fatigue damage accumulation due to sustained unsteady load applications caused by separation and cyclic vortex shedding, and that the noise and airframe responses created by these are, at best, uncomfortable for the crews who must fly the aircraft. *Fair everything is the good design motto*, and then take care that neither strong adverse pressure gradients nor shock-boundary layer interactions can undo the good work.

In assuring a full understanding of strong mutual aerodynamic interactions, and of the local pressure and Mach number distributions, the subcritical inviscid panel flow analysis methods (reference 2, for example) have unmatched capability and versatility. They are recommended equally for basic configuration decision making and for local detailed design, yielding useful information on overall lift, drag, pitching and yawing moments and their contributions from individual components.

When properly corrected for wind tunnel flow constraint and model support system tares, small scale wind tunnel model tests can yield reliable aerodynamic design information. With the further addition of estimated increments for non-scaleable roughness items, Reynolds effects and aeroelasticity, good predictions of full scale aircraft performance and flight characteristics can be made. In common with many other aircraft programs, the vital predictions made for this complex combined vehicle were all very close or slightly conservative. A key factor in the testing of all small scale models is the best possible simulation of the real flow viscous effects. Great care must always be taken to determine and match (as closely as possible) the features of the model boundary layer to its full scale counterpart.

FUTURE POSSIBILITIES

The shuttle carrier aircraft, as presently configured, is capable of carrying a payload canister (reference 3) that can accommodate shuttle payloads or other bulky cargo. It can also be used to convey many large payloads that can be cradled (for mounting to the shuttle support struts) and faired (to prevent airflow separation and bothersome vortex shedding). Portions of the B-1 aircraft fuselage are possible examples. When not equipped with struts and horizontal tail tip fins, it can serve as a freighter with a normal 747 operating speed envelope.

The aircraft in its present form is highly versatile. Nevertheless, certain possible future needs could prompt a re-examination of the configuration in order to adapt it to fulfill an even wider range of uses. Examples include the space shuttle's external fuel tank carriage and lifting a small space plane for air launch.

A vee-tailed version of the SCA might be able to perform all foreseeable carrying missions and achieve greater economy, range and flexibility by operating at increased cruise speeds. An outline of such a configuration is shown in figure 26. The concept has not been developed, but, by promising to reduce interactions between the payload and the vertical stabilizer/yaw control surfaces, it does appear to merit further consideration.

REFERENCES

1. 747 Shuttle Carrier Aircraft - Type II. Boeing Report D180-20441-2, Flight Test Summary Analysis Report, February 1977. Revision A.

2. Derbyshire, T.; and Sidwell, K. W.: PAN AIR Summary Document (Version 1.0). NASA CR-3250, 1982.

3. Lindroth, John R.: Large Payload Transportation Study Final Report (SISC Special Study 82B002), Boeing Aerospace Company, August 1982.

Figure 1.- Shuttle carrier aircraft during ALT flight in 1977.

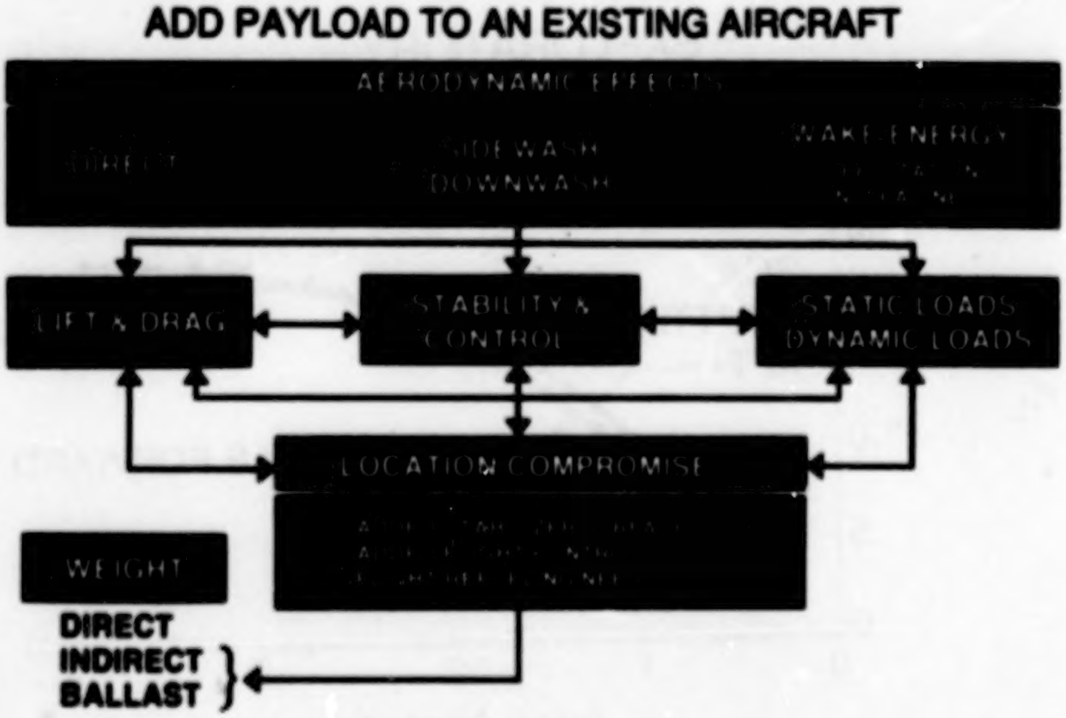
ADD PAYLOAD TO AN EXISTING AIRCRAFT
AERODYNAMIC EFFECTS
DIRECT
SIDEWASH
DOWNWASH
WAKE ENERGY
LIFT & DRAG
STABILITY &
CONTROL
STATIC LOADS
DYNAMIC LOADS
LOCATION COMPROMISE
WEIGHT
DIRECT
INDIRECT
BALLAST

Figure 2.- Major impacts of a large external payload.

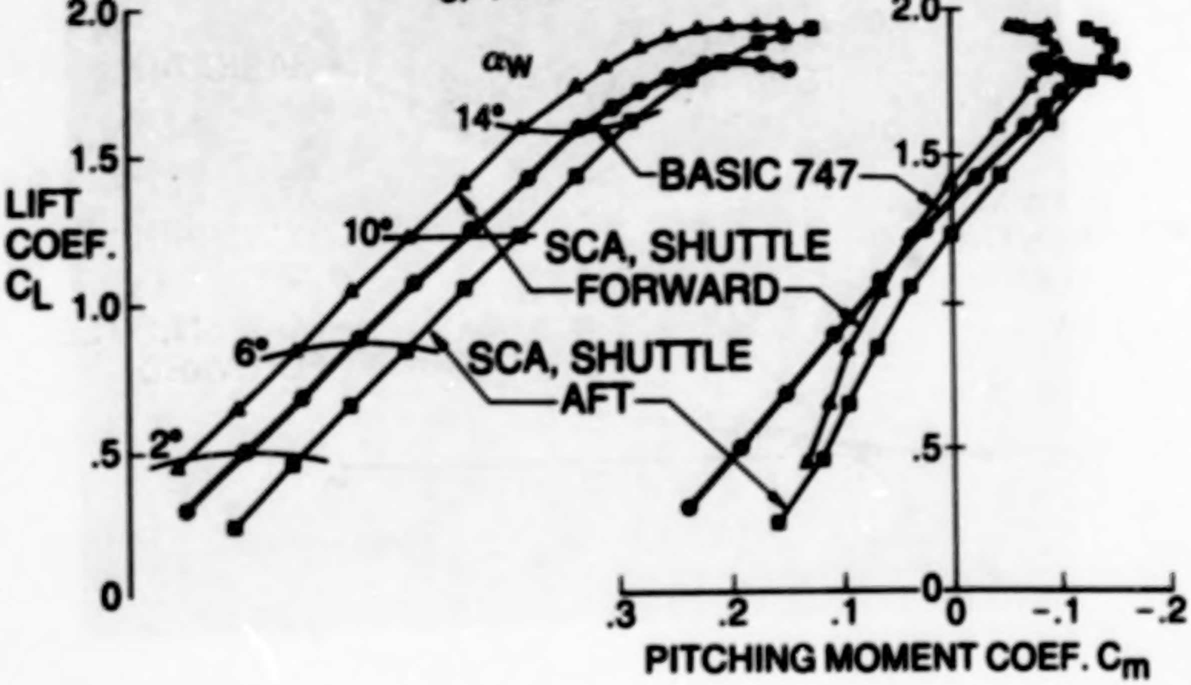

Figure 3.- Lift and pitch characteristics.

—EXPLORATORY—

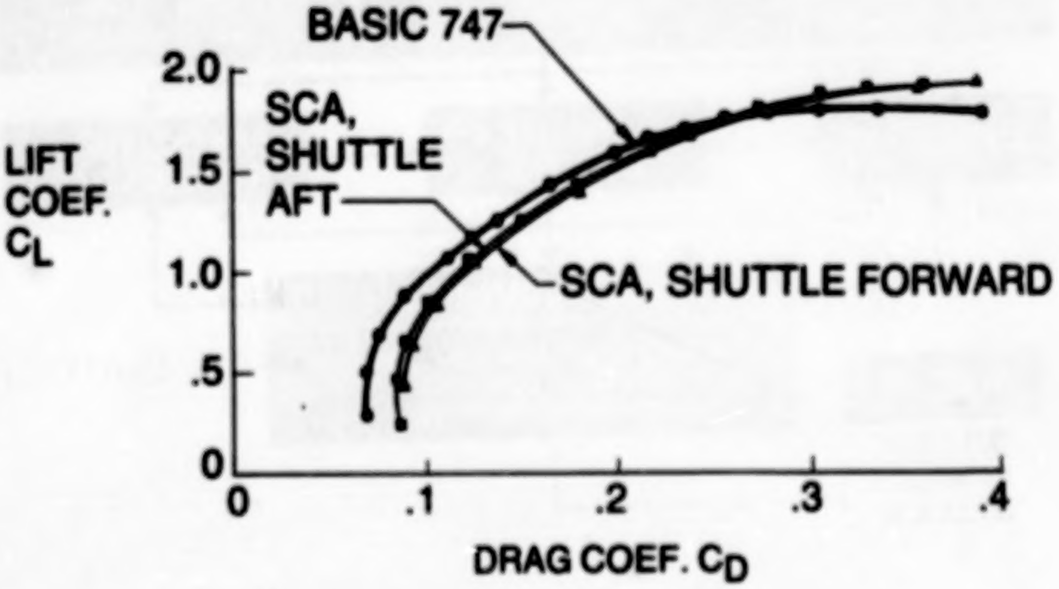

Figure 4.- Shuttle effects on drag.

-EXPLORATORY-

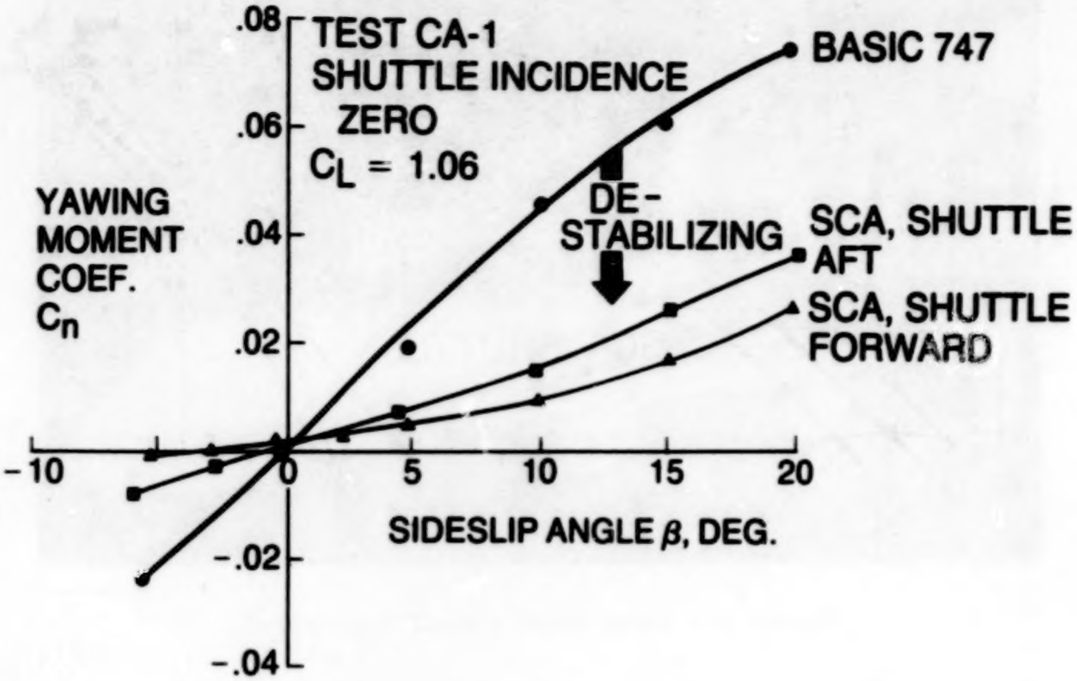

Figure 5.- Yawing moment due to sideslip at flaps 20.

-EXPLORATORY-

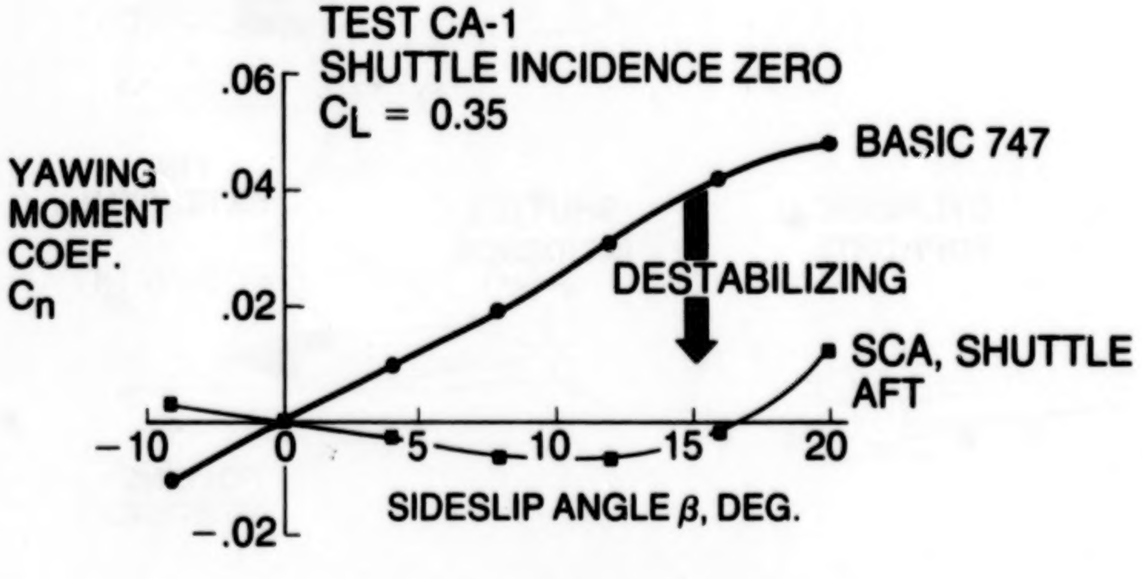

Figure 6.- Yawing moment due to sideslip at flaps up.

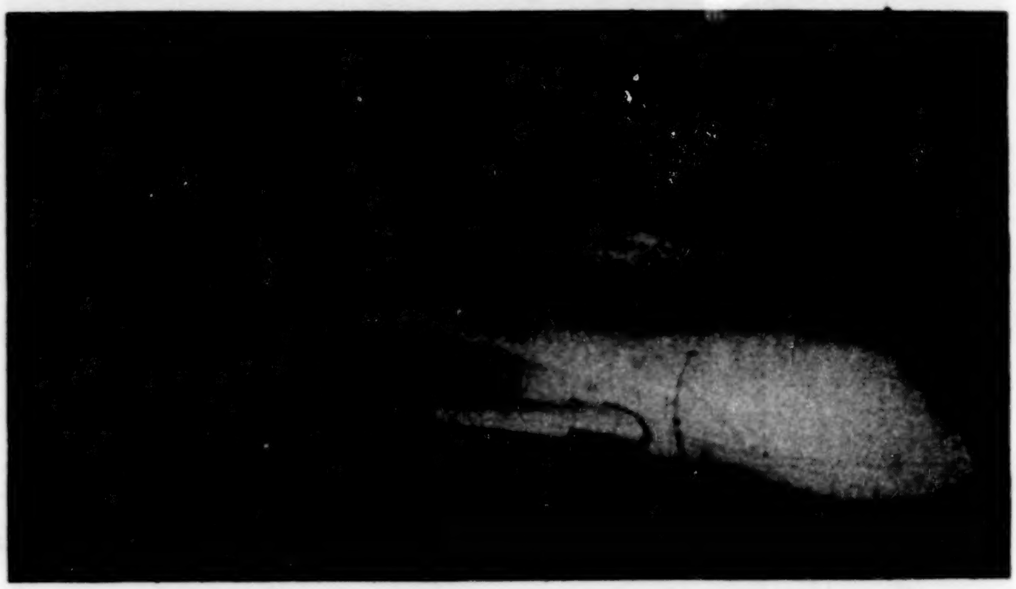

Figure 7.- First wind tunnel test model.

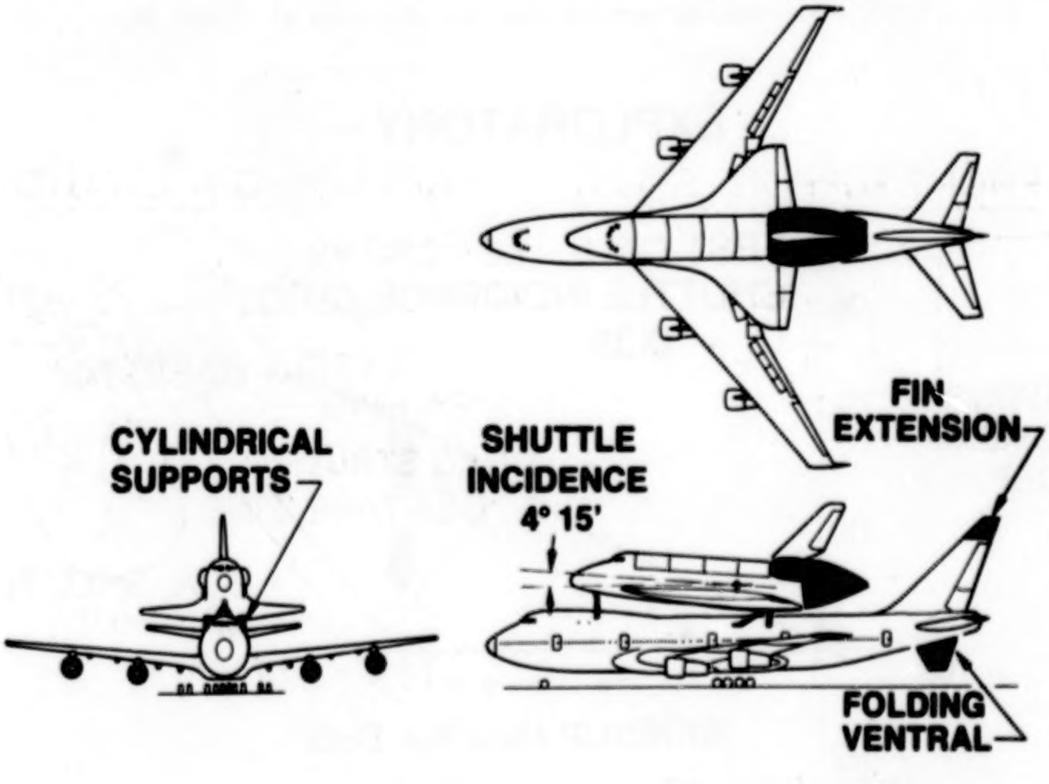
FIN
EXTENSION
CYLINDRICAL
SUPPORTS
SHUTTLE
INCIDENCE
4° 15'
FOLDING
VENTRAL

Figure 8.- Early SCA configuration.

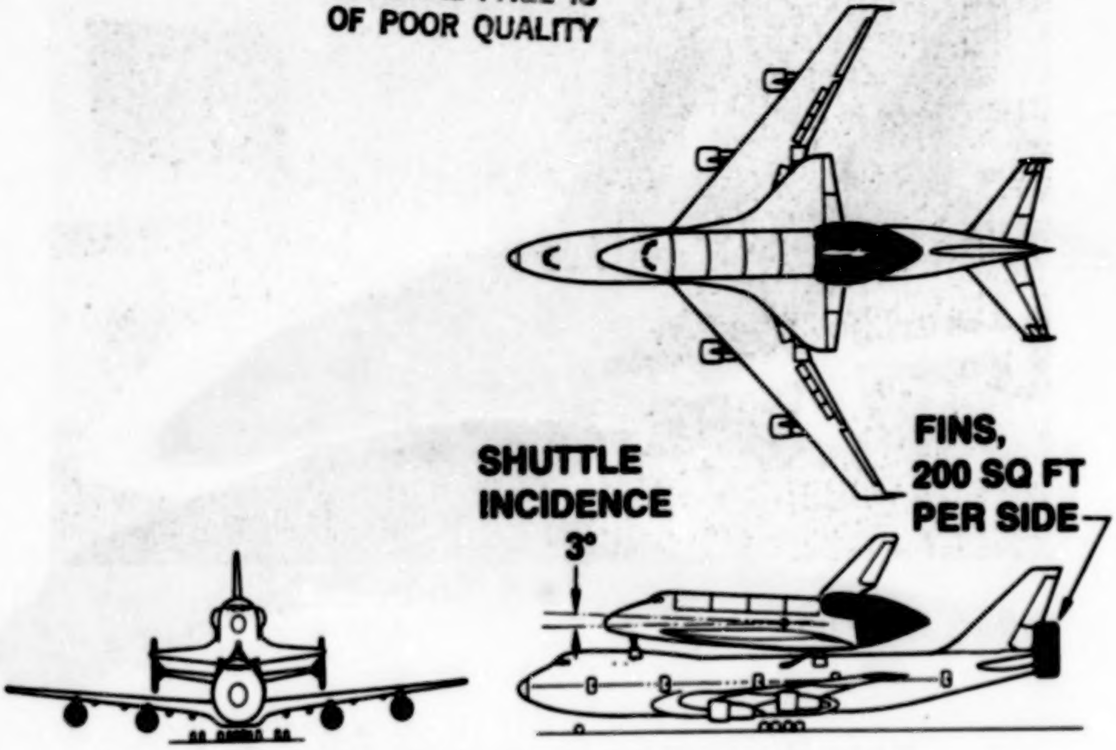
SHUTTLE
INCIDENCE
3°
FINS,
200 SQ FT
PER SIDE

Figure 9.- Final SCA configuration.

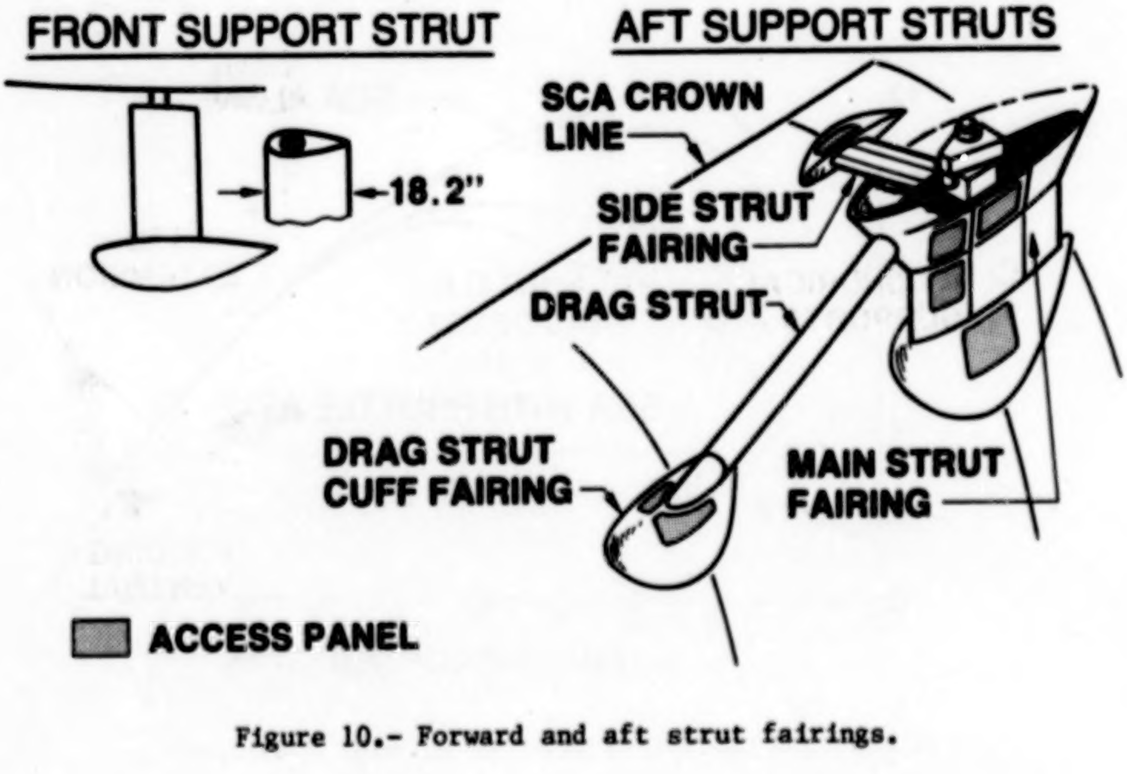
FRONT SUPPORT STRUT
18.2"
AFT SUPPORT STRUTS
SCA CROWN
LINE
SIDE STRUT
FAIRING
DRAG STRUT
DRAG STRUT
CUFF FAIRING
MAIN STRUT
FAIRING
▨ ACCESS PANEL

Figure 10.- Forward and aft strut fairings.

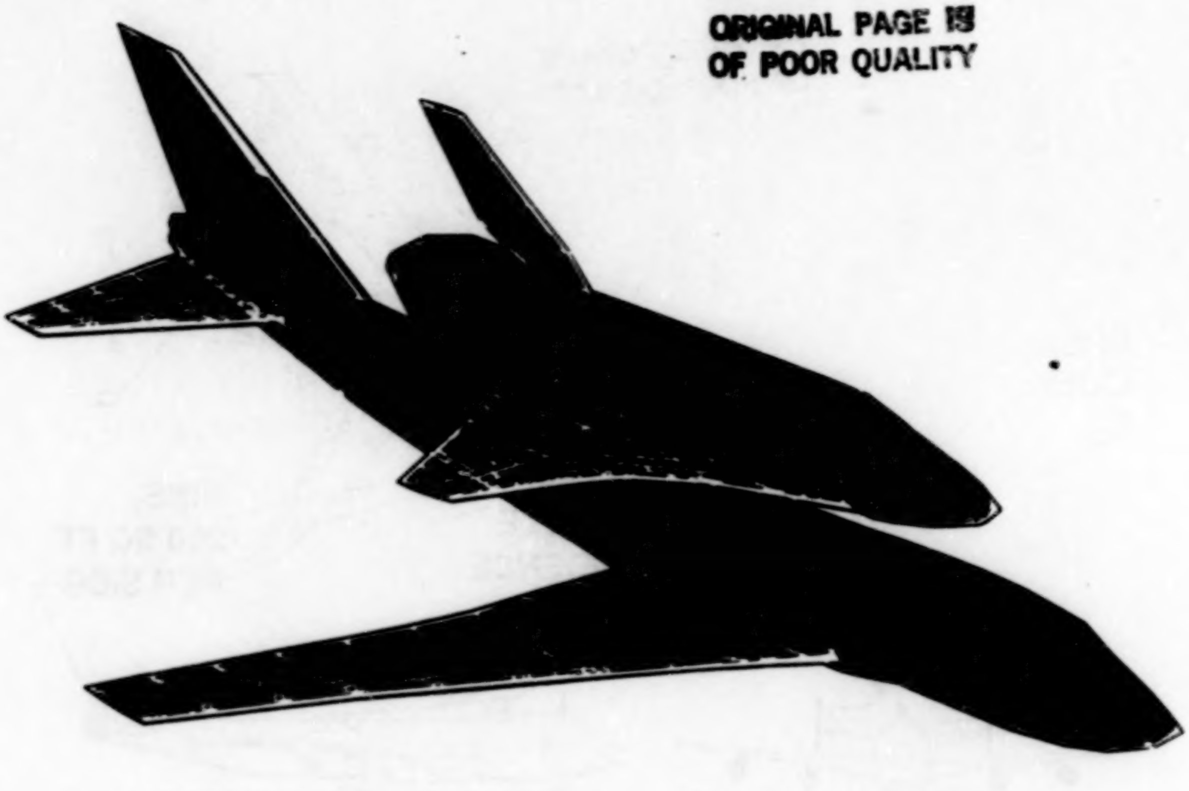

Figure 11.- Paneling for potential flow analysis.

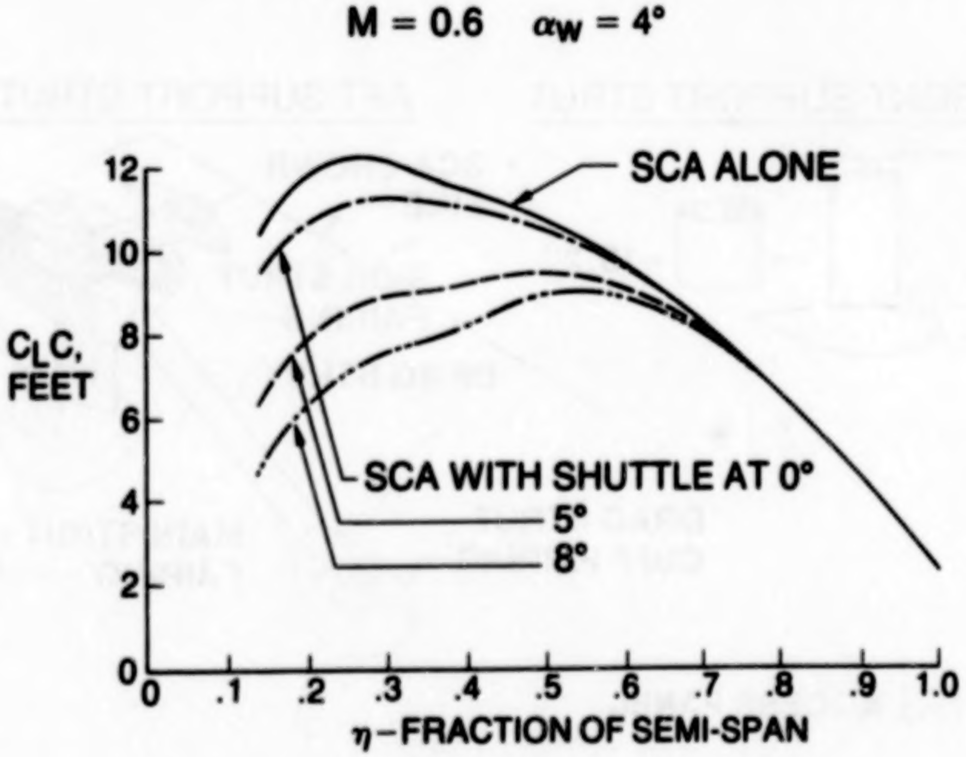

Figure 12.- Shuttle effects on SCA wing span loads.

ORIGINAL PAGE IS
OF POOR QUALITY

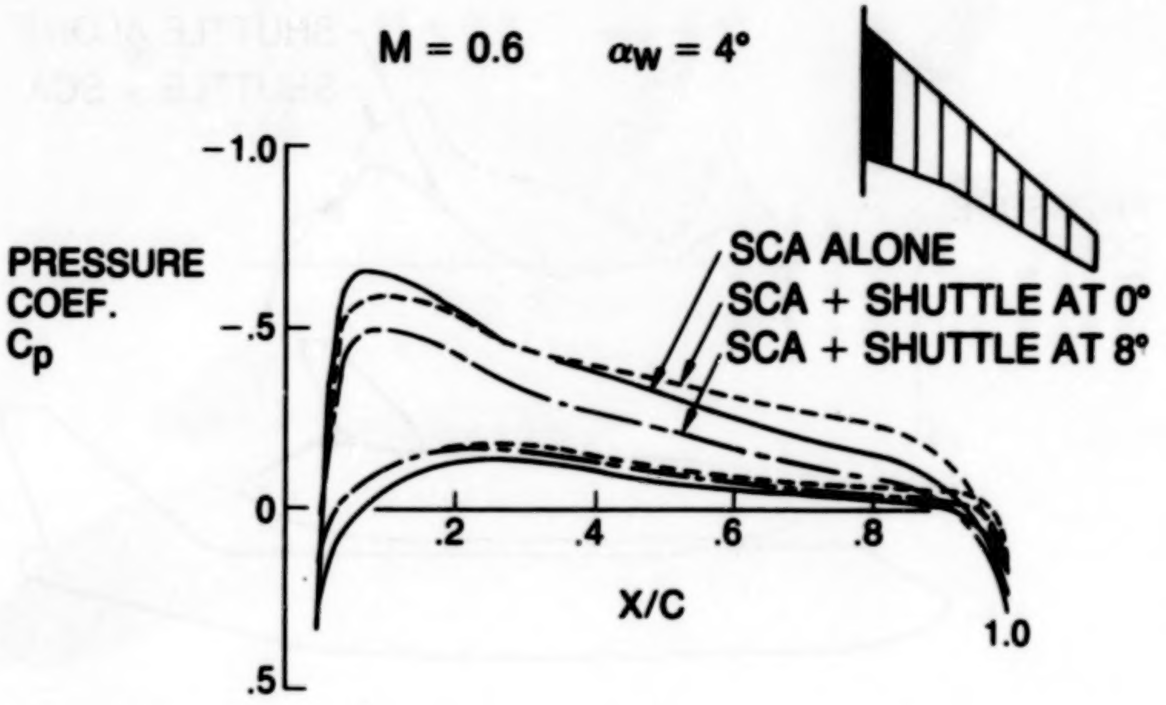

Figure 13.- Effect of shuttle on SCA wing pressures.

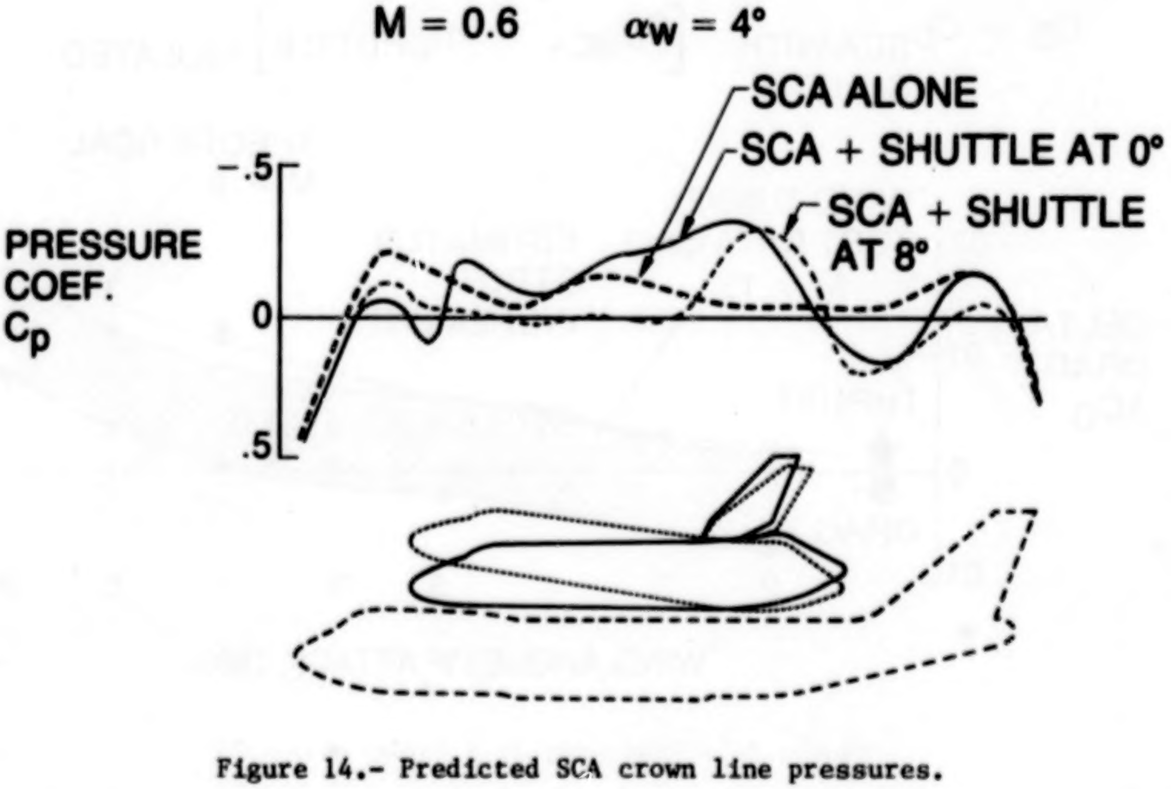

Figure 14.- Predicted SCA crown line pressures.

ORIGINAL PAGE IS
OF POOR QUALITY

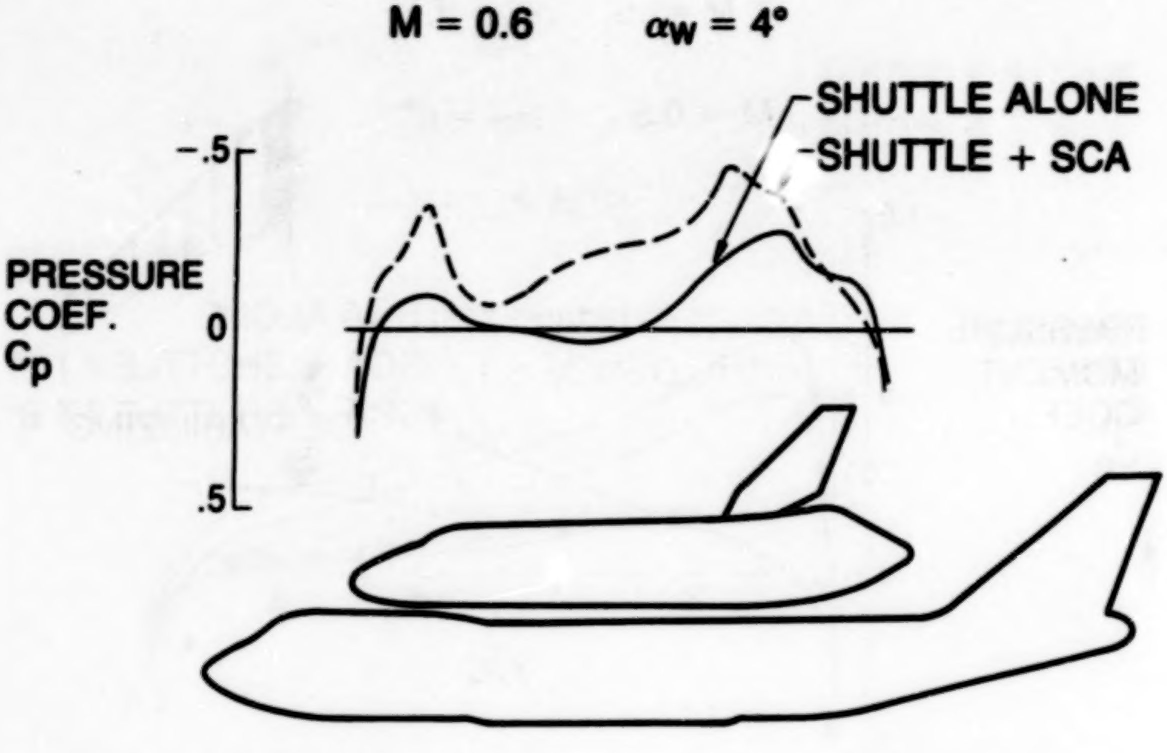

Figure 15.- Effect of SCA on shuttle lower surface pressures.

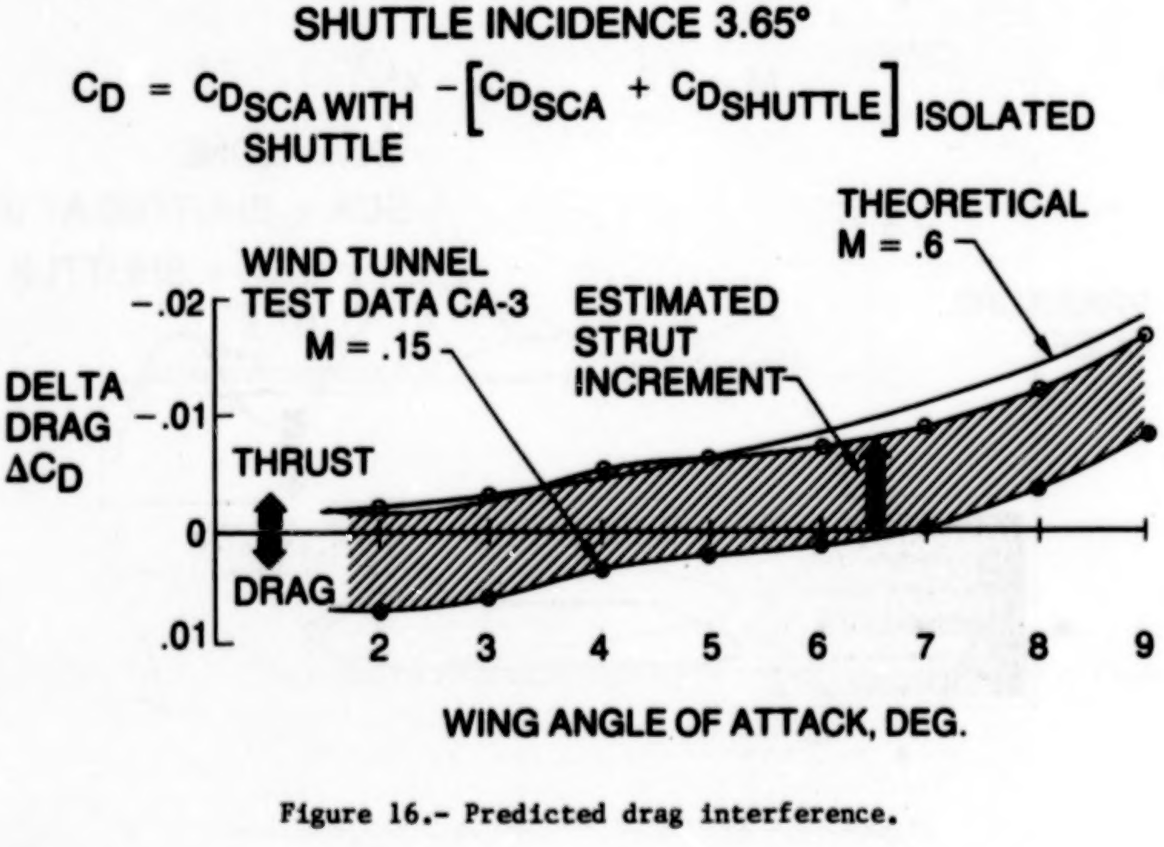

Figure 16.- Predicted drag interference.

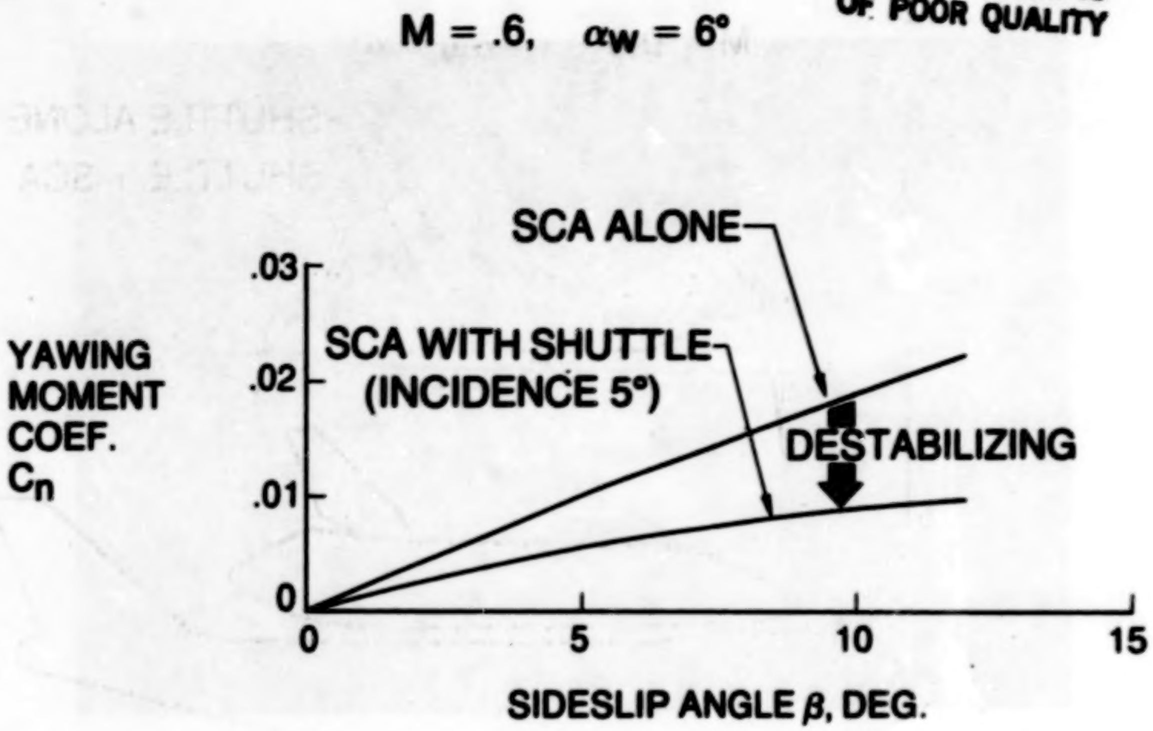

Figure 17.- Theoretical yawing moments.

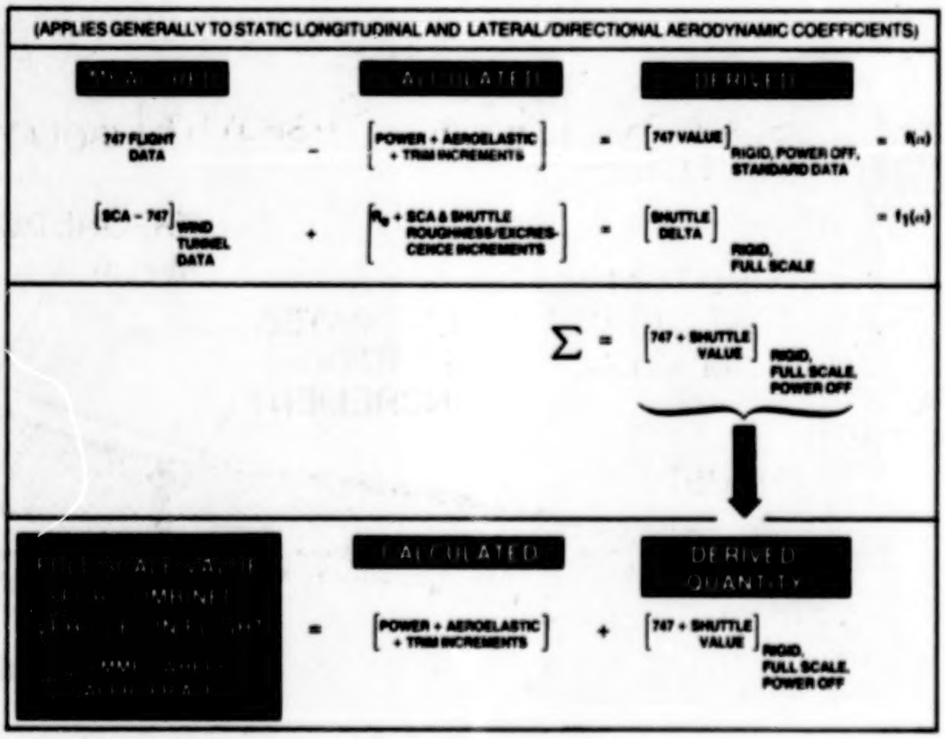
(APPLIES GENERALLY TO STATIC LONGITUDINAL AND LATERAL/DIRECTIONAL AERODYNAMIC COEFFICIENTS)
CALCULATED
DERIVED
747 FLIGHT DATA
-
[POWER + AEROELASTIC + TRIM INCREMENTS]
=
[747 VALUE] RIGID, POWER OFF, STANDARD DATA
= f₁(α)
[SCA - 747] WIND TUNNEL DATA
+
[R_e + SCA & SHUTTLE ROUGHNESS/EXCRESCENCE INCREMENTS]
=
[SHUTTLE DELTA] RIGID, FULL SCALE
= f₂(α)
Σ =
[747 + SHUTTLE VALUE] RIGID, FULL SCALE, POWER OFF
CALCULATED
DERIVED QUANTITY
=
[POWER + AEROELASTIC + TRIM INCREMENTS]
+
[747 + SHUTTLE VALUE] RIGID, FULL SCALE, POWER OFF

Figure 18.- Aerodynamic characteristics buildup.

ORIGINAL PAGE IS
OF POOR QUALITY

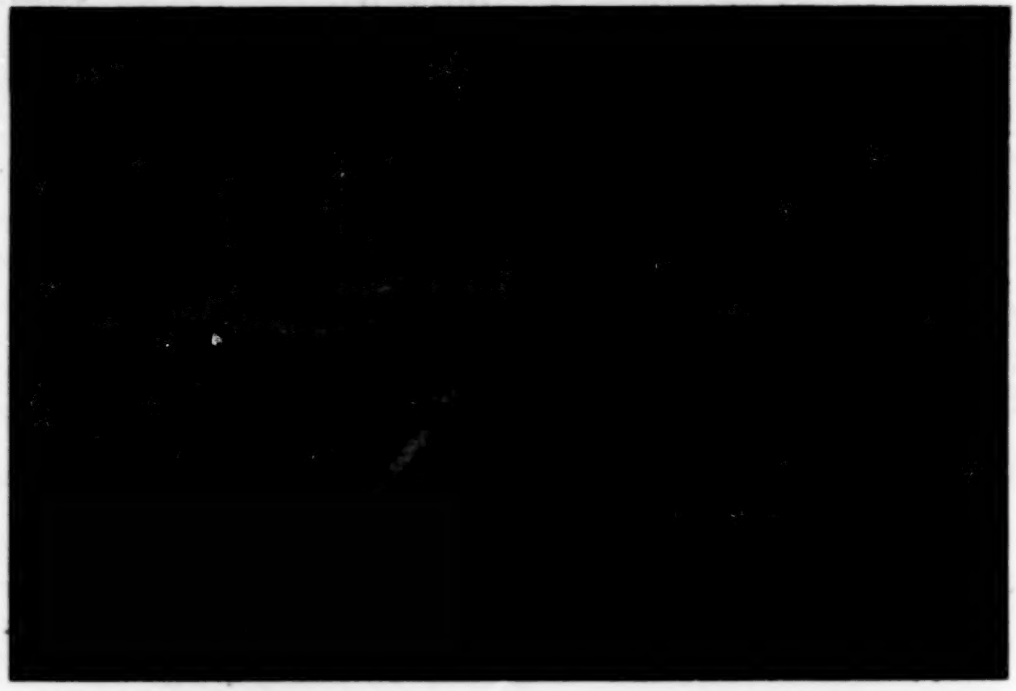

Figure 19.- SCA with ALT struts installed.

Figure 20.- First aft strut flight test fairing.

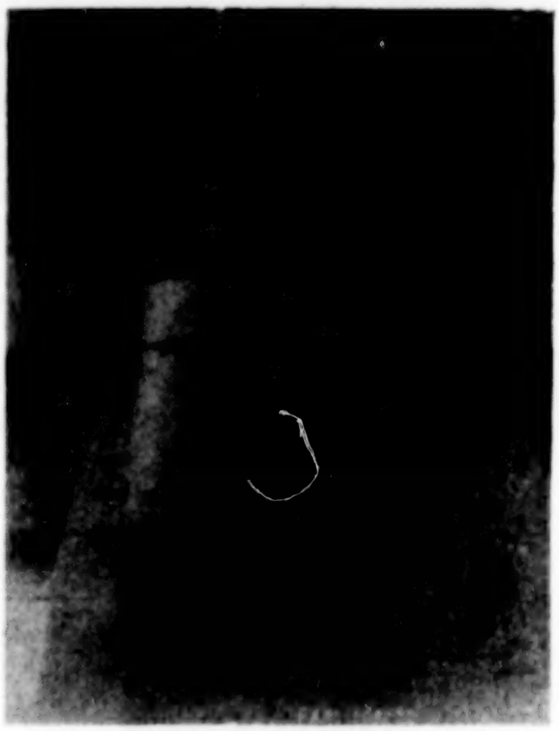

Figure 21.- First front strut flight test fairing.

ORIGINAL PAGE IS
OF POOR QUALITY

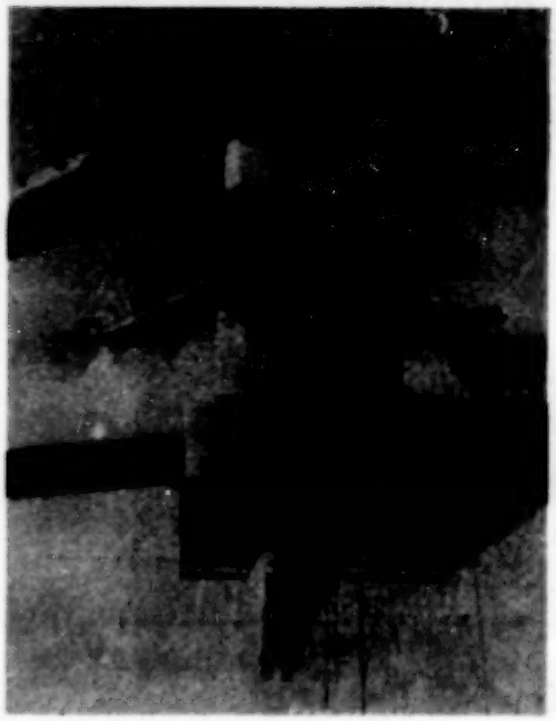

Figure 22.- Rebuilt aft strut fairing for FQF.

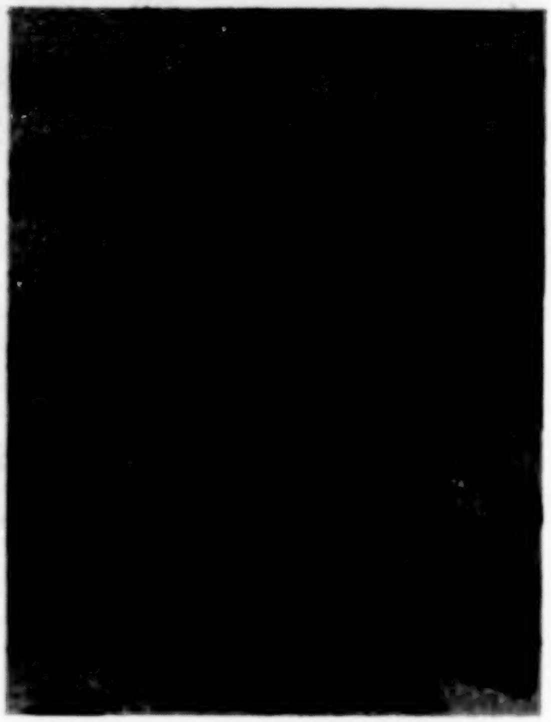

Figure 23.- Rebuilt front strut fairings for FQF.

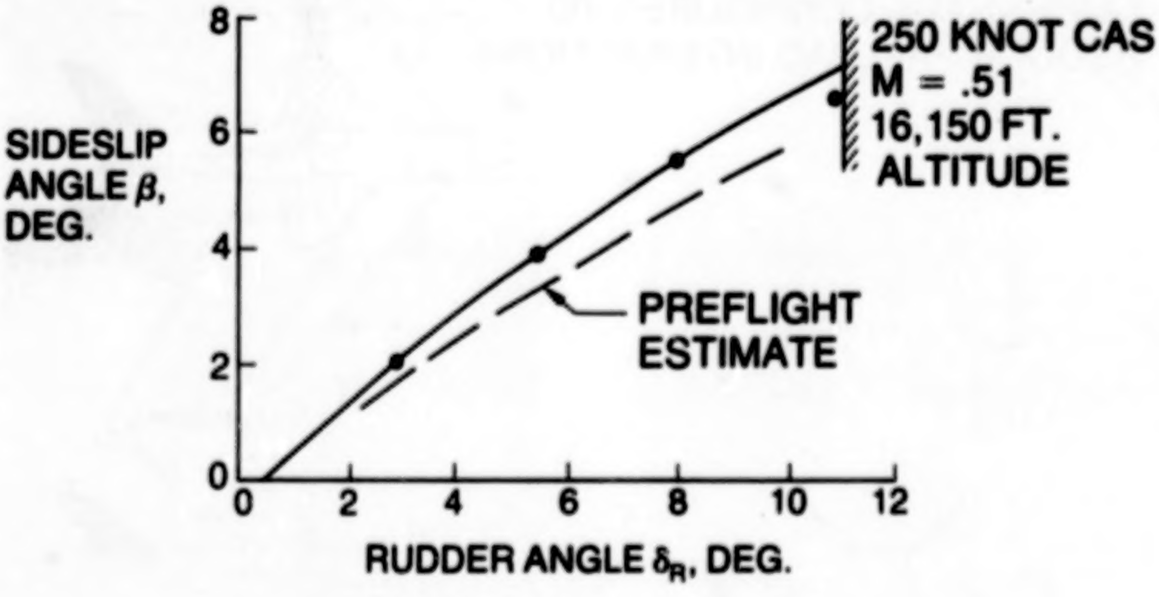

Figure 24.- Ferry configuration sideslip characteristics at cruise.

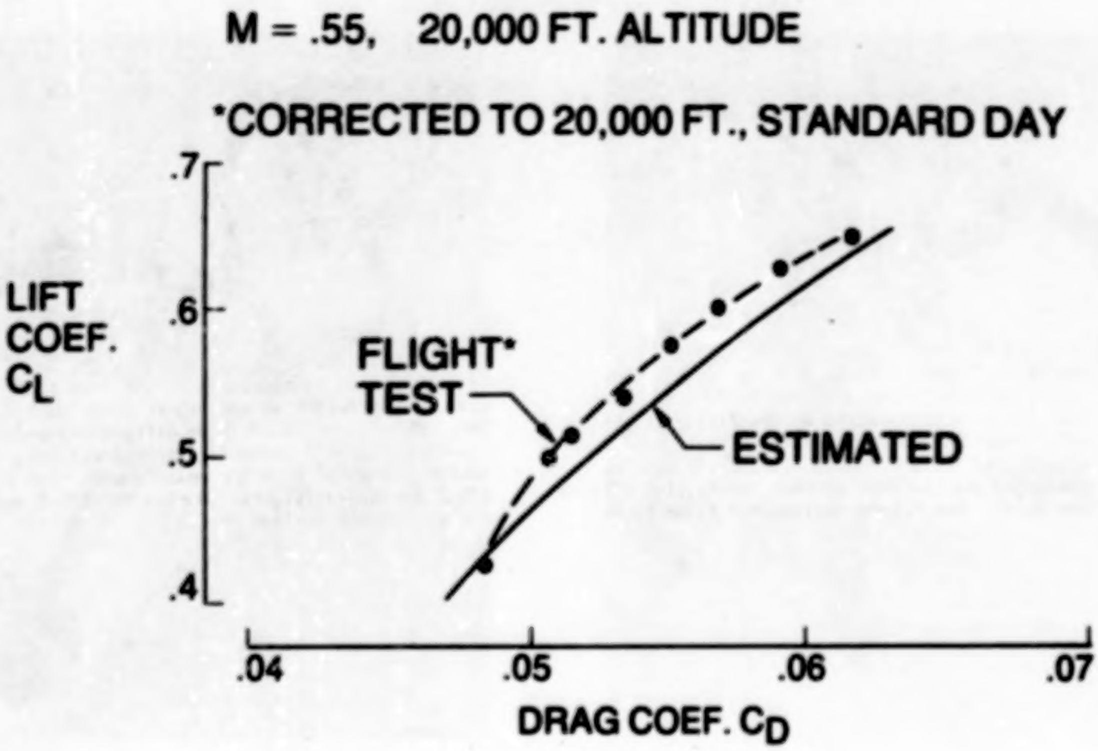

Figure 25.- Ferry configuration cruise drag.

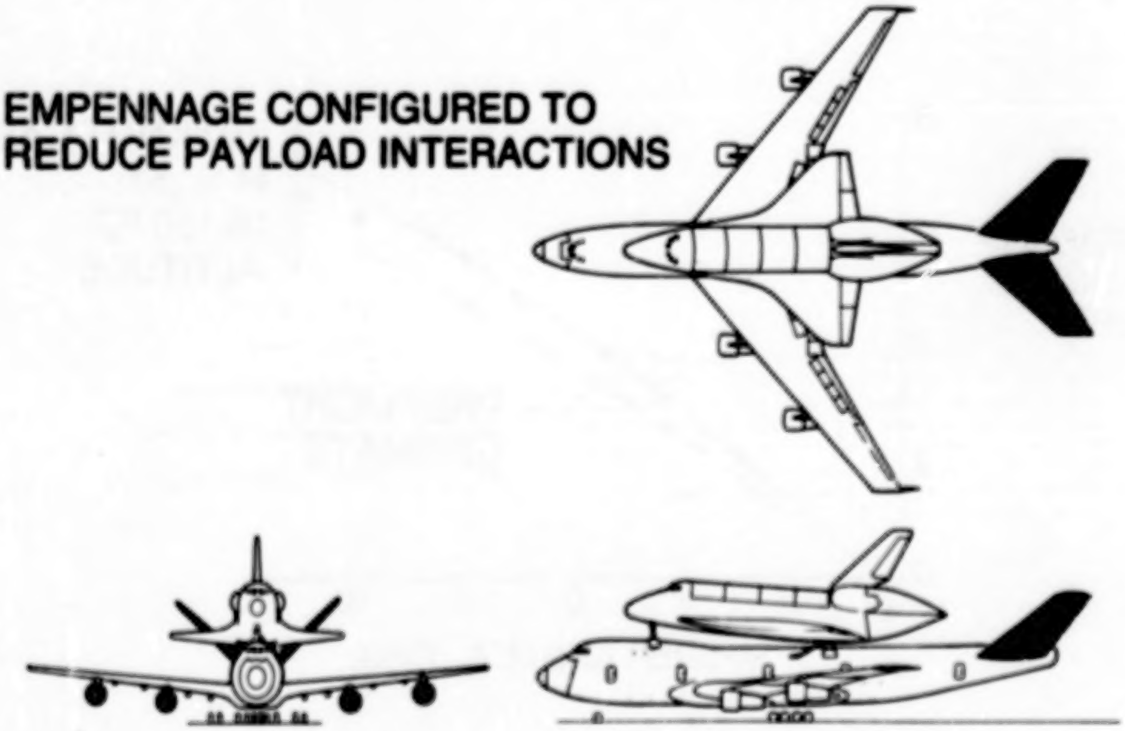
EMPENNAGE CONFIGURED TO REDUCE PAYLOAD INTERACTIONS

Figure 26.- A shuttle carrier alternative concept.

APPENDIX C

ORIGINAL PAGE IS
OF POOR QUALITY

SPACE SHUTTLE THIRD FLIGHT (STS-3) ENTRY RCS ANALYSIS*

W. I. Scallion, H. R. Compton, W. T. Suit,
R. W. Powell, T. A. Blackstock, and B. L. Bates
NASA Langley Research Center
Hampton, Virginia

Abstract

Flight data obtained from three Space Transportation System orbiter entries (STS-1, 2, and 3) are processed and analyzed to determine the roll interactions caused by the firing of the entry reaction control system (RCS). Comparisons between the flight-derived parameters and the predicted derivatives without interaction effects are made. The flight-derived RCS Plume flowfield interaction effects are independently deduced by direct integration of the incremental changes in the wing upper surface pressures induced by RCS side thruster firings. The separately obtained interaction effects are compared to the predicted values and the differences are discussed.

Introduction

During the years of development of the Space Shuttle Orbiter, the Space Systems Division at the NASA Langley Research Center actively supported the buildup of the aerodynamic data base required to design the vehicle and predict its flight characteristics. In addition to conducting supporting wind-tunnel tests throughout the entry speed range, detailed analyses of the data and their effects on the orbiter performance, stability and control characteristics were conducted. The Space Systems Division has also been processing and analyzing the actual flight measurements from the previous orbiter entries (STS-1 to STS-4).[1] The objective of this effort is to analyze the data from many orbiter entries, and compare the results with ground test data with a view toward improving ground-to-flight extrapolation techniques, and developing valid ground-to-flight correlation parameters. The current effort covers a wide variety of investigations of aerodynamic phenomena with special emphasis on hypersonic aerodynamics, across-the-speed-range performance, stability and control, and reaction control system (RCS) impingement and interaction effects. The investigation reported herein deals with the side-firing RCS thruster effectiveness and the interaction between its plume and the flowfield and wing upper surface.

Extraction of the total side-firing RCS effectiveness parameters from the STS-1 onboard inertial measurements indicated considerable differences between the rolling moments obtained from the flight data and those predicted by ground test data. In particular, the rolling-moment interactions as predicted by the preflight data base were considerably larger than those measured in flight at the higher entry Mach numbers (Mach 10 to 26). These differences were also confirmed by the RCS effectiveness parameters extracted from the measurements from the STS-2 and STS-3 flights. During the STS-1 entry the wing upper surface pressure instrumentation responded to the side-thruster firing; however, because of a recorder failure, there were insufficient data for analysis. This pressure instrumentation, although quite limited, offered a means by which the rolling-moment interactions produced by the side-firing thrusters could be deduced directly if sufficient data across the speed range could be obtained. No pressure data were obtained from the STS-2 flight, but the STS-3 flight produced upper wing surface pressure data from the beginning of the entry to around Mach 8.

The objective of this paper is to present an analysis of the effectiveness of the orbiter side-firing RCS thrusters at hypersonic speeds with emphasis on the plume flowfield interaction effects about the vehicle roll axis. Presented herein are the flight-determined lateral RCS control derivatives and rolling-moment interactions compared to the interactions derived from integrating flight-measured pressure distributions. These data are also compared to the preflight predicted values for the Mach number range of 26 to 8.

Nomenclature

ACIP	Aerodynamic Coefficient Identification Package
b	Reference wing span
ASI	Aerodynamic Stick Input
BET	Best Estimated Trajectory
$C_{\ell_{\delta_j}}$	Rolling-moment coefficient produced by firing the side thrusters, per thruster
$C_{n_{\delta_j}}$	Yawing-moment coefficient produced by firing the side thrusters, per thruster
$C_{Y_{\delta_j}}$	Side-force coefficient produced by firing the side thrusters, per thruster
$C_{\ell_{\delta_a}}$	Rolling-moment coefficient produced by aileron deflection, per deg.

---

*Paper not presented at conference.

ORIGINAL PAGE IS
OF POOR QUALITY

DFI	Development Flight Instrumentation
IMU	Intertial Measuring Unit
LAIRS	Langley Atmospheric Information Retrieval System
$\dot{m}_j/\dot{m}_\infty$	Mass flow ratio
MMLE-3	Modified Maximum Likelihood Estimation Program, Version 3
PTI	Programmed Test Input
RGA,AA	Rate Gyro Assembly, Accelerometer Assembly

Wind-Tunnel Data Base

The wind-tunnel tests to obtain the RCS performance and interference effects were conducted on several models at Mach numbers ranging from 2.5 to 10. The test models utilized nonmetric nozzles (thrust was isolated from the model balances) scaled to match jet exit momentum ratio as the primary parameter. Since the tests were limited to Mach 10, data corresponding to higher altitudes and Mach numbers were obtained by varying momentum ratio and mass-flow ratio to include those values applicable to the higher altitudes. Cold gas (nitrogen or air) was used to represent the rocket exhaust. The effects of the low molecular weight and high temperature of the exhaust were studied and are accounted for by including them in the variations (wind-tunnel-to-flight extrapolation uncertainties indicated in Fig. 1) in the predicted data base.

Rausch[2] in his analysis of the data found that the interactions resulting from the RCS side-firing thrusters correlated best with the mass-flow ratio parameter, $\dot{m}_j/\dot{m}_\infty$. The rolling-moment interactions from the side-firing thrusters as predicted from the wind-tunnel data[3] are shown as a function of this parameter in Fig. 1. The predicted curve, obtained from Ref. 3, represents a least-squares fit of all the wind-tunnel data without regard to the number of thrusters firing.

Vehicle Description

The Shuttle Orbiter, along with its entry aerodynamic controls and reaction control system (RCS), is shown in Fig. 2. The aerodynamic control system consists of split elevon surfaces (two moving in unison on each wing), a body flap, and a split rudder which also acts as a speed brake. The elevons and body flap become active at an entry dynamic pressure of 0.51 psf. The body flap is used for pitch trim.

The entry reaction control system is located on the aft section of the OMS pods (Fig. 3). This system consists of 12 vertical-firing thrusters (six up-firing and six down-firing) and eight side-firing thrusters (four per side). The vertical-firing thrusters are used only when the dynamic pressure is less than 10 psf and are used symmetrically with the elevon for pitch control and differentially for roll control. The side thrusters are used for yaw control from orbit down to Mach 1.0.

Entry Data System

The Shuttle Orbiter flight data were obtained from several sources. The primary source for body rates and accelerations was the aerodynamic coefficient identification package (ACIP). This package was designed to provide high quality rate and acceleration data at high sample rates for use in estimating the stability and control derivatives including the RCS effectiveness. Two other systems were also used to obtain stability and control derivatives, the inertial measuring unit, IMU, and the rate gyro and accelerometer assemblies, RGA and AA. The IMU data are highly accurate; however, the sample rate is very low (1 Hertz). Stability and control derivatives utilizing this source were obtained for STS-1, 2, and 3.[1] The RGA-AA data are not as accurate as the IMU or ACIP data and do not contain axial acceleration measurements, but the sample rate is of the order of 25 Hertz. Since the ACIP data for STS-2 were lost, the RGA-AA data were utilized along with interpolated axial acceleration data from the IMU to estimate the stability and control derivatives for that flight. The RCS control derivatives presented herein for flights 2 and 3 were determined from IMU and RGA-AA measurements. The STS-1 RCS derivatives were obtained from both ACIP and IMU data; however, only the IMU data are presented in this paper. The vehicle operational instrumentation (OI) system provided measurements of all the control positions and the RCS thruster chamber pressures. The summations of the chamber pressures divided by the nominal chamber pressure produced the nominal number of thrusters firing at any one instant. Surface pressure measurements were obtained from the development flight instrumentation (DFI) system as recorded during the STS-3 entry.

The flight conditions were obtained from the Langley best estimated trajectory (BET) described by Compton et al.[4] The BET utilized the onboard IMU measurements of attitudes, accelerations, and rates and the atmospheric properties generated by the Langley Atmospheric Information Retrieval program (LAIRS),[5] which processed meteorological data from National Oceanic and Atmospheric Administration radiosonde and sounding rocket measurements. Air data parameters were also obtained from the onboard air data system at the lower Mach numbers.

Method of Approach

Onboard Inertial Measurements

The measured accelerations and angular rates were used to extract the reaction control system derivatives. Utilization of the vehicle rates and accelerations to extract aerodynamic stability and control derivatives is dependent upon maneuvers in which precisely defined control inputs produce responses having adequate rates and amplitudes. No such maneuvers were performed during the STS-1 entry; however, the navigation bank maneuvers were utilized to extract derivatives. Specific maneuvers were performed during the STS-2 and -3 entries and they are tabulated in Tables 1 and 2.

The previously described rate, acceleration, control position, and trajectory data were time-correlated and combined into data files at a consistent frequency for each entry flight. These input files were used in a maximum likelihood estimation technique (MMLE-3) developed by Maine and Iliff[8] at the NASA Dryden Flight Research Center to determine the stability and control and RCS derivatives from the aforementioned maneuvers. The RCS parameters are treated herein in two ways, first as a linear control with the control deflection a function of the number of thrusters firing, that is $\delta_j = 1$ to 4 in the case of the side thrusters. The coefficients determined in this way are therefore on a per-thruster basis and are presented herein as a function of Mach number. Secondly, the rolling-moment coefficients are converted to dimensional data which are subtracted from the actual thrust moments to determine the magnitudes of the roll interactions. These interaction values are then presented as a function of mass-flow ratio for comparison with the interactions derived from the pressure data.

DFI Pressure Measurements

The DFI surface pressures measured during the STS-3 entry have been used directly to estimate the rolling-moment interactions induced by the firing of the yaw thrusters. The location of the pressure orifices are shown in Figs. 4 and 5. As can be noted from these figures, the number of orifices is quite small and considerable judgment was exercised as to how the pressure data would be treated. Additionally, the pressure orifices in the surfaces were covered by the thermal protection system insulation with holes drilled through to match the surface pressure taps. There was no way to determine how well these holes matched, or whether leakage under the insulation occurred during flight.

The first step in the process was to determine the extent of correlation between the side-thruster firings and the response of the pressure instrumentation. Examples of the correlation between the RCS and the surface pressures are given in Figs. 6 and 7, which show the number of yaw thrusters firing matched with the responses from representative pressure transducers located on the wing and on the fuselage and vertical tail, respectively. As can be seen from these figures, the pressure transducers responded to almost every instance in which the RCS thrusters fired. In instances where there was little or no response, the duration of the RCS firings was small. The minimum duration of an RCS pulse is 80 milliseconds for the range of Mach numbers shown on the figures, whereas the sampling rate of the surface pressures was 1 Hertz. Therefore, it is higly probable that many of the RCS firings were not recorded for all the pressure orifices at any given time. For most of the periods selected for analysis, all of the pressure transducers are believed to have responded; however, in some cases, a few of the responses were possibly not detected because of the low sample rate.

It is interesting to note (as Fig. 7 shows) that pressure transducers on the fuselage ahead of the center of gravity responded to the yaw-thruster firings. Some responses were noted as far as 22 percent of the body length ahead of the center of gravity; however, they were sporadic with small values. These were not included in the analysis. The responses of the transducers on the vertical tail were also sporadic, and sometimes indicated a negative increment in pressure. These results were also too limited for an analysis; however, all of these results, the responses from the wing, body, and tail transducers, indicate a significant interaction between the thruster plumes and the flowfield over the upper side of the vehicle. Although most of the transducers were saturated at the lower Mach numbers and could not be used in the analysis reported herein, some of them responded to the yaw-thruster firings all the way down to Mach 2.6. This indicated that the plume flowfield interactions were fairly significant down to near transonic speeds.

During this investigation, a total of 25 RCS firing periods were examined at Mach numbers ranging from 27 down to approximately 8, where about half of the transducer pressure ranges were exceeded (the gages became saturated). There were eight instances where four thrusters were firing, and the remainder consisted of periods where only two thrusters were firing.

The pressure data were converted to rolling moments by first determining the increment in pressure resulting from a side thruster firing. The increments in pressure, Δp, are represented by the differences between the peaks and the lower levels of pressure as shown on Fig. 6. These values of Δp were plotted chordwise at five spanwise stations on the wing as represented in Figs. 8, 9, 10, and 11. These figures show the chordwise distribution of Δp for several Mach numbers and for 2, 3, and 4 side thruster firings. It must be noted that the chordwise distribution shown at the wing root was derived by assuming that the pressures at the wing root were the same as those along the fuselage side at the orifice locations shown in Fig. 5. This does not represent the Δp values at the wing root exactly, but it was considered to be more representative than assuming the pressures at the wing root to be unaffected by the firing of the thrusters. Additionally, since the number of orifices was quite small, the manner in which these chordwise distribution curves are faired becomes extremely important in determining the final results.

For most of the chordwise distributions, the pressure increments did not vary greatly, and a straight line point-to-point fairing tended to suffice. There were some very high values of Δp (see Fig. 8) where straight line fairings would produce loadings considered to be unreasonable. In order to produce a consistent set of results, the curves were faired by assuming that each pressure measurement along the chord affected a length from the orifice to the halfway point to the next orifice. In this way, the peak pressures did not overly influence the loading along the total chord length. This method of fairing was consistently used for all data; however, for certain cases, alternate fairings were used and they will be discussed subsequently.

Note that on Figs. 9, 10, and 11 the letter "s" is located above the Δp for some of the orifices. This indicates that the local pressure exceeded the range of the gage. The curves for these cases were faired to the limit of the saturated gages which produced final results somewhat lower than the real case. An alternative method of fairing was used in which peak values of Δp (where they existed) were allowed to influence the entire chord by fairing in a straight line from the peak to the end of the chord. Thus, in the range where pressures began to exceed the capabilities of the gages (around Mach 17), two sets of results were obtained and are presented herein.

Once the chordwise pressure distribution curves were faired, they were integrated to obtain a chordwise loading that was multiplied by its moment arm from the center of gravity. These moments were then combined to form a spanwise moment diagram as shown in Fig. 12. The area under this curve represents the total interaction rolling moment produced by the firing of four yaw thrusters.

Discussion of Results

Inertial Data

The RCS derivatives $C_{Y_{\delta_j}}$, $C_{\ell_{\delta_j}}$, and $C_{n_{\delta_j}}$ as obtained from the measured rates and accelerations utilizing the maximum likelihood parameter estimation technique (MMLE-3) are presented in Fig. 13. The data sources, IMU and RGA-AA, are identified by different symbols in the figure. The data points are compared to the solid lines on the figure which represent predicted coefficients based upon the full thrust of the rockets corrected for altitude effects.

The side-force RCS derivatives tended to agree with the coefficients based on the thrust. The IMU values are somewhat low, and some nonagreement might be expected since this derivative depends upon side acceleration and the sample rates for the IMU data are of the order of one Hertz. The RGA-AA data generally exhibit values slightly more negative than the 100-percent thrust line, and this trend might also be expected, since the pressures on the fuselage side indicated some augmentation. For example, the augmentation in $C_{Y_{\delta_j}}$ was estimated to be about -.000056 at Mach 18.

The yawing moment RCS derivative, $C_{n_{\delta_j}}$, shows very good agreement with the full-thrust values shown as the solid line on Fig. 13. The data were fairly consistent and exhibited very little scatter throughout the Mach number range.

The variation of the RCS rolling-moment derivative $C_{\ell_{\delta_j}}$ with Mach number as shown in the middle of Fig. 13 was fairly consistent; however, considerable scatter of the data is evident at the lower Mach numbers. Generally, the RCS rolling-moment derivative becomes more difficult to extract at the lower Mach numbers by parameter estimation techniques because the ailerons move in conjunction with the firing of the side thrusters and they become relatively more powerful as Mach number decreases, that is, as dynamic pressure increases. Figure 14 shows that the ratio of aileron to side thruster effectiveness in roll increases by a factor of 4 from Mach 25 to Mach 8. By comparison then, the RCS signal becomes much more difficult to identify at the lower Mach numbers and altitudes, especially since the aileron signal is, for the most part, simultaneous with the RCS.

This type of problem was also encountered during the wind-tunnel tests to determine the pre-flight values of the interactions. At the lower values of mass-flow ratio, the simulated thrust magnitudes were below the quoted accuracy ranges of the balances used to measure the forces and moments. Reference 7 indicates that at low thrust coefficients corresponding to high dynamic pressures and lower altitudes, the errors in rolling-moment interaction values could range from 25 to 75 percent of the actual thrust-induced moments. Above Mach 6 (Fig. 13), where the results are more consistent, the difference between the solid line representing full thrust and the flight data points representing the flow-field interaction effects resulting from the firing of the side thrusters is shown. As can be seen from this figure, the rolling-moment interaction is quite large. The pre-flight predictions of the rolling-moment interactions were also large, and in order to compare them directly, the differences between the full-thrust curve and the flight data points were obtained and are presented along with the pre-flight estimate in Fig. 15. In this figure, the interaction coefficients (the differences) were converted to moments using the reference area and span and the appropriate dynamic pressures, and the moments were multiplied by four to represent the effects of four thrusters firing. The data are shown as functions of mass flow ratio and represent a Mach number range from about 3 to 26. As can be seen from this figure, a definite trend toward decreasing magnitudes of rolling-moment interactions is apparent between mass-flow ratios of 0.0012 and 0.01. Below this value, although the data are somewhat more scattered, the preponderance of points tends to indicate a trend toward larger interactions than the predicted values. An average fairing of these data would be represented by the heavy line drawn through the points. The resulting curve indicates interaction rolling-moments that are less than predicted for mass-flow ratios of 0.01 to 0.004, and are greater than predicted from $m_j/m_\infty = 0.004$ to the end of the faired curve at $m_j/m_\infty = 0.00015$.

Pressure Data

The rolling-moment interactions caused by the firing of four side thrusters as derived from

ORIGINAL PAGE IS
OF POOR QUALITY

integration of the wing upper surface pressure increments are presented in Fig. 16. The open symbols represent the effects of four thrusters derived by fairing the chordwise Δp curves to the value of the upper limit of the gages where saturation of the gages occurred. This occurred for values of m_j/m_∞ less than 0.004. The lower set of points (solid symbols) were obtained by letting the peak pressure increments influence the chordwise fairing of the curves for the full length of the chord as mentioned in a previous section. The two sets of points represent the spread between a minimum estimate and a maximum estimate of the rolling-moment interactions resulting from the firing of four side thrusters as obtained from the available data. The lower curve is probably the most reasonable representation of the trend in the interactions with varying values of the mass flow parameter, and is the one to compare with the curve obtained from the inertial data which is also presented in Fig. 16. For completeness, the preflight predicted variation of the rolling-moment interactions with mass-flow ratio along with the upper and lower uncertainties are also presented. Between mass flow ratios of about 0.003 to 0.01 the inertial data and the pressure data results compare fairly closely, and both curves indicate a trend toward lower values of interaction rolling moments than were predicted. Below m_j/m_∞ of 0.003, the interactions estimated from the inertial data are larger than the preflight estimates, although they are within the estimated uncertainties. The interactions derived from the pressure data, however, tend to follow the predicted curve. The trends shown by both sets of data in this range must be considered qualitative at best, since on the one hand the inertial results are quite scattered (see Fig. 15) and the pressure results are affected by the saturation of the gages and depend upon engineering judgment for consistent, but not absolute values. The trends in interactions for $m_j/m_\infty \geq 0.003$, can be considered to be fairly reliable, since both sets of data show essentially the same result.

The pressure data points representing the effect of two side thrusters firing (Fig. 17) do not show the degree of consistency as do those representing four thrusters. One mitigating factor may be that, generally, the duration of the firing pulses of two thrusters in many cases were shorter than those for four thrusters. This coupled with the low sample rate of this pressure data could have resulted in missing the peak pressure. This may have also been the reason for fewer cases in which some of the gages were saturated. As can be seen on Fig. 17, only four points (represented by the solid symbols) were adjusted to compensate for saturated gages. The curve representing the inertial results was obtained by dividing the values on the corresponding curve of Fig. 15 (representing the effects of four thrusters) by two to represent the effects of two thrusters. The assumption of a linear variation in rolling-moment interaction with the number of thrusters firing is not necessarily a valid one, but it is used here because it was originally extracted in that manner by the MMLE-3 parameter identification technique. The pressure data, although scattered, tend to confirm that the rolling-moment interactions resulting from side-thruster firing are dependent upon the number of thrusters firing, since the maximum absolute values of the points represent interactions considerably smaller than those resulting from four thrusters (Fig. 16). A comparison of the outer bound of the data points representing the effects of two thrusters (almost coincident with the curve for the inertial results) on Fig. 17 with the lower pressure curve of Fig. 16 also indicates that the effect of the number of thrusters firing, although evident, are not necessarily linear.

Concluding Remarks

An analysis of the rolling-moment interactions produced by the orbiter side-firing thrusters during entry was conducted utilizing data extracted from onboard inertial measurements and from integration of the left wing upper-surface pressures. In general, although the available pressure measurements were few in number, a reasonably good estimate of the rolling-moment interactions was obtained at mass-flow ratios corresponding to the higher altitudes and Mach numbers. The interactions compared favorably with those obtained from the inertial data in this altitude range, and both estimates indicate smaller magnitudes of the rolling-moment interactions than were predicted. At the lower altitudes, the pressure began to exceed the gage limits, and the results for four thrusters firing, although consistent and indicative of expected trends, must be considered qualitative in nature. A comparison of the effects of four thrusters with those of two thrusters shows that the rolling-moment interactions are dependent upon the number of thrusters firing. Finally, it is evident that with the proper distribution and range of instrumentation, the interactions caused by the firing of the RCS thrusters can be accurately determined in flight.

References

[1] Compton, H. R., Scallion, W. I., Suit, W. T., and Schiess, J. R., "Shuttle Entry Performance and Stability and Control Derivatives Extraction from Flight Measurement Data." AIAA Paper 82-1317, 1982.

[2] Rausch, J. R., "Space Shuttle Rear Mounted Reaction Control System Jet Interaction Study." General Dynamics Report No. CASD-NSC-77-003, 1977.

[3] "Aerodynamic Design Substantiation Report, Vol. I: Orbiter Vehicle," Space Division, Rockwell International Report No. SD-74-SH-0206-IL, Revision L-3, 1982.

[4] Compton, Harold R., Findlay, John T., Kelly, George M., and Heck, Michael L., "Shuttle (STS-1) Entry Trajectory Reconstruction." AIAA Paper 81-2459, 1981.

ORIGINAL PAGE IS OF POOR QUALITY

[5] Price, Joseph M., and Blanchard, Robert C., "Determination of Atmospheric Properties for STS-1 Aerothermodynamics Investigations." AIAA Paper 81-2430, 1981.

[6] Maine, Richard E., and Iliff, Kenneth W., "Users Manual for MMLE-3, A General FORTRAN Program for Maximum Likelihood Parameter Estimation." NASA TP-1563, 1980.

[7] Rausch, J. R., and Roberts, B. B., "Reaction Control System Plume Flow Field Interaction Effects on the Space Shuttle Orbiter." AIAA Paper 74-1104, 1974.

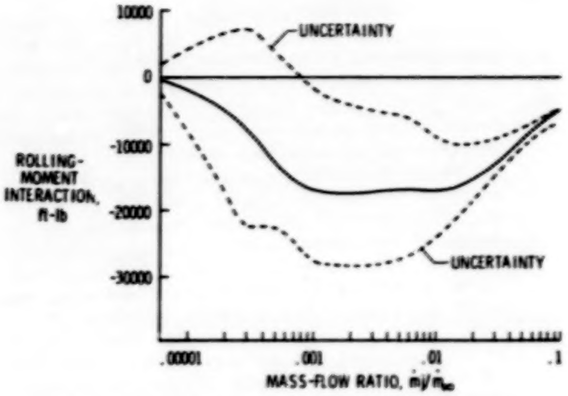

Fig. 1 Predicted rolling-moment interactions from side-firing RCS.

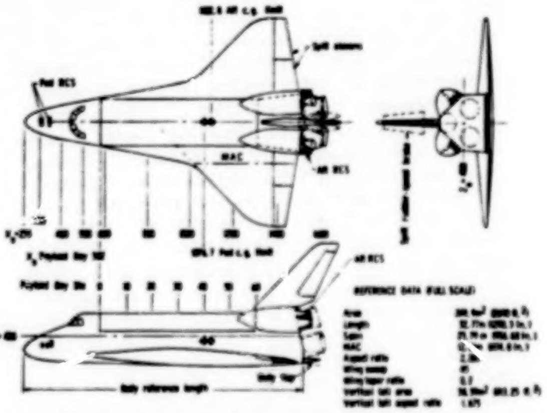
Fwd RCS
MAC
Aft RCS
REFERENCE DATA (FULL SCALE)

Fig. 2 The Space Shuttle Orbiter configuration.

Table 1 Schedule of STS-2 flight maneuvers

Event	Mach	Dynamic Pressure* (psf)	Altitude* (ft)
Roll Step	26.3	5.5	273431
Roll Step	26.2	9.1	263177
First Roll Maneuver	26.2	13.9	254612
Roll ASI	25.5	20.4	246628
PTI-1	24.6	26.5	239874
First Bank Reversal	19.7	46.9	218668
PTI-1	17.0	62.5	205246
PTI-1	12.0	105.1	174722
Second Bank Reversal	8.6	127.4	152414
PTI-1	7.4	131.5	144270
PTI-2	5.5	183.4	122053
Third Bank Reversal	4.7	206.7	111559
PTI-3	4.1	193.3	106502
PTI-4	3.1	199.8	92926

*From Langley BET

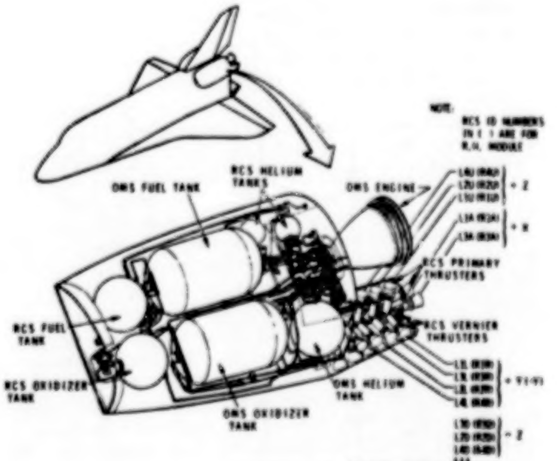
NOTE: RCS ID NUMBERS IN ( ) ARE FOR R.H. MODULE
RCS HELIUM TANKS
OMS FUEL TANK
OMS ENGINE
+Z
+X
RCS PRIMARY THRUSTERS
RCS VERNIER THRUSTERS
RCS FUEL TANK
RCS OXIDIZER TANK
OMS HELIUM TANK
OMS OXIDIZER TANK
-Z
THRUSTER LOCATION
PROPELLANT MANIFOLD NO.
THRUST REACTION

Fig. 3 The orbiter entry reaction control system.

Table 2 Schedule of STS-3 flight maneuvers

Event	Mach	Dynamic Pressure* (psf)	Altitude* (ft)
First Roll Maneuver	26.5	19.4	254150
PTI-1	25.2	22.9	244191
PTI-1	21.9	37.1	229207
PTI-1	17.9	62.2	210653
First Bank Reversal	16.6	75.7	204385
PTI-1	11.2	99.2	176077
Second Bank Reversal	8.2	122.9	156044
PTI-2	7.6	120.1	150414
Third Bank Reversal	4.3	210.2	112445
Fourth Bank Reversal	2.6	226.0	86182

*From Langley BET

ORIGINAL PAGE IS
OF POOR QUALITY

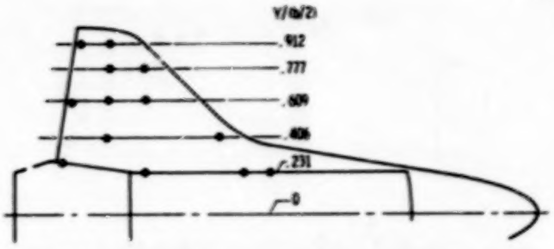

Fig. 4 Left wing upper surface pressure orifice locations.

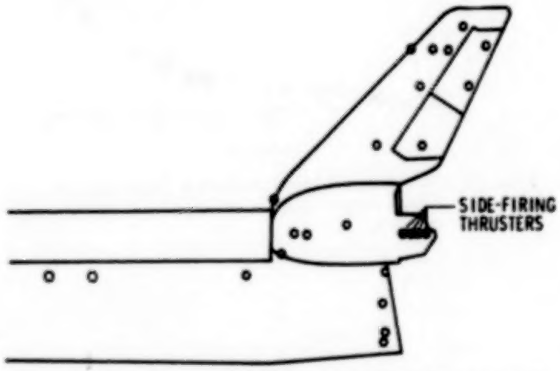

Fig. 5 Fuselage, OMS, and vertical tail pressure orifice locations.

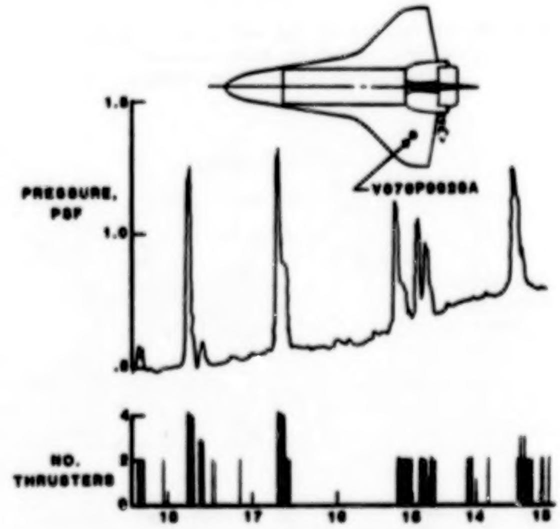

Fig. 6 Correlation of wing upper-surface pressure with RCS side-thruster firings.

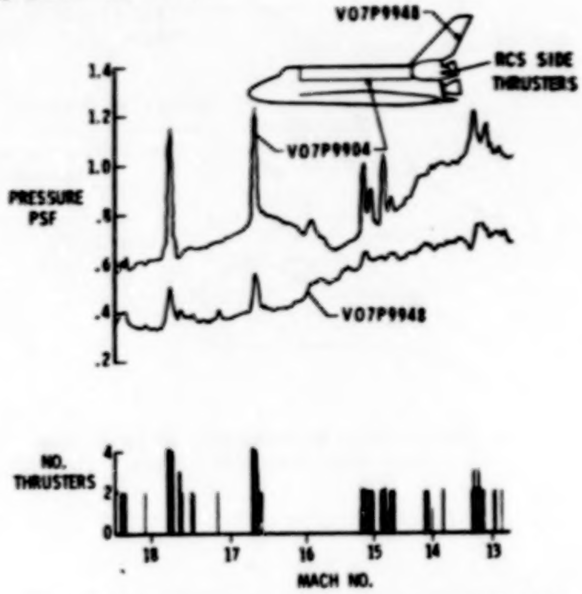

Fig. 7 Correlation of fuselage and vertical tail surface pressures with RCS side-thruster firings.

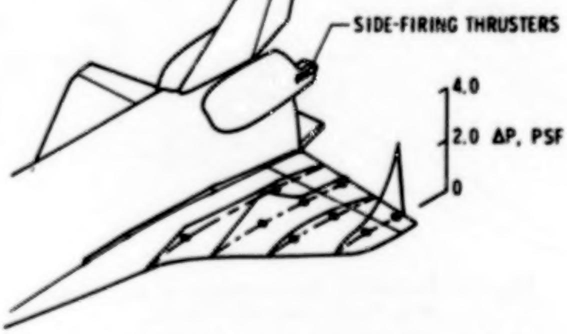

Fig. 8 Chordwise distributions of Δp at Mach 19.15, two thrusters firing.

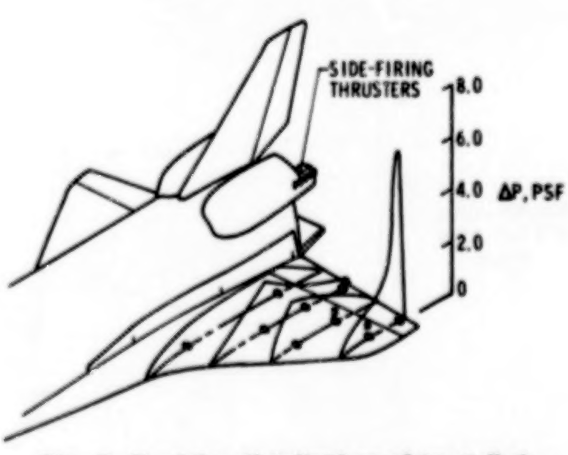

Fig. 9 Chordwise distributions of Δp at Mach 17.8, four thrusters firing.

ORIGINAL PAGE IS
OF POOR QUALITY

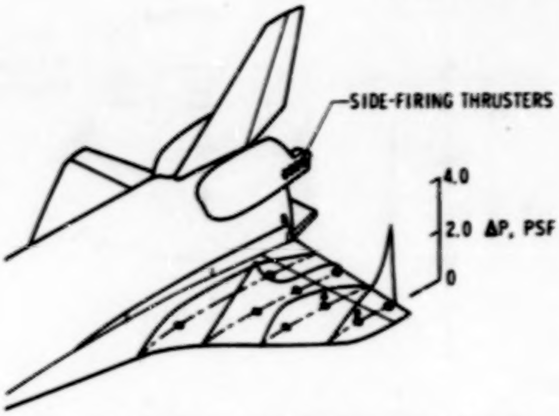
SIDE-FIRING THRUSTERS
4.0
2.0 ΔP, PSF
0

Fig. 10 Chordwise distributions of Δp at Mach 13.4, three thrusters firing.

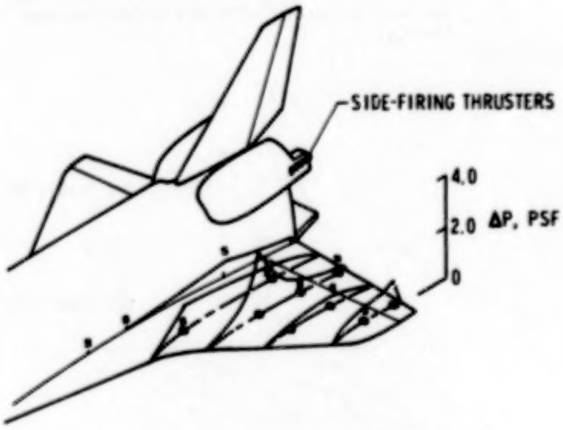
SIDE-FIRING THRUSTERS
4.0
2.0 ΔP, PSF
0

Fig. 11 Chordwise distributions of Δp at Mach 8.0, four thrusters firing.

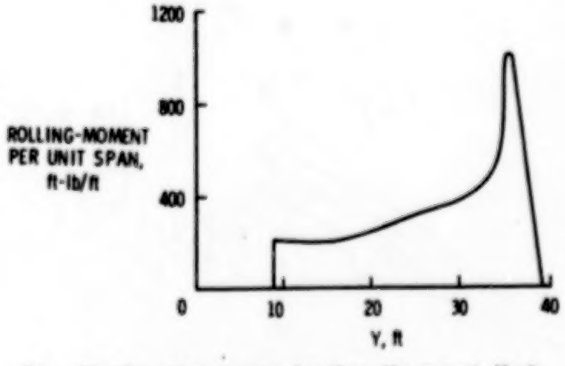

Fig. 12 Spanwise moment loading diagram at Mach 25, four thrusters firing.

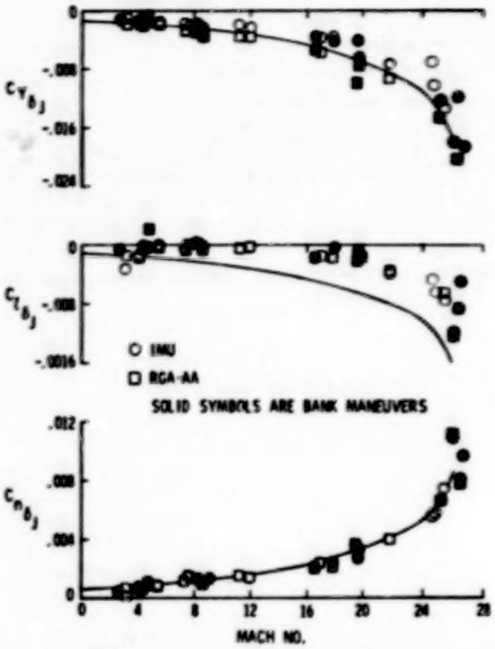

Fig. 13 RCS derivatives obtained from the on-board rates and accelerations utilizing MMLE-3.

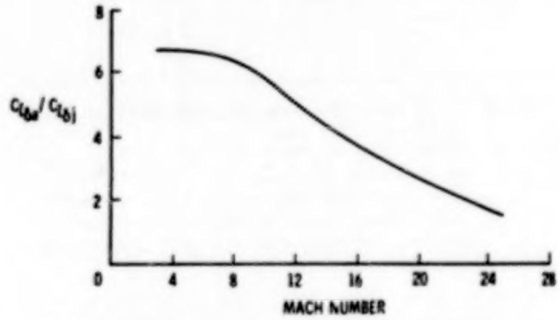

Fig. 14 Variations of the ratio of aileron effectiveness to side-thruster effectiveness with Mach number.

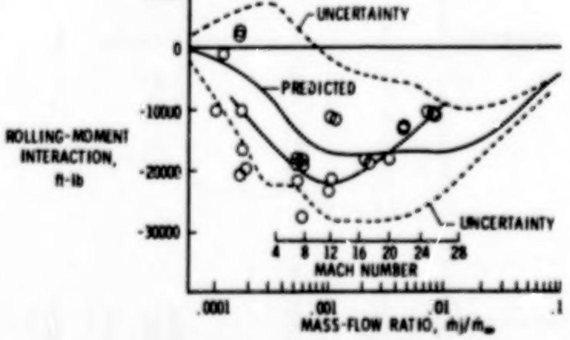

Fig. 15 Comparison of the rolling-moment interactions due to side thrusters firing as obtained from the on-board inertial measurements with the pre-flight predicted values.

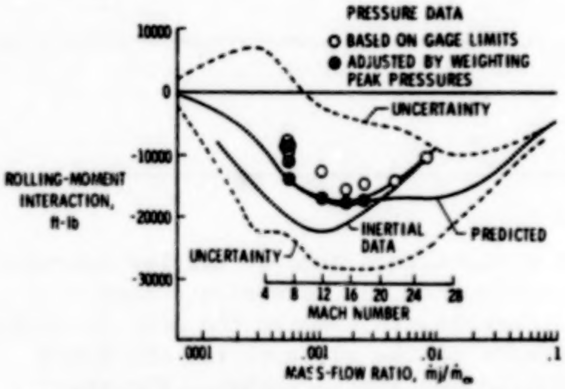

Fig. 16 Comparison of the rolling-moment interactions due to side thrusters firing as obtained from the pressure measurements with those from the inertial measurements, and with the pre-flight predicted values. Four thrusters firing.

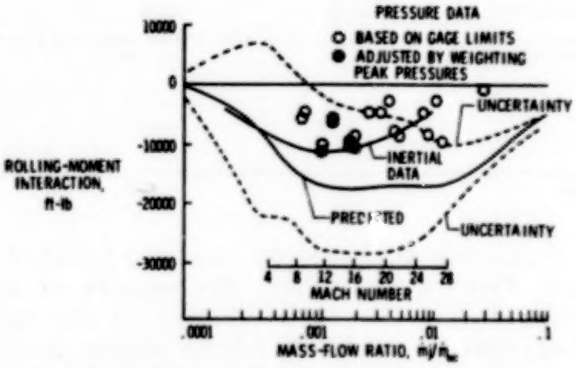

Fig. 17 Comparison of the rolling-moment interactions due to side-thrusters firing as obtained from the pressure measurements with those from the inertial measurements and with the pre-flight predicted values. Two thrusters firing.

☆U.S. GOVERNMENT PRINTING OFFICE: 1983-639-008/ 32

END

DATE

FILMED

DEC 3 1983